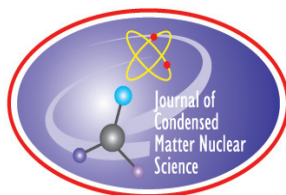


JOURNAL OF CONDENSED MATTER NUCLEAR SCIENCE

Experiments and Methods in Cold Fusion

**Proceedings of the ICCF 17 Conference,
August 12–17, 2012, Daejeon, Korea**

VOLUME 13, May 2014



JOURNAL OF CONDENSED MATTER NUCLEAR SCIENCE

Experiments and Methods in Cold Fusion

Editor-in-Chief

Jean-Paul Biberian
Marseille, France

Editorial Board

Peter Hagelstein
MIT, USA

Xing Zhong Li
Tsinghua University, China

Edmund Storms
KivaLabs, LLC, USA

George Miley
*Fusion Studies Laboratory,
University of Illinois, USA*

Michael McKubre
SRI International, USA

JOURNAL OF CONDENSED MATTER NUCLEAR SCIENCE

Volume 13, May 2014

© 2014 ISCMNS. All rights reserved. ISSN 2227-3123

This journal and the individual contributions contained in it are protected under copyright by ISCMNS and the following terms and conditions apply.

Electronic usage or storage of data

JCMNS is an open-access scientific journal and no special permissions or fees are required to download for personal non-commercial use or for teaching purposes in an educational institution.

All other uses including printing, copying, distribution require the written consent of ISCMNS.

Permission of the ISCMNS and payment of a fee are required for photocopying, including multiple or systematic copying, copying for advertising or promotional purposes, resale, and all forms of document delivery.

Permissions may be sought directly from ISCMNS, E-mail: CMNSEditor@iscmns.org. For further details you may also visit our web site: <http://www.iscmns.org/CMNS/>

Members of ISCMNS may reproduce the table of contents or prepare lists of articles for internal circulation within their institutions.

Orders, claims, author inquiries and journal inquiries

Please contact the Editor in Chief, CMNSEditor@iscmns.org or webmaster@iscmns.org



JOURNAL OF CONDENSED MATTER NUCLEAR SCIENCE

Volume 13

2014

CONTENTS

PREFACE

RESEARCH ARTICLES

- Cold Fusion – from the Laboratory to the World Setting the Stage for ICCF-17 1
S. Park and F. Gordon
- Detecting Energetic Charged Particle in D₂O and H₂O Electrolysis Using a Simple Arrangement of Cathode and CR-39 6
H. Aizawa, K. Mita, D. Mizukami, H. Uno and H. Yamada
- The Importance of the Removal of Helium from Nano-Pd Particles after Solid Fusion 13
X.F. Wang and Y. Arata
- Investigation of Radiation Effects in Loading Ni, Be and LaNi₅ by Hydrogen 19
Yu. N. Bazhutov, E.O. Belousova, A.G. Parkhomov, Yu.A. Sapozhnikov, V.P. Koretsky and A.D. Sablin-Yavorsky
- Erzion Model Interpretation of the Experiments with Hydrogen Loading of Various Metals 29
Yu. N. Bazhutov
- Possible Role of Oxides in the Fleischmann–Pons Effect 38
Jean-Paul Biberian, Iraj Parchamazad and Melvin H. Miles
- Cold Fusion 44
Jean-Paul Biberian
- Cu–Ni–Mn Alloy Wires, with Improved Sub-micrometric Surfaces 56
Francesco Celani, E.F. Marano, B. Ortenzi, S. Pella, S. Bartalucci, F. Micciulla, S. Bellucci, A. Spallone, A. Nuvoli, E. Purchi, M. Nakamura, E. Righi, G. Trenta, G.L. Zangari and A. Ovidi

LENR and Nuclear Structure Theory <i>N.D. Cook and V. Dallacasa</i>	68
Effect of Recrystallization on Heat Output and Surface Composition of Ti and Pd Cathodes <i>J. Dash, J. Solomon and M. Zhu</i>	80
Changes Observed in the Elemental Composition of Palladium and Rhenium Specimens Irradiated in Dense Deuterium by γ -Quanta with Boundary of Energy 23 MeV <i>A.Yu. Didyk and R. Wisniewski</i>	89
Measurement Artifacts in Gas-loading Experiments <i>O. Dmitriyeva, R. Cantwell and G. Moddel</i>	106
Anomalous Metals in Electrified Vacuum <i>E. Esko</i>	114
Patents and Cold Fusion <i>D.J. French</i>	118
Controlled Electron Capture and the Path toward Commercialization <i>Robert Godes, Robert George, Francis Tanzella and Michael McKubre</i>	127
Molecular D ₂ Near Vacancies in PdD and Related Problems <i>P.L. Hagelstein</i>	138
Basic Physics Model for PdH Thermodynamics <i>Peter Orondo and Peter L. Hagelstein</i>	149
Temperature Dependence of Excess Power in Two-laser Experiments <i>P.L. Hagelstein and D. Letts</i>	165
Models for Phonon–nuclear Interactions and Collimated X-ray Emission in the Karabut Experiment <i>P.L. Hagelstein and I.U. Chaudhary</i>	177
Isotope Effect for Heat Generation upon Pressurizing Nano-Pd/Silica Systems with Hy- drogen Isotope Gases <i>Tatsumi Hioki, Noriaki Sugimoto, Teppei Nishi, Akio Itoh and Tomoyoshi Motohiro</i>	223

Bose–Einstein Condensation and Inverted Rydberg States in Ultra-high Density Deuterium Clusters Related to Low Energy Nuclear Reactions <i>Heinrich Hora, George H. Miley and Xiaoling Yang</i>	234
Increase of Reaction Products in Deuterium Permeation-induced Transmutation <i>Y. Iwamura, T. Itoh and S. Tsuruga</i>	242
Neutron Burst Emissions from Uranium Deuteride and Deuterium-loaded Titanium <i>Songsheng Jiang, Xiaoming Xu, Liqun Zhu, Shaogang Gu, Xichao Ruan, Ming He, Bujia Qi and Xing Zhong Li</i>	253
Conventional Nuclear Theory of Low-energy Nuclear Reactions in Metals: Alternative Approach to Clean Fusion Energy Generation <i>Yeong E. Kim</i>	264
Recent Progress in Gas-phase Hydrogen Isotope Absorption/Adsorption Experiments <i>A. Kitamura, Y. Miyoshi, H. Sakoh, A. Taniike, Y. Furuyama, A. Takahashi, R. Seto, Y. Fujita, T. Murota and T. Tahara</i>	277
Potential Economic Impact of LENR Technology in Energy Markets <i>A. Kleehaus and C. Elsner</i>	290
A Change of Tritium Content in D ₂ O Solutions during Pd/D Co-deposition <i>Kew-Ho Lee, Hanna Jang and Seong-Joong Kim</i>	294
“Excess Heat” in Ni–H Systems and Selective Resonant Tunneling <i>Xing Z. Li, Zhan M. Dong and Chang L. Liang</i>	299
Nuclear Transmutation on a Thin Pd Film in a Gas-loading D/Pd System <i>Bin Liu, Zhan M. Dong, Chang L. Liang and Xing Z. Li</i>	311
Diamond-based Radiation Sensor for LENR Experiments. Part 1: Sensor Development and Characterization <i>Eric Lukosi, Mark Prelas, Joongmoo Shim, Haruetai Kasiwattanawut, Charles Weaver, Cherian Joseph Mathai and Shubhra Gangopadhyay</i>	319
Diamond-based Radiation Sensor for LENR Experiments. Part 2: Experimental Analysis of Deuterium-loaded Palladium <i>Eric Lukosi, Mark Prelas, Joongmoo Shim, Haruetai Kasiwattanawut, Charles Weaver, Cherian Joseph Mathai and Shubhra Gangopadhyay and Kyle Preece</i>	329
Calorimetric Studies of the Destructive Stimulation of Palladium and Nickel Fine Wires <i>Michael McKubre, Jianer Bao and Francis Tanzella and Peter Hagelstein</i>	337

Femto-atoms and Transmutation <i>A. Meulenberg</i>	346
Deep-Orbit-Electron Radiation Emission in Decay from $^4\text{H}^{*#}$ to ^4He <i>A. Meulenberg and K.P. Sinha</i>	357
Deep-electron Orbits in Cold Fusion <i>A. Meulenberg and K.P. Sinha</i>	368
New Visions of Physics through the Microscope of Cold Fusion <i>A. Meulenberg and K.P. Sinha</i>	378
Conventional Nuclear Theory of Low-energy Nuclear Reactions in Examples of Isoperibolic Calorimetry in the Cold Fusion Controversy <i>Melvin H. Miles</i>	392
Co-deposition of Palladium and other Transition Metals in H_2O and D_2O Solutions <i>Melvin H. Miles</i>	401
Use of D/H Clusters in LENR and Recent Results from Gas-Loaded Nanoparticle-type Clusters <i>George H. Miley, Xiaoling Yang, Kyu-Jung Kim, Erik Ziehm, Tapan Patel, Bert Stunkard, Anaïs Ousouf and Heinrich Hora</i>	411
Method of Controlling a Chemically Induced Nuclear Reaction in Metal Nanoparticles <i>Tadahiko Mizuno</i>	422
It is Not Low Energy – But it is Nuclear <i>Pamela A. Mosier-Boss</i>	432
Evidence from LENR Experiments for Bursts of Heat, Sound, EM Radiation and Particles and for Micro-explosions <i>David J. Nagel and Mahadeva Srinivasan</i>	443
Neutron Emission from Cryogenically Cooled Metals Under Thermal Shock <i>Mark A. Prelas and Eric Lukosi</i>	455
The Future May be Better than You Think <i>Jed Rothwell</i>	464
Hydrogen Isotope Absorption and Heat Release Characteristics of a Ni-based Sample <i>H. Sakoh, Y. Miyoshi, A. Taniike, Y. Furuyama, A. Kitamura, A. Takahashi, R. Seto and Y. Fujita, T. Murota and T. Tahara</i>	471

Statistical Analysis of Transmutation Data from Low-energy Nuclear Reaction Experiments and Comparison with a Model-based Prediction of Widom and Larsen <i>Felix Scholkmann and David J. Nagel</i>	485
Transmutations and Isotopic Shifts in LENR Experiments. An Overview <i>Mahadeva Srinivasan</i>	495
Sonofusion's Transient Condensate Clusters <i>Roger S. Stringham</i>	505
Demonstration of Energy Gain from a Preloaded ZrO ₂ -PdD Nanostructured CF/LANR Quantum Electronic Device at MIT <i>Mitchell R. Swartz and Peter L. Hagelstein</i>	516
Energy Gain From Preloaded ZrO ₂ -PdNi-D Nanostructured CF/LANR Quantum Electronic Components <i>Mitchell R. Swartz, Gayle Verner and Jeffrey Tolleson</i>	528
Forcing the Pd/ ¹ H- ¹ H ₂ O System into a Nuclear Active State <i>Stanislaw Szpak and Frank Gordon</i>	543
Nickel Transmutation and Excess Heat Model using Reversible Thermodynamics <i>Daniel S Szumski</i>	554
Physics of Cold Fusion by TSC Theory <i>Akito Takahashi</i>	565
Detection of Pr in Cs Ion-implanted Pd/CaO Multilayer Complexes with and without D ₂ Gas Permeation <i>Naoko Takahashi, Satoru Kosaka, Tatsumi Hioki and Tomoyoshi Motohiro</i>	579
Excess Heat Triggered by Different Current in a D/Pd Gas-loading System <i>Jian Tian, Bingjun Shen, Lihong Jin, Xinle Zhao, Hongyu Wang and Xin Lu</i>	586
A Self-Consistent Iterative Calculation for the Two Species of Charged Bosons Related to the Nuclear Reactions in Solids <i>Ken-ichi Tsuchiya</i>	594
Features and Giant Acceleration of "Warm" Nuclear Fusion at Interaction of Moving Molecular Ions (D-...-D) ⁺ with the Surface of a Target <i>Vladimir I.Vysotskii, Alla A.Kornilova and Vladimir S.Chernysh</i>	603
Stimulated (B ¹¹ p) LENR and Emission of Nuclear Particles in Hydroborates in the Region of Phase Transfer Point <i>Vladimir I.Vysotskii, Alla A. Kornilova, Vladimir S. Chernysh, Nadezhda D. Gavrilova and Alexander M. Lotonov</i>	608

On Problems of Widom–Larsen Theory Applicability to Analysis and Explanation of Rossi Experiments <i>Vladimir I. Vysotskii</i>	615
Application of Correlated States of Interacting Particles in Nonstationary and Periodical Modulated LENR Systems <i>Vladimir I. Vysotskii, Mykhaylo V. Vysotskyy and Stanislav V. Adamenko</i>	624

Preface

The theme for ICCF-17, “Cold Fusion-From the Laboratory to the World” was selected to highlight the recent advances in experimental results suggesting that useful products based on “Cold Fusion” were possible. By using nano-particles of nickel that were loaded with hydrogen gas under pressure, several groups were reporting significant production of excess energy in the form of heat and some had even predicted prototype units would be available within a year. In addition, other groups reported success with specially prepared cathodes. By the time of ICCF-17, the question was not “if” but “when” will the dreams of abundant, low-cost green energy be available. While progress toward commercialization has been slower than predicted, the dreams triggered by the 1989 announcement by Martin Fleischmann and Stanley Pons will be real. In addition to outstanding presentations, posters, and discussions, Francesco Celani displayed an operational demonstration of his device throughout the conference.

By the numbers, there were 157 participants at ICCF-17 representing 19 countries. Seventy-eight papers were given including posters. An excellent overview of ICCF-17 written by David J. Nagel was published in *Infinite Energy* (Issue 106, November/December 2012). For many attendees, this was their first visit to South Korea and cultural exchange tours were provided to historical sites near Daejeon. For one attendee, Roger Stringham, this was his second visit. His first was in 1950 when he served in the U.S. Army and he fought to defend what is now South Korea.

Unfortunately Dr. Fleischmann died a few days before the start of the conference. It was fitting and appropriate that we dedicated ICCF-17 to the memory of Martin Fleischmann and one of the outcomes from the conference was the establishment of the “Martin Fleischmann Memorial Project.”

We want to thank all those who have participated to make ICCF-17 a great success. Financial supports from Daejeon International Marketing Enterprise, Korea Tourism Organization and New Energy Foundation Inc. and our personal friends made it possible for us to hold an outstanding conference. We would also like to express our thanks to the personnel of Genicom Company and Daejeon Convention Center for their outstanding service for the successful conference. Finally, we also want to express our appreciation to the *Journal of Condensed Matter Nuclear Science* and especially Prof. Jean-Paul Biberian, the senior editor for publishing the papers from ICCF-17, making them available to everyone.

*Sunwon Park and Frank Gordon
May 2014*



Research Article

Cold Fusion – from the Laboratory to the World Setting the Stage for ICCF-17

Sunwon Park*

Korea Advanced Institute of Science and Technology, Daejeon, Republic of Korea

Frank Gordon^{†, ‡}

U.S. Navy SPAWAR Systems Center, San Diego, CA, USA

Abstract

The objective of ICCF-17 is to allow international groups of scientists to present their data to further the collective understanding of scientists working in the field and so that skeptical members of the mainstream scientific community, the media, and the public will see the evidence that “Cold Fusion” is real. Indeed several groups are currently developing commercial products that produce energy using the “Cold Fusion” phenomena. Ultimately, the reality of cold fusion will be determined by the public acceptance of commercial devices. People and companies who continue to deny the existence of cold fusion will become irrelevant as the applications are placed into service.

© 2014 ISCMNS. All rights reserved. ISSN 2227-3123

Keywords: Cold Fusion, ICCF-17

1. Introduction

The announcement by Fleischmann and Pons on March 23, 1989 that their experiments that produced more excess energy than could be accounted for via chemical means launched a frenzy of efforts around the world to confirm and improve upon their claims. If the phenomenon which was named as “Cold Fusion” by the media could be successfully developed, it offered the potential to supply the world with abundant, low-cost, green, and safe nuclear energy without hazardous waste.

*E-mail: swpark@kaist.ac.kr

†E-mail: dr.frank.gordon@gmail.com

‡Retired

1.1. The early months

Within hours of the press conference announcement, several universities and laboratories around the world initiated programs to replicate the results. Examples include the Bhabha Atomic Research Centre (BARC) in India where within a few days of the March 23rd announcement, 12 teams comprising about 50 scientists were formed to look for the nuclear origin of Cold Fusion. Less than 1 month later on 21 April, neutrons were first detected. Within a year, all 12 teams had detected both neutrons and tritium. The results were reported at ICCF-1 in August, 1990 [1]. In the U.S., the Electric Power Research Institute redirected contracts that were in place at Texas A&M University for fuel cell research to focus on “Cold Fusion”. Within two months, their experiments showed excess heat, tritium, and neutrons [2]. In Frascati, Italy, titanium shavings were placed in high pressure deuterium gas and then cooled to 77 K. As the samples warmed, neutrons were detected at 200 times background [3]. Groups in Hungary, the USSR, Japan, Brazil also conducted experiments. Several of the groups were successful in obtaining confirming experimental data but others including groups at California Institute of Technology and the Massachusetts Institute of Technology claimed that their experiments had not produced any excess heat. In spite of the many successful results, cold fusion was discredited by several speakers at the annual American Physical Society meeting in Baltimore in May. Ironically, the Caltech and MIT results were later analyzed by other groups to show that they had in fact produced excess heat but by late 1989, most scientists, the media, and the public considered cold fusion dead and cold fusion subsequently gained a reputation as pathological science [4].

1.2. DOE Reviews

In November, 1989 the Energy Research Advisory Board set up by the U.S. Department of Energy issued their report. Although most people believe that the report disproved “Cold Fusion,” that is not the case. There were several recommendations and conclusions but they summarized their finding with the statement: *“Consequently, with the many contradictory existing claims it is not possible at this time to state categorically that all the claims for cold fusion have been convincingly either proved or disproved.”*

Even though the DOE report *“recommended against establishment of special programs to develop cold fusion,”* the Panel was *“sympathetic toward modest support for carefully focused and cooperative experiments within the present funding system.”* However, to date proposals submitted to DOE for funding have all been ignored, in many cases without even reviewing the proposal or replying to the submitter. Additionally, the DOE findings and the resulting public opinion have had a chilling effect on other potential sources of support for cold fusion research.

The second DOE review was conducted in 2004 with a report issued in December, 2004. Although several of the individual reviewers believed that the experimental evidence provided significant support for the “Cold Fusion” phenomenon, the majority conclusion was: *“While significant progress has been made in the sophistication of calorimeters since the review of this subject in 1989, the conclusions reached by the reviewers today are similar to those found in the 1989 review.”* The details of these reports are beyond the scope of this paper but the complete reports are available along with reviews and analysis of the DOE findings by several individuals at: <http://newenergytimes.com/v2/government/DOE/DOE.shtml> and http://lenr-canr.org/wordpress/?page_id=455

1.3. Impact of the U.S. DOE decisions

The decisions by the DOE not to fund cold fusion research and the incorrect belief that cold fusion was bad science impacted funding for cold fusion research throughout the world. Governments and companies did not fund cold fusion research for fear of being accused of wasting money. And, the US patent office does not issue patents for cold fusion related inventions which reduces access to venture capital funding.

2. Research has Continued

In spite of the DOE reports, public opinion, and lack of funding, many groups around the world continued their experimental efforts while others worked on new theories to explain the phenomena. Scientists who had observed experimental results that could not be explained using conventional theories continued their efforts in spite of very limited funding. They were driven by the desire to be the first to understand and exploit cold fusion for whatever benefits it could provide.

In an attempt to more accurately describe the underlying physics and reduce the stigma associated with the name “cold fusion,” that had been used by the media, several names have been proposed including the Fleischman–Pons effect, Low Energy Nuclear Reactions, Lattice Assisted Nuclear Reactions, and Chemically Assisted Nuclear Reactions. The experimental evidence clearly shows is that nuclear reactions are involved but one of the challenges in selecting the best name is that the actual underlying nuclear processes that are occurring are not known. Suggestions range from “conventional” fusion on a nano-scale, fusion triggered by an unknown tunneling reaction, to other theories that do not even involve fusion. At the press conference, Fleischmann offered the opinion that it was an unknown nuclear reaction. Although Low Energy Nuclear Reactions (LENR) has the widest acceptance within the community, because of the media, the phenomenon is still best known to the public as “cold fusion.”

In the 23 intervening years, the body of worldwide experimental evidence has grown to include increased repeatability, increased levels of excess heat, transmutations to new elements, and nuclear emissions including X-ray, gamma radiation, alphas, protons, and neutrons. These experimental results have been published in 3500 technical papers, conference proceedings and articles [5]. A complete breakdown is available at: <http://lenr-canr.org/acrobat/RothwellJtallyofcol.pdf> Individually and collectively, these results provide compelling evidence that nuclear reactions are involved and they substantiate many of the original claims by Fleischmann and Pons.

3. Current Status

Within the last two years, the pace of development has increased, stimulated by new claims that a cell using Nickel powder in a high temperature Hydrogen gas environment could reliably produce significant excess heat. Although the initial claims have not been independently verified, multiple groups are reporting similar results using similar cell designs. At least one of the groups hopes to have a commercial product available by the end of 2012. These new results have reinvigorated research and new groups of scientists are joining in the race searching for a new energy source.

4. ICCF-17 Objectives

ICCF-17 promises to be a very exciting conference. Most of the groups who are known to be working toward commercial products will attend the conference and make presentations. In most cases, this conference will be the first public presentation of their results and plans for the future. In addition, leaders in the development of theories to explain the phenomenon will present their theories in individual presentations and as participants in a panel discussion. More than 80 abstracts were received from scientists in 15 countries for presentation in both oral and poster sessions. The conference schedule was adjusted to maximize the number of presentations and provide time for interaction between scientists.

The first objective of ICCF-17 is to carry on the tradition of the previous ICCF conferences to allow international groups of scientists to present their data to further the collective understanding of scientists working in the field. The second objective is to end the misunderstanding and the skepticism on the cold fusion of the mainstream scientific community, the media, and the public by showing the evidence that “cold fusion” is real. And the final objective is to start an international concerted effort to expedite the commercialization of energy generation devices based on LENR

to solve the immediate energy and environmental problems of the world and to prevent the possibility of misusing the LENR for the destructive purposes.

5. History of Scientific Revolutions

History is full of examples where scientific revolutions face resistance from the mainstream scientists and media. Galileo was charged with heresy because he supported Copernicanism at the time when the mainstream belief was that the earth was the center of the universe. He was convicted in a Roman inquisition, forced to recant, and spent the rest of his life under house arrest [6]. As a post-doc at the Paris observatory, Ole Roemer used Cassini's own data to conclude that the speed of light was approximately 186,000 miles/s, challenging the mainstream belief that the speed of light was infinite. He was ridiculed by Cassini and others and ultimately left his pursuit of a scientific career [7]. The Wright brothers were unable to even get the media to witness their flying demonstrations and Scientific American published an article calling them "the lying brothers" [8]. Many Nobel prize winners were ridiculed when they initially announced their discoveries [9]. These and many additional examples share a common theme starting with initial ridicule leading to acceptance only after the "old guard" of the scientific establishment has been replaced. A quote attributed to Max Planck applies: *"A new scientific truth does not triumph by convincing its opponents and making them see the light but rather because its opponents eventually die, and a new generation grows up that is familiar with it."* This quote has been shortened to *"Science advances one funeral at a time"* [10].

Cold Fusion has overcome many of the same issues that previous revolutionary scientific breakthroughs have confronted and the potential payoff could rank cold fusion as one of the greatest discoveries of all time.

6. The Future

At this point, it is impossible to predict the future impact of the successful implementation of cold fusion. When the first transistor was developed, it was used to replace radio tubes. No one imagined the solid state electronics industry which grew out of that device. The original transistors were approximately 5–10 mm in diameter and cost a few dollars each. Today, more than 1 billion transistors can be contained within a single chip costing less than 0.000001 cents per transistor [11]. Solid state electronics devices have contributed to a significant improvement in the standard of living throughout the developed world.

Cold fusion could have an even greater impact by providing green low-cost energy for both developed and developing countries. Some obvious examples which will become technically and economically possible include small energy devices to provide heat and electricity to remote locations, large scale desalination which can transform deserts into farm lands and meadows, and economical transportation. Cold fusion will increase the sustainable development of human civilization on the planet earth.

Cold Fusion is a scientific revolution of unimaginable impact. While it will provide tremendous benefits, it will also disrupt large segments of the current world economy. Many countries rely on the sale of oil and many companies exist to refine and transport oil to the consumers. A significant percentage of the world's current workforce is directly involved in energy-related enterprise. Just as what happened after the invention of transistor, some companies will disappear while new industries will evolve to take advantage of changing economics of energy. New products that were not possible in a world with limited, high-cost energy will appear.

The change will not be easy but the benefit to the public of safe, low-cost, abundant, green energy will drive the revolution.

The future starts now.

References

- [1] M. Srinivasan, Presentation at ICCF 14, August, 2008. Additional detail available at: http://lenr-canr.org/?page_id=463
- [2] Joe Santucci, EPRI presentation to Northern States Power Company, 24 May, 1989
- [3] A. De Ninno, F. Scaramuzzi, C. Pontorieri and P. Zeppa, Emission of neutron bursts from a titanium–deuterium gas system in a high-efficiency low-background experimental setup, *AIP Conf. Proc.* 228, pp. 122–129; doi: <http://dx.doi.org/10.1063/1.40712>
- [4] M.H. Miles and P.L. Hagelstein, New Analysis of MIT calorimetric errors, *J. Condensed Matter Nucl. Sci.*, accepted.
- [5] J. Rothwell, Tally of cold fusion papers, 2009, LENR-CANR.org
- [6] M. Finocchio, Galileo on the world systems, 1997.
- [7] L. Bobis and J. Lequeux, Cassini, Romer and the Velocity of Light, *J. Astronomical History and Heritage* **11**(2) (2008) 97–105.
- [8] <http://amasci.com/weird/vindac.html#j29>
- [9] <http://amasci.com/weird/vindac.html>
- [10] F. Gaynor, Science Quotes by Max Planck *Scientific Autobiography and Other Papers*, trans. (1950),
- [11] <http://www.anandtech.com/show/2549>



Research Article

Detecting Energetic Charged Particle in D₂O and H₂O Electrolysis Using a Simple Arrangement of Cathode and CR-39

H. Aizawa, K. Mita, D. Mizukami, H. Uno and H. Yamada*

Department of Electrical Engineering and Computer Science, Iwate University, Japan

Abstract

Electrolysis of D₂O and H₂O solutions is carried out under several DC current patterns using a Ni film cathode. A CR-39 track detector is set in close contact with the cathode to detect an energetic charged particle. An impressive increasing in number of etch pit is occasionally observed.

© 2014 ISCMNS. All rights reserved. ISSN 2227-3123

Keywords: CR-39, Low-energy nuclear reaction, Light-water electrolysis, Ni-film cathode

1. Introduction

The plastic track detector has become a popular method to detect energetic charged particles in low-energy nuclear reaction (LENR) studies especially in electrolysis experiments. In these studies, the evidence of the reaction is in the form of nuclear damage trails made visible by etching of the plastic chips. Oriani et al. [1,2], Lipson et al. [3,4] and Roussetski [5] have performed light and heavy-water electrolysis using the plastic track detector and have reported the generation of charged particle emission during the electrolysis.

However, there still exist technical complexities in using plastic detector in electrolysis experiment. In the previous studies, there have been a thin layer of electrolyte and/or a solid film between the cathode electrode and the plastic detector. Such construction could cause a considerable decrease in the energy of the charged particle emitted from the cathode.

In this present study, a chip of the plastic track detector CR-39 is positioned just under the Ni film cathode to limit energy decrease; a CR-39 chip of 30×30 mm in size is set in close contact with the rear surface of the cathode film. This construction avoids chemical attack on the chip by ions generated by the electrochemical reactions on the Ni film cathode. The present technique is simple but capable of detecting energetic charged particles produced on the cathode during electrolysis with higher efficiency. Using the present technique, we have studied energetic charged particle emission from the metal film cathodes for light and heavy-water electrolysis [6–8]. The primary purpose of this study is to establish a simple technique producing new convincing evidence that a nuclear reaction as LENR could accompany

*E-mail: yamadahi@iwate-u.ac.jp

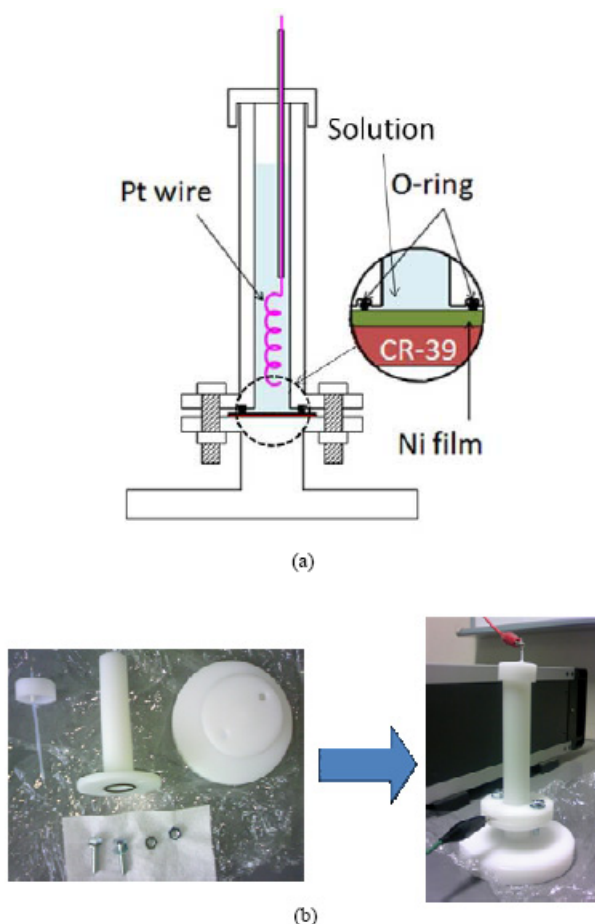


Figure 1. Test cell for the electrolysis, (a) vertical cross section, (b) the view of the component of the cell (*left*) and its assembled (*right*).

both heavy and light water electrolysis. Anomalous increase in number of etch pit has been observed in one out of seven and two out of five electrolysis conditions for D_2O and H_2O solutions, respectively.

2. Experimental

Electrolysis is carried out in a small plastic (polyoxymethylene) cell shown schematically in Fig. 1. It consists of a vertical plastic cylinder with 105 mm long and 10 mm inside diameter, a plastic stopper holding a wire anode, a lower portion of plastic base and a film cathode. The left-hand side and right-hand side of Fig. 1(b) display the components of the cell and the cell assembled, respectively. The top of cylindrical portion of the cell is covered by the plastic stopper with loose contact, which permits the escape of the gas produced by electrolysis. A $5\ \mu\text{m}$ thick Ni film is used as the metal cathode for both heavy and light-water electrolysis. The film forms the inner bottom of the test cell and serves as cathode; the diameter of the cathodes is 10 mm. The anode is $\phi\ 0.5\ \text{mm}$ Pt wire. The upper portion of it is sheathed by heat-shrinkable FEP tube surrounded with TFE and the lower part ($\sim 60\ \text{mm}$ long) is formed a crude spiral with the

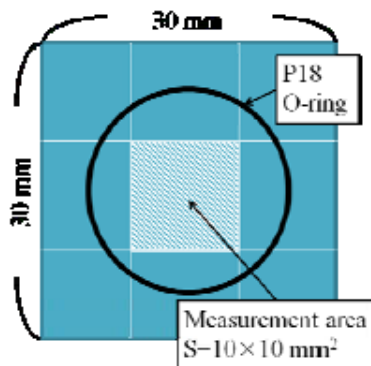


Figure 2. CR-39 chip.

diameter and length of ~ 5 mm and ~ 30 mm, respectively. The lower end of the spiral plane is parallel to the cathode surface with a gap distance of ~ 10 mm.

A 30×30 mm chip is cut from a sheet of the track detector CR-39, produced by Fukuvi Chemical Industry Co. The chip is carefully manipulated with tweezers. The center area of the front surface, which contacts to the metal film, is scratched to form a 10×10 mm square line, before removing the manufacture-supplied blue protective film. The CR-39 chip is mounted in the electrolysis cell immediately after removing the protective film. The scratched surface is referred to as the front surface upon which the metal film cathode is overlaid. The rear surface of the Ni film cathode area is set in close contact with the surface of the inside area bounded by the scratched 10×10 mm square line on the front surface of the CR-39 chip. Both the Ni film and the CR-39 chip are clamped together on the disc forming the bottom cap of the cell with an O-ring seal.

The arrangement of the cathode and the CR-39 chip is shown in the small circle of Fig. 1(a). This construction is able to avoid chemical attack on the CR-39 chip by ions generated in the electrolyte and keep the ideal distance between the cathode and the detector chip. Thus, the construction could minimize the energy loss of charged particle, which is produced on the surface of the thin Ni film and penetrates through it in the electrolysis process, and would maximize the efficiency of the detecting particle.

The electrolyte solutions for the heavy water electrolysis are $\text{Li}_2\text{SO}_4/\text{D}_2\text{O}$ and $\text{LiOH}/\text{D}_2\text{O}$. Those for the light water electrolysis are $\text{Li}_2\text{SO}_4/\text{H}_2\text{O}$, $\text{LiOH}/\text{H}_2\text{O}$ and $\text{Na}_2\text{SO}_4/\text{H}_2\text{O}$. The concentration of all the solutions is commonly 0.1-M. After the lower portion of the cell is assembled to form a small vessel, the ~ 6 ml electrolyte solution is poured into the cell. Then, the stopper cap holding the anode is put on the upper opening.

The electrolysis is conducted mainly for 168 h under DC current range 3–160 mA at voltage range 3–30 V. The current for the electrolysis is supplied by a constant-current power supply and no water is added during the electrolysis.

The CR-39 chip used for control experiments is always cut from the same sheet, neighboring to that for the corresponding electrolysis experiment and is carefully handled in exactly the same way as that used in the electrolysis experiment. In the control experiment, which is designated “Control” in the figures, the CR-39 chip is mounted in the same designed test cell as that for the electrolysis with an unused Ni film and a solution and is positioned in the near the ongoing electrolysis cell during the electrolysis. The exposure time of CR-39 for the control experiments in the absence of electrolysis is same length as that for the electrolysis experiment. After the electrolysis and control experiments, the cell assemblies are immediately disassembled to remove the CR-39 chips and the Ni films used.

The CR-39 chip is etched in 6 N NaOH solution for 7 h at 70°C immediately after each experiment. The measurement

Table 1. Electrolysis condition and result

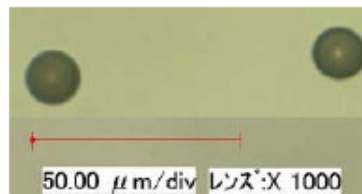
Solvent	Electrolyte	Current pattern	Total electrolysis period/run	Number of runs	Number of impressively positive runs
D ₂ O	Li ₂ SO ₄	20 mA	168 h	5	0
		20 mA/20 min-R	200 min	5	0
		20 mA/24 h-R	168 h	5	1
		3–160 mA	168 h	5	0
	LiOH	20 mA	168 h	5	0
		20 mA/24 h-R	168 h	5	0
H ₂ O	Li ₂ SO ₄	3–160 mA	168 h	3	2
		20 mA	168 h	5	0
	LiOH	3–160 mA	168 h	5	1
		20 mA/24 h-R	168 h	5	0
	Na ₂ SO ₄	3–160 mA	168 h	5	0
		3–160 mA	168 h	5	0

of etch pit is carried out using a digital microscope system (KEYENCE VHX-200), consisting of an optical microscope with a camera and a PC. The measurement area 10×10 mm is the center of the chip surface as shown in Fig. 2.

The electrolysis experiment is performed under total 12 electrolysis conditions for H₂O and D₂O solutions and all the electrolysis conditions are compiled into Table 1. There are 4 DC application patterns in the 12 electrolysis conditions. The patterns are designated “20 mA”, “20 mA/20 min-R”, “20 mA/24 h-R” and “3–160 mA”, as indicated in Table 1. The “20 mA” means that the application current is constant DC 20 mA for one week. The “20 mA/20 min-R” consisted of eight cycles; the application current is DC 20 mA with negative cathode for 20 min, followed by DC 20 mA with positive cathode for 5 min in each cycle. Thus, the total electrolysis time is 200 min. The “20 mA/24 h-R” consisted of seven cycles; the application current is DC 20 mA with negative cathode for 23 h and 55 min, followed by DC 20 mA with positive cathode for 5 min in each cycle. The total electrolysis time is 168 h. The “3–160 mA” means that DC is changed from 3 to 160 mA in stepwise every 24 h.

3. Result and Discussion

It may generally be necessary to distinguish nuclear pits produced during electrolysis from artifacts caused by manufacturing defects in the detector plastic. The appearance of the nuclear pits is thought to have much darker wide rim in the microscope. Because the pit has a relatively deeper bottom and the diameter of the bottom is rather small compared with that of the rim. However, there still exist many ambiguous pits whose origin, nuclear or artifactual, is hardly determined. Thus, the etch pits with narrow darker rim are not excluded in counting in this study; all the etch pits observed are counted. The pits are counted only within the inside area bounded by the scratched 10×10 mm square

**Figure 3.** Photomicrograph of a surface of the CR-39 chip, providing a pair of etch pits.

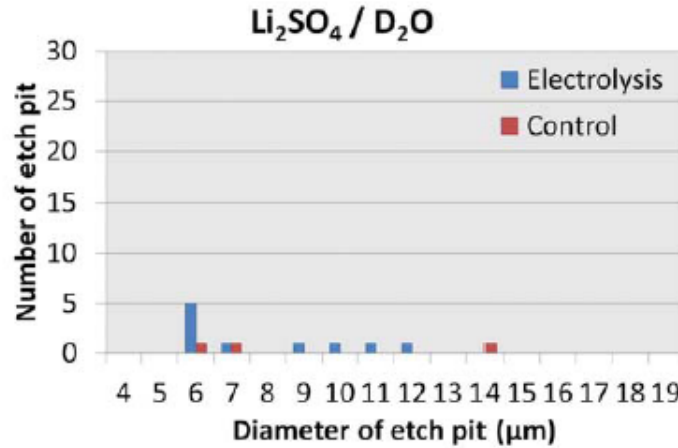


Figure 4. Distribution of etch pit diameter, indicating no difference in number of etch pit between electrolysis and control experiment.

line on the front surface of the CR-39 chip. The number of pit in the inside area is compared with that found in the control chip. Figure 3 shows the typical photomicrograph of pits, which are thought to have the nuclear origin.

The control experiment is expected to give some nuclear tracks already present in the CR-39 sheet as received from the supplier, as well as those produced during the entire experimental process by radioisotopes such as radon in the environment. Some of the pits originating from manufacturing defects will unavoidably have a similar form to that of nuclear pits. For instance, one of the lot of CR-39 sheets has provided higher density of etch pit in almost all the control CR-39 chips from the beginning [8].

The result for all the 12 electrolysis conditions is compiled into Table 1. Most of the experiments for 12 electrolysis

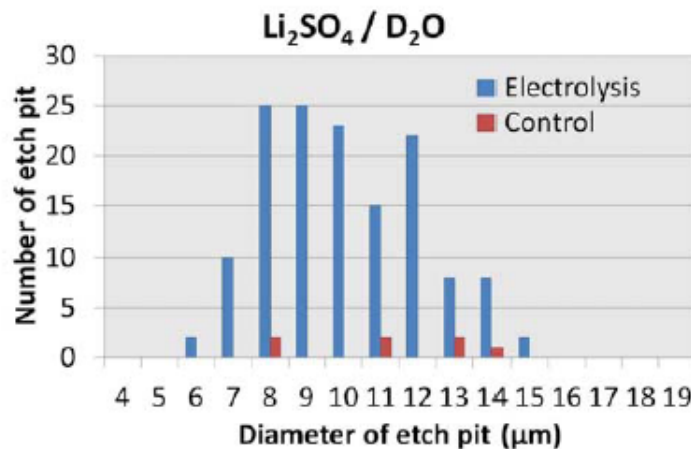


Figure 5. Distribution of etch pit diameter, indicating a marked difference in number of etch pit between electrolysis and control experiment.

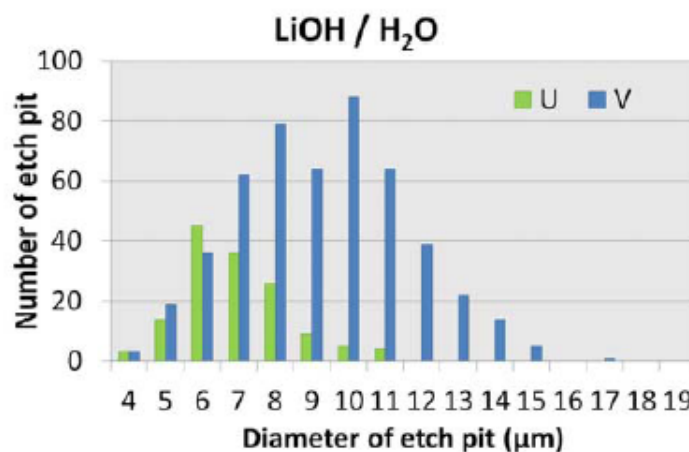


Figure 6. Distribution of etch pit diameter with a marked increase in number of etch pit for electrolysis experiment.

conditions using both solutions have revealed no apparent increase in number of etch pit as well as no apparent difference in the distribution of etch pit diameter between the electrolysis and control experiments. Figure 4 shows such typical relation between total number and the diameter of the etch pit for electrolysis and the corresponding control experiment. The electrolysis has been carried out under constant DC 20 mA application for 168 h with Li₂SO₄/D₂O solution, in this case.

Besides, there are several ambiguous runs hard to be excluded from positive result. Accordingly, we have focused our interest on only the impressive positive result in this study. The marked difference in number of etch pit and in the distribution of etch pit diameter between electrolysis and control experiment has been observed in one out of seven electrolysis conditions for D₂O solution.

The only significant difference is obtained from the current pattern “20 mA/24 h-R” by the Li₂SO₄/D₂O electrolysis, as shown in Table 1. Figure 5 provides the distribution as the relation between total number and the diameter of the etch pit for these electrolysis and control experiments. The number of etch pit for electrolysis quite different from that for control experiment is seen in the figure. There exists no peak in the distribution for the control experiment, similar to that in Fig. 4. While a semi-Gaussian distribution with large number of etch pit ranging 7–12 μm is seen for the electrolysis experiment. It should be pointed out, as mentioned above, that the difference of etch pit diameter between electrolysis and control experiment will not always appear in each run, even though the electrolysis is carried out under the same experimental condition.

The impressive difference in number of etch pit has been occasionally observed in two out of five electrolysis conditions for H₂O solution as well as D₂O solution. The marked increase in number of etch pit for electrolysis experiment has been obtained commonly using the current pattern “3–160 mA” for the H₂O solution, as shown in Table 1. Figure 6 shows one of these distributions for LiOH/H₂O electrolysis. Only two etch pits have been observed for the control experiment. Contrary, considerable large number of 638 has been observed on single CR-39 chip for electrolysis experiment. Thus, the data for control experiment is excluded from the figure; it presents rare but possible feature.

Even though the pits with shallow form having narrow darker rim in the microscope are usually not distinguished from those with deeper bottom having much darker wide in this study, the 638 pits are classified into two types. One with shallow form and the other with deeper bottom are designated “U” and “V” in Fig. 6, respectively. Similar semi-

Gaussian distribution to that seen in Fig. 5 with a large number of etch pit ranging 6–12 μm is also seen in Fig. 6. It is interesting to note that the distribution of “U” looks different from that of “V”. There exists a possibility that the two distributions correspond to two particles with different energies of the order of MeV.

It is demonstrated that the impressive increasing number of pit on the CR-39 chips could be attributed to a nuclear process occurring at the Ni film electrode in the operating electrolysis cell. The common key factors to increase number of the anomalous etch pit for both D_2O and H_2O solutions might be Ni film cathode, the long electrolysis time of 168 h and Li in the electrolyte solution. The diffusion constant of D/H in Ni is so small that the density of D/H in near surface of Ni film cathode could be saturated in short time. Consequently, the density of D/H in the uppermost surface region of Ni film might become large enough for the LENR to occur within the 168 h after beginning of electrolysis.

It has already been confirmed that the current flowing through the metal cathode, the solution temperature and mechanical stirring of solution have no effect on producing tracks at all [6].

4. Conclusion

A simple experimental technique using thin Ni film in conjunction with the track detector CR-39 is presented to detect energetic charged particles produced by a nuclear reaction in heavy and light water electrolysis. Anomalous increase in number of etch pit has been observed in one out of seven and two out of five electrolysis conditions for D_2O and H_2O solutions, respectively.

The result suggests a LENR occurring on the Ni film cathode during the light-water electrolysis as well as the heavy water one. The common factors to increase number of the anomalous etch pit in the CR-39 chip might be Ni film cathode, the long electrolysis time and Li in the electrolyte solution. All the results indicate a characteristic of LENR in the electrolysis that the reaction does not always takes place in every electrolysis experiment but occasionally does under the same experimental condition.

Acknowledgment

This work is financially supported by a Grant-in-Aid for a Challenging Exploratory Research (23656205) in the Scientific Research Foundation from MEXT in Japan.

References

- [1] R.A. Oriani et al., *Jpn. J. Appl. Phys.* **41** (2002) 6180.
- [2] R.A. Oriani, *Proc. 14th Int. Conf. Cold Fusion* (2008), p. 250.
- [3] A.G. Lipson et al., *Proc. 10th Int. Conf. Cold Fusion* (2003), p. 539.
- [4] A.G. Lipson et al., *Proc. 11th Int. Conf. Cold Fusion* (2004), p. 324.
- [5] A.S. Roussetski, *Proc. 11th Int. Conf. Cold Fusion* (2004), p. 274.
- [6] H. Yamada et al., *Proc. 10th Meeting of Japan CF Research Society* (2010), p. 41.
- [7] H. Yamada et al., *Proc. 11th Meeting of Japan CF Research Society* (2011), p. 41.
- [8] K. Mita et al., *Proc. 12th Meeting of Japan CF Research Society* (2012), p. 43.



Research Article

The Importance of the Removal of Helium from Nano-Pd Particles after Solid Fusion

X.F. Wang and Y. Arata*

*Arata Research & Development Center, B302, Collaborative Research Building, Office for University–Industry Collaboration,
Osaka University, 2-1 Yamadaoka, Suita, Osaka 565-0871, Japan*

Abstract

According to the measuring results of our paper presented at ICCF15 (2009), helium as an important evidence of solid-state fusion has been confirmed clearly by mass analyzer “QMS”. After one solid fusion cycle, the produced helium remained inside the particles. To measure the quantity of helium correctly, the residual helium inside these particles must be completely removed. However, it is not very easy. In this paper, one of the methods to solve the problem of the removal from the nano-Pd particle is discussed.

© 2014 ISCMNS. All rights reserved. ISSN 2227-3123

Keywords: Helium, Nano-Pd particles, Removal, Solid fusion

1. Introduction

Gas loading experiment has been a very important research trend of Low Energy Nuclear Reactions (LENR). We published our nano-Pd studies of excess heat and helium-4 using a new vessel at ICC15 (2009) [1]. The nano-scale Pd particle is attracting more and more researchers to study due to its unique properties [2]. In that paper, throughout the investigation of excess heat and helium-4, we have confirmed the occurrence of “Solid Fusion” by applying nano-Pd powder in D₂ gas loading system. As to measure the quantity of helium correctly, the removal of helium-4 from nano-Pd powder are very important. Therefore, we try to discuss about how to dissolve this problem in this paper.

2. Experimental and Discussion

2.1. The importance of Pd/D ratio for Solid Fusion

Pd/D ratio is an very important factor for solid fusion. Deuteron diffusing into Palladium expands the lattice. Because of this counter force, most palladium takes-up 0.5–0.7 parts deuteron. Generally very high pressures are needed to get palladium to uptake deuteron beyond PdD0.7. And it is well known that the D/Pd ratio larger than 0.88 is favorable to observe an excess heat during the loading of palladium with deuterium [3,4].

*E-mail: arata@casi.osaka-u.ac.jp

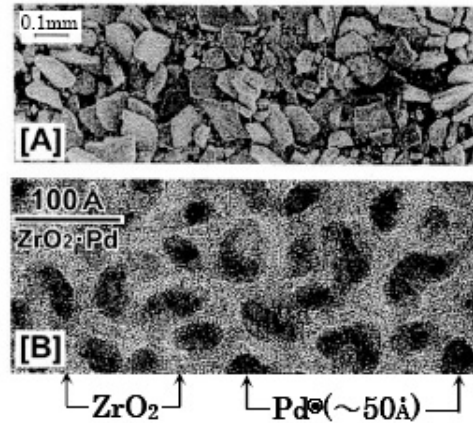


Figure 1. Nano-scale Pd embedded in ZrO_2 .

As shown in Fig. 1, the specimens, discussed in this paper, are nano-scale Pd particles with clusters of about 50 Å in diameter embedded in ZrO_2 matrix [5].

It is well known that nanometer-sized particles display intrinsic different characteristics from those of the corresponding bulk materials due to their unique nanometer-scale structure. The nano-Pd particles work more effectively to absorb large amounts of deuterium and then cause solid fusion attributing to the relative large specific surface area. Therefore, the “solid (state) deuterium”, namely the nuclear fuel, was successfully prepared. The “solid deuterium” is an ultrahigh density deuterium metallic lattice.

We have investigated that D atoms exhibit more stronger effect within host metal clusters and large amounts of D atoms more than 300% against the host atoms can be absorbed in nano-Pd particles, as shown in Fig. 2. Further

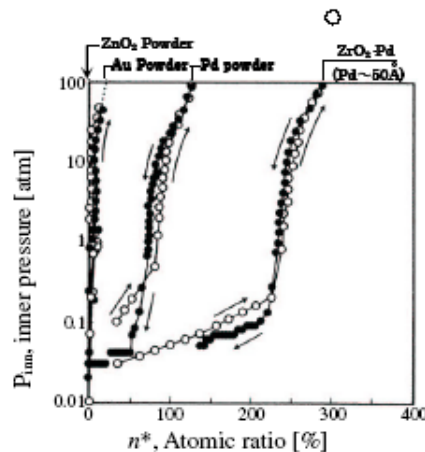


Figure 2. $\text{D(H)}/\text{Pd} = 2.9$ at 100 atm.

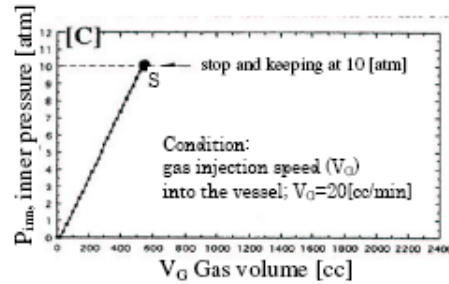


Figure 3. D/H Absorption characteristics of ZrO_2 powder.

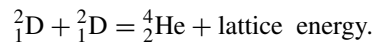
investigation shows that ZrO_2 powder did not absorb D_2 as shown in Fig. 3 (Fig. 1 (C) of [5]).

Figure 2 shows the relationship between the applied pressure and the atomic ratio of D/Pd. The results demonstrate that D_2 gas is quickly absorbed more than 200 and 250% in the number density of atoms into Pd clusters under the conditions of less than atmospheric pressure and around 3 atm, respectively. Furthermore, an enhancement of absorption up to 290% is gained under such high applied pressure as 100 atm.

2.2. The residual helium-4

As shown in Fig. 4, large amounts of D-atoms absorbed inside nano-Pd are solidified as ultrahigh deuterium-lump (Pynodeuterium) inside each octahedral space of unit cell of the host Pd lattice [5]. These pynodeuterium are dispersed to form "metallic deuterium lattice" with body centered cuboctahedron structure, as shown in the right photograph of Fig. 4.

Based on our previous experimental and theoretical analyses results, the high density solid-deuterium fused inside the host Pd lattice (Octa-vessel) by the reaction equation as follows [5],



According to our previous results of solid fusion, helium-4 remained inside both gas and particles after one solid fusion cycle [1]. Therefore, to measure helium-4, the measure process is divided into two parts (two steps), namely the removing of helium-4 from gas and Pd particles, respectively.

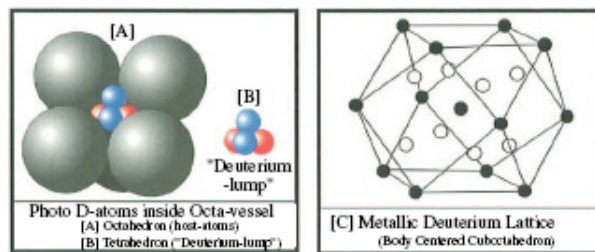


Figure 4. Existence position of deuterium in Pd.

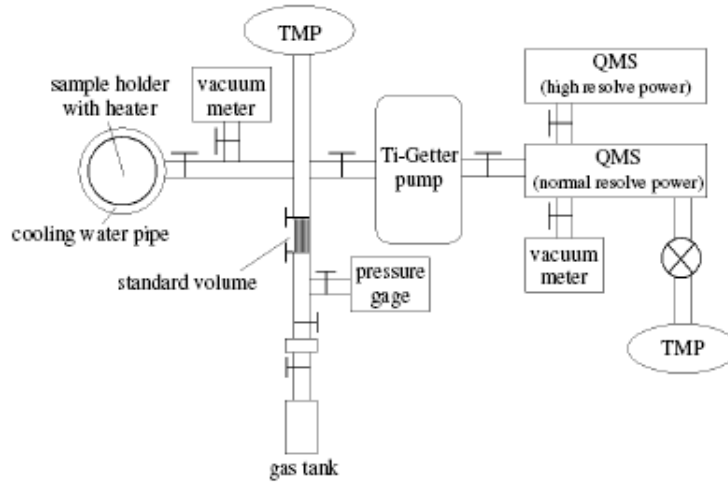


Figure 5. Schematic diagram of Mass analysis apparatus — “QMS”.

The exhausting of helium-4 from gas is relatively easy. Applying our measure apparatus, the quadrupole mass spectrometer (QMS) (Fig. 5), the amounts of helium-4 inside reaction gas after one solid fusion cycle can be detected [6].

However, the measurement of helium-4 inside Pd particles is not so easy as gas. According to the results of the previous analysis, it is extremely difficult to completely remove helium-4 from Pd particles. The removing of the residual helium-4 inside Pd particles could not be expected unless by heating up to high temperature and/or dissolving

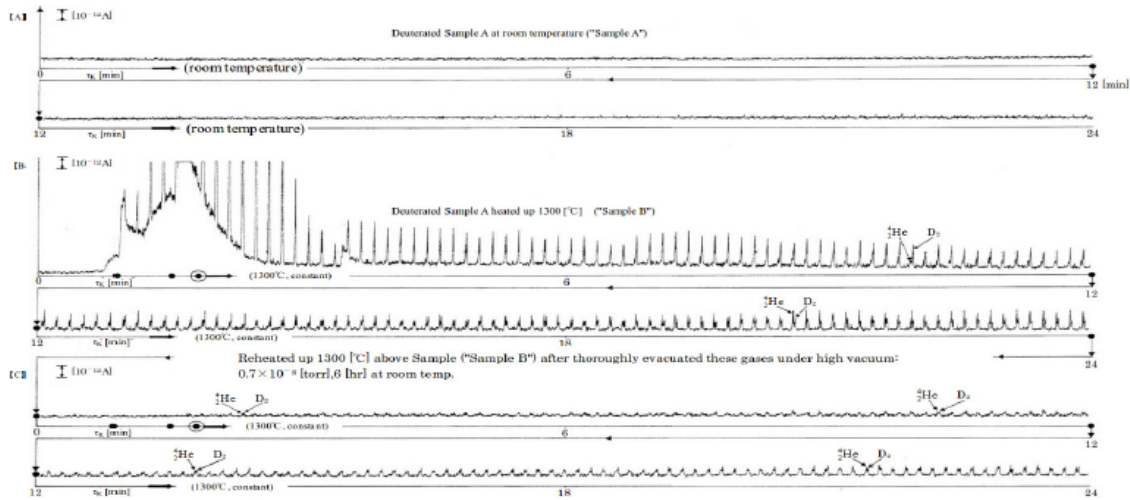


Figure 6. Characteristic of “released gases” (${}^4\text{He}$; D_2) discharged from “reheated sample”, using “limited QMS”.

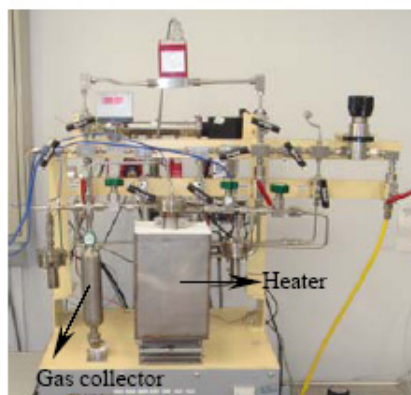


Figure 7. The photo of heating facility.

in liquid solution [5].

As stated in the previous report [7], elements released from highly deuterated sample placed in the “closed QMS” with high vacuum ($\approx 3 \times 10^{-9}$ Torr) are trapped inside the apparatus indefinitely. Helium will continue to exist under the effect of the “getter action” of Ti-Getter pump, shown in Fig. 5. However, the hydrogen series elements and others vanish or diminish to the limit of the Ti-Getter pump’s functional limit. Thus the existence of helium-4 is accurately determined.

In our previous works, we have investigated the releasing action of helium-4 using “limited QMS”(powder inside it can be heated up to over 1300°) from highly deuterated Pd sample [8], as shown in Fig. 6. In Fig. 6, (A) shows the characteristic of “Sample A” (highly deuterated Pd-black) at room temperature in high vacuum, long period ($\approx 10^{-8}$ Torr during 6 h. No “couple spectrum” (spectrum of helium-4 and deuteron) can be observed in this case. That is to say that no helium-4 released from sample A. (B) in Fig. 6 shows effect of only “heat” on the above “Sample A” and clear “coupled spectrum” (helium-4 and deuteron) takes place under high temperature and high vacuum ($\approx 1300^\circ\text{C}$, $\approx 10^{-8}$ Torr). (C) in Fig. 6 shows effect of “reheat” on the above heated sample A (“Sample B”) in (B). Before reheat, all gases released from “Sample B” were thoroughly evacuated under room temperature, high vacuum and long period (0.7×10^{-8} Torr, 6 h). And when “Sample B” is again heated under the same condition, “couple spectrum” was clearly regenerated.

That is to say, at present, helium-4 inside Pd particles cannot be completely released even heated ramping to 1300°C .

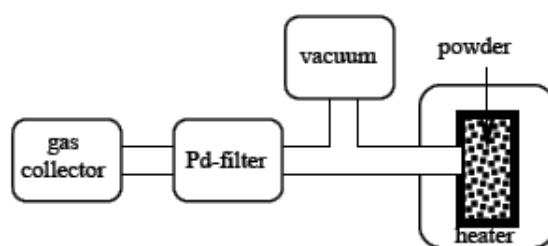


Figure 8. Schematic diagram of the apparatus.

2.3. Heating facility

On the basis of those considerations mentioned above, for the production analysis of Solid Fusion, the relationship between the temperature and helium-4 released from nano-Pd particles should be clarified firstly. Therefore, we designed a new heating facility, as shown in Fig. 7.

This heating facility consists of four major parts: heater, gas collector, gas filter and vacuum, as illustrated in Fig. 8. At present, the heat range is designed up to only 1300°C. This temperature is not enough to remove all of helium-4 inside Pd powders. And we are making our efforts to increase the heating ability of this apparatus to fit the temperature requirement.

This heating facility can be used to investigate the characteristic of the extraction of helium-4 from nano-Pd powder after one gas loading cycle. It can also be used to investigate the relationship between the temperature and the release of helium-4 after solid fusion.

Helium-4, due to its unique properties, has been used for leak detection, airships, balloon, scientific uses, and so on. Therefore, as bypass production of solid fusion, helium-4 production can also be expected. The concentrating and collecting of the helium-4 can also be made using this heating facility for use later.

In a word, it is necessary for us to make more efforts on the research of the residual helium-4 using above heating facility.

3. Conclusions

To measure helium-4 correctly, after one Solid Fusion cycle, one of the possible methods, heating is discussed in this paper.

Helium-4 inside Pd particles cannot be completely released even by heat ramping to 1300°. It is necessary to make more efforts on the research of the residual helium-4 inside nano-Pd particles.

A new heat facility is designed to investigate the characteristics of helium-4 inside nano-Pd particles after gas loading. And then concentrating and collecting of helium-4 can also be expected using this heat facility.

References

- [1] Y. Arata, Y.C. Zhang and X.F. Wang, Production of helium and energy in the “Solid Fusion”, *Proc. ICCF15*, Rome, Italy, pp. 72–81, 2009.
- [2] F. Celani, P. Marini et al, Towards a high temperature CMNS reactor: nano-coated Pd wires with D₂ at high pressures, *Proc. ICCF15*, Rome, Italy, pp. 82–87, 2009.
- [3] N. Hasegawa, K. Kunitatsu, T. Ohi and T. Terasawa, Observation of excess heat during electrolysis of IM LiOD in a fuel cell type closed cell, *Frontiers of Cold Fusion*, H. Ikegami (Ed.), Universal Academy Press, Tokyo, p. 377, 1993.
- [4] M. McKubre, F. Tanzella, P.L. Hagelstein et al, The need for triggering in cold fusion reactions, *Proc. ICCF10*, Cambridge, Massachusetts, USA, 2003, pp. 199–212.
- [5] Y. Arata, M.J.A and Y.C. Zhang, Formation of condensed metallic deuterium lattice and nuclear fusion, *Proc. Japan Acad.* **78B** (2002) 57–62.
- [6] Y. Arata and Y.C. Zhang, Helium (${}^4_2\text{He}$, ${}^3_2\text{He}$) within deuterated Pd-black, *Proc. Japan Acad.* **73B** (1997).
- [7] Y. Arata and Y.C. Zhang, Deuterium nuclear reaction process within solid, *Proc. Japan Acad.* **72B** (1996) 179–184.
- [8] Y. Arata and Y.C. Zhang, Solid-state plasma fusion (“cold fusion”), *Special Issue of High Temperature Society*, Special Volume, Vol. 23, Jan, 1997.



Research Article

Investigation of Radiation Effects in Loading Ni, Be and LaNi_5 by Hydrogen

Yu. N. Bazhutov*

Terrestrial Magnetism, Ionosphere and Radiowave Propagation Institute RAS (IZMIRAN), Moscow, Russia

E.O. Belousova, A.G. Parkhomov, Yu.A. Sapozhnikov and A.D. Sablin-Yavorsky

Lomonosov Moscow State University, Moscow, Russia

V.P. Koretsky

Erzion Scientific Research Center, Moscow, Russia

Abstract

The installation permitting to investigate gamma, X-ray and neutron radiations emitted by metals loaded with protium–deuterium mixture at temperature up to 750°C and pressure up to 100 bar is created. It was discovered that LaNi_5 powder, nickel and beryllium are radiated presumably X-rays and neutrons. Radiation emission occurs in the form of short bursts or series of bursts lasting up to several tens of minutes.

© 2014 ISCMNS. All rights reserved. ISSN 2227-3123

Keywords: Gamma, Metals loaded with protium–deuterium mixture, Short bursts or series of bursts, X-ray and neutron radiations

1. Introduction

Detailed study of nickel–hydrogen system properties, provided by F. Piantelli, S. Focardi, A. Rossi and other researchers, clearly showed that in this system occurs not only chemical but also Low-Energy Nuclear Reactions [1–3]. Based on these studies, installation emitting hundreds kilowatts of energy have been created with a very low hydrogen consumption [4,5].

Our researches have purposed to check the presence of nuclear transmutations in loading of different metals by hydrogen with registration of radiation with which the nuclear transformations should be accompanied. Apart from nickel, we investigated intermetallic compound type of LaNi_5 , which is able to absorb hydrogen multiply exceeds a pure nickel [6]. Beryllium was investigated as material which has ability to undergo cold transmutations is predicted by Erzion model [7–10].

*E-mail: erzion@mail.ru

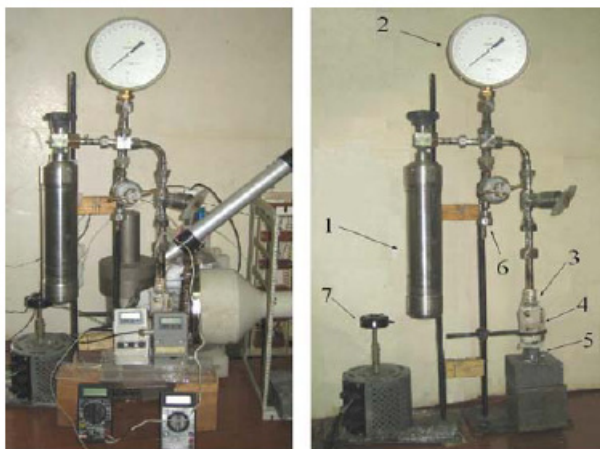


Figure 1. The experimental set-up. *Left*—a view with a complex of measuring apparatus, *right* — without it. 1- vessel with protium–deuterium mixture, 2- manometer, 3 – cylindrical cell containing substance under investigation, 4 – electric heater, 5 –collimator for gamma source, 6– offshoot to the vacuum pump, 7 – heater power regulator.

2. The Experimental Set-Up

The experimental set-up (Fig. 1) consists of a vessel with protium–deuterium mixture under the pressure of several tens of atmospheres: (1) the intermediate pipe and the cylindrical cell, (3) containing substance for investigation. The cell is surrounded by electric heater (4) that provides heating up to 700°C. The intermediate pipe has offshoots to the manometer (2) and oil-free vacuum pump (6). The temperature of the cell is measured using thermocouples mounted on it. Determination of investigated substance saturation degree was by dimension of hydrogen pressure changing in the vessel of known volume.

Particular attention was paid to the registration of radiation that may arise during experiments (Fig. 2). A counter with NaJ (Tl) scintillator $\varnothing 40 \times 40$ mm was used for detecting gamma radiation. In addition to it, four Geiger counters were used in the experiments. Two counters have a window made of thin mica (about 10 μm thick). Such counters are able to detect X-rays and gamma rays with quanta energies as low as several keV, beta radiation and even alpha particles. One of them was covered with 2 mm thick Teflon layer. In addition, two Geiger counters with metallic walls were also used with one of them also carrying additional 2 mm Teflon layer. These counters are able to detect gamma rays with quanta energies above 50 keV and beta particle energies above 0.5 MeV. For the detection of neutrons ^3He -counter, located in water serving as a moderating medium, is used. Such detector possesses high and approximately the same sensitivity to neutrons over a wide energy range – from 10s of eV to several MeV, coupled with extremely low sensitivity to gamma radiation.

We used a specially equipped computer for automatically recording temperature and count rate of radiation detectors information. The peculiarity of the used recording system is the ability to record short bursts.

3. Investigations of Thermodynamic Properties of Researched Substances

Figure 3 shows a typical course of interaction between doped LaNi_5 powder and hydrogen: loading and releasing when heated in fixed volume. Short-term opening of the vessel with hydrogen leads to a jump in pressure, which immediately begins to drop as a result of hydrogen absorption. This is accompanied by an increase of the cell temperature by

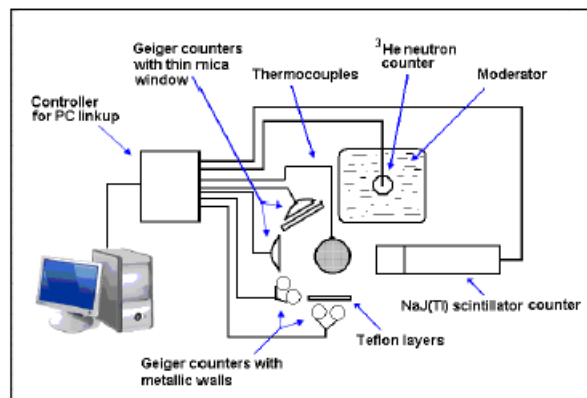


Figure 2. Equipment complex for radiation and thermal measurements.

several °C. After switching on the external heater at a temperature near 80°C begins a rapid release of absorbed hydrogen, resulting in rapid growth of the pressure. After reaching a temperature of 250°C, the pressure is almost stabilized and may even decline, despite the rising temperature. This effect can be explained by the fact that in this temperature range, absorption capacity of powder as the pressure increases faster than the release of hydrogen associated with the heating. After turning off the heater, a rapid decrease of pressure begins only after the temperature drops below 200°C. After cooling to room temperature, the pressure returns to a value close to the initial.

The pressure diagrams obtained in the experiments with nickel and beryllium are similar to the diagrams obtained in the experiments with LaNi_5 , but pressure modifications are less, as ability of these substances to absorb hydrogen is smaller than LaNi_5 .

4. Detection of Neutron Radiation

The character of signals registered by ^3He neutron counter in the experiments with nickel and beryllium foils and with nickel powder, is similar (Fig. 4). Registration of neutrons, is authentic exceeding background, is observed only at

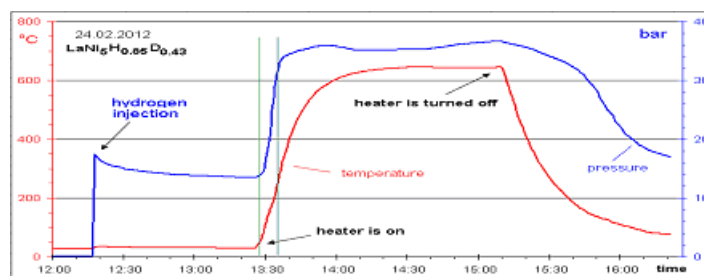


Figure 3. Typical course of interaction between doped LaNi_5 powder and hydrogen. Hydrogen injection leads to a jump in pressure, which immediately begins to drop as a result of hydrogen absorption. This is accompanied by an increase of the cell temperature by several °C. At temperature of 80°C begins a rapid release of absorbed hydrogen, resulting in rapid growth of the pressure. After reaching a temperature of 250°C, the pressure is almost stabilized. After cooling to room temperature, the pressure returns to a value close to the initial.

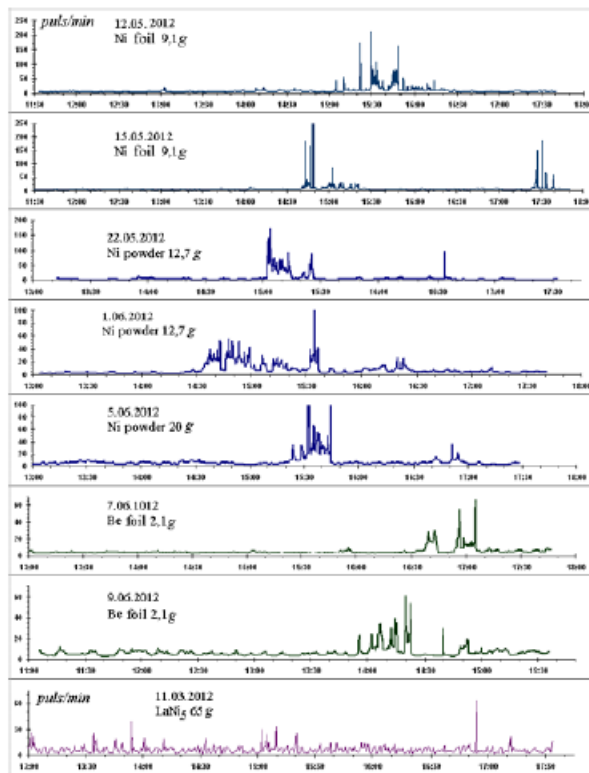


Figure 4. Character of signals registered by ^3He neutron counter. One registered impulse corresponds approximately 200 emitted neutrons.

temperatures above 200–300°C, and count rate fluctuates over a wide range. Common number of emitted neutrons - from several tens of thousands up to several hundred thousands in one experimental run.

Differently LaNi_5 powder exhibits. Signals from the counter of neutrons have an aspect of separate short bursts appearing even at room temperature. Let us consider some experiments closer. In Fig. 5, the outcomes one from experiments with nickel powder are shown. During 60 min, 1230 impulses over background are registered. It corresponds to 245,600 neutrons emitted from the sample. The intensive neutron counter impulses registration happened at pressure 64 bar and temperature 250–350°C.

In Fig. 6, the outcomes one from experiments with beryllium foil are shown. During 25 min, 232 impulses over background are registered. It corresponds to 46,400 neutrons emitted from the sample. The intensive neutron counter impulses registration happened at pressure about 56 bar and temperature 250–350°C.

In one experiment with nickel powder by means of alternative activation measuring technique, we checked that the used ^3He counter registered *just neutrons* (see Fig. 7). From 15:21 till 15:44 June 5 the neutron counter has registered 577 pulses over background. It corresponds to 11,5000 neutrons, emitted from the sample. The radiation of neutrons happened at pressure 61 bar and temperature about 350°C.

Same time on a distance about 4 cm from the sample, the indium foil by square 6.6 cm² and 0.35 mm thickness was placed. The measurement of indium activity was made by means of thin mica window Geiger counter. The measured

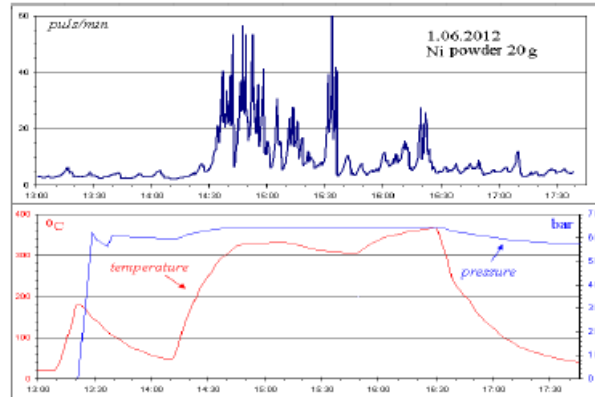


Figure 5. Experiment with nickel powder. From 14:30 till 16:30 1230 impulses over background are registered. Intensive neutron counter impulses registration happened at pressure 64 bar and temperature 200–350°C.

count rate of activated indium foil in view of a decay with a half-life 54 min was $(0.432 \pm 0.022 \text{ s}^{-1})$. Background was $(0.383 \pm 0.016 \text{ s}^{-1})$. With the account of beta particles absorption in a foil and counter window it corresponds to indium activity $(0.6 \pm 0.3) \text{ Bq}$. Such activity could be created by neutrons flux 2000 cm^{-2} . In view of geometry full number of the radiated neutrons $400,000 \pm 200,000$, which is equal $(115,000 \pm 500)$ neutrons.

Taking into account neutron spectrum uncertainty and weakness of activation effect, it is possible to recognize satisfactory fit of two methods measurements. It confirms the neutron reason of neutron counter impulses.

In difference from experiments with a nickel and beryllium, the signals from loaded by hydrogen LaNi5 sample has an aspect of separate short bursts (Fig. 8). It is visible that count rate bursts happen not only at high temperature and pressure, but also at room temperature and pressure close to atmospheric. It confirms experiment realized at room temperature in air environment at atmospheric pressure (Fig. 9).

Figure 10 shows time intervals distribution for small (four neutron events in counter) neutron bursts which gives us

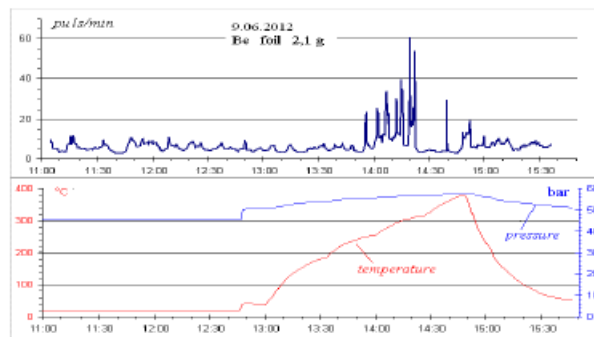


Figure 6. Experiment with beryllium foil. From 13:55 till 14:20 232 impulses over background are registered. It corresponds to 46,400 neutrons emitted from the sample. The intensive neutron counter impulses registration happened at pressure about 56 bar and temperature 250–350°C.

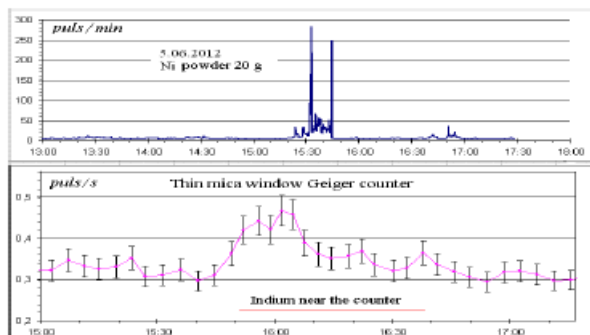


Figure 7. Experiment with nickel powder. Measurements of emitted radiation by two various techniques. Count rate of the neutron counter (*above*) and outcomes of indium activity measurement (*below*).

mean time interval value about 5 s in experiment with Ni powder loaded by hydrogen. Neutron bursts emission from LaNi_5 sample were found out in a wide range of temperatures (from room temperature to 650°C) and pressures (from

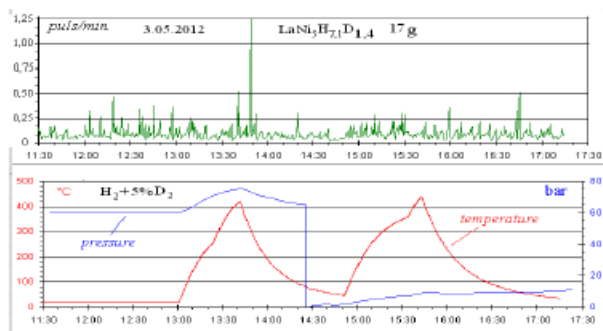


Figure 8. LaNi_5 powder. Signal from the neutron counter during temperature and pressure variations.

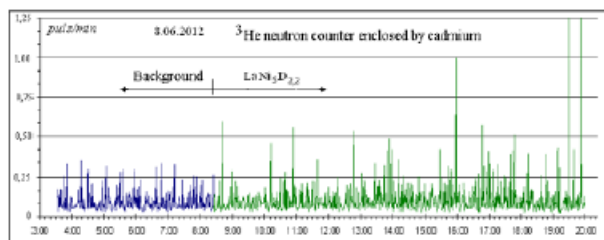


Figure 9. Count rate of ^3He neutron counter, wrapped up in cadmium sheet. Arrangement under cadmium of LaNi_5 sample, loaded by deuterium, increases significantly of bursts frequency and amplitude.

atmospheric pressure to 75 bar) and at different ratios of deuterium–protium (from tenths of percents up to 100%). Mandatory condition of bursts emission is sufficiently high saturation with hydrogen – greater than one hydrogen atom per one LaNi_5 cluster.

5. Gamma and X-ray Detectors Measurements

Detection of gamma radiation with photon energy with the threshold of about 50 keV by means of metallic Geiger counter and scintillation gamma-radiometer not found any effects. The most productive were Geiger counters with thin mica window, including a counter screened with Teflon. The emission occurs mainly in the form of short bursts or series of bursts lasting up to several minutes. Usually bursts in different detectors did not coincide in time. But several instances of quite credible coincide in two and three channels were registered.

In Fig. 11, two series of count rate bursts of the thin window Geiger counter and two series of a signal from the neutron counter which is not were synchronized to bursts, registered by the Geiger counter are visible. Two Geiger counters with metal walls not revealed noticeable effects at this time.

Figure 12 shows example of bursts synchronously recorded by three detectors. The strongest count rate bursts, as usual, gave a counter with a thin mica window – the excess above the background up to 200 times. Counter screened by Teflon gave peaks in excess of 10 times higher than the background value. Splash of more than four times of the background gave the metal counter, screened by Teflon, while the counter with metal walls and no Teflon layer did not give signals rising above background.

What did counters register? Detection of gamma radiation by means of metal Geiger counter and the scintillation

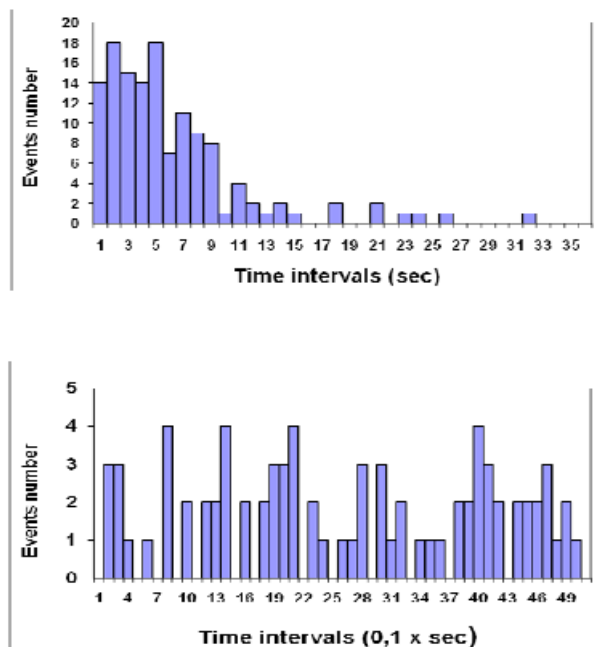


Figure 10. Time intervals distribution for which recorded every four events between 15:22 and 15:44, when the effect was strongest (06.06.12).

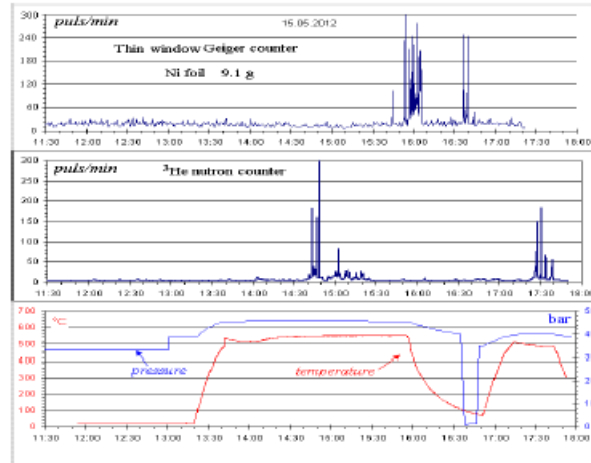


Figure 11. Bursts registered by thin window Geiger counter and ^3He neutron counter during experiment with nickel foil.

gamma-radiometer with energy threshold of about 50 keV did not reveal any effects, as noted above. Consequently, registered radiation cannot be gamma rays with energies above 50 keV. Such radiation would have made all the counters to respond. The assumption that it was beta radiation does not hold either, because beta particles with energies of less than 0.5 MeV, which cannot be registered by metallic Geiger counter, also would not have been registered by counters with a Teflon layer which is thick enough to absorb such beta particles completely. But they did show the effect. For the same reasons, any strongly ionizing radiation like alpha particles must be excluded from consideration.

The only radiation whose properties can explain the totality of the results is the X-rays with photon energies less

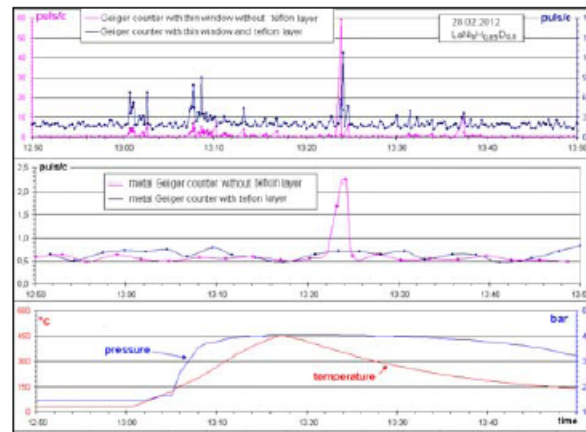


Figure 12. Synchronous count rate bursts of two Geiger counters with thin windows, one of which is screened with Teflon thickness of 2 mm (top) and count rate spike of Geiger counter with a metal wall (middle). Counter not covered with Teflon showed no discernible signals over the background level.

20 keV. It is almost completely absorbed by thin layers of materials with sufficiently high atomic weight, such as iron or copper, and only weakly attenuated by substances with low atomic weight, including Teflon. The walls of the metal used in our Geiger counters are made of stainless steel with a thickness of 0.1 mm. Such wall weakens X-rays with energies of 20 keV to more than 10 times, whereas the Teflon layer thickness of 2 mm reduces it only two times. It is clear that such radiation could hardly be registered by counters with metals walls but can easily produce significant effects in counters with thin window even if they are covered with Teflon.

However, analyzed sample cannot be the *immediate* source of registered X-rays with energies of about 20 keV because it is located in metallic vessel with walls thick enough to cause a complete absorption of this kind of radiation. It can be assumed that the powder emits a kind of radiation, having a relatively high penetrating power, which generates X-rays outside of the vessel, during interactions with Teflon or other substances. This may explain the fact that the bursts were observed in the metal counter, only if it was covered with Teflon.

6. Conclusions

- LaNi₅ powder loaded by hydrogen, and also nickel and beryllium in atmosphere of hydrogen at the increased pressure and temperature, are radiated presumably X-rays and neutrons. It indicates that in these substances under some conditions happen not only chemical or structural modifications, but also nuclear.
- Radiation emission occurs in the form of short bursts or series of bursts lasting up to several tens of minutes.
- Radiation emission occurs at different ratios of deuterium–protium (from 10s of percents up to 100%).
- Radiation emission from a nickel and beryllium are found out at pressure above 50 bar and temperature above 200°C.
- Radiation emission from LaNi₅ powder occur at a sufficiently high saturation with hydrogen – greater than one hydrogen atom per one LaNi₅cluster.
- Radiation emission from LaNi₅ powder occur in a wide range of temperatures (from room temperature to 650°C) and pressures (from atmospheric pressure to 75 bar).
- Neutron generation corresponds up to ~500,000 neutrons emitted from the sample during ~1 h.
- Time intervals distribution for small (four neutron events in counter) neutron bursts gives mean time interval value about 5 s

Acknowledgment

We would like to thank N.I. Khokhlov, V.O. Yapaskurat for help and support and A.A. Artyukhov, Ya.M. Kravets, A.V. Ryzhkov, A.Yu. Kazyonov, V.P. Martemianov, V.G. Tarasenkov, A.V. Zagnitko, M.V. Zemlyakov, S.A. Tsvetkov and V.N. Verbitsky for discussions and consultations.

References

- [1] S. Focardi, R. Habel and F. Piantelli Anomalous heat production in Ni–H systems, *Nuovo Cimento* **107A** (1993) 163.
- [2] S. Focardi et al., Large excess heat production in Ni–H systems, *Nuovo Cimento* **111A**(11) (1998) 1233.
- [3] S. Focardi and A. Rossi, A new energy source from nuclear fusion, *J. Nucl. Phys.* March 22 (2010).
- [4] A. Rossi, Method and apparatus for carrying out nickel and hydrogen exothermal reactions, World Intellectual Property Organization, Pub. No WO/2009/125444, Pub. Date 15.10.2009.
- [5] Yu. N. Bazhutov, Heat generator of Rossi and Focardi and its theoretical interpretation, *Izobretatelstvo* **12**(1) (2012) 49–59 (in Russian).
- [6] V.M. Azhazha, M.A. Tikhonovsky and A.G. Shepelev, Hydrogen storage materials, *Issues of Atomic Science and Technology*, No. 1 (2006), Series: Vacuum, clean materials, superconductors (15) 145–152 (in Russian).

- [7] Yu.N. Bazhutov, G.M. Vereshkov, R.N. Kuzmin and A.M. Frolov, Collection PPh&CPhSQ, TsNIIMash, 1990, 67–70.
- [8] Yu.N. Bazhutov and G.M. Vereshkov, The new stable hadrons in cosmic rays, their theoretical interpretation and possible role in catalysis of cold nuclear fusion, Preprint No. 1, TsNIIMash, 1990, 1–56.
- [9] Yu.N. Bazhutov and G.M. Vereshkov, A model of cold nuclear transmutation by the erzion catalysis, *Proc. of ICCF-4*, Hawaii, Vol. 4, 1993, pp. 8-1.
- [10] Yu.N. Bazhutov, A.B. Kuznetsov and E.V. Pletnikov, Spectroscopy of Erzion-catalytic nuclear transmutation, Preprint ¹ 1, SRC PhTP "Erzion" TsNIIMash, 1993, pp. 1–172.



Research Article

Erzion Model Interpretation of the Experiments with Hydrogen Loading of Various Metals

Yu. N. Bazhutov*

Terrestrial Magnetism, Ionosphere and Radiowave Propagation Institute RAS (IZMIRAN), 142190 Troitsk, Moscow, Russian Federation

Abstract

A short review of Cold Nuclear Transmutation for 22 years after its discovery is presented. I describe the main physical results of the Rossi–Focardi experiment and our experiment with hydrogen loading of various metals. I propose the Erzion Model of Catalytic Nuclear Transmutation as the theoretical explanation of the generation of excess heat, new chemical elements and isotopes, X-rays and neutron radiation in these experiments.

© 2014 ISCMNS. All rights reserved. ISSN 2227-3123

Keywords: Erzion model of catalytic nuclear transmutation, Hydrogen loading of various metals

1. Introduction

Twenty-three years ago Martin Fleischmann, Stanley Pons and Steven Jones declared the opening of a new nuclear physics phenomenon – cold nuclear fusion (CNF) [1,2], capable of becoming in the near future the basis for a new simple, safe and efficient form of nuclear power. In March 23 at the press conference in the University of Utah, Martin Fleischmann and Stanley Pons announced a simple electrolysis experiment with heavy water and excess heat up to 3 W with 1 W of input power.

To understand the mechanism of this new effect, it is possible that the most significant there were the results obtained in the Bombay Atomic Center by nuclear physicists of 11 independent groups, which a year later showed that the excess energy in high current heavy water electrolysis are observed with a very abnormal ratio of the neutron to tritium yield, relatively to a standard mechanism for nuclear fusion [3]. The yield of tritium relative to energy output is 1000 times smaller, and the neutron flux is suppressed, even a million times (3–11 orders of magnitude of suppression in different groups). After this, the researchers realized that they were dealing with a new mechanism in nuclear physics, and changed its name from CNF to CMNS or CNT.

By now the international CMNS community has discovered many different methods of stimulating this process. These methods include the use of laser illumination; thermodynamic and ultrasonic cavitation; temperature and pressure cycling in the gas phase; using plasma electrolysis, etc. Piantelli and Focardi spent 20 years investigating the mechanism

*E-mail: erzion@mail.ru

of nickel loaded with usual hydrogen, and had some success [4,5,11]. The Italian engineer Rossi saw the simplicity of the Piantelli cell and invested his own capital in this process. Together with Focardi, Rossi has been able to make an industrial variant of this cell even without a true understanding of the physical mechanism of it [9,10]. Thus, Rossi and Focardi may had great success in energy production, though perhaps not yet in the most optimal variant of it.

On 14 January 2011, the University of Bologna physics department held an online conference in which scientists and journalists were shown a working prototype of the reactor with a capacity of 12 kW, operating on the principle of cold nuclear transmutation [8]. Analysis with a spectrometer at the University in Uppsala, Sweden, showed that the initial powder consists mainly of pure nickel, while the used powder contains a number of other substances – 10% copper, 11% iron, and smaller percentages of cobalt and zinc. “Given that copper is not one of the additives used as a catalyst of copper, isotopes Cu^{63} and Cu^{65} can only be obtained during the nuclear process. This is evidence that nuclear reactions took place,” said Kullander. Swedish researchers concluded: “Given 25 kW from the container volume of 50 cm^3 any chemical process should be excluded. There is only one alternative explanation for the fact of the measured energy. This is a new nuclear process.”

On 6 October 2011 A. Rossi demonstrated a large set of E-Cat (37 modules, 3 cells each) with an output of thermal power $\sim 1 \text{ MW}$ [6,7]. On October 28, 2011, Rossi showed his first megawatt reactor for its first client, and the client’s engineers and scientists, checked his work. Due to some problems reactor produced 470 kW of continuous power for 5.5 h in self-sustaining mode [12]. Due to the use of a fully autonomous mode the reactor could not be run at full capacity, but what he did was quite impressive. He demonstrated for 5.5 h with the heat production capacity of 470 kW, a self-sustaining mode.

In our similar experimental studies (in a separate report presented at this conference) with hydrogenation and heating of various metals, we have conclusively identified the generation of X-rays, neutron radiation and we also obtained the possible indication of new isotopes and chemical elements generation.

2. Interpretation of Our Results and the E-Cat Results within Erzion Catalysis Model

To explain the phenomenon of Cold Nuclear Transmutation (CNT) over the 23 years about a hundred of theoretical models have been proposed. However, most of them only explain the mechanism of removing a potential barrier for nuclear fusion. Others suggested more radical new channels of nuclear reactions, thus providing a process CNT. The Erzion Catalysis Model [13–15], which appeared as early as 1990 is one of them.

The result of the E-Cat work and our similar experimental studies (in a separate report presented at this conference) with hydrogenation and heating of various metals give a natural explanation in the framework of the Erzion Catalysis Model, assuming the existence in nature of new hadrons – Erzions proposed even earlier (1982) in order to explain a number of cosmic ray anomalies [16,18–20].

Erzions are a pair of stable heavy mesons (E^0, E^-), the existence of which has a strong foundation in the framework of the Mirror Model [14,15,17]. A consequence of the quantum numbers of the Erzion doublet has a nuclear force of repulsion in the interaction with ordinary nuclei. Thus, the meson – Erzion cannot be captured by nuclei, and only with the nucleons can form a stable bound singlet state Erziobarion or 5-quark bag, which we called as Enion ($E_N = \{U^*, u, u, d, d\}$). As can be seen in Fig. 1, this particle can be dissociated or a charged pair ($E_N = E^- + p - \Delta E_1$), or in a neutral pair ($E^0 + n - \Delta E_2$) upon receipt by it of additional energy ($\Delta E_1 = 7.80 \text{ MeV}$) or ($\Delta E_2 = 6.15 \text{ MeV}$).

The basic model of the Catalytic Erzion Nuclear Transmutation (CENTM), created specifically to explain the phenomenon of cold fusion (or rather the Cold Transmutation of nuclei), is the assumption of the existence of matter in the bound state of Enions and nuclei with a very low concentration ($C \sim 10^{-15}$ per nucleon). The bound energies $-E_b = (1\text{--}100 \text{ eV})$ are very small. The Enion can bind to nuclei of some elements (donor isotopes) and can be stored for a long time for them to release due to a collision or impact of electromagnetic radiation. Enions are of relict origin, and came to earth mainly in the primary cosmic radiation.

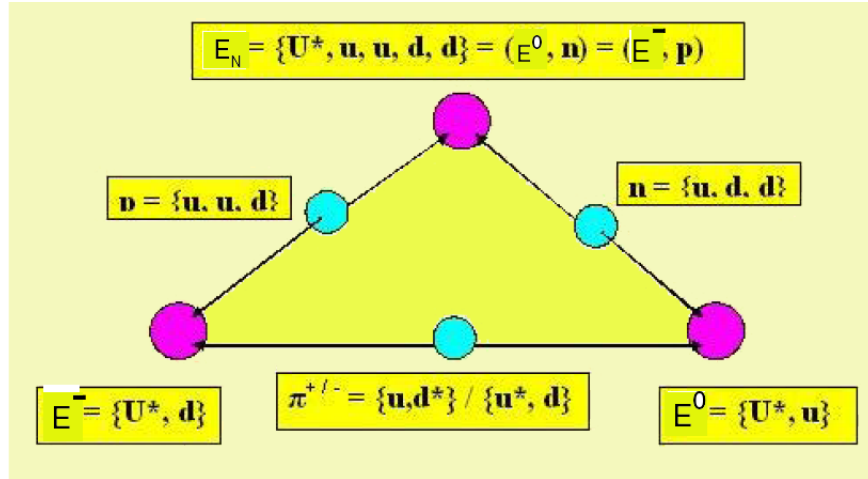


Figure 1. The Erzions and Enion structural quark scheme.

As previously reported, the Erzion nuclei cannot exist in principle and therefore Erzion and Enions can only participate in the exchange nuclear reactions (not capture) with preservation of “Erzion numbers”. Thus, Enions can become Erzion (E^- or E^0), and Erzion changes sign or charge ($E^- \Rightarrow E^0$; $E^0 \Rightarrow E^-$), or convert to E_N .

In principle, any possible implementation of the six Erzion-exchange reactions ($E_N \Rightarrow E^0$, $E_N \Rightarrow E^-$, $E^0 \Rightarrow E^-$, $E^0 \Rightarrow E_N$, $E^- \Rightarrow E^0$, $E^- \Rightarrow E_N$) [21].

3. Nuclear Transmutation and Calorimetry

Nuclear catalysis for metal hydride experiments is provided by heating nickel hydride to a high temperature (~ 700 K) at which due to the collision mechanism on the lightest donor isotope – proton ($E_{\text{bond}} \sim 1.5$ eV) Enions can become free, which has, in turn, triggers catalytic chain Erzion exothermic nuclear reactions [17].

At the 5th RCCNT conference in 1997 my report “Local and global transmutation of nuclei in Erzion model” was presented and later published in the Proceedings of RCCNT-5 [22]. I looked at the successive chain of nuclear transmutations, not only for all isotopes of the primary chemical element titanium (Ti), but in all of its daughter isotopes in the 14 stages of such a transmutation. Here it is done the same job, but for the original set of all stable isotopes of nickel. The fact is that for large nuclear sections of nuclear reactions of Erzion catalysis the daughter nuclei are accumulated at a very small (micron) distance from the primary reaction, and the frequency of their accumulation is huge (in the gigahertz range), so it quickly achieves a high concentration of daughter isotopes in this small volume, and effectively begins to produce second stage transmutation chains, third stage, and so on. Let us consider only two steps of the nickel nuclear transformations.

At the first stage, the five stable isotopes of nickel are as follows from Erzion-nuclear catalytic exchange reactions:

$$\text{Ni}^{58}(E^-, E^0)\text{Co}^{58}(\beta^+, \varepsilon) + 2.45 \text{ MeV}, \quad (1)$$

$$\text{Ni}^{58}(E_N, E^0)\text{Ni}^{59}(\varepsilon) + 2.95 \text{ MeV}, \quad (2)$$

$$\text{Ni}^{60}(\text{E}_\text{N}, \text{E}^0)\text{Ni}^{61} + 1.77 \text{ MeV}, \quad (3)$$

$$\text{Ni}^{61}(\text{E}_\text{N}, \text{E}^0)\text{Ni}^{62} + 4.55 \text{ MeV}, \quad (4)$$

$$\text{Ni}^{61}(\text{E}^-, \text{E}^0)\text{Co}^{61}(\beta^-) + 1.51 \text{ MeV}, \quad (5)$$

$$\text{Ni}^{62}(\text{E}_\text{N}, \text{E}^0)\text{Ni}^{63}(\beta^-) + 0.79 \text{ MeV}, \quad (6)$$

$$\text{Ni}^{64}(\text{E}_\text{N}, \text{E}^0)\text{Ni}^{65}(\beta^-) + 0.05 \text{ MeV}. \quad (7)$$

Thus, the first stage brings ever new nine subsidiaries of radioactive and stable isotopes, taking into account the β decay (β^+ , β^- - decays and ε - e capture): Fe^{58} , Co^{58} , Co^{59} , Co^{61} , Ni^{59} , Ni^{63} , Ni^{65} , Cu^{63} , and Cu^{65} .

At the second stage these nine radioactive and stable isotopes are the following, based on the Erzion-nuclear catalytic exchange reaction:

$$\text{Fe}^{58}(\text{E}_\text{N}, \text{E}^0)\text{Fe}^{59}(\beta^-) + 0, 53 \text{ MeV}, \quad (8)$$

$$\text{Co}^{58}(\text{E}_\text{N}, \text{E}^0)\text{Co}^{59} + 4.40 \text{ MeV}, \quad (9)$$

$$\text{Co}^{58}(\text{E}_\text{N}, \text{E}^-)\text{Ni}^{59}(\varepsilon) + 0.49 \text{ MeV}, \quad (10)$$

$$\text{Co}^{58}(\text{E}^-, \text{E}_\text{N})\text{Fe}^{57} + 1, 15 \text{ MeV}, \quad (11)$$

$$\text{Co}^{58}(\text{E}^-, \text{E}^0)\text{Fe}^{58} + 5.14 \text{ MeV}, \quad (12)$$

$$\text{Co}^{59}(\text{E}_\text{N}, \text{E}^0)\text{Co}^{60}(\beta^-) + 1.44 \text{ MeV}, \quad (13)$$

$$\text{Co}^{59}(\text{E}_\text{N}, \text{E}^-)\text{Ni}^{60} + 1.43 \text{ MeV}, \quad (14)$$

$$\text{Co}^{59}(\text{E}^-, \text{E}_\text{N})\text{Fe}^{58} + 0.74 \text{ MeV}, \quad (15)$$

$$\text{Co}^{59}(\text{E}^-, \text{E}^0)\text{Fe}^{59}(\beta^-) + 1.25 \text{ MeV}, \quad (16)$$

$$\text{Co}^{61}(\text{E}_\text{N}, \text{E}^0)\text{Co}^{62}(\beta^-) + 0.55 \text{ MeV}, \quad (17)$$

$$\text{Co}^{61}(\text{E}_\text{N}, \text{E}^-)\text{Ni}^{62} + 3.04 \text{ MeV}, \quad (18)$$

$$\text{Ni}^{59}(\text{E}_\text{N}, \text{E}^0)\text{Ni}^{60} + 5.34 \text{ MeV}, \quad (19)$$

$$\text{Ni}^{59}(\text{E}^-, \text{E}^0)\text{Co}^{59} + 3.91 \text{ MeV}, \quad (20)$$

$$\text{Ni}^{63}(\text{E}_\text{N}, \text{E}^0)\text{Ni}^{64} + 3.61 \text{ MeV}, \quad (21)$$

$$\text{Ni}^{65}(\text{E}_\text{N}, \text{E}^0)\text{Ni}^{66}(\beta^-) + 2.93 \text{ MeV}, \quad (22)$$

$$\text{Ni}^{65}(\text{E}_\text{N}, \text{E}^-)\text{Cu}^{66}(\beta^-) + 0.32 \text{ MeV}. \quad (23)$$

At the second stage and after, the generation of such radioactive isotopes is rather small. But as indicated below for $\text{Ni}^{65}\gamma$ -activity it may be dangerous (see next page). It is estimated that during the demonstration of only one module of the generator E-Cat (October 6, 2011) at only 3 kW of power for about 3 h, $\text{Ni}^{65}\gamma$ -activity on the order of the Curie ($\text{Cu} = 3 \times 10^{10} \text{ Bq}$ - decays per second) was produced. However, there are certain ways to suppress this, and perhaps Rossi et al. found a way intuitively.

The isotopes of hydrogen are also possible from the following reactions:

$$\text{H}^1(\text{E}^-, \text{E}^0) \text{n}(\beta^-) + 2.05 \text{ MeV}, \quad (24)$$

$$\text{H}^1(\text{E}^-, \text{E}_\text{N})\gamma + 8.10 \text{ MeV}, \quad (25)$$

$$\text{H}^2(\text{E}_\text{N}, \text{E}^0) \text{H}^3(\beta^-) + 0.21 \text{ MeV}, \quad (26)$$

$$\text{H}^2(\text{E}^0, \text{E}_\text{N}) \text{H}^1 + 3.83 \text{ MeV}, \quad (27)$$

$$\text{H}^2(\text{E}^-, \text{E}_\text{N}) \text{n}(\beta^-) + 5.88 \text{ MeV}, \quad (28)$$

$$\text{H}^3(\text{E}_\text{N}, \text{E}^-)\text{He}^4 + 11.70 \text{ MeV}. \quad (29)$$

Thus, the second stage, too, produces nine new subsidiaries of radioactive and stable isotopes, taking into account the radioactive β decay (β^- -decays and ε -capture e): Fe^{57} , Fe^{59} , Co^{60} , Co^{62} , Ni^{66} , Cu^{64} , Cu^{66} , and Zn^{66} .

At the third and subsequent stages, the accumulation of daughter isotopes in each subsequent phase will be reduced, and their concentration will decrease. Although these stages will continue more than 28 times and will work enough with this collection to produce of more than 95 new isotopes.

So for these first two stages, the most effective for production of new isotopes must have worked enough to produce four new chemical elements (Fe, Co, Cu, and Zn), which were observed by A. Rossi and C. Focardi in their demonstration experiments. Among the 18 newly established isotopes, there will be six radioactive isotopes, of which the most dangerous is the isotope Ni^{65} hard γ -rays with energy γ -quanta of 1.48 (25% – probability of emission of γ -ray) and 1.115 (16%).

Energy absorption of γ -rays in lead is a factor of 2.7 in its thickness of about 4 cm. It is estimated that during the demonstration work of only one module of the E-Cat generator (October 6, 2011) in only 3 kW of power for about 3 h should be established $\text{Ni}^{65}\gamma$ -activity of the order of the Curie ($\text{Cu} = 3 \times 10^{10}$ Bq - decays per second). However, there are methods to get rid of the γ -rays. Perhaps Rossi and Focardi used one of these methods, intuitively.

The above was stated in principle possible to provide Erzion Models catalysis of nuclear reactions to release of nuclear energy.

The order of magnitude of power in the Rossi experiment is in agreement with its estimation in the framework of the Erzion model.

According to references [6–10] in the E-cat about 100 g of Ni and 1.5 g of hydrogen are used, which is about 10^{24} of these atoms. In this case, the light nuclei of hydrogen are in a bound state of Enions (with concentration $C \sim 10^{-15}$ per nucleon) in the amount of 10^9 , which are very loosely connected with the nuclei ($E_b \sim 1.5$ eV), and when heated can let go and start a chain of exothermic catalytic Erzion nuclear reactions [17,18] at giant speeds (gigahertz). The frequency of Erzion chain of nuclear reactions in the E-Cat cell is $f \sim 10^{18}$ Hz, and the power of the energy released only 10% of Enions is about ~ 10 kW.

However, it should be borne in mind that the nuclear chain reaction will be closed only by a single reaction (27), in which neutral Erzion turns into Enion, but the responses to the transformation of Enions to Erzions – all the rest. Therefore, the deuterium is essential in the working body of the fuel system and in natural hydrogen to only $1.5 \times 10^{-4}\%$. The total amount of nuclear energy produced for the entire cycle of the E-cat with 1.5 g of hydrogen will be limited to the value of ~ 30 MJ, and a full time job at a power setting of ~ 10 kW will be only one hour.

In our first series of experiments, we used a metal hydride as a hydrogen absorbent metal intermetallic $\text{LaNi}_{4.75}\text{Al}_{0.25}$, very rich 20 years ago to the state of deuterium $\text{LaNi}_{4.75}\text{Al}_{0.25}\text{D}_{5.5}$ [23]. Therefore, we consider all Erzion-nuclear catalytic exchange reactions at the first stage on stable isotopes of La and Al, and Be used in the recent series of experiments:



$$\text{La}^{138}(\text{E}_\text{N}, \text{E}^0) \text{La}^{139} + 2.73 \text{ MeV}, \quad (35)$$

$$\text{La}^{138}(\text{E}^-, \text{E}_\text{N})\text{Ba}^{137} + 2.02 \text{ MeV}, \quad (36)$$

$$\text{La}^{138}(\text{E}^-, \text{E}^0)\text{Ba}^{138} + 4.58 \text{ MeV}, \quad (37)$$

$$\text{La}^{139}(\text{E}_\text{N}, \text{E}^-)\text{Ce}^{140} + 0.04 \text{ MeV}, \quad (38)$$

$$\text{La}^{139}(\text{E}^-, \text{E}_\text{N})\text{Ba}^{138} + 1.85 \text{ MeV}, \quad (39)$$

$$\text{La}^{139}(\text{E}^-, \text{E}^0)\text{Ba}^{139}(\beta^-) + 0.52 \text{ MeV}. \quad (40)$$

Twenty years after a sample was placed in storage, an analysis by a scanning electron microscope showed that it included about 5% copper and cerium. It is possible that the action of natural radioactivity and cosmic rays launched Erzion catalytic mechanisms of nuclear transmutation, which due to nuclear reactions(6), (7) and (38) provided the operating time of copper and cerium. By the way, this is just as it was at the Rossi and Focardi with operating 10% of copper from pure nickel, but for a shorter period due to the necessary process intensification temperature.

4. The Generation of Neutrons and X-ray

As is evident from the above, 40 Erzion nuclear exchange reactions with all stable isotopes of the major chemical elements involved in our experiments (except beryllium), neutron generation occurs only in the nuclei of atoms of light (proton) and heavy (deuteron) in the reactions of hydrogen, respectively (see reactions (24) and (28)).

In both these cases the reaction is provided by the negatively charged Erzion, which is generated by subsidiary nuclei formed by the isotopes of primary nickel and hydrogen in the reactions (10), (14), (18), (23) and (29) or on the primary isotope of La and Al in the intermetallic $\text{LaNi}_{4.75}\text{Al}_{0.25}$ in the reactions (34) and (38).

In the beryllium, neutrons are produced by an instantaneous collapse of the daughter isotope Be^8 two α -particles, neutrons, giving to the source nuclei in the reaction Be^9 :

$$\text{Be}^9(\alpha, n)\text{C}^{12} + 5.6 \text{ MeV}. \quad (41)$$

Although it is less likely to be formed in the reactions of hydrogen (24) and (28) through the preliminary formation of E^- on the child Be^{10} isotope in the reaction (32).

Because all neutrons generated in Erzion catalytic exothermic nuclear reactions chain from one initial Enion [17], they are born in bursts.

We observed mainly in the intermetallic $\text{LaNi}_{4.75}\text{Al}_{0.25}$ soft X-ray emission, which is due to the characteristic X-radiation of nuclear La ($E_\gamma \sim 40 \text{ keV}$) in their transmutation in the reactions (35)–(40) or as nuclear Ni ($E_\gamma \sim 8 \text{ keV}$) in reactions (1)–(23) with the emission of more soft X-rays.

5. Conclusion

As seen from the above, the Erzion Catalysis Model simply and naturally explains the Rossi and Focardi experiments on the fundamental level of a strictly scientific result. The model may also have a major prognostic potential for substantial optimization of future power plants [24–27].

In the near future we can expect rapid development of Cold Nuclear Transmutation, both in the theoretical and experimental plane. Large investments of financial capital will ensure a rapid breakthrough in the related fields of science and technology. Civilization is rapidly moving into a new Energy Era.

References

- [1] M. Fleischmann, S. Pons and M. Hawkins, *J. Electroanal. Chem.* **261** (1989) 301–308.
- [2] S.E. Jones, E.P. Palmer and J.B. Griss et al., *Nature* **338** (1989) 737.
- [3] BARC Studies in Cold Fusion, BARC-1500, Bombay, 1989.
- [4] S. Focardi, R. Habel and F. Piantelli, Anomalous heat production in Ni–H systems, *Nuovo Cimento* **107** (1994) 163–167.
- [5] S. Focardi, V. Gabbiani, V. Montalbano, F. Piantelli and S. Veronesi, Large excess in heat production in Ni–H systems, *Nuovo Cimento* **111 A** (1998) 1233–1241.
- [6] Link to the video report on the demonstration Rossi, October 6, http://www.nyteknik.se/nyheter/energi_miljo/energi/article3284823.ece
- [7] Testing the E-cat on October 6 at the site, <http://nyteknik.se/incoming/article328>
- [8] <http://4.bp.blogspot.com>
- [9] Patent Rossi “USECatPatentApplication”. The site: <http://ecatnews.com/.../USECatPatentApplication.pdf>
- [10] S. Focardi and A. Rossi, A new energy source from nuclear fusion, *J. Nucl. Phys.* March 22, 2010.
- [11] E.G. Campari, S. Focardi, V. Gabbiani, V. Montalbano, F. Piantelli, E. Porcu, E. Tosti and S. Veronesi, Ni–H systems, *Proc. of the 8th Conf. on Cold Fusion*, 2000, pp. 69–74.
- [12] Link to the video report on the October 28 demonstration Rossi, http://pesn.com/2011/10/28/9501940_1_MW_E-Cat_Test_Successful/
- [13] Yu.N. Bazhutov, G.M. Vereshkov, R.N. Kuzmin and A.M. Frolov, Collection PPh&CPhSQ, TsNIIMash, 1990, 67–70.
- [14] Yu.N. Bazhutov and G.M. Vereshkov, The new stable hadrons in cosmic rays, their theoretical interpretation and possible role in catalysis of cold nuclear fusion, *TsNIIMash* **1** (1990) 1–56 (preprint).
- [15] Yu.N. Bazhutov, G.M. Vereshkov, A model of cold nuclear transmutation by the erzion catalysis, *Proc. ICCF-4*, Hawaii, Vol. 4, 1993, p. 8-1.
- [16] Yu.N. Bazhutov, B.A. Khrenov and G.B. Christiansen, *Izv. USSR Academy of Sci. Ser. Fiz.* **46** (1982) 2425.
- [17] Yu.N. Bazhutov, G.M. Vereshkov and V.I. Kuksa, On the possible existence of new stable hadrons – hypothetical catalysts of cold nuclear transmutation, *Proc. RCCNT-3*, Moscow, 1996, pp.157–201.
- [18] Yu.N. Bazhutov, Erzion model catalytic nuclear transmutation and its interpretation of ball lightning and other anomalous geophysical phenomena, *Proc. RCCNT -3*, Moscow, 1996, pp.202–210.
- [19] Yu.N. Bazhutov, Possible consequences of the existence of Erzion within Erzion model of cold nuclear transmutation, *Proc. 7th Russian Conf. on Cold Nuclear Transmutation of Chemical Elements*, Moscow, 2000, pp.191–197.
- [20] Yu.N. Bazhutov, Erzion model and its application to Cold Nuclear Transmutation and other natural phenomena, *Proc. RCCNT & BL-14*, Moscow, 2008, pp. 37–47.
- [21] Yu.N. Bazhutov, A.B. Kuznetsov and E.V. Pletnikov, Spectroscopy of Erzion-catalytic nuclear transmutation, Preprint ¹ 1, SRC PhTP "Erzion" TsNIIMash, 1–172 (1993).
- [22] Yu.N. Bazhutov, Local and global nuclear transmutation in Erzion model, *Proc. 5th Russian Conference on Cold Nuclear Transmutation of Chemical Elements*, Moscow, 1998, pp. 142–149.
- [23] Yu.P. Chertov, Ya.B. Skuratnik and N.I. Khokhlov, Trying to gamma radiation during thermal cycling of the alloy D loading LaNi_{4.75}Al_{0.25}, *Proc. Int. Symposium on Cold Fusion and Advanced Energy Sources*, Minsk, Belorussia, 24–26 May 1994, pp. 118–121.
- [24] Yu.N. Bazhutov, Erzion – a mysterious and powerful messenger of Mirror World, *Inventing* **II**(7) (2002) 46–52.

- [25] Yu.N. Bazhutov and I.V. Goryachev, Cold Transmutation – a powerful reserve for development of breakthrough technologies, *Inventing* **VI**(7) (2006) 23–32.
- [26] Yu.N. Bazhutov and I.V. Goryachev, From cold fusion to cold nuclear transmutation – a possible alternative nuclear energy, *Nuclear Society* Nos. 4–5 (2006) 57–63.
- [27] Yu.N. Bazhutov, Generator Rossi and Focardi and its theoretical interpretation, *Inventing* **XII**(1) (2012) 49–59.



Research Article

Possible Role of Oxides in the Fleischmann–Pons Effect

Jean-Paul Biberian*

Aix-Marseille University, Jardin du Pharo - 58, bd Charles Livon - 13284 Marseille Cedex 07, France

Iraj Parchamazad[†] and Melvin H. Miles[‡]

University of LaVerne, 3rd St, La Verne, CA 91750, USA

Abstract

The mechanism of the Fleischmann–Pons effect is not yet fully understood. It appears that in many occasions an oxide layer or an insulating layer covers the surface of the active material. In this paper, we list a number of experiments displaying such situation and suggest possible roles of these oxide layers.

© 2014 ISCMNS. All rights reserved. ISSN 2227-3123

Keywords: Electrostatic fields, Excess heat, Insulating films, Zeolites

1. Introduction

It is well known that the Fleischmann–Pons effect needs specific situations where nuclear cold fusion reactions occur [1]. It has been established that high loading is necessary in order to observe excess heat [2]. However, this condition is not sufficient. For example, the variation of the flux of the deuterium through the surface of the palladium electrode is also a necessity [2]. In order to understand the mechanism of Cold Fusion many theories have been developed to explain the effect, but none of them is completely satisfactory. However, from an experimental point of view there are indications that the metals involved in the reaction are rarely free of impurities. Various oxide films often cover their surfaces. It is very possible that these layers play a role in the reaction. In this paper, we review some experimental results showing the existence of such oxide films on the active metal surfaces. The existence of these oxide layers has been observed both in electrolysis experiments and in gas-loading studies.

*E-mail: jpbiberian@yahoo.fr

[†]E-mail: iparchamazad@laverne.edu

[‡]E-mail: mmiles@laverne.edu

2. Electrolysis Experiments

2.1. The original Fleischmann and Pons experiment

The original Fleischmann and Pons experiments were performed in Pyrex cells using LiOD as an electrolyte. This solution being basic slowly etches the walls of the Pyrex container, and the etched material then deposits on the palladium cathode. This behavior has been discussed in details by Lonchamp et al. [3]. Analysis of the deposit on the electrode showed the presence of silicon, carbon, and oxygen [4]. The role of the oxide layer has been confirmed by the impossibility of getting excess heat with Teflon cells unless oxide materials were added [5]. Studies using polymer coated glass cells also failed to give any excess heat effects even when previously active electrodes were used [6].

The mechanism of formation of the oxide film can be described as follows: LiOD reacts with the Pyrex glass producing lithium silicates in the electrolyte solution. Silicon and lithium based deposits form on both the cathode and anode. Such deposits result in the production of a higher over-voltage on the electrodes. As a consequence, the input power increases due to the fact that most experiments are performed at constant currents; the temperature may then gradually rise up to boiling. On the other hand, the consequence of the cathodic deposit is an increase of the D^+ electrochemical potential at the cathode, which in turn increases the loading of deuterium. As mentioned previously, the higher loading helps the excess heat generation. This mechanism explains why long electrolysis times are required.

Fleischmann has proposed another approach to the role of the oxide layer [7]: the silicate deposit at the palladium cathode blocks the surface and prevents the flow of the current for most of the surface of the electrode. The current is then restricted to small regions of cracks in the silicate layer. In these regions, the current density becomes very high, and because the over-voltage increases with the current density, the deuterium loading greatly increases. Another advantage of the silicate layer is that it prevents de-loading by blocking the recombination of deuterium atoms at the palladium-solution interface. The deuterium atoms enter through the cracks and are blocked elsewhere by the silicate layer, therefore increasing the loading ratio, and this helps in producing excess heat.

2.2. Fleischmann/Imam/Miles

In order to help to create this surface oxide layer, Fleischmann/Imam/Miles [8] have added boron and cerium to the palladium. With this method, excess heat has been obtained nearly every time [8]. The boron composition ranged from 0.25 to 0.75 wt%, with boron/palladium atom ratios as high as 1:7. Excess power was observed much earlier than normal and was readily measurable during the first 57 h of electrolysis in an isoperibolic calorimeter [9].

3. Gas Diffusion Experiments

3.1. Yamaguchi and Nishioka

As early as 1990, Yamaguchi and Nishioka [10] observed a gigantic neutron burst of $(1-2) \times 10^6$ neutrons/s from deuterated palladium plates with heterostructures in a vacuum chamber. An explosive release of D_2 gas, biaxial bending of the samples, and excess heat was also observed at the same time. It was concluded that these phenomena are caused by the cooperative production of deuterium atoms accumulation layers at the palladium surfaces due to the controlled out-diffusion of deuterium atoms. Figure 1 shows a schematic of the palladium sample, with a thin film of manganese oxide on one side and a gold film on the other.

3.2. Lipson et al.

Lipson et al. [11] have shown the production of 3 MeV protons, X-ray emission when deuterium desorbs from Pd/PdO films. These observations are in agreement with those of Yamaguchi and Nishioka described above.

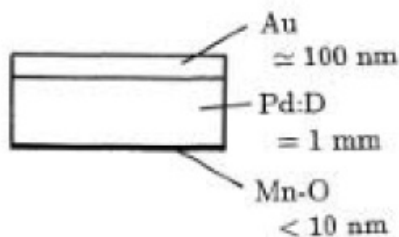


Figure 1. Schematic of the palladium sample involving a thin film of manganese oxide on one side and a gold film on the other side.

3.3. Iwamura et al.

Iwamura et al. [12] have observed the transmutation of cesium into praseodymium and strontium into molybdenum by permeation of deuterium gas through a palladium foil where a multilayer of palladium and CaO is deposited. Cesium and strontium were deposited on the surface of the last palladium layer as shown in Fig. 2. Further experiments showed the transmutation of barium into samarium [13].

3.4. Arata and Zhang

Arata and Zhang [14] using palladium and Pd–Ni nano-crystals embedded inside a zirconium oxide matrix have observed excess heat as well as production of helium-4 without any input energy. Figure 3 shows that the Pd–Ni nano-crystals produce more energy than the pure palladium. On the contrary no excess heat was observed with hydrogen.

3.5. Nickel–Copper–ZrO₂

At 523 K, Miyoshi et al. [15] have shown that Ni–Cu–Zr oxide compound + deuterium produces an excess heat of 300 eV/nickel atom, whereas the hydrogen run was endothermic.

3.6. Zeolites

Zeolites are interesting oxides containing substrates for LENR. They are micro-porous crystalline inorganic hydrated alumino-silicate materials having a highly regular structure of pores and chambers with extremely large surface areas.

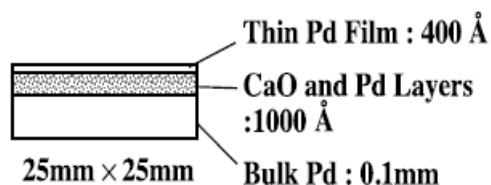


Figure 2. Transmutation experiments using multilayers of deposited palladium and calcium oxide.

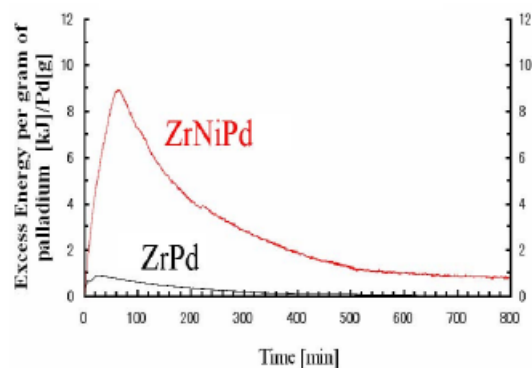


Figure 3. Comparison of excess heat results using palladium or Pd–Ni nanocrystals embedded inside a zirconium oxide matrix.

The zeolite framework structure encloses cavities or pores occupied by cations such as sodium, potassium, cesium, ammonium, and other ions. Figure 4 shows a schematic view of a zeolite.

Large internal electrostatic fields are present in the zeolite cages, making it an interesting nano-reactor to study the possibility of deuterium fusion at room temperature. Zeolites have a three-dimensional pore structure with strong electrostatic fields of 3 V/nm.

Addition of nano-particles of palladium in zeolite cavities produced significant temperature effects in the presence of deuterium gas, whereas no increase in temperature was observed in the presence of hydrogen [16].

3.7. Palladium in alumina

Excess heat was observed in an alumina powder impregnated with palladium upon loading of deuterium in the compound. No excess heat was observed when hydrogen was used [16].

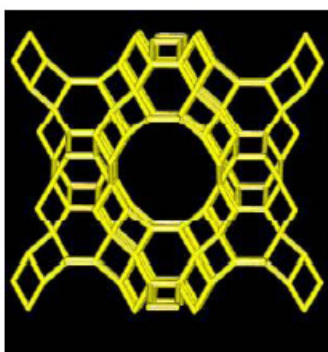


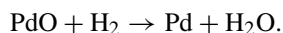
Figure 4. Schematic view of cavities and pores in a zeolite/oxide structure.

4. Discussion

Both electrochemical and gas phase experiments show that an insulating oxide layer on the palladium metal plays an important role. In the first experiments performed by Fleischmann and Pons, Johnson-Matthey palladium was prepared under cracked ammonia:



Hydrogen converts oxides to H_2O during melting



The palladium oxide is converted to H_2O vapor, minimizing PdO in the bulk palladium. This is probably the cause of the good success for excess heat in the first experiments of Fleischmann and Pons. These results also suggest that the oxides need to be present at the cathode surface rather than in the bulk palladium.

In the case of boron-doped palladium, the boron would react with and remove oxygen from the palladium bulk in the form of the substance, B_2O_3 , which would skim off the metal surface during the arc-melting process. It is possible that some boron remains on the surface as B_2O_3 . This may explain why it is not necessary to have long-term electrolysis to produce excess heat in the Pd–B system.. Good reproducibility has been observed with this system.

Several experiments have shown that an insulating oxide layer also plays an important role in gas-loading experiments.

5. Conclusion

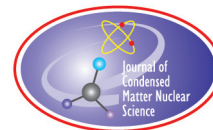
It seems important not to have any metal oxide inside the metal, whereas an oxide film at the surface of the metal is favorable for LENR. Excess heat has been observed in glass cells, but not in Teflon cells or polymer coated glass cells. In glass cells, a long loading time is necessary in order to build the silicon oxide layer at the surface of the cathode, or by adding aluminum oxide powder in the electrolyte in order to quickly build an insulating oxide layer.

The oxide layer has several roles that can be important. On one hand, the electric field at the interface can be very high and create conditions for LENR. On the other hand, it is difficult to say if the heat producing reactions occur mainly at the interface or at the near surface of the metal. However, important effects due to deuterium in the bulk palladium should not be ruled out.

References

- [1] M. Fleischmann and S. Pons, *J. Electroanal. Chem.* **261** (1989) 301–308.
- [2] M. McKubre, R.C. Rocha-Filho, S.S., F. Tanzella, J. Chao, B. Chexal, T. Passell and J. Santucci, *The First Annual Conference on Cold Fusion*, 1990, University of Utah Research Park, Salt Lake City, Utah: National Cold Fusion Institute.
- [3] G. Lonchampt, L. Bonnetrain and P. Hicter, Reproduction of Fleischmann and Pons experiments, in *Progress in New Hydrogen Energy*, Vol. 1, *ICCF-6 Proceedings*, Lake Toya, Hokkaido, Japan, October 13–18, M. Okamoto (Ed.), 1996, pp. 113–120.
- [4] P.L. Hagans, D.D. Dominguez, and M.A. Imam, *Progress in New Hydrogen Energy*, 1996, Lake Toya, Hokkaido, Japan.
- [5] D.D. Dominguez, D.A. Kidwell, D.L. Knies, K.S. Grabowski, G.K. Hubler, J.H. He and V. Violante, *J. Cond. Mat. Nucl. Sci.* **8** (2012) 219–223.
- [6] B.F. Bush, Unpublished and unauthorized experiments at NAWCWD, China Lake, CA, 1991.
- [7] M. Fleischmann, Private communication, 1999.
- [8] M.H. Miles and M. Fleischmann, *ICCF-6 Proceedings* **1** (1996) 113–120.
- [9] M.H. Miles, M.A. Imam and M. Fleischmann, *ICCF 14*, Washington D.C., USA, 2008. See also M.H. Miles, M.A. Imam and M. Fleischmann, NRL/MR/6320-01-8526, March 26, 2001.
- [10] E. Yamaguchi and T. Nishicha, *Jpn. J. Appl Phys. (Part 2)* **29**(4) (1990) L 666.

- [11] A.G. Lipson, G.H. Miley, A.S. Roussetski, B.F. Lyakhov and E.I. Saunin, *Proc. 12th Meeting of Japan CF Research Society, JCF12*, December 17–18, 2011, Kobe University, Japan, pp. 293–303.
- [12] Y. Iwamura, M. Sakano and T. Itoh, *Jpn. J. Appl. Phys.* **41** (2002) 4642–4650.
- [13] Y. Iwamura, T. Itoh, M. Sakano, N. Yamazaki S. Kuribayashi, Y. Terada, T. Ishikawa and J. Kasagi, *11th Int. Conf. on Condensed Matter Nucl. Sci.*, 2004. Marseille, France.
- [14] Y. Arata and Y.C. Zhang, *Proc. Jpn. Acad. Ser. B* **78** (2002) 57.
- [15] Y. Miyoshi, H. Sakoh, A. Taniike, A. Kitamura, A. Takahashi, T. Murota and T. Tahara, *Proc. 12th Meeting of Japan CF Research Society, JCF12*, December 17–18, 2011, Kobe University, Japan, pp. 1–9.
- [16] A. Sendis, Desktop fusion of D₂ in palladium nano-particles loaded in zeolites, Senior Thesis, Chemistry Department, University of LaVerne, May 25, 2011.
- [17] O. Dmitriyeva, R. Cantwell, M. McConnell and G. Moddel, *10th Int. Workshop on the Anomalies in Hydrogen Loaded Metals*, Siena, 2012.



Research Article
Cold Fusion

Jean-Paul Biberian*

Aix-Marseille University, 163 Avenue de Luminy, 13288 Marseilles Cedex 9, France

Abstract

This paper is a review of the work which I have performed on the subject of *Cold Fusion* alone or in collaboration with other scientists. It covers a number of techniques such as solid-state electrolytes, electrolysis and gas diffusion. The experiments described below produced positive results. I also tried many other techniques that failed, which are not described.

© 2014 ISCMNS. All rights reserved. ISSN 2227-3123

Keywords: Cold fusion, Deuterium diffusion, Mass flow calorimetry, Multi-layers, Solid state electrolyte

1. Introduction

My interest in *Cold Fusion* started on the day the discovery was announced, March 23, 1989. However, since I am not an electrochemist, I did not begin working in this field until 1993 when I met Francis Forrat, an engineer at the French Atomic Energy Commission in Cadarache. Following this encounter, I started working with solid-state electrolytes. Later, I continued with many different techniques including electrolysis and gas diffusion. In this paper, I described my work in this field, which has continued almost 20 years.

2. Proton Conductors

When I met Forrat in 1993, I was at the Lawrence National Berkeley Laboratory working on two-dimensional surface structures, a subject not related to LENR. Forrat had filed a French patent on a cold fusion technique using solid-state electrolytes [1]. This non-liquid technique gave me the opportunity to engage myself in the field. On a non-official way, I began experimenting with LaAlO_3 single crystals with lanthanum vacancies. LaAlO_3 single crystals with lanthanum vacancies have red color, whereas the stoichiometric crystals are white. As predicted by Forrat, when the samples are loaded with hydrogen or deuterium, the red crystals with vacancies turn into white. This behavior indicates that the lanthanum vacancies are filled with hydrogen or deuterium. LaAlO_3 has a perovskite structure: when stoichiometric which is an insulator, when it has vacancies it becomes a high temperature proton conductor.

The calorimeter for the first experiments in Berkeley was very simple and therefore open to criticism. The red LaAlO_3 single crystal, about 2 cm^2 , 1.5 mm thick, was squeezed between two tantalum foil electrodes. This ensemble

*E-mail: jpbiberian@yahoo.fr

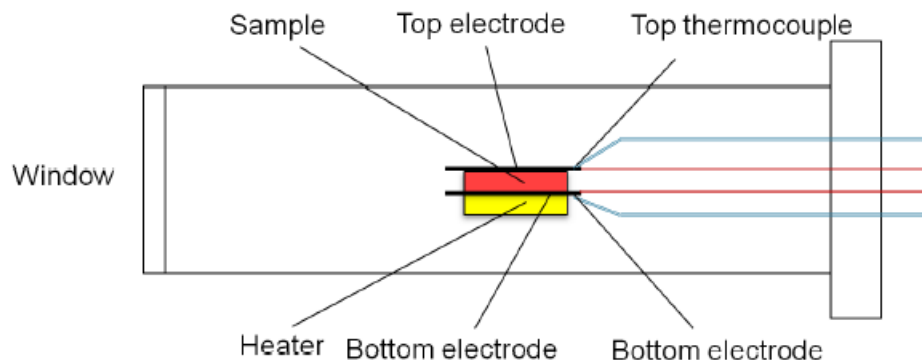


Figure 1. Chamber design].

was heated using a tungsten wire. Two thermocouples located on the bottom and the top electrodes measured the temperature of the sample. The system was positioned inside a 35 mm stainless steel chamber with electrical feed throughs on one side and a glass window on the other side. The chamber was evacuated with a mechanical pump down to 10^{-2} Torr, and filled with hydrogen or deuterium gas. Figure 1 shows a schematic of the set-up.

When a DC current was passed through the crystal, a deuterium concentration profile took place with more deuterium on the cathodic side than on the anodic side. The color of the crystal changes with the deuterium concentration. On the cathodic side it becomes blue, due to the overloading of the lanthanum vacancies with deuterium that generates F centers. The middle of the crystal becomes white, since all the vacancies are now filled with deuterium, and the anodic

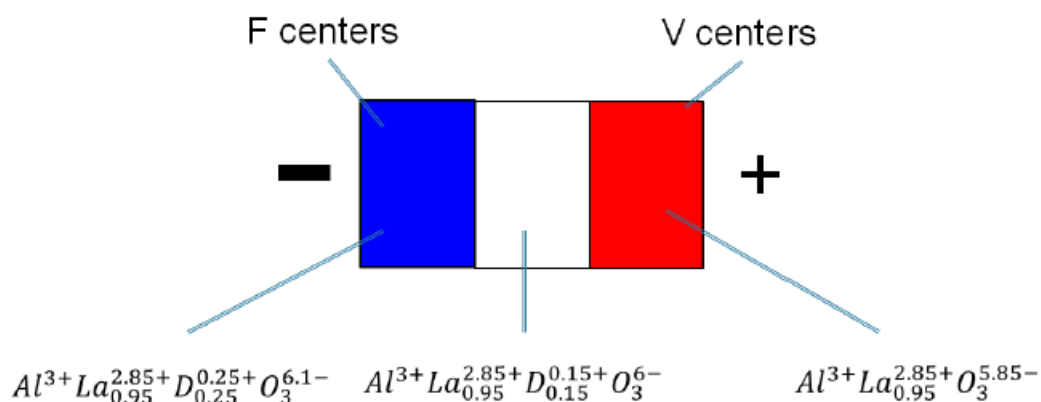


Figure 2. Sample colors during electrolysis.

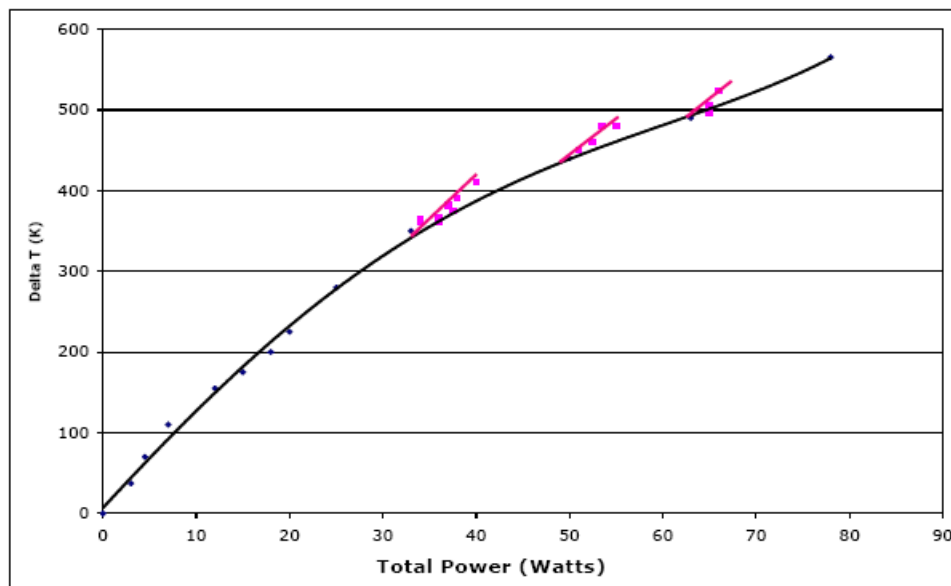


Figure 3. Bottom thermocouple temperature versus total power input.

side remains red, because there is no deuterium diffusing on this side of the crystal. Figure 2 shows the color changes of the crystal with the corresponding crystal compositions.

Figure 3 shows a typical result where the temperature difference between the bottom thermocouple and room temperature is plotted against total input power, which includes the heating power and the power delivered directly to the crystal. The curve without crystal current is plotted in black, and the curve with the added crystal current, in a deuterium atmosphere, is plotted in red. An additional temperature rise is observed when the crystal current is added, indicating excess heat. However, the experiments were only preliminary and were not published. In particular, I did not have a data acquisition system, and the data were recorded manually. Therefore, the measurements lacked precision.

These experiments were duplicated with Georges Lonchamp in Grenoble with a better calorimeter [2]. Figure 4 shows a schematic of the new design. In order to simplify the attachment of the samples, we used two identical crystals of LaAlO_3 with a common central cathode and two external anodes. The samples were placed inside a ceramic tube heated with a tungsten wire. The electrical power applied to the heater was maintained constant. When current was passed through the crystals, heat was produced and most of it passed through the ceramic tube. As the electrical power applied to the tube was constant, the extra heat changed the resistivity of the tungsten wire. By measuring the resistivity (voltage divided by current) of the tungsten wire, the heat generated by the crystals was calculated.

Figure 5 shows the production of excess heat. We performed experiments in constant current mode, and we observed “heat after death”, i.e. heat production that continued for almost 2 h after switching off the power supply. Based on this, we knew that constant input power was not necessary, so we changed to a pulsed mode, which gave excellent results. Every minute, we applied a 120 mW pulse lasting 1 s; this produced 150 mW of excess heat. The Coefficient of Performance (COP) was therefore 75!

These results were in agreement with the observations made by Mizuno et al. [3] with a different proton conductor crystal, but with similar crystallographic structures.

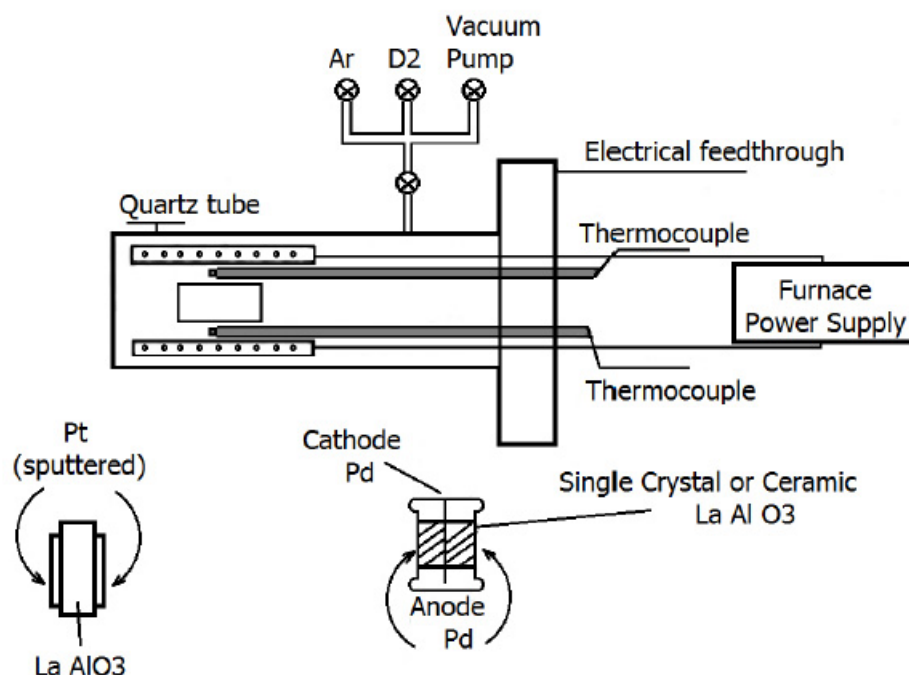


Figure 4. Schematic of the second chamber.

3. Patterson Type Experiments

Following James Patterson's work [4,5] showing excess heat and nuclear transmutation, we developed our own system [6]. The experimental set-up consisted of a cylindrical cell of 30 mm ID, with a nickel mesh cathode located at the bottom, and a platinum mesh anode at the top. The cathodic part of the cell was filled with 0.6 mm diameter beads; the anodic part was filled with ion exchange resins. The two compartments being separated by a nylon screen.

Three layers of nickel, palladium and nickel (about 1 μm each) were deposited on polystyrene beads pre-covered by a thin film of copper. The electrolyte (H_2O with Li_2SO_4) circulated through the cell, and the input and output temperatures were measured using two thermistors. Figure 6 shows a schematic of the whole system.

A blank experiment without electrolysis showed no excess heat, whereas during electrolysis excess heat was produced. The excess heat increased with increasing input power. However, the yield was the highest at low power. The excess heat was close to 100% at low power as shown in Fig. 7.

This experiment confirmed the results obtained by Patterson, but with a lower yield.

4. Pons and Fleischmann Boiling Experiments

In their original work, Fleischman and Pons [7] operated their cells below boiling temperature. Later, they let the cell go up to boiling, and by measuring the amount of water evaporated and the input electrical energy, they calculated the amount of excess heat produced [8,9]. In Grenoble we reproduced this type of experiment with success [10]. Figure 8

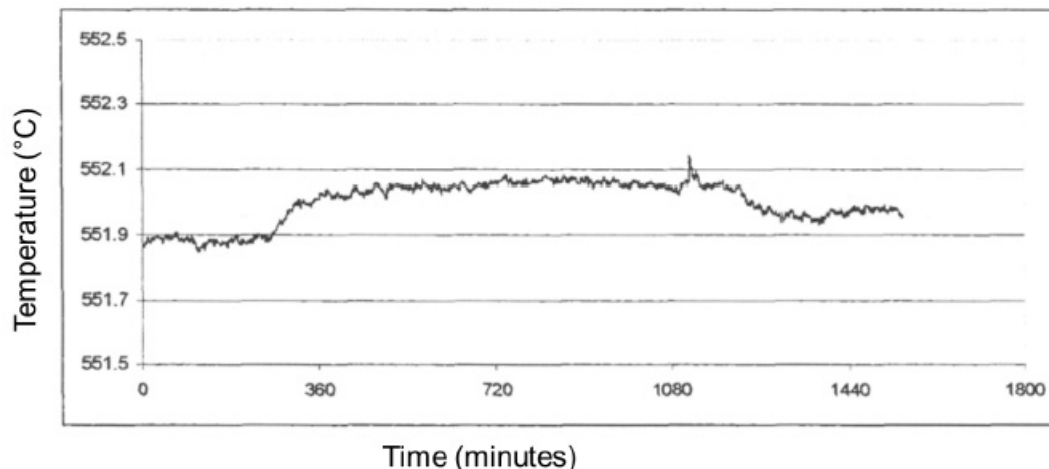


Figure 5. Temperature rise versus time. Input power: 2 mW (120 mW 1 s pulse every 60 s). Output power: 150 mW.

shows a schematic of the cell, which is identical to the one used by Fleischmann and Pons.

We measured excess heat up to 29% at boiling temperatures (see Table 1). This is in qualitative agreement with Fleischmann and Pons. However, the magnitude of the excess heat measured was less important than what they observed. Their analysis of the boiling off in two periods, assuming that the vast majority of the excess heat was produced at the end of the experiment, was difficult to evaluate.

As shown in Table 1, the experiments with Li_2SO_4 are surprising since they show that the palladium is more active, and that even platinum is active.

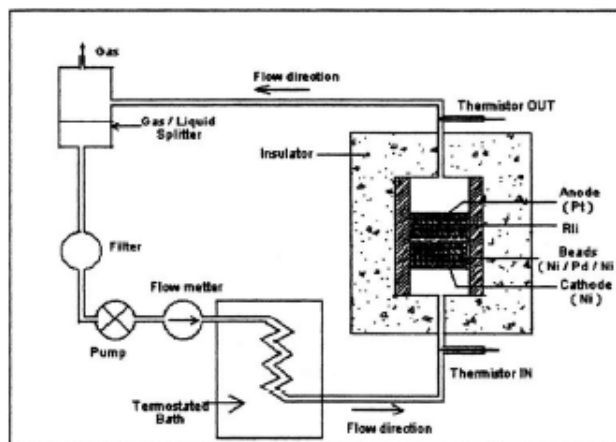


Figure 6. Schematic of the operation of the cell.

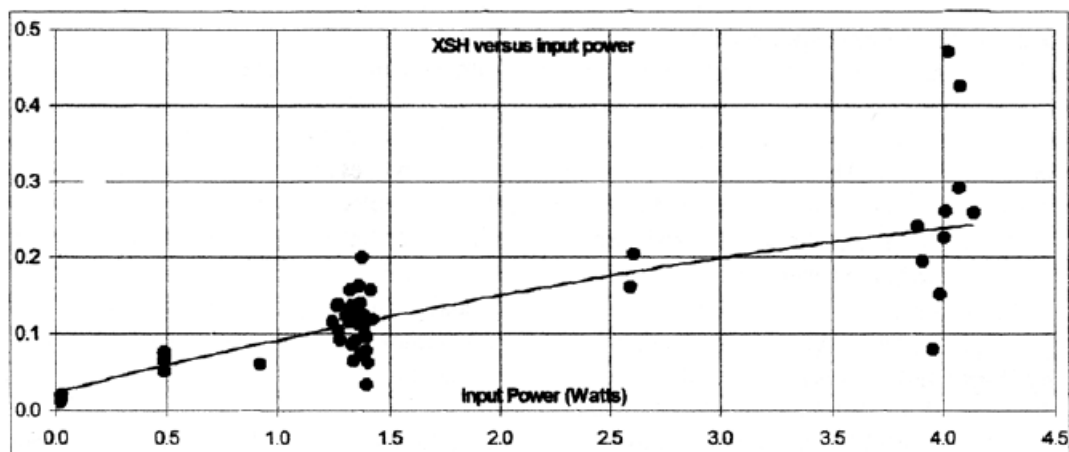


Figure 7. Excess heat versus input power (W).

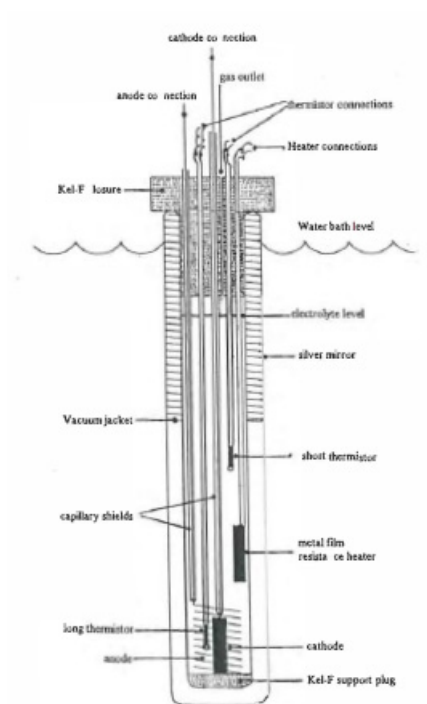


Figure 8. ICARUS II type cell.

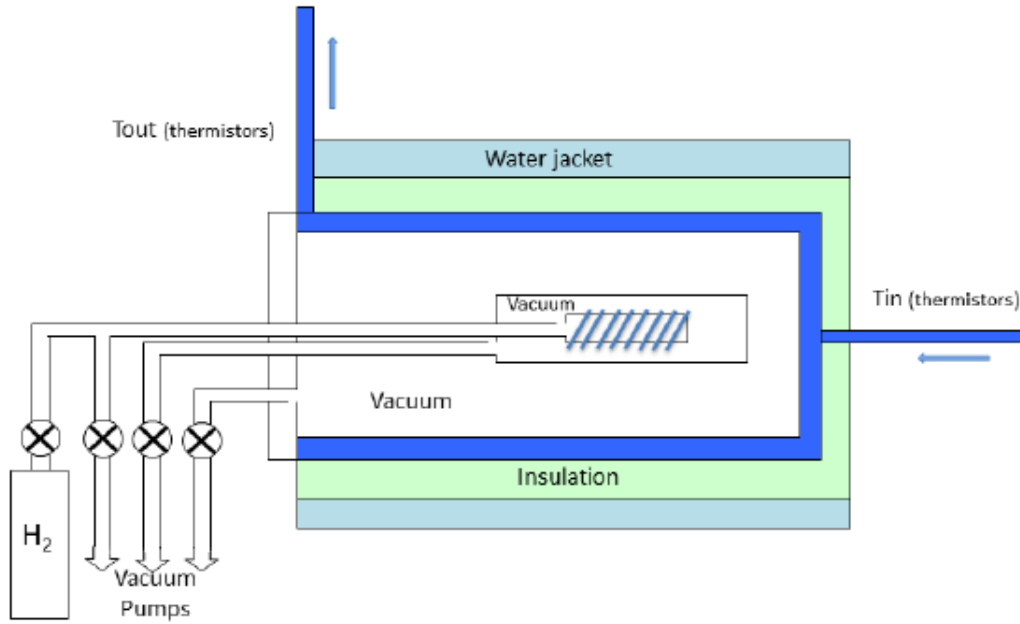


Figure 9. Mass flow calorimeter.

5. Diffusion of Deuterium through Palladium

In 1989, Fralick et al. [11] showed that when deuterium is pumped out from palladium tubes, a temperature rise is observed, whereas the same experiment with hydrogen showed no temperature change. It was therefore tempting to run a similar experiment with a method which allows continuous operation [12].

The experiment was performed in a mass flow calorimeter as shown in figure 9, where the thermal power was

Table 1. Excess heat in boiling cell

Boiling experiments in LiOD					
Cell P2			Cell P3		
Experiment	Cathode	XSH (%)	Experiment	Cathode	XSH (%)
88	Pt	0	93	Pt	0
90	Pd	12	96	Pd–Rh	8
91	Pd	20	97	Pd	7
95	Pd–Ce	5		Pd Li_2SO_4	9
98	Pd	14	99	Pd	14
107	Pd 1 mm	5	106	Pd–Pt–Cu	11
109	Pd	12	108	Pt	0
111	Pt	0	112	Pd	0
115	Pd	15	114	Pd	29
	Pd Li_2SO_4	13		Pd Li_2SO_4	0
			116	Pd wire	9



Figure 10. Palladium tube and external part of the calorimeter.

determined by measuring the temperature difference between output and input temperatures and the water mass flow. The palladium tube was 10 cm long and 2 mm in diameter closed at one end. See Fig. 10. The deuterium gas was introduced in the tube and diffused out through the walls of the tube in the vacuum chamber.

Figure 11 shows a 12-day experiment showing that the output power is lower than the input power when no deuterium is introduced in the tube, whereas the opposite happens when deuterium is introduced and diffuses through the palladium walls of the tube. An average of 4 W of excess power was measured with input power of 48 W for the tube heater.

6. Mass Flow Electrolysis Experiments

Isoperibolic calorimetry needs calibration; therefore it was tempting to develop a mass flow calorimeter for electrolysis experiments that measures the thermal power without depending on calibration. This is the reason I developed a mass

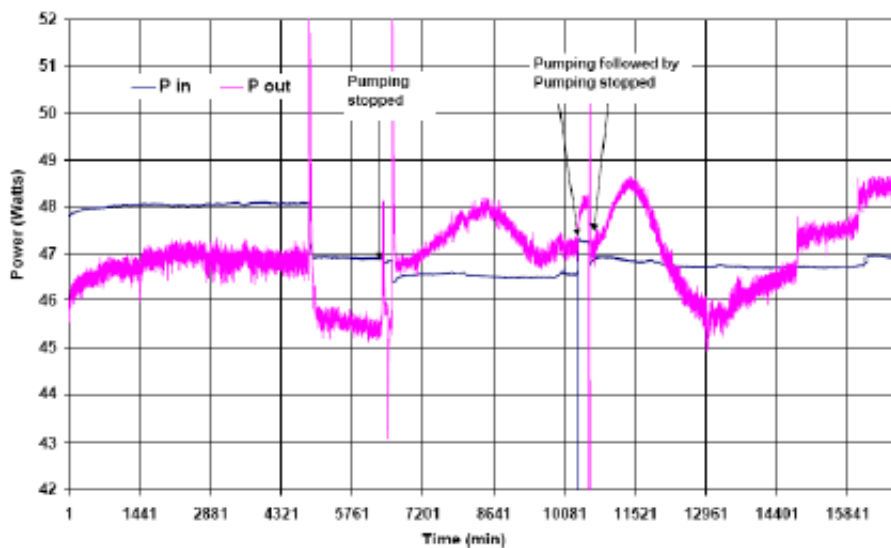


Figure 11. Input and output power versus time.

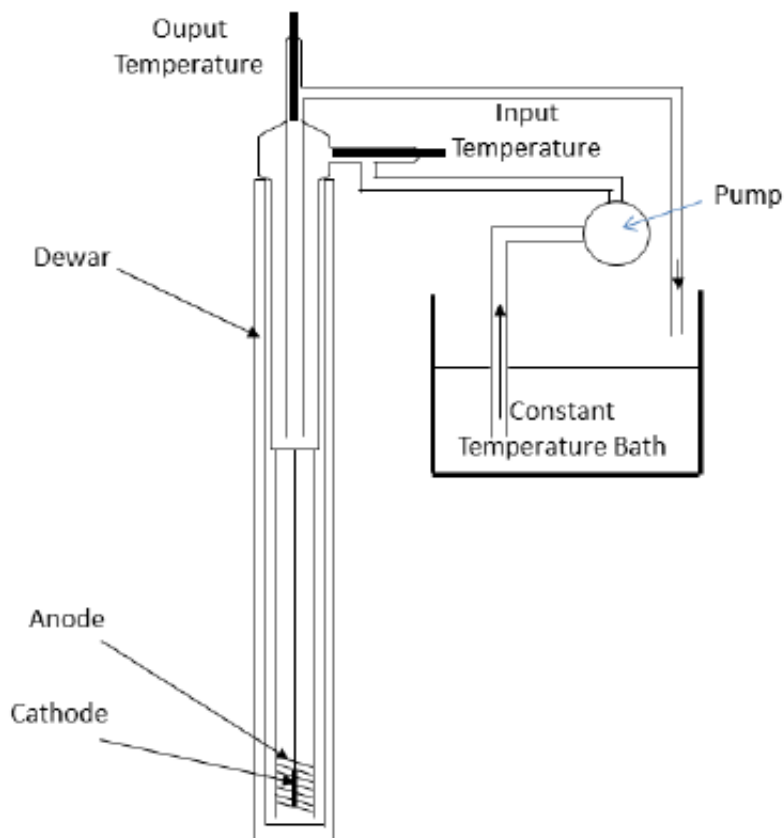


Figure 12. Mass flow calorimeter for electrolysis.

flow calorimeter that can operate up to boiling temperatures.

Figure 12 shows a schematic of the flow calorimeter. The cell is composed of a 50 cm long, 2.5 cm inner diameter Dewar. The palladium cathode is at the center of the cell, and the platinum anode wrapped around four glass rods. The water vapor condenses in a glass condenser positioned at the top of the cell. Cooling water from a constant temperature bath flows through the top portion of the cell at 100 ml/min.

Figure 13 shows a comparison between a set of experiments in light water and heavy water, both with a palladium cathode 12 mm long and 2 mm in diameter. The difference between the two sets of curves is about 20%, indicating excess heat of 20%.

7. Cell Explosion

In an attempt to replicate the results obtained with the palladium tube as described in Section 5, the 12 mm cathode was replaced by a palladium tube 10 cm long, 2 mm diameter, closed at one end [13]. Figure 14 shows the input and

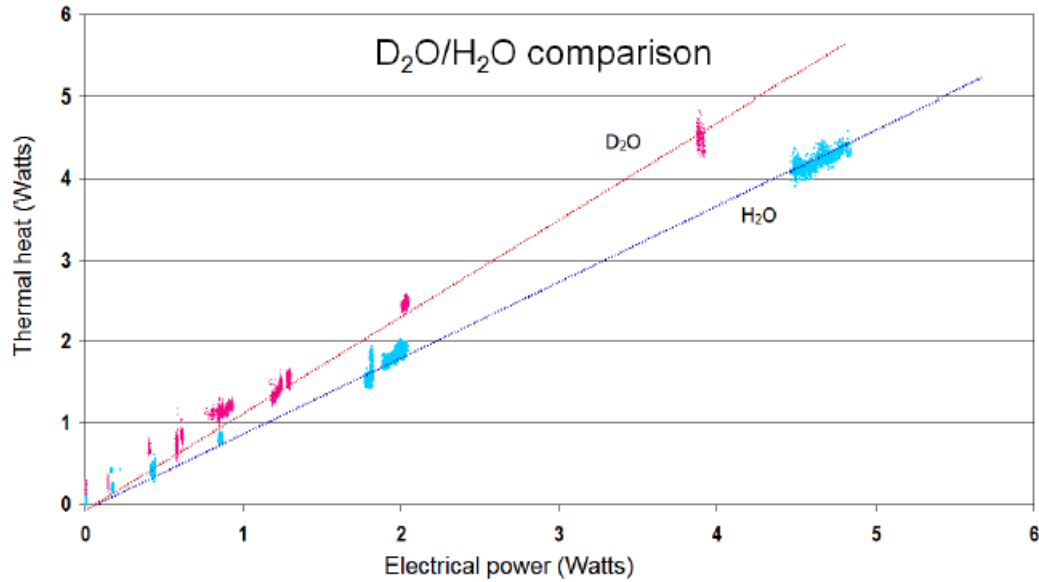


Figure 13. Comparison of experiments in light water and heavy water.

output power versus time. Up to hour 401 excess heat of a few watts appeared periodically (excess is $P_{in} - P_{out}$). Soon after hour 701, an explosion occurred.

Figure 15 shows the remains of the bottom of the cell after the explosion. Glass fragments were scattered meters

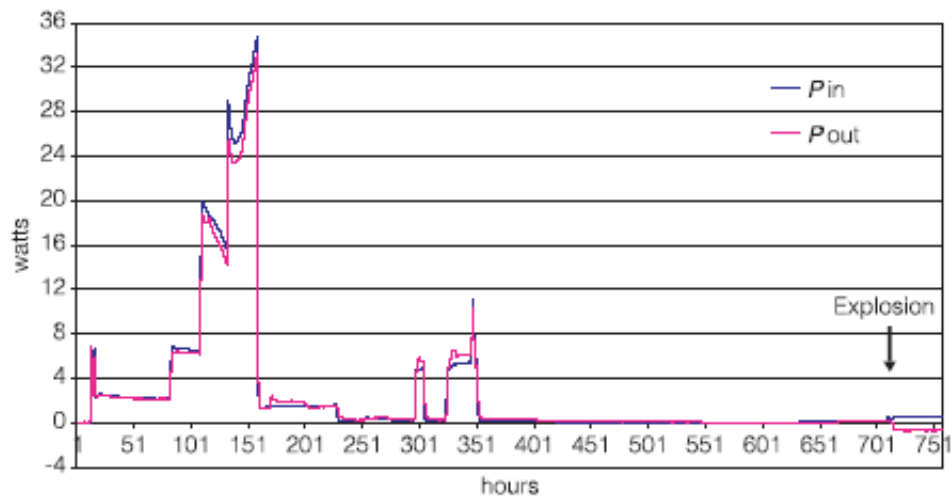


Figure 14. Power in and out versus time before the explosion.



Figure 15. Broken cell after the explosion.

away.

Figure 16 shows both the original Dewar and the broken interior of the cell with the cathode and anode. The cell was not sealed, so a deuterium-oxygen recombination explosion could not have broken the Dewar. To check this hypothesis, several explosions were deliberately triggered after adding a stoichiometric mixture of hydrogen and oxygen to a cell. No damage occurred to the cell as a result of these tests. It is therefore possible that in this case the explosion was of nuclear origin: some kind of chain reaction.

8. Conclusion

In this paper, I have reported several experiments that produced excess heat using various techniques. Some, such as the solid-state electrolyte experiments, had large COP, but low heat. On the other hand, deuterium diffusion experiments



Figure 16. Interior of the cell after the explosion.

showed larger excess heat, but a lower COP.

In this paper, I did not mention the collaboration with Roger Stringham and Russ George in sonofusion experiments. The results were very positive and interesting.

In addition to the positive work, I have performed many experiments which were negative with no excess heat.

Acknowledgements

I wish to acknowledge all the people who have participated in this work: Francis Forrat, Georges Lonchampt, Lucien Bonnetain and Nicolas Armanet.

References

- [1] F. Forrat, Réacteur pour fusion nucléaire électrolytique, French Patent, number FR 2647943, 1989.
- [2] G. Lonchampt, J.P. Biberian, L. Bonnetain and J. Delépine, Electrolysis of LaAlO_3 single crystals and ceramics in a deuterated atmosphere, *The Seventh Int. Conf. on Cold Fusion*, 1998, Vancouver, Canada, ENECO Inc., Salt Lake City, UT, p. 27.
- [3] T. Mizuno, T. Akimoto, K. Azumi, M. Kitaichi and K. Kurokawa, Excess heat evolution and analysis of elements for solid state electrolyte in deuterium atmosphere during applied electric field, *J. New Energy* **1**(1) (1996) 79.
- [4] J.A. Patterson, Systems for electrolysis, US patent #5,494,559, 27 Feb. 1996.
- [5] G.H. Miley and J.A. Patterson, Nuclear transmutations in thin-film nickel coatings undergoing electrolysis, *J. New Energy* **1**(3) (1996) 5.
- [6] G. Lonchampt, J.P. Biberian, L. Bonnetain and J. Delépine, Excess heat measurement with Patterson type cells, *the Seventh Int. Conf. on Cold Fusion*, 1998, Vancouver, Canada.
- [7] M. Fleischmann, S. Pons and M. Hawkins, Electrochemically induced nuclear fusion of deuterium, *J. Electroanal. Chem.* **261** (1989) 301 and errata in Vol. 263.
- [8] M. Fleischmann and S. Pons, Calorimetry of the $\text{Pd-D}_2\text{O}$ system: from simplicity via complications to simplicity, *Phys. Lett. A* **176** (1993) 118–129.
- [9] M. Fleischmann and S. Pons, *The Third Int. Conf. on Cold Fusion*, Nagoya, Japan, Universal Academy Press, Tokyo, 1992, p. 47.
- [10] G. Lonchampt, J.P. Biberian, L. Bonnetain and J. Delépine, *The Seventh Int. Conf. on Cold Fusion*, 1998, Vancouver, Canada, ENECO Inc., Salt Lake City, UT, p. 202.
- [11] G.C. Fralick, A.J. Decker and J.W. Blue, Results of an attempt to measure increased rates of the reaction $2\text{D} + 2\text{D} \rightarrow {}^3\text{He} + \text{n}$ in a nonelectrochemical cold fusion experiment, NASA Technical Memorandum, 1989.
- [12] J.P. Biberian and N. Armanet, Excess heat during diffusion of deuterium through palladium, *ICCF13 proceedings*, 2007, Sochi, Russia, pp. 170–180.
- [13] J.P. Biberian, Unexplained explosion during an electrolysis experiment in an open cell mass flow calorimeter, *J. Cond. Mat. Nucl. Sci.* **2** (2009) 1–6.



Research Article

Cu–Ni–Mn Alloy Wires, with Improved Sub-micrometric Surfaces, Used as LENR Device by New Transparent, Dissipation-type Calorimeter

Francesco Celani^{*,†}, E. F. Marano, B. Ortenzi, S. Pella, S. Bartalucci,
F. Micciulla and S. Bellucci

National Institute of Nuclear Physics, Frascati National Laboratories, Via E. Fermi 40, 00044 Frascati (RM), Italy

A. Spallone, A. Nuvoli, E. Purchi, M. Nakamura, E. Righi,
G. Trenta and G. L. Zangari

ISCMNS, Latium1 Group, Via Cavour 26, 03013 Ferentino (FR), Italy

A. Ovidi

Kresenn Ltd., 5a Frascati Way, SL6 4UY Maidenhead (Berkshire), UK

Abstract

Starting in February 2011, we studied the feasibility of new nickel-based alloys that are able to absorb significant amounts of hydrogen (H_2) and/or deuterium (D_2) and might, in principle, possibly generate anomalous thermal effects at temperatures $> 100^\circ C$. The interest in Ni alloys comes in part because there is the possibility to use H_2 instead of expensive D_2 . Moreover, a cross-comparison of results using H_2 instead of D_2 can be made and could help the understanding of the phenomena involved (and the possible nuclear origin).

© 2014 ISCMNS. All rights reserved. ISSN 2227-3123

Keywords: Calorimeter, LENR, Nickel-based alloys, Sub-micrometric surfaces

1. An Old Alloy Used For New Purposes

Based on some theoretical considerations, and thanks also to some sentences in a paper on catalysis not related to LENR studies [1], we decided to explore the possibility of using Ni–Cu alloys (including Constantan) as starting material that could fit our purposes.

^{*}E-mail: francesco.celani@lnf.infn.it; Also the personal e-mail: franzcelani@libero.it

[†]Also at: ISCMNS, Latium1 Group, Via Cavour 26, 03013 Ferentino (FR), Italy

One of the merits was, according to us, the ability to dissociate H_2 . One of the Ni–Cu alloys ($Ni_{37}Cu_{63}$), among the materials studied in [1], has the highest disassociation value (3.2 eV; in comparison, pure Ni and Pd have values of 1.74 and 0.42 eV, respectively). Moreover, even with large changes (a factor of about 2) in the relative atomic amounts of Ni with respect to Cu (i.e. from 0.37 to 0.62), the dissociation values remain at quite high levels (from 3.16 decreasing to 2.86 eV).

We focused on a commercial low-cost material, brand name ISOTAN®, CuNi44. The mass components in percent are $Cu_{55}Ni_{44}Mn_1$. This material was developed several years ago by Isabellenhutte Heusler, GmbH, KG-Germany. ISOTAN® was selected based on the following considerations, as we pointed out in April 2012, Ref. [2].

A. A measurable diffusion coefficient of hydrogen, even in the pure (not alloyed) elements, i.e. copper and nickel, at high temperatures: $Cu = 10^{-6} cm^2/s$ at $200^\circ C$, $10^{-4} cm^2/s$ at $700^\circ C$; $Ni = 10^{-7} cm^2/s$ at $200^\circ C$, $10^{-6} cm^2/s$ at $350^\circ C$. In comparison, good values for Pd are: $10^{-5} cm^2/s$ at $200^\circ C$, $10^{-4} cm^2/s$ at $420^\circ C$; at $600^\circ C$ reported values are as large as $8 \times 10^{-3} cm^2/s$, but are not reproducible. We suppose that the “flux” of H_2 or D_2 inside the lattice and/or near surface (either longitudinal or transversal) is one of the key factors needed to generate anomalous effects. Our opinion is based on the experimental observation that the anomalous effects increase with the increasing of R/R_0 value oscillations, i.e. loading and de-loading of hydrogen or deuterium.

B. Lower cost, overall, even considering the procedure to “build” nano-structured at the surface, compared to palladium, which is a very expensive precious metal.

C. This material has good mechanical properties and resistance to aging effects caused by cycles of both low→high→low temperatures, and cycles of H_2 absorption–desorption. Our first sample, (“generation one”) was used in a long duration experiment lasting for over 7 months; only after such a long time did we observe the beginnings of serious damage. Our results are, in that respect, different from those obtained by Szafranski [3]. He observed extreme brittleness in as-received Cu–Ni alloy that was only cold rolled from 200 to 20 μm . (Note that the penetration depth of H into Ni is about 30 μm .) His material was then cycled between 77 and 300 K under 1 GPa pressure of H_2 . We can only suppose that that high temperatures and/or adding manganese at 1% has the beneficial effect of reducing brittleness. We have never done experiments at 77 K, so it is difficult for us to judge.

D. Extremely large values of (computed) catalytic power (ΔE) in respect to the dissociation of H_2 [1], as shown in Table 1.

E. The possibility, at least in principle, of producing nano-micro structures (and voids) both at the surface and deeper into the bulk, with selective oxidation of Cu in such alloys at high temperatures (650 – $1050^\circ C$). Both segregation of pure Ni among to CuOx and the cooling rate are key aspects of the preparation need to be studied in deeper detail, even though we spent a lot of time and money investigating them.

Our exploratory studies were devoted to finding simple and reliable/reproducible procedures to get these kinds of structures. Experiments with the selected material were operated to last as long as possible: including “strength” and aging tests.

2. Sample Preparation (Procedures Used for the Experiment up to May 2012, “Generation One”).

Similar Composition Materials, All Nanometric, Developed Independently in Japan

In our exploratory preparations and tests, we used standardized wires: $\Phi = 200 \mu m$, $l = 105 cm$. Weight (307.4 mg enameled), Φ and resistance (17.16Ω) were carefully measured. The resistance measured in this batch was 5% higher

Table 1.

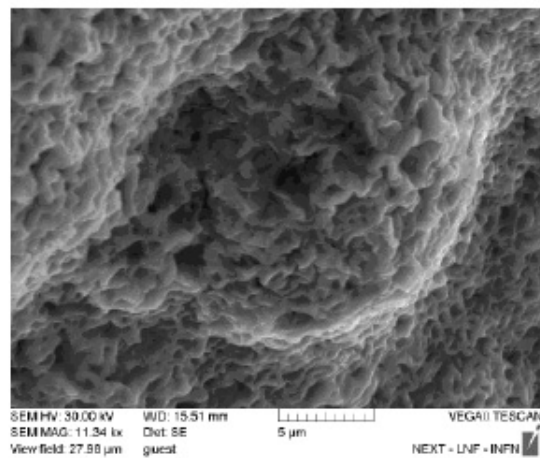
Alloy materials	Dissociation value (eV)
Ni0.3750–Cu0.6250	+3.16
Ni0.6250–Cu0.3750	+2.86
Ni0.8125–Cu0.1875	+2.10
Ni	+1.74
Ni0.1825–Cu0.8175	+1.57
Ag0.8125–Pd0.1875	+0.57
Ag0.625–Pd0.375	+0.51
Ag0.1875–Pd0.8125	+0.51
Pd	+0.42
Cu	–1.11
Ag	–1.42

than the nominal values reported by the manufacturer. We suppose the difference is related to iron impurities, which we detected by SEM-EDX analysis.

We point out that, although very promising results were obtained with pure Constantan, in our explorative test under H_2 gas (2–3 days of operations each, from February to June 2011), we *never* observed any type of anomaly, such as changing resistance, on wires with Joule heating up to 900°C under the following experimental conditions:

- (1) As received from the company (which we designate *ultra-virgin*); maximum temperature about 150°C .
- (2) With the enamel protection on the surface completely removed by burning up to 600°C in air, and stress released.
- (3) Acid etching of wire after treatment 2.

The wires in condition 2 at first were just “cleaned-up” with the original enamel insulating layer removed. This was done with Joule heating in air current up to 2000 mA, time 5 min.



SEM. Wire's surface after heat treatments at $I=2500\text{mA}$, 5m.

Figure 1. Wire surface after enhanced heat treatment, generation one experiments.

In these conditions, the power dissipated was about 70 W and the resistance ratio, with respect to the reference value at 100 mA of current, increased only 1%. This is expected for this type of material (which has the commercial name Constantan, i.e. constant resistance). After the first thermal treatment, the weight decreased by about 13 mg, the resistance decreased from 17.16 to 17.02 Ω .

We found that increasing both the current (up to 2500–3000 mA) and the duration at high power (5–1000 s), decreasing the cooling speed (from 100 s down to <1 s) had dramatic effects on the growing of nano-microstructures and their dimensions (see e.g. Fig. 1). The role of O_2 and H_2O , because of open air treatments, is important. The wire temperature, in some tests, was even larger than 1000°C (rough evaluation by color temperature; the melting point of pure copper in inert gas is 1083°C, and the melting point of ISOTAN® is 1280°C).

The quality of the wire produced by this method was evaluated by SEM observations. We determined that the better methods of preparation resulted in smaller particles at the surface, and a larger mass of particles compared to the mass the whole wire (i.e. the core).

The best material, we were able to produce at the end of July 2011 using DC thermal treatments, was put in our flow calorimeter (which has uncertainty of only 2%).

As previously noted, this material was extensively studied both in H_2 and D_2 gas as well as in calibrations and tests in helium, argon, air and in vacuum. The total time of experiments was quite long (about 10 months) and only toward the end of the tests, after 7 months, the damage to the wire increased to such an un-controlled level that it prevented reliable interpretation of the experimental results. These results were discussed in detail during the “X International Workshop...”, April 2012 [2].

Key information: we were happy to learn that Akito Takahashi (Osaka University) and Akira Kitamura et al. (Kobe University) studied in secret (as we did) an alloy of Ni–Cu. In their case, most of the materials were at nanometric size, i.e. 5–20 nm dispersed in an inert matrix of ZrO_2 . This work was performed in collaboration with Technova, a Toyota research group. We received brief information by them at the end of December 2011 about promising results from a specific alloy $(Ni_{85}-Cu_{15})_{35\%}-(ZrO_2)_{65\%}$ (for details see Ref. [4]).

We note that such material is a further development of the nanomaterial $Pd_{35\%}-ZrO_2_{65\%}$ made by Yoshiaki Arata at Osaka University since 2005. This material is made with complex melt spinning and quenching (cooling rate $>10^5$ °C/s) process.

Brief information about Ni–Cu– ZrO_2 came to my (FC) attention, for the first time, at the end of December 2011. I was invited to give a review talk on *Anomalous Effects in LENR Studies*, at the WSEC 2012 conference (January 10–12, 2012; Geneva) organized by the ISEO (Non-Governmental Organization cross-related to UN). I requested that everybody involved in LENR studies, worldwide, communicate the most recent and interesting results to include in the Review. Only Takahashi and Kitamura had performed experiments with Ni–Cu alloys and give permission to share their results, even though these results were qualitative and preliminary. A similar talk, with more technical and scientific details, was given at CERN (Geneva) on March 22, 2012 in the framework of the prestigious CERN Colloquium [5]. The overall behavior of Ni–Cu alloys, although at different ratios of the two main elements in response to H_2 and D_2 absorption, even with different geometrical shapes (powders used by the Japanese groups, wires from us) and amount of anomalous heat detected, were qualitatively similar.

Such evidence reinforced our intention to develop a better material from the point of view of nano-dimensionality, keeping the starting Ni–Cu composition “fixed”. Our efforts were devoted to increase the amount of active material at low dimensions (<100 nm) and, at the same time, reduce the adverse effect of “leakage” of the smallest particle from the surface due to: vacuum conditions, temperature cycling, loading, de-loading, etc.

3. New Transparent, Dissipation-Type Calorimeter

From the end of May 2012, we were able to produce sub-micrometric materials. Based on SEM observations, we expected performance several times better than the best material produced at the end of July 2011, with enough good reproducibility in the preparation procedures.

The new method, although similar to the old one in some key aspects, was really revolutionary in the practical parameters of mechanical stability (reduced leakage of the “good” material from the surface); and in the fraction of material at low dimensionality. The latter increased from 1 to 2% (*generation one*) up to about 30% of the whole material (*generation two*).

Such big improvements were obtained thanks to large financial help and man-power of an Italian company that “believed” in our previous results. We were able to design and build specific electronics and a mechanical set-up to produce sub-micrometric wires. Systematic, albeit very tedious and expensive experimental work was the key factor for success.

One of our goals was to see with the naked eye whether the wire was really stable in the rate of leakage of “good” materials even after several cycles of low→ high→ low temperatures and H₂ loading and de-loading. To this end, we build a new transparent reactor with borosilicate glass (Schott DURAN) of large (3 mm) wall thickness enough to withstand large pressure drops (up to 8 bar), at internal wall temperatures up to 280°C.

For the calorimetric measurements, we adopted the simplified approach of measuring the temperature on the outside of the glass wall. Taking into consideration the temperature of interest, i.e. $T_{\text{wall}} > 140^\circ\text{C}$, one of the main channels of heat exchange to the environment is heat radiation. In other words, we can use the Stefan–Boltzmann law:

$$P_{\text{out}} = \varepsilon \times 5.67 \times 10^{-8} \left(T_{\text{wall}}^4 - T_{\text{room}}^4 \right) \left[\frac{W}{m^2} \right]. \quad (1)$$

In this formula the temperatures T are in K and ε (the emissivity) is about 0.9. Calibrations were made using our usual procedure to add an “inert” wire, very close to the “active” one, and to make several measurements with inert gases. In the specific new set-up, the wires were parallel, alternatively and helicoidally shaped, with 22 turns. They were stepped through a range of input power levels in different gases (helium, argon and in a vacuum). Electric power was applied alternatively to the inert Ni–Cr wire and then to the active Constantan wire.

Because in our experimental set-up the geometrical dimension of the cell is constant (glass tube, external diameter 40 mm, internal diameter 34 mm, overall length of 280 mm and central active length of 100 mm), we can make a sort of simplified calibration curve just dividing formula (1) by the input power. Obviously, we neglected the contribution to heat dissipation by free air convection (which is 5–35 W m² K, in usual environments, at 12–15 W). We note that in the temperature range of our interest (internal cell 250–350°C), the thick borosilicate glass behaves like a black-body for the wavelengths of interest ($> 2.5 \mu\text{m}$). Moreover, the effects of pressure variations *inside* the reactor chamber, with related temperature variation due to different convection values (i.e. the internal temperature increases versus pressure decreasing), can be neglected at the external wall. Tests were performed in helium by varying the pressure between 6.5 and 2.5 bar. These tests were made at the beginning of the experiment, when the wire was new and the reactor glass wall “clean,” and again after a few months, when the wire was used and the glass wall lightly “dirty.”

4. Results with the New Wires (*generation 2*)

At the end of May 2012 two wires were produced: an old batch (with iron) with new procedures (*generation two*).

The first one was used a few days later to the experiment, the second one was just put inside a HDPE envelop and kept closed at Room Temperature (RT). We designated the experiments:

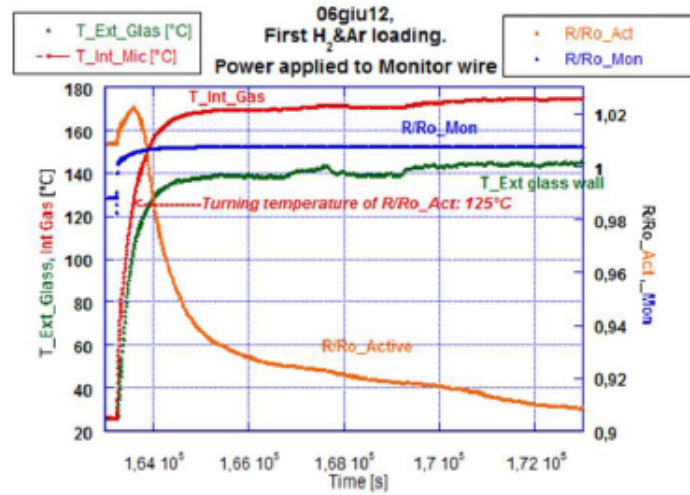


Figure 2. Details of first loading by H₂–Ar mixture.

[a] wire#1 (started in 06 June 2012);

[b] wire#2 (started in 10 July 2012).

The main improvements with respect to the previous procedure of fabrication, according to SEM observations, were multilayered structures, and total number of such layers, “which was extremely” large: “on” the order of 700. The thicknesses, of each multi-layers, were in the range of 20–100nm. The mechanical stability, against leakage of sub-micrometric materials, was improved.

The primary experimental procedures and results are as follows:

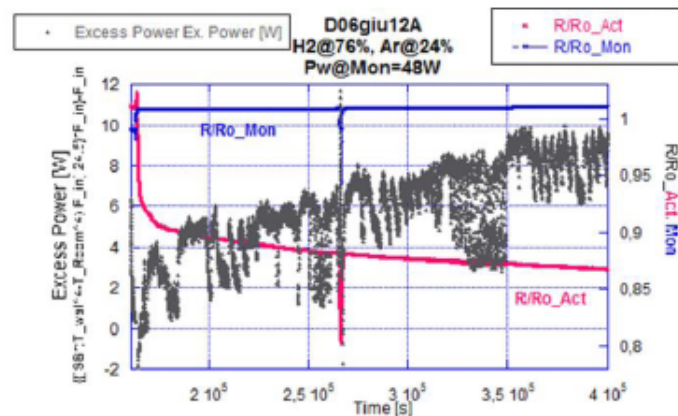


Figure 3. Behavior of anomalous power generation, using indirect heating, i.e. power (48 W) applied to Monitor wire.

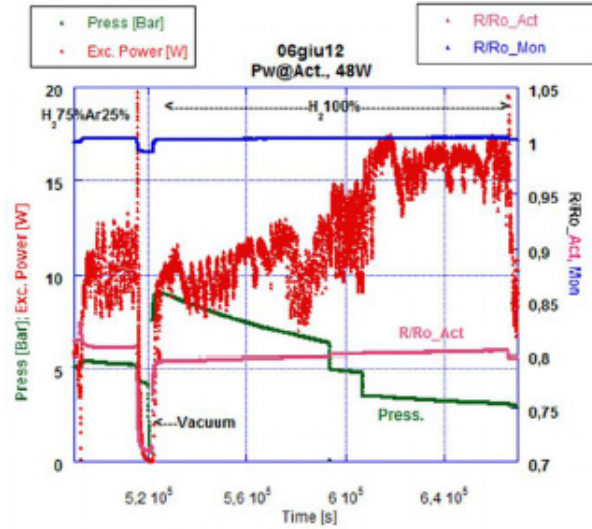


Figure 4. Experiment with 48 W applied to the active wire. Up to time 518 ks the gas mixture was H_2/Ar at a 75/25 ratio. Later, the power was reduced to zero and the cell was evacuated. The R/R_0 ratio was as low as 0.71. At time 522 ks pure H_2 was added: the excess power resumed, at the same level it was before the cell was evacuated. After a controlled reduction of pressure, excess power increased up to 16 W.

- (1) In order to use simple parameters easy to be managed by calculations, we adopted the usual term of R/R_0 . R_0 is the initial value of resistance at room temperature, i.e. at $23.5^\circ C$ (in that calibration), in a free air atmosphere, inside the reactor. With our wires ($l = 100$ cm) we measured, in situ ($I-V$ methods), a value of resistance of 16.9684 and 57.4394 Ω , respectively, for sub-micro_Costantan and Ni-Cr (presumably inert) wires. The

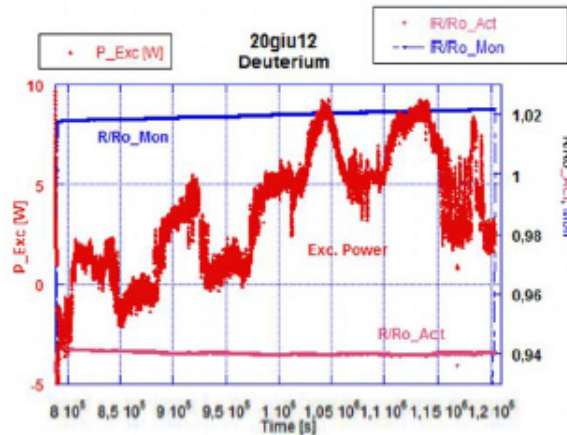


Figure 5. Experiments under D_2 gas. From the beginning, continuing for about a day, the reaction was endothermic; it later crossed the zero line and began to be exothermic, as it usually is with H_2 .

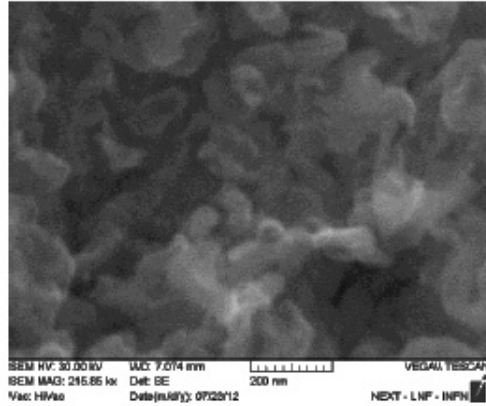


Figure 6. SEM after long H_2 interaction at HT. Experiment #1.

measuring currents were just 4 mA, to avoid self-heating of the wires.

- (2) We began the tests by calibrating with inert gases at the power levels of 5, 15, 30 and 48 W applied to the inert wire. The maximum internal temperature of the chamber was of the order of 180–250°C, depending on the gas composition and its pressure. Some tests, as cross references, were made with the active wire. Using the values of temperatures measured outside the glass cell and ambient it was possible to evaluate the “power exchange constant” (°C/W) of the small reactor by (1).
- (3) After adding a H_2/Ar mixture (75/25 ratio) at 7 bar of total pressure, while monitoring with the resistance ratio R/R_0 of both the active and inert wires, 48 W of power was applied to the inert wire. It was found (Fig. 2) that when the temperature inside the reactor was larger than 125°C, the resistance ratio of the active wire, after a very limited increase to 1.02, dropped to 0.92 at 2500 s. Later on, at about 100,000 s, the R/R_0 decreased to 0.88. We observed a correlated increase of anomalous excess heat, which was quite unstable with the R/R_0 decreasing. The temperature inside the cell was about 180°C.

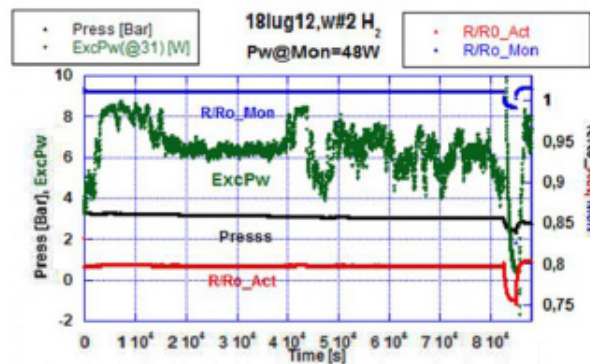


Figure 7. An example of anomalous heat from wire #2.

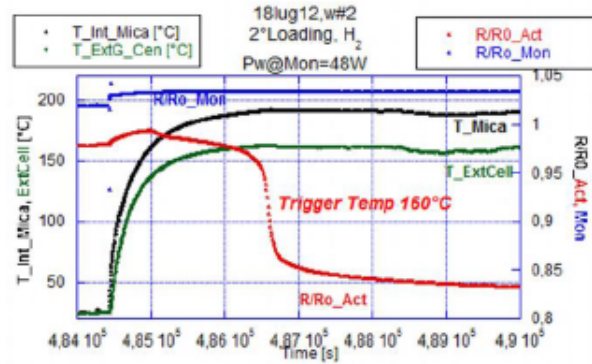


Figure 8. Behaviour of first re-loading of wire #2.

- (4) After 103,000 s (29 h) from the beginning (Fig. 3), we stopped the power to the inert wire and allowed the reactor and the wires to cool to room temperature. The R/R_0 value of the active wire decreased to 0.80.
- (5) Just after that, we powered the inert wire at the same power level and another 150,000 s (42 h) after the interruption we measured an R/R_0 value of 0.867. The anomalous excess power increased further (Fig. 3), in a way that, at a first observation, depends mainly on the time lasted and not to the R/R_0 value (low decrease). The instability of excess power, assuming there were no other uncontrolled parameters distorting it, had values quite large and was correlated to the small oscillations ($<1\%$) of R/R_0 values.
- (6) We observed that even the instabilities of room temperature (usually $23\text{--}27^\circ\text{C}$) helped anomalous heat production in some ways. We speculate this was because these instabilities introduced non-equilibrium conditions. To avoid errors in the interpretation of results, after a sufficiently long time, we note that the values of room temperature were the same as at the start of the experiment, while the anomalous heat increased over time.
- (7) The long-lasting positive effect with H_2 gas was also observed by the Takahashi and Kitamura groups (reports at X Pontignano Workshop and [4]). Depending on their conditions, constraints and materials, during 2-week

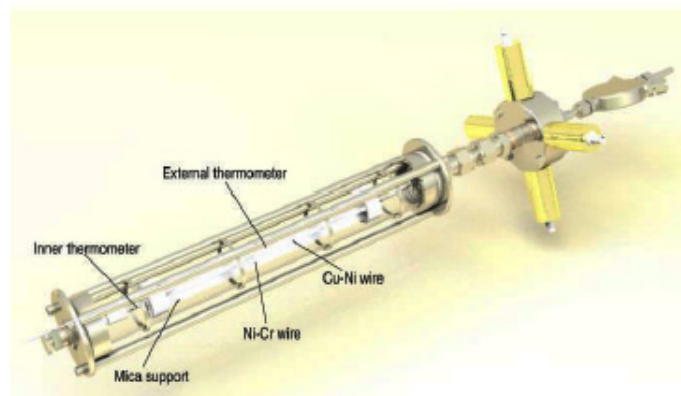


Figure 9. Schematic of the cell assembly.

- long experiments, the anomalous excess power slowly increased from 0 up to 3 W.
- (8) We observed that the minimum cell temperature at which anomalous heat is observed is around 120°C, i.e. close to the first “loading” temperature of 125°C.
 - (9) Around 330,000 s (4 days) after the first H₂/Ar intake, the active wire was powered (Fig. 4).
 - (10) We observed a further increase of anomalous power that, assuming no errors were made, was about twice that detected when the power was applied to inert wire; that is, of more than 10 W. The R/R_0 value, after initially increasing, stabilized at 0.808.
 - (11) A possible explanation was that the active wire’s temperature with Joule heating was larger than that when the power was indirect. The active wire temperature was 350–400°C, 200°C with indirect heating.
 - (12) If the explanation in 11 is correct, we see that the reaction, above from some temperature threshold, has a *positive feedback* with increasing temperature. Similar effects were found by our group with first generation wire/experiment, up to May 2012; and by the Takahashi and Kitamura group with Ni–Cu–ZrO₂ powders.
 - (13) After 360,000 s (4 days) from the H₂/Ar gas intake (Fig. 4), i.e. at time 515 ks, the power was switched off: the R/R_0 , at room temperature, dropped to 0.71. In other words, the direct heating (electro migration phenomena and/or larger temperatures) improved the loading, and then improved the anomalous power.
 - (14) After 410,000 s (5 days) from the first H₂/Ar intake, we evacuated the cell and then added H₂ at 100% concentration.
 - (15) The results were similar to H₂/Ar gas. The cell produced even more anomalous heat.
 - (16) We cannot discriminate whether the improvements in performance were due to effects of pure H₂, or due to more time under active gas, leading to increased embrittlement.
 - (17) After another week of miscellaneous tests, we decided to de-load the H₂ absorbed by the wire, to be sure that the resistance reduction observed was due to real absorption and not to a variation of resistance caused by the reduction of oxides (by H₂) at the nano-particles surfaces.
 - (18) To de-load we put the cell under a dynamic vacuum and increased the temperature.
 - (19) After several hours, we returned to the original starting value of R/R_0 at 1; the test was fully successful.
 - (20) We reloaded the wire again and observed the R/R_0 decrease and anomalous heat, similar to what we saw in the first cycle.
 - (21) Again we de-loaded H₂ from the wire, to do experiments with D₂ gas (Fig. 5). This time the final value of R/R_0 was 0.93, not 1.0 as expected. We suppose that some H₂ was stored somewhere in the lattice.
 - (22) After deloading the wire, we increased the temperature by powering the inert wire, as we usually do. Only a small amount of deuterium was absorbed.
 - (23) We observed, for the first time since 2011, some X and/or gamma ray emissions, coming from the reactor while the temperature increased from about 100°C to 160°C. We used an NaI(Tl) survey meter with an energy range 25–2000 keV, which was operated for safety purposes, not as a spectrometer. The total duration of this emission was about 600 s. The emission was burst-like and clearly detectable.
 - (24) We observed a very surprising thermal anomaly: the reaction was endothermic at first, not exothermic. On the second day the system crossed the zero line and later on become clearly exothermic. Similar effects were reported also by Takahashi and Kitamura.
 - (25) After about 350,000 s (4 days) from the beginning of D₂ intake the temperature abruptly increased and the wire broke. We noted that the pressure decreased, because there were problems with the seal, and the reactor was not perfectly gas tight, but this occurred at 80,000 s, *before the wire broke*. SEM observations showed fusion of a large piece of wire: ball shape. An SEM analysis after H₂ and/or D₂ interaction shows reduced size (Fig. 6).
 - (26) Starting on July 10, 2012, we used the second wire (#2) that had been stored in a plastic bag.
 - (27) In the meanwhile, we improved the overall detection of external temperatures by adding 3 more thermometers. The main thermometer was moved from the original position, which was not central over the wire length, to

- exactly at the center of the area of the glass tube.
- (28) The results were qualitatively similar to the first wire, although at lower intensity (Fig. 7). The starting temperature of loading increased from the value of 125°C of the wire #1, increased to about 160°C. In particular, the wire was not able to withstand direct heating conditions. We think that the surface was partially obstructed by something (perhaps HDPE plastic).
 - (29) On July 23 we de-loaded the wire, and on July 24 we loaded it again. The sequences were: (a) dynamic vacuum conditions, 220°C internal reactor temperature, power at Ni–Cr, 50,000 s duration; (b) H₂ filling.
 - (30) The results in Fig. 8 showed improvements in the speed of loading. It took only 2000 s for the R/R_0 ratio to fall from 1 to 0.85. The time necessary to get measurable anomalous heat was also reduced to less than 6 hours.
 - (31) The experiment with the cell shown in Fig. 9 was stopped on July 28, in order to package and ship the reactor to the National Instruments NI Week meeting at Austin, Texas in the US and later to the ICCF17 conference at Daejeon, South Korea.
 - (32) The wire #2 “overcame” the severe effects of shipping, especially the long time (8 days) without H₂, when it was exposed to free air. When we reconnected all the electrical connections at the NI Week conference, we realized that the R/R_0 value of the active wire remained almost unchanged (about 0.81). At the NI Week conference, all of the control and measurement electronics and software were provided by NI. In the previous experiments in Italy we used DAQ (6.5 digit) and MUX by Agilent; specific hardware and software were homemade.
 - (33) The maximum excess power reached after 3 days of operation in public at NI Week 2012 (Fig. 8) was about 21 W with indirect heating and about 25 W with direct heating of the sub-micrometric Constantan wire. The input power, as usual, was 48 W. These are the best values that we have observed up to now. We note that because we used the “old” value of calibration obtained in Italy, but a different experimental geometric set-up and instrumentation, the absolute value of excess power has to be scrutinized. In any case, the trend of increasing excess power versus elapsed time was reconfirmed.

5. Conclusions

It appears that the commercial Constantan alloy, with the surface geometry deeply modified (i.e. skeletonized) and size reduced to <100 nm, with multiple layers, is a good candidate for anomalous heat production due to:

- (1) Intrinsic low cost of raw materials;
- (2) Simple, low-cost procedures for growing nano-structures, as recently developed by our group at INFN-LNF, Italy;
- (3) Use of Hydrogen.

We observed that such materials exhibit “positive feedback” of anomalous power with increasing temperature.

The experiment has been shown to be reproducible as experienced both during the NI Week and the ICCF17 conferences. Several of the results we obtained were similar to those obtained using Ni–Cu alloy dispersed in a zirconia matrix by the Takahashi and A. Kitamura groups. (Both of these groups are in a collaboration with Technova, a research organization of the Toyota Company.) More systematic work is necessary to elucidate several open questions, first of all, the stability over time of the anomalous heat generation, safety and overall, third party independent confirmation about reproducibility, not to mention the “strange” endothermic behavior using deuterium gas.

Collaboration with the community involved in LENR studies is welcomed. A series of attempts to replicate the experiment is currently being performed by different organizations and laboratories worldwide.

The next step will be to use a quartz tube instead of the borosilicate now in use. Quartz will allow studies of temperatures over 300°C. Borosilicate glass begins to soften at around 280°C.

If positive results are reconfirmed with the wires made with the new procedures (i.e. “second generation” wires), it may be possible to reach regions of operation where even self-sustaining operation occurs, using larger amounts of materials.

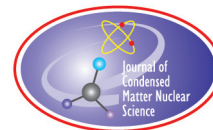
Acknowledgments

This work was done in collaboration with, and partly supported by:

- Metallurgical Company of NE, Italy.
- Kresenn Ltd., 5a Frascati Way, SL6 4UY Maidenhead (Berkshire), UK.
- Dennis Letts Laboratory, 12015 Ladrado Ln, Austin, TX 78727, USA.
- National Instruments, 11500 North Mopac Expressway, Austin, TX 78759, USA.
- Francesco Santandrea, ISCMNS, Latium1 Group, Via Cavour 26, 03013 Ferentino (Fr), Italy.
- We are indebted with Dr. James J. Truchard (CEO and President of National Instruments) and Dr. Stefano Concezzi (Director of Big Physics department): they convinced us to make a public demo both in USA and South Korea. The invaluable work of Brian Glass and his colleagues, among others, in making completely new software in a few days is deeply appreciated.

References

- [1] S. Romanowski et al., Density functional calculations of the hydrogen adsorption on transition metals..., *Langmuir* **15**(18) (1999) 5773–5780.
- [2] F. Celani et al., Experimental results on sub-micro structured Cu–Ni alloys under high temperatures hydrogen/deuterium interactions, at *X International Workshop on Anomalies in Hydrogen-Metal Systems*, Pontignano - Italy, April 10–14, 2012. http://www.22passi.it/downloads/X-WorksISCMNS_2012H4Pres.pdf
- [3] A.W. Szafranski et al., *J. Alloys Compounds* **404–406** (2005) 195–199.
- [4] A. Kitamura, A. Takahashi et al., Recent progress in gas phase hydrogen isotope absorption/adsorption experiments ICCF17, Daejeon, 10–17 August 2012, TUA2-1, in press.
- [5] F. Celani and Y. Srivastava, Overview of theoretical and experimental progress in low energy nuclear reactions (LENR), 22 March 2012; indico.cern.ch/conferenceDisplay.py?confId=177379



Research Article

LENR and Nuclear Structure Theory

Norman D. Cook*

Kansai University, 3-3-, R, T Yamatecho, Suita, Osaka, Prefecture 564-8680, Japan

Valerio Dallacasa

Verona University, Verona, Italy

Abstract

The significance of LENR research for understanding nuclear structure is discussed. In stark contrast to atomic-level Quantum Electrodynamics (QED), nuclear theory has remained a collection of mutually exclusive “models” lacking a rigorous foundation. We argue that LENR indicates the way forward to a quantitative theory of nuclear structure, Quantum Nucleodynamics (QND). © 2014 ISCMNS. All rights reserved. ISSN 2227-3123

Keywords: LENR, Nuclear structure theory, Piezonuclear fission, Quantum nucleodynamics

1. Introduction

The technological potential of LENR remains strong and progress in achieving experimentally stable LENR environments has recently been reported. Those developments are to be welcomed and should eventually lead to the long-awaited funding required for both basic and applied research. But, in light of experimental progress, the theoretical implications of LENR research for nuclear physics, in general, also deserve some attention.

LENR theorists have devoted most of their efforts to the explanation of mechanisms that would allow for the phenomena of “cold fusion.” What has not yet been studied is the significance of LENR for conventional nuclear physics. Here, we argue that LENR already indicates the direction in which progress in nuclear structure theory can be anticipated.

Three distinct aspects of nuclear theory are examined: (1) unanswered questions in conventional nuclear theory related to the nuclear force, (2) certain experimental findings in LENR research, and (3) the integration of LENR findings into conventional nuclear structure theory in the form of Quantum Nucleodynamics (QND).

*E-mail: cook@res.kutc.kansai-u.ac.jp

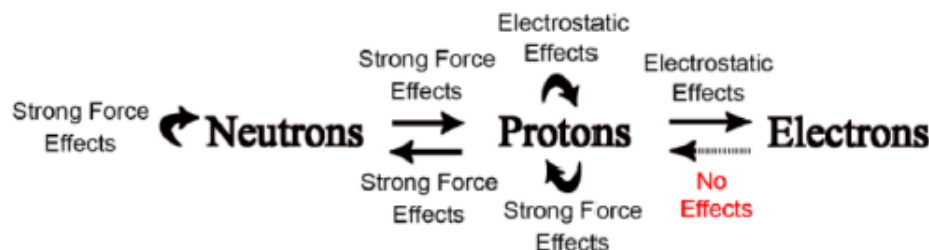


Figure 1. The central dogma of atomic physics (ca. 1932), where proton-electron attraction could be explained in terms of classical electrostatic theory, while the strong force effects were essentially new and inexplicable.

2. The Nuclear Force

No topic in nuclear physics is as important as that of the nuclear force. Already by the early 1930s, it was apparent that an extremely strong binding force allows for the stability of nuclei containing numerous positively charged protons. In contrast, the peripheral electrons were found to interact predominantly with the nuclear protons through the much weaker electrostatic force. These indubitable facts led to the so-called “central dogma” of atomic physics (Fig. 1).

Starting in the 1950s with the growing availability of particle accelerators capable of focusing beams of particles on nuclei at high energies, it became possible to characterize the nuclear force with great precision.

Theoretical reconstruction of the nuclear potential measured in nucleon-nucleon scattering experiments has typically resulted in Lennard–Jones type potentials (Fig. 2), where there is a strongly repulsive force (at least several hundred MeV) at short distances (<1 fm), a weaker attractive force (50–100 MeV) at 1–2 fm, and only weak effects beyond 3 fm. These characteristics have been formalized in the so-called Argonne, Paris and Bonn potentials. As of today, their approximate validity (and their spin-, isospin- and distance-dependence) is well-established.

It is relevant to note, however, that the powerful nuclear potential contrasts markedly with what is known from relatively low-energy experiments on the structure of stable nuclei. Specifically, the total binding energies of the 800+ stable isotopes indicate an average binding energy of less than 8 MeV per nucleon. Moreover, the average energy per nucleon implies a nearest-neighbor nucleon–nucleon interaction of less than 3 MeV in the high-density nuclear core (the region inside the arrow in Fig. 2). In other words, MeV-range nucleon interactions in stable nuclei are many orders of magnitude *weaker* than the effects measured in high-energy scattering experiments and many orders of magnitude *stronger* than the average eV interactions of electrons with their nuclei.

While there is still no consensus concerning the theory of the nuclear force, the essence of the “central dogma” of atomic physics throughout the 20th century was two-fold: (1) protons have strong effects on the peripheral electrons (but not vice versa), and (2) neutrons have little direct contact with the extra-nuclear world (Fig. 1). In fact, a weak chemical influence on nuclear decay rates had also become known by the early 1960s [2–5], but generally the nuclear realm and the atomic (electron) realm are still thought to be energetically distinct. That dogma is directly challenged by LENR findings and, today, the primary obstacle to the acknowledgement of the experimental evidence for induction of nuclear reactions at low energies is the *dogmatic* assertion that extra-nuclear effects on nuclear dynamics are theoretically impossible.

Unrelated to the issues of LENR, we have developed a lattice model of nuclear structure that was initially an attempt to integrate the diverse threads of modern nuclear structure theory [1, 6–8]. The implications of the lattice model for nuclear structure theory per se have been published many times, and are briefly summarized in the Appendix. Of direct relevance to LENR are the dimensions of the lattice and its implications regarding the nuclear force. That is,

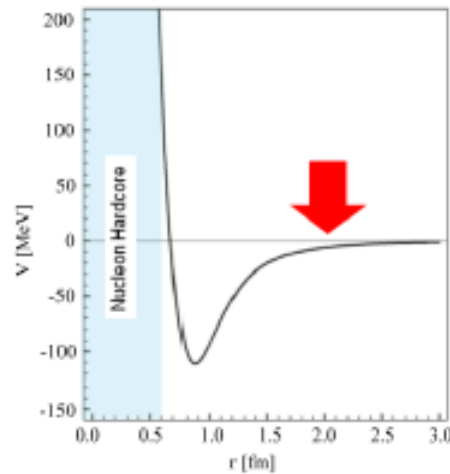


Figure 2. A realistic Lennard–Jones type nuclear potential deduced from nuclear scattering experiments. Small differences in the height, depth and distance of the potentials due to spin and isospin are known, but all such potentials have no effects beyond 3 fm. There is no doubt that the nuclear force is “short-range.”

in a lattice of nucleons, nucleon interactions are fixed within a narrow range of 1.0–3.0 fm. At that range, we have found a significant magnetic effect that is a microscopic (femtometer-scale) version of the Biot–Savart law of magnetic attraction between parallel currents (Fig. 3).

Under the assumption that the magnetic moments of the proton and neutron are consequences of the rotation of a *single* positive or negative valence charge, respectively, a significant magnetic contribution to nuclear binding energies is found. The main difference from the Biot–Savart law of classical electromagnetic theory is that, in copper wire coils containing continuous streams of electron charges, phase effects of the movement of individual charges need not be considered. With only one charge in each nucleonic “coil,” however, the magnetic interaction will necessarily depend strongly on the positions (phase relationship) of the two revolving charges – as they travel parallel or antiparallel relative to one another in their intra-nucleonic orbits. In effect, not only the distance and relative orientations of the magnetic poles, but also the phase relationship of the charge flow, determine the strength of the femto-scale magnetic interaction [9].

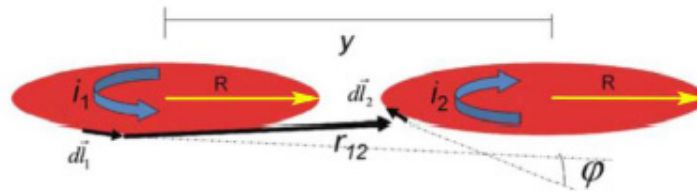


Figure 3. The magnetic force acting between two revolving charges depends not only on the distance and orientation of the electric currents, but also on their relative phases, φ [9].

The magnetic effects are attractive and repulsive for first and second neighbors in the lattice, respectively. That finding is consistent with the fact that the lattice model requires an *antiferromagnetic* ordering of nucleons in each isospin layer. Between layers of different isospin, there are necessarily both parallel and antiparallel nucleon pairs and differences in orientation of the magnetic dipole result in magnetic effects of varying magnitude. In this view, the magnetic force between nucleons is fundamentally short-range, because the dephasing of the charge “coils” with distance reduces the magnetic effects among distant neighbors. In effect the attractive magnetic force acts as a form of “strong screening” between like charges. These properties can be expressed by the force between two coils as, where r_{12} designates the center-to-center distance between the coils and R is the coil radius.

$$\vec{F}_{12} = \frac{\mu_0 i_1 i_2}{4\pi} \oint_{C_2} \oint_{C_1} \frac{d\vec{l}_1 d\vec{l}_2}{r_{12}^3} \vec{r}_{12}$$

In cylindrical coordinates

$$\vec{F}_{12} = \frac{\mu_0 i_1 i_2}{4\pi} \vec{j} \iint \frac{y R^2 \cos(\varphi_1 - \varphi_2) d\varphi_1 d\varphi_2}{[(y^2 + 2R^2(1 - \cos(\varphi_1 - \varphi_2)))^{\frac{3}{2}}]}$$

Note phases between currents

Expansion of the denominator

$$[(y^2 + 2R^2(1 - \cos(\varphi_1 - \varphi_2)))^{\frac{3}{2}}] = \frac{1}{y^3} (1 - \frac{3R^2}{y^2} (1 - \cos(\varphi - \varphi)) + \dots)$$

As summarized in Fig. 4, consideration of phase produces a strong increase well above the classical, Biot–Savart magnetic interaction between two circulating charges – leading to net attraction (repulsion) on the order of a few MeV at realistic internucleon distances of 1–3 fm. As we have previously reported [1], the mean nuclear binding force of nearest neighbor nucleons in the lattice is only 2.75–2.79 for nuclei as different as calcium, palladium and uranium. We therefore conclude that, regardless of the reality of pion-exchange binding effects and/or quark contributions, the magnetic effect alone is of sufficient strength to account for nuclear binding energies.

By definition, the clockwise rotation of negative charge gives an upward north pole, whereas similar rotation of a positive charge gives an upward south pole. The permutations of spin (up and down) and isospin (proton and neutron) result in the six fermi-level magnetic interactions shown in Fig. 5.

3. LENR

3.1. Magnetic effects

Some of the most interesting – and yet unexplained – findings in LENR research are indications that external magnetic fields can have a strong influence on heat generation. Letts and colleagues have reported [10] the ability to turn LENR excess heat-generation on-and-off simply by 90° rotation of the cathode (not anode) with respect to an external magnetic field of 500 Gauss. The significance of that effect lies in the fact that, in terms of conventional physics, a magnetic field of that strength should have little influence on intranuclear dynamics, being orders of magnitude weaker than nuclear

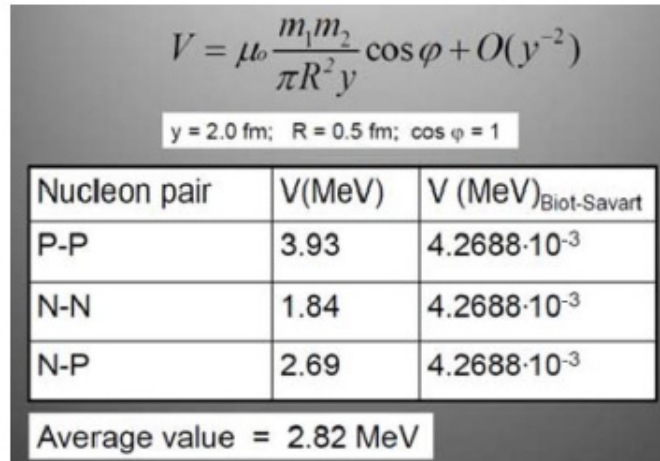


Figure 4. Summary of the strength of the magnetic attraction between nucleon pairs separated by 2.0 fm and lying in the same plane (as in Fig. 3). The classical Biot–Savart effect is weak, but, when phase is considered, there is an increase of three orders of magnitude in the strength of the magnetic interaction.

force effects. To the contrary, however, relatively low-energy changes in the magnetic environment have been shown to influence heat generation in LENR.

Questions remain unanswered concerning the location of the LENR effects that produce excess heat (the nuclear active environment, NAE, proposed by Storms [11]) and the mechanism of their susceptibility to magnetic fields, but manipulations of magnetic fields are clearly a promising direction for future LENR research.

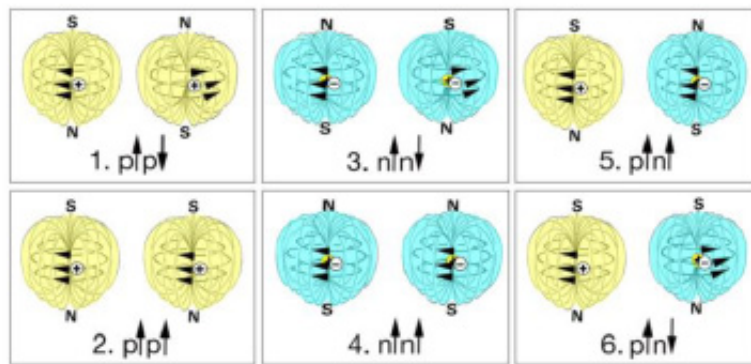


Figure 5. The six permutations of spin and isospin. The upper and lower rows show the attractive and repulsive magnetic interactions, respectively, at a center-to-center internucleon distance of 2.0 fm.

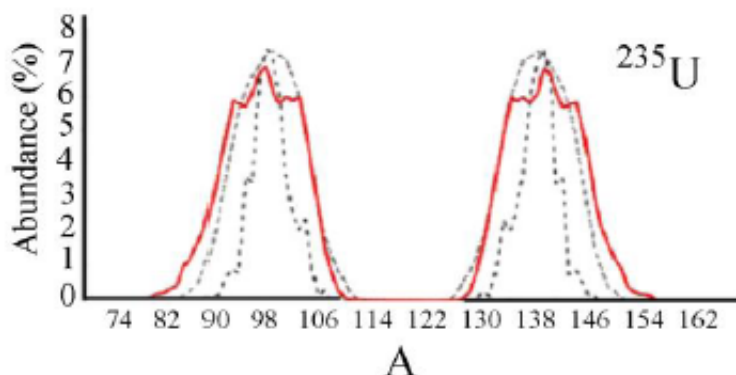


Figure 6. Results of the lattice simulation of thermal fission of ^{235}U . Lattice coordinates for nucleons in the nuclear core were fixed, while surface positions were occupied at random. The fission process was undertaken for each configuration along all available lattice planes and repeated for statistical study. The red lines are the experimental data, the dotted lines are the results of lattice simulations [1,19].

3.2. Transmutations

The most unambiguous indications of specifically nuclear involvement in “cold fusion” experiments are findings of nuclear transmutations. The appearance of elements in a reaction system where they are originally absent and/or measurement of abnormal isotopic ratios are decisive indications of nuclear effects [12,13]. As was true of early experiments on the fission of uranium in the 1930s, the possibility of contaminants must first be excluded, but the presence of unnatural isotopic ratios is alone indication of nuclear reactions. Both unnatural isotopic ratios and the presence of unanticipated elements in uncontaminated LENR experiments have been reported in several dozen LENR

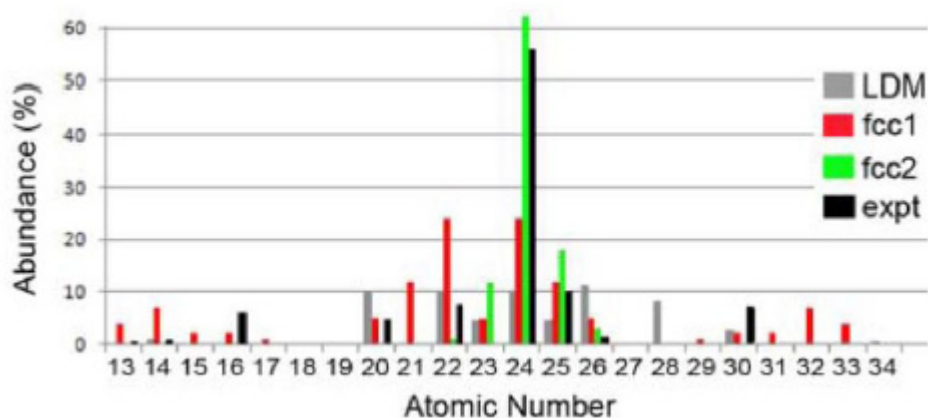


Figure 7. A comparison between the experimental findings on the low-energy fission of palladium and several theoretical models [1]. The liquid-drop model (LDM, grey lines) fails to account for the dominance of fragments at $Z = 22$ to 25. Qualitatively better results are obtained in lattice simulations where the deuterium triggers the fission but does not bind to either fragment (fcc1, red lines) and where the deuterium triggers the fission and binds to fragments (fcc2, green lines). Experimental data (black lines) from Mizuno [12].

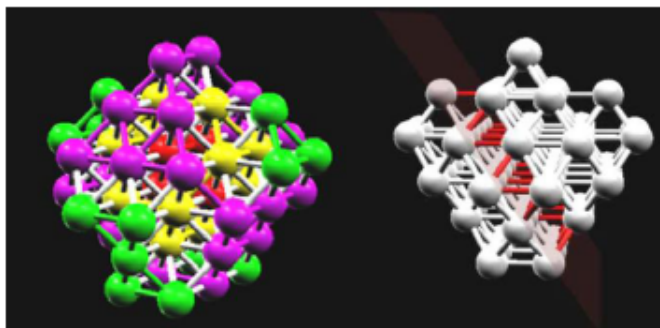


Figure 8. The lowest-energy lattice structure of ^{56}Fe that is consistent with the known IPM structure of this isotope. On the left is shown the color-coded ^{56}Fe nucleus (16 green nucleons on the surface of the doubly-magic ^{40}Ca nucleus). On the right is shown the lattice simulation of a low-energy fission plane, leading to stable daughter isotopes (^{27}Al and ^{29}Si). (The NVS software is available at [27].)

studies [11]. Unfortunately, the physical mechanisms underlying nuclear transmutations in LENR remain obscure and, primarily because of political, rather than experimental difficulties, their implications for nuclear structure theory have not been thoroughly explored. But the obvious needs to be stated: if nuclear transmutations can be elicited in the experimental conditions of LENR research, much of modern nuclear structure theory will need to be rewritten.

3.3. Piezonuclear fission

Over the past four years, Carpinteri and colleagues have reported on a new form of LENR. On the basis of geological findings and laboratory experimental studies, they have argued that a previously unknown type of solid-state nuclear fission has occurred in iron-containing rocks over geological time, and can be induced in high-impact compression experiments [14–18]. They report that a 2–4-fold increase in neutron emission over normal background levels has been consistently found in otherwise-conventional experiments on the tolerance of granite and other familiar rocks subjected to high pressure impact. Insofar as background neutron radiation is normally produced by the spontaneous fission of small amounts of radioactive elements, Carpinteri surmised that the non-radioactive elements in their samples were undergoing fission due to compression.

That hypothesis was confirmed in subsequent laboratory tests in which both neutron emission and nuclear “ash” suggestive of the fission of iron were found. Carpinteri has emphasized the geological significance of their findings and,

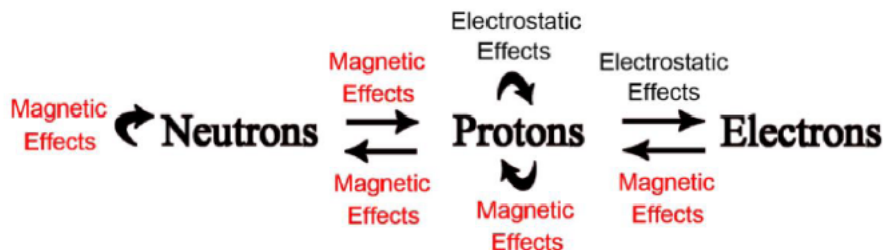


Figure 9. The modern “central dogma” of atomic physics implied by lattice calculations of magnetic effects [9] and magnetic field manipulations in LENR experiments [10].

like most LENR researchers, he has not speculated on the underlying nuclear mechanisms, but again the implication is that nuclear reactions can be induced at relatively low energies. Clearly, if low-level fission of the elements in the Earth's crust has occurred over geological time, there should be indication of elemental and isotopic changes. That is indeed the case in well-established geological findings on the distribution of elements on the Earth's surface. Specifically, a depletion of iron isotopes, together with an excess of magnesium, aluminum and silicon isotopes, in certain geological locations is circumstantial evidence of low-energy fission of iron nuclei, with the accumulation of nuclear “ash” corresponding to the binary fission of iron. Confirming results were then obtained along the compression fissures in rock samples undergoing laboratory tests: increases in background neutron counts, a decrease in the abundance of iron isotopes, together with an increase in magnesium, silicon and potassium isotopes. Their conclusion is that LENR effects – unrelated to the more usual palladium and nickel electrolytic findings of cold fusion research – result in the fission of iron, and the deposit of daughter fragments. An understanding of the significance of the Carpinteri results for both geology and LENR has only recently begun.

4. Putting LENR and the Magnetic Nuclear Force Together

While the focus of most experimental and theoretical LENR research has, for obvious reasons, been on the factors that lead to the production of excess heat in “table-top” LENR experiments, the *theoretical* implications of LENR are potentially revolutionary for nuclear structure physics, in general. Alone, the reconfiguration of nuclear structure theory within the framework of a lattice model (a “frozen liquid-drop”) would appear to have little relevance for theoretical developments in LENR, but the nuclear force properties that are implied by the lattice may be important.

The original claim of the lattice model was simply that a mathematical isomorphism exists between the entire set of nucleon states (as described in the independent-particle model, IPM) and a specific lattice (see the Appendix for a summary and literature references). The significance of the isomorphism lies in the fact that, unlike the gaseous phase models of the nucleus (the conventional Fermi gas, shell model and IPM), there is a precise geometrical configuration of nucleons in the lattice version of the IPM. As a direct consequence of that geometry, any quantum mechanical nuclear state that can be described in the IPM necessarily has a structural analog in the lattice. That fact, in turn, implies that the entire set of local nucleon-nucleon interactions for any given number of protons and neutrons in the lattice can be calculated. It is the precise, quantitative nature of nucleon interactions that distinguishes the lattice version of the IPM from the gaseous version.

Although the relevance to LENR studies is not obvious at first glance, there are two main arguments that suggest a deep connection between the lattice model and LENR. The most important point, in terms of nuclear structure theory, is the fact that the lattice IPM lends itself to implementation of a fully realistic nuclear force at the dimensions of the lattice, with no need to postulate a gaseous nuclear interior or a fictitious, long-range “effective” nuclear force unlike the force that is known experimentally. Since a nearest-neighbor internucleon distance of 2.026 fm in the lattice gives the nuclear core density of 0.170 nucleons/fm³ and reproduces nuclear charge radii and binding energies [1], the magnitude of the nuclear force at specifically 2.0 fm becomes crucial. Examination of magnetic effects at that scale (Section 2) clearly shows the relevance of femto-magnetic phenomena for explaining total nuclear binding energies.

The second, more direct, connection between the lattice model and LENR is found in the simulation of LENR phenomena using the lattice structures for specific nuclei, notably palladium and iron isotopes. While the energetic basis for all forms of LENR remains a theoretical puzzle, the specific types of nuclear “ash” that have been reported find relatively straight-forward explanations in terms of fission products, as deduced from systematic severing of nuclei along lattice planes.

Lattice simulations began with the thermal fission of uranium and plutonium isotopes [19], where the lattice structures were shown to produce asymmetrical fission fragments close to the 3:2 ratio that is known experimentally (Fig. 6). Notably, unlike the conventional liquid-drop and shell model explanations of asymmetrical fission, the lattice

results are produced *without* the use of an “asymmetry parameter” or other adjustable parameters of the nuclear potential well that are typically used to reproduce experimental findings. On the contrary, the asymmetrical fragments produced in the lattice model are a direct consequence of the lattice geometry itself, insofar as certain oblique planes passing through the actinide structures are energetically favored because they contain fewer nearest-neighbor bonds that cross the fission plane than vertical or horizontal planes.

Using the same lattice fission technique as used for the actinides, the simulation of the fission of the palladium isotopes (with a deuteron added at random to surface positions) produces approximately symmetrical fission fragments (Fig. 7). The rough agreement with the transmutation data published by Mizuno [12] is apparent. Again, “fission parameters” adjusted to reproduce the experimental data are *not* needed. While the energetic basis for the presumed fission of palladium remains unclear in LENR, the findings on the masses of the isotopes in the nuclear “ash” are consistent with the lattice model.

Finally, the newest of the LENR fission results are those of Carpinteri and colleagues [14–18]. Their basic finding is that there is a depletion of iron isotopes specifically along the fracture planes that are revealed in the high-pressure compression “failure” of granite and similar rocks. Together with isotopic analysis that reveals an excess of magnesium, aluminum and silicon along those same planes, they have argued that there is strong circumstantial evidence for the piezonuclear fission of iron ($Z = 26$), the production of daughter fragments ($Z = 12$ to 14) and low-level neutron radiation. Again, questions about mechanisms remain unanswered, but the phenomenology is consistent with nuclear fission.

Using the lattice model for the fission of iron isotopes, prediction of the high- and low-probability planes along which nuclear fission may occur is straightforward. As shown in Fig. 8, the lowest energy (maximal compactness) lattice structure for ^{56}Fe that is consistent with the lattice model can be fractured along 17 lattice planes that pass through or near the nuclear center. Already at this relatively gross level, the lattice model indicates an abundance of $Z = 12$ to 4 stable isotopes as the products of fission along nuclear lattice planes. Simulation results are summarized in Table 1.

Table 1. The main products generated by fission of ^{56}Fe along lattice planes using the NVS software

Fragment 1			Fragment 1			Interfragment effects	
Z	N	A	Z	N	A	Q (MeV)	Bonds
13	14	27	14	15	29	53.21	38
11	12	23	16	17	33	52.98	38
19	20	39	8	9	17	43.42	32
14	14	28	14	14	28	53.88	40
19	22	41	7	8	15	42.50	36

The current status of the lattice model in the realm of nuclear structure theory is approximately equivalent to the status of LENR in the realm of experimental nuclear physics. Conventional nuclear theorists are vociferous that the many models of the atomic nucleus are, if mutually contradictory, nonetheless “complementary” and suffice to explain nuclear phenomena. Similarly, experimental nuclear physicists are vociferous that the empirical claims in LENR research for excess heat and nuclear transmutations cannot possibly be true in light of the “central dogma” of atomic physics, and must reflect experimental error and/or wishful thinking. In other words, both the theorists’ and the experimentalists’ rejection of LENR are based upon the presumed inviolability of the nucleus via relatively low-energy mechanisms. There are, however, both experimental and theoretical grounds for skepticism concerning such dogma.

5. Conclusions

The experimental finding that initiated the “cold fusion” revolution was the generation of heat in electrolytic experiments far in excess of what could be explained conventionally on a chemical basis. Subsequent work indicated nuclear products – including low-level radiation and nuclear transmutations. Two decades of further experimentation has not led to theoretical clarity, but the involvement of the atomic nucleus in various ostensibly chemical phenomena is now unambiguous [11]. Significantly, conventional nuclear theory does *not* predict the phenomena of LENR and many conventional physicists remain unconvinced of the reality of LENR since the energy domains of chemistry and nuclear physics remain so far apart. The negative bias with regard to LENR is clearly a consequence of the familiar, but apparently incomplete, theoretical framework of the “central dogma” of atomic physics from the 1930s. Our own calculations (strictly within the realm of nuclear structure theory) indicate a previously unrecognized magnetic contribution to nuclear binding energies. Time, concerted effort and low-level funding for basic research will eventually tell what mechanisms are important, but it is already clear that a revision of the dominant “dogma” of atomic physics is in the making (Fig. 9).

Appendix A.

Details of the lattice model have been published in the physics literature [e.g., 6,7, 19–26], summarized in spreadsheets and PowerPoint presentations available over the internet [8,27], illustrated in cross-platform software that is freely available [27,28], and thoroughly discussed in a recent monograph [1]. The model has been advocated as a possible *unification* of nuclear structure theory – a field notorious for its continuing use of numerous, mutually-contradictory macroscopic analogies – the notorious gaseous, liquid, and cluster models of nuclear theory. Unfortunately, despite the widely acknowledged disarray of nuclear “modeling,” the argument for the unification of nuclear theory within the lattice model has fallen on deaf ears in light of the many successful applications of nuclear energy over the course of many decades. It may indeed be true that the many modern applications of nuclear phenomena are too numerous to discredit the entire field, but developments in LENR have again brought the “completeness” of current nuclear orthodoxy into question. Not only have unanticipated, low-energy nuclear phenomena been detected, but the reconfiguration of the central paradigm of nuclear structure theory, the IPM, within a lattice suggests the form in which a modern theory of quantum nucleodynamics (QND) might eventually take [29].

Whatever the ultimate outcome of current theoretical debates, it can be said that the central pillar in support of the lattice model – largely unappreciated, but uncontested by conventional theorists – is that the antiferromagnetic fcc lattice uniquely reproduces the entire “independent-particle texture” of the nucleus, as originally described in the IPM (ca. 1950). The mathematical identity between the lattice and the standard view of nuclear quantum mechanics means that the quantal states of nucleons (*n*, *l*, *j*, *m*, *s*, *i* and *parity*) can be deduced solely from nucleon coordinates in the lattice, and vice versa [7]. That fact is illustrated in the following seven equations:

$$n = |x| + |y| + |z| - 3)/2, \quad (\text{A.1})$$

$$l = |x| + |y| - 2)/2, \quad (\text{A.2})$$

$$j = |x| + |y| - 2)/2, \quad (\text{A.3})$$

$$m = |x|^*((-1) \wedge ((x - 1)/2))/2, \quad (\text{A.4})$$

$$s = (-1) \wedge ((x - 1)/2)/2, \quad (\text{A.5})$$

$$i = (-1) \wedge ((x - 1)/2), \quad (\text{A.6})$$

$$\text{parity} = \text{sign}(x^*y^*z), \quad (\text{A.7})$$

where nucleon coordinates (x, y, z) are the odd-integers that define a face-centered cubic lattice. The simplicity of the equations is self-evident, and leads to various nuclear-level geometrical symmetries of the nuclear shells and subshells (spherical n -shells, cylindrical j -shells, conical m -shells, orthogonal layering of spin and isospin). Even the non-classical concept of nucleon **parity** finds a geometrical definition in the lattice. *A priori*, it is not obvious which version of the independent-particle model – a lattice or a gas – is a more suitable description of nuclear reality, and further research is still needed.

References

- [1] N.D. Cook, *Models of the Atomic Nucleus*, 2nd Edn., Springer, Berlin, 2010 (the entire text is available free-of-charge at: www.res.kutc.kansai-u.ac.jp/~cook/MAN2.pdf).
- [2] G. Harbottle, Chemical effects of nuclear transformations in inorganic solids, *Ann. Rev. Nucl. Sci.* **15** (1965) 89.
- [3] S. DeBenedetti, F.D. Barros and G.R. Hoy, Chemical and structural effects on nuclear radiations, *Ann. Rev. Nucl. Sci.* **16** (1966) 31.
- [4] G.T. Emery, Perturbation of nuclear decay rates, *Ann. Rev. Nucl. Sci.* **22** (1972) 165.
- [5] P.K. Hopke, Extranuclear effects on nuclear decay rates, *J. Chem. Education* **51** (1974) 517.
- [6] N.D. Cook and V. Dallacasa, Face-centered-cubic solid-phase theory of the nucleus, *Phys. Rev. C* **35** (1987) 1883.
- [7] N.D. Cook, The inherent geometry of the nuclear Hamiltonian, <http://arxiv.org/abs/1101.4251v1>, 2011.
- [8] N.D. Cook and V. Dallacasa, The fcc structure of the nucleus and the magnetic interaction among nucleons. http://iccf15.frascati.enea.it/ICCF15-PRESENTATIONS/S8_O2_Cook.pdf, Rome, 2009.
- [9] V. Dallacasa, P. DeSia and N.D. Cook, In *Models of the Atomic Nucleus*, 2nd Edn., Springer, Berlin, 2010, pp. 217–221.
- [10] S.R. Chubb and D.G. Letts, Magnetic field triggering of excess power in deuterated palladium, *Infinite Energy* **95** (2011) 40.
- [11] E. Storms, *The Science of Low Energy Nuclear Reaction*, World Scientific, Singapore, 2007.
- [12] T. Mizuno, *Nuclear Transmutation: The Reality of Cold Fusion*, Tuttle, Concord NH, 1998.
- [13] G.H. Miley and J.A. Patterson, Nuclear transmutations in thin-film nickel coatings undergoing electrolysis, *J. New Energy* **1** (1996) 5.
- [14] A. Carpinteri, F. Cardone and G. Lacidogna, Piezonuclear neutrons from brittle fracture: early results of mechanical compression tests, *Strain* **45** (2009) 332.
- [15] F. Cardone, A. Carpinteri and G. Lacidogna, Piezonuclear neutrons from fracturing of inert solids, *Phys. Lett. A* **373** (2009) 4158.
- [16] F. Cardone, G. Cherubini and A. Petrucci, Piezonuclear neutrons, *Phys. Lett. A* **373** (2009) 862.
- [17] A. Carpinteri et al., Compositional and microchemical evidence of piezonuclear fission reactions in rock specimens subjects to compression tests, *Strain* **47** (2011) 282.
- [18] A. Carpinteri, G. Lacidogna, A. Manuello and O. Borla, Piezonuclear fission reactions from earthquakes and brittle rocks failure: Evidence of neutron emission and nonradioactive product elements, *Exp. Mechanics* 29 June, 2012.
- [19] N.D. Cook, Asymmetric fission along nuclear lattice planes, In, *Fission and Properties of Neutron-Rich Nuclei*, J.H. Hamilton, W.R. Phillips and H.K. Carter (Eds.), World Scientific, Singapore, 1999, pp. 217–226.
- [20] N.D. Cook, An fcc lattice model for nuclei, *Atomkernenergie* **28** (1976) 195.
- [21] V. Dallacasa, FCC lattice model for nuclei, *Atomkernenergie* **37** (1981) 143.

- [22] N.D. Cook, Quantization of the fcc nuclear theory, *Atomkernenergie* **40** (1982) 51.
- [23] V. Dallacasa and N.D. Cook, The fcc nuclear model, *Il Nuovo Cimento* **97** (1987) 157.
- [24] N.D. Cook, Nuclear binding energies in lattice models, *J. Phys. G* **20** (1994) 1907.
- [25] N.D. Cook, Is the lattice gas model a unified model of nuclear structure? *J. Phys.* **25** (1999) 1.
- [26] N.D. Cook, Computing nuclear properties in the fcc model, *Computers Phys.* **3** (1989) 73.
- [27] N.D. Cook, Homepage: <http://www.res.kutc.kansai-u.ac.jp/~cook>
- [28] N.D. Cook, T. Hayashi and N. Yoshida, Visualizing the atomic nucleus, *IEEE Computer Graphics Appl.* 7 (1999) 54.
- [29] N.D. Cook, Quantum nucleodynamics. <http://arxiv.org/ftp/arxiv/papers/1310/1310.3338.pdf>



Research Article

Effect of Recrystallization on Heat Output and Surface Composition of Ti and Pd Cathodes*

J. Dash,[†] J. Solomon and M. Zhu

Portland State University, Portland, OR, USA

Abstract

The microstructure of Pd and Ti foils was altered by cold rolling followed by heating at temperatures up to $\sim 700^{\circ}\text{C}$. The surface topography and microchemical composition of these foils was studied before and after electrolysis with heavy water electrolyte. Temperature measurements during electrolysis showed that Ti and Pd cathodes which had been heated to $\sim 700^{\circ}\text{C}$ gave about 1W excess power relative to a control.

© 2014 ISCMNS. All rights reserved. ISSN 2227-3123

Keywords: Composition, Heat output, Recrystallization, Topography

1. Introduction

It is well known that the microstructure of metals can be altered by deformation which produces point defects (vacancies and interstitials) and line defects (dislocations). Crystal size can vary from single crystals to nanocrystals. The presence of defects and grain boundaries results in slight expansion of the crystal lattice which may enhance diffusion of elements such as hydrogen and deuterium into titanium and palladium, thus increasing the rate and degree of loading. This may increase the excess thermal power produced during electrolysis of heavy water–sulfuric acid electrolyte with Ti or Pd cathodes. The purpose of this research was to determine if heating at elevated temperatures after cold rolling affects the thermal output and surface composition produced during electrolysis with Ti or Pd cathodes.

In a collaborative research effort between scientists at ENEA and SRI International, it has been shown that annealing palladium foil at temperatures between 800 and 1100°C increases the maximum D/Pd loading ratio by reducing the internal stress generated during deuteron sorption by the Pd lattice [1]. Annealing cold rolled metal foils such as Pd and Ti over a Bunsen burner flame should produce a similar reduction in the stress field via recrystallization. The effect of this process on excess enthalpy production, surface morphology, and elemental composition of Pd and Ti cathodes was studied herein.

*This work was supported by a grant from the New York Community Trust.

[†]E-mail: dashj@pdx.edu

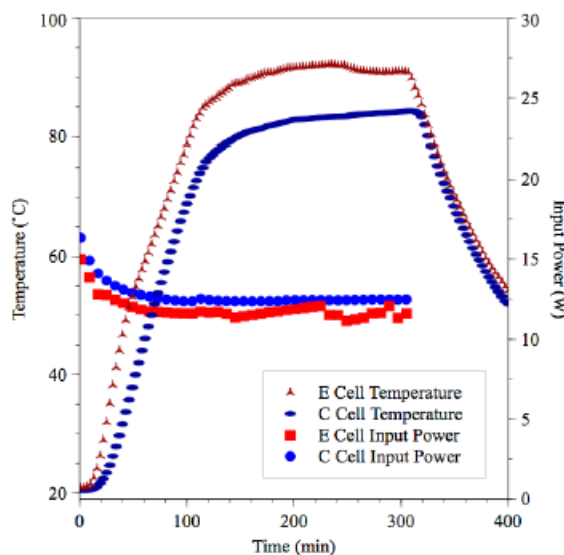


Figure 1. Temperature and input power evolution of an experimental (E) cell containing a thermally treated titanium cathode and a control (C) cell containing a Pt cathode.

2. Experimental

Ti foil (Alfa Aesar stock #43676, 99.99%, metals basis) and Pd foil (Alfa Aesar stock #11514, 99.9%, metals basis) were cold rolled from 0.5 mm thickness to about 0.3 mm thickness. Strips ($10 \times 30 \text{ mm}^2$) were # 3 cut from the cold rolled foils to be used as cathodes during electrolysis. The electrolyte consisted of 1.5 M H_2SO_4 (Fisher Scientific, lot #050994) in D_2O (Aldrich stock #14764, 99.8% isotopic).

Two cells were constructed in order to determine if cathodes with recrystallized microstructure are effective in producing excess thermal power. A cell with a cathode made from cold rolled Ti was crimped to a Pt wire (Alpha Aesar stock #10285, 99.95%). A control cell was identical except that its cathode was a Pt foil (Alfa Aesar stock #11509 99.99%). Each cell used a Pt foil anode and the same electrolyte.

Recrystallization was achieved by heating the cold rolled foils for 40 min at an average temperature of $\sim 700^\circ\text{C}$ with a Bunsen burner, after which a recrystallized Ti foil was crimped to the Pt cathode wire. Electrolysis was performed with constant cathode current density of about 0.3 A/cm^2 . Cell voltage and temperature were monitored with an automated data acquisition system.

3. Results

The data for the thermocouples which were attached to the outsides of the cells, close to the cathodes, is shown in Fig. 1, along with the power input to each cell. The input power to the control cell (C cell) is slightly higher throughout the experiment than the input power to the experimental cell with the recrystallized Ti cathode (E cell). Even though the E cell received less power, its temperature was higher than that of the C cell throughout the experiment. The peak E Cell temperature was about 92°C , and the peak C cell temperature was about 82°C . These peaks were reached after about 200 min of electrolysis.

The input power fluctuations to the E cell were caused by a loose connection to the cathode wire. Note that there

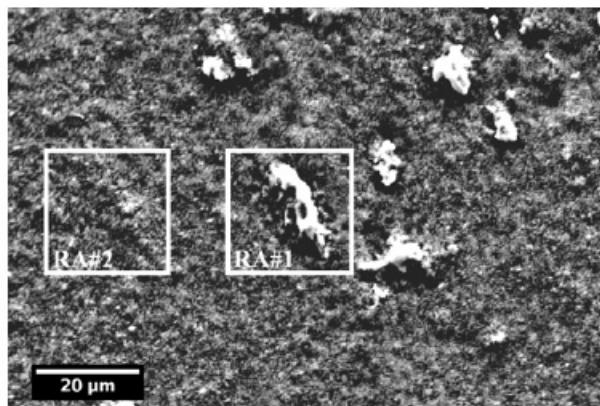


Figure 2. Surface topography of a cold rolled Ti substrate after 40 minutes of heating at 700°C over a Bunsen burner.

is less input power to the E cell than to the C cell throughout the entire run. Even so, the E cell produced about 1W of thermal power more than the C cell.

A second round of electrolysis was conducted using the same electrodes in order to test if the results obtained with this system were repeatable. The recombination catalyst was no longer effective after the first round of electrolysis, so it was replaced in both cells, and additional electrolyte was added to bring the cells to their initial electrolyte levels. The data obtained from this second experiment gave nearly identical results as the first.

A third experiment was conducted using the same electrodes. The recombination catalyst was replaced and the electrolyte was replenished before this run was made. This experiment did not replicate the first two. The maximum temperature was about 100°C for the E cell and 85°C for the C cell. The reason why the third run did not replicate the first two may be because the Ti cathode in the E cell slowly dissolved, thus reducing the surface area. Higher power input was required to maintain the constant current.



Figure 3. Surface topography of a titanium cathode after cold rolling, heating, and electrolysis in H₂SO₄/D₂O.

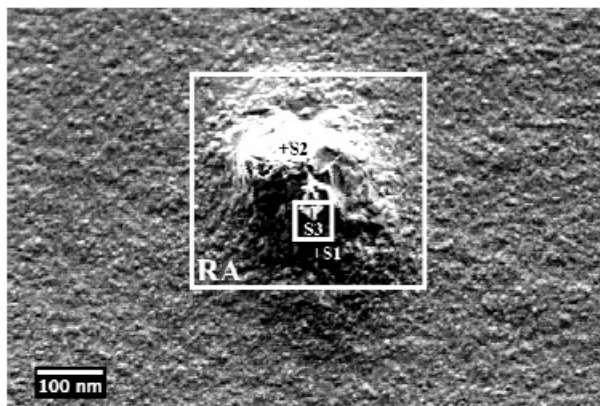


Figure 4. SEM image of a feature commonly found on the surface of a cold-rolled, heated titanium cathode following electrolysis in acidified heavy water.

The result was higher E cell temperature, which vaporized about 30 ml of the electrolyte. This loss made it impossible to calculate excess power accurately.

4. SEM and EDS Characterization

Using a scanning electron microscope (SEM) equipped with an energy dispersive spectrometer (EDS), we studied the surface topography and microcomposition of the thermally treated cathodes both before and after electrolysis. Figure 2 shows the typical surface topography of a titanium cathode after heating but before electrolysis.

EDS data was collected from the reduced areas outlined in Fig. 2. The EDS scan obtained from the center of the image (RA#1) contains about 2 at.% Fe, along with O, C, and Ti, whereas the reduced area to the left (RA#2) contains only O, C, and Ti (Table 1).

Figure 3 shows the surface topography of a Ti cathode that had undergone cold-rolling, followed by 40 min of heating at $\sim 700^\circ\text{C}$, and electrolysis. There are three similar pits (*black*) about $50\ \mu\text{m}$ diameter, with white rims which protrude above the surface. The surface eruptions have similar size and shape.

EDS spectra were taken from an eruption on a Ti cathode after cold rolling, heating, and electrolysis (Fig. 4). Spectra were obtained from the whole area, the reduced area (RA), the black spot S1, the white spot S2, and the triangular area in the small square near the center labeled S3 (Table 2). The detected elements consisted mainly of C, O, and Ti. Anomalous V was found in four of the five spectra at the 0.1 at.% level. Anomalous V, Cr, Fe, and Ni were found in the triangular particle within the small square near the center of the figure. Fe was at the 0.3 at.% level, and the other elements were at the 0.1 at.% level.

Table 1. Atomic composition of RA#1 and RA#2 in Fig. 2

Element	Atomic (%) composition reduced area #1	Atomic (%) composition reduced area #2
C	11.79	16.73
O	77.79	72.05
Ti	8.54	11.22
Fe	1.88	0

We performed similar experiments using Pd foils instead of Ti and obtained similar results. At steady state, the temperature of the cell with a heated Pd cathode was about 7°C higher than that of the control. With the same input power, this means that the heated Pd cathode was producing about 1 W more power than the control.

The topography of a Pd cathode after heating but before electrolysis is shown in Fig. 5a. It appears that surface melting has occurred, leaving a network of pores. Since the melting point of Pd is 1549°C and the Bunsen burner flame does not reach such temperatures, we speculate that a diffusion based process is responsible for the formation of the porous microstructure in Pd, namely spinodal decomposition [2, 3].

It is apparent that the heating of Pd over a Bunsen burner flame produces a high surface area, porous topography. More over, this morphology is stable since it has clearly maintained its structure even after 22.5 h of electrolysis at a current density of 340 mA/cm² (Fig. 5b). The white dots on the palladium surface seen in Fig. 5b are electroplated platinum deposits, which come from the dissolution of the anode.

Figure 6 shows another example of porous surface microstructure on a Pd cathode which had been heated in a Bunsen burner flame, then electrolyzed for 14.5 h. The pores seem to be concentrated in strands which meander over the surface. The square area in the center of the micrograph is shown enlarged in Fig. 6b, which has features suggesting

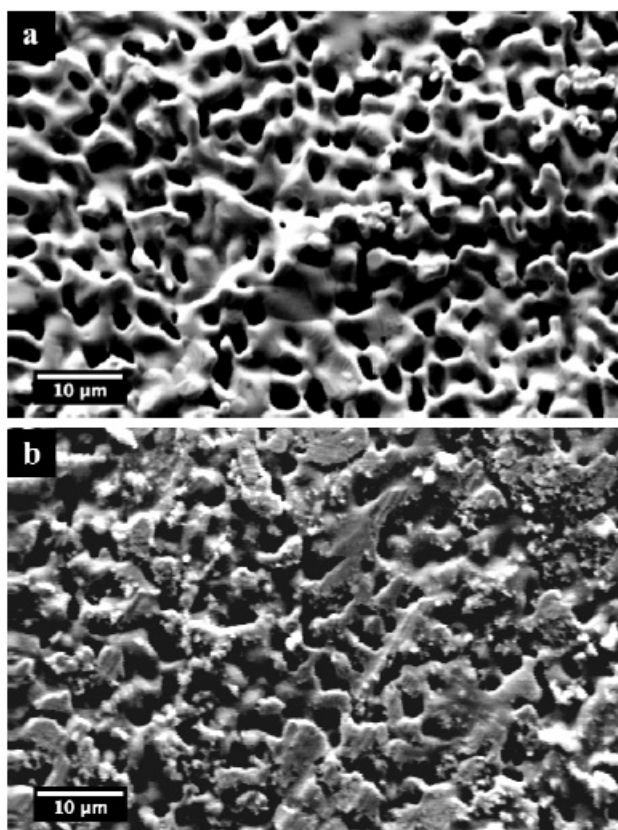


Figure 5. Surface topography of a Pd cathode after heating for 40 min under a Bunsen burner flame (a) before and (b) after electrolysis in H₂SO₄/D₂O.

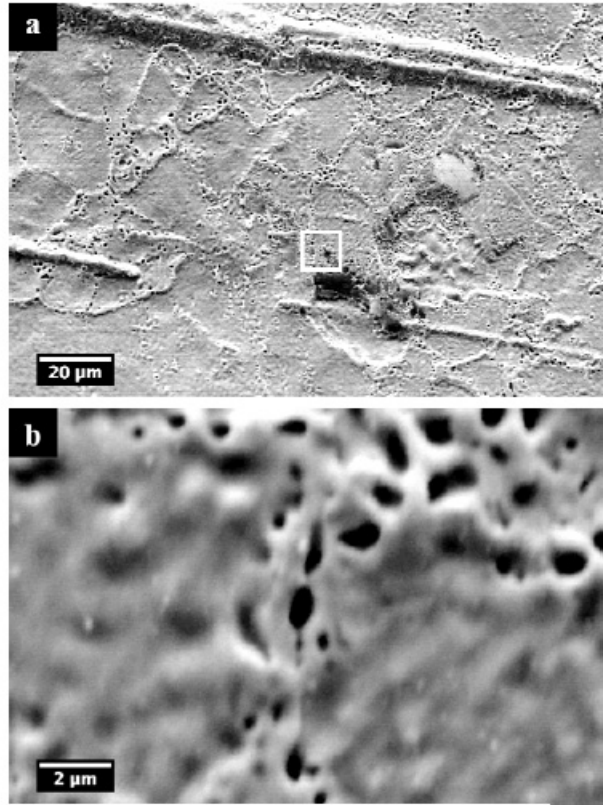


Figure 6. (a) Low magnification and (b) high magnification SEM image of a heated Pd sample following electrolysis in $\text{H}_2\text{SO}_4/\text{D}_2\text{O}$.

surface melting.

Figure 7 shows another view of a porous Pd cathode after electrolysis. Two of the pores were analyzed with the results given in Tables 3 and 4. Both contain significant amounts of Ag, which is consistent with our previous results [4].

Table 2. Atomic composition of the labeled regions in Fig. 4

Element	Atomic (%) composition reduced area	Atomic (%) composition black S1	Atomic (%) composition white S2	Atomic (%) composition whole area	Atomic (%) composition white triangle S3
C	26.71	43.78	35.72	22.25	41.21
O	64.60	52.93	59.55	68.92	52.60
S	0	0	0	0	0.04
Ti	8.69	3.23	4.67	8.73	5.60
V	0	0.06	0.07	0.11	0.08
Cr	0	0	0	0	0.10
Fe	0	0	0	0	0.33
Ni	0	0	0	0	0.04

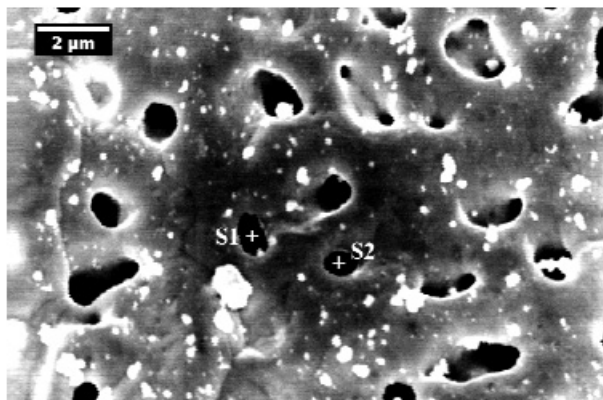


Figure 7. SEM image of a cold-rolled, heated Pd substrate following electrolysis in $\text{H}_2\text{SO}_4/\text{D}_2\text{O}$.

Table 3. Atomic composition of pore S1 in Fig. 7

Element	Weight %	Standard deviation	Atomic %
C	5.12	0.42	33.67
Al	0.7	0.16	2.03
Pd	70.76	1.52	52.51
Ag	7.04	1.68	5.15
Pt	16.39	0.79	6.63

As a final example, Fig. 8 shows the locations on the surface of a thermally treated, electrolyzed Pd cathode from which EDS spectra were obtained.

Quantitative results suggest that three of the five regions contain significant quantities of silver, with the highest concentrations located within pores (Table 5). Anomalous Ag is found in the black and gray features, but not in the

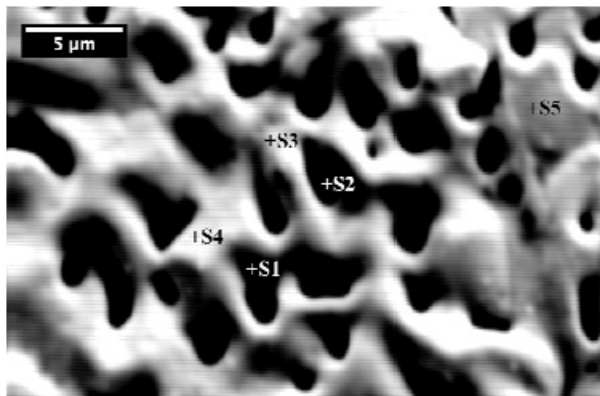


Figure 8. SEM image of the concave side of a heated palladium cathode after 14.5 h of electrolysis.

Table 4. Atomic composition of pore S2 in Fig. 7

Element	Weight %	Standard deviation	Atomic %
C	0.82	0.26	7.18
Pd	80.49	1.84	79.12
Ag	8.49	1.92	8.23
Pt	10.20	0.74	5.47

white features.

A primary objective of this research was to determine if there is an optimum time of heating at 700°C that produces a microstructure which maximizes excess heat during electrolysis. The results obtained for Pd cathodes are given in Table 6. Heating Pd for 40 min at 700°C gave 7°C higher steady-state temperature than no heating.

5. Discussion

The microstructure of the cathode in low energy nuclear reaction (LENR) studies is an important factor in loading hydrogen isotopes into the host lattice. In the case of nanocrystals, the goal is to prevent sintering of the microscopic particles so that a large surface area to volume ratio is maintained.

Cold rolled Ti foils, melting point 1668°C, and cold rolled Pd foils, melting point 1549°C, were used in this research. The goal of heating was to recrystallize the foils to form a new set of microscopic crystals with a large surface area to volume ratio.

Although the data are few, it seems that heating the foils for 40 min at 700°C produces microcrystals and unexpected microporosity which serve to increase excess heat and reproducibility for both Ti and Pd. In addition we continue to observe anomalous Ag in our EDS spectra, such as we reported previously [4].

It was suggested that the observed surface morphology is due to a compound of Pd, O, and C which has a low melting point [5]. Such a compound could form at elevated temperature if the free energy change is favorable. Rapid cooling to ambient would preserve the surface morphology in the form which was produced at elevated temperature.

6. Conclusion

This study shows that it is possible to enhance excess heat from metals such as Ti and Pd by thermal treatment to produce microstructure such as porosity which is favorable to diffusion of gases into the metals. Reproducibility of results may also be increased.

Acknowledgment

This research was supported by a grant from the New York Community Trust.

Table 5. Atomic composition of various spots on the sample shown in Fig. 8

Element	Atomic (%) composition black S1	Atomic (%) composition black S2	Atomic (%) composition white S3	Atomic (%) composition white S4	Atomic (%) composition gray S5
C	19.42	23.80	36.82	42.11	26.34
O	36.05	23.34	24.55	24.04	30.37
Pd	37.55	45.18	31.49	28.36	35.55
Ag	1.49	3.78	0	0	0.59
Pt	5.49	3.90	7.14	5.49	7.14

Table 6. Effect of recrystallization heat treatment of palladium cathodes on cell temperature during electrolysis

Duration of thermal treatment (minutes at $\sim 700^{\circ}\text{C}$)	Steady-state temperature during electrolysis ($^{\circ}\text{C}$)
0	64
20	65
40	71
60	68

References

- [1] M. Apicella, E. Castagna, L. D'Aulerio, G. Mazzitelli, F. Sarto, A. Rosada, E. Santoro, V. Violante, M. McKubre, F. Tanzella and C. Sibillia, Some Recent Results at ENEA, *Proc. of the 12th Int. Conf. Cold Fusion*, A. Takahashi, K. Ota and Y. Iwamura (Eds.), Yokohama, Japan, November 2005.
- [2] S.M. Allen, Spinodal decomposition, *Encyclopedia of Materials: Science and Technology*, K.H. Jergen Buschow et al. (Eds.), Elsevier, New York, 2001, pp. 8761–8764.
- [3] J. Dash, Electron transmission and diffraction observations of the microstructure of alnico alloys, Ph.D. Thesis, Pennsylvania State University, September 1966.
- [4] J. Dash, Q. Wang and D.S. Silver, Excess heat and anomalous isotopes and isotopic ratios from interaction of palladium with hydrogen isotopes, *Low Energy Nuclear Reactions and New Energy Technologies Sourcebook*, Vol. 2, J. Marwan and S. Krivit (Eds.), American Chemical Soc., Washington DC, 2009, pp. 61–80.
- [5] Private Communication.



Research Article

Changes Observed in the Elemental Composition of Palladium and Rhenium Specimens Irradiated in Dense Deuterium by γ -Quanta with Boundary of Energy 23 MeV

A.Yu. Didyk*

Joint Institute for Nuclear Research, 141980 Dubna, Russia

R. Wisniewski†

National Center of Nuclear Research, 05-400 Otwock, Poland

Abstract

We have studied the elemental composition of palladium and rhenium specimens irradiated in dense gaseous deuterium by γ -quanta of a continuous spectrum with the threshold energy of 23 MeV. Significant anomalies are found in the structure and elemental composition of the irradiated specimens. At both ends of the palladium wire considerable changes are observed in the form of blowouts (resembling congealed “Solar protuberances”) of molten metal with complex elemental composition. The palladium surface proved to be covered with small particles, approximately $1\text{--}2\ \mu\text{m}$ in size, composed of rhenium oxide Re_2O_7 , while near the cracks and fractures the surface was covered with rhenium, carbon and oxygen crystallites of hexagonal symmetry. The entire surface of the rhenium sample became cracked and coated with a thick layer of carbon compounds with rhenium as Re_xC_y . The phenomenological model of nuclear reactions leading to the observed elemental composition of rhenium and palladium is discussed. © 2014 ISCMNS. All rights reserved. ISSN 2227-3123

Keywords: Chain reaction of deuterium heating, Dense deuterium gas, Elastic and inelastic scattering, ^2H -induced reactions, High pressure, Photon absorption and scattering

1. Introduction

In previous works [1–6] the authors described a new approach to the study of nuclear reactions in deuterated materials saturated with atomic deuterium up to stoichiometric composition [7,8]. The authors described the creation of new structures in dense gaseous deuterium in metals. This approach is based on: (a) the use of Deuterium High Pressure Chambers (DHPC), see [6], which are capable of preserving molecular deuterium in a gaseous state for a long time

*E-mail: didyk@jinr.ru

†E-mail: roland.wisniewski@gmail.com

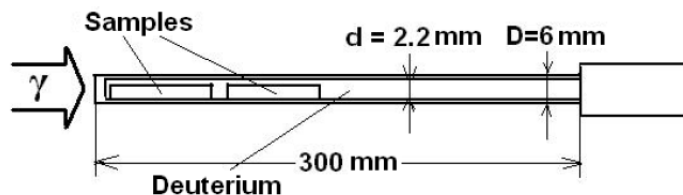


Figure 1. A schematic of the Deuterium High Pressure Chamber (DHPC) used to irradiate materials.

under pressure of up to 3–4 kbar, (b) application in HPC filled with dense gaseous molecular deuterium in which metallic or non-metallic specimens and special collectors for synthesized structures are placed, (c) irradiation of the DHPC by a flux of γ -quanta with a continuous energy spectrum, obtained at the tungsten braking target using electron beams of energies 10–25 MeV, i.e., in the region of a giant dipole resonance.

The aim of this work is to study the characteristics of nuclear reaction processes in pure metals in these conditions.

2. Experimental Technique

Palladium specimens (99.96%, in the shape of a wire of diameter 1 mm and length 110.7 mm) and rhenium specimens (99.97%, three wires of diameter 1 mm and lengths 12.5, 24.5 and 33.0 mm) were placed in a DHPC under the pressure of gaseous deuterium 2860 bar and irradiated at the electron accelerator MT-25 by electrons of energy 23.5 MeV at the average electron beam current 11–12 μA during 17.5 h of pure accelerator time.

Figure 1 shows a DHPC used for γ -quanta irradiation of specimens of various materials in the shape of wires and cylinders with relatively small diameters.

It should be noted that in the first experiment, which was described in detail in [1–5], a patented DHPC chamber [6] was used. In this experiment the walls of the DHPC constructed in frames of another project are made of 206 stainless steel to exclude chemical elements such as copper and zinc, which were observed in the first experiment. These elements formed contamination that made up a layer 80 μm thick on the palladium in the first experiment.

In the present experiment the thickness (W) of the braking target was set to 3 mm, while the aluminum electron absorber was 25 mm. Irradiation by γ -quanta with threshold energy 23 MeV was carried out for 19.5 h (7×10^4 s) at the average electron beam current 11–12 μmA . Calculation of γ -quanta spectra and fluxes as well as neutron yield from the $d(\gamma, n)p$ neutron photodisintegration reaction is described in detail in [1–5].

Before opening the DHPC (Fig. 1), the chamber pressure was measured to be 2860 bar. The palladium (99.96%, a wire of length 110 mm and diameter 1 mm) and rhenium (99.97%, three wires of lengths 12, 25 and 33 mm and diameter 1 mm) specimens placed in the chamber could be extracted only three days after deuterium desorption. The specimens, like the DHPC itself, proved to be highly activated, which prevented X-ray microelement analysis even after a long period of waiting for decreased induced activity: four full months for the palladium specimens and over eight months for the rhenium ones. As in previous studies [2–4], investigation of the structure and elemental composition of the virgin and irradiated specimens was done using scanning electron microscopy (SEM) and X-ray microelement analysis (XMA).

2.1. Experimental results for the palladium wire of length 110.7 mm

As shown in Fig. 2, the right edge of the specimen has undergone particularly considerable changes, namely, formation of an elongated part tapering towards the end from 1 to 0.461 mm in diameter with a strongly deformed frontal edge

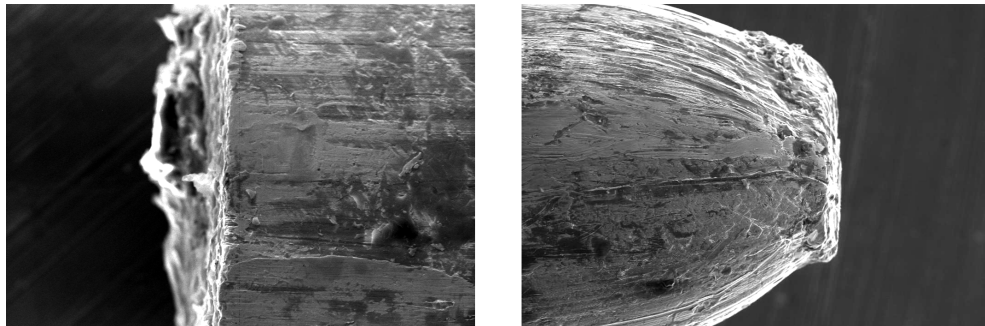
Table 1. Shows element concentrations at Points 1–3.

Element	Z	X-rayseries	Point 1		Point 2		Point 3	
			wt.%	at.%	wt.%	at.%	wt.%	at.%
C	6	K	–	–	65.24	76.22	48.31	66.42
O	8	K	15.24	27.95	18.04	15.77	14.30	14.76
F	9	K	–	–	–	–	7.52	6.28
Na	11	K	–	–	0.88	0.53	1.61	1.16
Mg	12	K	2.22	2.68	0.45	0.26	–	–
Al	13	K	50.18	54.56	12.06	6.26	12.99	7.95
Si	14	K	3.14	3.28	0.14	0.07	–	–
S	16	K	1.04	0.95	0.11	0.05	–	–
Cl	17	K	0.50	0.41	0.48	0.19	0.24	0.11
K	19	K	1.89	1.42	0.44	0.16	3.45	1.46
Ca	20	K	0.71	0.52	0.09	0.03	0.58	0.24
Cr	24	K	0.96	0.54	0.30	0.08	0.47	0.15
Mn	25	K	0.63	0.33	0.06	0.02	–	–
Fe	26	K	4.51	2.37	1.37	0.34	2.52	0.75
Ni	28	K	–	–	0.10	0.02	–	–
Cu	29	K	4.05	1.87	0.05	0.01	–	–
Zn	30	K	2.29	1.03	–	–	–	–
Pd	46	L	0.83	0.23	–	–	–	–
Re	75	L	11.82	1.86	–	–	8.32	0.74

about 100 μm wide. On both at the left (a) and right (b) ends of the wire one can observe smaller-scale inhomogeneities in the shape of congealed blowouts from the surfaces.

Figure 3 shows congealed-“Solar-protuberances” structures: (a) – blowout from the left surface in the direction opposite to the γ -quanta flux direction, (b) – blowout in the direction coinciding with the γ -quanta flux direction, and (c) – “pedestal” crystal structure on the surface from the direction of γ -quanta penetration.

Table 1 clearly shows that nuclear reactions in this experiment produce such palladium fission products as copper (^{29}Cu –1.87 at.%) and zinc (^{30}Zn –1.03 at.%). These results are similar to the results presented in [1–5]. One can also see that nuclear reactions in palladium yield light chemical elements ^{12}Mg , ^{13}Al , ^{14}Si , ^{16}S , ^{17}Cl , ^{19}K and ^{20}Ca , heavier elements ^{24}Cr , ^{25}Mn , ^{26}Fe , also ^{29}Cu and ^{30}Zn . The latter two chemical elements deserve special attention because they were found in significant quantities in the palladium cylinder surface in studies [1–5]. In order to check the reaction

**Figure 2.** SEM images of the left (a) and right ends of the palladium wire.

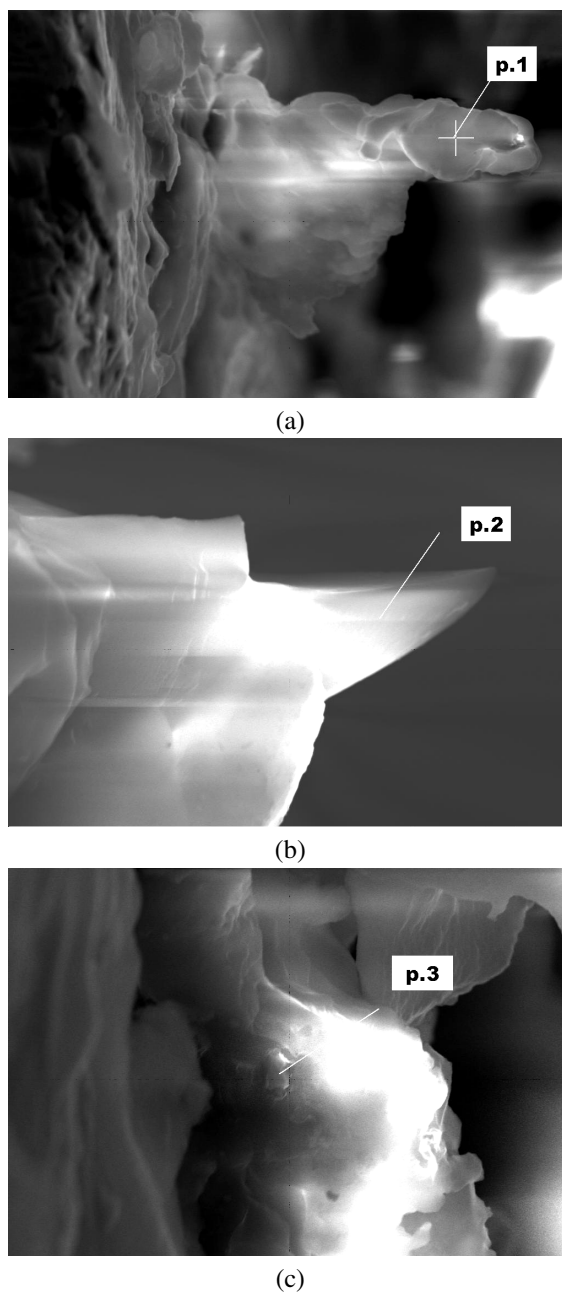


Figure 3. Two congealed blowouts from the direction of γ -quanta entry into the left end of the palladium wire and the “pedestal” of structure (Fig. 4).

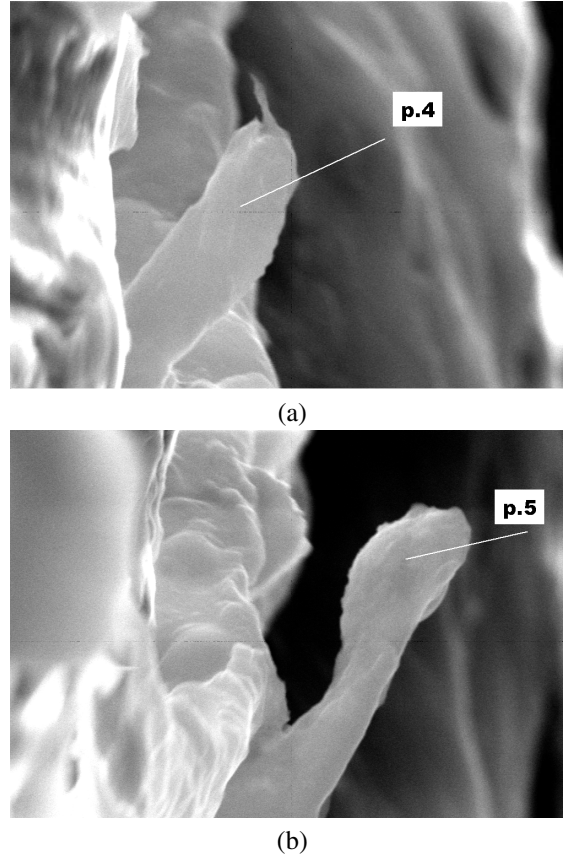


Figure 4. Two congealed blowouts from the direction of γ -quanta escape from the right end of the palladium wire.

processes in palladium with the production of ^{29}Cu and ^{30}Zn , all the materials containing these elements in the previous DHPC were replaced with stainless steel (see Fig. 1).

Figure 4 shows two photos of blowouts at the end surface, from the direction coinciding with the γ -quanta flux direction. As is shown, the elemental composition of the blowouts is comprised of a series of elements, which are lighter than palladium. Moreover, these elements are by no means coincidental. They can be obtained in nuclear reactions via fission of palladium isotopes which are described in [3,5]. The atoms of light chemical elements as ^{11}Na , ^{12}Mg , ^{13}Al , ^{14}Si , ^{16}S , ^{17}Cl , ^{19}K , ^{20}Ca , ^{24}Cr , ^{25}Mn , ^{26}Fe , and ^{28}Ni have greater volatility than the atoms of heavy chemical elements such as ^{46}Pd ; therefore, the palladium concentration is small or completely absent from the chemical composition of the congealed blowout (see Table 2). The speed of particle evaporation from the surface, introduced in [9], represents as

$$\frac{dn}{dt} = N \left(\frac{kT}{2\pi M} \right)^{1/2} \exp \left[-\frac{U_0}{kT} \right],$$

where N , k , T , M , and U_0 are the atomic density of particles in liquid phase, Boltzmann's constant, temperature on the surface, mass of the escaping particle and particle-surface binding energy, respectively.

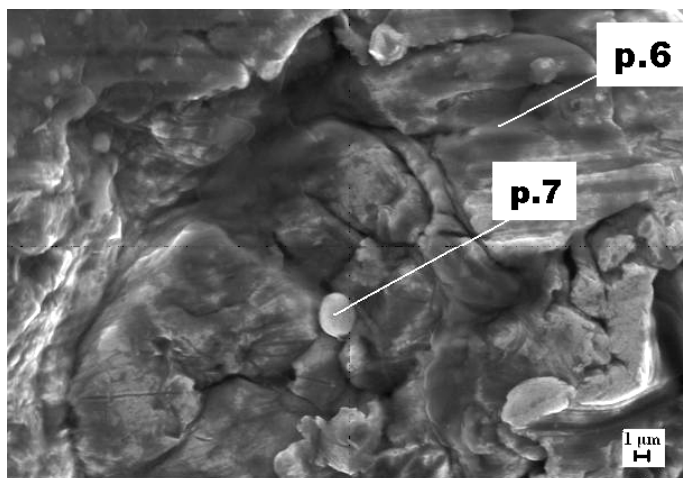


Figure 5. SEM image of surface patch near the tapering part from Fig. 2 (b).

Table 2 shows congealed blowouts of the elemental compositions in the cavities at Points 4 and 5. In Fig. 4, the SEM image shows a surface patch near the tapering part (Fig. 2 (b)) with two points where XMA analysis was carried out.

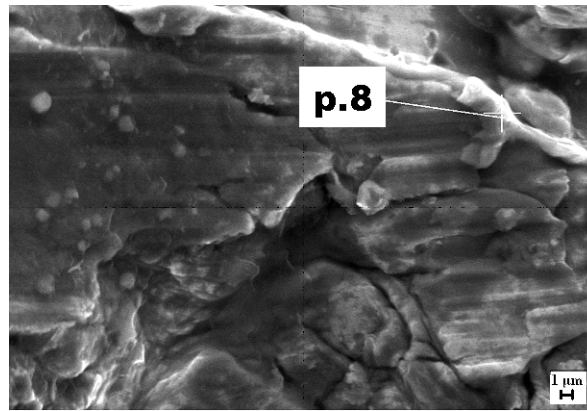
As is evident from Table 3 (Point 6), when the palladium concentration is significantly high, iron, nickel and chromium are also present. The composition of these elements is close to the elemental composition of the 206 stainless steel, which comprises the material of the DHPC wall: Fe-60.4%; Cr-30.5%, and Ni-9.0%. Nevertheless, the measured concentration of these elements is different from the original construction stainless steel composition. Apart from this, one can also observe significant amounts of aluminum (17.29 at.%) and copper (2.02 at.%). Analysis of a particle observed on the palladium wire surface (at Point 7) revealed a high concentration, for instance, of iron (38.39 at.%) and also carbon (37.76 at.%).

Table 2. Shows the elemental compositions in the cavities at Points 4 and 5.

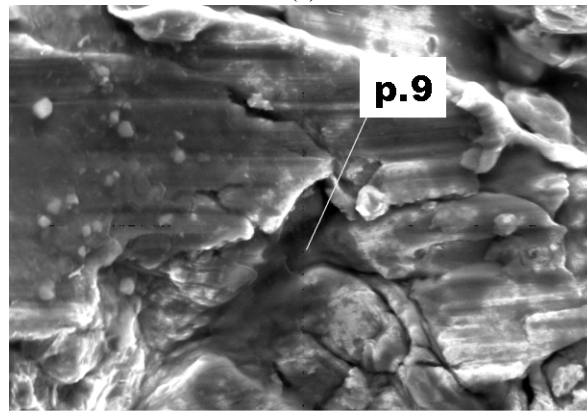
Element	Z	X-ray series	Point 4		Point 5	
			wt.%	at.%	wt.%	at.%
⁶ C	6	K	30.40	47.58	–	–
⁸ O	8	K	9.52	11.42	10.82	18.19
Na	11	K	–	–	1.36	1.59
Mg	12	K	1.32	1.02	1.67	1.85
Al	13	K	55.14	38.42	68.73	58.55
Si	14	K	0.37	0.45	1.58	1.51
S	16	K	0.11	0.07	0.29	0.25
Cl	17	K	0.74	0.39	0.77	0.58
K	19	K	0.43	0.20	0.64	0.44
Ca	20	K	0.27	0.13	5.74	3.86
Cr	25	K	0.29	0.10	0.83	0.43
Mn	25	K	0.36	0.12	0.58	0.28
Fe	26	K	0.82	0.28	2.20	1.06
Ni	28	K	0.02	0.01	0.95	0.44
Pd	46	L	–	–	3.84	0.97

Table 3. Provides elemental compositions for Points 6 and 7 from Fig. 5.

Element	Z	X-ray series	Point 6		Point 7	
			wt. %	at. %	wt. %	at. %
C	6	K	–	–	13.15	37.76
O	8	K	–	–	6.60	14.24
Mg	12	K	–	–	1.13	1.61
Al	13	K	5.18	17.29	0.46	0.62
Si	14	K	–	–	0.39	0.48
Cr	24	K	0.93	1.60	0.57	0.38
Fe	26	K	1.97	3.17	62.15	38.39
Ni	28	K	0.31	0.47	2.53	1.49
Cu	29	K	–	–	3.72	2.02
Pd	46	L	81.61	77.46	9.27	3.01



(a)



(b)

Figure 6. SEM images of a surface patch near the tapering part from Fig. 2(b).

Table 4. Provides elemental compositions for Points 8 and 9 marked in Fig. 6.

Element	Z	X-ray series	Point 8		Point 9	
			wt. %	at. %	wt. %	at. %
C	6	K	6.42	37.25	17.17	43.80
O	8	K	–	–	14.38	27.54
F	9	K	–	–	3.37	5.44
Na	11	K	–	–	0.82	1.03
Al	13	K	0.42	1.08	0.69	0.79
Si	14	K	–	–	0.40	0.44
P	15	K	–	–	0.26	0.26
Ca	20	K	–	–	0.93	0.71
Cr	24	K	0.39	0.52	–	–
Mn	25	K	–	–	0.18	0.10
Fe	26	K	0.66	0.82	0.33	0.18
Pd	46	L	92.11	60.32	59.52	17.14

As shown here, along with the relatively high palladium concentration, significant amounts of carbon are observed, as in the previously measured surface patch (${}^6\text{C}$ -37.25 at.%). Similarly to the congealed blowouts (see Fig. 2 (a,b)), there is an even greater variety of light atoms of chemical elements such as ${}^6\text{C}$ (43.80 at.%), ${}^7\text{N}$ $\uparrow(?)$, ${}^8\text{O}$, ${}^9\text{F}$, ${}^{10}\text{Ne}$ $\uparrow(?)$, ${}^{11}\text{Na}$, ${}^{12}\text{Mg}$, ${}^{13}\text{Al}$, ${}^{14}\text{Si}$, ${}^{15}\text{P}$, ${}^{16}\text{S}$, ${}^{17}\text{Cl}$, ${}^{18}\text{Ar}$ $\uparrow(?)$, ${}^{19}\text{K}$, ${}^{20}\text{Ca}$, ${}^{25}\text{Mn}$, ${}^{26}\text{Fe}$, and ${}^{46}\text{Pd}$. One can see that all chemical elements are present here, beginning with $Z = 6$ (${}^6\text{C}$), $Z = 20$ (${}^{20}\text{Ca}$), where symbols $\uparrow(?)$ indicate volatile elements which are impossible to register in a non-bound state by microelement analysis.

Figure 7 shows SEM images of two surface patches, also near the tapering part (Fig. 2(b)), with several particles on the palladium surface analyzed using XMA.

It should be noted that all foreign particles in both images are of approximately similar composition, containing significant amounts of rhenium up to 6.03 at.%. Moreover, since these particles are sufficiently small, being up to 1–2 μm in size, the XMA analysis naturally covers also the area around and under these particles. This might account for the “increase” in the palladium concentration, bearing in mind that these particles are most likely comprised of low-melt-point rhenium oxide (Re_2O_7) with the melting temperature around 200°C, which is confirmed by our observation of a very significant concentration of oxygen ${}^8\text{O}$ (64.08 at.%) apart from rhenium. It is known that rhenium oxide Re_2O_7 is formed at the temperatures over 150°C in presence of large amounts of oxygen. The boiling temperature for rhenium is slightly above 350°C.

Table 6 shows the elemental compositions for a monocrystal at Points 11 and 12. It is clear that due to the small size of the analyzed crystal, approximately 1.5–2 μm , and its relatively small thickness, the element analysis covers a larger volume than the crystal volume. But even taking account of this, the atomic concentration of rhenium reaches 6.61 at.%. Of special interest is the analysis of the elemental composition in the cracks formed in the palladium wire. It is precisely the areas with noticeable structural disturbances that suffered the most overheating and attendant mechanical stress.

Table 5. Provides the elemental composition for Point 10 indicated in Fig. 7.

Element	Z	X-ray series	wt. %	at. %
O	8	K	21.52	64.08
Na	11	K	1.04	2.15
K	19	K	4.22	5.14
Fe	26	K	0.90	0.77
Pd	46	L	48.75	21.83
Re	75	L	23.58	6.03

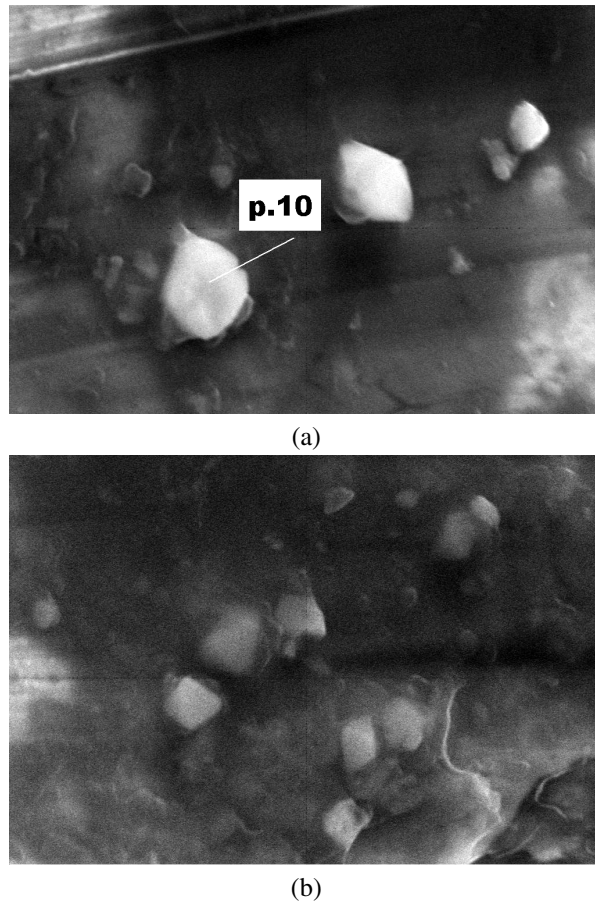


Figure 7. SEM images of two surface patches near the tapering part in Fig. 2(b) with foreign particles.

Consequently, this is where nuclear fission reactions with high energy release took place.

It is evident that the element analysis of the crack walls and bottom is not sufficiently reliable (Point 12) but it was not our goal to determine the element concentration with high accuracy. Also, one can observe in the crack significant amounts of silicon (^{14}Si –26.89 at.%) in combination with oxygen (^{16}O –51.11 at.%).

2.2. Experimental results for a rhenium wire of length 12 mm

It should be noted first and foremost that it was possible to carry out SEM and XMA studies only by using a rhenium wire 12.5 mm long because it had been placed at a distance of 110 mm (behind the palladium wire) from the back wall of the DHPC entrance window. And because it was smaller in size and, consequently, it had acquired a lower induced activity. The other rhenium specimens (of the length 25 and 33 mm) are not accessible for study at the moment due to their high activation level and slow decline of induced activity. Figures 9(a) and (b) provides SEM images of a rhenium wire with the place of entry of γ -quanta (a) and its reverse side (b), respectively.

Figure 10(a) shows a SEM image of surface patch of a rhenium wire 12 mm long near the crack. Once again it is of

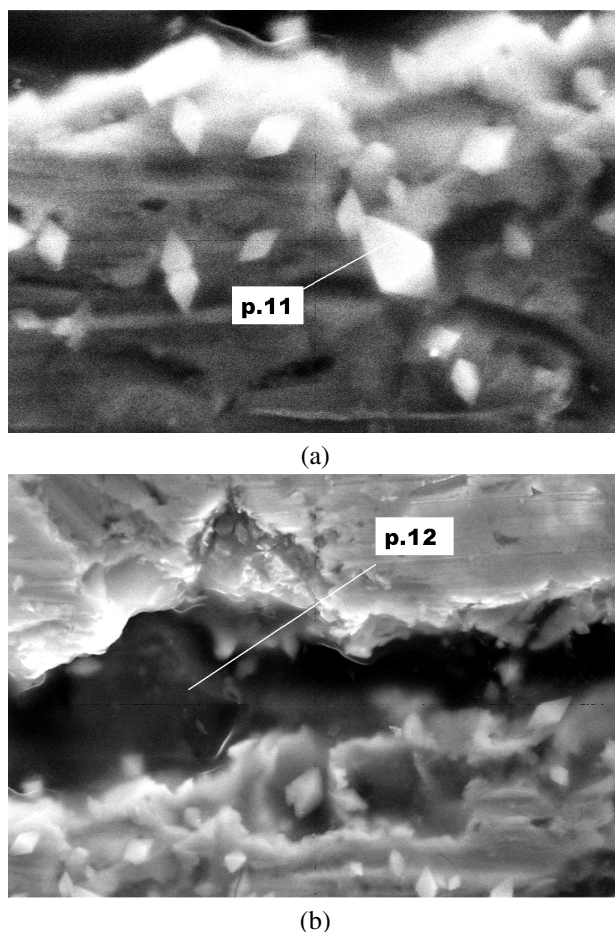


Figure 8. SEM images of the crack and hexagonal microcrystals on the side surface of the palladium wire.

interest to estimate the concentrations of impurities produced in nuclear reactions from the most degraded cavities, i.e. from the cracks one of which is presented in Fig. 10 (b). Averaged XMA analysis was carried out over three surface patches. Results are summarized in Table 7.

As one can see, the entire rhenium surface is coated with a carbon layer, with the carbon concentration reaching 80.94 at.%, a rhenium concentration of only 4.92 at.% and relatively high concentration of osmium up to 0.84 at.%

3. Discussions and Conclusions

The results obtained in this study on the changes in the surface structure, bulk properties and chemical composition of palladium and rhenium specimens under irradiation by γ -quanta of a continuous spectrum with the threshold energy 23 MeV confirm our conclusions from previously obtained data on the synthesis of a novel structure and the production of chemical elements lighter than palladium in the DHPC structures (see [1–5]).

In contrast to previous studies [1,2,4], the material of all the DHPC elements in these studies was replaced with

Table 6. The elemental compositions for a monocrystal at Points 11 and 12.

Element	Z	X-ray series	Point 11		Point 12	
			wt.%	at.%	wt.%	at.%
O	8	K	28.60	72.12	29.59	55.11
Na	11	K	0.54	0.95	–	–
Al	13	K	0.42	0.63	0.62	0.69
Si	14	K	–	–	25.35	26.89
S	16	K	0.19	0.23	1.11	1.03
Cl	17	K	0.12	0.14	1.09	0.91
K	19	K	5.60	5.77	1.65	1.26
Ca	20	K	–	–	2.42	1.80
Mn	25	K	0.76	0.56	1.48	0.80
Fe	26	K	1.09	0.79	4.23	2.26
Ni	28	K	–	–	0.68	0.34
Zn	30	K	–	–	0.74	0.34
Pd	46	L	32.19	12.20	30.05	8.41
Re	75	L	30.50	6.61	–	–
Pt	78	L	–	–	0.99	0.15

stainless steel (see Fig. 1) to exclude presence in the chamber of such chemical elements as copper and zinc. The energy of γ -quanta was increased up to 23 MeV to introduce into consideration (γ, n) processes in the giant dipole resonance energy interval [3,5].

Apart from the cracks, significant destruction of the palladium surface and the unusual changed form of the palladium wire end at the spots of entry and exit of γ -quanta (see Fig 2), there were also observed blowouts which resemble congealed “Solar protuberances” and are composed of lighter chemical elements than palladium: ${}^6\text{C}$, ${}^7\text{N}\uparrow(?)$, ${}^8\text{O}$, ${}^9\text{F}$, ${}^{10}\text{Ne}\uparrow(?)$, ${}^{11}\text{Na}$, ${}^{12}\text{Mg}$, ${}^{13}\text{Al}$, ${}^{14}\text{Si}$, ${}^{15}\text{P}$, ${}^{16}\text{S}$, ${}^{17}\text{Cl}$, ${}^{18}\text{Ar}\uparrow(?)$, ${}^{19}\text{K}$, ${}^{20}\text{Ca}$, ${}^{22}\text{Ti}$, ${}^{24}\text{Cr}$, ${}^{25}\text{Mn}$, ${}^{26}\text{Fe}$, and ${}^{28}\text{Ni}$. Observation of such “protuberances” attests to the presence on the DHPC inner walls from stainless steel (see Fig. 1) of congealed alloy drops composed from the “protuberances” material and to the presence of a synthesized structure on the back wall in the direction of γ -quanta flux, similarly to [1–5]. The “protuberances” allow us to both confirm and explain the formation of the synthesized structure in the special collector from the first experiments described in [1–5].

On the palladium surface one can observe rhenium particles of small size in considerable concentrations (see Figs. 7 and 8, Tables 1, 5 and 6).

As is well known, the melting and sublimation temperatures for rhenium are 3453 and 5873 K [6]. Rhenium has a hexagonal densely packed structure. Oxidation of rhenium occurs at 600°C while in presence of oxygen the metal burns out when heated at the temperature over 400°C. Rhenium oxidation with formation of oxides (ReO_3 , Re_2O_7) is observed starting with 300°C, proceeding intensively at the temperatures over 600°C. Rhenium does not interact with hydrogen up to the melting temperature and only absorbs it. However, rhenium can adsorb nine atoms of hydrogen or deuterium, forming $[\text{ReH}_9]^{2-}$ or $[\text{ReD}_9]^{2-}$ compounds [6,7]. *It is precisely this fact that motivated the authors to test rhenium along with palladium, as well as for the purpose of producing rhenium deuteride.*

Table 7. Results of averaged XMA analysis.

Element	${}^6\text{C}$	${}^8\text{O}$	${}^{12}\text{Mg}$	${}^{16}\text{S}$	${}^{19}\text{K}$	${}^{20}\text{Ca}$	${}^{26}\text{Fe}$	${}^{75}\text{Re}$	${}^{76}\text{Os}$
Initial	–	–	–	–	–	–	–	100	–
Spectrum 1	65.65	17.44	–	–	–	–	–	16.07	0.84
Spectrum 2	80.94	13.35	–	0.25	0.10	–	0.16	4.92	0.28
Spectrum 3	72.95	14.37	–	–	–	–	–	11.91	0.77
Spectrum 4	72.22	18.90	0.87	0.39	–	1.15	–	6.48	–

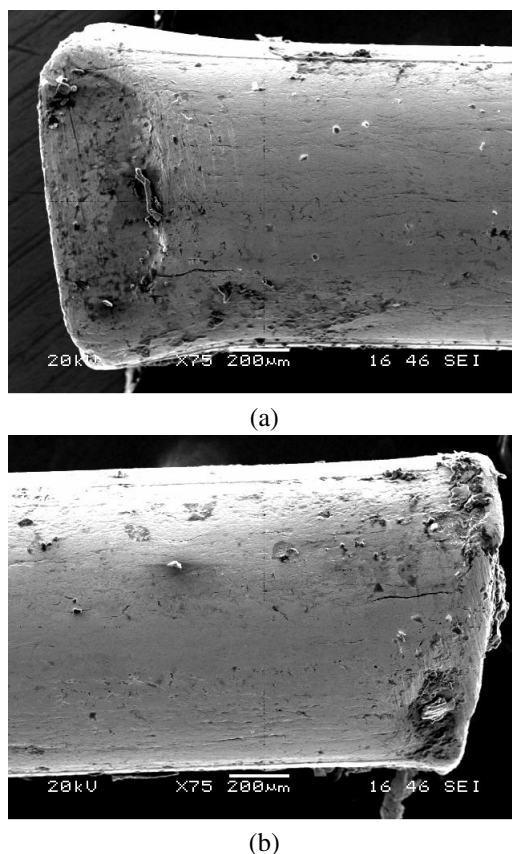


Figure 9. Two sides of a rhenium wire: (a) place of entry of γ -quanta and (b) reverse side.

Rhenium, as contrasted with other high-melting-point metals, does not form carbides. Let us consider specifically the rhenium oxide (VII) Re_2O_7 . Its melting and boiling temperatures are $t_{\text{melt}} = 301^\circ\text{C}$ and $t_{\text{boil}} = 362.4^\circ\text{C}$ [6,7]. Rhenium oxide Re_2O_7 is very volatile at relatively low temperatures; therefore, it evaporates very rapidly from the surface and does not protect rhenium from further oxidation, unlike most of rare-earth metal oxides [6,7]. It sublimates at temperatures above 220°C . Consequently, the rhenium-containing crystallites observed on the surface of palladium are apparently composed of rhenium oxide, which became crystallized near the cracks on cooling (see Figs. 8 and 9).

One can see that there are high concentrations of carbon (see Table 1 – 76.22 and 66.42 at.%, Table 2 – 47.58 at.%, Table 4 – 37.76, 37.25 and 42.80 at.%) and oxygen (Table 5 – 64.08 at.%, Table 6 – 72.12 and 55.11 at.%) in the palladium specimen. The rhenium specimens are marked by high concentrations of carbon (see Table 7 – 65.65, 80.94, 72.95 and 72.22 at.%). In these cases the high carbon concentration is generally accompanied by a significant concentration of oxygen. Conversely, a high oxygen concentration is usually accompanied by considerable carbon concentration. All basic reactions producing lighter elements than palladium are considered in works [3,5]. As was shown in [13,14], the formation of carbon and oxygen in large quantities in nuclear reactions with oxidation of rhenium and other elements is accompanied by the production of relatively heavy elements, which are however lighter than palladium and rhenium, such as ^{38}Sr , ^{40}Zr , ^{42}Mo , and the radioactive elements ^{39}Y , ^{41}Nb and ^{70}Yb , ^{71}Lu , ^{72}Hf in the

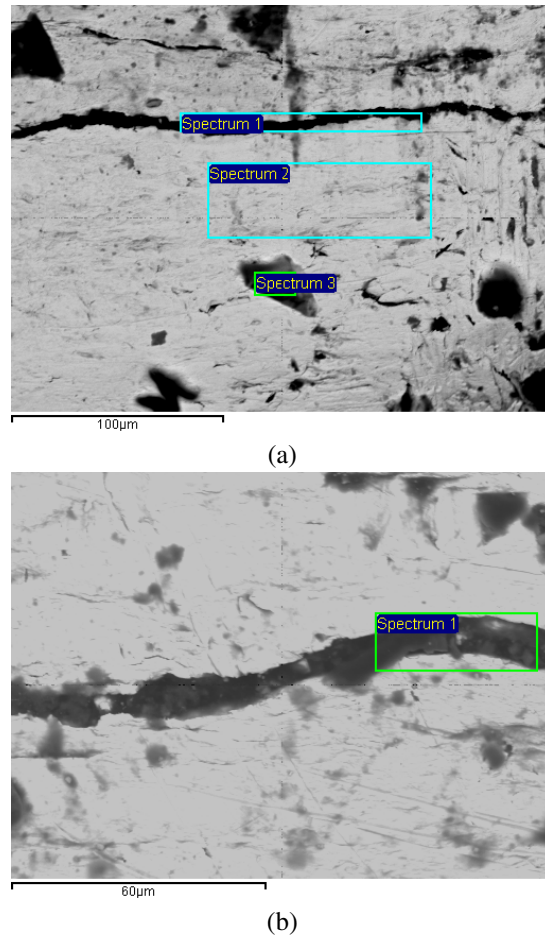


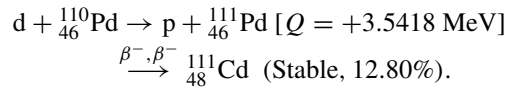
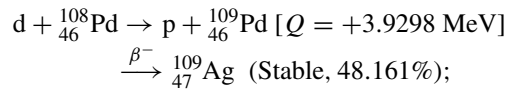
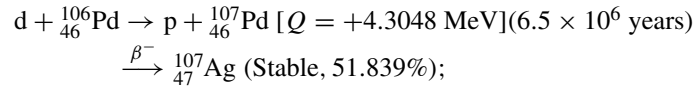
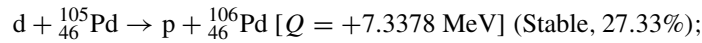
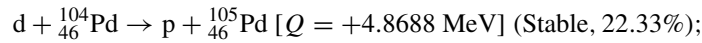
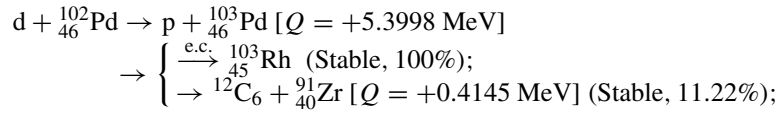
Figure 10. The surface structure of a rhenium wire with marked patches for XMA analysis.

^{75}Re specimen. In this case decay chains up to stable and long-lived decay products are registered. This provides exactly the grounds needed for a detailed presentation of possible Pd and Re fission reactions with decay chains.

It should be noted separately that under the irradiation of the DHPC with rhenium and palladium wires by γ -quanta of energies up to 23 MeV high temperatures with energy release were obtained. This opens up the possibility of constructing deuterated fission reactors (DFR) for power generation, based on deuterium-saturated metals under γ -quanta irradiation [8].

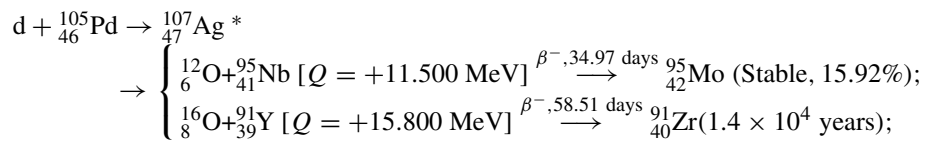
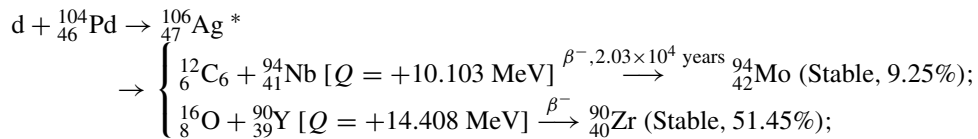
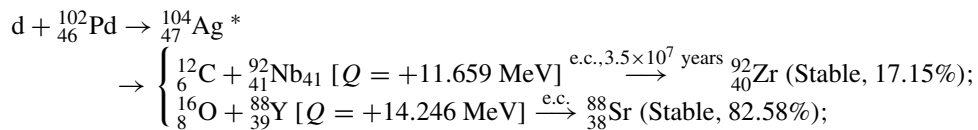
Appendix A.

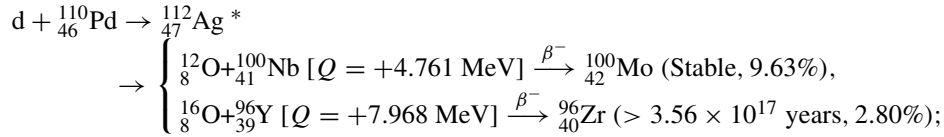
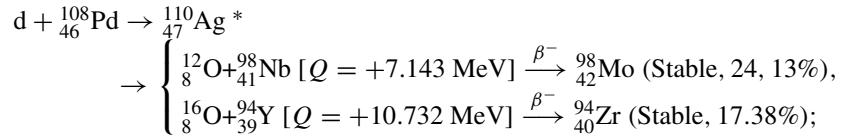
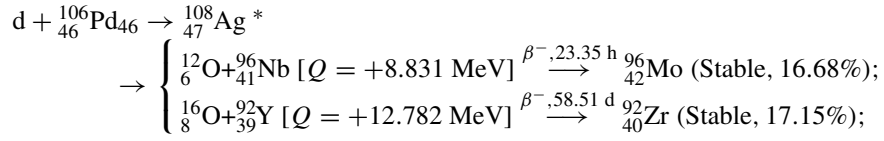
Consider the Oppenheimer reactions with deuterium [9] in Pd wire (see also [10–12]).



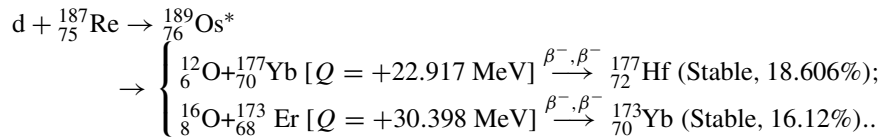
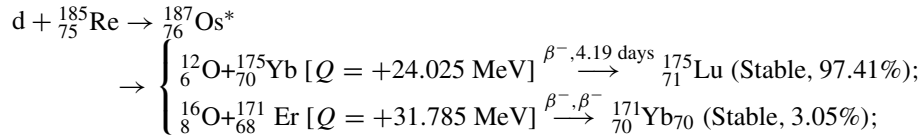
As one can see, carbon can be formed only in reactions with ${}^{102}_{46}\text{Pd}$, but the concentration of this isotope is only 1.02%. Correspondingly, in the Oppenheimer reaction it is difficult to obtain the concentrations of oxygen and carbon experimentally detected, since the nuclei forming in this case are stable.

We consider therefore the reactions of the subbarrier fusion of deuterium with the formation and fission of a compound nucleus to the scheme proposed in [10–12].

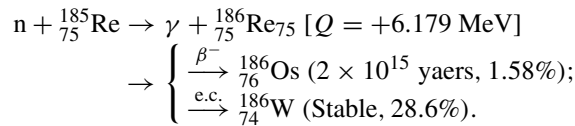
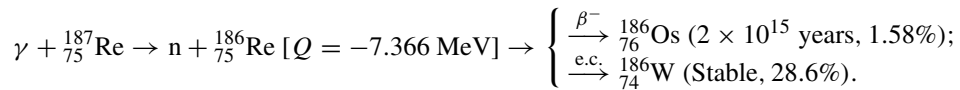


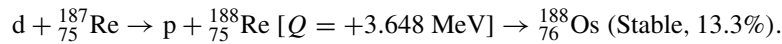
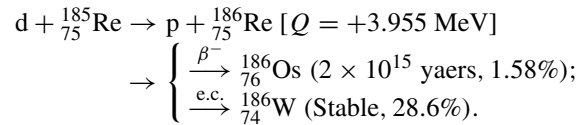
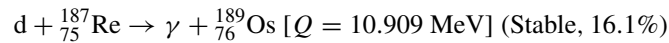
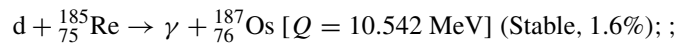
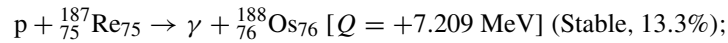
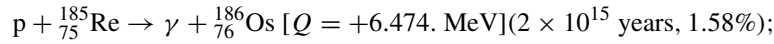
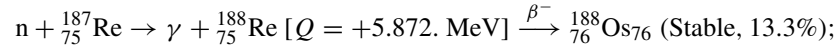


Consider the formation of carbon and oxygen upon the fission of an excited rhenium nucleus after subbarrier fusion with deuterium:



Now, let us consider reactions of the osmium (${}_{76}\text{Os}$) and tungsten (${}_{74}\text{W}$) formations:



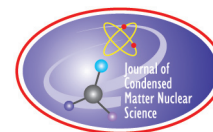


One can conclude that the formation of a large amount of carbon and oxygen upon the oxidation of rhenium (and other elements as the products of nuclear reactions) must be accompanied by the formation of a sequence of relatively heavy (but lighter than Pd and Re) atoms, such as ${}_{38}\text{Sr}$, ${}_{40}\text{Zr}$, ${}_{70}\text{Yb}$, ${}_{71}\text{Lu}$, and ${}_{72}\text{Hf}$ radioactive and stable nuclei. In addition, the disintegration chains up to stable or long-living products should also be registered. This motivates a detailed discussion of possible fission reactions in Pd, Re and the corresponding disintegration chains [13,14].

References

- [1] A. Yu. Didyk and R. Wisniewski, Nuclear reactions induced by g-quanta in palladium saturated with deuterium, surrounded by dense deuterium gas, *Eur. Phys. Lett.* **99** (2012) 22001-P1–22001-P6.
- [2] A. Yu. Didyk and R. Wisniewski, Chemical composition and structural phase changes of Pd sample and properties of novel synthesized structure at dense deuterium gas under irradiation by γ -quanta, *Phys. Particles and Nucl. Lett.* **9**(8) (2012) 615–631; Preprint E15-2012-34. Dubna. JINR, 2012. 26 p.
- [3] A. Yu. Didyk and R. Wisniewski, Phenomenological nuclear reaction description in deuterium saturated palladium and synthesized structure in dense deuterium gas under irradiation by γ -quanta, *Phys. Particles and Nucl. Lett.* **10**(4(181)) (2013) 603–611; Preprint E15-2012-35. Dubna. JINR, 2012. 25 p.
- [4] A. Yu. Didyk and R. Wisniewski, Synthesis of new structures in dense gaseous deuterium and saturated with deuterium palladium in nuclear reactions induced by γ -quanta, *Phys. Chemi. Materials Processing* **5**(5) (2012) 5–13; Preprint R15-2012-50, Dubna, JINR, 17 p.
- [5] A. Yu. Didyk and R. Wisniewski, Nuclear reactions in saturated with deuterium palladium and rhenium in dense deuterium gas under irradiation by γ -quanta of continuous spectrum with threshold energy 23 MeV, *Phys. Particles and Nucl. Lett.* **10**(4) (2013) 381–392; Preprint R15-2012-63. Dubna, 2012, 21 p.

- [6] A.Yu. Didyk and R. Wisniewski, Properties of Hydrogen and its Isotopes under High Pressure, and Technological Applications, Monograph, Dubna, 2013, 320 p.
- [7] Transition metal hydrides, edited by Earl L. Muetterties (Marcel Dekker, New York, 1971), 342 p.
- [8] A.Yu. Didyk, R. Wisniewski and T. Wilczynska-Kitowska, Device for energy production. Patent on Application Model, No. 122198, 21 May 2012.
- [9] J.R. Oppenheimer and M. Phillips, Note for the transmission functions for deuteron, *Phys. Rev.* **48**(15) (1935) 500–502.
- [10] J.G. Moretto, *Nucl. Phys. A* **247** (1975) 211.
- [11] A.J. Sierk, Mass-asymmetric fission of light nuclei, *Phys. Rev.* **55**(6) (1985) 582–583.
- [12] A.J. Sierk, Macroscopic model of rotating nuclei, *Phys. Rev.* **55**(6) (1986) 2039–2052.
- [13] A.Yu. Didyk and R. Wisniewski, Nuclear reactions in deuterided palladium and rhenium irradiated with a continuous spectrum at a threshold energy of 23 MeV in dense deuterium gas, *Phys. Particles and Nucl. Lett.* **10**(4) (2013) 381–392.
- [14] A.Yu. Didyk and R. Wisniewski, The study of changes in the elemental composition changes of Re and Pd samples, irradiated in dense deuterium by γ -quanta of threshold energy 23 MeV, *J. Phys. Sci. Appl.* **3**(4) (2013) 209–217.



Research Article

Measurement Artifacts in Gas-loading Experiments

O. Dmitriyeva ^{*†} and R. Cantwell

Coolscience, LLC, Boulder, CO, USA

G. Moddel

University of Colorado at Boulder, CO, USA

Abstract

Numerous reports on gas loading of hydrogen isotope into powdered materials indicate excess heat generation that could be the result of a low energy nuclear reaction (LENR). When the amount of generated heat is small, it is important to characterize the calorimeter to account for possible measurement errors, or artifacts, which can result in long-term apparent excess heat. In this paper we investigate one of those possible measurement artifacts applicable to the gas loading systems that (1) use thermometry as a proxy for energy flow measurements, and (2) run at elevated temperatures. When loading gas into Pd-impregnated alumina, we have found that thermal gradients inside the system result in apparent heating or cooling of the measuring system. We experimentally magnified this effect and confirmed that it was due to temperature nonuniformity inside the calorimetric system. We quantified the effect using a numerical simulation tool to show that a temperature gradient as small as 0.5 K/m might result in 50 mW of apparent excess heat “generation”. We suggest a simple approach for investigators to account for this measurement artifact by calibrating their systems with helium gas either prior to, or at the end of, the experimental sequence.

© 2014 ISCMNS. All rights reserved. ISSN 2227-3123

Keywords: Calibration, Gas-loading, Heat, Measurement, Palladium

1. Introduction

In recent years investigations have been reported on deuterium and hydrogen gas loading of a variety of nanoparticle materials including Pd- and Ni-based composites [1–6] because they have exhibited anomalous heat production and can potentially be used in the energy-generating devices. Excess heat observed in these systems is interpreted as an evidence of a low energy nuclear reaction (LENR). In the absence of reproducible data on nuclear byproducts, the majority of the reports are based on heat measurement results. The systems used for these experiments has varied but the basic concept of comparing the amount of heat generated by the system in the presence or in the absence of the reacting gas is common to all experiments.

^{*}E-mail: olga@coolscience.com

[†]Also at: University of Colorado at Boulder, CO, USA

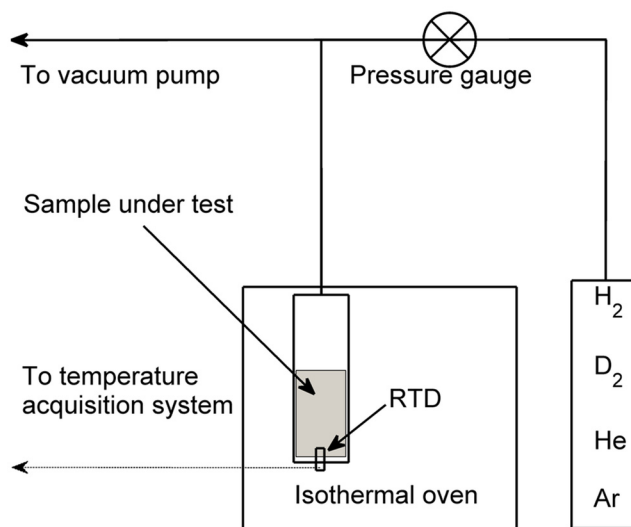


Figure 1. Schematic representation of the gas-loading system. The sample vessel is enclosed in an oven. Temperature is measured using resistance temperature detectors (RTDs).

We have replicated and analyzed the results of gas-loading reactions in Pd and Pt-impregnated alumina and zeolite powders and Pd-coated Ni-based composites. Earlier studies showed that some excess heat could be explained by the chemical reaction of substituting hydrogen with deuterium in residual water trapped in the material, known as an H/D exchange reaction [5,6]. However, at temperatures above 200°C we observed heating and cooling that could not be explained by conventional chemistry. Anomalous temperature shifts were observed as long as the sample was under gas pressure, with the longest run lasting 96 h, after which the sample was evacuated and the gas was removed. This run was performed at 390°C, and 50 mW of estimated excess heat was observed. The effect went away when the vessel was repositioned inside the experimental chamber, which gave rise to the question as to whether a measurement artifact could account for these observations. While we discovered this artifact in our setup, it is possible that any other gas loading system which uses thermometry to evaluate energy flow could be a subject to this error. Experiments that are run at elevated temperatures are more prone to this artifact since the temperature gradients are naturally higher. In this paper we describe our investigation of this measurement artifact and conclude by suggesting the calibration technique that can account for it.

2. Experiment

2.1. Experimental system and procedure

Figure 1 shows the block diagram of the experimental setup. The vacuum system was enclosed in an isothermal chamber (an HP 5890A gas chromatograph oven). This oven is designed for precise temperature control. The temperature uniformity across the oven is achieved by constant air flow produced by a heater and a fan at the back panel of the oven. The temperature of the oven can be set anywhere between 40°C and 400°C. We ran all the experiments at temperatures below 390°C.

Removable stainless steel vessels, which are part of the vacuum system, were placed inside the oven and connected to the gas line. Pipe plug resistance temperature detectors (RTDs) (Omega p/n RTD-NPT-72-E-MTP-HT) were welded

into the bottom of the vessels to measure temperature change. The sample material was loaded into the vessels.

Hydrogen, deuterium, helium, or argon were supplied through the gas line. The vacuum system was pressurized up to 1.6×10^5 Pa (1200 torr). A turbo-molecular pump was used to evacuate the system down to 10^{-5} Pa. System control, and temperature and pressure data acquisition were carried out with LabView software.

A typical run consisted of (1) pressurization by a gas of choice, (2) a period of time when the vacuum system remained under gas pressure, and (3) an evacuation step. Heat production or consumption was determined from temperature changes in the vessel, whose transient temperature can deviate from the constant oven temperature baseline. Net positive temperature change measured using the RTD was considered as heating, and negative as cooling.

2.2. Material

For this study we used three samples: alumina powder with no Pd content (Fisher Scientific P/N: CAS 1344-28-1), 2% by weight Pd-impregnated alumina powder, and commercially available Ni powder (Alfa Aesar P/N 43214). We tested these materials to see how their thermal conductivity affected the measurements. The chemistry and fabrication method of wet impregnation of Pd metal into alumina are beyond the scope of this paper, and a detailed description can be found in Ref. [6].

2.3. Hypothesis

We conducted our experiments in an isothermal oven. The sample vessel inside the oven then went through gas pressurization/depressurization cycles to detect a temperature change due to the gas-loading process. The assumption in gas-loading experiments is that heat produced under gas pressure is an indication of a reaction inside the vessel. This is a valid assumption as long as a stable temperature baseline is established, and temperature is uniform across the oven. However, at elevated temperature this uniformity is broken due to location-dependent variations in hot air flow from the oven heater. The effect becomes more noticeable as the temperature setting is raised. Local hot and cold spots are created as a result of this nonuniformity. Because the stainless steel vessel is a poor heat conductor when it is evacuated, such hot and cold spots couple weakly to the RTD. However, when the vessel is pressurized, the presence of gas changes drastically the heat conduction inside it and causes the RTD to couple more efficiently to the hot or cold spots in the oven than when under vacuum. This results in channeling of heat from or into the oven environment. This channeling effect can artificially shift the measurement baseline up or down, which can be mistaken for anomalous heating or anomalous cooling.

To test this hypothesis we artificially created and enhanced the hot and cold spot effect by placing a local heating or cooling element on the surface of the vessel that would later be pressurized with hydrogen, deuterium, helium, or argon. If our hypothesis is correct, then in the presence of the hot spot (dissipative resistor), the measurement baseline would shift upwards when the vacuum system was pressurized, and in the presence of the cold spot (Peltier element), downwards. Moreover, the difference in the heat conduction coefficients of supplied gases should affect the magnitude of the baseline shift. While hydrogen, deuterium and helium have similar thermal conduction coefficients, argon's thermal conductivity is ten times smaller. If our assumption is correct than an argon run would show a smaller baseline shift. The presence of material inside the vessel should also affect the conductive characteristics of the vacuum system, and thus the magnitude of a baseline shift. When evacuated, a loose powdered material is a poor heat conductor due to the spacing between the particles. When under pressure, however, the gas might establish a thermally conductive channel between particles. We expected the effect to be a result of a mixed contribution of the different factors such as the powder's packing density and the thermal conductivity of the sample.

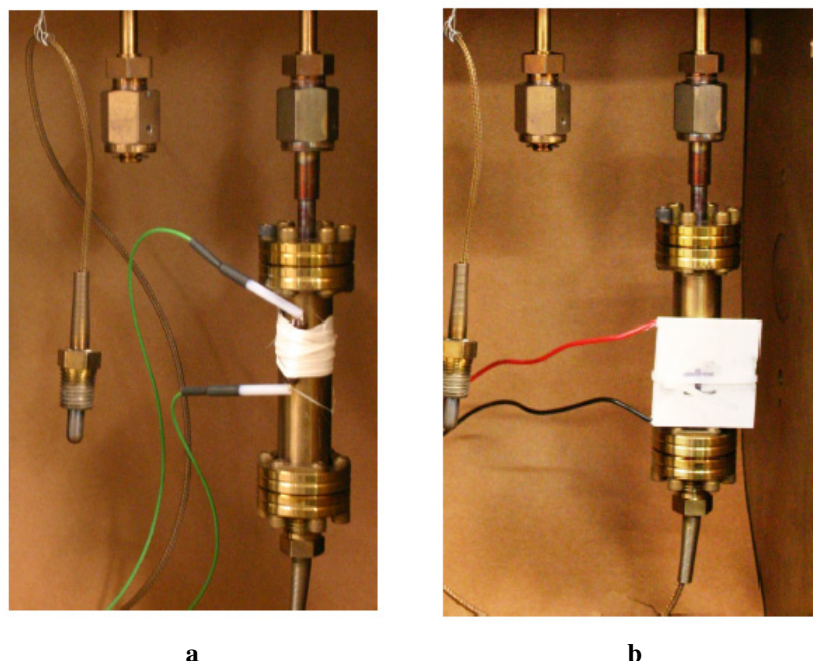


Figure 2. The vessel inside the oven with a (a) dissipative resistor, (b) cooling element.

3. Results

3.1. Hot spot

The hot spot was formed by placing a $150\ \Omega$ resistor on the surface of the vessel, containing 6 g of Pd-impregnated alumina powder. Figure 2 (a) shows the view inside the oven, with the resistor attached on the surface of the vessel.

The oven was kept at 100°C , and 1 W was dissipated in the resistor. The purpose of this exercise was to simply create a thermal gradient across the vessel. In Fig. 3 plot (a) shows the results of the gas pressurizations carried out in the absence of an artificially created thermal gradient.

The oven was kept at 100°C , and 1 W was dissipated in the resistor. In Fig. 3 plot (a) shows the results of the gas pressurizations carried out in the absence of an artificially created thermal gradient.

When no power was dissipated through the resistor the only temperature changes during pressurization cycles were due to absorption/desorption of the hydrogen isotopes in Pd [7] and the gas compression/expansion. Since neither helium nor argon is absorbed in Pd, the runs with those gases showed only temperature change associated with gas compression/expansion. The picture changes drastically when we powered the resistor. In Fig. 3, plot (b) shows a visible baseline shift whenever the vacuum system was pressurized. The baseline shift was similar for deuterium, hydrogen and helium runs and different for argon.

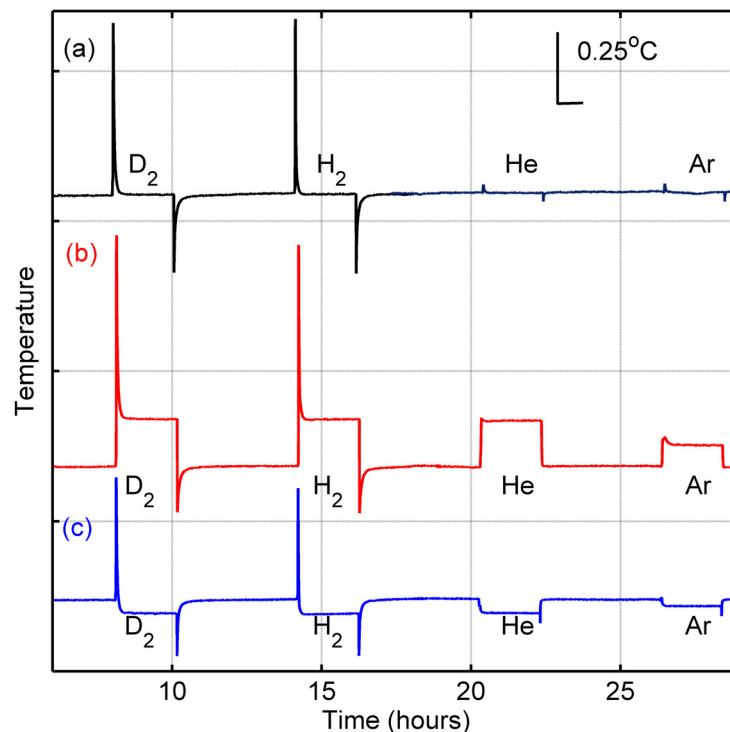


Figure 3. Experimentally observed temperature changes due to gas loading of Pd-impregnated alumina (a) in the absence of an artificially produced thermal gradient; (b) in the presence of a hot spot; (c) in the presence of a cold spot. Pressurizations were carried out with deuterium, hydrogen, helium and argon.

3.2. Cold spot

The cold spot was formed by a Peltier element (TEC1-12706) held against the vessel surface as shown in Fig. 2 (b). The oven temperature was set to 40°C and 0.1 W was dissipated through the Peltier element. We cycled hydrogen, deuterium, helium and argon through the vacuum system inside the oven, while having the Peltier element constantly on. The results are shown in Fig. 3, plot (c). Each pressurization resulted in the downward shift of the temperature baseline. The magnitude of the shift depended on the gas used in the experiment.

4. Numerical simulations

In order to quantify the measurement artifact caused by the temperature gradient inside the oven we used COMSOL commercial software to simulate heat conduction in the vessel. We interpolated the hot spot experimental data to evaluate the magnitude of a temperature nonuniformity that could cause the 50 mW baseline shift discussed in the Introduction. Figure 4 shows the result of the COMSOL simulation. In the solver the temperature of the surroundings was set to 390°C (663 K). A heating stripe at 390.084°C was simulated on the vessel's surface. Due to heat transfer and losses, the probe at the bottom of the vessel would read 390.060°C. Based on the simulations, a 0.5 K/m temperature gradient would result in 50 mW of apparent heating under the gas pressure. This noticeable effect was produced by

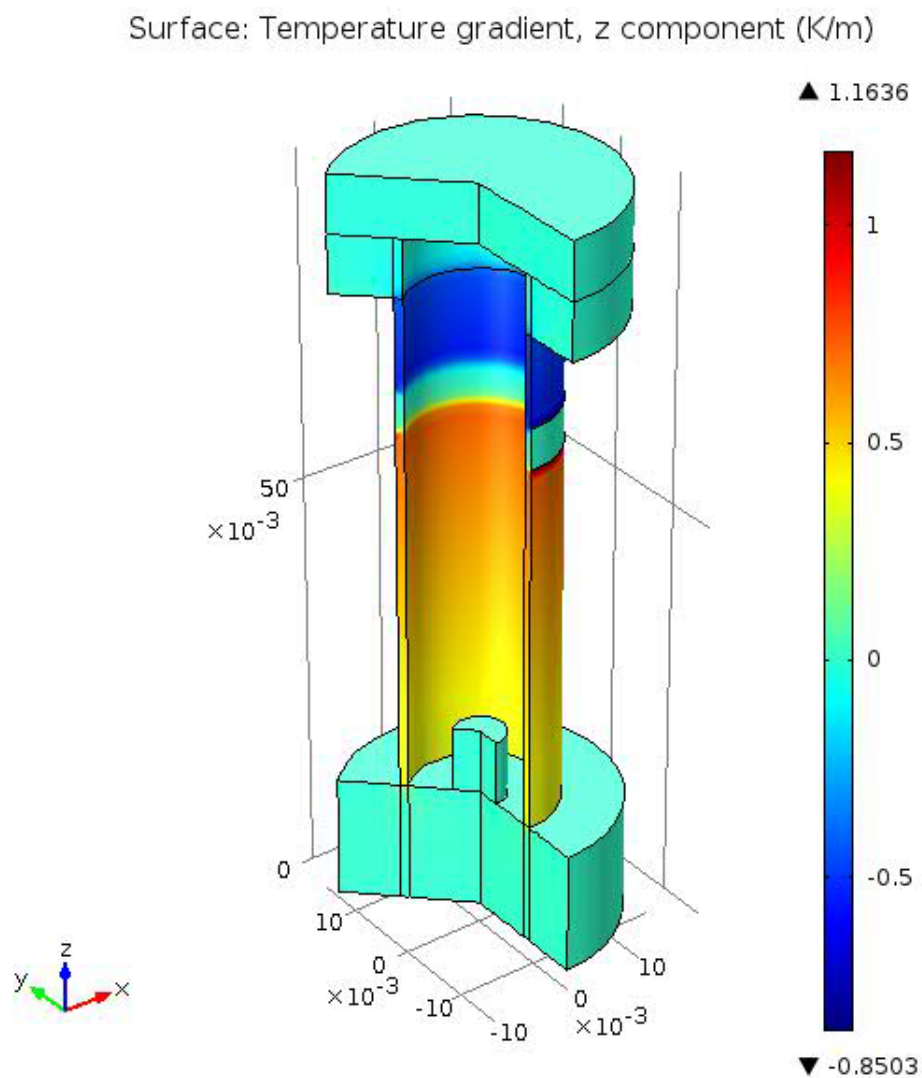


Figure 4. COMSOL simulation of the temperature gradient in the stainless steel vessel as a result of the local heating around the neck of the vessel. In this particular notation the temperature gradient is positive towards the bottom of the vessel. The portion of the vessel above the heating rings conducts heat as well, but the gradient is in the opposite direction, represented by the negative value.

relatively small temperature gradient of 0.024°C along the 4.5 cm long vessel wall. The purpose of this simulation was to show that relatively small temperature nonuniformity inside the experimental chamber would result in observable apparent heating by the temperature sensor.

5. Discussion

We enhanced the effect of the temperature gradient in order to study its ramification on the temperature measurements. Placing a resistor on the surface of the vessel formed a hot spot. The addition of gas to a previously evacuated system increased the thermal conductivity of the vessel and allowed better coupling to the local hot spot (resistor). As a result the measured temperature baseline shifted up. When the gas was removed, the coupling weakened due to the conductivity decline, and the temperature baseline shifted back to its initial position. We used a cooling Peltier element to confirm the downward baseline shift. Quantitative analysis of particular case of apparent heating was simulated using COMSOL Multiphysics.

The magnitude of the shift depended on (1) the magnitude of the thermal gradient, (2) the thermal conductivity of the gas, (3) the presence of material inside the vessel.

- (1) Increasing the local hot spot temperature resulted in an increased amount of heat available for channeling from/to the oven's environment (and opposite for the cold spot), affecting the magnitude of the baseline shift. We confirmed this hypothesis by dissipating different amount of power in the resistor. Doubling the power resulted in a doubling of the temperature baseline shift.
- (2) Gases of higher thermal conductivity (hydrogen, deuterium and helium) showed greater temperature baseline shifts, as compared to less-conductive argon. However, the trend was qualitative than quantitative. Even though argon's conduction coefficient is ten times smaller than that of helium, the baseline shift was only a factor of two smaller. We interpreted this as a mixed contribution of conductive and convective heat transfer mechanisms.
- (3) The presence of a sample inside the vessel resulted in a larger baseline shift as compared to the shift observed from gas loading in an empty vessel (results not shown). Three different materials were tested: Pd-impregnated alumina, un-impregnated alumina and Ni powder. Ni is three times more thermally conductive than alumina, but a simple proportionality between the thermal conductivity of the materials and the magnitude of the baseline shift was not observed (results not shown). We suggest that some other material properties (e.g., powder density) also affected the heat conduction process.

6. Conclusions

We studied the influence of the temperature gradient on heat measurements during gas-loading experiments. To clearly demonstrate the observed effect we enhanced the temperature gradient by placing a heating or cooling element on the surface of the sample vessel and later pressurized it either with hydrogen, deuterium, helium, or argon. We observed both upward and downward temperature baseline shifts. The magnitude of the shift depended on the magnitude of the temperature gradient and the thermal conductivity of the gas inside the vessel. While we discovered this artifact in our quasi-isothermal oven, the results are applicable to any other gas loading system that uses thermometry to evaluate energy release/consumption. Moreover, the experiments that are run at the elevated temperatures are more prone to this artifact since the temperature gradients are naturally larger.

We quantified the effect by simulating heat conduction inside the sample vessel using finite element software. According to the simulations at 390°C, the effect would become visible with a diminutive 0.024°C temperature difference along the 4.5 cm long vessel wall, and result in 50 mW of apparent heating.

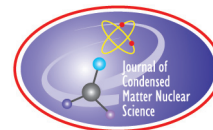
We conclude by emphasizing the importance of testing the measurement system with the material pressurized by helium gas, which has a thermal conductivity similar to hydrogen and deuterium, to identify potential measurement artifacts caused by temperature gradient.

Acknowledgments

The authors wish to acknowledge Gary Stanish for his technical support during the experimental work.

References

- [1] F. Piantelli, Energy generation and generator by means of anharmonic stimulated fusion, International Patent Classification G21B 1/00 and Publication Number WO 95/20816, (3 August 1995).
- [2] Y. Arata and Y. Zhang, Establishment of the “Solid Fusion” reactor, *J. High Temp Soc.* **34** (2008) 85–93.
- [3] A. Kitamura, T. Nohmi, Y. Sasaki, A. Takahashi, R. Seto and Y. Fujita, Anomalous effects in charging of Pd powders with high density hydrogen isotopes, *Phys. Lett. A* **373** (2009) 3109–3112.
- [4] T. Hioki, H. Azuma, T. Nishi, A. Itoh, J. Gao, S. Hibi, T. Motohiro and J. Kasagi, Hydrogen/deuterium absorption property of Pd fine particle systems and heat evolution associated with hydrogen/deuterium loading, *Proc. 15th Int. Conf. on Condensed Matter Nucl. Sci.* (2009), pp. 88–93.
- [5] D. Kidwell, D. Knies, A. Moser and D. Domingues, Yes, Virginia there is heat, but it is most likely of chemical origin, *Proc. 15th Int. Conf. on Condensed Matter Nucl. Sci.* (2009), pp. 100–109.
- [6] O. Dmitriyeva, R. Cantwell, M. McConnell and G. Moddel, Origin of excess heat generated during loading Pd-impregnated alumina powder with deuterium and hydrogen, *Thermochimica Acta* **543** (2012) 260–266.
- [7] Y. Sakamoto, M. Imoto, K. Takai, T. Yanaru and K. Ohshima, Calorimetric enthalpies for palladium-hydrogen (deuterium) systems at H(D) contents up to about $[H]/([D])/[Pd]=0.86$, *J. Phys.: Condens. Matter* **8** (1996) 3229–3244.



Research Article

Anomalous Metals in Electrified Vacuum

Edward Esko*

Quantum Rabbit LLC, USA

Abstract

Independent analysis of Quantum Rabbit (QR) vacuum arc test samples from an experiment conducted on Sept. 27, 2011 revealed the anomalous appearance of potassium (K) and gold (Au). These anomalies appeared in a prior QR vacuum arc test and raise the possibility of low energy transmutation.

© 2014 ISCMNS. All rights reserved. ISSN 2227-3123

Keywords: Fission, Fusion, Low energy nuclear reactions, Transmutation

1. Background

The 2011 experiment followed a test conducted at the Quantum Rabbit (QR) lab on July 30, 2009. In 2009, researchers performed a vacuum discharge test utilizing a copper anode—into which a pure lead insert had been pressed—a copper cathode, and pure lithium and sulfur test material. The tube was pumped down to vacuum, and pure oxygen admitted to approximately 3.5 torr. An electric arc was struck and a glow discharge with the characteristic color of lithium was produced. Analysis of test samples by Inductively Coupled Plasma Atomic Emission Spectroscopy (ICP) revealed the anomalous presence of germanium (Ge) at 3196 parts per million (ppm); potassium (K) at 750 ppm; and gold (Au) at 174 ppm [1].

2. Vacuum Tube Design

The 2009 experiment utilized the special vacuum tube designed by me and employed in previous metal vapor tests. The borosilicate glass tube was 150 mm long, with a 50 mm quartz midsection. A 3/8-inch diameter quartz straight section, perpendicular to the tube and 75 mm in length, connected the midsection with the vacuum manifold, and served as the entrance for a pure oxygen backfill. The 2011 test employed a vacuum tube with a different design. The 2011 tube was made entirely of quartz and fastened vertically atop the vacuum manifold. This eliminated the perpendicular joint that connected the 2009 tube with the manifold, thus reducing the possibility of breakage. The 2011 test employed the same inputs as the 2009 experiment, with several new features.

*E-mail: edwardesko@gmail.com



Figure 1. Sulfur and lithium atop the anode recess.

2.1. Anode recess

The first modification was the creation of a small recess at the center of the anode. The recess facilitated a more secure placement of test material in the tube. The recess helped confine the test material to the reaction zone. As was the case in 2009, a lead insert was placed in the center of the copper anode. The lead insert consisted of a lead slug approximately 0.25-inch diameter pressed into a 0.25-inch by 0.25-inch drilled hole. One piece of lithium was centrally placed atop the lead insert. The lithium was surrounded by sulfur pieces (Fig. 1).

Electrode (copper anode and cathode) separation was adjusted to a minimum value with just enough clearance to reduce shorting. Typically this was in the range of 0.30–0.60 inch.

2.2. Neon fill gas

The second modification was the use of neon as a fill gas to strike plasma before admitting oxygen as the catalyst. Oxygen was the sole fill gas in the 2009 test.

3. Experiment Timeline

The test proceeded in real time as follows (keep in mind that the data points are approximate.) The tube was pumped down to vacuum. Neon was admitted at the start to 2 torr. At 1 min in, the torr reading was 3.0, while power supply readings measured 53 V and 6.95 A. The inside of the tube was glowing red-purple, with what appeared to be the color of neon plasma. At about 2 min, the readings were as follows: 3.0 torr, 70 V, and 5.63 A. Intense heat was generated at this point; so that the test materials appeared to be melting. Oxygen was admitted between minute 3 and 4, and the torr reading went up to approximately 8.28. Following the oxygen fill, the test material began glowing a ruby red, the characteristic color of lithium plasma. At around 6 min, there was concern that the tube had failed. Power was disconnected. Thirty seconds later it was decided that the tube was still viable, and the decision was made to admit fresh oxygen and fire up the tube once again. At this point the tube began glowing blue–green (Fig. 2).



Figure 2. Blue–green discharge in vacuum tube.

Between 8 and 9 min, the power alternated between 45–55 V and 6.65 and 7.5 A. After 10 min, conditions in the tube appeared to stabilize. Voltage hovered around 77 and amps around 5.4. The test finished after a total time of approximately 14 min with a 3.5 torr reading. Upon conclusion of the experiment, the electricity was turned off, the vacuum pumps disconnected, and the samples allowed to cool.

4. Results

Two sets of samples were retrieved for testing: (1) the lead-tipped copper anode with lithium–sulfur residue in its center and (2) the copper cathode and the quartz tube which contained residue on the inner surface. The anode, cathode, and inside of the tube had undergone noticeable changes during the experiment. The samples were carefully packaged and sent to New Hampshire Materials Laboratory for ICP analysis. The 2011 result paralleled the result of 2009. Two of the three anomalous metals that appeared in 2009 were detected in 2011: potassium (K) at 181 ppm and gold (Au) at 252 ppm [2]. A comparison between the 2009 and 2011 experiments is shown in Table 1 (values in parts per million.)

Table 1. Comparison of 2011 and 2009 experiments.

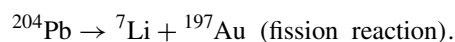
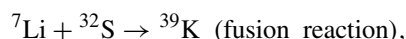
Element	Starting concentration*	Final concentration**
2011		
Au	< 0.51	252
K	< 1.615	181
2009		
Au	< 0.5	174
K	36.610	750

*Certificates of analysis of test components provided by Alfa Aesar; additional values for K provided by M & M Glassblowing.

**ICP Analysis by New Hampshire Materials Laboratory.

5. Conclusions

The 2011 results raise the question that was raised in 2009, namely, where did the anomalous metals come from? There are three possible sources for the anomalies: (1) contamination, or the presence of anomalies in test materials prior to experiment; (2) concentration, or the gathering of anomalous elements in the tested region and (3) transmutation, or the formation of anomalies through low energy nuclear reactions. The third possibility, that the anomalies appeared through a process of low energy transmutation, is not accepted by modern science. Placing the lithium-sulfur test material in contact with the lead anode, pumping down to vacuum, admitting oxygen as a catalyst and electrifying the tube, may have caused the lithium nuclei to fuse with sulfur nuclei, and produce nuclei of potassium (K). As fusion took place, a fission reaction occurred in which the lead (Pb) anode split into lithium and gold (Au). In other words, the process of low energy fusion, in which lithium and sulfur fuse to form potassium, initiates a process of low energy fission, in which nuclei of lithium are subtracted from nuclei of lead, thus forming gold:



Based on many studies, an electric arc apparently has the ability to cause transmutation resulting in an increase in mass of the target. Consequently, the observations reported above are important and contribute more support to this phenomenon.

However, it is premature to speculate as to how and why this process occurs. The enormous Coulomb barrier is not trivial and cannot be waved away by trivial explanations.

According to the standard model, the reaction $\text{Pb} \rightarrow \text{Li} + \text{Au}$ is endothermic, hence impossible. The reaction $\text{Li} + \text{S} \rightarrow \text{K}$, although it is exothermic, it would produce radioactive isotopes if it actually occurred. These radioactive isotopes need to be acknowledged and sought. Clearly additional research is required to test the hypothesis of low energy transmutation as postulated in the above paper.

Acknowledgments

The author wishes to thank George Ohsawa, Michio Kushi, and Louis Kervran for their pioneering work on low energy transmutation. I also thank Bill Zebuhr and Christy Frazier of the New Energy Foundation and *Infinite Energy* magazine for their continuing support and encouragement. Thanks also to Prof. Peter L. Hagelstein of MIT, Prof. George Miley of the University of Illinois, and Charles Entenmann for offering advice and guidance. I also thank my partners in Quantum Rabbit LLC, Alex Jack and Woody and Florence Johnson, for their ongoing support.

References

- [1] New Hampshire Materials Laboratory, Test Report, file number 26657, August 14, 2009.
- [2] New Hampshire Materials Laboratory, Test Report, file number 28929, October 14, 2011.



Research Article

Patents and Cold Fusion

David J. French*

CEO of Second Counsel Services, Ottawa, Canada

Abstract

Patents are available for any arrangement that exploits Cold Fusion. The arrangement must incorporate a feature which is new. However, for Cold Fusion inventions the Patent Office may require proof that the procedures described in the patent actually work. And the description must be sufficient to enable others to duplicate the invention.

© 2014 ISCMNS. All rights reserved. ISSN 2227-3123

Keywords: Cold fusion, Description, Patents, Utility

1. Introduction

The role of a Patent Agent is like that of a journalist who is also a detective. First you have to understand the story that is being presented by your client. Then you have to discover what it is in the story that is relevant in terms of being new and valuable. Finally, you have to write-up a disclosure that does justice to the idea according to the requirements of patent law.

This paper addresses patents as they relate to the field of Cold Fusion/LENR inventions. When reference is made to “Cold Fusion”, this is because this is a convenient term. The author has no opinion as to the mechanism that may be operating that provides unexplained excess energy. With that observation this paper will address some background points on the topic of patenting.

2. Why Patent?

Patenting the results of their work is frequently exciting for those engaged in research. They may have a dream of patenting as a path to generating vast riches. This can happen, but the road is not an easy one to follow.

A patent by itself does not provide financial success. You must have a successful technology before a patent becomes relevant. But if you do have such a technology success, patents can enhance the profitability of marketing that technology. Patents enhance profitability by allowing producers to charge customers more for the product. This may be trite to acknowledge but often people lose track of this objective. Patents are valuable if they are associated with a

*E-mail: David.French@SecondCounsel.com

successful business. This may lead to a buy-out at a higher price. It may appear that the patent has made the business more successful.

But the value of the patent and its ability to deliver enhanced profits only arise if the business itself is delivering a successful product to the marketplace. Patents cannot enhance profits if the product itself is not a success.

3. Patentable Subject Matter

Turning now to issues of patenting as they relate to Cold Fusion, a first misconception needs to be clarified. Patents must address products, processes or new compositions of matter. No patent is going to be issued for the person who finally provides the correct theory that explains the source of the Cold Fusion effect. That will properly be the subject for a Nobel Prize. Patents relate to products, articles, machines, or chemicals that are to be delivered to consumers or can be used by producers [1]. Patents also relate to procedures that can be carried-out industrially. It is possible to include all of these classes of “patentable subject matter” under the word “arrangement”. For an arrangement to become patentable, three critical conditions must be met:

- (1) There must be a feature or aspect of the arrangement which is new; a difference [2],
- (2) The arrangement must actually work and deliver a useful result, and
- (3) The patent disclosure document that accompanies a patent application must describe how others can obtain the promised useful result [3].

Those are the three requirements for patenting. They are simply stated but require careful contemplation to appreciate their effect completely.

4. Examination Requirements

In referring to patents as addressing new arrangements, it is critically important to understand that a patent must focus on some sort of physical structure or procedure. It is the responsibility of a patent applicant to define what it is about this structure or procedure that is new. Examination at the Patent Office always focuses on this issue: is the applicant’s proposed definition of exclusive rights limited to things that are new?

In the case of Cold Fusion, the Patent Office is also concerned about whether the new arrangement actually works and has been described in a manner that will enable others to achieve the promised results. This concern is not restricted only to patent applications directed to Cold Fusion technology. It exists for all inventions where the represented utility of the invention is dubious [4].

5. Patent Novelty Requirement

The Golden Rule of patent law is that a patent, once granted, cannot take away from the public anything that was previously available to the public. This principle goes back to the Statute of Monopolies [5] passed in England in 1624. No monopoly may be granted for something that is already available to the public.

A shocking consequence of this principle for many inventors is that their ideas, no matter how apparently creative they may appear to be, may not necessarily be patentable. Inventors may have subjectively conceived of a new idea, an “invention” from their perspective, but their ideas may not be patentable if such ideas have already been made available to the public anywhere in the world.

Prior ideas or art can never be patented if they have been disclosed previously to the degree that they have been made “available to the public”.

With the enactment of the America Invents Act [6] on September 16, 2011 this has become the law in the United States as of March 16, 2013. From that date on America will be on the same standard of novelty as the rest of the

world. This standard is: Absolute World Novelty. This means that an invention must be pristine in the sense that it has not been previously publicly disclosed, or even suggested in a way that would make it obvious, anywhere in the world by any means as of the date of filing of a patent application. This is a high standard to meet. This is the standard that Americans will have to live with. This is a standard imposed by patent laws elsewhere in the world.

Furthermore, it is wrong to assume that the objective is to slip something past the US Patent Examiner. Examination for novelty will occur at the Patent Office, but it has never been assumed that a Patent Examiner's ruling in favour of granting a patent is conclusive. A patent granted in error can be revoked or invalidated in the Courts. That is why patent litigation is so complicated, and expensive.

Examiners do not evaluate patents on the basis of whether the idea is valuable, or on the basis of whether the inventor deserves particular credit. Examiners evaluate patents for novelty to ensure that the exclusive rights being sought are restricted to things that are new. It is much easier to obtain a patent on a far-fetched or silly idea than a good idea. Good ideas are less likely to be novel. Good ideas are thought of by others regularly.

And Examiners, particularly in the case of Cold Fusion inventions, evaluate applications for the sufficiency of the disclosure, as referenced further, below.

6. Searching the Prior Art

Before filing for a patent, it is appropriate to search to see whether the idea being addressed is novel. Searches can be conducted anywhere in the world, but for convenience, searches are often initially done at a major patent office such as the United States Patent and Trademark Office [7].

It is important to appreciate that a prior patent or application is relevant as prior art not only for what it addresses in the claims but also for anything that is discussed anywhere in the patent document. A disclosure is a disclosure, no matter where it occurs.

Invention novelty searches are normally begun at a major patent office such as that in the United States where patent applications and granted patents are very well indexed and are easily accessible over the Internet. If you find your idea described in a patent document, your search is over. Your search is not over if you do not find your idea described in a patent document; in fact your search is never over as long as you do not find your idea described in the prior art.

If you get into litigation, your opponent may discover that references to your ideas have been made elsewhere. In one case in Canada, which went to Court on the subject of spiral nails, there was an additional disclosure in a prior Australian patent that was not found in corresponding patents filed in other countries around the world. It was, however, relevant to the validity of the Canadian patent. And that feature was not addressed in the claims of the Australian patent.

Examiners primarily review patent applications for novelty. But they are also entitled to question whether a patent disclosure addresses an invention which is useful and whether the disclosure is sufficient to obtain the promised results.

7. Invention Utility and Sufficiency of Disclosure

There has been a lot of discussion, and criticism, of the United States Patent Office for refusing to grant patents that address Cold Fusion inventions. This is not as unreasonable as it may first seem. A patent can only validly issue for an arrangement that delivers the useful result promised in the disclosure. Normally Examiners take it for granted that the applicant's description of a machine or process meets this requirement. But at any time, if an Examiner has good reason to suspect that the promised useful result is not available, or if the Examiner simply suspects that the disclosure is inadequate to allow other people to build the invention, then the Examiner may require that the applicant provide proof that these requirements are met [8].

In the case of applications that apparently are directed to perpetual motion mechanisms, the Examiner may require the applicant to provide evidence demonstrating that the system will work and that the description of how to achieve

the useful objective of the invention is sufficient. Fortunately or unfortunately, patent applications that are directed to Cold Fusion effects are treated as if they were equivalent to a claim to perpetual motion [9]. This means that any applicant who proposes to patent a specific arrangement that will produce unexplained excess energy from Cold Fusion will be subject to a challenge from the Examiner who will say: “Prove it!” The burden then shifts to the applicant to file evidence from reliable sources confirming the key representations being made in the patent application.

If you think about this last sentence, you will see that it is greatly in the interests of the patent applicant not to make extravagant representations in a patent application. In fact, you should never say that the invention is superior, cheaper or otherwise better in ways that will be hard to prove if challenged by the Examiner. It is sufficient to simply say: “I am achieving a useful result and there is something about what I am doing that is new.” A patent application is not a place to include a sales pitch.

8. Importance of a Complete Disclosure on Filing

At this point, it is important to observe that once a patent has been filed in final form, the “story” contained in the disclosure of the invention cannot be changed. Grammatical errors, however, can be corrected and any information that is already provided can be presented with different language. But the story itself is frozen. By way of contrast the claims can be amended.

The claims are the single sentences at the end of the patent that stipulate what the applicant believes to be new and for which the applicant seeks to obtain exclusive rights. Those claims can be rewritten, but only to the extent that they address what has been described in the story.

Once a final application has been filed, the disclosure content of the final application cannot be changed.

This is an extremely important consequence. The result is that you only have the flexibility of revising your application during the first year following the filing of a first Provisional application. After that, the application is frozen.

Technically, from then on, the inventor is no longer required. The application goes forward based on the words that are written and contained in the final text when the final application is filed. All over the world in various countries patent attorneys will engage in an exchange with the Examiner at the local national patent office based on the text in the final patent application. Those foreign patent agents do not really need to talk to the inventor as long as the application is comprehensible. The exchange with the foreign patent office will always take place on the basis of the final document as filed.

An applicant would be well advised to make a careful re-reading of his entire patent disclosure while there is still time to make amendments. If he has forgotten to mention something important at the time of filing, it will be too late to amend it during examination. But if he has said something that is incorrect it is permissible to delete the incorrect statement.

9. Parts of a Patent Specification

We could review individually the key parts of a patent disclosure: the Title, identifying the Field of the Invention, the Summary of the Invention, the listing of the Drawings and the Description of the Preferred Embodiment(s). But the most important part of any patent is the section containing the one or more claims at the end of the document [10]. These represent the “shooting end” of a patent.

In a patent application, a patent applicant must include proposed claims that define the exclusive rights that the applicant hopes to obtain. Some may think of the Claims as being too complicated to understand. This is not necessarily true. Claims are supposed to be logical and grammatically correct.

10. Structure and Function of Patent Claims

Each Claim constitutes a single sentence that serves as a check-off list for parts or components that constitute the arrangements which fall within the patent owner's exclusive rights. To infringe, competitors would need to adopt every element listed in a claim. Claims appear at the end of patent documents in the form of numbered sentences. Multiple claims are allowed. Each claim is a restatement of the inventor's exclusive rights with variations. The first claim is always critical.

The first Claim lists the minimum essential elements that need to be present in order for someone to infringe on the exclusive rights of the patent. Subsequent claims can refer back to the first claim and adopt its limitations by reference, adding something more. These are dependent claims. Thus, Claim 2 may read:

"The Cold Fusion apparatus as in Claim 1 additionally including an ultrasound generator positioned to introduce ultrasound vibrations into the Nickel/Palladium as previously referenced."

This second, dependent, claim may therefore appear to be quite short. It is in fact a longer claim than Claim 1 even though it uses fewer words because, being a dependent claim, it adopts all the limitations of the independent Claim 1 by reference. And it is narrower in scope.

If Claim 1 is not infringed, then none of the claims that refer back to Claim 1 will be infringed either. This is because claims that refer-back adopt all the limitations of the earlier claim or claims to which they refer. Therefore if somebody does not carry out all the limitations of the earlier claim, they do not infringe the later claim.

The referenced earlier claim itself may refer back to a yet earlier claim. Claim 1 is always independent because there is no prior claim to which it can refer-back. On this basis it can be seen why Claim 1 is so important. In fact, all of the claims that refer-back to an independent claim are potentially redundant. They are there merely backups in the event that Claim 1 fails, available as a consolation prize if the Examiner finds something which exists in the prior art that is described by Claim 1. In such a case Claim 1 will get a red "X".

But an applicant may be entitled to amend Claim 1. If you have multiple dependent claims previously drafted in the document, you can propose to add limitations from one or more of the dependent claims to Claim 1 to avoid the prior art. If the Examiner finds this is acceptable then you will get a patent with your modified version of Claim 1. But it will have a narrower scope of monopoly because it will have more limitations. Dependent claims are pre-planned positions of retreat.

11. Sample Patent Application

To assist in understanding the nature of a patent, it is helpful to examine an application of Robert Godes, the inventor associated with Brillouin Energy Corp [11] in California. The patent may be viewed at the US Patent Office website, www.USPTO.gov by entering the publication number: 20110122984 on the USPTO application search page [12].

This application has been rejected several times by the US Patent Examiner, most recently on the basis of failure to demonstrate that the invention works. That hurdle can still be overcome by filing further evidence. Meanwhile, we can use this reference to review the scope of potential patent coverage that might be obtained.

12. Godes Proposed Claim 1

In the Godes patent application [13] Claim 1 is written out as a block of words completing the preamble, "I claim ...". This claim is hard to read. But it is permissible to reorganize the layout of the words in this claim to identify the various elements for which exclusive rights are being sought. Here is a parsed version of that claim:

- (1) An apparatus for energy generation comprising:
 - (a) a body, referred to as the core, of a material capable of phonon propagation;

- (b) a mechanism for introducing reactants into said core;
- (c) a source of current pulses for establishing current pulses through said core, said current pulses inducing phonons in said core so that reactants, when introduced into said core, undergo nuclear reactions; and
- (d) a closed loop control system, coupled to said mechanism for introducing reactants and to said source of current pulses, for specifying operating parameters of said mechanism for introducing reactants and of said source of current pulses, for sensing one or more operating conditions, and for modifying one or more operating parameters

thereby controlling the number of nuclear reactions and the depth of the nuclear reactions in said core so as to provide a desired level of energy generation, while allowing energy released due to the nuclear reactions to dissipate in a manner that substantially avoids destruction of said core.”

Other independent claims in this application address operating the invention in a liquid phase. Claim 1, above, is not, however, so limited. Accordingly, Claim 1 has broader coverage. Correspondingly, Claim 1 risks being invalid if it describes anything present in the prior art.

As you run through the claim you will see that it is simply a check-off list of parts that have to be present in order for someone to infringe. If competitors omit one element listed in the claim, they will not infringe. The patent will be ineffective to prevent competition under those circumstances.

The art of good patent claim drafting is to draft a claim that addresses an essential collection of features that the competitors will have to adopt in order to compete. It is desirable for the claim to be short. Every time additional elements are added to the claim, competitors are provided with the opportunity of avoiding the claim by not adopting one of those additional elements. But elements may have to be added by an applicant in order to avoid the prior art.

Looking inside this claim we see that Godes has stipulated, or rather his patent attorney has stipulated based on instructions from Godes, that there must be “current pulses inducing phonons in said core”. This means that there must be an electric current running through the host material that contains the deuterium or hydrogen nuclei.

However the disclosure recites repeatedly that cold fusion may be precipitated by the use of ultrasound or heat. Nevertheless we see that the patent attorney has limited the claim to require the presence of a pulsed electrical current for inducing phonons in the core. With this limitation, the claim will not extend to or cover the precipitation of a Cold Fusion effect by means of ultrasound, heat or any other stimulant except the application of current pulses. The claim is narrower in its coverage than the disclosure.

We might ask why this would be done when it says in the document that the Cold Fusion effect could be precipitated by a variety of means, e.g. by current, ultrasonic energy or heat? By limiting Claim 1 to only one method of inducing phonons in the core, this claim leaves open the freedom for competitors to adopt other methods.

While this may appear to be a damaging initiative, there may be several explanations for why the claim has been so limited. If this were an oversight by the patent draftsman (not very likely), then it is still fixable as long as the applicant has a right to amend the patent claims and the amendments are based upon material contained in the disclosure. But we have to ask how this could have happened in the first place.

There is also a possibility that this stipulation for the presence of: “current pulses inducing phonons in said core” is an essential requirement to ensure the invention will work. In which case we have to go back to the disclosure and see whether the disclosure warns that there must be a pulsating electric current passing through the metal lattice as an

essential feature. Having looked through this disclosure I have not found such a warning. But this is nevertheless a possibility.

And this limitation may be present because the applicant knows about the existence of something in the prior art that prevents the claim from being broadened to include ultrasound as an alternative to current pulses for precipitating a Cold Fusion reaction within the core. If such a prior art example does exist, then, unless covered by a patent obtained by someone else, the technology described in the prior art will be in the public domain and available to the public as an alternative to the technology claimed in the Godes application.

A further possibility, particularly available under US law, is that the claim may have been limited to its most important variant, removing alternatives only for the purposes of prosecution of an initial application. Such a procedure can simplify examination, removing the possibility that the Examiner may cite the other means for inducing phonons if the Examiner can find such references in the prior art. If a patent were to issue on this stripped-down claim focus, then US law permits the filing of an additional patent for the alternate variants. Such further one or more applications would be called “Continuations” based on the same disclosure and original filing date.

13. Inclusion of a Theory in Patent Claims

As one last observation on Claim 1 referenced above, this claim adopts a theory of operation of the invention described earlier in the disclosure.

It is not necessary to include a theory of operation in a patent disclosure. The disclosure need only be sufficient in the sense that a recipe for baking cookies in a cookbook will eventually produce cookies. There is no need to explain the physics of the transformation from cookie dough to cookie that occurs in the oven.

Godes proposes a theory based on electron capture by protons to produce neutrons. This is followed by neutron capture to form higher hydrogen isotopes, e.g. ^4H which then, through beta decay, produce ^4He . Claim 1, however, adopts a broader theory.

Claim 1 addresses infringers who pursue the steps of providing: “current pulses inducing phonons in said core so that reactants, when introduced into said core, undergo nuclear reactions”. While a theory may be optionally present in a disclosure, in order to enforce this claim it will be necessary to demonstrate that this mechanism is occurring in an infringer’s apparatus. Without such a demonstration, the claim will fail to achieve the objective of shutting-down the activities of a competitor.

It is dangerous to include in a claim theoretical requirements that are hard to prove. It is better just to stipulate the ingredients and their order of mixing if you want to control the making of cookies by others.

14. Future of Godes Application

This application has gone through several cycles of amendment, with the applicant paying special fees in order to amend. It still stands rejected because the Examiner says that the applicant’s attempt to prove the utility of the invention was not good enough.

This application is not being presently rejected because of applied prior art, although that could occur later. It is being rejected because it addresses a Cold Fusion invention and the Examiner is of the opinion that insufficient evidence has been filed to date in order to prove that the invention works.

The assessment of the Examiner is not necessarily conclusive or even correct. Eventually, if the applicant has nothing better to present to the Examiner, the only recourse that an applicant has is to file an appeal to the Patent Trial and Appeal Board. But this is only justified if the applicant has filed adequate evidence that is sufficiently robust to satisfy the members of the Board that the invention works and that the disclosure is adequate. Otherwise, the application may have to be abandoned. Because it was published as of 18 months from its earliest priority date, it may be too late to file a fresh application for the same invention.

On the other hand, the inventor may already have filed one or more further applications that have not yet been published. Such applications will only be published as of 18 months from the earliest priority date upon which they are based, allowing that there may also be a processing time delay particularly in the US Patent Office.

In this specific case, the Examiner is not applying any prior art to the claims. The Examiner has rejected the patent for failure to file sufficient evidence to demonstrate that the invention works. In such cases, an Examiner may choose to avoid investing effort in searching the prior art and assessing the claims for lack of novelty or lack of inventive step. But such an objection on these bases could still be raised subsequently.

15. Conclusion

Patents can be valuable. The value starts with a working invention that will serve people's needs. If an invention is a success, a patent can enhance the profitability of exploiting that success. But patents cannot make an invention succeed. It all starts with the invention.

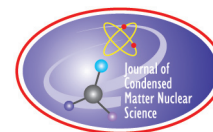
A good invention combined with a good prior art situation must be supported by a properly prepared patent disclosure; otherwise a valuable opportunity may go to waste. Patent applications that aspire to control the generation of energy through the effect of "Cold Fusion" are subject to the special procedure of demonstrating that the invention works as promised and that the instructions provided in the patent disclosure are sufficient to enable others to reproduce the invention.

Inventors embarking on the process of patenting should understand these requirements in advance and prepare their applications accordingly.

References

- [1] Section 101 of the US Patent Act allows patents to issue for: "any new and useful process, machine, manufacture, or composition of matter, or any new and useful improvement thereof".
- [2] Section 102 of the US Patent Act provides for "Conditions For Patentability; Novelty And Loss Of Right To Patent" in extensive detail.
- [3] Section 112 of the US Patent Act establishes the disclosure requirements for a patent Specification.
- [4] The Manual Of Practice And Examination Procedure - MPEP - published by the United States Patent Office provides in section 2107 extensive "Guidelines for Examination of Applications for Compliance with the Utility Requirement".
- [5] Statute of Monopolies, 1623 CHAPTER 3 21 Ja 1.
- [6] Leahy-Smith America Invents Act signed into law by President Barack Obama on September 16, 2011.
- [7] The United States Patent and Trademark Office accessible on the Internet at www.USPTO.gov.
- [8] MPEP endnote 4.
- [9] MPEP Section 2107, endnote 4: "...the Office considered the asserted utility to be inconsistent with known scientific principles or "speculative at best" as to whether attributes of the invention necessary to impart the asserted utility were actually present in the invention. ... Examples of such cases include: an invention asserted to change the taste of food using a magnetic field (*Fregeauv.Mossinghoff*, 776 F.2d 1034, 227 USPQ 848 (Fed. Cir. 1985)), a perpetual motion machine (*Newmanv.Quigg*, 877 F.2d 1575, 11 USPQ2d 1340 (Fed. Cir. 1989)), a flying machine operating on "flapping or flutter function" (*In re Houghton*, 433 F.2d 820, 167 USPQ. 687 (CCPA 1970)), a "cold fusion" process for producing energy (*In re Swartz*, 232 F.3d 862, 56 USPQ2d 1703, (Fed. Cir. 2000)), a method for increasing the energy output of fossil fuels upon combustion through exposure to a magnetic field (*In re Ruskin*, 354 F.2d 395, 148 USPQ 221 (CCPA 1966)), uncharacterized compositions for curing a wide array of cancers (*In re Citron*, 325 F.2d 248, 139 USPQ 516 (CCPA 1963)), and a method of controlling the aging process (*In re Eltgroth*, 419 F.2d 918, 164 USPQ 221 (CCPA 1970))".
- [10] The MPEP sets-out claim requirements in section 608.01(i).

- [11] The Web site for that company is: <http://www.brillouinenergy.com/>.
- [12] The USPTO patent application publication number search page is available at “<http://appft.uspto.gov/netahtml/PTO/srchnum.html>”.
- [13] A link to this application as filed and published may be found at the USPTO website “by entering this publication number 20110122984 on the Internet page of Ref. [12]”.



Research Article

Controlled Electron Capture and the Path toward Commercialization

Robert Godes* and Robert George

Brillouin Energy Corporation, 2625 Alcatraz Avenue, Suite 296, Berkley, CA 94705, USA

Francis Tanzella and Michael McKubre

SRI International, Menlo Park, CA 94025-3493, USA

Abstract

We have run over 150 experiments using two different cell/calorimeter designs. Excess power has always been seen using Q pulses tuned to the resonance of palladium and nickel hydrides in pressurized vessels. Excess energies of up to 100% have been seen using this excitation method.

© 2014 ISCMNS. All rights reserved. ISSN 2227-3123

Keywords: CANR, Cold neutrons, Electrolysis, Electron capture, Excess heat, LENR

1. Background

We started with the hypothesis that metal hydrides stimulated at frequencies related to the lattice phonon resonance would cause protons or deuterons to undergo controlled electron capture. If this hypothesis is true then less hydride material would be needed to produce excess power. Also, this should lead to excess power (1) on demand, (2) from light H_2O electrolysis, and (3) from the hydrides of Pd, Ni, or any matrix able to provide the necessary confinement of hydrogen and obtain a Hamiltonian value greater than 782 keV. Also, the excess power effect would be enhanced at high temperatures and pressures.

A Brillouin zone is an imaginary polyhedron whose shape is a function of the molecule's or metal's unit cell. Electrons (or X-rays) of a wavelength close to or smaller than this polyhedron's inter-planar distance will interact with and potentially excite the lattice's atoms. We postulate that, in NiH_x , this will also excite the interstitial hydrogen atoms. If the energy is greater than 782 keV we further postulate that the interstitial protons will interact with the electron to form a neutron.

This lattice stimulation reverses the natural decay of neutrons to protons and Beta particles, catalyzing this endothermic step. Constraining a proton spatially in a lattice causes the lattice energy to be highly uncertain. With the Hamiltonian of the system reaching 782 keV for a proton or 3 MeV for a deuteron the system may be capable of capturing

*E-mail: reg@brillouinenergy.com

an electron, forming an ultra-cold neutron or di-neutron system. The almost stationary ultra-cold neutron(s) occupies a position in the metal lattice where another dissolved hydrogen is most likely to tunnel in less than a nanosecond, forming a deuteron/triton/quadium by capturing the cold neutron and releasing binding energy.

This would lead to helium through a beta decay. The expected half-life of the beta decay: if $J_{-}(^4\text{H}) = 0-, 1-, 2-, \tau_{1/2} \geq 10$ min; if $J_{-}(^4\text{H}) = 0+, 1+, \tau_{1/2} \geq 0.03$ s [1]. The β^{-} decay of a quadrium atom is expected to lead to ^4He .

Early Pd/H₂O electrolysis experiments used a well mixed, open electrolysis cell in a controlled flowing air enclosure. The temperature probes were verified to $\pm 0.1^\circ\text{C}$ at 70°C and $\pm 0.3^\circ\text{C}$ at 100°C . We simultaneously ran live and blank (resistive heater) cells, maintaining identical constant input power in both cells. High voltage, bipolar, narrow pulses were sent through the cathode and separately pulse-width modulated (PWM) electrolysis through the cell (between the anode and cathode).

Input power was measured using meters designed to measure power high frequency (HF) PWM systems. NaOH solutions were used for high conductivity. Differential thermometry suggested excess power up to 42% and 9 W (Fig. 4 in Ref. [21]).

2. Experimental Methods

Our recent test data is generated autonomously through the use of a fully instrumented pressurized test vessel that permits much greater control over experiments than was possible using the “open container” test cells from Phase One experiments.

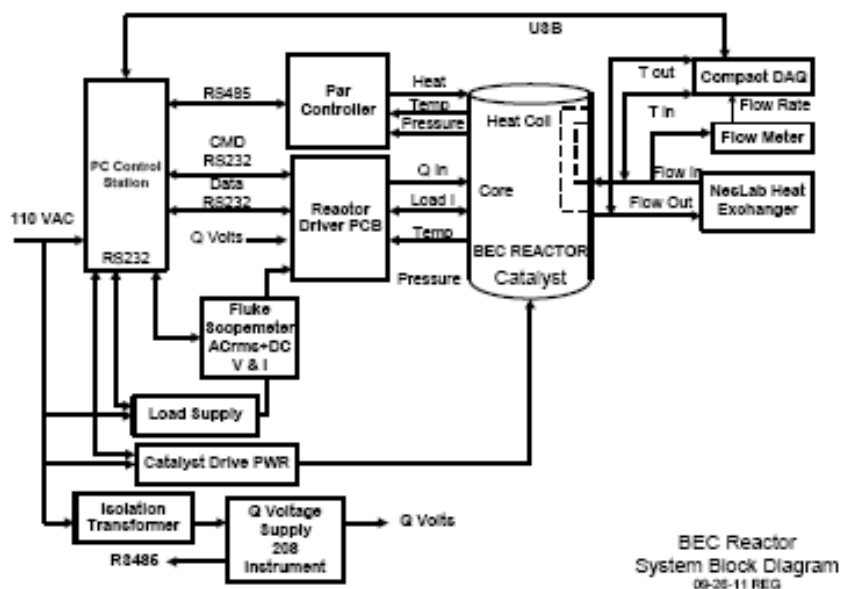


Figure 1. Components of the brillouin wet boiler.

2.1. Reactor components

The components of the most recent closed-cell Wet Boiler are shown in Fig. 1.

Those components include:

- A 130 bar pressure vessel with a band heater
- A 28AWG (0.31 mm) Ni 270 cathode
- Ni 270 wire mesh anode
- 0.5 l of 0.15–0.5 M NaOH solution
- Thermal transfer oil coolant loop with a heat exchanger. MobilTherm 603
- Platinum resistive temperature detector's (RTD's) measuring input and output coolant temperatures
- Mass Flow meter in the coolant line
- A catalytic recombiner, used for safety
- Resistance heater for calorimetric calibration

2.2. Power measurements

We performed conservative measurement of the input power into the reaction chamber and the control board. All inputs, including inductive and logic circuits losses, are counted as power applied to the system.

All power used for stimulation and control of the cell is measured. The power delivered to the band heater is provided by a Chroma 61602 programmable AC source. A 100 MHz Fluke 196C oscilloscope meter, operating in “AC (rms) + DC” mode, was used to measure the all input cell power applied to the primary control system.

Output power is calculated from the heat removed from the inside of the test cell by pumping an organic fluid (MobileTherm 603) through a heat exchanger immersed in the electrolyte inside the cell. The electrolyte is heated by the stimulation of the electrodes. An external heat exchanger extracts heat from the circulating organic fluid. The net heat in and out is carefully measured and the difference is tabulated. The flow rate is measured by a positive displacement flow sensor (Kytola 2950-2-AKT-N). 100 Ω platinum RTD's are used to measure the cooling fluid's inlet and outlet temperatures, placed just before and just after the cooling loop, respectively. Room temperature in the immediate environment of the test cell is also measured using a 100 Ω platinum RTD.

Heat also escapes from the test cell via conductive and radiative losses. Heat flows out of the test cell through the top of the test cell, its supporting brackets to a shelf, and through its insulation. This is accounted for in the software, following extensive calibrations of the cell running without stimulation pulses (Q).

The bias of the measurement scheme is to under-report thermal output. The electrolysis recombination activity in the headspace of the vessel increases the amount of the conduction and radiative losses at the top of the cell as it heats up and conducts more thermal energy through its mechanical supports. These losses become less significant at higher operation rates as the recombination heat layer moves down to the point where the heat exchange can begin to pick up more of that recombination energy.

2.3. Cell calibration and operation

This system recovers 98% of the heat input by the control band heater alone. The circulating oil is not able to remove all of the recombination energy in the test cell. A significant amount of the recombination energy escapes by conduction through the brackets that secure the cell to the shelf that holds it in place.

The method chosen to measure these parasitic heat losses is simple and accurate. The test cell has an electric resistance heating unit called the band heater. The band heater uses a known quantity of watts to heat the entire system to a selected temperature: 70, 80 or 100°C. It takes 132 W from the band heater to heat and hold the vessel to 70°C with

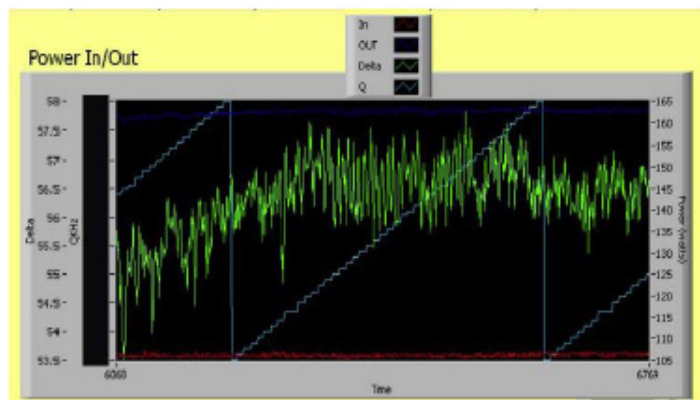


Figure 2. Calorimetric results from Experiment 1.

the cooling oil circulating in the cooling circuit. Measurements of the circulating oil show that the oil continuously removes 90 W at this set point. The difference (delta) is 42 W and this is the amount heat is “lost” from the vessel by thermal conduction and radiated heat. At 80°C, the calculated parasitic loss figure is 45 W and at 100°C the parasitic loss is 47 W.

Using this simple technique, at these three set points the amount of heat leaves the system in excess of that removed by the circulating oil is quantified to calibrate the measurements. This information is used in the data shown below. Table 1 shows the parasitic heat losses at 70, 80 and 100°C. Given the uncertainty in the calorimetric method in the Phase II reactor we feel that we need at least 20% excess power in order to be believable.

The cell/calorimeter is designed to operate at up to 200°C and up to 130 bar. The pressurized cell is controlled using LabView[®] software (National Instruments, Austin, TX, USA) that continuously and automatically collects information about energy flow in and out of the test cell. All experimental data are methodically and systematically archived and recorded to disk. The thermal load due to radiative and conductive losses, in addition to that collected by the heat exchanger, is approximately 400 W at a vessel temperature of 100°C but can achieve more than 2000 W at 200°C. The working fluid’s inlet temperature is maintained using a re-circulating chiller (Neslab RTE111).

During operation we have applied up to 800 W. The only input to the system is electric power and the only output from the system is heat. The AC stimulation consists of alternating high voltage positive and negative pulses, approximately 100 ns wide, of duty cycles up to 1% or repetition rates of up to 100 kHz

3. Results

Representative results of experiments operated in our pressurized cell/calorimeter are described below. Excess power is defined as the number of watts generated in the cell exceeding that supplied to the cell. The ratio of output to input

Table 1. Table of calibration power loss terms

A	B	C	D
Vessel temp. (°C)	Heater power (W)	Output power (W)	Lost power (W)
100	294	247	47
80	174	129	45
70	132	90	42

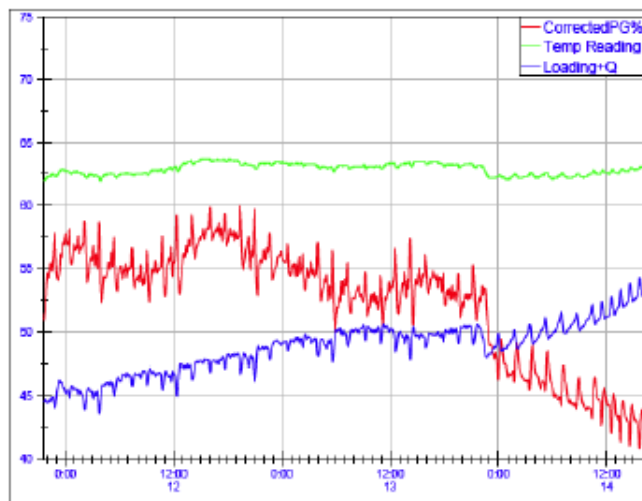


Figure 3. Plot of power gain (% , *red*), temperature (°C, *green*), and proprietary pulse parameter (*blue*) versus time of day for Experiment 1.

power is often plotted as percentage. When the output, for example, is twice that of the input, the amount of excess power is 100%.

The following experiments described herein were designed to measure excess power produced using proprietary electrical stimulation of nickel containing dissolved hydrogen.

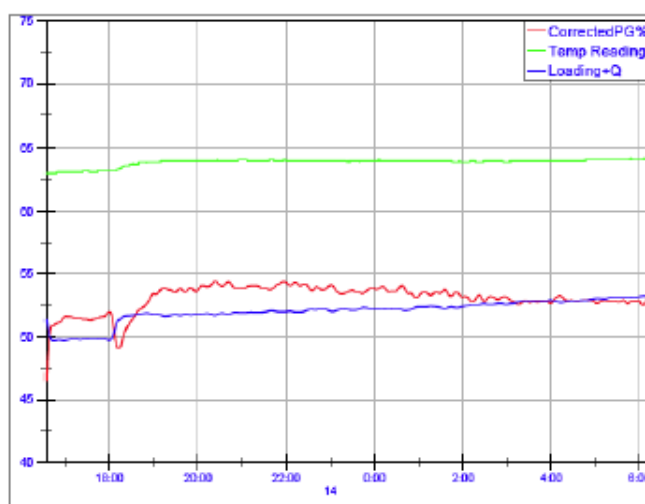


Figure 4. Plot of power gain (% , *red*), temperature (°C, *green*), and proprietary pulse parameter (*blue*) versus time of day for Experiment 3.

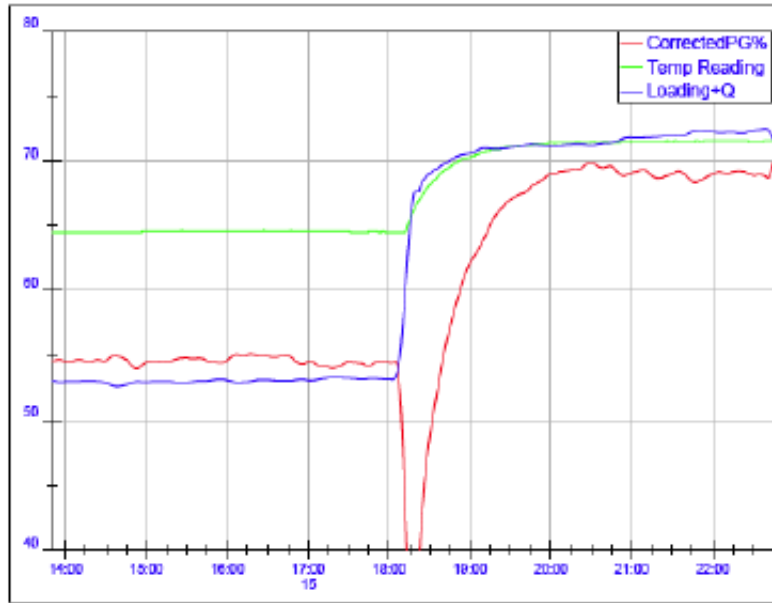


Figure 5. Plot of power gain (% , *red*), temperature (°C, *green*), and proprietary pulse parameter (*blue*) versus time of day for Experiment 3 continued.

3.1. Experiment 1

Experiment 1 which yielded excess power of over 50% for approximately 2 days. Figure 2 shows the calorimetric results and effect of stimulation frequency soon after 50% excess power was measured in the cell.

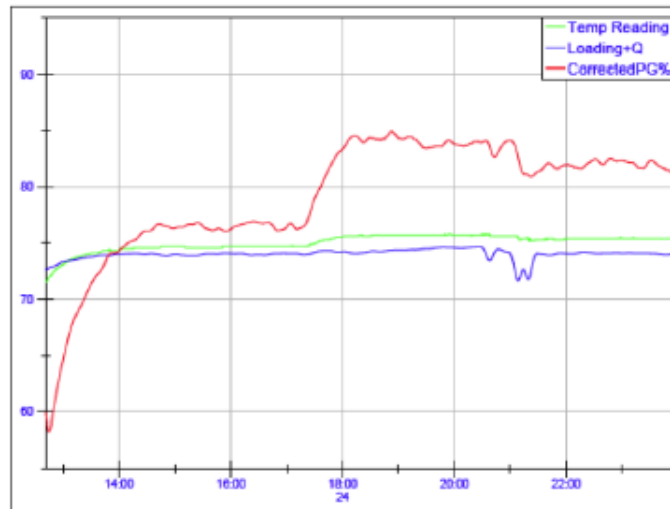


Figure 6. Plot of power gain (% , *red*), temperature (°C, *green*), and proprietary pulse parameter (*blue*) versus time of day for Experiment 4.

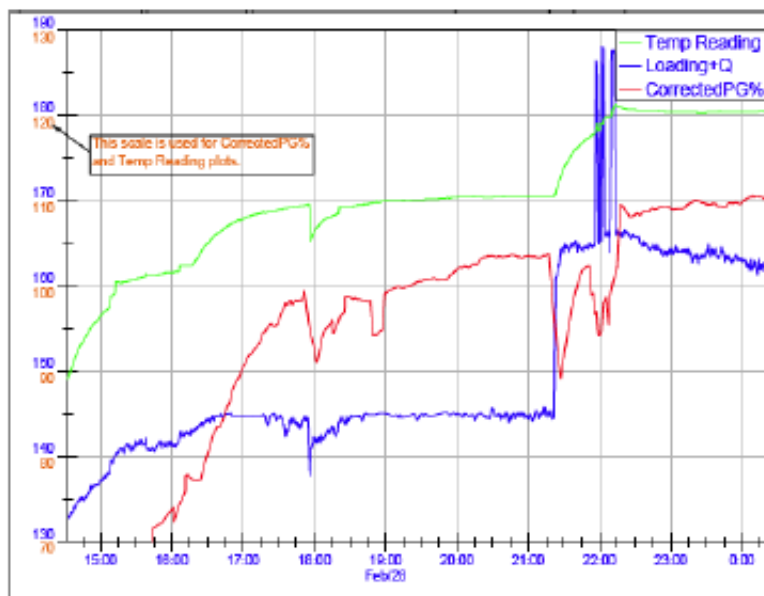


Figure 7. Plot of power gain (% , red, on red scale), temperature ($^{\circ}\text{C}$, green), and proprietary pulse parameter (blue) versus time of day for Experiment 5.

The amount of excess power shown on the screen is approximately 57%. During this time period there was 107 W in, 170 W out, yielding 63 W excess power, with the cell temperature at 76°C and pressure of 84 bar. Approximately 32 W power was applied to the catalyst and is included in the 107 W total input power.

3.2. Experiment 2

Figure 3 plots the power and temperature recorded during a complete 66-hour Ni/H₂O electrolysis experiment. Excess power of over 50% was recorded for much of this experiment. We repetitively swept Q repetition rate while stepping up Q amplitude and then a third parameter affecting Q shape to examine the effects and interplay among them.

The excess heat produced during this run shown in Fig. 3 declined as additional power was applied. The red line plots the percentage of excess power, blue the sum of the electrical inputs, and green the temperature of the test cell. The repetitive spikes in the data are due to the cycling of Q repetition rate and the downward sloping trend indicates the increase in power to a change in the shape of the Q pulses. This figure indicates that the level of the production of excess power does not rely exclusively on input power since increasing input power reduced absolute amount of excess power. The automated test system now has the ability to automatically sequence four separate input variables. When the Q pulse shape stepped out of an optimal operating point the red and blue plots crossed.

3.3. Experiment 3

In this experiment we examined the effect of changing specific input parameters. This plot shows a thermal output 50% greater than input for 14 h. A gradual increase in temperature tracks small incremental increases in both the DC and AC currents. This continued for 12 h past the end of this plot as seen in Fig. 5.

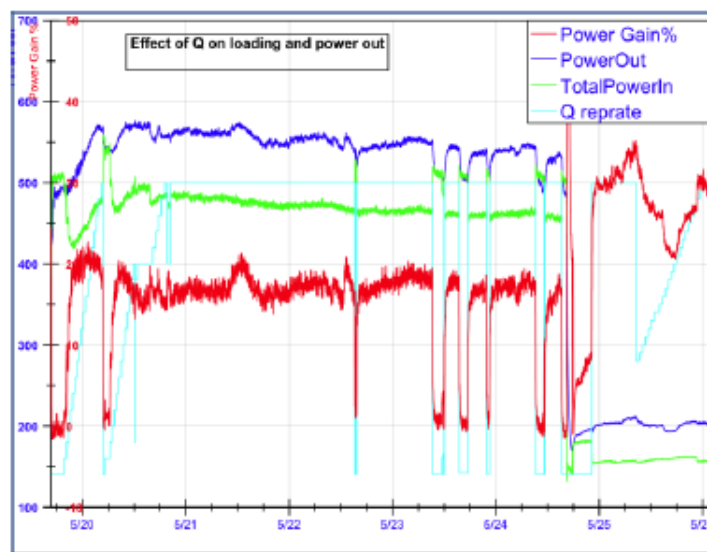


Figure 8. Effect of repetition rate on excess power; power gain (% , red, on red scale), power out (W, dark blue), power in (W, green), and proprietary pulse parameter (light blue) versus date.

Figure 5 shows the sharp response of the system to input power while everything else was held constant. A jump in excess heat from less than 55% to almost 70% was produced using the settings input during the second half of the experiment on 15 February. Learning from this data, we modified electric inputs to exceed these results.

3.4. Experiment 4

Figure 6 plots the calorimetric and temperature data for part of a Ni/H₂O electrolysis experiment. While holding total input power constant Q pulse shape was changed which yielded excess power production in excess of 75% for approximately 11 h. After achieving a thermal steady state, system performed well for the duration of the test. Subsequently a new set of input parameters were utilized in this experiment, after which the excess power peaked at approximately 85% and was above 80% for more than 7 h.

3.5. Experiment 5

Figure 7 plots the calorimetric and temperature data for part of a Ni/H₂O electrolysis experiment. This was the first time the excess power exceeded 100%, meaning the “watts out” were twice the “watts in.” Certain electrical inputs to the cell were changed deliberately in a proprietary manner effecting Q frequency content.

This experiment is important because it shows both our upward discovery trend and because it exceeded the important 100% milestone. These sets of representative experiments showed that we have progressed well beyond the results with the open-cell experiments described in the Background section.

3.6. Experiment 6

Experiment 6 shows the effect of changing the repetition rate of the high voltage stimulation pulses. Figure 8 plots the input and output powers, percent excess power, and the Q pulse repetition rate. Output power is shown in blue, input

power is shown in green, and excess is shown in red as a percentage. The proprietary repetition rate of the pulses is plotted without scale in turquoise.

For five days, excess power from the induced thermal reaction in nickel hydride averaged approximately 20% during times when the wave form at a given repetition rate was applied to the nickel hydride. Total applied power was above 450 W. When the repetition rate was reduced excess power fell significantly, even though the input power rose. On seven different occasions when total applied power to the system was above 450 W, and the repetition rate was reduced, excess power dropped from approximately 20% to close essentially 0%. Excess power returned quickly to approximately 20% when the repetition rate was restored to its original value.

This plot demonstrates a cause and effect relationship exists between the frequency of the applied waveform pulses (Q) and the amount of excess power produced in the test cell.

4. Conclusions

We have run the nickel-light-water system is able to achieve more than 100% excess heat production (“2X”). Recent data shows that excess heat production was in the range of 110% for 2 h.

We run over 150 experiments using two different cell/calorimeter designs. Excess heat was always seen [?] in experiments where Q pulses, which have been tuned to the resonance of the hydride conductors (“core”), are present. Using our open cell design it is now possible to get excess heat on demand using light water and hydrided nickel and palladium.

Pulsed power in the cathode is the preferred method to raise the energy of the Brillouin zones confining hydrogen nuclei in the metal lattice [?]. We postulate that conversion of this energy to mass, results in the production of cold to ultra-cold neutrons. The removal of charge from the system by absorption of an electron by a proton makes a current pulse the preferred source of pulsed power because it provides an explicit source of electrons for capture.

In all cases, the application of a suitable Quantum Compression waveform enables active hydrided materials to produce excess power on demand without regard to the grain structure. While it is common for “gross loading” systems to work with some pieces of material and not others from the same batch, Quantum Reactor technology caused every centimeter in all 15 m of Pd wire to immediately produce excess heat while exposed to properly pulsed currents in light water. Quantum Reactor technology also allows for significant modulation of the power out of the cell.

Leveraging the results of the open cell experiments, the proprietary circuitry was attached to hydrided conductors in high-pressure, high-temperature systems for the sealed cell experiments [?].

The data taken from nickel–hydrogen system that was stimulated by our proprietary electronic inputs show that the thermal output is statistically significantly greater than the electrical input. Measurable and repeatable surplus thermal output is found in the nickel–hydrogen system when all other inputs to the cells remain constant. We have shown 100% excess energy and hope to achieve 200%, which would make the technology industrially useful. It is believed that the moderately elevated pressure and temperature environment of the pressurized cell provides higher probabilities for proton–electron captures, than the conditions at ambient temperature and pressure, because the electrolyte can be heated to over the boiling point of the electrolyte at atmospheric pressure. In addition to elevated temperature and pressure, the dimensions of the metal cathode inside the test cell, is much larger than what was used in the “open container”, first- round experiments.

We conclude that the reaction producing excess power in the nickel hydride is related to and very dependent upon the frequency of the Q pulses applied. We have thus demonstrated that there is a repeatable and measurable relationship between excess heat production from the stimulated nickel hydride in the test cell and the repetition rate of the applied electronic pulses. When the repetition rate is changed from the optimum frequency, excess power production ceases in the nickel hydride lattice. When that repetition rate is restored, significant excess power production resumes.

No helium measurements were made from either Phase I or Phase II reactor experiments.

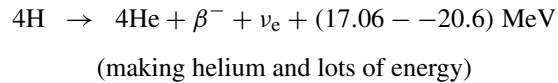
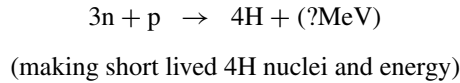
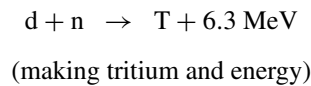
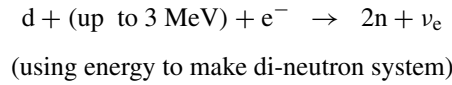
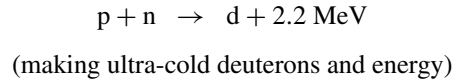
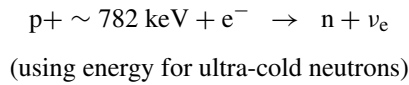
5. Future Work

We are looking closely at the experimental data from Experiment 5 and will use it to attempt to break through the next threshold 200% (“3X”) hopefully soon.

We have started to perform experiments in a third cell/calorimeter design in collaboration with SRI that we believe will lead to more useful heat by operating at higher temperatures. We feel that the first commercial applications expected will be hydronic heating systems that require grid power and produce lower quality heat as well as higher quality heat systems that will be used to re-power existing dirty generation assets.

In addition to Pd and Ni, the Q -pulse reactor system should work with other transition metals that confine hydrogen nuclei enough in a lattice to yield electron capture events.

Appendix: Controlled Energy Capture Hypothesis

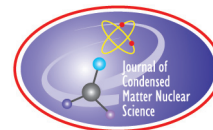


Acknowledgment

The authors acknowledge the ICCF-17 organizers for their generous support in allowing the presentation of this paper.

References

- [1] R. Godes, Brillouin Energy Corp. Phase One Data, http://brillouinenergy.com/Docs1/Phase_1-VerificationData.pdf.
- [2] R. Godes, Quantum Reactor Technology, Exciting New Science, Potential Clean Energy Source, <http://brillouinenergy.com/Docs1/BE25Tec.PPS>.
- [3] R. Godes, Brillouin Phase II Data, http://brillouinenergy.com/Docs1/Brillouin_Second_Round_Data.pdf.



Research Article

Molecular D₂ Near Vacancies in PdD and Related Problems

Peter L. Hagelstein *

Research Laboratory of Electronics, Massachusetts Institute of Technology, Cambridge, MA 02139, USA

Abstract

Excess heat is observed correlated with ⁴He in PdD excess heat experiments, consistent with proposed D₂/⁴He reaction mechanisms. The electron density is too high in PdD for molecular D₂ to form, so we consider the problem of D₂ formation in a monovacancy, and related problems involving other metal deuterides and hydrides.

© 2014 ISCMNS. All rights reserved. ISSN 2227-3123

Keywords: Donor and receiver model, Excess heat production, Lossy spin–boson model, Theory

1. Introduction

At present there is no general agreement among those working on cold fusion as to what physical mechanism is responsible for excess heat [1], or for other anomalies. In our work, we have tended to separate the associated theory issues into those requiring new physical mechanisms, and those which involve conventional aspects of physics, materials science, or chemistry [2]. For example, it is possible in our view to understand many important aspects of cold fusion experiments by focusing on the conventional issues.

From experiment we know that ⁴He is produced in amounts commensurate with the excess energy produced [3]. In these experiments the ⁴He is measured in the gas phase, which implies that the active sites must be close to a surface since helium diffusion is slow in PdD near room temperature. Once helium is trapped in defects, it is hard to remove it near room temperature since the binding energy can be an electron volt or more. Consequently the determination of the ratio of energy produced to ⁴He observed is not a simple experiment since it becomes problematic to get all of the ⁴He out [4]. It is now 2012, and it remains the case that only two measurements exist in which a significant effort was made to scrub all of the helium out of the cathode in such a measurement. The results from both of these experiments are consistent with a ratio of 24 MeV. This ratio is significant since it is the mass difference between two deuterons and a ⁴He nucleus. In this case this experimental evidence is consistent with proposed physical mechanisms involving two deuterons as reactants, and ⁴He as a product.

As we have remarked upon previously, the absence of energetic particles in amounts commensurate with the energy produced [5] means that no reasonable conventional Rutherford picture nuclear reaction can be consistent. There is no

*E-mail: plh@mit.edu

Rutherford-type mechanism possible in which a 24 MeV reaction energy can be shared among a modest number of final state particles in a manner consistent with experiment. As a product particle, the ^4He nucleus must be born with an energy less than 10–20 keV to produce few enough secondary neutrons to be consistent with measurements. If we were to propose that a 24 MeV quanta were somehow shared among nearby deuterons, we would have to find a way that the reaction energy be divided up and given to at least 25,000 of them so that the resulting neutron emission from subsequent dd-fusion reactions could be low enough to be consistent with experiment.

Given this situation, we might reasonably assert that some kind of new mechanism is responsible; one that involves two deuterons locally, produces ^4He , and communicates the reaction energy to low energy condensed matter degrees of freedom. Theoretical models that we have pursued work in this way; however details associated with the reaction mechanisms are discussed elsewhere [6], and are generally not needed in connection with the discussion to follow. We already have enough in such an ansatz to provide a foundation for addressing conventional physics, materials science, and chemistry issues associated with the experiments.

2. Background Electron Density

There is a school of thought that says that the local background electron density is an important parameter in understanding hydrogen as an interstitial in metals [7]. In essence, hydrogen is looking for a specific background electron density; at the optimum electron density the energy is minimized, so that at either lower or higher electron densities the energy increases. Of course, the mathematical formulation of the associated model includes two-body potentials along with the embedding energy. Nevertheless, we can make substantial progress in understanding many basic issues in metal hydrides simply by focusing single-mindedly on the background electron density.

We have described a version of this argument previously in the case of hydrogen and deuterium in Pd [8] (for the arguments that follow, hydrogen will be largely interchangeable with deuterium). We focused first on the diatomic molecule PdH where the interatomic separation at minimum energy is 1.53 Å; the corresponding background electron density in a single configuration relativistic Dirac Fock calculation is 0.069 electrons/Å³. According to the line of argument that we are following, we now know the background electron density preferred by hydrogen. It may be useful to see how this value compares with the density-dependent embedding energy from embedded atom theory, which is shown in Fig. 1. We see that the minimum embedding energy occurs at an electron density of 0.069 electrons/Å³, which is consistent with our estimated of the background electron density in the PdH molecule. This is encouraging.

The background electron density along the [111] direction in PdD as calculated using a simple superposition of atomic Pd electron density profiles is shown in Fig. 2. One sees that the lowest electron density occurs at the O-site, and that local minima occur at the T-sites. The electron density at the O-site in this model is 0.079 electrons/Å³, which is a bit higher than the optimum electron density (a bit higher than 0.070 given in [9], and a bit lower than the DFT result of Orondo, which is near 0.095 electrons/Å³ [10]). Based on the arguments above, we would expect hydrogen occupation of the O-sites in preference to T-sites (this argument is well known), since the electron density is too high at the T-sites. The corresponding difference in the embedding energy is 164 meV (and about 322 meV for the DFT densities, which suggests that the O–T excitation energy if measured from experiment will tell us something about the electron density at the O-site).

Nickel is known to have a lower solubility for hydrogen and deuterium. Based on the discussion above, we might conjecture that the electron density is higher, which is checked through an analogous superposition calculation for the background electron density in Ni shown in Fig. 3. We see that the background electron density is higher in this model, with the minimum (0.132 electrons/Å³) found at the O-site. Once again we would expect that O-site occupation would be preferred over T-site occupation because the electron density is even higher at the T-site. It is probable that one could use the difference in solubility between Ni and Pd to estimate the increase in the O-site electron density in Ni.

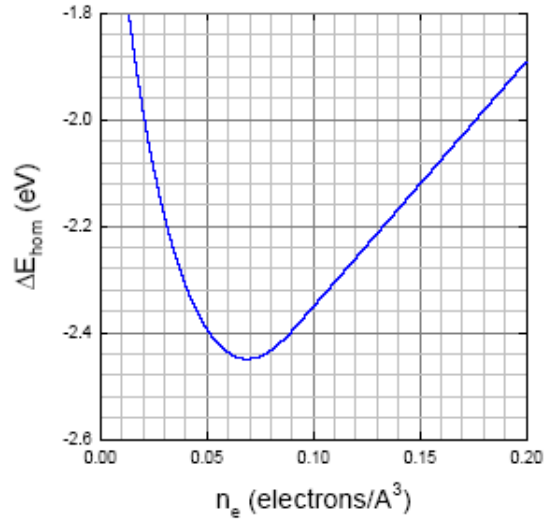


Figure 1. Embedding energy for hydrogen as a function of the background electron density from [7].

Alternatively, one could likely develop a systematic determination of O-site electron densities from experimental He solubility data.

A similar calculation for H in Au is shown in Fig. 4. In this case we might imagine that the solubility might be higher since the electron density seems to be lower. However, a check with the literature shows that the solubility is much lower, suggesting that this superposition model probably underestimates the electron density at the O-site.

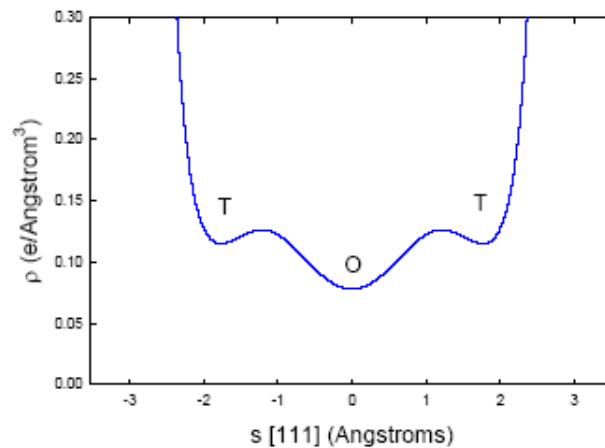


Figure 2. Background electron density along the [111] for PdD (with $a = 4.081 \text{ \AA}$).

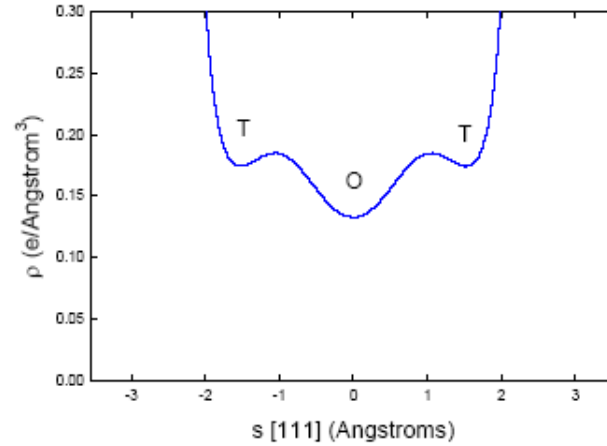


Figure 3. Background electron density along the [111] for Ni (with $a = 3.52 \text{ \AA}$).

It seems reasonably clear that we are seeing a commonality in the background electron density along the [111] direction in these simple fcc metals. The shape is nearly the same in all cases, and the only major difference is in what the minimum electron density at the O-site is. Based on the embedding energy of Fig. 1, we note that a modest increase in the minimum electron density above the optimum can produce a large reduction in the hydrogen solubility.

3. Molecular H_2 with Background Electrons

It would be useful to consider the extension of these ideas to the case of molecular H_2 embedded in an environment with some background electron density. Unfortunately the situation in this case is a little more complicated. For example, a

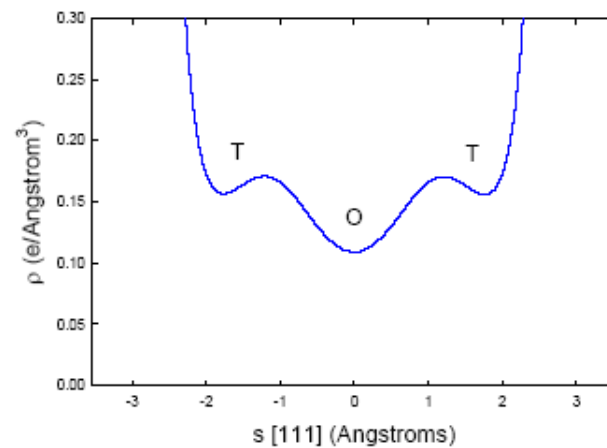


Figure 4. Background electron density along the [111] for Au (with $a = 4.0788 \text{ \AA}$).

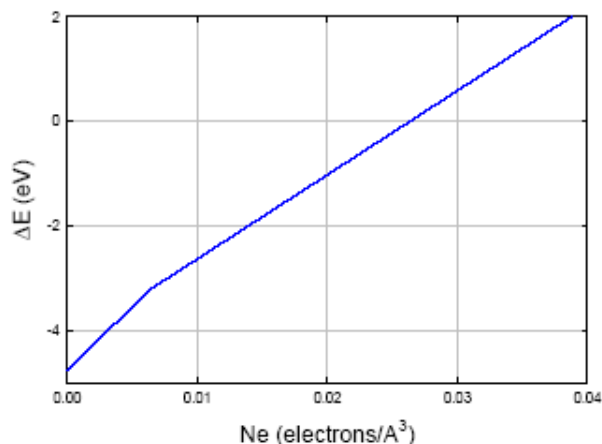


Figure 5. Embedding energy for H_2 with vacuum separation [12].

hydrogen atom experiences a significant attractive energy due to the background electron density alone, while there is no such effect for the H_2 molecule. Instead, the H_2 molecule is much more polarizable [11], so that there is a long-range attractive dipole–dipole interaction which dominates the potential when the molecule is separated from the atom.

The dipole–dipole interaction changes how we think about the H_2 molecule problem qualitatively then. It is no longer the case that the molecule is looking for the optimum electron density. Instead, we should begin with the long-range dipole–dipole interaction. Consider in the discussion that follows the case of a triatomic molecule formed by an atom with molecular H_2 . When this interaction is weak, as in the case of rare gas–diatomic hydrogen molecules, then the molecule approaches the atom seeing an increasingly attractive potential up to the point where the electron density becomes sufficiently high that a substantial increase in the embedding energy occurs.

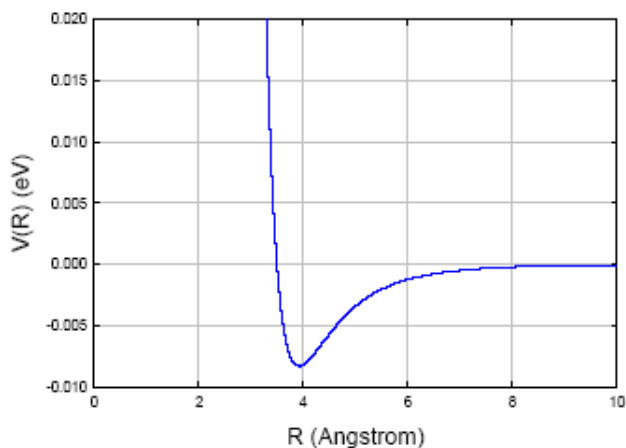


Figure 6. Lennard–Jones model potential for $Xe-H_2$ as a function of the $Xe-H_2$ separation.

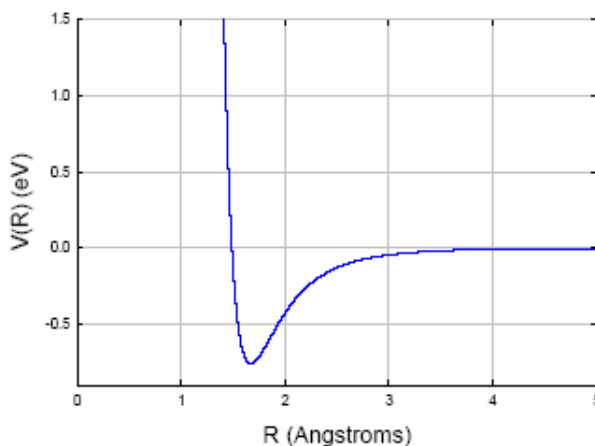


Figure 7. Lennard-Jones model potential for Pd-H₂ as a function of the Pd-H₂ separation.

For example, in the case of Xe-H₂, the potential minimum occurs at a separation of 3.9214 Å. We compute the background electron density of Xe at this radius to be 2.1×10^{-5} electrons/Å³, corresponding to an embedding energy of about 8.1 meV. The binding energy is 8.3 meV. Note that models that take into account dipole-dipole coupling have long been used to model the spectra of molecular hydrogen rare gas molecules [13].

In the case of Pd-H₂ the potential minimum occurs at 1.67 Å, at which point we estimate the background electron density is 0.033 electrons/Å³. The associated embedding energy is about 1.4 eV for a 0.74 Å H-H separation (and perhaps 1.1 eV for a 1.48 Å separation); and the binding energy is about 0.76 eV [14]. In this case, the Pd-H₂ configuration is a more strongly bound than the bent H-Pd-H configuration by about 0.19 eV [15]. The minimum energy found in a Quantum Espresso calculation of PdH₂ corresponds to a binding energy of about 1.6 eV [16]. We have wondered for some time why the binding should be so strong in this DFT model; in light of the discussion above we suspect that the Pd polarizability is overestimated in the DFT calculation.

Finally, in the case of NiH₂ the binding of molecular H₂ is more than 2 eV at the local minimum corresponding to Ni-H₂ according to Niu et al. [17]. In this case, the stronger dipole-dipole attraction pulls the molecule to higher electron density where the bent H-Ni-H configuration is favored; in this case the binding energy is near 2.7 eV. Consequently NiH₂ is unstable against decay to the lower bent H-Ni-H configuration.

We know that the H-H separation increases as the electron density increases. A calculation of the potential for H₂ in jellium at an electron density of 0.0628 electrons/Å³ is given in Christensen et al. [18], where the potential minimum is about 1 Å; this density is just below the threshold (near 0.10 electrons/Å³ in Dechiaro's calculation) where no potential minimum occurs in this density regime [19]. We note that the H-H separation in atom-H₂ molecules tends to be larger than what might be expected in a jellium calculation due to the dipole-dipole interaction which can produce additional stretching of the H-H bond.

4. D₂ in Vacancies

The electron density is too high in bulk Pd for molecular D₂ to form; hence it seems reasonable to consider the lower electron density available in vacancies [8]. Our focus has been on the monovacancy, since it is in a sense the simplest theoretical problem, and since there seems to be indirect evidence from high-current co-deposition experiments that

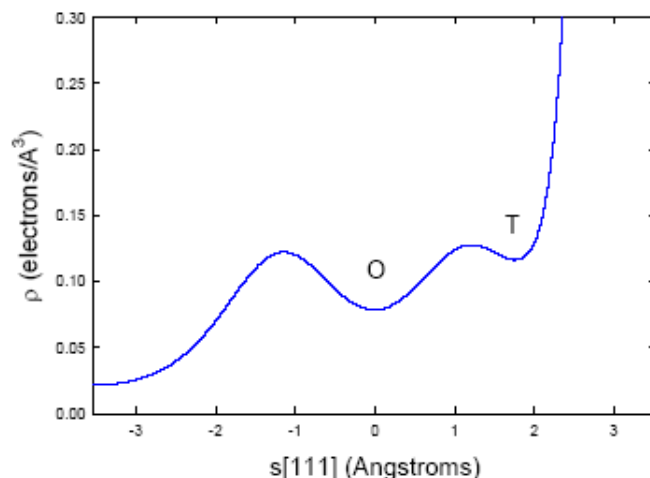


Figure 8. Background electron density along the [111] for PdD (with $a = 4.081 \text{ \AA}$) in the vicinity of a monovacancy.

conditions under which they are expected correspond to conditions under which excess heat is observed [20,21]. A lower electron density occurs in more complicated vacancy structures, such as divacancies and microvoids; such structures are less interesting to us, since larger amounts of volume are present where the electron density is "too low," such that we would expect internal D_2 gas formation which seems to us uninteresting.

Let us begin by considering the electron density in the vicinity of a Pd vacancy in PdD. The simple superposition estimate based on Dirac–Fock Pd electron densities is shown in Fig. 8. The minimum electron density at the vacancy site has now dropped to $0.022 \text{ electrons/\AA}^3$, which is below the background electron density for H_2 formation in PdH_2 (this density would be relevant in the case of a molecule in the vacancy closest to one Pd atom, as long as the polarizability of the atom in the solid is similar to the polarizability of the isolated atom). This compares with 0.020 in [9], 0.015 electrons/\AA^3 in Dechiaro’s DFT calculation [16].

Based on the discussion above, whether molecular H_2 or D_2 will behave similarly in a monovacancy then depends critically on whether the Pd atomic polarizability is impacted because of bonding to other atoms. To investigate, we consider first the calculation of Nakatsuji and Hada [22], where the binding of an H_2 molecule on molecular Pd_2 was analyzed. The binding in the case of an H_2 molecule aligned and centered with a Pd_2 molecule leads to a binding energy of 0.63 eV, which is a bit less than the 0.76 eV energy of Ref. [14] for PdH_2 ; this might indicate a minor reduction in the Pd polarizability due to bonding.

To pursue this, we consider the calculations of Wilke and Scheffler [23] for H_2 above a Pd [100] surface. The potential isocontours are seen to correspond to a binding energy no more than about 0.35 eV under conditions where the H–H separation is less than 1 \AA . Such a result seems consistent with a further reduction in the Pd atomic polarizability due to additional bonding. There are many related computations in the literature of H_2 over a clean Pd surface in different orientations, and in general the binding energy is only a few tenths of an eV under conditions where the separation is less than 1 \AA .

Based on this there seems to be no reason not to expect D_2 formation in principle in the vicinity of a monovacancy. The question of the associated binding energy is more interesting; for example, we might expect the binding energy to be similar to that of H_2 on a clean Pd surface. In the literature there is theoretical and experimental support for a molecular H_2 adsorbed state on Pd [210] with a binding energy of 0.27 eV [24,25].

To pursue this we have carried out some exploratory calculations based on an embedded molecule model based on

$$E_{\text{tot}} = \sum_{j < k} \phi_{jk}(r) + \Delta E_{\text{hom}}(\rho).$$

The interaction between the Pd atom and the molecule is dominated by dipole–dipole interactions at large distance, with a reduction in strength at smaller distances; this motivated us to adopt

$$\phi_{jk} = -\frac{C}{(r^2 + r_0^2)^3}.$$

One can develop a reasonable fit to molecule, cluster, and surface Pd–H₂ calculations with such an empirical interaction potential. Inside the metal we expect a screening of the long range interaction for distant atoms due to the conduction electrons (the associated Thomas–Fermi screening length is less than 1 Å).

If we neglect screening, the resulting models show a strong binding of the H₂ or D₂ molecule due to attractive Van der Waals contributions from many nearby Pd atoms. With screening the minimum energy occurs for the molecule at the center of the vacancy, and the molecule energy is above the vacuum level. Since part of the attractive interaction is bonding rather than dipole–dipole interaction, we tried working with models where exponential screening was deferred. Perhaps it is useful to consider one such calculation (see Fig. 9). In this case we have selected the parameters C and r_0 close to the PdH atom values, with screening deferred to about $4r_0$, and no correction for the reduction in embedding energy at increased H–H separation. This model was selected since it gives a minimum energy in the vicinity of what would be required to connect with the excess power as a function of loading curves from experiment. In this kind of a model, the total energy can be lowered when the molecule goes away from the center of the monovacancy since there are more Pd atoms that are closer in this direction. The O-site is located at 2.04 Å in the [100] direction, and we see that the minimum effective potential occurs for a displacement on the other side, closer to the Pd atom at the center of the next cell. The electron density in this model is very high at the O-site, around 0.066 electrons/Å, so that the H–H separation will be more than 1 Å in the absence of a cage effect. Note that something of a cage effect is expected in this configuration due to the five Pd atoms that surround the molecule. The potential in this calculation is defined relative to the vacuum molecule. According to the calculations of Orondo, the bulk O-site potential per hydrogen atom is about –250 meV at a loading near 0.85 [10]. If the excess power versus loading curves are a result of D₂ occupation of a monovacancy in this sense, then the molecule potential needs to be somewhere near 300 meV [8]; in Fig. 9 it goes down to –370 meV which is a little too deep. Note that under discussion here is D₂ binding that is a little stronger than for adsorbed H₂ on Pd[210] discussed above.

Dechiaro has carried out Quantum Espresso calculations for this configuration [16], and obtains a minimum potential near 1.45 Å away from the vacancy center, of close to –1 eV relative to the energy at the vacancy center. Since these DFT calculations overestimate the well depth in the PdH molecule, we might expect a similar overestimate for the attraction in the monovacancy calculation; hence, a corrected version of the calculation might give a reduction in energy near 400 meV. If so, then there would begin to be a connection between the models and the excess power versus loading curves from experiment.

We have noted previously that the molecule is unstable if nearby O-sites are unoccupied in the monovacancy [8]. We recently noticed a discussion of this effect in the early paper of Rosato and Cleri [9].

In a recent paper by He et al. [26], there is a discussion of H₂ in a monovacancy in Pd at different loadings. The 5+2 occupation of the monovacancy was not considered in this work, but one can find a discussion of 6+2 occupation. While the H–H separation is small for this configuration, the molecule is well separated from the Pd atoms. We consider this to be significant in connection with screening effects. The overlap probability between two deuterons is impacted strongly by screening, as has been often noted in the literature. One would expect screening due to conduction electrons, but the Thomas–Fermi screening length for an electron in the center of a monovacancy is near 0.7 Å, which is too small to

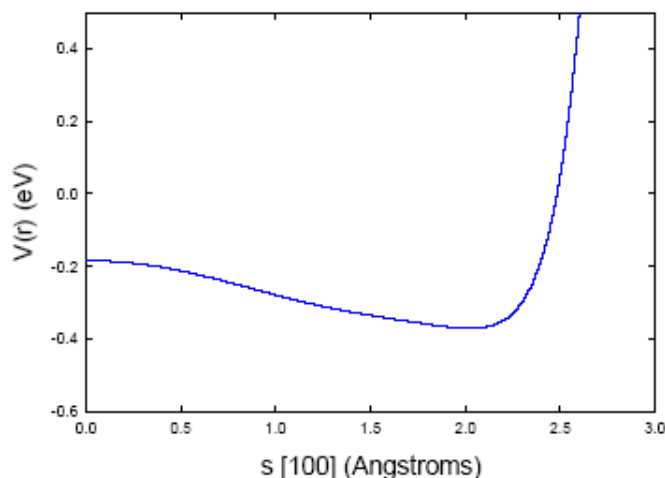


Figure 9. Model H_2 or D_2 potential in as a function of distance in the $[100]$ direction of a monovacancy with seven interstitials.

make much of a difference. A molecule at higher electron density would be expected to see increased screening, but the Thomas–Fermi length scales very slowly with density.

In our view the key issue is the proximity with a higher- Z metal atom. In our models for the reaction mechanism, the maximum reaction rate is proportional to the phonon exchange matrix element for the $D_2/{}^4\text{He}$ transition, which is proportional to $\exp(-G)$, where G is the associated Gamow factor. Hence, any increase in screening impacts the reaction rate exponentially. Consequently, the minor increase in screening near the O-site due to the higher electron density will already lead to a significant enhancement in the coherent reaction rate over the screening at the vacancy center. If the deuterons tunnel together at even higher electron density closer to the Pd atoms then one would expect even more screening. There may be the possibility of even more enhancement due to orbital hybridization with an inner shell if the one sigma orbital is close to a metal atom when the deuterons get close to each other. In the exploratory calculations we have done so far looking for such hybridization we have found only minor effects.

If so, then the goal would be to arrange for a D_2 molecule to be close to nearby metal atoms, and not keep them distant near the center of a monovacancy. A similar comment could be made in response to the recent proposals by Storms for hydrogen and deuterium in voids; from our perspective where the electron density is low the problem looks very much like vacuum physics.

Note that we would expect similar effects associated with monovacancies in other metal deuterides and hydrides. Dechiaro has carried out calculations of molecule formation in monovacancies in many metal hydrides. In the case of Ni and Au, the DFT calculations show effects similar to those in Pd, and H_2 or D_2 molecule formation is predicted very much like in the case of Pd.

5. Thoughts on the Piantelli Protocol for NiH

There has been much recent interest in excess heat in NiH experiments with gas phase hydrogen loading [27]. At present there is no agreement as to what mechanism is responsible for the excess heat observed. We have proposed that excess heat in this system is based on $HD/{}^3\text{He}$ transitions, as an analog of the $D_2/{}^4\text{He}$ transitions for PdD systems [2,6]. While the latter has some support in ${}^4\text{He}$ observations connected with the energy produced, there is as yet no experimental

clarification as to whether such a correlation exists (or does not exist) between ^3He and energy in the NiH system.

In the event that HD/ ^3He transitions are involved, then we face the problem of HD formation (similar to the problem of D_2 formation in PdD). The electron density in Ni is higher at the O-sites than in Pd, so it is much more difficult to load. On the other hand, the interstitial density doesn't need to be as high for the stabilization of the vacancies. The question is how might we arrange for HD in Ni, given that a protocol has been put forth by the Piantelli group [27].

In this protocol, the Ni is loaded with hydrogen and then deloaded repeatedly, with an increase in hydrogen uptake each cycle. Given that the solubility of hydrogen in bulk Ni is so low (parts in 10^{-4}) [28], what is responsible for increasing hydrogen uptake at the percent level? We have conjectured that vacancies are being produced during this cycling, and that the observed uptake is due to a loading in the vacancies. Note that since there is low electron density available within the monovacancy, hydrogen can find its optimum electron density with a corresponding solubility per vacancy O-site higher than that of Pd. One might ask how the local hydrogen density gets sufficiently high to stabilize vacancies in Ni since the solubility is so low. Apparently segregation occurs in the miscibility gap in NiH_x , where either there is no H, or regions with $\text{NiH}_{0.7}$ occur [29]. Consequently the hydrogen density gets to be sufficiently high locally so that vacancies can be stabilized [20]. In contrast to the PdD experiments done near room temperature, at the elevated temperature of the Piantelli experiments, some limited vacancy diffusion can occur.

6. Discussion

The deuterium molecule requires low electron density to form, which motivates our interest in vacancies in PdD and other metal hydrides and deuterides. We have argued previously that inadvertent codeposition can create monovacancies if the loading is sufficiently high (above 0.95 near room temperature in PdD). The D_2 molecule in the vacancy is unstable if there are unoccupied O-sites present, so we require a substantial loading (above 0.85 if the binding energy is close to the observed H_2 surface state in PdH) to stabilize the molecule. The situation in Au seems similar qualitatively; but Ni seems to show a higher polarizability, so that the HD may be a bit less stable in a Ni vacancy. It remains the case that we need experimental evidence to clarify whether sigma-bonded dideuterium molecules actually form along the lines discussed. Magic angle NMR at least has the potential to resolve the issue. Within the picture outlined here there should be many more candidates than just Pd or Ni for showing excess heat. Ni alloys with good hydrogen solubility (such as demonstrated by Celani at this conference) have the potential to be important in the future. We have made use of a simple empirical model to try to understand the calculations of Dechiaro, which we think gives too strong of a binding energy for dideuterium near the O-site of a monovacancy with the other O-sites occupied. Progress on the development of a potential model derived from DFT calculations will allow for realistic tunneling calculations in the future.

References

- [1] S. Pons, M. Fleischmann and M. Hawkins, *J. Electroanal. Chem.* **261** (1989) 301.
- [2] P.L. Hagelstein, Bird's eye view of phonon exchange models for excess heat in the Fleischmann–Pons experiment, *J. Cond. Mat. Nucl. Sci.* **6** (2012) 169–180.
- [3] M. Miles, R.A. Hollins, B.F. Bush, J.J. Lagowski and R.E. Miles, *J. Electroanal. Chem.* **346** (1993) 99.
- [4] P.L. Hagelstein, M.C.H. McKubre, D.J. Nagel, T.A. Chubb and R.J. Hekman, *Proc. ICCF11* **23** (2004).
- [5] P.L. Hagelstein, Constraints on energetic particles in the Fleischmann–Pons experiment, *Naturwissenschaften* (2010) 345–352.
- [6] P.L. Hagelstein and I.U. Chaudhary, Models for excess heat in PdD and NiH, *Proc. ICCF17* (in press).
- [7] F. Besenbacher, S.M. Myers and J.K. Nørskov, Interaction of hydrogen with defects in metals, *Nucl. Instr. Meth. Phys. Res. B* **7/8** (1985) 55.

- [8] P.L. Hagelstein and I.U. Chaudhary, Arguments for dideuterium near monovacancies in PdD, *Proc. ICCF15* (2009) 282.
- [9] V. Rosato and F. Cleri, Deuterium clusters in a strained Pd lattice, *J. Mater. Res.* **5** (1990) 2094.
- [10] P. Orondo, PhD Thesis, MIT, USA, 2012.
- [11] A. Dalgarno, A.L. Ford and J.C. Browne, *Phys. Rev. Lett.* **27** (1971) 1033.
- [12] R. Diez Munio and A. Salin, Self-consistent screening of diatomic molecules in an electron gas, *Phys. Rev. B* **60** (1999) 2074.
- [13] R.J. Le Roy and J. van Kranendonk, *J. Chem. Phys.* **61** (1974) 4750.
- [14] C. Jarque, O. Novaro, M.E. Ruiz and J. Garcia-Prieto, On the stability of the PdH₂ molecule, *J. Am. Chem. Soc.* **108** (1986) 3507.
- [15] K. Balasubramanian, P.Y. Feng and M.Z. Liao, *J. Chem. Phys.* **88** (1988) 6955.
- [16] L. Dechiaro, Private communication.
- [17] J. Niu, B. K. Rao, P. Jena and M. Manninen, Interaction of H₂ and He with metal atoms, clusters and ions, *Phys. Rev. B* **51** (1995) 4475.
- [18] O.B. Christensen, P.D. Ditlevsen, K.W. Jacobsen, P. Stolze, O.H. Nielsen and J.K. Norskov, *Phys. Rev. B* **40** (1989) 1993.
- [19] S.A. Bonev and N.W. Ashcroft, Hydrogen in jellium: First principles pair interactions, *Phys. Rev. B* **64** (2001) 224112.
- [20] D. Letts and P.L. Hagelstein, Modified Szpak protocol for excess heat, *J. Cond. Mat. Nucl. Sci.* **6** (2012) 44.
- [21] M.H. Miles, Codeposition of palladium and other transition metals in H₂O and D₂O solutions, *Proc. ICCF17* (in press).
- [22] H. Nakatsuji and M. Hada, Interaction of a hydrogen molecule with Pd, *J. Am. Chem. Soc.* **107** (1985) 8264.
- [23] S. Wilke and M. Scheffler, Potential energy surface for H₂ over Pd (100), *Phys. Rev. B* **53** (1996) 4926.
- [24] P.K. Schmidt, K. Christmann, G. Kresse, J. Hafner, M. Lishka and A. Gross, Coexistence of atomic and molecular chemisorption states: H₂/Pd(210), *Phys. Rev. Lett.* **87** (2001) 096103-1.
- [25] M. Lischka and A. Gross, Hydrogen on palladium: A model system for the interaction of atoms and molecules with metal surfaces, *Recent Developments in Vacuum Science and Technology*, J. Dabrowski (Ed.), 2003, p. 111.
- [26] J.H. He, L.F. Dechiaro, D.L. Knies, G.K. Hubler, K.S. Grabowski, A.E. Moser, D.D. Dominguez, D.A. Kidwell and P.L. Hagelstein, Stability of a hydrogen molecule in a vacancy of palladium hydrides, *Int. J. Hydrogen Energy* **37** (2012) 12351.
- [27] S. Focardi, V. Gabbani, V. Montalbano, F. Piantelli and S. Veronesi, Large excess heat production in NiH systems, *Il Nuovo Cimento* **111A** (1998) 1233.
- [28] M.L. Wayman and G.C. Weatherly, The H–Ni (nickel hydrogen) system, *Bulletin of Alloy Phase Diagrams* **10** (1989) 569.
- [29] R. Juskenas, A. Selskis and V. Kadziauskiene, In situ X-ray diffraction investigation of nickel hydride formation during cathodic charging of Ni, *Electrochimica Acta* **43** (1998) 1903.
- [30] B. I. Dunlap, D.W. Brenner, R.C. Mowrey, J.W. Mintmire and C.T. White, *Phys. Rev. B* **41** (1990) 9683.
- [31] M. Apicella, E. Castagna, L. Capobianco, L. D'Aulerio, G. Mazzitelli, F. Sarto, A. Rosada, E. Santoro, V. Violante, M. McKubre, F. Tanzella and C. Sibilía, *Proc. ICCF12* (2005) 117.



Research Article

Basic Physics Model for PdH Thermodynamics

Peter Orondo and Peter L. Hagelstein*

Research Laboratory of Electronics, Massachusetts Institute of Technology, Cambridge, MA 02139, USA

Abstract

We made use of the very powerful modern density functional code Quantum Espresso for an ab initio calculation of the thermodynamics of PdH. There is an energy offset of about 100 meV in the calculation as compared to experiment. We developed an empirical correction to the theoretical energies which allowed us to fit the experimental results for excess enthalpy and excess entropy with some success. We also explored a new model that posits a weak binding between absorbed hydrogen atoms in PdH, and is able to provide a better fit to the experimental results. The model provides a simple physical explanation of observed phase diagram, and also of the observed dependence of the thermodynamic variables (excess enthalpy and excess entropy) on loading.

© 2014 ISCMNS. All rights reserved. ISSN 2227-3123

Keywords: Density functional calculation, Phase diagram, Quantum espresso, Thermodynamics

1. Introduction

Palladium hydride is one of the most studied and best understood of the metal hydrides. However, a complete picture of the physics and thermodynamics of absorbed hydrogen still eludes us.

Early work on the theory of absorbed interstitial hydrogen was done by Fowler [1] and Lacher [2]. They attempted to model the properties of absorbed hydrogen using a statistical interpretation. From this point of view, a distribution of the gas and hydrogen in metal phases may be derived from the partition function after assuming that the lattice contains potential energy holes into which the hydrogen is absorbed [2]. A challenge, however, arises because the energy of the absorbed hydrogen has to be known a high degree of accuracy if such a scheme is to give good results.

Earlier workers have tackled the problem with varying degrees of success. Christensen employed an effective medium-type model within the same partition function formalism as Lacher's [3] while Salomons has employed molecular dynamics [4]. There are also Monte Carlo models, for example [5]. In this work we make use of an ab initio calculation based on modern density functional methods as implemented in Quantum Espresso.

2. Basic Model Formulation

In this work, we employ the basic Lacher model to describe the entire problem, so we write

*E-mail: plh@mit.edu

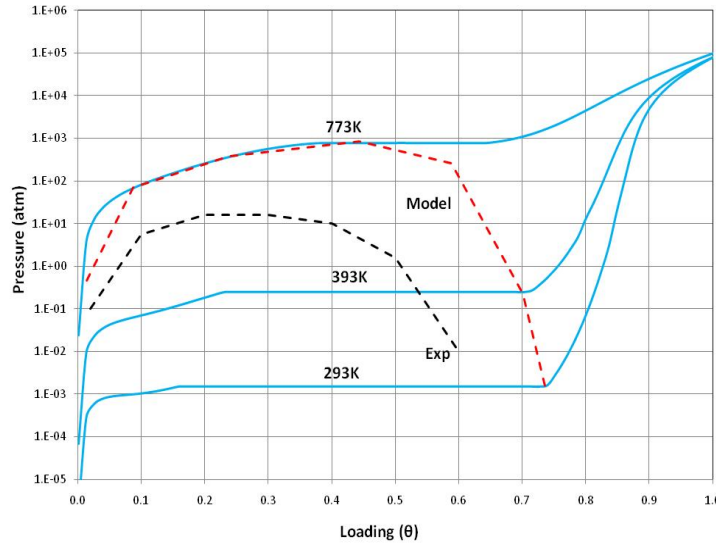


Figure 1. Pressure-composition-temperature isotherms; phase boundary from experiment (black); model isotherms (blue); model phase boundary (red).

$$Z_H(\tau, \mu) = \sum_{n_o} \sum_{n_t} \sum_{ASN} e^{\frac{(n_o+n_t)\mu - \epsilon_h}{\tau}} z^{(n_o+n_t)}. \quad (1)$$

In Eq. (1), $Z_H(\tau, \mu)$ is the grand partition function of the full PdH system; $n = n_o + n_t$ is the number of occupied sites, of which there are two types, shown in subscripts (octahedral and tetrahedral); τ is the normalized temperature $\kappa_B T$; μ is the chemical potential of absorbed proton; Z is the partition function of an absorbed proton; $\epsilon_h(n)$ is the total interaction energy of the configuration containing n absorbed protons; and “ASN” signifies all configurations containing $n_o + n_t$ absorbed protons.

From the grand partition function, the system is fully characterized (if we could determine the interaction energy accurately). Thus, the chemical potential of the interstitial proton is, for example, for the occupied octahedral sites,

$$\mu_o(\tau, n_o, n_t) = -\tau \frac{\partial \ln Z_H(\tau, n_o, n_t)}{\partial n_o}, \quad (2)$$

which must equal that of the tetrahedral species. The result is, after using the Stirling approximation:

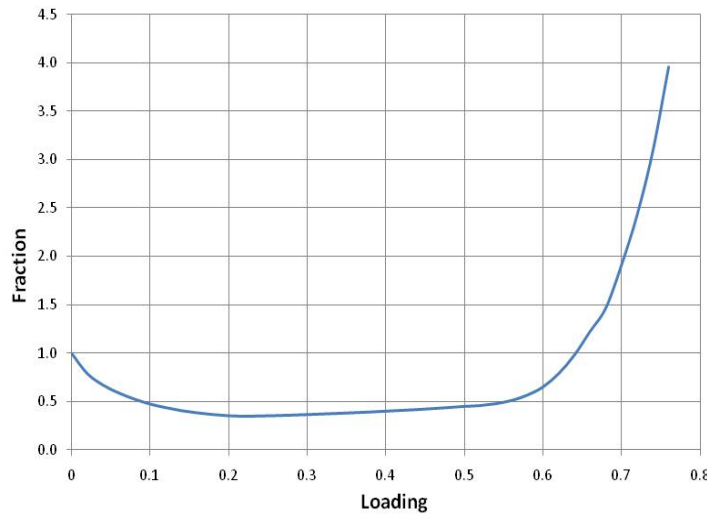


Figure 2. Incremental number of accessible microstates for data from [11].

$$\mu_H(\theta) = -\tau \ln z + \tau \ln \frac{\theta}{1-\theta} + \theta \frac{\partial}{\partial \theta} \epsilon_h(\theta) + \epsilon_h(\theta), \quad (3)$$

where $\theta = n/N$ is fractional occupation or loading, and N is the total number of available interstitial sites.

Matching the chemical potential at the gas–solid boundary then yields an analytical expression for the pressure–composition–temperature isotherm. The gas phase chemical potential is well known, for example [6]:

$$\mu_{H_2} = -\tau \ln \left[\left(\frac{2\pi m \tau}{h^2} \right)^{3/2} \frac{\tau}{P} \right] - \tau \ln \frac{e^{\frac{\epsilon_{0v}}{2\tau}}}{1 - e^{\frac{\epsilon_{0v}}{\tau}}} - \tau \ln \left(\frac{8\pi^2 I \tau}{\sigma h^2} \right) - \epsilon_D. \quad (4)$$

In Eq. (4), the right-hand side terms are, respectively, the translational, vibrational, rotational and dissociative contributions to chemical potential of hydrogen gas. At high pressure, we must use fugacity instead of pressure in Eq. (4).

3. Density Functional Theory: State Energies

For the dissolved hydrogen, we calculate the state energies by developing approximate solutions to the many-body time-independent Schrodinger equation:

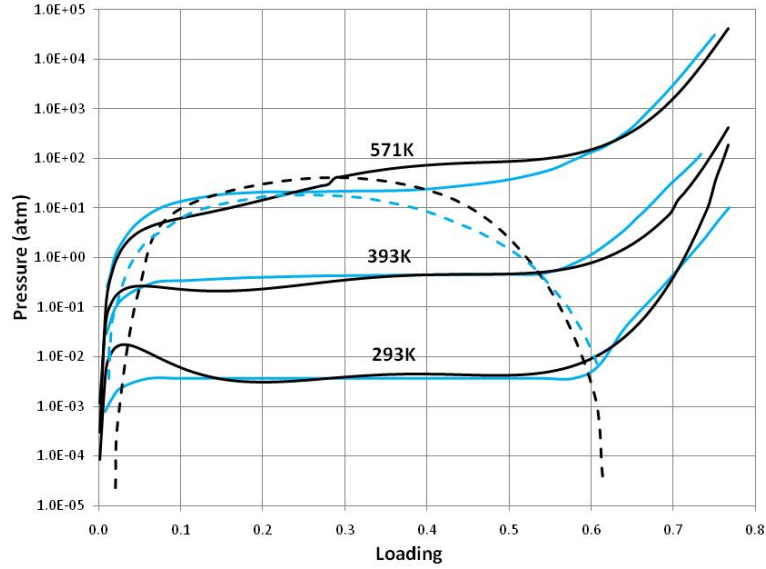


Figure 3. P–C–T isotherms; model (*black*); experiment (*blue*).

$$\hat{H}\psi(r_i) = E_i\psi(r_i), \quad (5)$$

where

$$\hat{H} = -\sum_i \frac{\hbar^2 \nabla_i^2}{2m_e} - \sum_{i,I} \frac{Z_I e^2}{|\mathbf{r}_i - \mathbf{R}_I|} + \sum_{i \neq j} \frac{e^2}{|\mathbf{r}_i - \mathbf{r}_j|} - \sum_I \frac{\hbar^2 \nabla_I^2}{2M_I} + \frac{1}{2} \sum_{I,J} \frac{Z_I Z_J e^2}{|\mathbf{R}_J - \mathbf{R}_I|}. \quad (6)$$

The Hamiltonian is made up of kinetic and Coulomb potential energy contributions in a nonrelativistic approximation.

Given the substantial progress made in recent years in density functional codes, we decided to make use of Quantum Espresso and work with density functional theory (DFT) to obtain approximate solutions to Eq. (5). Additionally, we need to give a meaning to the interaction energy term, $\epsilon_h(n)$. For that, we make a simple definition that corresponds to the energy change when one proton is absorbed, referenced to the gas energy in vacuum, ϵ_{2H}^{Vac} :

$$\epsilon_h(n) = \epsilon_{(n+1)H}^{Pd} - \left(\epsilon_{nH}^{Pd} + \frac{1}{2} \epsilon_{2H}^{Vac} \right). \quad (7)$$

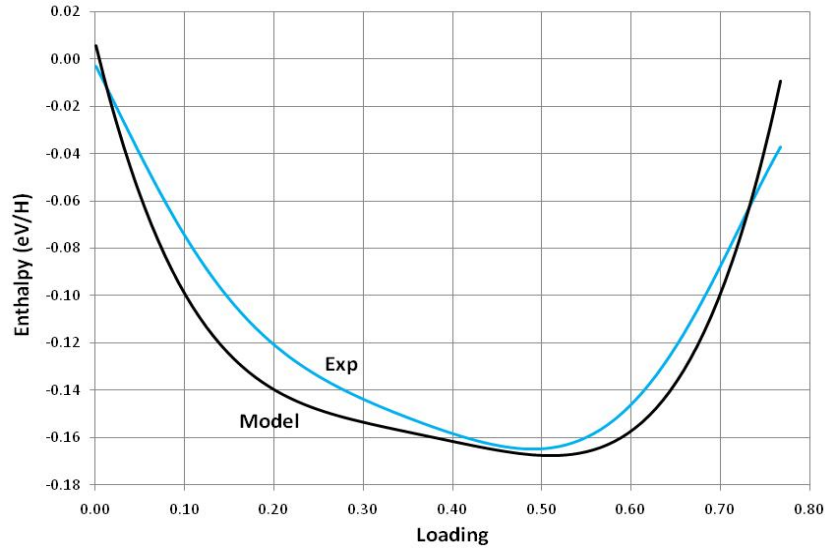


Figure 4. Model excess enthalpy at 571 K; experimental data is from [11].

From the solution for this energy we obtain the pressure–composition–temperature isotherm of Fig. 1 from Eqs. (3) and (4). We find that the DFT results are correct qualitatively; but corrections will be required in order to obtain agreement with experimental results for the chemical potential.

4. Corrected Energy

We would like to take this basic DFT result above and correct it in a manner consistent with the expected relevant physics. We assume that the biggest errors are associated with the DFT calculation of the state energies. Apart from the constant offset in calculated DFT energies which are intrinsic in the model (see e.g. [7]), there will be corrections from the interaction of H with the Pd lattice. These errors are plausibly expected to be linear in loading. We should also expect that DFT will not correctly predict elasticity that is inevitable when the lattice expands with loading. We expect these errors to be quadratic. Lastly, DFT will not capture any temperature dependence of the energy; we recall that band energies in semiconductors are often linear in temperature (see [8] e.g.), and there is no reason to expect the energies in PdH to behave differently.

This discussion motivates us to consider a corrected energy model given of the form [9]

$$\epsilon_h(\theta, T) \rightarrow \epsilon_h(\theta) + \left[\epsilon_\delta^0 + \epsilon_\delta^0(T - T_c) \right] + \left[\epsilon_\delta^1 + \epsilon_\delta^1(T - T_c) \right] \theta + \left[\epsilon_\delta^2 + \epsilon_\delta^2(T - T_c) \right] \theta^2 + O(\theta^3), \quad (8)$$

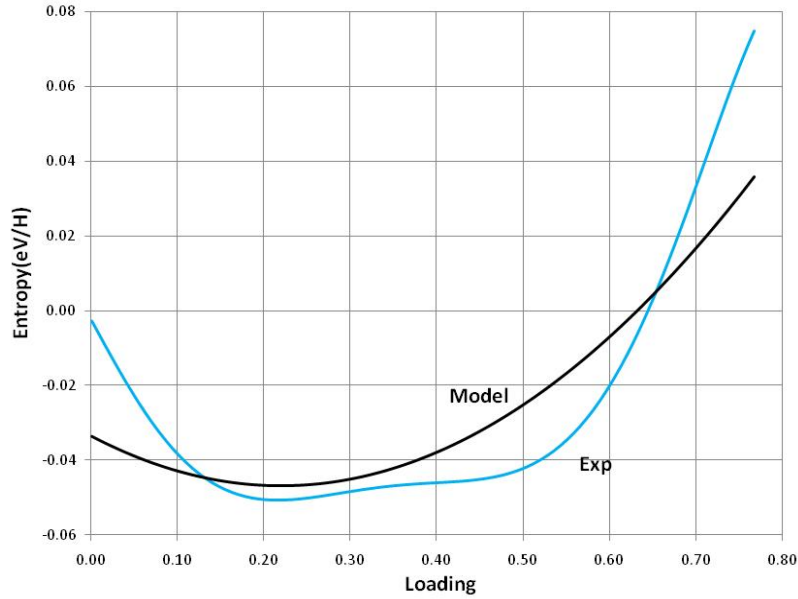


Figure 5. Excess enthalpy at 571 K; model (black) ; experiment [11] (blue).

where, $\epsilon_{\delta}^0, \epsilon_{\delta}^1, \epsilon_{\delta}^2, \epsilon_{\delta}^0, \epsilon_{\delta}^1, \epsilon_{\delta}^2$ are fitting parameters that are determined based on a global fit to experimental P–C–T, and enthalpy and entropy data and T_c is set to the critical temperature for convenience.

5. Excess Enthalpy, Excess Entropy

In a straightforward manner, we can calculate excess entropy and excess enthalpy [9] from the pressure derived analytically from Eqs. (3) and (4). The results are

$$H = -T^2 \left(\frac{\partial(G/T)}{\partial T} \right)_{P,n}. \quad (9)$$

In Eq. (9), H is enthalpy and G is the Gibbs energy. From this, we can derive excess \overline{H}_H^E enthalpy, via [10]

$$\Delta \overline{G}_H = \overline{G}_H^{\text{Ideal}} + \Delta \overline{G}_H^{\text{Excess}} \quad (10)$$

and

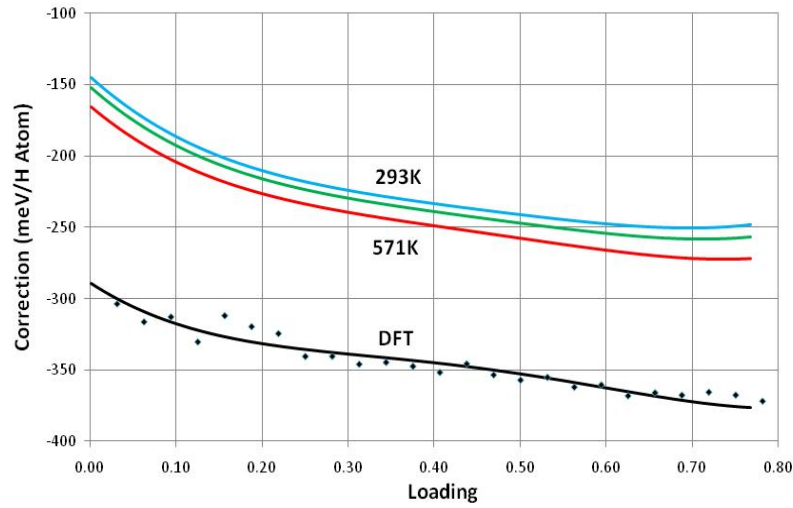


Figure 6. DFT interaction energy (*black*); corrected interaction energy (in color, showing temperature dependence).

$$\overline{G}_H^{Ideal} = RT \ln \frac{\theta}{1 - \theta} \quad (11)$$

as

$$\overline{H}_H^E = \Delta \overline{H}_H^E - \Delta \overline{H}_H^0, \quad (12)$$

where $\Delta \overline{H}_H^0$ is the enthalpy at zero loading [11] and we have converted Eq. (9) to the usual molar format.

Excess entropy may be derived similarly [9]. Thus,

$$-S = \left(\frac{\partial G}{\partial T} \right)_{P,n} \quad (13)$$

and, similar to Eq. (12)

$$\overline{S}_H^E = \Delta \overline{S}_H^E - \Delta \overline{S}_H^0. \quad (14)$$

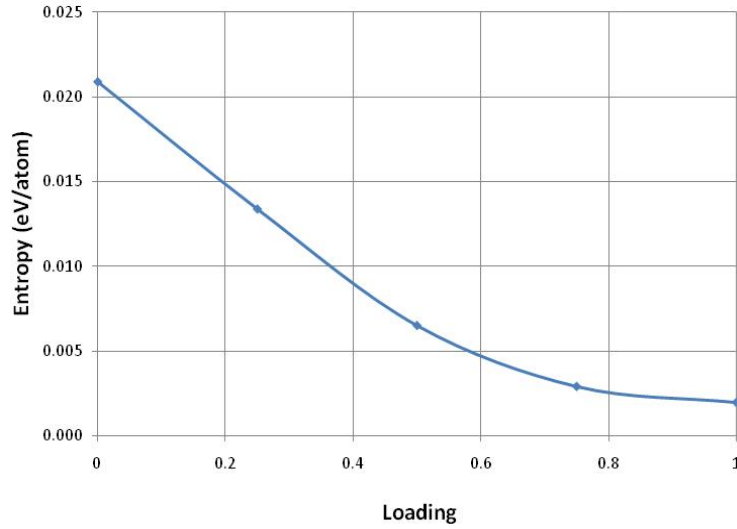


Figure 7. Model electronic entropy at 571 K.

Now, we interpret the excess entropy as telling us something about the incremental number of accessible proton microstates in metal hydride [9]. To see this, we apply the fundamental definition of entropy to write:

$$\bar{S}_H^E = \kappa_B \ln \Omega^E, \quad (15)$$

where Ω^E may now be thought of as the incremental number of accessible microstates from the gas phase (initial) to the absorbed state (final), i.e.,

$$\Omega^E = \frac{\Omega^{\text{final}}}{\Omega^{\text{initial}}}. \quad (16)$$

For the experimental data we used in this work [11], we can depict Eq. (16) in Fig. 2. From this point of view, we see that the experimental excess entropy is consistent with a reduction of about half the number of accessible microstates in the miscibility gap. As the loading increases above the miscibility gap, the number of accessible microstates also increases.

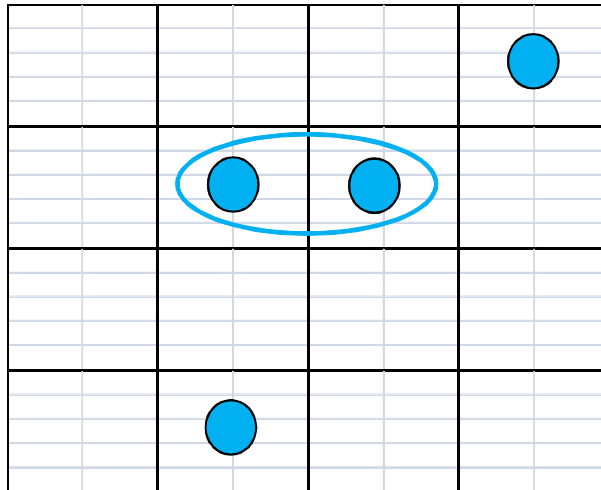


Figure 8. Hydrogen quasi-molecule based on a proposed attractive interaction between neighboring interstitial hydrogen in PdH at low H concentration.

6. Results

Applying these corrections to the basic model, Eqs. (1), (7) and (8), we get a marked improved in our match to experiment; Fig. 3 shows the improved PCT isotherms. From Eqs. (12) and (15), we may derive excess enthalpy and entropy analytically; the results are shown in Fig. 4.

The results for excess entropy and enthalpy compare well with experiment. The corrected interaction energy in this model is shown in the colored curves of Fig. 6; we see that the correction is roughly 100 meV, with a weak dependence on the temperature. DFT results for specific configurations are shown as dots, with the average shown as a black line.

A spread in the energies associated with the different configurations would by itself produce a temperature dependence in the weighted average that would produce corrections that would increase with temperature. The corrections obtained by matching this model to data decrease in temperature. In the Appendix we discuss a different model that assumes possible pairing between interstitial hydrogen; in that model the corrected energy increases with temperature.

7. Electronic Contributions to Entropy

Kuji [11] has proposed that electronic contributions to entropy might dominate at high loading. We have attempted to evaluate this position in a couple of ways. First, we modeled the electronic contributions to entropy as a correction to the proton chemical potential. Thus, we formulated the problem using the partition function

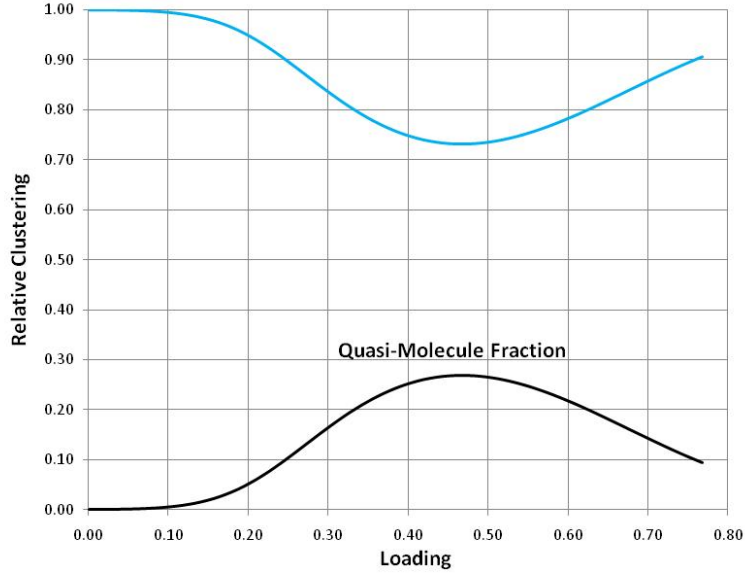


Figure 9. Quasi-molecule fraction from optimization of the model.

$$Z_H(\tau, \mu) = \sum_k \sum_{\sigma} \left(\sum_{n_{nc}=0}^{N_o} \sum_{k=0}^{\frac{N_o-n_{nc}}{\alpha+\gamma}} \sum_{n_T=0}^{N_t} \sum_{ASN} e^{\frac{(n_{nc}+n_t+k\gamma)\mu-\epsilon_h(n)}{\kappa_B T}} z_o^{n_{nc}} z_t^{n_t} z_c^{k\gamma} z_{e,t}^{n_t} z_{e,c}^{k\gamma} \right) g_k^{\sigma} e^{\frac{\epsilon_{\sigma}(n,k)-\mu_F(n,\tau)}{\kappa_B T}}. \quad (17)$$

In this formulation, g_k^{σ} is the degeneracy of the k^{th} electronic band with spin α . After evaluating the electronic contribution obtained from this model, we found that it was negligible [9].

A second approach is to consider the electronic and proton contributions as approximately independent and write [13]

$$\bar{\mu}_H^E(\theta, T) = \bar{\mu}_{H^+}^E(\theta, T) + \bar{\mu}_F^E(\theta, T), \quad (18)$$

where the proton contribution, $\bar{\mu}_F^E(\theta, T)$, was previously modeled above. For the electronic portion, we use the basic theoretical result [14], and calculate it from first principles using DFT [9]:

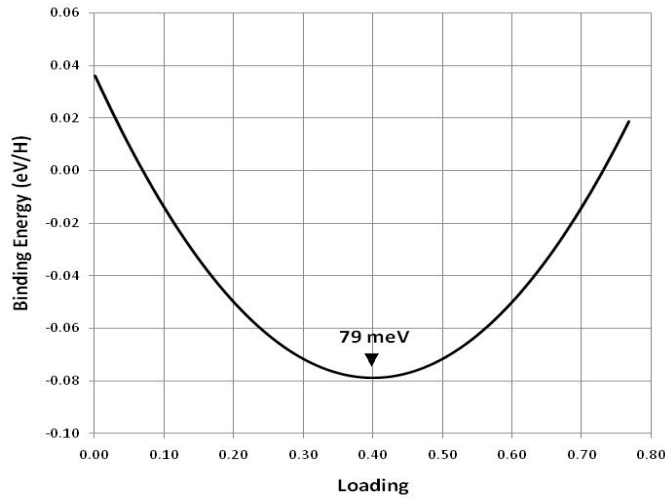


Figure 10. Quasi-molecule binding energy at 571 K.

$$S_E(x) = - \int g(\epsilon) d\epsilon \left[f_{FD} \ln f_{FD} + (1 - f_{FD}) \ln(1 - f_{FD}) \right], \quad (19)$$

where f_{FD} is the Fermi Dirac function, $g(\epsilon)$ is the density of states, and

$$x(\tau) = \frac{\mu - \epsilon_l(n)}{\tau}. \quad (20)$$

The results are shown in Fig. 7; this is inconsistent with Kuji [11], but consistent with Wallace [14].

8. Discussion

In the work outlined here, we developed a physics-based model that describes the hydrogen absorption into palladium lattice. Using a statistical mechanics and the grand partition function formalism, we are able to obtain a theoretical expression for basic properties of hydrogen absorption in equilibrium.

In recent years density functional theory has become much more widely used for applied problems in materials science in general, and for hydrogen in metals in particular. We have taken advantage of the availability of Quantum Espresso, and of the increasing power of modern computers, to use DFT to study hydrogen absorption in palladium.

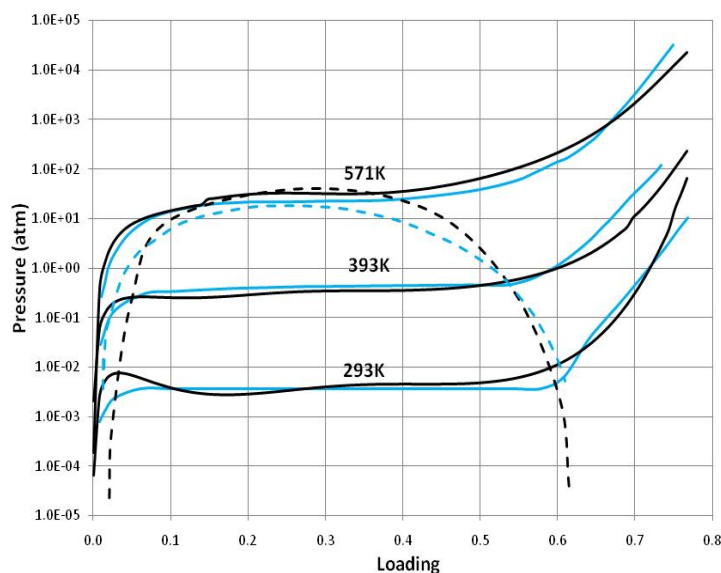


Figure 11. P–C–T Isotherms; model (*black*); experiment [12] (*blue*).

We know that modern DFT calculations are very good; however, the independent particle approximation has limitations as an approximation, and we would not expect the DFT energies to match experimental ones. Since PdH is one of the best studied metal hydrides, we have thermodynamic data that allows us to compare the DFT results with experiment (since there are no experimental results for the interaction energy). Based on the initial comparison illustrated in Fig. 1, we know that there are errors in the DFT results, and we were hoping to quantify them. As the research progressed, it became apparent that we could do more than just quantify DFT errors, we found that we could correct them in a meaningful way, leading to a corrected energy that seems to give results globally that are close to experiment. This is interesting, and results in a new physics-based model that can be used in future work.

This kind of model is in some sense the simplest possible that might be relevant to PdH; hydrogen occupation of interstitial sites is essentially random with a thermal weighting associated with the average energy. In this model the occurrence of the miscibility gap is due to the dependence of the underlying chemical potential as a function of loading, following the argument of Lacher. However, we know that segregation occurs in NiH in the miscibility gap, which indicates that hydrogen–hydrogen attraction occurs. Since NiH and PdH are closely related, it would be natural to consider the possibility of a hydrogen–hydrogen attraction in PdH. For example, quasi-molecule formation due to singlet electronic state occupation which is not included in the DFT calculation could provide a physical basis for such an effect. If we interpret the excess entropy in the miscibility gap in terms of a reduction in the number of accessible microstates as illustrated in Fig. 2, we might conclude that ordering of some kind occurs; a model with pairing would

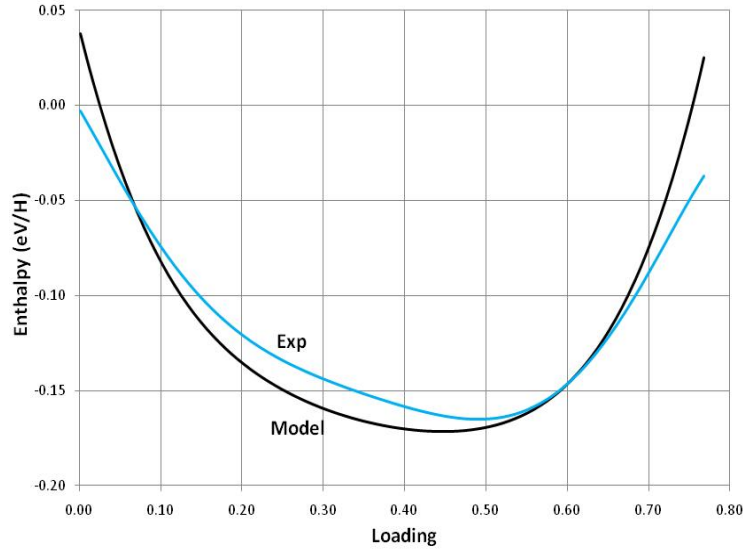


Figure 12. Excess enthalpy at 571 K; model (*black*); experiment [11] (*blue*).

be expected to show such a reduction in excess entropy naturally. In the Appendix we discuss a model for PdH which works in this way.

Appendix A.

As part of our research on PdH work, we investigated a model whereby a weak binding between neighboring absorbed protons [9] through the sharing of a localized electron pair to form a quasi-molecule as shown in Fig. 8. Such a binding is might occur due to electronic occupation of a quasi-molecule singlet state, or perhaps due to simple polarization effects; occupation of quasi-molecule states constitutes an ordering that is consistent with the excess entropy in the miscibility gap. We assume that the binding energy has a dependence on loading and temperature similar to the interaction energy discussed in the main text; the form of the binding is taken to be

$$E_B^c(\theta) \rightarrow \epsilon_c^c + \delta_c^c(T - T_c) + \left[\epsilon_c^1 + \delta_c^1(T - T_c) \right] \theta + \left[\epsilon_c^2 + \delta_c^2(T - T_c) \right] \theta^2 + O(\theta^3). \quad (\text{A.1})$$

In Eq. (A.1), ϵ_c^0 , ϵ_c^1 , ϵ_c^2 , δ_c^0 , δ_c^1 , and δ_c^2 are fitting parameters that are determined based on a global fit to experimental P–C–T, and enthalpy and entropy data.

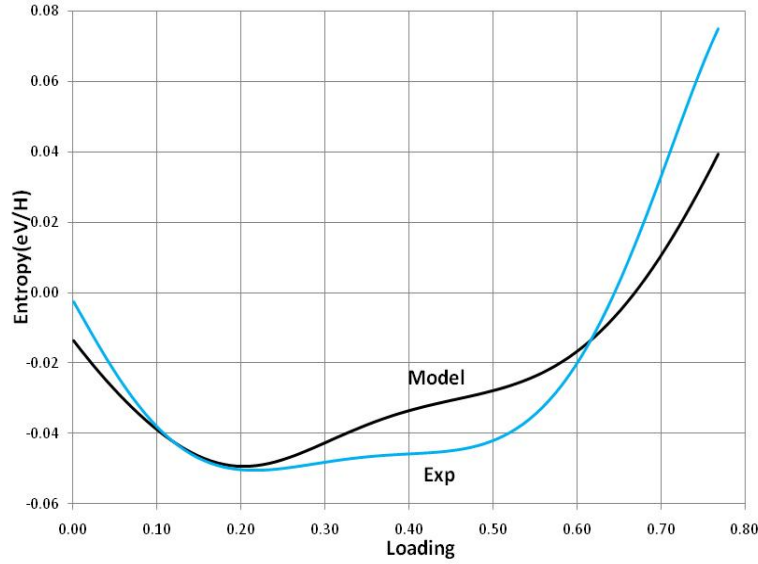


Figure 13. Excess entropy at 571 K; model (black); experiment [11] (blue).

If one postulates the existence of a quasi-molecule at low concentration, then there are issues about what occurs at high concentration (where additional hydrogen occupation of nearby states occurs). We have investigated two different models, the most interesting of which is one where we assume that the quasi-molecule is destroyed when additional protons are present in adjacent sites. The resulting exclusion model is then [9]

$$Z_H(\tau\mu) = \sum_{n_{nc}=0}^{N_0} \sum_{k=0}^{\frac{N_0-n_{nc}}{\alpha+\gamma}} \sum_{n_t=0}^{N_t} \sum_{ASN} e^{\frac{(n_{nc}+n_t+k\gamma)\mu-\epsilon_H}{\tau}} z_0^{n_{nc}} z_t^{n_t} z_c^{k\gamma} z_{e,0}^{n_{nc}} z_{e,t}^{n_t} z_{e,c}^{k\gamma}, \quad (\text{A.2})$$

where γ is a clustering factor, α is a nearest-neighbor exclusion factor, and we have added electronic contribution terms to the partition function – for example $z_{e,0}^{n_{nc}}$ is the electronic contribution to the partition function of an electron ‘associated’ with a non-clustered proton [9].

The model we posit in Eq. (A.2) predicts a quasi-molecule population given by the following isotherm [9].

$$\frac{\varphi^{\frac{1}{\gamma}} \theta_c^{\frac{1}{\gamma}} (1 - \theta_{nc})^{\frac{\gamma\varphi-1}{\gamma\varphi}}}{\theta_{nc} (1 - \theta_{nc} - \varphi\theta_c)^{\frac{\varphi-1}{\gamma\varphi}}} = \frac{1}{2} \left(1 - e^{-\frac{\epsilon_{ov}}{k_B T}} \right)^3 e^{-\frac{E_B^C(n)}{k_B T}}, \quad (\text{A.3})$$

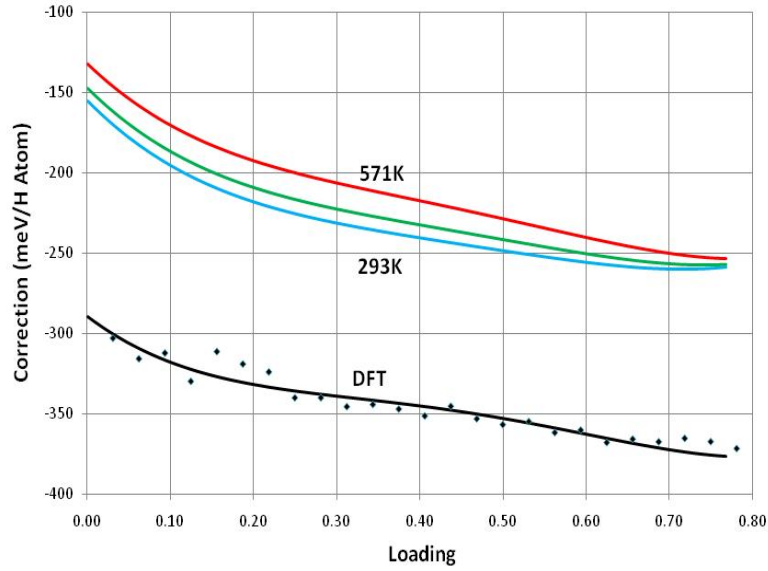


Figure 14. Interaction energy corrections for the pairing model.

where

$$\varphi = \frac{\alpha + \gamma}{\gamma}. \quad (\text{A.4})$$

Equation (A.3) predicts significant fractional quasi-molecule population in the miscibility gap, after optimization of the model against experimental P–C–T data, excess entropy, and excess enthalpy. Results at 571 K are shown in Fig. 9.

The model predicts a quasi-molecule population that peaks around the middle of the miscibility gap. It may be that with a more sophisticated version of this kind of model that we might think of the two phases in the miscibility gap as random and ordered, where the ordering is due to quasi-molecule formation. The binding energy for the quasi-molecule is shown in Fig. 10. From this result, we see that the model binding energy is relatively weak (79 meV), as expected. The binding profile has a minimum near the middle of the miscibility gap. We also show the results based on a global, simultaneous fit to P–C–T isotherms at three temperatures (Fig. 11), and excess enthalpy (Fig. 12) and excess entropy (Fig. 13).

We can obtain somewhat better agreement between model and data with this more complicated model, although this does not adequately bring out how the model accomplishes this. In the simpler model described in the main text, the excess entropy is matched by decreasing the interaction energy with temperature; in this model the excess entropy

is matched in the miscibility gap by reducing the number of accessible microstates, and the interaction energy increases with temperature (Fig. 14).

Note that the apparent divergence between model and experiment in the high loading regime in the plots in this paper is due in part to the weights used in the least squares fits. These results are in a sense preliminary due to the way the fits were obtained.

References

- [1] R. Fowler, *Proc. Camb. Phil. Soc.* **32** ((1936) 144.
- [2] J. Lacher, *Proc. R. Soc. Lond. A* **161** (1937) 525.
- [3] O. Christensen, P. Stoltze and W. Jacobsen, *Norskov J. Phys. Rev. B* **41** (1990) 12413.
- [4] E. Salomons, *J. Phys.: Cond. Mat.* **2** (1990) 845.
- [5] R. Wolf et al., *Phys. Rev. B* **48** (1993) 12415.
- [6] Silbey, Alberty and Bawendi, *Physical Chemistry* (Wiley, New York).
- [7] R. Martin, *Electronic Structure* (Cambridge University Press, Cambridge, 2004).
- [8] F. Stern and S. Sarma, *Phys. Rev. B* (1984) 840.
- [9] P. Orondo, MIT Ph.D. Thesis, 2012.
- [10] G. Boureau, O. Kleppa and P. Dantzer, *J. Chem. Phys.* **64** (1976) 5247.
- [11] T. Kuji, W. Oates, B. Bowerman and T. Flanagan, *J. Phys. F: Met. Phys.* **13** (1983) 1785.
- [12] E. Wicke and F. Brodowsky (*Hydrogen in Metals II.*, 1978).
- [13] W. Oates and A. Stoneham, *J. Phys. F: Met. Phys.* **13** (1983) 2427.
- [14] D. Wallace, *Phys. Rev. B* **46** (1992) 5242.



Research Article

Temperature Dependence of Excess Power in Two-laser Experiments

Peter L. Hagelstein *

Research Laboratory of Electronics, MIT, Cambridge, MA 02139, USA

Dennis Letts [†]

12015 Ladrido Ln, Austin, TX 78727, USA

Abstract

Data published previously on the two-laser experiment shows that the excess heat depends on temperature, and is mostly zero in the absence of a magnetic field. A new experiment shows higher excess power at higher temperature. We augment our previous empirical model with temperature dependence. A picture for the temperature dependence is described in terms of the elimination of ^4He which blocks active sites when the excess power is high.

© 2014 ISCMNS. All rights reserved. ISSN 2227-3123

Keywords: Active site blocking by helium, Letts 2-laser experiment, Temperature dependence of excess heat

1. Introduction

Excess power in the Fleischmann–Pons experiment [1,2] has been studied around the world following the initial announcement of the effect in 1989. Excess heat was observed to depend on the cathode loading [3], and also on the maximum loading during the cathode history [4]. Fleischmann and Pons described a positive feedback effect in which the excess power was increased at the end of a heater calibration pulse [5], suggesting that the effect was dependent on the cell temperature. Subsequently measurements from different groups showed that in some experiments the excess power increased with temperature [6–8].

As a separate discussion that has taken place over many years, people have been interested in how excess heat is triggered in these experiments. In early experiments, excess heat bursts seemed to occur randomly for the most part. Excess heat events at SRI seemed to be triggered by current ramps; subsequently more systematic studies yielded a linear dependence of excess power on current density above a threshold. Excess power was seen to be correlated with

*E-mail: plh@mit.edu

[†]E-mail: lettslab@sbcglobal.net

the surface deuterium current flux [9], and later on many experiments have sought to use this mechanism to stimulate excess power. Electrical current has by now been seen to stimulate excess power [10,11].

Letts and Cravens noticed that excess power could be stimulated using a weak laser incident on the cathode surface under conditions where the cathode was below threshold for excess power production [12]. Subsequent experimental work confirmed the existence of the effect. Some years later Letts and Cravens showed that excess power could be stimulated by two lasers [13]. A multi-year campaign to study the effect was carried out by Letts, which found a set of three “sweet spots” in frequency difference where excess power was maximized [14]. Two of these resonances were found to correspond to the Γ -point and L-point of the PdD optical phonon modes, which had been predicted to be favored since the compressional mode group velocity is zero. As yet it has not been clarified what the origin of the third peaks is. Conjectures have been made that it is due to H contamination (which would produce an impurity-related L-point close to the observed peak), or perhaps D in the codeposited Au layer. A detailed analysis of the data set was published [14,15].

2. Possible Temperature Dependence

Some of the two-laser experiments carried out as part of this study were done at different temperatures. If excess power in the two-laser experiment is sensitive to temperature, then perhaps we might improve the analysis of the data by taking this into account. For example, we remarked on a data point at 521 mW that was sufficiently high that it did not fit on the plot [14]; the corresponding experiment was done at a higher temperature than most of the others.

We begin by working with the data set discussed previously in [14], and we now fit to an excess power model of the form

$$P_{xs} = \exp\left(-\frac{\Delta E}{k_B T}\right) \sum_j A_j \frac{\gamma_j^2}{(f - f_j)^2 + \gamma_j^2}.$$

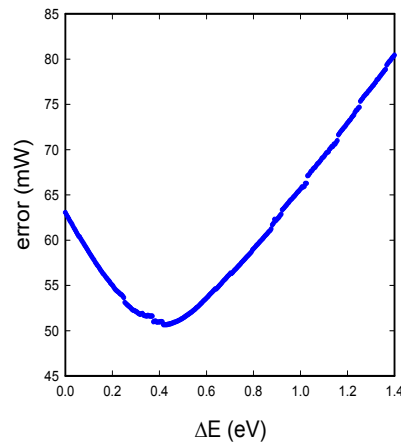


Figure 1. Error in the fit for excess power in mW as a function of ΔE in eV.

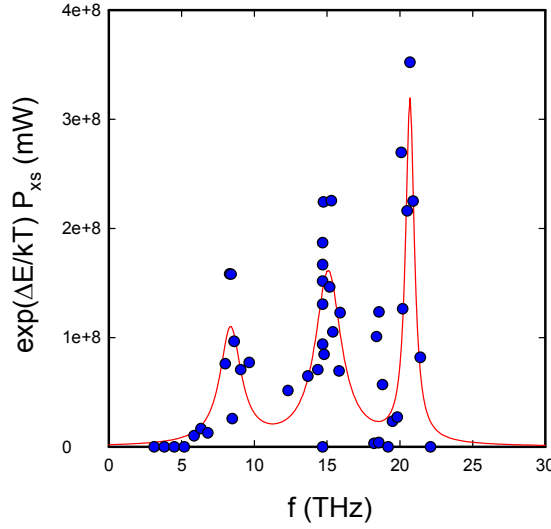


Figure 2. Scaled spectrum compared with empirical model for $\Delta E = 0.42$ eV.

By least-squares fitting to the data we find that the error is reduced when ΔE is in the vicinity of 0.42 eV as shown in Fig. 1.

The scaled spectrum that results is shown in Fig. 2. Note that now all of the data points fit on the graph. A few of the data points have been corrected following a re-examination of the data set. The center frequencies in this model are 8.4, 15.1, and 20.7 THz, which are close to what we found earlier.

In his study of Fleischmann–Pons excess power as a function of temperature, Storms parameterized the results according to [7]

$$P_{xs} = P_0 e^{-\Delta E / K_B T}$$

consistent with $\Delta E = 670$ meV. Swartz reported a similar value consistent with 630 meV [8]. In earlier work ΔE was interpreted as the barrier energy for helium diffusion, in a picture where helium build up plugs active sites and must be removed. This is discussed further in Section 8. Given the relatively shallow dependence of ΔE around the minimum for this data set, such values used in the above fitting model would not lead to a substantial degradation of the fit.

3. Possible Magnetic Field Dependence

Letts has found that excess power tends to work better when a magnetic field is present generally in his experiments. In looking through the data set associated with the spectrum, the majority of the associated experiments included a magnetic field; however, some were done without a magnetic field. In general we might include the magnetic field dependence in our model through

$$P_{xs} = F(B) \exp\left(-\frac{\Delta E}{k_B T}\right) \sum_j A_j \frac{\gamma_j^2}{(f - f_j)^2 + \gamma_j^2}.$$

Now, in the experiments under discussion the magnetic field strength was always the same when present. Consequently, we might make use of a reduced function of the form

$$F(B) = \begin{cases} 0 & \text{no magnetic field,} \\ 1 & \text{magnetic field.} \end{cases}$$

Letts has conjectured that the excess power should be linear in the magnetic field. However, given that excess power is known to occur with no applied magnetic field, probably a better general fit might be

$$F(B) = 1 + \frac{B}{B_0}$$

if Letts is correct. It will take a dedicated set of experiments to sort this out.

If we eliminate data points with no magnetic field present, the optimum ΔE is again 0.42 eV, and the resulting spectrum is nearly identical (since these points mostly gave zero excess power at the same difference frequency points as existing points). The frequencies of the resonances in this case are 8.3, 15.3 and 20.7 THz.

4. A New Test for Temperature Dependence

In more recent work, Letts (in this case stimulated by Cravens) carried out a two-laser experiment (669u,v) in which temperature dependence was explored. The cathode was first stimulated with two lasers at a difference frequency of 21.0 THz, which occurred at minute 58 while the electrolyte was at 62.0°C. The cathode responded with about 220 mW of excess power that can be seen drifting upward slowly. The lasers were turned off at minute 948, following which the excess power drifted down over the course of about 8 h. The heater power was increased which raised the cell

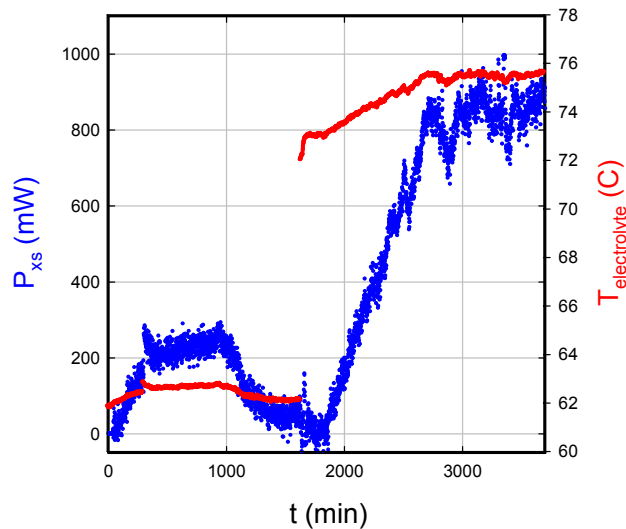


Figure 3. Excess power for experiment 669u,v in mW (blue); electrolyte temperature in °C (red).

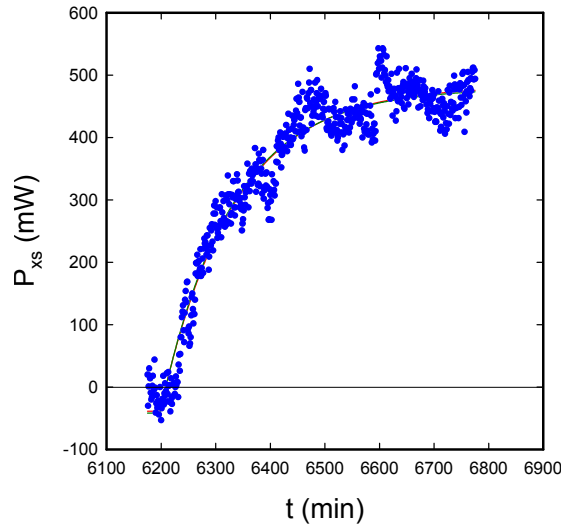


Figure 4. Excess power for experiment 662a (blue); analytic models (red line, green line).

temperature to 72.05°C at minute 1633. The lasers were turned on again at minute 1849, with a difference frequency of 21.6 THz, which stimulated a second excess power event. The excess power produced in this case was higher, around 840 mW, as can be seen in Fig. 3.

If the difference in excess power is attributed in this experiment only to the different initial temperature as

$$P_{xs} = F(B) \exp\left(-\frac{\Delta E}{k_B T}\right).$$

then the associated value for ΔE is 1.33 eV. If we repeat this calculation based on the electrolyte temperature at the time of the excess heat (which includes the positive feedback effect), then we get 1.27 eV. These values are much higher than we found in the discussion above, and motivates us to go back and reconsider the data set.

5. Examination of a Single Set of Data

When we analyzed the data set previously, the approach that we used was to fit the data to a thermal relaxation model, which was useful to get systematic excess power estimates along with error bars. This procedure is discussed in [14,15].

However, given the temperature dependence of experiment 669u,v discussed above, Letts was motivated to go back through the data once again to see whether this temperature dependence had been overlooked somehow. In order to understand what Letts found, we need to consider an example. Perhaps most illuminating is the case of an experiment labeled 662a, which gave the highest excess power (521 mW) as mentioned in [14]. The analysis of that paper can be summarized as in Fig. 4. We see the excess power increasing following laser stimulation with a beat frequency of 14.75 THz, and the excess power follows the two analytic model results reasonably well. The value 521 mW in this case is the asymptote for the simpler analytic model. Similar data sets following laser stimulation were provided by Letts for analysis at MIT at the time Refs. [14,15] were written.

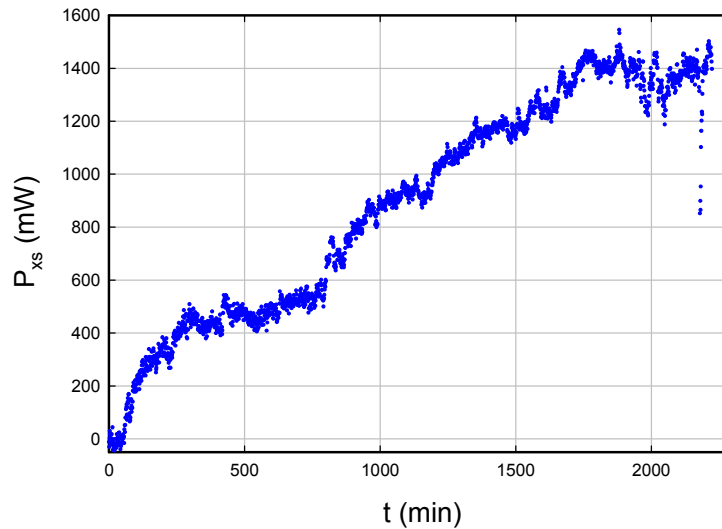


Figure 5. Excess power for experiment 662a (blue) for longer time.

However, in this case the experiment was allowed to continue running, so that it is possible to see how close the experiment came to the predicted asymptote. The results are shown in Fig. 5. We see that the excess power subsequently started to rise again.

So, should we use the 521 mW number as was done previously, and which could reasonably be argued to represent the initial level of excess power; or should we use a higher number in the vicinity of 1400 mW? Since Letts was comparing against a predictor based on the ΔE value from 669u,v discussed above, he was expecting the excess power for the elevated temperature conditions of this experiment to be a good bit greater than 521 mW. In fact, the excess power in this experiment ended up going to a level relatively close to what might be expected based on $\Delta E = 1.33$ eV.

The conjecture in this case was that rather than looking at the initial excess power as was done before, perhaps the better thing to do in response to 669u,v would be to make an estimate of the maximum power that the cell seems to equilibrate to.

6. Max Equilibrium Power Spectrum

These arguments led to the construction of a different kind of spectrum from the data. In this case, the maximum equilibrium excess power is reported as discussed above; however, only data sets with magnets present are now included, not all of the data sets used previously were judged suitable, and results from 669u,v are now included. The excess power data points in this case are shown in Fig. 6.

Since the two experiments with very high excess power correspond to runs done at elevated temperature, let us first consider the fitting of the spectrum in the absence of these points. Results are shown in Fig. 7. The minimum error occurs for $\Delta E = 0.54$ eV, and we see that the error in this case is much lower than what we found previously. The spectrum that results is shown in Fig. 8. The peaks in this fit are centered at 8.4, 15.2, and 20.8 THz. This result is consistent given the shallowness of the error curve as a function of ΔE with the earlier ΔE results of Storms, and of

Swartz.

As expected, when the two highest power points are included in the spectrum, the fit becomes dominated by their contribution. This is illustrated in Fig. 9, where the minimum error occurs for $\Delta E = 1.0$ eV. Given this situation there are a number of obvious candidate interpretations. One interpretation might be that the barrier associated with the two-laser experiment is in the range of 0.85–1.05 eV, and we should think of it as being higher than the barrier found in the experiments of Storms and of Swartz.

Another interpretation might be that for the majority of the two-laser experiments the barrier is around 0.6 eV, so that we have reasonable consistency with the experiments of Storms and of Swartz; while the two outliers at higher power do so because some additional and different sites are involved in the excess power production. One could imagine that the excess power in Fig. 5 stays for a while at the lower power value (around 500 mW) perhaps consistent with a lower ΔE number, then increases later on due to extending the reactions to a new batch of sites with a higher associated ΔE .

Finally, there is yet another point of view. Not all experiments show a dependence on the operating temperature. For example, excess heat at SRI in the 1990s seemed not to show any particular sensitivity to temperature. Perhaps it is that the temperature sensitivity shows up when the excess power is “high” relative to the experiment under study (suppose all the active sites available are plugged up with ^4He , so that the temperature dependence comes about due to barriers associated with getting the helium out); and there is little temperature sensitivity when the excess power is “low” (suppose that there are many active sites available, so that scrubbing out the helium is not at issue). Certainly this data set would be consistent with such a picture.

7. Mechanism Issues and Vacancies

Over the years much effort has been put into the development of theoretical models for excess heat production. At present there is no consensus within the field as to what reaction or mechanism is responsible. Outside of the field,

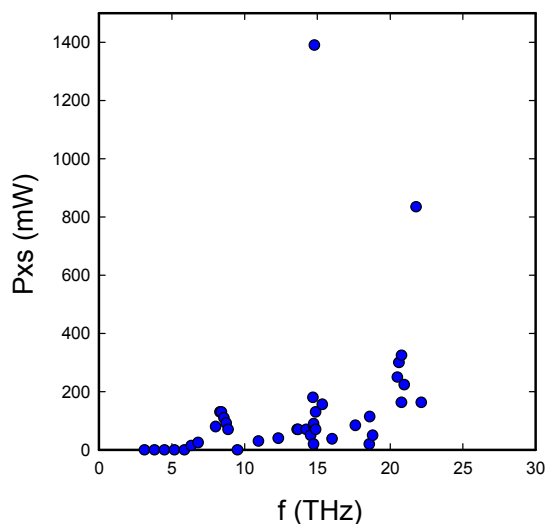


Figure 6. Spectrum of maximum equilibrium excess power as a function of frequency (*blue*).

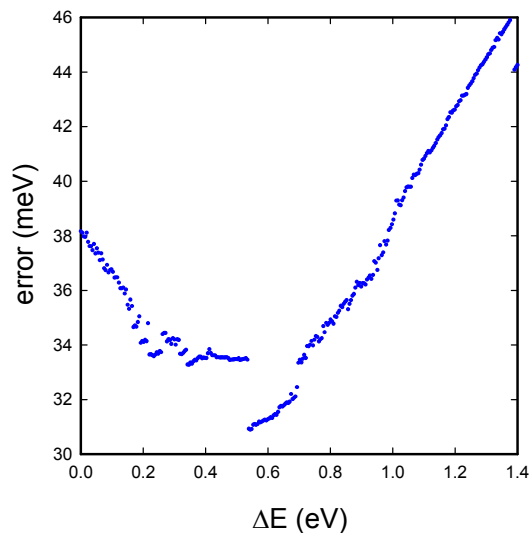


Figure 7. Error in the fit for excess power in mW as a function of ΔE in eV for the spectrum of Fig. 6 without the two highest points.

the scientific community generally still regards excess heat Fleischmann–Pons experiments to be impossible, with all positive results attributable to experimental error. Those in the field at this point are sure it works, and that new physics is emerging in the associated studies.

From our perspective, the issue of how it works can be divided into two sets of issues [16]: conventional issues (electrochemical, materials science, applied physics, and so forth) that relate to loading and how deuterium behaves in the cathode; and unconventional issues that relate to the microscopic reaction mechanism. If we adopt the point of view generally that two deuterons react to make ^4He in connection with the new unconventional issues (consistent with theoretical models that we have pursued), then many experimental issues become purely conventional. This is the view we take in what follows.

For example, in order for two deuterons to interact in the first place, they probably need to be physically close to one another. Since the electron density in bulk PdD is too high to support D_2 formation, our focus has been on the lower electron density region available in the vicinity of a host Pd vacancy [17]. The vacancy formation energy in bulk Pd is around 1 eV, which one might think could be related to the ΔE value associated with the excess heat in experiment 669u,v, except that atomic self-diffusion is sufficiently slow near room temperature that it would take a great many years for thermal equilibrium to be established.

When Pd is loaded with hydrogen or deuterium, the vacancies become stabilized more with each additional interstitial until at a loading near 0.95 the vacancies become thermodynamically preferred. This could account for the requirement observed at SRI that the maximum cathode D/Pd loading over the course of the loading history must reach about 0.95 for excess heat to be observed [4]. Even when stabilized, the diffusion rate remains very slow near room temperature; so we contend that the most plausible mechanism for the production of vacancies in these experiments is inadvertent codeposition at high surface loading [16].

8. Active Sites and Helium

From this perspective, the active sites are vacancies, and molecular D_2 formation is expected near room temperature at sufficiently high loading that the other O-sites around the vacancy are occupied (which we suspect occurs above a loading around 0.84). In the two-laser experiment there is codeposition of Au at substantial current density, and it may be that vacancies are formed at high surface deuterium chemical potential similar to Pd and Ni in the case of Au close to PdD. Density functional calculations support the conjecture that molecular D_2 formation occurs in an Au vacancy similar to the situation in a Pd vacancy [18].

If this picture is basically sound, then the active sites of the system are the vacancies, which we expect to be created in the course of the experiment (since Au is codeposited at high current density). According to the unconventional reaction mechanism that we have focused on, the reaction energy is fractionated and transferred to the optical phonon modes prior to thermalization [14,16]. If so, then the ^4He produced remains roughly in place where the D_2 molecule had been previously (since the local interaction of the ^4He is different than molecular D_2 , we would expect some relaxation of the equilibrium position to lower electron density). The ^4He produced will eventually “plug up” the active sites [16].

If there were no way to remove the ^4He , we might imagine that after some amount of energy is produced that all active sites would end up blocked. We can see from Fig. 11 that the production of 10 kJ corresponds to 2.6×10^{15} ^4He atoms, which may be in the vicinity of the number of vacancies present (although we know that sufficient Au is present on the surface to change the color, we do not have an estimate for the associated number of vacancies produced).

To remove ^4He atoms from the active sites, we would expect first that we would have to arrange for it to get out of the vacancy, and then for it to diffuse away from the active sites. In the case of He binding in a single vacancy in Pd, there has been a recent density functional calculation by Zeng et al. [19] which gives a binding energy of about 2.4 eV for a single helium atom, about 1.5 eV for two, and about 0.6 eV for three. In a different calculation by Laakmann et al. [20], the binding energy for a single helium atom in a monovacancy in Au is about 2.3 eV. One would expect

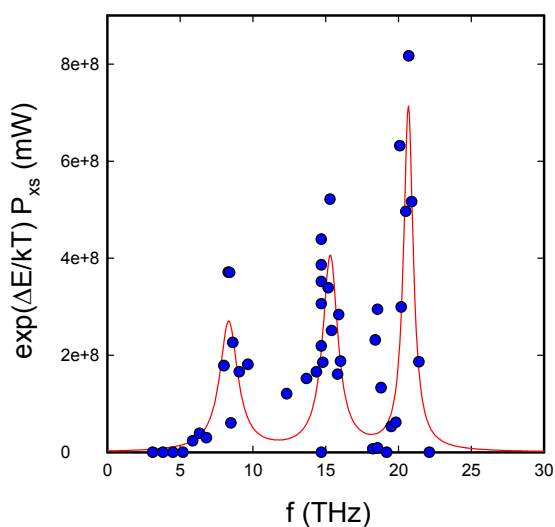


Figure 8. Scaled spectrum without two highest power points compared with empirical model for $\Delta E = 0.54$ eV.

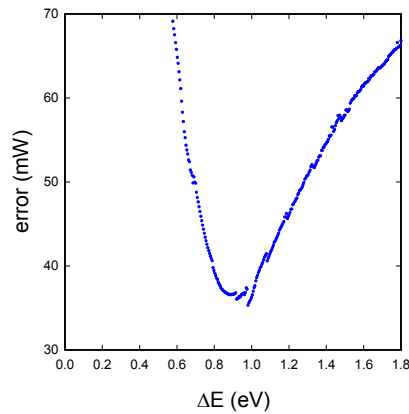


Figure 9. Error in the fit for excess power in mW as a function of ΔE in eV for the spectrum of Fig. 6 including all points.

these binding energies to change in the case of a monovacancy with substantial deuterium occupation.

Next, the helium atoms must diffuse away. Xia et al. (2006) calculated the barrier energy for helium diffusion in Pd as 0.72 eV. A similar value (0.72 eV) is reported by Laakmann et al. [20] for helium migration in Au.

Based on this we might conjecture that the 0.67 eV value for ΔE found by Storms [7], and the 0.63 eV number found by Swartz [8], may be associated with helium diffusion in Pd away from the active sites. The higher ΔE number (near 1.3 eV) associated with experiment 669u,v may be associated with the binding energy of helium in a vacancy (where Pd and Au appear to be similar, and where the presence of deuterium in the other O-sites of the vacancy is conjectured to reduce the binding energy).

Such a picture might be appropriate if the active sites in the two-laser experiment are closer to a nearby surface

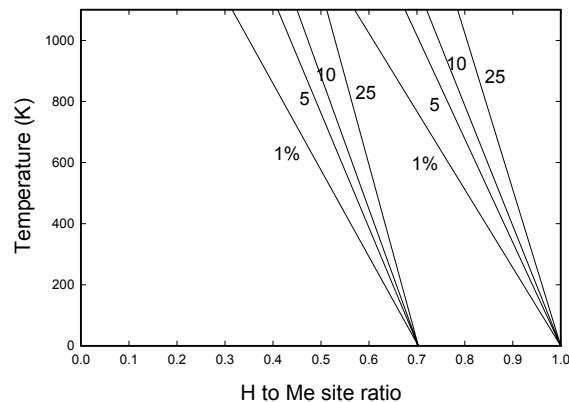


Figure 10. Estimated vacancy fraction in equilibrium in NiH and PdH at different temperatures as a function of loading.

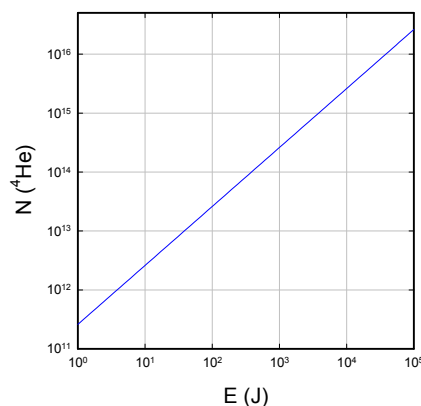


Figure 11. Number of ^4He atoms as a function of the excess energy produced.

(so that diffusion is not limiting), while the active sites in the experiments of Storms and of Swartz involve active sites further away from a nearby surface (so that diffusion is limiting).

Of course we would like to see additional experimentation that focuses on the question of the temperature dependence; and also measurements aimed at determining the number of vacancies, deuterium occupation of the vacancies, and showing that molecular D_2 forms under the conditions proposed. Within the basic picture under discussion we can readily identify helium removal and diffusion mechanisms, and we have the ability to pursue relevant density functional calculations; however, at some point we are going to need additional experimental results to have confidence in the proposed picture.

Finally, we note that the excess power in 669u,v is seen to go away (slowly) following beat laser irradiation. This is in contrast to previous experience with the two-laser experiment in which the excess power remains on at the same level when the lasers are turned off.

9. Magnetic Field Dependence

The issue of why excess heat should depend on an externally applied magnetic field deserves some consideration. By now there are several observations of an enhancement of the excess heat with the application of relatively small external magnetic fields, and also a substantial increase in excess heat with the application of a large magnetic field. In addition, excess heat in the two-laser experiment was sensitive to an applied magnetic field with the proper orientation [14].

At issue is why there should be any dependence at all. For example, one would not expect the local $\text{D}_2/^4\text{He}$ problem to be impacted at all by such weak fields. In the phonon theory, nuclear transitions between a molecular D_2 state embedded in the lattice and the stationary final ^4He state is made possible through the fractionation of the large nuclear quantum into a great many low energy phonons [16]. Relatively recently, a new model has been introduced that allows for the computation of physical parameters (such as matrix elements) in connection with the theory [21]. It was noted in the calculation of the \mathbf{a} -matrix element of the deuteron [22] that the selection rules were consistent with the magnetic field orientation effects observed in the two-laser experiment. The idea is that if the deuteron is involved in the fractionation of the large nuclear quantum, then only two out of the three spin states can participate. A magnetic field can lead to an increase in the number of deuterons that have a favorable spin alignment. In the event that fractionation

limits the reaction rate, then the rate is exponential in the number of deuterons with in a favorable spin state. This could account for the extreme sensitivity of excess heat to such weak magnetic fields seen in the experiments.

References

- [1] M. Fleischmann, S. Pons and M. Hawkins, *J. Electroanalytical Chem.* **261** (1989) 301, errata **263** (1990) 187.
- [2] M. Fleischmann, S. Pons, M.W. Anderson, L.J. Li and M. Hawkins, *J. Electroanalytical Chem.* **287** (1990) 293.
- [3] M.C.H. McKubre, S. Crouch-Baker, A.M. Riley, S.I. Smedley and F.L. Tanzella, *Proc. ICCF3* **5** (1993).
- [4] M.C.H. McKubre, Cold fusion (LENR) one perspective on the state of the science, *Proc. ICCF15* **1** (2009) xv–xxvii.
- [5] M. Fleischmann and S. Pons, Calorimetry of the Pd D₂O system: from simplicity via complications to simplicity, *Proc. ICCF3* (1992), pp. 47–66.
- [6] S. Szpak, P. Mosier-Boss, M.H. Miles and M. Fleischmann, Thermal behavior of polarized Pd/D electrodes prepared by codeposition, *Thermochemica Acta* **410** (2004) 101–107.
- [7] E. Storms, Some characteristics of heat production using the cold fusion effect, *Proc. ICCF4* **2** (1993) 4-1.
- [8] M. Swartz, Photo-induced excess heat from laser-irradiated electrically polarized cathodes in D₂O, *Proc. ICCF10* (2003) 213–224.
- [9] M.C.H. McKubre, S. Crouch-Baker, A.K. Hauser, S.I. Smedley, F.L. Tanzella, M. S. Williams and S. Wing, Concerning reproducibility of excess power production, *Proc. ICCF5* (1995) 17–33.
- [10] F. Celani, Who explained that excess heat could be stimulated by axial electrical current in the demonstration shown at ICCF17.
- [11] M. Swartz and P.L. Hagelstein, Demonstration of energy gain from a preloaded ZrO₂–Pd nanostructured CF/LANR quantum electronic device at MIT, *Proc. ICCF17* (in press).
- [12] D. Letts and D. Cravens, Laser stimulation of deuterated palladium: past and present, *Proc. ICCF10* (2003) 159.
- [13] D. Letts and P.L. Hagelstein, Dual laser stimulation and optical phonons in palladium deuteride, in *Low Energy Nuclear Reactions and New Energy Technologies Sourcebook*, Volume 2, J. Marwan and S.B. Krivit (Eds.), Washington, DC, American Chemical Society (2009) p. 81.
- [14] P.L. Hagelstein, D. Letts and D. Cravens, Terahertz difference frequency response of PdD in two-laser experiments, *J. Cond. Mat. Nucl. Sci.* **3** (2010) 59.
- [15] P.L. Hagelstein and D. Letts, Analysis of some experimental data from the two-laser experiment, *J. Cond. Mat. Nucl. Sci.* **3** (2010) 77.
- [16] P.L. Hagelstein, Bird's eye view of phonon models for excess heat in the Fleischmann–Pons experiment, *J. Cond. Mat. Nucl. Sci.* **6** (2012) 169.
- [17] P.L. Hagelstein and I.U. Chaudhary, Arguments for dideuterium near a monovacancy in PdD, *Proc. ICCF15*, Rome, Italy, October 5–9, 2009.
- [18] L. Dechiaro, unpublished.
- [19] C. Zeng, H. Deng, and W. Hu, First-principles approach to the properties of point defects and small helium-vacancy clusters in palladium, *Nuc. Instr. and Methods in Phys. Res. B:* **267** (2009) 3037.
- [20] J. Laakmann, P. Jung and W. Uelhoff, Solubility of helium in gold, *Acta Metall.* **35** (1987) 2063.
- [21] P.L. Hagelstein and I.U. Chaudhary, Including nuclear degrees of freedom in a lattice Hamiltonian, *J. Cond. Mat. Nucl. Sci.* **7** (2012) 35.
- [22] P.L. Hagelstein and I.U. Chaudhary, Coupling between a deuteron and a lattice, *J. Cond. Mat. Nucl. Sci.* **9** (2012) 50.



Research Article

Models for Phonon–nuclear Interactions and Collimated X-ray Emission in the Karabut Experiment

Peter L. Hagelstein *

Research Laboratory of Electronics, Massachusetts Institute of Technology, Cambridge, MA 02139, USA

Irfan U. Chaudhary

Department of Computer Science and Engineering, University of Engineering and Technology, Lahore, Pakistan

Abstract

Excess heat in the Fleischmann–Pons experiment occurs without commensurate energetic nuclear radiation, which motivated us to seek mechanisms capable of fractionating a large quantum, resulting in the lossy spin-boson model. Collimated x-ray emission in the Karabut experiment we interpreted as demonstrating the conversion of vibrational energy to nuclear excitation, as predicted from the lossy spin-boson model; this motivated us to seek physical models that could account for the effect. We found that the coupling strength associated with electron–nuclear and electron–electron coupling was too weak to fractionate keV quanta into 100 MHz vibrations, which motivated us to seek a theory in which nuclear transitions coupled directly to vibrations. These considerations led us to a lattice model with a relativistic description of compound nuclei, in which a strong phonon-nuclear interaction is present. This interaction is normally rotated out with the Foldy–Wouthuysen transformation, but in the presence of strong loss mechanisms this transformation becomes unhelpful. The model that results describes the coupling of vibrational energy to nuclear excitation, but earlier efforts to apply it to the Karabut experiment resulted in inconsistencies. This motivated us to analyze fluctuations due to electron-phonon coupling in metals, which we find here to be a weak effect for Bloch picture phonon exchange, and a somewhat stronger effect with Born–Oppenheimer phonon exchange. As no new physics were found to substantially enhance fractionation, we returned to the basic theory, and carried out a systematic analysis of the three different degrees of freedom that result from simple product approximations for the wavefunction. We find that when there are more virtual phonons than real, a significant enhancement of the coupling strength occurs, corresponding to a new anomalous regime. Conditions on the coupling matrix element and relative state occupation are derived for the anomalous regime, which favors strongly-coupled low energy transitions which constitute a large fraction of all nuclei present. The fractionation power of a sample in the anomalous regime is very much constrained, which allows us to be able to make predictions with the new model. We find that the 30.77 keV transition in ^{93}Nb is likely to be in the anomalous regime in a Nb cathode; that the threshold fractionation energy is too low for excitation of the 30.77 keV transition; but that the threshold fractionation energy is high enough to result in the excitation of the 1565 eV transition in ^{201}Hg , and x-ray emission in the few keV regime consistent with Karabut’s observations.

© 2014 ISCMNS. All rights reserved. ISSN 2227-3123

Keywords: Collimated X-rays, Fractionation, Karabut experiment, Phonon–nuclear coupling, Phonon theory

1. Introduction

We have been interested for years in mechanisms by which a large quantum can be fractionated, and quantum systems that exhibit efficient coherent energy exchange under conditions of fractionation. The initial motivation for this came from the excess heat effect in the Fleischmann–Pons experiment [1–3]; in which a great deal of energy is seen which is thought to have a nuclear origin; where ^4He has been observed correlated with the excess energy [4–7]; but energetic nuclear radiation is not seen in amounts commensurate with the energy produced [8,9]. As this problem is highly nontrivial, probably the place to start is with simple idealized models in which the mechanism can be studied independently of the distractions associated with a real physical system. For example, in the course of our research we focused on the idealized problem of equivalent two-level systems linearly coupled with an oscillator. The two-level systems in such a model stand in for the nuclear transitions, where the transition energy is large; and the oscillator stands in for a condensed matter degree of freedom, such as a highly excited phonon mode, where the characteristic oscillator energy is much smaller.

This simple idealized model is well studied in the literature [10–12], and it is known as the spin–boson model. Without modification the spin–boson model describes coherent energy exchange between the two-level systems and oscillator when appropriate resonance conditions are satisfied. The basic effect in this model is not particularly strong [13,14]. For example, modest rates for coherent energy exchange are predicted under conditions where the large two-level system quantum is exchanged for tens of oscillator quanta; but unfortunately the model seems to run out of steam under conditions of greater fractionation. We were interested in the question of what limited the effect in the spin–boson model. After some investigation, we found that the problem was that destructive interference limited the rate of coherent energy exchange under conditions of fractionation [15,16]. If we think of it in terms of perturbation theory, coherent energy exchange requires indirect coupling between two nearly-resonant states separated by a large number of intermediate off-resonant states. Contributions to the indirect coupling come from all possible pathways between the two nearly resonant states, of which there are many when a large quantum is fractionated. Some of the contributions come with one sign, and some with another, so that in the end there is exquisite cancellation so that the sum is orders of magnitude smaller than the individual contributions.

In the Brillouin–Wigner formalism [17], loss mechanisms are dependent on how far off of resonance a basis state is. Hence, basis states with much more energy than available to the system see slow or negligible decay rates, while basis states with much less energy than available to the system can see increased decay rates [16]. In the event that decay mechanisms are fast, it is possible for loss to cause some of the off-resonant basis states to have much reduced occupation. The absence of the contribution to the indirect coupling spoils the cancellation effect discussed above, and we find that the resulting indirect coupling can be very strong when such loss is added to the spin–boson model [18–21].

Once this mechanism was understood, our attention turned to the problem of finding a physical system which could support the mechanism, and which had something to do with the anomalies seen in connection with Fleischmann–Pons studies [22]. It turns out that many physical systems are consistent with this fractionation mechanism, and there is no difficulty in arguing that most of the anomalies seen in experiment can be predicted to occur in suitably designed experiments. For example, there are known weak couplings between nuclear transitions and lattice vibrations, and under appropriate conditions there is no difficulty in calculating that large quanta can be fractionated. Such models predict coherent processes in which two deuterons make ^4He , with the energy going into vibrations; lattice-induced

*E-mail: plh@mit.edu

nuclear excitation, leading to gamma emission and nuclear disintegration; and lattice-induced nuclear excitation leading to collimated x-ray emission, as seen in the Karabut experiment [23–28]. However, such models are not particularly close to experiment quantitatively. Although anomalies are predicted, the coupling implied in the experiments is orders of magnitude larger than available in the conventional models.

This motivated us to consider unconventional models, which eventually led us to focus on the very strong coupling between vibrations and internal nuclear degrees of freedom present in relativistic models for composite nuclei [29–31]. Normally this strong coupling is eliminated by a generalized Foldy–Wouthuysen transformation, resulting in a dressed picture in which only a very weak residual second-order coupling remains. However, a Foldy–Wouthuysen transformation also eliminates the strong first-order coupling in the spin–boson model [13]. But when loss is present, coherent energy exchange under conditions of fractionation proceeds at a rate determined by the first-order coupling [20]. In a sense, the Foldy–Wouthuysen transformation becomes unhelpful for the lossy spin–boson model, primarily because the transformed loss operator in the rotated picture is large and complicated. In the presence of strong loss, it is simpler not to use the Foldy–Wouthuysen transformation and just analyze the problem in the original unrotated basis.

The resulting phonon–nuclear model is very interesting. As was the case for conventional coupling, this new model predicts coherent energy exchange under conditions of fractionation, which means that pretty much the full array of the anomalies observed in experiment are predicted. To check whether the new theory might have predictive capability, we decided to check against collimated X-ray emission in the Karabut experiment. As remarked upon previously, such a comparison relies on the underlying theory, the interpretation of the experiment, and on the details of the model and model parameters used. Once again we did not obtain consistency between theory and experiment (but things are very much closer than with earlier models before the new relativistic model); a version of this comparison is given below in Section 8. This lack of agreement provided us with motivation in an earlier work [32], and also in this work, to double check issues with the basic theory to see whether something was missing.

The focus of our efforts was on the issue of phonon fluctuations that result from the coupling between vibrations and electrons in a metal. In a sense, coherent energy exchange in the phonon–nuclear model occurs through phonon fluctuations produced as a second-order effect which results from the strong phonon–nuclear coupling (as seen in the

$$\frac{g}{(\Delta n)^2} \frac{d^2}{dz^2}$$

term that appears in the continuum model of Ref. [20]). It seems pretty clear in the model that if there are additional mechanisms capable of producing phonon fluctuations, that these might impact coherent energy exchange in the phonon–nuclear model.

As a result of all of this, we became interested in the development of a model for phonon fluctuations in a metal [32]. This problem is easily stated, but very quickly technical issues arise. The problem that we face at the outset has to do with the basic picture (or rather, two basic pictures) of the coupled system of conduction electrons and phonons in the literature. One basic approach to the problem follows from the Born–Oppenheimer approximation, in which the nuclear motion is assumed slow, so that an adiabatic model can be used for the electrons. In the Born–Oppenheimer picture, there is a static screening effect associated with the conduction electrons (that does not involve phonon exchange), and phonon exchange is responsible for dynamical effects at second order and higher. The other basic approach involves the Bloch picture, in which conduction electrons respond to the dynamical motion of the metal ions through phonon exchange. Electron screening in the Bloch picture then comes about as a result of phonon exchange. Over the years there has been occasional discussions about these two pictures [33,34]; nearly all calculations are done in the Bloch picture (because it is much simpler), and it is generally agreed that basic results for screening and phonon decay are the same in the two pictures [35].

The development of a fluctuation model in the Bloch picture is conceptually simple, since we have available explicit expressions for the relevant coupling matrix elements [35,36], and we know how to evaluate the parameters that describe

fluctuations [32]. Fluctuations in the Bloch picture are very strong (we will see in Section 6 that fluctuations due to phonon-nuclear coupling can be stronger still). This can be attributed to how phonon dynamics in the Bloch model come about in the first place. Coulomb repulsion at long wavelength between the ions would result in vibrations at the ion plasma frequency for longitudinal modes, but electron screening in the resonant sector very nearly cancels out this contribution and reduces the vibrational frequency to much lower values. Off of resonance the screening of the electrons is reduced, the lattice stiffens up, and the vibrational frequency increases (approaching the ion plasma frequency if the screening were eliminated completely). In a calculation which is referenced to the phonon mode basis of the resonant sector, we would find little difference in the mode structure in the case of a simple monatomic metal as we go off of resonance; however the frequency changes in the off-resonant sectors, and off-diagonal coupling arises. This gives rise to the phonon fluctuations. A model for these fluctuations is discussed in Sections 2 and 3.

The situation in the Born–Oppenheimer picture at the outset is much less clear, primarily since there has been much less in the way of analysis in this picture to draw from. We know that in the resonant sector the static part of the screening comes about due to conventional interactions with electrons that involves no phonon exchange [32]. Non-adiabatic and phonon exchange contributions in this case results in a weak dynamical correction. It was unclear to us initially how the Born–Oppenheimer version of the model works in the off-resonant sectors. For example, since phonon exchange effects are so weak in the resonant sector, we imagined that they could become even weaker in the off-resonant sectors.

However, by now we have some experience with the Born–Oppenheimer picture (both on and off of resonance), as well as with the Bloch picture. We also know much more about the issues involved in accessing off-resonant states in connection with the phonon-nuclear interaction. We can develop a fluctuation model for this case similarly to the one for the Bloch picture. In Section 3 we present the results of a calculation of the associated shift for the fixed-point picture, in which the phonon exchange is Born–Oppenheimer. The results are interesting. While the Bloch picture and Born–Oppenheimer picture give similar results in many calculations as mentioned above, for fluctuations the two models give very different results at low frequency. In the Bloch picture, fluctuations are modest in comparison to the nonphysically large fluctuations resulting from the fixed-point formula in the low frequency limit. This motivates us to propose that the validity of the Born–Oppenheimer approximation might be at issue for the slow electrons which dominate the contributions to the fluctuations.

Now that we have a fluctuation model, we can address the question as to whether these fluctuations substantially enhance the ability of the system to fractionate a large quantum. In Section 6 we find that the fluctuations in the Bloch picture have only a small impact in comparison to fluctuations already present due to the strong phonon-nuclear coupling. On the one hand this might be viewed as discouraging, since we had hoped to see an enhancement of fractionation power due to electron–phonon interactions. On the other hand, the fact that electron–phonon interactions make little difference means that the problem simplifies, and that we should consider the phonon–nuclear interaction as a very strong and robust effect in its own right.

Since the inclusion of additional phonon fluctuations in the phonon-nuclear model makes little difference, we are faced once more with the issue of a lack of agreement between theory and experiment in connection with X-ray emission in the Karabut model. We recall that the test involved the underlying theory, the interpretation of the experiment, and the specification of a model and model parameters. As we found no issue with the underlying theory, our attention turns to the interpretation and the associated model. This provides us with the motivation to go back to the basic theory systematically, and more carefully, and see whether something was missed in the earlier models (in Sections 4–7), or perhaps in the interpretation (in Section 8). As will be seen, we have found a new regime in which the model shows an enhanced ability to fractionate large quanta (Sections 7 and 8).

2. Phonon–nuclear Model and Phonon Fluctuations

The addition of a phonon fluctuation model to the phonon–nuclear model is straightforward; however, it seems appropriate here to consider the problem in the context of the reduction from the fundamental Hamiltonian. In previous papers we have considered different parts of this reduction and associated issues in some detail. Rather than reproducing the full calculation, we are then motivated here to develop a shortened version of the development. This will hopefully be useful in providing a distillation of what has come before, and also in providing a foundation for the discussion in the following sections.

While this paper was under development, we had put together a detailed description of the reduction of the second-order phonon exchange contribution for both the diagonal and off-diagonal cases for the fixed-point picture with Born–Oppenheimer phonon exchange [32], and also for the Bloch picture equivalent. For the Bloch picture case, the results were the same for the diagonal case in the resonant sector (which might be thought of as on the mass shell, or involving real states) as appear in the literature. The generalization to the off-resonant case (which correspondingly might be thought of as off the mass shell, or involving virtual states) is trivial, and essentially identical expressions result for the off-diagonal interaction. After some thought, it became clear why this should be so; a force model that is different from the diagonal resonant sector can only come into the problem off of resonance in one way. The frequency shift off of resonance is very closely related to the off-diagonal coupling parameters, which simplifies the model considerably. Once we recognize this, the generalization to a fixed-point model becomes straightforward. Since the fixed-point phonon exchange interaction is so closely related to the Bloch phonon exchange interaction, the same basic approach can be used for either. Because of this, it seemed much less important to include a detailed reduction of the fixed-point interaction, as the end result is reasonably obvious given developments already in the literature. This allows us to focus on the results here, rather on the associated development of the fixed-point expressions.

2.1. Fundamental Hamiltonian

We begin with the fundamental Hamiltonian [29–32]

$$\begin{aligned} \hat{H} = & \sum_j \left(\mathbf{M}c^2 + \mathbf{a} \cdot c\hat{\mathbf{P}} \right)_j + \sum_k \frac{|\hat{\mathbf{p}}_k|^2}{2m} + \sum_{j < j'} \frac{Z_j Z_{j'} e^2}{4\pi\epsilon_0 |\mathbf{R}_{j'} - \mathbf{R}_j|} \\ & + \sum_{k < k'} \frac{e^2}{4\pi\epsilon_0 |\mathbf{r}_{k'} - \mathbf{r}_k|} - \sum_{j,k} \frac{Z_j e^2}{4\pi\epsilon_0 |\mathbf{r}_k - \mathbf{R}_j|}. \end{aligned} \quad (1)$$

We see a relativistic matrix description for the composite nuclei which includes all rest frame basis state energies in $\mathbf{M}c^2$ (including negative energy states), and all internal transitions due to coupling with the center of mass momentum in the \mathbf{a} matrix. The description of the electronic system here is nonrelativistic. Included are simple Coulomb interactions between nuclei and other nuclei, electrons and other electrons, and between electrons and nuclei. This model provides a direct generalization of the conventional solid-state Hamiltonian to include vibrational coupling between the lattice and internal nuclear degrees of freedom.

2.2. Isolation of the preferred transition

The fundamental Hamiltonian above is very complicated, but it provides us with a more complete description of the nuclear part of the problem. Normally we would make use of a generalized Foldy–Wouthuysen transformation to decouple the vibrations and internal nuclear degrees of freedom [31]

$$\hat{U}^\dagger \left(\mathbf{M}c^2 + \mathbf{a} \cdot c\hat{\mathbf{P}} \right) \hat{U} = \mathbf{M}c^2 \sqrt{1 + \frac{|c\hat{\mathbf{P}}|^2}{(\mathbf{M}c)^2}}. \quad (2)$$

We have found that in the presence of strong loss mechanisms (which increase rapidly off of resonance for basis states with less energy than available in the resonant sector), the Foldy–Wouthuysen transformation becomes unhelpful [31]. In this case the rotation still decouples the strong first-order coupling between vibrations and internal nuclear degrees of freedom, but the rotated loss becomes very hard to work with. This was the situation in the case of the spin–boson model, which can be decoupled with a Foldy–Wouthuysen transformation [13]. However, in the presence of strong loss the model behaves differently qualitatively, and it is simplest to simply analyze the problem directly in the unrotated basis [16,18–20].

We now have some experience with this kind of problem in connection with the phonon–nuclear problem under consideration here. What we find is that for most transitions included in the \mathbf{a} matrix, one arrives at the same answer as would have been obtained had a Foldy–Wouthuysen rotation been used [31]. Even though loss mechanisms makes it so we cannot take advantage of the Foldy–Wouthuysen transformation, it is not easy to arrange for something much different to happen on any particular transition (for example, anomalies are not seen from day to day in mainstream laboratories; and according to the models rather specialized conditions are needed for the coherent dynamics under discussion to occur).

As a result, we would expect coherent dynamics on only a small number of special transitions (those with strong coupling, relatively low transition energy, reasonably stable upper and lower states, with very strong occupation of at least one of the states). All other transitions are benign; consequently it seems a reasonable approximation to isolate the preferred (dynamic) transitions from all of the others (which are static) [31]

$$\mathbf{a} \rightarrow \mathbf{a}_{\text{static}} + \mathbf{a}_{\text{dynamic}} \quad (3)$$

Since only a tiny part of the \mathbf{a} matrix is involved in the dynamic transitions, we would expect (and calculations support) that it would be a good approximation (even in the presence of loss) to take

$$\begin{aligned} \hat{U}^\dagger \left(\mathbf{M}c^2 + \mathbf{a}_{\text{static}} \cdot c\hat{\mathbf{P}} \right) \hat{U} &\rightarrow \mathbf{M}c^2 \sqrt{1 + \frac{|c\hat{\mathbf{P}}|^2}{(\mathbf{M}c)^2}} \\ &\rightarrow \mathbf{M}c^2 + \frac{|\hat{\mathbf{P}}|^2}{2\mathbf{M}}, \end{aligned} \quad (4)$$

where \hat{U} is an incomplete Foldy–Wouthuysen transformation (since a few transitions are not included). The idea is that for the static transitions, when we compute the associated occupation, we get the same result we would have gotten in the absence of the loss term that prevents us from exploiting the Foldy–Wouthuysen transformation globally. Hence, it is as if Foldy–Wouthuysen works for all transitions that are not dynamic (an exception to this will be required later in this paper in Section 8 where transitions that make it into an anomalous regime, but are otherwise static, need to be included with the dynamic transitions).

We make use of this argument then to write

$$\begin{aligned} \hat{H} \rightarrow & \sum_j \frac{|\hat{\mathbf{P}}_j|^2}{2\mathbf{M}_j} + \sum_k \frac{|\hat{\mathbf{p}}_k|^2}{2m} + \sum_{j < j'} \frac{Z_j Z_{j'} e^2}{4\pi\epsilon_0 |\mathbf{R}_{j'} - \mathbf{R}_j|} + \sum_{k < k'} \frac{e^2}{4\pi\epsilon_0 |\mathbf{r}_{k'} - \mathbf{r}_k|} - \sum_{j,k} \frac{Z_j e^2}{4\pi\epsilon_0 |\mathbf{r}_k - \mathbf{R}_j|} \\ & + \sum_j \left(\mathbf{M}c^2 + \mathbf{a}_{\text{dynamic}} \cdot c\hat{\mathbf{P}} \right)_j. \end{aligned} \quad (5)$$

This Hamiltonian in practice is then one that we can work with for analyzing coherent dynamics that result from phonon-nuclear coupling.

2.3. Counter term

We might work with this kind of Hamiltonian under conditions where the transitions that could be dynamic happen to be static (and also in the conventional regime to be described later in Section 7.3 of this paper). In this case we could rotate the interaction out to second order, which would result in a decoupling of the dynamic transitions and leave us with a second-order contribution of the form

$$\hat{U}^\dagger \left(\mathbf{M}c^2 + \mathbf{a}_{\text{dynamic}} \cdot c\hat{\mathbf{P}} \right) \hat{U} \rightarrow \mathbf{M}c^2 + \frac{(\mathbf{a}_{\text{dynamic}} \cdot c\hat{\mathbf{P}})^2}{E - \hat{H}} + \dots \quad (6)$$

This contains the contribution of the dynamic transitions to the kinetic energy. It is the dominant term that is missing in our earlier incomplete Foldy–Wouthuysen transformation. As a result, it seems reasonable to subtract it out in the Hamiltonian if we are interested in studying the system right when it begins to become dynamic

$$\begin{aligned} \hat{H} \rightarrow & \sum_j \frac{|\hat{\mathbf{P}}_j|^2}{2\mathbf{M}_j} + \sum_k \frac{|\hat{\mathbf{p}}_k|^2}{2m} + \sum_{j < j'} \frac{Z_j Z_{j'} e^2}{4\pi\epsilon_0 |\mathbf{R}_{j'} - \mathbf{R}_j|} + \sum_{k < k'} \frac{e^2}{4\pi\epsilon_0 |\mathbf{r}_{k'} - \mathbf{r}_k|} - \sum_{j,k} \frac{Z_j e^2}{4\pi\epsilon_0 |\mathbf{r}_k - \mathbf{R}_j|} \\ & + \sum_j \left[\mathbf{M}c^2 + \mathbf{a}_{\text{dynamic}} \cdot c\hat{\mathbf{P}} - \frac{(\mathbf{a}_{\text{dynamic}} \cdot c\hat{\mathbf{P}})^2}{E - \hat{H}} \right]_j. \end{aligned} \quad (7)$$

The counter term here is equivalent to what we have discussed previously in [30,31]. From experience we have had with this kind of model, we know that the counter term is very small compared to the first-order coupling term under conditions where the system undergoes coherent dynamics. So good results can be obtained for rate estimates away from threshold if the counter term is not included.

2.4. Phonons and conduction electrons in the resonant sector

Next we consider the electronic and vibrational degrees of freedom. In the case of a metal the problem has been well-studied, and we know that it is possible to work with a dressed system in which the electronic and vibrational degrees of freedom are approximately separated [35–37]. We indicate this by writing

$$\begin{aligned}
& \sum_j \frac{|\hat{\mathbf{p}}_j|^2}{2M_j} + \sum_k \frac{|\hat{\mathbf{p}}_k|^2}{2m} + \sum_{j < j'} \frac{Z_j^* Z_{j'}^* e^2}{4\pi \epsilon_0 |\mathbf{R}_{j'} - \mathbf{R}_j|} + \sum_{k < k'} \frac{e^2}{4\pi \epsilon_0 |\mathbf{r}_{k'} - \mathbf{r}_k|} - \sum_{j,k} \frac{Z_j^* e^2}{4\pi \epsilon_0 |\mathbf{r}_k - \mathbf{R}_j|} \\
& \rightarrow \sum_{\mathbf{q},s} \hbar \omega_{\mathbf{q},s} \left(\hat{a}_{\mathbf{q},s}^\dagger \hat{a}_{\mathbf{q},s} + \frac{1}{2} \right) + \sum_{\mathbf{k},\sigma} E(\mathbf{k}) \hat{c}_{\mathbf{k},\sigma}^\dagger \hat{c}_{\mathbf{k},\sigma}.
\end{aligned} \tag{8}$$

We will use this for the resonant sector, as there can be a modification of the vibrational frequencies for a highly excited mode off of resonance.

From earlier work we know that coherent dynamics are unlikely to develop as a result of thermal excitation of a phonon bath; in general highly excited (nonthermal) phonon modes are required. Our work has focused so far on models where a single highly excited phonon mode interacts with a few dynamical transitions; consequently, we will isolate a single highly excited phonon mode according to

$$\sum_{\mathbf{q},s} \hbar \omega_{\mathbf{q},s} \left(\hat{a}_{\mathbf{q},s}^\dagger \hat{a}_{\mathbf{q},s} + \frac{1}{2} \right) \rightarrow \hbar \omega_0 \left(\hat{a}^\dagger \hat{a} + \frac{1}{2} \right) + \sum_{\mathbf{q}',s'} \hbar \omega_{\mathbf{q}',s'} \left(\hat{a}_{\mathbf{q}',s'}^\dagger \hat{a}_{\mathbf{q}',s'} + \frac{1}{2} \right) \tag{9}$$

As the other phonon modes have so far not played a role in the coherent dynamics, we can take them to be unexcited or thermal as we wish.

2.5. Frequency shift off of resonance and phonon fluctuations

Because the Foldy–Wouthuysen transformation is unhelpful for analyzing coherent dynamics, we need to model this part of the problem in an unrotated basis. Since the coupling is strong in general, we end up coupling to a great many states that are far off of resonance. At issue then is what changes are needed in the off-resonant sectors.

In a metal, the conduction electrons screen the interaction between the ions. Since the conduction electrons constitute an independent quantum mechanical system, the part of the interaction associated with dynamical screening will change off of resonance, which will result in a change in the phonon frequency off of resonance. Associated with the frequency changes will be corresponding terms that create and destroy phonons, which results in phonon fluctuations. We have been very interested in these phonon fluctuations, as we had hoped that they would produce an enhancement in the ability of the phonon–nuclear system to fractionate a large quantum (we will see that only a small effect results from this).

At issue then is the frequency shift of the highly-excited phonon mode off of resonance, which we will denote through

$$\omega_0 \rightarrow \omega_0(E_{\text{off}}), \tag{10}$$

where E_{off} is the amount of off-resonant energy per phonon in the highly excited phonon mode relative to the resonant sector (with a sign defined to be positive for basis states with more energy than in the resonant sector). There is a technical issue involved here as to how to deal with the off-resonant energy in connection with the phonon frequency. The argument we have relied on is one that makes use of a configuration space picture for individual phonons, with a corresponding optimization for each phonon individually. In this kind of picture on average the total off-resonant energy will be divided up between them, so that the frequency shift will be determined by how far off of resonance a single phonon is.

We will take the contribution of this frequency shift to the Hamiltonian to be

$$\hbar\omega_0 \left(\hat{a}^\dagger \hat{a} + \frac{1}{2} \right) \rightarrow \hbar\omega_0 \left(\hat{a}^\dagger \hat{a} + \frac{1}{2} \right) + \frac{1}{2} \hbar \Delta\omega_0(E_{\text{off}}) \left(\hat{a}^\dagger + \hat{a} \right)^2. \quad (11)$$

This kind of a model is consistent with a force constant model that changes off of resonance

$$\frac{1}{2} \sum_j \sum_k (\mathbf{R}_j - \mathbf{R}_j^{(0)}) \cdot \mathbf{K} \cdot (\mathbf{R}_k - \mathbf{R}_k^{(0)}) \rightarrow \frac{1}{2} \sum_j \sum_k (\mathbf{R}_j - \mathbf{R}_j^{(0)}) \cdot \mathbf{K}(E_{\text{off}}) \cdot (\mathbf{R}_k - \mathbf{R}_k^{(0)}), \quad (12)$$

where \mathbf{K} is a force matrix (and where the force matrix indices are suppressed). If we choose to define the phonon basis based on \mathbf{K} in the resonant sector, then the interaction off of resonance will be

$$\hat{H}_{\text{int}}(E_{\text{off}}) = \frac{1}{2} \sum_j \sum_k (\mathbf{R}_j - \mathbf{R}_j^{(0)}) \cdot [\mathbf{K}(E_{\text{off}}) - \mathbf{K}] \cdot (\mathbf{R}_k - \mathbf{R}_k^{(0)}), \quad (13)$$

Once again there are technical issues; however, if we make use of phonon modes defined in the off-resonant sectors, then for the highly excited mode we may write

$$\frac{1}{2} \sum_j \sum_k (\mathbf{R}_j - \mathbf{R}_j^{(0)}) \cdot [\mathbf{K}(E_{\text{off}}) - \mathbf{K}] \cdot (\mathbf{R}_k - \mathbf{R}_k^{(0)}) \rightarrow \frac{1}{2} \hbar \Delta\omega_0(E_{\text{off}}) \left(\hat{a}^\dagger + \hat{a} \right)^2. \quad (14)$$

Of interest in connection with this argument is that the phonon fluctuations are connected with the frequency shift. Although at this point there is no problem in calculating the frequency shift, or the dynamical change in the force constant, conceptually it is much simpler to focus on (and to estimate) the frequency shift. Because of this close connection between the frequency shift and the fluctuations, we understand that any vibrating system in which the frequency shifts off of resonance will also have fluctuations. Hence, there is no reason to believe that the fluctuations under discussion for a metal here would be absent in an insulator.

In a strict fixed-point model, the interaction is mediated by momentum operators rather than position operators. In this case, we would use instead

$$\frac{1}{2} \sum_j \sum_k \hat{\mathbf{P}}_j \cdot [\mathbf{L}(E_{\text{off}}) - \mathbf{L}] \cdot \hat{\mathbf{P}}_k \rightarrow \frac{1}{2} \hbar \Delta\omega_0(E_{\text{off}}) \left(\frac{\hat{a} - \hat{a}^\dagger}{i} \right)^2, \quad (15)$$

where the \mathbf{L} matrix is discussed in [32]. This will result in a sign change in the off-diagonal terms.

We note that there is yet another subtle issue in all of this. We are using a model in which the off-resonant energy is divided among the different phonons in the highly excited mode to produce the frequency shift. There may be thermal phonons, so the question might arise as to whether the off-resonant energy should also be shared among them as well. We might go further and point out that there are also conduction electrons which might also be considered as candidates. From our perspective, in connection with coherent dynamics associated with phonon–nuclear interactions, what contributes to the effect are interactions between the highly excited phonon mode and the nuclear system; consequently, the thermal phonon modes are independent degrees of freedom that are not involved (and hence out of the picture for practical purposes). The same can be said of the conduction electrons, once the dynamic response (which comes about from the response of the electrons to the highly excited phonon mode) has been extracted.

2.6. Loss

We first introduced (our version of) the lossy spin–boson model by augmenting the lossless spin–boson model with a Brillouin–Wigner loss operator [16]. The empirical loss added to the model was intended to account for the myriad of fast loss mechanisms (electron promotion, atomic displacement/ejection, and nuclear loss channels) available when a large quantum of excess off-resonant energy became available.

Now that we have a physical model for the system, it is possible for the loss terms to be developed directly from the model (instead of adding them empirically). Consider for example the specific case of phonon loss due to electron promotion. Since our model includes electron–phonon interactions, it also includes this phonon loss channel. In the fixed-point picture [32] we can determine the phonon loss in the resonant sector that results from second-order phonon exchange from

$$-\frac{\hbar}{2}\hat{\Gamma}(E) = \text{Im}\langle n| - \sum_j \sum_k \hat{\mathbf{P}}_j \cdot \left\{ \sum_{X \neq 0} \frac{\hbar^2}{M_j M_k} \frac{\langle \Phi_0 | \nabla_j \Phi_X \rangle_0 \langle \Phi_X | \nabla_k \Phi_0 \rangle_0}{E - \hat{H}} \right\} \cdot \hat{\mathbf{P}}_k | n \rangle, \quad (16)$$

where the denominator here is understood to keep track of phonon and electron energies appropriately. In a more general (complex) computation of the phonon mode frequencies that included the imaginary parts of the transformed generalized force matrix, the resulting frequency would be complex. In this case we could determine the loss numerically on resonance from

$$-\frac{1}{2}\Gamma = n_0 \text{Im}\{\omega_0\}. \quad (17)$$

Off of resonance for basis states with higher energy than the resonant sector, it would probably make sense to compute loss rates with the off-resonant energy spread over all of the phonons, as was discussed for the frequency shift above. Since the frequency shift can be thought of as an average quantity (averaged over all phonons), making use of the per phonon energy deficit seems reasonable. Loss in the presence for resonance states with an energy deficit can probably be thought of similarly, since an energy deficit results in a net reduction of the loss rate. However, in the case of an energy surplus (where the basis states have less energy than available in the resonant sector), the system would be able to make a transition to a final state in the (post-loss) resonant sector by losing the excess energy. Hence, there is a net benefit for the system in exchanging substantial excess energy in a single loss for these basis states, rather than spreading the excess energy over all phonons. In this case we could make use of an appropriate off-resonant version of Eq. (16) to compute the associated (very fast) decay rate. As discussed above, such fast loss can reduce state occupation where an energy excess is present, which makes the problem behave qualitatively differently. In future work it will be of interest to revisit the estimation of decay rates based on realistic models.

We have argued that the Foldy–Wouthuysen transformation becomes unhelpful in the presence of fast decay mechanisms that reduces or eliminates occupation of basis states needed for the rotation [31]. In essence a generalized Foldy–Wouthuysen transformation of the loss turns into a complicated operator that is very hard to deal with. We have such an example here already in Eq. (16). In the unrotated problem with strong coupling, we have a wide range of basis states involved; some with weak decay rates, and some with very fast decay rates. Whether a decay rate is fast or slow depends on the energy offset from resonance. There is no good way to keep track of the states that are unoccupied because of loss in a Foldy–Wouthuysen transformation. This is the reason that the transformation becomes unhelpful in this situation.

2.7. Reduced models

If we make use of the various simplifications above, then the model under consideration can be written as

$$\begin{aligned} \hat{H} \rightarrow & \hbar\omega_0 \left(\hat{a}^\dagger \hat{a} + \frac{1}{2} \right) + \frac{1}{2} \hbar \Delta\omega_0(E_{\text{off}}) \left(\hat{a}^\dagger + \hat{a} \right)^2 + \sum_{\mathbf{q}', s'} \hbar\omega_{\mathbf{q}', s'} \left(\hat{a}_{\mathbf{q}', s'}^\dagger \hat{a}_{\mathbf{q}', s'} + \frac{1}{2} \right) \\ & + \sum_{\mathbf{k}, \sigma} E(\mathbf{k}) \hat{c}_{\mathbf{k}, \sigma}^\dagger \hat{c}_{\mathbf{k}, \sigma} + \sum_j \left[\mathbf{M}c^2 + \mathbf{a}_{\text{dynamic}} \cdot c\hat{\mathbf{P}} - \frac{(\mathbf{a}_{\text{dynamic}} \cdot c\hat{\mathbf{P}})^2}{E - \hat{H}} \right]_j - i \frac{\hbar}{2} \hat{\Gamma}(E). \end{aligned} \quad (18)$$

Since the coherent dynamics of interest here do not involve electron promotion (beyond that included in the loss term), there is little reason to retain conduction electrons in the model. Similarly, we are not including interactions with the unexcited or thermal phonon modes, so we will not keep them in our model.

We have already presumed that the nuclear masses are well approximated by the ground state mass in connection with the kinetic energy

$$\frac{|\hat{\mathbf{P}}_j|^2}{2\mathbf{M}_j} \rightarrow \frac{|\hat{\mathbf{P}}_j|^2}{2M_j}, \quad (19)$$

when we introduced the phonon modes above. However, this model contains a large mass matrix with far more information (about all of the rest frame states) than we require. All we really need is a description of the masses of the states which participate in the coherent dynamics. Hence, we can reduce in this case to

$$\mathbf{M}_j \rightarrow \begin{cases} M_j & \text{if no coherent dynamics} \\ \text{smaller } \mathbf{M}_j & \text{if coherent dynamics.} \end{cases} \quad (20)$$

There is also no reason to keep the rest masses in the Hamiltonian, as they simply contribute a large constant offset (but do not impact the dynamics).

After all of this, the model that remains can be written as

$$\begin{aligned} \hat{H} \rightarrow & \hbar\omega_0 \left(\hat{a}^\dagger \hat{a} + \frac{1}{2} \right) + \frac{1}{2} \hbar \Delta\omega_0(E_{\text{off}}) \left(\hat{a}^\dagger + \hat{a} \right)^2 - i \frac{\hbar}{2} \hat{\Gamma}(E) \\ & + \sum_j \left[\mathbf{M}c^2 + \mathbf{a}_{\text{dynamic}} \cdot c\hat{\mathbf{P}} - \frac{(\mathbf{a}_{\text{dynamic}} \cdot c\hat{\mathbf{P}})^2}{E - \hat{H}} \right]_j. \end{aligned} \quad (21)$$

This model could reasonably be taken as the starting point for future analyses of anomalies in condensed matter nuclear science. Even though it is much simpler than where we started, the physics in this model is very rich. This model can be used for example to describe coherent dynamics and fractionation involving multiple transitions with spatial nonuniformity, which is likely to include most problems of interest well into the future.

2.8. Uniform interaction and two-level systems

Although much simpler than what we started with, this model is still extremely complicated. We would like to develop even simpler models that can be analyzed more easily. Consequently, the final step in our reduction is to assume a uniform interaction, so that

$$\hat{\mathbf{P}} \rightarrow \frac{d\mathbf{P}}{da} \left(\frac{\hat{a} - \hat{a}^\dagger}{i} \right) \quad (22)$$

and to assume that only two levels are involved so that

$$\begin{aligned} \sum_j \left[\mathbf{a}_{\text{dynamic}} \cdot c \hat{\mathbf{P}} \right] &\rightarrow \sum_j \begin{pmatrix} 0 & \mathbf{a} \\ \mathbf{a} & 0 \end{pmatrix}_j \cdot \frac{d\mathbf{P}}{da} \left(\frac{\hat{a} - \hat{a}^\dagger}{i} \right) \\ &= \mathbf{a} \cdot c \frac{d\mathbf{P}}{da} \frac{2\hat{S}_x}{\hbar} \left(\frac{\hat{a} - \hat{a}^\dagger}{i} \right). \end{aligned} \quad (23)$$

In the last line we make use of a pseudo-spin notation

$$\hat{S}_x = \frac{\hbar}{2} \sum_j \begin{pmatrix} 0 & 1 \\ 1 & 0 \end{pmatrix}_j. \quad (24)$$

There is a notational issue in that previously \mathbf{a} was used to describe a very large matrix of vectors, and now \mathbf{a} is a single vector matrix element for a single nuclear transition. For the mass matrix contribution, we can write

$$\begin{aligned} \sum_j \mathbf{M} c^2 &\rightarrow \Delta M c^2 \sum_j \begin{pmatrix} 1/2 & 0 \\ 0 & -1/2 \end{pmatrix}_j \\ &= \Delta M c^2 \frac{\hat{S}_z}{\hbar}, \end{aligned} \quad (25)$$

where

$$\hat{S}_z = \frac{\hbar}{2} \sum_j \begin{pmatrix} 1 & 0 \\ 0 & -1 \end{pmatrix}_j. \quad (26)$$

The model that results is

$$\begin{aligned} \hat{H} &\rightarrow \Delta M c^2 \frac{\hat{S}_z}{\hbar} + \mathbf{a} \cdot c \frac{d\mathbf{P}}{da} \frac{2\hat{S}_x}{\hbar} \left(\frac{\hat{a} - \hat{a}^\dagger}{i} \right) + \hbar \omega_0 \left(\hat{a}^\dagger \hat{a} + \frac{1}{2} \right) + \frac{1}{2} \hbar \Delta \omega_0 (E_{\text{off}}) (\hat{a}^\dagger + \hat{a})^2 \\ &\quad - i \frac{\hbar}{2} \hat{\Gamma}(E). \end{aligned} \quad (27)$$

The counter term is suppressed here. We recognize this as a lossy spin–boson model augmented with phonon fluctuations.

2.9. Basic lossy-spin boson model

As we will see in what follows, the impact of the phonon fluctuations due to electron-phonon coupling is minor, so one could reasonably neglect them resulting in the basic lossy-spin boson model [16]

$$\hat{H} \rightarrow \Delta M c^2 \frac{\hat{S}_z}{\hbar} + \mathbf{a} \cdot \mathbf{c} \frac{d\mathbf{P}}{da} \frac{2\hat{S}_x}{\hbar} \left(\frac{\hat{a} - \hat{a}^\dagger}{i} \right) + \hbar \omega_0 \hat{a}^\dagger \hat{a} - i \frac{\hbar}{2} \hat{\Gamma}(E). \quad (28)$$

This model is perhaps the simplest to describe coherent energy exchange between nuclear and vibrational degrees of freedom. As we have remarked upon previously, the augmentation of the basic spin-boson model with appropriate loss results in efficient coherent energy exchange under conditions of fractionation.

3. Fluctuation Model for Long Wavelength Phonons

In order to evaluate the impact of phonon fluctuations on the phonon–nuclear problem, we require a model for the associated fluctuation parameters. From the discussion of the previous section we understand that this is equivalent to determining the frequency shift off of resonance. This motivates us to pursue the problem here.

As it turns out, models for vibrations in metals are much simpler for long wavelength phonons, since in this limit the interaction between conduction electrons and ions is “softer” so that a simple Coulomb interaction becomes appropriate. For shorter wavelength phonons, interactions at short range are important so we would require a more accurate pseudo-potential description.

3.1. Bloch picture frequency shift

The simplest place to start is with the Bloch picture, where the acoustic frequency for a monatomic simple metal lattice can be written as [37]

$$\omega_0(E_{\text{off}}) = \omega_i \sqrt{\frac{\epsilon_0}{\epsilon(\mathbf{q}, \omega_0 - E_{\text{off}}/\hbar)}}, \quad (29)$$

where the ion plasma frequency satisfies

$$\omega_i^2 = \frac{(Z^* e)^2}{\epsilon_0 N M}. \quad (30)$$

For small excursions off of resonance we can use a Taylor series to write

$$\omega_0(E_{\text{off}}) = \omega_0 + E_{\text{off}} \left[\frac{d}{dE} \omega_0(E) \right]_{E=0} + \dots \quad (31)$$

The first derivative can be evaluated to give

$$\begin{aligned} \frac{d}{dE} \omega_0(E) &= -\frac{1}{2} \omega_i \frac{\epsilon_0^{1/2}}{[\epsilon(\mathbf{q}, \omega_0 - E/\hbar)]^{3/2}} \frac{d}{dE} \epsilon(\mathbf{q}, \omega_0 - E/\hbar) \\ &= -\frac{1}{2} \omega_0(E) \frac{1}{\epsilon(\mathbf{q}, \omega_0 - E/\hbar)} \frac{d}{dE} \epsilon(\mathbf{q}, \omega_0 - E/\hbar). \end{aligned} \quad (32)$$

To lowest order the frequency shift is

$$\begin{aligned}\Delta\omega(E_{\text{off}}) &= \omega_0(E_{\text{off}}) - \omega_0 \\ &\rightarrow -\frac{1}{2} \left\{ \omega_0(E) \frac{1}{\epsilon(\mathbf{q}, \omega_0 - E/\hbar)} \frac{d}{dE} \epsilon(\mathbf{q}, \omega_0 - E/\hbar) \right\}_{E=0} E_{\text{off}}.\end{aligned}\quad (33)$$

The relative frequency shift can be expressed as

$$\frac{\Delta\omega(E_{\text{off}})}{\omega_0} \rightarrow -\frac{1}{2} \left\{ \frac{d}{dE} \ln \epsilon(\mathbf{q}, \omega_0 - E/\hbar) \right\}_{E=0} E_{\text{off}}.\quad (34)$$

3.2. Longitudinal dielectric constant

In the random phase approximation, the longitudinal dielectric constant for a simple plane wave model for the electrons can be written as

$$\frac{\epsilon(\mathbf{q}, \omega)}{\epsilon_0} = 1 - \sum_{\mathbf{k}, \sigma} \frac{2e^2}{\epsilon_0 V |\mathbf{q}|^2} \frac{n_F(\mathbf{k})[1 - n_F(\mathbf{k} + \mathbf{q})]}{\hbar\omega + E(\mathbf{k}) - E(\mathbf{k} + \mathbf{q})}.\quad (35)$$

We can write this in a continuum approximation as

$$\frac{\epsilon(\mathbf{q}, \omega)}{\epsilon_0} = 1 + \frac{4e^2}{\epsilon_0 |\mathbf{q}|^2} \int \frac{n_F(\mathbf{k})[1 - n_F(\mathbf{k} + \mathbf{q})]}{E(\mathbf{k} + \mathbf{q}) - E(\mathbf{k}) - \hbar\omega} \frac{d\mathbf{k}^3}{(2\pi)^3}.\quad (36)$$

If we take the $T = 0$ limit, we may write

$$\frac{\epsilon(\mathbf{q}, \omega)}{\epsilon_0} \rightarrow 1 + \frac{4e^2}{\epsilon_0 |\mathbf{q}|^2} \frac{1}{(2\pi)^2} \frac{k_F^3}{E_F} \int_{-1}^1 dx \int_0^1 \kappa^2 d\kappa \left\{ \frac{\Theta(\sqrt{\kappa^2 + \eta^2 + 2\kappa\eta x} - 1)}{\eta^2 + 2\kappa\eta x - \Omega} \right\},\quad (37)$$

where

$$\kappa = \frac{|\mathbf{k}|}{k_F}, \quad \eta = \frac{|\mathbf{q}|}{k_F}, \quad \Omega = \frac{\hbar\omega}{E_F}.\quad (38)$$

From direct numerical computations for a model for long wavelength vibrations in Na (as a representative metal often used for this kind of model), we can estimate

$$\left\{ \frac{d}{dE} \ln \epsilon(\mathbf{q}, \omega_0 - E/\hbar) \right\}_{E=0} \rightarrow -\frac{0.013}{\hbar\omega_0}.\quad (39)$$

The numerical parameter in this formula depends on the Fermi energy E_F , the Fermi wave vector k_F , and the effective mass of the electrons in this model; consequently we expect similar values for other metals. This result, combined with the relative frequency shift of Eq. (34) is sufficient to specify a fluctuation model.

3.3. Frequency shift in the fixed-point picture

Perhaps the simplest way to make progress toward a fixed-point picture calculation is to go back to the dispersion relation calculation in the Bloch picture, and write it as

$$\begin{aligned}\omega_0^2 &= \frac{\omega_i^2}{\epsilon_0} \left[1 - \frac{\epsilon(\mathbf{q}, \omega) - \epsilon_0}{\epsilon(\mathbf{q}, \omega)} \right]_{\omega=-\omega_0} \\ &= \frac{\omega_i^2}{\epsilon_0} \left[1 + \frac{\pi(\mathbf{q}, \omega)}{\epsilon(\mathbf{q}, \omega)} \right]_{\omega=-\omega_0}\end{aligned}\quad (40)$$

with

$$\frac{\pi(\mathbf{q}, \omega)}{\epsilon_0} = \sum_{\mathbf{k}, \sigma} \frac{2e^2}{\epsilon_0 V |\mathbf{q}|^2} \frac{n_F(\mathbf{k})[1 - n_F(\mathbf{k} + \mathbf{q})]}{\hbar\omega + E(\mathbf{k}) - E(\mathbf{k} + \mathbf{q})} \quad (\text{Bloch}). \quad (41)$$

The interpretation here is that π in this model is associated with the ion–electron interaction, and ϵ is associated with the screening by the conduction electrons.

In the fixed-point picture phonon exchange between the electrons and ions works differently (as appropriate for a Born–Oppenheimer picture), which we can take into account for long wavelengths in the phonon exchange contribution through

$$\frac{\pi(\mathbf{q}, \omega)}{\epsilon_0} = \sum_{\mathbf{k}, \sigma} \frac{2e^2}{\epsilon_0 V |\mathbf{q}|^2} \frac{(\hbar\omega_0)^2 n_F(\mathbf{k})[1 - n_F(\mathbf{k} + \mathbf{q})]}{[E(\mathbf{k}) - E(\mathbf{k} + \mathbf{q})]^2 [\hbar\omega + E(\mathbf{k}) - E(\mathbf{k} + \mathbf{q})]} \quad (\text{Fixed – point}). \quad (42)$$

We cannot make use of the phonon exchange contribution in the fixed-point model to determine the phonon frequency as in the Bloch picture, but there is no difficulty in using the phonon exchange contribution to estimate the frequency shift. To lowest order we may write

$$2\omega_0 \Delta\omega = \frac{\omega_i^2}{\epsilon_0} \left[\frac{d}{dE} \frac{\pi(\mathbf{q}, \omega_0 - E/\hbar)}{\epsilon(\mathbf{q}, \omega_0 - E/\hbar)} \right]_{E=0} \Delta E_{\text{off}}. \quad (43)$$

This can be rewritten as

$$\frac{\Delta\omega}{\omega_0} = \frac{1}{2} \frac{\epsilon(\mathbf{q}, \omega_0)}{\epsilon_0} \left[\frac{d}{dE} \frac{\pi(\mathbf{q}, \omega_0 - E/\hbar)}{\epsilon(\mathbf{q}, \omega_0 - E/\hbar)} \right]_{E=0} \Delta E_{\text{off}}. \quad (44)$$

The evaluation of this derivative is made complicated by the fact that the continuum integral is (logarithmically) singular. If we assume that the lowest compressional mode of a plate is highly excited (and use an appropriate cut-off), then over a modest range of long wavelength modes (around $\eta = 10^{-2}$) we can estimate from numerical calculations for Na

$$\frac{\epsilon(\mathbf{q}, 0)}{\epsilon_0} \left[\frac{d}{dE} \frac{\pi(\mathbf{q}, -E/\hbar)}{\epsilon(\mathbf{q}, -E/\hbar)} \right]_{E=0} \rightarrow \left(\frac{0.000234 \text{ eV}}{\hbar\omega_0} \right)^4 \frac{1}{\hbar\omega_0}. \quad (45)$$

We conclude that phonon fluctuations can be much larger at long wavelengths in the fixed-point model.

3.4. Discussion

As we can see from the discussion above, one expects a different frequency shift off of resonance in the Bloch picture versus the Born–Oppenheimer based fixed-point picture. In the literature the Bloch picture and Born–Oppenheimer pictures give similar answers for most problems that have been studied; here we get a qualitatively different behavior.

Our intuition suggests that the Bloch picture with the low fluctuations is appropriate for a macroscopic sized metal at long wavelengths, and that Born–Oppenheimer picture is probably inappropriate in this regime (in connection with fluctuations). At this point it may be useful to think a bit about the adiabatic approximation itself. The premise of the Born–Oppenheimer approximation is that the nuclear velocity is slow compared to the electron velocity, so that the use of electronic wavefunctions determined with fixed nuclei is sensible. However, in the simple models under discussion here, the relevant velocity in the longitudinal wave direction is the compressional sound speed c_L . If the sample is large, then there are many electrons that contribute with electron velocities in the same direction less than the compressional sound speed. It is not difficult to imagine that the Born–Oppenheimer approximation is ill-suited for these electrons.

We could imagine working with a thin film for which localization due to the film boundaries would eliminate these slow electrons. We could estimate the plate thickness at threshold from

$$v = \frac{\hbar k}{m^*} \rightarrow \frac{\hbar \pi}{m^* L} = c_L. \quad (46)$$

The lowest phonon frequency at this threshold would satisfy

$$\hbar \omega_0 = \hbar c_L \frac{\pi}{L} = m^* c_L^2. \quad (47)$$

For Na, the threshold thin film thickness is about 1000 Å, and the threshold phonon energy is about 60 μeV. For example, if we were to require that this threshold be exceeded by an order of magnitude or so, then the relative shift consistent with Eq. (45) would be plausible.

Consequently, we can imagine that compressional vibrations in a nano-scale metal sample could be reasonably described within a Born–Oppenheimer type of picture. Thicker samples that are 1 μ or greater are probably well described using a Bloch picture for long wavelength acoustic phonons. From this point of view, the appearance of a characteristic energy in the fixed point formula for the relative frequency shift is then not surprising. When the phonon energy gets to be much less than the characteristic energy, which is where the frequency shift becomes anomalously large, the Born–Oppenheimer approximation itself may well be inappropriate.

4. Local Approximation

Our attention now returns to the coupled phonon–nuclear model, which now includes an additional term that accounts for phonon fluctuations. We are interested in developing approximate solutions for eigenfunctions of the model, and ultimately to determine the rate of coherent energy exchange under conditions of fractionation. In previous work we have analyzed very similar models, so we can take advantage of this earlier analysis for this model. The basic idea is that when n is very large, we can analyze the rate at which coherent energy exchange occurs by working with a periodic approximation in n and m space [19].

4.1. Finite basis approximation

We are interested in developing approximate solutions for the time-independent Schrödinger equation

$$E\Psi = \left\{ \Delta M c^2 \frac{\hat{S}_z}{\hbar} + \left(\mathbf{a} \cdot c \frac{d\mathbf{P}}{da} \right) \frac{\hat{S}_x}{2\hbar} \left(\frac{\hat{a} - \hat{a}^\dagger}{i} \right) + \hbar\omega_0 \left(\hat{a}^\dagger \hat{a} + \frac{1}{2} \right) + \frac{\hbar\Delta\omega(E)}{2} \left(\hat{a}^\dagger + \hat{a} \right)^2 - i \frac{\hbar}{2} \hat{\Gamma}(E) \right\} \Psi. \quad (48)$$

We make use of a finite basis approximation of the form

$$\Psi = \sum_m \sum_n e^{i\frac{\pi}{2}n} c_{m,n} |S, m\rangle |n\rangle. \quad (49)$$

The expansion coefficients then satisfy an eigenvalue equation of the form

$$\begin{aligned} E c_{m,n} = & \left\{ \Delta M c^2 m + \hbar \left[\omega_0 + \Delta\omega(E) \right] \left(n + \frac{1}{2} \right) - i \frac{\hbar}{2} \Gamma(E) \right\} c_{m,n} \\ & + \left(\mathbf{a} \cdot c \frac{d\mathbf{P}}{da} \right) \sqrt{(S-m)(S+m+1)} \left[\sqrt{n+1} c_{m+1,n+1} + \sqrt{n} c_{m+1,n-1} \right] \\ & + \left(\mathbf{a} \cdot c \frac{d\mathbf{P}}{da} \right) \sqrt{(S+m)(S-m+1)} \left[\sqrt{n+1} c_{m-1,n+1} + \sqrt{n} c_{m-1,n-1} \right] \\ & - \frac{1}{2} \hbar \Delta\omega(E) \left[\sqrt{(n+2)(n+1)} c_{m,n+2} + \sqrt{n(n-1)} c_{m,n-2} \right]. \end{aligned} \quad (50)$$

4.2. Approximate form

As before we will assume that

$$n \gg 1 \quad (51)$$

and also that

$$|S \pm m| \gg 1. \quad (52)$$

In this case the eigenvalue equation is approximated by

$$\begin{aligned} E c_{m,n} = & \left\{ \Delta M c^2 m + \hbar \left[\omega_0 + \Delta\omega(E) \right] n - i \frac{\hbar}{2} \Gamma(E) \right\} c_{m,n} - \frac{n}{2} \hbar \Delta\omega(E) \left[c_{m,n+2} + c_{m,n-2} \right] \\ & + \frac{1}{i} \left(\mathbf{a} \cdot c \frac{d\mathbf{P}}{da} \right) \sqrt{n} \sqrt{S^2 - m^2} \left[c_{m+1,n+1} - c_{m+1,n-1} + c_{m-1,n+1} - c_{m-1,n-1} \right]. \end{aligned} \quad (53)$$

4.3. Resonance condition and periodic approximation

Suppose now that there is a resonance of the form

$$\Delta M c^2 = \hbar\omega_0 \Delta n \quad (54)$$

(since $\Delta\omega(E)$ is zero in the resonant sector) with Δn odd. In this case, the eigenvalue equation becomes locally approximately periodic; in this case we require [19]

$$\left(\mathbf{a} \cdot c \frac{d\mathbf{P}}{da}\right) \sqrt{n} \sqrt{S^2 - m^2} \quad (55)$$

and

$$\frac{n}{2} \hbar \Delta\omega(E) \quad (56)$$

to be approximately constant locally for indirect transitions of the form

$$(n + \Delta n, m - 1) \rightarrow (n, m) \rightarrow (n - \Delta n, m + 1). \quad (57)$$

In this case, we can make use of an approximate local solution of the form

$$c_{m,n} \rightarrow e^{im\phi} v_{n+m\Delta n}, \quad (58)$$

which is consistent with an approximate local wavefunction of the form

$$\Psi = \sum_m \sum_n e^{im\phi} v_{n+m\Delta n} |n\rangle |S, m\rangle. \quad (59)$$

The eigenvalue equation for the v coefficients in this local approximation satisfy

$$\begin{aligned} E(\phi) v_n = & \left\{ \hbar \left[\omega_0 + \Delta\omega(E) \right] n - i \frac{\hbar}{2} \Gamma(E) \right\} v_n - \frac{n}{2} \hbar \Delta\omega(E) \left[v_{n+2} + v_{n-2} \right] \\ & + \left(\mathbf{a} \cdot c \frac{d\mathbf{P}}{da} \right) \sqrt{n} \sqrt{S^2 - m^2} \left[e^{i\phi} \left(v_{n+\Delta n+1} + v_{n+\Delta n-1} \right) + e^{-i\phi} \left(v_{n-\Delta n+1} + v_{n-\Delta n-1} \right) \right]. \end{aligned} \quad (60)$$

Although we have used the notation $E(\phi)$ for the energy eigenvalue here, if we wish to relate it to the energy eigenvalue E above we will need to remember that a constant offset of $\Delta M c^2 m$ has been suppressed.

4.4. Implementing loss as a boundary condition

There seems to be nothing to prevent us from making use of a realistic loss model for $\hat{\Gamma}(E)$ in this approximation, and computing the sector eigenfunctions and eigenvalues in the Brillouin-Wigner formalism that we are using. However, we know that when the loss is very large for basis states with an energy below the resonant sector energy $E(\phi)$, that the state occupation will be very small. We implement this boundary condition approximately by omitting basis states with n less than n_0 . We therefore consider the local eigenvalue equation

$$\begin{aligned} E(\phi) v_n = & \hbar \left[\omega_0 + \Delta\omega(E) \right] n v_n - \frac{n}{2} \hbar \Delta\omega(E) \left[v_{n+2} + v_{n-2} \right] \\ & + \left(\mathbf{a} \cdot c \frac{d\mathbf{P}}{da} \right) \sqrt{n} \sqrt{S^2 - m^2} \left[e^{i\phi} \left(v_{n+\Delta n+1} + v_{n+\Delta n-1} \right) + e^{-i\phi} \left(v_{n-\Delta n+1} + v_{n-\Delta n-1} \right) \right] \end{aligned} \quad (61)$$

with

$$v_n \rightarrow 0 \quad \text{for } n \leq n_0 \quad (62)$$

This version of the local approximation eigenvalue equation is a bit different than previous versions [19,20]. Here we are interested in taking into account the \sqrt{n} dependence of the coupling strength in the second line, so that n in this version of the model will be the number of phonons (instead of an incremental number of phonons).

4.5. Approximate model for the nuclear state distribution

Historically our focus has been on the phonon distribution, since the solution of the local problem determines the indirect matrix element (from which the rate of coherent energy transfer is determined). However, it has become clear that if we have an approximate solution for the v_n coefficients, these could be used to develop a consistent model for which m states are occupied. Such a model could be quite useful to determine the m distribution near the threshold for coherent dynamics.

For this we propose an approximate product solution of the form

$$c_{m,n} = (-1)^m d_m v_{n+m\Delta n}. \quad (63)$$

We propose to find a constraint on the d_m by using the variational principle on an approximate total energy. For this we start with

$$\begin{aligned} \langle \hat{H} \rangle = & \sum_{m,n} \left\{ \Delta M c^2 m + \hbar \left[\omega_0 + \Delta \omega(E) \right] \left(n + \frac{1}{2} \right) \right\} |c_{m,n}|^2 \\ & + \sum_{m,n} \left(\mathbf{a} \cdot c \frac{d\mathbf{P}}{da} \right) \sqrt{(S-m)(S+m+1)} \left[\sqrt{n+1} c_{m,n} c_{m+1,n+1} + \sqrt{n} c_{m,n} c_{m+1,n-1} \right] \\ & + \sum_{m,n} \left(\mathbf{a} \cdot c \frac{d\mathbf{P}}{da} \right) \sqrt{(S+m)(S-m+1)} \left[\sqrt{n+1} c_{m,n} c_{m-1,n+1} + \sqrt{n} c_{m,n} c_{m-1,n-1} \right] \\ & - \sum_{m,n} \frac{1}{2} \hbar \Delta \omega(E) \left[\sqrt{(n+2)(n+1)} c_{m,n} c_{m,n+2} + \sqrt{n(n-1)} c_{m,n} c_{m,n-2} \right], \end{aligned} \quad (64)$$

where the summations are over allowed states. This we adapt to a product approximation using

$$\begin{aligned} \langle \hat{H} \rangle = & \sum_{m,n} \left\{ \Delta M c^2 m + \hbar \left[\omega_0 + \Delta \omega(E) \right] \left(n + \frac{1}{2} \right) \right\} |d_m|^2 v_n^2 \\ & - \left(\mathbf{a} \cdot c \frac{d\mathbf{P}}{da} \right) \left[\sum_n \sqrt{n+1} v_n v_{n+1} + \sqrt{n} v_n v_{n-1} \right] \\ & \left[\sum_m \sqrt{(S-m)(S+m+1)} d_m d_{m+1} + \sqrt{(S+m)(S-m+1)} d_m d_{m-1} \right] \\ & - \sum_{m,n} \frac{1}{2} \hbar \Delta \omega(E) |d_m|^2 \left[\sqrt{(n+2)(n+1)} v_n v_{n+2} + \sqrt{n(n-1)} v_n v_{n-2} \right]. \end{aligned} \quad (65)$$

Minimization of the energy with respect to the d_m coefficients results in

$$\begin{aligned}
 E_d d_m = & \sum_n \left\{ \Delta M c^2 m + \hbar \left[\omega_0 + \Delta \omega(E) \right] \left(n + \frac{1}{2} \right) \right\} v_n^2 d_m \\
 & - \left(\mathbf{a} \cdot c \frac{d\mathbf{P}}{da} \right) \left[\sum_n \sqrt{n+1} v_n v_{n+1} + \sqrt{n} v_n v_{n-1} \right] \\
 & \left[\sqrt{(S-m)(S+m+1)} d_{m+1} + \sqrt{(S+m)(S-m+1)} d_{m-1} \right] \\
 & - \sum_n \frac{1}{2} \hbar \Delta \omega(E) \left[\sqrt{(n+2)(n+1)} v_n v_{n+2} + \sqrt{n(n-1)} v_n v_{n-2} \right] d_m.
 \end{aligned} \tag{66}$$

This provides an improved constraint over one proposed previously in [38].

4.6. Reduction of the constraint

We would like to isolate terms in this eigenvalue equation that depend on m . For example, consider

$$\sum_n \left\{ \hbar \left[\omega_0 + \Delta \omega(E) \right] \left(n + \frac{1}{2} \right) \right\} v_n^2 \rightarrow \hbar \omega_0 \left(\langle n \rangle + \frac{1}{2} \right) + \hbar \langle n \Delta \omega \rangle + \frac{1}{2} \hbar \langle \Delta \omega \rangle. \tag{67}$$

This term has no m dependence, and only provides a constant offset. Our constraint is then equivalent to

$$E'_d d_m = \Delta M c^2 m d_m - 2 \left(\mathbf{a} \cdot c \frac{d\mathbf{P}}{da} \right) \langle \sqrt{n} \rangle \left[\sqrt{(S-m)(S+m+1)} d_{m+1} + \sqrt{(S+m)(S-m+1)} d_{m-1} \right], \tag{68}$$

which we can write in normalized form as

$$\lambda_d d_m = m d_m - 2 \frac{\left(\mathbf{a} \cdot c \frac{d\mathbf{P}}{da} \right) \langle \sqrt{n} \rangle}{\Delta M c^2} \left[\sqrt{(S-m)(S+m+1)} d_{m+1} + \sqrt{(S+m)(S-m+1)} d_{m-1} \right]. \tag{69}$$

4.7. Specialization for threshold calculations

In the case of lattice-induced nuclear excitation, the population of the nuclei to be excited is localized near the ground state. In previous work we pursued models specific to this limit; to proceed, we recall the relation between the Dicke parameters S and m and the number of nuclei in the two states

$$S - m = N_0 - N_1, \quad S + m = N_1, \tag{70}$$

where N_0 is the total number of nuclei, and where N_1 is the number of excited state nuclei. We will assume that the number of nuclei in each state is much greater than unity

$$N_0 - N_1 \gg 1, \quad N_1 \gg 1 \tag{71}$$

in which case the Dicke factors reduce to

$$\sqrt{(S-m)(S+m+1)} \rightarrow \sqrt{(N_0-N_1)N_1}, \quad (72)$$

$$\sqrt{(S+m)(S-m+1)} \rightarrow \sqrt{N_1(N_0-N_1)}. \quad (73)$$

The eigenvalue equation can be written in terms of the number of excited nuclei as

$$\lambda'_d d_{N_1} = N_1 d_{N_1} - 2 \frac{\left(\mathbf{a} \cdot c \frac{d\mathbf{P}}{da} \right) \langle \sqrt{n} \rangle \sqrt{(N_0-N_1)N_1}}{\Delta M c^2} (d_{N_1+1} + d_{N_1-1}). \quad (74)$$

We can make use of this constraint to estimate state distributions for the computation of average quantities that show up later on. This version of the constraint is most closely related to those of [38] (note that a factor of N_1 is missing in the potential of Eqs. (57) and (58) and several following equations in [38]).

Although we have considered a similar constraint in our earlier work, this new version of the constraint works very differently. We will see an enhancement in the fractionation power resulting from this constraint.

5. Pulse and Amplitude Approximation

Since the solutions to the local eigenvalue equation includes a series of pulses that are very nearly the same, we have found it effective to make use of a pulse and amplitude approximation [20,39]. Adapting the pulse and amplitude approximation to the present case we may write for the $\phi = \pi$ case

$$v_n^{(-)} \rightarrow \sum_{j=0}^{\infty} \sum_{k=0}^{\Delta n-1} \delta_{j\Delta n+k-n} a_j u_k, \quad (75)$$

For the other case ($\phi = 0$) we have

$$(-1)^n v_n^{(+)} \rightarrow \sum_{j=0}^{\infty} \sum_{k=0}^{\Delta n-1} \delta_{j\Delta n+k-n} a_j u_k. \quad (76)$$

5.1. Total energy

To optimize the pulse and amplitude solutions individually, we would like to use an appropriate variational method based on the total energy. We start with the total pulse energy in terms of the v_n , which is

$$\begin{aligned} \langle v_n | \hat{H} | v_n \rangle = & \sum_n \hbar \left[\omega_0 + \Delta \omega_n \right] n v_n^2 - \sum_n \frac{n}{2} \hbar \Delta \omega_n v_n \left[v_{n+2} + v_{n-2} \right] \\ & \pm \left(\mathbf{a} \cdot c \frac{d\mathbf{P}}{da} \right) \sqrt{S^2 - m^2} \sum_n \sqrt{n} v_n \left[v_{n+\Delta n+1} + v_{n+\Delta n-1} + v_{n-\Delta n+1} + v_{n-\Delta n-1} \right]. \end{aligned} \quad (77)$$

In the pulse and amplitude approximation we adapt this to

$$\begin{aligned} \langle v_n | \hat{H} | v_n \rangle = & \sum_j \sum_k \hbar \left[\omega_0 + \Delta \omega_{j\Delta n+k} \right] (j\Delta n + k) a_j^2 u_k^2 \\ & - \sum_j \sum_k \frac{j\Delta n + k}{2} \hbar \Delta \omega_{j\Delta n+k} a_j^2 u_k \left[u_{k+2} + u_{k-2} \right] \\ & - \left(\mathbf{a} \cdot c \frac{d\mathbf{P}}{da} \right) \sqrt{S^2 - m^2} \sum_j \sum_k \sqrt{j\Delta n + k} \left[a_j a_{j+1} + a_j a_{j-1} \right] \left[u_k u_{k+1} + u_k u_{k-1} \right]. \end{aligned} \quad (78)$$

5.2. Optimization of the amplitudes

We begin with the optimization of the amplitudes, which is accomplished by minimizing the energy to give the constraint

$$\begin{aligned} E_a a_j = & \left\{ \sum_k \hbar \left[\omega_0 + \Delta \omega_{j\Delta n+k} \right] (j\Delta n + k) u_k^2 - \sum_k \frac{j\Delta n + k}{2} \hbar \Delta \omega_{j\Delta n+k} u_k \left[u_{k+2} + u_{k-2} \right] \right\} a_j \\ & - \left(\mathbf{a} \cdot c \frac{d\mathbf{P}}{da} \right) \sqrt{S^2 - m^2} \left\{ \sum_k \sqrt{j\Delta n + k} \left[u_k u_{k+1} + u_k u_{k-1} \right] \right\} (a_{j+1} + a_{j-1}). \end{aligned} \quad (79)$$

In general we are interested in this model under conditions where

$$j \gg 1 \quad (80)$$

so that

$$\sum_k \hbar \left[\omega_0 + \Delta \omega_{j\Delta n+k} \right] (j\Delta n + k) u_k^2 \rightarrow j \hbar \left[\omega_0 + \Delta \omega_{j\Delta n} \right] \Delta n, \quad (81)$$

$$\sum_k \frac{j\Delta n + k}{2} \hbar \Delta \omega_{j\Delta n+k} u_k \left[u_{k+2} + u_{k-2} \right] \rightarrow j \Delta n \hbar \Delta \omega_{j\Delta n}, \quad (82)$$

$$\sum_k \sqrt{j\Delta n + k} \left[u_k u_{k+1} + u_k u_{k-1} \right] \rightarrow 2\sqrt{j} \sqrt{\Delta n}. \quad (83)$$

This leads to

$$E_a a_j = j \Delta M c^2 a_j - \left\{ 2 \left(\mathbf{a} \cdot c \frac{d\mathbf{P}}{da} \right) \sqrt{\Delta n} \sqrt{S^2 - m^2} \right\} \sqrt{j} (a_{j+1} + a_{j-1}). \quad (84)$$

It would seem reasonable to normalize this equation, and also modify it into the form

$$\lambda_a a_j = j a_j - 2 \frac{\left(\mathbf{a} \cdot c \frac{d\mathbf{P}}{da} \right) \sqrt{\Delta n} \sqrt{S^2 - m^2}}{\Delta M c^2} \left(\sqrt{j+1} a_{j+1} + \sqrt{j} a_{j-1} \right), \quad (85)$$

where

$$\lambda_a = \frac{E_a}{\Delta M c^2} \quad (86)$$

Note that this model generalizes the result obtained previously in [39].

Once again, it seems worth emphasizing that this version of the amplitude constraint differs in an important way from what we considered previously; this one includes the enhancement of the coupling when the number of phonons increase.

5.3. Pulse optimization

We next optimize the pulse by minimizing the energy to obtain the constraint

$$\begin{aligned} E_u u_k = & \left\{ \sum_j \hbar \left[\omega_0 + \Delta \omega_{j \Delta n + k} \right] (j \Delta n + k) a_j^2 \right\} u_k \\ & - \left\{ \sum_j \frac{j \Delta n + k}{2} \hbar \Delta \omega_{j \Delta n + k} a_j^2 \right\} (u_{k+2} + u_{k-2}) \\ & - \left\{ \left(\mathbf{a} \cdot c \frac{d\mathbf{P}}{da} \right) \sqrt{S^2 - m^2} \sum_j \sqrt{j \Delta n + k} \left[a_j a_{j+1} + a_j a_{j-1} \right] \right\} (u_{k+1} + u_{k-1}), \end{aligned} \quad (87)$$

Once again we assume that j is large, and approximate

$$\sum_j \hbar \left[\omega_0 + \Delta \omega_{j \Delta n + k} \right] (j \Delta n + k) a_j^2 \rightarrow \Delta n \hbar \left[\omega_0 \langle j \rangle + \langle j \Delta \omega \rangle \right] + \hbar \left[\omega_0 + \langle \Delta \omega \rangle \right] k, \quad (88)$$

$$\sum_j \frac{j \Delta n + k}{2} \hbar \Delta \omega_{j \Delta n + k} a_j^2 \rightarrow \frac{1}{2} \Delta n \hbar \langle j \Delta \omega \rangle + \frac{1}{2} \Delta n \hbar \langle \Delta \omega \rangle k, \quad (89)$$

$$\sum_j \sqrt{j \Delta n + k} \left[a_j a_{j+1} + a_j a_{j-1} \right] \rightarrow 2 \sqrt{\Delta n} \langle \sqrt{j} \rangle. \quad (90)$$

The pulse equation that results can be written as

$$\begin{aligned}
\left[E_u - \Delta n \hbar \left(\omega_0 \langle j \rangle + \langle j \Delta \omega \rangle \right) \right] u_k &= \hbar \left[\omega_0 + \langle \Delta \omega \rangle \right] k u_k \\
&- \left\{ \frac{1}{2} \Delta n \hbar \langle j \Delta \omega \rangle + \frac{1}{2} \Delta n \hbar \langle \Delta \omega \rangle k \right\} (u_{k+2} + u_{k-2}) \\
&- 2 \left\{ \left(\mathbf{a} \cdot c \frac{d\mathbf{P}}{da} \right) \sqrt{S^2 - m^2} \sqrt{\Delta n \langle \sqrt{j} \rangle} \right\} (u_{k+1} + u_{k-1}). \quad (91)
\end{aligned}$$

We would like to take advantage of the fact that

$$k \ll j \Delta n \quad (92)$$

in this constraint. To do this, we will use the approximation

$$\begin{aligned}
&\hbar \left[\omega_0 + \langle \Delta \omega \rangle \right] k u_k - \left\{ \frac{1}{2} \Delta n \hbar \langle j \Delta \omega \rangle + \frac{1}{2} \Delta n \hbar \langle \Delta \omega \rangle k \right\} (u_{k+2} + u_{k-2}) \\
&\rightarrow \hbar \omega_0 k u_k - \frac{1}{2} \Delta n \hbar \langle j \Delta \omega \rangle (u_{k+2} + u_{k-2}). \quad (93)
\end{aligned}$$

The approximate pulse constraint that results can be written as

$$\begin{aligned}
E'_u u_k &= \hbar \omega_0 k u_k - \frac{1}{2} \Delta n \hbar \langle j \Delta \omega \rangle (u_{k+2} + u_{k-2}) \\
&- 2 \left\{ \left(\mathbf{a} \cdot c \frac{d\mathbf{P}}{da} \right) \sqrt{S^2 - m^2} \sqrt{\Delta n \langle \sqrt{j} \rangle} \right\} (u_{k+1} + u_{k-1}). \quad (94)
\end{aligned}$$

As before it seems useful to have a normalized version of this constraint, which we can write as

$$\lambda_u u_k = k u_k - \frac{\Delta n \langle j \Delta \omega \rangle}{2 \omega_0} (u_{k+2} + u_{k-2}) - 2 \left[\frac{\left(\mathbf{a} \cdot c \frac{d\mathbf{P}}{da} \right) \sqrt{S^2 - m^2} \sqrt{\Delta n \langle \sqrt{j} \rangle}}{\hbar \omega_0} \right] (u_{k+1} + u_{k-1}). \quad (95)$$

This is similar to what we obtained previously in Ref. [39], but is generalized to include the effects of phonon fluctuations. Since we have analyzed this kind of problem previously, our attention is drawn here to the prefactors of the fluctuation terms (those containing $u_{k'}$ with $k' \neq k$), as these determine the indirect coupling matrix element which determines the coherent energy exchange rate [20].

6. Estimation of the Indirect Coupling Matrix Element

We are interested in developing estimates for the coherent energy exchange rate under conditions of fractionation. This rate is proportional to the indirect coupling matrix element, and from previous work we know that the pulse and amplitude approximation can be used to obtain accurate estimates for the indirect coupling matrix element. As we have seen above, there are three constraints that describe the different distributions of states that are relevant to the problem (pulse, amplitude and nuclear excited state distribution). In this section we will examine these constraints, and use them to estimate the indirect coupling matrix element.

6.1. Amplitude constraint

We will work with the amplitude constraint in the form

$$\lambda_a a_j = j a_j - 2\gamma_a \left(\sqrt{j+1} a_{j+1} + \sqrt{j} a_{j-1} \right) \quad (96)$$

with

$$\gamma_a = \frac{\left(\mathbf{a} \cdot c \frac{d\mathbf{P}}{da} \right) \sqrt{\Delta n} \sqrt{S^2 - m^2}}{\Delta M c^2} \quad (97)$$

subject to the boundary condition

$$a_j = 0 \quad \text{for } j < j_0, \quad (98)$$

where

$$j_0 = \frac{n_0}{\Delta n}. \quad (99)$$

We have discussed this kind of problem previously [20,39], so we know how it works and how to use it. We are not interested in the eigenvalue; however, we are very interested in the expansion coefficients a_j because they can be used to determine expectation values needed for the model.

6.2. Scaling relations

There is no difficulty solving this eigenvalue equation numerically, which is of interest here to develop scaling laws for the expectation values that we need for the pulse constraint. From the numerical solutions we can estimate

$$\langle \sqrt{j} \rangle \rightarrow \sqrt{j_0 + (2\gamma_a)^2}. \quad (100)$$

We also require the expectation value of the frequency shift

$$\begin{aligned} \langle \Delta\omega \rangle &= \left[\frac{d}{dE} \Delta\omega \right] \frac{\Delta M c^2}{j \Delta n} (j \Delta n - n_0) \\ &= \left[\frac{d}{dE} \Delta\omega \right] \hbar \omega_0 \left\langle \frac{j - j_0}{j} \right\rangle. \end{aligned} \quad (101)$$

There are three regimes of interest; we may write

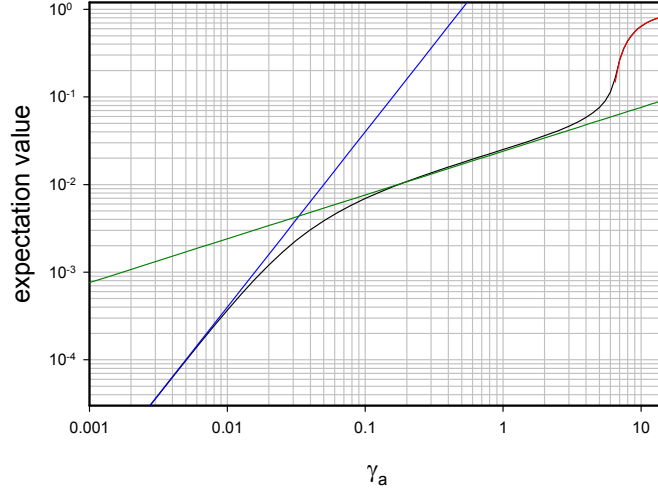


Figure 1. Numerical (black) and analytic (blue, green, and red) results for $\langle (j - j_0)/j \rangle$ as a function of γ_a , for $j_0 = 144$.

$$\left\langle \frac{j - j_0}{j} \right\rangle = \begin{cases} 4\gamma_a^2, & \gamma_a < \frac{1}{4^{2/3}\sqrt{j_0}}, \\ \frac{\sqrt{\gamma_a}}{j_0^{3/4}}, & \frac{1}{4^{2/3}\sqrt{j_0}} < \gamma_a < \frac{\sqrt{j_0}}{2}, \\ 1 - \frac{j_0}{4\gamma_a^2}, & \gamma_a > \frac{\sqrt{j_0}}{2}. \end{cases} \quad (102)$$

The different limits are compared with exact numerical results in Fig. 1. Finally, we require

$$\langle j \Delta \omega \rangle = \left[\frac{d}{dE} \Delta \omega \right] \hbar \omega_0 \langle j - j_0 \rangle \quad (103)$$

Once again there are three regimes of interest; we have the estimates

$$\langle j - j_0 \rangle = \begin{cases} 4\gamma_a^2 j_0, & \gamma_a < \frac{1}{4^{2/3}\sqrt{j_0}}, \\ j_0^{1/4} \sqrt{\gamma_a}, & \frac{1}{4^{2/3}\sqrt{j_0}} < \gamma_a < \frac{\sqrt{j_0}}{2}, \\ 4\gamma_a^2 - j_0, & \gamma_a > \frac{\sqrt{j_0}}{2}. \end{cases} \quad (104)$$

Once we have the scaling relations for the expectation values, we have everything with need from the amplitude constraint.

6.3. Pulse constraint

We can write the pulse constraint as

$$\lambda_u u_k = k u_k - \frac{g'_u}{2} (u_{k+2} + u_{k-2}) - 2g_u (u_{k+1} + u_{k-1}) \quad (105)$$

with

$$\begin{aligned} g_u &= \frac{\left(\mathbf{a} \cdot c \frac{d\mathbf{P}}{da} \right) \sqrt{S^2 - m^2} \sqrt{\Delta n} \langle \sqrt{j} \rangle}{\hbar \omega_0} \\ &= \gamma_a \Delta n \langle \sqrt{j} \rangle, \end{aligned} \quad (106)$$

$$g'_u = \Delta n \frac{\langle j \Delta \omega \rangle}{\omega_0}. \quad (107)$$

Once again, we have encountered this kind of constraint previously [20,39], and we know that the indirect coupling matrix element can be derived from the g_u and g'_u parameters.

Since we are interested in situations where Δn is very large, and since we know that the u_n vary slowly when the coupling is strong, we can develop a continuum version of the constraint according to

$$\lambda_u u(z) = \Delta n z u(z) - \frac{g'_u}{2} \left[2u(z) + \frac{4}{\Delta n^2} \frac{d^2}{dz^2} u(z) \right] - 2g_u \left[2u(z) + \frac{1}{\Delta n^2} \frac{d^2}{dz^2} u(z) \right]. \quad (108)$$

This can be simplified to

$$\epsilon u(z) = z u(z) - \frac{2(g_u + g'_u)}{(\Delta n)^3} \frac{d^2}{dz^2} u(z). \quad (109)$$

6.4. Impact of fluctuations

We are interested in understanding under what conditions fluctuation might be important. To study this, we examine the ratio of the two dimensionless coupling constants

$$\frac{g'_u}{g_u} \rightarrow \hbar \left[\frac{d}{dE} \Delta \omega \right] \begin{cases} \gamma_a \sqrt{j_0}, & \gamma_a \sqrt{j_0} < \frac{1}{4^{2/3}}, \\ \frac{1}{\sqrt{j_0} \gamma_a}, & \frac{1}{4^{2/3} \sqrt{j_0}} < \gamma_a < \frac{\sqrt{j_0}}{2}, \\ 2, & \gamma_a > \frac{\sqrt{j_0}}{2}. \end{cases} \quad (110)$$

Earlier we obtained an estimate for the frequency shift for Na in the Bloch picture, which we write here as

$$\hbar \left[\frac{d}{dE} \Delta\omega \right] = 0.013. \quad (111)$$

We see that fluctuations will have the largest impact in the outer two regions generally, and for Na in the Bloch model in particular we can write

$$\frac{g'_u}{g_u} \rightarrow \begin{cases} 0.013\gamma_a\sqrt{j_0}, & \gamma_a\sqrt{j_0} < \frac{1}{4^{2/3}}, \\ \frac{0.013}{\sqrt{j_0}\gamma_a}, & \frac{1}{4^{2/3}\sqrt{j_0}} < \gamma_a < \frac{\sqrt{j_0}}{2}, \\ 0.026, & \gamma_a > \frac{\sqrt{j_0}}{2}. \end{cases} \quad (112)$$

In general, fluctuations contribute only a minor correction in the Bloch picture. The fluctuations can be larger in the Born–Oppenheimer approximation where appropriate, which suggests that we should think about them further in connection with experiments involving nanoparticles.

6.5. Indirect coupling matrix element

We can write for the indirect coupling matrix element [20]

$$\frac{V_{\text{eff}}}{\Delta M c^2} = 4 \frac{2(g_u + g'_u)}{(\Delta n)^3} \Phi \left[\frac{2(g_u + g'_u)}{(\Delta n)^3} \right], \quad (113)$$

where the Φ function was defined previously in connection with the lossy spin–boson problem [20], and illustrated in Fig. 2.

The coherent energy exchange rate is proportional to this indirect coupling matrix element [20]. From earlier work we view the indirect coupling matrix element as involving a prefactor which is sufficiently large as to allow for very fast reactions as long as the large quantum can be fractionated; and a hindrance factor, which in this case is the Φ function, which approaches unity only when the associated coupling is sufficiently strong. The hindrance factor here is then associated with the fractionation of the quantum, which is the most difficult thing accomplished by the model.

7. Threshold Condition for Lattice-induced Nuclear Excitation

From the beginning of the field back in 1989, the key issue in our view has always been whether a large quantum can be fractionated. Based on the analysis in the previous sections, and also in previous papers, we are in a position to evaluate the threshold condition for fractionation. The basic argument is that the coupling has to be sufficiently strong in order for a large quantum to be fractionated, and now we can quantify this.

7.1. Threshold condition

The Φ function that shows up in the evaluation of the indirect coupling matrix element is essentially a hindrance factor, one that goes approximately to unity when the coupling is strong

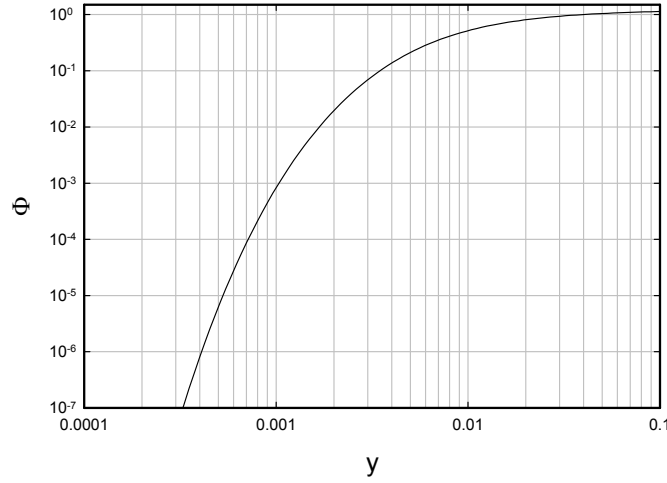


Figure 2. Function $\Phi(y)$ as a function of y .

$$\lim_{x \rightarrow 0.03} \Phi(x) \rightarrow 1. \quad (114)$$

Alternatively, when the coupling is weak, the hindrance function Φ goes to zero. We will adopt a threshold condition here based on

$$\frac{2(g_u + g'_u)}{(\Delta n)^3} \geq 4 \times 10^{-4}. \quad (115)$$

In the event that can neglect fluctuations, this becomes

$$\frac{2g_u}{(\Delta n)^3} = \frac{2\gamma_a \langle \sqrt{j} \rangle}{(\Delta n)^2} \geq 4 \times 10^{-4}. \quad (116)$$

This then is the mathematical requirement that needs to be satisfied for the large quantum $\Delta M c^2$ to be fractionated into Δn smaller quanta $\hbar \omega_0$. In what follows our goal is to relate this mathematical constraint to the relevant parameters of a physical system.

7.2. Expectation value of the Dicke number

If we expand out this constraint, we obtain

$$\frac{2 \left(\mathbf{a} \cdot c \frac{d\mathbf{P}}{da} \right) \sqrt{\Delta n} \sqrt{S^2 - m^2} \langle \sqrt{j} \rangle}{\Delta M c^2 (\Delta n)^2} \geq 4 \times 10^{-4}. \quad (117)$$

Before proceeding, we require an estimate for the Dicke factor $\sqrt{S^2 - m^2}$. We recall that

$$\sqrt{S^2 - m^2} = \sqrt{(N_0 - N_1)N_1}. \quad (118)$$

The total rate will be obtained by averaging the N_1 -dependent rate over the relevant distribution; however, for the simple argument in this section, we will be satisfied with an average.

To proceed, we need to determine the population distribution from the eigenvalue equation that we derived previously

$$\lambda'_d d_{N_1} = N_1 d_{N_1} - 2 \frac{\left(\mathbf{a} \cdot c \frac{d\mathbf{P}}{da} \right) \langle \sqrt{n} \rangle \sqrt{(N_0 - N_1)N_1}}{\Delta M c^2} \left(d_{N_1+1} + d_{N_1-1} \right). \quad (119)$$

At issue here is the fact that $\langle \sqrt{n} \rangle$ depends on N_1

$$\begin{aligned} \langle \sqrt{n} \rangle &\rightarrow \sqrt{\Delta n} \langle \sqrt{j} \rangle \rightarrow \sqrt{\Delta n} \sqrt{j_0 + 4\gamma_d^2} \\ &= \sqrt{n_0} \sqrt{1 + \frac{4 \left(\mathbf{a} \cdot c \frac{d\mathbf{P}}{da} \right)^2 \Delta n (N_0 - N_1) N_1}{j_0 (\Delta M c^2)^2}}. \end{aligned} \quad (120)$$

It will be useful to write this as

$$\sqrt{n} \rightarrow \sqrt{n_0} \sqrt{1 + \frac{(N_0 - N_1)N_1}{N_0 N_c}}, \quad (121)$$

where

$$N_c = \frac{j_0 (\Delta M c^2)^2}{4 \left(\mathbf{a} \cdot c \frac{d\mathbf{P}}{da} \right)^2 \Delta n N_0} = \frac{n_0 (\hbar \omega_0)^2}{4 \left(\mathbf{a} \cdot c \frac{d\mathbf{P}}{da} \right)^2 N_0}. \quad (122)$$

The eigenvalue equation for the d_{N_1} then becomes

$$\lambda'_d d_{N_1} = N_1 d_{N_1} - 2\gamma_d \sqrt{\frac{(N_0 - N_1)N_1}{N_0}} \sqrt{1 + \frac{(N_0 - N_1)N_1}{N_0 N_c}} \left(d_{N_1+1} + d_{N_1-1} \right), \quad (123)$$

where

$$\gamma_d = \frac{\left(\mathbf{a} \cdot c \frac{d\mathbf{P}}{da} \right) \sqrt{n_0} \sqrt{N_0}}{\Delta M c^2}. \quad (124)$$

As before in the case of the amplitude eigenvalue equation, we are not interested in the eigenvalue; however, we are interested in the expansion coefficients, since we can use them to calculate the expectation value $\left\langle \sqrt{S^2 - m^2} \langle j \rangle \right\rangle$.

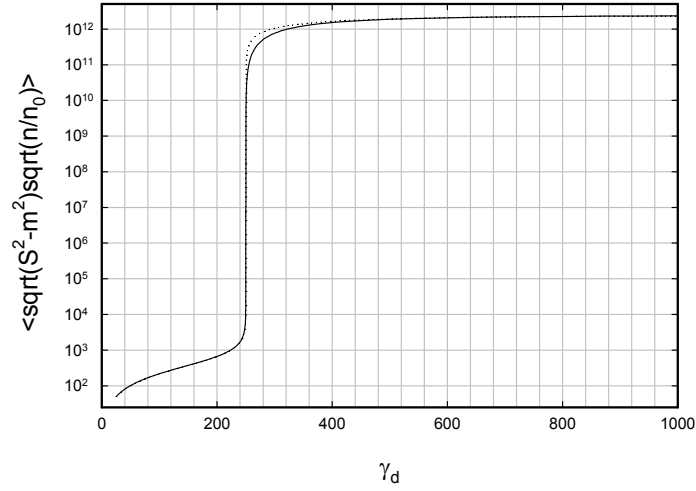


Figure 3. Numerical result for $\left\langle \sqrt{S^2 - m^2} \frac{\langle \sqrt{n} \rangle}{\sqrt{n_0}} \right\rangle$ as a function of γ_d (solid line) compared with empirical result of Eq. (125); in this calculation we have taken $N_0 = 10^{16}$ and $N_c = 10^6$.

We have solved numerically for the excited state distribution by now many times, and we have found empirical formula for the required expectation value of the form

$$\left\langle \sqrt{S^2 - m^2} \langle \sqrt{n} \rangle \right\rangle = \sqrt{\Delta n} \left\langle \sqrt{S^2 - m^2} \langle \sqrt{j} \rangle \right\rangle$$

$$\rightarrow \begin{cases} \sqrt{n_0 N_0} \frac{2\gamma_d}{\sqrt{1 - \left(\frac{4\gamma_d}{\sqrt{N_c}}\right)^2}}, & 4\gamma_d < \sqrt{N_c}, \\ \frac{1}{4} \sqrt{n_0 N_0} \frac{N_0}{\sqrt{N_c}} \sqrt{\frac{1 - \left(\frac{\sqrt{N_c}}{4\gamma_d}\right)^2}{1 + \left(\frac{\sqrt{N_c}}{4\gamma_d}\right)^2}}, & 4\gamma_d > \sqrt{N_c}. \end{cases} \quad (125)$$

We have not considered this expectation value before; it is new to this analysis of the model. Note from Fig. 3 that this matrix element increases suddenly at $\gamma_d = \sqrt{N_c}/4$, which implies for us a corresponding sudden increase in the ability of the system to fractionate a large quantum.

7.3. Threshold constraint including the averaged Dicke factor

We can make use of the results above and write the constraint in the form

$$4 \times 10^{-4} \leq \frac{2 \left(\mathbf{a} \cdot c \frac{d\mathbf{P}}{da} \right) \sqrt{n_0 N_0}}{\Delta M c^2 (\Delta n)^2} \times \begin{cases} \frac{2\gamma_d}{\sqrt{1 - \left(\frac{4\gamma_d}{\sqrt{N_c}} \right)^2}}, & 4\gamma_d < \sqrt{N_c}, \\ \frac{1}{4} \frac{N_0}{N_c^{1/2}} \sqrt{\frac{1 - \left(\frac{\sqrt{N_c}}{4\gamma_d} \right)^2}{1 + \left(\frac{\sqrt{N_c}}{4\gamma_d} \right)^2}}, & 4\gamma_d > \sqrt{N_c}. \end{cases} \quad (126)$$

Let us first consider the case of $4\gamma_d < \sqrt{N_c}$, which we might consider to be a conventional regime (conventional in the sense that the number of virtual phonons is less than the number of real phonons, and there is no large enhancement of virtual nuclear excited state population). Away from the boundary the constraint becomes

$$\frac{2 \left(\mathbf{a} \cdot c \frac{d\mathbf{P}}{da} \right) \sqrt{n_0 N_0}}{\Delta M c^2 (\Delta n)^2} (2\gamma_d) = \frac{4(\hbar\omega_0)^2 \left(\mathbf{a} \cdot c \frac{d\mathbf{P}}{da} \right)^2 n_0 N_0}{(\Delta M c^2)^4} \geq 4 \times 10^{-4}, \quad 4\gamma_d \ll \sqrt{N_c}. \quad (127)$$

Next we examine what happens when $4\gamma_d > \sqrt{N_c}$, which will consider to be in the anomalous regime (anomalous because there are more virtual phonons than real, and a large enhancement of virtual nuclear excitation can occur). Away from the boundary we may write

$$\frac{2 \left(\mathbf{a} \cdot c \frac{d\mathbf{P}}{da} \right) \sqrt{n_0 N_0}}{\Delta M c^2 (\Delta n)^2} \left(\frac{1}{4} \frac{N_0}{N_c^{1/2}} \right) = \frac{\hbar\omega_0 \left(\mathbf{a} \cdot c \frac{d\mathbf{P}}{da} \right)^2 N_0^2}{(\Delta M c^2)^3} \geq 4 \times 10^{-4}, \quad 4\gamma_d \gg \sqrt{N_c}. \quad (128)$$

Note that this anomalous regime condition can be obtained from the conventional regime condition from the replacement

$$n_0 \rightarrow \frac{N_0 \Delta M c}{4\hbar\omega_0}. \quad (129)$$

In essence, there are more virtual phonons than real in the anomalous regime [to see this, note that the effects under discussion follow from the enhancements in $\langle \sqrt{n} \rangle$ of Eqs. (120) and (121)], and we can get an estimate of how many virtual phonons are present from this replacement.

7.4. Boundary between the conventional and anomalous regimes

The boundary between the conventional and anomalous regime satisfies

$$4\gamma_d = \frac{4 \left(\mathbf{a} \cdot c \frac{d\mathbf{P}}{da} \right) \sqrt{n_0} \sqrt{N_0}}{\Delta M c^2} = \sqrt{N_c} = \sqrt{\frac{n_0 (\hbar\omega_0)^2}{4 \left(\mathbf{a} \cdot c \frac{d\mathbf{P}}{da} \right)^2 N_0}}. \quad (130)$$

We can recast this as

$$8 \left(\mathbf{a} \cdot c \frac{d\mathbf{P}}{da} \right)^2 N_0 = \hbar \omega_0 \Delta M c^2. \quad (131)$$

In the case of a simple monatomic crystal, we may write for $d\mathbf{P}/da$ in the special case of the highly excited uniform vibrational mode

$$\frac{d\mathbf{P}}{da} = \mathbf{u} \sqrt{\frac{M \hbar \omega_0}{2N}}. \quad (132)$$

In this case the boundary is determined from

$$4 (\mathbf{a} \cdot \mathbf{u})^2 \frac{N_0}{N} = \frac{\Delta M c^2}{M c^2}. \quad (133)$$

This is very interesting for a number of reasons. We interpret this as a constraint on the strength of the transition as determined by the associated matrix element. In the event that the transition matrix element and vibrational mode are aligned (so that $\mathbf{u} \cdot \mathbf{a} = |\mathbf{a}|$) then we can determine a condition for the anomalous regime as

$$|\mathbf{a}| \geq \sqrt{\frac{1}{4} \frac{N}{N_0} \frac{\Delta M c^2}{M c^2}} \quad (\text{anomalous regime}). \quad (134)$$

In the case of a transition showing coherent dynamics, we require in addition that the transition must be stable on a relevant time scale. A static transition that satisfies the constraint may be able fractionate a large quantum for a dynamic transition (for example, in a donor and receiver scheme [40]) even if it has fast loss.

7.5. Conventional regime threshold energy

Since the basic issue in this discussion is the ability of the system to fractionate a large quantum, we would like to interpret the threshold constraint in terms of how large a quantum can be fractionated. For example, in the conventional regime we can rewrite the constraint as

$$\delta E^4 = \frac{4(\hbar \omega_0)^2 \left(\mathbf{a} \cdot c \frac{d\mathbf{P}}{da} \right)^2 n_0 N_0}{4 \times 10^{-4}} \geq (\Delta M c^2)^4, \quad (135)$$

where

$$\delta E = 10(\hbar \omega_0)^{1/2} \left(\mathbf{a} \cdot c \frac{d\mathbf{P}}{da} \right)^{1/2} (n_0 N_0)^{1/4}. \quad (136)$$

In the case of a monatomic crystal this becomes (assuming the transition is aligned with the vibrations)

$$\delta E = 8.41 (M c^2)^{1/4} |\mathbf{a}|^{1/2} (\hbar \omega_0)^{1/2} \left(\frac{n_0 \hbar \omega_0}{N} \right)^{1/4} N_0^{1/4}. \quad (137)$$

Although an evaluation of this will be discussed in the following section, perhaps it is useful to note here that fractionation of a large quantum is pretty difficult in the conventional regime, and that this constraint is not so easy to satisfy for keV energy quanta.

7.6. Anomalous regime threshold energy

In the anomalous regime the threshold constraint can also be expressed in terms of an energy; we may write

$$\delta E^3 = \frac{\hbar\omega_0 \left(\mathbf{a} \cdot c \frac{d\mathbf{P}}{da} \right)^2 N_0^2}{4 \times 10^{-4}} \geq (\Delta M c^2)^3. \quad (138)$$

The threshold energy is now

$$\delta E = 2500^{1/3} (\hbar\omega_0)^{1/3} \left(\mathbf{a} \cdot c \frac{d\mathbf{P}}{da} \right)^{2/3} N_0^{2/3}. \quad (139)$$

In the case of a monatomic crystal this becomes (again assuming alignment)

$$\delta E = 1250^{1/3} (M c^2)^{1/3} |\mathbf{a}|^{2/3} (\hbar\omega_0)^{2/3} \left(\frac{N_0^2}{N} \right)^{1/3}. \quad (140)$$

We will see in the next section that this constraint is much easier to satisfy for keV quanta, and that we might understand collimated X-ray emission in the Karabut experiment in terms of a very similar constraint derived for the donor and receiver model.

7.7. Simple monatomic crystal threshold condition

If we adapt the general threshold condition above for a simple monatomic crystal, we find that it can be written in the form

$$4 \times 10^{-4} \leq \frac{1}{4} \frac{1}{(\Delta n)^3} \times \begin{cases} n_0 \frac{r}{\sqrt{1-r^2}}, & r < 1, \\ \frac{1}{4} \left(\frac{N_0 \Delta M c^2}{\hbar\omega_0} \right) r \sqrt{\frac{r^2-1}{r^2+1}}, & r > 1, \end{cases} \quad (141)$$

where the ratio r is defined according to

$$r = 4|\mathbf{a}|^2 \frac{M c^2}{\Delta M c^2} \frac{N_0}{N}. \quad (142)$$

Before proceeding, we would like to draw attention to this version of the fractionation constraint for a number of reasons. The basic lossy spin–boson model under discussion is reasonably complicated, especially when we take into account

all three of the constraints; so to obtain an approximate version of the threshold constraint in such a simple form was unexpected. Additionally, we see that this threshold condition depends only on four basic parameters of the system: the number of phonons present n_0 ; the number of phonons Δn produced by the fractionation of the large quantum; the ratio r which depends on the \mathbf{a} matrix element, and which determines whether the system is in the conventional or anomalous regime; and finally the number of virtual phonons

$$\frac{N_0 \Delta M c^2}{4 \hbar \omega_0}.$$

We see from this that when r is less than unity, the system is in the conventional regime, and the threshold constraint becomes

$$\frac{1}{4} \frac{r}{(\Delta n)^3} n_0 \geq 4 \times 10^{-4}, \quad r \ll 1. \quad (143)$$

To reach the threshold in this regime, the number of phonons needs to be increased to satisfy

$$n_0 \geq 1.6 \times 10^{-3} \frac{(\Delta n)^3}{r}, \quad r \ll 1. \quad (144)$$

In the anomalous regime the threshold condition is

$$\frac{1}{4} \frac{r}{(\Delta n)^3} \left(\frac{N_0 \Delta M c^2}{4 \hbar \omega_0} \right) \geq 4 \times 10^{-4}, \quad r \gg 1. \quad (145)$$

The threshold condition in the anomalous regime is similar in form to that of the conventional regime; we could write it in the form

$$\frac{1}{4} \frac{r}{(\Delta n)^3} n_V \geq 4 \times 10^{-4}, \quad r \gg 1, \quad (146)$$

where n_V is the number of virtual phonons

$$n_V = \frac{N_0 \Delta M c^2}{4 \hbar \omega_0}. \quad (147)$$

The coupling between the phonons and excited nuclei result in the generation of a large number of virtual phonons in the anomalous regime, as well as a large number of virtual excited nuclei. Roughly a quarter of all of the nuclei involved in the transition are excited in the anomalous regime in this model.

8. Theory and the Karabut Experiment

Back in 1989 we understood that the observation of excess heat in the Fleischmann–Pons experiment [1,2] probably implied that a large MeV quantum was being fractionated into a great many small quanta. This provided us with the motivation to seek models capable of efficient coherent energy exchange under conditions of fractionation, leading ultimately to the lossy spin–boson model. However, it was collimated X-ray emission in the Karabut experiment [23–28], which we interpreted as showing direct conversion of vibration to nuclear energy, that motivated us to explore the new condensed matter model with relativistic coupling to internal nuclear degrees of freedom [29–31].

Once the new theory had gone through a preliminary development, we applied it to a model corresponding to our interpretation of the Karabut experiment, and found that the experimental conditions we estimated to be consistent with our interpretation were inconsistent with sufficient fractionation according to the model. This motivated us to seek stronger fractionation, first in the model of last summer [30] (which was found to be in error [31]), and then in fluctuations due to electron-phonon coupling [32] (which was found to be a small effect earlier in this paper). However, from the development of the previous sections we now understand that there can be a large enhancement in the fractionation power due to virtual phonon generation. This motivates us to revisit collimated X-ray emission in the Karabut experiment, to examine our earlier interpretation, and to suggest a new interpretation.

8.1. Fractionation by the 1565 eV transition in ^{201}Hg

Our earlier interpretation of the Karabut experiment focused on the 1565 eV transition in ^{201}Hg , which we proposed was present on the surface in small amounts. This transition is unique in that it is the lowest energy transition from a stable ground state nucleus. However, based on the discussion in the previous section, our attention is drawn to the fact that ^{201}Hg is present in the Karabut experiment as an impurity, so that

$$r = 4|\mathbf{a}|^2 \frac{Mc^2}{\Delta Mc^2} \frac{N_0}{N} \ll 1. \quad (148)$$

Although we do not have a value for the \mathbf{a} matrix element in this case, we can quantify what value would be needed to reach the anomalous regime; $r = 1$ for an impurity level of 10 ppm (and optimistically assuming that all of the ^{201}Hg is initially in the same spin state) when $|\mathbf{a}|$ satisfies

$$|\mathbf{a}_{\text{thresh}}| = \sqrt{\frac{1}{4} \frac{N}{N_0} \frac{\Delta Mc^2}{Mc^2}} \rightarrow \sqrt{\frac{1}{4} \left(\frac{1}{0.132 \cdot 10^{-5}} \right) \left(\frac{1565 \text{ eV}}{201 \text{ amu}} \right)} = 0.04. \quad (149)$$

This seems much too high to be plausible, so we conclude that ^{201}Hg as an impurity would fractionate in the conventional regime.

We can use the analysis of the previous section to determine what energy can be fractionated by the 1565 eV transition. Results are shown in Fig. 4. These results are interesting in the sense that we see threshold energies of more than 40 eV in the upper right corner, which is a highly nontrivial amount of fractionation power given that we are starting from $\hbar\omega_0 = 0.13 \mu\text{eV}$. On the other hand, clearly the transition is well short of the keV regime needed to be relevant to the experimental results. Our conclusion is that Hg on the surface or in the bulk as an impurity simply cannot fractionate a sufficiently large quantum to be relevant to the observed collimated X-ray emission. We note that there would be no problem with the 1565 eV transition being the source of the radiation as long as fractionation is accomplished on some other transition (e.g., in a donor and receiver type of model).

8.2. Fractionation in the anomalous regime

Let us consider briefly a different experiment intended to access the anomalous regime, where Hg is no longer an impurity. Suppose that we consider a difficult physics experiment in which a frozen sample of isotopically pure ^{201}Hg is initialized in a single nuclear spin state; the magnitude of the $|\mathbf{a}|$ matrix element needed to reach the anomalous regime in this case is

$$|\mathbf{a}_{\text{thresh}}| = \sqrt{\frac{1}{4} \frac{N}{N_0} \frac{\Delta Mc^2}{Mc^2}} \rightarrow \sqrt{\frac{1}{4} \left(\frac{1565 \text{ eV}}{201 \text{ amu}} \right)} = 4.57 \times 10^{-5}. \quad (150)$$

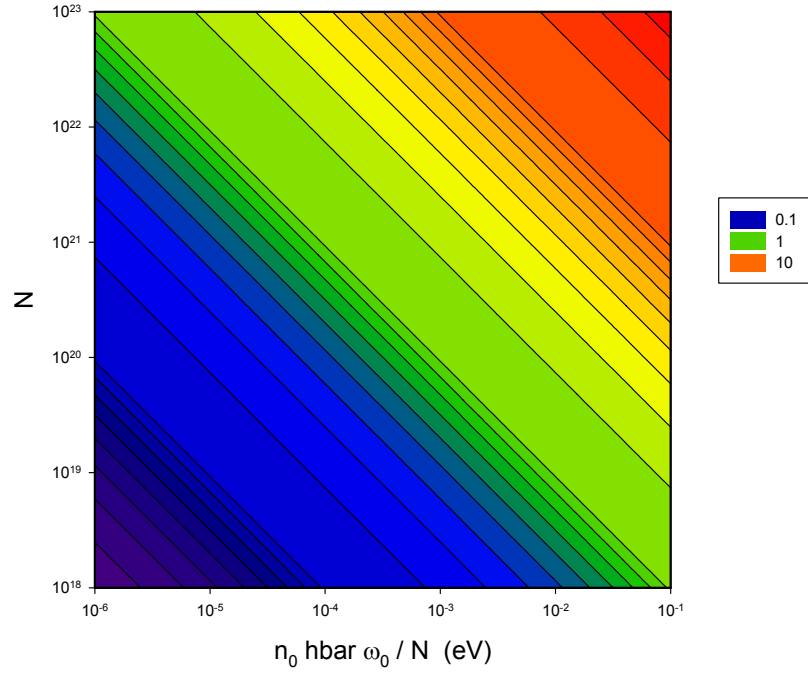


Figure 4. Threshold energy δE (eV) as a function of number of sample atoms and energy (eV) per atom; assumed for this calculation is $r = 10^{-6}$, a frequency $\omega_0/2\pi$ of 100 MHz, and a cathode material with a mass A close to 201.

As noted above the \mathbf{a} matrix element is not known at present; however, it seems to us that it is likely to be larger than this threshold value.

The fractionation energy δE in this case is shown in Fig. 5. We see that the fractionation energy is independent of how highly excited the lattice is (keeping in mind that it must be highly excited for the model to be relevant in the first place), and that a fractionation energy in the vicinity of 1565 eV in this example requires about 5×10^{17} nuclei.

8.3. Fractionation on other low-energy transitions

We are motivated from the discussion above to consider other low-energy nuclear transitions that occur in some of the isotopes which are not impurities in the cathodes. Our attention turns immediately to the case of Nb, which gave positive results in Karabut's experiment. This element is interesting because it has only a single stable isotope (^{93}Nb), and there is an M4 transition to a low-energy metastable state at 30.77 keV (which is a candidate transition for fractionation). We can determine a constraint on the \mathbf{a} matrix element to get into the anomalous regime

$$|\mathbf{a}_{\text{thresh}}| = \sqrt{\frac{1}{4} \frac{N}{N_0} \frac{\Delta M c^2}{M c^2}} \rightarrow \sqrt{\frac{1}{4} (9) \left(\frac{30.77 \text{ keV}}{93 \text{ amu}} \right)} = 8.94 \times 10^{-4}, \quad (151)$$

where we note that the ground state has a spin of 9/2 (and we consider for this estimate that each sub-level transition

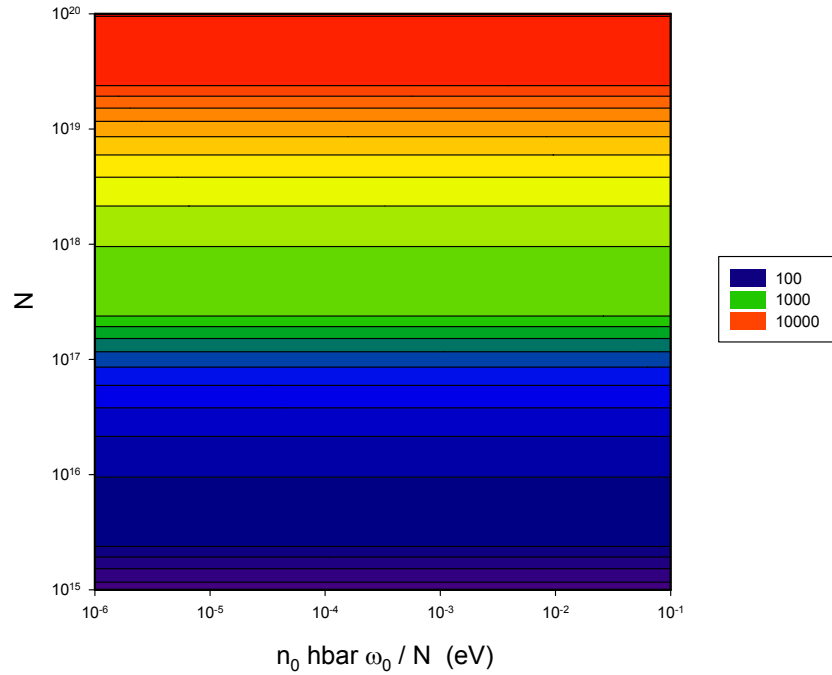


Figure 5. Threshold energy δE (eV) as a function of number of sample atoms and energy (eV) per atom; assumed for this calculation is $r = 2$, a frequency $\omega_0/2\pi$ of 100 MHz, and a cathode material with a mass A close to 201.

be considered independently). This threshold seems sufficiently low that there is a good chance that the 30.77 keV transition can exceed this value.

Let us suppose now that the 30.77 keV transition in ^{93}Nb can reach the anomalous regime; if so, then what kind of fractionation energy might we expect. Results are shown in Fig. 6. Since the longitudinal sound speed is 4.92×10^5 cm/s, a 25 μ thick cathode has a fundamental frequency at 98.4 MHz. For a cathode diameter of 1 cm, the total number of Nb atoms present is 1.1×10^{20} ; if we assume that about half of these nuclei experience motion sufficiently uniform to be accounted for by a Dicke model, then we estimate N to be about 5.5×10^{19} . From Fig. 6 we see that the fractionation energy δE is about 5 keV. This fractionation energy is too low to support efficient excitation of the 30.77 keV transition (consistent with experiment). From data presented by Karabut, we see that X-ray emission is seen up to about 4 keV in Nb [28], which we would expect to be consistent with the threshold fractionation energy (although the X-rays would not be from the 30.77 keV transition). The relation between threshold fractionation energy and number of nuclei participating in the transition (once r has been fixed) in the anomalous regime is

$$\delta E = \left[\frac{1}{(16)(4 \times 10^{-4})} r \sqrt{\frac{r^2 - 1}{r^2 + 1}} N_0 \right]^{1/2} \hbar \omega_0. \quad (152)$$

There is an E3 transition to a metastable state in ^{103}Rh at 39.73 keV, which does not seem to be among the cathode

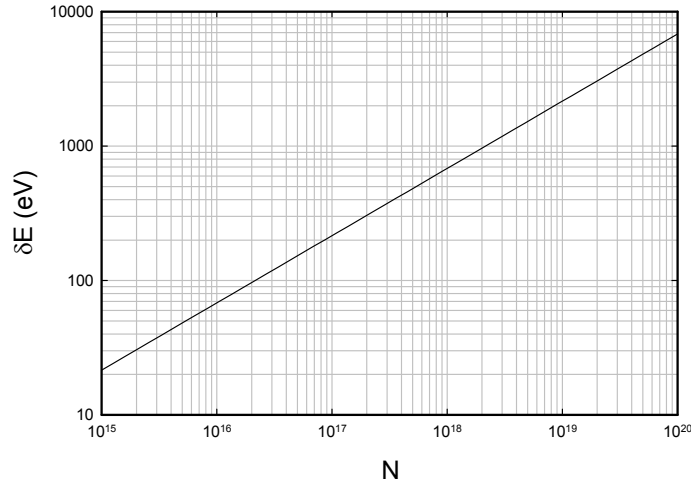


Figure 6. Threshold energy δE (eV) as a function of number of sample atoms and energy (eV) per atom; assumed for this calculation is $r = 2$, a frequency $\omega_0/2\pi$ of 100 MHz, and a cathode material made of Nb.

materials worked with by Karabut. A similar computation to what we did above leads to

$$|a_{\text{thresh}}| = \sqrt{\frac{1}{4} \frac{N}{N_0} \frac{\Delta M c^2}{M c^2}} \rightarrow \sqrt{\frac{1}{4} (2) \left(\frac{39.73 \text{ keV}}{102 \text{ amu}} \right)} = 4.57 \times 10^{-4}. \quad (153)$$

This threshold **a** matrix value is even lower, and may be consistent with anomalous regime operation.

8.4. Donor and receiver model

We proposed the donor and receiver model [40] to account for fractionation in the case of excess heat production. In this model, the donor transition is assumed to be weakly coupled to the highly excited phonon mode, consistent with the weakness of the $D_2/{}^4\text{He}$ transition on account of hindrance by the Coulomb barrier. Since the donor transition in this case is much too weak to fractionate a large quantum, we proposed that a second much stronger transition was present which would fractionate the large quantum in the donor and receiver model. Subsequently, we have noted that this model has wider applicability to any situation where strong and weak transitions are coupled to the same highly excited phonon mode.

In light of the discussion above, we are motivated to apply the model to lattice-induced excitation in the Karabut experiment. The weakly coupled transition in this case is the 1565 eV transition in ${}^{201}\text{Hg}$ present as an impurity. The strongly coupled transition is as yet unidentified, except perhaps in the case of ${}^{93}\text{Nb}$ where we can identify a plausible candidate. However, we can take advantage of an important feature of the models described above; if a transition makes it into the anomalous regime, then the response is pretty much fixed independent of the details of the transition. We can make use of this in an examination of the donor and receiver model with a receiver transition assumed to be in the anomalous regime.

From previous work, we know that the indirect coupling matrix element for the weakly coupled transition can be written as

$$\begin{aligned} \frac{V_1^{\text{eff}}}{(\Delta M c^2)_1} &= 2g_1 |\langle v_n | v_{n+\Delta n} \rangle_2| \\ &= 2 \frac{\left(\mathbf{a}_1 \cdot c \frac{d\mathbf{P}}{da} \right) \sqrt{n} \sqrt{S_1^2 - m_1^2}}{(\Delta M c^2)_1} |\langle v_n | v_{n+\Delta n_1} \rangle_2|. \end{aligned} \quad (154)$$

The indirect coupling matrix element is determined by the dimensionless coupling parameter associated with the weak transition, and an overlap matrix element that depends on the strongly coupled transition. This overlap matrix element serves as a hindrance factor that depends on the ability of the strongly coupled transition to fractionate the large quantum associated with the receiver transition.

In the pulse and amplitude approximation [39] we can use the pulse to approximate

$$|\langle v_n | v_{n+\Delta n_1} \rangle_2| \rightarrow |\langle u_n | u_{u+\Delta n_1} \rangle_2|. \quad (155)$$

If we further make a continuum approximation, then

$$|\langle u_n | u_{u+\Delta n_1} \rangle_2| \rightarrow \left| \left\langle u(z) \left| u \left(z + \frac{\Delta n_1}{\Delta n_2} \right) \right\rangle_2 \right|. \quad (156)$$

Since the continuous $u(z)$ are well approximated by Airy functions, we can evaluate the overlap matrix element using [38]

$$\left| \left\langle u(z) \left| u \left(z + \frac{\Delta n_1}{\Delta n_2} \right) \right\rangle_2 \right| \rightarrow f \left(\frac{\Delta n_1}{(2g_u)_2^{1/3}} \right), \quad (157)$$

where the function $f(y)$ is defined according to

$$f(y) = \frac{\int_{-2.33810}^{\infty} \text{Ai}(x) \text{Ai}(x+y) dx}{\int_{-2.33810}^{\infty} \text{Ai}^2(x) dx}. \quad (158)$$

This function is illustrated in Fig. 7.

As before, it seems useful to define a threshold fractionation energy for the strongly coupled transition. We might adopt a constraint of the form

$$\frac{\Delta n_1}{(2g_u)_2^{1/3}} \leq 10. \quad (159)$$

This can be compared to the constraint above for lattice-induced nuclear excitation, which can be recast as

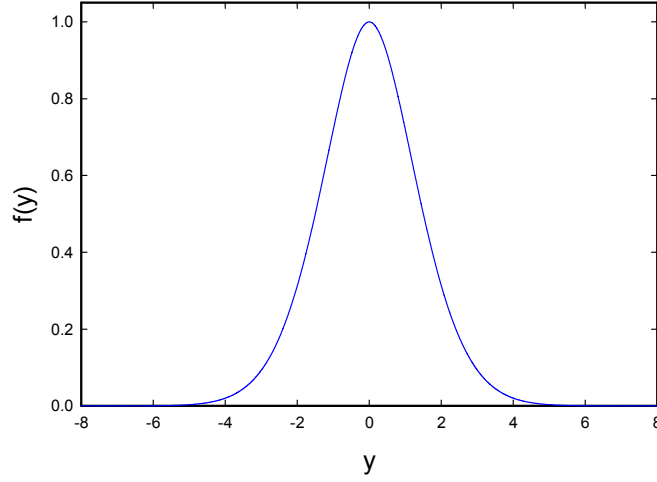


Figure 7. Plot of $f(y)$ as a function of y .

$$\frac{\Delta n}{(2g_u)^{1/3}} \leq \left(\frac{1}{4 \times 10^{-4}} \right)^{1/3} = 13.57. \quad (160)$$

We see from this that the fractionation threshold energy for a transition in lattice-induced nuclear excitation is essentially the same fractionation threshold energy when it serves as the strongly coupled transition in a donor and receiver scheme.

We can rewrite the donor and receiver constraint assuming that the strongly coupled transition is in the anomalous regime using

$$(g_u)_2 = \frac{\left(\mathbf{a}_2 \cdot c \frac{d\mathbf{P}}{da} \right) \left\langle \sqrt{S_2^2 - m_2^2} \langle \sqrt{n} \rangle \right\rangle}{\hbar \omega_0}. \quad (161)$$

In the anomalous regime we can write

$$\begin{aligned} \left\langle \sqrt{S^2 - m^2} \langle \sqrt{n} \rangle \right\rangle &\rightarrow \frac{1}{4} \sqrt{n_0 N_0} \frac{N_0}{\sqrt{N_c}} \sqrt{\frac{1 - \left(\frac{\sqrt{N_c}}{4\gamma_d} \right)^2}{1 + \left(\frac{\sqrt{N_c}}{4\gamma_d} \right)^2}} \\ &= \frac{\sqrt{n_0} N_0^{3/2}}{16\gamma_d} r \sqrt{\frac{r^2 - 1}{r^2 + 1}}, \end{aligned} \quad (162)$$

which leads to

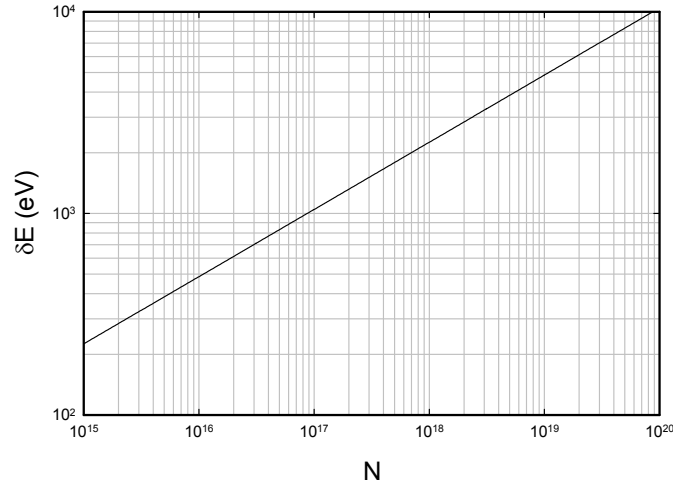


Figure 8. Threshold energy δE (eV) for a donor and receiver model, with the 30.77 keV transition in ^{93}Nb as the strongly coupled transition, and the 1565 eV transition in ^{201}Hg as the weakly coupled transition, as a function of number of sample atoms and energy (eV) per atom; assumed for this calculation is $r = 2$, a frequency $\omega_0/2\pi$ of 100 MHz, and a cathode material made of Nb (with Hg as an impurity).

$$(g_u)_2 \rightarrow \frac{1}{16} \left(\frac{\Delta M c^2}{\hbar \omega_0} N_0 r \sqrt{\frac{r^2 - 1}{r^2 + 1}} \right)_2, \quad r_2 > 1. \quad (163)$$

We can use this to recast the threshold constraint for transitions on the weakly coupled system in terms of a threshold fractionation energy

$$\delta E = 5 \left(\frac{\Delta M c^2}{\hbar \omega_0} N_0 r \sqrt{\frac{r^2 - 1}{r^2 + 1}} \right)_2^{1/3} \hbar \omega_0 \geq (\Delta M c^2)_1. \quad (164)$$

This constraint is illustrated in Fig. 8. We see that the threshold for excitation of the ^{201}Hg transition is about 3×10^{17} Nb atoms.

The models considered so far have primarily been concerned with coherent dynamics, but there should be no difficulty extending them slightly for excitation of the ^{201}Hg transition and subsequent superradiant decay. In this case, the energy transferred from the strongly coupled transition could go into exciting the ^{201}Hg 1565 eV transition off of resonance, with the total transferred energy emitted as an X-ray. The same constraints should apply in this case as well, so that collimated X-ray radiation up to a few keV would be expected, consistent with experiment [28].

9. Summary and Conclusions

As outlined in the Introduction and in subsequent sections, the Fleischmann–Pons experiment motivated us to consider mechanisms through which a large quantum could be fractionated, and led to the lossy spin–boson model and the

generalization to the donor and receiver model. Similarly, collimated X-rays in the Karabut experiment motivated us to seek stronger coupling between vibrational and nuclear degrees of freedom, which led to the new relativistic theory under discussion in this work.

Once we had the new relativistic theory, we had expected it to make sense out of the Karabut experiment and other anomalies. However, when we applied it to our interpretation of the Karabut experiment, the results were discouraging. This led to an effort last year to seek an enhancement of the fractionation effect due to coupling with very strong static transitions, resulting in a model that agreed reasonably well with experiment but contained an internal error. This also led to a substantial effort to include phonon fluctuations due to coupling with conduction electrons in metals. We found in this work that phonon fluctuations from the Bloch model are small compared to phonon fluctuations induced by phonon–nuclear coupling on dynamic transitions.

All of this brought us back to reconsider the basic model once more, this time more systematically than in previous work. The analyses of early last year focused on using the pulse and amplitude approximation on the phonon distribution in the local approximation, and did not lead to agreement with experiment. In this work we described the associated models in more detail than was done in previous publications. However, this time we considered a self-consistent model for the nuclear excited state distribution, including the possibility that the number of virtual phonons might be large. Although we had constructed models for the nuclear excited state distribution previously, we had not imagined that so many virtual phonons might be present.

This new self-consistent model for the nuclear excited state distribution showed clearly that there are two basic regimes. In the conventional regime, the excited state distribution closely resembles what one would obtain with simple static coupling. The fractionation of a large quantum in the conventional regime is difficult in the sense that a large number of nuclei are needed, and the system has to be driven very hard. In the anomalous regime, the number of virtual phonons can exceed the number of real phonons, and the increased coupling strength that results from these additional phonons has a profound impact on the nuclear excited state distribution. The fractionation of a large quantum in the anomalous regime is very much easier, and depends on the number of nuclei present and the mode frequency. Since the number of virtual phonons in this regime can be large, fractionation becomes independent of the number of real phonons (except that enough must be present for the highly excited mode to avoid interference from all the other modes).

With this new analysis, we returned once again to the problem of collimated X-ray emission in the Karabut experiment. In earlier work we had interpreted the experiment (erroneously) as showing coherent energy exchange between vibrations and nuclear excitation due to fractionation on the 1565 eV transition in ^{201}Hg as an impurity. As discussed above, a transition in an impurity at low concentration is most like going to fall into the conventional regime, and we find (as we have found before) that the fractionation strength of the 1565 eV transition is just too low to be relevant to the experimental results. However, a frozen mercury sample with enough ^{201}Hg nuclei initialized in the same nuclear spin state would very likely make it into the anomalous regime. Vibrational excitation in the 100 MHz regime of the fundamental resonance of a thin sample would be a very interesting, although perhaps technically challenging.

We applied the model to the 30.77 keV transition in ^{93}Nb , and developed a constraint on the \mathbf{a} matrix element for the system to be in the anomalous regime; our conclusion from this is that there is a substantial likelihood that the transition can make it. If so, the question is whether coherent dynamics would be expected under the conditions of the Karabut experiment. We concluded that the threshold fractionation energy in this case is lower than what would be needed, which is consistent with the absence of strong collimated emission at 30.77 keV in the experiment.

On the other hand, if the 30.77 keV transition can operate in the anomalous regime, then one would expect it to be able to fractionate large quanta to support coherent dynamics on the 1565 eV transition, in a donor and receiver model. The threshold fractionation energy for lattice-induced nuclear excitation is pretty much the same as for fractionation in a donor and receiver model (as expected since the hard part of both models is the fractionation of the same quantum), so while the 30.77 keV transition may not be able to fractionate a 30.77 keV quantum in the Karabut experiment, it should be able to fractionate large quanta up to about 5 keV. This corresponds well to the nearly 4 keV quanta observed

in collimated emission with a Nb cathode by Karabut.

Karabut sees collimated emission with a variety of different metal cathodes. In all cases, we would expect the 1565 eV ^{201}Hg transition to be on the receiving end of the converted vibrational energy in a donor and receiver kind of model, present as an uncontrolled impurity at low levels. However, in these cases we do not have an identification of the strongly coupled transition in the host cathode lattice. Since the fractionation energy depends weakly on the details of the transition once the system is in the anomalous regime, we have some ability to apply the model in these cases. Perhaps the biggest implication is that for the collimated emission to occur, there must be at least one transition that operates in the anomalous regime (even if we don't know which transition). Karabut's experiment interpreted in this way provides the important result that many metals have such transitions, suggesting that they are reasonably common. It will remain for future work to develop estimates for **a** matrix element from nuclear structure models. However, if controlled experiments can be developed that show collimated X-ray emission, then we should be able to extract equivalent information directly from experiment.

To date **a** matrix elements have been calculated for transitions in the deuteron [41], and for the $\text{D}_2/{}^4\text{He}$ transition [42]. In the case of the deuteron transition, the magnitude of the **a** matrix element was estimated to be about 3×10^{-3} , which is too small for anomalous regime operation, since

$$r = 4|\mathbf{a}|^2 \frac{Mc^2}{\Delta Mc^2} \frac{N_0}{N} \rightarrow 4(3 \times 10^{-3})^2 \left(\frac{2 \text{ amu}}{127 \text{ MeV}} \right) \left(\frac{1}{3} \right) = 1.76 \times 10^{-4}. \quad (165)$$

However, it may be that the **a** matrix element in this case might be too low, since in the computation it was presumed that the proton and neutron act as Dirac particles (for the reduction of the α matrices). We know that the proton and neutron are instead composites (and not Dirac particles), and that we should probably take this into account in calculating the **a** matrix element. To be philosophically consistent with our fundamental Hamiltonian of Eq. (1), perhaps we should think instead of a model for the deuteron based instead on

$$\hat{H} = \mathbf{M}_n c^2 + \mathbf{a}_n \cdot c\hat{\mathbf{P}}_n + \mathbf{M}_p c^2 + \mathbf{a}_p \cdot c\hat{\mathbf{P}}_p + \hat{V}_{np}. \quad (166)$$

One motivation for such a consideration is that excess heat in the Fleischmann–Pons model would seem to make sense if transitions in the deuteron could fractionate the large quantum. We might expect an increase on the general order of the ratio of the proton to quark mass, which might be sufficient to allow the system to make it into the anomalous regime. One wonders where transitions to negative energy states might be relevant, as long as real transitions are not allowed (there should be no problem with virtual transitions).

More relevant to the discussion in this paper is the issue of how the different elements used by Karabut might fractionate in the anomalous regime, since for most there are not obvious low-energy transitions available. Based on our experience with the deuteron, we know that it is problematic to develop a large **a** matrix element; yet, if our new interpretation of the Karabut experiment is correct, then somehow this it is not a rare occurrence. To address this issue systematically, we would imagine making use of a nuclear model based on

$$\hat{H} = \sum_j \left(\mathbf{M} c^2 + \mathbf{a} \cdot c\hat{\mathbf{P}} \right)_j + \sum_{j < k} \hat{V}_{jk}. \quad (167)$$

Although easily stated, the development of such models would take considerable effort.

Although we have not pursued the issue in this work, we note that the scaling laws are very favorable for fractionation with smaller number of nuclei in the THz regime, which is where we think that fractionation occurs in the Fleischmann–Pons experiment.

References

- [1] M. Fleischmann, S. Pons and M. Hawkins, *J. Electroanal. Chem.* **201** (1989) 301; errata **263** (1990) 187.
- [2] M. Fleischmann, S. Pons, M.W. Anderson, L.J. Li and M. Hawkins, *J. Electroanal. Chem.* **287** (1990) 293.
- [3] E. Storms, *Science of Low Energy Nuclear Reaction: A Comprehensive Compilation of Evidence and Explanations about Cold Fusion*, World Scientific, New Jersey, 2004.
- [4] B.F. Bush, J.J. Lagowski, M.H. Miles and G.S. Ostrom, Helium production during the electrolysis of D₂O in cold fusion, *J. Electroanal. Chem.* **304** (1991) 271.
- [5] M.H. Miles and B. Bush, Search for anomalous effects during D₂O Electrolysis using palladium cathodes, *Proc. ICCF3* (1992) 189.
- [6] M.H. Miles, R.A. Hollins, B.F. Bush, J.J. Logowski and R.E. Miles, Correlation of excess power and helium production during D₂O and H₂O electrolysis using palladium cathodes, *J. Electroanal. Chem.* **346** (1993) 99.
- [7] M.H. Miles, B. Bush and J.J. Lagowski, Anomalous effects involving excess power, radiation and helium production during D₂O electrolysis using palladium cathodes, *Fusion Technol.* **25** (1994) 478.
- [8] P.L. Hagelstein, M.C.H. McKubre, D.J. Nagel, T.A. Chubb and R.J. Hekman, New physical effects in metal deuterides, *Proc. ICCF11* (2004) 23.
- [9] P.L. Hagelstein, Constraints on energetic particles in the Fleischmann–Pons experiment, *Naturwissenschaften* **97** (2010) 345.
- [10] F. Bloch and A. Siegert, Magnetic resonance for nonrotating fields, *Phys. Rev.* **57** (1940) 522.
- [11] J. Shirley, Solution of the Schrödinger equation with a Hamiltonian periodic in time, *Phys. Rev.* **138** (1965) B979.
- [12] C. Cohen-Tannoudji, J. Dupont-Roc and C. Fabre, A quantum calculation of the higher order terms in the Bloch–Siegert shift, *J. Phys. B: Atom. Molec. Phys.* **6** (1973) L214.
- [13] P.L. Hagelstein and I.U. Chaudhary, Level splitting in association with the multiphoton Bloch–Siegert shift, *J. Phys. B: At. Mol. Phys.* **41** (2008) 035601.
- [14] P.L. Hagelstein and I.U. Chaudhary, Models relevant to excess heat production in Fleischmann–Pons experiments, *Low-energy nuclear reactions sourcebook ACS Symp. Ser.* **998** (2008) 249.
- [15] P.L. Hagelstein, A unified model for anomalies in metal deuterides, *Proc. ICCF9* (2002) 121.
- [16] P.L. Hagelstein and I.U. Chaudhary, Energy exchange in the lossy spin–boson model, *J. Cond. Mat. Nucl. Sci.* **5** (2011) 52.
- [17] H. Feshbach, A unified theory of nuclear reactions, II *Ann. Phys.* **19** (1962) 287.
- [18] P.L. Hagelstein and I.U. Chaudhary, Second-order formulation and scaling in the lossy spin–boson model, *J. Cond. Mat. Nucl. Sci.* **5** (2011) 87.
- [19] P.L. Hagelstein and I.U. Chaudhary, Local approximation for the lossy spin–boson model, *J. Cond. Mat. Nucl. Sci.* **5** (2011) 102.
- [20] P.L. Hagelstein and I.U. Chaudhary, Coherent energy exchange in the strong coupling limit of the lossy spin–boson model, *J. Cond. Mat. Nucl. Sci.* **5** (2011) 116.
- [21] P.L. Hagelstein and I.U. Chaudhary, Errata and comments on a recent set of papers in *J. Condensed Matter in Nucl. Sci.*, *J. Cond. Mat. Nucl. Sci.* **7** (2012) 1.
- [22] P.L. Hagelstein, Bird's eye view of phonon models for excess heat in the Fleischmann–Pons experiment, *J. Cond. Mat. Nucl. Sci.* **6** (2011) 169.
- [23] A.B. Karabut, Research into powerful solid X-ray laser (wave length is 0.8–1.2nm) with excitation of high current glow discharge ions, *Proc. 11th Int. Conf. on Emerging Nuclear Energy Systems*, 29 September–4 October 2002, Albuquerque, New Mexico, USA, pp. 374–381.
- [24] A.B. Karabut, Experimental research into characteristics of X-ray emission from solid-state cathode medium of high-current glow Discharge, *Proc. 10th Int. Conf. on Cold Fusion*, August 24–29, 2003, Cambridge, MA, USA.
- [25] A.B. Karabut, Research into characteristics of X-ray emission laser beams from solid-state cathode medium of high current glow discharge, *Proc. 11th Int. Conf. on Cold Fusion*, 31 October–5 November, France, 2004, pp. 253–257.
- [26] A.B. Karabut, Study of energetic and temporal characteristics of x-ray emission from solid state cathode medium of high current glow discharge, *Proc. 12th Int. Conf. on Cold Fusion*, December 2–7, 2006, Japan, pp. 344–350.
- [27] A.B. Karabut, E.A. Karabut, Research into energy spectra of X-ray emission from solid cathode medium during the high current glow discharge operation and after the glow discharge current switch off, *Proc. 14th Int. Conf. on Cold Fusion*, August

- 10–15, 2008, USA.
- [28] A.B. Karabut, E.A. Karabut and P.L. Hagelstein, Spectral and temporal characteristics of X-ray emission from metal electrodes in a high-current glow discharge, *J. Cond. Mat. Nucl. Sci.* **6** (2012) 217.
 - [29] P.L. Hagelstein and I.U. Chaudhary, Including nuclear degrees of freedom in a lattice Hamiltonian, *J. Cond. Mat. Nucl. Sci.* **7** (2011) 35.
 - [30] P.L. Hagelstein and I.U. Chaudhary, A model for collimated emission in the Karabut experiment, *Proc. ICCF17* (in press).
 - [31] P.L. Hagelstein and I.U. Chaudhary, Phonon–nuclear coupling for anomalies in condensed matter nuclear science, *J. Cond. Mat. Nucl. Sci.*, submitted.
 - [32] P.L. Hagelstein and I.U. Chaudhary, Born–Oppenheimer and fixed-point models for second-order phonon exchange in a metal, *J. Cond. Mat. Nucl. Sci.*, submitted.
 - [33] J.M. Ziman, The electron-phonon interaction, according to the adiabatic approximation, *Math. Proc. Cambridge Philosophical Soc.* **51** (1955) 707.
 - [34] J.C. Taylor, The electron–phonon interaction, according to the adiabatic approximation, *Math. Proc. Cambridge Philosophical Soc.* **52** (1956) 693.
 - [35] L.J. Sham and J.M. Ziman, The electron–phonon interaction, *Solid State Phys.* **15** (1963) 221.
 - [36] S.K. Joshi and A.K. Rajagopa, Lattice dynamics of metals, *Solid State Phys.* **22** 159 (1969).
 - [37] G. Mahan, *Many-Particle Physics*, Plenum Press, New York, 1990.
 - [38] P.L. Hagelstein and I.U. Chaudhary, Lossy spin–boson model with an unstable upper state and extension to N-level systems, *J. Cond. Mat. Nucl. Sci.* **11** 59 (2013).
 - [39] P.L. Hagelstein and I.U. Chaudhary, Pulse and amplitude approximation for the lossy spin–boson model, *J. Cond. Mat. Nucl. Sci.* **9** 30 (2012).
 - [40] P.L. Hagelstein and I.U. Chaudhary, Generalization of the lossy spin–boson model to donor and receiver systems, *J. Cond. Mat. Nucl. Sci.* **5** 140 (2011).
 - [41] P.L. Hagelstein and I.U. Chaudhary, Coupling between a deuteron and a lattice, *J. Cond. Mat. Nucl. Sci.* **9** 50 (2012).
 - [42] P.L. Hagelstein and I.U. Chaudhary, Central and tensor contributions to the phonon-exchange matrix element for the $D_2/{}^4\text{He}$ transition, *J. Cond. Mat. Nucl. Sci.* **11** 15 (2013).



Research Article

Isotope Effect for Heat Generation upon Pressurizing Nano-Pd/Silica Systems with Hydrogen Isotope Gases

Tatsumi Hioki *, Noriaki Sugimoto, Teppei Nishi, Akio Itoh and Tomoyoshi Motohiro

Toyota Central R & D Laboratories Inc., Japan

Abstract

The isotope effect for heat generation upon pressurization with hydrogen isotope gases was clearly observed in a reproducible manner for nano-Pd/silica systems. For Pd/zeolite, the isotope effect decreased with increasing cycle of pressurization and almost disappeared at several cycles, whereas the effect was observed up to 15 cycles or more for Pd/FSM. Pd particles with sizes less than 2 nm are suggested to be essential for the isotope effect to be clearly observable.

© 2014 ISCMNS. All rights reserved. ISSN 2227-3123

Keywords: Heat, Isotope effect, Nano-palladium, Porous silica

1. Introduction

Arata and Zhang have reported that the heat arising from nuclear fusion reaction in solid is observed simply by pressurizing a nano-Pd/ZrO₂ system with deuterium gas [1]. Nano-sized Pd particles have been expected to absorb sufficient deuterium to induce low energy nuclear phenomena. Actually, a high value of hydrogen absorption capacity has been reported for the nano-Pd/ZrO₂ system [2].

Similar experiments with that by Arata and Zhang have been performed in several laboratories [3–6]. Kitamura et al. have constructed a twin type flow calorimeter and have measured quantitatively the heat generated upon pressurizing a nano-Pd/ZrO₂ system synthesized by Santoku Corporation [5]. They have observed a remarkable difference in the heat evolution between deuterium and hydrogen, i.e., a clear isotope effect for heat, which seems to support strongly the claim by Arata and Zhang. They have also reported a D/Pd or H/Pd ratio of 1.1, which far exceeds the literature value of 0.7 for Pd bulk [5].

Using a flow calorimeter, we have measured the heat generation for nano-Pd powder obtained from Tanaka Kikinzoku Kogyo, nano-Pd / γ -Al₂O₃ synthesized by us [6] and nano-Pd/ZrO₂ [7] obtained from Santoku Corporation. However, we have not observed any clear isotope effect for the heat with pressurization. Using Sievert's method, we have also measured hydrogen absorption capacity of these nano-Pd systems and have obtained values of H/Pd not exceeding that

*E-mail: l6908@mosk.tytlabs.co.jp

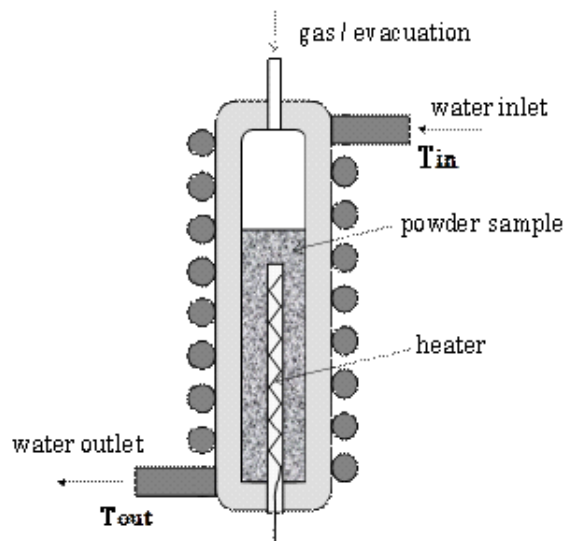


Figure 1. Schematic of the calorimeter.

of Pd bulk. Since nano-Pd particles are easy to coalesce and grow once they are exposed to hydrogen environment, it is not easy to pressurize nano-Pd systems keeping the initial size of the Pd particles. In this context, it should be mentioned that the nano-Pd/ZrO₂ powder used by Arata and Zhang may be different from the powders of Santoku Corporation, because the nano-Pd particles in Arata's sample seem to be embedded in ZrO₂ matrix, thus may be difficult to grow upon exposure to hydrogen. The growth of nano-Pd particles may be considerably suppressed if the particles are inside the pores of porous matrices. Kidwell et al. have used zeolite and γ -Al₂O₃ as porous matrices and observed a large, reproducible isotope effect for the heat using the porous matrices dispersed with small concentrations of Pd [8].

In this study, as the porous matrices we have used two silica's: zeolite and FSM (Folded Sheet Mesoporous silica) [9] with pores of about 1 nm and 1.5–2 nm, respectively. A clear isotope effect for heat with pressurization has been observed for both Pd/zeolite and Pd/FSM systems in a reproducible manner.

2. Experimental

2.1. Materials

The samples used in this study were 5.0 wt% Pd/ zeolite and 9.85 wt% Pd/FSM. Zeolite powder of Y-type (Faujasite) was obtained from Toso Corporation. The composition was SiO₂/Al₂O₃ (mol/mol) = 5.5, Na₂O/ Al₂O₃ (mol/mol) = 1.0, and the size of the pore ~1.1 nm. The zeolite powder was dispersed with 5.0 wt% Pd by wet method using palladium nitrate.

Powder samples of FSM (3D-hexagonal type, P6₃/ mmc, pore size; 1.5–2 nm) synthesized in our laboratory were dispersed with 9.85 wt% Pd by wet method using palladium chloride.

2.2. Calorimetry

The heat generation with loading of hydrogen isotope gases was measured with a flow calorimeter. Figure 1 shows the schematic of the calorimeter.

The volume of the sample vessel was about 50 cm³. The difference in the temperature between the inlet (T_{in}) and outlet (T_{out}) of the cooling water was measured with thermocouples of alumel-chromel. The flow rate of water was measured using a Coriolis-force type flow meter. The temperature difference, $T_{out} - T_{in}$, and the flow rate of water were recorded every 1–10 s and used to calculate the heat power. An electric heater was mounted at the center of the sample vessel and used to determine the recovery rate of heat, i.e. the ratio of the calculated heat power with the measured temperature difference and the flow rate of water to the heat power supplied by the electric heater. A value of 0.68 was used as the recovery rate, which was almost independent of the species of the gases (H₂, D₂, and He) used, of the gas pressure in the range 0–1 MPa, and of the electric heater power in the range of 1–5 W. In order to suppress the fluctuation and the drift of the measured output power, the calorimeter system was installed in a room of constant temperature. The accuracy of the calorimeter was ± 50 mW [6]. The gases were supplied into the sample vessel through a mass flow controller. The flow rate of the gas was about 20 ml/min.

3. Results

3.1. Heat measurement for 5 wt% Pd/zeolite

An as-synthesized 5 wt% Pd/zeolite sample of 30.7 g (Pd: 1.5 g) was loaded in the sample vessel of the calorimeter. The sample was first evacuated for two days at room temperature and heated up to 623 K in vacuum and maintained at the temperature for about 3 h, followed by natural cooling to room temperature. Then, deuterium gas was firstly supplied to the sample up to 1 MPa at room temperature (300K) and at a flow rate of 20 ml/min with a mass flow controller. When the pressure reached 1 MPa, the gas supply was stopped and the sample was maintained under the fixed pressure of 1 MPa for a period of about 1 h. Here, we define the first stage as the period where the pressure is raised from 0 to 1 MPa, the second stage as the period where the sample is maintained under the constant pressure of 1 MPa. The measurements of the heat power upon pressurizing with deuterium or hydrogen gases were repeated 16 times for the same sample without exposing the sample to air. Prior to each cycle of pressurization, the sample was always heat treated in vacuum at 623K for 3 h. The procedure of the heat measurements is shown in Fig. 2.

In Fig. 3, as a typical example, the heat power as a function of time is shown for the fourth cycle pressurization with deuterium gas. It is seen in Fig. 3 that the heat power rapidly increases as the supply of the gas is started, reaches a broad peak value, and then rapidly decreases followed by a small, nearly constant value. In the second stage, where the gas pressure is kept at 1 MPa, any heat power exceeding the detection limit is not observed.

From the variation of the gas pressure with time, the behavior of heat power is suggested to correlate with the palladium–hydrogen phase diagram; α -phase, coexisting phase of α - and β -phases, and β -phase, as shown in Fig. 3. This finding seems to indicate that the behavior of the heat power is dominantly caused by the metallic Pd particles at and after the second cycle.

The heat generated during pressurization is obtained by integrating the heat power in the first stage. Figure 4 shows the heat generated upon pressurizing the 5 wt% Pd /zeolite sample with hydrogen isotope gases up to 1 MPa as a function of pressurization cycle. In Fig. 4, the first cycle measurement was done with D₂, the second cycle was done again with D₂, the third cycle with H₂, and so forth.

It is seen in Fig. 4 that the heat generated in the first cycle is remarkably large. This is due to the fact that in the as-synthesized state, the nano-Pd particles are in the form of PdO. When the oxidized Pd particles are exposed to hydrogen isotope gases, they are reduced to metallic Pd. This chemical reaction produces a large amount of heat. After the first cycle, it is expected that Pd particles are in metallic state and the heat obtained at and after the second cycle

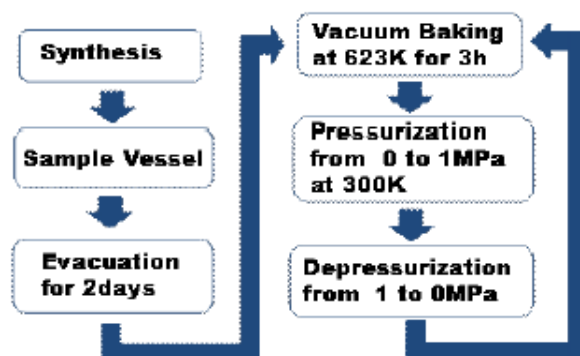


Figure 2. Procedure of the heat measurement.

pressurization is the heat for zeolite dispersed with *metallic* Pd.

It is noted in Fig. 4 that the heat generated with D₂ is clearly larger than the heat with H₂. This difference, i.e., the isotope effect for heat with pressurization is observed up to several cycles in a reproducible manner. However, the difference decreases with increasing cycle and no isotope effect is seen at increased number of cycles above around 7–10.

Figure 5 compares the TEM images for the sample before and after the 16-cycle's measurement. In the as-synthesized state, Pd particles exist inside the pores, although Pd particles are also seen on the surface of zeolite grains (Fig. 5(a)). As seen in Fig. 5(b), almost all the Pd particles seem to precipitate on the surface of the zeolite grains after the 16-cycle's heat measurement. The size of the precipitated Pd particles is about 10nm or more, which is much larger than the size

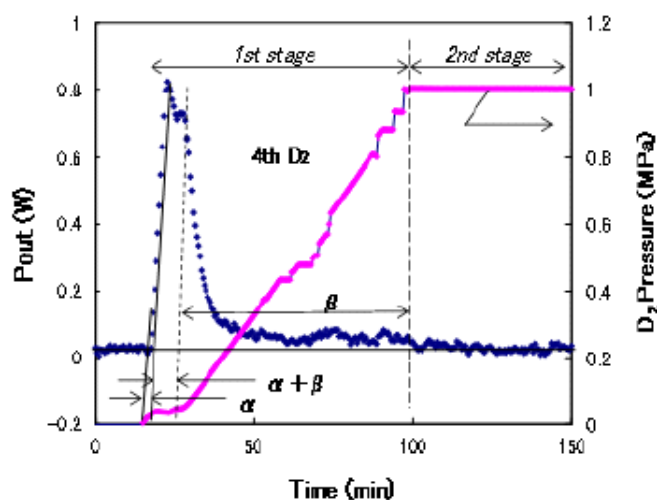


Figure 3. Heat power and gas pressure as a function of time for the fourth cycle pressurization with D₂ for 5 wt% Pd/zeolite.

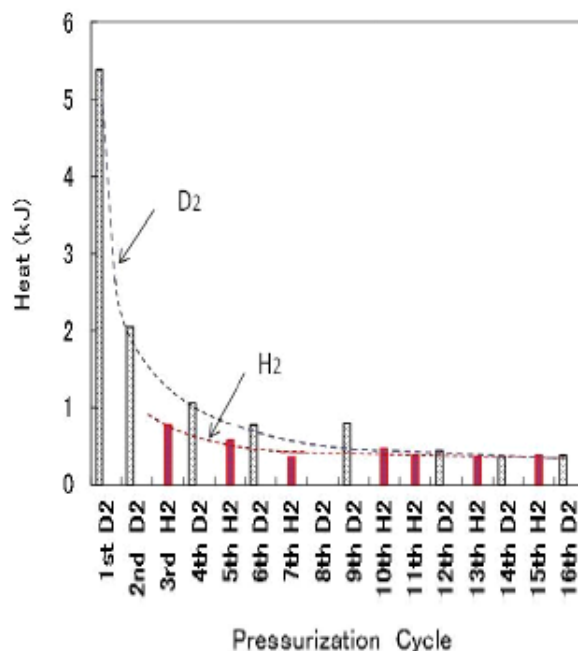


Figure 4. Heat as a function of pressurization cycle for 5 wt% Pd/zeolite.

of the pore of the zeolite ~ 1.1 nm.

3.2. Heat Measurement for Pd/FSM

Similar measurements were also performed for 9.85 wt% Pd/FSM. The measurements were repeated up to 15 cycles, following the same procedure shown in Fig. 2.

In Fig. 6, the heat generated with pressurization up to 1 MPa is plotted against pressurization cycle. The data of the first cycle is omitted in the figure, because the first cycle includes the heat of reduction for PdO. Prior to each measurement, the sample was always heat-treated in vacuum at 623 K for 3 h without exposing the sample to air.

It is seen in Fig. 6 that the heats with D₂ are clearly larger than those with H₂. Furthermore, the difference does not seem to become smaller with increasing cycle of measurement. The heat averaged over the cycles of D₂ pressurization is larger than the heat averaged over the cycles of H₂ by 29%.

Figure 7 compares the TEM images for the sample before and after the 15-cycle's measurement for heat with pressurization. In the as-synthesized state, Pd particles exist inside the pores of FSM. Some Pd particles with the size of several nm are also seen on the surface of the grains. As seen in Fig. 7(b), it is noted that Pd particles still stay inside the pores of FSM even after the 15-cycle's measurement. This is in contrast with the results for the 5 wt% Pd/zeolite sample.

4. Discussion

In Fig. 4, the isotope effect for heat is seen only up to several cycles of pressurization for the 5 wt% Pd/zeolite sample. At higher cycles, the heat with D_2 is almost equal to the heat with H_2 , i.e., no isotope effect is observed.

First, we consider the heat generation at the increased number of pressurization. As the possible mechanisms at the

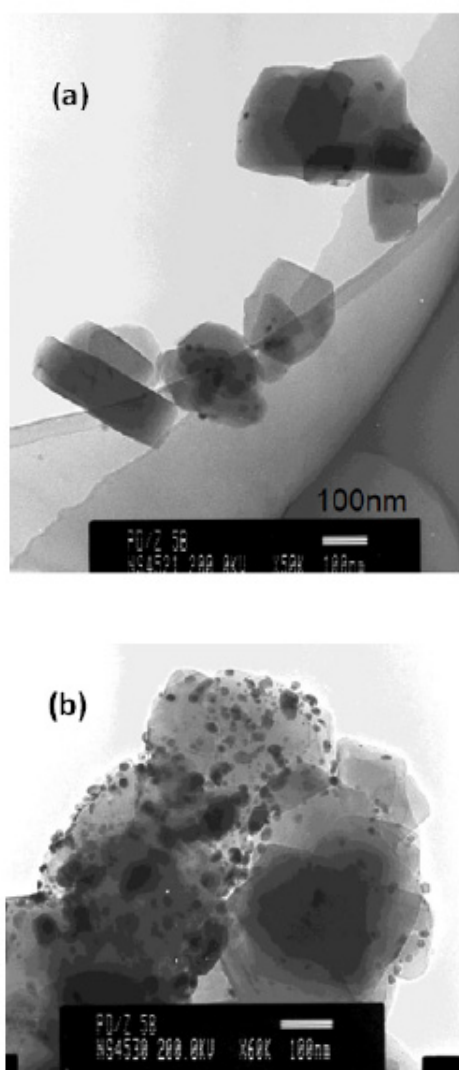


Figure 5. TEM images for 5 wt% Pd/zeolite: (a) as-synthesized and (b) after the 16 cycle's measurement of heat generation with pressurization. Dark spots are Pd particles.

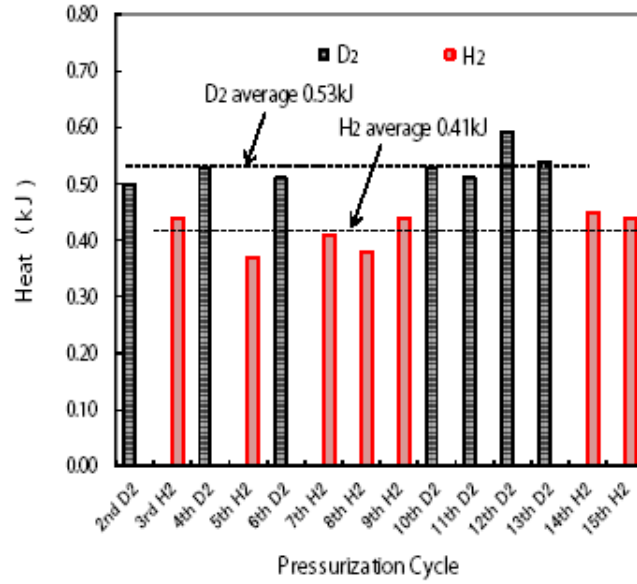


Figure 6. Heat as a function of pressurization cycle for 9.85 wt% Pd/FSM.

higher cycles, the followings are considered.

$$Q_{\text{out}}^{\text{hi-cycl}} = Q_{\text{abs}} + Q_{\text{ads}} + Q_{\text{mech}}. \quad (1)$$

Here, Q_{abs} is the heat of hydrogen absorption for Pd, i.e.,

$$\text{Pd} + 0.35 \text{H}_2 = \text{Pd H}_{0.7} - Q_{\text{abs}}, \quad (2)$$

Q_{ads} is the heat of hydrogen adsorption of zeolite matrix, Q_{mech} the mechanical work with pressurization by hydrogen/deuterium. It is known $Q_{\text{abs}} = 40 \text{ kJ/mol H}_2$ [10]. In the present study, we experimentally obtained Q_{ads} for pure zeolite using the calorimeter. We obtained $Q_{\text{ads}}(\text{H}_2) = 2.7 \text{ kJ/mol}$, and $Q_{\text{ads}}(\text{D}_2) = 2.9 \text{ kJ/mol}$. The mechanical work was also measured to be 1.15 J/cm^3 using the blank sample vessel. Using these values, Eq. (1) was estimated and compared in Table 1 to the experimental value averaged over higher cycles from 11th to 16th. The calculated value agrees to the experimental one, suggesting that Eq. (1) is good for zeolite at higher cycles, where almost no isotope effect is observed.

Next, we consider the heat at the first cycle where Pd is assumed to be in the state of PdO. We can assume that

$$Q_{\text{out}}^{\text{1st}} = Q_{\text{abs}} + Q_{\text{ads}} + Q_{\text{mech}} + Q_{\text{red}} + Q_{\text{liq-sol}}. \quad (3)$$

Table 1. Estimated and experimental heats at high cycles for 5 wt% Pd/zeolite sample (J).

	Q_{mech}	Q_{ads}	Q_{abs}	$Q_{\text{out}}^{\text{hi-cycl}}$
Estimation	44	130	198	372
Experiment				375

Here, Q_{red} is the heat of reduction for PdO, i.e.

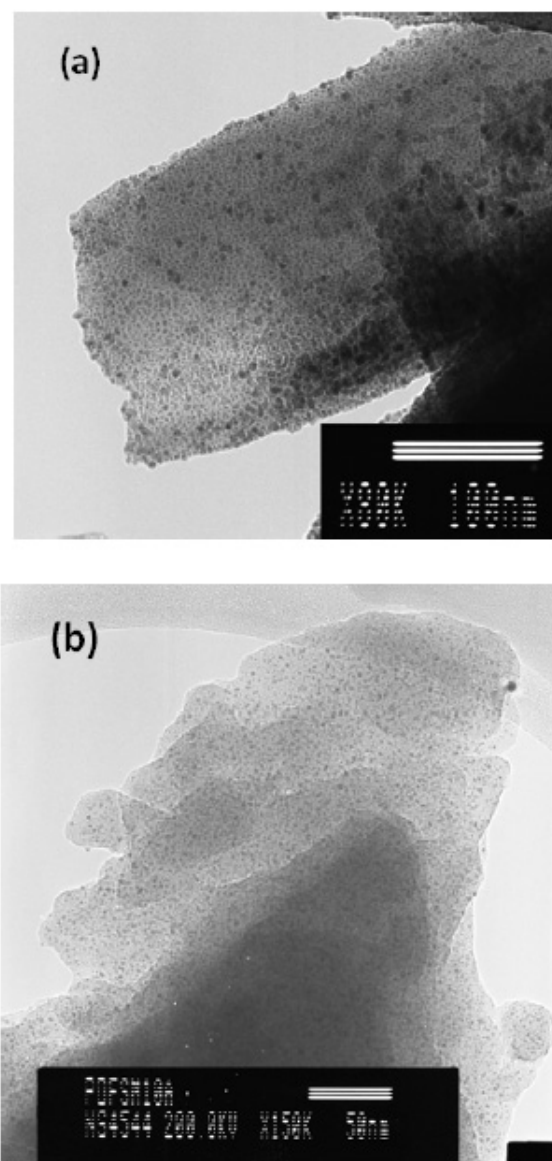
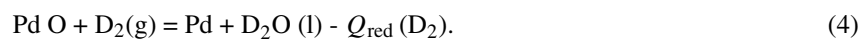


Figure 7. TEM images for 9.85 wt% Pd/FSM: (a) as-synthesized and (b) after the 15 cycle's measurement of heat generation. Dark spots are Pd particles.

Table 2. Estimated and experimental heats at the first cycle for 5wt% Pd/zeolite sample (J).

	Q_{mech}	Q_{ads}	Q_{abs}	Q_{red}	$Q_{\text{liq-sol}}$	$Q_{\text{out}}^{\text{1st}}$
Estimation	44	130	198	2520	707	3600
Experiment						5380

Here, $Q_{\text{red}}(\text{D}_2) = 178 \text{ kJ/mol Pd}$ [11]. The water produced by the reducing reaction is thought to be absorbed inside the pore of zeolite and becomes solid water. We assume $Q_{\text{liq-sol}} = 40 \text{ kJ/mol D}_2\text{O}$.

Table 2 compares the estimated value with the experimental one for $Q_{\text{out}}^{\text{1st}}$.

It is seen that the experimental value is considerably larger than the estimation. This fact suggests that there is an unknown source of heat to be taken into account. The unknown heat, Q_{unknown} , is 1780 J, which is about 33% of the experimental value.

In the second cycle, we assume that Pd particles exist in metallic state. Therefore, we assume

$$Q_{\text{out}}^{\text{2nd}} = Q_{\text{abs}} + Q_{\text{ads}} + Q_{\text{mech}} + Q_{\text{unknown}}. \quad (5)$$

If we further assume $Q_{\text{unknown}}^{\text{2nd}} = Q_{\text{unknown}}^{\text{1st}}$, we can estimate the value of $Q_{\text{out}}^{\text{2nd}}$, which is compared to experiment in Table 3.

The estimated value agrees approximately with the experimental one, although the estimation is a little larger than the experiment.

From these estimations, it is suggested that Q_{unknown} appears in the early cycles of pressurization in the case of 5 wt% Pd/zeolite. Figure 4 suggests that Q_{unknown} must become smaller with increasing cycle and disappears at higher cycles. The isotope effect observed at early cycles arises mainly from Q_{unknown} .

A possible candidate of Q_{unknown} is the D–H exchange reaction which has been discussed by Kidwell et al. [8] and Dmitriyeva et al. [12] in explaining the anomalous heat observed for low concentration Pd in oxide matrices including zeolite [8]. They estimated the heat due to D–H exchange reaction using gas analysis data and found that in some matrices the likely source of the anomalous heat is D–H exchange with the water present in the matrix [8,12]. In other matrices, however, no simple explanation of the excess heat could be made [8]. In the present study, the amount of water included in the matrix is negligible because the sample was always baked at 623 K in vacuum. However, silica's contain surface silanols and D/H exchange reaction of the silanols may generate a significant amount of heat and hence an isotope effect for heat generation. Therefore, it is required to estimate quantitatively the contribution from D–H exchange reaction of the silanols.

Isotope effect for heat with pressurization has also been clearly observed for 9.85 wt% Pd/FSM. It was noted for this sample that the difference in the heat between deuterium and hydrogen did not decrease with an increase of cycle up to at least 15 cycles, whereas the difference disappeared at several cycles for 5 wt% Pd/ zeolite.

The origin of these apparently different behaviors of the isotope effect seems to be correlated with the size of the Pd particles, i.e., the isotope effect is negligible if the size of the Pd particle is larger than about 10 nm. For the 5 wt% Pd/zeolite sample, a significant amount of Pd initially existed inside the pore of zeolite with a size of $< \sim 1.1 \text{ nm}$ and

Table 3. Estimated and experimental heats at the second cycle for 5 wt% Pd/zeolite sample (J).

	Q_{mech}	Q_{ads}	Q_{abs}	Q_{unknown}	$Q_{\text{out}}^{\text{2nd}}$
Estimation	44	130	198	1780	2150
Experiment					2050

precipitated onto the surface of zeolite grain with increasing cycle of pressurization, resulting in the growth of Pd up to sizes of more than 10 nm. In the 9.85 wt% Pd/FSM sample, on the contrary, the Pd particles inside the pores of FSM kept staying there even after the 15-cycle's measurement, suggesting the size of Pd particles was mostly less than the size of the pore, i.e. 2 nm. These facts suggest that nano-sized Pd particles mainly cause the isotope effect for heat generation upon pressurization. The size of the Pd particles favorable to a clear observation of the isotope effect is less than about 2 nm.

Thus, it has been demonstrated that isotope effect for heat generation upon pressuring nano-Pd systems is strongly dependent on the size of Pd particles, which is easy to increase upon exposure to hydrogen. To suppress the growth of Pd particles, incorporation of Pd particles into the pores of porous materials is effective, although the stability of Pd particles is dependent on the size of the pores of the porous material. Therefore, to clarify the origin of the observed isotope effect for heat generation in nano-Pd systems, the influence of the Pd particle size on the isotope effect should be properly explained.

5. Conclusions

Differences in the heat generation upon pressurization with H₂ and D₂, i.e., the isotope effect, were clearly observed for both Pd/zeolite and Pd/FSM systems in a reproducible manner. For Pd/zeolite, the difference decreased with increasing cycle of pressurization and almost disappeared at higher cycles, whereas it was almost constant for Pd/FSM. It was indicated that when exposed to hydrogen, the nano-Pd particles in the pores of zeolite migrated onto the surface of zeolite grain, whereas nano-Pd particles inside the pores of FSM kept staying there. It is suggested that the existence of Pd particles with sizes of less than 2nm is essential for the isotope effect to be clearly observable.

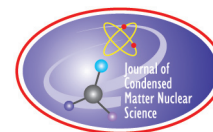
Acknowledgement

We would like to thank S. Hibi, N. Takahashi, S. Kosaka and S. Oshima for discussion and experimental supports. We are also grateful to J. Kasagi of Tohoku University and Y. Fukada and N. Nakamura of Toyota Motor Corporation for discussion and encouragement.

References

- [1] Y. Arata and Y. Zhang, The establishment of solid nuclear reactor *J. High Temp. Soc.* **34** (2008) 85–93.
- [2] S. Yamaura, K. Sasamori, H. Kimura, A. Inoue, Y. Zhang and Y. Arata, Hydrogen absorption of nanoscale Pd particles embedded in ZrO₂ matrix prepared from Zr-Pd amorphous alloys, *J. Mater. Res.* **17** (2002) 1329–1334.
- [3] J. Biberian and N. Armanet, Excess heat during diffusion of deuterium through palladium, *Proc. 13th Int. Conf. on Condensed Matter Nucl. Sci.*, Dagomys, Russia, June25–July1, 2007, pp.170–180.
- [4] F. Celani et al., High temperature deuterium absorption in palladium nano-particles, *Proc. 13th Int. Conf. Condensed Matter Nucl. Sci.*, Dagomys, Russia, June25–July1, 2007, pp.181–201.
- [5] A. Kitamura, T. Nohmi, Y. Sasaki, A. Taniike, A. Takahashi, R. Seto and Y. Fujita, Anomalous effects in charging of Pd powders with high density hydrogen isotopes, *Phys. Lett.* **A373** (2009) 3109–3112.
- [6] T. Hioki, H. Azuma, T. Nishi, A. Itoh, S. Hibi, J. Gao, T. Motohiro and J. Kasagi, Absorption capacity and heat evolution with loading of hydrogen isotope gases for Pd nanopowder and Pd/ceramics nanocomposite, *J. Condensed Matter Nucl. Sci.* **4** (2011) 69–80.
- [7] T. Hioki, H. Azuma, T. Nishi, A. Itoh, J. Gao, S. Hibi, T. Motohiro and J. Kasagi, Hydrogen/deuterium absorption capacity of Pd fine particle system and heat evolution associated with hydrogen/deuterium loading, *Proc. 15th Int. Conf. Condensed Matter Nucl. Sci.*, Rome, Italy, Oct.5–9, 2009, pp. 88–93.
- [8] D. Kidwell, D. Knies, K. Grabowski and D. Dominguez, Yes, Virginia there is heat, but it is likely of chemical origin, *Proc. 15th Int. Conf. Condensed Matter Nucl. Sci.*, Rome, Italy, Oct.5–9, 2009, pp. 100–109.

- [9] S. Inagaki, A. Koiwai, N. Suzuki, Y. Fukushima and K. Kuroda , Syntheses of highly ordered mesoporous materials, FSM-16, derived from kanemite, *Bul. Chem. Soc. Japan* **69** (1996) 1449–1457.
- [10] Y.Fukai, K.Tanaka and Y.Uejida, *Suiso to Kinzoku*, Uchida Rokakudo Publishing Co.Ltd., Tokyo, 1998, p.38.
- [11] HSC Chemistry 6.1, Chemical simulation and reaction software with extensive thermo-chemical database, Outokumpu Research, Oy, Finland, 2007.
- [12] O. Dmitrieva, R. Cantwell, M. McConnell and G. Moddel, Origin of excess heat generated during loading Pd-impregnated alumina powder with deuterium and hydrogen, *Thermochimica Acta* **543** (2012) 260–266.



Research Article

Bose–Einstein Condensation and Inverted Rydberg States in Ultra-high Density Deuterium Clusters Related to Low Energy Nuclear Reactions

Heinrich Hora*

Department of Theoretical Physics, University of New South Wales, Sydney 2052, Australia

George H. Miley and Xiaoling Yang

Department of Nuclear, Plasma and Radiological Engineering, University of Illinois, Urbana, IL 61801, USA

Abstract

Results about low energy nuclear reactions (LENR) are related to very high density clusters of deuterons where properties of Bose–Einstein condensation and/or inverted Rydberg states are compared. A modification of Bohr’s atom model is used to overcome the problem that a quantum state with $n = 1$ does not emit radiation from an “orbiting” electron. This permits then the description of the inverted state of Rydberg matter in agreement with the recent measurements of Holmlid et al. for deuterium clusters with ultra-high deuteron densities in the range of 10^{29}cm^{-3} . A virtual oscillation model for laser excitation clusters explains the low intensity ionization threshold in clusters. MeV particle emission from LENR can then be compared with measurements from inverted Rydberg states.

© 2014 ISCMNS. All rights reserved. ISSN 2227-3123

Keywords: Bose–Einstein condensation, Generalized Bohr model, Low energy nuclear reactions, Rydberg matter, Ultra-high density deuterium clusters

1. Introduction

Ultra-high density states of deuteron clusters are considered which generation in empty crystal positions (Schottky defects) were measured [1]. Similar ultra-high density states of deuteron clusters in surface defects were measured [2–4] where the distance between the deuterons in these states was measured from deuteron emission using mass spectrometry. The distances between the deuterons within the clusters in the range of 2 pm were explained as the result of inverted Rydberg states. These states may be compared with Bose–Einstein-Condensations (BEC) [1,2,5,6]. This was studied in connection with low energy nuclear reactions (LENR) beginning with a two body Bose–Einstein

*E-mail: h.hora@unsw.edu.au

mechanism [7] with general consequences [8]. The essential property for BEC was opened by the very small deuteron distance of 2 pm for nuclear reactions with probability times in the kilosecond range [9] which could be concluded from experiments with plasma loading processes in palladium grains [10] even before the convincing LENR processes were discovered [11,12]. This all was leading to the recent significant progress about LENR [13] using gas loading of deuterium in palladium nano-grains.

The interest in the deuteron interaction processes in the 2 pm distance range needs a comparison with the different properties of the involved models for explaining the phenomenon and may finally lead to an interaction process where a virtual oscillation model of quantum states is applied.

2. Basic Experimental Proof of LENR

In view of the complex developments of low temperature nuclear reactions of deuterons in gaseous-plasma loaded palladium crystals [10,13], it should first be underlined on what crucial experimental result LENR [11,12] is based. It was the discovery that the deuterium loaded palladium is generating nuclei up to gold and higher proton numbers Z with nucleon numbers A . Thanks to the very sophisticated diagnostics facilities of the Frederick Seitz center at the University of Illinois at Urbana, IL, the generation probability $P(Z)$ could be measured where the maxima and minima were similar to the element distribution in the Universe [14]. The large scale minimum at A around 155 could be compared with the minimum of the uranium fission products at A of 119 [6]. While this large scale minimum is standard knowledge for fission of unexcited uranium nuclei, it was discovered [15,16], that a difference occurs if the fissioning uranium is in an excited state of up to MeV energy. The $P(Z)$ curve has then a little local maximum peak at the large scale minimum. It is very surprising that this Maruhn–Greiner-maximum at uranium fission [15] was also measured for LENR at A of 155. This fact is a very convincing experimental proof of LENR.

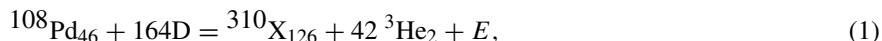
After this solid experimental fact, it could be speculated how this result may be understood. It could be suggested, that LENR may be via a compound nuclear reaction [17] where indeed a very hypothetical nucleus with $A = 310$ may be involved. What was interesting, is that the new model for derivation of the nuclear magic numbers [14] was possible from the few maximum curves of $P(Z)$ similar to the astrophysics case, where higher magic numbers above 126 were 184 and further. Both were fitting a double magic number nucleus with $A = 310$ [5,6] as a initial hypothetical result.

3. Two Picometer Deuteron Distance

The significance of a 2 ps deuteron distance was initially based on an evaluation [9] of gas phase loading of deuterium in palladium crystals [10]. The reduction of Coulomb screening by a factor 5 is well known in high temperature plasmas [18]. Evaluating the semi-empirical DD reaction probability for the usual hot fusion, for muon-catalized fusion and what could be concluded from deuterium loaded palladium [9] was that the Coulomb screening is resulting in a factor 13 for the deuterons within the crystal, in which case the DD reaction probability is given by a time t^* of kiloseconds (ks) to nearly Ms and the distance of the reacting deuterons are in the range r^* of about 2 pm. It is remarkable that the K-shell capture of electrons at the inverse radioactive beta-decay have similar ranges t^* and r^* .

After this semi-empirical derivation of the screening factor 13, this was derived in a detailed quantum mechanical study by Czerski, Huke et al. [19,20]. This means that the deuterons are screened like neutral particles, e.g. like neutrons, moving within the palladium lattice like spheres of 2 pm diameter following Maxwell statistics. For smaller diameters the screening of the deuterons is lost and then electrical repulsion will occur. These screened deuterons may then cling together by attractive forces where the Casimir effect is a possibility. But it well can be that these clusters have the properties of inverted Rydberg states as concluded from the measured 630 eV emission of deuterons as a kind of Coulomb explosion [2]. In contrast to larger distances [7,8], the 2 pm distances of deuterons in clusters may also

lead to the description as Bose–Einstein condensation. This state is ideal to understand the nonlocality of the deuterons within the clusters. More than 100 deuterons can then be in a cluster of about 10 pm diameter moving around within the palladium lattice like cold neutrons. If one cluster moves to a distance of about 2 pm to a palladium nucleus, all the deuterons in the cluster can react as if in 2 pm distance due to the quantum property of BEC within the cluster. A compound nuclear reaction could then be [5,6]



where E is the energy release. The mass per nucleon expressed in proton masses in X is derived to be 1.004946 (ignoring the minor contribution associated with E). This compares favourably with the value of uranium 1.0001868 or with the very low value comparing favourably with iron of 0.9988376.

4. Discussion about the BEC Model in View of Inverted Rydberg States

The here presented BEC model is one possible model with several open questions in order to explain the clear fact of the Maruhn–Greiner result in Miley’s LENR measurement. What has not yet been solved is, e.g., what happens with the screening electrons in their Fermi–Dirac background within the ultra-high density clusters. The screened deuterons are not really neutral atoms or molecules. A contrast may be the inverted Rydberg state for the clearly measured ultra-high density deuterium in the clusters for which case the following modification of Bohr’s atom model may be given.

The alternative approach to clusters in void-defects of solids was the experimental discovery of cluster states with ultra-high deuterium densities of up to 10^{29} per cm^3 in near-surface crystal defects of iron oxide. This was found [2] from measurements of the emission of 630 eV deuterium ions during laser irradiation with the conclusion that these clusters are in an inverted Rydberg state. It may be assumed that the clusters in these surface defects are related to the ones we have described relative to the defects formed by loading-unloading methods [1].

The generation of Rydberg matter in the universe as interstellar clusters has been discussed over recent years. These are molecular structures where the electrons are in orbital states with a orbital quantum number $m = 1$ or higher. It is difficult to produce these states in the laboratory because the atoms needed an energetic excitation much higher than the molecular binding energy for joining to a molecule. However, the statistics in interstellar space does permit this. Such RM clusters in space cannot be detected by spectroscopic methods but may be dark matter which only are measured by gravitation. Indeed, this may be the dark matter predicted to have some concentration inside and near the discs of galaxies.

A special method was developed by Holmlid et al. [2–4] to use the catalytic property at the surface of ion oxide for producing Rydberg states. Then within voids of the crystal defects it is possible, that hydrogen or deuterium atoms obtain an $m = 1$ excitation, leading to a RM molecular compound catalytically without counterproductive higher energies as in vacuum. It is calculated [2] that the proton distance of 74 pm in a H–H molecule with valent binding is changed into a distance

$$d = 150 \text{ pm} \quad (2)$$

in the RM state. This state is a metallic modification of hydrogen H(1) where the number one expresses the $m = 1$ state.

The inverted RM is using an inversion of the role of the electron and proton to form a hydrogen atom. The normal atom is based on the electric field of a central proton and the electron is attracted by this field. In Bohr’s model, the electron is considered in a point-mechanical treatment as rotating with an angular momentum p at a radius r such that the quantum relation

$$rp = nh/2\pi = \hbar \quad (n = 1, 2, 3 \dots) \quad (3)$$

is fulfilled. This rotation is not true in the ground state for $n = 1$ because the electron would then emit energy by radiation. This problem was solved by Schrödinger's quantum mechanics where the electron orbiting is possible only for $n = 2$ and higher. The merit of both models should not be ignored. The transition of a rotating electron from a higher to lower orbit described the radiation emission to arrive at the measured times of about 10^{-8} s for spontaneous emission. This was difficult to be derived in quantum mechanics and was achieved only by Dirac's introduction of the quantization of the electromagnetic field energy density (second quantization).

The following quantum mechanical modification of Bohr's semiclassical atom model is possible in the following way in order to overcome the orbiting problem for $n = 1$. The electric field energy gained by an electron when falling into the proton depends on the distance r and can be compared with the Fermi–Dirac energy for squeezing the electron into a sphere of radius r . The difference of the exponents of the energies arrives at a radius where both energies are the same. This is just the value [21]

$$r_B = \hbar^2/me^2 \quad (4)$$

of the Bohr radius where m is the rest mass and e the electric charge of an electron (see Section 2.3 of [21]). Using this model, the measured polarization shift of spectral lines in plasma (Inglish–Teller effect) for hydrogen can be theoretically explained [22] with higher accuracy than by the earlier derived model by Griem.

The inverted hydrogen atom occurs when an electron produced the central electric field and the proton (or deuteron) falls into the electron until a radius is reached where the electric field energy gained is equal to the increase of the Fermi–Dirac quantum energy. The radius is then different from the normal Rydberg case by the square root of the ratio of the mass of the proton p or deuteron D , see the equations between 2.16 and 2.17 of Ref. [22]. Instead of the distance d , Eq. (2), in a Rydberg cluster, the distance d^* in the inverted deuterium RM cluster D(-1) is then expressed with the deuteron mass m_D

$$d^* = (m/m_D)^{1/2}d. \quad (5)$$

Remarkably, this value is 2.5 pm as was initially calculated [2] from the orbital motion within the clusters.

The direct experimental proof of this distance was obtained from measurements using laser irradiation of the catalytic produced D(-1) clusters [2]. The mechanism can be seen when photons from a laser beam irradiate the cluster and photo-electrically removing electrons at binding centers for the deuterons in the inverted RM. The remaining deuterons are then to repel each other by Coulomb repulsion causing a Columbic Explosion (CE) and are subsequently emitted into the vacuum above the iron oxide. Time of Flight (TOF) measurements show energies of 630 eV. This exactly corresponds to an initial distance of the deuterons in the cluster of

$$d_{\text{exo}}^* = 2.3 \text{ pm}. \quad (6)$$

The quantum mechanical explanation of the laser produced electron emission process is given with fitting the parameters obtained in this experiment. The threshold of the laser intensity is found to be close to or a little higher than [23]

$$I_{\text{three}} = 10^{10} \text{ W/cm}^2 \quad (7)$$

for a wave length of 565 pm. It should be noted that this experiment did not work with H(1) and H(-1) RM at the low intensities (7). This indicates that the D(-1) clusters have properties of BEC which is not normally possible with protons as fermions while deuteron are bosons. As suggested by Kim [8], at the densities involving pseudo bosons, this may result form allowing condensation.

5. Oscillation Model for Quantum States Analogue to Free Electrons

Low energy laser excitation may be another way of exciting LENR reactions in RM states. This requires development of efficient methods for coupling the laser photon energy with the inverted RM state of D(-1) clusters in order to remove electrons, and cause the D-atom in the cluster to fuse. The mechanisms to explain removal of the electrons by the laser field from the inverted surface RM state of D(-1) clusters is explained from the oscillation of the electron in an electromagnetic field (quiver motion at laser irradiation) in combination with a quantum relation to obtain a correspondence principle for the electromagnetic interaction [24].

A free electron in space, e.g. in a plasma, quivers in a laser field with the amplitude E of the laser field having a maximum elongation

$$r = eE/m\omega^2 \quad (8)$$

with a maximum momentum $p = mv$ from the quiver velocity v

$$p = mv = eE/\omega, \quad (9)$$

where ω is the radian frequency of the laser. Indeed, free electrons in vacuum perform the quiver motion as detected also from Thomsen scattering where the oscillation energy of the electrons

$$\varepsilon_{\text{osc}} = (eE/\omega)^2/2m \quad (10)$$

is the quiver energy.

A basic difference between this analysis as classical point mechanical motion in vacuum occurs when the electron is bound in an unexcited hydrogen atom or any bound state including the Rydberg state. If the laser field has a sufficiently high intensity $I > I_i$ above the ionization threshold I_i , in vacuum the electron will be ionized and the motion of the electron will then follow the quiver motion where I_i is defined by the ionization energy ε_i . At lower intensities photon interaction of the laser light can occur quantum-electro-dynamically with the electron in the hydrogen atom by resonance for energy levels given by energy eigen-values of the quantum states of the electron within the bound atom. At these lower intensities one cannot describe the electron interaction with the photons in the point-mechanical classical way as quiver motion. Nevertheless the correspondence to the quiver motion might be considered as a virtual oscillation (with all caution not to over-stress this description until it is studied further). It is therefore interesting to see when the product of the length of the quiver motion, r of Eq. (8), with the momentum $p = mv$, Eq. (9) reaches the value of Planck's constant h

$$rmv = \hbar = h/2\pi. \quad (11)$$

This quantum relation permits substitution of the laser field E of the quiver velocity v in Eq. (9) with the quiver energy (10) to arrive at

$$\varepsilon_{\text{osc}} = \hbar^2/2mr^2. \quad (12)$$

For low laser intensities, this can be considered as a “virtual” quiver motion of the electron which is fundamentally different from the quantum states of the electron when bound in the atom. Based on this virtual description it is interesting to see what happens if r assumes the value of the Bohr radius, Eq. (4). This arrives at a value of a “Bohr”-quiver oscillation energy

$$\varepsilon_{\text{B,osc}} = me^4/2\hbar^2 = \alpha^2 mc^2/2 = 13.6 \text{ eV}; \quad \alpha = e^2/\hbar c \quad (13)$$

using the vacuum speed of light c and the fine structure constant α . This is just the ionization energy of hydrogen. It is worth noting that this value is simply expressed by the fine structure constant α and the electron rest energy mc^2 . It is remarkable that this ionization energy for hydrogen marks a border line between the classical and the quantum mechanical state now expressed by the quiver motion, i.e. by the virtual electron oscillation.

The state of the inverted Rydberg cluster D(-1) [2] with distance d^* of 2.3 pm between the deuterons (as measured from the 630 eV energy of the emitted deuterons with the TOF mass spectrometer) is a rather complicated quantum state for the electrons and deuterons. In fact it is the state of the electron of an unexcited hydrogen atom. Using the radius $r^* = d^*/2 = 1.15 \text{ pm}$ as a first approximation in the inverted Rydberg deuterium cluster in the same way as the Bohr radius (4) was used for hydrogen, we arrive at a virtual oscillation energy for the electron for “ionization” from the bound state in the inverted Rydberg state cluster.

$$\varepsilon_{\text{DD,osc}} = \varepsilon_{\text{B,osc}}(m_e/m_D)(d/2r_B)^2. \quad (14)$$

The laser intensity for producing a quiver energy $\varepsilon_{\text{B,osc}}$ for the boron ionization Eq. (14) at the wave length 565 pm is $2.298 \times 10^{14} \text{ W/cm}^2$ resulting with the same ratios as Eqs. (13) and (14) to arrive at a laser intensity

$$I^* = 3.1 \times 10^{10} \text{ W/cm}^2. \quad (15)$$

This is close to the measured threshold in the experiment [23]. We assumed an ad hoc distance d^* for the inverted D-clusters in these calculations in order to work with the radius $r^* = d^*/2$. The correct value may be somewhat different, leading to a slightly different threshold I^* . When very precise measurements of the threshold intensity are at hand, the more precise elongation of the virtual quivering in the D(-1) cluster could be calculated and may give more important information about the inverted Rydberg state of the D- which definitely will not be a “clumping” together of spheres but with much more complicated structures. This result and the corresponding theory also provide exciting new insights the correspondence principle of electromagnetic interactions [24].

It is very important to realize that the measured [2] $d^* = 2.3 \text{ pm}$ value is lower than the initially expected theoretical value. This shows qualitatively that the radius of an inverted deuterium atom is larger than for an inverted Rydberg state of free deuterium. This confirms the implied overlap between the cluster members with neighboring states within the D(-1) state under the assumption of a cubic deuteron lattice structure in the cluster. The degree of overlap can be defined quantitatively from this type of analysis and should be carefully studied when more precise measurements are obtained.

Compared to the very long time of the resonance transition of electrons in atoms, the virtual-quiver-model ionization process is indeed extremely fast, roughly in the femto-second range. The electric field amplitude of the laser of 10^{10} W/cm^2 is $2.7 \times 10^6 \text{ V/cm}$ in good consistence to a laser driven field emission process. The laser intensity threshold near 10^{10} W/cm^2 for removing the electrons in the inverted Rydberg state for the subsequent 630-eV Coulomb explosion

of the deuterons arrives at the virtual electron oscillation energy in full analogy to the ionization of hydrogen. This represents a characteristic of the correspondence principle of electromagnetic interaction [24,29]. The inverted Rydberg state model may be considered at least as a heuristic. The essential same results are seen all in a direct Bose–Einstein cluster model.

6. Discussion and Conclusions

We underline the following open questions about comparison of 2 pm deuteron distance results for nuclear interaction. The first case of 2 pm was the semi-empirical fitting [9] of binary DD reactions using Coulomb screening by a factor 13 as confirmed in details by the complete quantum mechanical derivation by Czerski, Huke et al. [20,21]. The second case was the hypothetical model for explaining the Maruhn-Greiner local maximum of measured $P(Z)$ LENR heavy nuclear generation by assuming that the 2 pm screened distance motion of deuterons in the palladium crystal are “clumping” together to clusters with 150 deuterons of about 10 pm diameter to arrive at a Bose–Einstein state with nonlocality such that a compound nuclear reaction, Eq. (1), may produce the measured heavy nuclei. The third case is the inverted Rydberg state as a heuristic approach where there is a cubic lattice of Rydberg-inverted deuterium molecules in contrast to the BEC nonlocality.

The question may be whether there is some complementarity between BEC and inverted Rydberg states. This may be suggested from experimental results from the emission of nuclear reaction products using the volume clusters [1] for deuterons, where an increase of the fusion neutrons was measured when these states in targets for usual laser driven fusion were used [25,26]. Using surface state deuterium clusters, emission of MeV neutrons was measured at laser irradiation at about 20 times higher laser intensities I above the threshold, Eq.(15) where the following gain of the MeV neutron numbers N was increasing [27]

$$N \sim I^3. \quad (16)$$

This proportionality is comparable with the conclusion (see Fig. 1 of Ref. [28]) of the large scale laser fusion of spherically compressed thermal ignited direct drive volume ignition laser fusion with the proportionality

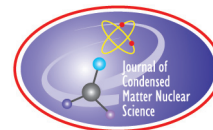
$$N \sim I^2. \quad (17)$$

This was confirmed [28] for ns laser pulses of about 10 kJ and is concluded for present experiments with up to 2 MJ pulses.

References

- [1] A. Lipson, B. J. Heuser, C. Castano, G. Miley, B. Lyakhov and A. Mitin, *Phys. Rev. B* **72** (2005) 212507.
- [2] S. Badiei, P.L. Andersson and L. Holmlid, High-energy Coulomb explosion in ultra-high dense deuterium: Time-of-flight mass spectrometry with variable energy and flight length, *Int. J. Mass Spectr.* **282** (2009) 70–76.
- [3] L. Holmlid, H. Hora, G.H. Miley and X. Yang, Ultra-high-density deuterium of Rydberg matter clusters for inertial confinement fusion targets, *Laser and Particle Beams* **27** (2009) 529–532.
- [4] L. Holmlid, *Laser and Particle Beams* **31** (2013) 715–722.
- [5] H. Hora and G.H. Miley, Maruhn–Greiner maximum from uranium fission for confirmation of low energy nuclear reactions LENR via a compound nucleus with double magic numbers, *J. Fusion Energy* **26** (2007) 349–353, 357.
- [6] George H. Miley, Heinrich Hora, Karl Philberth, Andrei Lipson and P.J. Shrestha, Radiochemical comparisons on low energy nuclear reactions and uranium, In *Low-Energy Nuclear Reactions and New Energy Technologies Source Book*, Vol. 2, Jan Marwan and Steven B. Krivit (Eds.), American Chemical Society/Oxford University Press, Washington DC, ISBN 978-0-8412-2454-4 (2009), pp. 235–252.

- [7] Y.E. Kim and A.L. Zubarev, *Phys. Rev. A* **66** (2002) 053602.
- [8] Yeong E. Kim, Theory of Bose–Einstein condensation mechanism for deuteron-induced nuclear reactions in micro/nano-scale metal grains and particles, *Naturwissenschaften* **96**(7) (2009) 803–811.
- [9] H. Hora, J.C. Kelly, J.U. Patel, Mark A. Prelas, G.H. Miley and J.W. Tompkins, Screening in cold fusion derived from D–D reactions, *Phys. Let. A* **175** (1993) 138–143.
- [10] M.A. Prelas, F. Boody, W. Gallaher, E. Leal-Quiros, D. Mencin and S. Taylor, *J. Fusion Energy* **9** (1990) 309.
- [11] G.H. Miley and J.A. Patterson, *J. New Energy* **1** (1996) 11.
- [12] G.H. Miley, G. Narne, M.J. Williams, J.A. Patterson, J. Nix, C. Cravens and H. Hora, *Progress in New Hydrogen Energy*, M. Okamoto (Ed.), New Energy and Industrial Technology, Tokyo, 1997, p. 629.
- [13] H. Hora, Magic numbers and low energy nuclear transmutations by protons in host metals, *Czechosl. J. Phys.* **48** (1998) 321.
- [14] H. Hora and G.H. Miley, *Czechosl. J. Phys.* **50** (2000) 433.
- [15] J. Maruhn and W. Greiner, *Phys. Rev. Lett.* **32** (1974) 548.
- [16] J.A. Maruhn, W. Greiner and W. Scheid, Theory of fragmentation in fission, fusion and heavy ion scattering, in *Heavy Ion Collisions*, R. Bock (Ed.), Vol. II (North- Holland, Amsterdam, 1980), pp. 387–465.
- [17] G.H. Miley, *Trans. Am. Nucl. Soc.* **76** (1997) 155.
- [18] S. Ichimaru. Nuclear fusion in dense plasmas, *Rev. Mod. Phys.* **65** (1993) 255–299.
- [19] K. Czerski, A. Huke and A. Biller et al., *Europhys. Lett.* **54** (2001) 449.
- [20] A. Huke, K. Cerski and P. Heide et al., *Phys. Rev. C* **78** (2008) 015803.
- [21] H. Hora, *Plasmas a High Temperature and Density*, Springer, Heidelberg, 1991.
- [22] H. Hora and B.I. Henry, Polarization shift of spectral lines in high density plasmas, *Opt. Comm.* **44** (1983) 218–222.
- [23] L. Holmlid, Private communication.
- [24] Heinrich Hora and Peter H. Handel, Kapitza–Dirac effect with lasers and non-resonant interaction for quantum modulation of electron beams (Schwarz–Hora effect) , *Appl. Phys. Lett.* **102** (2013) 141119/1–4.
- [25] X. Yang. G.H. Miley, K.A. Flippo and H. Hora, Energy enhancement for deuteron beam fast ignition of a pre-compressed inertial confinement fusion (ICF) target, *Phys. Plasmas* **18** (2011) 032703/1–5.
- [26] Xiaoling Yang, George H. Miley, Kirk A. Flippo and Heinrich Hora. Hot spot heating process estimate using a laser-accelerated quasi-Maxwellian deuteron beam, *Laser and Particle Beams* **30** (2012) 31–38.
- [27] Patrik U. Andersson and Leif Holmlid, Fusion generated fast particles by laser impact on ultra-dense deuterium: rapid variation with laser intensity, *J. Fusion Energy* **31** (2012) 249–256.
- [28] H. Hora, Extraordinary jump of increasing laser fusion gains experienced at volume ignition for combination with NIF experiments, *Laser and Particle Beams* **31** (2013) 228–232.
- [29] B.W. Boreham and H. Hora, Energy spectra of electrons emitted from laser irradiated low density gas and the correspondence principle of electromagnetic interaction, *Laser and Particle Beams* **13** (1995) 71–85.



Research Article

Increase of Reaction Products in Deuterium Permeation-induced Transmutation

Y. Iwamura, T. Itoh and S. Tsuruga *

Advanced Technology Research Center, Mitsubishi Heavy Industries Ltd., Japan

Abstract

Low-energy nuclear transmutations have been observed in the nano-sized Pd complexes, which are composed of Pd and CaO thin film and Pd substrate, induced by D₂ gas permeation. In order to increase the transmutation products, an electrochemical method was applied to increase deuterium density near the surface of the nano-structured Pd multilayer film. Transmutation products were successfully increased by this approach. Laser irradiation method was also applied to make surface Plasmon on the Pd multilayer, however, the effect of laser irradiation was not so prominent.

© 2014 ISCMNS. All rights reserved. ISSN 2227-3123

Keywords: Deuterium permeation-induced transmutation, Increase of reaction products, Nano-structured Pd multilayer thin film, Transmutation

1. Introduction

Transmutation reactions in nano-structured material have been observed in nano-structured Pd multilayer thin film which is composed of Pd and CaO thin film and Pd substrate, induced by D₂ gas permeation [1–5]. Experimental data that indicates the presence of transmutation have been accumulated and experimental conditions for inducing low-energy transmutation reactions are gradually becoming clear, although systematic experimental study is still insufficient. Replication experiments have been performed by some researchers and similar results have been obtained [6–8]. Potential applications would be expected as an innovative nuclear transmutation method of radioactive waste and a new energy source.

Figure 1 shows schematic of our experimental method. Our approach can be characterized by the permeation of D₂ gas through the nano-structured Pd complex and the addition of an element that is specifically targeted to be transmuted. Permeation of deuterium is attained by exposing one side of the Pd multilayer thin film to D₂ gas while maintaining the other side under vacuum conditions. The surface of the plate was covered by layers of CaO and Pd, which were obtained by five times alternately sputtering 2-nm-thick CaO and 20-nm-thick Pd layers. Then a 40-nm-thick Pd layer was sputtered on the surface of the CaO and Pd layers. These processes were performed by the Ar ion beam sputtering

*E-mail: Yasuhiro_Iwamura@mhi.co.jp

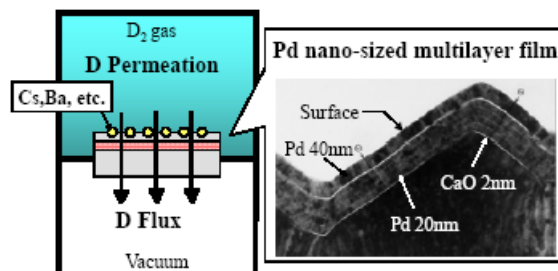


Figure 1. Experimental method for permeation-induced nuclear transmutation.

method. After fabricating a Pd complex, Cs was deposited on the surface of the thin Pd layer. After fabricating a Pd complex, Cs, Ba, or other element is deposited on the surface of the top thin Pd layer. The added elements can be transmuted.

Reactions observed so far in our group are shown in Table 1. Based on these experimental results, alkali elements seem to be transmutable by our method. In other words, chemically active elements that can easily emit electrons might be transmutable. And the obtained experimental results so far suggest that a certain rule seems to exist. We can notice that 2d, 4d or 6d look like reacting with deposited elements. Multi-body reactions like 2d, 4d and 6d require sufficient number of d. Therefore, we can see that sufficient deuterium density would be important to induce transmutation reactions.

Table 2 shows correlation between intermediate material in Pd multilayer film and transmutation results. If we replaced CaO with MgO, we did not obtain any positive transmutation products; we could not observe any transmutation reactions. It means that MgO cannot work instead of CaO. Three cases out of the three experiments using MgO show no Pr by ICP-MS measurements, although D₂ gas Flow rates were enough (2–3 sccm) in all cases. However, if we replaced CaO with Y₂O₃, we could observe transmutation reactions from Cs to Pr. Y₂O₃ works like CaO. Work functions for MgO, Y₂O₃ and CaO are shown in the Table 2. Although it is difficult to make conclusive results, the existence of low work function of intermediate material might have some effects to induce transmutation.

The permeation-induced transmutation technology would be expected as an innovative nuclear transmutation method for radioactive waste and a new energy source. However, it is necessary to increase the amount of transmutation products for commercialization.

The author is now assuming that the following two conditions are important to increase up transmutation products based on the experimental results.

- (1) Local deuterium density is sufficiently high.

Table 1. Typical reactions observed so far.

Elements		Assumed reactions
Cs	4d	$^{133}_{55}\text{Cs} \xrightarrow{4d(2\alpha)} ^{141}_{59}\text{Pr}$
Ba	6d	$^{138}_{56}\text{Ba} \xrightarrow{6d(3\alpha)} ^{150}_{62}\text{Sm}$, $^{137}_{56}\text{Ba} \xrightarrow{6d(3\alpha)} ^{149}_{62}\text{Sm}$
W	4d or 2d	$^{182}_{74}\text{W} \xrightarrow{4d(2\alpha)} ^{190}_{78}\text{Pt}$, $^{186}_{74}\text{W} \xrightarrow{2d(\alpha)} ^{190}_{76}\text{Os}$

Table 2. Correlation between intermediate material in Pd multilayer film and transmutation results.

Intermediate material	Work function (eV)	Results for analysis after permeation
CaO	1.2	Pr detected > 100 cases
Y ₂ O ₃	2.2	Pr detected > 10 cases
MgO	3.3	No Pr (3 cases)

(2) Electron rich state is important.

According to these assumptions, we tried to increase the amount of transmutation products by the increase of deuteron density and the excitation of surface Plasmon on the Pd multilayer.

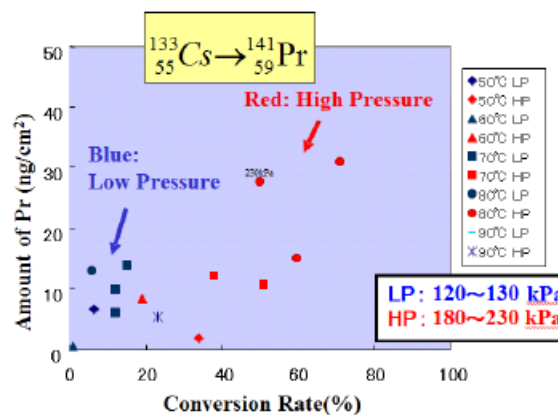
2. Increase of Deuteron Density Using an Electrochemical Method

Figure 2 shows the transmutation products dependence on D₂ gas pressure in the case of Cs transmutation into Pr. Conversion rate means how much portion of initial Cs was transmuted into Pr. Amount of Pr is expressed as the mass of Pr divided by the permeated surface area. Typical permeated surface area is about 1.0 cm².

It is possible to see that the amount of Pr and conversion rate increase as the D₂ gas pressure increase. It is reasonable that multi-body reactions observed in the permeation-induced transmutation require sufficient number of deuterium. Therefore we need high D₂ gas pressure since it gives much deuterium near the surface.

An electrochemical method is applied to increase deuterium surface density as shown in Fig. 3. A photo of our apparatus is shown also in Fig. 3. If we apply this method, we can provide very high deuterium density by controlling applied voltage between the Pd/CaO multilayer thin film and the anode made of Platinum. Simple pressurization is, off course, one of the solutions which give high deuterium density, however, it needs relatively large-scale apparatus. Therefore, we choose this electrochemical method for giving high deuterium density to the Pd surface, taking into the consideration of future commercialization.

An example of experimental results is shown in Figs. 4 and 5. A 0.1 M CsNO₃–D₂O solution was used for this experiment. Purity for both NO₃ and D₂O is more than 99.9%. Mass distributions by Secondary Ion Mass Spectrometry

**Figure 2.** Pr Dependence on D₂ gas pressure.

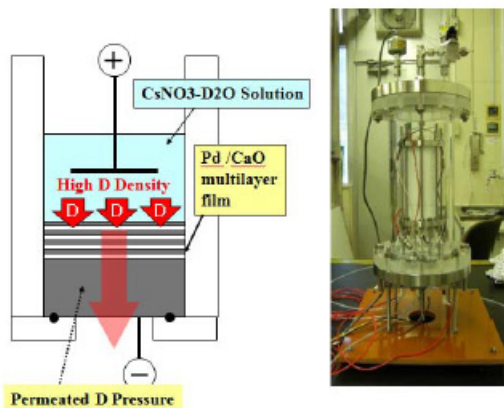


Figure 3. Electrochemical deuterium permeation apparatus aiming the increase of deuterium density.

(SIMS) are plotted in Fig. 4 and mass distributions by Inductively Coupled Plasma Mass Spectrometry (ICP-MS) for the same sample: E006 are shown in Fig. 5.

We can postulate that nuclear transmutation reactions occur at the permeated part of the Pd multilayer sample (center), however, no reactions occur at the part where no D permeated (corner). In advance, Cs ion implantation (20 kV , $10^{16} \text{ ions/cm}^2$) were applied to Pd multilayer.

SIMS counts are plotted in a logarithmic scale in Fig. 4(a). SIMS analysis was performed by O^{2+} ions and the analyzed area was circle in $60 \mu\text{m}$ diameter. Mass 133 corresponds to Cs and SIMS counts for mass 133 of E006-corner are larger than those of E006-center as shown in Fig. 4(a). It means that ^{133}Cs decreased at the center of E006. On the contrary, SIMS counts around mass 140 of E006-center are larger than those of E006-corner. It means that elements or molecular compounds that have mass number around 140 increased at the deuterium permeated point where SIMS analysis was performed. As a reference, SIMS mass distributions for no Cs implantation sample are plotted for both center and corner. The increase of SIMS counts around mass 140 cannot be seen as for the no implantation sample.

The magnified mass spectra from mass 130 to mass 150 is shown in Fig. 4(b) where SIMS counts are plotted in a linear scale. It can be seen that SIMS counts around mass 140 are greatly increased only for the E006-center.

We performed ICP-MS analysis to confirm the obtained results by SIMS analysis. Basically, the mass information obtained by SIMS is at the analyzed small point. In contrast, the information obtained by ICP-MS is from the sample surface because mass distribution was analyzed for the HNO_3 solution that contains the surface of Pd multilayer thin film. In the ICP-MS analysis, we cut a permeated Pd multilayer sample into 1/4 size and put it into 68% high purity HNO_3 solution and analyzed the HNO_3 solution that contained the surface part of it.

Figure 5 (a) shows ICP-MS results for E006 and the no Cs implantation and D permeated sample. ICP-MS counts around mass 140 of E006 are larger than those of no Cs implantation sample. It means that elements or molecular compounds that have mass number around 140 increased on the dissolved surface by HNO_3 . The magnified mass spectra from mass 130 to mass 150 are shown in Fig. 5(b) where ICP-MS counts are plotted in a linear scale. It would be possible to say that Figs. 4 and 5 are similar around mass 140, although the difference of signals between E006 and no Cs implantation is smaller for Fig. 5. It is reasonable because SIMS data is taken from the point where transmutation reactions were supposed to occur, however, ICP-MS results contained corner part where no D was permeated and therefore no transmutation reactions were supposed to occur.

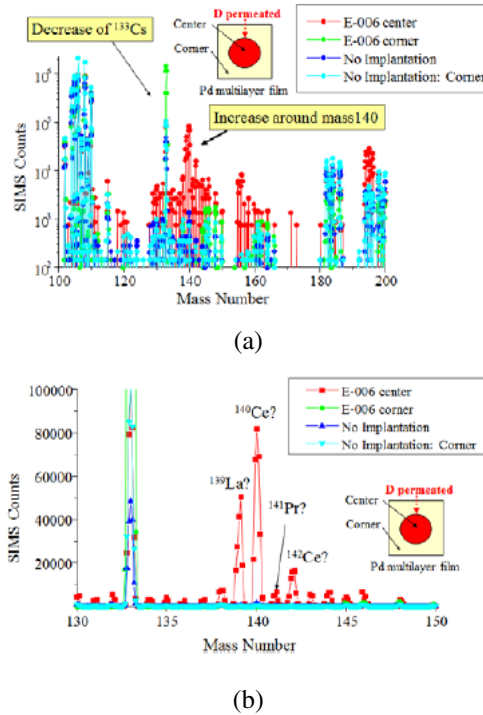


Figure 4. Comparison of SIMS mass spectra between E006 and No Cs implantation sample. (a) Wide SIMS Spectra in a logarithmic scale. (b) Magnified SIMS Spectra from mass 130 to mass 150 in a linear scale.

Next we examined the formations of compound species for mass 139 and 140 that large increases were observed. Possible compounds for mass 139 and 140 are shown in Table 3. If we carefully examine and take natural abundances for each element into consideration, mass 139 and 140 cannot be explained by these compounds. Therefore, mass 139 and 140 would be ^{139}La and ^{140}Ce , respectively. Of course, it is preferable to make cross check by the other analysis methods that have other measurement principle, for example, XRF or XPS. It is the next step work to confirm these results by the other methods.

Table 3. Possible compounds for mass 139 and 140.

Possible compounds for mass 140		
^{138}Ba (71.7%) D	^{133}Cs (100%) ^7Li (92.4%)	^{110}Pd ^{30}Si (3.1%)
^{106}Pd ^{34}Si (4.3%)	^{109}Ag (48.1%) ^{31}P (100%)	^{104}Pd ^{36}Ar (0.33%)
^{102}Pd ^{38}Ar (0.06%)	^{110}Pd ^{28}Si (92.3%) D	^{108}Pd ^{30}Si (3.1%) D
^{105}Pd ^{33}Si (0.8%) D	^{102}Pd ^{36}Si (0.02%) D	^{102}Pd ^{36}Ar (0.3%) D
Possible compounds for mass 139		
^{137}Ba (11.2%) D	^{133}Cs (100%) ^6Li (7.6%)	^{110}Pd ^{29}Si (4.7%)
^{106}Pd ^{33}Si (0.8%)	^{104}Pd ^{35}Cl (75.8%)	^{102}Pd ^{37}Cl (24.2%)
^{110}Pd ^{27}Al (100%) D	^{106}Pd ^{31}P (100%) D	^{105}Pd ^{32}S (94.9%) D
^{104}Pd ^{33}Si (0.8%) D	^{105}Pd ^{32}Si (94.9%) D	^{102}Pd ^{35}Cl (75.8%) D

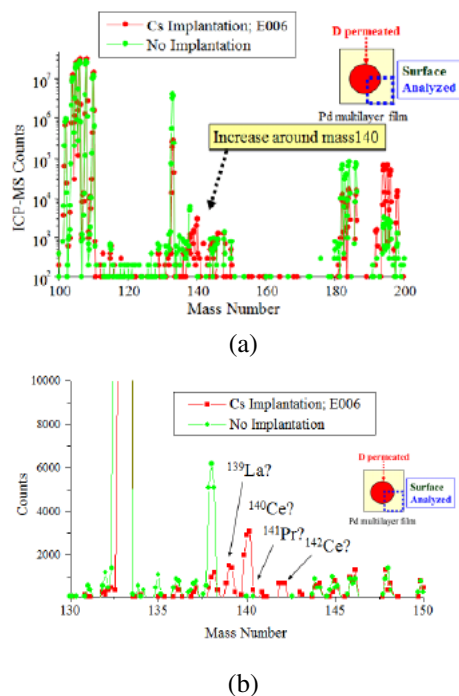


Figure 5. Comparison of ICP-MS Mass Spectra between E006 and No Cs Implantation sample. (a) Wide ICP-MS Spectra in a logarithmic scale. (b) Magnified SIMS Spectra from mass 130 to mass 150 in a linear scale.

According to our experimental results using D_2 gas permeation, we usually observed transmutation of Cs into Pr, in other words, mass 133 decreased and mass 141 increased. In this new apparatus, however, mass 139, 140, 141 and 142 increased while mass 133 decreased. The differences between D_2 gas permeation and electrochemical D permeation can be attributed to the effective deuterium density and/or source of deuterium.

Let us consider about contamination due to the $CsNO_3$ – D_2O solution. If we analyzed the $CsNO_3$ – D_2O solution, we could not see any mass numbers of 139, 140, 141, 142 (La, Ce, Pr). Furthermore, we make comparison between E006 and the D permeated sample. The D permeated sample was contacted with $CsNO_3$ – D_2O solution and almost the same current was applied. The other experimental conditions except Cs implantation were all the same. However, the only permeated part of E006 has different mass distribution as shown in Figs. 4 and 5. So it is very difficult to assume that obtained mass difference between D_2 gas permeation and electrochemical D permeation are derived from the contamination of $CsNO_3$ – D_2O solution. Therefore, we might consider the effective deuterium density make effects on the transmutation reaction pass. Anyway, we should make more experiments using the other measurement methods and improve the reliability of our experiments.

Let us move onto the next point. We describe an example of gamma-ray detection during an electrochemical D permeation experiment. In Fig. 6, applied voltage and corresponding current between Pd multilayer thin film and Pt anode, pressure at the exit side of Pd multilayer cathode are plotted as a function of time. Deuterium permeation rate is proportional to the pressure described here. At the beginning of the experiment, applied voltage was 3 V and the current was low. If we increased the voltage up to 4 V, the current increased and permeated D increased correspondingly, as shown in Fig. 6. If we increased the voltage up to 4.5 V, current amounted to 70 mA and deuterium permeation

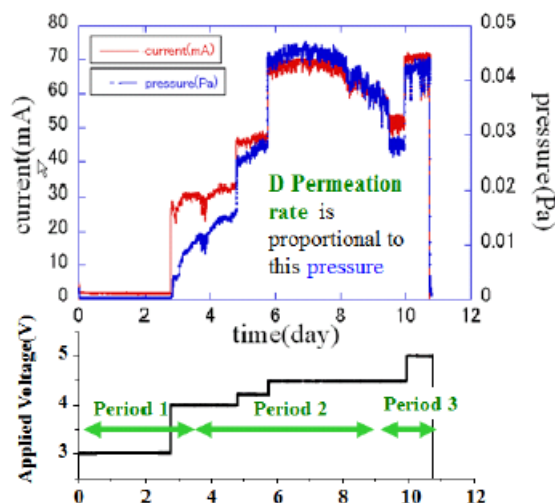


Figure 6. Time variation of applied voltage, current and pressure during an experiment E16.

increased, however, the current and D permeation decreased gradually even though we did not change the applied voltage.

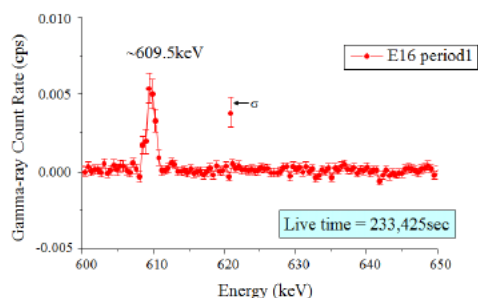
In this experiment, Pd/Y₂O₃/Pd multilayer thin film with Cs implantation and 0.5 M CsNO₃–D₂O solution were used.

Gamma-ray measurements using a Germanium detector were performed during electrochemical D permeation experiments. In this experiment (E16), gamma-ray energy spectra were obtained for three periods shown in Fig. 6. We deducted background energy spectra from obtained gamma-ray spectra during periods 1–3.

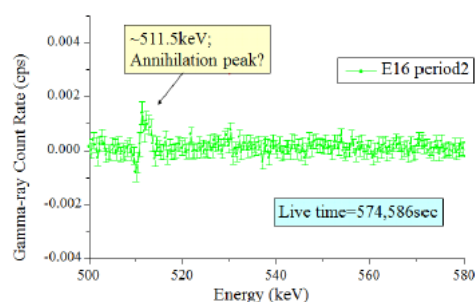
Emitted gamma-ray spectra are plotted in Fig. 7 (a)–(c), which correspond to periods 1–3, respectively. Standard deviations are also plotted for each point in all spectra. During period 1, very low current and low permeation rate, a clear gamma-ray peak around 609 keV exceeding statistic error was detected. During periods 2 and 3, relatively high current and large amount of D permeation, the 609 keV gamma-ray vanished and a peak around 511 keV was detected. There was no 511 keV peak during period 1.

Gamma-rays were not always detected. Energy spectra, in most cases, were exactly the same as background spectra, which were taken several times using the same set-up without D permeation. In the case of experiment E16, as well as a few experiments, gamma-rays exceeding statistical errors were detected. Ge detector and experimental apparatus were fixed during the experiments, off course.

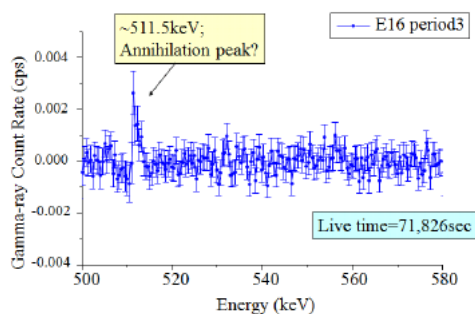
We could not observe clear gamma-ray emissions for D₂ gas permeation experiments for long time. What does it mean that we can observe weak gamma-ray emissions recently from the electrochemical D permeation? The electrochemical D permeation method gives us more transmuted products than D₂ gas permeation method. Detection of gamma-ray might be correlated to the increase of the transmuted products. The 511 keV gamma-ray is closed to annihilation energy and we might have some unstable nuclear species that emit positron. Further study is necessary to identify the source of the gamma-ray emitter. We are now planning to suppress the background gamma-rays in order to obtain better statistic results.



(a)



(b)



(c)

Figure 7. Gamma-ray emissions during an electrochemically D permeation experiment E16. (a) Gamma-ray energy spectrum emitted during period 1. (b) Gamma-ray energy spectrum emitted during period 2. (c) Gamma-ray energy spectrum emitted during period 3.

3. Effect of Laser Irradiation

As I described in Table 2, work function of the intermediate layer seems to be important. Then we assumed that electron rich state was important. In order to make electron rich state near surface of the Pd multilayer thin film, we tried to use laser stimulation method that was reported by Letts [9] to enhance excess heat generation.

If we irradiate the surface of the Pd multilayer, surface Plasmon is excited. So we would have a lot of high electron

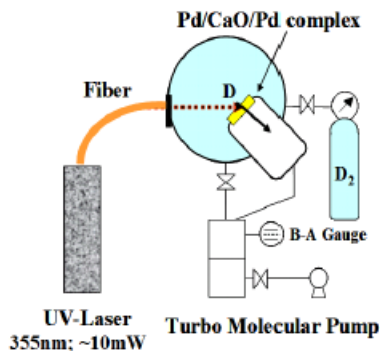


Figure 8. Schematic of the experimental set-up for plasmon excitation by laser irradiation.

density region by the Plasmon excitation. As the Plasmon has pico-second order wave and typical nuclear reaction occurs within the order of femto-second, high electron density region would be kept high during nuclear transmutation reaction proceed. Therefore it might be possible to enhance the rate of nuclear transmutation reaction by laser irradiation.

Figure 8 shows a schematic of the experimental set-up for Plasmon excitation by laser irradiation. A fiber UV-laser that has 355 nm wave length was applied. The multilayer Pd complexes are Pd/CaO/Pd and D₂ gas permeation experiments with laser irradiation were performed 3 times.

An example of experimental results is shown in Fig. 9. SIMS spectra for the permeated with laser irradiation and no permeation samples are plotted. As you can see, ¹³³Cs decreased and ¹⁴¹Pr emerged in a very similar way to the original D₂ gas permeation experiments. According to this result, we cannot find enhancement by laser irradiation.

The effect of laser irradiation on D₂ gas permeation rate is shown in Fig. 10. The laser-irradiated periods are painted with blue color. The D₂ gas permeation rate decreased when the laser was irradiated for all the cases as shown in Fig. 10. The mechanism for this phenomenon is not clear but deuterium absorption process might be influenced by

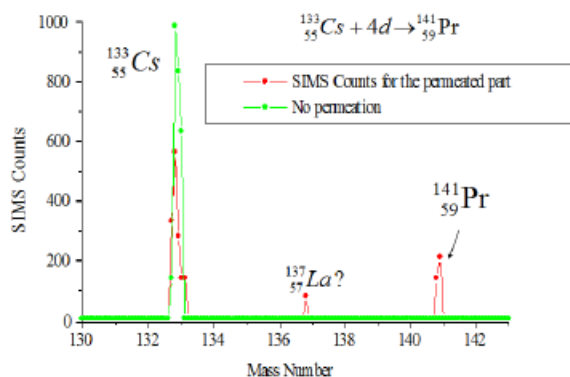


Figure 9. SIMS spectra for the permeated with laser irradiation and No permeation samples.

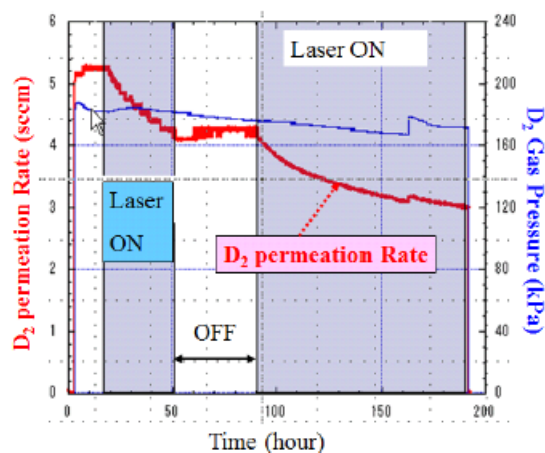


Figure 10. Effect of laser irradiation on D₂ gas permeation rate.

laser irradiation. D₂ gas permeation rate is one of the important factors to induce permeation transmutation reactions [4]; laser irradiation method is not so desirable in the view of the permeation rate.

4. Concluding Remarks

We tried two types of experimental approaches in order to increase transmuted products in the deuterium permeation induced transmutation reactions. One is the electrochemical deuterium permeation method to increase the surface deuterium density near the surface of the nano-structured Pd multilayer film. The other is the laser irradiation method for making electron rich state near the surface. The electrochemical deuterium permeation method gave us increased transmutation products, although the effect of the laser irradiation method was not clear. Many kinds of transmuted products were obtained and gamma-ray emissions were observed by the electrochemical deuterium permeation method. It is necessary to perform more experiments from different viewpoints using the other measurement methods and improve the reliability of our experiments.

Acknowledgments

The authors would like to acknowledge Prof. K. Fukutani, Prof. D. Sekiba, Dr. C. Nishimura, Prof. A. Takahashi, Prof. J. Kasagi, Dr. Hioki, Dr. F. Clelani, Prof. M. Melich, Dr. K. Grabowski, Prof. H. Yamada and Prof. S. Narita for their supports and valuable discussions.

References

- [1] Y. Iwamura, M. Sakano and T. Itoh, Elemental analysis of Pd complexes: effects of D₂ gas permeation, *Japanese J. Appl. Phys.* **41** (2002) 4642–4650.
- [2] Y. Iwamura, T. Itoh, N. Yamazaki, J. Kasagi, Y. Terada, T. Ishikawa, D. Sekiba, H. Yonemura and K. Fukutani, Observation of low energy nuclear transmutation reactions induced by deuterium permeation through multilayer Pd and CaO thin film, *J. Condensed Matter Nucl. Sci.* **4** (2011) 132–144.

- [3] Y. Iwamura, T. Itoh, M. Sakano, S. Kuribayashi, Y. Terada and T. Ishikawa, Observation of surface distribution of products by X-ray fluorescence spectrometry during D₂ gas permeation through Pd complexes, *Condensed Matter Nuclear Science*, A. Takahashi et al. (Ed.), World Scientific, New Jersey (2006), pp.178–187.
- [4] Y. Iwamura, T. Itoh, M. Sakano, S. Sakai and S. Kuribayashi, Low Energy Nuclear transmutation in condensed matter induced by D₂ gas permeation through Pd complexes: Correlation between deuterium flux and nuclear products, *Condensed Matter Nuclear Science*, P. H. Hagelstein and S. Chubb (Eds.), World Scientific, New Jersey (2006), pp. 435–446.
- [5] Y. Iwamura, T. Itoh, N. Yamazaki, N. Watari, H. Yonemura, K. Fukutani and D. Sekiba, Recent advances in deuterium permeation transmutation experiments, *Proc. ICCF16*, to be published.
- [6] N. Takahashi, S. Kosaka, T. Hioki and T. Motohiro, Detection of Pr in Cs ion-implanted Pd/CaO multilayer complexes with and without D₂ gas permeation, *Proc. ICCF17*, to be published..
- [7] T. Higashiyama, M. Sakano, H. Miyamaru and A. Takahashi, Replication of MHI Transmutation experiment by D₂ gas permeation through Pd complex, *Proc. 10th Int. Conf. on Condensed Matter Nuclear Science*, P.H. Hagelstein et al. (Eds.), *Condensed Matter Nuclear Science*, World Scientific, New Jersey (2006), pp. 447–454.
- [8] H. Yamada et al., Producing transmutation elements on plain Pd-foil by permeation of highly pressurized deuterium gas, *Proc. 12th Int. Conf. on Condensed Matter Nuclear Science*, A. Takahashi et al. (Eds.), *Condensed Matter Nuclear Science*, World Scientific, New Jersey (2006), pp. 196–205.
- [9] D. Letts and D. Cravens, Laser stimulation of deuterated palladium: past and present, *Proc. ICCF10*, 2003. Cambridge, World Scientific, Singapore (2006), pp.159–170.



Research Article

Neutron Burst Emissions from Uranium Deuteride and Deuterium-loaded Titanium

Songsheng Jiang *, Xiaoming Xu, Liqun Zhu, Shaogang Gu, Xichao Ruan, Ming He and Bujia Qi

China Institute of Atomic Energy, People's Republic of China

Xing Zhong Li

Tsinghua University, People's Republic of China

Abstract

This paper reports new results of anomalous neutron bursts (high-frequency neutron bursts) from deuterium-loaded titanium and uranium deuteride samples at room temperature. The number of neutrons in the large bursts is up to 2800 in an interval of less than 30 s, and the highest frequency of neutron bursts is 13 bursts in 7 min. Accidental artifact noise and cosmic-ray sources are ruled out. We suggest that the anomalous neutron bursts are correlated with deuterium-loaded metals and probably the result of nuclear reactions occurring in the samples.

© 2014 ISCMNS. All rights reserved. ISSN 2227-3123

Keywords: Deuterated metals, Low-energy nuclear reaction, Neutron burst emission, Normal temperature

1. Introduction

In 1989, Fleischmann and Pons, and Jones et al. claimed the production and detection of neutrons from D–D nuclear reactions in deuterated palladium and titanium by using the electrolytic method. Since then, the actual emission of neutrons from deuterium-loaded metals has been a matter of discussion among scientists. Because of the difficulty of detecting low-level neutrons and infrequent neutron-production from nuclear reactions, the results were often contradictory or not reproducible. However, some positive results have been reported [1–4].

Measuring neutrons in low-energy nuclear reactions (LENR) requires particular care and expertise. Because of the low level and infrequency of neutron production, it is difficult to measure energy spectra at a high confidence level. Therefore, each individual neutron burst must be evaluated to determine whether its origin was electronic noise, environmental gamma-rays, cosmic-ray background, environment neutrons, accidental artifact noise or a legitimate signal.

*E-mail: ssjiang@ciae.ac.cn

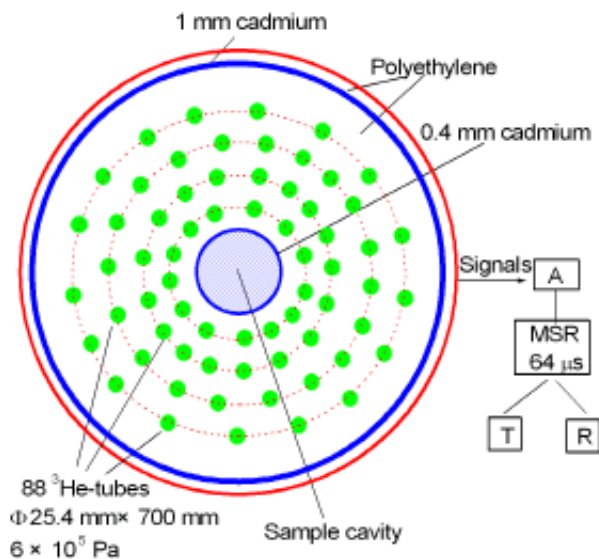


Figure 1. A top view of the neutron detector system. The A, MSR, T and R denote amplifiers, multiply shift registers, counter for time-correlated signals and counter for random signals, respectively.

In this work, measurements of neutron emission from uranium deuteride and deuterium-loaded titanium samples are carried out by using a high-efficiency neutron detector and update time-correlated (coincidence) counting technique. The experimental result provides strong evidence for neutron burst emissions from deuterated metals at room temperature. Observation of nuclear products, such as neutrons, protons and tritium in metal hydride (deuteride) [5,6] will be helpful to study the mechanism of LENR and origin of excess ^3He and tritium in the deep earth [7–9].

2. Experimental Details

2.1. Neutron detection

The detector has high neutron detection efficiency and a good ability to reject γ -ray background and eliminate electrical noise. The multiplicity shift register circuit [10] was used for recording both the random and time-correlated neutrons, and is able to quantitatively measure a single burst of neutrons lasting a few microseconds. The multiplicity shift register has a better ability than the common shift register [11]. It can record all time-correlated (coincidence) neutron events, not just single and double neutron events. The time interval of the coincidence gate was $64 \mu\text{s}$ in this work. The detector consists of 88 ^3He -tubes with pressure of $6 \times 10^5 \text{ Pa}$, embedded in the polyethylene moderator (Fig. 1). The sample cavity located at the center of the detector has a diameter of 16.5 cm and height of 40 cm, and is lined with 0.4 mm cadmium. A graphite cylinder with diameter of 16.5 cm and height of 18 cm fills the bottom end of the cavity and another cylinder is used as a plug at the top of the cavity to reflect neutrons emitted from the sample. The detector body has an outside diameter of 70 cm and height of 80 cm, and the whole detector body is shielded from thermal neutrons with 1 mm of cadmium. The neutron detection efficiency was calibrated by using a ^{252}Cf neutron source (average neutron energy 2.3 MeV) and found to be greater than 50%.

Another neutron detector (also called the neutron monitor) was used for monitoring the environmental neutron background and accidental artifact noise during sample measurements. The detector consists of three polyethylene

slabs of $30 \times 30 \times 6 \text{ cm}^3$. Four ^3He -tubes were embedded in each slab. The relative efficiency of the neutron monitor to the main neutron detector is about 40% for detection of the environmental neutron background. The monitor has the electronic circuitry and a multiplicity shift register similar to that of the main neutron detector. Thus, the two detectors have similar sensitivity to the signals of accidental artifact noise. The two detectors were 2 m apart. The neutron monitor was used for monitoring the variation of the environmental neutron background and accidental artifact vibration noise.

There are two nuclear processes for nuclear reactions occurring in the deuterium-loaded metals: burst (time-correlated) and continuous (random or accidental) reactions. We use multiplicity shift register for recording both time-correlated neutron burst and random events.

2.2. Uranium deuteride and deuterium-loaded titanium samples

We measured two sorts of deuterium-loaded metal samples: deuterium-loaded uranium (uranium deuteride) and deuterium-loaded titanium samples. Uranium deuteride has a high D/U atom ratio of 3, which is a factor of 2 greater than D/Ti ratio. The uranium (^{238}U) metal machine-chips (about 10 g) were used to prepare the uranium deuteride sample. The procedures used for preparation of uranium deuteride were performed as described in the previous work [12]. After loading deuterium in uranium chips, the chips were broken into fine powder. The uranium-deuteride powder was sealed into a stainless-steel cylinder with an inner diameter of 2 cm and length of 18 cm, and the thickness of the stainless-steel was 5 mm. The deuterium-loaded titanium foil sample consists of a set of various types of foils. These include one deuterium-loaded titanium foil with a thickness of 0.1 mm and weight of 150 mg and the D/Ti atomic ratio in 10 μm depth of the surface layer of the foil was estimated to be 1. The other types were six Ti–Mo foils. The Ti–Mo foils were prepared by vaporizing titanium onto the molybdenum discs, which had a thickness of 0.5 mm and a diameter of 20 mm. The thickness of titanium varied from about 1.5–4.5 mg/cm^2 , and the D/Ti atom ratios were ~ 1.4 . The total weight of titanium for all of the deuterium-loaded titanium foils was about 250 mg. All of the deuterium-loaded titanium foils were placed in a 0.5-mm thick aluminum container having a diameter of 9 and 6 cm high. The procedures for loading deuterium into titanium were described in the previous work [5]. Industrial deuterium gas was used for the preparation of the deuterium-loaded titanium samples. The experiment result shows that hydrogen isotopes in the chemical forms of DH, H_2 and H_3 were also mixed in the deuterium gas. The atomic ratio of H/D in the deuterium gas was evaluated to be greater than 5% [5]. Thus, a considerable amount of hydrogen was also loaded into the titanium together with the deuterium.

2.3. Control samples

Control experiments were carried out using uranium oxide and deuterium-unloaded titanium foil samples. The uranium oxide ($\sim 30 \text{ g}$) was sealed into a plastic square box with a volume of 50 cm^3 and a plastic thickness of 1 mm. The deuterium-unloaded titanium foil with 0.1 mm thickness ($\sim 3 \text{ g}$) is sealed into an aluminum can with diameter of 9 cm, height of 6 cm and aluminum thickness of 0.5 mm.

3. Results

Five runs were taken for the background measurements and five runs were also taken for the uranium deuterium and deuterium-loaded titanium samples, respectively. Each run lasted about 20–50 h, or about 2500–6500 cycles. The period of a cycle is 30 s.

3.1. Measurement of neutron random emissions

The results of the random neutron (including ^{238}U spontaneous fission neutrons in the samples) count rates for the samples and background are plotted in Fig. 2. The random neutron count rates for the five background runs were

measured from 1.660 to 1.775 counts/s, and the average random count rate is (1.712 ± 0.030) counts/s. The average random count rate was 1.798 ± 0.030 and 1.716 ± 0.030 for the uranium deuteride and deuterium-loaded titanium sample, respectively. As a result of ^{238}U spontaneous fission, the average random count rates for the uranium oxide and uranium deuteride samples are greater than the rates for the deuterium-loaded titanium and deuterium-unloaded titanium samples. Based on the ^{238}U spontaneous-fission neutron rate of 0.0136 neutron/s·g [10] and a neutron detector efficiency of 0.55, the neutron production rate is calculated to be 0.16 neutrons/s, or 0.88 counts/s, a value equivalent to the number of neutrons emitted from spontaneous fission in the ~ 10 g uranium metal sample. Two runs were taken for the measurement of uranium oxide (~ 30 g). The average random count rate for uranium oxide sample was (1.971 ± 0.03) counts/s, a value of (0.26 ± 0.03) counts/s greater than the background value. The higher value is the result of ^{238}U spontaneous fission in the uranium oxide sample. On the other hand, no difference in average count rates between the deuterium-loaded titanium sample and background is observed within an uncertainty of 2%. Therefore, no excess random neutron emission is observed for either uranium deuteride or deuterium-loaded titanium samples at the background level in this work.

3.2. Time-correlated neutron events for background

The results of time-correlated (coincidence) neutron counts versus the counting cycle in four background runs are given in Fig. 3.

These results show that the intensity and frequency of neutron bursts have irregular variations. The number of neutrons in a burst varies from about 10–750 counts or 18–1400 neutrons in the 30 s in the 5 runs. The frequency of the large bursts (more than 30 neutrons) is about 1–5 bursts per day, and time intervals between two individual bursts are longer than 2 h. The large neutron bursts may originate from spallation induced by high energy (1–100 GeV) cosmic rays in the detector body matter, i.e. polyethylene moderator and other components [1].

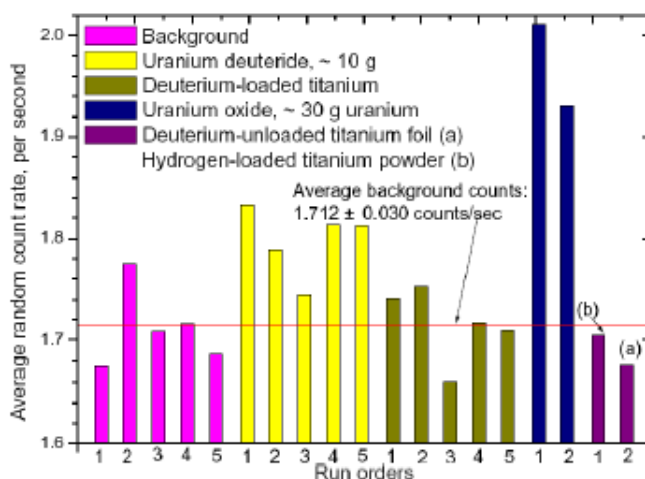


Figure 2. Random neutron count rates for sample measurements. Five runs were taken for background, uranium deuteride and deuterium-loaded titanium samples, respectively, and two runs for uranium oxide and deuterium-unloaded titanium samples, respectively.

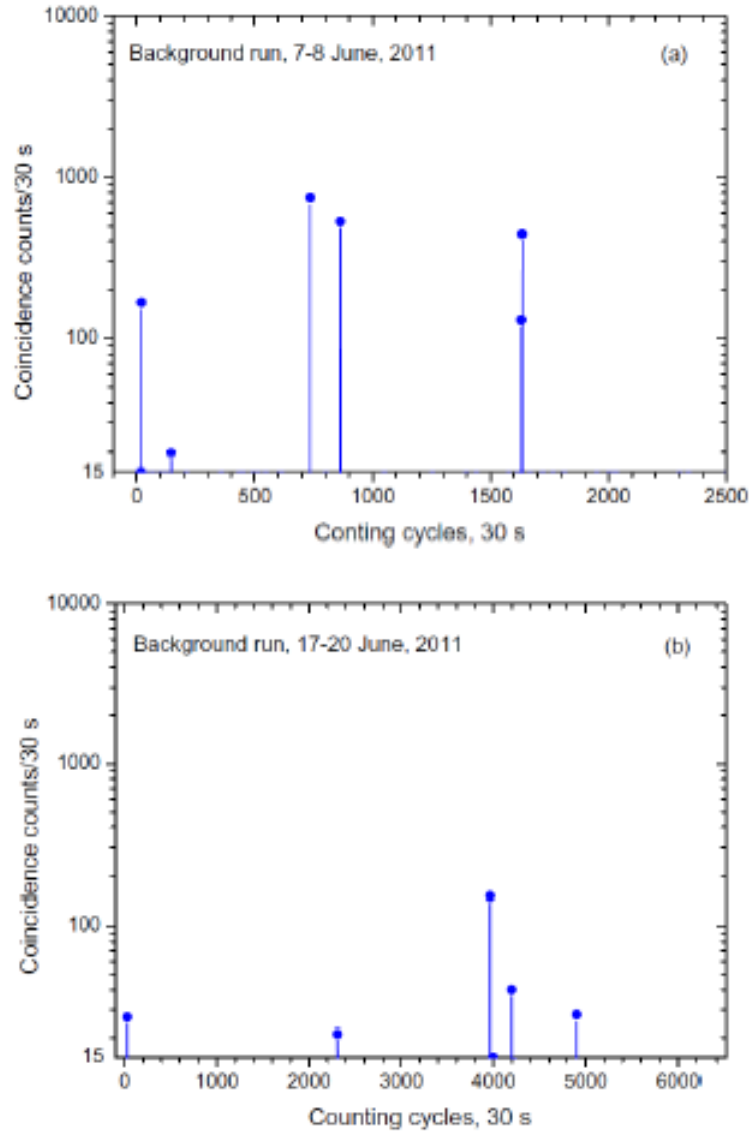


Figure 3a–b

3.3. Anomalous neutron burst emissions for uranium deuteride and deuterium-loaded titanium samples

The four results for uranium deuteride and deuterium-loaded titanium samples are plotted in Fig. 4, and the anomalous neutron bursts are shown. Eight bursts occurred between cycles 365–380 (~ 7 min), and 13 bursts occurred between cycles 2400–2415 (~ 7 min) for a uranium deuteride sample on 8–9 June, 2011 (Fig. 4a). Such high-frequency neutron

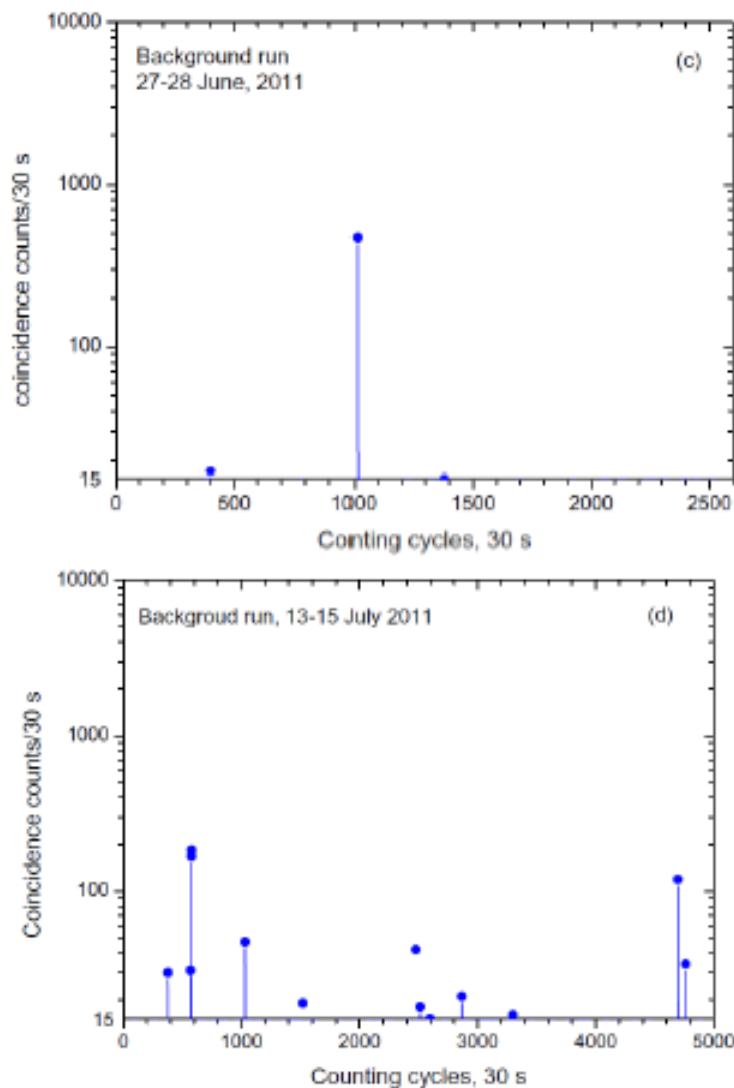


Figure 3c–d

Figure 3. Coincidence neutron counts versus counting cycles for the background measurements.

bursts have never been observed for the background runs at our laboratory, and they are not reported in the literature. The high-frequency neutron bursts are also observed for the other runs. Eleven neutron bursts occurred between cycles 1798–2949 (~120 min), and 5 bursts occurred between cycles 2819 and 2863 (~20 min) on 22–24 June, 2011 (Fig. 5b). The largest intensity of neutron bursts for the uranium deuteride sample was 1181 counts or 2150 neutrons in the 30 s (Fig. 5b). The high-frequency neutron bursts are also observed for deuterium-loaded titanium sample. Three bursts occurred between cycle 449 and 479 (~15 min) and between cycles 1616 and 1624 (~4 min), and four bursts

occurred between cycles 2511 and 2530 (~ 10 min) on 11–13 July, 2011 (Fig. 4c). Six bursts occurred between cycles 2511 and 2715 (~ 100 min) and five bursts occurred between cycles 5053 and 5074 (~ 10 min) on 19–22 July, 2011 (Fig. 4d). The highest intensity of neutron bursts for deuterium-loaded titanium sample was 1541 neutrons, or 2800 neutrons in the 30 s (Fig. 4c). The two high-frequency neutron burst events observed on 8–9 June are enlarged in Fig. 5.

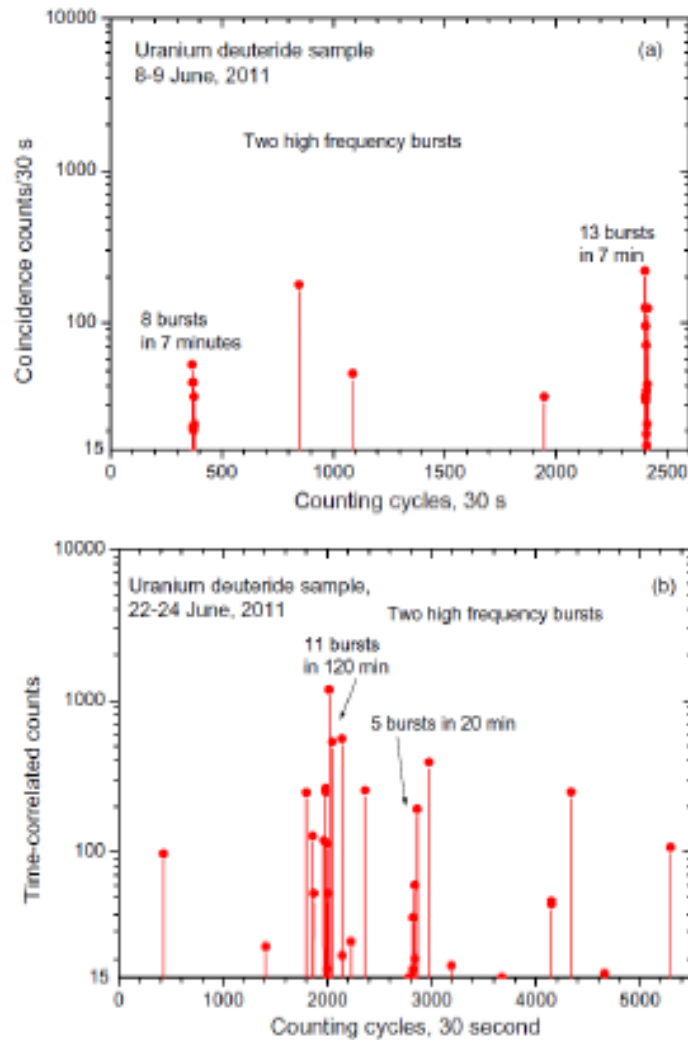


Figure 4a–b

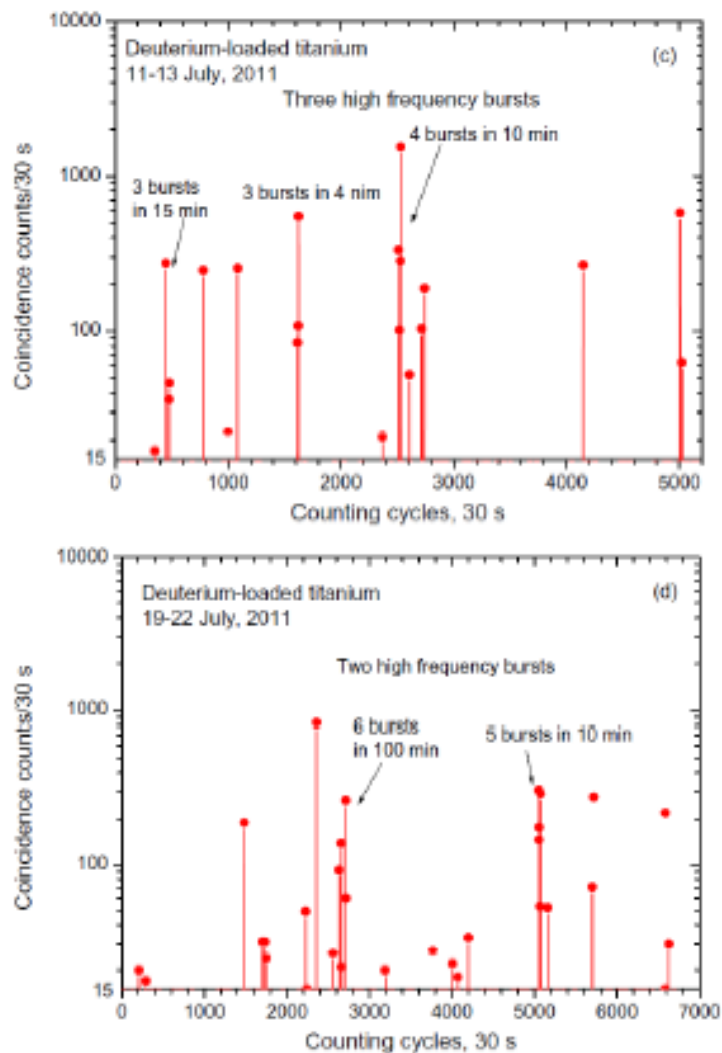


Figure 4c–d

Figure 4. Coincidence neutron counts versus counting cycles for uranium deuteride and deuteride-loaded titanium samples.

3.4. Time-correlated Neutron burst events for the control samples

Control experiments were carried out using uranium oxide and deuterium-unloaded samples. Total numbers of neutron bursts in 24 and 50 h were 4 and 10 for the uranium oxide sample on 21–22 June, 2011 (Fig. 6a) and 28 June–1 July, 2011, respectively (Fig. 6b). The total number of bursts was 12 for the deuterium-unloaded titanium foil sample in ~50 h (Fig. 6c). No high-frequency neutron burst emissions are observed for either of the control samples.

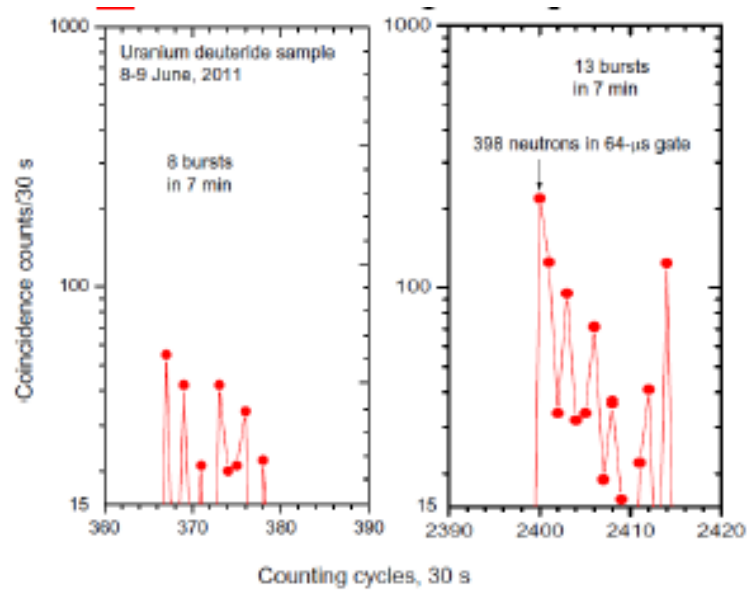


Figure 5. The two enlarged cascade neutron burst events for uranium deuteride sample (see original plot in Fig. 4a).

4. Conclusions

We have reported new results of neutron burst emission from deuterium-loaded metals. In addition to normal neutron bursts induced by cosmic-ray spallations, high-frequency neutron bursts are observed occasionally for uranium deuteride

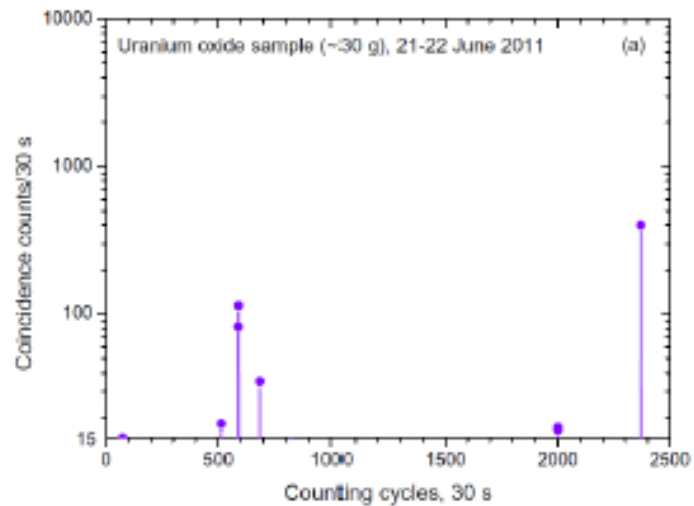


Figure 6a

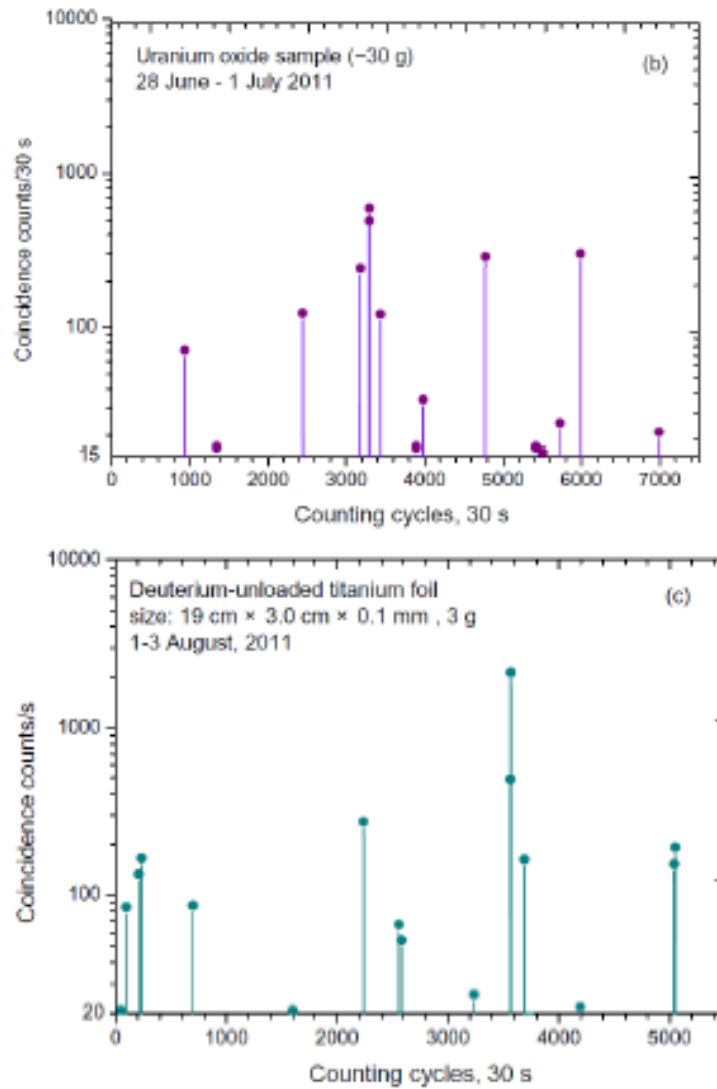


Figure 6. Coincidence neutron counts versus counting cycles for uranium oxide and deuterium-unloaded titanium samples (Fig. 6a–c).

and deuterium-loaded titanium samples. In this measurement, another neutron detector, i.e. neutron monitor, was used for monitoring the variation of the environmental neutron backgrounds and accidental artifact vibration noise. No anomalous signals were observed. Therefore, the accidental artifact burst events may be ruled out in sample measurements. We suggest that the high-frequency neutron bursts are correlated with the deuterium-loaded metals and may originate from a nuclear reaction occurring on the metal surface with a micro-nanometer size[5,13], but do not occur in the bulk materials and whole surface. The number of neutrons in the large bursts was measured as being up to 2800 in an interval of less than 30 s. On the other hand, random neutron emissions are not observed in this work.

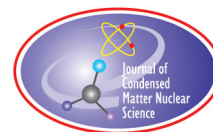
Measurement of neutron burst emission may have special significance in understanding the mechanism of LENR and heat production. The mechanism of neutron burst emission in deuterium-loaded metals remains an open question. Although reaction mechanisms have been supposed, as yet no theory has gained wide acceptance [14].

Acknowledgements

We are grateful to Dr. Takahashi for his kind pre-review and helpful comments. This work was supported by President Foundation of the China Institute of Atomic Energy (No. YZ-0704).

References

- [1] H.O. Menlove, M.M. Fowler, E. Careia, A. Mayer, M.C. Miller, R.R. Ryan and S.E. Jounes, The measurement of neutron emission from Ti and Pd in pressurized D₂ gas and D₂O electrolysis cells, *Journal of Fusion Energy*, vol. 9, pp. 495–506. 1990.
- [2] G. Mengoli, M. Fabrizio, C. Manduchi, E. Milli and G. Zannoni, Absorption–desorption of deuterium at Pd95%–Rh5% alloy. \ddagger U: Neutron emission, *J. Electroanal. Chem.* **10** (1995) 249–260.
- [3] P.A. Mosier-Boss, S. Szpak, F.E. Gordon and L.P.G. Forsley, Triple tracks in CR-39 as results of Pd/D Co-deposition: evidence of energetic neutrons, *Naturwissenschaften* **96** (2009) 135–142.
- [4] S.-S. Jiang, J.-H. Li, J.Q. Wang, M. He, S.-Y. Wu, H.T. Zhang, S.-H. Yao and Y.-G. Zhao, Measurement of anomalous nuclear reaction in deuterium-loaded metal, *Chinese Phys. B* **18** (1999) 1428–1435.
- [5] S.-S. Jang, M. He, S.-Y. Wu and B.-J. Qi, Anomalous high isotope ratio $^3\text{He}/^4\text{He}$ and tritium in deuterium-loaded metal: evidence for nuclear reaction in metal hydrides at low temperature, *Chinese Phys. Lett.* **29** (2012) 12503–1–3.
- [6] S.-S. Jiang, L. Jin and M. He, A possible in situ ^3H and ^3He source in Earth's interior: an alternative explanation of origin of ^3He in deep Earth, *Naturwissenschaften* **97** (2010) 655–662.
- [7] S.E. Jones and J.E. Ellsworth, Cold (metal-enhanced) fusion, geo-fusion, and cold nucleosynthesis, *Condensed Matter Nuclear Science*, World Scientific, London, 2005, p. 617.
- [8] S.-S. Jiang and M. He, Anomalous nuclear reaction in Earth's interior: a new field in physics science? , *Plasma Sci. Technol.* **14** (2012) 438–441.
- [9] N. Ensstin, W. Harker, M.S. Krick, D.G.. Langner, M.M. Pickrell and J.E. Stewart, Application guide to neutron multiplicity counting , *LA-13422-M Manual*, Los Alamos, 1998.
- [10] H.O. Menlove and M.C. Miller, Neutron-burst detector for cold fusion experiments, *Nucl. Instr. Meth. A* **299** (1990) 10–16.
- [11] P. Seungwoo, D.H. Ahn, K.R. Kim and H. Chung, Characteristics of reaction between hydrogen isotopes and depleted uranium, *J. Ind. Eng. Chem.* **8** (2002) 12–16.
- [12] Y.E. Kim, Theory of Bose–Einstein condensation mechanism for deuteron-induced nuclear reactions in micro/nano-scale metal grains and particles, *Naturwissenschaften* **96** (2009) 803–811.
- [13] E. Storms, *The Science of Low-energy Nuclear Reaction*, World Scientific, Singapore, 2007.



Research Article

Conventional Nuclear Theory of Low-energy Nuclear Reactions in Metals: Alternative Approach to Clean Fusion Energy Generation

Yeong E. Kim *

Department of Physics, Purdue University, West Lafayette, IN 47907, USA

Abstract

Low-energy nuclear reactions (LENRs) in metals are described using conventional nuclear theory based on the optical theorem formulation. It can be applied to both deuteron and proton induced LENRs. Cryogenic ignition of deuteron fusion in metal particles is proposed as an alternative approach to clean fusion energy generation.

© 2014 ISCMNS. All rights reserved. ISSN 2227-3123

Keywords: Deuteron fusion in metals, Nuclear theory, Nuclear transmutations, Optical theorem formulation

1. Introduction

Over the last two decades, there have been many publications reporting experimental observations of excess heat generation and anomalous nuclear reactions occurring in metals at ultra-low energies, now known as ‘low-energy nuclear reactions’ (LENRs). After a review of key experimental observations, theoretical explanations of the LENR phenomena will be described by conventional nuclear theory based on the optical theorem formulation of LENRs (OTF-LENRs) [1] and theory of Bose–Einstein condensation nuclear fusion (BECNF) in micro/nano-scale metal particles [2–11]. Proposed experimental tests of the basic assumption and theoretical predictions as well as potential application to cryogenic ignition of deuteron fusion in micro/nano-scale metal particles will be described [11,12].

The OTF-LENRs [1,2] can be applied to both conventional nuclear beam experiments and also to LENRs in metals. The BECNF theory [2–12] is merely one of many potential applications of the OTF-LENRs, which we will be exploring in future. The OTF-LENRs can also be applied to proton–nucleus transmutation reactions, etc. It can be applied possibly to biological transmutations

*E-mail: yekim@purdue.edu

2. Anomalous Experimental Results

2.1. D + D reaction channels in free space

The conventional deuterium fusion in free space proceeds via the following nuclear reactions:

- {1} $D + D \rightarrow p (3.02 \text{ MeV}) + T (1.01 \text{ MeV}),$
- {2} $D + D \rightarrow n (2.45 \text{ MeV}) + {}^3\text{He} (0.82 \text{ MeV}),$
- {3} $D + D \rightarrow {}^4\text{He} + \gamma (23.8 \text{ MeV}).$

The cross-sections for reactions {1}–{3} are expected to be extremely small at low energies ($\leq 10 \text{ eV}$) due to the Gamow factor arising from Coulomb barrier between two deuterons. The measured cross-sections have branching ratios: $(\sigma\{1\}, \sigma\{2\}, \sigma\{3\}) \approx (0.5, 0.5, \sim 10^{-6})$.

Experimental values of the conventional hot-fusion cross section $\sigma(E)$ for reaction {1} or {2} have been conventionally parameterized as [13]:

$$\sigma(E) = \frac{S}{E} e^{-2\pi\eta} = \frac{S}{E} e^{-\sqrt{E_G/E}} \quad (1)$$

with

$$\eta = \frac{1}{2kr_B}, \quad r_B = \frac{\hbar^2}{2\mu e^2}, \quad \mu = m/2,$$

where $e^{-2\pi\eta}$ is known as the “Gamow factor”, and E_G is the “Gamow energy” given by

$$E_G = (2\pi\alpha Z_d Z_d) \mu c^2 / 2 \quad \text{or} \quad \sqrt{E_G} \approx 31.39 \sqrt{\text{keV}}$$

for the reduced mass $\mu = m/2$ for reactions {1} or {2}.

The value E is measured in keV in the center-of-mass (CM) reference frame. The S -factor, $S(E)$, is extracted from experimentally measured values [14] of the cross section $\sigma(E)$ for $E \geq 4 \text{ keV}$ and is nearly constant [15]; $S(E) \approx 52.9 \text{ keV-barn}$, for reactions {1} or {2}, in the energy range of interest here, $E \leq 100 \text{ keV}$. The S -factor is known as “astrophysical S -factor” [13].

2.2. D + D Reaction channels in metals

From many experimental measurements by Fleischmann and Pons [16] in 1989, and many others [17–19] over 23 years since then, the following experimental observations have emerged from experimental results reported from electrolysis and gas-loading experiments. They are summarized below (as of 2011, not complete: exit reaction channels {4}–{6} are defined below and are shown in Fig. 1):

- (1) The Coulomb barrier between two deuterons are suppressed.
- (2) Production of nuclear ashes with anomalous rates: $R\{4\} \ll R\{6\}$ and $R\{5\} \ll R\{6\}$.
- (3) ${}^4\text{He}$ production commensurate with excess heat production, no $23.8 \text{ MeV } \gamma$ -ray.
- (4) Excess heat production (the amount of excess heat indicates its nuclear origin).
- (5) More tritium is produced than neutron $R\{4\} > R\{5\}$.
- (6) Production of hot spots and micro-scale craters on metal surface.
- (7) Detection of radiations.

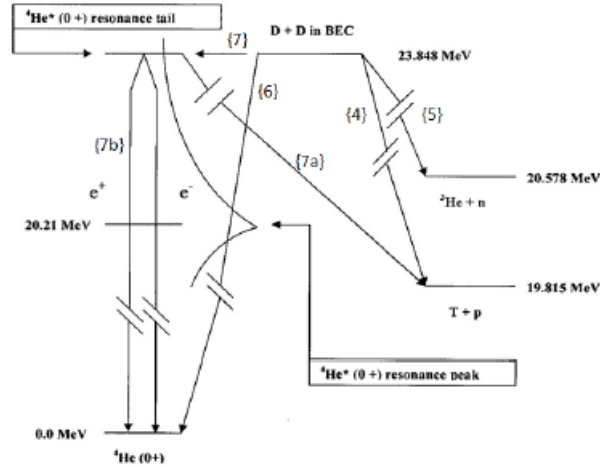


Figure 1. Exit reaction channels for D + D reactions in metal. Parallel bars indicate break in energy scale.

- (8) “Heat-after-death”.
- (9) Requirement of deuteron mobility ($D/Pd > \sim 0.9$, electric current, pressure gradient, etc.).
- (10) Requirement of deuterium purity ($H/D \ll 1$).

All of the above experimental observations are explained either quantitatively or qualitatively in terms of theory of BECNF in previous publications [2–12].

As shown in Fig. 1, at ambient temperatures or low energies (≤ 10 eV), deuterium fusion in metal proceeds via the following reactions:

- {4} $D(m) + D(m) \rightarrow p(m) + T(m) + 4.03 \text{ MeV (m)}$,
- {5} $D(m) + D(m) \rightarrow n(m) + {}^3\text{He}(m) + 3.27 \text{ MeV (m)}$,
- {6} $D(m) + D(m) \rightarrow {}^4\text{He}(m) + 23.8 \text{ MeV (m)}$,

where m represents a host metal lattice or metal particle. Reaction rate R for {6} is dominant over reaction rates for {4} and {5}, i.e., $R\{6\} \gg R\{4\}$ and $R\{6\} \gg R\{5\}$.

3. Optical Theorem Formulation

In this section, we introduce a low-energy “partial-wave” optical theorem and use it to develop the optical theorem formulation (OTF) of LNERs.

3.1. Optical theorem for positive energy scattering

The conventional optical theorem first introduced by Feenberg [20] is given by

$$\sigma_t = \frac{4\pi}{k} \text{Im} f(0), \quad (2)$$

which shows that the total cross section is related to the elastic scattering amplitude in the forward direction, $f(0)$. To avoid complications associated with the singularity of the forward Coulomb scattering amplitude $f_c(0)$ as in the case of the conventional optical theorem, for two-potential scattering involving two charged nuclei, we used a different formulation based on a partial-wave optical theorem involving angle-integrated and/or angle-independent quantities to obtain the following optical theorem formula [1]

$$\text{Im } f_l^{n(\text{el})} \approx \frac{k}{4\pi} \sigma_l^r, \quad (3)$$

where $f_l^{n(\text{el})}$ and σ_l^r are the l -th partial wave nuclear elastic scattering amplitude and reaction cross-section, respectively. The above formula is rigorous at low energies.

The elastic scattering amplitude can be written in terms of t-matrix as

$$f_l^{n(\text{el})} = -\frac{2\mu}{\hbar^2 k^2} \langle \psi_l^c | t_l | \psi_l^c \rangle, \quad (4)$$

where ψ_l^c is the Coulomb wave function for scattering between two charged particles. From Eqs. (3) and (4), we obtain the optical theorem formula for the dominant s-wave state as :

$$\frac{k}{4\pi} \sigma^r = -\frac{2\mu}{\hbar^2 k^2} \langle \psi_0^c | \text{Im } t_0 | \psi_0^c \rangle \quad (5)$$

and

$$\sigma^r = \frac{S}{E} e^{-2\pi\eta} \quad \text{with } \text{Im } t = -\frac{S r_B}{4\pi^2} \delta(\vec{r}). \quad (6)$$

The reaction rate is given by

$$R = v \sigma^r = -\langle \psi^c | \text{Im } V | \psi^c \rangle \quad (7)$$

with Fermi potential

$$\text{Im } V = -A \delta(\vec{r}_{ij}), \quad A = \left(\frac{2}{\hbar} \right) \frac{S r_B}{\pi},$$

where S is related to the nuclear force strength and the delta-function represents the short-range nature of the nuclear force.

3.2. Generalization to LENRs in metals

The above result (7) can be generalized to D + D fusion reactions in metals to obtain

$$R_t = -\frac{2}{\hbar} \frac{\sum_{i < j} \langle \psi | \text{Im } V_{ij}^F | \psi \rangle}{\langle \psi | \psi \rangle} \quad (8)$$

with Fermi potential

$$\text{Im } V_{ij}^F = -\frac{A \hbar}{2} \delta(\vec{r}_{ij}), \quad A = \left(\frac{2}{\hbar} \right) \frac{S r_B}{\pi}$$

Ψ is the bound-state solution of the many-body Schroedinger equation

$$H\Psi = E\Psi \quad (9)$$

with

$$H = T + V^{\text{confine}} + V^{\text{Coulomb}} \quad (10)$$

The above general formulation can be applied to (i) D + D reactions in metals, (ii) proton–nucleus transmutations, etc. It could also possibly applied to (iii) biological transmutations. For each case of (i)–(iii), an appropriate Hamiltonian is to be chosen for Eqs. (9) and (10). To be realistic to a chosen physical system, H could include many degrees of freedom for electrons, metal lattice structures, etc. However, we may have to choose a simpler model Hamiltonian for which Eq. (9) can be solved approximately.

3.3. Importance and significance of OTF-LENRs

It is important to note differences between Eqs. (7) and (8). Equation (7) is for nuclear reactions at positive energies (such as for nuclear scattering experiments using beam of nuclei), while Eq. (8) is for nuclear reactions between two nuclei in a bound state (such as deuterons bound in a metal). In the past, Eq. (7) is inappropriately used to argue that LENRs in metals are impossible. It should be emphasize that the use of Eq. (8) is more appropriate for LENRs in metals.

4. Bose–Einstein Condensation Nuclear Fusion Theory

In this section, as an application of the OTF-LENRs (Eqs. (8)–(10)), we describe theory of BECNF.

4.1. Deuteron mobility in metals

Experimental proof of proton (deuteron) mobility in metals was first demonstrated by Coehn in his hydrogen electro-migration experiment [21,22]. A theoretical explanation of Coehn's results [21,22] is given by Isenberg [23]. The Coehn's results are not well known in review articles and textbooks. Velocity distributions of protons (dueterons) in metal have not been measured as a function of temperatures.

4.2. Theory

For applying the concept of the BEC mechanism to deuteron fusion in a micro/nano-scale metal particle, we consider N identical charged Bose nuclei (deuterons) confined in an ion trap (or a metal grain or particle). Some fraction of trapped deuterons are assumed to be mobile as discussed above. The trapping potential is 3-dimensional (nearly sphere) for micro/nano-scale metal particles, or quasi-two-dimensional (nearly hemi-sphere) for micro-scale metal grains, both having surrounding boundary barriers. The barrier heights or potential depths are expected to be an order of energy (≤ 1 eV) required for removing a deuteron from a metal grain or particle. For simplicity, we assume an isotropic harmonic potential for the ion trap to obtain order of magnitude estimates of fusion reaction rates. N -body Schroedinger equation is given by Eq. (9) with the Hamiltonian H for the system given by

$$H = \frac{\hbar^2}{2m} \sum_{i=1}^N \Delta_i + \frac{1}{2} m \omega^2 \sum_{i=1}^N r_i^2 + \sum_{i < j} \frac{e^2}{|r_i - r_j|} \quad (11),$$

where m is the rest mass of the nucleus.

The approximate ground bound-state (GBS) solution of Eq. (9) with H given by Eq. (11) is obtained using the equivalent linear two-body method [4–6]. The use of an alternative method based on the mean-field theory for bosons yields the same result (see Appendix in [3]). Based on the optical theorem formulation of low energy nuclear reactions [1], the ground-state solution is used in Eq. (8) to derive the approximate theoretical formula for the deuteron–deuteron fusion rate in an ion trap (micro/nano-scale metal grain or particle). The detailed derivations are given elsewhere [2,3].

4.3. Reaction rate

Our final theoretical formula for the total fusion rate R_t for large N case is given by [2,3]

$$R_t = \frac{1}{4} \left(\frac{3}{\pi} \right)^{1/2} S B \Omega V n_D^2, \quad (12)$$

where $B = 2\hbar/(\pi m e^2) = 1.4 \times 10^{-18} \text{ cm}^3/(\text{sec-keV-barn})$, S is the S -factor for the nuclear fusion reaction between two deuterons, n_D is the deuteron number density, and V is the total volume. For $D(d,p)T$ and $D(d,n)^3\text{He}$ reactions, we have $S \approx 55 \text{ keV-barn}$. We expect also $S \approx 55 \text{ keV-barn}$ or larger for reaction {6}. Only two unknown parameters are (i) the probability of the ground bound-state (GBS) occupation, Ω , and (ii) the S -factor. Equation (12) shows that the total fusion rates, R_t , are maximized when $\Omega \approx 1$.

Equation (12) was derived analytically (no numerical calculations were involved). Equation (12) provides an important result that nuclear fusion rates R_t for large N case do not depend on the Gamow factor in contrast to the conventional theory for two-body nuclear fusion in free space. There is a simple classical analogy of the Coulomb field suppression. For an uniform spherical charge distribution, the Coulomb field diminishes toward the center and vanishes at the center.

4.4. Reaction mechanism

For a single trap (or metal particle) containing a large number N of deuterons, the deuteron–deuteron fusion can proceed with the two reaction channels {6} and {7}. We will discuss {6} in this section. {7} will be discussed in the next section.

For the large N case, the deuteron–deuteron reaction {6} in a GBS proceeds via



where the Q -value of 23.84 MeV is shared by ^4He and all D 's in a GBS state, thus maintaining the momentum conservation in the final state. This implies that the deuteron GBS state undergoes a micro/nano-scale explosion (“micro-explosion” or “nano-explosion”). For a micro/nano-scale metal particle of 10 nm diameter containing $\sim 3.6 \times 10^4$ deuterons, each deuteron or ^4He will gain only $\sim 0.7 \text{ keV}$ kinetic energy, if the excess kinetic energy of 23.84 MeV is shared equally. For a larger metal particle, $\sim 0.7 \text{ keV}$ is further reduced. This mechanism can provide an explanation for constraints imposed on the secondary reactions by energetic ^4He , as described by Hagelstein [24].

Furthermore, as these deuterons slow down in the host metal, they can release electrons from the host metal atoms, thus providing extra conduction electrons which may reduce the resistivity of the host metal.

Other exit channels, {4} and {5}, are expected to have much lower probabilities than that of the exit channel {6}, since both {4} and {5} involve centrifugal and Coulomb barrier transmissions of exit particles in the exit channels, while {6} does not, thus providing a theoretical explanation for the observation (2).

4.5. Role of Bose–Einstein condensation of deuterons

For BECNF processes, Bose–Einstein condensation of deuterons in metal is not required, but desirable for enhancing the fusion reaction rates as discussed below.

For $0.5 < \Omega < 1.0$, the GBS becomes a BEC state while for $\Omega < 0.1$ we have a GBS. For experimental results with very slow reaction rates observed so far, we have GBSs with $\Omega \ll 0.1$. For making Ω larger to improve reaction rates for scaling up the reaction rates and also improving reproducibility, it will require cooling (1) by lowering temperatures using coolants, or (2) by removing high velocity particles (evaporation cooling) with application of pressure gradients or with application of EM field gradients (including laser), etc.

5. Anomalous Tritium and Neutron Production

There have been many reports of anomalous tritium and neutron production in deuterated metal from electrolysis experiments [25–29] and gas/plasma loading experiments [30–36]. The reported branching ratio of $R(T)/R(n)$ ranges from 10^7 to 10^9 in contrast to the conventional free-space reactions branching ratio of $R\{1\}/R\{2\} \approx 1$. In this paper, we consider reaction rates for two exit channels to ${}^4\text{He}$ (0+, 0, 0.0 MeV) and ${}^4\text{He}^*$ (0+, 0, 20.21 MeV) states.

5.1. Sub-threshold resonance reaction channel

In this section, we present a theoretical explanation of observed anomalous tritium production based on the BECNF theory, utilizing a sub-threshold resonance (STR) state ${}^4\text{He}^*$ (0+) at 20.21 MeV with a resonance width of $\Gamma(T + p) = 0.5$ MeV [37] as shown in Fig. 1.

For the entrance channel {7}, exit channels are {7a} and {7b} as described below:

$$\begin{aligned} \{7\} \quad \Psi_{\text{GBS}} \{ (D + D) + (N - 2)Ds \} &\rightarrow \Psi^* \{ {}^4\text{He}^* (0+, 0) + (N - 2)Ds \} (Q = 0.0 \text{ MeV}), \\ \{7a\} \quad {}^4\text{He}^*(0^+, \text{STR}, 23.85 \text{ MeV}) &\rightarrow T(1.01 \text{ MeV}) + p(3.02 \text{ MeV}), \\ \{7b\} \quad {}^4\text{He}^*(0^+, \text{STR}, 23.85 \text{ MeV}) &\rightarrow {}^4\text{He}(0^+, \text{g.s., } 0.0 \text{ MeV}) + e^+ e^- \text{ pair}. \end{aligned}$$

5.2. Anomalous tritium production

For this section (Eqs. (13)–(15)), we use a new energy level scale which sets $E = 0$ for (D + D) state, and $E = -23.85$ MeV for the ${}^4\text{He}$ ground state. Q -value remains same since $Q = E_i - E_f$.

It is important to note that reaction {6} cannot occur in free space due to the momentum conservation, while reaction {7} can occur with $Q = 0$ in free space without violating the momentum conservation, due to the resonance width of $\Gamma(T+p) = 0.5$ MeV [37] for the 20.21 MeV state of ${}^4\text{He}^*$.

Reaction {7} can proceed via a sub-threshold resonance reaction [38,39]. The cross section for the sub-threshold resonance reaction is given by Breit–Wigner expression [39]

$$\sigma(E) = \pi \tilde{\lambda}^2 w \frac{\Gamma_1(E) \Gamma_2}{(E - E_R)^2 + (\Gamma/2)^2}, \quad (13)$$

where $\tilde{\lambda} = \lambda/2\pi$, $\lambda = h/mv$ (de Broglie wavelength), w is a statistical factor, E_R is the sub-threshold resonance energy. Γ_2 is a partial decay width and Γ is the total decay width to the final states. If E is measured from the threshold energy $E = 0$ of (D + D) state, $E_R = (20.21 \text{ MeV} - 23.85 \text{ MeV}) = -3.64 \text{ MeV}$.

After combining Eq. (1) with Eq. (13), the $S(E)$ can be written

$$S(E) = E e^{\sqrt{E_G}/\sqrt{E}} \pi \kappa^2 w \frac{\Gamma_1(E) \Gamma_2}{(E - E_R)^2 + (\Gamma/2)^2} \quad (14)$$

from Eq. (14), we obtain the $S(E)$ factor near zero energy as [38]

$$\begin{aligned} S(E) &= \frac{\pi^2 \hbar^4}{4\mu^2 R_n^2} \frac{1}{K_1^2(x)} w \theta_0^2 F_{BW}(E) \\ F_{BW}(E) &= \frac{\Gamma_2}{(E - E_R)^2 + (\Gamma/2)^2} \end{aligned} \quad (15)$$

where μ is the reduced mass in units of atomic mass unit (931.494 MeV), R_n is the nuclear radius, and $K_1(x)$ is the modified Bessel function of order unity with argument

$$x = (8Z_1 Z_2 e^2 R_n \mu / \hbar^2)^{1/2}$$

We note that $F_{BW}(E_R)$ is a maximum at $E = E_R = -3.64$ MeV. At $E = 0$, $F_{BW}(0)$ is reduced to $F_{BW}(0) = 0.47 \times 10^{-2} F_{BW}(E_R)$. Equation (15) shows that the $S(E)$ factor has a finite value at $E = 0$ and drops off rapidly with increasing energy E . θ_i^2 is the reduced width of a nuclear state, representing the probability of finding the excited state in the configuration i , and the sum of θ_i^2 over i is normalized to 1. The dimensionless number θ_i^2 is generally determined experimentally and contains the nuclear structure information. $S(E)$ factors are calculated from Eq. (15) using $E = 0$ at a tail of the ${}^4\text{He}^*$ ($0^+, 0$) resonance at 20.21 MeV. $E = 0$ corresponds to 23.85 MeV above ${}^4\text{He}$ ($0^+, 0$) ground state. The calculated $S(E)$ can be used in Eq. (12) to obtain the total fusion reaction rate. We will estimate $S(E)$ factors for the decay channels, {7a} and {7b}, using Eq. (15) in the following.

For the decay channel {7a}, $\Gamma_2 = \Gamma_a = 0.5$ MeV [37]. When this value of Γ_2 is combined with other appropriate inputs in Eq. (15), the extracted S-factor for the decay channel {7a} is $S\{7a\} \approx 1.4 \times 10^2 \theta_0^2$ keV-barn for $E \approx 0$. Since (${}^3\text{He} + n$) state has a resonance width of Γ_2 (${}^3\text{He} + n$) = 0 [37], this value of $S\{7a\}$ may provide an explanation of the reported branching ratio of $R(T)/R(n) \approx 10^7 - 10^9$ [30–36] or $R(n)/R(T) \approx 10^{-7} - 10^{-9}$. If we assume $S\{6\} \approx 55$ keV-b (this could be much larger), we expect the branching ratio $R\{7a\}/R\{6\} = R(T)/R({}^4\text{He}) \approx 2.6 \theta_0^2 \approx 2.6 \times 10^{-6}$ if $\theta_0^2 \approx 10^{-6}$. Experimental measurements of $R(T)/R({}^4\text{He})$ are needed to determine θ_0^2 . If $S\{6\}$ ($=S({}^4\text{He})$) is determined to be larger from future experiments, $R(T)/R({}^4\text{He})$ is reduced accordingly. From a previous estimate [9], we have theoretical prediction that $R(n)/R({}^4\text{He}) < 10^{-11}$. Combining this with the above theoretical prediction of $R(T)/R({}^4\text{He}) \approx 2.6 \theta_0^2$, we have $R(n)/R(T) < 0.38 \times 10^{-11} / \theta_0^2$. If we assume $\theta_0^2 \approx 10^{-6}$, we have $R(n)/R(T) < 0.38 \times 10^{-5}$, which is consistent with reported values of $10^{-7} - 10^{-9}$.

5.3. Internal e^+e^- pair conversion

For the decay channel {7b} ($0^+ \rightarrow 0^+$ transition), γ -ray transition is forbidden. However, the transition can proceed via the internal e^+e^- pair conversion. The transition rate for the internal electron pair conversion is given by

$$\omega = \frac{1}{135\pi} \left(\frac{e^2}{\hbar c} \right)^2 \frac{\gamma^5}{\hbar^5 c^4} R_N^4, \quad R_N^2 = \left| \left\langle \psi_{\text{exc}}, \sum_i r_i^2 \psi_{\text{norm}} \right\rangle \right| \quad (16)$$

where γ is the transition energy. Equation (16) was derived by Oppenheimer and Schwinger [40] in 1939 for their theoretical investigation of $0^+ \rightarrow 0^+$ transition in ^{16}O . The rate for the internal electron conversion is much smaller by many order of magnitude. For our case of $0^+ \rightarrow 0^+$ transition {7b}, we obtain $\omega \approx 1.75 \times 10^{13}/\text{s}$, and $\Gamma_b = \hbar\omega \approx 1.15 \times 10^{-2} \text{ eV}$ using appropriate inputs in Eq. (16). Using $\Gamma_2 = \Gamma_b = 1.15 \times 10^{-2} \text{ eV}$ in Eq. (15), the extracted S-factor for decay channel {7b} is $S\{7b\} \approx 3.3 \times 10^{-6} \theta_0^2 \text{ keV-barn}$ for $E \approx 0$, yielding a branching ratio, $R\{7b\}/R\{7a\} \approx S\{7b\}/S\{7a\} \approx 2.4 \times 10^{-8}$. Experiments are needed for testing this predicted branching ratio.

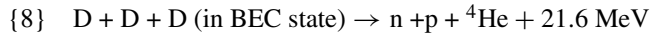
5.4. Anomalous neutron production

Experimental observation of $R(n)/R(T) \approx 10^{-7} - 10^{-9}$ [31–37] is anomalous since we expect $R(n)/R(T) \approx 1$ from “hot” fusion reactions, {1} and {2}. In this section, we explore nuclear reactions producing neutrons at anomalously low rates.

There are three possible processes that can produce neutrons:

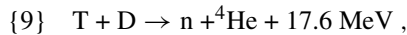
The first process is the secondary “hot” fusion reaction {2} producing 2.45 MeV neutrons. The rate for this secondary reaction is extremely small, $R\{2\}/R\{6\} = R(n)/R(^4\text{He}) < 10^{-11}$, as shown previously [9].

The second process is a 3D BECNF reaction:



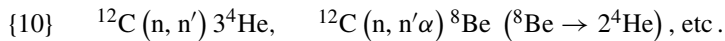
This reaction is a secondary effect since the probability for {8} is expected to be much smaller than the 2D BECNF reaction {6}.

The third process is a “hot” fusion reaction



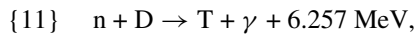
which is induced by 1.01 MeV T produced from reaction {7a}. Since the cross-section for reaction {9} is large and is a maximum (several barns) at $E_D \sim 100 \text{ keV}$ [41], neutrons from this process may contribute substantially to the branching ratio $R(n)/R(T) = 10^{-7} - 10^{-9}$.

Energetic neutrons from the third process {9} described above could induce the following reactions:



as reported recently by Mosier-Boss et al. [42].

To test the above theoretical interpretation, based on the third process {9}, we need to measure/detect (i) tritium production, (ii) Bremsstrahlung radiations from energetic electrons going through metal, (iii) 0.51 MeV γ -rays from e^+e^- annihilation, (iv) energetic electrons from e^+e^- pair production, (v) γ -rays from the following reaction:



and (vi) γ -rays from reaction {12} induced by 0.3 MeV protons from {7a}:



The cross-section for {11} is $\sim 0.5 \text{ mb}$ with thermal neutrons.

6. Experimental Observation of Formation of Micro-craters

6.1. Experimental observations

There have been many reports of experimental observation of micro-craters [31,43,44]. In the following, estimates of energetics involved in a micro-crator formation observed by Szpak et al. [43] is presented.

6.2. Estimates of energetics

For the micro-crator shown in Fig. 2, we have the ejecta volume of $V = 1.6 \times 10^{-8} \text{ cm}^3$ which contains 1.1×10^{15} deuterons, corresponding to $N_{\text{moles}} = 1.8 \times 10^{-9}$ moles of deuterons. The total energy E_T required for vaporization is $E_T = 6.5 \times 10^{-4} \text{ J}$. Since $Q = 23.8 \text{ MeV}$ per nuclear reaction, the total number N_R of D + D reactions is $N_R = E_T/Q = 1.7 \times 10^8$ DD reactions. Explosion time estimated from Eq. (12) is $\sim 1.2 \times 10^{-13} \text{ s}/\Omega$.

7. Proposed Experimental Tests

BECNF theory is based on a physical observation of deuterons mobility in a metal grain/particle which may lead to possibility of forming a Bose–Einstein condensate of deuterons in metals. Two types of experimental tests (Proposed Experiments 1 and 2) are proposed as experimental tests of this possibility of observing BEC of deuterons in metals. For both types of experiments, the dependences on the temperature and pressure are to be measured. In addition, Proposed Experiment 3 is proposed to probe possibilities of cryogenic ignition of deuterons loaded in micro/nano-scale metal particles.

7.1. Proposed experiment 1

As is the case for the atomic BEC experiments, experiments are proposed to measure the velocity distribution of deuterons in metal. An enhancement of low-velocity deuterons in the deuteron velocity distribution is expected when the BEC of deuterons occurs. Inelastic Compton scatterings of neutrons and of X-rays are suggested for this proposed experimental test 1. At the present we do not know the velocity distribution of deuterons in metal, which is expected to be different from the Maxwell–Boltzmann distribution for an ideal gas. This experimental demonstration of the BEC of deuterons in a metal based on the velocity distribution may lead to a new discovery. In 1995, this type of experiments for measuring the velocity distribution was used to establish the existence of the BEC of atoms in a magnetic trap at extremely low temperatures, for which the Nobel prize was awarded in 2000.

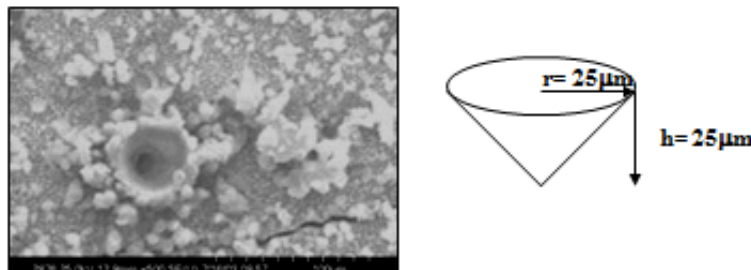


Figure 2. A micro-crator observed in co-deposit electrolysis experiment with applied external electric field [43].

7.2. Proposed Experiment 2

To explore the superfluidity of the BEC of deuterons in metal, experiments are proposed to measure the diffusion rates of both deuterons and protons in a metal as a function of temperature. When the BEC of deuterons in a metal occurs, it is expected that the deuteron diffusion rate will increase substantially more than that of proton. We need to explore a number of other experimental methods for observing the superfluidity, such as the use of torsional oscillators. Experimental demonstration of the superfluidity of deuterons in the BEC state in metal may lead to a new discovery. In 1996, the Nobel prize was awarded for the discovery of superfluidity of ^3He .

7.3. Proposed Experiment 3

To explore possibilities of constructing a practical BECNF reactor for energy generation, both experimental and theoretical investigations are proposed to study the possibility of BECNF mini-explosion (or ignition) at extremely low temperatures. At ^4He liquid temperature, from estimates of reaction rates using Eq. (12), DD fusions are expected to occur nearly simultaneously from each of micro/nano-scale metal particles contained in a bulk volume. This can cause a mini-explosion (or ignition). An ignition fuel of $\sim 1\text{ cm}^3$ volume containing $\sim 10^{18}$ of $\sim 10\text{ nm}$ metal particles (each loaded with $\sim 10^{4\sim 5}$ deuterons) could be used to ignite $\sim 10^{18}$ DD fusions in a very short time period at ^4He liquid temperature or cooling by electromagnetic field gradients, etc. If the proposed experimental test proves this theory to be correct, the ignition fuel can be used in a series of reactor chambers similar to the ignition chamber containing a cryogenic-target at the National Ignition Facility, Livermore National Laboratory [45].

If successful, Proposed Experiment 3 could lead to alternative approach to clean nuclear fusion energy generation technology at commercial and industrial scales.

8. Conclusions

The optical theorem formulation (OTF) of low energy nuclear reactions (LENRs) has been generalized to describe LENRs occurring in deuterium/hydrogen loaded metal systems.

It is pointed out (in Section 3.3) that previous theoretical objections of LENR phenomena made in the past are inappropriate, since they are based on a theoretical description which is not applicable to LENR phenomena.

As a first application of the OTF-LENRs, theory of Bose–Einstein condensation nuclear fusion (BECNF) is developed to explain deuteron-induced nuclear reactions observed in metal. It is based on a single physical observation of deuteron mobility in metals, which may lead to the possibility of Bose–Einstein condensation of deuterons in metals.

It is shown that the BECNF theory is capable of explaining qualitatively or quantitatively all of ten experimental observations (listed in Section 2.2) reported from electrolysis and gas-loading experiments.

It is also shown that observed anomalous tritium and neutron productions can be explained by incorporating a sub-threshold resonance reaction mechanism into the BECNF theory.

The BECNF theory has also predictive powers as expected for a quantitatively predictive physical theory. Experimental tests of theoretical predictions are proposed.

As a potential practical application of BECNF theory, experimental tests of predicted cryogenic ignition are proposed for the purpose of achieving scaling-up of LENRs rates, which may lead to an alternative technology for clean nuclear fusion energy generation at commercial and industrial scales.

Applications of the OTF-LENRs to hydrogen loaded metal systems are in progress.

References

- [1] Y.E. Kim, Y.J. Kim, A.L. Zubarev and J.H. Yoon, Optical theorem formulation of low-energy nuclear reactions, *Phys. Rev. C* **55** (1997) 801.

- [2] Y.E. Kim and A.L. Zubarev, Nuclear fusion for Bose nuclei confined in ion traps, *Fusion Technol.* **37** (2000) 151.
- [3] Y.E. Kim and A.L. Zubarev, Ultra low-energy nuclear fusion of Bose nuclei in nano-scale ion traps, *Italian Physical Soc. Proc.* **70** (2000) 375.
- [4] Y.E. Kim and A.L. Zubarev, Equivalent linear two-body method for many-body problems, *Phys. B: At. Mol. Opt. Phys.* **33** (2000) 55–69.
- [5] Y.E. Kim and A.L. Zubarev, Ground state of charged bosons confined in a harmonic trap, *Phys. Rev. A* **64** (2001) 013603-1.
- [6] Y.E. Kim and A.L. Zubarev, Equivalent linear two-body method for Bose–Einstein condensates in time-dependent harmonic traps, *Phys. Rev. A* **66** (2002) 053602-1.
- [7] Y.E. Kim and A.L. Zubarev, *Condensed Matter Nuclear Science*, Proc. 11th Int. Conf. on Cold Fusion, Marseilles, France, 31 October–5 November, 2006, World Scientific, New York, pp. 711–717.
- [8] Y.E. Kim, Theory of Bose–Einstein Condensation mechanism for deuteron-induced nuclear reactions in micro/nano-scale metal grains and particles, *Naturwissenschaften* **96** (2009) 803 and references therein.
- [9] Y.E. Kim, Bose–Einstein condensate theory of deuteron fusion in metal, *J. Condensed Matter Nucl. Sci.* **4** (2010) 188, Proceedings of Symposium on New Energy Technologies, the 239th National Meeting of American Chemical Society, San Francisco, March 21–26, 2010.
- [10] Y.E. Kim, Theoretical interpretation of anomalous tritium and neutron productions during Pd/D co-deposition experiments, *Eur. Phys. J. Appl. Phys.* **52** (2010) 31101.
- [11] Y.E. Kim, Nuclear reactions in micro/nano-scale metal particles, invited paper presented at the 5th asia-pacific conference on few-body problems in physics (APFB2011), Seoul, Korea, August 22–26, 2011; to be published in the Proceedings of APFB2011.
- [12] Y.E. Kim, Cryogenic ignition of deuteron fusion in micro/nano-scale metal particles, purdue nuclear and many body theory group (PNMBTG) Preprint PNMBTG-11-2011 (November 2011). Invited paper presented at Topical Meeting of the 2012 Nuclear and Emerging Technologies for Space (NETS), the 43rd Lunar and Planetary Science Conference, March 19–23, 2012, the Woodlands, Texas.
- [13] W.A. Fowler, G.R. Caughlan and B.A. Zimmermann, Thermonuclear reactions rates, *Annu. Rev. Astron. Astrophys.* **5** (1967) , 525; see also .Thermonuclear reaction rates II, *Annu. Rev. Astron. Astrophys.* **13** (1975) 69.
- [14] A. von Engel and C.C. Goodyear, Fusion cross-section measurements with deuterons of low energies, *Proc. R. Soc. A*, **264** (1961) 445.
- [15] A.Krauss, H.W. Becker, H.P. Trautvetter and C. Rolfs, Low energy fusion cross-sections of D + D and D + ³He reactions, *Nucl. Phys.* **465** (1987) 150.
- [16] M. Fleischman and S. Pons, Electrochemically induced nuclear fusion of deuterium, *J. Electroanal. Chem.* **261** (1989) 301; Errata, *J. Electroanal. Chem.* **263** (1989) 187.
- [17] P.L. Hagelstein et al., New physical effects in metal deuterides, *Proc. ICCF-11*, Marseille, France, *Condensed Matter Nuclear Science*, World Scientific, Singapore, 2006, pp. 23–59 and references therein.
- [18] Y. Arata and Y.C. Zhang, *J. High Temp. Soc.* **34**(2) (2008) 85.
- [19] A. Kitamura et al., *Phys. Lett. A* **373** (2009) 3109, and references therein.
- [20] E. Feenberg, *Phys. Rev.* **40** (1932) 40.
- [21] A. Coehn, Proof of the existence of protons in metals (with discussion), *Z. Electrochem.* **35** (1929) 676–680.
- [22] A. Coehn and W. Specht, Ueber die Beteiligung von Protonen an der Elektrizitaetsleitung in Metallen (Role of protons in electric conductivity of metals), *Z. Phys.* **83** (1930) 1–31.
- [23] I. Isenberg, The ionization of hydrogen in metals, *Phys. Rev.* **79** (1950) 736.
- [24] P.L. Hagelstein, *Naturwissenschaften* **97** (2010) 345.
- [25] E. Storm and C. Talcott, Electrolytic tritium production, *Fusion Technol.* **17** (1990) 680.
- [26] K. Cedzynska, S.C. Barrowes, H.E. Bergeson, L.C. Knight and F.W. Will, Tritium analysis in palladium with an open system analytical procedure, *Fusion Technol.* **20** (1991) 108.
- [27] F.G. Will, K. Cedzynska and D.C. Linton, Reproducible tritium generation in electrochemical-cells employing palladium cathodes with high deuterium loading, *J. Electroanalytical Chem.* **360** (1993) 161: .Tritium generation in palladium cathodes with high deuterium loading, *Trans. Fusion Technol.* **26** (1994) 209.
- [28] J.O'M. Bockris, C.-C. Chien, D. Hodko and Z. Minevski, Tritium and helium production in palladium electrodes and the

- fugacity of deuterium therein, *Frontiers Science Series No. 4, Proc. Third Int. Conf. on Cold Fusion.*, October 21–25, Nagoya Japan, Ed. H. Ikegami, Universal Academy Press Tokyo Japan., 1993, pp. 23.
- [29] R.Szpak, P.A. Mosier-Boss, R.D. Boss and J.J. Smith, On the behavior of the Pd/D system: evidence for tritium production, *Fusion Technol.* **33** (1998). 38-51.
- [30] M. Srinivasan et al., Observation of tritium in gas/plasma loaded titanium samples, *AIP Conf. Proc.* **228** (1990) 514.
- [31] A. DeNinno, A. Frattolillo, G. Lollobattista, L. Martinis, M. Martone, L. Mori, S. Podda and F. Scaramuzzi, Emission of neutrons as a consequence of titanium–deuterium interaction, *Il Nuovo Cimento*, **101A** (1989) 841.
- [32] T.N. Claytor, D.G. Tuggle, H.O. Menlove, P.A. Seeger, W.R. Doty and R.K. Rohwer, Tritium and neutron measurements from a solid-state cell, LA-UR-89-3946, October 1989, Presented at the NSF-EPRI workshop.
- [33] T.N. Claytor, D.G. Tuggle, H.O. Menlove, P.A. Seeger, W.R. Doty and R.K. Rohwer, Tritium and neutron measurements from deuterated Pd–Si, *AIP Conf. Proc.* **228**, Anomalous Nuclear Effects in Deuterium/Solid Systems, S. Jones, F. Scaramuzzi and D. Worledge (Eds.), Provo Utah, (1990), p. 467.
- [34] T.N. Claytor, D.G. Tuggle and S.F. Taylor, Evolution of tritium from deuterided palladium subject to high electrical currents, *Frontiers Science Series No. 4, Proc. Third Int. Conf. on Cold Fusion.*, October 21–25 Nagoya Japan, H. Ikegami (Ed), Universal Academy Press, Tokyo, Japan., 1993, p. 217.
- [35] T.N. Claytor, D.G. Tuggle and S.F. Taylor, Tritium evolution from various morphologies of deuterided palladium, *Proc. Fourth Int. Conf. on Cold Fusion*, December 6–9, 1993, Maui, Hawaii, T.O. Passel (Ed.), EPRI-TR-104188-V1 Project 3170, Vol 1 7-2 (1994).
- [36] T.N. Claytor et al., Tritium production from palladium alloys, *Proc. ICCF-7*, 1998, p. 88.
- [37] D.R. Tilley, H.R. Weller and G.M. Hale, Energy level of light nuclei $A=4$, *Nucl. Phys. A* **541** (1992) 1.
- [38] C.E. Rolfs and W.S. Rodney, *Cauldrons in the Cosmos: Nuclear Astrophysics*, University of Chicago Press (1988), chapter 4.
- [39] J.M. Blatt and V.F. Weisskopf, *Theoretical Nuclear Physics*, Wiley, 1952., 8th Printing (1962).
- [40] J. R. Oppenheimer and J. S. Schwinger, *Phys. Rev.* **56** (1939) 1066.
- [41] G.S. Chulick, Y.E. Kim, R.A. Rice and M. Rabinowitz, Extended parameterization of nuclear-reaction cross sections for few-nucleon nuclei, *Nucl. Phys. A* **551** (1993) 255–268.
- [42] P.A. Mosier-Boss, S. Szpak, F.E. Gordon and L.P.G. Forsley, Triple tracks in Cr-39 as the result of Pd–D Co-deposition: evidence of energetic neutrons, *Naturwissenschaften* **96** (2009) 135; .Characterization of Tracks in CR-39 detectors as a result of Pd/D co-deposition, *Eur. Phys. J. Appl. Phys.* **46** (2009) 30901.
- [43] S. Szpak, P.A. Mosier-Boss, C.Young and F.E.Gordon, *J. Electroanal. Chem.* **580** (2005) 282.
- [44] D.J. Nagel, Characteristics and energetics of craters in LENR experimental materials, to be published; this paper contains many other references on micro-craters.
- [45] National Ignition Facility Project: <http://www.llnl.gov/nif/nif.html>



Research Article

Recent Progress in Gas-phase Hydrogen Isotope Absorption/Adsorption Experiments

A. Kitamura ^{*†}, Y. Miyoshi, H. Sakoh, A. Taniike and Y. Furuyama

Graduate School of Maritime Sciences, Kobe University, Kobe 6580022, Japan

A. Takahashi [‡], R. Seto and Y. Fujita

Technova Inc., Tokyo 1000011, Japan

T. Murota and T. Tahara

Santoku Corp., Kobe 6580013, Japan

Abstract

To enhance reusability of the nanopowder samples for heat generation by gas-phase hydrogen isotope absorption, porous-silica-inclusion has been applied to Pd nanopowders (PSII) and Pd-Ni nanocomposite (PNS) samples. Absorption parameters repeatedly obtained in the repeated runs including repeated oxidization-hydridation cycles suggest interesting role of admixed minority atoms in the nanoparticles.

© 2014 ISCMNS. All rights reserved. ISSN 2227-3123

Keywords: Hydrogen isotope absorption, Inclusion, Nanoporous-silica, Pd nanoparticles

1. Introduction

Gas-phase hydrogen isotope absorption/adsorption experiments have been performed since 2008 at Kobe University to elucidate the mechanism of anomalously large heat release. The samples include 0.1- μm -diam. Pd particles (PP, Nilaco Corp.), Pd-black (PB, Nilaco Corp.), oxide nanocomposites of Pd-ZrO₂ (PZ, Santoku Corp.), ternary oxide compound of Pd-Ni-ZrO₂ (PNZ, Santoku Corp.), binary oxide compound of Ni-ZrO₂ (NZ, Santoku Corp.), Pd-Ni nanoparticles dispersed in ZrO₂ powders provided by B. Ahern (PNZ2B), and porous-silica-included Pd nanoparticles (PSII, Admatechs Co. Ltd.).

^{*}E-mail: kitamuraakira3@gmail.com

[†]Also at: Technova Inc, Tokyo 1000011, Japan

[‡]Also at: Osaka University, Suita 5650871, Japan

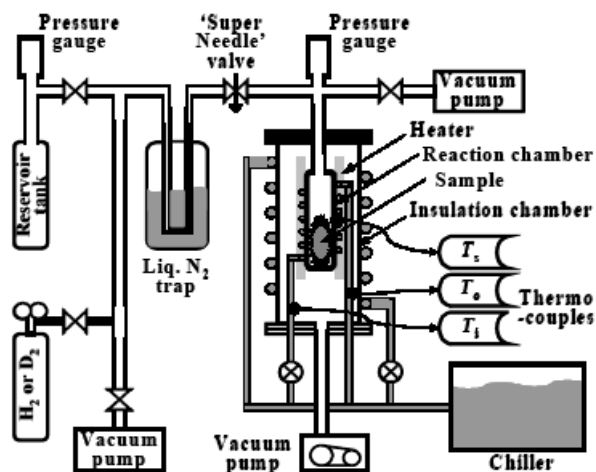


Figure 1. Schematic of one-part of the twin system.

Based on the results of the extended measurements, the effects of the sample structure on the absorption/adsorption characteristics have been discussed; particle size, oxide formation on the Pd samples, the silica-inclusion of Pd nanoparticles, and Ni-substitution for Pd. Anomalously large values of the evolved heat, the total D/Pd (H/Pd) loading ratios and the η -values have been repeatedly observed in the absorption runs at room temperature using the samples of PZ [1–3], PSII [4] and PNZ2B [5]. It has been found that addition of a small amount of Pd to the Ni nanoparticle sample changes the absorption characteristics of Ni drastically to enhance the loading ratio and heat release [5].

These results have prompted examination of two kinds of the sample; ternary oxide compound of Cu-Ni-ZrO₂ (CNZ, Santoku Corp.) and porous-silica-included Pd-Ni nanoparticles (PNS, Admatechs Co. Ltd.).

The CNZ sample was fabricated for the purpose of checking whether Cu atoms can substitute for Pd atoms in the PNZ2B sample. Preliminary results show that the CNZ sample requires elevated temperature to absorb hydrogen isotopes. Slight and long-term increase in temperature have been observed in some runs operated at above 500 K. Detailed description of the experiments using this sample is given in another presentation by H. Sakoh [6] in this Conference.

In the present paper the characteristics of the nanoporous-SiO₂-included samples, PSII and PNS, are discussed in detail. It is well known that Pd nanoparticles clump together to become agglomerated, when simple nanoparticle samples of Pd are subjected to repeated use for gas-phase hydrogen isotope absorption experiments. This causes substantial decrease in absorbed amount of hydrogen isotopes and induced heat release for the second use or more.

It has been reported that large heat release with isotopic difference was observed under hydrogen isotope absorption by Pd nanopowders included in the basket structure of zeolite [7]. Purpose of inclusion in the basket structure is to prevent agglomeration of nanoparticles of Pd under repeated use. In the present study we have used nanoporous-silica-included Pd (PSII) or Pd-Ni (PNS) nanoparticles manufactured by Admatechs Co., Ltd. instead of zeolite-included one to study effect of such structure on absorption and heat release characteristics. The latter PNS sample was fabricated to have a mixture of Pd and Ni with a molar fraction of about 0.01 and 0.06, respectively, in expectation of the similar function of the Pd atoms in the PNZ2B sample.

2. Experimental Apparatus and Procedure

The PSII sample is composed of nanoparticles of Pd and nanoporous-silica with a mean size of $4\ \mu\text{m}$. The size of Pd ranges from about 3 nm to about 150 nm, with 90% being 3–10 nm.

We have used a twin absorption system consisting of two equivalent chambers for hydrogen isotope gas absorption/adsorption experiments. Figure 1 shows a schematic of one-part of the twin system. The samples are put in the reaction chamber, and the outer chamber is evacuated for thermal insulation during hydrogen isotope absorption/adsorption. Sheath heaters with resistance of 37.9 and 53.8 Ω wound around the reaction chambers in the A_1 and A_2 systems, respectively, are used for sample heating in the cases of baking, forced deoxidization, forced oxidization and absorption runs at elevated temperatures. Alumel-chromel thermo-couples are used to measure temperatures.

For the PSII samples, mass flow calorimetry was employed. The coolant water temperature is maintained constant ($\pm 0.1^\circ\text{C}$) at near-room temperature with a chiller, and the flow rate is controlled with a digital coolant transmitter at a rate of $12\ \text{cm}^3/\text{min}$, which recovers heat with an efficiency of $90.0 \pm 1.7\%$. Calorific power is calculated from temperature difference between the exit and the entrance of water-coolant. There is a delay in the response of the temperature difference due to the indicial response with a time constant of 2.2 min. The calibrated conversion factor is 0.929 W/K.

On the other hand, since we expected that the PNS sample exhibits better performance at elevated temperatures [8], the power measurement in the PNS absorption runs were performed by isothermal calorimetry. In this case, water was taken out of the coolant pipe, and the output power was deduced from the relation between the temperature of the reaction chamber wall and the thermal power. The thermocouples were rearranged to measure the temperatures of the surface of the reaction chamber at the bottom, the side and the top.

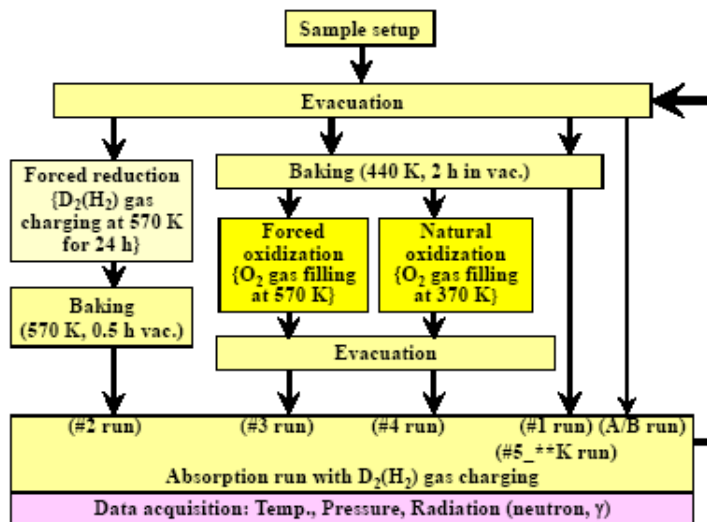


Figure 2. Flowchart of the experimental procedure.

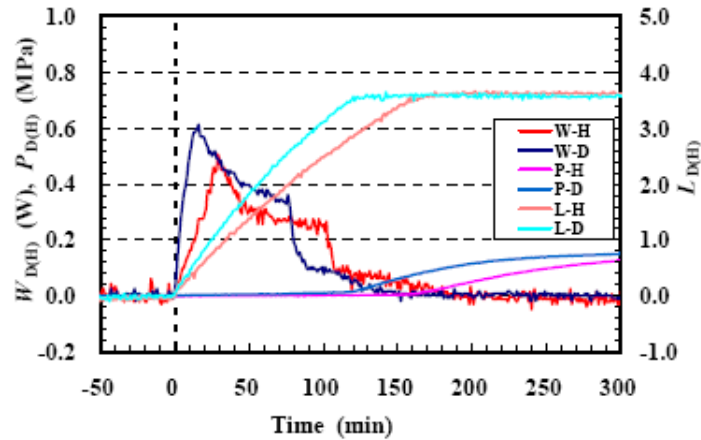


Figure 3. Evolution of thermal power $W_{D(H)}$, pressure $P_{D(H)}$ in the reaction chamber after introduction of D_2 (or H_2) gas and the time-dependent loading ratio $L_{D(H)}$ in runs D-PSII3#1 and H-PSII4#1.

This relation was obtained beforehand in the calibration runs using the power supplied to the heater, and is shown in Table 2 of ref. [6]. The conversion factor to the power depends on temperature, and is 0.16 W/K at room temperature, and about 1.0 W/K at 573 K.

Since the major path for the heat loss is absent, the time constant becomes much longer than in the case of the mass-flow calorimetry. It was measured in the above calibration using a stepwise variation of the heater power to reveal two components in the temperature decay curve with time constant of 16 and 45 min due to radiation and conduction, respectively.

Figure 2 shows the experimental procedure. The run number expresses the conditions of the sample used in the run, using the letters defined in Table 1. The as-received sample is baked at 440 K for 2 h in vacuum, and subjected to the D_2 (H_2) absorption run (#1 run). The sample is reused either without any treatment (A or B run) or after the specified treatment; forced deoxidization (#2 run) or forced oxidization (#3 run) or passive oxidization (#4 run). For Ni-based samples, NZ, CNZ and PNS, high temperature was required for appreciable absorption of hydrogen. The run at an elevated temperature of T K is called “# n _TK” run.

The detailed descriptions of the run procedures are found in other papers; e.g., [4] for the room-temperature runs with mass flow calorimetry, and [6] for the high-temperature runs with isothermal calorimetry.

Table 1. Nomenclature for the run number.

#1	Absorption run using a virgin sample
#2	Absorption run after forced de-oxidization
#3	Absorption run after forced oxidization
#4	Absorption run after natural oxidization
# n A	Absorption run following # n without baking
# n B	Absorption run following # n A without baking
# n (N)d	Desorption run by evacuation after an absorption run # n (N)
#5_TK	Absorption run at an elevated temperature of T K

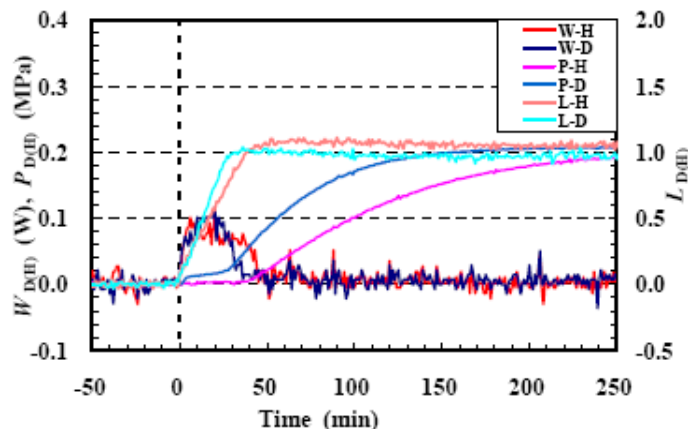


Figure 4. The runs after forced deoxidization, D-PSII#2 and H-PSII#2.

3. Results and Discussion

3.1. PSII sample

First we discuss the effect of silica inclusion of the Pd nanopowders. Figure 3 shows typical variation of the heat output, $W_D(t)$ and $W_H(t)$, pressure in the reaction chamber, $P_D(t)$ and $P_H(t)$, and the loading ratio, $L_D(t)$ and $L_H(t)$, in the hydrogen isotope absorption run for ten-gram aliquots of as-received samples, D-PSII3 and H-PSII4, respectively. The D(H)-PSII3(4)#1 runs have extraordinary large loading ratios $L_{D(H)}(t)$ which reach D(H)/Pd \approx 3.6 (3.5) at the end of the exothermic phase. This phase is thought to be dominated by chemical process, and is called the first phase in the present work. The 1st phase involves processes of surface adsorption, oxygen pickup reaction and absorption into the bulk. Contributions of these processes to the time-dependent parameters, $W_{D(H)}(t)$ and $L_{D(H)}(t)$, and their time-integrated parameters, $E_{1D(H)}$ and D(H)/Pd, are discussed later in this paper.

The specific heat release $E_{1D(H)}$ is also very large; $E_1 \approx 2.7$ (2.4) eV/atom-Pd for D(H). The values of the loading ratio are more than 4 times larger than the maximum value of 0.85 ever observed for loading bulk Pd metal, while the values of the specific heat release evaluated as the energy per one D(H) atom absorption give 0.75 (0.69) eV/atom-D(H), which is also about 4 times larger than the value of 0.2 eV/atom-H for the bulk-Pd metal, and even a factor of 1.5 (1.4) larger when compared with the surface adsorption energy of 0.5 eV/atom-H for bulk-Pd metal.

After finishing the #1 run, we made forced deoxidization at 573 K. Figure 4 shows the #2 absorption runs using these samples. The values of D(H)/Pd and E_1 were 0.95 (1.02) and 0.21 eV/atom-Pd, respectively. The loading ratio is slightly larger than that for the bulk Pd, and the values of the released heat give 0.22 (0.20) eV/atom-D(H) which are nearly equal to the bulk value. It appears that the deoxidized samples have fewer adsorption sites, and/or very small adsorption energy. If the former is the case, a higher temperature and/or a longer period of heating are/is necessary in the deoxidizing process for purging the D(H) atoms in the adsorption sites on the PSII sample surface.

Forced oxidation of the samples was performed by keeping them in the O_2 atmosphere at a temperature of 570 K for 30 h. The degree of oxidation, x (\equiv PdO/Pd), is calculated from the pressure difference between the beginning (0.3 MPa) and the end of the exposure to O_2 in the closed system. The values of x ranged from 0.69 to 0.79. Figure 5 shows the traces of the parameters in the #3 absorption runs using the oxidized samples. The oxidized samples has almost recovered the large values of E_1 and D(H)/Pd.

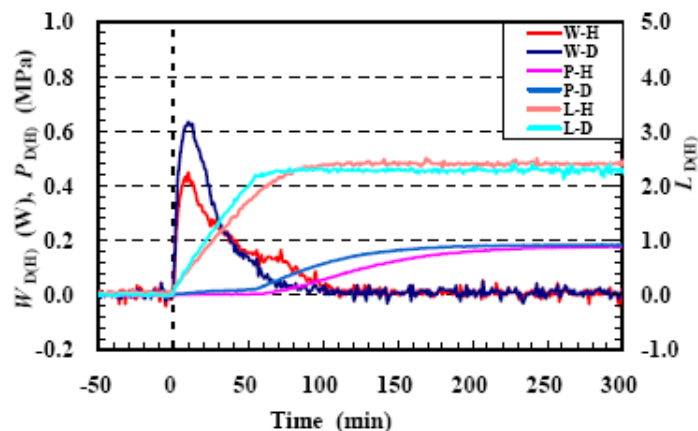


Figure 5. The absorption runs after forced oxidation, D-PSII3#3_3 and H-PSII4#3_3.

Next, the samples were left outside the chamber for 24 h to allow natural oxidation in the ambient air, and subjected to the #4 absorption runs. Then the samples were subjected to forced oxidation again, followed by #3_2 absorption runs, which were also followed by passive oxidation runs twice, #4_2 and #4_3.

Figures 6 and 7 show the parameters E_1 and $D(H)/Pd$, respectively, for runs #1 through #4_3 as histograms. In the PSII#1 run the released heat and the loading ratio were both considerably large in comparison with the bulk Pd as described above. The loading ratios of the A, B and #2 runs were about 1.0 and slightly larger than that of the bulk Pd, while the released heat remained the bulk value. In the two runs after the forced oxidation of the samples, #3 and #3_2, the released heat and the loading ratio were largely recovered. However, the passive oxidation was not effective for substantial recovery of the large values of the loading ratio and the released heat.

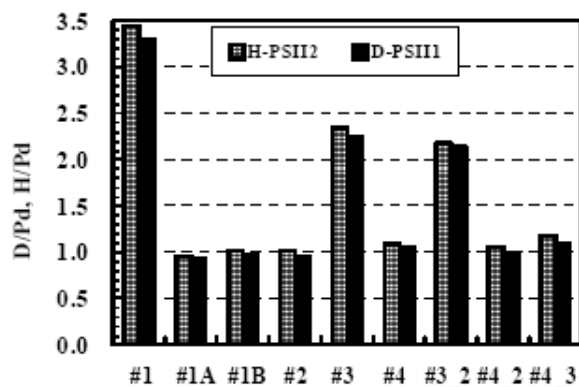


Figure 6. Specific heat release E_1 for the samples D-PSII1 and H-PSII2.

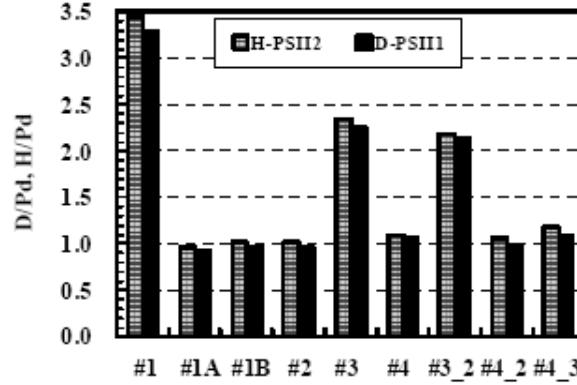


Figure 7. Loading ratio D(H)/Pd for the samples D-PSII1 and H-PSII2.

These results show that the PSII sample can be repeatedly used with little deterioration. The PSII sample serves our purpose.

Next, we discuss time-resolved parameters. The time-resolved specific sorption energy, or differential heat of hydrogen uptake, $\eta_{D(H)}$, is defined as the output energy per one hydrogen isotope atom absorbed/adsorbed [2];

$$\eta(t) \equiv \frac{\int_t^{t+\Delta t} W_{\text{true}}(t) dt}{L(t + \Delta t) - L(t)}. \quad (1)$$

The time-variation of $\eta_{D(H)}$ values is shown in Fig. 8 together with the thermal power evolution in the D-PSII1 and H-PSII2 runs.

Qualitative time-variation of η_D/η_H values is similar to that for the PZ sample [2]. In the #1 run the first phase is clearly divided into two sub-phases, 1a and 1b. In the 1b-phase both η_D and η_H values are nearly equal to those for the bulk Pd expressed as the chain lines, while they are extraordinarily large in the 1a-phase. However, the #2 run loses the 1a-phase. And in the #3 absorption run of the oxidized sample, the 1a-phase with the large values of $\eta_{D(H)} \approx 1.0$ eV/atom-D(H) is recovered. Using Fig. 11 later, we will discuss $L_{D(H)}(t) - P_{D(H)}(t)$ (loading ratio vs. pressure) diagrams to show that the 1b-phase is identified as the phase when only absorption into bulk takes place, and the surface adsorption and/or oxygen pickup reaction could be involved in the 1a-phase.

As for the isotope effect, the value of η_D/η_H sometimes exceeds unity especially in the beginning of the 1a-phase of the #1 runs, and also in the 1a-phase of the #3 run with a maximum of about 1.3, as is seen in the third graph. In addition, the value of η_D/η_H sometimes differs from unity also in the 1b-phase. However, η_D/η_H is erroneous in the 1b-phase, since the change in the loading ratio, the denominator of Eq. (1), is sometimes very small in this phase. It is thought that η_D/η_H exceeding about 1.1 can hardly be explained solely by chemical isotope effect.

We have changed the extent of oxidization to examine effect of oxygen on hydrogen isotope absorption/adsorption. Figures 9 and 10 show the released heat E_1 and the loading ratio D(H)/Pd, respectively, as a function of the oxidizing fraction x . Here any decrease in the pressure is regarded as an increase in D(H)/Pd.

The lines in the figures show the least-square fittings of the relevant dependencies, where x is the fraction of Pd atoms oxidized as defined above. The parameter D(H)/Pd is the ratio of the number of D(H) atoms used for oxygen pickup and hydridation (absorption and adsorption including spillover effect) to that of the host Pd atoms. We see that D(H)/Pd and E_1 linearly increase with x . As indicated in the figure, the intercepts to the y-axes, or

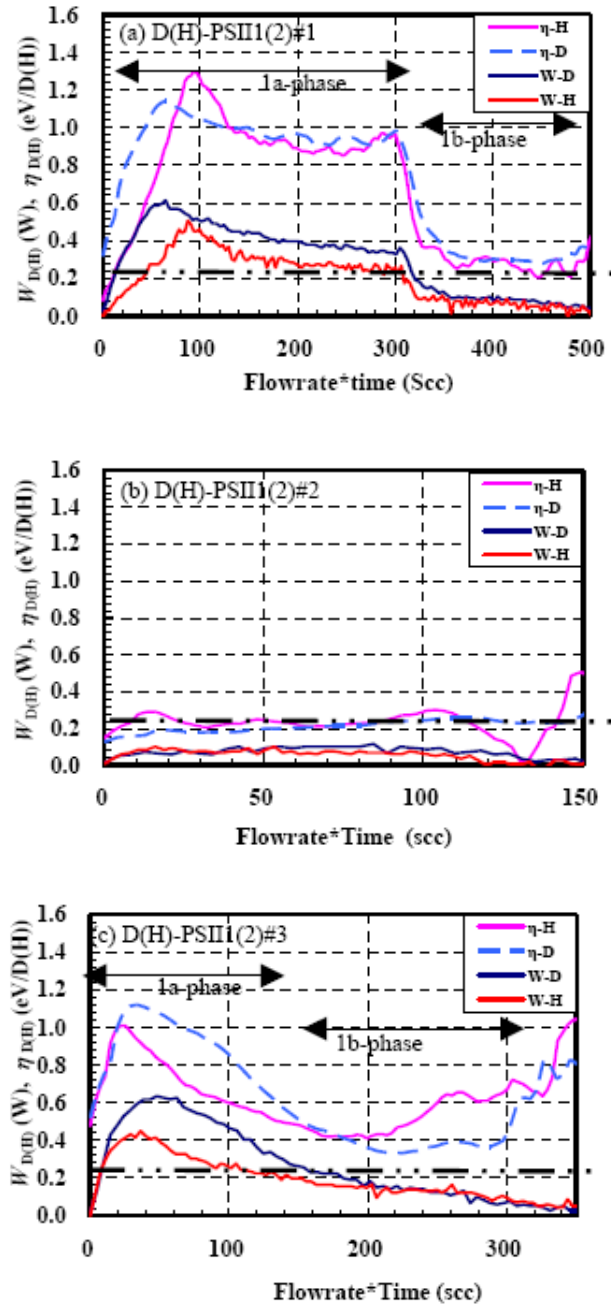


Figure 8. Evolution of heat, W , and the time-dependent absorption energy, η , for D_2 gas and H_2 gas absorption runs D(H)-PSII(2)#1 (a), D(H)-PSII(2)#2 (b), and D(H)-PSII(2)#3 (c).

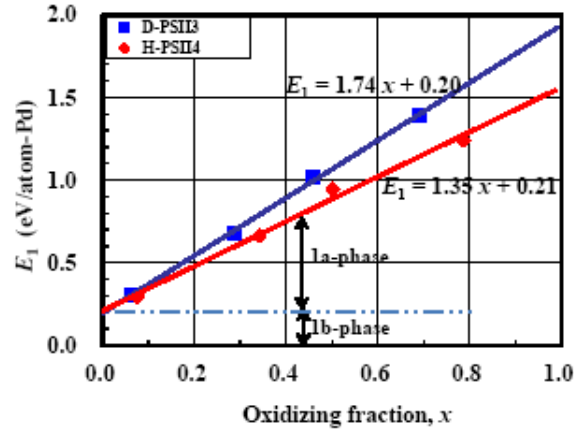


Figure 9. Relation between the specific output energy E_1 and the oxidizing fraction x for the PSII samples.

the values at $x = 0$, correspond to the #2 runs, and therefore to the 1b-phase, while the portions linearly increasing with x correspond to the 1a-phase in which surface adsorption and oxygen pickup take place.

The oxygen pickup reaction from PdO are considered to proceed in the following manner:

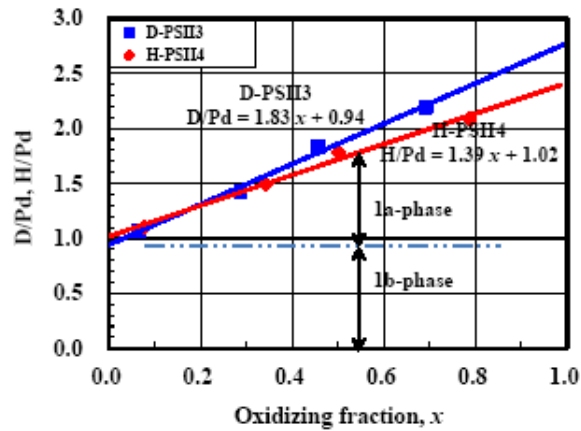
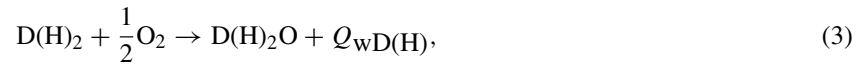
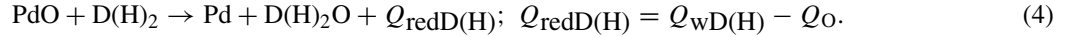
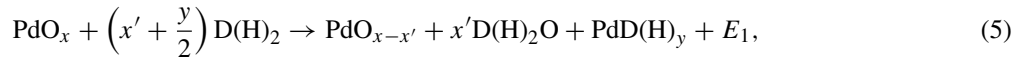


Figure 10. Relation between loading ratio and the oxidizing fraction x for the PSII samples.

where the oxide formation energy $Q_O = 0.886$ eV for the bulky Pd, and the water formation energy $Q_{wD(H)} = 2.654$ (2.511) eV. Summing up these formulae, we have the following as the oxygen pickup reaction:



For the bulky Pd the oxygen pickup reaction energy $Q_{\text{redD(H)}} = 1.768$ (1.625) eV. If hydridation follows the oxygen pickup from PdO with a fraction of x' out of x , we have the following for the output energy $E_{1D(H)}$:



$$E_1 = x' Q_{\text{redD(H)}} + y Q_{D(H)}. \quad (6)$$

Using the above formulae, we can make some discussion under some assumptions.

First, we note that the values of the intercepts to the vertical axes corresponding to the #2 and #4 runs with no oxygen, or the 1b-phase, agree very well to the published absorption energy of 0.2 eV/atom-D(H). From this fact, we can infer that contribution of the surface adsorption should be included in the first term proportional to x' . Namely, the number of hydrogen isotopes adsorbed on the PdO_x surface is considered to be proportional to x .

The water formation does not change the pressure measured with a piezoelectric gauge, as far as the water remains in the gas phase, since H_2O has the same volume as H_2 . In this case, the pressure decrease in the 1a-phase is caused by adsorption exclusively. This appears to be the case in the present measurements, as is shown in Fig. 11. Even so, it is difficult to deduce the adsorption energy, since the oxygen pickup also contributes to the first term in Eq. (6).

In contrast, the water molecules could be adsorbed on the sample surface. In this case the water formation yields no volume, and decreases the pressure to be measured as a part of $L_{D(H)}(t)$. Anyway, it is difficult to separate adsorption and oxygen pickup from each other in the first term in Eq. (6) without further assumption.

Now we discuss $L_{D(H)}(t) - P_{D(H)}(t)$ diagrams in comparison to those for another sample to show that the 1b-phase is identified as the phase when only absorption into bulk takes place. Figures 11 and 12 show the time-resolved relation between the loading ratio $L_{D(H)}(t)$ and the pressure $P_{D(H)}(t)$ for the PSII and the PNZ2B samples, respectively. The latter is a sample of nanoparticles of Pd·Ni compound dispersed in ZrO_2 prepared by B. Ahern with the melt-spinning method [8]. The hydrogen absorption characteristics of the PNZ2B sample was described partly in Refs. [5,9]. Here we refer only to the $P_{D(H)}(t) - L_{D(H)}(t)$ diagram. After hydrogen isotope gas introduction, pressure increases without significant increase in $L_{D(H)}(t)$ up to about 50 kPa, at which the pressure abruptly decreases down to 7–8 kPa, making a pressure hump. This pressure hump is considered to be typical of supersaturation followed by condensation of the $\text{D(H)}_2\text{O}$ vapor into liquid with a static vapor pressure of about 4 kPa (for H_2O) at room temperature. For the water molecules to condensate, the partial pressure has to exceed more than several times the static vapor pressure to become supersaturation condition.

On the other hand, the pressure hump is not observed in the PSII sample runs. After $L_{D(H)}(t)$ increases above 1.0, $P_{D(H)}(t)$ rises above 10(4) kPa with a large isotope effect, which is never related to oxygen pickup reaction, but is common to bulk absorption [2,5]. The former phase with $P_{D(H)}(t) < 10(4)$ kPa is identified as the 1a-phase with the larger $\eta_{D(H)}$, and the latter to the 1b-phase with the smaller $\eta_{D(H)}$ which gives the intercepts to the y-axes in Figs. 9 and 10, or equivalently the lower values of E_1 and $\text{D(H)}/\text{Pd}$ for oxygen-free runs other than #1 and #3 in Figs. 6 and 7. The isotope effect in the bulk absorption (1b-) phase could be explained by the difference in velocity leading to a difference in probability of tunneling through the periodic potential barriers between the lattice atoms. It is therefore inferred that $\text{D}_2\text{O}(\text{H}_2\text{O})$ formation has negligible effect on the pressure for the present PSII sample.

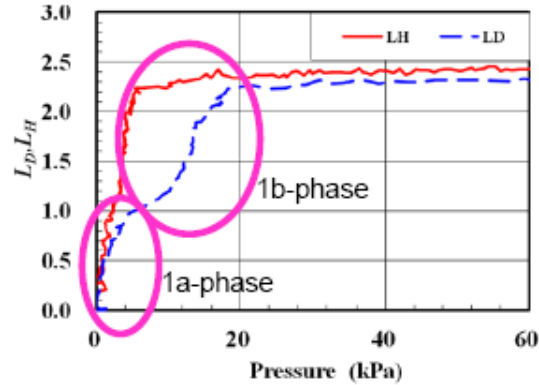


Figure 11. Relation between the loading ratio and the pressure in the D(H)-PSIII(2)#3 runs.

3.2. PNS sample

At the instant of presentation at this conference we did not complete the absorption experiments at elevated temperatures. In the present paper only the room-temperature runs are described.

As mentioned earlier, the isothermal calorimetry has been employed in absorption runs using the PNS samples including the room-temperature runs. Figure 13 shows evolution of the absorption parameters in the room-temperature runs using 10-g aliquots of the PNS sample containing 0.78 g of the Pd_1Ni_6 nanopowders.

We see clearly the sharp 1st-phase peaks of the thermal power output $W_{D(H)}(t)$ with a width of about 35 min, which are coincident with the sharp rising-up of the loading ratio $L_{D(H)}(t)$ to the saturation value of 0.43 (0.39). The powers are integrated to give the specific output energy $E_{1D(H)} = 0.51$ (0.39) eV/atom-M, where M stands for the metal host atom with the averaged composition of Pd_1Ni_6 . These are reevaluated as the energy per one hydrogen isotope atom absorbed to be $Q_{D(H)} = 1.2$ (1.0) eV/atom-D(H).

The values of $L_{D(H)}(t)$ and $E_{1D(H)}$ are rather modest in comparison with those for the PSII sample. However, if we assume that Ni atoms had no effect on the hydrogen absorption, the values would be seven times larger, which could

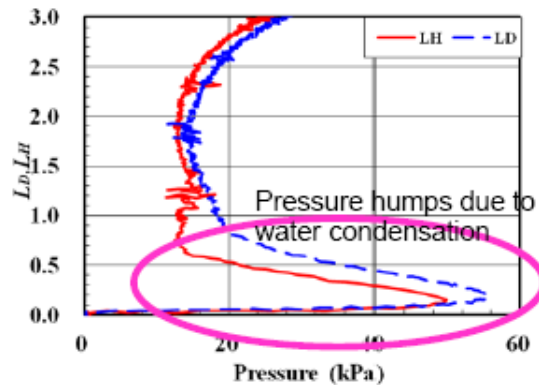


Figure 12. Relation between the loading ratio and the pressure for the PNZ2B samples.

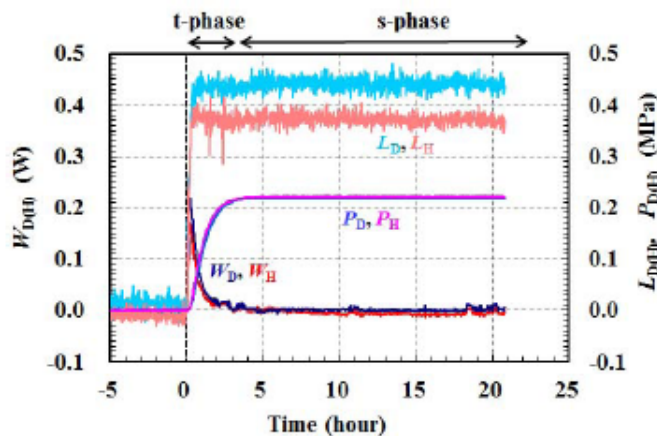


Figure 13. PNS absorption runs at room temperature, D-PNS1#1 and H-PNS2#1. The isothermal calorimetry is used.

be unacceptable. We can conclude therefore that the Pd atom in the present configuration is acting as a catalyzer for hydrogen absorption of Ni nanoparticles.

It is also interesting to note that $Q_{D(H)}$ are comparable to or even larger than those not only for the PSII sample but also for the PNZ2B sample. The potential of the hydrogen absorption sites in the present configuration is comparable to or deeper than in those samples.

The above comparisons with the other samples are tentative, since the different method of calorimetry has been employed for the PNS sample. Further study is needed to confirm the interesting conclusion.

4. Conclusion

The PSII samples have shown distinguishing absorption characteristics summarized in the following:

- (1) The as-received PSII samples showed very large loading ratio reaching 3.5 and absorption energy exceeding 2.5 eV/atom-Pd, both being much larger than other Pd nanoparticle samples ever used [2–4].
- (2) Subsequent runs without baking and runs after forced de-oxidization showed almost the same characteristics; $D(H)/Pd \approx 1.0$, and $E_1 \approx 0.2\text{--}0.3$ eV/atom-Pd. These are slightly larger than or equal to those of bulk Pd. However, forced oxidation recovered large values of $D(H)/Pd$ exceeding 2.2 and E_1 exceeding 1.3 eV.
- (3) Silica-inclusion of nanoparticles of Pd is effective to make the sample reusable to the hydrogen isotope absorption/adsorption.
- (4) The isotope effect in the released heat in the first phase is rather large.

The PNS samples have also shown interesting, though tentative, absorption characteristics:

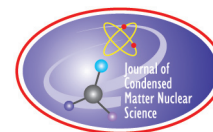
- (1) Pd atoms are acting as a catalyst for hydrogen absorption of Ni nanoparticles.
- (2) The potential of the hydrogen absorption sites in the present configuration is comparable to or deeper than in other samples ever tested.

Acknowledgements

The authors thank Dr. Brian Ahern for supplying the PNZ2B sample and valuable discussions. They also appreciate Admatechs Co. Ltd. which provided the silica-included sample.

References

- [1] A. Kitamura, T. Nohmi, Y. Sasaki, A. Taniike, A. Takahashi, R. Seto and Y. Fujita, *Phys. Lett. A* **373** (2009) 3109–3112.
- [2] A. Kitamura, Y. Miyoshi, A. Taniike, A. Takahashi, R. Seto and Y. Fujita, *J. Condensed Matter Nucl. Sci.* **4** (2011) 56–68.
- [3] A. Kitamura, Y. Miyoshi, H. Sakoh, A. Taniike, A. Takahashi, R. Seto and Y. Fujita, *J. Condensed Matter Nucl. Sci.* **5** (2011) 42–51.
- [4] H. Sakoh, Y. Miyoshi, A. Taniike, A. Kitamura, A. Takahashi, R. Seto and Y. Fujita, *Proc. 12th Meeting of Japan CF Research Society, JCF12* (2012), pp. 10–18.
- [5] Y. Miyoshi, H. Sakoh, A. Taniike, A. Kitamura, A. Takahashi, R. Seto and Y. Fujita, *J. Condensed Matter Nucl. Sci.* **10** (2013) 46–62; A. Takahashi et al., *Session of New Energy Technology, 241st ASC National Meeting*, Mar. 2011.
- [6] H. Sakoh, Y. Miyoshi, A. Taniike, A. Kitamura, A. Takahashi, R. Seto and Y. Fujita, *17th Int. Conf. Condensed Matter Nucl. Sci.*, Daejeon, Korea, Aug. 2012.
- [7] D. A. Kidwell, A. E. Rogers, K. Grabowski and D. Knies, *17th Int. Conf. Condensed Matter Nucl. Sci.*, ENEA, Rome, Italy, 2009.
- [8] B. Ahern, Private communication.
- [9] A. Takahashi, A. Kitamura, Y. Miyoshi, H. Sakoh, A. Taniike, R. Seto and Y. Fujita, *ICCF16*.
- [10] R. Laesser and K. H. Klatt, *Phys. Rev.* **B28** (1983) 748–758.



Research Article

Potential Economic Impact of LENR Technology in Energy Markets

Alexander Kleehaus*

Ecorium GmbH, Germany

Christian Elsner†

CHM, Germany

Abstract

There has been a huge discussion about the technology of Low Energy Nuclear Reaction (LENR) devices. Some of the common assumptions about this technology discuss the projected major transformation of our present society in points of infrastructure, cost of power and power storage, but a clear economic impact simulation in a business plan systematic review manner with different parameters and scenarios is still missing. The question is how will the lives of people be affected by LENR and how will power industry adapt the potential huge changes in infrastructure and cost of power. There is no doubt that access to LENR will change the lives of average citizens for that matter. The here described model is a monte-carlo simulation scenario model to find a proposed business and socio-economic value of the LENR technology as impact on current infrastructure, economy and citizens of a given country. The simulation is a good tool for pricing discussions, price modeling and predictive modeling on the technology impact. The validation of the model over common mechanisms is work-in-progress.

© 2014 ISCMNS. All rights reserved. ISSN 2227-3123

Keywords: Commercialization of LENR, LENR Pricing, LENR Economy, Technology assessment

1. Introduction

Simulation Models are a good way to calculate the impact of a technology. For the calculation there are different ways to model simulations. Modeling simulations classically needs 4 different categories of validations to determine simulation accuracy. In detail:

- (1) Face validation which means plausibility check with experts groups in interdisciplinary workshops and different expert interviews in the field

*E-mail: alexander.kleehaus@ecorium.de

†E-mail: ch.elsner@gmail.com

- (2) Internal validation which means the reproducibility of results with different methods and cross over validation with other models
- (3) Predictive value validation of the simulation, which means the ability of the simulation to predict outcomes in a simulated pre-post comparison with real data and a fictive future, and
- (4) The pure plausibility and mathematical validation, which means the validation of the model in terms of pure technical correct functionality

The here described simulation model was developed following the methodology of FDA approved health care simulations and adopts different scenarios for the German energy market. It includes a part simulating the gross economic and business value simulation, a part on the simulation of the socio-economic impact for the single households and a geographical simulation to project the impact on different geographical regions in Germany. In this paper only a rough overview of meta-results is given and the broad geographical and detailed result distribution is kept out, as of too much data and detail validation still being in progress.

The validation of the simulation is still in progress, as different expert interviews are conducted and the different validation methods are in progress.

2. Technical Work Preparation

The adopted simulation was programmed in common tools using Microsoft Office and .NET Technology / Microsoft Maps and is able to project effects of LENR on different countries.

The simulation was done with the example country of Germany but can also be projected over common parameters to any other country.

2.1. Input parameters of the simulation and computation

The Input Parameters of the simulation are:

- (1) The Present Value of the Countries Power Infrastructure with fixed rate for yearly maintenance.
- (2) The Cost of Energy for the average family and number of families in the country for heating and other scenario purposes.
- (3) Cost of the LENR Device with consumption and maintenance.

The simulation is then able to compute different scenarios with different assumptions on the possibility of the break down of power infrastructure and different scenarios of LENR use just for heating and/or for all other purposes like power generation and other energy purposes.

The saved money is then distributed over the available income of the population and generates local spill-over effects on the economics of the given country.

The economics effect is then computed as a increase in QALCs (Quality adjusted Lifetime Consumptions) of the average family.

The model further assumes, that the work force freed in the power industry is completely absorbed in other or the new LENR market and will be neutral for the economy.

2.2. Data sources for the simulation

The simulation input parameters were pulled from the German statistical database Destatis. This paper cites only the major data sources used for the model and skips the detailed geographical statistical data, that was gathered in an individual tailored analysis requested from the German Statistical Bureau.

Table 1. Present value of German energy infrastructure

No.	Type of energy	p.a. Investments in MIO Euro	Investment multiple for infrastructure value	Value of infrastructure in billion Euros
1	Electricity	8.279	24.3	201.2
2	Gas	1.280	22.6	29
3	Warm/Cold Supply	325	19.5	6.3

In detail three main data sets were used for the basic simulation model. Using the Hoppenstedt data source [1], a set of different financial statements of the different participants of the power industry was analyzed and a consistent assumption on the value of the power infrastructure was done. The meta assumption is pictured in Table 1.

The validation of the data and the computation of the multiples was done with additional data from Destatis/Section of Energy Infrastructure Investments [2].

3. Results of the Simulation

Overall the simulation was used to determine the business value of a LENR unit being installed in a normal household with 2 or more persons being able to perform the complete heating and power resource supply and to do only the heating supply for the household.

For simplicity reasons only these two scenarios are plotted here in Table 2. The source data of the simulation would also allow the modeling of other scenarios including industry power consumption and different gradations of power equivalents for power/heating substitution by LENR.

Additionally we tried to calculate a substrate of wealth being distributed over the population. Therefore it was assumed that all workforce finds a new allocation in the German System and the cost of power can be reduced by 43%, as the value of LENR systems will not fully translate into pricing.

Following this model, the wealth of a typical German household would increase by 6.1% in the full substitution model and by 2.2% in the heating substitution model, which would both mean a significant increase and acknowledgeable increase in value of life for each single household.

4. Conclusions And Discussion

The programmed simulation is able to compute different scenarios with different assumptions on the possibility of the break down of power infrastructure and different scenarios of LENR use just for heating and/or for all other purposes.

We were able to do a simple cross-check with common methods of simulation validation, but further evaluation of the model is needed. The geographical sub-simulation turned out not be of too much value, as the meta-data is sufficient for a gross evaluation of the technology.

Overall the first results of the simulation show promising results as for the big business and social-economic value of the technology.

Table 2. Output parameters of the simulation - extract

No.	Parameter name	Value (in Euros)	Comment
1	Value of a LENR device for private house hold for power and heating substitution	52. 632	Total cost of ownership value for a life-time of 10years including consumption and maintenance of the device
2	Value of a LENR device for private household for heating substitution	18.421	Total cost of ownership value for a life-time of 10 years including consumption and maintenance of the device

The model assumes, that production of the technology is cheaper than the value generated and saved money is then distributed into the available income of the population and generates local spill-over effects on the economics of the given country. The model needs further cross-validation and also a business-calculation for the cost of distribution and manufacturing of the LENR technology. Therefore, the flexible simulation model is an ideal basis for performing target costing and pricing simulations in the field of LENR technology.

Acknowledgment

Thanks to the team of Ecorium GmbH for providing the CPU power for performing the SQL Database simulations and the statistical data gathered over Destatis and Ecorium.

References

- [1] www.bilanzen.de data source of Hoppenstedt company informations “Hoppenstedt Firmeninformationen GmbH Havelstrasse 9 in 64295 Darmstadt, Postfach 10 01 39 in Germany visited online on April 25th in the year 2012.
- [2] Destatis German statistical data driven taken from the web <https://www.destatis.de/DE/ZahlenFakten/Wirtschaftsbereiche/Energie/BeschaeftigteUmsatzInvestitionen/Tabellen/KSEDaten.html> visited online on April 25, 2012



Research Article

A Change of Tritium Content in D₂O Solutions during Pd/D Co-deposition

Kew-Ho Lee^{*,†}, Hanna Jang and Seong-Joong Kim[‡]

Green Chemistry Division, Korea Research Institute of Chemical Technology, 100 Jang-dong, DaeJeon 305-343, South Korea

Abstract

In this study electrochemical co-deposition of Pd/D on nickel electrodes was performed to determine whether a nuclear fusion reaction occurs in the palladium deposit. Co-deposition was performed with a palladium salt/D₂O solution. The content of tritium in D₂O solution was varied depending on the electrolysis procedure during co-deposition. A comparison between the co-deposition of Pd/D and the simple electrolysis of D₂O was performed to investigate the change of tritium concentration in the D₂O solution. © 2014 ISCMNS. All rights reserved. ISSN 2227-3123

Keywords: Electrolysis, Palladium co-deposition, Tritium

1. Introduction

An early report on experiments with the Pd/D system suggested that fusion of deuterium atoms occurs within the Pd-lattice when the system is under prolonged cathode polarization [1]. Among the observed results attributed to nuclear events, a significant amount of tritium was found. Questions were raised concerning the origin of the tritium [2–4,10].

In this study, the electrochemical co-deposition of Pd/D on nickel electrodes was performed to determine whether a nuclear fusion reaction occurred in palladium metals that were co-deposited from a palladium salt/D₂O solution [6–9]. The content of tritium (³T) in the D₂O solution was varied depending on the electrolysis procedure of Pd/D co-deposition. A comparison between the co-deposition of Pd/D and the simple electrolysis of D₂O with a Pd foil cathode was performed to investigate the change of tritium concentration in the D₂O solution.

2. Experimental

Two types of palladium electrodes on porous Ni cathodes of 3 mm O.D. were prepared by electrodeposition in the cell design shown in Fig. 1 [5]. One type is PdCl₂–LiCl–D₂O solution and the other type is Pd(en)Cl₂(palladium

*E-mail: khlee@kriect.re.kr

[†]Also at: University of Science and Technology, 176 Gajeong-dong, Yuseong-gu, Daejeon, South Korea

[‡]Also at: University of Science and Technology, 176 Gajeong-dong, Yuseong-gu, Daejeon, South Korea

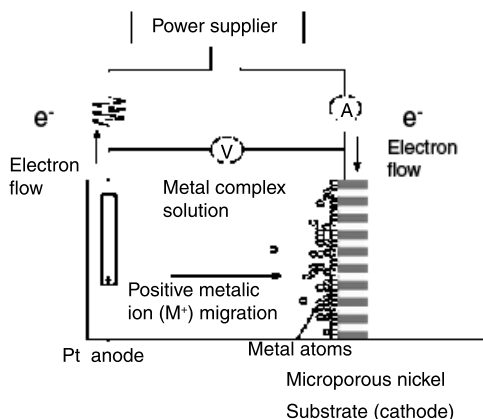


Figure 1. Electrolytic co-deposition cells.

ethylenediamine chloride)–LiCl–D₂O solution. Palladium foil electrodes (7 × 20 mm) were subjected to D₂ evolution from D₂O + 0.3 M LiCl electrolysis. The co-deposition experiments were carried out in a closed system with a recombination catalyst. The resulting solutions were examined for tritium. Samples of liquid electrolyte were measured using liquid scintillation counting. In all cells, measurements were made for the activity of ³H in solution. The resulting liquid was analyzed the same way as the electrolyte samples were. Platinum gauze anodes (99.9% pure), used in all cases, were washed and allowed to dry in air.

All of the cells were first run at low-current density. After a few days, current density was increased up to 300 mA. Samples of electrolyte were withdrawn for tritium analysis from the cell. Tritium analysis was performed on the alkaline electrolyte by in situ Liquid Scintillation Counting (LSC). A 1 ml sample of electrolyte is added to 2 ml of Ready safe, Beckman LSC cocktail in a vial. The prepared solutions were counted for 1 min in a Beckman LS 6000 TA scintillation Counter. The results are given as counts per minute (cpm) per ml of samples.

3. Results and Discussion

3.1. Pd/D co-deposition

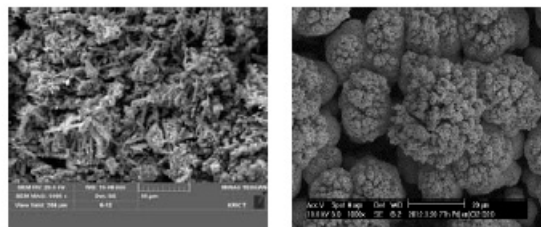
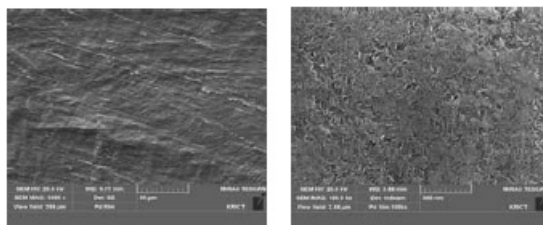
Pd/D co-deposition with two different conditions was performed. One is Pd/D co-deposition with PdCl₂ and the other is Pd(en)Cl₂. The same type cathode (porous Ni) and anode (Pt gauze) was used and the current density conditions are only a little different. Experimental conditions and results are summarized in Table 1. Pd/D co-deposition using PdCl₂ was conducted from 1 up to 300 mA of current density. The tritium level was decreased from the initial level of 596–235 cpm after the reaction. Pd/D co-deposition using Pd(en)Cl₂ was conducted from 1 up to 200 mA and the tritium level was decreased from 489 to 160 cpm. Figure 2 shows SEM images of the surfaces of cathodes after Pd/D co-deposition. This is an unexpected result. The tritium content should have remained constant or increased [11]. These results suggest that tritium was consumed or adsorbed in the electrodes. The surface of a cathode co-deposited with PdCl₂ (Fig. 2(a)) was somewhat rough like branches of acicular shape, while the shape of cathode co-deposited with Pd(en)Cl₂ (Fig. 2(b)) was like aggregates of spherical globules.

Table 1. Change of tritium concentration of Pd/D co-deposition.

Conditions	PdCl ₂ 0.03 M LiCl 0.3 M D ₂ O 100 mL Ammonia water 1.8 mL	Pd(en)Cl ₂ 0.03 M LiCl 0.3 M D ₂ O 100 mL Ammonia water 1.8 mL
Electrodes (cathode/anode)	Porous Ni/ Pt gauze	Porous Ni/ Pt gauze
Current	1–50 mA (4 h)-200 mA (7 h)-300 mA (1 h)-1 mA	1–10 mA (6 h)-50 mA (1 h)-100 mA (1.5 h)-150 mA (1 h)-200 mA (1 h)-1 mA
Time	97 h	77 h
Before	596.00 cpm	489.00 cpm
After	235.00 cpm	160.00 cpm

3.2. D₂O electrolysis

Electrolysis was performed with 0.3 M lithium chloride in D₂O. The cathode was palladium foil, and the anode was platinum gauze. The experimental conditions and results are summarized in Table 2. D₂O electrolysis was conducted from 20 up to 400 mA of current density. As a result, an increase in the tritium level was seen from the initial tritium level of 10.00 up to 167.00 cpm after the reaction. Despite the short duration of electrolysis and the initial low level of tritium, the tritium level increased a great deal. Figure 3 shows SEM images of the surface of the cathode after D₂O electrolysis. Band split vertically appeared on the surface of cathode (Fig. 3(a)). The change of the surface was observed clearly at high magnification. Small defects appeared, along with what looks like small uniform patterns.

**Figure 2.** SEM image of Pd/D co-deposition cathodes. (a) PdCl₂ (b) Pd(en)Cl₂.**Figure 3.** SEM image of D₂O electrolysis cathode. (a) 1000× and (b) 100 000×.

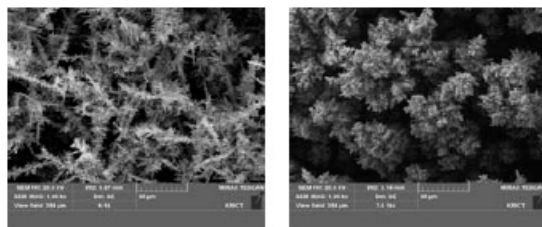


Figure 4. SEM image of Pd/D co-deposition and D₂O electrolysis cathode. (a) PdCl₂ and (b) Pd(en)Cl₂.

3.3. Pd/D co-deposition and D₂O electrolysis

Pd/D co-deposition under two different conditions was performed. One condition is Pd/D co-deposition with PdCl₂ and the other is with Pd(en)Cl₂. The Pd/D co-deposition was conducted at a current of 1 mA for 1 week, and D₂O electrolysis was conducted by increasing current density. The same type of cathode (porous Ni) and anode (Pt gauze) was used and the current density conditions were the same. Experimental conditions and results are shown in Table 3. Pd/D co-deposition with only low current does not change the tritium concentrations. Tritium levels were not changed with either of the Pd/D co-deposition cathodes at a current of 1 mA. But the tritium level after D₂O electrolysis increased greatly. The tritium level using PdCl₂ increased from the initial at 28–314 cpm. The tritium level using Pd(en)Cl₂ increased from the initial level of 30–258 cpm. Figure 4 shows SEM images of the initial of 28–314 cpm after reaction surface of the cathode after Pd/D co-deposition and D₂O electrolysis. The surface of 30 cpm to the final level of 258 cpm the cathode was fine and weak forms compared with Pd/D co-deposition cathodes (Fig. 2). The surface shape of cathode co-deposited with PdCl₂ (Fig. 4(a)) was somewhat rough, with long branches of acicular shape; while the surface shape of the cathode co-deposited with Pd(en)Cl₂ (Fig. 4(b)) was short with sparse shapes.

4. Conclusions

Pd/D co-deposition with only low current did not change the tritium level at the concentrations studied in this work. Contrary to our expectations, Pd/D co-deposition with higher current, up to 300 mA, decreased the tritium concentration of D₂O solutions, when highly tritiated D₂O was used. When D₂O with lower levels of tritium was used, both palladium foil and Pd co-deposited electrodes increased tritium content during D₂O electrolysis

Table 2. Change of tritium concentration of D₂O electrolysis cells

Conditions	LiCl 0.3 M D ₂ O 100 mL
Electrodes (cathode/anode)	Pd foil/ Pt gauze
Current	20–250 mA (2h)-20 mA-200 mA (0.5 h)- 400 mA (0.5 h)
Time	65h
Before	10.00 cpm
After	167.00 cpm

Table 3. Change of Tritium concentrations of Pd/D co-deposition and D₂O electrolysis

Conditions	PdCl ₂ 0.03 M LiCl 0.3 M D ₂ O 100 mL Ammonia water 1.8 mL	Pd(en)Cl ₂ 0.03 M LiCl 0.3 M D ₂ O 100 mL Ammonia water 1.8 mL
Electrodes (cathode/anode)	Porous Ni/ Pt gauze	Porous Ni/ Pt gauze
Current	1 mA	1 mA
Time	168 h	168 h
Before	40.00 cpm	24.00 cpm
After	35.00 cpm	26.00 cpm
Conditions	LiCl 0.3 M D ₂ O 100 mL	LiCl 0.3 M D ₂ O 100 mL
Electrodes (cathode/anode)	Porous Ni/ Pt gauze	Porous Ni/ Pt gauze
Current	20–250 mA (2 h)-20 mA- 200 mA (0.5 h)-400 mA (0.5 h)	20–250 mA (2 h)-20 mA- 200 mA (0.5 h)-400 mA (0.5 h)
Time	65 h	65 h
Before	28.00 cpm	30.00 cpm
After	314.00 cpm	258.00 cpm

Acknowledgment

The authors wish to thank K.Y. Kim (KRICT) and J.S. Ahn (KRIBB) for help in making many of the tritium measurements.

References

- [1] M. Fleischmann and S. Pons, Electrochemically induced nuclear fusion of deuterium, *J. Electroanal. Chem.* **261** (1989) 301 and errata **263** (1989) 187.
- [2] N.J.C. Packham, K.L. Wolf, J.C. Wass, R.C. Kainthla and J.O'M. Bockris, Production of tritium from D₂O electrolysis at a palladium cathode, *J. Electroanal. Chem.* **270** (1989) 451.
- [3] K.-H. Lee and Y.M. Kim, The change of tritium concentration during the electrolysis of D₂O in various electrolyte cells, *Proc. Third Int. Conf. on Cold Fusion*, 1992, p. 511.
- [4] K.-H. Lee, A study on cold fusion reaction report- 0234, KRICT (1991).
- [5] S.-E. Nam and K.-H. Lee, *J. Membrane Sci.* **170** (2000) 91.
- [6] S. Szpak et al., *J. Electroanal. Chem.* **379** (1994) 121.
- [7] S. Szpak, P.A. Mosier-Boss, R.D. Boss and J.J. Smith, On the behavior of the Pd/D system: evidence for tritium production, *Fusion Technol.* **33** (1998) 38–51.
- [8] P.A. Mosier-Boss, S. Szpak, F.E. Gordon and L.P.G. Forsley, Use of CR-39 in Pd/D co-deposition experiments, *Eur. Phys. J. Appl. Phys.* **40** (2007) 293.
- [9] P.A. Mosier-Boss, S. Szpak, F.E. Gordon and L.P.G. Forsley, Characterization of tracks in CR-39 detectors obtained as a result of Pd/D co-deposition, *Eur. Phys. J. Appl. Phys.* **46** (2009) 30901.
- [10] Y.E. Kim, Theoretical interpretation of anomalous tritium and neutron productions during Pd/D codeposition experiments, *Eur. Phys. J. Appl. Phys.* **52** (2010) 31101.
- [11] J.O'M. Bockris, C. Chien, D. Hodko and Z. Minevski, Reproducible Nuclear Reactions during Interaction of Deuterium with Oxide Tungsten Bronze, *Proc. Third Int. Conf. on Cold Fusion*, part 1, 231 (1992).



Research Article

“Excess Heat” in Ni–H Systems and Selective Resonant Tunneling *

Xing Z. Li[†], Zhan M. Dong and Chang L. Liang

Department of Physics, Tsinghua University, People's Republic of China

Abstract

Selective resonant tunneling model is applied to Ni–H systems to explain the “excess heat” without strong neutron and gamma radiations. In combination with Bethe’s solar model of weak interaction, the reaction rate is estimated, and compared with experiments. An experimental test is further suggested.

© 2014 ISCMNS. All rights reserved. ISSN 2227-3123

Keywords: Bethe’s solar model of weak interaction, Internal conversion electron, Resonant electron capture, Selective resonant tunneling

1. Introduction

Excess heat in Ni–H systems was discovered in Piantelli’s biological experiments in a cryogenic environment [1], and in Mastromatteo’s chip of integrated circuits when electrical current was passing through the nickel foil in the hydrogen gas [2]. Thanks to Professor Focardi, my visits to Bologna University and Siena University were arranged to see their Ni–H systems for detecting excess heat and nuclear radiations in 1999 and 2000. Rossi’s demonstrations in 2011 motivated us to study the resonant tunneling [3–8] through Coulomb barrier with high charge number $Z = 28$. Although the resonant tunneling model is still valid to explain the excess heat without strong neutron and gamma radiation, it needs additional consideration to calculate the reaction rate for $Z = 28$.

The resonant tunneling model introduces three parameters: U_r , U_i , and a_0 , i.e. the real and imaginary part of nuclear potential well and its radius, respectively. The imaginary part, U_i , would be extremely small for a resonant tunneling with $Z = 28$, because U_i is supposed to be in the order of $(1/\theta^2)$ in order to have a resonant tunneling. Here $(1/\theta^2)$ is the Gamow penetration factor, an extremely small number for $Z = 28$. Indeed, it is not legitimate to use U_i for this case, because the weak interaction is dominant, and the imaginary part of nuclear potential is no longer a suitable tool for describing the weak interaction. The intermediate heavy boson makes the range of weak interaction much shorter

*Supported by Natural Science Foundation of China #21153003 and by Tsinghua University Basic Research Fund (985-III).

[†]E-mail: lxz-dmp@tsinghua.edu.cn

than the range of strong interaction (a_0). We have to calculate the overlapping of the initial wave function with the final wave function in order to estimate the reaction rate instead of using U_i .

2. Overlapping of Wave Functions

In Bethe's solar model [9], the overlapping of wave functions was calculated to estimate the fusion reaction rate for $p + p \rightarrow d + e^+ + \text{neutrino}$, because the weak interaction dominates. The cross-section of reaction, σ , is written as

$$\sigma = \frac{g f(W) \left| \int \Psi_f \Psi_i d\tau \right|^2}{v}. \quad (1)$$

Here, g is the coupling constant for weak interaction, which is about 10^{-4} 1/s, $f(W)$ is a function of emitted β -particle's energy, W and v is the speed of incoming proton. The integration $\int \Psi_f \Psi_i d\tau$ shows the overlapping of the initial wave function, Ψ_i , with the final wave function, Ψ_f . In Bethe's calculation, Ψ_i is the $p + p$ elastic scattering wave function which is in a continuous state normalized to the incoming beam intensity, and Ψ_f is the $n + p$ confined state wave function (i.e. deuteron) which is in a discrete state normalized in its confined region. The transition from $p + p$ to $n + p$ with positron emission implies that a proton is transformed into a neutron, and a positron is created. Both of these two processes need energy, which is provided by the binding energy of deuteron. There is no heavy electron involved at all. Hence, if $n + {}^{58}\text{Ni}$ confined state would provide enough binding energy, the $p + {}^{58}\text{Ni}$ might be transformed into $n + {}^{58}\text{Ni}$ confined state in terms of electron capture as well:



We learned two points from Bethe's calculation: (??) the contribution from the overlapping of wave functions outside the nuclear potential well was much greater than the contribution from the overlapping of wave functions inside the nuclear potential well. Hence, the resonance of transition would appear when the overlapping of wave functions outside the nuclear potential well reaches a maximum; (??) in a hydrogen-storage metal (Ni-H system), $p + {}^{58}\text{Ni}$ is in a confined state in lattice which is different from an incoming proton beam; hence, the initial wave function must be normalized in its confined region (including the lattice region) as well. The cross-section in Eq. (??) is supposed to be replaced by the probability of transition, T :

$$T \propto g \cdot \frac{\left| \int \Psi_f \Psi_i d\tau \right|^2}{\int |\Psi_f|^2 d\tau \cdot \int |\Psi_i|^2 d\tau}. \quad (3)$$

Searching the resonance means searching for the maximum of T in Eq. (3). Mathematical theorem says that the ratio of integrations in Eq. (3) would reach its maximum value 1, if and only if

$$\Psi_i = \text{Constant} \cdot \Psi_f, \quad (4)$$

Ψ_f is a confined state of $n + {}^{58}\text{Ni}$ or the excited ${}^{59}\text{Ni}$. The neutron wave function would extend to outside of the nuclear potential well (thick dashed curve in Fig. 1). It is an exponentially decaying wave function outside the nuclear well; hence, the resonance condition (??) requires an exponentially decaying wave function, Ψ_i , in the region under the Coulomb barrier (thick solid curve in Fig. 2). In other words, the irregular Coulomb wave function, G_0 , must be dominant in this region.

Figure 2 shows $p + {}^{58}\text{Ni}$ wave function in a down-shifted Coulomb field and a square nuclear potential well, when the wave function reaches almost the maximum on the boundary of the nuclear potential well. The resonance condition, Eq. (??), implies a similar logarithmic derivative for Ψ_i and Ψ_f . The logarithmic derivative of Ψ_f at the border of nuclear potential well is determined by the binding energy of $n + {}^{58}\text{Ni}$ confined state. If this binding energy is too large

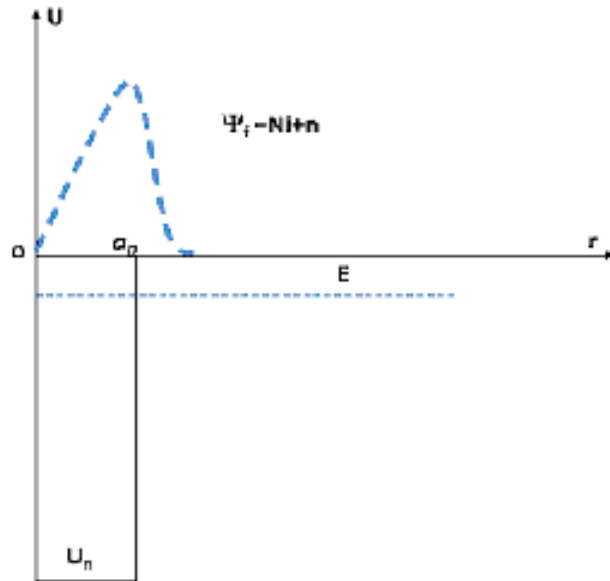


Figure 1. $n + {}^{58}\text{Ni}$ wave function in a square nuclear potential well.

or too small, it might be not suitable to have a good overlapping in the integration of the numerator of Eq. (3), because

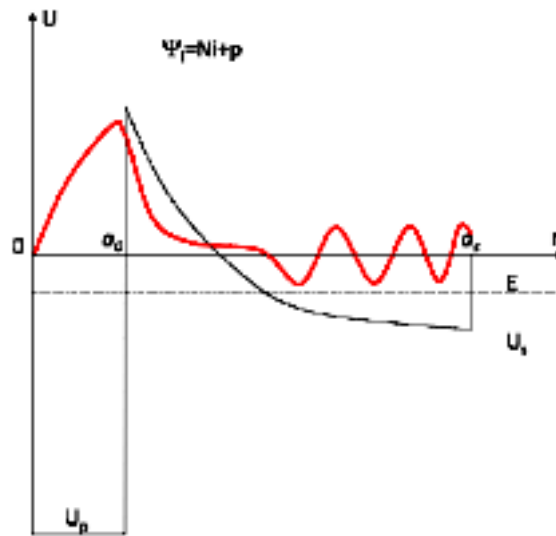


Figure 2. $p + {}^{58}\text{Ni}$ wave function in a down-shifted Coulomb field and a square nuclear potential well, when the wave function reaches almost the maximum on the boundary of the nuclear potential well.

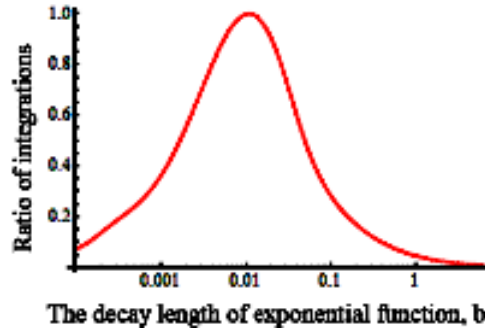


Figure 3. Qualitatively showing the maximum of overlapping was reached when binding energy of $n + {}^{58}\text{Ni}$ is of order of MeV.

the logarithmic derivative of Ψ_f at the border of nuclear potential well has to be close to

$$\frac{1}{G_0} \cdot \frac{\partial G_0}{\partial r} \bigg|_{r=a_0}.$$

Figure 3 shows the normalized overlapping of $G_0[\eta, \rho]$ with an exponentially decaying function, $\exp[-\rho/b]$, varies with the decay length, b , which depends on the binding energy of $n + {}^{58}\text{Ni}$ confined state.

In Fig. 2, the Coulomb potential is down-shifted by the electron-screening effect to form a potential well in lattice. The wave function in this lattice well is a combination of irregular Coulomb wave function, G_0 and the regular Coulomb wave function, F_0 , $\Psi_i = F_0 + K \cdot G_0$. The coefficient of linear combination, K , would eventually determine the overlapping of the initial and final wave functions. Figure 4 shows that the normalized overlapping ratio of wave functions, R , for $p + {}^{58}\text{Ni}$ may approach its maximum when K is greater than $(10000/\theta)$.

$$R = \frac{|\int \Psi_f \Psi_i d\tau|^2}{\int |\Psi_f|^2 d\tau \cdot \int |\Psi_i|^2 d\tau}. \quad (5)$$

It is evident that even if the Gamow factor is very small for the $p + {}^{58}\text{Ni}$ system, it is still possible to reach the resonance by controlling the linear combination coefficient. Thus the probability of transition, T , in Eq. (3), would be in the order of $10^{-5}/s$, if and only if G_0 is dominant at the interface between nuclear potential well and the Coulomb barrier in the initial wave function, Ψ_i .

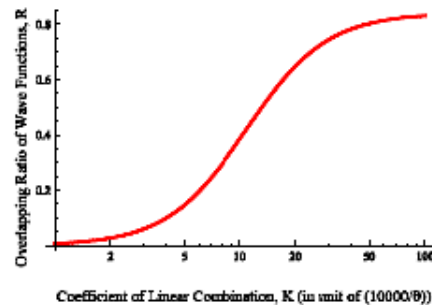


Figure 4. The overlapping of wave functions is a function of the linear combination coefficient, K .

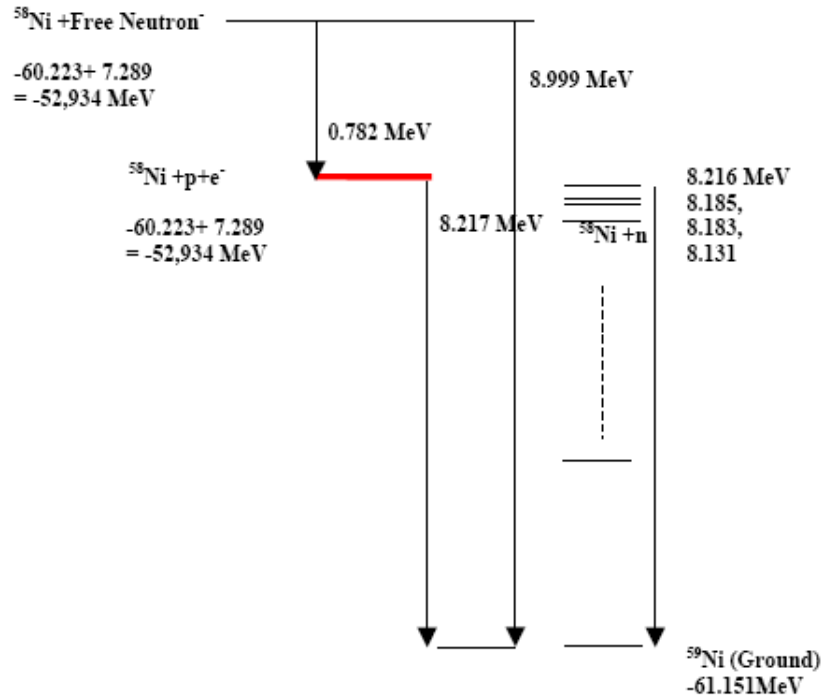


Figure 5. $n + ^{58}\text{Ni}$ (top line) and $p + ^{58}\text{Ni} + e$ states (thick line) on the ^{59}Ni energy spectrum(right).

3. Energy Transfer

When $p + ^{58}\text{Ni}$ forms a mother nuclear state for transition, it is important to discuss the daughter nuclear state of $n + ^{58}\text{Ni}$, because the energy spectrum of the daughter state determines the energy transfer from nuclear energy to lattice energy. If the energy is taken away by a neutrino during the transition, it is not good for heating the lattice, because neutrino would escape with its energy. Hence, it is important to have a $n + ^{58}\text{Ni}$ confined state just between the $p + ^{58}\text{Ni}$ confined state and ground state of ^{59}Ni in order to reduce the escaping energy carried by the neutrino. Figure 5 shows the $n + ^{58}\text{Ni}$ state and $p + ^{58}\text{Ni} + e$ state on the ^{59}Ni energy spectrum. For the lattice confined hydrogen in nickel, $p + ^{58}\text{Ni}$ state is below the “ $^{58}\text{Ni} + \text{Free neutron}$ ” state by 0.782 MeV . Hence, the energy defect prohibits the transition from proton to free neutron. However, there is a series of excited states of ^{59}Ni , which are just below $p + ^{58}\text{Ni}$ state by keV to MeV. Indeed this binding energy assists the transition from a proton to a confined neutron. During this *resonant electron capture* process only about 1 keV – 1 MeV is taken away by the neutrino, and most of excited energy still remains in the excited ^{59}Ni nucleus. Now the question is how this energy ($\sim 7 \text{ MeV}$) would be preferably transferred to the lattice during its de-excitation processes.

The de-excitation processes are in two categories: (1) releasing the energy to internal conversion electron; (2) emitting photon through gamma decay. If the energy is transferred to orbital electrons through internal conversion electron, it is good for heating the lattice. However, if the energy is taken by photons, and photons penetrate the nickel lattice; then, it is not good for heating the lattice, and causes the problem of radiation protection. They are the competing processes. The result of the competition is determined by the energy difference between two energy levels.

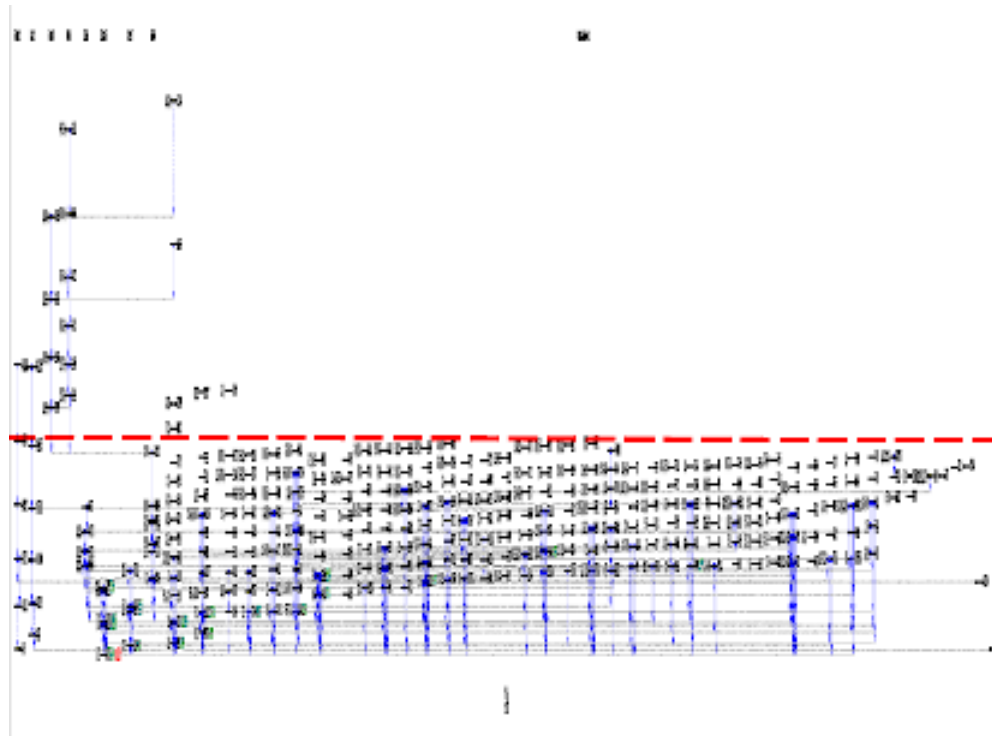


Figure 6. More than 276 energy levels are below the dashed line in ^{59}Ni energy spectrum.

When the energy difference is getting smaller and smaller, the internal conversion electron dominates. That is, the orbital electrons would take away most of the de-excitation energy and heat the lattice eventually. Figure 6 shows the whole energy spectrum of ^{59}Ni . The long thick dashed line shows the energy level of $p + ^{58}\text{Ni}$ state. A lot of energy levels are below this dashed line (each short dash represents an energy level in Fig. 6). Roughly speaking, more than 276 energy levels are below that dashed line. It implies that the average difference between two neighboring energy levels is around 30 keV. Thus the internal conversion electrons would dominate the de-excitation process by a factor of up to 10^5 . This is shown in Fig. 7. The ratio of internal conversion probability to the gamma transition is depicted in Fig. 7 for K-orbital electrons. At the low energy, the internal conversion process dominates for all modes of gamma emission [10].

The electron capture or the internal conversion would capture or kick out an orbital electron and create a vacancy which would introduce the characteristic X-rays and Auger electrons. Table 1 shows the ionization energy for all the orbits of nickel and copper. They are all below 12 keV [11]. Now we may answer the question whether the nickel powder cylinder of diameter of 5 cm and the lead plate of 3 mm thickness are enough to reduce all the gamma radiations and the energetic electrons to the background level? [12] The dose of background radiation is about 1 mSv/year which corresponds to an energy flux density of 1–6 MeV/cm²/s of 30–60 keV photons (Fig. 8) [13]. However, 10 kW of heating power corresponds to an energy flux density of 8×10^{14} MeV/cm²/s on the surface of the copper tube of 5 cm diameter in the case of E-cat demonstration in 2011 if there was no attenuation of γ radiation. Hence, it is necessary to provide a reduction of the order of 10^{14} in order to reach a background dose outside the E-cat device. The mass attenuation coefficient for 60 keV photon just provides such a reduction of the order of 10^{14} (the dashed

line in Fig. 9 [14]). However, if the excited ^{59}Ni de-excites to the ground state directly and emit a gamma photon with 8.216 MeV; then, the mass attenuation coefficient would be reduced by a factor of 40 or more in comparison with that of 30–60 keV photons (the dashed line in comparison with dotted line in Fig. 9). As a result, the 8.216 MeV photon would not leave the energy to lattice, and the radiation dose would be higher than the background in E-cat demonstrations

4. Excess Power

When the weak interactions dominate the de-excited processes; then one might worry if it would give 10 kW power in a volume of 85 cm^3 [12]. Indeed the nickel ($\sim 10\text{ mol}$) is more than enough. The resonant electron capture has a rate of 10^{-5} per second in Eq. (3). It would provide a power of 10 MW if all of nickel nuclei are in the resonant electron capture process. In reality, the resonance happens only in the surface layer of 10^{-8} m (100 \AA) thickness. If we do not use nickel powder, only 10^{-6} of total nickel nuclei are involved. They are able to provide 10 W at most. However if we use the powder of diameter of 10^{-5} m ($10\text{ }\mu\text{m}$); then, it would provide 10 kW of excess heat. This is just the size of the powder revealed in the patent.

The 10 kW E-cat is supposed to be in operation for half a year ($\sim 10^7\text{ s}$). The number of nickel nuclei in resonance would decrease dramatically, because the total number of nickel nuclei in the surfaces of powder would decrease by e-fold after every 10^5 s . We expect that the powder would split gradually during the process of absorbing and desorbing; then, a constant power of 10 kW might be maintained with the assistance of some wave fields.

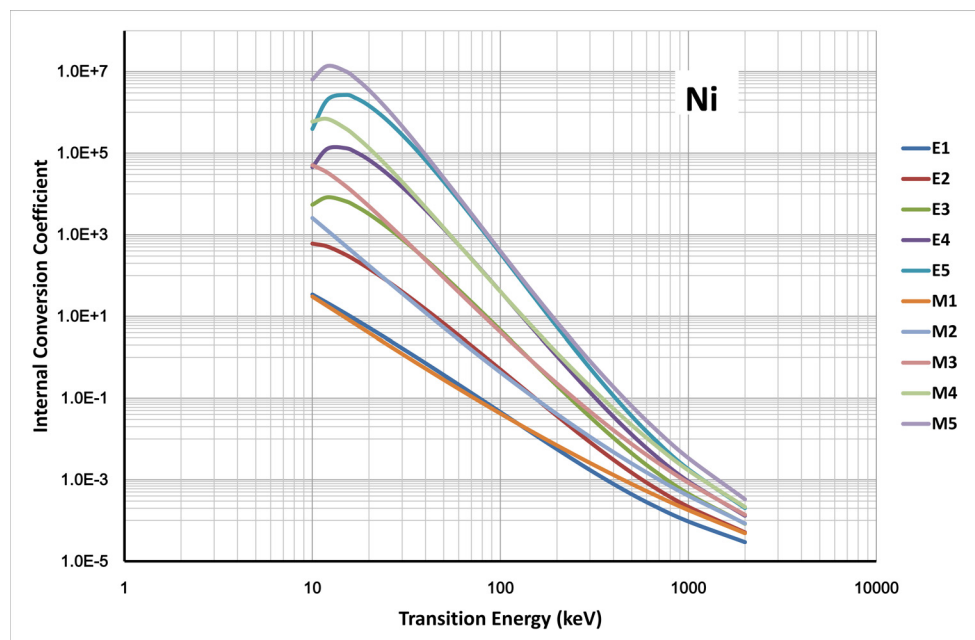


Figure 7. The internal conversion coefficient versus transition energy (in keV) for nickel.

Table 1. Ionization energies of atoms and atomic ions (in unit of eV)

Neutral atoms to + 7 ions neutral		I	II	III	IV	V	VI	VII	VIII
Z	Element								
28	Ni	7.6398	18.16884	35.19	54.9	76.06	108	133	162
29	Cu	7.72638	20.2924	36.841	57.38	79.8	103	139	166
+ 8 Ions to + 15 ions									
Z	Element	IX	X	XI	XII	XIII	XIV	XV	XVI
28	Ni	193	224.6	321.0	352	384	430	464	499
29	Cu	199	232	265.3	369	401	435	484	520
+ 16 Ions to + 23 ions									
Z	Element	XVII	XVIII	XIX	XX	XXI	XXII	XXIII	XXIV
28	Ni	571.08	607.06	1541	1648	1756	1894	2011	2131
29	Cu	557	633	670.588	1697	1804	1916	2060	2182
+ 24 Ions to + 29 ions									
Z	Element	XXV	XXVI	XXVII	XXVIII	XXIX			
28	Ni	2295	2399.2	10288.8	10775.40				
29	Cu	2308	2478	2587.5	11062.38	11567.617			

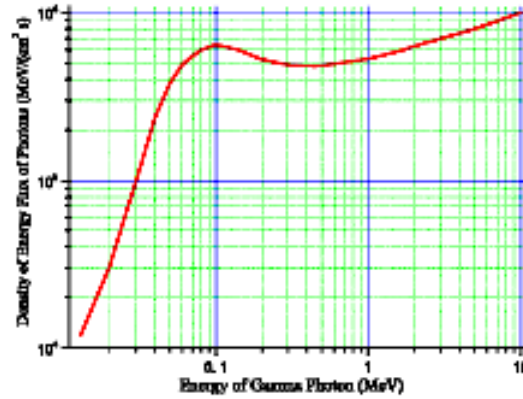


Figure 8. The energy flux density of gamma radiation versus photon energy for 1 Roentgen/hour dose in air. (1 Roentgen/hour is about 76212 mSv/year).

5. Eigen Equation

In Fig. 2 the lattice potential well is approximated by a down-shifted Coulomb field in an electron screening sphere. The wave function of proton in this potential well is a linear combination of irregular and regular Coulomb wave functions: $F_0 + KG_0$. The coefficient of linear combination, K , is determined by the eigen equations (6) and (7). Here,

$$k_1 = \sqrt{\frac{2\mu(E - U_p)}{\hbar^2}},$$

μ is the reduced mass for $p + {}^{58}\text{Ni}$ system; E and U_p are the energy and nuclear potential of $p + {}^{58}\text{Ni}$ system, respectively, \hbar is the Planck constant divided by 2π , $\eta = 1/(ka_c)$ and $\rho = kr$ are Coulomb variables with

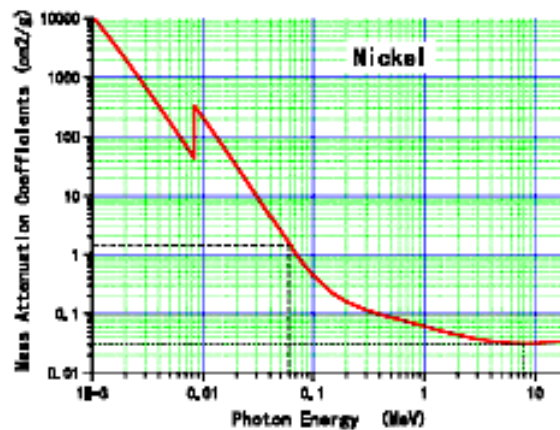


Figure 9. The necessary mass attenuation coefficient to reduce the gamma radiation dose to the background level.

$$k = \sqrt{\frac{2\mu(E - U_s)}{\hbar^2}} \quad \text{and} \quad a_c = \frac{4\pi\epsilon_0\hbar^2}{Ze^2\mu}, \quad \epsilon_0 = 8.8542 \times 10^{-12} \text{ F/m};$$

U_s is the depth of the lattice potential well for p + ^{58}Ni system; a_s is the radius of the electron screening sphere.

$$\frac{F_0[\eta, \rho_0]}{G_0[\eta, \rho_0]} \cdot \frac{\frac{\rho_0}{F_0[\eta, \rho_0]} \cdot \frac{\partial F_0[\eta, \rho]}{\partial \rho} \Big|_{\rho=\rho_0} - k_1 a_0 \cot[k_1 a_0]}{\frac{\rho_0}{G_0[\eta, \rho_0]} \cdot \frac{\partial G_0[\eta, \rho]}{\partial \rho} \Big|_{\rho=\rho_0} - k_1 a_0 \cot[k_1 a_0]} = \frac{F_0[\eta, \rho_s]}{G_0[\eta, \rho_s]} \cdot \frac{\frac{\rho_s}{F_0[\eta, \rho_s]} \cdot \frac{\partial F_0[\eta, \rho]}{\partial \rho} \Big|_{\rho=\rho_s} + \beta a_s}{\frac{\rho_s}{G_0[\eta, \rho_s]} \cdot \frac{\partial G_0[\eta, \rho]}{\partial \rho} \Big|_{\rho=\rho_s} + \beta a_s}, \quad (6)$$

$$K = -\frac{F_0[\eta, \rho_0]}{G_0[\eta, \rho_0]} \cdot \frac{\frac{\rho_0}{F_0[\eta, \rho_0]} \cdot \frac{\partial F_0[\eta, \rho]}{\partial \rho} \Big|_{\rho=\rho_0} - k_1 a_0 \cot[k_1 a_0]}{\frac{\rho_0}{G_0[\eta, \rho_0]} \cdot \frac{\partial G_0[\eta, \rho]}{\partial \rho} \Big|_{\rho=\rho_0} - k_1 a_0 \cot[k_1 a_0]}. \quad (7)$$

$$\rho_0 = ka_0, \quad \rho_s = ka_s, \quad \text{and} \quad \beta = \sqrt{\frac{2\mu(-E)}{\hbar^2}}$$

Equation (6) determines the eigen value of energy E , and Eq. (7) determines the coefficient, K , of the linear combination. In general,

$$\frac{F_0[\eta, \rho_0]}{G_0[\eta, \rho_0]} \sim \frac{2\pi\eta}{\exp[2\pi\eta] - 1} = \frac{1}{\theta^2} \ll 1.$$

It makes $K \sim (1/\theta)^2$. In order to meet the resonance condition in Fig. 4, the denominator in Eq. (7) must satisfy

$$\left(\frac{\rho_0}{G_0[\eta, \rho_0]} \cdot \frac{\partial G_0[\eta, \rho]}{\partial \rho} \Big|_{\rho=\rho_0} - k_1 a_0 \cot[k_1 a_0] \right) \ll 1/10000 \theta. \quad (8)$$

This is the boundary condition for the p + ^{58}Ni wave function at $r = a_0$. Equation (??) corresponds to its smooth connection to an irregular Coulomb wave function, $G_0[\eta, \rho_0]$, in the lattice well. That is the necessary condition for a resonance, because it makes the good overlapping with an exponentially decaying n + ^{58}Ni wave function (Figs. 3 and 4). Equation (??) is indeed a relation between U_r and a_0 when $U_i \rightarrow 0$. We may suggest that an experimental test on this relation should be performed.

6. Experimental Test

In the above-mentioned sections, all discussions are based on a fundamental assumption, i.e. there is a resonance in the p + ^{58}Ni system near the zero energy. This resonance allows proton to penetrate Coulomb barrier, and pick up the weak interaction only among various interactions – selective resonant tunneling. If we have a set of good data for p + ^{58}Ni non-elastic scattering; then, we might use the 3-parameter formula [6]

$$\sigma_r = \frac{\pi}{k^2} \cdot \frac{1}{\theta^2} \frac{-4w_i}{w_i^2 + (w_i - \frac{1}{\theta^2})^2} \quad (9)$$

to fit this set of data in order to find the real and imaginary part of nuclear potential well and its radius, respectively (i.e. U_r , U_i , and a_0) because w_r and w_i depend on these three parameters only. We have successfully applied this method to the $p+{}^6\text{Li} \rightarrow {}^3\text{He} + {}^4\text{He}$ fusion reaction data [8], and showed that U_r, U_i , and a_0 satisfy the resonance condition (??). Unfortunately, there is no such data set for $p + {}^{58}\text{Ni}$ at low energy. The only available low-energy data for $p + {}^{58}\text{Ni}$ is the $p+{}^{58}\text{Ni} \rightarrow {}^{59}\text{Cu} + \gamma$ data published in 1977 [10], which is not accurate enough to find this fit. Hence, a better experiment for $p + {}^{58}\text{Ni}$ system is desirable to confirm this resonance.

In addition, we may detect the neutrino emission from the resonant electron capture process. The mono-energetic neutrino might make this difficult test a little easier [15].

7. Conclusion

A resonant electron capture model is proposed to explain the “excess heat” in Ni–H system without strong neutron and gamma radiation. It has four main features:

- (1) Proton penetrates the Coulomb barrier of ${}^{58}\text{Ni}$ in terms of selective resonant tunneling; hence, the resultant resonance state should be a $p + {}^{58}\text{Ni}$ state with no strong neutron or gamma emission. Only the state governed by the weak interaction would be created as a mother nucleus.
- (2) The $p + {}^{58}\text{Ni}$ state would transit to $n + {}^{58}\text{Ni}$ confined state in terms of electron capture processes $p + {}^{58}\text{Ni} + e^- \rightarrow {}^{59}\text{Ni}^* + \text{neutrino}$ with the neutrino emission. The neutrino would take away part of the binding energy if the newly created ${}^{59}\text{Ni}^*$ state is still in an excited state of ${}^{59}\text{Ni}$. The de-excitation of this ${}^{59}\text{Ni}^*$ state would provide the observed “excess heat” in Ni–H system.
- (3) The internal conversion electron process would dominate the de-excitation, because ${}^{59}\text{Ni}^*$ state is submerged in a sea of energy levels of excited ${}^{59}\text{Ni}$ state. The energy difference between two neighboring levels is around 30–60 keV, the internal conversion electron process would win over the gamma decay in the competition (this is consistent with Defkalion and E-cat measurements published during or after ICCF-17).
- (4) In a word, proton is transformed into a neutron to gain the binding energy from $(p + {}^{58}\text{Ni})$ to $(n + {}^{58}\text{Ni})$. The energy level of $(p + {}^{58}\text{Ni})$ system near zero energy plays a key role. It may be verified in a beam-target experiment.

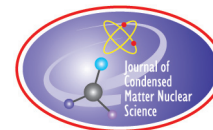
Notes

- (1) The assumption of resonance level might be verified by $d + (d + d)$ reaction as well, when low-energy data is not accurate enough to determine the boundary condition of nuclear potential well for $(d + d)^*$ state.
- (2) The probability in resonance would be greatly enhanced when we consider the transition from energy band of proton in lattice and the dynamic feed-back mechanism.
- (3) F. Piantelli and W. Collis *Some results from the Nichenergy Laboratory. 10th Int. Workshop on Anomalies in Hydrogen Loaded Metals*, 10–14 April 2012, Certosa di Pontignano, Loc. Pontignano, 53010 Vagliagli, Siena – Italia, described the potential well in the lattice as well.

References

- [1] F. Piantelli, Anomalous energy production, *Atti Accad. Fisiocritici*, Serie XV, Tomo XXII, 1993, pp. 89–98.
- [2] U. Mastromatteo, Hydrogen loaded nickel layers show high temperature hot spots, *Proc. of Asti Workshop on Anomalies in Hydrogen/Deuterium Loaded Metals*, W.J.M.F. Collis (Eds.), Villa Riccardi, Rocca d’Arazzo, 27–30 Nov. 1997, pp. 63–69.
- [3] X.Z. Li, A new approach towards fusion energy with no strong nuclear radiation, *J. New Energy* **1**(4) (1996) 44–54.
- [4] X.Z. Li, J. Tian, M.Y. Mei and C.X. Li, Sub-barrier fusion and selective resonant tunneling, *Phys. Rev. C* **61** (2000) 024610.

- [5] X.Z. Li et al., Study of nuclear physics for nuclear fusion, *J. Fusion Energy* **19** (2002) 163.
- [6] X.Z. Li, Q.M. Wei and B. Liu, A new simple formula for fusion cross-sections of light nuclei, *Nucl. Fusion* **48** (2008) 125003.
- [7] X.Z. Li, Z. M. Dong, C.L. Liang, H. Yi and Y.P. Fu, A clean nuclear energy using hydrogen and condensed matter nuclear science, *Trans. Fusion Sci. Technol.* **61** (1T) (2012) 446–451.
- [8] X.Z. Li, Z.M. Dong and C.L. Liang, Studies on $p + {}^6\text{Li}$ fusion reaction using 3-parameter model, *J. Fusion Energy* **29**(??) (2010) DOI 10.1007/s 10894-01-9483-3.
- [9] H.A. Bethe, The formation of deuterons by proton combination, *Phys. Rev.* **54** (1938) 248–254.
- [10] Data retrieved from *National Nuclear Data Center*, Brookhaven National Laboratory.
- [11] *CRC Handbook of Chemistry and Physics*, D.R. Lide (Ed.), 2010, pp. 10–203.
- [12] H. Mills, *Pure Energy Systems News*, Transcription of the anniversary E-Cat interview, <http://www.pesn.com>, Jan. 14, 2011
- [13] *Handbook of Gamma Radiation Protection*, edited by Institute of Mechanic Engineering, Chinese Academy of Science (Atomic Energy Press, 1976), p. 9 (in Chinese).
- [14] J.H. Hubbell⁺ and S.M. Seltzer, Radiation and Biomolecular Physics Division, PML, NIST, 1996.
- [15] X.Z. Li, The conjecture of the neutrino emission from the metal-hydrides, *J. Cond. Mat. Nucl. Sci.* **1** (2007) 1–5.



Research Article

Nuclear Transmutation on a Thin Pd Film in a Gas-loading D/Pd System

Bin Liu *

Department of Science and Technology, Chief Engineer's Office, Shenhua Group Corporation Limited, Beijing 100011, China

Zhan M. Dong, Chang L. Liang and Xing Z. Li

Department of Physics, Tsinghua University, Beijing 100084, China

Abstract

This paper discusses the deformation and elemental distribution of different palladium film surfaces after loading and unloading many times deuterium gas in the system.

© 2014 ISCMNS. All rights reserved. ISSN 2227-3123

Keywords: Deformation, Gas loading, Nuclear transmutation

1. Introduction

When deuterium gas permeates through a thin palladium film, it was thought as a diffusion process only. However, after about 80 times absorption and desorption processes accompanied with permeations, nuclear transmutation was discovered on the surface of palladium film using Scanning Electron Microscopy (SEM).

At first glance, it was noticed that the macroscopic deformation of palladium was very large that the palladium film might increase its thickness while decrease its diameter of a rounded palladium film. The stress at the rounded sealing line might be so strong that it even cuts the palladium film into two pieces: the central rounded piece and the ring-shape edge piece.

The SEM analysis revealed that new elements (Cu, Zn, Si, etc.) were detected in the permeation area, but there were no such elements in the original palladium film or in the ring-shape area where no deuterium permeation happened. The temperature of palladium film was much higher than that of Iwamura experiments in Advanced Technology Research Center, Mitsubishi Heavy Industries [1,2]. Besides, there was no super lattice on the surface of our palladium films. Metallography analysis will be shown as well [3].

*E-mail: liub01@shenhuachina.com

2. Apparatus

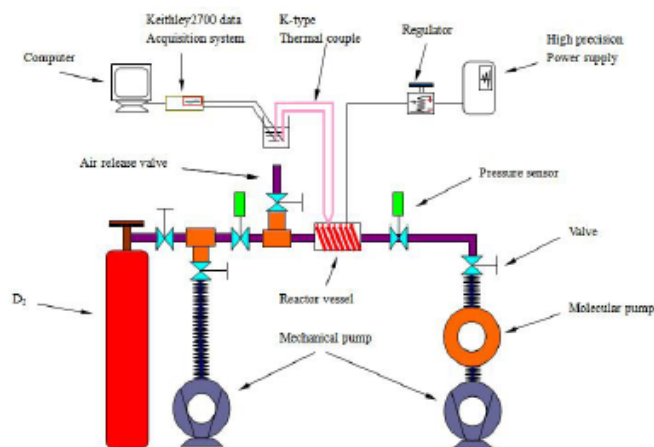


Figure 1. Deuterium gas loading palladium film system.

Figure 1 shows the sketch of deuterium gas loading palladium film system. The reactor vessel is separated by a $\phi 20 \text{ mm} \times 0.1 \text{ mm}$ palladium film into two parts. One is gas room, and the other is vacuum room. There is a 4 MPa

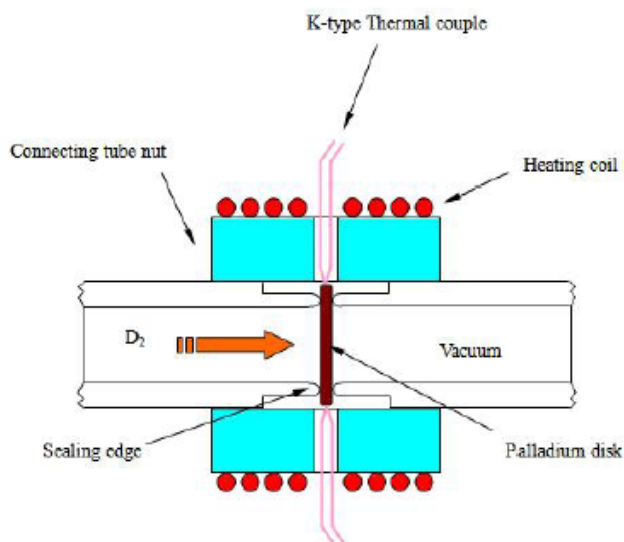


Figure 2. Palladium sealing part.

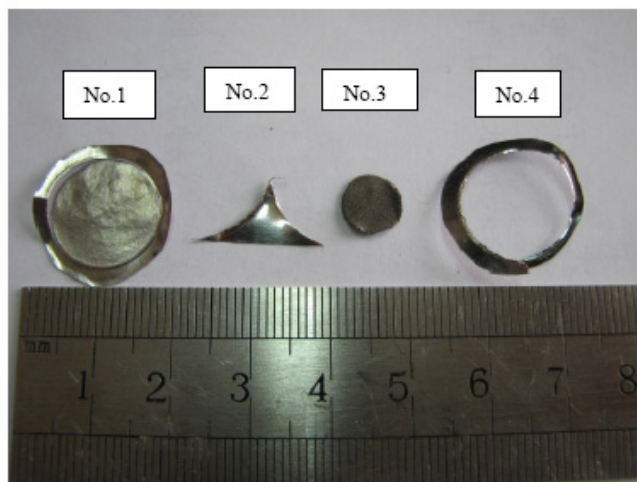


Figure 3. Palladium film samples.

D₂ gas bottle with purity of 99.5% at gas room side. Some valves are connected into pipes for checking or changing the system. When we begin to load sample gas into gas room, we have to use mechanical pump to evacuate the pipes first in order to avoiding gas pollution.

There is a molecular pump and a mechanical pump connected in series for high vacuum at vacuum room side. We set a power supply with high precision of $\pm 1\%$ in front of a voltage regulator, so we can add variable power to a heating coil which is equably wound on the swagelok sealing reactor vessel. We use K-type thermo couple to measure the temperature at some places where we think necessary. The required temperature includes the edge of Pd film, heating coil and connecting tube nut.

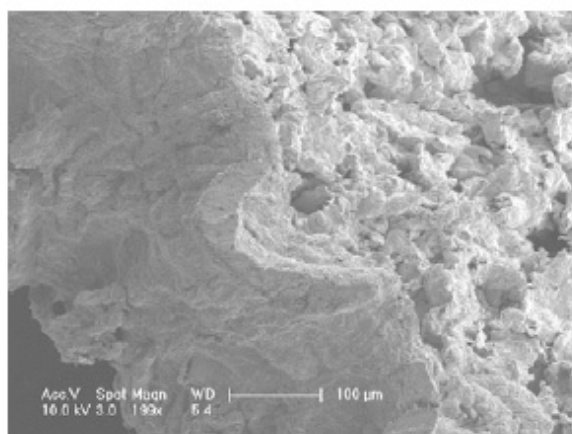


Figure 4. No. 3 sample 100 μm SEM.

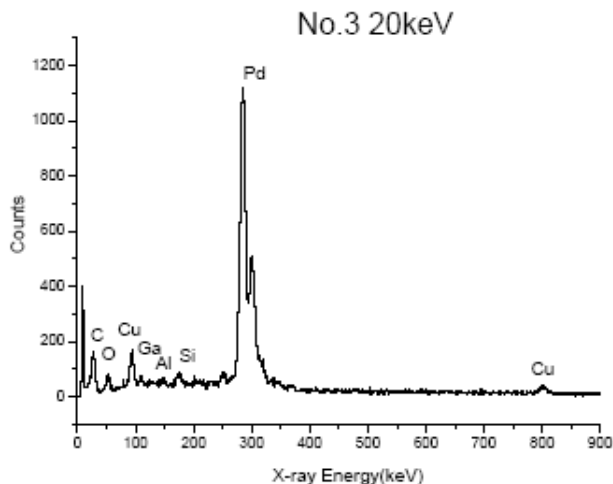


Figure 5. No. 3 sample 20 keV EDS.

Some pressure sensors are placed in pipes to monitor the gas loading pressure or vacuum. Figure 2 gives the structure of palladium film sealing part.

The palladium film is sealed by Swagelok stainless steel sealing edges when the connecting tube nut screws down conjuncting gas room and vacuum room. A round sealing mark forms at each surface of palladium film. The diameter of the mark is $\phi 16$ mm. We put the K-type thermo couple into tiny hole in the nut to measure temperature. The experimental process is described as below:

- (1) Evacuate the whole system (both gas room and vacuum room).
- (2) Stop pumping all the tubes, then load deuterium gas into gas room.
- (3) After the solution of deuterium finished, add power to heating coil to raises system temperature.

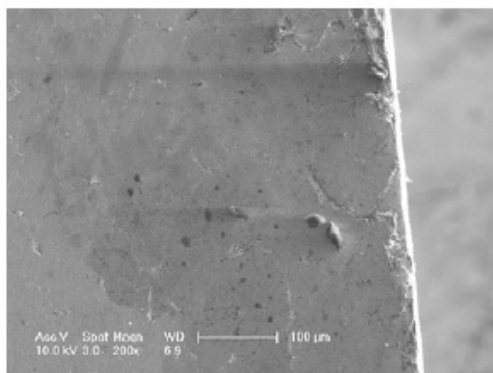


Figure 6. No. 4 sample 100 μ m SEM.

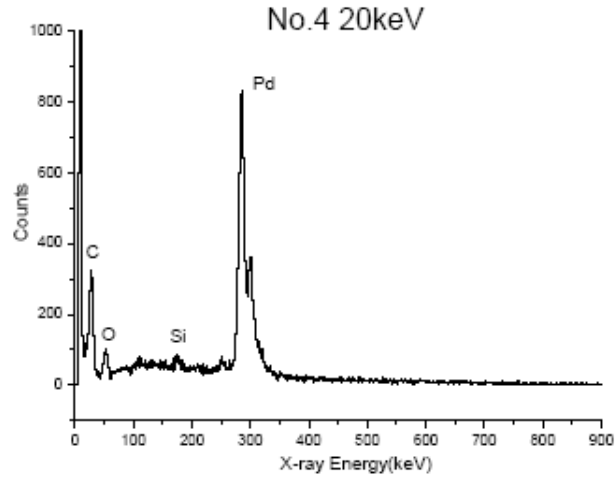


Figure 7. No. 4 sample 20 keV EDS.

- (4) After the temperature increases higher than 300°C , keep heating power unchanged and wait temperature stable [4,5].
- (5) Pumping the system with both gas room and vacuum room.
- (6) Decrease the heating power slowly until the system temperature equals the atmosphere temperature.

3. Results

Figure 3 shows the virgin sample and experimental sample. After many times deuterium gas loading and unloading, the surface of palladium film shows great change and deformation [6]. No. 1 sample has been loaded and unloaded by deuterium gas for more than 10 cycles. We can clearly see that the round area which has met deuterium gas becomes rough on surface, but the outside ring which is cut by sealing line mark keeps unchanged. No.2 sample is the virgin

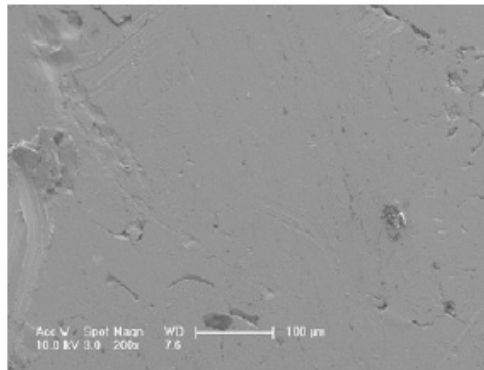


Figure 8. No. 2 sample 100 μm SEM.

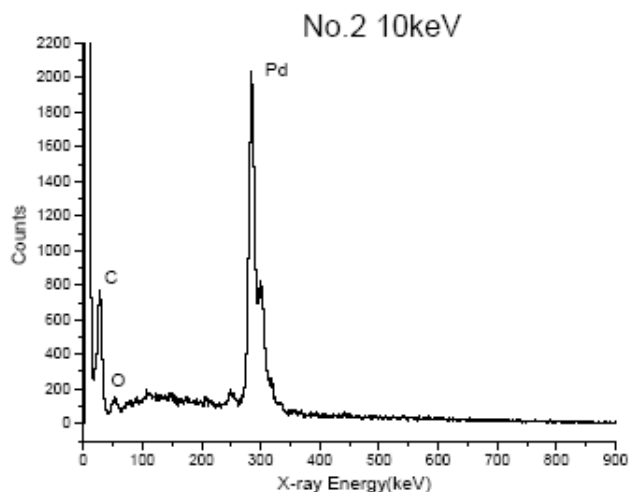


Figure 9. No. 2 sample 10 keV EDS.

palladium film. No. 3 sample has been loaded and unloaded by deuterium gas for about 80 cycles. It was cut by sealing line mark with thickness increasing and diameter decreasing. No. 4 sample is an outside ring of No.3 round piece. It nearly remains unchanged.

Figure 4 shows No. 3 sample 100 μm SEM figure. Because it suffered about 80 times deuterium gas loading, the metallic phase of palladium surface and edge shows great change. The smooth surface becomes porous and loose. A 20 keV EDS analysis gives the chemical element distribution (Fig. 5). There are two characteristic peaks of Cu distributing at both sides of Pd peak. Iwamura has found Cu many times in his research work [1,2]. Si peak is also observed in the curve.

Therefore, we are interested in No. 4 sample surface element distribution. It was separated from No. 3 sample by

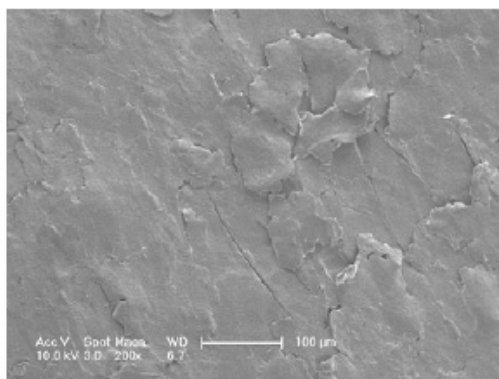


Figure 10. No. 1 sample 100 μm SEM.

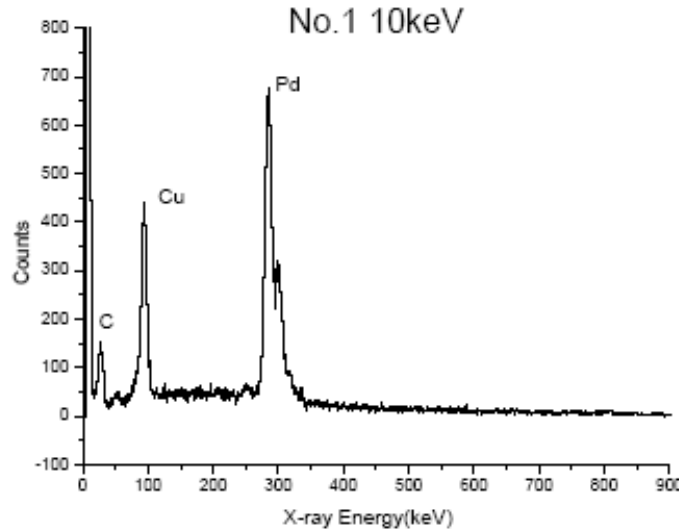


Figure 11. No. 1 sample 10 keV EDS.

sealing line mark and keeps isolated from deuterium gas. Its surface keeps smooth after the experimental cycles. The edge cut by sealing line mark is formal. We can see that in Fig. 6. Figure 7 20 keV EDS shows only Si peak besides Pd, C and O peak.

Figures 8 and 9 separately show the virgin palladium film SEM and EDS. The surface of No. 2 sample is the smoothest of all. The spectrometer curve looks like No. 4.

Figure 9 indicates that No. 2 virgin palladium film is clear. No. 4 outside ring piece shows no Cu signal on the surface but No. 3 round piece dose. Therefore, Cu may be caused by nuclear transmutation. Both on No. 3 and No. 4 sample surface we detect weak Si signal like a lot of other gas loading research groups. No. 1 sample central surface becomes loose and flaked as shown in Fig. 10. Its EDS curve also appears Cu peak seen in Fig. 11.

4. Discussion

Through SEM analysis of different palladium film and virgin sample, we study the gas loading D/Pd system. The deformation of palladium film is observed when deuterium flux generates. The element distribution of experimental palladium film surface is analyzed by X-ray EDS, and some elements (Cu, Si, etc.) show anomalous distribution. Stepped work is to find correlation between anomalous heat and element, and to eliminate noise and pollution of experiments.

Acknowledgment

I would like to thank Prof. Fan Shoushan, who has provided help in SEM analysis in his laboratory. I extend my thanks to all my teachers and team mates who have helped me to develop the fundamental and essential academic competence.

References

- [1] Y. Iwamura, Observation of surface distribution of products by X-ray fluorescence spectrometry during D₂ gas permeation through Pd complexes, in the *12th International Conference on Condensed Matter Nuclear Science*, Yokohama, Japan, 2005.
- [2] Y. Iwamura, T. Itoh and M. SakaNo, Nuclear products and their time dependence induced by continuous diffusion of deuterium through multi-layer palladium containing low work function material, in *8th International Conference on Cold Fusion*, 2000, Lerici (La Spezia), Italy: Italian Physical Society, Bologna, Italy.
- [3] Y. Arata and Y.C. Zhang, Formation of condensed metallic deuterium lattice and nuclear fusion, *Proc. Jpn. Acad. Ser. B* **78** (2002) 57.
- [4] Francesco Celani, A. Spallone, E. Righi et al., High temperature deuterium absorption in palladium nano-particles, LNF-07/18(P)[2007-09-19].
- [5] Jean-Paul Biberian and Nicolas Armanet, Excess heat during diffusion of deuterium through palladium, *Proc. ICCF13*, 2007-06-10,15], Sochi, Russia.
- [6] A. De Ninno, A. La Barbera and V. Violante, Deformations induced by high loading ratios in palladium–deuterium compounds, *J Alloys and Compounds* **181** (1997) 253–254.



Research Article

Diamond-based Radiation Sensor for LENR Experiments. Part 1: Sensor Development and Characterization

Eric Lukosi*, Mark Prelas, Joongmoo Shim, Haruetai Kasiwattanawut,
Charles Weaver, Cherian Joseph Mathai and Shubhra Gangopadhyay

SKINR, University of Missouri, Columbia, MO 65211, USA

Abstract

There have been many reports on charged particle and neutron production in LENR experiments but as of yet they have not been correlated in time with excess heat generation. Diamond sensors with palladium electrodes can be utilized to address this need. First results using a diamond sensor are presented.

© 2014 ISCMNS. All rights reserved. ISSN 2227-3123

Keywords: Charged particle spectroscopy, Diamond sensors, Low energy nuclear reactions

1. Introduction

LENR experiments are done in three basic ways: gas loading, plasma loading/co-deposition, and electrochemically. If radiation is a by-product of LENR then their detection is limited by a few basic factors. In the case of neutrons the detection efficiency of the sensor for the source of interest must be statistically higher than background. For charged particles, the system must also be designed to keep background noise and count levels as low as possible. In addition, the distance between the detector and the charge particle emitting source should be minimized to limit energy loss outside of the sensing medium. This is especially important if spectroscopic analysis is going to be conducted.

Experimental analyses of charged particle and neutron production in LENR have utilized CR-39. At first the sensors were placed near electrodes in electrochemical cells and later were placed in direct contact. Results of this work indicate that there seems to be charged particle production by single track analysis using unfolding software, but later experiments placed the sensor in direct contact with the electrode [1–4]. Neutron production was also considered a possibility at a minimum energy of 7.89 MeV due to triple tracks produced by three alpha particles from the breakup of ^{12}C [1,2,5].

There are many limitations in using CR39 for radiation detection as outlined by Durrani in 2008 [6]. In this application the major limitation is the limited spectroscopic capabilities of CR39. To understand better, the mechanism

*E-mail: edlf3f@mail.missouri.edu

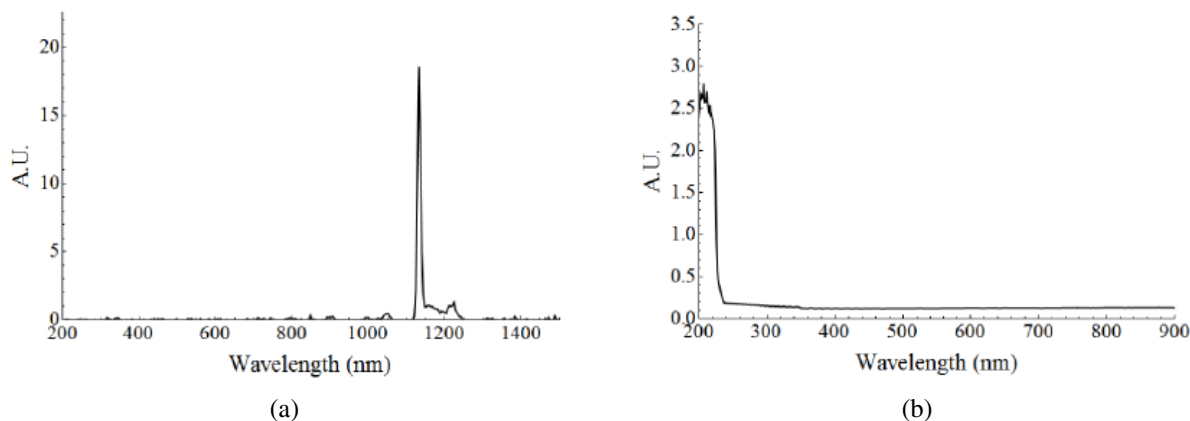


Figure 1. Count rate data for the hydrogen exposures of the palladium coated sensor for (a) the entirety of the experiment and (b) during the count rate burst.

of LENR it is vital to conduct spectroscopy on the created charged particles and/or neutrons in an LENR experiment and to correlate them in time with excess heat generation in order to provide definitive evidence whether or not the two are correlated. If they are correlated, conducting an analysis of the change in energy due to the supposed nuclear reaction would be a great step in understanding the reaction mechanism(s) of LENR reported by so many in recent history.

2. Diamond Sensor Background

To begin to answer the identified need, it is proposed that diamond be used for radiation detection in LENR experiments. Diamond is a wide band gap semiconducting material that is radiation hard, mechanically the strongest material known to man, chemically inert, and exhibits an extremely high thermal conductivity [7]. These properties allow a diamond sensor to be used in a variety of environments and operated at various temperatures. Diamond can act as a radiation sensor because of its semiconducting properties and the commercial availability of intrinsic grade single crystal diamond plates. This makes diamond suitable for both charged particle and neutron detection.

Charged particles and photons can be detected by diamond through the collection of electron–hole pairs created within its band structure as any charged particle slows down within it. The statistically averaged ratio of electron–hole pairs created versus total energy deposition is 0.42 for diamond. There have been several reports on the interactions of charged particles or photons with diamond in recent history as the capabilities of synthetic diamond growth have allowed for electronic grade diamond to become available [8–14]. This work has shown that energy resolutions for alpha particle interactions approach 0.6% [13,15] and 4% for 14.1 MeV neutrons through reaction number 8 in Table 1 [14,16]. This table indicates all the neutron–carbon interactions that can take place in a center of mass energy range from 0–20 MeV. Since diamond is a low- Z material gamma rays are not readily detectable in small diamond plates for low to moderate energies in low flux environments operating in pulse mode.

The capabilities of diamond outlined indicate that diamond could be very suitable as a radiation sensor to replace CR39 in LENR studies. It is also excellent compared to other solid-state or gas sensors because it is wide band-gap, corrosion and radiation resistant and made with low atomic mass atoms. Among its capabilities are low thermal noise at room temperature (does not need cooling) high sensitivity (has an excellent signal to noise ratio), and is able to detect multiple types of radiation in the same sensor including charged particles and neutrons (recoil detection). However,

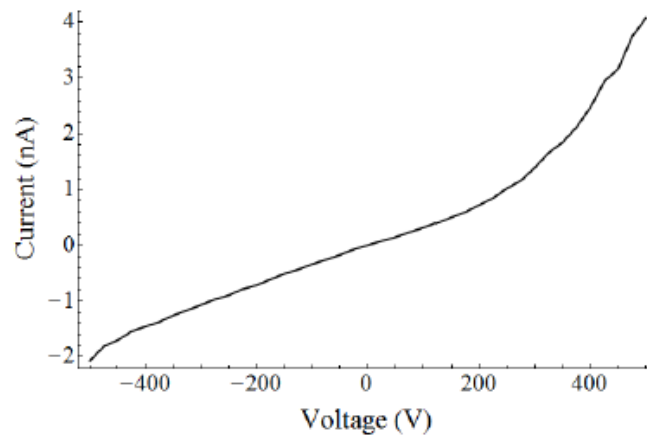
Table 1. Neutron interactions with natural carbon¹.

Reaction number	Reaction	Q-value (MeV)	Threshold energy (MeV)
1	$^{12}\text{C}(\text{n},\gamma)^{13}\text{C}$	4.946	0
2	$^{12}\text{C}(\text{n},\text{el})^{12}\text{C}$	0	0
3	$^{12}\text{C}(\text{n},\text{n}')^{12}\text{C}^*$	–	4.450 ²
4	$^{12}\text{C}(\text{n},\text{n}')^{12}\text{C}^*(3\alpha)$	–7.275	7.886
5	$^{12}\text{C}(\text{n},\text{n}')^{12}\text{C}^*(3\alpha)$	–	9.64 ²
6	$^{12}\text{C}(\text{n},\text{n}')^{12}\text{C}^*(3\alpha)$	–	10.8 ²
7	$^{12}\text{C}(\text{n},\text{n}')^{12}\text{C}^*(3\alpha)$	–	11.8 ²
8	$^{12}\text{C}(\text{n},\alpha)^9\text{Be}$	–5.701	6.181
9	$^{12}\text{C}(\text{n},\alpha)^9\text{Be}^*$	–7.381	8.800
10	$^{12}\text{C}(\text{n},\text{p})^{12}\text{B}$	–12.59	13.64
11	$^{12}\text{C}(\text{n},\text{d})^{11}\text{B}$	–13.73	14.89
12	$^{12}\text{C}(\text{n},\text{np})^{11}\text{B}$	–15.96	17.30
13	$^{13}\text{C}(\text{n},\gamma)^{14}\text{C}$	8.176	0
14	$^{13}\text{C}(\text{n},\text{el})^{13}\text{C}$	0	0
15	$^{13}\text{C}(\text{n},\alpha)^{10}\text{Be}$	–3.835	4.132
16	$^{13}\text{C}(\text{n},\alpha)^9\text{Be}$	–10.65	11.47
17	$^{13}\text{C}(\text{n},\text{t})^{11}\text{Be}$	–12.42	13.39
18	$^{13}\text{C}(\text{n},\text{p})^{13}\text{B}$	–12.66	13.64
19	$^{13}\text{C}(\text{n},\text{d})^{12}\text{B}$	–15.31	16.50
20	$^{13}\text{C}(\text{n},\text{np})^{12}\text{B}$	–17.53	18.89

¹All data, unless otherwise specified, were obtained from the National Nuclear Data Center maintained by Brookhaven National Laboratory [17].

²Data reported obtained from Pillon et al. reported in 1995 [18].

electrochemical cells are not the best environment to obtain better information about charged particle energy in the current design because of the loss of energy in the fluid which separates the sensor from the deuterium loaded film and the various path lengths that charged particles can take. This is also a problem in the gas loading LENR experiments

**Figure 2.** $I - V$ characteristics of the diamond sensor.

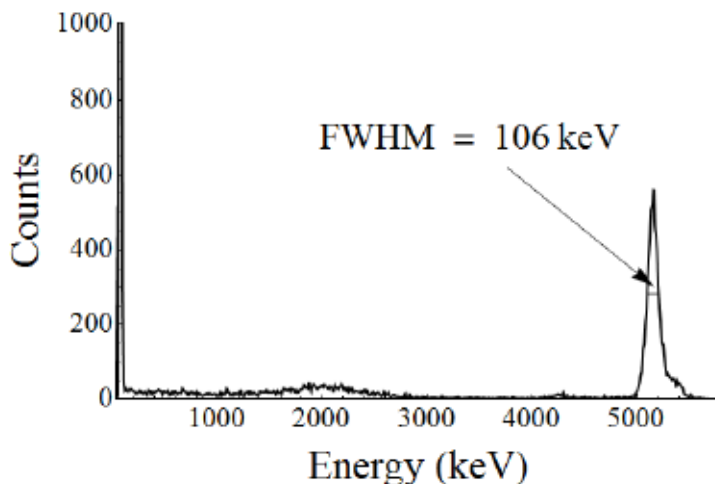


Figure 3. Pu-239 spectrum obtained with the diamond sensor.

as well and can only be overcome by operating in a vacuum for current experimental techniques.

To get past this difficulty a palladium film will be used as an electrode on the diamond sensor so that the detection efficiency of any charged particles coming from the system will be 0.5 and is also the geometrical detection efficiency of any neutrons coming from the palladium film. In this configuration the energy lost by the charged particles will be minimized and well controlled, occurring only within the thin (100 nm) palladium film. In this manner diamond can be utilized in both gas loaded and electrochemical experiments. In the former the detector is merely introduced to a high pressurized deuterium environment and in the latter one of the diamond electrodes can be utilized as an electrode such that it creates a parallel component to the electrochemical cell. The high resistance of diamond makes current flow into

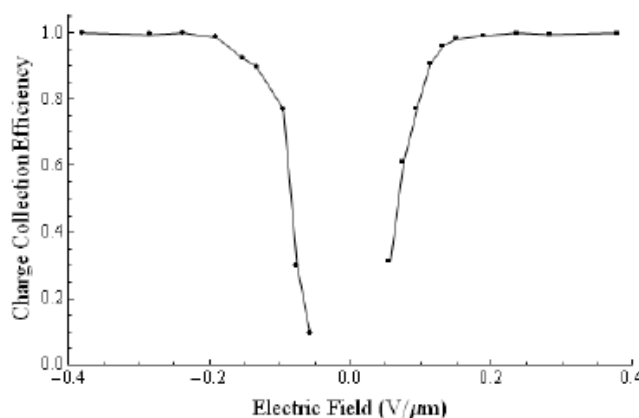


Figure 4. Charge collection efficiency versus applied bias across the diamond sensor during Pu-239 exposures.

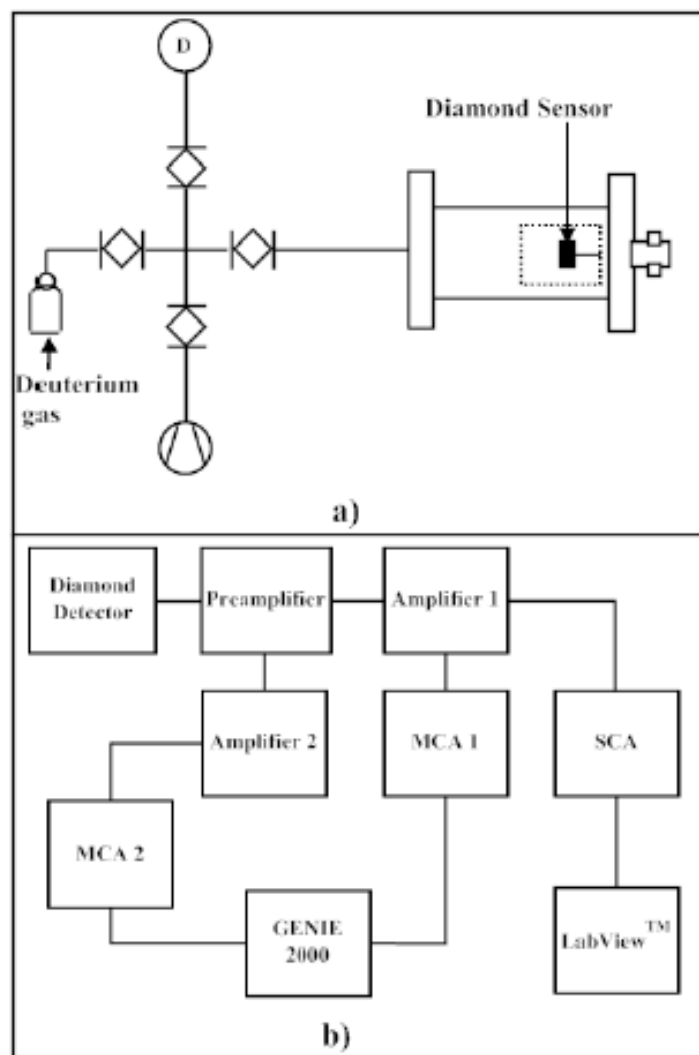


Figure 5. In (a) the experimental setup is described and the electronic pathways are shown in (b).

the detection system very low unless a radiation interaction occurs in which case one type of charge carrier (electrons or holes) will be collected by the detection system.

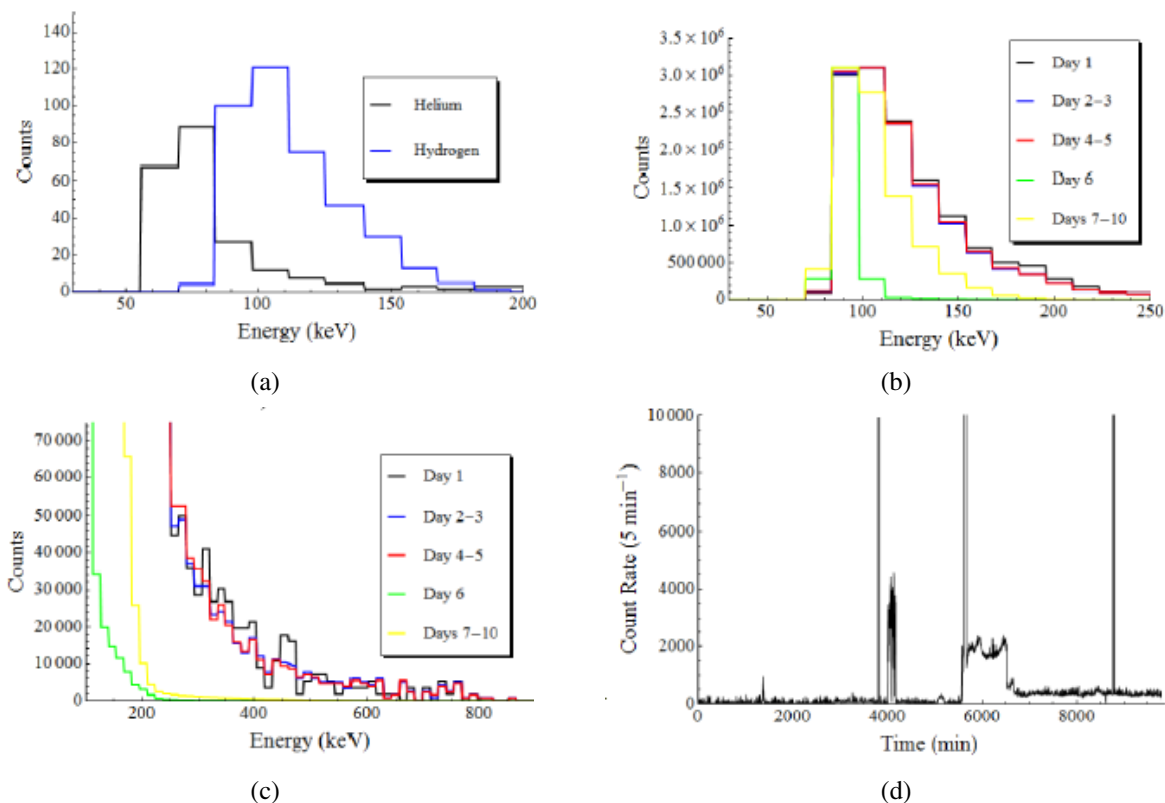


Figure 6. Experimental results obtained in the gas loading palladium electrode on a diamond sensor. Here the results are shown for (a) the background spectra obtained for hydrogen and helium, (b) and (c) the low-energy spectra from the deuterium run, and (d) the count rate of pulses observed in the diamond sensor over time for the deuterium run.

3. Experimental Technique

3.1. Sensor material

Two $3 \times 3 \times 0.5$ mm semiconducting diamond plates were obtained from Element Six for this work [19]. The diamonds were characterized through Raman and spectrophotometry to verify its structure and detect any band gap impurities. The results shown in Fig. 1 indicate that the samples have no energy levels within the band gap that are above the detection threshold for the spectrophotometer used.

The diamond samples were chemically cleaned with the following process and were rinsed with deionized water between each step. The first two steps are meant to clean the diamonds and remove any stray metal and organic materials. The last two steps are utilized to remove any graphitization layers on the surface and to oxygen terminate the surface to increase the surface resistivity of the diamond.

- (1) Aqua Regia at 150°C for 20 min.
- (2) $\text{NH}_3\text{OH}/\text{H}_2\text{O}_2/\text{H}_2\text{O}$ (1:1:5) at 150°C for 20 min.
- (3) Piranha at 150°C for 20 min.
- (4) $\text{H}_2\text{SO}_4/\text{HNO}_3/\text{HClO}_4$ (1:1:1) at 150°C for 30 min.

The diamonds were metalized through sputtering carbon at 400°C to create an approximate 10 nm diamond-like carbon (DLC) layer and then coated with a palladium top layer 100 nm thick. The DLC layer provides two functions. First, it provides a junction between the electrode and diamond for mechanical adhesion. Second, it provides a tunneling junction for electrons to escape the diamond material when a large work function metal is used as the electrode [13]. This allows for the creation of a contact that should behave Ohmically.

3.2. Sensor electrical characterization

The diamond was mounted on a transistor head and wire bonded with aluminum. Its current–voltage properties were characterized using a Keithley 6487 picoameter and the results are shown in Fig. 2. It can be seen that the sensor does behave Ohmically for lower voltages but that a somewhat Schottky behavior is observed at voltages above +250 V. This was found to be due to the conductive silver epoxy on the diamond outside of the palladium contact area and was verified by reversing the circuit configuration for this measurement and seeing the same effect with an opposite applied voltage. In any case, it is shown in the following alpha particle exposures that a bias of 200 V is all that is required to gain 100% charge collection efficiency and so the observed Schottky behavior is unimportant.

The diamond sensor was then tested for its energy resolution and charge carrier characteristics through the use of a Pu-239 alpha source and Hecht's theory (Eq. (1)), which relates the charge collection efficiency to the properties of the semiconductor. It can then be used to characterize the mobility-trapping time constant product of the sensor (Eq. (2)) and therefore the required bias to collect 100% of the charge generated. The energy resolution of the diamond sensor used is pictorially shown in Fig. 3 to be 2.1%.

By exposing the diamond to alpha particles and varying the applied bias used for charge collection a plot can be created that relates the charge collection efficiency to the applied electric field. The diamond sensor was utilized with an Ortec 142PC preamplifier, Canberra 2026 spectroscopy amplifier, and Genie 2000 for data acquisition. A plot of these results is given in Fig. 4.

$$Q_c = Q_0 \left[\frac{\mu_e \tau_e E}{W} \left(1 - e^{-x/\mu_e \tau_e E} \right) + \frac{\mu_h \tau_h E}{W} \left(1 - e^{-(W-x)/\mu_h \tau_h E} \right) \right], \quad (1)$$

$$\frac{\mu_e \tau_e}{h} = \frac{W}{E}. \quad (2)$$

The result of the alpha particle exposures yielded the data shown in Table 2. These exposures also allowed the characterization of the energy resolution of the diamond sensor, which was 2.43 and 2.37% for a positive and negative applied bias, respectively. The sensor did not exhibit polarization effects at a positive bias of 200 V over a one-hour exposure. Further, it has been shown experimentally that diamond responds linearly with deposited energy and agrees with theory such that the location of the Pu-239 alpha particle peak can be used for a one-point energy calibration [20]. The location of the Pu-239 peak in the pulse height spectrum was determined for various amplification factors and it was found to be linear, as expected.

3.3. Experimental setup and procedure

A schematic of the experimental apparatus and the electronic acquisition system setup for the deuterium gas loading experiment are shown in Fig. 3. In (a) the experimental set-up is shown where the diamond is placed inside of a small pressure vessel that can handle up to 690 kPa. The voltage applied to the sensor was +200 V during all experimental runs where the top electrode carries the positive potential with respect to ground. Here, the signal from the preamplifier was

Table 2. Charge carrier characteristics of the diamond sensor.

	Electrons	Holes
Median $\mu\tau$ ($10^{-6}\text{cm}^2/\text{V}$)	59.3	67.6
Maximum $\mu\tau$ ($10^{-6}\text{cm}^2/\text{V}$)	60.4	71.1
Minimum $\mu\tau$ ($10^{-6}\text{cm}^2/\text{V}$)	58.2	64.8

split and sent to two different amplifiers. This allowed for simultaneous measurement of fine low-energy spectroscopy as well as very high-energy spectroscopy. The high-energy and low-energy signals are denoted as Amplifiers 1 and 2 with full scales of 59 and 5.7 MeV, respectively. The low-energy spectrometer had its signal split from its output to go to both the MCA and an SCA and then to a digital counter that allows for some timing information on the pulses. Although this method does not allow each pulse to be time-stamped, it does allow the quantification of rapid increases of count rates during experiments as it has been indicated in several LENR experiments that excess heat generation often takes place in pulses.

The experimental procedure started with loading the diamond sensor into the test chamber and the chamber was evacuated using a mechanical pump to approximately 1 mTorr. The chamber was then filled with the process gas to a pressure of approximately 5100 Torr and placed into a lead shield three inches thick above the chamber and one and a half inches thick else. Three gases were utilized in this experiment: helium, hydrogen, and deuterium. The first process gas was used to determine the background counts that can be expected and was conducted for 1 h. Then natural isotopic abundance hydrogen was used as a check for a secondary background count experiment. Then the system was evacuated to 1 mTorr for 3 h to unload any light hydrogen from the electrode and the final run using deuterium was conducted. The pressure used in the gas loading is expected to lead to a D/Pd loading ratio of approximately 75%. This was not verified during the experiment but can be a future addition to the system through resistance measurements of the top electrode.

4. Results

The spectra obtained in this experiment are shown in Fig. 6. The background spectra for helium and hydrogen, taken for one hour each, are shown together in part (a). The background spectra for each of the process gases give the general shape. The Ortec 142PC preamplifier has a sensitivity with diamond at its input of 80 mV/MeV and for the helium run this indicates that the peak of the noise lies around 16 mV. For the hydrogen run the noise shifted by a channel number and so the noise floor of the MCA had to be shifted by one channel to keep the dead time down and is the reason for the difference between the spectra.

The deuterium run spectra are shown in parts (b) and (c). Spectra were taken at various times in this experiment to provide a measure of spectral change over time. The spectra obtained were normalized to each other and the ratio of the run time and maximum count in a channel to the largest count rate spectrum is given in Table 3. This data clearly indicates that the count rate seen is not constant over the ten-day run.

In part (b) the low-energy spectrum obtained for the deuterium gas loading experiment is shown. It can be seen that the run using deuterium process gas differs from the background runs by a tail of pulses that extends into higher energies. This can be seen clearly in part (c) that shows a low total count scale on the ordinate. The energy of the pulses seen are distributed and do not match what is expected for a nuclear reaction, such as a narrow peak from alpha decay. Further, the data obtained for day six clearly shows a massive jump in counts versus the other spectra obtained at the

Table 3. Normalized time and count data of all experimental data obtained for the pressurized deuterium runs.

Run	Day 1	Days 2–3	Days 4–5	Day 6	Days 7–10
Time	4.24	2.15	1.96	5.00	1.00
Counts	1788.2	861.3	787.7	17.8	1.00

location of the peak of all spectra shown. The actual peak of this spectrum was 209,775 counts at channel number 6, corresponding to 80 keV.

Only one spectrum was obtained after day six and it was conducted for 3 days. There is an interesting effect in this spectrum in that the location of the peak is now pushed against the lowest channels, as if it has been shifted to lower energies even though there is no cause for this shift due to equipment changes or faults and was verified with other sensors. The high-energy spectra are not shown here because no high energy counts were registered in any of the experimental runs at any time.

To compare the obtained spectra, the rate of counts registered per 5 min period from day three and on is displayed in part (d). It can be clearly seen that the count rate is very low for about the first 3800 min and at about this time the count rate increases rapidly for a short period. This occurs a second time shortly after at about 4000 min with a large width and then a third time at about 4600 min with a very long high count rate plateau ending at about 6600 min. There is also a final fourth count rate burst as well at about 8700 min and after the third count rate burst the background count level floor is increased by about a factor of two. This seems to indicate that there are possible spontaneous reactions of some kind depositing energy (or more accurately charge in the conduction band of the diamond or into the high input of the preamplifier) within the diamond sensor. It is possible that the burst in count rate is some sort of electronic noise and further analysis is required in future experiments. However, all electronics associated with these measurements were plugged into a power conditioner and so this seems unlikely.

A visual representation of the electrode before and after the experiment is shown in Fig. 7. After inspection it becomes clear that some sort of reaction has indeed occurred between the diamond sensor electrode and the deuterium gas. At this point it is unclear whether the damage to the electrode is chemical or nuclear in nature.

It is not expected to be directly due to the potential on the electrode, although there may be some indirect effects of having a positively charged electrode in a pressurized deuterium atmosphere. It is possible that the effect of a higher background count rate between the third and fourth count rate bursts could be due to vibrational effects on a partially delaminated palladium electrode. The sensor was tested for operability after the deuterium run was halted and it responded as expected to a Pu-239 alpha particle source. However, when another background run in hydrogen was tried the palladium top electrode was lost during chamber evacuation and/or pressurization.

5. Conclusion

In this work the preparation and application of a diamond sensor to a gas loading palladium LENR experiment has been presented. The results obtained indicate that some sort of reaction has taken place when the sensor was in the deuterium environment due to electrode deformation and delamination and due to the different pulse height spectra seen between runs conducted in hydrogen and deuterium. Further analysis of the observed effects is required. In part two of this report the diamond sensor will be exposed to a pressurized hydrogen environment for several days to see if the observables are due to chemical reactions with the palladium electrode. A better experimental procedure will be conducted and second run results will be presented.

Acknowledgements

We would like to thank everyone within the Sidney Kimmel Institute for Nuclear Renaissance for their support in this project. This especially includes Joseph Mathai and Shubhra Gangopadhyay for their support in palladium electrode deposition.

References

- [1] P.A. Mosier-Boss et al., Characterization of tracks in CR-39 detectors obtained as a result of Pd/D Co-deposition, *Euro. Phys. J. Appl. Phys.* **46** (2009) 1–12.
- [2] P.A. Mosier-Boss et al., Use of CR-39 in Pd/D co-deposition experiments, *Euro. Phys. J. Appl. Phys.* **40** (2007) 293–303.
- [3] A.G. Lipson et al., In-situ charged particles and X-ray detection in Pd thin film-cathodes during electrolysis in $\text{Li}_2\text{SO}_4/\text{H}_2\text{O}$, in *Ninth Int. Conf. on Cold Fusion*, 2002, Beijing, China.
- [4] R.A. Oriani and J.C. Fisher, Generation of nuclear tracks during electrolysis, *Japanese J. Appl. Phys.* **41** (2002) 6180–6183.
- [5] P.A. Mosier-Boss et al., Comparison of Pd/D co-deposition and DT neutron generated triple tracks observed in CR-39 detectors, *Euro. Phys. J. Appl. Phys.* **51** (2010) 1–10.
- [6] S.A. Murrari, Nuclear tracks today: Strengths, weaknesses, challenges, *Radiation Measurements* **43** (2008) S26–S33.
- [7] R.S. Balmer et al., *J. Phys: Cond. Matter* **21** (2009) 364221.
- [8] J. Isberg et al., *Science* **297**(5587) (2002) 1670–1672.
- [9] J. Isberg et al., *Diamond and Related Materials* **13** (2004) 872–875.
- [10] M. Pomorski et al., Charge carrier transport properties of single crystal CVD-diamond particle detectors, *Diamond and Related Materials* **16** (2007) 1066–1069.
- [11] E. Pace, R.D. Benedetto and S. Scuderi, Fast stable visible-blind and highly sensitive CVD diamond UV photodetectors for laboratory and space applications, *Diamond and Related Materials* **9** (2000) 987–993.
- [12] R.D. Benedetto et al., Influence of metal–diamond interfaces on the response of UV photoconductors, *Diamond and Related Materials* **10** (2001) 698–705.
- [13] A. Galbiati et al., *IEEE Trans. Nucl. Sci.* **56**(4) (2009) 1863–1874.
- [14] M. Pillon et al., Radiation tolerance of a high quality synthetic single crystal chemical vapor deposition diamond detector irradiated by 14.8 MeV neutrons, *J. Appl. Phys.* **104** (2008) 054513.
- [15] A. Murari et al., Measuring the radiation field and radiation hard detectors at JET: Recent developments, *Nucl. Instr. Methods in Phys. Res. A* **593** (2008) 492–504.
- [16] S. Almaviva et al., Thermal and fast neutron detection in chemical vapor deposition single-crystal diamond detectors, *J. Appl. Phys.* **103** (2008) 054501.
- [17] National Nuclear Data Center: p. www.nndc.bnl.gov.
- [18] M. Pillon, M. Angelone and A.V. Krasilnikov, 14 MeV neutron spectra measurements with 4% energy resolution using a type II a diamond detector, *Nucl. Instr. Methods in Phys. Res. B* **101** (1995) 473–483.
- [19] Element Six, King's Ride Park, Ascot, UK.
- [20] M. Pillon et al., *Nucl. Instr. Methods in Phys. Res. A* **640** (2011) 185–191.



Research Article

Diamond-based Radiation Sensor for LENR Experiments. Part 2: Experimental Analysis of Deuterium-loaded Palladium

Eric Lukosi*, Mark Prelas, Joongmoo Shim, Haruetai Kasiwattanawut,
Charles Weaver, Cherian Joseph Mathai and Shubhra Gangopadhyay

SKINR, University of Missouri, Columbia, MO 65211, USA

Kyle Preece

University of Tennessee, Knoxville, TN 37996, USA

Abstract

The purpose of this paper is to report on the continued work on utilizing a palladium electrode on a diamond sensor in a pressurized hydrogen or deuterium environment to investigate the release of radiation during low energy nuclear reactions (LENR). In this investigation we conducted a long hydrogen exposure to see if palladium electrode delamination occurred due to chemical reactions and it was found that after seven days the electrode did not delaminate. A pressurized deuterium run was conducted immediately following the hydrogen exposure on the same sensor and some interesting count burst data was observed. Further analysis is required to determine what the observed effect could be attributed to.

© 2014 ISCMNS. All rights reserved. ISSN 2227-3123

Keywords: Charged particle spectroscopy, Diamond sensors, Low energy nuclear reactions

1. Introduction

There is the possibility that radiation particles can be created in low energy nuclear reactions (LENR) experiments and that a correlation (or anti-correlation) between the creation of radiation particles and excess heat may exist. To try and understand the underlying mechanism of LENR, a sensor was developed for gas loading experiments that is further described in [1]. In this work a palladium electrode was made on the diamond sensor for deuterium loading through pressurized environments. In this report it was shown that the diamond sensor had an energy resolution for 5.4 MeV ^{239}Pu alpha particles of 2.1% and that the diamond material seemed to be stable in the hydrogen-like environment. However, the initial test run showed that the palladium electrode was sensitive to the pressurized hydrogen environment but it was unclear what reaction caused the delamination of the electrode, specifically if it was chemical or nuclear in

*E-mail: edlf3f@mail.missouri.edu

origin. To continue the work this report presents the results obtained in the second experimental run with modified experimental technique to help answer some of the questions that were raised in the first test run.

2. Pressurized Hydrogen Experiment

2.1. Experimental set-up and procedure

In this experimental run, the diamond sensor was prepared with a metallization pattern of Diamond/DLC/Au/Pd (10/100/100 nm) to try and increase mechanical adhesion of the palladium electrode through the addition of the intermediary gold layer between the palladium and diamond-like-carbon (DLC) layers.

In each run (hydrogen and deuterium) the sensor was placed in a pressurized gaseous environment and this chamber was encased in several inches of lead on all sides to reduce cosmic ray interactions. There were two main runs in this experiment; one in hydrogen and another in deuterium. Based on the first trial results previously reported [1], it was shown that delamination occurred. To see if this effect was due to a palladium–deuterium chemical reaction the sample was placed in a hydrogen environment at 690 kPa with a stainless steel 316 boundary. After a set period of time, usually around one day, the system was depressurized, removed from the chamber and the electrode was inspected. Then the system was restored to its previous state and the experiment continued. This process was repeated until a total exposure time of 7 days was reached.

2.2. Experimental results

The spectra obtained for a lower and higher amplifier gain are shown in Fig. 1 and the count rate data obtained is given in Fig. 2. The spectra were normalized to a single spectrum and the normalization factors in time and total peak counts are given in Tables 1 and 2 for the low and high gain amplifier output signals, respectively. It can be seen in the supplied data that there are some differences in the spectra obtained, specifically in the tail end of one or more spectra reaching into higher energies and it can be seen that the count rate seems to be growing slightly over the entirety of the experiment with few high count rate spikes that are currently unexplained. In Fig. 3, a picture of the top palladium electrode at various times is shown. It can be seen that some damages do show up on the electrode in the form of missing sections that represent a small area over the entire electrode. This could account for the count rate bursts as electrode flaking during experimentation would produce significant voltage spikes. However, the results seem to not be out of the normal operation and the fluctuations seen are due to electronic noise and drifting but needs to be further verified.

Table 1. The normalization factors in time and total peak counts low gain amplifier output signals for “Pressurized hydrogen experiment”.

Run	Time	Counts
Day 1	1.23	15.04
Days 2–3	0.54	12.56
Day 4	–	–
Day 5	1.00	1.00
Day 6	1.17	1.01
Day 7	1.21	2.07

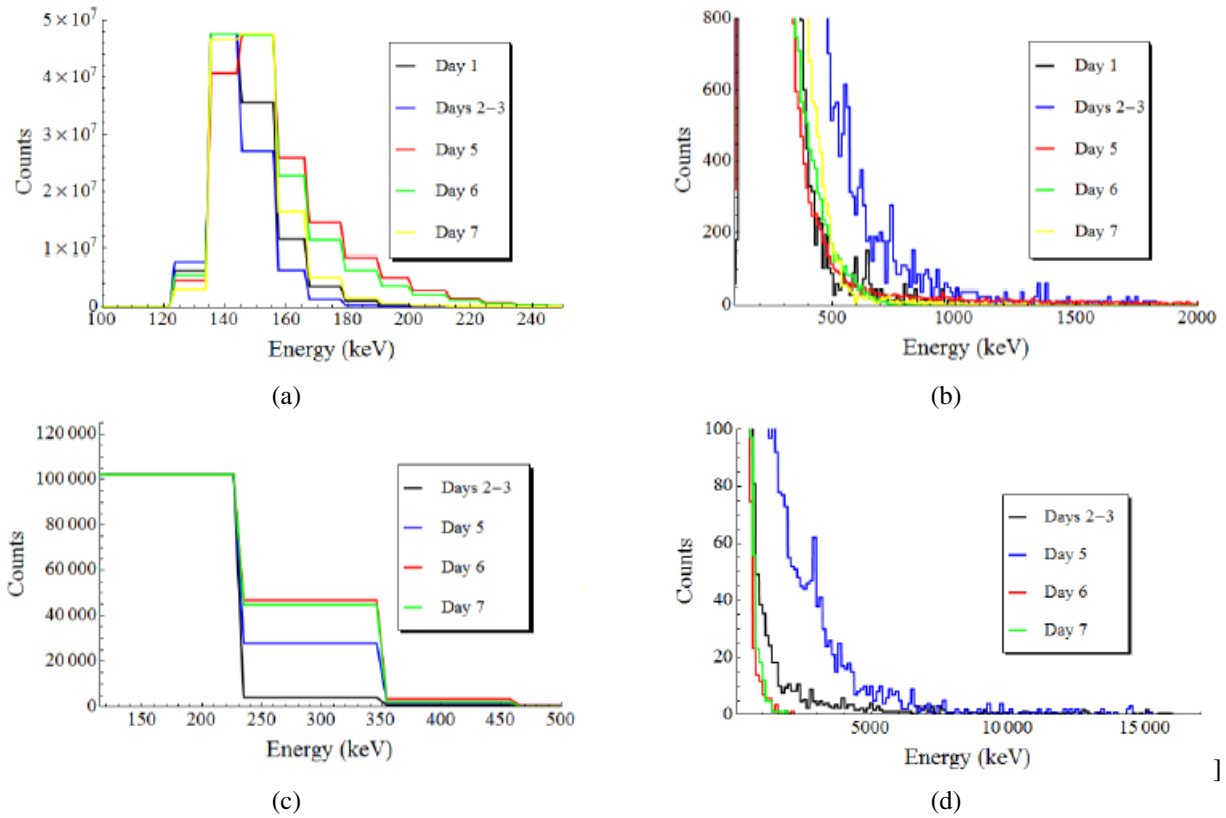


Figure 1. Spectra obtained during hydrogen exposures of the palladium coated diamond sensor with (a)–(b) low sensor gain and (c)–(d) high sensor gain.

3. Pressurized Deuterium Experiment

After the hydrogen exposure the palladium electrode on the diamond sensor seemed to be unaffected from the hydrogen exposure for 7 days. At this point the experiment was continued except that the hydrogen was replaced with deuterium. The spectra obtained for these exposures are shown in Fig. 4 and the normalization data are displayed in Tables 3 and 4

Table 2. The normalization factors in time and total peak counts high gain amplifier output signals for “Pressurized hydrogen experiment”.

Run	Time	Counts
Day 1	–	–
Days 2–3	0.51	5.75
Day 4	–	–
Day 5	0.86	1.44
Day 6	1.00	1.00
Day 7	1.04	1.09

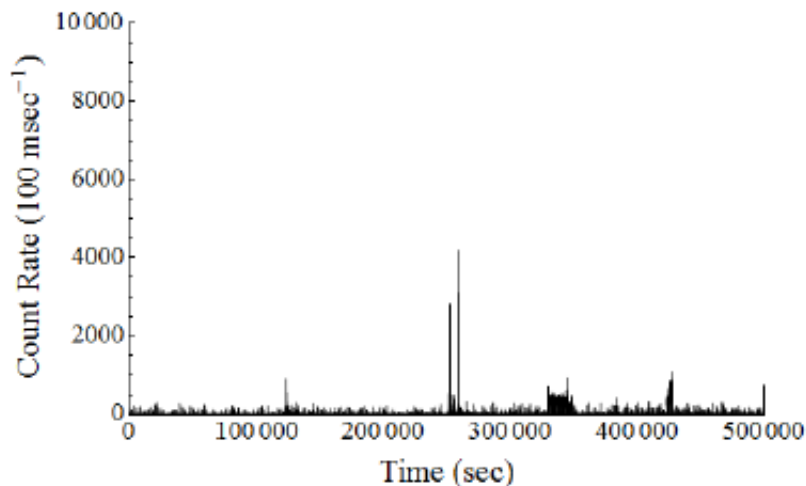


Figure 2. Count rate data for the hydrogen exposures of the palladium coated sensor.

mimicking the method of data presentation for the hydrogen experiment run. In addition, the count rate data collected for this experimental run are shown in Fig. 5 and the palladium electrode on the diamond between exposure days is displayed in Fig. 6.

From the results and from the deuterium exposures, it can be seen that the data collected are similar to the hydrogen runs until day 5 is reached. In the high gain data obtained it can be seen that there is many more counts than in any of the other days in the experimental run but this is not seen in the low gain data collected.

This is because the noise floor of the high gain data in the obtained spectra is higher and therefore the peaks seen

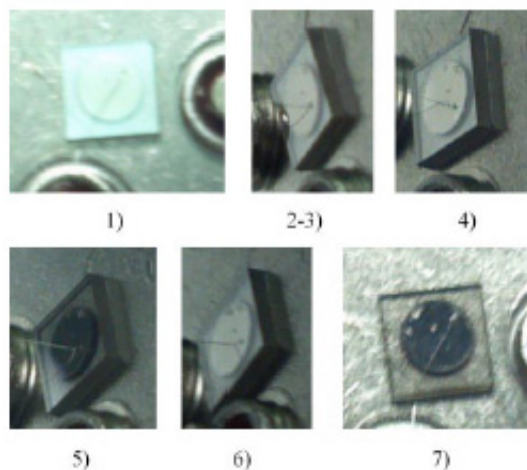


Figure 3. Pictures of the electrode on the diamond sensor between each data acquisition from the pressurized hydrogen run. The indexes of the pictures represent the days of exposure that has been completed.

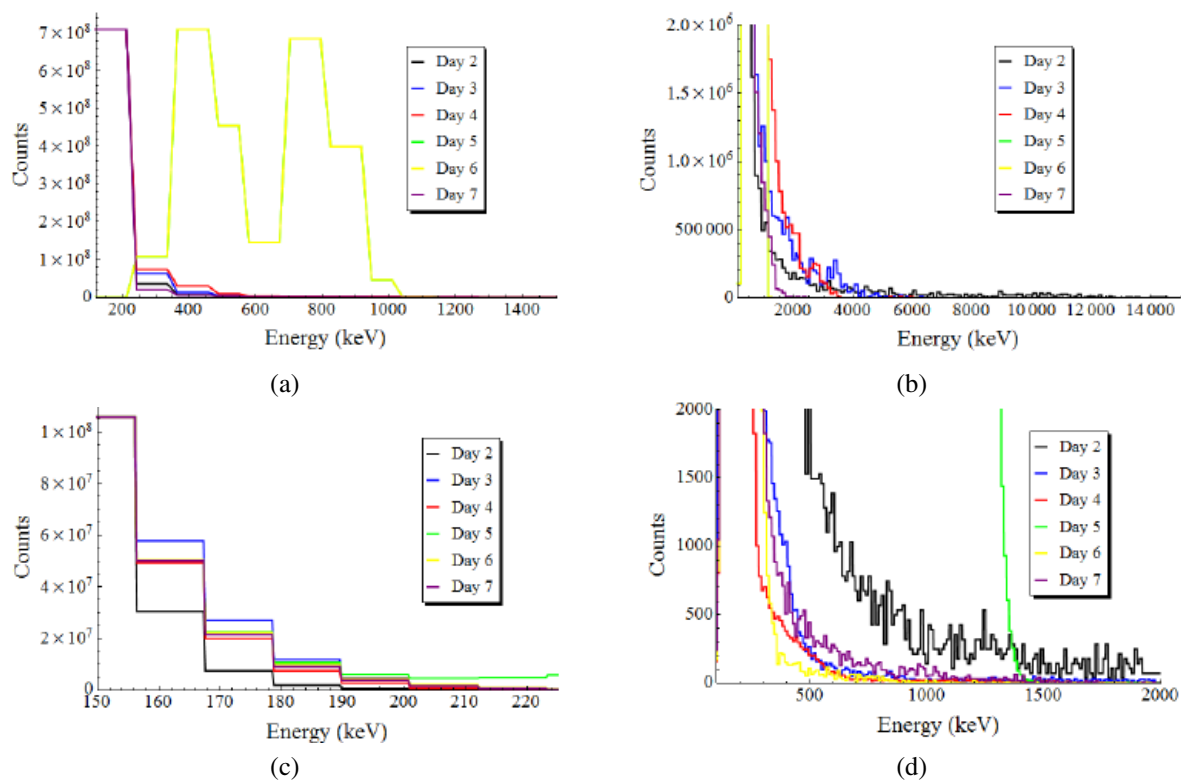


Figure 4. Spectra obtained during deuterium exposures of the palladium coated diamond sensor with (a)–(b) low sensor gain and (c)–(d) high sensor gain.

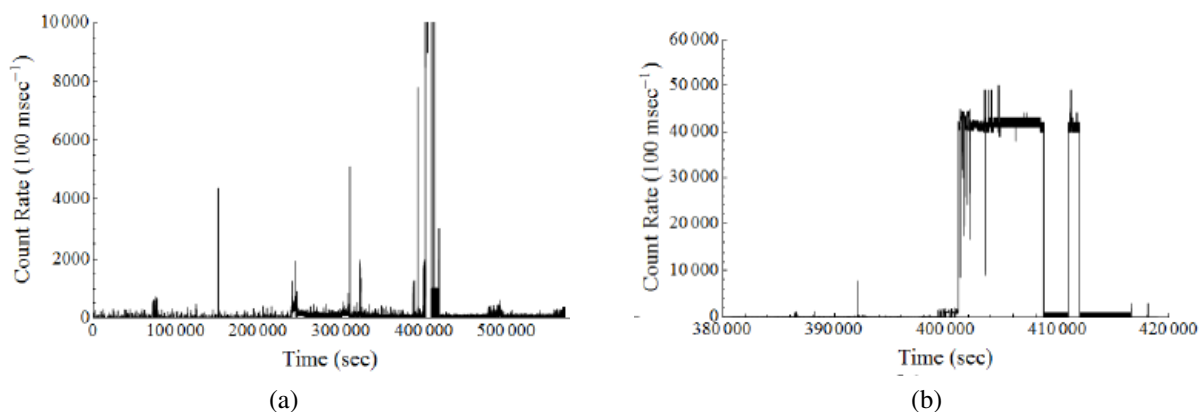


Figure 5. Count rate data for the hydrogen exposures of the palladium coated sensor for a) the entirety of the experiment and b) during the count rate burst.

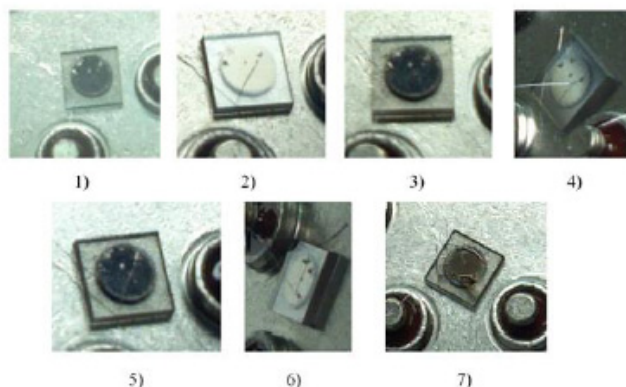


Figure 6. Pictures of the electrode on the diamond sensor between each data acquisition from the pressurized hydrogen run. The indexes of the pictures represent the days of exposure that has been completed.

in Fig. 4(b) account for this large difference. Still, the resolution of these peaks is poor due to the gain and the better resolution is in the low gain data collected but the curve is not shown in Fig. 4 but is shown in Fig. 7 with an interpolation order of one. In this figure, it can be seen that there are three peaks seen. The results are interesting in that the peaks increase in intensity as the energy increases. The three peaks seen are at 312.5, 658.5, and 881.7 keV. With the count rate data shown in Fig. 5, it is suspected that these peaks occurred during a 20 000 s interval in day 5. The count rate seems to jump quickly and plateau as can be seen in Fig. 5(b) but an analysis of the hardware used implies that the count rate ceiling was not reached.

After day 5, the count rate lowered back down to expected levels and then the cathode delaminated after day 7. The surface was scanned with a microscope to identify any anomalies, such as crater formation reported in other reports in LENR. There are two regions where there seems to be some sort of feature that could be regarded as crater formation but at this time it is not clear because the electrode was not scanned immediately before the experiment was conducted.

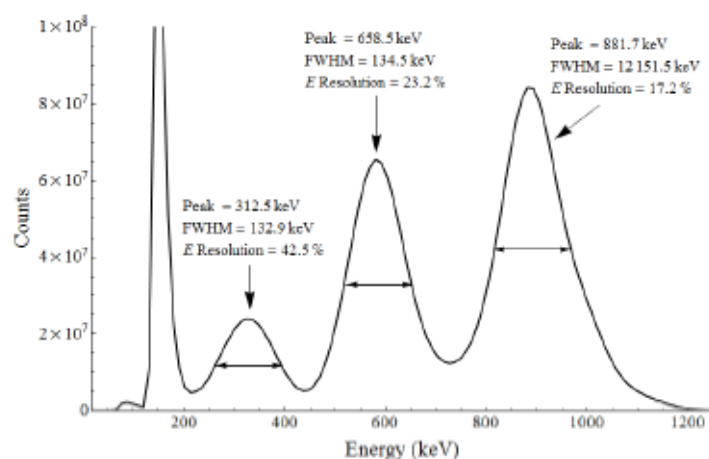


Figure 7. Spectrum obtained from day five of the deuterium run with low amplification of the acquired signal.

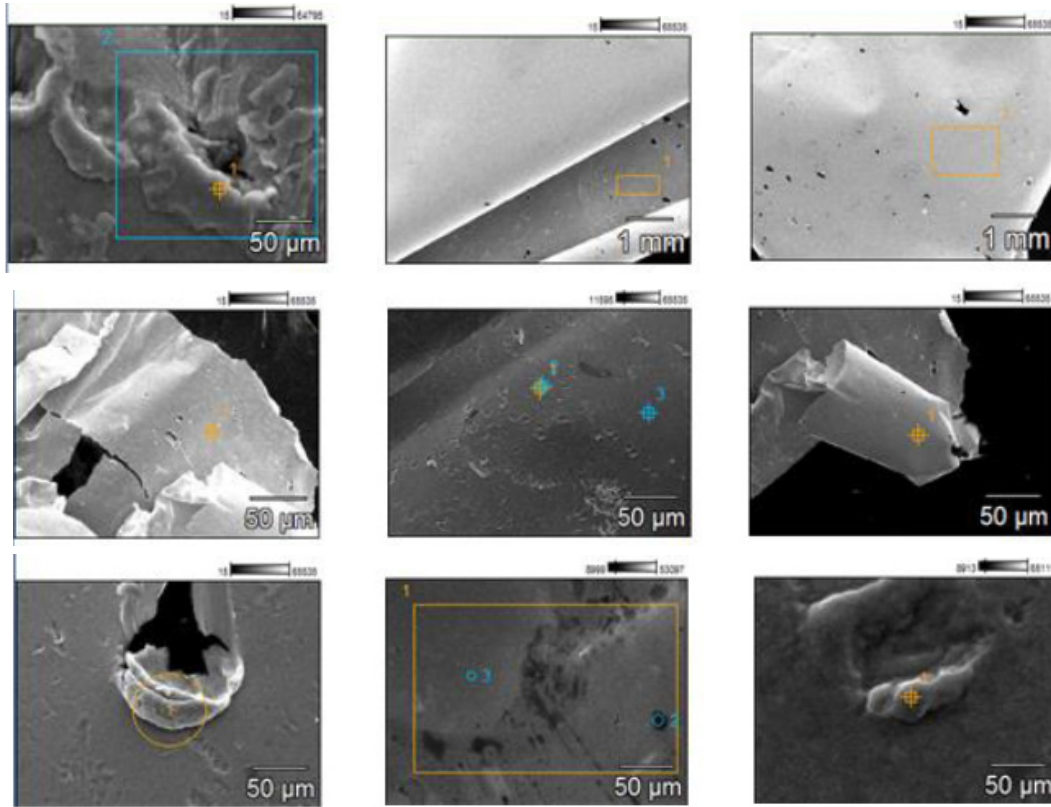


Figure 8. Microscopic analysis of the delaminated palladium electrode of the deuterium run after day seven.

4. Conclusion

The results shown for the deuterium run raise some important questions. First, if the radiation released were monoenergetic then this type of spectral response would not be seen. This suggests that the results are from a polyenergetic source such as beta particles or is a facsimile of the system. Since there was only one result from two experimental

Table 3. The normalization factors in time and total peak counts low gain amplifier output signals for “pressurized deuterium experiment”.

Run	Time	Counts
Day 1	–	–
Day 2	0.58	35.57
Day 3	0.92	4.00
Day 4	1.00	1.00
Day 5	0.62	1.26
Day 6	0.77	5.79
Day 7	0.79	8.07

Table 4. The normalization factors in time and total peak counts high gain amplifier output signals for “pressurized deuterium experiment”.

Run	Time	Counts
Day 1	–	–
Day 2	1.01	139073
Day 3	1.58	124573
Day 4	1.56	105499
Day 5	1.00	1
Day 6	1.33	307092
Day 7	1.38	327650

runs that produced this result, it is very possible that the data seen is due to spikes that overtook the power conditioner from the electrical lines in the building or even a loose cable. The former is a definite possibility while the latter is less likely because of when the effect took place in time in the experimental run. If the spectra seen was indeed from beta particles then there is the question of why there is a sharp spike in count rate and correspondingly, a sharp decrease. If any sort of transmutations were occurring to produce radioactive beta emitters such as Ag-104, then it begs to reason that the count rate should follow some sort of exponential decay. Still, there could be another mechanism that does not correspond to this type of reaction mechanism.

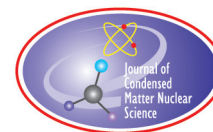
Suffice it to say there are many questions raised by these results. The results may be from charged particles, RF noise, or from some other phenomena and the experiment must be reproduced with more scrutiny and detailed analysis of the system to verify the source of these signals. Further, a correlation of any count rate spikes with excess heat generation should be made to help better define what reactions could be responsible for the observed results.

Acknowledgements

We would like to thank everyone within the Sidney Kimmel Institute for Nuclear Renaissance for their support in this project. This especially includes Joseph Mathai and Shubhra Gangopadhyay for their support in palladium electrode deposition.

References

- [1] Eric Lukosi, Mark Prelas, Joongmoo Shim, Haruetai Kasiwattanawut, Charles Weaver, Cherian Joseph Mathai and Shubhra Gangopadhyay, Diamond-based radiation sensor for LENR experiments Part 1: sensor development and characterization, *17th ICCF Conf. Proc.*, Seoul, South Korea, August 12–17, 2012.



Research Article

Calorimetric Studies of the Destructive Stimulation of Palladium and Nickel Fine Wires

Michael McKubre*, Jianer Bao and Francis Tanzella

SRI International, Menlo Park, CA 94025-3493, USA

Peter Hagelstein

Research Laboratory of Electronics, Massachusetts Institute of Technology, Cambridge, MA 02139, USA

Abstract

An experimental program was designed and performed to test three aspects of CMNS studies. A fourth objective was added in the light of reports from Rossi regarding large scale heat release from the nickel – natural hydrogen system, that prompted re-evaluation of earlier work on this system performed by Piantelli, and later claims by Defkalion.

© 2014 ISCMNS. All rights reserved. ISSN 2227-3123

Keywords: Deuterium, Hydrogen, Nickel, Palladium

1. Background

- (1) The conditions causing the Fleischmann–Pons Heat Effect in Condensed Matter Nuclear Science (CMNS) experiments have been well established by empirical study. In a suitable lattice one needs to achieve (and maintain) a large D/Pd loading ratio and then stimulate a rapid disequilibrium condition causing a deuteron flux. In the experiments of Fleischmann and Pons the electrochemical process achieves both conditions. Of interest is whether the loading and stimulation conditions can be decoupled.
- (2) CMNS experiments have been demonstrated to produce over 20 keV of thermal energy per host Pd atom or interstitial D [1]. This is approximately 10,000 times larger than the largest possible chemical energy release. In experiments previously performed the rate of energy release has been limited by mechanisms unknown, to a few 10's or 100's of Watts per cm³ of Pd. We remain interested in evaluating potential limits on the rate of thermal energy release by optimizing then freezing lattice conditions and applying large and abrupt stimuli.
- (3) One reason for the slow development of the CMNS field is the unavailability of a robust experiment that can be performed rapidly and repeatedly to evaluate the influence of potentially relevant experimental parameters; the physical scientists equivalent of the biologists “lab rat”. The experiments described here were designed with

*E-mail: Michael.mckubre@sri.com

the potential to play this role, allowing more rapid empirical exploration and rationalization of experiment with theory.

- (4) Initial and repeatable success with the Pd/D system and outside claims of success with Ni/H (or Ni natural H/D) systems, possibly involving structures having nano-dimensions, prompted an expansion of our study to include prefabricated, superficial, dendritic nano-structures, and the rapid stimulation of pre-loaded NiH and PdH wires with and without such nano-structures.

2. Introduction

Considerable progress has been made in elucidating the conditions necessary to produce the Fleischmann–Pons heat effect (FPHE or FPE) [2–7] in which heat is produced in amounts substantially larger than the sum of all possible chemical reactions by the prolonged and extensive electrolytic loading of deuterium into palladium. In such heat releases, energy densities have been measured more than 10,000 times larger than known chemistry [1]. An open question is, what imposes an upper limit on the rate of energy release? What, if anything, limits the power of the FPHE? In the history of the field going back now over 20 years several explosive incidents have been noted. Are there circumstances under which the energy release of the FPHE can be explosive? The experiments reported here were performed with very small samples, starting at low (liquid nitrogen) temperatures, in designed safety closures, to evaluate this possibility.

As reported previously [3, 4] the FPHE requires three conditions to be met^a simultaneously:

Loading. The cathode must achieve and maintain a D/Pd atom ratio greater than ~ 0.9 for times longer than ~ 10 times the deuterium diffusional time constant.

Flux. The heat effect appears to correlate closely, and approximately linearly [4], with the diffusive motion of deuterium atoms irrespective of direction.

Stimulation. The effect requires a trigger or stimulus to move the D/Pd system from its equilibrium or steady-state condition, or to populate appropriate energy modes in the lattice or on its surface [5].

In moving this experiment out of the laboratory and advancing towards utility application two practical questions are relevant:

- (1) (How) can we simultaneously achieve the *Loading* and *Flux* conditions? This problem is complicated by the severe degree of non-linearity in electrochemical kinetics and mass transport processes. In the attempt to obtain flux through the surface by partially loading and unloading the cathode, one generally achieves less loading than unloading with simple periodic functions and the cathode quickly falls below the threshold-loading requirement. Although not utilized heavily in the experimental set described here, the only waveform that we have found so far to be effective in creating simultaneously both loading and flux is the SuperWave developed and described by Dardik [1].
- (2) (How) can we decouple the *Loading* and *Stimulation* processes? In the electrochemical FPE experiments performed to date, both the loading and the stimulation were provided by the electrolytic current (density). Loading is a direct (although not inevitable) consequence of the net cathodic charge passed, but the current density of maximum loading is well below that needed to trigger the FPHE. Additional current is needed apparently for stimulation, possibly by means of an exchange flux in which areas of the cathode surface

^aThese conditions are necessary but not sufficient. Further elucidation of a sufficient set of condition can be found in [2–4].

preferentially absorb, while others (perhaps grain boundaries) desorb. Of interest is whether we can use electrochemistry for the effect that it performs highly efficiently, loading, and provide stimulation by other means perhaps more energetically efficiently and more easily controlled.

Another concern is that “traditional” Fleischmann–Pons experiments take weeks or months to complete. Even if successful we have been faced frequently with the possibility and reality of learning only one new thing per experiment, per month. Fleischmann and Pons recognized this and attempted to offset this difficulty by performing large matrix experiments incorporating up to 32 cells operating simultaneously. At SRI we operated a matrix of 3×4 cells in a single thermostated enclosure connected electrically in series. This is an expensive approach, and still too slow. Of interest is an experimental scheme that allows us to learn faster and with lower expense. Basically we are looking for the physico-chemical equivalent of the biologists “lab rat” that allows us to perform experiments that are: relevant, repeatable, rapid and unambiguous.

Of final concern is the final answer to the following questions. What is the process that drives the FPHE? What is the detailed reaction mechanism and what are the products of presumably nuclear reactions that drive the non-chemical heat effect? What is the quantum-based, solid-state, nuclear physics model and theory for this process? One of us (PLH) has been concerned with finding rational and complete answers to these questions since it became evident that the Fleischmann Pons heat effect is both real and non-chemical in origin [7]. The hypothesis to be tested is the conjecture that a significant Pd vacancy^b (point defect) population is required to produce measurable excess heat generation. A final condition for our “lab rat” experiment is the requirement to fully interrogate the “metabolic” (in this case, presumably nuclear) products of any such reaction.

The experiments and protocol described below were designed to answer the various questions addressed above.

3. Experimental

Experiments were performed with fine wires pre-loaded with hydrogen or deuterium, and were designed to be performed in six steps:

- (1) *Loading.* When Pd wires were used as a substrate or as test objects these were pre-loaded electrolytically with either H or D in low molarity SrSO_4 electrolytes ($50 \mu\text{M}$) using procedures developed previously at SRI [8] and elsewhere [9].
- (2) *Sealing.* The atomic loading of H or D can be sealed inside the Pd lattice for extended periods (several hours or days) with the addition of very small concentrations of Hg_2SO_4 to the SrSO_4 electrolyte and continued cathodic electrolysis [8,9]. The deposited Hg at monolayer coverage is a highly effective poison for hydrogen atom recombination, effectively preventing desorption by inhibiting molecule formation.
- (3) *Co-deposition.* As first noted by Fukai [10], vacancies in FCC metals can be stabilized thermodynamically by high activities of hydrogen and its isotopes. Szpak and Boss [11] developed a co-deposition method to deposit Pd and H (or D) simultaneously onto a cathode surface under appropriate potential control. This provides a rapid and almost ideal way of both forming and stabilizing a high population of H or D-filled vacancies and was adapted for this purpose. Co-deposits were not used in all experiments, and were formed on Pd, Ni and Ag substrate wires. At the end of the codeposition process, Hg_2SO_4 was also added to stabilize the loading of the co-deposited layer.
- (4) *Transfer.* The wires were quickly transferred to a stainless steel dewar filled with liquid N_2 as a cryogenic calorimeter (see Fig. 1) for excess energy measurement. SEM characterization, EDX analysis, and optical

^bVacancies in the lattice provide a suitable host structure for diatomic molecular D_2 or H_2 states rather than atomic D or H. These states are required for the Hagelstein nuclear energy release mechanism [7].

microscope observations were generally carried out after the calorimeter testing to determine the quality of the deposited film as well as any possible relationship between the surface morphology and excess energy production.

- (5) *Calorimetry.* As a matter of safety and to preserve high loading, we chose to examine the energy release from PdD_x and other wires at 77 K in liquid nitrogen. For that reason we developed, calibrated, and utilized a cryogenic calorimeter for measuring the amount of heat released when a pulse of current is sent through a loaded wire (with and without co-deposit). In this way the loading (by electrochemistry) and the stimulation (by a sharp current pulse) are effectively decoupled. The calorimeter and its calibration are described below.
- (6) *Nuclear Product Analysis.* From previous experience [2,3,6] the anticipated products of FPE experiments are ^3H , ^3He and ^4He , with only ^4He expected to be present commensurate with the amount of released thermal energy. The experiment was designed to facilitate the search for ^3He and ^4He and boiling liquid N_2 provides an almost ideal medium in which to do this^c. Instrumental difficulties prevented us from completing this important step.

The means of calorimetry selected was to measure the output energy as the enthalpy of vaporization of liquid N_2 . The heat of vaporization of liquid N_2 at 77 K is 5.56 kJ/mol so that 4.32 ml of N_2 gas evolves at STP per Joule of energy. With no other parameter needed, energy release can be measured directly from the mass flow of evolving gas. This was accomplished by sealing the sample to be tested in liquid N_2 inside a thermally isolated enclosure. Excess energy is the difference between the enthalpy of evolved N_2 gas and the measured electrical stimulation.

As shown in Fig. 1, the calorimeter is comprised of a stainless steel Dewar flask, a silicone rubber gasket, a DelrinTM adapter plate, a thick DelrinTM cap for good insulation, a $\frac{1}{4}$ " diameter tube for boiling off N_2 gas, and two copper current rods with blocks to fix the loaded Pd wire in place for the excess heat measurement. The gas outlet was sent to an Aalborg GFM-17 0–5 l/min calibrated mass flow meter with a 0–5 V analog output. The Dewar flask was filled with a fixed amount of liquid N_2 . The copper rods and gas outlet were exposed to the environment to be connected to the electrical cables and gas mass flow meter. The parts exposed to the room temperature environment can transfer heat to the liquid nitrogen, especially through the copper, so that the N_2 evolves at a certain rate.

An integration of the mass flow rate gives the total amount of N_2 gas evolved. The whole system is placed inside a cylindrical acrylic shield to minimize the ambient environmental fluctuations.

After attaining a near constant^d N_2 evolution rate signaling thermal equilibrium, loaded and unloaded wires (for calibration) were stimulated and ruptured by passing current axially along the wires mounted between the copper blocks. The input energy is provided by a 50 V, 8 A, four-quadrant power supply (Kepco BOP 50-8, Flushing, New York) for all the 50- μm wires. For thicker 250- μm wires we used an 8 V, 125 A Sorenson DCS 8-125 power supply. The voltage and current were measured using a high-speed oscilloscope and transferred digitally to the computer. The analog output of the gas mass flow meter was also measured by the high-speed data acquisition systems. Further details of the calorimeter design and calibration verification can be found in [12].

4. Results and Discussion

Calorimeter calibrations were performed using a 50 W, 10 Ω resistor or a number of thin 50- μm -diameter Pd wires. Figure 2 shows the measured N_2 gas evolved vs. input heat to the 10 Ω resistor. The data fall close to the straight line of expected slope of 4.32 ml/J, indicating that the calorimeter maintains its accuracy within a wide energy input range.

^cBecause boiling occurs in the liquid volume, liquid N_2 is self-sparging and the concentration of other dissolved gases rapidly falls to unmeasurably small values.

^dThe system does not reach a steady state because the N_2 is constantly evaporating, thus reducing level in the dewar. Analysis indicates that a quasi-steady state is attained when the variation of flow rate becomes negligible within the time period tested.

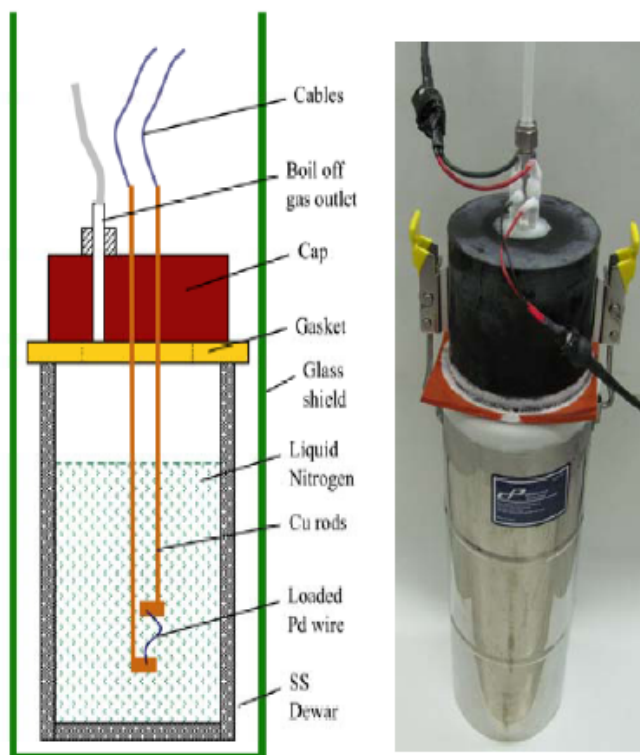


Figure 1. Schematic diagram and photograph of the cryogenic calorimeter.

Statistical analysis indicates that up to 0.25 ml of error could result due to sudden temperature fluctuations, either in excess or deficiency, when the base flow rate is below 1.8 l/min, which is equivalent to 0.06 J in energy. An upper bound and lower bound of 0.25 ml error range is also added to the plot. Figure 3 shows the calibration result with 10 unloaded 50 μm Pd wires. It is seen that all of the calculated evolved gas volumes match well with the input energy (except for one data point when the base flow rate was too high), and no excess energy is seen. The input energy for pulses that break the wires is usually between 0.4 and 0.8 J, and it usually breaks the wire in 3–6 ms.

Figure 4 plots the input vs. the measured output energy from all of the loaded wires studied. The different symbols represent the different materials tested. The results show clearly that excess energy is generated both from Pd and Ni wires loaded either with deuterium or natural hydrogen^e. However, data from Pd/D co-deposited onto highly loaded Pd wires (solid triangles) sit on top of the plot, indicating that this category of wires generates the most excess heat. Interestingly, the Ni co-deposited system also yields significant amounts of excess heat.

^eThe set of data Ni/NiH_x + Additive were generated by the addition of impurity species to the H₂O (natural) loading electrolyte. It is anticipated that these had poor H loading, and thus small or zero excess energy. This set provides good internal calibration of the calorimeter.

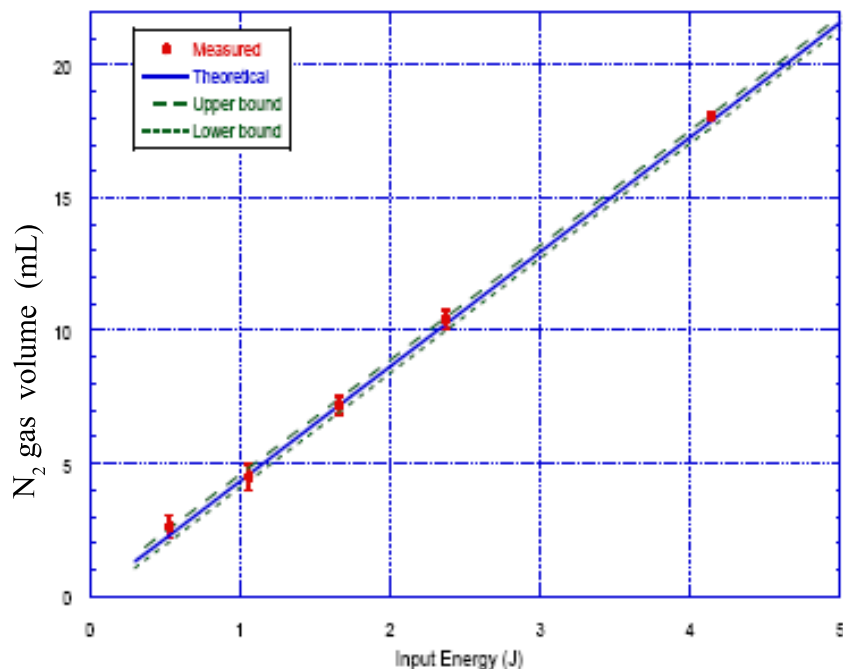


Figure 2. Wide range calibration of the cryogenic calorimeter with a 10 Ω resistor. Error range is ± 0.06 J.

5. Conclusions

A total of 30 experiments demonstrated output energy release in excess of input by amounts larger than can be accounted for by known chemical effects. Because Pd is a very dense material, the gravimetric energy density for these energy releases per gram of bulk Pd is quite low. That is, 2 joules released from ~ 1 mg of pure Pd ($50\ \mu\text{m}$ diameter \times 5 cm long) only yields ~ 2 kJ/g^f. However we have reason to believe that the active region is primarily the co-deposited material, which is present at much lower quantities (mass) than the bulk supporting wire. Hence, the 5–8 ml of 7×10^{-5} M PdSO₄ that was deposited on the wire would correspond to 34–57 kJ/g of co-deposited Pd if all participated in the reaction.

Even this larger number is likely low for two reasons: (i) wires generally ruptured at a single point consuming only a small fraction of the total length; (ii) the amount of energy input stimulation used was likely much greater than that needed to trigger the effect. Clearly this is an experimental method that shows considerable promise in evaluating nuclear heat release from solid-state hydrides and deuterides, and should be further explored.

The purpose of the experimental program was not just to seek a tool to evaluate potential heat-producing systems, we were hoping for a means to elucidate the underlying mechanism. On a theoretical basis we have identified what we believe to be the key to the new effects, which is a novel and fundamental coupling mechanism that allows for coherent energy exchange between vibrational excitation and nuclear excitation (see Ref. [7] and Appendix A of Ref. [12]). A key detail of the experimental protocol was left incomplete, the evaluation of product gases and residual metal mass for

^fFor reference 1 g of TNT yields ~ 4.6 kJ.

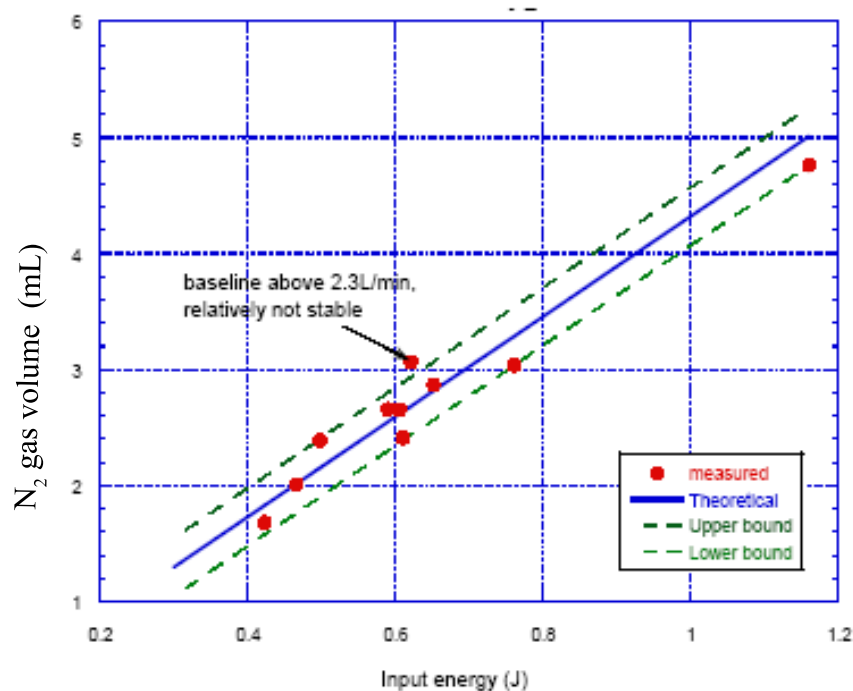


Figure 3. Calibration of the cryogenic calorimeter with thin Pd wires.

^3H , ^3He and ^4He . It is hoped that in future experimentation this task can be completed, allowing for full rationalization of theory with experiment.

Observation of excess energy from Pd wires heavily loaded with D, and particularly those with PdD co-deposits is consistent with our previous experimental experience and with theoretical conjecture. As such these results provide support and comfort, and also validation that this new experimental method may play a useful role in progressing the field forward. Although not the major focus of the present activity, one interesting observation was the evidence of excess energy from Ni wires coated with co-deposited Ni and H from normal water electrolytes (in two out of three experiments).

Although supported by theory as resulting from lattice-vacancy mediated interaction between H and the minor component D in natural water, in no previous experiments at SRI has excess heat been measured either for systems with Ni electrodes or in electrolytes or gas systems containing only natural hydrogen. This suggests that the nickel/deuteride or mixed nickel deuteride/hydride systems may be appropriate materials to produce excess energy, in potentially useful amounts.

Results of these preliminary studies suggest that very high rates of energy release signaling high explosive powers do not normally or necessarily result from extreme electrical stimulation of metal wires highly loaded with hydrogen and/or deuterium. Experimental support is given for the claims of nuclear level excess heat both from Pd wires loaded with isotopically enriched D, and Ni wires loaded with H at natural isotope levels. The excess heat effect was larger for PdD, and largest for PdD with dendritic PdD surface structure, but was nevertheless clear and present for Ni wires

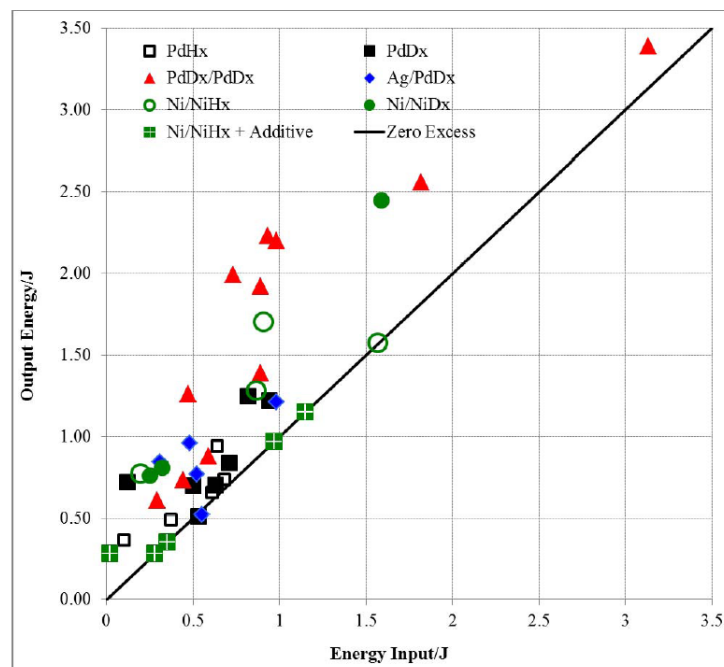


Figure 4. Summary of excess heat from all wires tested.

loaded in “normal” H_2O containing natural isotopic D concentrations providing further experimental support for the work and claims of Piantelli, Rossi, Defkalion and Brillouin.

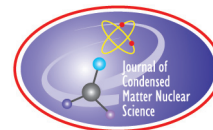
Acknowledgment

The authors gratefully acknowledge the support of the Defense Threat Reduction Agency and Dr. William Wilson on Contract No. HDTRA1-08-1-0050.

References

- [1] I. Dardik et al., Excess heat in electrolysis experiments at Energetics Technologies, *Proceedings of ICCF11*, pp. 84–101, 2004.
- [2] E. Storms, *The Science of Low Energy Nuclear Reaction*, World Scientific, Singapore, 2007.
- [3] M. McKubre et al., Cold Fusion (LENR) one perspective on the state of the science, *Proceedings of ICCF15*, p. XV, 2009.
- [4] M. McKubre, Concerning reproducibility of Excess Power Production, *Proceedings of ICCF5*, p. XV, 2009.
- [5] M. McKubre et al., Excess power observations in electrochemical studies of the D/Pd System; the influence of Loading, *Proceedings of ICCF8*, p. 3, 2000.
- [6] M. McKubre et al., The emergence of a coherent explanation for anomalies observed in D/Pd and H/Pd systems, *Proceedings of ICCF8*, p. 17.
- [7] P. Hagelstein, *ibid*, 2012.
- [8] P. Tripodi et al., Temperature coefficient of resistivity at compositions approaching PdH, *Phys. Lett. A*, **276**(1–4) (2000) 122–126.

- [9] F. Celani et al., Reproducible D/Pd ratio > 1 and excess heat correlation by 1-micro s-pulse, high-current electrolysis, *Fusion Technol.* **29**(3) (1996). 398–404.
- [10] Y. Fukai, *The Metal-hydrogen System: Basic Bulk Properties*, Springer, Berlin, 2005.
- [11] S. Szpak et al., On the behavior of palladium deposited in the presence of evolving deuterium, *J. Electroanalytical Chem.* **302**(1–2) (1991) 255–260.
- [12] F. Tanzella et al., Triggered nuclear energy release from palladium deuteride, SRI Final Report to DTRA on Contract HDTRA1-08-0050, 2012.



Research Article

Femto-atoms and Transmutation

A. Meulenberg*

Science for Humanity Trust Inc., Tucker, GA, USA

Abstract

The low-energy nuclear-reaction (LENR) fusion process for a deep-electron orbit femto-hydrogen atom, $H^\#$, with an atomic nucleus yields new isotopes and femto-atoms. The multi-body interaction, strong near-field radiation from tightly bound electrons, and low input energies, make energetic particle emission less common than for normal fusion or neutron-activation processes.

© 2014 ISCMNS. All rights reserved. ISSN 2227-3123

Keywords: Deep-electron levels, Femto-atoms, Fusion, Transmutation

1. Introduction

In addition to the fusion of hydrogen atoms, the present Lochon [1] and Extended-Lochon Models [2] are consistent with the formation of multi-femto-meter size ions and atoms, $H^{\#+}$ or $D^{\#+}$ and $H^\#$ or $D^\#$, and of femto-hydrogen molecules and ions, $H_2^\#$ or $D_2^\#$ and $H_2^{\#+}$ or $D_2^{\#+}$. Femto-atoms, with very high electron-binding energies, have been proposed for over 50 years [3,4]. They are based on a solution of the standard Schrodinger, Klein–Gordon, and Dirac equations. This particular solution has been rejected by mathematical physicists for nearly as many years because, assuming a $1/r$ Coulomb potential, it is singular at $r = 0$. Since, a $1/r$ potential implies that all of the energy of the universe is tied up in a single electron, a real, non-singular, potential must be used. Once a realistic potential is used, such as those used in nuclear physics, the argument against this ‘anomalous’ solution fails and legitimate deep-Dirac level (DDL) electron orbitals emerge with binding energies on the order of 500 keV [5].

The 500 keV energy levels have not been observed for several reasons. The primary one is that the population is extremely low [6]. If these levels were as stable as the atomic orbitals, the number of DDL electrons would only be on the order of parts-per-billion relative to the atomic orbitals. However, with electron orbital radii in the fermi range, the lifetime of femto-hydrogen in matter could be less than picoseconds. In this case, the ratio of femto-hydrogen atoms to normal ones might be 10^{-20} to one. This would make detection, via photon absorption (e.g., from annihilation radiation at 511 keV), very difficult.

Detection of radiation from the decay of an electron in an atomic orbital to the DDL would be similarly problematic. The difference in energies between these levels is ~ 5 orders of magnitude. More problematic is the fact that electrons

*E-mail: mules333@gmail.com

in the H ground-state, and below, do not have sufficient angular momentum with which to form photons. This means that such transitions are highly forbidden. Thus, the transition probability is another 6–8 orders of magnitude less likely than a similar transition with sufficient angular momentum. Only if the atoms can interact inelastically with matter can their electrons decay to the lower levels.

Once formed, the number of subsequent fusion products for a femto-hydrogen or femto-deuterium ion or molecule with other nuclei is immense. This reduces the femto-atom population much faster than would reexcitation of DDL electrons to the atomic levels. Of perhaps greatest importance in this regard is the interaction of two femto-hydrogen atoms. This is the most probable interaction because the population of the DDLs is primarily a result of phonon-induced H–H or D–D interactions in the lattice during which the paired protons with DDL electron(s) will greatly enhance p–e–p or p–e–p fusion. If the two converging nuclei have too much angular momentum to fuse immediately, it is proposed that they will form a meta-stable femto-molecule with the deep-orbit electrons binding them. At even higher angular momentum levels, the protons can separate and the spin-coupled electron pair may go with one or the other. This would produce a negative femto-hydrogen ion along with a proton.

Femto-hydrogen molecules may be slowed from self-fusing by the centrifugal force countering the dipole–dipole Coulomb attraction of the composite femto-atoms and the strong interaction of their nucleons. They have a finite lifetime that, in matter, would be primarily limited by chance interactions with lattice nuclei. Femto ions, atoms, and molecules are highly mobile in the lattice because of their near-nuclear size. The interaction of $H_2^\#$ or $D_2^\#$, with atomic nuclei of the lattice would greatly increase the possible LENR products. There will be new selection rules because of this process that may be guidelines rather than rigid rules. The formation and stability of alpha particles, and even neutron-proton pairs, in the product nucleus will be important. However, some of the femto-hydrogen may not fuse with other nuclei. They may form femto-molecular hydrides. The negative femto-hydrogen ion would also do that readily.

This paper will describe a number of representative transmutations in the NiH system and their energy and radiation release. A unique feature of this model is the selectivity of the femto-hydrogen for radioactive isotopes. The paper finally gives examples of how the low-energy transmutation process works to move isotopes (both stable and unstable) toward stable nuclear configurations.

2. Deep-electron Orbits

The deep-electron energy level predicted by the Klein–Gordon equation is alone and far below the $n = 1$ levels, so we will call it interchangeably the $n = 0$, or ‘nought’, or ‘naught’ orbit or level. What are some of its properties and problems? Assuming a single electron, bound to a proton, the ‘anomalous’ solution of the K–G equation predicts a binding-energy level of about –507 keV and a characteristic orbit with $r_0 = 390$ fm [7]. However, the high-magnitude binding energy requires a deeper orbit; the effective electron-charge center must be in the low fermi range from the proton [8].

The deep-orbit solution of the Dirac equations has been shown to be problematic assuming the obviously idealized $1/r$ dependence of the Coulomb potential, with its point-charge singularity at $r = 0$. Maly and Va’vra [5] selected a modified Coulomb potential that nuclear hysicists had been using for years. This non-singular potential reflected a charge distribution within the nucleus (rather than a point charge) and still matched the $1/r$ Coulomb potential beyond the surface of the nucleus. With a non-singular potential, the solution of the relativistic Schrodinger and Dirac equations, which had been rejected by mathematical physicists for over five decades, must now be considered as having low population [6], but being as valid [4] as the normally accepted solutions of the equations.

3. Femto-hydrogen Transmutation Pathways

If the deep orbits do exist, and can be occupied, then a new physics discipline with immense practical implications can result. This version of atomic physics opens new pathways to both nuclear physics and femto-chemistry. The nuclear physics opens from a version of muon catalysis. The tight-electron orbit allows a proton (or deuteron) and this electron to be close enough to another nucleus, for long enough, to initiate fusion reactions. The plural here is used because now, instead of just catalyzing a hydrogen-fusion reaction, new options are open. Proximity to a nucleus by a proton, plus deep-orbit electron(s), leads to at least three-body interactions. The proton–electron pair ($H^\#$, the # indicates a deep-orbit electron and similarly for a deuteron–electron pair, $D^\#$) can be captured by nucleus ${}^A N_Z$ to become:

- (1) ${}^A N_Z + H^\# \rightarrow {}^{A+1} N_Z + \text{neutrino}$ if the proton + deep-orbit electron is transformed to a neutron.
- (2) ${}^A N_Z + H^\# \rightarrow {}^{A+1} N_{Z+1} + e$ if the deep-orbit electron is ejected (as in the muon case) and the proton is retained in the new nucleus.
- (3) ${}^A N_Z + H^\# \rightarrow {}^A N_{Z-1} + p + \text{neutrino}$ if the deep-orbit electron is retained to form a neutron from an existing proton and the incident proton is ejected.
- (4) ${}^A N_Z + H^\# \rightarrow {}^A N_Z H^\#$ if the deep-orbit electron and proton are both retained just outside of the nucleus to form a halo nucleus, a femto-hydride.
- (5) ${}^A N_Z + H^\# \rightarrow {}^A N_Z^\# + p$ if the deep-orbit electron alone is retained in orbit to form a femto-atom.

The choice of paths depends on the energy levels and the ‘needs’ of the ${}^A N_Z$ nucleus. Pathway 1 requires enough energy to form a neutron from the proton–electron pair. Pathway 2 is for neutron-rich nuclei that gain stability by adding a proton. Pathway 3 is for proton-rich nuclei that gain stability by adding a neutron and subtracting a proton. Pathways 4 and 5 are for nuclei that cannot move to a lower nuclear energy state by internal addition of the proton–electron pair or parts thereof. However, the addition of a femto-atom or deep-orbit electron reduces the total system energy, from the dipole/monopole Coulomb interaction of the atoms, and from reducing the proton–proton repulsion within the nucleus. This selectivity and multiple-path availability provides an energy source, a potential source of stable rare elements, and the means of remediation for radioactive waste products.

Pathways 4 and 5 lead to a new femto-chemistry, to new femto-atoms, and thus to femto-molecules. Presently, pico-second chemistry is of interest using sono-luminescent ‘bubbles’ as the reactors. Some of the femto-atoms and femto-molecules suggested here may be longer lived. There is even evidence of biological systems producing transmutations that may be available by these pathways.

4. Transmutation (Examples)

Just as thermal neutrons in a nuclear reactor are a major source of useful isotopes that do not occur, or no longer exist, naturally, the nought-orbit atoms can also produce useful transmutations. The thermal neutrons can operate only in the manner of Pathway 1 (but without a neutrino). A tight-orbit hydrogen atom has all five options. As an example of the use of these pathways, it is possible to demonstrate an actual implementation that has claimed some actual results against which we can compare our model.

Figure 1 provides an example of these multiple actions in a system that is of particular interest today. The first claimed sale and delivery of a mega-Watt Low-Energy Nuclear Reaction heat source was announced in late 2011.^a Other, smaller units are also being advertised.^b The systems start with metallic nickel powder and creation of significant quantities of stable copper has been claimed. Mention has been made of iron and cobalt by-products as well, with little to no

^ahttp://www.leonardo-ecat.com/fp/Products/1MW_Plant/index.html

^b<http://www.defkalion-energy.com/products>

radioactivity beyond the initial startup period. The figure displays the percentage concentration or half-life of, major decay path for, and energy released in positron emission, or as negative values in beta emission, by isotopes about nickel on the chart.

We will start with the major isotope, ($^{58}\text{Ni}_{28}$, red box outline) and identify the pathways available from a local ‘flood’ of femto-hydrogen. The top white box outline represents Pathway 2. The bottom white box represents Pathway 3. The middle white box represents Pathway 1. Pathway 5 is experimentally indistinguishable from Pathway 3 unless extremely fine instrumentation is used. Pathway 4 is nearly indistinguishable from pathway 1 except for the lack of a neutrino, again, not an easy observable.

The open arrows indicate transmutation paths induced by a flux of nought-orbit hydrogen. The ‘x’ed arrows indicate paths that are improbable because the product would naturally decay in the opposite manner from the suggested arrows (not all improbable paths are marked). The colored arrows indicate natural radioactive decay paths that would compete with the induced transitions. The availability of options greatly improves the probability of femto-hydrogen attraction to and subsequent transition of radioactive isotopes. The stable isotopes have fewer natural paths along which to transmute. Therefore, they are less likely to attract and fuse with a femto-hydrogen atom (Appendix A). Thus, any natural or process-induced radioactivity dies off as the concentration of nought-orbit hydrogen builds to high levels. This initial radioactivity and subsequent die-off is reported in the type of heat-generation units presently being prepared for commercialization.

There are other differences in the deep-orbit electron pathways from those of presently accepted physics for neutron activation. A most important one is that, because of the high binding energy of the nought orbit, the energy available for the fusion/transmutation reaction may be significantly less (up to 1.5 MeV) than that for thermal-neutron activation. This means that the many nuclei, which would be ‘energized’ by addition of a neutron, would not be as receptive to reaction with a proton plus deep-orbit electron. Thus, instead of creating radioisotopes, the lower-energy fusion process selectively deactivates radioactive nuclei by the above processes (Pathways 1–3, and even 4 and 5).

5. Energetics and Radiation Products of Various Pathways

The predicted nought orbit electron’s total energy is $E_t = 3.7$ keV, kinetic energy is $\text{KE} \approx 1$ MeV, potential energy is $\text{PE} = -1.5$ MeV (derived from the binding proton), and its binding energy of $E_b = E_t - m_e c^2 = -507$ keV. With this information, it is possible to look at the energetics of, and radiation from, femto-hydrogen in a nickel lattice (Fig. 1). We look at the possible paths assuming a local, but prolific, source of $\text{H}^{\#}\text{H}$ or of $\text{H}^{\#}$ in the lattice assuming only ^{58}Ni for this discussion. We reserve the more probable pathways of the femto-molecule $\text{H}_2^{\#}$ for later papers. Similarly, we do not discuss here the results for $^4\text{He}^{\#}$ in either a Ni or Pd lattice.

Assuming >8.7 MeV net gain for each addition of a proton or neutron,^c a single ^{58}Ni nucleus in the presence of the femto-hydrogen ‘field’ could transmute 6 times to reach $^{64}\text{Zn}_{30}$. This would provide >52 MeV net energy in this chain. However, four of the transmutations may involve forming neutrons with a portion of the gain in nuclear energy. Consequently, a neutrino is formed and escapes with a portion of the excess energy. This would be lost from the heat generated locally in the process.

Most of the chain remains as atomic nickel, so that the lattice is not greatly disturbed. There are intermediate paths possible for transmutation from one Ni isotope to the next. Nevertheless, they are improbable and therefore marked with a red X in Fig. 1. An example of an improbable path is ^{58}Ni to ^{59}Cu via proton capture. It is going against the natural decay path of the ^{59}Cu , which is to emit a positron, not to capture a proton. The proton + electron weak interaction to a neutron is energetically more probable (Table 1); however, it may not be the preferred path, since the weak interaction to form a neutron from the $\text{H}^{\#}$ is much slower than the capture of an electron alone (to go to ^{59}Co).

^c<http://www.nndc.bnl.gov/chart/reColor.jsp?newColor=beda>

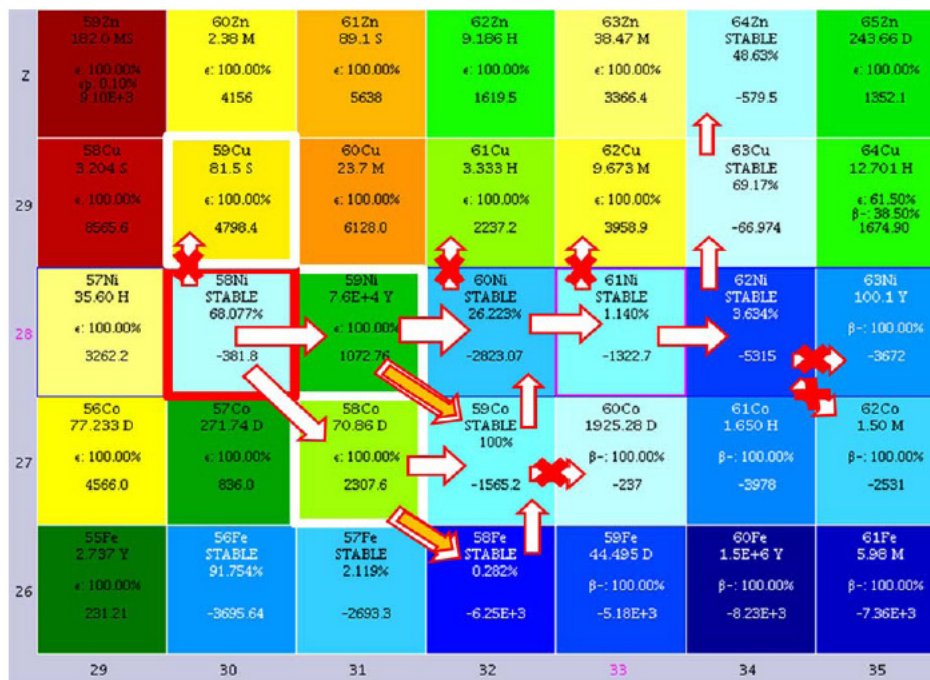


Figure 1. Chart of nuclides (see http://www.leonardo-ecat.com/fp/Products/1MW_Plant/index.html) indicating the femto-hydrogen-induced transmutation paths leading from ^{58}Ni (<http://www.nndc.bnl.gov/chart/reColor.jsp?newColor=qec>).

Although the process could go through additional paths, the total energy produced is the same, if it gets to the same final result. Stopping part way, because of insufficient femto-atom flux, will reduce the energy gain per starting Ni atom but not the gain per femto-atom. This first condition, e.g., transmutation from Ni to Co or Fe and back to Ni, would affect the amount of Ni ‘used up’ over a given period of time producing energy. The second condition is related to the production of the femto-atoms and therefore the rate of getting energy from a system. It could also alter the chemical structure of the cold-fusion source region.

Two of the nuclides along the probable paths are radioactive, ^{59}Ni and ^{58}Co . It is possible for some of these to decay before they are transmuted to stable isotopes or if they are left over when the system is shut down. In both cases, they will decay by positron emission ($\epsilon = 100\%$), which would produce small amounts of energetic and penetrating electron–positron annihilation radiation. The half life of this characteristic radiation (511 keV gammas) would be proof of the process. Since ^{59}Ni has a much longer half life than does ^{58}Co , even if it is produced in orders of magnitude greater quantities, the 71-day half life of ^{58}Co decay could be a clear signature.

6. Path Selection by a Femto-hydrogen Atom

The natural questions arise as to if, why, and how the tight-orbit $\text{H}^\#$ determines what nucleus to enter and which of the above paths will result from such an intrusion. Possible answers come from both physical and QM causes. Random-walk paths through the nickel lattice and non-selective nuclear encounters would produce a dominance of nickel isotopes, some of which are radioactive. If the $\text{H}^\#$ has to ‘sample’ the deep nuclear potential it encounters, then

‘selectivity’ is too late and any change in interaction volume, $V_n = 4\pi r_n^3$, from such selection would be too small. On the other hand, if selectivity is based on the bound Maxwellian radiation [9] of the nuclear protons and if the interaction drops off as $1/r^6$ for a dipole-dipole interaction (see Appendix B), then, even in the pico-meter range, the interaction should be significant. If so, the evanescent waves (virtual photons) from the protons in the nuclear well should be able to affect the $H^\#$ and alter its path through the lattice, since the femto-atom kinetic energy will only be at the lattice temperature.

If this EM radiation field is able to give up energy and lower the total system energy, by drawing the $H^\#$ into its source nucleus, then it can increase the interaction cross section by $k_{EM}(r_{EM}/r_n)^3$. The coupling coefficient of the EM interaction, k_{EM} , between nuclei is small relative to that of a nuclear potential or even that of a Coulomb potential; yet there are no barriers impeding motion of the neutral femto-atom within the lattice and its inertia is only that from the thermal environment. Since the femto-atom’s motion through the lattice is non-linear, the interaction volume, not its cross-section, is important. Thus, comparing the near-picometer virtual-photon range to the fermi nuclear size, the capture volume could be increased by > 7 orders of magnitude.

How does this hypothesis work out in practice? The ‘preferred’ paths based on Table 1 were identified based on the known decay modes of both starting and product nuclides where radioactivity is present. If the starting nuclide is a positron emitter, it is unlikely that it will accept a proton from the femto-hydrogen. On the other hand, it would like the DDL electron from that entity. If the ending nuclide is a beta emitter, it is an unlikely goal for accepting the electron of the femto-atom (except as a portion of a halo nucleon). Anything leading to a stable nuclide would be considered a preferred path. Anything leading from a stable nuclide is considered a lower probability transition. It will only occur when the concentrations of the femto-hydrogen and/or the stable nuclide are high.

Table 1 gives some examples of the energetics of many of the transitions examined in Fig. 1. The table values are based on an earlier estimate of the femto-hydrogen properties where the electron energy was 0.5 MeV lower and the proton mass was 0.5 MeV higher. However, the binding energy was the same. The table does not include starting nuclides that are radioactive or electron-capture transitions. Nevertheless, it does indicate preferred paths in agreement with those marked in Fig. 1.

The table shows pairs of transitions. In each pair, the starting nuclide is combined with either an $H^\#$ or an H. These choices correspond to the equivalent of adding a neutron (a proton and nought-orbit electron) or a proton from the femto-hydrogen. With only a single exception, the preferred path is unambiguous. The exception is that of ^{62}Ni . Based on energetic alone, the choice of continuing along the Ni path to a long-lived isotope, ^{63}Ni , or changing to a stable copper isotope, ^{63}Cu , is not clear-cut. However, continuation along the Ni path beyond ^{64}Ni (not shown in the figure) appears closed by the energetics. The stable ^{65}Cu nuclide gives a strong preference over the short-lived ^{65}Ni branch in the table.

The QM answer to the preferential interaction of radioisotopes for the femto-hydrogen comes from the small size of the nucleon wave functions (in the multi-fm range) versus that of the EM portion of the nuclear protons and the relativistic deep-orbit electron(s) (in the multi-hundred fm range). The difference between the femto-atom case and the normal atomic interaction is in the electron orbit. If the inter-nuclear separation is larger than the atomic-electron orbitals, the dipole–dipole interaction is stronger than the ‘screened’ nuclear Coulomb repulsion. For smaller separations, the screening is inadequate and the repulsion dominates and keeps atoms apart. This explanation is simply described in terms of electrostatics. For the femto-atom case, the screening is complete down to nearly nuclear dimensions, so that electrostatics play little role beyond the dipole–dipole attraction. However, with the strong acceleration experienced by deep-orbit electron(s) and by excited-state protons, the EM fields now becomes more important than even a dipole–monopole interaction [9]. To my knowledge, this contribution to the QM wave function(s) has never been recognized or applied in the past.

Assuming the larger EM-field interaction volume, how does the potential for radioactive decay affect the nuclear evanescent waves? (See Appendix A.) Since the nuclear potential can be approximated by a square well, the excited

Table 1. Nuclide and femto-hydrogen transitions and energies

Starting nuclide	Product nuclide	Q (MeV)
$^{58}\text{Ni}(68.1\%) + \text{H}^\#$	\rightarrow ^{59}Ni	+7.717
$^{58}\text{Ni}(68.1\%) + \text{H}$	\rightarrow ^{59}Cu	+2.919
$^{59}\text{Co}(100\%) + \text{H}^\#$	\rightarrow ^{60}Co	+6.210
$^{59}\text{Co}(100\%) + {}^1\text{H}$	\rightarrow $^{60}\text{Ni}(26.2\%)$	+9.032
$^{60}\text{Ni}(26.2\%) + \text{H}^\#$	\rightarrow $^{61}\text{Ni}(1.14\%)$	+6.538
$^{60}\text{Ni}(26.2\%) + {}^1\text{H}$	\rightarrow ^{61}Cu	+4.300
$^{61}\text{Ni}(1.14\%) + \text{H}^\#$	\rightarrow $^{62}\text{Ni}(3.64\%)$	+9.314
$^{61}\text{Ni}(1.14\%) + {}^1\text{H}$	\rightarrow ^{62}Cu	+5.355
$^{62}\text{Ni}(3.64\%) + \text{H}^\#$	\rightarrow ^{63}Ni	+5.555
$^{62}\text{Ni}(3.64\%) + {}^1\text{H}$	\rightarrow $^{63}\text{Cu}(69.2\%)$	+5.622
$^{64}\text{Ni}(0.93\%) + \text{H}^\#$	\rightarrow ^{65}Ni	+4.816
$^{64}\text{Ni}(0.93\%) + {}^1\text{H}$	\rightarrow $^{65}\text{Cu}(30.8\%)$	+6.954
$^{63}\text{Cu}(69.2\%) + \text{H}^\#$	\rightarrow ^{64}Cu	+6.634
$^{63}\text{Cu}(69.2\%) + {}^1\text{H}$	\rightarrow $^{64}\text{Zn}(48.6\%)$	+7.213
$^{65}\text{Cu}(30.8\%) + \text{H}^\#$	\rightarrow ^{66}Cu	+5.784
$^{65}\text{Cu}(30.8\%) + {}^1\text{H}$	\rightarrow $^{66}\text{Zn}(27.9\%)$	+8.425
$^{64}\text{Zn}(48.6\%) + \text{H}^\#$	\rightarrow ^{65}Zn	+6.697
$^{64}\text{Zn}(48.6\%) + {}^1\text{H}$	\rightarrow ^{65}Ga	+3.443

states will have higher frequencies than the filled states. Electrons in excited states will radiate more and stronger EM-fields at higher frequencies and therefore at higher nuclear energies. Any energy transfer, which could lower the system energy by bringing the bodies closer together, would provide an attraction between nucleus and femto-atom. Thus, excited nuclei, or those with excess kinetic energy, would have a stronger EM field and therefore a larger capture cross-section.

The force driving this action is expressed simply as $F = -dV/dr$, where V is the potential energy of the nucleus at distance r from the femto-atom. The potential energy is the ability to do work. Radioisotopes have excess energy relative to their ground state. Work that *can* be done includes moving the femto-hydrogen closer to the radioactive nucleus. This pathway to lower energy levels does not only compete with gamma transitions, it interferes with them and therefore suppresses them by altering time spent at the resonant frequencies.

While the hydrogen or femto-hydrogen nucleus is not radioactive, the combination with another femto-hydrogen,

as a molecule, is a lower energy state; therefore, work can be done in bringing them closer together. Thus, there will be a significant attractive potential (and force) between these atoms because of their proximity relative to that of normal molecular atoms.

In Eq. (1), the lower probability solar fusion p–e–p reaction^d is shown with the deuteron and neutrino fusion result along with the mass defect energy, Q . By comparison, Eq. (2) shows production of a femto-hydrogen molecule. I do not believe that the similarity in Q values is a coincidence. The ‘less than’ symbol is used in Eq. (2) because, while the potential energy loss in bringing the electron to the DDL is ~ 1.5 MeV, some of that energy is translated into kinetic energy of the protons (~ 1 MeV is added to the deep-orbit-electron kinetic energy and mass).

$$p + e + p = d + \nu, \quad Q = 1.44 \text{ MeV}, \quad (1)$$

$$p + e + p = H_2^\#, \quad Q < 1.5 \text{ MeV}. \quad (2)$$

The reason to mention this is that a deuteron is considered to be a ‘halo’ nucleus.^e The neutron and proton wave functions do not have strong overlap. Therefore, they do not spend much time in the nuclear potential well that they make when close to each other. The halo nucleus is not, but could be, considered a femto-molecule. Seen as a femto-molecule, the neutron and femto-hydrogen could be names for the two molecular s-orbitals that are separated in energy by the quadratic-Stark effect. The Stark effect is the splitting of energy levels by an external electric field (such as that provided by a nearby nucleus).^f

For the case where a proton has two deep-orbit electrons bound to it, the pair is considered a boson (a lochon, or local charged boson). As such, the Klein–Gordon equation provides the proper mathematical model and this then becomes a nought orbit with the electrons strongly coupled by their magnetic moments as well as by the proton’s Coulomb field. The difference in isotopic transition paths induced by the femto-hydrogen atom versus that of the negative femto-hydrogen ion is very small in the case described in Fig. 1. The major difference is that ^{58}Fe has a higher probability of being created by the ion with its two electrons. It can be created by a flood of the femto atoms in a 2-step process; but the negative femto-ion can do it with a single ‘hit’. A major difference in the femto-ion vs. the femto-atom interactions is the charge. The negative ion has long-range attraction (100s of fm) to any nucleus. Thus, the selective attraction to radio-active nuclides is no longer a dominant feature.

We have shown a simple example of nought-orbit (or femto-hydrogen) induced transmutation. It gets more complicated when deuterium (as $D^\#$) or femto-molecular hydrogen (as $H_2^\#$) is considered. With femto-helium (e.g., $^4\text{He}^\#$ resulting from fusion of two deuterium atoms), the changes in atomic number can be ± 2 and changes in atomic mass can be up to 4 (with multiples and variations thereof). Thus, the breadth of nuclear-waste remediation gets broader very rapidly. While heavier isotopes of H and He are expected to be useful, nothing with more than a pair of electrons is expected to provide a useful nought orbit.

Heavier halo nuclei are not uncommon; however, in the present model, they would be created by interactions with femto-hydrogen, either as direct femto-molecular formation or as a by-product of a nuclear reaction of the parent nucleus with a femto-hydrogen or helium atom or ion.

7. Conclusions

Transmutation associated with cold-fusion results was a surprise. However, on closely examining the consequences of the deep-orbit electrons postulated to provide the low-energy fusion of repulsive hydrogen nuclei, the possibility of

^dhttp://en.wikipedia.org/wiki/Proton-proton_chain#The_pep_reaction

^ehttp://en.wikipedia.org/wiki/Halo_nucleus

^fhttp://en.wikipedia.org/wiki/Stark_effect#Second_order

transmutation became clear. The discovery of relativistic deep-electron orbits for both the Klein–Gordon and Dirac equations confirmed the cold-fusion predictions of deep electrons involved in the process.

These orbits, long-lived relative to the multiple pass-by electron transits originally postulated, greatly amplify the numbers and types of transmutations available. The creation of low-kinetic-energy neutral femto-atoms and femto-molecules allows a long-range selective attraction to radio-active nuclei and thereby provides a means of distributing these newly created transmutants far from their originating site.

One difference between the system of a ‘radioactive nucleus and a femto-atom’ relative to the system of a ‘non-radioactive nucleus and the femto-atom’ has to do with the amount of energy released by the fusion of the two. Another difference between these systems is the excitation level(s) of the components causing the evanescent wave(s) that serve as an attractant to the femto-atoms. A third difference is in the ‘orbital’ frequency of the excited nucleon(s) relative to that of the ground-state nucleons. A fourth difference involves the angular momentum of the different states. These differences are generally related, but not necessarily so.

The second and third differences lead to a most important feature of the model: selectivity of nuclei by the femto-particles. This possibility means that these femto-atoms can be used to produce energy from nuclear transmutations with a minimum of radioactivity resulting. It also gives the possibility for nuclear-waste remediation and, more important for the future, it allows us to tailor elements and isotopes for specific applications.

In addition to having a limitless source of inexpensive, non-polluting energy from cold fusion, humanity will never run short of rare-earth metals.

Appendix A. Evanescent-wave Coupling between Neutral Nuclei

Evanescent waves (or virtual particles) convey no energy unless there is an absorber within its range. What is an absorber? It could be something as simple as a two energy-level system (such as used in [10]).

However, just as there are simple coupled oscillators (such as the atoms in the reference), there are also more complex systems. In the present system, the excited nucleus (one able to decay radioactively) is an obvious 2-level system. The second oscillator is not a 2-level system. The neutral femto atom has a fixed final state, i.e., fusion with the excited nucleus. However, its excited state is related to the distance between it and the radioactive nucleus. Even without knowing the coupling coefficient, we can still look at the potential V for doing work.

Assume any position-dependent potential, $V(r_{ij})$. The force between two ‘actors’ (i and j) creating this potential is related to the potential, $F_{ij} = -dV(r_{ij})/dr$. There is an energy related to this potential. Thus, the second excited-energy level is not a fixed energy; it is a variable, dependent on r . In addition, the system is not strictly an oscillator; but it could be. The major point to be made is that, if there is no possibility of a net energy change, it is a conservative system and the interaction is greatly reduced (but not necessarily zero).

The exchange of virtual photons between two atoms in the ground state is an example of a low-impact interaction. Pion-exchange between a neutron and proton is an example of a high-impact interaction. Both are interactions between ‘identical’ particles. However, the coupling mechanism between them (related to the virtual energy exchanged) is quite different. This also affects the range of the interaction. However, the 2-level oscillators in the identical particles cases are the energy related to the spacing between the particles.

The two distinct energy levels are related in time, before and after, rather than in space. The energy difference between the two cases presented is fractions of an eV versus > 100 MeV. In the latter case, the cause and shape of the nuclear potential is unknown. Nevertheless, use of the internal resonance associated with a virtual-exchange particle, the pion, predicts very well the effective potential between nucleons. The potential shows an ability to do work, to move nucleons and to accelerate them to high energies (by some means, even if unknown).

The system that we are studying is different, but similar enough to provide a model [8–10]. We are not studying identical particles; neither the targets nor the ‘projectiles’ are identical. Therefore, we have sacrificed two major

components of a resonant-energy transfer. On the other hand, we know more about the nature of our proposed energy-exchange fields, the evanescent waves of the bound protons and electrons. These are the Maxwellian near-field EM wave of an oscillating and/or rotating electric dipole.

Appendix B. Near-field Dipole–Dipole Electromagnetic Coupling [10]

For computation, we shall confine ourselves to two adjacent systems (1 and 2), each with two-levels (n & p and m and o). We assume that E_{pn} ($p \rightarrow n$) is larger than E_{om} ($o \rightarrow m$), i.e., the excited-state proton has more energy to lose than the nought-orbit electron can gain. Averaging over all polarizations and angles leads to the effective interaction between two randomly oriented dipoles at a distance R apart in free space. Then, the near-field interaction can be recast as

$$U_{eg}^{NZ}(R) = -\frac{2}{3} \frac{1}{R^6} \frac{|\mu_{mo}(2)|^2 |\mu_{np}(1)|^2}{(|E_{np}(1)| - |E_{om}(2)|) = \Delta E_{12}}, \quad (B.1)$$

where ΔE_{12} is a positive number and μ_{ij} are the matrix elements of the transition-dipole moments.

It is important to note that it could be the frequencies that are more important for this interaction than are the energies. In normal transitions, the bound-electron energy is converted to and from photons (with $E = h\nu$) so that the frequencies are related to the change in energy of the states involved. The $\Delta E_{12} = 0$ satisfies energy conservation and establishes the balances between photon energies and bound-electron levels,

Because of the proximity of the radioactive nuclide and the femto-hydrogen (fractions of a nanometer), the energy transfer may not be via photonic transition. Furthermore, in the presence of the strongly varying local electric fields, the DDL electrons and nearby nuclei may not have well-defined energy levels. Energy must still be conserved, but resonance is key: $\nu_1 \approx \nu_2$ and $\Delta\nu_{12} \approx 0$. Resonance can stimulate emission of energy from an excited state. Since the two oscillators, the excited nucleon and the DDL electron, do not have the same mass, $\Delta\nu_{12} \approx 0$ does not imply that $\Delta E_{12} = 0$ or that E_1 is the same as E_2 . It implies that the frequency of the excited state (nucleon) is the same as that of the DDL electron which electric field would be stimulating it. The equation change necessary to adapt to direct stimulation, rather than to photonic stimulation, is shown in Eq. (B.2). Since the frequencies are of ‘bodies’ rather than photons, the use of Planck’s h to provide the energy base may not be appropriate. A new normalization constant might have to be determined.

$$U_{eg}^{NZ}(R) = -\frac{2}{3} \frac{1}{R^6} \frac{|\mu_{mo}(2)|^2 |\mu_{np}(1)|^2}{h(|\nu_p(1)| - |\nu_m(2)|) = \Delta h\nu_{12}}. \quad (B.2)$$

The important features of (B.2) are the R^{-6} dependence and the resonance established between frequencies of the two oscillators (i.e., $\Delta\nu_{12}$ is small).

Acknowledgment

This work is supported in part by HiPi Consulting, New Market, MD, USA; by a USM International Grant from the Science for Humanity Trust, Bangalore, India; and by the Science for Humanity Trust, Inc, Tucker, GA, USA. I am very appreciative of the support and work that William Collis has provided in the nuclear mass calculations for the femto-hydrogen transmutations of Table 1.

References

- [1] K. Sinha and A. Meulenberg, A model for enhanced fusion reaction in a solid matrix of metal deuterides, in *ICCF-14 Int. Conf. on Condensed Matter Nuclear Science*, 2008, Washington, DC, 2009.
- [2] A. Meulenberg and K. Sinha, Tunneling beneath the $^4\text{He}^*$ fragmentation energy, *J. Cond. Mat. Nucl. Sci.* **4** (2010) 241–255.
- [3] R. Loudon, One-dimensional hydrogen atom, *Am. J. Phys.* **27**(9) (1959) 649–655.
- [4] A. Meulenberg, From the naught orbit to the ^4He excited state, in *Proc. 16th Int. Conf. on Condensed Matter Nuclear Science*, 2011, Chennai, India; and in *J. Cond. Mat. Nucl. Sci.* **10** (2013) 15–29. <http://www.iscmns.org/CMNS/publications.htm> This reference's discussion of the nought orbit and the arguments against it include citations back to 1985. The cited story actually goes back to 1959.
- [5] J. Maly and J. Vavra, Electron transitions on deep Dirac levels I, *Fusion Technol.* **24**(3) (1993) 307.
- [6] R. Rice, Y. Kim, Rabinowitz and Zubarev, Comments on exotic chemistry models and deep dirac states for cold fusion, *Proc. 4th Int. Conf. on Cold Fusion*, Volume 4, Theory and Special Topics Papers, p. 4-1 December 6–9, 1993, Lahaina, Hawaii lenr-canr.org/acrobat/RiceRAcommentsona.pdf
- [7] J. Naudts, On the hydrino state of the relativistic hydrogen atom, <http://arxiv.org/abs/physics/0507193>.
- [8] A. Meulenberg and K.P. Sinha, Deep-electron orbits in cold fusion, *17th Int. Conf. on Condensed Matter Nuclear Science*, Daejeon, Korea, 12–17 August, 2012.
- [9] A. Meulenberg and K.P. Sinha, Deep-orbit-electron radiation emission in the decay from $^4\text{H}^*$ to ^4He , *17th Int. Conf. on Cond. Matter Nucl. Sci.*, Daejeon, Korea, 12–17 August, 2012.
- [10] K. Sinha and A. Meulenberg, Radiative-field quantum-coupling between closely-spaced surfaces, preprint arXiv:0902.0682, 2009.



Research Article

Deep-Orbit-Electron Radiation Emission in Decay from ${}^4\text{H}^{*}\#$ to ${}^4\text{He}$

A.Meulenberg*

Science for Humanity Trust Inc., Tucker, GA, USA

K.P. Sinha[†]

Indian Institute of Science, Bangalore 560012, India

Abstract

The process of nuclear energy transfer to the lattice involves near-field electromagnetic coupling of energy from energetic charged nuclei to deep-Dirac level electrons. From there, the energetic electrons near-field and far-field couple energy into adjacent Pd-bound electrons causing intense local ionization, but no energetic radiation beyond the multi-keV level.

© 2014 ISCMNS. All rights reserved. ISSN 2227-3123

Keywords: Deep-Dirac levels, Near-field coupling, Nuclear radiation, Relativistic radiators

1. Introduction

A major problem in the acceptance of Cold Fusion, CF, by the Nuclear Physics community is the widely accepted claim for CF in the PdD system to be nuclear. The most commonly proposed CF fusion reaction, $\text{D} - \text{D} \Rightarrow {}^4\text{He}^*$ but without energetic-particulate radiation, violates the well-known deuterium-fusion reactions. This apparent contradiction has been demonstrated by the present authors to be a ‘sign-post’ for a model proposed to show how CF can occur without release of energetic radiation [1]. The Lochon Model provided the pathway for deuterons in a palladium (Pd) lattice to overcome the Coulomb barrier that prevented all prior low-energy fusion reactions from occurring [2]. The natural extension of this model was able to identify the means of tunnelling beneath the proton fragmentation level (19.8 MeV above the ${}^4\text{He}$ ground state) to avoid the expected energetic particles [3]. The extended-lochon model also provided a qualitative description of how the nuclear energy (~ 20 MeV) could be transferred from the excited ${}^4\text{He}^*$ (and ${}^4\text{He}^{*}\#$, the excited state with lochon present) to the lattice without destroying it [4]. This paper continues the development of the cold fusion models based on these assumptions by using dissipation of the nuclear energy via direct and EM radiation-coupling to the lattice. β

*E-mail: mules333@gmail.com

[†]E-mail: Kritpsinha@gmail.com

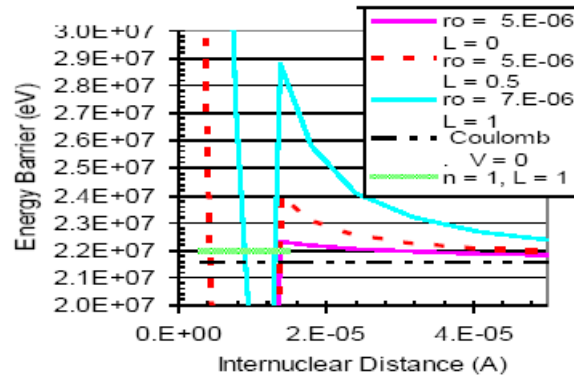


Figure 1. The Coulomb and centrifugal-energy barriers for d-d collision ($l = 0, 0.5$, and 1). The solid curve, with the highest barrier, is for $l = 1$.

Fundamental to these proposed models and their development is the ability of one (or two) electrons to move deeply into the nuclear Coulomb potential and remain there long enough to allow two protons (or deuterons) to penetrate their mutual barrier. A theoretical basis, from the relativistic Dirac equations for actual orbits within fermis of the nucleus has been provided [5] and developed [6]. Figure 1 shows a representative view of the near-nuclear region with energy plotted from the ^4He ground state.

The fuchsia curve ($L = 0$) identifies the Coulomb barrier and nuclear potential well for two protons in a head-on collision (no angular momentum). The dashed line indicates the centrifugal barrier within the nuclear potential well (at ~ 0.4 fm) and the raising of an effective Coulomb barrier through which the hydrogen must tunnel to reach the nuclear well.

For an even higher angular momentum (top, aqua, curve), only a near-circular orbit is possible and a further increase in effective barrier is noted. Higher-energy orbits are not bound. The real potentials for deuterium collisions are not this clean since the neutrons, providing nuclear potential without Coulomb effects, are a major perturbation. The quantum mechanical wave function for a nucleon extends well beyond the 2-fm point and is not strongly affected by the shape of the potential well. The closely bound electrons, on the other hand, are able to follow the protons' motions and thus, over time, are spread well beyond the radius that we will use as an average for both the protons and deep-Dirac level electrons (R_p and $R_{DDL} \approx 1$ fm).

Once non-resonant tunnelling^a has occurred in the proposed D-D fusion process and the excited state, $^4\text{He}^*$, is formed below the fragmentation levels (below 20 MeV, as proposed by the extended lochon model [3]), then the means of dissipating the excess nuclear energy and getting to the ^4He ground state must be considered. The initial process of energy transfer from the excited nucleus to the lattice involves the near-field electromagnetic coupling [7] of energy from the energetic charged nuclear dipoles to tightly confined (~ 1 fm) electron dipoles (possibly in deep-Dirac levels, DDLs [5]). From there, the energetic electrons near-field-couple energy into the adjacent Pd-bound electrons and cause intense local ionization. Because of the 0.5 MeV binding energy of a DDL electron and its extreme proximity to the charged nucleus, significant radiant-energy transfer is possible, both into the DDL electrons and, from there, into the atomic electrons. However, since no resonances other than the Pd atomic-electron binding energies are obvious, no energetic radiation beyond their keV level is expected from this process. The lack of any nuclear-energy levels below the proton fragmentation level, the steady loss of nucleon energy to the DDL electron(s), and their disturbing presence

^aThe reduced tunneling probability of non-resonant tunneling is compensated by the greatly reduced tunneling distance of the model.

in the nuclear region, prevent formation of any semi-stable nuclear orbits required for creation of energetic gamma rays. This paper seeks to better describe and quantify the proposed decay process and to identify the conditions and limits required to permit stable and efficient conversion processes from nuclear energy to thermal energy in the lattice via DDL electrons. In particular, it will describe the near-field EM coupling that will take place within the nuclear region of these ‘femto-atoms’ (a nucleus with an electron bound at the deep-Dirac level). While nucleon dipole coupling has been well studied [8], the coupling of nucleons with tightly bound electrons and from there with nearby lattice electrons may be new.

2. Near-field Coupling: DDL Electrons to Atomic Orbital Electrons

Radiant nuclear energy transfer first involves near-field electromagnetic coupling of energy from the energetic charged nuclear dipoles to tightly-confined electron dipoles (in nought orbits or deep-Dirac levels [6]). These energized electrons subsequently near-field-couple energy into adjacent Pd-bound electrons, thereby causing intense local ionization. However, they produce little energetic radiation beyond the multi-keV level of the inner Pd electrons. This far-field photonic-radiation process is closer to what we may be familiar with, so we begin our analysis with the relativistic radiated-electric field^b of the DDL electrons at the Pd atomic electrons.

$$E(x, t) = e \left(\frac{n - \beta}{\gamma^2(1 - \beta \cdot n)^2 R^2} + \frac{n \times [(n - \beta) \times \dot{\beta}]}{c\gamma^2(1 - \beta \cdot n)^2 R} \right)_{ret} \quad (1)$$

The β and $\dot{\beta}$ ($= \beta$ dot) terms are the source velocity and acceleration, respectively, divided by the velocity of light, c . R is the distance along the unit vector n between the source and ‘test’ or target positions and $\gamma = 1/\sqrt{(1 - v^2/c^2)}$. All of these are at the ‘retarded’ time position, which does not enter into the present picture. An important part of Eq. (1) is the relative weight of the two terms from a common nuclear-proton source. The first is the electrostatic Coulomb field modified for relativistic velocities of the radiating charge. The second is the radiation field that depends on both relativistic velocity and charge acceleration ($a = F/m$ or $\dot{\beta} = F/mc$). The radiation field, for our purposes is divided into the near-field (fields at approximately the same distance as the emitted wavelength) and the far-field (fields much greater than the emitted wavelength).

Figure 2 identifies three regions of electron resonance in the hydrogen atom. The atomic orbitals (radius in the angstrom range $= R_a$) are known and accepted. The deep-Dirac levels (radius in the low fermi range $= R_{DDL}$) are predicted by the relativistic Schrodinger, the Klein–Gordon, and the Dirac equations. They have not been recognized yet, except within CMNS. They are in the region of nucleon motion and of halo nuclei.^d The Compton resonance (radius in the 380 fm range, but not discussed here), related to the electron mass energy equivalence and wave nature, is not explicitly found in the Schrodinger formulation of quantum mechanics. Nevertheless, one of the present authors has suggested it as a resonance (to explain Zitterbewegung) and it is proposed and suggested in the literature [9].

The primary energy storage and exchange mechanisms discussed in this paper are those of the protons and DDL electrons in the nuclear region and the coupling between these levels and those of the atomic electrons. The Compton resonance is only suggested as a transition point between the collision-dominated and photonic-radiation-dominated energy-exchange regimes. Note the five orders of magnitude between the proton and DDL electron motion and dipole moments and those dimensions of the atomic and neighbouring electrons.

We will first compare the radiant \mathbf{E} field of the non-relativistic ($\gamma = 1$) atomic electrons (second term of Eq. (1)) relative to the proton and atomic-electron Coulomb fields (first term of Eq. (1)) at the bound atomic electrons. In (2),

^bhttp://en.wikipedia.org/wiki/Li%C3%A9nard%E2%80%93Wiechert_potential#Corresponding_values_of_electric_and_magnetic_fields^c

^dhttp://en.wikipedia.org/wiki/Halo_nucleus

the ratio of the two terms eliminates the velocity effect and only leaves a comparison between the atomic electron's orbit radius and, strangely enough, its classical radius. At atomic distances;

$$\begin{aligned} \frac{\text{atomic Coulomb term}}{\text{atomic EM radiation term}} &= \frac{1/R_a^2}{\dot{\beta}/R_a c} = \frac{c}{R_a F/mc} = \frac{mc^2}{R_a(e^2/R_a^2)} = \frac{R_a}{R_c} \\ &= \sim \frac{10^{-10}}{2.8 \times 10^{-15}} = 3.5 \times 10^4, \end{aligned} \quad (2)$$

where R_c is the classical electron radius ($R_c = e^2/m_e c^2 = \sim 2.8$ fm), F/mc is the atomic-electron acceleration from the Coulomb field, and R_a is the atomic-electron orbital radius (~ 0.1 nm). The latter is the radius for the acceleration term of the atomic electrons and a rough figure for the inter-electron distances. This indicates that the radiation **E**-field strength between atomic electrons is only a small fraction of the Coulomb field between the electrons or between the electrons and nucleus. How does the radiation field from the DDL electron at the atomic orbits compare with the Coulomb field from the proton?

Two differences between the DDL-electron and the proton or atomic-electron Coulomb and radiation fields in Eq. (1) are in the factors of γ and β . For the relativistic DDL electron, they are 2–3 and ~ 0.9 , respectively. The relativistic contribution from these terms is to multiply the maximum Coulomb and radiation field by an order of magnitude. This comes from $(n - \beta)/\gamma^2(1 - \beta \cdot n)^3$ where the maximum magnitudes give the particular relativistic correction $\Re = \sim (1 - 0.9)/3^2(1 - 0.9)^3 = \sim 11$.

Making a comparison of the Coulomb binding of an atomic electron relative to the maximum far-field radiation (assume distance $R_a = 0.1$ nm) from the relativistic DDL electrons (for $\gamma = 3$ and relativistic correction $\Re = 11$), we get (3):

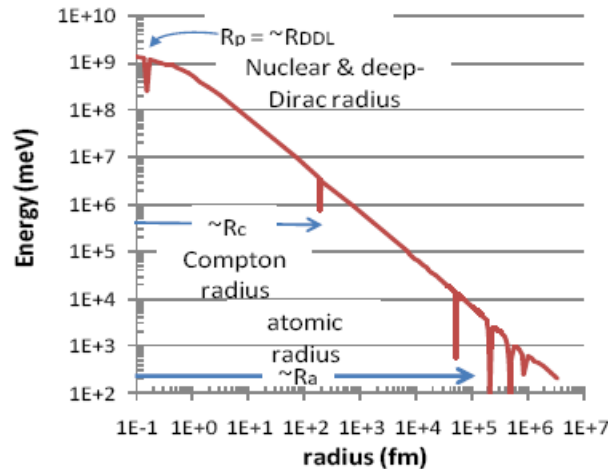


Figure 2. The bound-electron energy levels for hydrogen as a function of radius from the center of force.

$$\begin{aligned}
\frac{\text{Proton Coulomb}}{\text{DDL EM far-field}} &= \frac{1/R_a^2}{(n-\beta)\dot{\beta}_{\text{DDL}}/\gamma^2(1-\beta \cdot n)^3 R_a c} = \frac{\gamma m c^2}{\Re R_a (e^2/R_{\text{DDL}}^2)} \\
&= \frac{R_{\text{DDL}}^2}{11 R_a R_c} = \frac{\sim 0.27(10^{-15})^2}{10^{-10} \times 2.8 \times 10^{-15}} \sim 10^{-6}.
\end{aligned} \tag{3}$$

In this case, the DDL-electron radiated-field strengths are orders-of-magnitude larger than that of the atomic-electron, the nuclear Coulomb, or even the DDL-electron Coulomb fields. The distances from the DDL electrons to the local atomic electrons and to the deeper Pd-bound electrons of the adjacent Pd nuclei are not much different. The distances to the nearby lattice atoms are only factors of 2–4 greater. This could mean that, if screening were ignored, (3) indicates that ionization could take place hundreds of lattice sites from a DDL electron. This is clearly not observed; so either DDL electrons do not exist (the standard response), the calculation is wrong, or something else interferes with the ionization process. Assuming the last, what can prevent total ionization near a DDL electron?

Actually, several things prevent total local ionization. First, the relative frequencies of the DDL and atomic electrons mean that the interaction probability is very high; but the ability to transfer energy is very low (as much energy is taken away as is added in each cycle). It is not possible to have the uncompensated $1/2$ cycle (or portion thereof) required for net energy transfer. The relative frequencies ν are $\sim 10^{16}/\text{s}$ for atomic electrons vs. $\sim 10^{22}/\text{s}$, in (4), for DDL electrons.

$$v_{\text{DDL}} = \frac{0.9c}{2\pi r_{\text{DDL}}} = \frac{0.9 \times 3 \times 10^8 \text{ m/s}}{3 \times 10^{-14} \text{ m}} = \sim 10^{22}/\text{s}. \tag{4}$$

With 5–6 orders of magnitude difference in frequency, if the far-field radiation from the DDL electron gives the electron enough energy for ionization during one-half cycle, it takes it back during the next half. This is why an energetic gamma ray can go through matter with little ionization along its path. On the other hand, gamma rays *do* cause some ionization in matter. Therefore, an excited DDL electron, which produces the equivalent of a standing-wave gamma ray, can still cause ionization from interactions in the small volume about its femto-atom.

Since this frequency difference is a major limitation in the energy transfer to atomic electrons, it is worth exploring it further. Photons have a diameter of $\lambda/2\pi$ [10]; therefore, gamma rays, with wavelengths comparable to nuclear dimensions, have only small interaction with electrons in matter. DDL electron orbits are of similar dimensions. Therefore, only if an electron comes close enough to a femto-atom (within 10s of fm) for direct interaction (net fractional EM cycle) will significant energy transfers become possible. The differences between a gamma ray and the DDL electron near-field is that the gamma ray is transient, but it traces out a path through matter. The DDL field is long-lived, but has only a small interaction volume. However, since the atomic electron density gets higher as the femto-atom approaches a lattice nucleus, and more electrons means more energy exchange and more lowering of the excited femto-atom's energy, there is an attractive force ($F = -dV/dr$) that draws femto-atoms to nuclei.

The second reason that total ionization does not occur over large volumes is the screening effect of the bound and free electrons in the lattice. The calculated Debye length, which has been used in an attempt to allow penetration of the proton–proton Coulomb barrier for cold fusion, now becomes the factor that prevents massive disruption of large volumes in the lattice.

The third reason why the DDL electrons do not radiate all of their energy away and collapse into the nucleus is the same reason that the atomic ground states do not radiate away their energy and drop into the nucleus or into the DDLs. The answer is not the standard QM statement that the electron is at an energy minimum. The ground state is like all other orbitals; it is a minimal, a *local* minimum, not a general minimum. However, there is insufficient angular momentum in the ground state and below to create photons. A transition with $0 \Rightarrow 0$ angular momentum transfer is highly forbidden.

What prevents a 2-p electron, which does have enough angular momentum to form a photon, from dropping to the DDLs? There are three reasons:

- (1) there is the 10^6 -frequency difference between the DDLs and atomic orbitals mentioned earlier;
- (2) if there is a vacant s-orbital at closer to the same energy (frequency), the 2-p electron will go there, not to a DDL;
- (3) if there are no unfilled atomic orbitals below a p-electron, then the EM fields (standing waves) from the deeper atomic electrons prevent the higher-orbit electrons from losing energy.

Likewise, the DDL electrons are at a local minimum. However, because the Coulomb potential is no longer proportional to $1/r$ within the nucleus, because of the centrifugal barrier at small r , Fig.1, and because of relativistic effects, the DDLs may actually *be* at an energy minimum, not just a minimal point.

3. Near-field Coupling: Protons to DDLs

Protons, being more massive than electrons, have much less acceleration when exposed to the same \mathbf{E} field as an electron. This factor of $\sim 1800\times$ is the reason that we can normally ignore radiation from protons. However, we know that nuclear protons in a compound nucleus can generate very energetic gamma rays. We also know that the deep nuclear potential well (for ${}^4\text{He}$, $V \sim 80$ MeV?) can cause great acceleration of the protons. And, while the exact shape of the potential well has little effect on the nucleon's wave functions, it does have an impact on the magnitude and type of radiation fields that it produces.

Going back to (1) for this new situation, we can do the same as we did for the atomic electrons. If we use the equivalent of (2) for Coulomb binding of a DDL electron to, and the radiation from, a nuclear proton, assuming it to be bound by a $100\times$ Coulomb potential ($F_p = 100 \times F_{\text{DDL}}$, for ease of calculation by similarity) with another proton in a ${}^4\text{He}$ nucleus, we obtain a ratio for the forces. This calculated ratio for the protons' effects on a DDL electron using $R_p = R_{\text{DDL}} \sim R_c/3$ is

$$\begin{aligned} \frac{\text{p Coulomb}}{\text{p radiation}} &= \frac{1/R_{\text{DDL}}^2}{\dot{\beta}_p/R_p c} = \frac{c}{R_{\text{DDL}} F_p / m_p c} = \frac{m_p c^2}{R_{\text{DDL}} 100 F_{\text{DDL}}} \\ &= \frac{m_p c^2}{R_{\text{DDL}} (100 e^2 / R_p^2)} \sim \frac{m_p R_p}{300 m_e R_{\text{DDL}}} \sim 6. \end{aligned} \quad (5)$$

The central attraction of the nuclear potential for the proton, or the Coulomb attraction between the proton and DDL electrons, is again greater than the maximum radiant fields that the proton can generate at its limited location relative to the center of attraction. Thus the proton-generated EM-field at the DDL electron(s) will not be sufficient to overcome the Coulomb attraction by direct interaction. This provided another 'sanity check' for the DDL electron model.

What effect does our assumption of a $1/r$ potential have on the calculation for maximum radiation field strength? It provides a lower limit for the term. The value used for the acceleration term in (5) assumed a circular orbit. If it were not circular, the maximum radiation would be at the minimum radius and that could be a fraction of the 1 fm used. However, it cannot be a small fraction since the repulsive nuclear 'hard-core' would prevent that. The DDL electron would normally be in a near-circular orbit (perhaps as a rosette). Since it is tightly bound to a proton, it can transit a compound nucleus and perhaps even penetrate deeply into a proton. Radiation under these circumstances gets complicated. The result of (5) is large enough that the order-of-magnitude variations in the various near-nuclear R 's will not alter the conclusion of Coulomb forces greatly exceeding the proton radiation forces.

How does the proton's Coulomb field strength at the Pd-electron orbits compare with the Coulomb and EM-field strengths at and from the DDL electrons? The proton and electron Coulomb fields are similar in the DDL region.

However, the electron has a contribution from its relativistic velocity that affects both the radiation field and its effective mass, $\mathfrak{N} = 11$ and $\gamma = 3$. We will, consider the larger of the two Coulomb fields. If we do a similar exercise as in (5) above for the relativistic DDL electrons ($\gamma = 3$), \mathfrak{N} cancels out and we see (6):

$$\begin{aligned} \frac{\text{DDL Coulomb}}{\text{DDL near field}} &= \frac{1/R_{\text{DDL}}^2}{\dot{\beta}/R_{\text{DDL}}c} = \frac{c}{R_{\text{DDL}}F_{\text{DDL}}/\gamma mc} = \frac{\gamma mc^2}{R_{\text{DDL}}(e^2/R_{\text{DDL}}^2)} = \frac{\sim 3R_{\text{DDL}}}{R_c} \\ &= \frac{\sim 3 \times 10^{-15}}{2.8 \times 10^{-15}} = \sim 1. \end{aligned} \quad (6)$$

In this case, the radiated-field strength of a relativistic DDL electron at the nucleus or at another DDL electron is of the same order-of-magnitude as its Coulomb field, and ~ 4 times greater than the Coulomb field of a non-relativistic proton at the DDL. This could cause serious perturbation, or major resonances, if more than one DDL electron is present. However, the spin-spin coupling – not included here – would likely dominate in this range.

4. Relative Field Strengths: of Protons at DDL Electrons vs. that of DDLs at Atomic Electrons

This section addresses the relative field strengths radiated from excited nuclei and measured at DDL electrons to those radiated from excited DDL electrons and measured at atomic and free electrons in the vicinity. This provides a basis for determining the flow of excited-nucleus energies into the lattice.

Even though the nuclear-proton radiated **E**-field strength at the deep-Dirac orbit $R_{\text{DDL}} = R_p$ is less than its Coulomb field strength there (5), it is still much greater at the near field than the radiant field of a DDL electron at an atomic electron's orbit R_a (7).

$$\begin{aligned} \frac{\text{DDL far-field}}{\text{p near-field}} &= \frac{\dot{\beta}_{\text{DDL}}/R_a c}{\dot{\beta}_p/R_{\text{DDL}}c} = \frac{\mathfrak{N}R_{\text{DDL}}m_p}{R_a\gamma m_e} = \frac{11R_{\text{DDL}}m_p}{R_a\gamma m_e} \\ &= \frac{11 \times 10^{-15}}{10^{-10}} 600 = \sim 7 \times 10^{-2}. \end{aligned} \quad (7)$$

Therefore, the protons should be able to transfer energy more easily to the DDL electrons than the DDL electrons can to the Pd-bound electrons. However, if this is so, could the protons not also transfer energy directly to the atomic electrons, even if no DDL electrons were present? The large ratio of DDL-electron to proton energy transfer to atomic electrons with $R_{\text{DDL}} = \sim R_p$, (8) is indicated by the large difference in effective EM-field strengths ($6700\times$).

$$\frac{\text{DDL far-field}}{\text{p far-field}} = \frac{\mathfrak{N}\dot{\beta}_{\text{DDL}}/R_a c}{\dot{\beta}_p/R_a c} = \frac{11m_p}{\gamma m_e} = \sim 6700. \quad (8)$$

Nevertheless, when compared with (3) the maximum proton radiant force is still $\sim 130\times$ greater than the Coulomb force holding the atomic electrons to the adjacent Pd nuclei. Why does not the radiant **E**-field eject all the local atomic electrons? The reason is that, because of the extremely high nuclear frequencies relative to the electron orbital frequencies, the electrons are pulled back into their original orbit (or lower) before they can escape. The net force of a very high-frequency field on a bound electron is zero. Only if the DDL **E**-field is instantaneously in proper phase with an atomic s-orbit electron, so that it can move the atomic electron during its transit of the nuclear region, can net energy be directly transferred from a DDL electron to an atomic-orbit electron.

While the proton far-field forces are much less than those provided by the DDL electrons, the non-excited-proton frequencies are much closer to those of the Pd electrons, particularly of the keV-range inner electrons. Therefore, the

excitation of atomic electrons by the proton radiation still needs to be considered. Nevertheless, the large difference in energy levels for the inner electrons makes them less susceptible to excitation by the still higher-frequency proton radiation fields.

5. Decay Rates of $^4\text{He}^*$ to the Ground State

This section extends the last section where the field *strengths* were considered and addresses the relative energy transfer *rates* from excited nuclei to DDL electrons as compared to those from excited DDL electrons to atomic and free electrons in the vicinity. If the energy transfer were dependent on field strength alone, then the near-field energy transfer from the protons to the DDL electrons would always be much faster than the electrons can transfer energy to the far-field bound Pd electrons. Therefore, the excited nuclei should deliver enough energy to the DDL electrons to eject them almost immediately despite their high binding energy (~ 500 keV). What prevents this from happening? How does energy actually transfer from the nuclear potential to the lattice? Why does it not happen with normal (unexcited) nuclei?

As energy is transferred from the excited protons to the DDL electrons, the electrons move out of their meta-stable orbit to higher levels within the Coulomb potential. As they rise in the potential well, their orbital radius, R_p in (7), also increases. Consequently, the ratio of proton to electron energy transfer changes. However, as seen in (1), the dependence is not entirely as might be expected.

The field strength at the excited DDL electrons from the protons depends on the distance between charges (R_{DDL}^{-1}); but the field strength generated by the DDL electrons depends on their acceleration, $a = F_{\text{DDL}}/m = e^2/R_{\text{DDL}}^2/m$, hence the orbital radius squared (so R_{DDL}^{-2}). Furthermore, as the excited DDL electrons move out with the newly added nuclear energy, they slow down and lose the relativistic component, $\mathfrak{R} = 11$, of their radiation field. This means that, as the DDL-electron increases its orbital radius, its radiation fields decrease faster than does the proton radiation field at that location.

The nuclear-proton radiated E-field strength at an expanded deep-Dirac orbit (e.g., $R_{\text{DDL}*} \approx 400R_p$) is still less than its Coulomb field at that point – substitute $R_{\text{DDL}*}$ for R_{DDL} in (5). It is also much greater at that point than is the radiant field from an excited DDL* electron measured at an atomic-electron's orbit R_a , (9). Therefore, the ratio of EM field strengths from nuclear-to- $R_{\text{DDL}*}$ (p mid-field) to the DDL* radiant fields at atomic distances (in the DDL* far-field) actually increases as the DDL electrons move out under the influence of the EM fields of excited proton(s). Thus, we must look beyond this simple algorithm to determine the actual energy-transfer rates.

$$\begin{aligned} \frac{\text{DDL* far-field}}{\text{p mid-field}} &= \frac{\dot{\beta}_{\text{DDL}*}/R_a c}{\dot{\beta}_p/R_{\text{DDL}*} c} = \frac{R_p^2 R_{\text{DDL}*} m_p}{R_{\text{DDL}*}^2 R_a m_e} = \frac{R_p m_p}{400 R_a m_e} \\ &= \frac{\sim 10^{-15}}{4 \times 10^{-8}} 2000 \approx 5 \times 10^{-4}. \end{aligned} \quad (9)$$

As an example, let us give the DLL electron sufficient energy to raise its orbit from $R_{\text{DDL}} \approx 1$ fm, with a binding energy of 507 keV, to $400R_{\text{DDL}}$, with a binding energy in the low keV range. Its initial kinetic energy of ~ 1 MeV is decreased to ~ 4 keV. Its initial potential energy of ~ 1.5 MeV is decreased to ~ 8 keV.^e What has happened to this deep-orbit electron? It is still 'deep', just not as deep as it was initially.

As the DDL electron orbit grows with energy fed from the nuclear proton(s), its interaction volume grows too. In the example chosen ($R_{\text{DDL}*} = 400R_p$), the interaction volume with transiting bound electrons has increased by $\sim (400)^3 > 1 \times 10^7$. This increase in interaction volume is the first step in the dissipation of excited-nuclear energy. Until, or

^eThese are back-of-the-envelope calculations, since there are no steady state values and calculations involve relativistic electrons. Values that are more accurate will have to be provided later.

unless, the femto-atoms drift close to a lattice atom, the primary source of collisions is with the numerous Pd d-orbital electrons. These are more likely to get within range of the DDL* electrons and have less binding energy. Therefore, they are the best means of transferring energy from a DDL* electron to the lattice.

As the excited DDL electron slows down and its orbital frequency decreases with expanding orbit with energy fed from the nuclear proton(s), it now has orbital frequencies closer to that of photons with the resonant energies of the Pd inner orbital electrons. It also has a dipole moment that may have increased by two orders of magnitude and, since the photo-transition probability increases with the square of the dipole moment [11], both effects greatly feed photonic energy coupling between the DDL electrons and the lattice electrons.

A DDL electron has always had sufficient energy and field strength to ionize nearby atomic electrons; but now it has near-field resonant coupling and a larger dipole moment with which to work. The energy transfer between excited DDL electron and atomic electrons may go up by many orders of magnitude. The dominant transfer mechanism has changed from collision mode to photonic radiation mode. However, the latter is still dependent on the former. Only by collisions can the DDL* electrons obtain the angular momentum necessary for photon emission. On the other hand, it may be possible for double-photon emission from the intense EM fields to satisfy those requirements. However, it is not likely that this would be a major source of energy transfer.

The additional energy drain may still not be sufficient to keep up with the nuclear energy being fed to the excited DDL electron(s) – perhaps because the equilibrium population of the Pd inner electrons is depleted faster than they can be refilled. The excited DDL electron would then gain more energy from the excited proton(s), expand its orbit further, and slow its orbital velocity. It would thus be able to produce photons with lower frequencies. These lower frequencies are resonant with the much higher population of p- and even d-orbital Pd electrons of the $n = 2$ and 3 orbits.

If the process continues, with the stimulated DDL electrons getting pushed further from the ${}^4\text{He}^*$ nucleus, their orbital frequency decreases further and the photons generated are able to penetrate deeper into the local plasma being generated by the intense local ionization. This plasma actually reduces the Debye length and therefore the non-photonic EM field strength about the femto-atom. At some point in this process, the DDL electron frequency will drop below that of the excited nucleons and the rate of energy transfer between them will decrease greatly. Energy transfer between the excited nucleus and the lattice will now be limited by the emission rate of the DDL electrons and that, in turn, will depend on the DDL electron(s) acquiring sufficient angular momentum to form photons.

Since the strong EM fields convey information about the excitation state of the femto-atom and its nucleus, they also provide a basis for attraction and selectivity of radioactive nuclei relative to stable nuclei. A similar mechanism provides selectivity in the attraction of ground-state femto-atoms by radioactive nuclei [12]. This relative variation in the exchange of EM energy between bodies is a known variation on the Casimir effect.^f Therefore, while the DDL electron provides a means for dissipating energy of excited nuclei, it also is the means of, and basis for selective, transmutation.

6. More Representative Numbers

As an example of the desired quantitative results, consider the $\text{D} + \text{D} \Rightarrow {}^4\text{He}$ nuclear energy of ~ 24 MeV to be distributed into an average 5 eV Pd d-orbital electron ionization to the conduction band. This implies $\sim 5\text{E}6$ ionizations. Assuming that the vacant d-orbital is refilled from the conduction band and adjacent d-orbitals within a picosecond and that there are, on average, four d-orbital electrons close enough for rapid energy transfer, then a decay time of ${}^4\text{He}^*$ to ${}^4\text{He}$ of more than a microsecond would not cause any damage to the lattice. However, to attain the ‘magic’ number of 1×10^{-12} fusions per second, to produce a watt of thermal energy, this would require a steady level of 1×10^6 actively decaying ${}^4\text{He}^{*}\text{###}$ nuclei. If there were $1 \times 10^{14}/\text{cm}^2$ surface Pd atoms of material and only one in a million were part of a nuclear

^fhttp://en.wikipedia.org/wiki/Casimir_effect#Analogies_and_the_dynamic_Casimir_effect^g

active environment (NAE) consisting of 100 Pd atoms, then the NAEs could be continuously productive at a rate of 1 W/cm² and still be at 1/10 the lattice-damage level.

7. Summary

Bound-radiation field strengths are an important part of the ⁴He* nuclear-energy transfer dynamics. The near-field radiation from the excited protons in a newly fused D–D pair is very strong at the deep-Dirac levels (DDLs). Only the 0.5 MeV binding energy of the electron(s) and the difference in frequencies between the DDL electrons and excited nucleons keep them from being immediately ejected. The far-field radiation from these relativistic DDL electrons is much stronger than that from the excited protons. However, the recipients of those energies, the atomic-orbital electrons, are generally orders of magnitude further away from these energy sources than are the DDL electrons and therefore less able to receive this energy. Thus, to first order, a nuclear proton can transfer energy to its DDL electron much faster than the electron can transfer it out to atomic orbital electrons. The major means of energy transfer from the DDL electrons in the early stages of ⁴He* decay to ground state is by direct collision (near-field interaction) or instantaneous phase coupling of atomic and DDL electrons.

With more energy coming from the protons than can be dissipated and by direct interactions with the transiting bound Pd electrons, the DDL electrons can pick up sufficient energy and angular momentum to radiate photons as well as producing bound EM fields. The very energetic electrons, with their expanding orbits and therefore larger dipole moments, can then radiate much greater average energy per unit time (photonicallly) than possible by direct collisions or off-resonant EM stimulation. Since the photonic emission rises rapidly as the DDL* electron orbit increases and orbital frequency approaches that of the numerous Pd-d electrons, it is unlikely that the femto-atom will eject their electron(s) without some abrupt change in the local system. Thus, a balance is established between the proton and DDL-electron, radiant-energy transfer. This is maintained until the protons get low enough into the ⁴He potential well that resonant exchange between the protons and DDL* electrons overwhelms the electron binding energy and the DDL* electron(s) are ejected. This leaves the ⁴He* atom in a slightly excited state from which proton radiation can bleed off energy into the Pd electrons to reach the stable ground state.

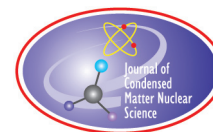
Acknowledgment

This work is supported in part by HiPi Consulting, New Market, MD, USA; by a USM International Grant from the Science for Humanity Trust, Bangalore, India; by the Science for Humanity Trust Inc., Tucker, GA, USA, and by the Indian National Science Academy.

References

- [1] A. Meulenberg and K. Sinha, New visions of physics through the microscope of cold fusion, in *17th Int. Conf. on Cond. Matter Nucl. Sci. (ICCF-17)*, Daejeon (Korea), 2012a.
- [2] K. Sinha and A. Meulenberg, A model for enhanced fusion reaction in a solid matrix of metal deuterides, in *ICCF-14 Int. Conf. on Condensed Matter Nuclear Science*, 2008, Washington, DC. (USA), 2008, Vol. 2, pp. 633–638.
- [3] A. Meulenberg and K. Sinha, Tunneling beneath the ⁴He* fragmentation energy, *J. Cond. Mat. Nucl. Sci.* **4** (2010) 241–255.
- [4] A. Meulenberg, From the naught orbit to the ⁴He excited state, in *16th Int Conf on Cond Matter Nucl Sci (ICCF-16)*, Chennai, India, 2011.
- [5] J. Maly and J. Vavra, Electron transitions on deep Dirac levels I, *Fusion Technol.* **24**(3) (1993) 307.
- [6] A. Meulenberg and K. Sinha, Deep-electron orbits in cold fusion, in *17th Int. Conf. on Cond. Matter Nucl. Sci. (ICCF-17)*, Daejeon, Korea, 2012c.
- [7] K. Sinha, A. Meulenberg and P. Hagelstein, Quantum-coupling between closely-spaced surfaces via transverse photons, *Arxiv preprint cond-mat/0606184*, 2006.

- [8] W.S. Veeman, Nuclear magnetic resonance, a simple introduction to the principles and applications, *Geoderma* **80** (3–4) (1997) 225–242.
- [9] J. Naudts, On the hydrino state of the relativistic hydrogen atom, *Arxiv preprint physics/0507193*, 2005.
- [10] A. Meulenberg, Appendix A of “Creation and fusion of photons,” Paper 8121-29, SPIE Optics + Photonics 2011, Conference 8121 The Nature of Light: What are Photons? IV, 21–25 August 2011, San Diego, CA, USA.
- [11] K.P. Sinha and A. Meulenberg, Radiative-field quantum-coupling between closely spaced surfaces, <http://arxiv.org/abs/0902.0682>.
- [12] A. Meulenberg, Femto-atoms and transmutation, in *17th Int. Conf. on Cond. Matter Nucl. Sci. (ICCF-17)*, Daejeon, Korea.



Research Article

Deep-electron Orbits in Cold Fusion

A. Meulenberg *

Science for Humanity Trust Inc. Tucker, GA, USA

K.P. Sinha

Department of Physics, Indian Institute of Science, Bangalore 560012, India

Abstract

The lochon models of cold fusion, among others, propose deep-energy electrons as necessary for low-energy nuclear reactions (LENR). Relativistic Schrodinger equations, e.g., the Klein–Gordon (K–G) and Dirac equations, have ‘irregular’ solutions that predict such levels at ~ 500 keV. The basis for such a level and its implications are presented.

© 2014 ISCMNS. All rights reserved. ISSN 2227-3123

Keywords: Deep-Dirac levels, Femto-atom, Irregular solutions, Klein–Gordon

1. Introduction

One theory of cold fusion, CF, based on the lochon (a local charged Boson, e.g., paired-electrons) and the model’s extension into the nucleus have proposed deep-energy electrons as the active agent in producing a fusible result. While the model does not require stable electron orbits to mediate the fusion of colliding hydrogen nuclei, the existence of such orbits would support the deep-energy-electron portion of the lochon models, would increase the fusion probabilities, and would explain other results observed in CF experiments.

The Schrodinger equation is made relativistic in two forms: the Klein–Gordon (K–G) equation for spinless particles and the Dirac equation for spin-1/2 particles. These pairs of equations each have two solutions. In each case, for the $1/r$ Coulomb potential, one of the two equations has been rejected for various reasons (primarily having to do with the singularity at $r = 0$). In the rejection of these solutions, recognition of the existence of very-deep (~ 500 keV) electron orbits has been lost.

Details and implications of the single-electron deep-orbits predicted by the ‘anomalous’ K–G and Dirac models are described below in terms of binding energy and electron orbital radius. The assumed applicability of both models to the lochon models is explained in terms of the tightly bound lochons (Bosons), and electrons (Fermions). The lochon model, for successful cold fusion, depends on the spatially paired electrons remaining together for as long as possible

*E-mail: mules333@gmail.com

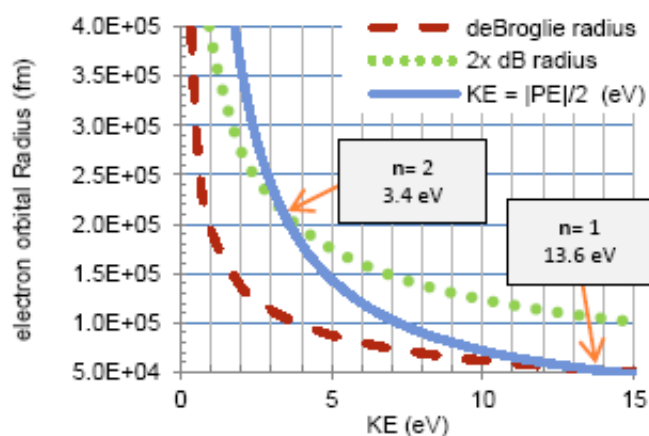


Figure 1. First two atomic orbitals (of many) associated with the common points of integer de Broglie radii (momentum based) and kinetic energy.

during the H–H collision process. The normally rejected K–G solution would allow the decay from a filled 1s orbital (e.g., the lochon in an H^- ion) to the boson-occupied nought orbit. The anomalous Dirac equation solution would allow deep-orbit electrons to combine two protons in fusion or a molecule.

Two multi-femtometer-spaced hydrogen atoms, as a femto-molecule, would share the electron(s). The transition pathways and probabilities for both possibilities must be explored. Cold fusion results provide experimental evidence for the proposed deep-orbit and their theoretical basis comes from relativistic quantum mechanics. The consequences for hydrogen of such transitions are indicated below and implications for transmutations are explored in other papers [1].

2. Resonances

What are electron orbitals? They are resonances; in some respects standing waves. In the case of atomic orbitals, they are orbits in which the electron de Broglie wavelengths are ‘completed’ within the cycle about the nucleus. This means that it is in the identical condition (position, energy, momentum, spin, etc.) at the same point in every cycle. This is an energy minimal point and, therefore, more stable than adjacent points. Figure 1 indicates this ‘resonance’ by having the known orbitals identified with the crossing of the electron’s kinetic energy and the deBroglie radius that gives one-half the potential energy required to give the kinetic energy. This is a stable configuration according to the virial theorem.

There are other stable configurations. Figure 2 shows some of these related to the kinetic energies associated with the Compton radius and de Broglie radius (small boxes). The large box includes common solutions (and large uncertainty) with the classical electron radius with and without relativistic correction. These last solutions are the ones that represent the deep-electron orbits predicted by the K–G and the Dirac equations.

3. Nought Orbits

A deep atomic orbital at a binding energy of about mc^2 is predicted from one solution of the K–G equation [2]. Earlier studies of the relativistic 1-D hydrogen atom [3], of a normally rejected solution to the Schrodinger equation [4], and in an independent development [5], had predicted a similar deep orbit (in some cases infinitely deep [3]). The deep-orbit

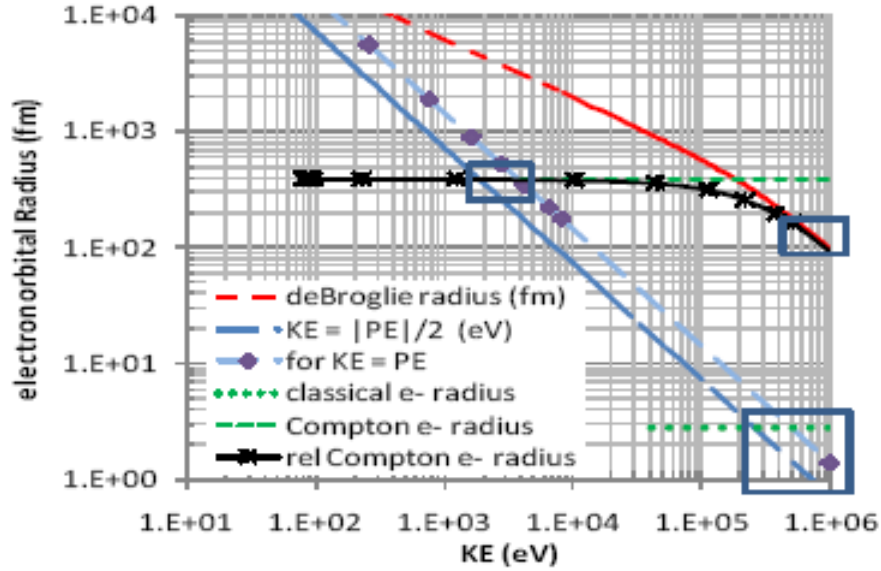


Figure 2. Possible atomic orbitals associated with the common points of de Broglie, Compton, and classical radii with higher kinetic energies.

solution of the K–G equation has been rejected by other authors [6,7] as: being from an equation that is not applicable to particles with spin, being non-square integrable, and being singular at the origin (and therefore not normalizable). Thus, by their definition, it cannot be applied to an electron and it could not be real even if it did pertain. Nevertheless, the same K–G model predicts two sets of energy levels. One set is ‘acceptable’ (even without considering spin) because it provides levels consistent with known values for bosons (e.g., pions) and is not singular. The other set is ‘unacceptable’ because, along with predicting the known atomic-electron levels to within milli-electron volts, it predicts a level at >500 keV that has not been observed.

The deep-orbital level predicted by the K–G equation is far below the $n = 1$ level, so we will call it interchangeably the $n = 0$, or ‘nought’, or ‘naught’ level. Some of its predicted properties (and problems?) are provided in Eqs. (??) and (??) (the fine-structure constant $\alpha \approx 1/137$). The total nought-orbit energy, TE_0 , equals the mass energy plus the binding energy ($E_b = \text{potential energy} - \text{a negative value} + \text{the kinetic energy}$). Therefore, the binding energy of the orbit (a negative value for an attractive potential and a single charge without spin) is $E_0 - m_0c^2$ and the proposed nought-orbit values from the K–G equation are:

$$TE_0 \cong m_0c^2\alpha \cong 3.7\text{keV} \Rightarrow \text{binding energy} = E_b = TE_0 - m_0c^2 \cong -507.3\text{ keV} \quad (1)$$

and

$$r_0 \cong \hbar/m_0c \cong 390\text{ fm}. \quad (2)$$

A more recent paper [8] has established theoretical criteria for accepting the deep-orbit solution in the K–G equation, but not in the Dirac equation for which such a solution had been claimed earlier [9].

4. Deep-Dirac Levels (DDLs)

In 1993, recognizing that deep-orbit electrons were an important element in the cold-fusion dilemma, Maly and Va'vra [9] made a break from one of the traditional mathematical physicists' 'mind games' that had been going on since the early recognition of deep orbits was presented in 1957 [10]. Instead of the obviously idealized $1/r$ dependence of the Coulomb potential, with its point-charge singularity at $r = 0$, Maly and Va'vra selected a modified Coulomb potential that nuclear-physicists had been using for years. This non-singular potential reflected a charge distribution within the nucleus (rather than a point charge) and still matched the $1/r$ Coulomb potential beyond the surface of the nucleus. With a non-singular potential, the solution of the relativistic Schrodinger and Dirac equations, which had been rejected by the mathematical physicists for over three decades, must now be considered as valid as the accepted solution.

While the 1993 paper is largely ignored today because it is relativistic quantum mechanics, and therefore 'suspect' on two counts, it was not ignored at the time. In a challenging argument [11], Rice, Kim, and Rabinowitz did not suggest on mathematical grounds that the orbit could not exist. They argued that the equilibrium population was too low to be significant (2×10^{-9} times that of the accepted atomic orbitals). However, they then discount the possibility of the DDLs, because the fusion rate would be too high not to be observable.

If their calculation is within orders of magnitude of a real value, we could consider that the density of these DDLs for hydrogen in a metal matrix might be in the range of $10^{-13}/\text{cm}^3$. However, the Dirac equation does not consider nuclear fusion or even the weak interaction; therefore, the equilibrium value between the regular and irregular solutions will be quite different from that predicted from the simple Dirac equations with Coulomb potential. The number of populated DDLs will be much lower, because the transition rate is very low between atomic levels and DDLs (i.e., from a weak overlap of the respective wave functions) and the steady flow of electrons from the atomic to the nuclear level and its consequences must be considered.

The deep-orbit solutions for the relativistic Schrodinger and the Dirac equations have multiple deep levels [9,12] with higher angular-momentum. These additional orbits also have higher binding energy for hydrogen ($509 < E_b < 511$) than the nought-orbit level, or ground-state DDL, as distinct from the atomic orbits that have lower binding energies as n increases.

5. Deep-electron Orbits and QM

A point not mentioned in the nought-orbit papers is the need for the electron orbit to be in the Fermi range, not the picometer range, to attain the ~ 1 MeV energies required for the solution. This important concept is addressed briefly in [12] and below.

The non-relativistic QM predictions are based on the de Broglie wavelengths and the associated resonances of a bound electron. The addition of a (perhaps) single Compton wavelength for the electron (Fig. 2) could give a new orbit (a solution or resonance) and still not violate the old QM models (they may just not be the general solution). Since the strict Coulomb potential has no minimum and nothing except the perceived singularity at $r = 0$ prevents the electron from passing through the nucleus, the normal ground state is a minimal (not a minimum) only as a result of 'mechanical' resonance states of the electrons in a potential well. The photon and its requirements for $E = h\nu$ and $\ell = 1$, which are critical to a proper understanding of the atom, do not directly enter the standard Schrodinger-equation picture.

This resonance of an electron in a Coulomb potential is a consequence of the de Broglie relation ($\lambda_{dB} = h/mv$) that is often used, but seldom explained. Alternatively, it is answered in the form of a mathematical solution of the Schrodinger equation with 'no further discussion required' (allowed?). The relativistic addition of the Compton relation ($\lambda_C = h/mc$) does not alter the former solutions. However, instead of multiple resonances (as in Fig. 1), made possible by a variable (v , the electron velocity) in the *de Broglie* wavelength definition, there may be only a single K–G resonance for the single *Compton* wavelength ($v \leq C$). On the other hand, just as there are beat frequencies when two frequencies are combined, it is possible that there are multiple resonances (and higher angular-momentum states) that

can be associated with the relativistic-electron (near-nuclear) regime [9].

We have given a logical basis for the existence of very-deep energy levels for atomic electrons that are predicted by the relativistic corrections to the Schrodinger equation. What keeps electrons from filling it and precipitating high rates of fusion in H-rich material? The Heisenberg Uncertainty Principle (HUP) is often used to explain the lack of energy levels below the known atomic orbitals. However, this ignores some important features of the atom (see Appendix A). A partial key, which is never discussed in the QM development of atomic orbitals, is in the inability to transfer photonic energy without the simultaneous transfer of angular momentum. This limitation exists in energy transfer via photons between one or more bound electrons or between a bound electron and a proton. Both photons and phonons are bosons and have angular momentum of 1 (\hbar). Therefore, they are not candidates for energy transfer in this $\ell = 0$ case (ground state and below). To fit theoretical results, but without momentum transfer, all the Coulomb potential energy difference between levels must be converted into the electron's kinetic energy or a portion ($\sim 50\%$) must be used to do work within a fundamentally conservative system.

6. Field Nature of DDL Electrons

The Maxwellian radiation, bound to the electron, cannot exceed the velocity of light in vacuum. The DDL electron is moving at $>0.9 C$ in a multi-fermi orbit. The radius that includes $\sim 99\%$ of its EM field (by some criterion) is nearly 400 fm. Thus, the field cannot keep up with the electron and the field lines must be tightly 'wrapped' about the charge pair. They cannot stay there. They must terminate on a positive charge. In a static, or a non-relativistic, or a single pass-by case (e.g. scattering experiment), this 3-D 'flow' of field lines is not too difficult to picture. For a bound, relativistic-electron, orbit, the picture is less clear.

The cyclic 'disturbance-front' in the dipole field propagates out less than the distance around the DDL orbit circumference before the next front is initiated. Since the DDL electron may take 100 orbital cycles to return to the exact orientation of the equivalent point in its de Broglie cycle, resonance cannot occur in one or even a few cycles. This 100-cycle time frame establishes the resonant condition in the multi-hundred fermi EM field about the tightly bound electrons.

At the close-in DDL range, most of the field lines are closed between the electron and the local nuclear proton(s). The dipole potential drops off as $1/r^2$, rather than the $1/r$ of the Coulomb potential. (Thus, in the presence of a proton, an electron, defined by its potential or field, 'shrinks' in size.) Field lines are a potential gradient. As such, they are 'directional' and cannot cross one another without violating the limitations of 3-dimensional space. They must 'close' on the adjacent proton(s); but, since the distributed potential is dependent on the relative position of the two charges, both it and the associated field lines may be highly dynamic.

A problem with the simple field-line model exists for the dipole field lines extending to >10 fm and with the return time of a change in the source being greater than the cycle time. How does the DDL electron avoid its own outward-radiating field lines (on their return to the proton) and find, over time, a path of minimum energy? The answer must lie in the ability of the charge's potential to change the field lines at both the source region and then again at all other places locally, perhaps even before the original perturbation reaches them. This does not violate any causality; but it does set up some interesting conditions for resonance between the DDL electron and its bound EM radiation. It means that the potentials and field lines have a short-term 'memory' and, at least to some extent, this memory can affect the EM fields at a given location.

The dipole's far-field radiation ($r \gg 2\pi r_{DDL}$) is seen only as a fluctuating bipolar field and closed field lines cannot make sense under that condition. Another unanswered question is, "while this field derives its energy from the dipole and is in a sense bound to the dipole, does it contribute to the electron's kinetic energy and effective mass?" (The proton's mass is too great relative to that of the electron to be affected by the field.) This same question can be posed about atomic electrons. However, the energy tied up in that far-field radiation is too small to be of concern. This may

not be so, in the case of DDL electrons where the field energy may exceed the mass energy of the source electron.

The point of this section is to indicate that a bound electron is quite different from an energetic incident electron. Its creation of, and interaction with, its own radiant field is complicated and perhaps the source of some aspects of nuclear and quantum physics not presently being explained. Conservation and symmetry considerations are able to provide much of the predictive power available in mathematical physics today. Nevertheless, we must not be bound by preconceived ideas that may not pertain to the specific system that we are seeking to describe.

7. Deep Orbits and Cold Fusion

Deep-orbit electrons are the ultimate Coulomb screen. Atomic or ‘free’ electrons cannot spend sufficient time close to a proton to shield its positive charge from another proton. The deep-orbit electrons can. They make a proton look like a ‘fat-neutron’. Fusion becomes inevitable; however, there are many kinds of fusion possible with this proton combined with a DDL electron, $p^\#$ or $H^\#$ [1]. We will only sample the cases of hydrogen.

7.1. Interaction of $p^\#$ with H

The major differences between $p^\#$ and H are that the proton has given up about 1.5–2 MeV of its mass (in the form of potential energy) to give the DDL electron about 1–1.5 MeV of kinetic and mass energy and a binding energy of ~ 0.5 MeV. This means that there is insufficient mass energy to form a neutron despite the electron’s > 1 MeV of kinetic energy. On the other hand, if $p^\#$ meets H in a low-energy, low-angular-momentum encounter, then production of a deuteron is probable.

The DDL electron draws the two protons together (dipole–monopole attraction). Both protons do work through the DDL electron and lose mass. The electron gains kinetic energy as it moves to deeper (now femto-molecular) levels. The deep-orbit electron shifts toward the heavier proton and, in the sharing process, the proton masses are equalized. However, there is now sufficient total mass energy to form a deuteron. (We can ignore any atomic electron in this, because it is not in the action.)

7.2. Interaction of $p^\#$ with $p^\#$ (or H^+ with $H^{\#\#}$)

It is unlikely that two $p^\#$ would encounter unless there were a strong nuclear active environment (NAE) capable of producing this femto-atom in large quantities. However, the lochon model, utilizing $p^+ + p^- \Rightarrow p_2^{\#\#}$, produces this entity by preference, unless fusion occurs.

Again, there is not sufficient mass energy in the potential-energy-depleted protons alone to form a deuteron. Nevertheless, with the DDL electron energies and proximity available, fusion is expedited. If fusion does not occur, the resultant neutral, but polarizable, femto-molecule is highly penetrating of both atomic-electron screens and of nuclei. Thus, $H_2^{\#\#}$ is a strong transmutation agent.

8. Interaction of $p^\#$ with D or $d^\#$ with H

While both ${}^3\text{He}^\#$ and ${}^3\text{H}$ can result from either of these combinations, the end product will be ${}^3\text{He}$ in both cases. In the first case, the DDL electron will assist in dissipating the excess nuclear energy and will finally be ejected from the deep orbit – to leave the ${}^3\text{He}$ nucleus in its ground state. In the second case, the tritium formed, with conversion of a proton into a neutron and neutrino, would ultimately decay into a ${}^3\text{He}$ atom.

8.1. Interaction of $d^+ + d^- \Rightarrow {}^4\text{He}^*, {}^4\text{He}^{*#} \text{ or } {}^4\text{He}^{*##}$

This starting point is the principle candidate for the formation of DDLs. If the lochon process does not achieve the proper depth of the bound electrons, it is generally reversible. However, even during a reversible process, there is still a slight probability for the deuterons to tunnel through their mutual Coulomb barrier, without DDL formation, and produce ${}^4\text{He}^*$ by the conventional hot-fusion process. The result, however, would be the expected 50/50 split in the n and p fragmentation levels.

If the $d^+ + d^-$ process is only partially successful, but one electron had to absorb the other electron's energy so that one of them could attain the DDL, then a single-DDL-electron ${}^4\text{He}^{*#}$ state could result. This state is beneath the ${}^4\text{He}^*$ neutron fragmentation level, but not that of the proton fragmentation. Few or no neutrons would be observed; but a goodly number of energetic protons and tritium would result. The single DDL electron could still provide an alternative path to the ${}^4\text{He}$ ground state and so a significant amount of heat would be produced along with the fragments and ${}^4\text{He}$.

A fully successful $d^+ + d^- \Rightarrow {}^4\text{He}^{*##}$ process would produce a 'decaying' neutral nucleus with many MeV excess nuclear energy. It is also a powerful transmutant. Since it would penetrate nuclei easily and has four nucleons to contribute, the extra energy available could split many of the isotopes that it would encounter. On the other hand, with its many bodies, including the DDL electrons, it could also create many combinations of decay paths to allow the excess nuclear energy to be dissipated without highly energetic particles being emitted [4].

8.2. Interaction of $d^+ + d^- \Rightarrow d_2^{##} + e \text{ or } d_2^{##} \text{ or } {}^4\text{He}^{*##}$

Two deuterons bound by DDL electron(s) cannot have too much angular momentum to fuse. Nevertheless, they may be metastable in the femto-molecular or fused, but excited, state, where they can exist as such in the lattice for a brief period (fs?). The $d_2^{##}$ neutral femto-molecule or ${}^4\text{He}^{*##}$ would be a powerful transmutant.

9. Conclusions

The deep-orbit electron levels, which have been rejected for more than five decades because of mathematical physicists' inability to see the inappropriate use of a singular potential, were properly revealed (again) two decades ago. Since this information was published in the context of cold fusion, it was ignored outside of the CF field. Similarly, no experimental evidence, outside of the CF literature, has been accepted to validate these levels and this knowledge has remained dormant.

With the recognition that a non-singular Coulomb potential provides acceptable deep-orbit solutions of the K–G, Schrodinger, and the Dirac equations, we must also look at the consequences and any experimental evidence to validate and refine these solutions and/or the input potential. The K–G nought orbits and deep-Dirac levels (DDLs) provide properties that explain many of the experimental observations of low-energy nuclear reaction (LENR) research and condensed-matter nuclear science (CMNS). The strongest support for these deep-Dirac levels is the number of transmutation products observed in the cold fusion work. It would appear that experimental support for these levels already exists and validation may not be far away.

Accepting the reality of these deep-orbit electrons and utilizing them will provide a century of new growth in both Physics and Chemistry (and perhaps in Biology). The practical benefits could far exceed those in the last century from QM and Relativity combined.

Appendix A. Appendix: Deep-Dirac Levels and the HUP

The HUP, or Relation, is sometimes an obstacle to those asked to consider a deep-orbit or nuclear electron. The HUP indicates that to confine an electron to the fermi range requires a high kinetic energy ($> 100 \text{ MeV}$) so that the uncertainty in momentum is large enough to satisfy the relation. How is this challenge solved?

Classically, the nought-orbit electron can have angular momentum. However, it will be much lower than Planck's constant divided by 2π (where $h/2\pi = \hbar$). Therefore, since $0 < \ell \ll \hbar$ and the uncertainty in angular momentum is $\hbar/2$, it would be classified as an $\ell = 0$ orbit. The nought orbit is thus both an $n = 0$ and an $\ell = 0$ orbit.

There are other interesting points about this orbit relative to normal atomic orbitals. 'Circumferences' of the Bohr orbits are integer multiples of the electrons' *de Broglie* wavelength ($\lambda_{dB} = h/p$, where p is the electron momentum). However, the naught orbit in one development [2] has a predicted circumference close to that of the electron's *Compton* wavelength (Eq. (??) $\Rightarrow \lambda_C = h/m_0c$). As such, nought-orbit electrons still fit within the wave mechanics regime and are consistent with the Heisenberg Uncertainty Relation (see below).

The problem with a Compton radius (~ 380 fm) for the deep-electron orbit is that it does not provide the potential energy needed to establish the binding energy predicted by either the K–G or the Dirac equations. That must come from a radius in the low fermi range. How are these apparently mutually exclusive conditions reconciled? Part of the answer comes from recognition that Δx does not represent the uncertainty in position of a point particle (or even its centroid of distribution) but the extent of the wave function (wave packet?) associated with that particle. Since a wave packet has no well-defined edges, Δx can be much larger than an average, a weighted-mean, or an otherwise-defined position distribution. The 'distribution of what' is also not defined. Do we define a particle by its mass, by its field, by its potential? Therefore, the value cannot be single valued. This concept allows both values for orbital radius.

Looking at the 1 MeV kinetic energy region of Fig. 2, one can see two resonances. Both the Compton and classical electron radii are involved. Both involve the electron mass, but at different radii: one with the electron momentum, the other with the kinetic energy as defined by the electrostatic potential. It would appear that this is a region of significance, where an electron's KE and PE are close to twice its mass energy.

The HUP implies that to confine an electron to the nuclear region would require such a high momentum that the Coulomb potential cannot contain it. However, an electron, to be confined to a nucleus, will have enough kinetic energy (from the Coulomb potential) to create electron–positron pairs that will spread the effective mass energy – and therefore increase the uncertainty in position – as the positron is ejected by the nuclear Coulomb field. Since the electrons are identical particles, when one electron combines with the positron, it is impossible to determine which electron it is. Again, the uncertainty in position is increased sufficiently to fulfill the HUP. A 'modern-physics' view of the model, when extended to lower energies, would say that virtual electron–positron pairs are constantly being created and annihilated about every electron. The nuclear Coulomb field polarizes the virtual pair further increasing the uncertainty of location, because, once again, there is no means of distinguishing the virtual from the real electron.

The use of virtual particles is a QM technique for using 'quantized' entities, rather than fields, to describe phenomena. A stationary electron or positron can be described by only one of the two Dirac equations. As soon as an electron begins to move, a contribution to the combined wave function from the second coupled equation begins to grow. This second equation describes the positron (or a 'portion' thereof). Thus the concept of virtual 'particles', a portion of the linear superposition of 'eigen states' (the electron and positron in this case), can be used in place of Maxwell's equations to describe the EM-energy field that grows with velocity and acceleration of a charge. The 'range', a limit of existence, of the virtual particles corresponds to the evanescent wave from a classical photon of the electron's mass energy. When the energy of the EM field reaches $2mc^2$, then real particles, can be created. This transition from virtual to real has dramatic and, perhaps, not-easily explicable consequences [13].

Classically, a moving electron creates a magnetic field (a description of the relativistic changes to the electrostatic \mathbf{E} field – even at low velocities). If it is not moving linearly, additional field components are required to describe the resulting disturbance to the radial Coulomb field. Since another charge is required to accelerate an electron (any \mathbf{E} field is created by, or composed of, charges), the field lines of both charges are greatly distorted during this process. Once the source of acceleration is removed, the field lines return to their original configuration (in the rest frame of the electron). Viewed from another frame moving relative to the electron, the fields appear distorted to reflect a higher energy level. When bound to a nucleus, the electron is constantly accelerating and therefore its field lines reflect the

constant change. This is the basis of the ‘bound’ EM field described by Maxwellian radiation. It is bound both to the electron and to the positive charge(s) to which the electron is attracted.

Only under special conditions can the Maxwellian radiation ‘leave’ the electron. Maxwell did not believe in the corpuscular nature of light and therefore did not include the option of photons in his formulation. QM also ignores the photon in its time-independent calculation of the hydrogen atom. The difference is that Maxwell predicts EM fields extending to infinity (radiation) and, strictly, QM says there is no radiation at all (that is covered in QED!).

The HUP, based on wave mechanics, has often been misused by assuming that the uncertainty in location of a particle is only defined by its distribution as predicted by its wave function. If it is recognized that particles are composed of waves, then the HUP applies to them as well. The electron is the easiest example of this. If we recognize that the electron with its $1/r$ potential can be considered as infinite in extent, then the HUP is a tautology. If $\Delta x = \infty$, then, $\Delta x \Delta p = \infty > \hbar/2$. This is not very useful. If, however, we consider the electron to be composed of a photonic shell structure with $E = h\nu = hc/\lambda = mc^2 = 511 \text{ keV}$, and having a radius $r = \lambda/2\pi = \lambda_c$ and $p = E/c$, then the uncertainty in location is $2\pi r \geq \Delta x \geq 2r$ and in momentum is $2p \geq \Delta p \geq p = E/c = h/\lambda$. The HUP becomes $2\pi \lambda_c \hbar/\lambda \geq \Delta x \Delta p \geq 2\lambda_c \hbar/\lambda = 2\hbar > \hbar/2$ and is then satisfied. This is a useful and instructive definition and condition. However, since the electron has no strict boundaries, the use of a Compton radius ($r_c = \lambda_c/p$) is no more valid than that of the classical electron radius ($r_c = e^2/mc^2$). Is full-width half-maximum (FWHM) a better description of a pulse shape than half-width half-maximum (HWHM), or full-width at $1/e$ of maximum value? Nevertheless, usage of the Compton radius when imposing the HUP has merit in that both are related to the wave-mechanical (photonic) description of an electron.

Too often, competent physicists use the HUP with little or no understanding of what it means or even represents. They use the de Broglie wavelength as the uncertainty in position because there is a QM wave function related to it. Recognition of what the wave function represents, or how it relates to the physical world is generally missing (it is seldom taught). Therefore, like engineers, they use the equations and assume that this is proper, always giving the correct answer.

In atomic physics, such procedure gives the electron orbitals to great accuracy. This gives great assurance of the procedure’s correctness in using the de Broglie wavelength and its multiples. Approaching the nuclear case, where the Compton wavelength is more important if in resonance, the de Broglie wavelength of an electron is only a perturbation in an ill-defined region. Thus, the sum and difference between the Compton and de Broglie frequencies ($\nu_c \pm \nu_{dB}$) may be the dominant feature. Furthermore, interaction of an electron’s frequencies with the nuclear frequencies can play a major role.

For high-energy scattering experiments (e.g., 100 MeV), the electron deBroglie frequencies greatly exceed the Compton frequency. This allows them to be used in the HUP as a useful indicator of limitations in ‘resolution’ of experiments. For DDLs, the electron kinetic energy ($\sim 1 \text{ MeV}$ each) and momentum is small relative to that of scattering experiments, but large relative to the rest mass. Thus, the positional limitation imposed by the de Broglie wavelength would appear to forbid such nuclear orbits. However, just as the $n\lambda_{dB}$ criterion provides sharp resonances within the atomic-electron orbits (e.g., Fig. 1), a λ_{dB}/n criterion, where n may be ~ 100 , could provide a very broad resonance (composed of many states) within the deep-electron orbits. The point is that, as in the atomic orbitals, the electron orbit is not defined by HUP with Δx equal to the DDL electron’s radial distance from the nucleus. It is defined by the integer circumferential lengths of the electron orbit and $\Delta x = 2\pi rn = \lambda_{dB}$, where n can be large and therefore r can be small.

When referring to the Coulomb attraction between nucleus and electron, the distance between centers of charge is the critical feature, unless the charge is distributed over a larger volume than that occupied by the centers of two bodies. The fact that the electron charge is distributed over many fermi and the proton charge over nearly a fermi puts the DDL electrons in this category. Some weighted-average distance between charges determines the potential energy between them. At some point ($r = 1 \text{ fm}$?), the electron may no longer be distinguishable as a separate entity and then the HUP

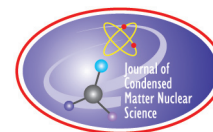
must apply to the modified proton rather than to the electron. To say that confinement to an average distance violates the HUP, unless the momentum is sufficiently high, is mixing and misunderstanding physical and resonant sources of the HUP.

Acknowledgment

This work is supported in part by HiPi Consulting, New Market, MD, USA; by a Universiti Sains Malaysia Research Grant [1001/PNAV/817058 (RU)]; by a USM International Grant from the Science for Humanity Trust, Bangalore, India; by the Science for Humanity Trust Inc, Tucker, GA, USA, and by the Indian National Science Academy.

References

- [1] A. Meulenberg, Femto-atoms and transmutation, *17th Int. Conf. on Cond. Mat. Nucl. Sci.* (ICCF-17), Daejeon, 2012.
- [2] J. Naudts, On the hydrino state of the relativistic hydrogen atom, *Arxiv preprint physics/0507193*, 2005.
- [3] H.N. Spector and J. Lee, Relativistic one-dimensional hydrogen atom, *Am. J. Phys.* **53** (1985) 248.
- [4] Z.L. Zhang, W.S. Zhang and Z.Q. Zhang, Further study on the solution of Schrödinger equation of hydrogen-like atom, in *Proc. 9th Int. Conf. on Cold Fusion*, Beijing, China, 2002, pp. 435–438.
- [5] J. Kadeisvili, The Rutherford–Santilli Neutron, *Hadronic J.* **31**(??) (2010) 1.
- [6] A.S. de Castro, Orthogonality criterion for banishing hydrino states from standard quantum mechanics, *Phys. Lett. A*, **369** (5–6) (2007) 380–383.
- [7] N. Dombey, The hydrino and other unlikely states, *Phys. Lett. A* **360** (??) (2006) 62–65.
- [8] T. Nadareishvili and A. Khelashvili, Some problems of self-adjoint extension in the Schrodinger equation, *Arxiv preprint arXiv:0903.0234*, 2009.
- [9] J. Maly and J. Vavra, Electron transitions on deep Dirac levels I, *Fusion Technol.* **24** (3) (1993) 307.
- [10] R. Loudon, One-dimensional hydrogen atom, *Am. J. Phys.* **27** (9) (1959) 649–655.
- [11] R. Rice, Y. Kim and M. Rabinowitz, Comments on electron transitions on deep dirac levels I, *Fusion Technol.* **26**(1) (1994) 110.
- [12] J. Maly and J. Vavra, Electron transitions on deep Dirac levels II, *Fusion Technol.* **27**(1) (1995) 59.
- [13] A.D. Alhaidari, Resolution of the Klein paradox, *Physica Scripta* **83** (2) (2011) 025001.



Research Article

New Visions of Physics through the Microscope of Cold Fusion

A. Meulenberg*

National Advanced IPv6 Centre, Universiti Sains Malaysia, Malaysia

K.P. Sinha

Department of Physics, Indian Institute of Science, Bangalore 560012, India

Abstract

Cold-Fusion (CF) Research is not hindered as much by what we do *not* know as it is by what we *know too well*. This paper identifies several standard physics models, which must be extended beyond present practice, and indicates condensed-matter nuclear science (CMNS) work in this direction.

© 2014 ISCMNS. All rights reserved. ISSN 2227-3123

Keywords: Deep-Dirac levels, Deuterium fusion, Fragmentation, Transmutation

1. Introduction

The authors of this article have been involved in this controversial field from the beginning of the cold fusion (CF) era and one has continually followed its progress over the years very closely. It can be said that, by now, adequate evidence has been accumulated, e.g. [1,2], to confirm a variety of fascinating “near radiationless Low Energy Nuclear Reactions” (LENRs) occurring in deuterated (and even hydrided) metallic lattices under certain conditions. The phenomenon has been found to occur primarily on the surface of the deuterated/hydrided samples and that too only in certain highly localized sites, which seem to provide what has been characterized as a “Nuclear Active Environment” (NAE). Reproducibility has significantly improved over the years, approaching almost 100% levels in some configurations. Nevertheless, universal reproducibility and satisfactory theoretical understanding of the phenomenon are lacking even today.

Rather than cover again the evidence for LENR (the nuclear explanation for heat generated in CF), this paper will address the arguments presented against it over two decades ago. It will show how those arguments helped to guide the theoretical work needed to explain the results. Answers to those arguments in terms of experimental results and theoretical models are presented in the following development.

*E-mail: mules333@gmail.com

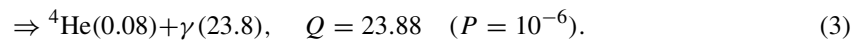
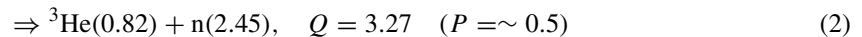
Soon after the announcement of anomalous heat attributed to nuclear sources and initial attempts to repeat the results failed, scientists collected and presented the physics concepts showing why such a thing could not happen. As a result, Cold Fusion was considered impossible and rejected as science. In the two decades since then, mounting evidence indicates that low-energy nuclear reaction (LENR) *can* happen. Furthermore, there is now evidence that transmutation can occur from this process and could even be taking place in biological systems. Therefore, present physics, chemistry, and perhaps even biology models need to be both reexamined and extended or must be supplemented with new models. This paper identifies some standard models, which can be extended, and indicates results of some condensed-matter nuclear science (CMNS) work in this direction. In particular, three experimental results of this work, which indicate a decay mode not permitted by present nuclear physics models, will be explained in terms of several extended-physics models:

- (1) the ability of two low-energy protons or deuterons to penetrate their mutual Coulomb barrier;
- (2) the production of heat is far in excess of that permitted based on the measured particulate radiation;
- (3) the high levels of ^4He measured are much beyond background and at levels consistent with ~ 20 MeV per ^4He atom measured.

The first argument against LENR was the *inability of protons or deuterons to overcome the MeV-sized Coulomb barrier between them* without having energies in the 10s of keV to MeV range. There was no evidence in any of the early cold-fusion work to indicate lattice-hydrogen energies above the eV range. Thus, according to the well-known nuclear physics at the time, the interaction cross-section claimed for the cold fusion results was more than 100 orders of magnitude higher than anything that could be explained by room-temperature D–D fusion. The ‘known’ physics was based on extrapolation from experimental results of high-energy ($E > 1$ MeV range) d–d collisions.

The reason for the high rates, given by the believers at the time, was that the presence of the solid-state environment was different from that in which the nuclear theories were engendered. Nevertheless, many critical papers were written showing (with notable exceptions) that this environment could make no difference. Subsequently, these cross-section predictions, while good for $E > 25$ keV, have been over-turned by lower-energy collision experiments during the last two decades. Extrapolation from the new results is much closer to the measured Cold-Fusion results than to that of the early ‘Gospel’.

The second argument against LENR has several sub-topics. The general argument involved the *incompatibility of the known radiation of protons, neutrons, tritium, ^3He , and gammas with the measured heat generated from the CF process*. These radiations, by-products known as “nuclear ash” result from the $\text{D} + \text{D} \Rightarrow ^4\text{He}^*$ fusion-decay process (Eqs. (1)–(3), respectively). While protons and deuterons –p and d – or hydrogen and deuterium – H and D – are often used generically and interchangeably in this paper to describe the interacting particles, when specificity is required, it will be applied.



The Q s in the equations are the mass deficit between the decay product atoms and the helium atom ground state, ^4He . It is seen that the decay to ^4He produces the greatest Q (and therefore has the greatest heating potential) of the three paths.

The first sub-topic of the second argument is characterized by the statement, “if there were nuclear reactions generating the claimed heat, then the only ones ‘possible’ in that situation would have provided *enough penetrating*

radiation (neutrons) to kill everyone in the building.” Neutrons had subsequently been measured, but at a rate many orders-of-magnitude too low to account for the heat generated.

Associated with the dearth of neutrons was the second sub-topic, an *unusual measured fragmentation ratio of neutrons to protons or tritium* (P_n/P_p or $P_n/P_t \approx 10^{-7}$ where the P s are the probability of choosing a decay path). All known D–D fusion reactions provided a 1 to 1 ratio ($P_n = P_p$). The observed CF results gave 10^7 – 10^9 tritium atoms for every neutron [3]. According to accepted nuclear physics, since the 1 to 1 ratio is not observed in CF as prescribed by (1) and (2), D–D fusion “cannot” be occurring.

There seemed to be a “disconnect” in the logic of the argument against cold fusion. Instead of seeing the anomalous ratio as an *explanation* for the low number of neutrons produced for the amount of heat observed, the critics added it to the list of arguments against nuclear reactions. Nuclear physicists neglected to consider well-known excited states of helium below the neutron fragmentation level because they ‘knew’ that d–d collisions could not populate these states.

The third argument, somewhat related to the second, was the *high amount of ^4He measured in many experiments*. Nuclear physics has accurate and repeated measurements indicating the forbidden-transition nature of the gamma-ray decay from the excited state $^4\text{He}^*$ to the ground state resulting from the D–D fusion (3). Thus, the probability of forming ^4He from D–D fusion is less than one per million fusions. This is almost as low as the percent of neutrons that were “missing” in the CF experiments. Nevertheless, the image of “sloppy” experimental work of CF researchers was confirmed in the minds of its critics by these “impossible” results.

Assuming that the Coulomb barrier could be tunneled through by minimum-energy, minimum-angular-momentum, deuterons, the available excited-state energy levels $^4\text{He}^*$ are well-known zero-angular-momentum ($l = 0$) levels with decay characteristics that led to the second argument (a nearly equal number of neutrons and protons and almost no ^4He). There was “no conceivable” means of resonant tunneling below these levels because there are no states between them and the ground state. (This argument is explained further in Section 3.) *Only by tunneling below the fragmentation levels can a deuteron pair attain the ^4He ground level* by other than the highly-forbidden energetic $l = 0$ to $l = 0$ gamma transition.

The critics have declared that the high levels of ^4He observed in the LENR experiments, where it was sought and measured, were only contamination from atmospheric helium or were from ‘bad’ measurements and techniques. The fact that it correlated with the heat produced, and did not show up in the control experiments, was ignored.

These arguments, based on a mature field of study (one that produced nuclear weapons and power plants with a high level of reproducibility and predictability) and supported by at least two other fields with equivalent credentials, appeared incontrovertible; therefore, the books were closed on cold fusion. “It is only pseudo-science.”

While the three arguments showing that the LENR results could not be fusion were strong and based on experiment and theory, other information was available at the time and subsequently led to even stronger answers. The low-energy experimental work was just beginning at that time. However, some theoretical work [4] goes back 4 decades before the Pons–Fleischman experiment.

Quantum mechanics declares that the ground state of hydrogen is its lowest energy level. However, mathematically, it is a ‘minimal’, not the minimum, level. The relativistic Schrodinger equations (the Klein–Gordon and Dirac equations) are solved for a charged body in a Coulomb ($1/r$) potential. The solutions that are singular at $r = 0$ have been repeatedly rejected and ignored. Nuclear physics, many decades ago, decided that the Coulomb potential must be different when $r \Rightarrow 0$. There is no singularity! These rejected solutions predict a deep atomic level (binding energy of ~ 500 keV) for relativistic electrons.

This paper will address these arguments against CF and show how they have been repeatedly proven incorrect and how a self-consistent explanation, based on known physics may be emerging. No model for CF, in general, and for LENR, in particular, has yet been universally accepted, even by the LENR community. Moreover, new experimental

results that are just as outrageous as the earlier ones have been more-recently confirmed. Nevertheless, it must be clear to all who are willing to examine the issue that something new and different is going on - and - it holds immense promise on many levels.

2. The Coulomb Barrier

The Coulomb barrier problem dominated much thought for many years. To get fusion, one must get the two nuclei close enough together for the short-range, charge-independent, attractive nuclear force to overcome the weaker, but long-range Coulomb repulsion of the positive nuclear charges. At normal atomic and molecular separations, negatively charged atomic electrons neutralize the nuclear charges and stable configurations (molecules) result from the balance between the attractive dipole-dipole interaction of the atoms (pairs of positive and negative charge) and the repulsive Coulomb field. The latter prevents atoms from getting too close because the electrons have too much kinetic energy to be confined in the space between. Therefore, their ability to neutralize the positive nuclear charges, sufficiently to allow tunneling through the remaining barrier to resonant energy levels inside, is limited at short nuclear distances and the universe does not collapse.

It was recognized, early on, that the palladium lattice must have something to do with the proximity problem. Initial thoughts revolved about the concept that, if protons could exist comfortably in lattice sites within the Pd crystal, then, when those sites were nearly full, two protons could be forced into a single site and therefore become pushed together by the lattice. Careful calculations from the mature field of Solid-State Physics showed that even if a second proton could be forced into an already filled site, rather than into a higher-energy, but empty, adjacent site, the pair would still be forced into a distant configuration within the lower-energy site. Something different must be going on, either in the normal hydrogen sites or within the newly paired site, if low-energy (e.g., room-temperature) nuclear reactions are to occur in the lattice.

Another possible explanation offered for the ability of hydrogen nuclei to get close enough to fuse has been the screening effect of electrons (bound and free) in the palladium lattice. The high number of electrons near the hydrogen atoms in the lattice would reduce the Coulomb barrier between them. This argument has been contested; but, in various forms, it is still going on today (see below).

There are hints from both the natural world and man's industry as to what might be happening to allow the Coulomb barrier to be breached. Catalysts are known to accelerate processes without being greatly affected by the system that they altered. This acceleration can be by many orders of magnitude. However, since nuclear physics states that D–D fusion probability at low energies is more than 100 orders of magnitude below the observed CF results, critics have said that catalytic enhancements are unlikely to be noticed. Nevertheless, at the time of the announcement in 1989 by Pons and Fleischman that started the whole cold fusion adventure, there was already work going on that cast doubt on the standard model's extrapolation to low energies that was the basis of nuclear physics prediction of the extreme difference.

The nuclear physics model was/is based on accelerator data for particles with energy greater than 1 MeV. The cold fusion particle energies were assumed to be close to that associated with room temperature thermal motion (i.e., in the range of 25 meV). Actual data at lower beam energies (down to 25 keV) had confirmed the model; so the critics assumed that they were on firm ground with their arguments. Nevertheless, early astro- and nuclear-physics papers, e.g., [5–7], showed a major deviation from the model beginning below 25 keV for D–D fusion experiments in the presence of matter. Thus, multiple works (at <10 keV) had been ignored by nuclear physics because that energy range was of interest only to the astrophysics community. The new low-energy D + D collision result has now been fully confirmed in the low-keV range for a large range of elements [8, 9].

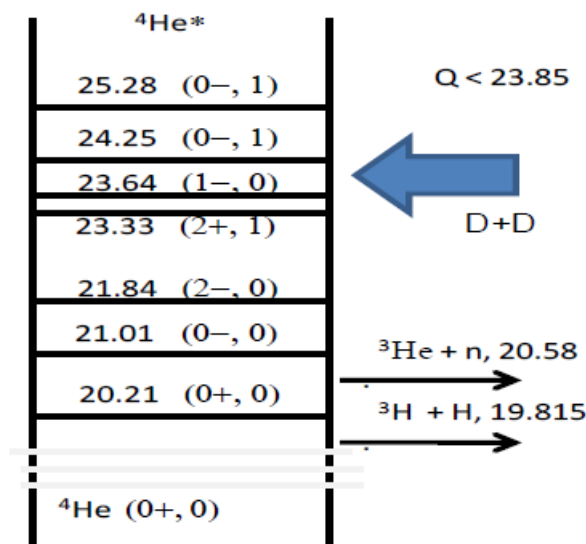
The model preferred by the nuclear physicists to explain these new low-energy results is one of electron screening by the material in which the deuterons are being implanted. Note that the observed fusion interaction is now taking

place at low energies (keV range) and in dense matter, rather than at high energies (> 1 MeV) and generally in low-pressure gases. Originally, the deviation below 10 keV was small, almost within experimental error of an individual measurement. However, as data accumulated over many successively refined experiments [9,10], the trend has become clear. The expected exponential fall of fusion cross section *does not continue to lower energies*. The mechanism of electron screening that had been rejected as “not possible to have any major impact on fusion reactions” suddenly is observed and modeled to make nearly 100 orders of magnitude difference in the data conventionally extrapolated down below the 100 meV range. The critics would say, that does not matter, the cross-sections are still 30–50 orders of magnitude too low to account for the claimed CF results to be nuclear in origin. They would like to ignore the fact that they had been 100 orders of magnitude off in the basis of their criticism and that all CF results are closer to the present extrapolated fusion cross-section prediction than 20th Century nuclear physics was. It is likely that few nuclear physicists are aware of this discrepancy even today.

Many of the arguments against the proximity of hydrogen in the lattice have been based on quantum mechanical (QM) calculations. However, any such calculation depends strongly on what is put into the model. Early models typically looked at equilibrium conditions that did not include the dynamic or non-linear contributions to the system. Phonon interaction (resonant mechanical-motion modes) of the collective atoms, ions, and electrons of the lattice is such a contributor [11]. Individual phonon energies are in the 10s-of-meV energy range and therefore would not be expected to make any difference in the fusion mechanism that requires keV-range incident-particle energies. Nevertheless, phonons (as bosons) have collective action and the net energy could get much higher (multi-eV range). Furthermore, the induced motions are coherent and therefore additive over time (within limits imposed by non-linearities and damping). The collective coherent modes can be incorporated into the QM calculations and, suddenly, deuterons have a much higher probability of getting closer together than had ever been calculated before [12,13]. Here is another mature field of physics that, when updated to a realistic model, should suddenly change its predictions about Cold Fusion.

Two additional aspects of phonons can contribute to LENR. The first is that the phonon field intensity can be enhanced by application of a resonant “driver.” The increased heat output of an experiment, when subjected to this enhancement has been observed with the application of laser pairs with frequencies set so that the beat frequencies are at the lattice-phonon frequencies [14]. Individual lasers also can increase the measured heat output by increasing the electron energies and electric fields of the lattice. Thus, even though the deuterons cannot respond directly to the higher frequencies of the single laser, the atom can move as a whole into the stronger electric-field regions that the laser induces locally in the lattice. This second effect is related to the field enhancement associated with structural defects in a lattice. Electric fields, at surface or lattice defects, may be concentrated by orders of magnitude. The increased fields align charge pairs, or simply orient motion of the deuterium atoms, and thereby increase the interaction cross section [15]. The pair alignment (forming a 1-D structure) and increased local electric fields also deepen the bound-electron energy levels (particularly the ground-state levels) by the Stark effect. Experimental evidence for this effect comes from post CF-experiment surface studies and other results that indicate the prior existence of both “hot spots” and localized radiation sources on an apparently otherwise uniform surface.

A final point on penetrating the Coulomb barrier is also related to the phonon effects. Phonon fields can polarize the electron populations in a crystal lattice. It is known that some phonon modes (longitudinal-optical modes) cause the lattice atoms to oscillate in opposition to their immediate neighbors (resulting in a “collision” mode). The two effects are generally synchronous and phased so that the polarizing fields are maximal at the same time that two colliding deuterons are closest together. It is then possible for the previously covalently bonded s-electrons of the deuterons (shared with 4d-electrons in adjacent palladium atoms) to be confined to one of the deuterons, while the electrons of the other deuteron are more closely confined to an adjacent Pd atom. The net result is that, at a time when the deuterons are closest, they become charge polarized [16,17] so that they are effectively attracted to one another rather than being repelled by the Coulomb barrier [18]. This phonon-catalyzed attraction draws the deuterons closer together than otherwise possible. Work done by the electrons in pulling the deuterons together allows the paired-electron paths to



shrink (electrons going deeper into the deuteron's Coulomb potential well) and thereby increase the electron screening of the Coulomb barrier [19]. The “bare” deuteron easily penetrates the Pd-lattice barrier and is drawn closer to the now shrinking negative part of the deuteron pair. Once through the lattice barrier, the bare deuteron now is part of a shrunken polarized pair that can easily fit into the lattice site that would not normally hold two deuterons. From here, the process to $D^- D^+$ fusion continues [20,21].

It seems that the three mature fields of physics that rejected cold fusion (Nuclear, Solid-State, and Quantum Physics) are presently in the embarrassing situation of having provided a basis for its operation – and not having recognized it. Furthermore, there are still other arguments made against CF and LENR that are now turned around. In examining two of them, we find the difference between hot fusion and cold fusion that simply overcoming the Coulomb barrier, by whatever means, does not address.

3. 'Nuclear Ash' Problem

The nuclear ash problem has to do with known energy levels and decay patterns of the excited helium nucleus. Figure 1 shows these levels and the accepted decay paths [22,23]. The energy level of interest in the standard high-energy D–D fusion reaction starts at the “ Q ” level and extends upward as the collision energy of the deuterons is increased. The Q value (arrow at ~ 23.85 MeV) is determined from the total (center-of-mass kinetic and mass) energies of the deuterium atoms relative to those of the ^4He atom ground state. Note that the usage today in nuclear physics is to include the electron(s) in the total energy of the atom. When used consistently, this makes no difference in the predicted and measured energy levels.

All of these levels are well and accurately known. The decay paths and the ratios of the different paths from these levels are also well known. Therefore, when nuclear physicists claimed that the energies of the CF reaction were incompatible with the energies available and the fragments (particulate residue or ash) of the reaction, they were

not talking about theories; they were talking about years of solid, reproducible, experimental *evidence*. The pathway leading to the $l = 0$ ^4He ground state from low-energy, $l = 0$, D–D fusion is highly forbidden. Therefore, the lower-energy-release alternative decay paths (to $^3\text{He} + n$ and $^3\text{H} + H$) become the paths of choice. And, from years of D–D collision measurements, these paths have nearly equal probabilities (a 1:1 ratio).

When CF claimed that large energy releases were observed and nobody in the lab was killed or sickened by radiation damage, the inconsistencies became clear. As particulate radiation from the LENR experiments became more accurately measured, the n/p ratio observed was “wrong.” There were almost no neutrons relative to the number of measured protons (or of tritium). On the other hand, this phenomenon (if real) would account for the low level of neutron radiation in CF experiments. It also would be a very valuable asset for a nuclear power source. Furthermore, measurements of ^4He indicated anomalously high levels of this isotope in LENR experiments. This observation could have helped to explain the low neutron radiation levels (and perhaps low proton, tritium, and ^3He levels as well). However, by this time, CF had been “declared” pseudo science and nobody seems to have noticed the strong signature of a different situation from the normal D–D fusion.

Table 1 shows the fragmentation ratio for different excited ^4He energy levels with $E < Q$ [24]. It tells a clear story of what is happening. The table identifies neutron- and proton-decay percentages for levels below the Q value that is the lower limit of hot fusion theory. Notice that, as the energy level approaches Q (at 23.85 MeV), from below, the decay path approaches the high-energy-physics predicted values of 50/50% for neutron/protons. When the energy level (e.g., at 20.21 MeV) is below the neutron fragmentation level (at 20.58 MeV, from Fig. 1), the decay path is 100% via protons.

The expected monotonic-increasing n/p transition ratio exists between these lower levels and the Q levels. Above the Q level, the near 50/50 ratio is universal. However, it is obvious that, if there existed an energy level below 19.3 MeV (or > 0.5 MeV below the proton fragmentation level at 19.82 MeV, from Fig. 1), the decay path could no longer be via protons either. Without this fragmentation, another path to ^4He ground would dominate (perhaps via energetic-gamma emission). Such lower-energy levels (or even resonances) had been proposed, and sought, to explain the observed CF results. They have not been found and such measurements have been made in CF and other experiments; therefore, such levels probably do not exist. (No LENR advocate has suggested that nuclear physicists have done sloppy work or hidden data to block a viable LENR model.) However, recent work [25] has suggested that, even in keV-energy D–D collisions, these n/p ratios may depend on the target material. This sub-fragmentation-level injection, or some similar, explanation must be proposed to account for the observed CF results.

Table 1. ^4He Energy levels and decays

E level (MeV)	J (parity)	Decay
23.64	1 (-)	% n = 45 % p = 55
23.33	2 (-)	% n = 47 % p = 53
21.84	2 (-)	% n = 37 % p = 63
21.01	0 (-)	% n = 24 % p = 76
20.21	0 (+)	% p = 100
0.0	0 (+)	Stable

4. Below Fragmentation Levels

If the Q value for $D + D \Rightarrow {}^4\text{He}$ forces fusion into excited states above the fragmentation levels, and if fragments and energetic gammas are not observed in the quantities and ratios expected, then, according to the critics, the deuterons must not have tunneled through the Coulomb barrier and D–D fusion has not occurred.

Several models, including the Lochon Model described below, have addressed the means of getting the deuterons through their Coulomb barrier. However, if they cannot address the fragmentation issue, they cannot be complete explanations for the observed CF effect. Purely quantum-mechanical models, with wave-function overlap of the deuterons, indicate the probabilities of fusion through the barrier; but, without proper interpretation, they say nothing about the fragmentation-ratio dilemma. One model of direct D–D fusion that seems to have promise in being able to do both is the Extended-Lochon Model [20,21].

The Lochon Model provides a means of, and calculated results for, D–D fusion from the Pd-lattice-defect sites [19]. Deuterons are embedded in the Pd lattice and are highly confined and electrically screened from one another by the bound Pd electrons. Older models of hydrogen mobility in a lattice assumed that the ionized hydrogen (a bare proton) had the high observed mobility. Modern models for PdD show that the ground state of the hydrogen atom is nearly 8 eV below the Fermi level of the Pd lattice [26] and is therefore unlikely to contribute its electron to the conduction band. However, it can share electrons with the broad Pd 4d orbital. Thus, it allows the Pd atoms to contribute more of their electrons for conduction. The point is “the proton in a Pd lattice is almost never ‘bare’”. It must migrate because of the Pd-lattice phonon field and must be ‘handed’ over from one Pd atom to the next in the lattice. With increased filling of hydrogen into the lattice, fewer sites are able to receive these D atoms and thus hydrogen transport nearly ceases even though its mobility has increased because of the expanded lattice and enhanced ‘sub-lattice’ phonon fields.

As the local Pd lattice becomes fully ‘loaded’ with hydrogen (deuterium), a uniformly spaced D sub-lattice forms within and the Pd lattice stretches to its greatest extent. When the hydrogen concentration matches the Pd concentration, all of the readily accessible interstitial sites are filled and each D has eight other deuterons in adjacent ‘octahedral’ sites. This forms large sections of a complete sub-lattice. A full lattice will generally have greater average collective sub-lattice motion. A ‘break’ in the sub-lattice can often produce even larger local motion. One form of resonant motion has adjacent lattice elements moving against each other rather than with each other. This ‘longitudinal optical-phonon’ mode is the one used by the Lochon model to produce the conditions needed for LENR.

The lattice and sub-lattice atoms can interact with each other to enhance or interfere with the collective motion. This may produce the final piece of the puzzle. Since the lattices are composed of charged atoms, their relative motion can create polarization of the atoms and electric fields between different elements of the lattice and the sub-lattice. If the local electric field caused by motion of the lattice is in one direction over a lattice spacing, and two deuterium atoms are coming together from adjacent sites in the D sub-lattice region, one D may be in phase with the field and the other D in opposite phase. The result is dynamic charge polarization with the momentary result being a $D^+ D^-$ pair. Because of screening and electron sharing, these are not unit charges. Nevertheless, the Coulomb barrier between the deuterons is thereby greatly reduced in length and somewhat in height.

Key to the model is the stability of electron pairs in the 1s ground state. This spin-coupled electron pair is a boson (integer-spin system \Rightarrow local charged boson = Lochon). It is similar in concept to the Cooper-pairs, electrons coupled in momentum space that produce superconductivity. However, these electrons are coupled in physical space and, because of the much stronger spin-coupling and shared Coulomb potential well, this pairing exists even at high temperatures. Its stability permits momentary charge polarization of interstitial D–D pairs by the phonon-induced electric fields into an attracting $D^+ D^-$ pair. Being at adjacent sites in the D sub-lattice, these deuterons are initially embedded in the Pd lattice among the bound Pd electrons. Because they are well screened, the deuterium atoms may not even be aware of the other’s charge state most of the time. However, when they do get close enough for charge separation of the polarized atoms to shift the interaction from a dipole–dipole to a monopole–monopole interaction, they appear to be

oppositely charged ions. The ionic-deuterium energies at simultaneous contact with the lattice barrier at this point of their phonon collision mode are much higher than for neutral deuterium atom collisions. Thus, for multiple reasons, fusion probability is greatly enhanced by the lattice phonons and the resulting local electric fields.

While it provides a mechanism for fusion, the basic Lochon Model does not address the nuclear interaction after fusion. However, when it is extended into this regime, it fits very naturally and helps to explain the mechanism involved in tunneling below the fragmentation levels. This extension uses a concept introduced by Tom Barnard^a that enhances aspects of the lochon model to deepen the atomic-electron energy levels during a portion of the phonon-induced oscillations of the deuterons within their individual lattice sites. Part of this energy goes into the electron kinetic energy and part into the work of accelerating and drawing two deuterons together (work = $F \times \text{Distance}$). The deepened energy levels also mean that the electron orbitals are greatly reduced in size. Therefore, the D^- electrons: are no longer shared with the Pd 4d electrons; are much better at screening the deuterons' Coulomb field; and are a lesser impediment to the negative ion in passing into or through the minimum in the lattice barrier between hydrogen sites. It is at this point that either: the deuterons reflect from the barriers (lattice or nuclear Coulomb) and return to their individual sites; or, the two deuterium ions can fall back (now together) into a single site under conditions much more conducive to fusion; or, fusion can take place directly.

The extended-lochon model recognizes that this net energy transfer (from deuterons to now-energetic electrons) comes from the total energy (E-field and mass as potential energy) of the deuterons and the electrons. However, the electrons gained kinetic energy (~ 1 MeV each) and binding energy ($\sim 1/2$ MeV each) at the same time [27]. This energy comes from the potential energy of the proton binding them to itself. Therefore, when the mass–energy values of the fusion reaction is calculated, the result must be lower for the *nuclei* (< 1 MeV from the D^+ and > 2 MeV from the D-nucleus), but not for the atoms. This separation of mass and energies, and its attribution to the individual electrons and nucleons, is not normally considered in nuclear physics, since the atomic electrons seldom change orbit or energy very much relative to the fusion-process energies. The total *nucleon* Q value in the extended-lochon model can decrease by ≥ 3 MeV before fusion ever occurs.

A 3-MeV reduction in Q is not sufficient to get the deuterons beneath the proton-fragmentation level. However, the much greater electron density within the nuclear region (from the deep-electron orbitals) reduces the proton-proton repulsion and thereby increases the effective attractive nuclear potential by ~ 0.7 MeV for the first electron [28] and ~ 0.3 MeV for the second. The ${}^4\text{He}^{\#\#}$ ground state energy (the double # indicates both of the deep-orbital electrons are present in the nuclear region), dominated by the nucleon momenta, is also lowered until the deep-orbit electrons are ejected. Furthermore, the reduced repulsion from this neutralizing charge, which allows the protons to move deeper into their nuclear potential well, does raise the fragmentation levels: relative to the ${}^4\text{He}^*$ (excited-state) levels, relative to the ${}^4\text{He}^{\#\#*}$ levels, and relative to the total initial energy of the deuteron pair.

Figure 2 indicates the adjusted energy levels and $Q^{\#}$ value for the incident deuterons and the resultant nucleus (all excited states are with the deep lochon present), not for the atoms. However, the ground state used is that of the final nucleus (without lochon or electrons), hence the use of ${}^4\alpha$, since the deep-orbit electron(s) would have been ejected by the time ground-state energy is achieved. The excited nuclear levels are taken to be relative to the final nucleus, but with the 'less-than' sign added to indicate that the deep-orbit electrons are allowing the protons, and thus the neutrons, to be closer together and thereby spend more time in the nuclear potential well (with greater nuclear-wavefunction overlap).

Fragmentation is also identified with the nucleons, ${}^3\alpha + n$ and ${}^3t + p$, not with the atoms. These fragmentation levels have been raised (~ 1 MeV) relative to the nuclear energy levels because of the reduced proton–Coulomb repulsion [28–30] and greater nuclear-potential attraction with the deep-orbit electrons present.

Because of its importance and difference from normal practice, we re-emphasize - the value of $Q^{\#}$, for deuterons, $d^{\#}$, but with the deep-orbit electron(s) present, is relative to the normal ${}^4\text{He}$ nucleus with atomic electrons present.

^a<http://www.ichaphysics.com/the-science-of-cold-fusion>

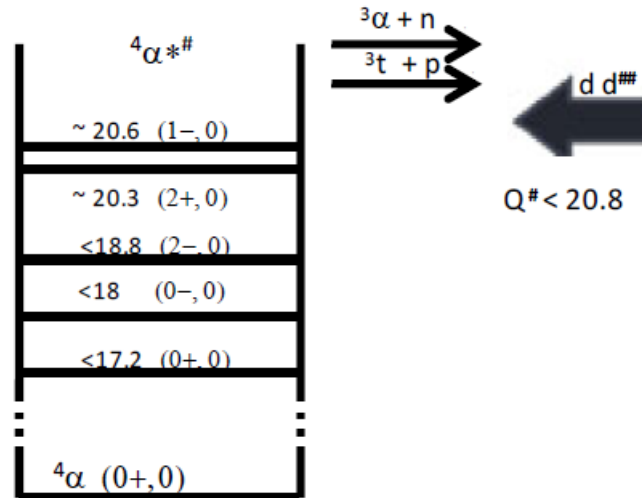


Figure 2. ${}^4\text{He}$ nucleus (see text for notation): incident $d\text{-}d^{\#}$, excited-state ${}^4\text{He}^{\#*}$, and fragmentation levels.

The electrons are present but *not* included in the $Q^{\#}$ value. This $Q^{\#}$ value has been lowered (~ 4 MeV) relative to the fragmentation level by the two processes: reduction of input nucleon mass and reduction of proton-proton repulsion in the nucleus. Since the $dd^{\#}$ insertion level is now below the neutron fragmentation level and perhaps the proton fragmentation level as well, we can see how the pattern of low neutron flux is possible in cold-fusion experiments. This reduced value of $Q^{\#}$ provides the answer to the question of nearly eliminated neutrons and reduced protons and tritium relative to the observed levels of heat and ${}^4\text{He}$ from cold fusion.

The actual values for $Q^{\#}$ and the fragmentation levels depend on details of the lochon model, at what point one or both of the electrons are ejected, and an additional factor mentioned in Section 5. The nuclear resonance states at and above the proposed $dd^{\#}$ entry level are high angular-momentum states that cannot be accessed by the low-energy process of CF. Therefore, the forming ${}^4\text{He}^{\#}$ nucleus immediately begins transferring energy to the nucleons, and from the accelerating protons to the lattice via near-field radiation from their extremely tight EM coupling with the deep-orbit electrons. The first accessible metastable states that would allow momentary pause in the rush to the ground state are the (0, 0) states now well below the fragmentation level. These are the states most likely tunneled to. This is another major difference between CF and normal hot fusion processes. If energetic deuterons are collided at $Q > 23.85$ MeV ($\text{KE} > 0$), both the expected incident particles and available excited resonant states have angular momentum (Fig. 1). For tunneling at $Q = 23.85$ MeV (i.e., CF without the lochon model), there is no $l = 0$ nuclear state into which the deuterons can resonantly tunnel and no levels below fragmentation.

The extended-lochon model permits weak resonant tunneling into the ~ 18 MeV (0, 0) level. There is insufficient angular momentum to tunnel to the levels between 18 MeV and $Q^{\#}$ and not enough energy to reach the higher (0, 0) levels ($E > Q^{\#}$). However, neither the nuclear nor the collision parts of the model have developed far enough to determine either the actual nuclear levels or the $Q^{\#}$ values yet. Furthermore, the variability and poor reproducibility of the CF data indicate that these values might not be fixed. For example, if only one electron is deeply bound, or if the electrons don't penetrate deeply enough into their Coulomb wells before D–D tunneling occurs, or if one or both electrons are ejected early in the fusion process, then the deuterons would fuse above the proton fragmentation level. Neutrons would not then be observed in CF, but protons and tritium would be. This would account for observations.

If in Fig. 2, the nuclear levels were raised relative to $Q^\#$, then the tunneling probability would go up; but perhaps the proton fragmentation would also. Thus, while the extended-lochon model provides an explanation for observed effects, it does not yet have sufficient information to suggest a ‘best’ path to the goal of radiationless heat from LENR. Nevertheless, it also provides more possibilities to explain the ‘inexplicable’. But, how does the excited ${}^4\text{He}^\#$ nucleus decay to ground state and how can CF produce transmutations?

5. ${}^4\text{He}^\#$ to ${}^4\text{He}$

The lochon, being tightly coupled to the fusing nucleons, provides a new path for their decay to the ${}^4\text{He}$ ground state that is not much different from internal conversion [31]. However, there *are* differences. The primary one being that, after D–D tunneling, the nucleons and electrons are not in a stable configuration. Therefore, instead of a resonant transfer of energies in internal conversion, the transfer of nuclear energy from the protons to the electrons, via the electric and magnetic field coupling, is chaotic. If this were the only consideration, it could take longer. On the other hand, the average electron–proton separation is orders-of-magnitude less, if the lochon model is correct; thus, the amount of energy transferred during each pass can be many orders higher and the number of passes per second is also orders of magnitude higher. The second difference is that the electrons (lochons) are very energetic (near the MeV range) and tightly bound, instead of in the many-eV range of the normal, loosely bound, k-conversion electron. Thus, their acceleration-induced EM field is perhaps tens of orders of magnitude higher. Furthermore, when they interact with the protons and the adjacent lattice phonons and electrons (as a multi-body system), they may acquire sufficient angular momentum to radiate photons and to (more efficiently) proximity-couple this energy to the neighboring Pd electrons [32]. The expected energetic gamma ray needed to de-excite a nuclear level requires a more stable state as a starting point. Furthermore, since the only states accessible to the low D^+D^- entry energy and angular momentum in the lochon model are (0, 0), these highly forbidden (i.e. very slow to form) $0 \Rightarrow 0$ transition gamma rays are not observed. This process explains the high concentration of ${}^4\text{He}$ atoms that violates the nuclear physics data based on electron-free energetic-particle collisions. It also explains the dearth of fragmentation products *and* energetic gammas.

A consequence of the only available path to ground is the continued presence of the tightly bound electrons during the extended decay process. This gives the ${}^4\text{He}^\#$ nucleus a net zero charge and a multi-Fermi sized charge distribution. In the case of hydrogen, rather than deuterium fusion, a $2\text{p}+2\text{e}^\#$ nucleus, a femto-sized $\text{H}_2^\#$ molecule, will be present. Thus, a neutral, but active, nucleus can drift at will through the lattice-atom’s electron clouds and it can drift into range of the nearby nuclear potentials. Entering another nucleus means transmutation. Since the now-compound nucleus has excess energy available and several combinations of loosely bound protons, neutrons, and electrons, the paths to a minimum energy level nucleus are multiple and varied [33]. The ability to shed excess energy by forming bound neutron(s), by proximity coupling to lattice electrons, and/or by emission of tightly bound electrons and heavy particles, means that long-range energetic radiation is not a common by-product.

The Extended-Lochon Model is based on starting assumptions that must be validated. The Lochon Model assumes that, in a lattice-phonon field, electron pairing in deepened ground states is of sufficient strength to provide a continuing attractive potential (for protons, as well as deuterons) rather than just a screening potential between hydrogen nuclei. Since a consequence of this effect is not normally observed (often even when sought), it is likely that a special condition or structure must exist to make this possible. Identifying such a structure is one of the CF priorities today.

6. Steps Beyond

The steps to low-energy nuclear reactions are well delineated; the mechanisms to carry them out are less well identified. Nevertheless, there is evidence from other fields that supports the proposed mechanisms. Evidence of transmutation resulting from these reactions is now nearly ubiquitous and incontrovertible [34]. This is a natural consequence of tightly bound electrons easing protons or energetic deuterium and helium nuclei into adjacent atoms and their nuclei.

Another line of support for this effect, from quantum physics, is a here-to-for-rejected deep (relativistic) atomic level [35]. Figure 2 uses values predicted by this model. This level has been rejected for several reasons, lack of experimental evidence for the predicted 500 keV binding energy being one of them. The recognition of halo nuclei [36] as femto-molecules would be clear evidence of the deep-Dirac levels that would explain so much in CF.

7. Conclusion

Three major objections were made over two decades ago against the cold fusion claims of a nuclear source for the observed excess heat in the CF experiments. These objections have been carried over against the last 20 years of low-energy nuclear reaction (LENR) research conducted to provide evidence to support the nuclear hypothesis. It has been subsequently shown; but as yet unproven, that these objections might be overcome with more detailed analysis, by experimental evidence, and by extension of known physical processes.

The Coulomb-barrier problem is addressed in terms of dynamic processes in a solid-state environment. One main ‘new vision’ is the ability of atomic electrons to change energy levels without emitting photons. Experimental work over the last 25 years within the field of low-energy nuclear- and astro-physics has led to a new extrapolation from the well-known and accepted high-energy model into a region far from its base. The ‘standard’ prediction of the Coulomb barrier effects (for $E < 1$ eV) is much further from the new predictions based on the recent nuclear data (at $E < 10$ keV) than is the prediction based on Cold Fusion data.

The nuclear-ash problem actually identifies the CF process, rather than proving it wrong. The production of ^4He and the dearth of neutrons relative to the heat produced is a natural consequence of a particular LENR model that extends the solution of these problems into the nucleus. The ‘new vision’ identifies proton mass as a source of electrostatic potential energy and sees it lowered as the atomic electron(s) comes close.

Other objections and solutions not detailed here, particularly those involving p–p fusion, can be treated similarly. Observed transmutations in LENR, and even in biological systems have immense implications. The differences between ‘hot’ fusion, with its known physics but very difficult technology, and cold fusion, with its ‘unknown’ physics and simple technology, are worth noting [37]. There are even some surprises coming from quantum mechanics that now support LENR by providing the theoretical basis for a relativistic deep-electron orbit. It is to be hoped that, with the new knowledge obtained over the last two decades, more physicists and chemists (and biologists) will recognize something real here and will look for ways of applying their specialties to the expanding field.

Acknowledgement

This work is supported in part by HiPi Consulting, New Market, MD, USA; by a Universiti Sains Malaysia Research Grant [1001/PNAV/817058 (RU)]; by a USM International Grant from the Science for Humanity Trust, Bangalore, India; by the Science for Humanity Trust Inc., Tucker, GA, USA, and by the Indian National Science Academy.

References

- [1] E. Storms, *The Science Of Low Energy Nuclear Reaction*, World Scientific, Singapore, 2007.
- [2] M. McKubre, Cold Fusion (LENR) One Perspective on the State of the Science. This is the Forward to V. Violante and F. Sarto (Eds.), *Proc. 15th Int. Conf. on Cond. Matter Nuclear Sci* (Part 1), 2009, ENEA: Rome, Italy, p. 385.
<http://lenr-canr.org/acrobat/ViolanteVproceeding.pdf>
- [3] M. Srinivasan, Wide-ranging studies on the emission of neutrons and tritium by lenr configurations: An historical review of the early BARC results, *Low-Energy Nuclear Reactions and New Energy Technologies Sourcebook, Volume 2*, ACS Symposium Series 1029, pp. 35–57, American Chemical Society, 2009.
- [4] R. Loudon, One-dimensional hydrogen atom, *Amer. J. Phys.* **27** (9) (1959) 649–655.

- [5] A. Krauss, H. Becker, H. Trautvetter et al., Low-energy fusion cross sections of $D+D$ and $D+^3\text{He}$ reactions, *Nucl. Phys. A* **465** (1) (1987) 150–172.
- [6] H.J. Assenbaum, K. Langanke and C. Rolfs, Effects of electron screening on low-energy fusion cross sections, *Zeitschrift für Physik A Hadrons and Nuclei* **327** (4) (1987) 461–468.
- [7] S. Ichimaru, Nuclear fusion in dense plasmas, *Rev. Modern Phys.* **65** (2)(1993) 255.
- [8] K. Czerski, A. Huke, P. Heide et al., The $2H(d, p)3H$ reaction in metallic media at very low energies, (*Europhys. Lett.*) **68** (2004) 363.
- [9] F. Raiola, L. Gang, C. Bonomo et al., Enhanced electron screening in $d(d,p)t$ for deuterated metals, *Euro. Physical J. A* **19** (2) (2004) 283–287.
- [10] A. Huke, K. Czerski and P. Heide, Measurement of the enhanced screening effect of the $d+d$ reactions in metals, *Nucl. Instr. Methods Phys. Res. Section B* **256** (2) (2007) 599–618.
- [11] K. Sinha, A theoretical model for low-energy nuclear reactions in a solid matrix, *Infinite Energy* **5** (2000) 29–54.
- [12] V. Vysotskii and S. Adamenko, Correlated states of interacting particles and problems of the Coulomb barrier transparency at low energies in nonstationary systems, *Tech. Phys.* **55** (5) (2010) 613–621.
- [13] K. Sinha and A. Meulenber, Quantum-correlated fluctuations, enhanced tunneling, and low-energy nuclear reactions in condensed matter (alloys), in *16th Int. Conf. on Cond. Matter Nucl. Sci.* (ICCF-16), Chennai, 2011, pp. 132–141; and *JCMNS-8*, 2012, pp. 105–114.
- [14] D. Letts, D. Cravens and P.L. Hagelstein, Dual laser stimulation of optical phonons in palladium deuteride, *J. Sci. Exploration* **23** (4) (2009) 459–461.
- [15] K. Sinha and A. Meulenber, Laser stimulation of low-energy nuclear reactions in deuterated palladium, *Current Sci.* **91** (7) (2006) 907–912.
- [16] P.W. Anderson, Model for the electronic structure of amorphous semiconductors, *Phys. Rev. Lett.* **34** (15) (1975) 953–955.
- [17] A.S. Alexandrov and N.F. Mott, *Polarons and bipolarons*, Singapore; River Edge, NJ: World Scientific, 1995.
- [18] K. Sinha and A. Meulenber, Lochon catalyzed DD fusion in deuterated Pd in the solid state, *Nat. Acad. Sci.(India) Lett.* **30** (7,8) (2007) 243–246.
- [19] K. Sinha and A. Meulenber, A model for enhanced fusion reaction in a solid matrix of metal deuterides, *arXiv e-print* (2009) 1–5.
- [20] A. Meulenber and K. Sinha, Tunneling Beneath the Fragmentation Level, V. Violante and F. Sarto (Eds.), *Proc. 15th Int. Conf. on Cond. Matter Nuclear Sci.* (Part 2), pp.337-341, 2009, ENEA: Rome, Italy. p. 385.
<http://lenr-canr.org/acrobat/ViolanteVproceedinga.pdf>
- [21] A. Meulenber and K. Sinha, Tunneling beneath the 4He^* fragmentation energy, *J. Cond. Matt. Nucl. Sci.* **4** (2016) 241–255.
- [22] D.R. Tilley, H.R. Weller and G.M. Hale, Energy levels of light nuclei $A = 4$, *Nucl. Phys. Section A* **541** (1) (1992) 1–104.
- [23] A. Csótó and G. Hale, Nature of the first excited state of ^4He , *Phys. Rev. C* **55** (5) (1997) 2366.
- [24] J. Kelley, D. Tilley, H. Weller et al., Adopted levels of ^4He , National Nuclear Data Center, 2011.
<http://www.nndc.bnl.gov/nudat2/getdataset.jsp?nucleus=4HE&unc=nds> (Accessed 17/05/2014).
- [25] K. Czerski, A. Huke, P. Heide et al., Experimental and theoretical screening energies for the $2H(d, p)3H$ reaction in metallic environments, *Euro. Phys. J.* **27** (1) Supplement (2006) 83–88.
- [26] I. Chernov, Y. Koroteev, V. Silkin et al., Evolution of the electron structure and excitation spectrum in palladium as a result of hydrogen absorption, *Doklady Phys.* **53** (6) (2008) 318–322.
- [27] J. Maly and J. Vavra, Electron transitions on deep Dirac levels I, *Fusion Technol.* **24**(3) (1993) 307.
- [28] F. Oner and B.A. Mamedov, Evaluation of Coulomb energy difference for light mirror nuclei using Slater-type orbitals, *Commun. Theoret. Phys.* **37** (3) (2002) 327–330.
- [29] S. DeBenedetti, *Nuclear Interactions*, Wiley, New York, 1964.
- [30] V.R. Shaginyan, Coulomb energy of nuclei, *Phys. Atomic Nuclei* **64** (3) (2001) 471–476.
- [31] P. Kálmán and T. Keszthelyi, Solid state internal conversion, *Phys. Rev. C* **69** (3) (2004) 031606.
- [32] A. Meulenber and K. Sinha, Deep-orbit-electron radiation emission in decay from 4H^* to 4He , in *17th Int. Conf. on Cond. Matter Nucl. Sci.* (ICCF-17), Vol. 13, Daejeon, 2012, pp.378–391.
- [33] A. Meulenber, Femto-atoms and transmutation, in *17th Int. Conf. on Cond. Matter Nucl. Sci.* (ICCF-17), Vol. 13, Daejeon, 2012, pp. 378–391.

- [34] M. Srinivasan, G. Miley and E. Storms, *Nuclear energy encyclopedia*, Wiley Online Library, 2011.
- [35] J. Maly and J. Vavra, Electron transitions on deep Dirac levels II, *Fusion technol.* **27** (1) (1995) 59.
- [36] Halo Nucleus, http://en.wikipedia.org/wiki/Halo_nucleus.
- [37] D.J. Nagel, Hot and cold fusion for energy generation, *J. Cond. Matter Nucl. Sci.* (Review Article) **4** (2011) 1–16.



Research Article

Examples of Isoperibolic Calorimetry in the Cold Fusion Controversy

Melvin H. Miles*

University of LaVerne, Laverne, CA 91750, USA

Abstract

The Dewar isoperibolic calorimetry developed by Fleischmann and Pons can achieve an accuracy of ± 0.1 mW. This accuracy requires the use of seven power terms to adequately describe the rate of enthalpy flowing into and out of the calorimetric system. The isoperibolic calorimetry reported by Caltech, MIT, and Harwell neglected important power terms leading to large errors.

© 2014 ISCMNS. All rights reserved. ISSN 2227-3123

Keywords: Caltech, Harwell, MIT, Power

1. Introduction

The initial cold fusion controversy centered around claims by Fleischmann and Pons for anomalous excess enthalpy and excess power produced in Dewar-type isoperibolic calorimetric cells during the electrolysis of $D_2O + LiOD$ using palladium cathodes [1]. This was soon followed by counter claims of no excess enthalpy produced in the calorimetric cells used by MIT, Caltech, and Harwell [2–4]. These and other examples will be examined in terms of the complete equation for isoperibolic calorimetry expressed by Eq. (??) [1,5,6].

$$P_{\text{calor}} = P_{\text{EI}} + P_X + P_H + P_C + P_R + P_{\text{gas}} + P_W. \quad (1)$$

The net power that flows into and out of the calorimetric system (P_{calor}) is determined by the electrochemical power (P_{EI}), excess power (P_X), the internal heater power (P_H), the heat conduction power (P_C), the heat radiation power (P_R), the power carried away by the gases generated (P_{gas}), and the power due to pressure-volume work (P_W). Each power term is a function of time (t) such as $P_{\text{calor}} = C_p M dT/dt$, thus Eq. (??) is a differential equation that can be used directly or numerically integrated for greater accuracy. Equation (??), originally developed by Fleischmann and Pons, has not been challenged, yet many groups have not considered or have ignored important terms by making various approximations.

*E-mail: melmiles1@juno.com

2. Power Terms

2.1. Calorimetric System, P_{calor}

This is the thermodynamic system under consideration and usually consists mainly of the electrochemical cell, electrolyte, and electrodes. The rate of enthalpy flowing into or out of this system determines the rate of temperature change within the calorimeter. This term is modeled by the equation

$$P_{\text{calor}} = C_p M \, dT/dt, \quad (2)$$

where $C_p M$ is the heat capacity of the system (J/K) and dT/dt is the rate of change of the cell temperature in degrees Kelvin per second (K/s). The heat capacity is expressed in the number of equivalent moles (M) of H_2O or D_2O that would yield the correct total heat capacity, and C_p is the molar heat capacity of either H_2O or D_2O (J/mol K) [1,5]. At standard conditions, the molar heat capacities (C_p) are 75.29 J/mol K for H_2O and 84.35 J/mol K for D_2O .

2.2. Electrochemical Power, P_{EI}

Power must be added to the cell to electrochemically change D_2O into D_2 and O_2 gases, $2\text{D}_2\text{O} \rightarrow 2\text{D}_2 + \text{O}_2$. Furthermore, the chemical energy contained in the D_2 and O_2 gases that flow out of an open isoperibolic calorimeter must be included in the calorimetric analysis. Thus, the equation for this term is given by [1,5–8].

$$P_{\text{EI}} = (E - E_{\text{H}}) I, \quad (3)$$

where E is the cell potential (V), I the cell current (A), and E_{H} is the thermoneutral potential (V) that is based on the chemical enthalpy of the D_2 and O_2 gases. In a closed isoperibolic cell with a recombiner, there would be no enthalpy carried out of the cell, thus $P_{\text{EI}} = EI$.

2.3. Excess power, P_{X}

This is the anomalous excess power that cannot be explained by recombination or any other chemical effects. It is often referred to as the Fleischmann–Pons Effect (FPE) excess power and generally requires the presence of both palladium and D_2O in electrolysis experiments [9,10].

2.4. Heat conduction power, P_{C} , and heat radiation power, P_{R}

Heat can be carried out of the cell into the constant temperature water bath either by thermal conduction or by electromagnetic radiation that is mostly in the infrared region [8]. The cell construction determines the dominate heat transfer pathway. For cells with thermal insulation, heat conductance to the water bath should be the major pathway. For the Dewar cells with a good vacuum between the cell walls, the heat transfer should be mainly by electromagnetic radiation. The power term for the rate of enthalpy transferred by conduction is given by

$$P_{\text{C}} = -k_{\text{C}} (T - T_{\text{b}}), \quad (4)$$

where k_{C} is the conductive heat transfer coefficient (W/K), and $T - T_{\text{b}}$ is the difference in the cell temperature and the bath temperature (K). Radiative heat transfer power is given by

$$P_{\text{R}} = -k_{\text{R}} (T^4 - T_{\text{b}}^4), \quad (5)$$

where k_{R} is the radiative heat transfer coefficient (W/K⁴) and both the T and T_{b} temperatures must be expressed in Kelvin, K. The radiative heat transfer coefficient can be estimated using the Stefan–Boltzmann constant

($5.670373 \times 10^{-8} \text{ W m}^{-2} \text{ K}^{-4}$) and the surface area of the Dewar cell [5,11]. Prior to the calorimetric cell construction, calculations should be made to determine the appropriate cell dimensions and the amount of cell insulation or Dewar-cell surface area that will ensure that the main heat transfer pathway is from the cell to the constant temperature water bath and not through the cell top to the room or through any other unwanted pathway. The clear advantage of the Dewar cell is that it allows visual observations inside the cell.

2.5. Other power terms (P_H , P_{gas} , P_W)

The heater power term, P_H , is simply the exact power in watts supplied by the resistance heater when it is operating. A typical value for the heater power is 0.2500 W [5].

The most difficult power term to express by an equation is P_{gas} [1,5,6,11]. This term includes the power carried out of the cell by the transport of the heated D_2 and O_2 gases as well as by the D_2O vapor. The power required for the vaporization of D_2O makes the largest contribution to this term [8,11]. This complicated power term is generally small except when the cell temperature exceeds about 70°C [5,8]. It can, however, become very large for cells driven to boiling [5, 8]. The complete equation for the P_{gas} term is given in Appendix A.

The power term for the rate of pressure–volume work done by the electrolysis gases is given by.

$$P_W = -RT (0.75 I/F) \quad (6)$$

assuming ideal gas behavior [8,12]. The 0.75 is the total number of moles of electrolysis gases produced by one Faraday (96,485 C) of current, R is the molar gas constant (8.3145 J/mol K) and T is the cell temperature (K). This power term is small and often neglected. However, it can produce an error if the calorimetric cell is calibrated using a small current and then a much larger electrolysis current is applied. For example, this term is -3.1 mW for $I = 0.150 \text{ A}$ at 323 K and increases to -20.9 mW for $I = 1.000 \text{ A}$ at this same temperature. The neglect of this term gave an erroneous small negative excess power of -5.0 mW for Day 61 of the NHE Pd–B study [5]. Negative experimental excess power results were very rare for the accurate Fleischmann and Pons Dewar calorimetry, and the only adequate explanation was that the excess power was nearly zero and the P_W term had become significantly more negative when the cell current was increased to 1.000 A on Day 61 [5]. The negative quantities in Eqs. (??)–(??) have their usual thermodynamic significances in showing that the power or heat is transferred from the system to its surroundings.

3. Fleischmann–Pons Dewar Calorimetry

Fleischmann and Pons had perfected their isoperibolic Dewar calorimetry over at least five years prior to their 1989 announcement. This included the determination of the best size and shape of their calorimetric cell, attaining a good Dewar vacuum, improving their temperature measurements, acquiring good instrumentation, setting up a reliable data acquisition system, modeling their calorimetry with correct equations, and, especially important, improving their methods for the analysis of the calorimetric data. Improvements continued after 1989 such as the silvering of the top portion of their calorimetric cell that provides a constant radiative heat transfer surface from the liquid electrolyte to the water bath [12]. It should not be surprising that the limited cold fusion research by MIT and others fell far short of the calorimetric accuracy obtained by Fleischmann and Pons [1,12].

The calibrated thermistors used for temperature measurements by Fleischmann and Pons were accurate to $\pm 0.001 \text{ K}$, cell voltages were measured to within $\pm 0.0001 \text{ V}$, and current measurement were reported to within $\pm 0.00001 \text{ A}$ [5]. The limiting accuracy, therefore, was the measurement of the cell temperature. Based on a 10 K difference in cell and bath temperatures, the calorimetric accuracy should approach $\pm 0.01\%$. This accuracy was attained where an experiment with 800 mW of input power was capable of measuring the power output to within $\pm 0.1 \text{ mW}$ [13]. Besides very accurate measurements, methods of data analysis were perfected to reach this high accuracy. This included the use of averaging

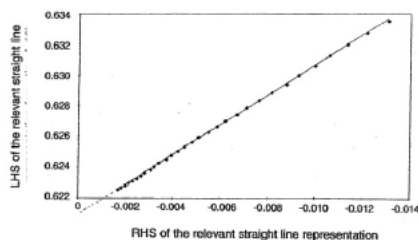


Figure 1. Straight-line from backward integration of calorimetric data (see Fig. 8 of Ref. [13]).

methods for the data, casting the calorimetric equation into a straight-line form, and the numerical integration of the calorimetric differential equation [5,11,13]. No other group or calorimetric system has come close to the ± 0.1 mW precision and accuracy of the Fleischmann–Pons isoperibolic Dewar system. It was found that backward integration that includes the internal heater period yields the best results [5,13]. The heat capacity of the system ($C_p M$) is obtained from the slope of the straight line, and the line intercept accurately gives the radiative heat transfer coefficient, k_R , to five significant figures [5,13].

An example of the straight line obtained from the backward integration of the calorimetric data for a platinum/D₂O control experiment is shown in Fig. 1. This line is in the form $y = C_p M x + k_R$, and Fig. 1 shows the left-hand side (LHS) versus the right-hand side (RHS). The line intercept at $x = 0$ yields $k_R = 0.620187 \times 10^{-9}$ W/K⁴ and the slope of this line yields $C_p M = 341.1$ J/K [13]. For this graphical representation, the straight-line equation was modified by an estimate of $C_p M$ to give a slope of near unity instead of the large slope equal to $C_p M$. The mathematical details of Fleischmann's straight-line method are given in Appendix B. Many other examples of these methods are given elsewhere [5,11,13].

Claims of large errors for isoperibolic calorimeters are not valid as long as the measurements of the cell temperature, cell voltage and cell current are accurate. Reported calorimetric errors often trace back to the failure to consider all of the power terms presented in Eq. (??) or to poor cell designs. Adequate stirring by the electrolysis gases requires tall and narrow cells as used by Fleischmann and Pons. Typical cell dimensions were 25.0 cm in height with an inner diameter of 2.5 cm for Dewar cells [5]. The cathode and anode should be positioned near the bottom of the calorimetric cell to provide the best stirring by the electrolysis gases. The data analysis methods used for isoperibolic calorimetric results may also lead to different conclusions. This is generally due to errors in determining the key calorimetric parameters involving the conductive heat transfer coefficient, k_C , the radiative heat transfer coefficient, k_R , and the heat capacity of the calorimetric system, $C_p M$ [5, 6]. In response to stirring questions, as many as seventeen thermistors were placed at various locations within the cell, and all gave the same temperature readings when properly calibrated [14]. Typically two thermistors are used in each cell [5,6]. In many isoperibolic calorimetric measurements reported, the important P_{calor} term is ignored. This term, however, can be large at the beginning of an experiment, when additional D₂O is added, when the cell heater is operating, when the cell voltage is changing, or when the cell current is changed. There is no steady state where $dT/dt = 0$ exactly, thus the P_{calor} term cannot be ignored. The use of the P_{gas} term requires the measurement of the atmospheric pressure in the laboratory (see Appendix), but this has seldom been reported. In short, the reports of large errors for isoperibolic calorimeters are, in fact, errors made by those conducting such experiments.

The largest experimental measurement error in the Fleischmann–Pons Dewar calorimetry resides in the cell temperature measurement. This temperature error can be used to calculate how this error limits the calorimetry. This is done by using Eq. (??) and assuming a typical radiative heat transfer coefficient of $k_R = 0.8000 \times 10^{-9}$ W/K⁴, a bath temperature of 298.150 K (25°C), and a cell temperature of 313.150 K (40°C). Results are shown in Table 1.

For the Fleischmann–Pons temperature error of ± 0.001 K, the resulting calorimetric error would be ± 0.1 mW as experimentally determined [13]. This calorimetric error increases to about ± 1.0 mW for the cell temperature error of ± 0.01 K and to about ± 10 mW if the cell temperature error is ± 0.1 K. Similar calorimetric errors due to cell temperature measurements are found with heat conduction calorimeters if $k_C = 0.1000$ W/K. These limiting errors will be smaller for smaller calorimeters that have smaller heat transfer coefficient, but the smaller cell size results in a larger electrolyte level effect error. Trade offs are necessary in the dimensions of the calorimetric cell.

4. Caltech, MIT, and Harwell Calorimetric Errors

The Caltech, MIT, and Harwell calorimetric errors have been fully documented in previous publications [6,12], thus this is only a brief summary.

The Caltech isoperibolic calorimetry publications show only fragments of Eq. (1), thus only P_{EI} and a term for the total power similar to P_C could be identified. The Caltech cell required electrical stirring due to its large diameter, and this introduced a poorly defined heat source. The most disturbing aspect of the Caltech experiments was that the cell constant was arbitrarily allowed to change with time. This alone will serve to zero out any possible excess power [6]. The MIT isoperibolic calorimetry used terms corresponding to P_{EI} , P_H , and P_C in Eq. (??) and P_{calor} would be small or zero in their constant temperature system. However, a large error in the MIT calorimetry was that the major heat transfer pathway was out of the cell top due to the thick glass wool insulation that was used for the cell walls [12]. Temperature measurements accurate to only ± 0.1 K were also a large source of error for the MIT calorimetry. The Harwell isoperibolic calorimetry shows only the use of the P_{EI} term and approximations for P_{gas} , P_R , and P_C . Other error sources include their method of cell calibration and the unfavorable geometry of various cathodes used [6].

In contrast to Caltech, MIT, and Harwell, the Grenoble work in France succeeded in obtaining excess power using Dewar cells [15]. The only power terms of Eq. (??) neglected was the small P_W term. Five out of 18 experiments by the Grenoble group produced excess enthalpy. The measured excess power ranged from 50 to 300 mW and the percent of excess power reached 150% during the boiling phase [15].

The actual power terms used by various groups in their isoperibolic calorimetry is shown in Table 2.

The power terms for heat conduction (P_C) could be left out for the three groups using Dewar calorimetric cells

Table 1. Effects of cell temperature errors

T_C (K)	ΔT_C (K)	P_R (W)*	ΔP_R (W)
313.150	–	1.37144	–
313.151	0.001	1.37154	0.00010
313.160	0.010	1.37242	0.00098
313.250	0.100	1.38127	0.00983
314.150	1.000	1.47018	0.09874

*Assuming $k_R = 0.8000 \times 10^{-9}$ W/K⁴ and $T_b = 298.150$ K.

Table 2. Calorimetric power terms reported

Group	P_{calor}	P_{EI}	P_X	P_H	P_C	P_R	P_{gas}	P_W
F–P *	Yes	Yes	Yes	Yes	–	Yes	Yes	No
Miles	Yes	Yes	Yes	Yes	Yes	–	Yes	Yes
Caltech	No	Yes	No	No	Yes	–	No	No
MIT	No	Yes	No	Yes	Yes	–	No	No
Harwell	No	Yes	No	No	–	Yes	No	No
Grenoble	Yes	Yes	Yes	Yes	–	Yes	Yes	No

*Fleischmann–Pons.

(Fleischmann–Pons, Harwell, and Grenoble). Similarly, for the three groups using heat conduction calorimetry (Miles, Caltech, MIT), the power terms for radiation (P_R) could be ignored. It is obvious from Table 2 that the three groups that reported no excess power (Caltech, MIT, and Harwell) failed to include several power terms in their analysis. For Caltech, the power terms P_{calor} , P_H , P_{gas} , and P_W were not discussed. The MIT calorimetry failed to mention P_{calor} , P_{gas} and P_W . Harwell missed the P_{calor} , P_H , P_{gas} and P_W power terms. In contrast, the Grenoble group left out only the small P_W power term.

5. The Thermoneutral Potential

Perhaps the most controversial term for open isoperibolic calorimetry is the use of the thermoneutral potential, E_H , in the P_{EI} power term (Eq. (3)). For the exothermic and spontaneous reaction at standard conditions,



the change in enthalpy (heat at constant pressure) is $\Delta H^\circ = -294.600$ kJ per mol of D_2O produced [16]. Thus, the thermoneutral potential is given by

$$E_H = -\Delta H^\circ / 2F = 1.52666 \text{ V}. \quad (8)$$

This is the potential at which the cell filled with D_2O could remain at standard temperature (298.15 K) during electrolysis without any heat exchange with its surroundings (thermoneutral). The actual cell potential during electrolysis is greater than E_H , and this adds heat to the cell. If one mole of D_2O is electrochemically converted into D_2 and O_2 gases that escape from the open cell, then the chemical enthalpy contained in these gases is given by $\Delta H^\circ = -2FE_H = -294.600$ kJ. Suppose for example that the electrolysis current is 0.500 A. The rate of D_2O electrolysis is then 2.5911×10^{-6} mol/s ($I/2F$). This yields -0.76333 W ($I\Delta H^\circ/2F = -E_H I$), thus the $-E_H I$ term in Eq. (??) provides a convenient method for accurately calculating the chemical power carried out of the cell in the form of the D_2 and O_2 electrolysis products. There is no other potential except E_H that will exactly account for the rate of chemical enthalpy leaving the cell in the form of the D_2 and O_2 electrolysis gases. If these gases are recombined in a closed calorimetric cell, then this calculation is not required. Appendix C provides additional information about the thermoneutral potential.

Another controversial point often raised is that 100% of the current is not always used for D_2O electrolysis. This can be checked by measuring the volume of gases produced per unit time and comparing this with Faraday's law. An integrated method over the entire experiment is the measurement of the volume of D_2O that is consumed [10]. There may be other reactions such as recombination or oxygen reduction at the cathode that interfere with the D_2O electrolysis. Thus Eq. (??) could be modified to give

$$P_{\text{EI}} = (E - \gamma E_H) I, \quad (9)$$

where γ is the current efficiency for D_2O electrolysis. Our experiments have shown that γ is very close to 1.00 and can be neglected except for a few co-deposition studies. A control study using a platinum cathode in D_2O has reported the small value of 1.1 ± 0.1 mW for recombination that is attributed to the electrochemical reduction of oxygen at the cathode [13]. This experiment used a current of 0.2000 A, thus the correction for the current efficiency yields $\gamma = 0.9964$. This small error is readily corrected by the cell calibrations [13].

6. Conclusions

The accuracy of electrochemical isoperibolic calorimetry should approach the accuracy of the cell and bath temperature measurements. For the Fleischmann–Pons isoperibolic Dewar calorimetry, this accuracy limit is $\pm 0.01\%$ or ± 0.1 mW. The cold fusion controversy traces back to the poor calorimetry and methods of data analysis used in the Caltech, MIT

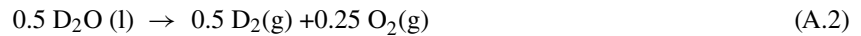
and Harwell studies. Important calorimetric terms were omitted in their experimental analyses. Even today, the reports of large errors for isoperibolic calorimeters are due mainly to the errors made by those conducting the experiments. These errors often include the neglect of important calorimetric terms, poor design of the calorimetric cells, large errors in temperature measurements, and inadequate analysis of the calorimetric data.

Appendix A.

Another pathway for the transfer of enthalpy from the open cell to the surroundings is by the heated gases that vent from the cell top through a small glass exit tube. These gases are the electrolysis gases, D_2 and O_2 , as well as D_2O vapor carried out of the cell. The evaluation of this enthalpy transfer requires the molar heat capacities of D_2 gas (C_{p,D_2}), O_2 gas (C_{p,O_2}), and D_2O vapor ($C_{p,D_2O(g)}$) as well as the enthalpy of vaporization (L) of $D_2O(L)$. The gas pressure within the cell, P^* , is approximately equal to the atmospheric pressure in an open system. Using Dalton's law of partial pressure

$$P^* = P_{D_2(g)} + P_{O_2(g)} + P, \quad (A.1)$$

where P is the partial pressure of D_2O gas at the cell temperature. The pressure terms are bolded to minimize confusing them with power terms. The electrolysis reaction per Faraday (F)



consumes 0.5 mol of D_2O and produces a total of 0.75 mol of $D_2 + O_2$ gases. The amount of $D_2O_{(g)}$ carried away per Faraday is then given by Eq. (A. 3)

$$\text{mol } D_2O (g) = 0.75(P/(P_{D_2} + P_{O_2})) = 0.75(P/(P^* - P)). \quad (A.3)$$

The rather complicated power term, P_{gas} , for the rate of enthalpy transfer by the gases leaving the cell is given by

$$P_{\text{gas}} = -(I/F)[\{0.5C_{p,D_2} + 0.25 C_{p,O_2} + 0.75 (P/(P^* - P)) C_{p,D_2O (g)}\} \Delta T + 0.75 (P/(P^* - P))L], \quad (A.4)$$

where $\Delta T = T - T_b$. The first term multiplied by ΔT represents the rate of enthalpy transfer by the D_2 , O_2 , and D_2O gases leaving the cell. The second term multiplied by the heat of vaporization of $D_2O (L)$ represents the power for the change of D_2O from a liquid to a gas. This second term makes the largest contribution to the P_{gas} power term [11]. Assuming $I = 0.2000$ A and $T_b = 22.00^\circ\text{C}$, the P_{gas} term is -5.65 mW at $T = 40.00^\circ\text{C}$ and increases to -57.83 mW at $T = 80.00^\circ\text{C}$ [11]. As seen by Eq. (A.4), these numbers would be doubled for $I = 0.4000$ A.

Appendix B.

Martin Fleischmann's straight-line method begins with the calorimetric Eq. (??) expressed as

$$C_p M dT/dt = -k_R f(T) + P_{\text{net}} + P_X \quad (B.1)$$

for Dewar cells where $P_R \gg P_C$ and where $P_{\text{net}} = P_{EI} + P_H + P_{\text{gas}} + P_W$ and $f(T) = T^4 - T_b^4$. Rearrangement of this differential equations yields

$$(P_{\text{net}} + P_X) dt/f(T) dt = C_p M dT/f(T) dt + k_R. \quad (B.2)$$

Let

$$y = (P_{\text{net}} + P_X) dt / f(T) dt \quad \text{and} \quad x = dt / f(T) dt,$$

where y has units of W/K^4 and x has units of $\text{K}^{-3} \text{s}^{-1}$. This gives a straight-line form for the differential equation

$$y = C_p M x + k_R. \quad (\text{B.3})$$

The substitution $y = C_p M' y'$ where $C_p M'$ is an estimated value for $C_p M$ gives y' and x the same units ($\text{K}^{-3} \text{s}^{-1}$), thus

$$C_p M' y' = C_p M x + k_R. \quad (\text{B.4})$$

Multiplying Eq. (B.4) by 10^9 removes the large exponents for each term, and numerical integration over a selected time period yields

$$10^9 C_p M' [y'] = 10^9 C_p M [x] + 10^9 k_R, \quad (\text{B.5})$$

where $[y']$ and $[x]$ represent numerically integrated values for these variables. At $[x] = 0$, $10^9 k_R$ equals the intercept value.

An advantage of this straight-line method is that possible errors from $C_p M$ are eliminated at $[x] = 0$. The slope of the straight line is $C_p M / C_p M'$ and is near unity when a good estimate of $C_p M'$ is used. The actual heat capacity value is given by $C_p M = (\text{slope}) (C_p M')$. Various integration methods have been reported by Fleischmann [5,11,13], but backward integrations from the midpoint of the two-day cycle (t_2), through the heating pulse, to near the beginning of the cycle (t) gives the best results. Furthermore, the k_R value obtained is for the mid-point of the two-day cycle. The cell is refilled with D_2O at the beginning of each measurement cycle ($t = 0$). Fleischmann's straight-line method assumes that the excess power (P_X) is zero or constant over the selected time period. It is not possible to accurately calibrate any calorimetric system when the excess power is changing.

Appendix C.

In addition to the heat carried out of the cell by the D_2 , O_2 , and D_2O gases (P_{gas}), there is also chemical energy contained in the D_2 and O_2 gases that could be obtained if they react outside the cell (see Eq. (??)). Therefore, in an open cell

$$P_{\text{EI}} = EI + (I/2F) \Delta H, \quad (\text{C.1})$$

where ΔH is negative for Eq. (??). As usual, power added to the system (cell) is positive and power carried away from the system is negative. This equation using ΔH (J mol^{-1}) for the chemical reaction of D_2 and O_2 outside the cell can be used directly. However, it is more convenient to use the relationship $\Delta H = -2F E_H$ (Eq. (??)) to obtain

$$P_{\text{EI}} = EI + (I/2F)(-2F E_H) = EI - E_H I \quad (\text{C.2})$$

or

$$P_{\text{EI}} = (E - E_H)I \quad (\text{C.3})$$

for these calculations. Note that at $E = E_H$, $P_{\text{EI}} = 0$, and no heating effect is provided by the electrolysis (thermo neutral). Both Eqs. (C.1) and (C.3) will give exactly the same results. At standard conditions, $E_H = 1.52666 \text{ V}$ for D_2O as given in Eq. (??) and 1.48121 V for H_2O . Thermodynamic equations (Kirchhoff's law) allow the calculation of ΔH for other temperatures, thus also E_H . For example $E_H = 1.52150 \text{ V}$ at 50°C for D_2O experiments.

Acknowledgement

This work was supported from an anonymous fund at the Denver Foundation. An adjunct faculty position at the University of LaVerne is also acknowledged. The author especially thanks Professor Martin Fleischmann for very helpful communications over many years.

References

- [1] M. Fleischmann, S. Pons, M.W. Anderson, L. Li and M. Hawkins, Calorimetry of the palladium–deuterium–heavy water system, *J. Electroanal. Chem.* **287** (1990) 293–348.
- [2] N.S. Lewis et al., Searches for low-temperature nuclear fusion of deuterium in palladium, *Nature* **340** (1989) 525–530.
- [3] D. Albagli et al., Measurements and analysis of neutron and gamma-ray emission rates, other fusion products, and power in electrochemical cells having Pd cathodes, *J. Fusion Energy* **9** (1990) 133–148.
- [4] D.E. Williams et al., Upper bounds on cold fusion in electrolysis cells, *Nature* **342** (1989) 375–384.
- [5] M.H. Miles, M. Fleischmann and M.A. Imam, Calorimetric analysis of a heavy water electrolysis experiment using a Pd–B alloy cathode, Naval Research Laboratory Report Number NRL/MR/6320-01-8526, Washington, DC, pp. 1–155, March 26, 2001.
- [6] M.H. Miles, B.F. Bush and D.E. Stilwell, Calorimetric principles and problems in measurements of excess power during Pd–D₂O electrolysis, *J. Phys. Chem.* **98** (1994) 1948–1952.
- [7] M.H. Miles and M. Fleischmann, New approaches to isoperibolic calorimetry, in *ICCF-15 Proceedings*, V. Violante and F. Sarto (Eds.), Rome, Italy, October 5–9, 2009, pp. 22–26.
- [8] M.H. Miles and M. Fleischmann, Measurements of excess power effects in Pd/D₂O systems using a new isoperibolic calorimeter, *J. Cond. Mat. Nucl. Sci.* **4** (2011) 45–55.
- [9] M.H. Miles, Electrochemistry and calorimetry of ruthenium co-deposition, *J. Cond. Mat. Nucl. Sci.* **8** (2012) 115–123.
- [10] M.H. Miles, Co-deposition of palladium and other transition metals in H₂O and D₂O solutions, *ICCF-17*, Daejeon, Korea, 2012 (submitted).
- [11] M.H. Miles and M. Fleischmann, Accuracy of isoperibolic calorimetry used in a cold fusion control experiment in *Low-Energy Nuclear Reactions Sourcebook*, J. Marwan and S.B. Krivit (Eds.), Washington, DC: American Chemical Society, 2008, pp. 153–171.
- [12] M.H. Miles and P.L. Hagelstein, New analysis of MIT calorimetric errors, *J. Cond. Mat. Nucl. Sci.* **8** (2012) 132–138.
- [13] M. Fleischmann and M.H. Miles, The instrument function of isoperibolic calorimeters: excess enthalpy generation due to the parasitic reduction of oxygen in *Condensed Matter Nuclear Science*, P.L. Hagelstein and S.R. Chubb (Eds.), *ICCF-10 Proceedings*, New Jersey: World Scientific, 2006, pp. 247–268.
- [14] M. Fleischmann, personal communication, 2000.
- [15] G. Lonchampt, L. Bonnetrain and P. Hicter, Reproduction of Fleischmann and Pons experiments, *ICCF-6 Proceedings*, Hokkaido, Japan, Vol. 1, 1996, pp. 113–120.
- [16] D.D. Wagman et al., The NBS table of chemical thermodynamic properties, *J. Phys. Chem. Ref. Data* **11** (1982) 38,



Research Article

Co-deposition of Palladium and other Transition Metals in H₂O and D₂O Solutions

Melvin H. Miles*

University of La Verne, La Verne, CA 91750, USA

Abstract

The co-deposition of palladium, ruthenium, rhenium, nickel, and iridium were investigated in H₂O and D₂O ammonia systems (NH₄Cl/NH₃). Significant amounts of excess power were observed only in the deuterated Pd/D₂O system. There was no anomalous excess power observed for the co-deposition of ruthenium, rhenium or nickel in any H₂O or D₂O experiment.

© 2014 ISCMNS. All rights reserved. ISSN 2227-3123

Keywords: Calorimetry, Nickel, Rhenium, Vacancies

1. Introduction

Anomalous effects for Pd/D co-deposition were first reported by Szpak and Mosier-Boss using the PdCl₂ + LiCl/D₂O system [1]. However, commercial electroplating baths for palladium are often based on aqueous ammonia solutions (NH₄Cl/NH₃) at pH 7–10 [2]. The related PdCl₂ + ND₄Cl + ND₃/D₂O deuterated ammonia system previously produced large reproducible excess power in three out of three experiments [3]. This co-deposition excess power was similar to the anomalous effects observed in other Pd–D systems [4]. Recent experiments have shown that these anomalous excess power effects were absent in Pd/H₂O controls as well as for the co-deposition of ruthenium (Ru) in both H₂O and D₂O ammonia solutions [5,6]. This study reports results for the co-deposition of rhenium (Re), nickel (Ni), and iridium (Ir) in both H₂O and D₂O ammonia systems and the use of high currents for palladium co-deposition.

The Pd/D co-deposition term implies that both palladium and deuterium are simultaneously deposited at the cathode in an electrochemical cell. Thermodynamically, palladium deposition can occur at a smaller cell voltage than D₂O electrolysis (0.5362 V vs. 1.2615 V at standard conditions). Therefore, the use of small cell currents or linear potential scan may result in the deposition of palladium without the generation of deuterium gas at the cathode, thus there would be no co-deposition. For our studies, however, the cell currents used were always sufficient for the simultaneous generation of deuterium and the deposition of palladium or other transition metals at the cathode.

*E-mail: melmiles1@juno.com

2. Experimental

Calorimetric studies used a heat conducting isoperibolic design and electrochemical instrumentation as previously reported [7,8]. The deuterated chemicals used were Cambridge Isotope Laboratories or ACROS D₂O (99.9 at% D), ACROS ND₄Cl (98 at% D) and ACROS ND₄OD (99 at% D). The deposition of transition metals used Alfa-Aesar PdCl₂, Ru(NO)(NO₃)₃, ReCl₃, NiO, NiCl₂·6H₂O, and IrCl₃. The transition metal solution concentrations were near 0.025 M except for two of the high current depositions using PdCl₂ where the concentration was significantly smaller (about 0.006–0.009 M). The metal deposition process generally used a constant current of 6 mA or higher where deuterium gas production can be visually observed at the cathode. However, ruthenium could not be deposited until the current was increased to 400 mA [6]. The IrCl₃ solution remained dark in color and could not be completely deposited even at high currents. Recent experiments have used a large current (200 or 300 mA) for palladium deposition in an effort to increase metal vacancy formation that may promote the production of large excess power effects [9].

3. Results

Previous studies of ruthenium co-deposition in H₂O and D₂O produced no measurable excess power [6]. These studies have now been extended to the co-deposition of other transition metals as well as to the high current deposition of palladium.

3.1. Co-deposition of rhenium

The use of 0.020 M ReCl₃ + 0.15 M NH₄Cl + 0.45 M NH₄OH + H₂O formed a very dark red solution with a pH = 9.58 at 19°C. Co-deposition at 6 mA produced a black deposit of Re at the cathode and a clear solution within 24 h. The solution became acidic (pH = 1.36), as expected, following completion of the rhenium deposition and after increasing the current to 100 mA which drives off the ammonia. Some chlorine production was also detected during this period. The ammonia and chlorine evolution events are both endothermic processes that could only produce small negative effects on excess power measurements. This cell was then placed into the calorimeter and ran for 12 days using an electrolysis current of 300 mA. As shown in Fig. 1, no excess power was detected within the experimental error of ± 5 mW.

The mean excess power using thermistor 4, as shown in Fig. 1, was -1.1 ± 4.2 mW. This thermistor was placed directly in the solution within the glass cell. A second thermistor was placed in the usual position on the outside surface of the glass cell in a secondary compartment filled with Mobil-1 oil (5–30 W) as reported previously [6,7]. This second thermistor gave a mean excess power of 1.4 ± 5.7 mW. Both thermistors agree that there was no excess power within experimental error for this rhenium co-deposition study. In fact, the small departures from exactly zero excess power can be related to errors in the calculation of the electrolyte volume. Long periods between re-filling this cell were used in this rhenium co-deposition experiment to obtain the value for the effect of the electrolyte volume on the heat transfer coefficient. This study yielded the value of $\Delta k_C / \Delta V = 0.0002$ W/K mL that was used in this and following experiments [10].

3.2. Co-deposition of palladium at high currents

Recent experiments have involved the co-deposition of palladium at high currents in an effort to produce a larger number of metal vacancies and possible large excess power effects [9]. Two Pd/D₂O experiments have been completed using a high co-deposition current of 200 or 300 mA, and both produced large excess power effects. Figure 2 shows the results for one of these studies.

From Fig. 2, it is estimated that there was a total of 150 kJ of excess enthalpy in this co-deposition experiment. It appears that even larger excess enthalpy amounts could have been measured by running the experiment longer. A

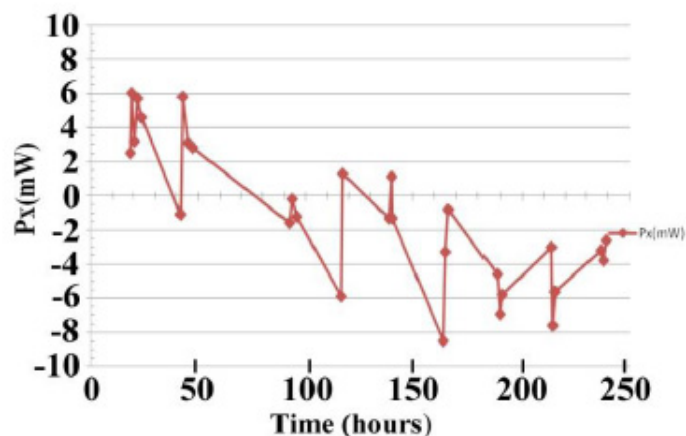


Figure 1. Calorimetric results for rhenium co-deposition in H₂O (thermistor 4).

second Pd/D₂O experiment using 200 mA for the co-deposition process produced a similar excess power effect and a total excess enthalpy of about 170 kJ. This exceeds the amount found in any other co-deposition experiment using the ammonia system. The calorimetric results for this second Pd/D₂O experiment is shown in Fig. 3. A smaller concentration of PdCl₂ (0.0091 versus 0.0264 M) was used in this second experiment.

The current profile for the results in Fig. 2 was 300 mA up to 118.77 h, then 400 mA until 194.00 h, then 300 mA again up to 221.50 h, and finally 500 mA to the end of the experiment. The second experiment shown in Fig. 3 used 200 mA up to 30.62 h, then 300 mA to 123.18 h, then 200 mA again until 152.32 h, 350 mA until 176.40 h, and then 300 mA to the end of this experiment. The slight dip in the excess power seems to be related to the lower current of 200 mA for this period. The cell voltage ranged from 3.898 V at 300 mA to 7.906 V at 500 mA in the first Pd/D₂O experiment (Fig. 2), and 7.092 V at 200 mA to 8.550 V at 350 mA in the second Pd/D₂O study (Fig. 3). The more

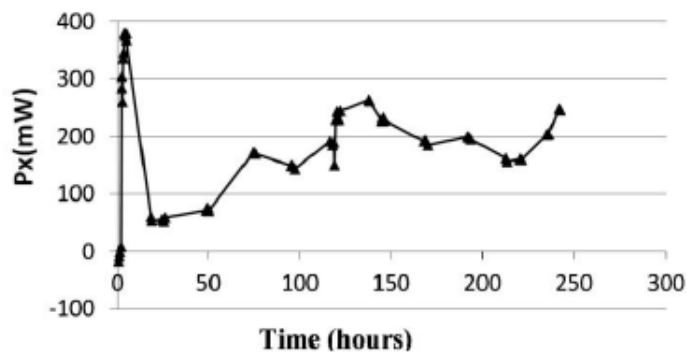


Figure 2. Calorimetric results for the co-deposition of palladium in D₂O at 300 mA.

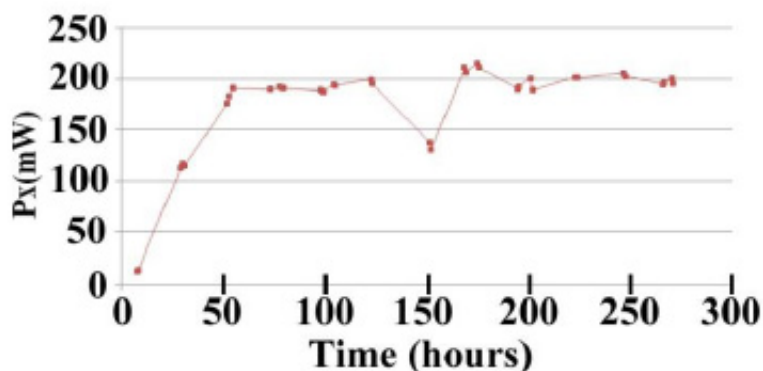


Figure 3. Calorimetric results for the second co-deposition of palladium in D₂O at 200 mA.

constant excess power effect in the second experiment (Fig. 3) may be related to the more narrow range in the cell voltage.

Control studies of Pd/H₂O using co-deposition at 300 mA unexpectedly yielded small excess power effects. The consumption of H₂O was also smaller than calculated suggesting possible recombination. It was found that not all of the palladium remains on the cathode substrate with high current deposition, and small palladium particles were visible in the solution that may cause recombination. The excess enthalpy in this Pd/H₂O experiment was about 60 kJ. In a second Pd/H₂O study, a smaller concentration of PdCl₂ (0.0063 M versus 0.0247 M) was used. In this experiment, the H₂O consumed slightly exceeded the theoretical amount (28.0 mL versus 27.28 mL). The excess enthalpy produced was also significantly smaller at 35 kJ. This still leaves, however, a small unexplained excess power effect for the Pd/H₂O control system. Further experiments are needed to resolve these findings. However, another laboratory has reported excess power in light water experiments using high current co-deposition [11].

Experimental cooling curves at the end of studies produced by shutting off the electrolysis current provide a tool that may distinguish between the Fleischmann–Pons excess power effects (FPE) and other types of excess power such as recombination [7]. At this zero current, the calorimetric equation simplifies to

$$C_p M \frac{dT}{dt} = -k_C(T - T_b) + P_X, \quad (1)$$

where $C_p M$ is the heat capacity of the calorimetric system (J/K), T is the cell temperature (K), T_b is the constant bath temperature (K), k_C is the conductive heat transfer coefficient (W/K), and P_X is the excess power effect (W). For FPE excess power, P_X often continues after the current is set to zero (Heat-After-Death, see [16]). In contrast, other types of excess power go to zero immediately when $I = 0$. By assuming $P_X = 0$, Eq. (1) can then be integrated to give

$$\ln(T - T_b) = -(k_C/C_p M)t + \ln(T_0 - T_b). \quad (2)$$

The rearrangement of Eq. (2) yields

$$\Delta T = \Delta T_0 \exp(-k_C t / C_p M), \quad (3)$$

where $\Delta T = T - T_b$ and $\Delta T_0 = T_0 - T_b$. This exponential decrease in ΔT is shown experimentally in Fig. 4 for the cell temperature using thermistor 2 (T_2).

The time constant (τ) for the calorimetric cell can be determined directly from Fig. 4 or calculated from $\tau = C_p M / k_C$ and yields 51 min (3060 s) for this experiment.

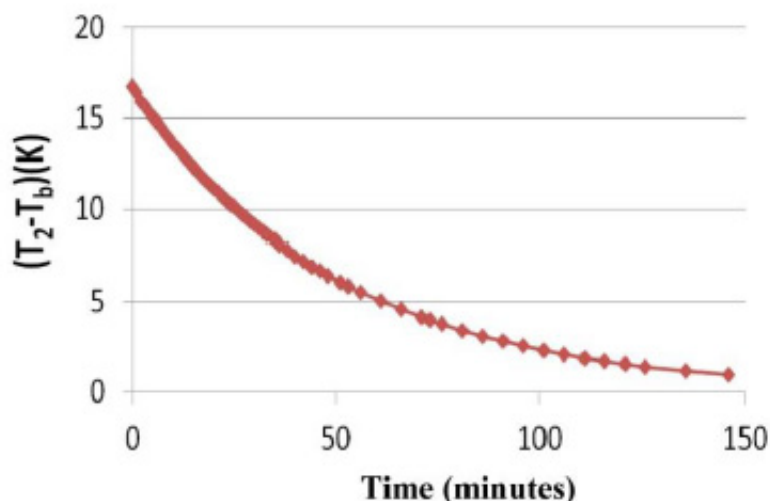


Figure 4. Experimental cooling curve for the Pd/H₂O experiment.

Figure 5 shows the application of the integrated Eq. (2) to the cooling curve for the Pd/H₂O co-deposition control that showed excess power. The experimental data fits almost perfectly with Eq. (2) ($R^2 = 0.99992$). This suggests that there was no “Heat-After-Death” and likely no FPE excess power in this Pd/H₂O control ($P_X = 0$). This is also evidence that almost all of the heat is transferred by conduction through the walls of the calorimeter to the water bath. Furthermore, the equation for this line provides for the calculation of the heat capacity of the system and yields $C_p M = 402$ J/K. A theoretical calculation of this heat capacity for this same experimental volume of H₂O in the cell (42.0 mL) yields $C_p M = 404$ J/K. Cooling curve studies for other Pd/H₂O control cells have also given near perfect agreement with the integrated Eq. (2) [7,8].

Figure 6 shows the same application of Eq. (2) to the cooling curve for the Pd/D₂O experiment involving high current co-deposition. It is readily apparent that the line fit is not as good. Furthermore, the equation for the line yields $C_p M = 476$ J/K, a value that is much too high. The presence of a lingering excess power effect distorts the fit of the data with Eq. (2) and prolongs the cooling process. This reduces the slope of the line and yields a high $C_p M$ value. Based on these cooling curves, there was likely real FPE excess power for the Pd/D₂O experiment but not for the Pd/H₂O experiment.

3.3. Nickel and iridium co-deposition

The Rossi E-Cat [12] claims for a nickel–hydrogen system spurred interest in Ni/H₂O co-deposition experiments. Several co-deposition experiments were completed in the ammonia system using either NiO or NiCl₂·6H₂O. The NiO was mostly insoluble and required increasing the current to 100 mA to obtain complete deposition and a clear solution. The NiCl₂·6H₂O was much more soluble, but there was no excess power produced in any of the nickel co-deposition experiments involving H₂O and D₂O.

The iridium co-deposition experiment proved to be a challenge. The initial 0.024 M IrCl₃ ammonia solution resulted in a black, insoluble suspension. Complete deposition could never be achieved even with the use of large currents up to 500 mA. Reversible Ir³⁺/Ir⁴⁺ reactions are known as a “source of annoyance” for iridium chemistry that block further

reactions [13]. The calorimetry showed measurable excess power, but this may be explained by the dark color of the insoluble suspension. The dark iridium particles may partially block the transmission of visible and infrared radiative power from the cell, but more work is needed to test this assumption. There could also be iridium reactions that interfere with the electrolysis of H_2O , but this was not obvious by the measured H_2O consumption.

Iridium is one of the most resistive metals to hydrogen absorption with a very low value of $\text{H}/\text{Ir} = 0.005$ even at 90,000 atm hydrogen pressure at 250°C [14]. Based on this property, the small excess power in the iridium study was likely due to the dark solution color, the incomplete deposition, or some factor other than real FPE excess power.

Prior to the iridium experiment and the palladium co-deposition at high currents, the only excess power observed was for $\text{Pd}/\text{D}_2\text{O}$ in the ammonia co-deposition system. Excess power was measured for $\text{Pd}/\text{D}_2\text{O}$ in six out of six (6/6) experiments, while no excess power was found in 2/2 $\text{Pd}/\text{H}_2\text{O}$ studies, 4/4 ruthenium H_2O or D_2O studies, 2/2 rhenium H_2O or D_2O studies and 4/4 nickel H_2O or D_2O experiments. Statistical calculations at this point showed only a small probability (0.0000106) that random errors could have restricted the excess power effect to only the $\text{Pd}/\text{D}_2\text{O}$ co-deposition system. However, the $\text{Pd}/\text{H}_2\text{O}$ co-deposition studies at high currents as well as the iridium results complicates these statistical calculations. Further experiments are needed to determine if these new small excess power effects for $\text{Pd}/\text{H}_2\text{O}$ and $\text{Ir}/\text{H}_2\text{O}$ are real.

3.4. Consumption of H_2O and D_2O

Recombination or other chemical reactions can yield false measurements of anomalous excess power for open, isoperibolic calorimeters. This can be checked by simultaneous measurements of the electrolysis gases produced and comparisons with theoretical amounts based on Faraday's law. In the Navy experiments at China Lake using palladium rod cathodes, the experimental amounts of electrolysis gases always agreed within experimental errors with Faraday's Law [15]. However, some co-deposition experiments occasionally gave evidence of recombination [15]. This was attributed to the small palladium particles formed by co-deposition floating loose in the solution and reaching the top of the electrolyte and leading to the direct recombination of a portion of the electrolysis gases.

It has been found that careful measurements of the total volume of H_2O or D_2O consumed also provides a rea-

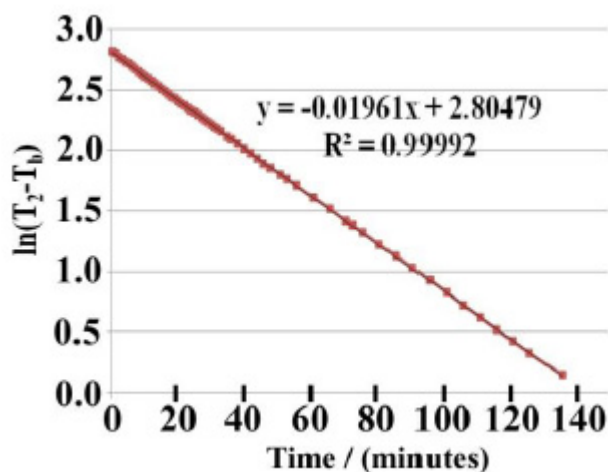


Figure 5. Integrated cooling curve results for the $\text{Pd}/\text{H}_2\text{O}$ experiment.

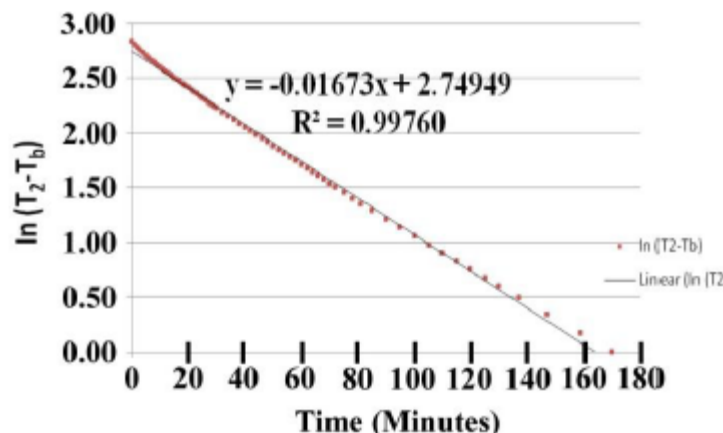


Figure 6. Integrated cooling curve results for the Pd/D₂O experiment.

sonable integrated check over the entire experiment for recombination or other chemical reactions [5,16]. Previous measurements of the volume of H₂O or D₂O consumed compared with the theoretical calculation gave a mean ratio of 1.09 ± 0.11 [5]. There are always small extra amounts of H₂O or D₂O that are evaporated and carried out of the cell by the electrolysis gases. This can vary with the geometry and the temperature at the top of the gas outlet tube, but typical measurements usually give about a 5% loss of H₂O or D₂O due to evaporation [16]. Measured and theoretical consumptions of H₂O or D₂O in recent co-deposition experiments are presented in Table 1. Several values are higher than normal due to foaming (Colorado) or due to problems with measuring the volume of electrolyte consumed.

The mean value for the measured/theoretical ratios from Table 1 is a near normal 1.04 ± 0.07 . However, the low values found in the first two experiments with Pd + D₂O or Pd + H₂O for depositions at 300 mA are quite unusual and suggest that some recombination occurred. The last two experiments using less PdCl₂ for high current depositions gave near normal ratios within the experimental error range (± 1.0 mL). It was visually observed that the use of smaller concentrations of PdCl₂ led to better deposits of palladium and much smaller amounts of palladium particles present in

Table 1. Experimental and theoretical consumptions of H₂O and D₂O

Experiment	Measured (mL)	Theoretical (mL)	Ratio
Ru (H ₂ O)	45.5	40.73	1.12
Ru (D ₂ O)	43.0	41.83	1.03
Re (H ₂ O + D ₂ O)	34.5	31.40	1.10
Ni (H ₂ O)	26.0	23.62	1.10
Ni (H ₂ O + D ₂ O)	23.8	23.06	1.03
Ir (H ₂ O)	21.5	20.78	1.04
Pd (D ₂ O), Colorado	11.3	9.94	1.14
Pd (D ₂ O, High I)	25.7	28.46	0.90
Pd (H ₂ O, High I)	14.6	15.30	0.95
Pd (D ₂ O, High I)*	25.0	25.41	0.98
Pd (H ₂ O, High I)*	28.0	27.28	1.03

*Used small concentrations of PdCl₂.



Figure 7. Photo of the two Colorado cells.

the solutions. Except for the high current co-deposition experiments, the measured consumption of H_2O or D_2O does not support any significant recombination in these studies.

3.5. Colorado Pd/ D_2O experiment

A replication of the large excess power effect with Pd/ D_2O co-deposition [3–5] was attempted by taking this calorimeter to the Coalescence Laboratory in Boulder, Colorado. The experimental protocol of low-current deposition at 6 mA followed by 100 mA and then 20 mA for three days before again increasing the current was performed exactly as previously at NHE in Japan [3,4]. The excess power results up to this point (140 h) were very similar to the experiments in Japan. However, the following increases in the current produced periods of negative excess power effects that were larger than normal experimental errors. This was never previously observed using this calorimeter and was quite confusing as well as thermodynamically impossible. This strange behavior was finally explained when bubbles of foam were observed emerging from the top of the gas outlet tube. It was later determined that this foaming problem produced an additional heat leak of about 4% for this calorimeter (k_C increased from 0.1340 W/K to about 0.1390 W/K). Because of this foaming problem, it was not possible to clearly identify any excess power production. At the end of this experiment, it was found that the epoxy used on the electrodes had not cured properly, swelled considerably in size, and likely was the source of this foaming problem. This Colorado Pd/ D_2O experiment is included in Table 1 and shows a somewhat higher than normal amount of D_2O consumed that can be attributed to the foaming effects. Figure 7 shows the photo of the two cells at the end of the experiments in Colorado that used the same epoxy. The Coalescence cell using this same epoxy is on the right. The epoxy swelled by at least a factor of 10 as seen by the light colored material above the electrodes in Fig. 7. This epoxy problem was never observed in any previous experiment, but in an effort to maintain everything exactly the same as a previous excess power study, an older epoxy material was used. Later experiments using the same bottle of D_2O but no epoxy produced no foaming.

The actual calorimetric results for the Colorado Pd/ D_2O experiment are given in Fig. 8. The same heat transfer coefficient (k_C) was used as in previous experiments (0.1340 W/K at 50.0 mL) because it was not possible to determine the extent of foaming and its precise effect on k_C .

The calorimetric results looked similar to the previous NHE results [3,4] up to 140 h when the current was increased from 20 to 100 mA. This suggests that there was no significant foaming early in this experiment. The effect at 100 mA produced the first significant negative excess power ever measured with this calorimeter. Although the calorimeter recovered to near zero excess power, it was not possible to evaluate how this foaming effect could mask any real excess

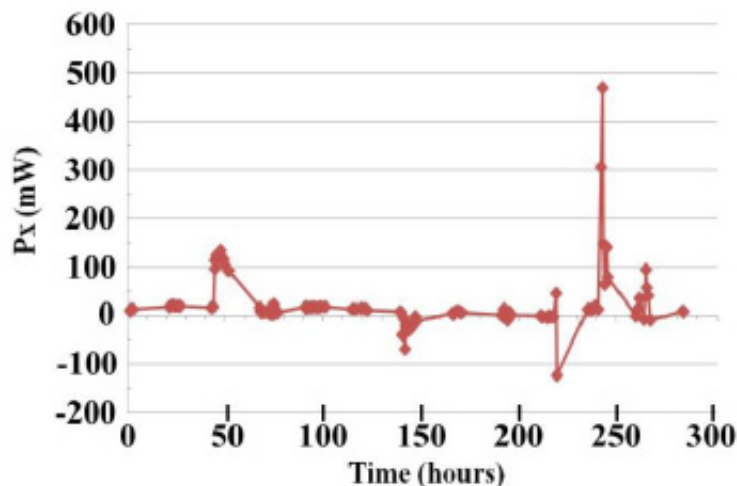


Figure 8. Calorimetric results for the Colorado Pd/D₂O co-deposition experiment.

power. Increasing the current to 400 mA at 217 h produced an even larger negative excess power effect due to the visible foaming carrying heat out of the vent tube at the top of the cell. At times the cell voltages became very large and approached the limit of the electrochemical instrumentation (30 V), thus the cell current had to be scaled back. Due to the unusually high cell voltage, encountered, additional ND₄Cl + D₂O was injected into the cell at 241 h. This significantly lowered the cell voltage. At least part of the following excess power peak up to 470 mW at $I = 400$ mA could be due to a new episode of chlorine evolution that was detected and possible NCl₃ formation. Normally, there is no need to add additional ND₄Cl, and there is no measurable chlorine production at this stage of the experiment. However, large increases in the cell voltages have been observed in other excess power producing experiments for Pd/D₂O co-deposition in the deuterated ammonia system [3–5]. In contrast, the measured cell voltages have always been normal for the Pd/H₂O studies. Something unusual other than chemistry is likely implicated in these large cell voltage increases in the Pd/D₂O system while normal cell voltages were always observed in Pd/H₂O systems.

There are several possible explanations for the large cell voltages observed in the Pd/D₂O ammonia co-deposition systems. One explanation is the loss of most of the electrolyte by the net reaction



where D₂ is formed as normal at the cathode but Cl₂ is produced at the anode while the electrolysis gases drive off the ND₃. A second more unusual explanation involves the very large electrode area up to 10⁶ cm² formed by the palladium deposition [17]. It can be shown that an electrode surface this large could absorb all ions present in the cell into the electrode double layer and leave practically no ions in the solution. In the Colorado experiment, the addition of another 0.15 M of ND₄Cl created a sudden decrease in the cell voltage from 22.2 to 2.84 V for a cell current of 20 mA. This effect could be rationalized by either of these two explanations. It is not known why this large loss of electrolyte has only been observed in the Pd/D₂O system. The Pd/D₂O and Pd/H₂O system both show similar amounts of chlorine production and display similar chemistries. Is it possible that hot spots or some type of nuclear radiation in the Pd/D₂O system promotes decomposition of the ammonia electrolytes?

4. Conclusions

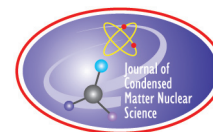
Large amounts of excess power and excess enthalpy have only been observed in the deuterated Pd/D₂O co-deposition system. There was no excess power observed for the co-deposition of ruthenium, rhenium, or nickel in any H₂O or D₂O experiment. High current deposition of Pd in D₂O has produced large excess power and excess enthalpy effects. In fact, the total excess enthalpy of 170 kJ exceeds that of any previous co-deposition experiment in the deuterated ammonia system. Similar high current deposition studies of palladium in H₂O, however, have produced smaller excess power and excess enthalpy effects. Cooling curves of both the Pd/D₂O and Pd/H₂O systems indicate that the smaller excess power effects for Pd/H₂O are likely due to recombination or other chemical effects. Numerous problems were encountered in the attempted co-deposition of iridium. This is the only study where complete deposition of the metal was unattainable.

Acknowledgment

This work was supported from an anonymous fund at the Denver Foundation. Dixie State University and the Dixie Foundation, especially Kalynn Larson, assisted in the administration of the Fund and the purchase of equipment and supplies. The Naval Air Warfare Center Weapons Division at China Lake, California provided laboratory space and Navy equipment that helped with this research. Helpful discussions with Dennis Letts and Peter Hagelstein are also acknowledged. The author also appreciate the opportunity provided by Rick Cantwell and Matt McConnell to visit and run experiments at the Coalescence Laboratory in Boulder, Colorado.

References

- [1] S. Szpak, P.A. Mosier-Boss and J.J. Smith, On the behavior of Pd deposited in the presence of evolving deuterium, *J. Electroanal. Chem.* **302** (1991) 255–260.
- [2] R. LePenven, W. Levason and B. Pletcher, Studies of the electrodeposition of palladium from baths based on {Pd(NH₃)₂X₂} salts I. Pd(NH₃)₂Cl₂ baths, *J. Appl. Electrochem.* **20** (1990) 399–404.
- [3] S. Szpak, P.A. Mosier-Boss and M.H. Miles, Calorimetry of the Pd + D co-deposition, *Fusion Technol.* **36** (1999) 234–241.
- [4] S. Szpak, P.A. Mosier-Boss, M.H. Miles and M. Fleischmann, Thermal behavior of polarized Pd/D electrodes prepared by co-deposition, *Thermochimica Acta* **410** (2004) 101–107.
- [5] M.H. Miles, Investigations of possible shuttle reactions in co-deposition systems, *J. Cond. Mat. Nucl. Sci.* **8** (2012) 12–22.
- [6] M.H. Miles, Electrochemistry and calorimetry of ruthenium co-deposition, *J. Cond. Mat. Nucl. Sci.* **8** (2012) 115–123.
- [7] M.H. Miles and M. Fleischmann, New approaches to isoperibolic calorimetry, in *ICCF-15 Proceedings*, V. Violante and F. Sarto (Eds.), Rome, Italy, pp. 22–26, October 5–9, 2009.
- [8] M.H. Miles and M. Fleischmann, Measurements of excess power effects in Pd/D₂O systems using a new isoperibolic calorimeter, *J. Cond. Mat. Nucl. Sci.* **4** (2011) 45–55.
- [9] D. Letts and P.L. Hagelstein, Modified Szpak protocol for excess heat, *J. Cond. Mat. Nucl. Sci.* **8** (2011) 1–11.
- [10] M.H. Miles and P.L. Hagelstein, New analysis of MIT calorimetric errors, *J. Cond. Mat. Nucl. Sci.* **8** (2012) 132–138.
- [11] D. Letts, Email communications, 2012.
- [12] S.K. Ritter, Reviving cold fusion, *Chem. Eng. News* **90** (2012) 42–44.
- [13] N.N. Greenwood and A. Earnshaw, *Chemistry of the Elements*, Pergamon Press, Oxford, UK, 1984, p. 1296.
- [14] V.E. Antonov, I.T. Belash, V. Yu. Malyshev and E.G. Ponyatovsky, The solubility of hydrogen in the platinum metals under high pressure, *Int. J. Hydrogen Energy* **11** (3) (1986) 193–197.
- [15] M.H. Miles, B.F. Bush and K.B. Johnson, Anomalous effects in deuterated systems, NAWCWPNS TP 8302, September 1996.
- [16] M.H. Miles, M. Fleischmann and M.A. Imam, Calorimetric analysis of a heavy water electrolysis experiment using a Pd–B alloy cathode, Report number NRL/MR/6320-01-8526, Naval Research Laboratory, Washington, DC, March 26, 2001.
- [17] M.H. Miles, Investigations of co-deposition systems, in *ICCF-15 Proceedings*, V. Violante and F. Sarto (Eds.), Rome, Italy, October 5–9, 2009, pp. 32–37.



Research Article

Use of D/H Clusters in LENR and Recent Results from Gas-Loaded Nanoparticle-type Clusters

George H. Miley^{*,†}, Xiaoling Yang, Kyu-Jung Kim, Erik Ziehlm,
Tapan Patel, Bert Stunkard and Anais Ousouf

Department of Nuclear, Plasma and Radiological Engineering, University of Illinois at Urbana-Champaign, IL 61801, USA

Heinrich Hora

Department of Theoretical Physics, University of New South Wales, Sydney, Australia

Abstract

Anomalous heat, attributed to Low-energy Nuclear Reactions (LENRs), is obtained by pressurizing metal alloy nanoparticles with deuterium gas. The reactions are enhanced by creation of ultra-high density deuterium clusters in the nanoparticles. Experiments comparing various nanoparticles and plans for a proof-of-principle unit are presented.

© 2014 ISCMNS. All rights reserved. ISSN 2227-3123

Keywords: Gas-loading system, Low-energy nuclear reaction, Nanoparticles

1. Introduction

Our previous experimental results have demonstrated the formation of ultra-high density hydrogen/deuterium nanoclusters with 10^{24} atom/cm [3] in metal defects (Fig. 1) [1,2,4–6]. Both experimental [7–11] and theoretical studies [12] have demonstrated that due to the close distance (ca. 2.3 pm) [7] between ions in the cluster, they can easily be induced to undergo intense nuclear reactions among themselves and some neighboring lattice atoms. In view of their multi-body nature, such reactions are termed Low-energy Nuclear Reactions (LENRs) – a terminology generally accepted by workers in the cold fusion field. Because the interacting ions have little momentum, the compound nucleus formed in these reactions is near the ground state so few energetic particles are emitted from its decay. Triggering excess heat generation, i.e., heat generation from nuclear reactions, in LENR experiments has been accomplished in various ways, all involving the loading of protons or deuterons into a solid metal or alloy material.

^{*}E-mail: ghmiley@illinois.edu

[†]Also at: Lenuco LLP, Champaign, IL 61821, USA.

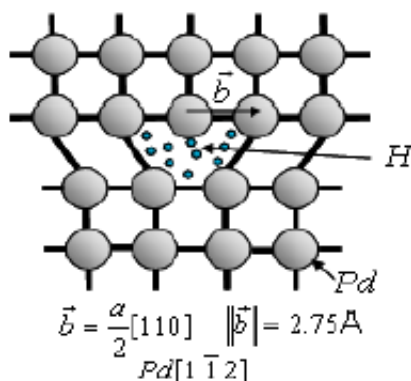
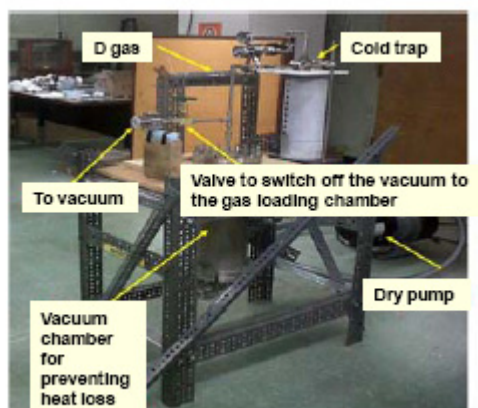


Figure 1. Scheme of edge dislocation loops in Pd containing.

Electrochemical loading was the initial approach of the experiment, and remains the most practiced approach. Gas loading is also widely used [13–23]. It is currently gaining more attention due to its smaller heat capacity and thereby higher temperature change as compared to an electrolysis system. In addition, a gas can be easily heated to temperatures greater than 100°C without excess pressure production. Therefore, the excess energy production from a gas-loading system can be observed more efficiently and in a relatively higher temperature range, making the technology compatible with existing energy conversion methods. Although the nuclear physics of LENRs is independent of the loading method, advantages of the gas-loading system described above using Ultra-High Density Deuterium (UHD-D) clusters can be taken advantage of to move the field towards a practical power unit. In this study, we report the anomalous heat generated from metal alloy nanoparticles loaded with deuterium through pressurizing the sample chamber.

Our gas-loading system is based on the design we first developed for thin film studies in 2010. Figure 2 shows the setup. Inside the large outer chamber (8-inch diameter) shown in Fig. 2(A) is a much smaller cylindrical pressure chamber (1-inch diameter), shown in Fig. 2(C). This arrangement uses a vacuum between the two cylinders to minimize heat losses and also provided a basis for measurement of heat flow for the calorimeter measurement. The nanoparticles are placed in the smaller chamber and loaded with deuterium (D_2) or hydrogen (H_2) gas. Three thermocouples are attached to the small cylinder – two at the sides and one at the bottom – to record the temperature during the loading and unloading process. The experiments described here used D_2 gas and Pd rich nanoparticles. Other work with H_2 uses Ni-rich nanoparticles. A cold trap is connected between the smaller cylindrical chamber and the D_2 gas cylinder in order to provide extra purification for the flowing D_2 gas. During the D_2 gas loading and unloading process, the large chamber remained under a vacuum to reduce heat losses. The remaining heat loss is predominantly by radioactive heat transfer which can be calculated for calorimetric purposes from the thermocouple data. Figure 3 provides a further explanation of the operation of this gas-loading system.

Initial experiments with this system employed a “dynamic” loading where the system is first rapidly pressurized and after about 500 s depressurized. This is intended to study the initial adsorption effect, followed by desorption. The results shown in Fig. 4 loaded high purity D_2 gas at 60 psi into 20 g of Pd-rich nanoparticle powder (termed #1 nanoparticles). Figure 4 shows the raw data of this dynamic experiment – the temperature profiles shown recorded by three thermocouples attached to different locations on the sample cylinder. The slower increase of the temperature in two of the three thermocouples was later attributed to a poor connection to the cylinder surface. The initial rapid D_2 gas pressurization caused the temperature increase from ca. 20°C to ca. 50°C which produced ca. 1480 J energy



(A)



(B)



Diameter = 1 inch
Length = 3.69 inch,
Volume = 47.5 cm³

(C)

Figure 2. (A) Gas-loading system, (B) students working on the system and (C) sample cylinder that contains nanoparticles in (B).

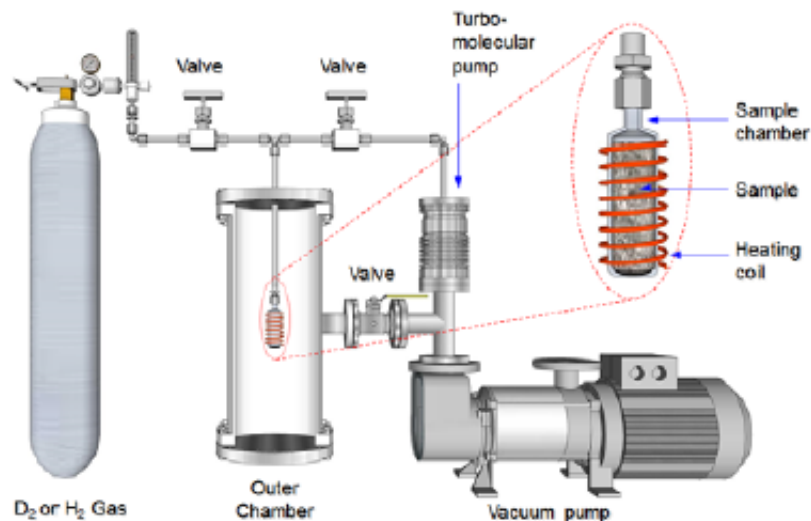


Figure 3. Sketch of the gas-loading system.

release, and is well above the exothermal energy 690 J that is calculated as the maximum possible from chemical reactions involving hydrating. (Note that the total heating energy was calculated by considering the heat capacity of both the sample cylinder and the nanoparticle powder, and the chemical exothermal energy was calculated using $\Delta H = \sim 35,100$ J per mole of D_2 for the formation of PdD_x for $x < 0.6$.) The further rise in temperature from ca. 50°C to ca. 140°C during unloading D_2 gas is important because it is opposite from what would occur normally as deloading is an endothermic process. Thus, the heating is thought to be due to LENRs that are enhanced because of the increased deuterium flux inside the nanoparticles. However, more experiments are needed to eliminate side reactions such as oxygen and deuterium reactions. In this experiment, the input power, including power consumed by gas compression process and vacuum pumping process, is negligible compared to the output power. For example, considering the pumping process, the whole system can reach ca. 10^{-2} Torr within one minute. The volume of the sample chamber is less than one percent of the whole system, thus the power needed for vacuum pumping is negligible. The exact power used for gas compression is difficult to determine exactly, but calculation of the energy required is approximated by the power required to compress deuterium. Although many more studies are needed to unveil the source of the excess heat during the first step rise in temperature shown in Fig. 4, this result has provides evidence of significant excess energy gain [(Total energy out – energy in)/energy in]. In this short run the gain is already >1.0 . Since the input energy is mainly due to exothermal heating during adsorption of the gas into the nanoparticles at the beginning of the run, the gain can be significantly increased by longer run times. Some data from such runs is shown next.

2. Parametric Gas-Loading Nanoparticle Experiments

We have performed various experiments to study the effect of changing some key parameters and to study longer run times. Each run involves loading and de-loading deuterium gas into nanoparticles by pressurizing and vacuuming

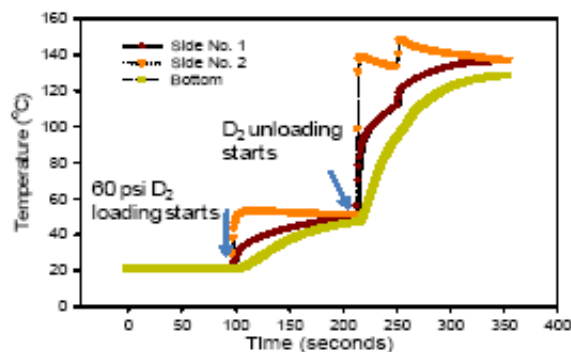


Figure 4. Raw data (temperature profile) from the dynamic experiment of the gas-loading system. The purpose of this very short dynamic run was to demonstrate the rapid temperature rise following a sharp pressure rise and the same upon sudden depressurization.

the sample cylinder. Two sets of different particles were used. The temperature profile for 23 g of nanoparticle #1 (same as in the dynamic run of Fig. 4) during the 60 Psi deuterium loading is shown in Fig. 5. We can see that the temperature rises right after gas-loading starts. The increasing rate is low at the start, but then exponentiates until reaching ca. 115°C. The initial slow rise is attributed to exothermal heating during the loading process, while the fast rise is attributed to LENRs. This is consistent with the theory that the LENRs are instated once a certain threshold temperature is reached. The temperature rising phase lasts about half an hour and then begins to decrease. The total energy produced in this 4.2-hour run was ca. 4770 J. The maximum exothermic energy from chemical reactions is calculated to be 690 J, suggesting the LENRs dominated with a gain (LENR energy out/Chemical energy in) of ~ 6 . This is viewed to be conservative. For example, if the calculation was based on the observed desorption energy, the value will be roughly twice of the above value (the value is quoted later in Table 1 using the latter technique). In this run, the averaged power density about 15 W/g.

The run in Fig. 5 was followed by another three runs using the same set of #1 nanoparticles. Figure 6 shows the

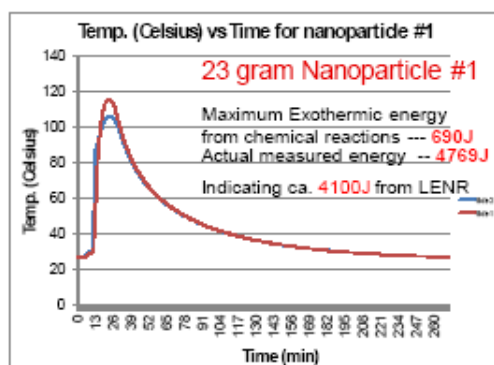


Figure 5. Temperature profile during the 60 Psi deuterium loading of the #1 nanoparticles. Two different curves were recorded by two thermocouples attached to the sample cylinder at different sites. In this case, 99.99% deuterium gas was used.

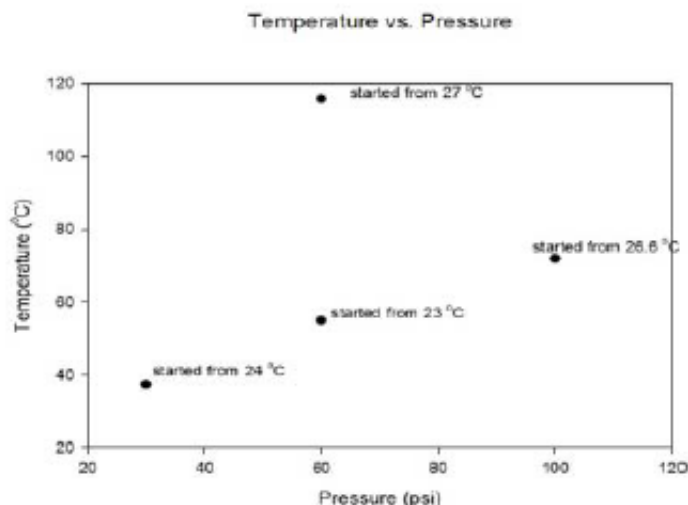


Figure 6. Temperature versus pressure for #1 nanoparticles. The one data point at the highest temperature is from fresh nanoparticles, whereas the other data are from the same particles after using first run.

peak temperature versus pressure for these runs. These three runs all have relative low temperature rises compared with the first run, but the three rises follow a linear relationship. The decreased temperature rise in the latter runs suggests the nanoparticles may be deteriorating, or sintering due to repeated use.

Figure 7 shows a SEM image of #1 nanoparticles before (Fig. 7(A)) and after (Fig. 7(B)) deuterium loading experiments. We can see that after deuterium loading, some nanoparticles, especially at the top layer, stick together compared with their loose-packed state before deuterium loading. The sintering of the layer may be blocking the deuterium gas from effectively going further into nanoparticles below the top layer, causing a lower temperature rise in the repeated experiment runs with the same packed nanoparticles. The sintering seems to occur at a lower temperature than expected, but hot spots may be caused by the localized loading cluster reactions. It is difficult to tell from the SEM image if there are any melted spots, but such local heating should not be neglected.

Following the experiment summarized in Fig. 6, improvements were made in nanoparticle manufacturing to provide much smaller size. In this case, three different alloys were employed for the nanoparticles, Type A is Pd rich similar to Type #1 used earlier, Types B and C contain both Pd and Ni, but with different percentages, along with small percentage of additional metals. As shown in following data, these new nanoparticles are much more reactive than that shown in Fig. 5. Table 1 lists a series of experiments performed to compare various types of nanoparticles. For these runs the outer vacuum chamber shown in Fig. 2 was removed and smaller weight of nanoparticles was employed in order to save total experiment time. A set of runs for the Type A nanoparticle is shown in Fig. 8. Only the initial run times up to 100 s from start of pressurization are analyzed for the comparisons. Note that with the decreased weight of nanoparticles used here and the faster heat loss due to the outer chamber removal, the temperature increase phase is much shorter than that in the runs of Fig. 5. As our main purpose for these experiments is to determine the best nanoparticles and to overcome sintering problems, the current adiabatic conditions with outer chamber removed are acceptable for such short times. Moreover, due to the fast heat loss, the analysis of the data is only done for the period of temperature increase as shown in Fig. 8. Three different types of nanoparticles (Types A–C) were employed in the comparison. Some were reused, either with or without treatment, following initial use. This was done to study the effect of sintering

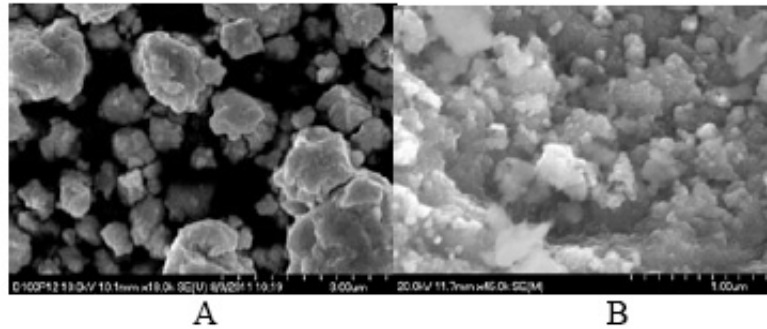


Figure 7. SEM image of the #1 nanoparticles before (A) and after (B) the deuterium loading experiment. Note: The white color in (B) is because the distance of the nanoparticles to the electron gun is different. The closer, the brighter. Also note that the nanoparticles employed in the adiabatic experiments described here are considerably smaller than those shown here.

and possible treatment of sintered particles. As seen in Table 1, the highest gain achieved (LENR energy out/estimated maximum possible chemical energy in) was 15.1 using Type C nanoparticles. The gain in these new sets of experiments more than doubled compared with previous ones due to the improved procedure of making nanoparticles. Note that this gain was achieved in only 98 s of the run. Since the adsorption (chemical) energy release occurs at the beginning of the run and then ends, longer runs than employed for these comparisons can give gains of many thousands. The highest power density achieved was 42.7 W/g using Type A particles. This is largely due to the rapid heating achieved with these particles (about 10 s to the peak vs. 70–100 s for other particles.) Runs 2 and 6 used the same nanoparticle employed in Runs 1 and 5, respectively. Both suffered a significant reduction in performance, e.g. gains reduce roughly an order of magnitude. This is attributed to sintering effects caused in the initial run, even though it was fairly short.

However, results from run 3 suggest that the sintering problem seems solvable. In this run, particles from Run 2 were treated by reheating in the air for 2 h. When these particles were run they were able to release energy of 426 J/g, only 3% less than that achieved by the fresh particles in Run #1. This is very encouraging, and we are continuing study of ways to treat (added coatings, etc.) the nanoparticles to achieve longer initial runs prior to their re-treatment. Initial

Table 1. Adiabatic experiments for nanoparticle evaluation.

Run Nos.	Nanoparticle type	Gas	Pressure (Psi)	Mass (g)	Average ΔT ($^{\circ}\text{C}$)	Joules (Peak)	Peak En-ergy /mass (J/g)	Run time - initial temp. to peak temp. (s)	W/g	Chemical energy (J)	Measured peak en-ergy (J) minus chemical energy (J)	Gain
1	Type A	D ₂	90	2.2	31.55	972.05	441.84	14.00	31.56	74.85	897.21	12.0
2	Type A (same particles from Run 1)	D ₂	100	1.9	4.95	151.96	79.98	16.00	5.00	64.64	87.32	1.3
3	Type A (same particles as Run 2, but after heat treatment)	D ₂	105	1.8	25.05	768.01	426.67	10.00	42.67	61.24	706.77	11.5
4	Type B	D ₂	60	11.1	90.90	3588.88	323.32	95.00	3.40	271.29	3317.59	12.2
5	Type C	D ₂	100	6.4	84.90	2754.00	430.31	98.00	4.39	170.76	2583.24	15.1
6	Type C (same particles from Run 5)	D ₂	100	6.4	6.80	220.58	34.47	76.00	0.45	170.76	49.82	0.3
7	Type C	D ₂	100	3.2	27.10	846.04	264.39	78.00	3.39	85.38	760.66	9.3

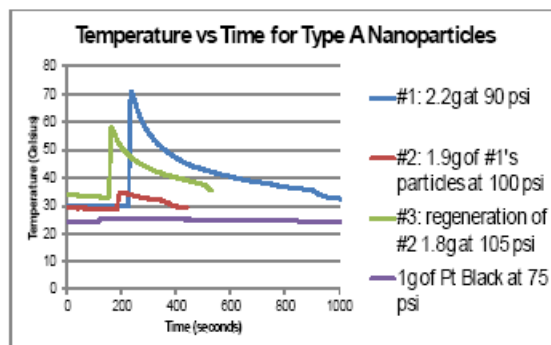


Figure 8. Typical adiabatic experiment with Type A nanoparticles. Included is a Pt black reference run data from these runs as well as others for different nanoparticles is summarized in Table 1.

results seem promising, but much more study and long run experiments are required to fully evaluate long run time issues.

To investigate possible gas impurity effects, another deuterium loading and unloading run followed using the same nanoparticles but low-purity (99.7%) deuterium gas at 60 Psi. The temperature only raised to ca. 30°C, suggesting excess heat production might be affected by the purity of deuterium gas. More study is needed, though, to confirm this and to identify the impurities involved that affect the reaction rate. This result also indicates that the heat from other reactions, such as a catalyzed deuterium oxidation reaction, is not a dominant reaction in the heat production process.

3. Comparison of Energy Output to other Power Sources

So far, our experiments suggest a remarkable proof-of-principle power unit at ca. 40 W/g, when using deuterium gas. This projection is based on the assumption that with an appropriate control system, the gas-loaded cell is able to maintain a steady-state temperature profile once it reaches the peak temperature.

This also requires nanoparticles with coating permitting long runs before removal for re-treatment. These methods are currently under study.

For perspective, it is useful to compare the envisioned LENR unit to a heat source such as Pu^{238} used for RTGs in NASA's deep space probes. Assuming a linear power/weight scaling, a 3-kW LENR unit (not including the gas tank) would use 0.5 kg or 0.3 L of nanoparticles compared to a 3-kW Pu^{238} unit which would be 5.6 kg or 0.28 L. However, this assumes the power obtained in the short LENR runs can be extended using control strategy and improve the nanoparticles as illustrated in Fig. 9. In that figure, the periodic oscillation pressure is employed to maintain the required flux in the nanoparticles giving a theoretical quasi-steady-state run. Note that the LENR data used is based on very preliminary experiments so improvements should be possible. Thus, it is foreseen that power densities for LENR can be expected to increase with further research development.

A new company, LENUCO has been set up in Champaign to commercialize this technology. The first goal is to develop units in the 1.5 kW_e range for house use. These would be stackable to form 30 kW_e units for small business applications. Thermoelectric energy conversion to electricity would be employed and the units would have cooling stream to allow use for co-generation operation. An earlier conceptual design for such a unit is shown in Fig. 10. While this design is for gas loading of thin films, it can easily be transformed to the device using nanoparticles.

Like other nuclear energy sources such as fusion and fission, a LENR cell offers a very high-energy density. However, LENR power sources offer other distinct advantages. Fission power faces limitations due to the need for

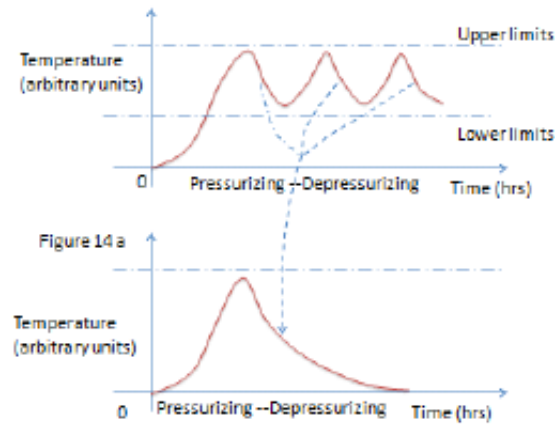


Figure 9. Illustration of pressure control to maintain flux of ions required for continuous long time operation. As seen once the temperature starts to decrease, the pressure is reduced to initiate flow via desorption. These periodic pressure variations maintain a time-averaged temperature at the desired set-point.

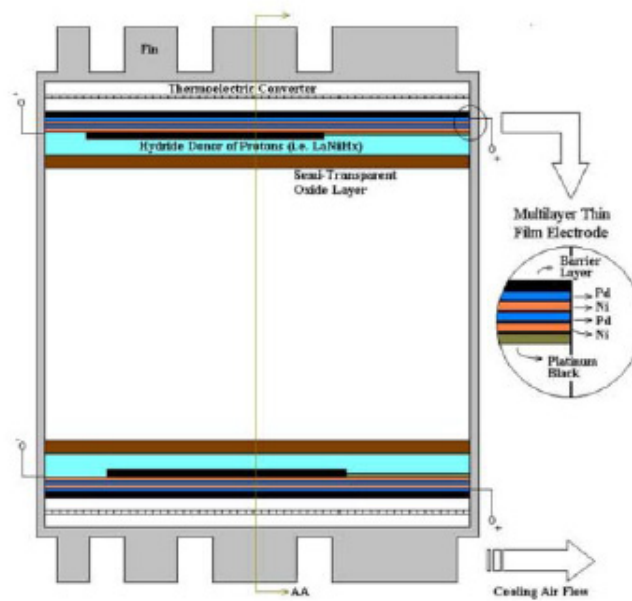


Figure 10. Conceptual design of a gas loaded thin film cell using thermoelectric energy conversion and air cooling. This base 1.5 kW_e module can be stacked to provide a 30 kW_e unit for use in distributed commercial power units.

long-term storage of its radioactive waste. Fusion has less radioactivity involvement but with the planned initial use of D–T fuel still faces tritium containment issues and induced radioactivity of plant materials due to the intense flux of 14.7 MeV neutrons.

Also, scaling down to smaller power units is virtually impossible with these two nuclear sources. A LENR-based power source has reaction products that are mildly radioactive, mainly from low-energy beta decay from transmutation reactions. But with the short range of the betas, this radioactivity can easily be contained and quickly decays. The fuel it used, such as D₂, or H₂, is virtually inexhaustible. For LENR power sources, both scaling down and up in power are possible, and the huge energy released in the nuclear reactions (versus chemical reactions) makes this an extremely compact, long-lived energy source.

4. Conclusion

The primary result thus far is that the excess energies obtained in all experiments to date are all well above the maximum estimate of what could be attributed to chemical reactions. The external power/energy involved, such as deuterium gas compression and vacuum pumping, is minimal compared to the output, suggesting very large energy gain. This result is extremely encouraging relative to this gas-loaded cell becoming a remarkable power unit. The prime issue under study is to extend the run times using revised nanoparticle treatment combined with a pressure control to maintain a flux of ions in the nanoparticles following the initial loading. Finally optimization of the particle alloy and gas needs study involving the many system trade-offs. Along this line, our ongoing experiments are designed to compare Ni-rich-alloy-H₂ with the present Pd-rich-alloy-D₂ system. Also, in order to understand the power scaling with pressure and weight of the nanoparticles, the earlier studies reported here need to be refined. In view of the many remaining issues at this point, it is premature to identify the best potential application. However, assuming the issues identified are resolved, numerous game-changing applications can be envisioned, for both space and terrestrial power. There are also numerous commercial uses on land, e.g. use in small power units for residential use including hot water heaters, use in larger power units for local power sources in commercial plants, and even DOD forward operating bases. Space applications, ranging from station keeping on to propulsion would also be revolutionized with such power units.

Acknowledgment

The support from New York Community Trust, NPL Associates Inc., and Lenuco is greatly appreciated.

References

- [1] G.H. Miley and J.A. Patterson, Nuclear transmutations in thin-film nickel coatings undergoing electrolysis, *J. New Energy* **1**(3) (1996) 5.
- [2] G.H. Miley, Product Characteristics and Energetics in Thin-Film Electrolysis Experiments, *Proc. Int. Conf. on Cold Fusion*, Vancouver, Canada, 1998, pp. 241–246.
- [3] A. Lipson, B.J. Heuser, C. Castano, G.H. Miley, B. Lyakhov and A. Mitin, Transport and magnetic anomalies below 70 K in a hydrogen-cycled Pd foil with a thermally grown oxide, *Phys. Rev. B* **72** (2005) 212507.
- [4] A.G. Lipson, B.J. Heuser, C.H. Castano and A. Celik-Aktas, Observation of a low-field diamagnetic contribution to the magnetic susceptibility of deformed single crystal PdH_x ($x \simeq 4.0 \times 10^{-4}$), *Phys. Lett. A* **339** (2005) 414–423.
- [5] G.H. Miley, X. Yang and H. Hora, A potentially game changing green power source based on low energy nuclear reactions (LENRs), *Nuclear and Emerging Technologies for Space 2012*, The Woodlands, TX, March 19–23.
- [6] G.H. Miley and X. Yang, Deuterium cluster target for ultra-high density, *18th Topical Meeting on the Technology of Fusion Energy*, San Francisco, CA, 2009.
- [7] L. Holmlid, H. Hora, G. Miley and X. Yang, Ultra HIGH-DENSITY DEUTERIUM OF RYDBERG MATTER CLUSTERS FOR INERTIAL CONFINEMENT FUSION TARGETS, *Laser and Particle Beams* **27** (2009) 529–532.

- [8] G.H. Miley, G. Narne, M.J. Williams, J.A. Patterson, J. Nix, D. Cravens and H. Hora, Multilayer thin-film microspheres after electrolysis, *Proc. Int. Conf. on Cold Fusion*, Vol. 2, edited by New Energy and Industrial Tech. Dev. Org., Japan, 1996, p. 529.
- [9] A.G. Lipson, A.S. Rusetskii, A.B. Karabut and G.H. Miley, D–D reaction enhancement and X-ray generation in a high-current pulsed glow discharge in deuterium with titanium cathode at 0.8–2.45 kV, *J. Exp. and Theoret. Phys.* **100** (6) (2002) 1175–1187.
- [10] A.B. Karabut, A.G. Lipson and A.S. Roussetsky, Correct measurement of D–D reaction yield and in high current pulse-periodic deuterium glow discharge operating at 0.85–1.20 keV voltage applied, *Proc. 8th Int. Conf. of Cold Fusion*, Italy, 2000, p. 335.
- [11] G.H. Miley, N. Luo, A.G. Lipson and A.B. Karabut, A Unique Plasma Discharge Driven Solid-State X-ray Laser, *SPIE Ablation*, Taos, NM, 2004.
- [12] Y.E. Kim, Theory of Bose–Einstein condensation mechanism for deuteron-induced nuclear reactions in micro/nano-scale metal grains and particles, *Naturwissenschaften* **96** (2009) 803.
- [13] Y. Arata and Y. Zhang, The establishment of solid nuclear fusion reactor, *J. High Temp. Soc.* **34** (2) (2008) 85.
- [14] Y. Arata, Y. Zhang and X. Wang, Production of helium and energy in the ‘solid fusion’, *15th Int. Conf. Condensed Matter Nuclear Science*, Rome, Italy, 2009.
- [15] Y. Sasaki et al., Anomalous heat generation in charging of Pd powders with high density hydrogen isotopes (i) results of absorption experiments using Pd powders, *15th Int. Conf. Condensed Matter Nuclear Science*, Rome, Italy, 2009.
- [16] Y. Sasaki et al., Deuterium gas charging experiments with Pd powders for excess heat evolution (i) results of absorption experiments using Pd powders, *9th Meeting of Japan CF-Research Society*, Shizuoka, Japan, 2009.
- [17] A. Takahashi et al., Deuterium gas charging experiments with Pd powders for excess heat evolution (ii) discussions on experimental results and underlying physics, *9th Meeting of Japan CF-Research Society*, Shizuoka, Japan, 2009.
- [18] A. Kitamura, T. Nohmi, Y. Sasaki, Y. Taniike, A. Takahashi, R. Seto and Y. Fujita, Anomalous effects in charging of Pd powders with high density hydrogen isotopes, *Phys. Lett. A* **373** (35) (2009) 3109–3112.
- [19] D. Kidwell, Trace analysis of elements in a palladium matrix, *Int. Conf. Condensed Matter Nuclear Science*, Washington, DC, 2008, p.1.
- [20] D. Kidwell et al., Does gas loading produce anomalous heat? *15th Int. Conf. Condensed Matter Nuclear Science*, Rome, Italy, 2009, p. 41.
- [21] F. Celani et al., Deuteron electromigration in thin Pd wires coated with nano-particles: evidence for ultra-fast deuterium loading and anomalous, large thermal effects, *Int. Conf. on Condensed Matter Nuclear Science*, Washington, DC, 2008, p.2.
- [22] F. Celani et al., Towards a high temperature CMNS reactor: nano-coated Pd wires with D₂ at high pressures, *15th Int. Conf. on Condensed Matter Nuclear Science*, Rome, Italy, 2009, p. 25.
- [23] X. Li et al., Progress in gas-loading D/Pd system—the feasibility of a self-sustaining heat generator, *10th Int. Conf. on Cold Fusion*, 2003, p.1.



Research Article

Method of Controlling a Chemically Induced Nuclear Reaction in Metal Nanoparticles

Tadahiko Mizuno*

Hydrogen Engineering Application and Development Company, Japan

Abstract

A nuclear reaction can occur when metal nanoparticles are exposed to hydrogen isotopes in the gas phase. When hydrogen isotopes (light hydrogen and deuterium) enter the nanoparticles and are exposed to electron irradiation, the hydrogen reacts inside the lattice, producing energy. The reaction also produces neutrons, gamma rays and transmutations. Protons and heavy electrons take part in the reaction. The method of control and the experimental results are reported here.

© 2014 ISCMNS. All rights reserved. ISSN 2227-3123

Keywords: Gas loading, Heat, Nanoparticles

1. Experimental Method

Excess heat is observed when nanoparticles of nickel or palladium undergo glow discharge electrolysis in hydrogen or deuterium gas. After glow discharge ends, when additional gas is admitted to the cell, another burst of heat is sometimes observed.

This method produces nanoparticles by bombarding the electrodes with electrons during roughly 30 h of glow discharge. The nanoparticles are created in situ in electrodes [1–3]. The electrodes have already been cleaned and purified, and they are kept in a high-purity gas environment, so the nanoparticles have little contamination on the surface and they are highly absorbent. With other methods, the nanoparticle material is fabricated elsewhere and exposed to air and contamination before being placed in the cell.

The particle size and number of particles is controlled by varying the strength and duration of initial glow discharge. This, in turn, controls the reaction rate. In a typical run with a fine wire palladium electrode, the cell produced 4.4 kJ of anomalous heat at first. After polarity was reversed, making the electrode positive, 54 kJ more excess heat was produced. After glow discharge finished, 10 ml of additional deuterium gas was added to the cell, and an extra 15 kJ of anomalous heat was produced.

Excess heat was produced in most test runs (47 out of about 70 tests).

*E-mail: head-mizuno@lake.ocn.ne.jp

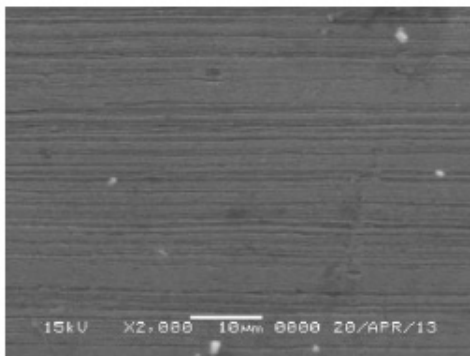


Figure 1. Palladium wire before use. The wire has been scored.

2. Materials and Equipment

2.1. Materials

The materials used in the deuterium–palladium experiments are described here. The deuterium gas (Japan Fine Products) purity is 99.99% for D, or for D₂, 99.8%, with 0.2% HD). Heavy water vapor (Across, 100.0 at%) is also used. Commercial grade nickel mesh made from 0.2 mm wire is used to cover the inside walls of the reactor, to prevent the glow discharge plasma from touching the steel reactor walls.

For the palladium tests, commercial grade palladium wire, 0.1–1.0 mm thick, 99.9% pure was used. The wires are scored before use. Figure 1 shows a palladium wire sample before exposure to glow discharge. This wire is 300 mm long. It is wrapped in a spiral around a rod, and then exposed to glow discharge which forms nanoparticles on the surface.

2.2. Nanoparticle size

The smaller the nanoparticles in a sample are, the more effectively they absorb hydrogen, and the faster the reaction will occur. I believe the reaction rate increases exponentially. On the other hand, the overall reaction size depends on the number of particles in the active site. As the metal particle size decreases, both the particle volume and the number of hydrogen atoms absorbed by the particle decrease by the third power (cubically).

We can calculate the optimum particle size taking into account these two factors. It comes out to be 2–5 nm, where the number of atoms per particle is 10^3 – 10^4 .

2.3. Reactor and electrodes

Two reactors were used in this study, a small one and a large one. This paper describes the large reactor and electrodes. The reactor is stainless steel. Grade 316 stainless steel is preferred. The vessel is about as wide as it is tall, (50 cm × 50 cm) being cross-shaped with the gas inlet and window ports. Electrodes are introduced from the top, and there are a variety of connection terminals at the sides, including the gas inlet, pressure gauge and vacuum exhaust. The viewing window is made of Kovar glass. ICF flanges are used throughout, with oxygen-free copper gaskets. The reactor volume is 15 L, weight 50 kg.

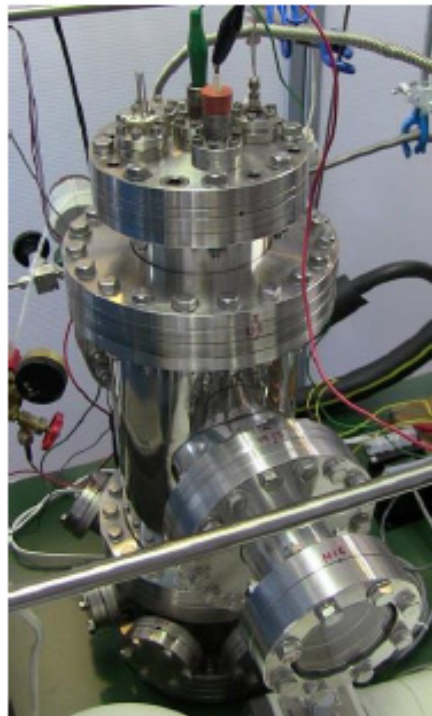


Figure 2. The reactor.

As shown in Fig. 3, the two electrodes enter the cell through the lid. Both are insulated. The polarity of the electrodes can be reversed. The entire reactor vessel is grounded for safety.

The core of the electrode is a square alumina ceramic holder, 30 mm per side, 2 mm thick, with palladium wire wrapped around it. The wire is 0.2 mm thick, 1000 mm long, and is coiled around the ceramic holder about 15 times. The other electrode is made with 300 mm of palladium wire wrapped in a tight spiral around a palladium tube, which is 50 mm long, 3 mm in diameter.

Counter-electrode: With nickel wire the counter-electrode is either 1 mm diameter 30 mm long wire, or thinner 0.1 mm diameter, 1000 mm long wire, both wrapped in a spiral around a rod. The wire is wrapped as tightly as possible. It is arranged so there are no protruding or pointed surfaces. Before use, the entire electrode assembly is washed in alcohol and acetone, in particular to eliminate contamination from fats and oils.

2.4. Nanoparticle size

The smaller the nanoparticles in a sample are, the more effectively they absorb hydrogen, and the faster the reaction will occur. I believe the reaction rate increases exponentially. On the other hand, the overall reaction size depends on the number of particles in the active site. As the metal particle size decreases, both the particle volume and the number of hydrogen atoms absorbed by the particle decrease by the third power (cubically). We can calculate the optimum

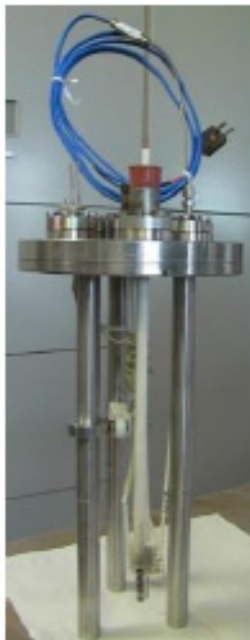


Figure 3. The reactor lid and electrodes.

particle size taking into account these two factors. It comes out to be 2–5 nm, where the number of atoms per particle is 10^3 – 10^4 . A cross-section of the reactor is shown in Fig. 4.

2.5. Equipment configuration

Figure 5 shows a block diagram of the reactor, the control system, the vacuum exhaust and mass spectroscopy system, and the measurement and control systems. Voltage is applied from the high voltage (HV) power supply (left-hand side of diagram). Also shown on the left is the computer, data logger, power analyzer and waveform analyzer. Along the top of the cell is a neutron detector and gamma detector, and a pressure gauge. In this diagram, the cell is shown in the lower portion.

The temperature of the electrodes is measured directly with a thermocouple (shown in the upper right pin in Fig. 4). This is a K-type thermocouple, 1.6 mm diameter, 300 mm long, in a stainless steel jacket. It touches the surface of the electrode wrapped around the ceramic holder.

On the right-hand side is shown one of the two K-type thermocouples measuring the reactor vessel wall temperature (T5 is shown; T6, at the base, is not). Another thermocouple is inside the cell, in direct contact with the electrode surface. The bottom right of the diagram shows the gas supply and quadrupole mass analyzer used to analyze the gas withdrawn from the cell. Temperature is measured in four locations total, including ambient temperature. Temperature, voltage, power, pressure, the neutron and gamma count, and the gas analysis is collected by the logger and recorded in the computer every few seconds.

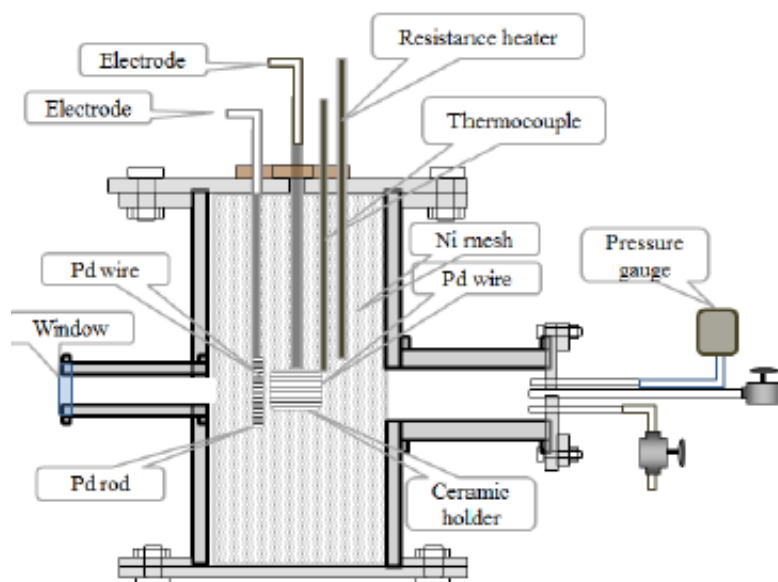


Figure 4. Cross section of the reactor.

3. Method

3.1. Heater calibration

Figure 6 shows the results of a calibration performed with the joule heater that is placed up against the electrode. The cell is filled with D_2 gas at 10 or 100 Pa, and the power is stepped from 0 to 50 W in 5 W increments. The results for 10

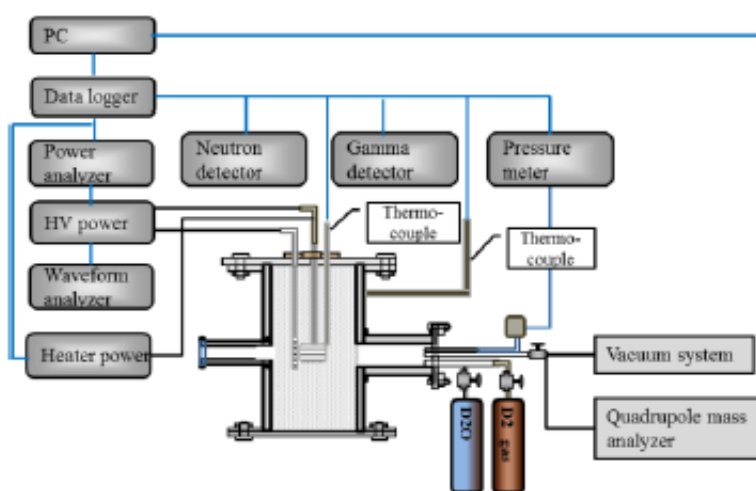


Figure 5. System.

and 100 Pa are close. The temperature is held at each step for about 18 h to ensure that it is stable. This graph shows the stable temperature minus ambient temperature for each step, recorded on the three K-type thermocouples listed above.

3.2. Electrode activation treatment

The electrode is treated by the following method to produce nanoparticles and activate the surface: The reactor vessel is evacuated down to several Pascals. After evacuating the reactor, the gas level is held at several Pascals, and electrons from the central electrode are used to bombard the counter-electrode. This activation treatment step exposes the metal, cleaning off impurities and oxides. Voltage and current are applied to the electrodes. At first the 0.1 mm thin wire palladium mesh is made the positive electrode at 600 V, and glow discharge at 20 mA is continued for 600 s. Then the mesh is switched to negative terminal, and glow discharge continues for 1200 s, again at 600 V and 20 mA.

This glow discharge cycle is repeated for about 15 h with electrodes made from thin 0.1 mm diameter wire, or for 30 h with the 1 mm wire. Glow discharge continues until many nanoparticles form on the surface, and the surface is activated. The vessel is then evacuated to a lower pressure while the electrodes are hot, to remove additional impurities. The electrodes are then activated by being heated with the resistance heater, to temperatures between 100°C and 200°C for about 3 h. This continues until light hydrogen, H₂O, and gaseous hydrocarbons are driven out of the electrodes and are no longer detected by the mass spectrometer at significant levels.

3.3. Glow discharge heating

Glow discharge is then performed to produce nanoparticles on the electrode surface. The thin wire palladium electrode is the positive terminal. Direct current glow discharge is maintained at about 20–30 mA and 600–800 V for about 10 ks (~27 h). After this, D₂ gas is admitted into the cell, and it absorbs into the electrode surface.

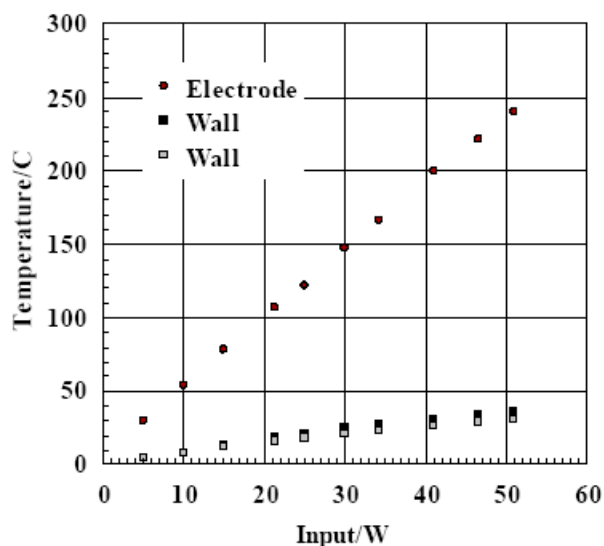


Figure 6. Heater calibration.

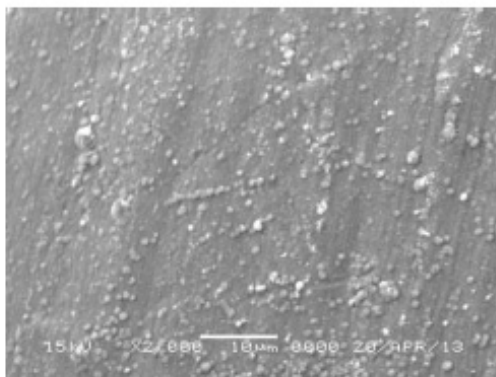


Figure 7. Palladium wire after activation.

Figure 6 shows a SEM photo of the palladium wire electrode surface after this treatment. Fine metal particles (nanoparticles) are formed on the metal surface. The magnification here is 2000 times, which is enough to reveal nanoparticles of less than $1\text{ }\mu\text{m}$. When the SEM magnification is increased, even smaller particles can be seen. Particles on the nanometer scale are ideal. Figure 7 shows a SEM photo of the nickel wire, with even more nanoparticles than the palladium sample.

This method produces nanoparticles in situ after cleaning and purifying the electrode material, in a high-purity gas environment. So the nanoparticles have little contamination on the surface and they are highly absorbent. With other methods, the nanoparticle material is fabricated elsewhere and exposed to air and contamination before being placed in the cell.

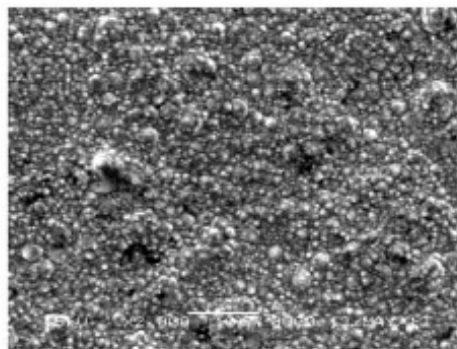


Figure 8. Nickel wire after activation.

4. Results

4.1. Anomalous exothermic reaction

Figure 9 shows an example experimental run. Input power is shown in the right axis, with the broken dashed line. It is roughly 46 W. The grey line indicates gas pressure, which begins with a vacuum and is increased to 320 Pa at 2000 s. When gas pressure is raised, the reactor electrode temperature (the difference between the electrode and room temperature) increases from 220°C to 300°C. Later, as shown in Fig. 10, the reactor wall temperature increases from 38°C to 44°C, and then stabilizes.

The amount of heat can be calculated based on the electrode temperature calibration, as follows. With 46 W of input, the calibration shows that the electrode temperature difference should reach 250°C, but it climbs to 300°C instead, which indicates 60 W of power. Therefore, excess power is $60 - 46 \text{ W} = 14 \text{ W}$. This excess power can sometimes continue for over 50,000 s (14 h). Excess heat can also be computed based on the reactor wall temperature, and this also indicates $\sim 14 \text{ W}$ excess.

Figure 11 shows single points representing the stable (equilibrium) temperature differences from several tests. That is, the electrode minus room temperature, and cell wall minus room temperature. These temperatures were recorded in various experiments 2000–10,000 s after gas is admitted into the cell, after the temperature reaches equilibrium. The two straight lines in the figure indicate the calibration curves from control runs for the electrode (*top*) and cell wall (*bottom*), where the data was taken before the metal was activated. This shows that the temperatures are considerably higher for samples that have been activated.

In one example data point in Fig. 11, where input as 30 W, the average output temperature was 150°C during calibration. After the electrode was activated, the temperature difference rose as high as 280°C. In the control runs, 280°C indicates 50 W of input. In other words, $50 - 30 \text{ W} = 20 \text{ W}$ excess heat. During the control run, with 30 W input, the cell wall temperature is 17°C, but with activated material it reaches 26°C, which again indicates about 50 W of excess heat.

Excess heat first becomes apparent when the cathode temperature goes above 50°C. However, when the cathode temperature exceeds 300°C the metal is deactivated and the excess heat goes away, probably because of structural

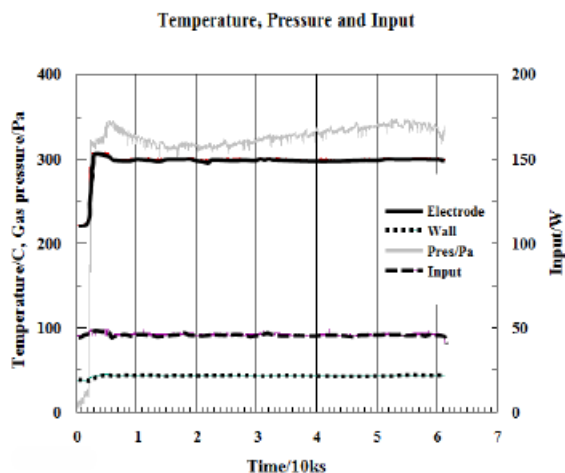


Figure 9. Electrode temperature, wall temperature, gas pressure (*left axis*) and input power (*right axis*).

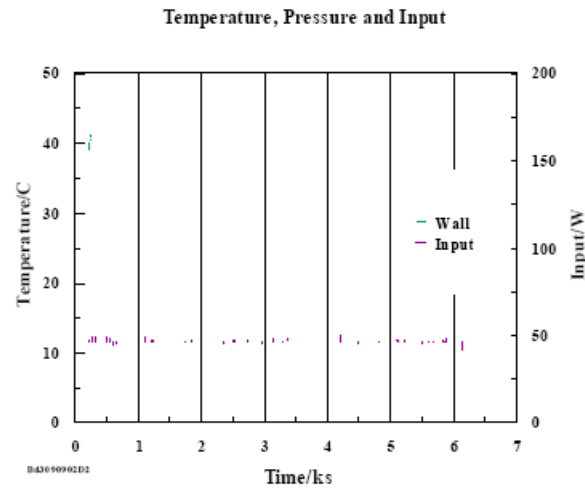


Figure 10. Detail showing reactor wall temperature and input power.

changes. At present the reason is unclear. Table 1 shows a summary of recent tests. These were all conducted with the large reactor. The electrodes were palladium, either a rod or a wire. D_2 gas or D_2O or H_2O vapor was used. The tests were performed after the electrode was activated with glow discharge for many hours. The electric power was either direct current or alternating current at 50 Hz. Output is calculated based on the calibration curves during the control

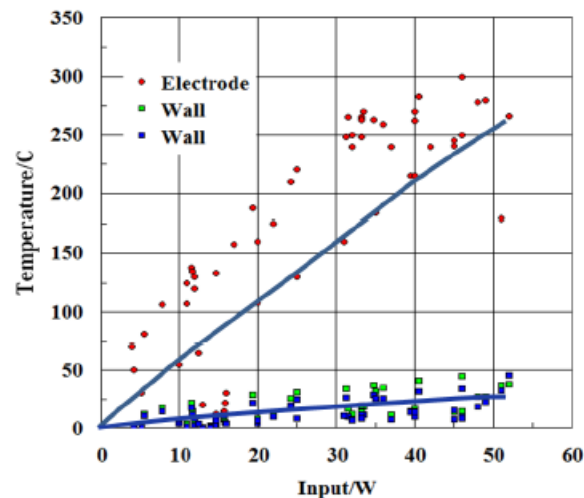


Figure 11. Equilibrium temperature of the electrode in several experimental runs.

run. The “Out/in” columns show the ratio of output heat to input power, estimated from the electrode temperature, and the cell wall temperature.

As shown in Fig. 9, after the sample has undergone heat treatment and activation with glow discharge, excess heat sometimes continues for 24 h or longer. In some cases output exceeds 10^6 kJ, and continues longer than 100,000 s. Heat has been observed with both heavy water vapor and D_2 gas. This indicates that palladium wire that has undergone surface treatment to produce nanoparticles can produce anomalous excess heat.

Table 1. Summary of recent successful tests with large reactor, palladium electrodes

Gas		Applied V		Power (W)		Heat out (W)		Time	H_{out}/H_{in}		Temp.(°C)
Cathode—	Component	Pressure (Pa)	Heater (W)	Plasma (V)	Heater input	Plasma input	By electrode temp.	By reactor temp.	By electrode temp.	By reactor temp.	Electrode
Wire	D ₂ O	70	30.7	0	30.7	0	51	34	7	1.65	240
Wire	D ₂ O	70	30.7	780	30.7	13.9	61	48	2.8	1.37	260
Wire	D ₂ O	275	31	0	31	0	58	35	58	1.87	260
Wire	D ₂ O	50	31	0	31	0	46	34	78.3	1.48	200
Wire	D ₂ O	50	31	0	31	0	43	31	12.8	1.38	210
	D ₂ O	100	45.7	0	45.7	0	53	55	64.7	1.15	275
	D ₂ O	20	44.6	0	44.6	0	36	50	1.2	0.82	190
Rod	D ₂ O	50	45.8	790	45.8	16.6	62	62	2.48	0.99	320
Wire	D ₂ O	50	46.6	772	46.6	14.6	60.4	60	1.44	0.99	320
	D ₂ O	50	47	0	47	0	55	55	1.17	1.28	315
Wire	D ₂ O	145	45.9	0	45.9	0	124	114	75.2	2.7	280
Wire	D ₂	330	45.8	0	45.8	0	64	63	62.5	1.4	325
Wire	H ₂ O	20	46	0	46	0	46	70	8.2	1	250
Rod	D ₂	400	49	770	49	12	66	70	6.5	1.08	330
	D ₂	200	49	0	49	0	61	60	1.3	1.24	300
	D ₂	300	25	0	25	0	41	30	6.5	1.64	250
Rod	D ₂	300	36	0	36	0	54	48	1.5	1.5	300
	D ₂	330	36	0	36	0	54	44	2.8	1.5	285
	D ₂	330	51.2	0	51.2	0	58	80	8	1.13	298
	H ₂ O	20	35.5	0	35.5	0	42	60	1.18	1.18	230
Wire	H ₂ O	150	15.6	825	0	15.6	4.3	10	16	0.28	45
Rod	H ₂ O	145	16	800	0	16	3.1	10	9.4	0.19	44

References

- [1] Tadahiko Mizuno, Tadashi Akimoto, Tadayoshi Ohmori, Akito Takahashi, Hiroshi Yamada and Hiroo Numata, Neutron evolution from a palladium electrode by alternate absorption treatment of deuterium and hydrogen, *Jpn. J. Appl. Phys.* **40** (2001) L989–L991
- [2] Tadahiko Mizuno, Tadashi Akimoto, Kazuhisa Azumi, Tadayoshi Ohmori, Yoshiaki Aoki and Akito Takahashi, Hydrogen evolution by plasma electrolysis in aqueous solution, *Jpn. J. Appl. Phys.* **44**(1A) (2005) 396–401.
- [3] Tadahiko Mizuno, *Transmutation Reaction in Condensed Matter; Low-Energy Nuclear Reactions Sourcebook*, American Chemical Society symposium series 998, Jan Marwan and Steven B. Krivit (Eds.), 2008, pp. 271–294.



Research Article

It is Not Low Energy – But it is Nuclear*

Pamela A. Mosier-Boss[†]

Research Laboratory of Electronics, Massachusetts Institute of Technology, Cambridge, MA 02139, USA

Abstract

In this communication, CR-39 track results obtained as a result of Pd/D co-deposition are discussed and criticisms of those results are addressed. Implications of the CR-39 results with reports of transmutation are explored.

© 2014 ISCMNS. All rights reserved. ISSN 2227-3123

Keywords: CR-39, Energetic particles, Pd/D co-deposition, Transmutation

1. Introduction

Anomalous effects observed in the Pd/D system include heat, helium-4, energetic charged particles, tritium, neutrons, gamma/X-ray emissions, and transmutation. It was later shown that the heat did not correlate with either neutrons or tritium [1]. Instead it was found that the heat correlated with helium-4 [2]. These results indicated that there were at least two channels – an aneutronic channel that produced heat (the so-called true Fleischmann–Pons effect) and another channel that favored formation of energetic charged particles, neutrons, and tritium. It was Swartz [3] who suggested that, by adjusting the experimental parameters, one could switch from one channel to the other.

In the Pd/D co-deposition process that was pioneered by Szpak, both the heat [4,5] and energetic particle [6,7] producing channels have been observed. The focus of this communication is on the experimental observations of energetic particles as detected using CR-39 solid-state nuclear track detectors (STNTDs). In particular, methods used to identify the charged particles are discussed. In addition, criticisms of the Pd/D co-deposition CR-39 results are addressed in this communication. The implications of these results on the nuclear processes occurring inside the Pd lattice are explored.

*This work was funded by the Defense Threat Reduction Agency.

[†]E-mail: pboss@san.rr.com

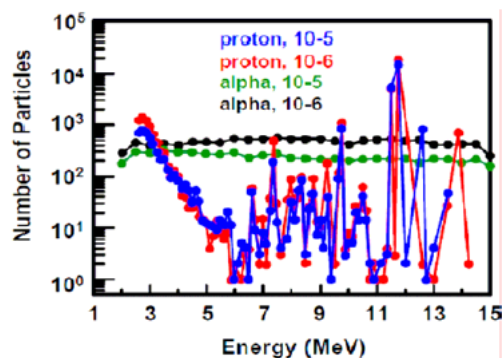


Figure 1. Results of LET spectrum analysis of the front side of CR-39 detectors 10-5 and 10-6 used in the SRI replication.

2. Summary of CR-39 Experimental Observations

2.1. Summary of Pd/D co-deposition results

The Stanford Research Institute (SRI) conducted several Pd/D co-deposition experiments that used CR-39 detectors. The experiments were conducted in the presence of a magnetic field. Two experiments were done with the detector inside the cell. In these experiments a 60 μm thick polyethylene film separated the Ag cathode from the detector. These detectors, identified as 10-5 and 10-6, underwent microscopic examination by our group. Tracks were observed on both sides of the detectors. These detectors were also scanned using an automated scanner.

Afterwards, the detectors were sent to Lipson and Roussetski. Using sequential etching, Lipson and Roussetski identified tracks due to 3 MeV protons as well as 12 and 16 MeV alphas [8]. Zhou of NASA subjected the scanned data to a linear energy transfer (LET) spectrum analysis [9]. The results, for the front side of detectors 10-5 and 10-6, are summarized in Fig. 1. From his analysis, Zhou concluded that there were 3–10 MeV protons as well as a continuum of alpha energies.

In another SRI experiment, The CR-39 detector was placed outside the cell. A 6 μm thick Mylar film was placed between the detector and the Ag cathode. The detector used in this experiment also underwent sequential etching analysis by Lipson and Roussetski. In their analysis, they identified proton recoil tracks due to 2.45 MeV (DD) neutrons.

Besides tracks due to energetic charged particles, triple tracks have also been observed in CR-39 detectors used in Pd/D co-deposition experiments. Triple tracks have not been observed in blank detectors or in detectors used in control experiments. These triple tracks are diagnostic of 14.1 MeV neutrons. Figure 2 shows a side-by-side comparison of a Pd/D co-deposition generated triple track and a similar DT neutron generated triple track. The top images were obtained by focusing the microscope optics on the surface of the detector. The bottom images are an overlay of two images taken on the surface of the detector and the bottom of the tracks. In both images, it can be seen that three tracks are breaking away from a center point.

2.2. Addressing the critiques of the Pd/D co-deposition CR-39 results

The three criticisms of the CR-39 results addressed in this communication are: (1) chemical damage vs. nuclear origins of the tracks; (2) why the Pd/D co-deposition tracks are predominantly circular in shape; and (3) the absence of Pd K-shell X-ray emissions that should simultaneously occur with the energetic charged particles.

A series of control experiments had been done to demonstrate that the tracks observed in CR-39 detectors used

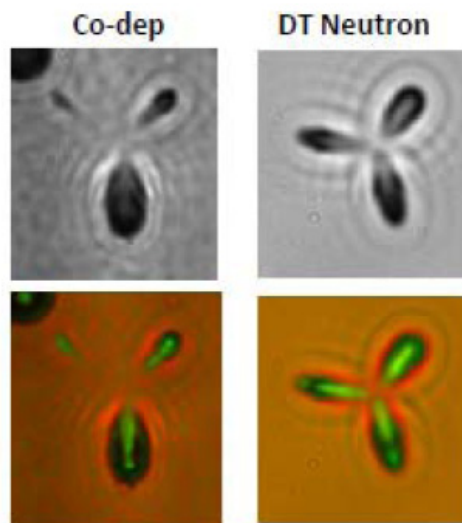


Figure 2. Microphotographs of Pd/D co-deposition and DT neutron generated triple tracks.

in Pd/D co-deposition experiments were not the result of chemical damage [6]. The most notable control experiment involved replacing PdCl_2 with CuCl_2 . In both the PdCl_2 and CuCl_2 systems, the same chemical and electrochemical reactions are occurring. At the anode, oxygen and chlorine gases are evolved. At the cathode, metal plates out in the presence of evolving deuterium gas. Both Pd and Cu form dendritic metal deposits with a high surface area. The significant difference is that Pd absorbs deuterium and copper does not. Tracks in CR-39 were only observed in Pd/D co-deposition. This control experiment indicated that the tracks were not due to the dendrites piercing into the CR-39 or to localized production of hydroxide ions etching into the CR-39. Although the control experiments indicated that the tracks were not the result of chemical damage, these conclusions have been questioned. To address this, a Pd/D

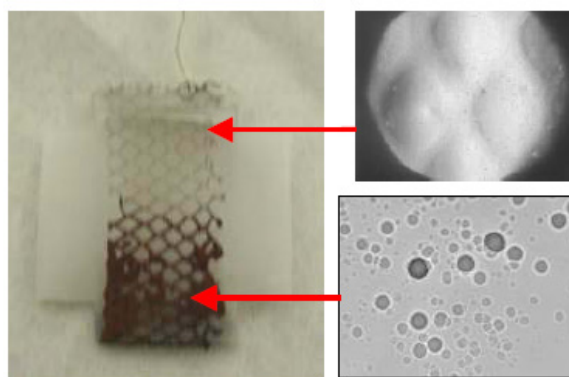


Figure 3. Ni/Au composite electrode used in a Pd/D co-deposition experiment and the resultant observations.

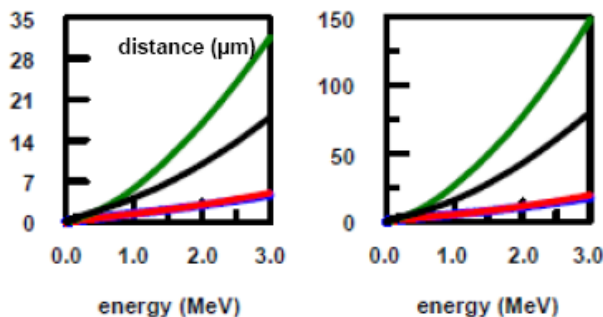


Figure 4. LET curves for protons (green), tritons (black), helium-4 (blue), and helium-3 (red) in palladium and water.

co-deposition experiment was conducted using a Ni/Au composite electrode, shown in Fig. 3.

Earlier it was shown that in the absence of an external E/B field, no tracks were obtained on a Ni screen cathode. Instead the impression of the Ni screen was observed on the CR-39 detector. For Au, Ag, and Pt cathodes, tracks were obtained in both the presence and absence of an external E/B field. In the composite cathode experiment, Au was electroplated on half of the Ni screen, as shown in Fig. 3. This composite cathode was placed in contact with a CR-39 detector and used in a Pd/D co-deposition experiment. At the end of the experiment, the detector was etched and analyzed. The results show that no tracks were obtained on the bare Ni half of the cathode. The impression of the Ni screen is observed. However, tracks were observed on the Au-coated Ni screen. Both halves of the cathode experienced the same chemical and electrochemical environment at the same time. If the pitting in CR-39 was due to chemical attack, those reactions would have occurred on both the bare Ni and Au-coated Ni halves of the cathode and both halves would have shown pitting of the CR-39 detector. But this was not observed. Therefore, the tracks observed in the CR-39 detectors are not the result of chemical attack.

The tracks observed in CR-39 detectors used in the Pd/D co-deposition experiments are predominantly circular in shape. After their birth, charged particles have to pass through the Pd lattice and a water layer before impinging upon the detector. LET curves were used to determine the magnitude of the effect of Pd and water on the energies of the particles. These LET curves, shown in Fig. 4, show that thin layers of Pd and water greatly slow down the

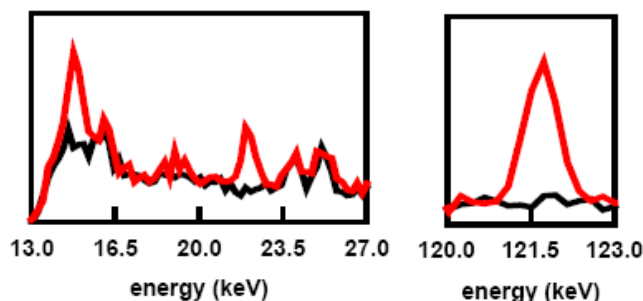


Figure 5. Gamma ray spectra of the lead cave obtained in the presence (red) and absence (black) of a ^{210}Po source.

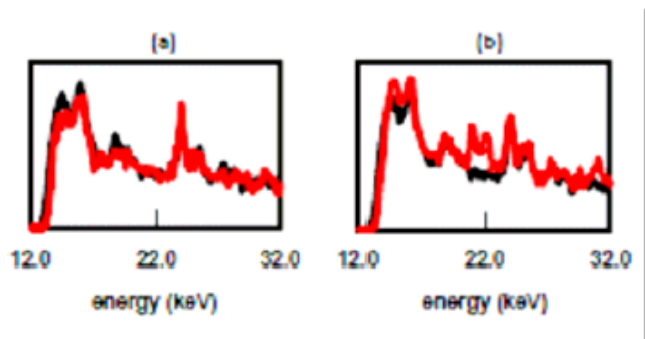


Figure 6. Gamma ray spectra obtained with the ^{210}Po -Pd sample (a) oriented perpendicular to the detector window and (b) facing the detector window. Background and sample spectra are in black and red, respectively.

charged particles. They also indicate that, CR-39 will only detect charged particles that are born near the surface of the Pd. Circular tracks indicate that the charged particles are entering perpendicular to the surface of the detector. These charged particles are the only ones with enough energy to get through the water layer to reach the detector. In one simulation, a CR-39 detector was exposed to an ^{241}Am source [10]. Placing $24\ \mu\text{m}$ of Mylar between the detector and the ^{241}Am source slows the alphas by 4.41 MeV. The resultant tracks were primarily circular in shape and greatly resembled the tracks obtained as a result of Pd/D co-deposition.

It has been shown that X-rays are generated by the refilling of the K shell electron orbits ionized by the passage of charged particles. In 1989, Bennington et al. [11] and Deakin et al. [12] used SiLi detectors to detect these K-shell X-rays in Pd/D electrolysis experiments. No X-rays above background were detected. If the CR-39 is detecting charged particles, where are the concurrent Pd X-ray emissions? To address this apparent discrepancy, simulation experiments were conducted using a $0.1\ \mu\text{Ci}$ ^{210}Po source, a pure alpha particle emitter.

A CR-39 detector was exposed to the ^{210}Po source. The observed number of tracks was consistent for a $0.1\ \mu\text{Ci}$ source. A gamma-ray spectrum of the ^{210}Po source was obtained by placing the source inside the lead cave and pressed against the Be window of a HPGe detector. Figure 5 shows the time-normalized spectra obtained for the lead cave with and without the ^{210}Po source. From the spectra, it can be seen that three new gamma/X-ray lines at 14.8, 21.9, and 121.7 keV are present in the ^{210}Po source spectrum. As ^{210}Po is a pure alpha emitter, these new lines cannot be due to ^{210}Po . Both gamma rays and alpha particles will stimulate the K shell X-ray emission. While the presence of the contaminant in the ^{210}Po source was unexpected, it did present an opportunity to separate and quantify the alpha/gamma contributions in stimulating the Pd K shell X-rays.

The ^{210}Po source was placed in contact with a Pd foil. Spectra were obtained by placing the sample perpendicular to the Be window of the HPGe detector, Fig. 6(a), and directly facing the detector, Fig. 6(b). No Pd K shell X-rays were observed with the ^{210}Po -Pd sample facing away (perpendicular to) the detector. However, when the Pd foil and ^{210}Po source were facing the Be window of the HPGe detector, the Pd $K\alpha$ line at 21.1 keV was observed as was the 21.9 keV line due to the contaminant in the ^{210}Po source. Consequently, the orientation of the cell relative to the HPGe detector will determine whether or not tracks will be observed.

Experiments were then conducted by placing $100\ \mu\text{m}$ thick acrylic film between the Pd foil and the ^{210}Po source. The acrylic film will block the alphas from ^{210}Po but not the gammas from the unknown contaminant. Figure 7 summarizes the results. Figure 7(a) is the spectrum of the Pd foil in the lead cave. The fluorescence from the lead bricks is stimulating the Pd K shell X-ray emissions. Figure 7(b) is the spectrum obtained for the ^{210}Po source and shows

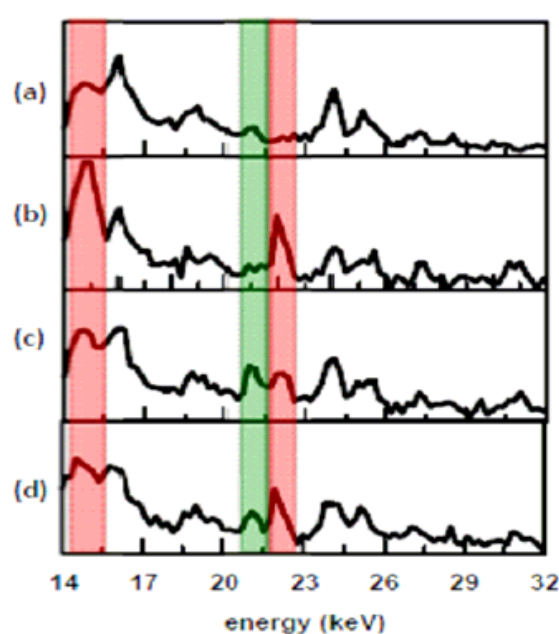


Figure 7. Summary of the ^{210}Po -Pd experiments where the red bars indicate the gamma lines of the unknown contaminant(s) and the green bar indicates the Pd K shell X-ray. Experiments were conducted by placing the samples in direct contact with the HPGe detector. (a) Pd foil in the lead cave, (b) ^{210}Po source, (c) Pd foil in contact with the ^{210}Po source, and (d) a 100 μm thick acrylic film is between the Pd foil and the ^{210}Po source.

the gamma lines due to the unknown contaminant(s). Figure 7(c) is the spectrum obtained when the ^{210}Po source is in contact with the Pd foil. The Pd K-shell emissions are stimulated by the lead cave background, the ^{210}Po alphas, and the gamma rays from the unknown(s). Figure 7(d) is the spectrum obtained when the 100 μm thick acrylic film is between the ^{210}Po source and the Pd foil. The Pd K-shell emissions are stimulated by the lead cave background and the gamma rays from the unknown(s). It is assumed that the background, ^{210}Po α -particle, and unknown contaminant γ -ray stimulations contribute additively to the Pd K α emissions of the Pd- ^{210}Po sample, Fig. 7(c). With this assumption, the estimated contributions of each source, in stimulating the Pd K shell X-ray emissions, are 35.2% due to background (lead fluorescence), 44.4% due to the ^{210}Po α -particles, and 20.4% due to the unknown contaminant gamma rays.

The results of the ^{210}Po -Pd experiments discussed *vide supra* can be used to determine whether or not Pd K shell X-rays should have been observed in the Pd/D co-deposition experiments. Figure 8(a) shows a photomicrograph of tracks obtained by scanning a CR-39 detector used in a Pd/D co-deposition experiment. The scanner identifies and numbers objects in the scanned image, Fig 8(b). Based upon measurements of object symmetry and contrast, the computer algorithm identifies tracks whose properties are consistent with those of nuclear generated tracks. Positively identified tracks are indicated by green rectangles, Fig. 8(c).

In a 1 mm \times 20 mm area of the CR-39 detector, the total number of tracks positively identified by the scanner in this area was 1079. The scanner does not count overlapping tracks. To determine whether or not Pd K shell X-rays would have been observed in the experiment, it is assumed that the observed tracks are due to charged particle interactions with the detector and not neutrons. As shown in Fig. 8(c), the number of tracks in this one image is undercounted by a factor of ~ 3 . Therefore, at a minimum, the number of tracks is undercounted by a factor of 3. However, the charged

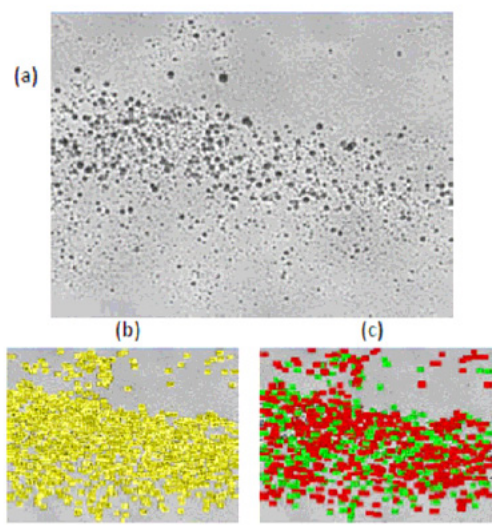


Figure 8. Scanned image of CR-39 detector used in a Pd/D co-deposition experiment: (a) raw image, (b) objects identified in the image, (c) after processing, identified tracks are *green*, non-tracks are *red*.

particle stimulation of the Pd K shell X-rays will occur throughout the Pd deposit. Ignoring absorption of the Pd K-shell X-rays by the Pd deposit and cell components, in the worst-case scenario, it is estimated that the charged particles are undercounted by a factor of 1000. The total area of the detector is 10 mm \times 20 mm. Taking this larger area into account, the charged particles are estimated to be undercounted by a factor of 10 000. Therefore, in this worst-case scenario, the number of charged particles is 1.079×10^7 . These experiments typically run for 2 weeks. For a two-week experiment (1.2096×10^6 s), the rate of particle production is estimated to be $8.9 \text{ particles s}^{-1}$.

Figure 7(a) and (d) is the time normalized spectra measured, in the Pb cave, for the Pd foil and for the experiment in which the 100 μm thick acrylic sheet was placed between the Pd foil and the ^{210}Po source. The measured peak areas for the line due to the Pd K-shell X-rays are tabulated in Table 1. From the data, the peak area, resulting from stimulation by the γ -rays from the unknown contaminant in the ^{210}Po source, is measured to be 5.31×10^{-5} . As discussed *vide supra*, the contribution of the unknown gamma contaminant to the Pd K-shell X-ray line is 20.4%. The ^{210}Po α -particles are responsible for 44.4% of the signal. A 0.1 μCi ^{210}Po α source will have 3700 decays s^{-1} . For the time-normalized spectra, this means that 3700 α particles will result in a Pd K-shell X-ray line with a peak area of 1.156×10^{-4} . In contrast, the increase in peak area of 8.9 charged particles, in the time-normalized spectrum, is calculated to be 2.8×10^{-7} . This is too small an increase in peak area to see in the measured spectrum. In addition, in this particular experiment, the cathode would have been oriented perpendicular to the HPGe detector. In this configuration, no Pd K-shell X-rays would have been observed, i.e. Fig. 6(a).

Measurement of K-shell X-rays occurs in real-time. In contrast CR-39 is an example of a constantly integrating detector, which means that when an event occurs, it is permanently stamped in the detector. The results discussed *vide supra* indicate that, although tracks significantly above background were observed in CR-39 detectors used in Pd/D co-deposition, the rate of charged particle production is too low to be detected by measuring the Pd K-shell X-ray emissions.

Table 1. Measured peak areas of the Pd K α line shown in the time-normalized spectra in Fig. 7(a) and (d).

Sample	Area of Pd K-shell X-ray line	Cause of stimulation ^{a,b}
Pd foil	9.22×10^{-5}	b kg
^{210}Po -100 μm acrylic-Pd foil	1.453×10^{-4}	b kg + γ

^ab kg is the background stimulation, γ is the gamma rays from the unknown contaminant(s) in the ^{210}Po source.

^bThe peak area resulting from stimulation by the unknown γ source is 5.31×10^{-5} .

2.3. Implications of the CR-39 results

In the absence of a magnetic field, the Pd deposit has a uniform “cauliflower”-like structure that consists of aggregates of spherical micro-globules. Figure 9(a) is an SEM microphotograph that shows the morphology of a Pd deposit that has been subjected to an external magnetic field. The Lorentz forces of the magnetic field have caused the Pd micro-globules to form the star-like features seen in Fig. 9(a). The development of these structural features in the magnetic field experiments requires high-energy expenditure.

EDX analysis of one of the spots is shown in Fig. 9(b). A very small peak due to Pd is observed. Larger peaks due to Fe, Cr, Ni, and Al are also observed. EDX detection limits are on the order of 0.1% [13]. Given the insensitivity of the EDX technique, the inhomogeneous distribution of the new elements, and the fact that the experiment was done using

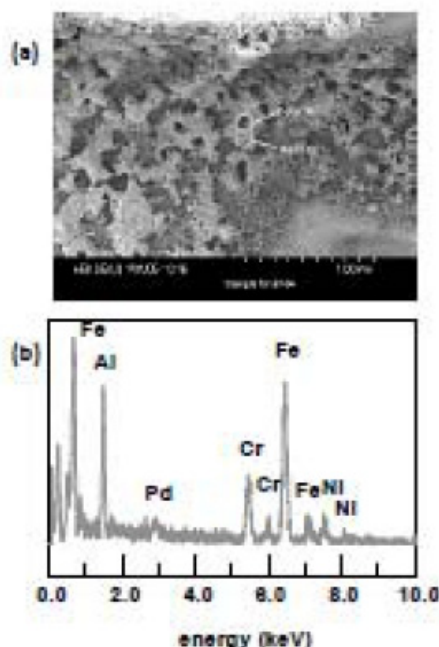
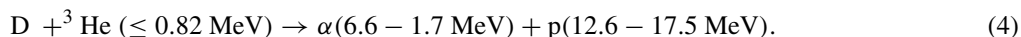
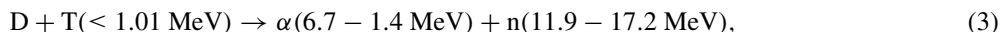
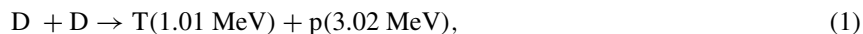


Figure 9. (a) SEM photomicrograph of the Pd deposit subjected to a magnetic field. (b) EDX analysis of one of the circled spots on the deposit.

a plastic cell, these new elements cannot be due to contamination. These same elements have been reported by others using a wide variety of conditions, e.g. different electrode materials and loading methods such as electrolysis, surface plasma electrolysis, gas pressure, plasma discharge, ion implantation, bubble collapse loading, and laser initiation [14]. But are the new elements observed the result of multi-body deuteron fusion or the disintegration of the Pd lattice? The energetic particles detected by solid-state nuclear track detectors such as CR-39 provide some insight as to the nature of the processes occurring inside the Pd lattice.

As discussed *vide supra*, the tracks in CR-39 used in Pd/D co-deposition experiments in the presence of a magnetic field were identified as being caused by 3–10 MeV protons, 2–15 MeV alphas, 2.45 MeV neutrons, and 14.1 MeV neutrons. Others have also reported detecting these energetic particles in their experiments. Roussetski [15] reported seeing triple tracks, which are diagnostic of 14.1 MeV, in his CR-39 experiments involving Pd/PdO:D heterostructures. Using CR-39 and Au/Pd/PdO:D heterostructures, Lipson et al. [16] reported seeing tracks due to 3 MeV protons and 1 MeV tritons. They also detected 2.5 MeV neutrons using NE213 detectors. In experiments using Si surface barrier detectors, including a dE-E telescope, Lipson et al. [17] detected 8–14 MeV alpha emissions from Au/Pd/PdO samples that had been loaded electrolytically with deuterium. Lipson et al. [18] conducted *in-situ* electrolysis experiments in which the Pd foil cathode was in direct contact with a CR-39 detector. Using Cu and Al spacers between the cathode and the detector, they identified the particles emitted as being 1.7 MeV protons and 11–16 MeV alphas.

The 2.45 MeV neutrons, 3–10 MeV protons, 14.1 MeV neutrons, and 1–7 MeV alphas can be accounted for by the following primary (1) and (2) and secondary fusion reactions (3) and (4):



The 7–16 MeV alphas can only come from another nuclear process. Fission reactions are known to produce these ‘long-range alphas.’ The EDX analysis of a cathode used in a magnetic field experiment, Fig. 9(b), shows that the peak due to Pd is significantly smaller than those for Fe, Al, Cr, and Ni. This implies that the Pd has been consumed. Both the sequential etching analysis and LET spectrum analysis of a CR-39 detector used in a magnetic field detector, discussed *vide supra*, showed the presence of long-range alphas. As the source of the long-range alphas is fission, it is very likely that the new elements seen in the EDX spectrum result from fissioning of the Pd nucleus.

3. Conclusions

In this communication, the use of microscopic examination, sequential etching, and LET spectrum analysis to identify the energetic charged particles and neutrons responsible for the tracks in CR-39 detectors used in Pd/D co-deposition experiments were discussed. These analytical techniques gave complementary results. The energetic particles were identified as 2.45 MeV neutrons, 3–10 MeV protons, 2–15 MeV alphas, and 14.1 MeV neutrons.

There have been questions/critiques about the Pd/D co-deposition CR-39 results. These have been addressed in this communication. In one criticism, the nuclear origin of the tracks has been questioned. Using a bare Ni, Au-plated Ni

screen composite cathode in a Pd/D co-deposition experiment, it was demonstrated that the observed pitting in CR-39 detectors were not the result of chemical damage. There have been questions as to why the Pd/D co-deposition tracks are predominantly circular in shape. LET curves for charged particles in Pd metal and water showed that only particles traveling perpendicular to the CR-39 detector have sufficient energy to impact the detector. As a result, the tracks are primarily circular in shape. It has been noted that charged particles traversing through a metal will stimulate K-shell X-rays. Yet these X-rays are not observed. Using a ^{210}Po source, it was shown that the experimental configuration determined whether or not X-rays would be seen. It was also shown that the rate of charged particle production was too low to detect measurable Pd K shell X-ray emissions.

The neutrons, protons, and 2–7 MeV alpha particles that have been detected in CR-39 used in Pd/D co-deposition have energies that are consistent with both primary and secondary fusion reactions. The alphas with energies between 7 and 15 MeV are referred to as long range alphas. These alphas have also been detected in CR-39 detectors used in Pd/D co-deposition reactions. The only known source of these long-range alphas is fission reactions. This suggests that the new elements observed on the cathodes are caused by fissioning of the Pd nucleus.

Currently within the CMNS community there has been disagreement as to what constitutes LENR. There are those in the community who contend that LENR is only heat and helium-4. Energetic particles with energies in the MeV range are clearly not low energy. However, they can only result from nuclear processes.

Acknowledgments

This communication is dedicated to the memory of Andrei Lipson. Replication of the co-deposition experiment by SRI is acknowledged as well as the sequential etching analysis of the detectors done by Lipson and Roussetski and the LET spectrum analysis done by Zhou. Steve Krivit of New Energy Times is acknowledged for organizing the SRI replication and subsequent analysis by Lipson and Roussetski. She is grateful for the support and encouragement she has received from both Frank Gordon and Dr. J.W. Khim. She also acknowledges thought provoking discussions she has had with Peter Hagelstein, Mitchell Swartz, Fran Tanzella, Roger Boss, Pat McDaniel, and Larry Forsley.

References

- [1] J.O'M. Bockris, G.H. Lin, R.C. Kainthla, N.J.C. Packham and O. Velez, Does tritium form at electrodes by nuclear reactions? in *The First Annual Conference on Cold Fusion*. 1990. University of Utah Research Park, Salt Lake City, Utah: National Cold Fusion Institute.
- [2] M.H. Miles, R.A. Hollins, B.F. Bush, J.J. Lagowski and R.E. Miles, Correlation of excess power and helium production during D_2O and H_2O electrolysis using palladium cathodes, *J. Electroanal. Chem.* **346** (1993) 99–117.
- [3] M. Swartz, Three physical regions of anomalous activity in deuterated palladium, *Infinite Energy* **14** (2008) 19–31.
- [4] S. Szpak, P.A. Mosier-Boss and J.J. Smith, On the behavior of Pd deposited in the presence of evolving deuterium, *J. Electroanal. Chem.* **302** (1991) 255–260.
- [5] S. Szpak, P.A. Mosier-Boss, M.H. Miles and M. Fleischmann, Thermal behavior of polarized Pd/D electrodes prepared by co-deposition, *Thermochimica Acta* **410** (2004) 101–107.
- [6] P.A. Mosier-Boss, S. Szpak, F.E. Gordon and L.P.G. Forsley, Use of CR-39 in Pd/D co-deposition experiments, *Eur. Phys. J. Appl. Phys.* **40** (2007) 293–303.
- [7] P.A. Mosier-Boss, S. Szpak, F.E. Gordon and L.P.G. Forsley, Triple tracks in CRT-39 as the result of Pd–D co-deposition: evidence of energetic neutrons, *Naturwissenschaften* **96** (2009) 135–142.
- [8] A.G. Lipson, A.S. Roussetski, E.I. Saunin, F. Tanzella, B. Earle and M. McKubre, Analysis of the CR-39 detectors from SRI's SPAWAR/Galileo type electrolysis experiments #7 and #5. Signature of possible neutron emission, *8th International Workshop on Anomalies in Hydrogen/Deuterium Loaded Metals*, pp. 182–203, October 2007.
- [9] D. O'Sullivan, D. Zhou, W. Heinrich, S. Roesler, J. Donnelly, R. Keegan, E. Flood and L. Tommasino, Cosmic rays and dosimetry at aviation altitudes, *Radiation Measurement* **31** (1999) 579–584.

- [10] P.A. Mosier-Boss, S. Szpak, F.E. Gordon and L.P.G. Forsley, Characterization of tracks in CR-39 detectors obtained as a result of Pd/D co-deposition, *Eur. Phys. J. Appl. Phys.* **46** (2009) 30901.
- [11] S.M. Bennington, R.S. Sokhi, P.R. Stonadge, D.K. Ross, M.J. Benham, T.D. Beynon, P. Whitney, I.R. Harris and J.P.G. Farr, A search for the emission of X-rays from electrolytically charged palladium-deuterium, *Electrochimica Acta* **34** (1989) 1323–1326.
- [12] M.R. Deakin, J.D. Fox, K.W. Kemper, E.G. Myers, W.N. Shelton and J.G. Skofronick, Search for cold fusion using X-ray detection, *Phys. Rev. C* **40** (1989) R1851–R1853. .
- [13] <http://www.web.pdx.edu/~jiao/phy451/Lect7.pdf>
- [14] G. Miley and P.J. Shrestha, Review of Transmutation Reactions in Solids, *Condensed Matter Nuclear Science*, World Scientific, New York, pp. 361–378, 2006.
- [15] A.S. Roussetski, Application of CR-39 plastic track detector for detection of DD and DT-reaction products in cold fusion experiments, 8th *International Conference on Cold Fusion*, 2000.
- [16] A.G. Lipson, B.F. Lyakhov, A.S. Roussetski, T. Akimoto, T. Mizuno, N. Asami, R. Shimada, S. Miyashita and A. Takahashi, Evidence for low-intensity D–D reaction as a result of exothermic deuterium desorption from Au/Pd/PdO:D heterostructure, *Fusion Technol.* **38** (2000) 238–252. .
- [17] A.G. Lipson, B.F. Lyakhov, A.S. Roussetski and N. Asami, Evidence for DD-reaction and a long-range alpha emission in Au/Pd/PdO:D heterostructure as a result of exothermic deuterium desorption, 8th *International Conference on Cold Fusion*, 2000.
- [18] A.G. Lipson, A.S. Roussetski, G.H. Miley and C.H. Castano, In-situ charged particles and X-ray detection in Pd thin film-cathodes during electrolysis in Li₂SO₄/H₂O, 9th *International Conference on Cold Fusion*, 2002.



Research Article

Evidence from LENR Experiments for Bursts of Heat, Sound, EM Radiation and Particles and for Micro-explosions

David J. Nagel*

The George Washington University, 2121 I St NW, Washington, DC 20052, USA

Mahadeva Srinivasan^{†,‡}

Bhabha Atomic Research Centre, Trombay, Mumbai 400085, India

Abstract

We examined published evidence for power production by LENR, which occurred too fast to be captured by calorimeters. That evidence includes observations of craters in materials, measurements of sound emission, recordings of radio-frequency, infrared and X-ray emissions, measurements of neutrons and charged particles and micro-explosions. The energy emission times, some below 1 ms, are tabulated.

© 2014 ISCMNS. All rights reserved. ISSN 2227-3123

Keywords: Energy bursts, Low energy nuclear reactions, Micro-explosions, Power bursts

1. Introduction

The energy released in low energy nuclear reactions (LENR) experiments and generators is unavoidably pulsatile on the scale of atoms. This is because some amount of energy is released during each LENR event at some point in time and space. If there are many LENRs occurring simultaneously, the power production on mesoscopic and macroscopic levels can occur in bursts. Or, if there are numerous LENRs occurring sequentially, the power production can have an apparently continuous and smooth time history. So, there are four basic modes of uncontrolled energy release: (a) a constant rate (ignoring shot noise), (b) a slowly varying (pseudo-steady) rate, (c) bursts of various durations and magnitudes, and (d) a mix of the more-or-less steady output plus the occurrence of some bursts.

The time scale over which energy is released in LENR experiments and anticipated products is important for both scientific and practical reasons. The basic mechanisms for the occurrence of LENR are still not understood. Hence, fast energy releases might help in understanding what is happening at a fundamental level. For example, are energy

*E-mail: nagel@gwu.edu

[†]E-mail: chino37@gmail.com

[‡]Retired.

releases, which require the near-simultaneous occurrence of numerous LENR, the result of many uncorrelated events, or are they due to some type of a fast cascade of reactions, essentially a chain reaction? This is a very basic question.

The practical importance of temporal variations in LENR power production seems clear. Comparisons with the release of chemical energy are instructive. There are some chemical heat production situations that are more-or-less steady, such as the burning of coal, oil or gas in a boiler. Others are pulsed, but tightly controlled. Explosions of petrol vapors in automobile engines at rates of hundreds of Hz are a common example. At this early stage in commercialization of LENR power generators, it is unclear what power production profiles will be employed for the many possible applications of the new sources. However, it is clear that both reproducible behavior and adequate control will be needed. Hence, the time histories of heat production in LENR experiments are directly relevant to later applications.

There are four different classes of evidence for the occurrence and characteristics of LENR, some of which are relevant to the question of fast energy releases. The first is production of heat that cannot be explained by chemistry. Because of the long time constants of calorimeters, most thermal measurements cannot resolve LENR energy releases that occur in fast bursts. However, there are some other rapid thermal phenomena, such as crater production and infrared emission, which require nuclear events for their explanation. The second kind of evidence is the residue of nuclear reactions, that is, the nuclear ash left from transmutation reactions. Here again, data from transmutations cannot provide evidence of bursts of energy production because the sensitive chemical analysis methods needed to quantify nuclear ash can only be used after an experiment. That is, localization in time cannot be detected, but localization in space can be discerned by post-run scanning spectroscopy of materials. Measurements of energetic particles and hard electromagnetic radiation, which cannot be due to chemistry, are the third foundation for LENR. In this case, it is possible to see bursts of energetic quanta, so that something can be learned about the time history of the occurrence of LENR. The fourth class of information on LENR includes acoustic emission. Bursts of sound from LENR experiments have been measured, and will be discussed below.

In this paper, we examine the available evidence that illuminates the short-time history of the energy production by LENR and, for some cases, the spatial distribution of power production. Fast thermal events, including characteristics of craters left in cathode surfaces and the emission of infrared radiation from cathodes during electrolysis, are surveyed.

The characteristics of pulsed sound emission, electromagnetic radiation and fast particles from LENR experiments are studied. The goal of this review is to compare the temporal extent of bursts from LENR experiments that are measured in these various ways.

Section 2 discusses evidence for energy releases, both slow and fast. Sound emission is the subject of Section 3. Temporal measurements of electromagnetic radiation in the radio-frequency, infrared and X-ray regions are reviewed in Section 4. Section 5 deals with neutron and fast ion measurements. References to papers discussing micro-explosions are in Section 6. A summary and discussion of evidence for the relatively fast measured phenomena constitutes Section 7.

2. Energy Releases

Much of the experimental literature on LENR includes measurements of energy going into and out of experimental electrochemical and other cells, and the excess energy, gotten as the difference between output and input energies. The calorimeters used for such measurements are diverse in type and specific design. They can be remarkably sensitive, with the ability to measure powers to less than a milliwatt in some cases. However, even that remarkable threshold is too high to capture events involving relatively small numbers of reactions and associated energy releases or emissions.

The thermal masses, and associated time constants, of calorimeters are such that it is not possible to temporally resolve events that occur on the time scale of one minute or less. This is simply understandable by considering how long it takes for a cup of hot coffee to cool to room temperature. Water has a high thermal capacity, and loss of its

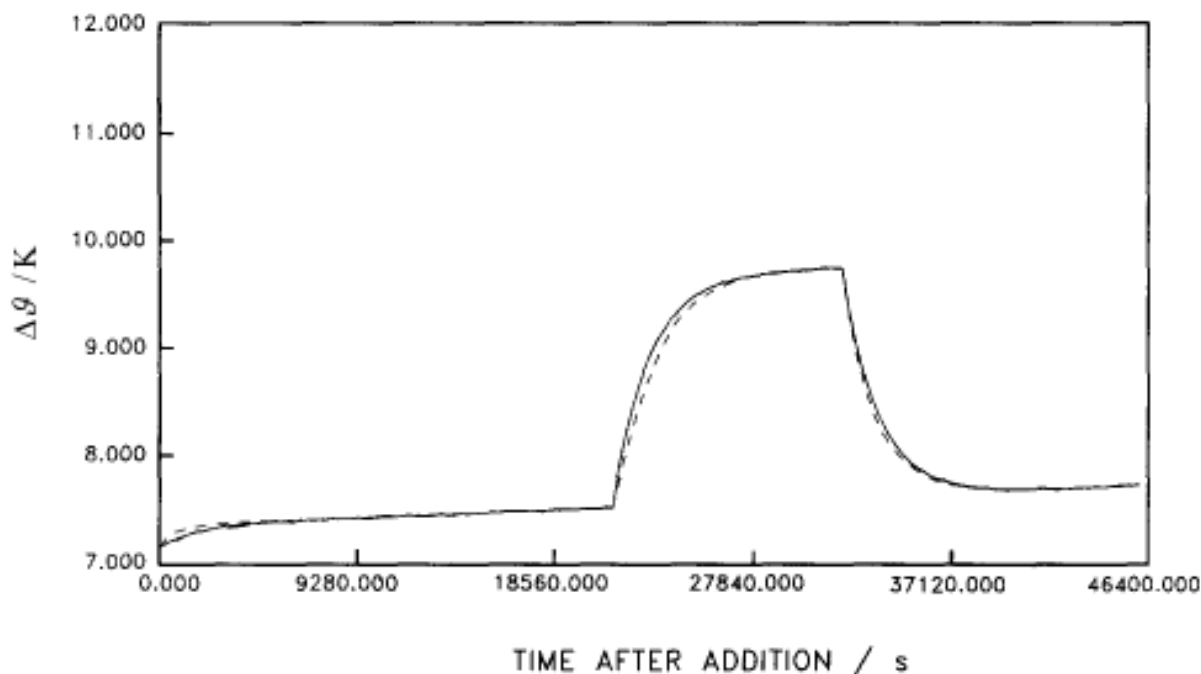


Figure 1. Cell temperature (K) vs time for about 12.5 h showing the response to application and removal of a heater pulse [1]. The horizontal bar shows the time between tick marks on the horizontal axis. See text for discussion in details.

thermal energy by conduction, convection and radiation takes times on the scale of minutes for volumes such as those within calorimeters.

Many LENR calorimeters have time constants on the scale of hours. Figure 1 is from a very important 1990 publication by Fleischmann, Pons and three colleagues [1]. It shows the time history of temperature in one of their isoperibolic calorimeters before, during and after the application of a heater pulse. The figure contains two curves, the solid experimental line and the fit using their equations for behavior of the calorimeter. The close similarity shows that, early in the field, Fleischmann and Pons understood the quantitative behavior of their instrumentation very well.

Even though calorimeters are too slow to capture energy emission events on time scales fast enough for mechanistic understanding and practical utilization, many LENR experiments have evidenced burst-mode behavior. Figure 2 is one example [2]. It shows bursts of energy as measured by a sealed Seebeck envelope calorimeter with a recombination catalyst. The overshoot after each burst is ascribed to the possible loss (leakage) from the cell of the gases produced during bursts. Such leakage would reduce the energy recovered from recombination and give apparent negative excess power for a period of time. The main point here is that LENR experiments often produce bursts of energy of a few hours duration. The pulses occur at seemingly random times, with highly variable amplitudes. However, the authors found that a plot of the number of pulses with specific excess powers (<0.5 W) had a $1/f$ character, where f is the frequency of occurrence. Such behavior is seen in many natural and man-made situations. It has been attributed to “self organized criticality” [3]. Whether or not the $1/f$ behavior seen in these experiments reveals anything about the creation of nuclear active regions, or the dynamics within such regions, remains to be explored.

There is one phenomenon widely observed after LENR experiments, which indicates fast thermal energy releases.

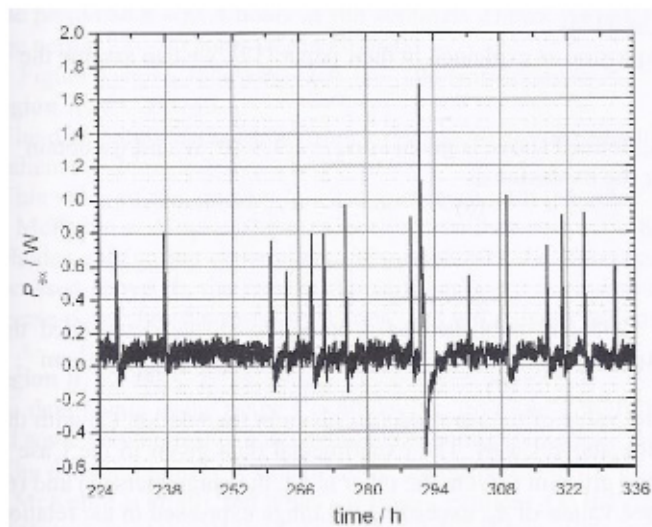


Figure 2. Excess power for 112 h of a 14-day experiment showing bursts of emitted energy [2].

It does not involve the use of inevitably slow calorimeters. And, it can be employed to set a limit on the duration of an energy emission event. The phenomenon is the production of small craters on the surfaces of cathodes used in electrochemical LENR experiments.

Craters have been observed for a very wide variety of materials and conditions in LENR experiments. Figure 3 gives a sampling of craters from co-deposition experiments (top three images) and super-wave experiments (bottom

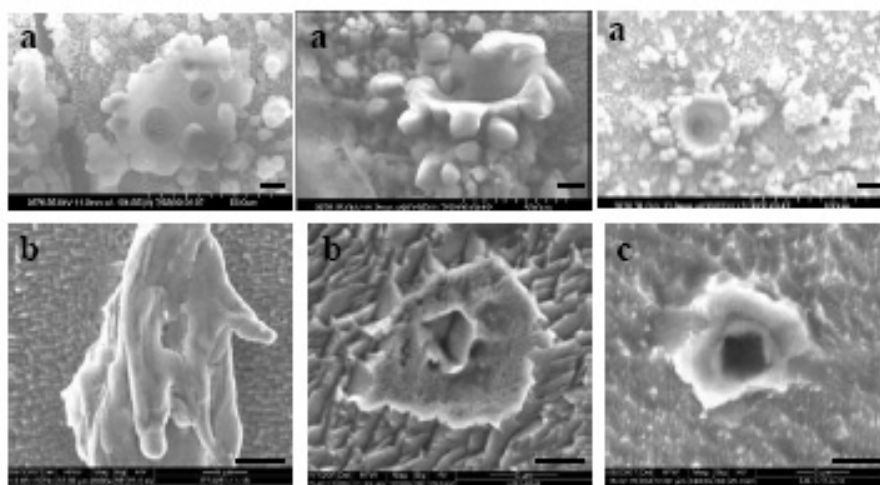


Figure 3. Scanning electron micrographs of craters in cathodes from LENR experiments. (a) shows craters from co-deposition experiments with 10 μ bar [4]. (b) [5] and (c) [6] are from super-wave experiments with 2 μ bar.

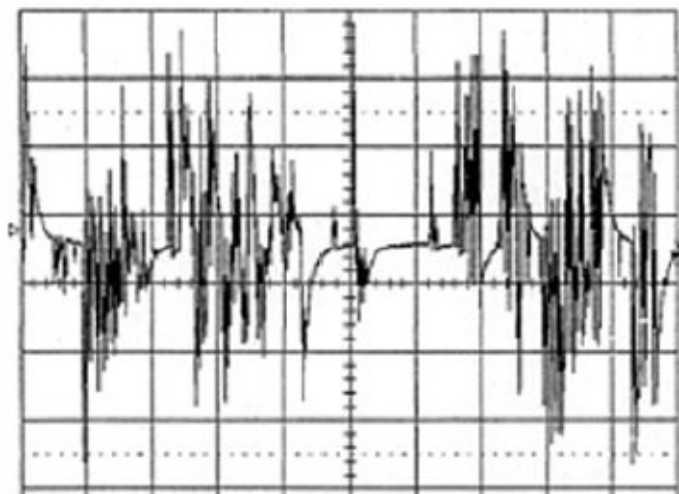


Figure 4. Record of sound emission from a LENR experiment [10]. Time is horizontal (200 ms/div) and voltage is vertical (5 V/div).

three images). The rounded character of parts of most of these and many other crater images indicates that melting probably occurred during production of the craters. A study of LENR micro-craters showed that they have diameters generally in the 1–100 μm range [7]. Two methods were used to estimate the energies needed to produce such craters. They were in reasonable agreement, and showed that the energies necessary to make the observed craters fall in the range from 1 nJ (1 μm craters) to 1 mJ (100 μm craters). However, neither that study nor any other has reported on estimates of the time for crater formation. Those times could be computed using modern thermal analysis software [8,9]. Such computations should be straightforward and would be valuable.

3. Sound Emission

A rapid release of energy, sufficient to form a crater, would also result in the emission of sound, possibly a click. For this reason, as well as to exploit all avenues for the experimental study of LENR, measurements of sound from active cells could be important.

There seems to be only one study that included measurements of sound from a LENR experiment. The scientists at the US Navy SPAWAR Laboratory co-deposited Pd and D on the surface of a piezoelectric transducer [10]. This enabled them to efficiently pick up and record the sounds emitted within the cell. Figure 4 shows one of the resultant oscilloscope records. It contains apparently random spikes with widely varying peak height and time of occurrence.

It should be worthwhile to do the same kind of analysis of such acoustic data as was done for the heat bursts seen in Fig. 2. It might also be possible to correlate the number of craters observed by post-run microscopy with the number of sound bursts measured in the same experiment. Such a correlation, and statistical analyses of both the crater and sound data, could establish a quantitative relationship between the craters and sound. Finally, spectroscopy of the sound emission is possible using very fast modern digitization hardware and methods. The spectrum of individual bursts of sound might be instructive.

4. Electromagnetic Radiation

Emission of electromagnetic radiation, like sound emission, occurs on a fast time scale. Hence, it is potentially valuable for understanding the mechanisms active in LENR energy releases. Many experimenters in the field have sought to measure radiation within several regions of the EM spectrum. Emission for short periods has been recorded in the radio-frequency, infrared and X-ray ranges. Samples of such data are given below.

Afonichev performed experiments in which deuterium-saturated Ti samples were deformed during measurements of neutron and radio-frequency (RF) emission [11]. At ICCF-10 in 2003, he showed time traces over about half an hour that exhibited what look like random bursts of neutron emission during deformation, but not when the deformation was interrupted. There were three systems measuring the RF emission at the same times. His paper states that the RF emission “had a sporadic character; the same character was noted when detecting neutrons.”

More recently, Dominguez and ten colleagues sought to measure RF emissions during electrochemical LENR experiments [12]. They performed over 300 runs, many with a spectrum analyzer in place to search for RF emission. In one run, they observed two episodes of excess heat, both of about two hours duration. Each heat burst was accompanied by RF signals near 400 MHz. There is clearly a need for more attempts to listen for RF signals from LENR experiments.

Infrared (IR) radiation from LENR experiments was measured with a camera sensitive to such long wavelength radiation [13]. Figure 5 shows one frame from the video record. The temperature range for the image is from 29 to 49°C. It is seen that some small spots of the image are white, so they have temperatures near 49°C, that is, about 2°C higher than the region in which they occur (the red area). These temperatures imply energy releases on the scale of nuclear values. The video shows that the small spots turn on and off as time progresses. It is as if there are very local releases of energy at different point of the cathode at different times. Presumably, the relatively hot, red-colored region covering most of the viewed area of the cathode was heated by such bursts or by conduction from locations of earlier bursts. It is highly desirable to make more IR measurements and to thoroughly analyze them spatially and temporally. Spectral measurements of IR emission from LENR experiments should also be made.

X-ray (XR) emission from LENR experiments is especially interesting because, unlike RF or IR photon energies, the energy in a single XR photon is much greater than chemical energies. There have been many measurements of XR emission from LENR experiments with mixed success. But, some of the observations are very noteworthy. Karabut

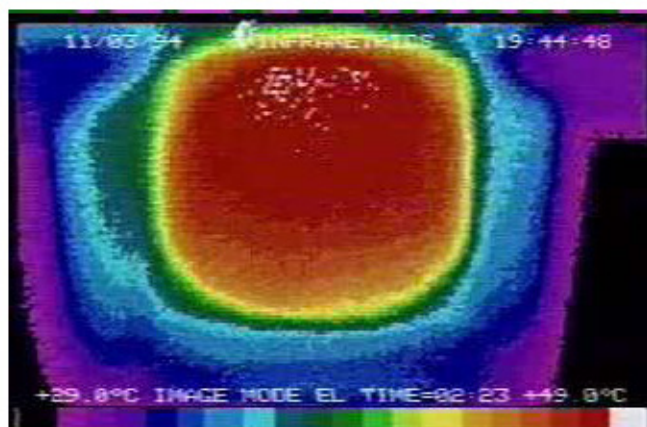


Figure 5. Image recorded by an infrared camera viewing the cathode in a co-deposition experiment [13].

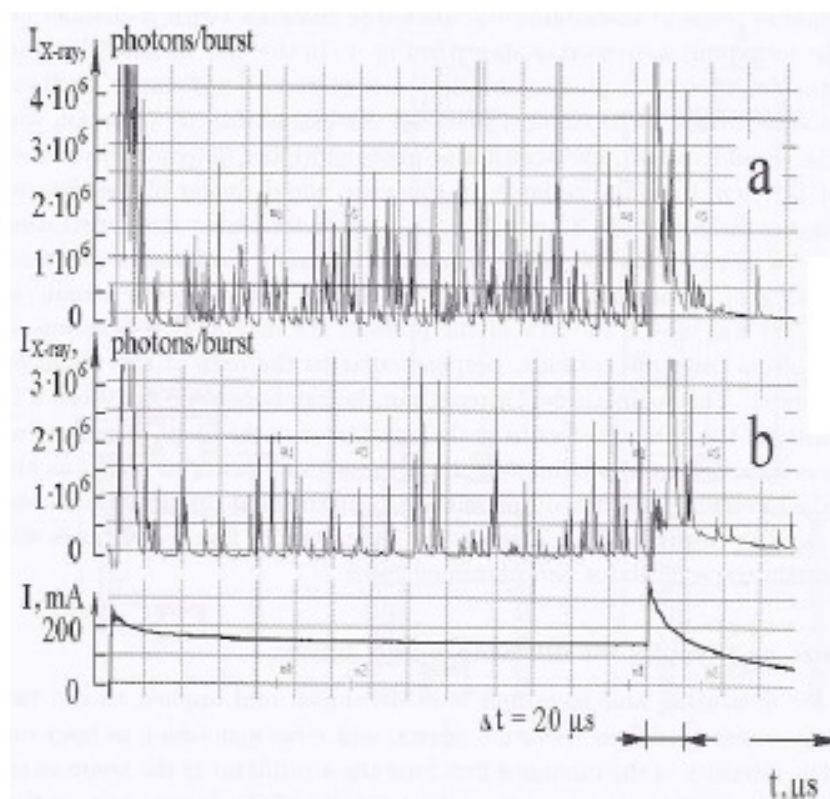


Figure 6. Two time traces of X-ray emission, as measured by a Photo Multiplier Tube viewing a scintillator covered with a Be foil to exclude light. The grid lines on the horizontal time axis are $20\ \mu\text{s}$ wide, as indicated. The current history for the glow discharge is shown at the bottom [15].

has been performing glow discharge LENR experiment for over 20 years. He measured the spectral, spatial and temporal characteristics of such emissions with “100% reproducibility” [14].

Karabut found that the emitted X-rays are in the 0.6–10 keV region. They are collimated, which is truly remarkable. Figure 6 shows one of the many time histories, which Karabut and his colleagues have published [15]. It is not possible to fully resolve the time variations of the fastest pulses. However, they appear to have full widths at their half maxima of about 10% of the grid line spacing, that is, about $2\ \mu\text{s}$. Here again, as with the slow heat pulses (Fig. 2) and the sound emission (Fig. 4), both the appearance times and the magnitudes of the pulses appear to be quite random. However, a detailed analysis of those two parameters and their relationship ought to be done.

We sought to locate published gamma ray data from LENR experiments, which showed rapid time variations. However, there is relatively little gamma ray data and it is almost always time integrated because of low count rates. Fast gamma ray data would be of great interest.

It is possible to instrument various LENR experiments to simultaneously record electromagnetic radiation in several spectral regions. Potential time correlation of such measurements would be valuable.

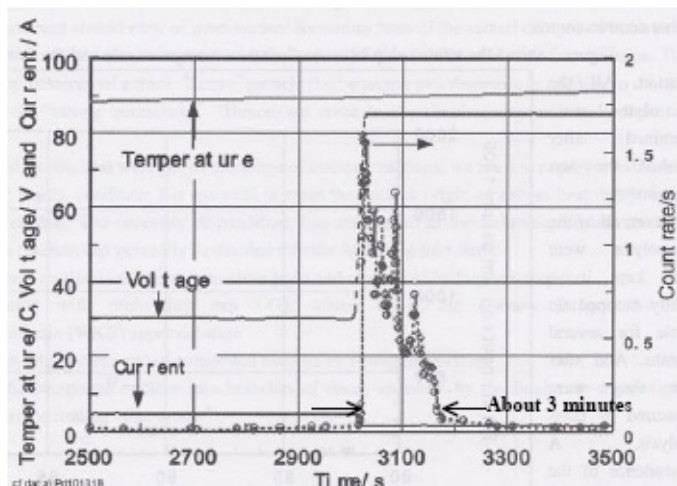


Figure 7. Time variation of neutron count rate (*right axis*) [16]. The burst of neutrons was triggered by change in the voltage (*left axis*).

5. Particle Emissions

As with emission of EM radiation, particle emissions occur individually on very fast atomic time scales. So, measurements of the time histories of the emission of neutrons and ions might also be instructive. We begin with two kinds of neutron data. The first is direct measurements of time variations. The second involves measurements of neutron multiplicities.

There are neutron detectors able to capture the variations in neutron signals with time resolutions well below 1 s. Hence, it is possible to record fast neutron emissions from LENR experiments. Figure 7 is one example of neutron emission that varies in times as short as about 10 s [16]. It might be difficult to obtain neutron time variation data for much shorter times because of relatively low count rates.

The overall history of neutron measurements from LENR experiments is a complex story. Many attempts were made to record evidence of neutron emissions, some of them in underground laboratories with low cosmic ray background and others with veto detectors over the experiments. Very generally, it has proven difficult to obtain neutron data. The time trace in Fig. 7 was one of the exceptions, until recently. Remarkably, there were three papers at ICCF-17, which reported high neutron count rates.

Jiang et al. [17] performed a complex and careful set of experiments and obtained strong neutron data. They employed samples of uranium deuteride and D-loaded Ti, and cycled the experiment. The materials were surrounded by 88 ^3He neutron detection tubes in a polyethylene moderator. Bursts of neutrons were measured in a short time window. Up to 2800 neutrons were observed in a 64 μs interval for D-loaded Ti.

Prelas and Lukosi reported on neutron emission from Ti in deuterium gas that was thermally shocked from liquid nitrogen temperature to 100°C [18]. These researchers used a pair of ^3He detectors. Two million neutrons were recorded in 5 min. It remains to be learned if the D-loaded Ti common to both the Jiang et al and Prelas–Lukosi experiments reported at ICCF-17 was key to such intense neutron production, or if the protocols used (cycling and thermal shocking) caused the large measured intensities.

Yuri Bazhutov et al. measured radiation emission from a variety of materials loaded with mixtures of hydrogen and

deuterium gases [19]. The samples included LaNi_5 , Ni and Be. Neutrons were recorded using one ^3He tube. Pulses of neutrons exceeding 100 per minute were observed for short periods for LaNi_5 and Ni samples. For some runs, roughly one-half million neutrons were registered in about 1 h.

The equipments for the measurements of neutrons discussed so far in this section were qualitatively similar. That is, pulses from neutron detectors were recorded as a function of time for the duration of an experiment. A different approach to obtaining data on the simultaneous, or very nearly simultaneous, emission of neutrons was taken by researchers at the Bhabha Atomic Research Center (BARC) very early in the field [20]. That approach produced some qualitatively different results.

It is possible to distinguish between single neutron emission events and multiple neutron emission events by carrying out a frequency analysis of the neutron pulse train issuing from a thermal neutron detector embedded inside a hydrogenous moderator. A cluster of fast neutrons incident simultaneously on such a detector assembly will get temporally resolved due to the statistical nature of the neutron slowing down process in the moderator. The resultant time spread is typically of the order of $100\ \mu\text{s}$. For statistical analysis, the neutron counts in 10 ms time bins were recorded to yield a frequency spectrum of counts. It was concluded that over 20% of the neutrons generated in Pd- D_2O electrolytic cells and gas loaded TiD samples could be due to multiple neutron events wherein 20 to about 400 neutrons were possibly released in each “burst”.

Besides neutrons, it is also possible to measure energetic ions from LENR experiments. This has been attempted much less frequently than neutron measurements, because the ranges of ions in solids and even gases, are relatively short. However, attempts to measure ions have still resulted in worthwhile data. Figure 8 shows the count rate obtained from a D-loaded Ti foil subjected to 400 mA DC current [21]. It can be seen that temporal variations on the time scale of a few minutes were recorded. Particle energies up to more than 10 MeV were obtained. It is not known specifically which particles produced these data. The authors speculated that they may be tritons, ^3He or possibly alpha particles.

There are some other ion measurements, but without time resolution. As in the case of gamma rays, ion count rates are low, making it difficult to obtain good time histories showing fine temporal structure. However, more attempts to

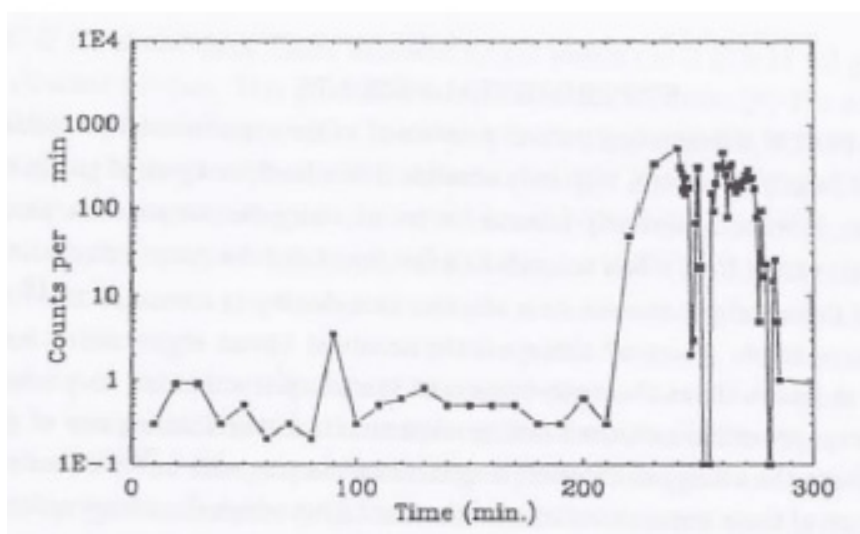


Figure 8. Time history of the count rates for ions from an LENR experiment [21].

measure ions might be made from gas loading experiments by use of differential pumping, a common practice in mass spectrometers.

6. Micro- and Macro-explosions

The papers noted above deal with measurements of phenomena in LENR experiments that occur too fast, or involve too little energy, to be captured by calorimeters. They have caused some scientists dealing with such data to speculate on the occurrence of small explosions on or in materials within LENR experiments. The earliest such surmise was based on the neutron multiplicity data measured at BARC and discussed in the last section. Piecing together all the BARC findings, it was concluded that micro-nuclear explosions are probably occurring, wherein 10^8 – 10^{10} tritons are generated in a sharp highly localized event. It was speculated that neutrons arise from secondary reactions involving the interaction of energetic tritons with deuterons in the lattice. A recent discussion of the early BARC data, and whether it is the signature of micro-nuclear explosions, is available [22].

The authors of several other papers were lead to contemplate small explosions as the source of what they and others measured [23–29]. The last of these papers is especially interesting. At ICCF-17, Biberian reported on his experimental attempts to understand an explosion that happened in his laboratory with an open cell [25,28]. Thrice, he triggered purposeful explosions using a mixture of hydrogen and oxygen, but the test cell was not damaged. Biberian concluded “It is therefore possible that in this case the explosion was of nuclear origin: some kind of a chain reaction.” The recent study of the energies required to form small craters on the surfaces of electrolytic LENR materials was already noted [7]. The micro-craters are *prima facie* evidence for small explosions on or near the surface of LENR cathodes.

The most notable macroscopic event was described in a paper by Fleischmann and Pons in 1989 [30]. They were conducting an electrolytic LENR experiment in which the cathode was a cube of Pd 1 cm on a side. During a weekend, the experiment suffered a thermal runaway, which lead to the following statement in their paper. We have to report here that under the conditions of the last experiment, even using D₂O alone, a substantial portion of the cathode fused (melting point 1554°C), part of it vaporized, and the cell and contents and a part of the fume cupboard housing the experiment were destroyed.” After burning through the table, the event left a hole in the concrete floor about 3 inches deep and 8 inches wide [31].

7. Summary and Discussion

A compilation of the various measurements, which show time variations faster than a calorimeter can respond, is given in Table 1. The order is the same as discussed above. The last column gives the authors’ views of what should be done for each type of observable. Straightforward simulations should give limits on the times for crater formation. The annotations “More Work” mean both additional measurements and sophisticated data analysis would be valuable. Actually, the need for initial or better data analysis applies to all of the entities. There are X-ray detectors with sub-

Table 1. The shortest reported times and further work needed for the indicated measurements from LENR experiments.

Observations	Shortest time	Needs
Craters	$\ll 1$ s	Simulations
Sound	About 20 ms	More work
RF emission	A few seconds	More work
Infrared emission	$\ll 1$ s	Spectroscopy
X-ray emission	About 2 μ s	Fast detectors
Neutrons	$< 64 \mu$ s	More work
Energetic ions	About few min.	New designs

nanosecond response times that should be used. The outstanding neutron apparatus of Jiang et al. should be used for more measurements. New experiment designs to capture ions with little attenuation are both possible and needed.

The overall message from the tabulation is that some processes happen in LENR experiments on the time scale of microseconds.

Bursts, such as studied in this review, will probably be of most use scientifically. That is, they serve to guide and constrain theories about the mechanisms that lead to LENR. This may be most true for the fastest energy releases, which set limits on the durations of energy release events. Fast recordings might turn out to have something to say about the difference between near-simultaneous reactions and cascaded (chain) reactions. However, it is also likely that bursts of power that occur over much longer times, including those resolvable with calorimetry, will be important. The use of LENR generators for myriad applications will be influenced by large variations on longer time scales. It is already clear that the ultimate disposition (as heat, sound, radiation, etc.) of the energy released from nuclear binding energies will be significant, at least scientifically, and probably practically. Such energy branching ratios are needed.

References

- [1] M. Fleischmann et al., Calorimetry of the palladium–deuterium-heavy water system, *J. Electroanal. Chem.* **28** (1990) 293–350.
- [2] H. Kozima, W.-S. Zhang and J. Dash, Precision measurement of excess energy in electrolytic system Pd/D/H₂SO₄ and inverse power distribution of energy pulses vs. excess energy, *Proc. of the 13th Int. Conf. on Condensed Matter Nuclear Science*, MATI Moscow, 2008, pp. 348–358.
- [3] Per Bak, *How Nature Works*, Springer, Berlin, 1999.
- [4] S. Szpak, P.A. Mosier-Boss, J. Dea and F.E. Gordon, Polarized D⁺/Pd-D₂O system: hot spots and mini-explosions, *Proc. 10th Int. Conf. on Cond. Matter Nucl. Sci.*, World Scientific, Singapore, 2006, pp. 13–22.
- [5] I. Dardik et al., Ultrasonically-excited electrolysis experiments at energetics technologies, *Proc. ICCF-14*, 2020, pp. 106–122 at www.iscmns.org/iccf14/ProcICCF14a.pdf.
- [6] M. Tsirlin, Private Communication.
- [7] D.J. Nagel, Characteristics and energetics of craters in LENR experimental materials, *J. Cond. Mat. Nucl. Sci.* **10** (2013) 1–14.
- [8] <http://www.ansys.com/>.
- [9] <http://www.solidworks.com/>.
- [10] S. Szpak, P.A. Mosier-Boss and F.E. Gordon, Experimental evidence for LENR in a Polarized Pd/D Lattice, presented at the *National Defense Industry Association Conference*, Washington DC, 2006, and available for downloading at http://lenr-canr.org/wordpress/?page_id=1081.
- [11] D.D. Afonichev, High-frequency radiation and tritium channel, *Proc. 10th Int. Conf. on Cond. Mat. Nucl. Sci.*, World Scientific, Singapore, 2006, pp. 353–359.
- [12] D. D. Dominguez et al., Evidence for excess heat in Fleischmann–Pons-type electrochemical experiments, *J. Electroanal. Chem.* (submitted).
- [13] P.A. Mosier-Boss and S. Szpak, The Pd/^mH system: transport processes and development of thermal instabilities, *Nuovo Cimento Soc., Ital. Fis.* **112 A** (1999) 577–586.
- [14] A.B. Karabut, Research into Excited long-lived 0.6–10 keV energy levels in the cathode solid medium of glow discharge by X-ray spectra emission, *Proc. ICCF-17*, 2012.
- [15] A.B. Karabut and S.A. Kolomeychenko, Experiments characterizing the X-ray emission from a solid-state cathode using a high-current glow discharge, *Proc. 10th Int. Conf. on Cond. Mat. Nucl. Sci.*, World Scientific, Singapore, 2006, pp. 585–596.
- [16] T. Mizuno et al., Relation between neutron evolution and deuterium permeation of a palladium electrode, *Int. Conf. on Cond. Mat. Nucl. Sci.*, 2003, pp. 265–270.
- [17] S. Jiang et al., Neutron burst emissions from uranium deuteride and D-loaded titanium, *Proc. ICCF-17*, 2012.
- [18] M.A. Prelas and E. Lukosi, Neutron emission from cryogenically cooled metals under thermal shock, *Proc. ICCF-17*, 2012.
- [19] Y. Bazhutov et al., Investigation of radiation effects at loading Ni, Be and LaNi₅ by hydrogen, *Proc. ICCF-17*, 2012.
- [20] P.K. Iyengar and M. Srinivasan, Overview of BARC studies in cold fusion, *The First Annual Conference on Cold Fusion*, Salt Lake City, Utah, USA, March 1990, pp. 62–81.

- [21] F. W. Keeney et al., Charged-particle emission from deuterided metals, *Proc. 10th Int. Conf. on Cond. Mat. Nucl. Sci.*, World Scientific, Singapore, 2006, pp. 509–523.
- [22] Mahadeva Srinivasan, Neutron emission in bursts and hot spots: signature of micro-nuclear explosions? *J. Cond. Mat. Nucl. Sci.* **4** (2011) 161–172
- [23] W. Dalun et al., Experimental studies on the anomalous phenomenon in Pd metal loaded with deuterium, *Proc. ICCF-3*, 1992, pp. 169.
- [24] X. Zhang et al., On the explosion in a deuterium/palladium electrolytic system, *Frontiers of Cold Fusion*, Universal Academy Press, 1992, pp. 381–384.
- [25] S. Szpak et al., Polarized D^+ /Pd- D_2O system: hot spots and mini-explosions, *Proc. ICCF-10*, 2006, pp. 13–22.
- [26] J.-P. Biberian, Explosion during an electrolysis experiment in an open cell mass flow calorimeter, *6th Int. Workshop on Anomalies in H/D Loaded Metals*, (2005).
- [27] R.W. Kuhne, The extended micro hot fusion scenario, *Proc. of the 13th Int. Conf. on Cond. Mat. Nucl. Sci.*, MATI Moscow, 2008, pp.704–708.
- [28] S. Szpak and F. Gordon, Forcing the Pd/ 1H - 1H_2O system into a nuclear active state, *Proc. ICCF-17*, 2012.
- [29] J.-P. Biberian, Cold fusion, *Proc. ICCF-17*, 2012.
- [30] M. Fleischmann and S. Pons, Electrolytically induced nuclear fusion of deuterium, *J. Electroanal. Chem.* **261** (1989) 301–308.
- [31] Chase N. Petersen, *The Guardian Poplar*, University of Utah Press, 2012, p. 218.



Research Article

Neutron Emission from Cryogenically Cooled Metals Under Thermal Shock

Mark A. Prelas and Eric Lukosi*

University of Missouri, Columbia, MO 65211, USA

Abstract

During the summer of 1991, intense neutron bursts were observed after temperature shocking titanium chips which had been saturated with deuterium gas. The titanium chips were cooled and loaded with deuterium at 77 K and then rapidly heated to 323 K. The rapid heating produces a large pressure increase inside the crystalline lattice of the host metal. An Event Timer/Counter (ETC) card was designed and developed which counted and kept a time distribution of the neutron pulses as they occurred from a helium-3 neutron counter embedded in a paraffin moderator [1]. The experiment produced copious neutron counts. During one cooling and heating cycle, over 2 million neutrons were counted over a 5 min time period. In subsequent cooling and heating cycles using the same titanium chips, significant neutron bursts were observed with diminishing counts after each subsequent cycle. This paper will discuss the 1991 experiments and the status of ongoing experiments. .

© 2014 ISCMNS. All rights reserved. ISSN 2227-3123

Keywords: Deuterium, Neutrons, Phase Change, Surface preparation, Thermal shock, Titanium

1. Introduction

Reports indicated that low level neutron bursts occurred in titanium [2] and palladium [3]. Both experiments, designed to look at neutron production from deuterium fusion, created a highly stressed lattice prior to the observed neutron bursts. Experiments were designed by our group to take advantage of a potentially large pressure build-up in the crystalline lattice of metals created by phase changes during a thermal shock from liquid nitrogen temperature (-190°C) to 50°C . The palladium hydride phase diagram is distinctly different from that of titanium hydride. Palladium hydride retains its face centered structure throughout the few phase changes it experiences. The changes of phase are simply a distortion of the crystalline lattice from face centered cubic to face centered tetragonal. Information on titanium is not as plentiful as with palladium but its hydride phase diagram is much more complex, with phases going from hexagonal close pack, to face centered cubic, to body centered cubic, with intermediate phases being combinations of these. Titanium, containing a high level of hydrogen, will have yet another phase transition between 77 and 300 K which can achieve greater than 60% atomic hydrogen loading at cryogenic temperatures [4]. The experiments were based on an interesting thermal

*E-mail: Eric Lukosi- elukosi@utk.edu

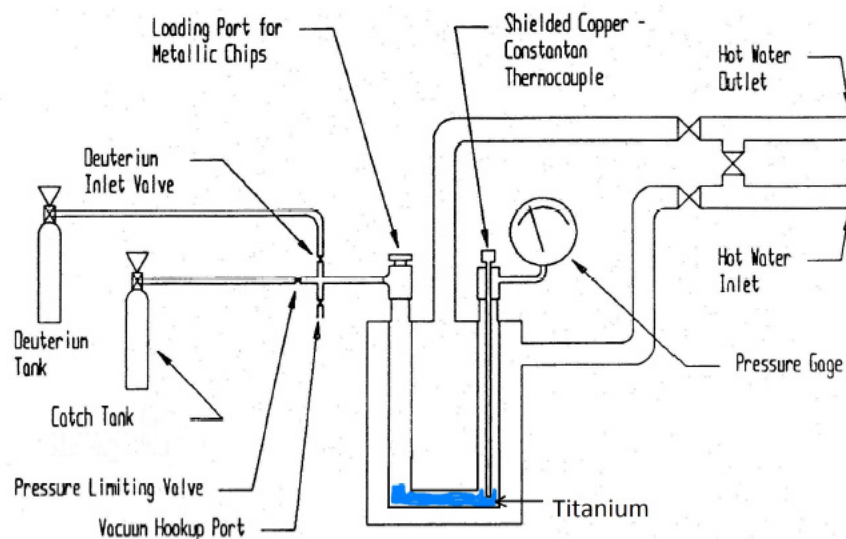


Figure 1. Sketch of the testing chamber used for the pressure shock experiment. The pressure gauge was a bourbon tube with a 1000 psi maximum and an accuracy of 3%. The catch tank was evacuated and used to capture the D_2 gas from the test chamber for analysis. The hot water inlet and outlet were used to thermally shock the samples.

shock scenario. For example, if palladium were saturated with hydrogen at liquid nitrogen temperature (-199°C), the atom ratio of H/Pd would approach 1. If the temperature were quickly raised above 25°C , the internal pressure would exceed 14 kbar. Titanium hydrides have not been as extensively studied as palladium hydrides, and low temperature charts are not available, but given the complex phase structure of titanium, the generation of high pressures under thermal shock was thought to be feasible.

2. Experiment

The initial cryogenic thermal shocking experiments used 42 g of 99.5% pure titanium sponge (from Alfa Aesar) which was broken into 1/8 inch or smaller chips by hand in a glove box under argon overpressure and then placed in a glass jar. The jar was sealed and agitated using a paint shaker for several minutes and the pieces further fragmented. A double-walled chamber was built with the inner container made of high-pressure copper tubing bent into a U-shape and an outer chamber made of 304 stainless steel. A T-joint was placed on the ends of the U-shaped copper tubing. On one side there was a loading port at the top of the T (where the titanium chips were loaded) and a gas manifold on the side. On the other part of the U a thermocouple was inserted and a pressure gauge (Fig. 1).

The test chamber was designed to be moved from a liquid nitrogen bath and placed in the center of a neutron

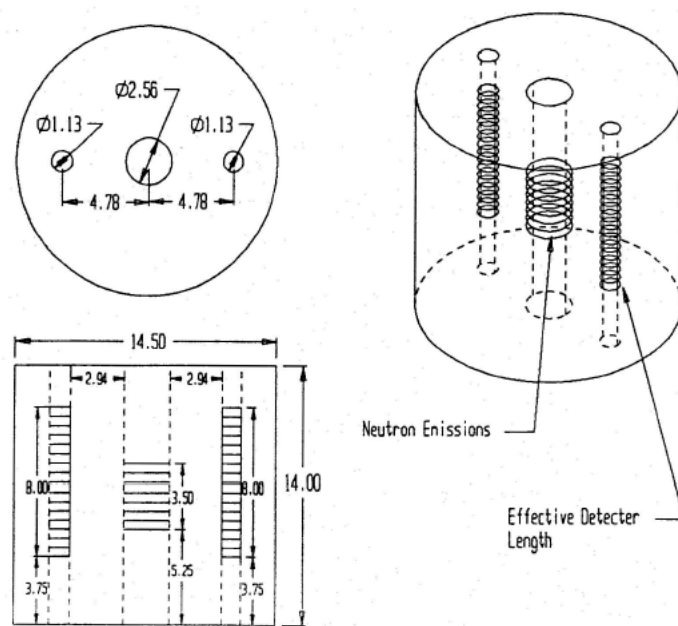


Figure 2. A solid paraffin block was fitted with two helium-3 detectors in the position labelled as “effective detector length.” The dimensions are in inches.

counting chamber, using two helium-3 detectors, built to detect low-level neutron bursts (Fig. 2).

The helium-3 detector signals were amplified, shaped and then sent to the ETC card in a Macintosh II computer and to a decade counter. The ETC was designed to achieve one microsecond resolution and a 32,000 count storage capacity [1]. It was designed to run unattended until its storage capacity was filled and then shut down. Data was then transferred to a storage file on the hard drive. Afterwards the card could be cleared and restarted. The decade counter simply accumulated counts over a set period of time. Once it reached its capacity of 1 million counts, it reinitialized and started the count cycle over. Given that all experiments had shown low level bursts, it was believed that the 32,000 count capacity of the ETC and the 1 million count capacity of the decade counter were sufficient.

3. Results

Timing of the various measurements was complicated. The computer clock was started by software when the test chamber was placed in the neutron counter. The temperature and pressure were timed and observations recorded by a student with a chronograph watch. The decade counter and ETC were located in a Faraday cage and the signals were brought into the room with BNC connectors. The student timed and recorded the decade counter data with a chronograph watch. All times were synchronized to a time zero corresponding the ETC start time.

A pressure loading with argon was run as a control where the test chamber was pressurized to 200 psi argon and

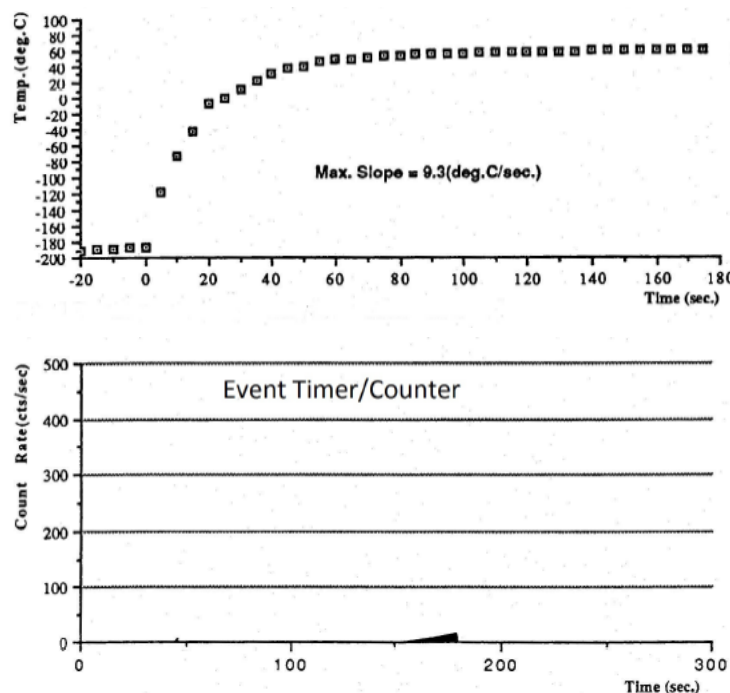


Figure 3. Thermal shocking using argon. ETC and decade counter show 45 counts in 240 s.

then cooled in the LN2 bath until pressure and temperature reached equilibrium. Then the test chamber was loaded into the neutron counting unit and hot water injected into the test chamber. The results from this test are shown in Fig. 3. The ETC data is plotted below the temperature data. The decade counter showed count rates consistent with the ETC and matched the results from prior extensive background counting runs (where the background was on the order of 0.15 counts per second).

As shown in Table 1, a procedure for loading the titanium with D₂ was developed to limit exothermic heat from the creation of titanium deuteride. The D₂ pressure was slowly increased to 200 psi (the valve was closed at 200 psi) while simultaneously running hot water (at 45°C). When the temperature stabilized, the water was drained and the test chamber was slowly lowered into an Liquid Nitrogen (LN2) bath on July 20, 1991 at 01:54. As temperature dropped, the D₂ pressure fell below 50 psi and at this point the D₂ pressure was increased to 100 psi and the valve closed. The D₂ pressure in the test chamber dropped and the temperature increased. At 310 min the decision was made to take the test chamber from the LN2 bath and place it in the neutron counter (even though pressure was still dropping and temperature increasing slowly). At 313 min, hot water was injected into the chamber causing the temperature to rise (Fig. 4). The hot water circulated for 15 min and then was shut off. The test chamber stayed in the neutron counting chamber for three days with the ETC and decade counter running. In the first cycle the neutron counts were at background level.

Since the test chamber was still showing changes in pressure and temperature when the test chamber was removed from LN2 during the first cycle, we thought that the chips had not been fully loaded. On July 23, 1991 at 18:42, the test chamber was then cooled to -186°C and the D₂ pressure was held at 50 psi for 160 min. The ETC was started and at 163 min, the test chamber was placed in the neutron detection chamber and the hot water flow started. Due to a freezing problem, the water flow was restricted and the rate of temperature change was reduced. As soon as the test chamber

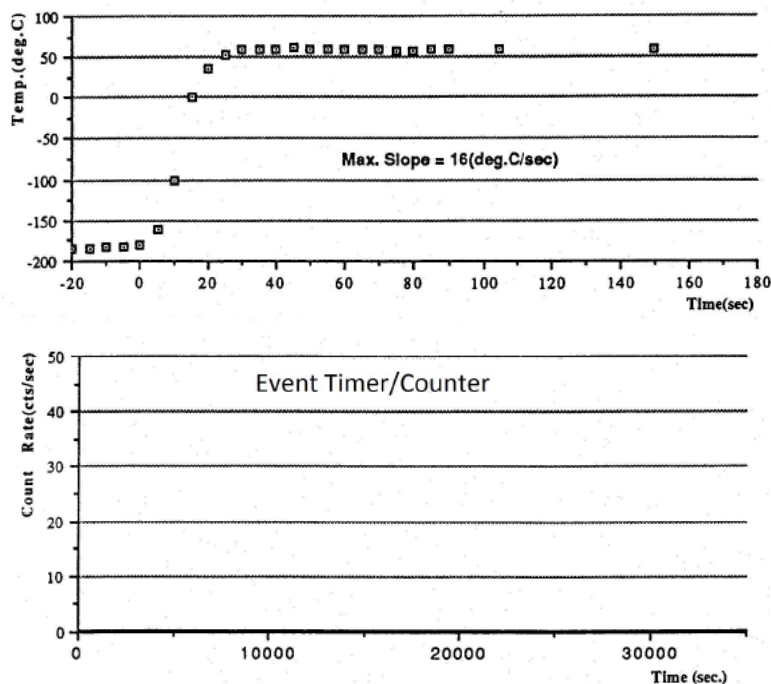


Figure 4. In the first thermal shock cycle, the ETC and decade counter were consistent showing no neutrons counts above background.

was in the neutron counting chamber, neutron counts were rapidly building up on both the ETC and the decade counter. The ETC's storage capacity was quickly saturated. The ETC had to be manually restarted about 42.8 s after saturation.

It again saturated in about 0.11 s. A computer glitch did not allow a restart after the second saturation. In the meantime the decade counter had exceeded its one million count capacity at least twice (the student recording decade counter data by hand was also the student who restarted the ETC three times likely missing other decade counter saturation events- the counts that were observed were at a consistently high count rates). After 5 min, it was decided to put the device back into the LN2 bath.

The results from the second temperature cycle had a minimum 2,486,500 neutron counts during the five-minute period. The detector efficiency was $\sim 4\%$ so this would correspond to a minimum of 62,163,000 neutrons produced. A more accurate indication of neutron counts was only possible during the two brief periods when the ETC was running and saturated. Figure 5 shows the two points in time where the ETC was saturated in about ~ 0.11 s. This data indicates 290,000 counts per second.

A third cycle was started by putting the test chamber in a LN2 bath for 35 min (cooled to -190°C). On July 23, 1991 at 19:25 the chamber was allowed to warm by natural convection. Everyone left for the night (due to fatigue) and returned 17 h later. The decade counter showed 50,883 counts and the ETC had saturated. The decade counter could have recycled itself multiple times during the event shown in Fig. 6 so the total count is at minimum 50,833, but could have orders of magnitude more. One small neutron burst occurred within 10 s of the convective warming process and a much larger burst which saturated the ETC occurred at 47,715 s into the cycle.

A fourth cycle was started on Wednesday July 24, 1991 at 17:20. The test chamber was cooled to -190°C for 190 min and the D_2 pressure held at 50 psi. The ETC was started and the test chamber put into the neutron counting

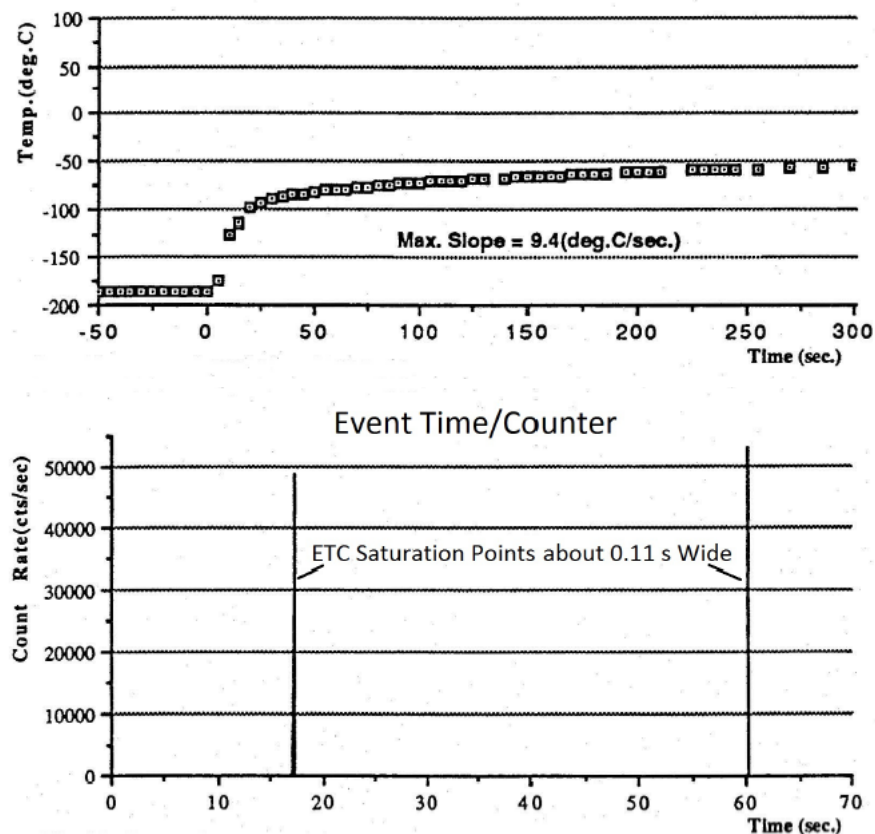


Figure 5. Second cycle neutron count rate.

chamber and at 20:25 hot water was injected. A neutron burst was seen about 10 s after the start of the heating cycle (Fig. 7).

At this point we collected the D₂ gas and titanium samples to check for tritium content. One hour and 26 min after removing the titanium, 9.6 g of the sample was placed in a Tri Carb 1600 TR Liquid Scintillation Analyzer. The minimum detectable level of tritium for this unit was $2.9 \times 10^{-6} \mu\text{Curi}$. The test sample yielded a reading of $12.8 \times 10^{-6} \mu\text{Curi}$. A control sample of the titanium yielded a reading of $11.9 \times 10^{-6} \mu\text{Curi}$. There was a difference of $0.9 \times 10^{-6} \mu\text{Curi}$.

4. Discussion and Conclusions

Cryogenically cooled metals under thermal shock yielded promising results. Three cooling and heating cycles using titanium yielded neutron counts significantly above background. The ETC was able to pinpoint when the bursts occurred and the count rate at the time of the burst. In the second cycle, a sustained burst of neutrons were observed that twice saturated the 32K storage limit of the ETC before a software failure and a decade counter at least twice exceeded its one million count capacity during the five minute period. The neutron production might have been sustained longer had we not put the test chamber back into the LN₂ bath in order to try to stop the reaction. At minimum, this event

Table 1. Data showing the procedure used to saturate the titanium with deuterium. D₂ pressure was slowly increased to 200 psi at which point the valve was closed. When D₂ pressure dropped below 50 psi, the valve was opened to increase it to 100 psi and was closed.

Time (min)	Pressure (psi)	Temperature (°C)
0	40	28.9
20	40	50.6
45	60	45.0
65	80	45.0
80	100	45.0
85	120	45.0
90	140	45.0
95	160	45.0
100	200	45.0
105	230	98.3
115	225	91.6
125	215	45
135	Drain water and slowly lower in LN2 bath	
140	200	−5.0
150	180	−72.0
155	140	−117.0
160	115	−136.0
180	45	−182.0
190	100 (add D ₂)	−190.0
280	100	−188.0
300	60	−186.0
310	55	−184.0

yielded >2,486,500 neutron counts (the student who was observing the decade counter was busy trying to restart the ETC and missed additional cycling of the decade counter). In addition the ETC was saturated twice. The saturation

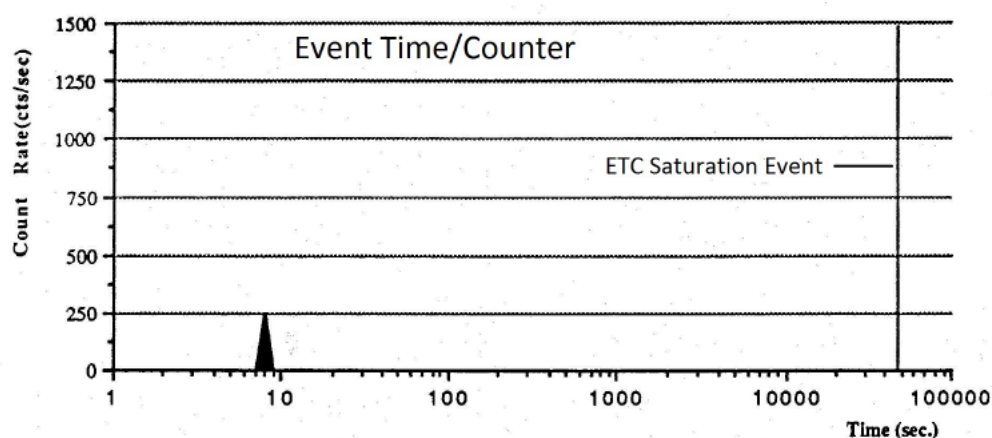


Figure 6. Event counter results from the third cycle.

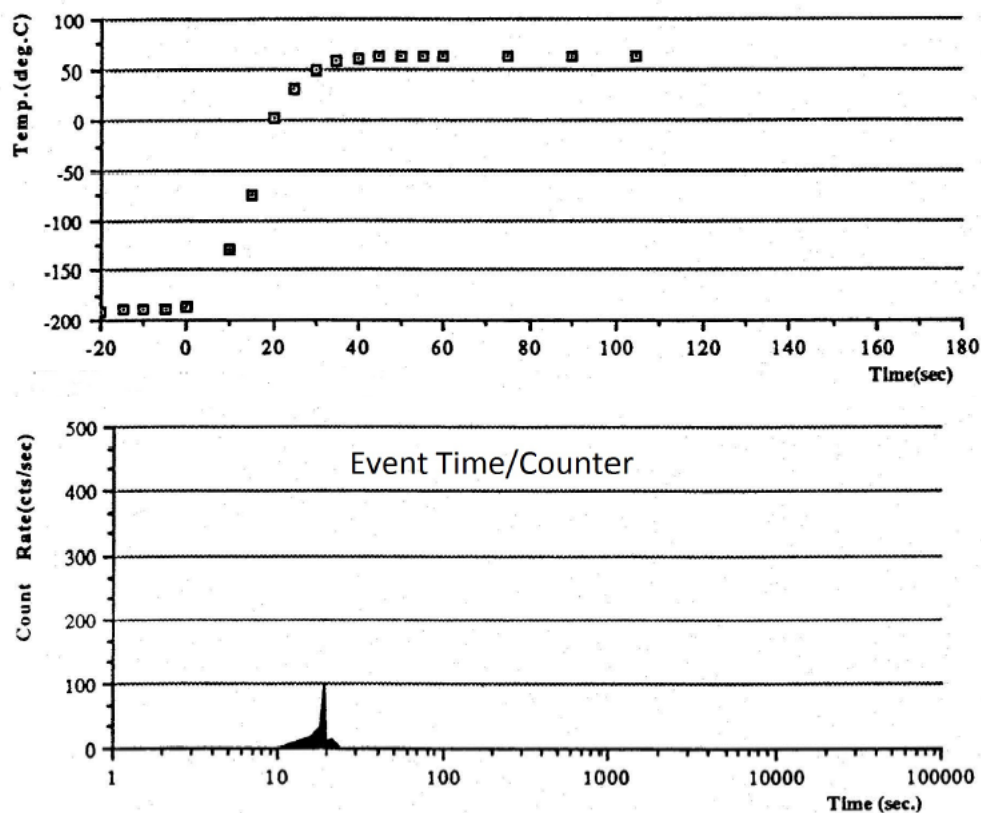


Figure 7. Fourth heating cycle.

time was 0.11 s which indicated a count rate of 290,000 counts per second. Our goal was to test other metals capable of forming hydrides (e.g., palladium). However, the experiments were discontinued due to circumstances beyond our control. In the 22 years since this work, others groups have seen neutron bursts in various metal hydrides. This particular experiment is unique in both magnitude and duration of neutron production.

As part of the Sydney Kimel Institute for the Nuclear Renaissance, a continuation of the cryogenically cooled metals under thermal shock experiments are underway. A team is developing a next generation testing system—some of which will be reported at future meetings and in future publications.

References

- [1] Scott Taylor, Event Timer/Counter (ETC) Card for the Study of Neutron Bursts, MS Thesis, Electrical Engineering, University of Missouri, Dec. 1991.
- [2] T. Izumida, H. Yamashita and H. Miyadera, A search for neutronemissions from cold fusion in a titanium–deuterium system, *Fusion Technol.* **18** (1990) 641–646.

- [3] Y. Arata and Y. Zhang, Achievement of intense cold fusion reaction, *J. Fusion Energy* **18** (1990) 95–102.
- [4] H.O. Menlove, M.M. Fowler, E. Garcia, M.C. Miller, M.A. Paciotti, R.R. Ryan and S.E. Jones, Measurements of neutron emissions from Ti and Pd in pressurized D₂ gas and D₂O electrolysis cells, *J. Fusion Energy* **20** (1990) 495–506.



Research Article

The Future May be Better than You Think

Jed Rothwell *

LENR-CANR.org, 1954 Airport Road, Suite 204, Chamblee, GA 30341, USA

Abstract

Cold fusion researchers are prone to be unduly pessimistic about the potential for cold fusion. They know too much; they are too close to the problem. They may also have unexamined assumptions. Researchers feel put-upon because of political opposition. The LENR-CANR.org web site log file proves there is a great deal of interest in this field. There is broad, untapped, latent support for it. The log shows that every week scientists and engineers download thousands of papers on cold fusion.

© 2014 ISCMNS. All rights reserved. ISSN 2227-3123

Keywords: Commercialization, LENR, Review

1. Introduction

Cold fusion is even more promising than many researchers realize. Many researchers fail to see, for example, that not only will it reduce the cost of energy; it will also reduce the cost of machines such as generators and water heaters. Researchers are also unaware that there is widespread interest in cold fusion. The prospects for revolutionary technology based on cold fusion are described in my book, *Cold Fusion and the Future* [1]. The book is a compilation of essays I wrote, many co-authored by Eugene Mallove. It is the result of conversations I had with many people especially Mallove, Arthur C. Clarke and Martin Fleischmann. I should also give credit to Edmund Storms, John O'M. Bockris, David Nagel, Adm. Sir Anthony Griffin, Tom Passel, Tadahiko Mizuno, Christopher Tinsley and others listed in the footnotes. Many of these ideas came from Arthur Clarke's masterpiece, *Profiles of the Future* [2]. In the final edition of 1999, Clarke added several pages about cold fusion [3].

2. Experts Tend to Overestimate the Difficulties

Researchers tend to be overly pessimistic about the future prospects for cold fusion *because they are experts*. They know too much about the problems. Some have not given much thought to the potential advantages. They know how difficult the research is. They know there is powerful political opposition to it. They find it hard to envision a world in which everyone agrees cold fusion is real and the opposition vanishes.

*E-mail: JedRothwell@gmail.com

Table 1. Intrinsic advantages of cold fusion.

Intrinsic Advantages of Cold Fusion
<ul style="list-style-type: none"> • Flexible, scalable, clean, safe, easy to use, with no emissions • Compact; power density is high • Energy density millions of times greater than chemical fuel • Can be located anywhere: inside a building, underwater, implanted in body, in outer space • Available nonstop, unlike solar or wind Fuel is inexhaustible • Fuel costs virtually nothing
Nickel-hydride cells have additional advantages
<ul style="list-style-type: none"> • Ni catalyst is cheap and available in unlimited amounts • Materials, manufacturing, distribution, maintenance, disposal all appear to be inexpensive and safe • Rossi cells made with simple copper pipes; precision manufacturing or clean rooms apparently not needed

Researchers are discouraged mainly because the effect is so hard to replicate and it seems to defy explanation. They have made great efforts, yet progress has been slow. In the book I envision a world with millions of ultra-reliable cold fusion devices, everything from pacemaker batteries to blast furnaces. I predict that not only will this drastically reduce the cost of energy; it will spur the development of countless revolutionary machines such as food factories; small autonomous robots that go around killing invasive insects; supersonic VTOL aircraft; desalination mega-projects that convert deserts into farmland, and many other marvels. I also predict it may give rise to some nightmare inventions that I hope can be prevented.

I ignore the technical difficulties. It is understandable that researchers who struggle to make an experiment work at milliwatt levels feel I am overdoing it. They think I am promising too much. I realize this is a leap comparable to the difference between the Curie's warm radium in 1898 and the first commercial fission reactor in 1956. I make this leap because I believe that any phenomenon that can be detected in the laboratory can, in principle, be understood, controlled and scaled up. Naturally, this will take more funding than we now have. It will take hard work and a measure of good luck. But it can be done.

My predictions are predicated on the many intrinsic advantages of cold fusion, shown in Table 1. There are so many advantages we lose track of them. We forget how promising this is. It is no wonder some skeptics feel cold fusion is too good to be true. It appears to be flexible, scalable, clean, safe, easy to use, with no emissions. It is millions of times more energy dense than chemical fuel. It is available nonstop, unlike solar or wind. The fuel is available in unlimited amounts; enough to vaporize the whole planet Earth. The nickel hydride version is even better: materials, manufacturing, distribution, maintenance and disposal appear to be inexpensive and safe. Cold fusion has many of these wonderful attributes already, even at this primitive stage of development. If researchers can learn to control the reaction, it will become the ideal source of energy.

These advantages are so obvious that if they become generally known, corporations will make frantic efforts to understand and control the reaction. They will launch crash projects. Nothing motivates people more than the prospect of making billions of dollars.

Researchers today are used to working on a shoestring. They should understand that if it becomes generally known this phenomenon is real, this field could soon be funded at the levels now spent on semiconductor R&D: *\$48 billion per year* [4]. That comes to \$132 million a day, which is more money than all of the funding for cold fusion in the last 23 years. Thousands of people in corporations, national laboratories and universities will be frantically working on this. A conference on cold fusion may resemble a major electronics trade show, such as the International CES, with thousands of exhibits and 150,000 attendees [5]. Many of the researchers who enter the field in a hurry will contribute little. But some will be smart, and some will be lucky. Progress will be far swifter than it has been up until now.

A Niagara Falls of money does not ensure progress, but it does ensure that if progress can be made, it will be made.

3. Researchers Overestimate the Timescale

Let us consider a major difference of opinion, where some researchers think I am wildly optimistic. How long will it be before most cars use cold fusion? Andrea Rossi predicts 60 years. James Dunn estimates 40 years. I predict only 20 years, as shown in the time-line in Fig. 1.

This time-line begins on the day researchers learn to control the reaction. It is impossible to know when that day will come. We cannot be sure it will come, but assuming it does, the events that follow are easier to predict. Starting that day, it will take roughly 10 years to develop and begin manufacturing cold fusion cars. This is how long it took Toyota to develop the Prius. No doubt a cold fusion car is more difficult to design than a hybrid. On the other hand there will be more pressure on Toyota and the other manufacturers to work quickly. They will know this is a fight for survival. No company can afford to be three years late going into this market.

The first cold fusion vehicles will be far more expensive than conventional ones. Hopefully, in a few years competition will drive down the cost. The premium for hybrids fell rapidly after Honda, Toyota and others began competing.

I predict that a few years after sales begin most people will select the cold fusion model. Gasoline car sales will languish. In the time-line I show this happening only three years after the introduction of cold fusion cars. Dunn predicts it will happen much later, perhaps 15 years after sales begin. This is why he thinks the overall transition will take 40 years.

I think cold fusion sales will soon overtake gasoline for several reasons:

- Even at this early stage the premium for cold fusion cars will be small thanks to competition. They may soon become cheaper than gasoline cars, mainly because with cold fusion efficiency does not matter. You can trade off efficiency for a lower cost, for example by using cheap, heavier steel instead of light, expensive alloys. The cars will be inherently inexpensive to manufacture.
- Cold fusion cars will have enormous consumer appeal, mainly because the fuel cost is zero, but also because

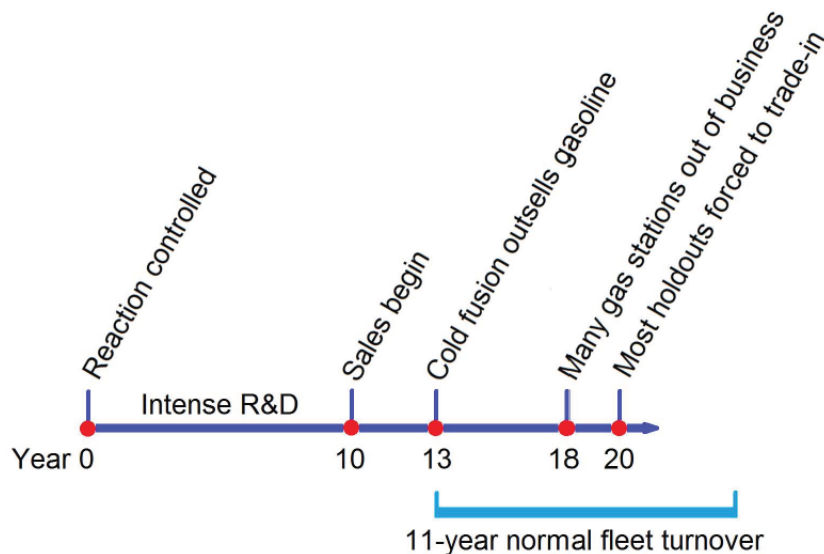


Figure 1. Time-line showing my estimate of how long it will take before most cars use cold fusion.

they will be simpler, more reliable, easier to maintain, and nonpolluting. They will be safer in accidents because they will not have flammable gasoline.

- Cold fusion heaters and generators are likely to be introduced during the 10-year period cars are being rushed to development. People will be used to the idea of cold fusion. They will see that it works, and that it is safe. This will generate pent-up demand for cold fusion cars. Especially among people who use a lot of gas, such as taxi drivers and people who use large pickup trucks to haul heavy loads every day. These people will be the first to buy cold fusion vehicles, so gasoline consumption will fall even faster than gasoline car sales.
- Dunn points to the small market share of Prius as evidence that cold fusion cars may have limited appeal. The Prius is only one model (a mid-sized hatchback) whereas I expect that manufacturers will quickly introduce a full range of cold fusion vehicles, from small cars to SUVs and trucks.

I expect that trying to sell gasoline cars in this market, at this stage, would be like trying to sell typewriters in 1985, after people realized how much better personal computers are. Assuming I am right, the pace of change will pick up a few years after cold fusion begins to outsell gasoline. It will increase with positive feedback, because

- (1) As shown in the time-line, normal fleet turnover is 11 years. With or without cold fusion, after 11 years most cars wear out.
- (2) During the 1970s oil shock, many gas stations went out of business. Their profit margins are thin. A 10–15% sales drop will knock many of them out of business.

Assume that people replace cars at the normal rate, without spending extra money. Five years after the tide turns, 20–30% of gasoline cars will be gone. Gasoline consumption will fall even more because, as noted above, cars that consume a lot of gasoline will be first to go. Gas stations will have lost roughly half their revenue. They will be going out of business in droves. In a dying industry, the number of retail outlets tends to fall even faster than sales do. Owners see the writing on the wall and they get out quickly.

At this stage, a person living in a city will have to drive miles to find a gas station every time he wants to fill up. A person driving on the Interstate in the middle of nowhere may find there are no gas stations left in business. He will run out of gas. When you take your gasoline car in for service, a young mechanic will say: “Gee, I have never worked on one of those. I wonder if we still have parts?” Maintaining obsolete technology is a nuisance. A reader who doubts this should try getting a film camera repaired. The hold-outs still driving gasoline cars will soon be forced to trade them in. People who normally hang on to cars for 11 years will be forced to trade-in a few years ahead of schedule.

This is not to suggest that every single gasoline car on the road will be gone after only 20 years. They will be rare, the way horses on the roads were in the 1930s.

My conclusion: A changeover forced by obsolete technology tends to accelerate in the last stages.

This is one of the general rules described in the book. It will apply not only to automobiles but to other machines enhanced by cold fusion. That includes nearly every machine.

4. Unexamined Assumptions

People say we cannot afford to replace all of the vehicles on the road, or all of the water heaters in our houses. They forget that we replace all this equipment anyway, because it wears out. These are unexamined assumptions. Kleehaus and Eisner recently described the cost of new cold fusion water heaters as an investment that a family might make to save money, with a certain rate of return (ROI) [6]. They forget that people must buy water heaters because they need hot water, and water heaters must be replaced every 15–20 years as they wear out. Cold fusion heaters will indeed save money but that is not why people will buy them. People will not spend any more on hot water heaters with cold fusion than they did previously with gas or electric heaters. In that sense there is no “investment” and no extra outlay of money, or burden on the consumer.

Here are some other unexamined assumptions I have heard from cold fusion researchers recently:

We will still need oil to run the equipment needed to mine palladium or nickel. People often say this, for some reason. It is not true. Mining equipment will also run on cold fusion.

We will still need oil for plastic feedstock. I doubt this. I predict it will be cheaper, faster and safer to synthesize hydrocarbons on site with cold fusion energy.

If it takes 10 min for a reactor to reach operating temperature, you cannot use it in a car because no one wants to wait that long before driving. This will not be a problem. The car will be a series electric hybrid, similar to the GM Volt. It will have a battery large enough to drive the car at least 10 min at top speed on battery power alone. After the car is parked, the cold fusion primary engine may continue to run for a while until the battery is fully charged again.

Cold fusion may not scale up. It has already been scaled up to commercially useful levels. That is, to 100 W by Fleischmann and Pons, and reportedly much more by Rossi and Defkalion.

The last and most interesting assumption is that *cold fusion will only reduce the cost of electricity, transportation, or space heating by the cost of fuel.* That is to say: if you spend \$100 a month heating your house with natural gas, you will save \$100 but the gas heater itself will not be cheaper. That is wrong. When the core technology in a machine improves dramatically, it often forces the rest of the machine to improve. That is why cold fusion will have a gigantic impact.

By “core technology” I mean the device that makes it possible to build the machine in the first place; the heart of the machine. In an automobile that is the internal combustion engine. In a mainframe computer it is the CPU. In a desktop computer it is the microprocessor. When the microprocessor drastically reduced the cost of computation, this in turn pushed down the price of everything else in the computer system. It created a mass market for peripherals such as screens, printers and especially hard disks. Then it went on to lower the cost of cell phones, photography and countless other things.

Cold fusion will lower the cost of electricity not only by eliminating the cost of fuel, but also by radically transforming the generator technology. It may spur the development of cheap, reliable thermoelectric devices. Or, if that proves to be a dead-end, some other type of cheap, simple generator will be discovered. When you spend \$ 132 million a day, things get discovered.

Cold fusion will simplify the design of water heaters, and make them safer. It will lower the total cost of ownership: hardware, installation and maintenance. You dispense with the high voltage electric circuit or the gas pipeline and chimney. You do not need hot water pipes because these will probably be tankless heaters, like the ones common in Japan. You put one in the kitchen and another in the bathroom. They are mounted on the wall or under the sink. They last for decades. Installation is simple compared to a conventional U.S. water heater. Tankless heaters are not popular in the U.S. because of technical problems such as our use of 120 V AC. Cold fusion will make these problems go away.

Cold fusion will begin by expanding the market for conventional energy uses such as hot water, space heating, cooking and process heat. Then designers will realize they can do many new things with it. The Brave New World I described will be upon us. The deserts will bloom. I hope it will be more utopia than dystopia, but you never know. People can turn any blessing into a curse.

5. The Opposition to Cold Fusion, and Latent Support for it

Political opposition is another reason researchers feel discouraged. There is tremendous opposition. It is one part academic politics and two parts human nature. Martin Fleischmann said, “People do not want progress. It makes them uncomfortable. They do not want it, and they should not have it” [7].

Political opposition is another reason researchers feel discouraged. There is tremendous opposition. It is one part academic politics and two parts human nature. Martin Fleischmann said, “People do not want progress. It makes them uncomfortable. They do not want it, and they should not have it” [7]. On the other side of the debate, Francis Slakey,

Table 2. Visits to LENR-CANR.ORG in 2006.

A look at visits to LENR-CANR.org in 2006

In the first 9 months of 2006 visitors came from over 12,000 ISPs in 42 countries. Examples:

- 4,000 visits from 3,700 colleges and university departments (.edu)
- 660 from about 150 U.S. military (.mil) sites at the Army Research Lab, the NRL, and so on.
- 241 visits from 89 National Lab divisions, mainly at LANL, ANL, SGONE, PNL, ORNL
- Government institutions in China, Canada, and the U.S.; several U.S. State Environmental Protection Agencies
- Defense Ministries of Australia, France, Canada, most other major nations; defense research establishments worldwide
- Hundreds of corporations, investment firms and banks

the Science Policy Administrator of the American Physical Society (APS), wrote in the New Scientist that cold fusion researchers are: “a cult of fervent half-wits.” He went on to say: “While every result and conclusion they publish meets with overwhelming scientific evidence to the contrary, they resolutely pursue their illusion of fusing hydrogen in a mason jar. . .” [8]. I have encountered many people like Slakey. It is my impression they mean what they say. They are sincere.

This is a horrible situation. It is no wonder researchers doubt that funding will soon arrive, and utopia is just around the corner. However, there is reason to hope. Behind the scenes, things are better than they seem. I can tell because I am the web master at LENRCANR. org.

When you access a web site, everything you do is recorded in the log file of the site you are visiting [9]. The log record does not list you as an individual, but it does show what Internet Service Provider (ISP) you come from. When you access from home using a major ISP, the person at the remote web site knows only that you came from a commercial ISP in a certain city (such as AT&T in Atlanta). When you access from an institution such as a university or bank, the log record often indicates which institution you came from. It also shows the date and time, the name of the screens you looked at, documents you downloaded and so on.

If the network technicians at an investment bank wish to, they can set up their computers to browse incognito. But at most universities, corporations, and other institutions they make no effort to cover their tracks. So, as web master, I can tell where our professional audience comes from, and what papers they are interested in.

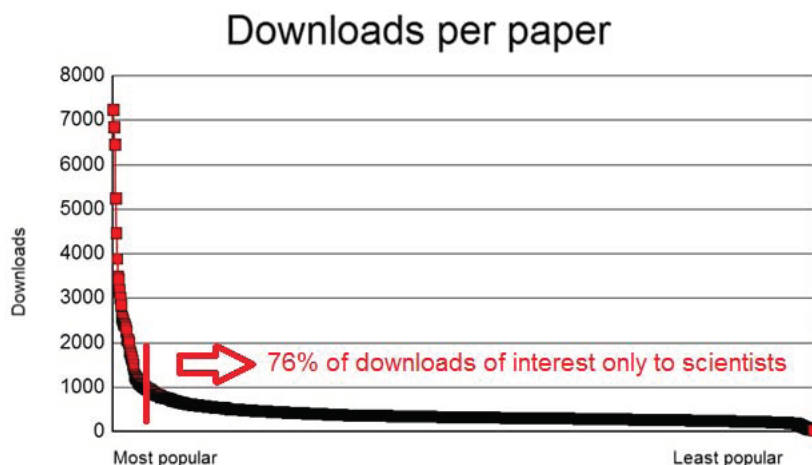
**Figure 2.** Downloads per paper from June 2011 through May 2012.

Table 2 shows a study of visitors for the first 9 months of 2006. Visitors came from more than 12,000 ISPs in 42 countries. They included people from many universities, military sites, national laboratories, and hundreds of corporations, investment firms and banks. This trend has continued.

Institutional visitors make about 10% of visits, but they download half to two-thirds of the papers; more in winter when universities are in session. I can estimate how many papers are downloaded by professionals and how many by the general public, using various methods. In Fig. 2 I did this by looking at the distribution of downloads over 1 year, from June 2011 to May 2012. During this period, 892 different papers were downloaded 401,196 times. The most popular paper was downloaded 7224 times. Item number 40 was downloaded 1007 times. Items 41 through 892 were less popular, and were downloaded fewer than 1000 times each, in a “long-tail” distribution. The less popular papers were downloaded 303,907 times, which is 76% of total downloads. Most of them are highly technical. Most people reading them come from professional organizations.

In 2012 so far, readers have been downloading 9700 papers per week on average. Since we began in 2002, readers have downloaded 2.4 million papers. Scientists and engineers worldwide know more about cold fusion than they let on. There is a great deal of interest in this research. There is goodwill, and latent support.

LENR-CANR.org lets researchers bypass the mass media, and the scientific journals. APS officials publish outlandish accusations in the New Scientist. Wikipedia is filled with misinformation about cold fusion. The public sees only misinformation, and knows nothing else. But week after week, scientists worldwide continue to download thousands of original source papers about cold fusion. LENR-CANR.org gives researchers direct, unfiltered access to their colleagues.

LENR-CANR.org is a library, not a journal. We do not review, judge or reject papers. We do not take sides in disputes. We publish no editorials, and no blogs.

If Rossi, Defkalion, Celani or someone else does a convincing demonstration of a commercial-scale device, they should provide us third-party data verifying this. During the August 2012 NI Week conference and the ICCF17 conference following it, Celani demonstrated a nickel hydride reactor that apparently produced between 14 and 21 W of heat for four days. Celani announced that he plans to try to run this reactor in self-sustaining mode soon. Ideally, he should provide LENR-CANR.org with data from a self-sustaining reaction. This could make a large impact on public opinion. Within months after we upload this data, hundreds of thousands of professional scientists and investors will read it. These people are friends of cold fusion. Cold fusion researchers will be believed. They will be funded, and this research will finally triumph.

References

- [1] J. Rothwell, Cold Fusion And The Future. 2004: LENRCANR. org. Three editions are available, in English, Japanese and Brazilian Portuguese.
- [2] A.C. Clarke, *Profiles of the Future*, Harper & Row, 1963.
- [3] A.C. Clarke, *Profiles of the Future*, Millennium Edition, Indigo, 1999.
- [4] IC Insights, The McClean Report 2012, <http://www.icinsights.com>. Data for 2011.
- [5] International CES electronics trade show, <http://www.cesweb.org/>
- [6] A. Kleeaus and C. Eisner, Potential economic impact of LENR technology in energy markets, in *17th International Conference on Cold Fusion*, Daejeon, South Korea, 2012.
- [7] Fleischmann said this in a conversation with me in October 1997.
- [8] F. Slakey, When the lights of reason go out – Francis Slakey ponders the faces of fantasy and New Age scientists, *New Scientist* 1993, **139**(1890) 49.
- [9] Apache HTTP Server Project, Log Files, <http://httpd.apache.org/docs/current/logs.html>



Research Article

Hydrogen Isotope Absorption and Heat Release Characteristics of a Ni-based Sample

H. Sakoh, Y. Miyoshi, A. Taniike, Y. Furuyama and A. Kitamura^{*,†}

Graduate School of Maritime Sciences, Kobe University, Higashinada-ku, Kobe 6580022, Japan

A. Takahashi[‡], R. Seto and Y. Fujita

Technova Inc., Chiyoda-ku, Tokyo 1000011, Japan

T. Murota and T. Tahara

Santoku Corp., Higashinada-ku, Kobe 6580013, Japan

Abstract

Recently, several researchers have claimed excess heat from Ni-based alloy nano-compound samples during gas-phase protium absorption. nickel is used instead of expensive Pd-based nano-compounds. We have performed hydrogen isotope absorption runs using the Cu–Ni–ZrO₂ and Ni–ZrO₂ nano-powders. We observed long-lasting temperature changes corresponding to astonishingly large output energy of several hundred eV/atom-Ni.

© 2014 ISCMNS. All rights reserved. ISSN 2227-3123

Keywords: Catalyst, Cu–Ni alloy nano-powder, Protium absorption

1. Introduction

Rossi and Focardi reported large heat generation on the order of kilowatts from a Ni-based alloy powder sample absorbing protium (H)–gas at elevated temperatures above 573 K [1]. Brian Ahern (private communication) infers that their sample would be a mixture of nickel and copper.

In contrast to these dramatic reports, our Ni–ZrO₂ samples did not show any appreciable absorption of hydrogen isotopes or heat release at room temperature [2,3]. Pd₁Ni₇ nano-particles dispersed in a ZrO₂ substrate, supplied by B. Ahern, showed a dramatic change in the amount of absorbed hydrogen to very large values [4–6] at room temperature.

^{*}E-mail: kitamuraakira3@gmail.com

[†]Also at: Technova Inc., Chiyoda-ku, Tokyo 1000011, Japan.

[‡]Also at: Osaka University, Suita 5650871, Japan.

Table 1. Characteristics of the NZ and CNZ samples.

	CNZ			NZ	
	Cu	Ni	Zr	Ni	Zr
Specific surface area (m ² /g)	25.3			20.6	
Composition (%)	7.9	36.0	56.1	35.8	64.2
Average grain size (nm)	6.8	24.5	–	23.2	–

This result gives a strong indication that significant improvement of absorption characteristics would be expected by adding a small amount of foreign atoms to the Ni–Zr sample.

In the present work, we used compounds of Ni–Zr mixed oxide (NZ) and Cu–Ni–Zr mixed oxide (CNZ) nanopowders fabricated by Santoku Corporation as samples for hydrogen isotope absorption experiments.

2. Experimental Apparatus and Procedure

The physical properties of the NZ and CNZ samples are shown in Table 1. Figure 1 shows a schematic of one part of the twin system. We have used a twin absorption system consisting of two equivalent chambers for hydrogen isotope gas absorption/adsorption experiments. The nickel samples are put in the reaction chambers, which are evacuated through filters to eliminate particles of sizes greater than about 5 μm . They are baked, to outgas them. The outer chambers are evacuated in order to thermally insulate the inner chamber during hydrogen isotope absorption/adsorption. Sheath heaters with resistance of 37.9 and 53.8 Ω are wound around the reaction chambers in the A₁ and A₂ systems, respectively. These are used to bake the sample before the run, and to heat it during runs at elevated temperatures.

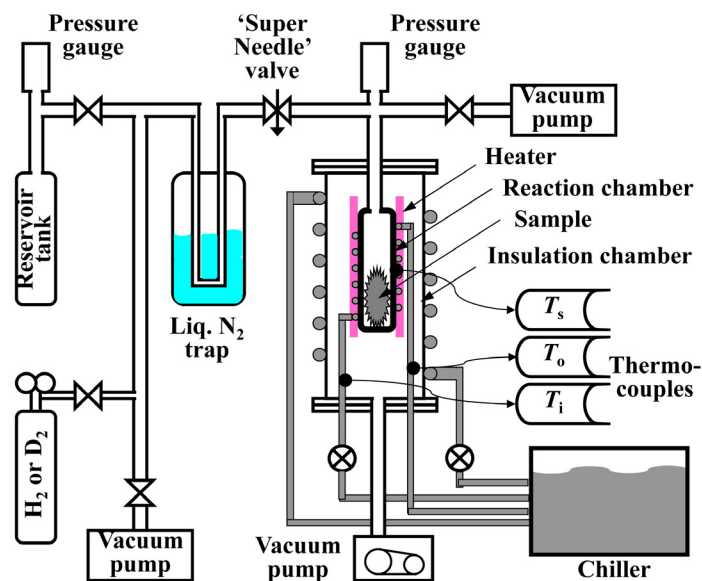


Figure 1. Functional view of the system A₁–A₂. Water cooling of the reaction chamber with a flow rate of 6 ml/min was done only in the #1 run at room temperature. The cooling water pipe was empty in the #5 runs at elevated temperatures.

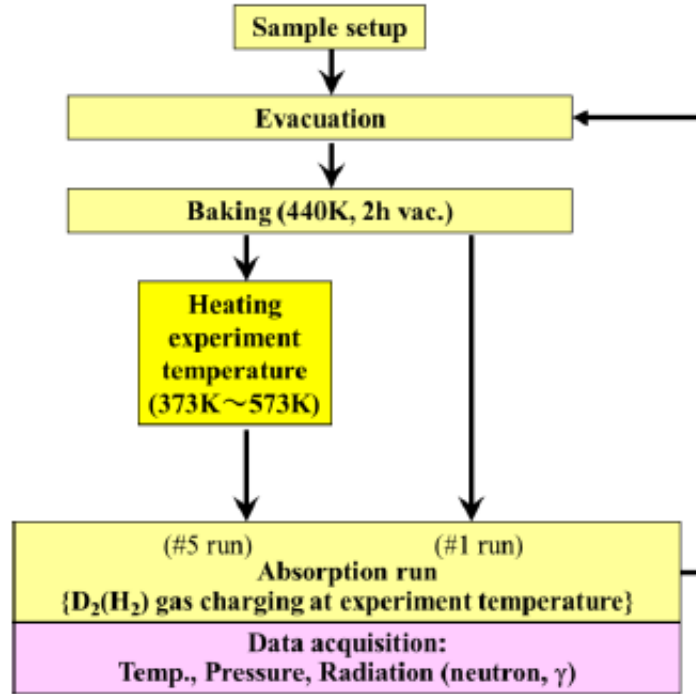


Figure 2. Flow-chart of the experimental procedure.

Alumel-chromel thermo-couples are used to measure temperatures. To reduce the influence of environmental temperature changes as small as possible, only the outer vacuum vessel was cooled with water at constant temperature

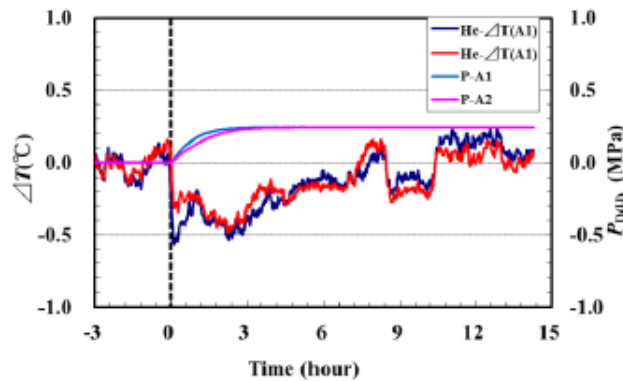


Figure 3. Variation of temperature and pressure in the blank runs with ^4He gas, at an input power of 70 W by the heater.

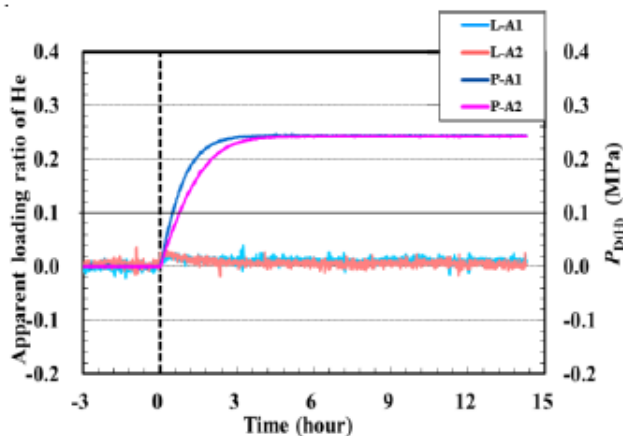


Figure 4. Pressure and apparent loading ratio in the blank run with ^4He gas at an input power of 70 W from the heater.

(regulated within 0.1°C variation), and the experimental room was air-conditioned to keep temperature change within 0.1°C variation.

Figure 2 shows the experimental procedure. The reservoir tank is filled with D_2 (H_2) gas at a pressure of 0.3 MPa, typically, before an absorption run starts. The reaction chamber and the outer chamber are evacuated, and the coolant water is run. The reaction chamber is then heated to a prescribed temperature. When the chambers attain the constant temperature, the D_2 (or H_2) gas is run with a flow rate adjusted and regulated with a “Super Needle” valve.

Blank runs for isothermal calorimetry were performed, with ohmic heating and ^4He gas charging instead of $\text{H}(\text{D})$ -gas. This data was used to correct the time-evolution data for the temperature and the pressure in the reaction chamber. Time variation of input power was recorded and used to correct the calorimetry. Any fluctuation of the temperature of

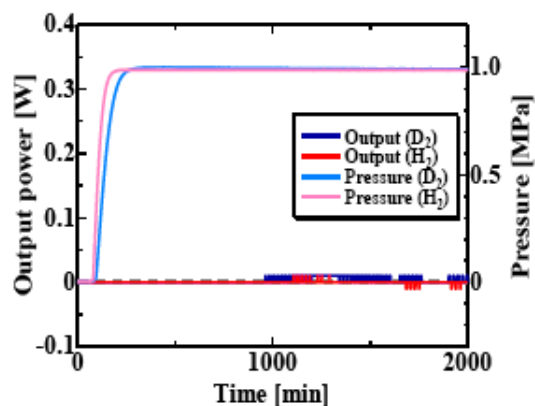
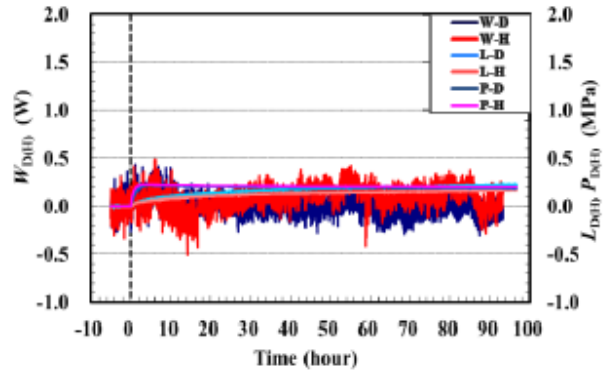
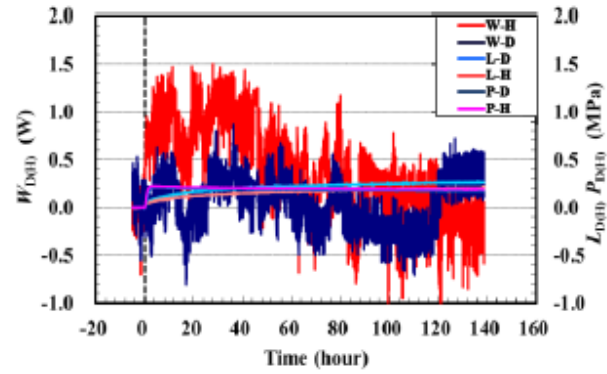


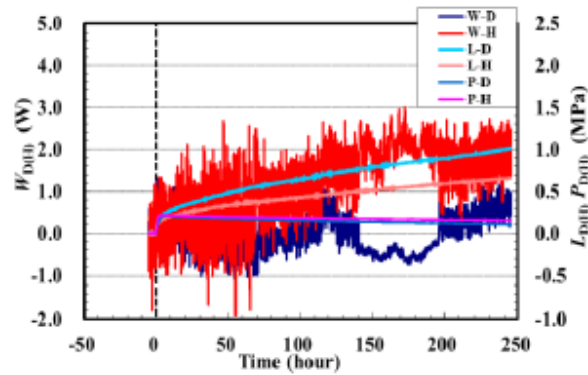
Figure 5. Results of D_2/H_2 absorption runs for Ni–Zr oxide compounds; the run numbers are D–NZ1#1 and H–NZ2#1.



(a)



(b)



(c)

Figure 6. Variation of the thermal output power $W_{D(H)}(t)$, the pressure $P_{D(H)}(t)$ and the time-dependent loading ratio $L_{D(H)}(t)$ in the runs (a) H(D)-NZ3(4)#5_473 K, (b) H(D)-NZ3(4)#5_523 K and (c) H(D)-NZ3(4)_573 K.

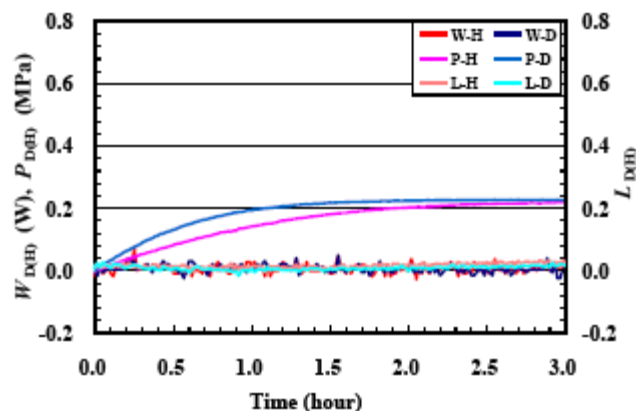


Figure 7. Evolution of the thermal power $W_{D(H)}$, pressure $P_{D(H)}$ in the reaction chamber after introduction of D_2 (or H_2) gas and the time-dependent loading ratio $L_{D(H)}$ in runs D–CNZ1#1 and H–CNZ2#1.

the reaction chamber not coincident with an intentional change in the heater input power is regarded as a maximum error, and was evaluated to be ± 0.5 W at 573 K. An example of such fluctuations is seen in Fig. 3.

The instantaneous amount of absorbed hydrogen atoms in each reaction chamber can be calculated by measuring the pressures of both the reaction chamber and the reservoir tank. Since the gas is supplied through the valves and pipes at room temperature, there is an apparent emission (or negative loading) of the gas from somewhere in the reaction chamber due to expansion by heating. The apparent helium loading ratio, which should be negligible, is minimized by suitably approximating the temperature distribution in the “reaction chamber” consisting of the bottle itself and the pipes downstream of the Super Needle.

An example of the apparent loading ratio $L_{D(H)}(t)$ in the blank run using ^4He at a heating power of 70 W is shown in Fig. 4. We use the marginal apparent loading ratio of helium to estimate the systematic error, to correct the loading ratios in the hydrogen absorption runs.

The temperature measurement is also affected by the introduction of cool gas. Therefore, blank runs in which ^4He gas was introduced into the reaction chamber under the same experimental conditions as in the cases of the hydrogen runs were necessary. Figure 3 is an example of a blank run using ^4He operated at 70 W. The fall of temperature, with the difference in the heat capacity of ^4He (20.8 J/mol K) and $D(H)_2$ (28.8 J/mol K) taken into account, is used for correction in the data processing to obtain the thermal output power $W_{D(H)}(t)$.

The relation between the evolving thermal power and the temperature was obtained beforehand. The temperature of the reaction chamber was measured for the heater input powers of 0, 15, 27, 43.5, 70, and 105 W. The results are shown in Table 2. Linear interpolation using the derivatives, $\Delta T/\Delta W$ values, is applied for an arbitrary value of the temperature other than the temperatures measured in the calibration. We estimated there is a ± 0.2 W systematic error in the calorimetry.

There is a delay in the response of the temperature. The transition curve is well approximated by a two-component exponential function with a time constant of 16 min and 45 min, each corresponding to thermal energy losses due to radiation and conduction.

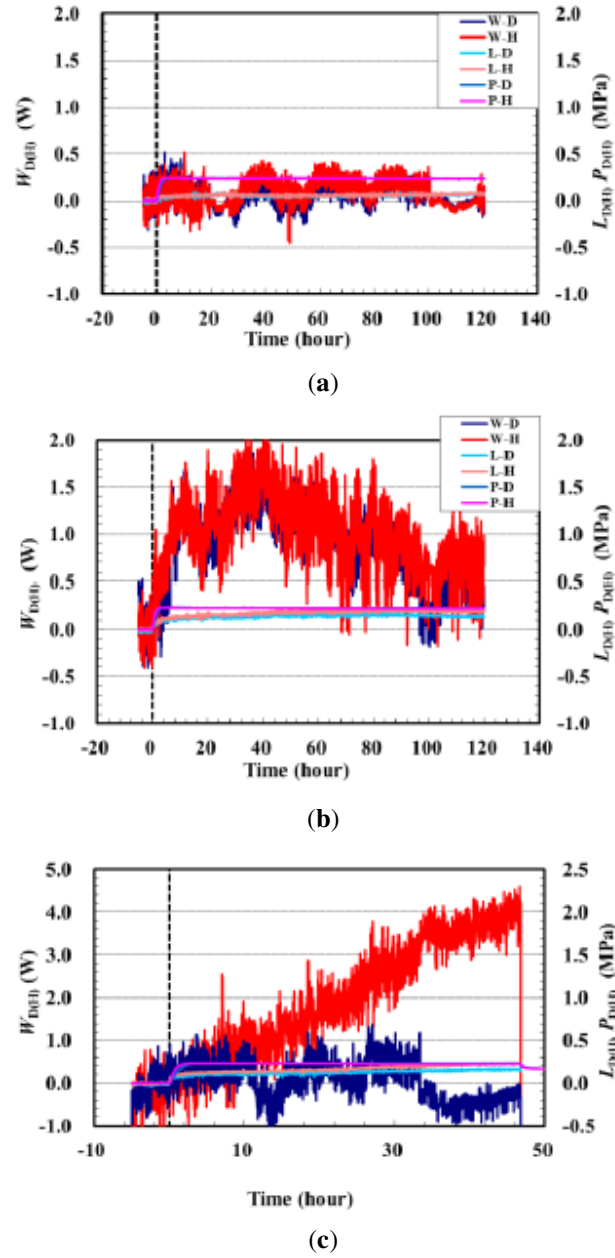


Figure 8. Variation of the thermal output power $W_{D(H)}(t)$, the pressure $P_{D(H)}(t)$ and the time-dependent loading ratio $L_{D(H)}(t)$ in the runs (a) H(D)-CNZ3(4)#5_473 K, (b) H(D)-CNZ3(4)#5_523 K, and (c) H(D)-CNZ3(4)#5_573 K_2.

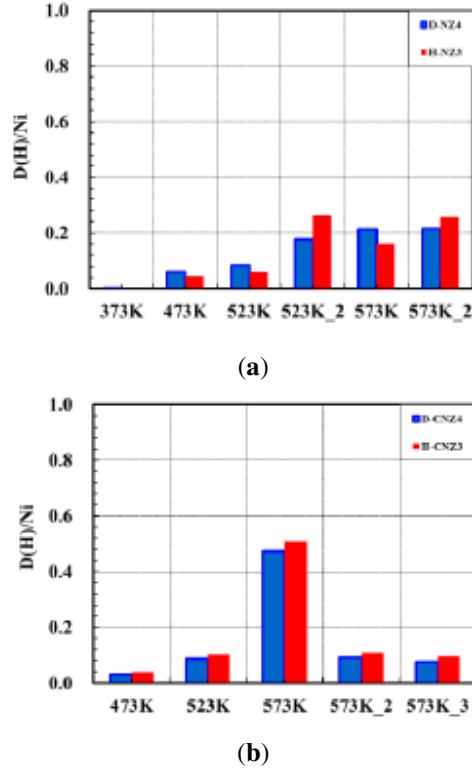


Figure 9. H(D)/Pd data for the t-phase of sample H(D)–NZ, upper figure (a) and H(D)–CNZ, lower figure (b).

3. Experimental Results

Figure 5 shows typical variation of the heat output, $W_D(t)$ and $W_H(t)$, pressure in the reaction chamber, $P_D(t)$ and $P_H(t)$, in the hydrogen isotope absorption run at 293 K for as-received samples, D-NZ1 and H-NZ2, respectively. We observed negligible absorption of hydrogen isotopes accompanied by exothermic temperature change, confirming that nickel does not absorb hydrogen at room temperature [7].

Activation of the H(D)-gas absorption reaction is expected at higher temperatures. Therefore, the experiments were

Table 2. Relation between the temperature of the reaction chamber and the heater input power for each subsystem, A_1 and A_2 . The differential value $\Delta T/\Delta W$ is the slope of the line connecting the neighboring points.

Input power (W)	T (K)		$\Delta T/\Delta W$ (K/W)	
	A_1	A_2	A_1	A_2
0	294.2	294.2	–	–
15	393.3	388.2	6.61	6.27
27	435.9	429.3	3.55	3.43
43.5	480.7	472.1	2.72	2.59
70	524.5	523.2	1.65	1.93
105	564.4	565.5	0.99	0.99

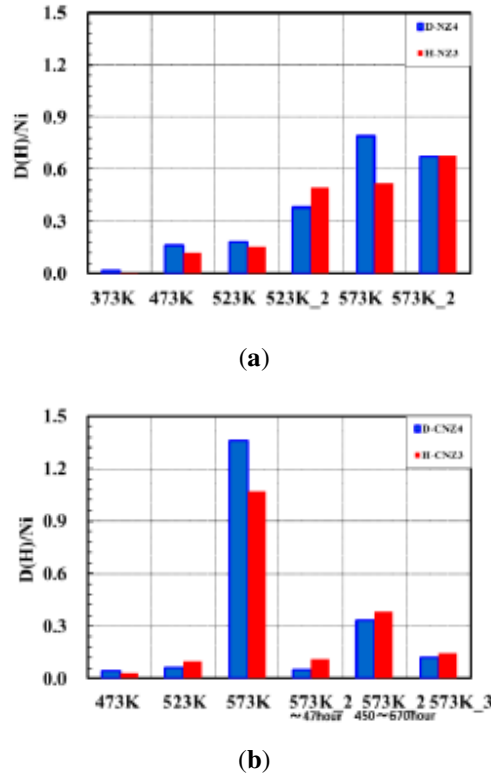


Figure 10. H(D)/Pd data for the s-phase of sample H(D)–NZ, upper figure (a) and H(D)–CNZ, lower figure (b).

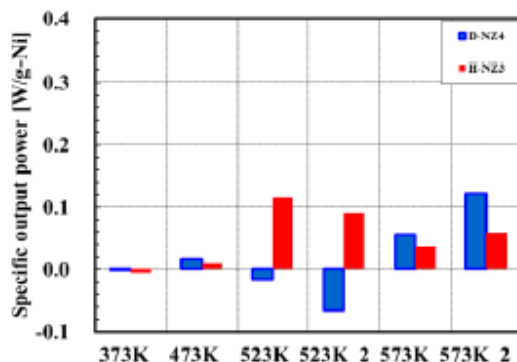
also conducted at elevated temperatures up to 573 K with use of the heater input power of up to 105 W. Figures 6(a)–(c) show typical variation of the heat output, $W_D(t)$ and $W_H(t)$, pressure in the reaction chamber, $P_D(t)$ and $P_H(t)$, and the loading ratio, $L_D(t)$ and $L_H(t)$, in the hydrogen isotope absorption runs, H(D)–NZ1(2)#5_373 K through H(D)–NZ1(2)_573 K, respectively.

At 473 K, we did not observe an appreciable exothermic reaction. In the protium absorption run at 534 K an exothermic reaction with the maximum output power exceeding 1.0 W was registered. Although it is only a small change compared with the input heater power of 70 W, it continued for about 40 h.

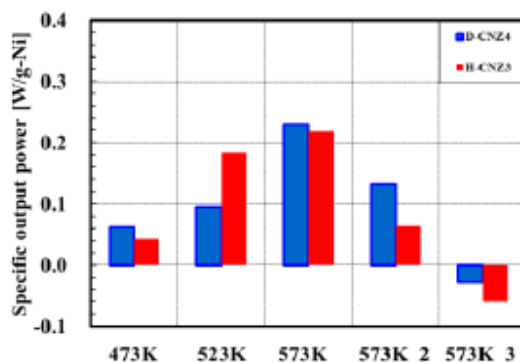
In the protium run at 573 K, the power increased gradually to reach about 2 W, and the exothermic reaction continued for 250 h. However, the sample absorbed/adsorbed deuterium with much less output power, sometimes even endothermically. The loading ratio was larger than in any other run. The D/Ni ratio reached 1.0.

We cannot distinguish absorption from adsorption with our present configuration. We admit that the “absorption” could include protium moving not only into interstitial sites but also into vacancies and vacancies clusters. However, it is hardly imagined that the sample has vacancies to accommodate hydrogen atoms as much as more than 10% of the host lattice atoms. It is natural therefore that the most hydrogen atoms are absorbed into the interstitial sites or adsorbed on the surfaces. In the following we mean “absorption and/or adsorption” by “absorption”.

The exothermic reaction was more prominent in the protium runs than in the deuterium runs in almost all cases including the helium blank runs.



(a)



(b)

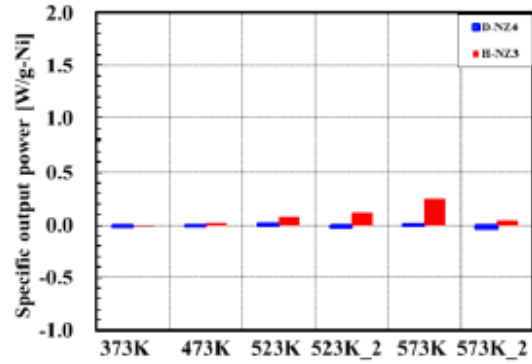
Figure 11. Specific output power data for the t-phase of sample H(D)–NZ, upper figure (a) and H(D)–CNZ, lower figure (b).

However, the system appears to lose long-term stability at temperatures higher than 500 K. The above temperature change regarded as the exothermic reaction is rather small, at most only about 2% of the input power. We are not very confident that it indicates a real exothermic reaction.

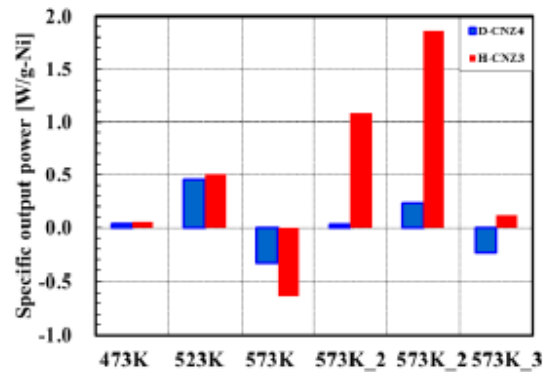
Next, the hydrogen absorption characteristics of the CNZ sample is described. Figure 6 shows the temporal behavior of the absorption parameters in the room temperature runs, D–CNZ1#1 and H–CNZ2#1. We have not observed absorption of hydrogen nor exothermic temperature change similarly to the NZ sample. We stopped the runs before we were able to collect much data, because we wanted to finish a certain number of experimental runs on a tight schedule.

After the #1 run, we performed hydrogen isotope absorption runs under conditions similar to the NZ sample. Figures 7(a)–(c) show the absorption parameters in the runs, H(D)–CNZ3(4)#5_473 K through H(D)–CNZ3(4)_573 K. At 473 K, we did not observe an exothermic reaction like the one we saw with the NZ sample. At 523 K the exothermic reaction appeared both in the protium and deuterium runs and continued for more than 100 hours. The power increased gradually to reach about 2 W.

At 573 K the sample absorbed gas-phase protium, and produced output power of 4.0 W maximum. This is twice as large as that of the NZ sample at the same temperature. Granted, it is only a small amount of power compared with



(a)



(b)

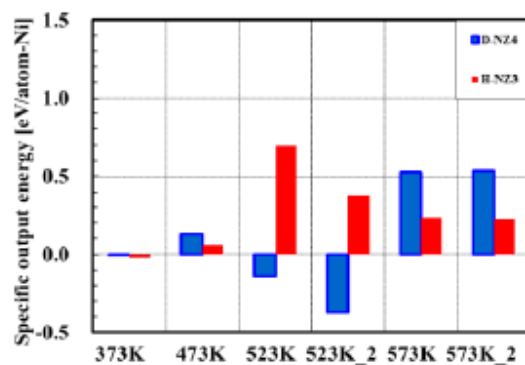
Figure 12. Specific output power data for the s-phase of sample H(D)–NZ, upper figure (a) and H(D)–CNZ, lower figure (b).

the input heater power. Note that the NZ sample had 5.41 g of net Ni, while the CNZ sample had 2 g of net Ni.

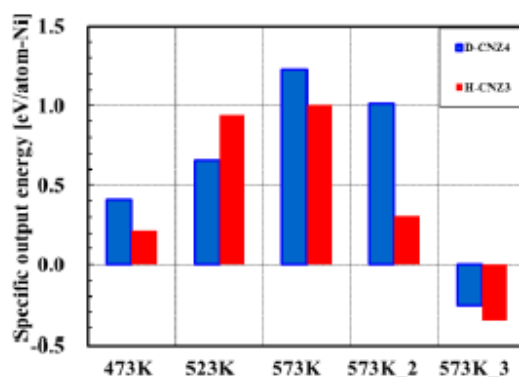
In evaluating the time-integrated output energy, we take notice of the fact that the CNZ-sample runs have an initial phase in which appreciable absorption takes place. We call this the t-phase, and distinguish between it and the rest of the run which has almost constant pressure. We call the latter the s-phase. The specific output energy $E_{D(H)}$ (eV/atom-Ni) is evaluated by integrating the specific output power $W_{D(H)}$ (W/g-Ni) until the time when the power becomes either almost zero or some constant value.

Figures 9, 11 and 13 are the histograms showing the loading ratio H(D)/Pd, the mean specific output power $W_{D(H)}$, and the specific output energy $E_{D(H)}$ in the t-phase of the four runs operated at temperatures 373–573 K. Figures 10, 12 and 14 are those in the s-phase of these runs. In Fig. 14 for $E_{D(H)}$, the integration times are shown in parentheses in the line below the x -axis.

The loading ratio for the sample CNZ is almost the same as that for the NZ sample both in the t-phase and the s-phase. On the other hand, the mean specific output power and the specific output energy for the CNZ sample are larger than those for the NZ sample operated at temperatures higher than 500 K. Especially, the specific output energy E_H reached about 800 eV/atom-Ni for the CNZ sample at 573 K, which is too high to be explained by any known



(a)



(b)

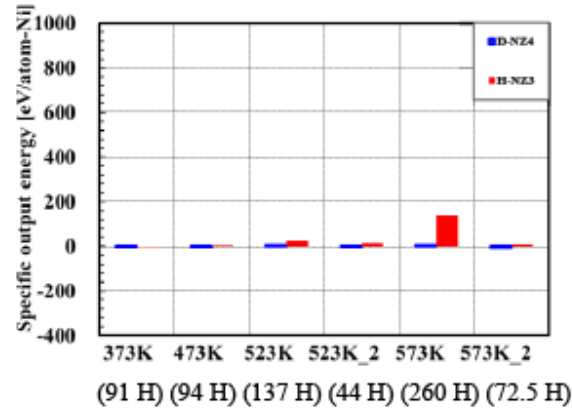
Figure 13. Specific output energy data for the t-phase of sample H(D)–NZ, upper figure (a) and H(D)–CNZ, lower figure (b).

chemical processes. The reason is as follows. All chemical processes including oxidation and de-oxidation proceed by exchanging outer electrons having binding energies at most 10 eV.

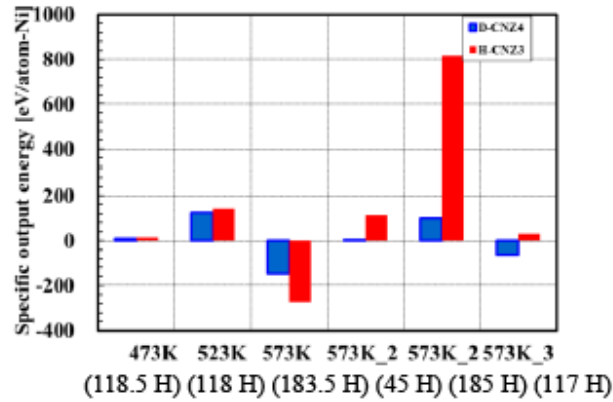
Therefore, we hardly suppose any atomic/molecular reaction energy greater than 10 eV/atom-H or 10 eV/atom-Ni. We admit that the oxygen pick-up reactions could be included. However, the reaction energies are lower than 1 eV or even negative; $\text{NiO} + \text{H}_2 \rightarrow \text{Ni} + \text{H}_2\text{O} + 0.7 \text{ eV}$, $\text{ZrO}_2 + 2\text{H}_2 \rightarrow \text{Zr} + 2\text{H}_2\text{O} - 6.4 \text{ eV}$.

Based on our results, we conclude that the copper atoms act as catalysts to produce the heat release under hydrogen isotope absorption/adsorption, presumably by substantially deepening the potential for interstitial hydrogen atoms inside nano-particles and/or surface atomic hydrogen. How the deeper potential relates to the nuclear reaction is the core question. We do not have the answer at the moment. A possible answer might be the Takahashi model [8].

In view of the large fluctuations of the observed temperatures, cautious reexamination of the absorption runs with a larger amount of the nickel sample material is necessary to confirm what appears to be continued, extraordinary large heat evolution.



(a)



(b)

Figure 14. Specific output energy data for the s-phase of sample H(D)-NZ, upper figure (a) and H(D)-CNZ, lower figure (b). The duration (integration time) of each run is designated below the temperature of the run in parenthesis.

4. Conclusion

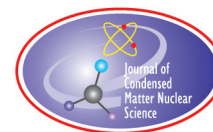
The results of the present work are summarized as follows:

- (1) Both NZ and CNZ samples showed apparent heat release at temperatures higher than 500 K.
- (2) Absorption of protium is more effective than deuterium absorption at producing a heat release.
- (3) The loading ratio for the NZ sample was almost the same as that for the CNZ sample, while for the heat release the CNZ sample was ten times more effective than the NZ sample. We infer that the copper atoms act as a catalyst for hydrogen absorption of the nickel nano-particles to deepen the potential well for the adsorption/absorption.

- (4) As the sample temperature was raised, the heat release and the loading ratio became larger. It may be possible that the sample will show an even larger heat release and a larger loading ratio at temperatures above 573 K.

References

- [1] For example, http://en.wikipedia.org/wiki/Energy_Catalyzer.
- [2] Y. Sasaki, Y. Miyoshi, A. Taniike, A. Kitamura, A. Takahashi, R. Seto and Y. Fujita; *Proc. JCF10*, 2010, pp. 14–19.
- [3] A. Kitamura, Y. Miyoshi, A. Taniike, A. Takahashi, R. Seto and Y. Fujita, *J. Condensed Matter Nucl. Sci.* 4 (2011) 56–68.
- [4] B. Ahern, private communication.
- [5] H. Sakoh, Y. Miyoshi, A. Taniike, A. Kitamura, A. Takahashi, R. Seto and Y. Fujita, *Proc. JCF11*, 2011, pp. 16–22.
- [6] Y. Miyoshi, H. Sakoh, A. Taniike, A. Kitamura, A. Takahashi, R. Seto and Y. Fujita, *Int. Conf. on Condensed Matter Nuclear Science, ICCF16*, Chennai, 2011, paper MT-02.
- [7] Y. Fukai, K. Tanaka and H. Uchida, *Hydrogen and Metals* (Uchida Rokakuho, Tokyo, 1998) (in Japanese).
- [8] A. Takahashi, *J. Condensed Matter Nucl. Sci.* 9 (2012) 108.



Research Article

Statistical Analysis of Transmutation Data from Low-energy Nuclear Reaction Experiments and Comparison with a Model-based Prediction of Widom and Larsen

Felix Scholkmann*

Bellariair 10, 8038 Zurich, Switzerland

David J. Nagel

The George Washington University, Washington DC, 20052, USA

Abstract

Nuclear transmutations were reported in many low-energy nuclear reaction (LENR) experiments. In the present study, we analyzed (i) whether three available nuclear transmutation data sets show a consistent pattern and (ii) whether this pattern correlates with a model-based prediction of Widom and Larsen. Our analysis revealed that the data sets (i) exhibit a similar pattern and (ii) correlate with the predicted function. The last three peaks as a function of atomic mass A (intervals: 64–70, 116–129, 191–208 A) were significantly ($p < 0.05$) correlated with the averaged data despite great differences in the experiments.

© 2014 ISCMNS. All rights reserved. ISSN 2227-3123

Keywords: Low-energy nuclear reactions (LENR), Neutron scattering strength, Statistical analysis, Transmutation, Widom–Larsen theory

1. Introduction

Experimental data are the basis for both scientific and commercial interest in low-energy nuclear reactions (LENR). There are four classes of evidences for the ability to induce nuclear reactions by the use of chemical energies: excess heat, transmutation products, energetic particles and radiation, and other low-energy phenomena. Excess heat data have received the most attention, but many studies of transmutation products are also available. A recent review summarizes some of the most relevant work reporting transmutations [1].

There are two major kinds of evidence for transmutations. The simplest, and possibly best-accepted, involves changes in the distribution of isotopes for specific elements, as measured with a mass spectrometer. Such data is useful even on a relative basis, that is, absolute calibrations and measurements are not needed. Measured relative distributions

*E-mail: felix.scholkmann@gmail.com

of isotopes are compared with natural distributions. Significant differences are taken as evidence of nuclear reactions, that is, transmutations. For example, Iwamura et al. apparently transmuted Sr into Mo [2]. The isotopic distribution of the Mo found after deuterium permeation of a complex Pd foil was similar to that of the initial Sr and very different from that of natural Mo.

The second type of transmutation data involves measurement of specific elements before and after LENR experiments. This type of LENR transmutation data requires sophisticated elemental analyses, which are open to more arguments than the relative data on isotope distributions. The analytical measurements can be done in either of two ways, with or without spatial resolution. Specific locations on samples can be examined analytically with a scanning electron microscopy (to get the location), which has the ability to do X-ray analyses (to obtain the elemental composition). Alternatively, analyses can be performed without spatial resolution by use of unfocussed instruments, or by dissolution of the surface or more of the materials from a LENR experiment followed by either wet or instrumental chemical assays. Sometimes, such spatially unresolved analyses are done for elements of particular interest [2]. Other times, they are performed for a wide range of elements spanning the periodic table. This paper is focused on the last type of transmutation data.

Miley [3–5], Mizuno [6,7], Little [8], Yamada [9] and their colleagues have published independent experimental transmutation data for elements across the periodic table. Their plots of nuclear transmutation production rates or final concentrations as a function of atomic mass number (A) appear to be qualitatively similar despite great differences in the experiments. However, these important data sets have never been compared with each other quantitatively.

In 2006, Widom and Larsen presented a model to predict the nuclear transmutation production rate [10] (here called ‘WL-prediction’). Although they pointed out that their prediction seems to correlate quite well with the experimental data of Miley [3,4], a statistical analysis for the agreement between the theoretical prediction and experimental data has not been done so far.

Thus, in order to gain further insights into the process of transmutations, and LENR in general, we analyzed (i) whether three available nuclear transmutation data sets show a consistent pattern, and (ii) whether this pattern correlates with the WL-prediction. We consider this study to be an example of ‘data mining’, a process which could be more widely applied to diverse data available from LENR experiments.

2. Data and Methods

2.1. Laboratory Data

The following transmutation data sets from electrolysis experiments were selected from publications and used for the present analysis: data obtained by (i) Miley (*Miley data set*), (ii) Mizuno (*Mizuno data set*), and (iii) Little and Puthoff (*Little-Puthoff data set*).

Very brief synopses of the methods and results for each of the three experiments follow.

Miley et al. [3–5] electrolyzed plastic beads coated with Pd and Ni in a packed bed configuration through which a light water (H_2O) electrolyte circulated. They used four analytical techniques, Secondary Ion Mass Spectrometry (SIMS), Auger Electron Spectroscopy (AES), and both Energy Dispersive X-Ray (EDX) and Neutron Activation Analyses (NAA), some both before and after 14-day runs. Production rates in atoms/s/cm³ were reported as a function of mass A .

Mizuno et al. [6,7] electrolyzed a Pd rod in a closed cell containing a heavy water (D_2O) electrolyte at high pressures, temperatures, and current densities for 32 days. They used the same analytical methods as Miley et al., except electron probe micro-analysis was employed in place of neutron activation analysis. Data were reported in SIMS count rates and gms of deposited material as a function of A . Both Miley et al. and Mizuno et al. observed excess heat and measured anomalous isotope ratios.

Little and Puthoff [8] used the same configuration as Miley et al. for runs of 2 weeks. They employed X-ray

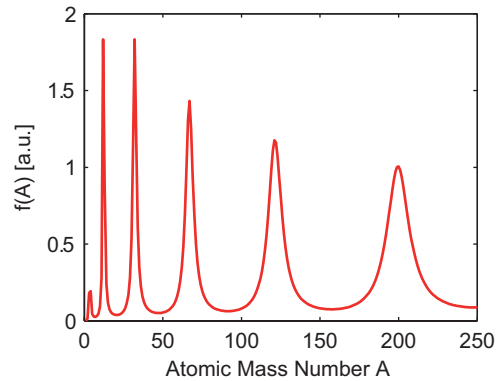


Figure 1. The $f(A)$ function according to Eq. (3) for $A \in \{1, 2, \dots, 250\}$.

fluorescence analysis, which has a relatively high minimum detection limit. Miley analyzed their materials using SIMS and obtained absolute production rates generally similar to what his team observed.

Since these data were not available as data files we used a Matlab (Mathworks, Natick, MA, USA) software ('grabit.m') written by J. Doke to extract the data from the published figures. For the *Miley data set* we used the figure given in [5], which is of higher quality than in [3], where the same data were reported. It consists of six runs (run numbers: #5, #7a, #8, #11, #13, and #18c) of the same experiment. We averaged over all six individual data sets to create the final data set. The *Mizuno data set* was created by using the figure in [7], consisting of two measurements (isotopic distribution of the top and the side of the electrode). We averaged over those two individual data sets to create the final data set ('combined data set'). The *Little-Puthoff data set* was created by using the corresponding figure given in [8].

2.2. Widom–Larsen prediction

That collective electron and proton or deuteron plasma modes on surfaces of fully loaded metallic hydrides produce ultra-low momentum neutrons ($< 10^{-10}$ eV) was put forward in a theoretical work in 2005 of Widom and Larsen [11]. According to this hypothesis, the reaction of radiation energy with electrons (e^-) gives rise to heavy electrons localized near the metal hydride surface (\tilde{e}^-). They can react with a proton (p^+) resulting in the formation of an ultra-low

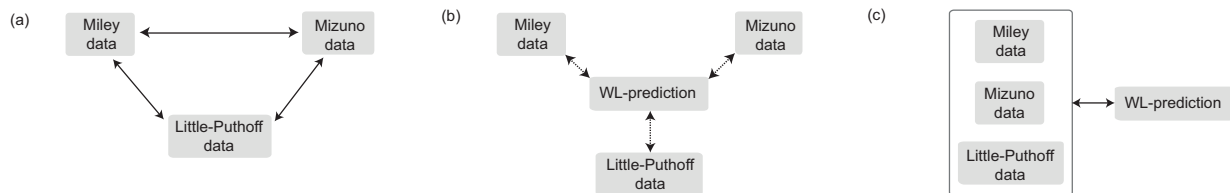


Figure 2. Visualization of the three different types (a–c) of data analyses performed in the present study.

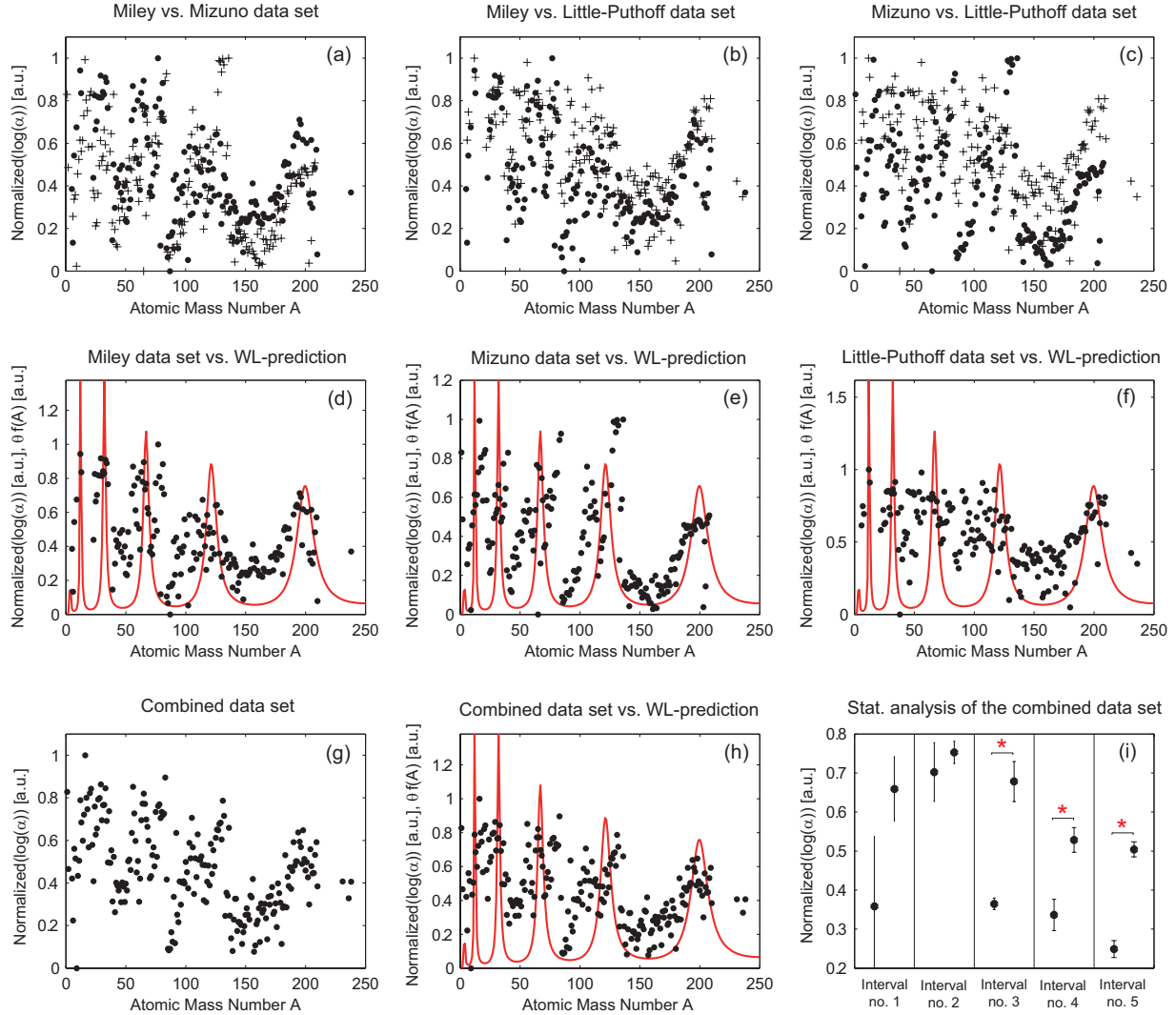


Figure 3. (a)–(c) Comparison of the each data set with each other. α is the scaling of the original data sets (isotopic abundance, ...). (a): Miley (•) vs. Mizuno data set (+). (b): Miley (•) vs. Little-Puthoff data set (+), (c): Mizuno (•) vs. Little-Puthoff data set (+). (d)–(f): Comparison of the each data set with the WL-prediction. Values obtained for the scaling parameter θ : case (d), $\theta = 0.751$; case (e), $\theta = 0.655$; case (f), $\theta = 0.3703$. (g)–(h): Comparison of the sum of all data sets with the WL-prediction. (g) Combined data set. (h) Combined data set vs. WL-prediction. (i) Result of the interval analysis. * Indicates statistically significantly ($p < 0.05$) differences.

momentum neutron (n) and an electron neutrino (ν_e):

$$\Delta E + e^- \rightarrow \tilde{e}^-, \quad (1)$$

$$\tilde{e}^- + p^+ \rightarrow n + \nu_e. \quad (2)$$

According to Widom and Larsen [11], the ultra-low momentum neutrons interact with the atoms on the metallic hydrides and cause nuclear transmutations.

Widom and Larsen proposed that the transmutation rates depend on the atomic mass number of the reacted element [10]. Based on an optical potential model for the effective neutron amplitude, they derived a function for the neutron scattering strength:

$$f(A) = 3m \left[\frac{\tan(zA^{1/3})}{z} \right] \quad (3)$$

with $z = 3.5 + 0.05i$. In their paper [10], they showed a remarkable similarity of the theoretically derived $f(A)$ function and results from two LENR experiment where a change in the isotopic distribution was observed [3,4].

Figure 1 shows the $f(A)$ function according to Eq. (3) for $A \in \{1, 2, \dots, 250\}$ comprising a spectrum with five main peaks at $A = 12, 32, 67, 121$, and 200.

2.3. Data Analysis

We performed three types of analyses: (i) comparison of each of the three data sets with each other, (ii) comparison of each data set with the WL-prediction (i.e. the function), and (iii) comparison of the combined data set with the WL-prediction. A visualization of these three analyses can be seen in Fig. 2.

All data sets used were first normalized to the range $[0,1]$ in order to enable the next data processing steps, i.e. to make the data comparable to each other.

2.3.1. Comparison of each data set with each other

Since the three different data sets contain missing values and show strong scattering, an interpolation function was calculated for each data set in order to be able to quantitatively compare the data sets. For the interpolation, a fully automated smoothing procedure based on a penalized least square method introduced by Garcia [12] was used. The correlations between the data sets were then quantified by calculating the Pearson correlation coefficient (r) and the significance level (p) of the correlation. A value of $p < 0.05$ was considered as statistically significant.

2.3.2. Comparison of each data set with the WL-prediction

First, the $f(A)$ function for $A \in \{1, 2, \dots, 250\}$ according to Eq. (3) was computed. Then, the $f(A)$ function was fitted to each data set by using a classical least squares optimization method. The fitting was realized by multiplying the $f(A)$ function with a scaling factor α , which then was changed until the sum of squared errors between the $f(A)$ function and the data was minimized. Finally, the correlation between each data set with the specific $f(A)$ function was quantified as described in the previous section.

2.3.3. Comparison of the combined data set with the WL-prediction

For this analysis, all three data sets were combined and an interpolation function was determined, according to the approach presented in [12], to obtain the missing values. Then, two types of data analyses were performed. *First data analysis:* The $f(A)$ function was fitted to the new data set and the strength as well as statistical significance (r , p) were determined. *Second data analysis:* The new data set was segmented into intervals corresponding to the peaks and troughs of the $f(A)$ function. Thus, ten intervals were determined. The borders of the intervals were chosen to cover the peak and troughs position of the $f(A)$ function optimally. The borders for the peak intervals were: 11–13 A,

30–34 A, 64–70 A, 116–129 A, and 191–208 A. The borders for the trough intervals were: 7–9 A, 19–22 A, 44–50 A, 88–101 A, and 153–180 A. To test whether the mean values of the new data set in the peak and trough intervals are statistically significantly different, a *t*-test was used.

3. Results

3.1. Comparison of each data set with each other

The three comparisons between the data sets revealed that all three combinations tested showed a positive correlation coefficient and a statistically significant correlation: (i) $r = 0.3823$, $p < 0.001$ (Miley vs. Mizuno data set), (ii) $r = 0.5392$, $p < 0.001$ (Miley vs. Little-Puthoff data set), and (iii) $r = 0.3545$, $p < 0.001$ (Mizuno vs. Little-Puthoff data set). The graphical visualizations of the data analysis results are given in Fig. 3(a)–(c).

3.2. Comparison of each data set with the WL-prediction

The comparison of each data set with the WL-prediction showed that each data set was significantly correlated with the predicted function. The obtained values were: (i) $r = 0.4360$, $p < 0.001$ (Miley data set vs. WL-prediction), (ii) $r = 0.2338$, $p < 0.001$ (Mizuno data set vs. WL-prediction), and (iii) $r = 0.3703$, $p < 0.001$ (Little-Puthoff data set vs. WL-prediction). The graphical visualizations of the data analysis results are given in Fig. 3(d)–(f).

3.3. Comparison of the combined data set with the WL-prediction

This analysis revealed that the sum of all data sets ('combined data set'), shown in Fig. 3(g), is statistically significantly correlated with the WL-prediction as depicted in Fig. 3(h) ($r = 0.3409$, $p > 0.001$). Fig. 3(i), which shows that when summing up the values for the five peaks and troughs according to the WL-prediction, the last three peaks are present in the data and correspond to the WL-prediction.

4. Discussion

This discussion addresses three topics. The first deals with the experimental challenges of transmutation studies. Next, we briefly summarize what was found in the present study, and an associated question raised at the conference (ICCF-17). Then, we consider how the peaked distributions seen in the three data sets and in the WL prediction can occur conceptually.

As a practical matter, getting transmutation rates experimentally is very challenging and expensive. Transmutations of one element into another are due to reactions. The amounts of materials that result from reactions, chemical as well as nuclear, depend both on the amounts of materials at the outset and the reaction rates. Hence, the reaction rates can only be obtained by measuring the amount of a given element or isotope present at the beginning and the end of a LENR experiment and forming the ratio of those numbers. That is possible in principle, but challenging in practice because of the sampling that is required. Rigorously, the same region (area and depth) of the sample must be analyzed before and after any nuclear reactions.

It is possible to do before and after analysis with non-destructive methods, such as X-ray analysis, but it is not possible for analytical methods that require consumption of the sample. Inductively coupled mass spectrometry is remarkably sensitive, but requires digestion of the sample. That is, pre-run analysis changes the sample, and it is that changed sample which goes into and out of the experiment. Of course, whatever analytical technique is used, it has to have an adequately low minimum detection limit, and offer good signal-to-noise performance for the analyte levels both before and after an experiment. It should be highlighted that the NAA method is able to examine the whole analyte

while also giving absolute values. Therefore, analysis with NAA is recommended for future LENR transmutation experiments. It remains remarkable that the three experimental data sets we studied have such great similarities in the face of these challenges.

In summary, we found that all three data sets, and the WL-prediction, correlated well with each other. Further, we found that peaks in three intervals of atomic mass are well correlated: 64–70 A, 116–129 A, and 191–208 A.

The fact that the data sets of the teams lead by Miley and by Mizuno, and also the Little-Puthoff data, all correlate well, each with the others, would seem to add strength to the value of these data. These LENR experiments, which differ widely in what was done and measured, apparently tell the same story, namely nuclear transmutations occur with results that resemble each other. However, there are two reasons to be cautious in adopting that viewpoint. At ICCF-17, right after presentation of this paper, David Kidwell of the Naval Research Laboratory raised a question about the data sets themselves [13]. He stated that, if all three of the transmutation experiments we studied were contaminated with dirt, which reflected the distributions of elements on the earth's surface, their similarity would be understandable and artifactual. That is, the peaked data sets might be due to impurities in the experiments and not reflective of transmutation rates, as stated by the authors. The absolute amounts of material for any given element in the transmutation experiments are very small. Kidwell's idea might seem preposterous to some, since the data that were used in this study were obtained by careful experimenters. However, the fact that the data sets are so similar, even though the experiments and analytical methods are so different, does give some people pause for thought. The anomalous isotope ratios measured by the teams lead by Miley and Mizuno argue for the probability that transmutations were actually produced. We plan to perform a statistical comparison of the same three data sets, as used above, with the distribution of elements and isotopes in the earth's crust. Such an analysis could indicate whether (i) the LENR transmutation results are artifacts due to contamination with dirt, dust, etc., (ii) or whether both processes (LENR transmutation and natural elemental abundances) share a common physical mechanism.

The other reason for being cautious in drawing conclusions from the correlations we found is conceptual. The measured peak distributions as a function of atomic mass could be due to peaks in the initial distribution of elements, peaks in the reaction rates or both these factors. As already noted, analyses before and after an experiment can eliminate the effects of the initial variations in sample composition, and give the mass-dependent reaction rates. The theoretical prediction of WL about the rates of reactions of nuclei with what they call ultra-low momentum neutrons deals only with the reaction rates, and not the initial distributions of the elements in an experiment. The good correlations of their reaction rates with the experimental data can lead to the conclusion that the initial distributions of elements before the three experiments might be quite flat, that is, independent of atomic mass. But, that is highly unlikely.

The discussion to this point assumes that there is only one reaction per starting nucleus. However, there might be sequential (cascaded) reactions during an experiment to produce the final measured distribution. Assume for the sake of discussion that the WL-prediction is correct. If there are enough ultra-low momentum neutrons for long enough times, there might be sequential nuclear reactions involving isotopes lighter than the positions of each peak. Any isotope to the left of a peak would react to give a larger A value, and then that product would again react, etc. The final elemental distribution would be the result of a cascade of sequential reactions. The probability of reactions would increase as the peaks are approached from the left. When masses at the peak values are achieved, then the declining probabilities for reactions at larger A values would leave a high concentration in the region of the theoretical valleys, where the reaction rates are lowest. Then, most atoms would be in mass regions away from the peaks, contrary to experiment.

If this scenario happened, then the final distribution would be either less dependent on the initial distribution of elements, or even independent of it. Because of the possibility of cascades of reactions, we sought to find papers that dealt with this scenario. There seems to be only one such study in this field [14,15]. Mishinsky and Kuznetsov consider individual transmutation reactions, which can involve several input nuclei as reactants and up to three output nuclei products. Different types of LENR experiments with different reaction times and energy densities were considered. Setting aside concerns about the mechanistic details of such reactions, we note that the authors do take into consideration

the necessary conservation requirements for exothermic single and sequential transmutation reactions. For the sequential reaction case, distributions of elements are shown as a function of time for multi-hour runs, implying knowledge and use of reaction rates. It should be possible to test experimentally the results computed by these authors.

There is one well-studied topic in science in which sequential nuclear reactions occur, namely stellar nucleosynthesis [16–19]. The basic idea in the astrophysical field is that all heavy elements in the universe are the result of cascades of nuclear reactions, which occur within stars, both during their lifetimes and also during the explosions (supernova) at the end of their lives. A great deal of modeling has been performed on cosmic nucleosynthesis. It is based on conventional nuclear reaction physics. The results have no direct utility to the understanding of LENR. However, the computational methodologies employed to understand the natural distributions of elements and isotopes are worth studying to see if those techniques could be applied to understand the distributions of interest in this paper.

The results we obtained in this study do not validate the basic concept of the Widom–Larsen theory of LENR [10,11, 20–26]. Their theory for the occurrence of LENR depends on the production of extremely high fields (100 V/nm) on the surfaces of lattices. According to Widom and Larsen, such fields would “mass renormalise” electrons in the surface region, making it possible for the reverse of the familiar neutron decay reaction to occur. This would, in their view, produce ultra-low momentum neutrons, which could then react with nearby elements during LENR. The WL-prediction, which we employed in this paper, is ancillary to their basic theory. That is, the correlation of their prediction with the results of three transmutation experiments does not validate the occurrence of the postulated very high surface fields, the production of heavy electrons or the appearance of ultra-low momentum neutrons.

If it were shown computationally that there are (a) appropriate conditions in LENR experiments to produce high densities of ultra-low momentum neutrons and (b) enough time for many cascaded reactions, then the WL prediction might be the basis for understanding the peaked experimental distributions, as discussed above. Then, the observed peaked distributions could be taken as evidence for the validity of the WL-prediction we used. That, in turn, would indicate the occurrence of ultra-low momentum neutrons, which would buttress the case for their production by mass renormalisation of electrons, which would indicate that the super-high surface fields might exist, as theorized. Of course, it would also be good to design experiments that might be able to more directly produce evidence, which can only be explained by the presence of such immense fields.

It would be also interesting to compare the findings of the present study with prediction of other theories about LENR. However, we are not aware of any other theory that predicted the pattern of peaks in LENR transmutation rates.

Although our study proved that there is a similar pattern in the LENR transmutation data, this study has raised more questions than it has answered. Knowledge of the quantitative comparisons we obtained is a useful advance in our understanding of LENR experiments that reportedly produce transmutations. However, we are left with two large questions about the observed distributions of elements across the periodic table. The first is the important, albeit disturbing, issue that was raised by Kidwell. He asserted that it might be possible for the measured distributions now available to be the result of contamination and not transmutations. That concern can be addressed experimentally by use of very pure initial samples, or more ordinary samples with very well characterized compositions. Doing such experiments would require the employment of sophisticated sampling and analytical methods before and then after the LENR experiments. It is expected that such experiments will not be possible until adequate funding is available for the field.

The second large question can be addressed theoretically and computationally. It deals with the possibility that the measured distributions are indeed due to transmutations and that they are attained by cascaded nuclear reactions, such as occur in stars by understood nuclear reactions. The question is whether or not it LENR can also occur by cascaded reactions. This is basically a scientific question. However, it might have practical consequences. If many sequential reactions occur in commercial LENR energy generators, then the materials left after operation would be different than if only one or very few reactions can occur, one after the other. The point is that the residual materials from operation of LENR power sources would depend on the answer to this question about cascaded reactions. The reclamation of

elements from spent LENR energy generators would be different both chemically and economically without or with sequential nuclear reactions. If such new generators do become as widely used as many hope and some expect, the character of their residues would be significant. These considerations also apply to the hope on the part of many people that LENR can be used to process current radioactive materials from fission reactors into something more benign, while extracting additional energy in the process.

References

- [1] M. Srinivasan, G.H. Miley and S. Storms, Low energy nuclear reactions: transmutations, in *Nuclear Energy Encyclopedia: Science, Technology and Applications*, S.B. Krivit, J.H. Lehr and T.B. Kingery (Eds.), Wiley, New York, 2011, pp. 503–540.
- [2] Y. Iwamura, M. Sakano and T. Itoh, Elemental analysis of Pd complexes: effects of D₂ gas permeation, *Japanese J. Appl. Phys.* **41**(7A) (2002) 4642–4650.
- [3] G.H. Miley, Possible evidence of anomalous energy effects in H/D-loaded solids—low energy nuclear reactions (LENR), *J. New Energy* **2**(3–4) (1997) 6–13.
- [4] G.H. Miley and J.A. Patterson, Nuclear transmutations in thin-film nickel coatings undergoing electrolysis, *J. New Energy* **1**(3) (1996) 5–3.
- [5] G.H. Miley, *Reaction product and heat correlation for LENRs*, Lerici (La Spezia), Italy, 2000.
- [6] T. Mizuno, T. Ohmori and M. Enyo, Isotopic changes of the reaction products induced by cathodic electrolysis in Pd, *J. New Energy* **1**(3) (1996) 31–45.
- [7] T. Mizuno, Isotopic changes of elements caused by various conditions of electrolysis. in *The 237th ACS National Meeting*, 2009, Salt Lake City, UT, USA.
- [8] S. Little and H.E. Puthoff, Search for evidence of nuclear transmutations in the CETI RIFEX Kit. <http://www.earthtech.org/experiments/rifex/rifex.pdf>, 1998.
- [9] H. Yamada et al., Production of Ba and several anomalous elements in Pd under light water electrolysis. in *ICCF-9*, Beijing, China, 2002.
- [10] A. Widom and L. Larsen, Nuclear abundances in metallic hydride electrodes of electrolytic chemical cells, arXiv:cond-mat/0505026, 2006.
- [11] A. Widom, A. and L. Larsen, Ultra low momentum neutron catalyzed nuclear reactions on metallic hydride surfaces, arXiv:cond-mat/0505026v1, 2005.
- [12] D. Garcia, Robust smoothing of gridded data in one and higher dimensions with missing values, *Computational Statistics and Data Analysis* **54**(1) (2010) 1167–1178.
- [13] D. Kidwell, Public Communication, 2012.
- [14] G.V. Mishinsky and V.D. Kuznetsov, Element distribution in the products of low energy transmutation, Nucleosynthesis, *Annales de la Fondation Louis de Broglie* **33**(3–4) (2008) 331–356.
- [15] G.V. Mishinsky and V.D. Kuznetsov, Phenomenological model of low energy element transmutation and element distribution in transmutation products, in *Proc. 13th Int. Conf. on Condensed Matter Nuclear Science*, Y. Bashutov, (Ed.), MATI, Moscow, 2008, pp. 718–737.
- [16] T. Rauscher and A. Patkós, Origin of the chemical elements, in *Handbook of Nuclear Chemistry*, A. Vértes et al. (Eds.), Springer, Berlin, 2011, pp. 611–665.
- [17] J.W. Truran, Nucleosynthesis, *Ann. Rev. Nucl. Particle Sci.* **34** (1984) 53–97.
- [18] A. Lépine-Szilya and P. Descouvemont, Nuclear astrophysics: nucleosynthesis in the Universe, *Int. J. Astrobiology* **11**(4) (2012) 243–250.
- [19] C.E. Rolfs and W.S. Rodney, *Cauldrons in the Cosmos: Nuclear Astrophysics*, University of Chicago Press, Chicago, 2005.
- [20] A. Widom and L. Larsen, Ultra low momentum neutron catalyzed nuclear reactions on metallic hydride surfaces, *Euro. Phys. J. C* **46** (2006) 107–111.
- [21] A. Widom and L. Larsen, Absorption of nuclear gamma radiation by heavy electrons on metallic hydride surfaces, arXiv:cond-mat/0509269 v1, 2005.
- [22] A. Widom and L. Larsen, Theoretical standard model rates of proton to neutron conversions near metallic hydride surfaces, arXiv:nucl-th/0608059v2, 2007.

- [23] A. Widom, Y.N. Srivastava and L. Larsen, Energetic electrons and nuclear transmutations in exploding wires, arXiv:0709.1222v1, 2007.
- [24] A. Widom, Y.N. Srivastava and L. Larsen, Errors in the quantum electrodynamic mass analysis of Hagelstein and Chaudhary, arXiv:0802.0466v2, 2008.
- [25] A. Widom, A., Y.N. Srivastava, and L. Larsen, High energy particles in the solar corona, arXiv:0804.2647v1, 2008.
- [26] Y.N. Srivastava, A. Widom and L. Larsen, A primer for electroweak induced low-energy nuclear reactions, *Pramana – J. Phy.* **75**(4) (2010) 617–637.



Research Article

Transmutations and Isotopic Shifts in LENR Experiments An Overview

Mahadeva Srinivasan *

Bhabha Atomic Research Centre (BARC) (Retired), Mumbai, India

Abstract

This overview presents a brief summary of observations of products of transmutation reactions, which occur in a variety of LENR configurations wherein the “host metal” nuclei react with loaded deuterium or hydrogen, resulting in the formation of new stable elements or isotopes not present prior to an experimental run.

© 2014 ISCMNS. All rights reserved. ISSN 2227-3123

Keywords: Isotopic anomalies, Multi-deuteron capture, Transmutation reactions

1. Introduction

The term “Transmutations” as used in the LENR field has come to refer to the occurrence of nuclear reactions between the loaded deuterium (or deuterons) or hydrogen (protons) on the one hand, and nuclei of the host metals such as Pd, Ni, Ti or of higher-Z nuclei present in the experimental environment such as those of alloyed elements or impurities in the cathode or even elements present in the electrolyte (in case of electrolysis experiments), on the other. Any nuclear reactions that occur among hydrogenous isotopes such as p or d (or even tritium) present in the reactive zone would generally be classified as “fusion” reactions. As understood in the context of the present discussion the basic difference between transmutations and fusion is that in the former the host metal lattice nuclei participate directly in the nuclear processes taking place while in fusion they merely serve a catalytic role but themselves do not get involved.

Interestingly there are a few instances wherein nuclear reactions do seem to occur even when neither p or d is externally injected into the system nor is any host metal present as such. Examples are the Carbon Arc under water experiments and the phenomenon called “Biological Transmutations”. But in both these cases hydrogen (and deuterium from natural abundance) are already present in the configuration.

When Fleischmann–Pons announced their discovery in 1989, as is well known, it was (and still is) met with considerable skepticism by the Nuclear Physics community. The postulated occurrence of nuclear reactions between two positively charged nuclei having nuclear charge of unity at normal temperatures was dismissed as impossible. Under

*E-mail: chino37@gmail.com

these circumstances any suggestion of the likelihood of a nuclear reaction occurring at room temperature between a deuteron (or proton) and any higher-Z nucleus would be considered as “preposterous”!

It is in the backdrop of this “intense disbelief” of the whole topic of LENR transmutations that we briefly review the experimental evidence gathered by several groups the world over, deploying a variety of different experimental configurations and analytical techniques, over the last couple of decades.

The present overview is a condensed version of a review paper published a year ago [1] jointly with George Miley and Edmund Storms (an electronic version of the preprint of this article which was distributed to participants of ICCF 16 conference is available in [2]). Miley had earlier published periodic status reports on Transmutations [3,4]. Storms had included in his book published in 2007 [5] an exhaustive tabulation of the nuclear products observed by various researchers as reported in a 101 references to LENR Transmutations related publications.

2. General Remarks on Experimental Methodology

Transmutation experiments generally involve two steps: The experimental run during which a target or test sample is loaded with deuterons or protons by a suitable technique such as electrolysis, gas/plasma loading or other. In the second step, on completion of the experimental run, the test sample is analyzed off line to determine if there is any evidence for transmutation reactions having occurred. This involves measuring the elemental composition and/or isotopic distribution of various components, which were present in the reaction zone. In the case of electrolysis and glow discharge experiments the cathode would be the one mainly investigated. Obviously mere detection of traces of a “new” element which was not present prior to the run does not imply occurrence of transmutations, since in principle cross contamination could have occurred through inadvertent transport of minute quantities of elements from elsewhere in the apparatus. For example during electrolysis trace quantities of impurities could easily have plated out from the electrolytic solutions. In glow discharge experiments plasma etching could have sputtered out some elements and redeposited them on the test sample. It is therefore important to ensure such type of contamination is not the cause of the observations. Having accurate elemental composition of the stock electrolytic solution, especially of trace elements, available prior to the commencement of the experimental runs, would be essential.

However, if the isotopic distribution of the newly found elements or for that matter of any of the materials previously present in the system, are found to be significantly different from their natural abundance values following a run, then it clearly points to anomalous nuclear processes having taken place. Such findings are often referred to as “isotopic anomalies”. Advanced mass spectrometric analytic tools available these days, such as Secondary Ion Mass Spectrometry (SIMS) permit accurate and often *in situ* isotopic distribution measurements. However, mass spectroscopy is known to be subject to errors arising from interference effects caused by molecular ion species having masses close to that of the isotope under measurement. This possibility has to be addressed before concluding that the observed “isotopic anomalies” are real.

Lastly the well-known characteristic of non-uniformity of the LENR phenomenon has to be recognized while interpreting the transmutation results. Ed Storms has propounded the interesting concept of Nuclear Active Environment (NAE), to explain this. Invariably the phenomenon is found to occur in one spot but not in a neighboring one. Also, a systematic variation of the reaction product concentrations is often discerned as one goes from outer layers to deeper layers. Depth profiling of new element concentrations and isotopic ratios has at times influenced acceptance of the genuineness of the transmutation results.

3. Russian Glow Discharge Measurements

Karabut and Savvatimova were among the earliest researchers to investigate LENR transmutation phenomena using glow discharge. Figure 1 is a schematic of their glow discharge apparatus, which is basically a double-walled quartz

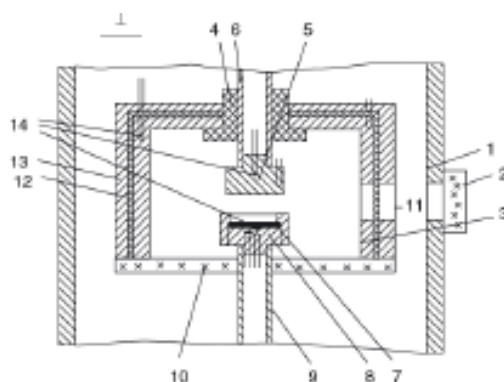


Figure 1. Glow discharge apparatus used by Karabut et al.

vacuum chamber with Mo anode and cathode. The design of the setup permitted use of different cathode material inserts for study [6]. The chamber was evacuated and filled with D_2 gas to a pressure of 3–10 Torr. The region of the cathode bombarded by the plasma ions was typically $\sim 1 \text{ cm}^2$ in area. Applied voltage varied from 50 V to 1.2 kV; discharge current was $\sim 100 \text{ mA}$.

The chamber and electrodes were water cooled to perform calorimetric measurements. The authors have reported observing excess heat consistently with near 100% reproducibility, but not detecting the normal (d–d) fusion reaction products such as neutrons, tritium, or even helium, commensurate with the magnitude of the heat generated. Hence their persistent quest for evidence of transmutation products.

Prior to commencement, the impurity content of virgin Pd cathode material was confirmed to be under 0.01%. Post-discharge Pd cathode buttons were analyzed using: Surface topography by scanning electron microscopy; elemental and isotopic composition using spark mass spectrometry, SIMS, Thermal Ionization Mass Spectrometry (TIMS) and XRF. Autoradiography was used for evidence of any remnant radioactivity. Results have consistently indicated significant deviations from natural abundance values for most elements.

At the Nagoya ICCF 3 meeting (1992), Karabut et al. reported finding as much as 0.1% of Na, Mg, Br, Zn, S, Mo, and Si in the upper crust of the Pd. The top $1 \mu\text{m}$ layer of the Pd sample was examined at several spots in the front portion, the back portion, and shielded area with a spatial resolution of $1 \mu\text{m}$ using an X-ray microprobe analyzer. It was found that the content of some elements increased by tens to hundreds of times relative to initial content in virgin Pd.

At ICCF 5 held in Monaco in 1995, they reported finding significant spot to spot variations using an X-ray microprobe analyzer. In some spots, the Ag content was as high as 12–15% and Mo about 5–7%. The concentration of elements such as As, Br, Rb, Sr, Y, and Cd, which were not present in any of the construction materials used in the experimental apparatus, was in the range of 0.1–0.2%. A new result reported at the Monaco meeting was that even with hydrogenous plasma, they observed elements not present in the virgin cathode, but in general the products' yield with deuterium gas was orders of magnitude higher.

At ICCF 9 held in Beijing in 2002, Karabut reported [7] new results obtained by subjecting the discharge device to an “impulsive periodical power source” (pulsed voltage), which led to generation of intense X-ray laser beams. The main impurity nuclides (with more than 1% content altogether) registered in the top 100 nm thick surface layer were Li^7 , C^{12} , N^{15} , Ne^{20} , Si^{29} , Ca^{44} , Ca^{48} , Fe^{56} , Fe^{57} , Co^{59} , Zn^{64} , Zn^{66} , As^{75} , Ag^{107} , Ag^{109} , Cd^{110} , Cd^{111} , Cd^{112} , and Cd^{113} . They identified two broad categories of impurity elements: those with masses roughly half of that of Pd (probably caused by deuteron induced fission) and those with masses close to but above that of Pd (possibly caused by

multiple deuteron captures).

At ICCF 12, held in Yokohama in December 2005, Karabut presented further results from discharges carried out with V, Nb, and Ta cathodes and in the inert gases of Xe and Kr besides D₂. In general, with cathodes other than Pd, “impurity” element yield was significantly lower. In these experiments, Karabut also measured the impurity content yield after peeling off some atomic layers using plasma etching and then again measuring the elemental content using SIMS.

At the same conference in Yokohama, Savvatimova presented [8] a very detailed and exhaustive account of her independently conducted glow discharge results with hydrogen, deuterium, argon, and argon-xenon mixture plasmas. The influence of various experimental parameters such as nature of plasma gas, total dose of bombarding ions, discharge current density (mA/cm²), and type of applied voltage (direct or pulsed) on the yield of “additional” elements was studied systematically. This time she also used multilayer cathodes comprising several foils of 100 μm thickness stacked one on top of the other to study differences in product yield characteristics with depth. The greatest changes in “additional” element content and isotope shifts were found in certain “hot spots” (mostly near grain boundaries) where a micro-explosion or plasma micro-discharges had appeared to have taken place. The author makes special mention of elements with mass numbers 59 (Co), 55 (Mn), and 45 (Sc), which were always found in plenty in the post-discharge samples but never in initial samples. One intriguing observation was that the isotopic changes continued to occur for at least three to five months after glow discharge exposure. Several isotopes with masses less than those of W and Ta increased by factors ranging from 5 to 1000 times.

On the whole, Savvatimova found that the more deeply she investigated the LENR glow discharge phenomenon, the more complex it was found to be, as brought out in the 13 tables of results included in her Yokohama paper.

4. Electrolysis Experiments

It was the Miley–Patterson paper first published in 1996 [9] that perhaps really opened the door to acceptance of Transmutation being possibly real even within the CMNS community. Industrial chemist James Patterson had invented a pebble bed cathode, circulating solution electrolytic cell wherein the cathode was made up of a bed of Pd-Ni multilayer thin film coated plastic microspheres (~1 mm dia). There were typically 1000 microspheres in the cell forming a four or five-layer bed constituting the cathode. Li₂SO₄ solution served as electrolyte as well as coolant. Figure 2 is a schematic of this cell. As this cell showed excess heat with both D₂O based as well as H₂O based electrolytic solutions, Patterson entrusted Miley’s group at the University of Illinois to perform elemental analysis of the coating of the post run beads to determine if any nuclear products could be identified.

When Miley found what appeared to be a gamut of new elements he repeated the electrolytic runs in his lab after fabricating his own version of multilayer thin film coated cathodes as well as a fresh electrolytic cell using no metallic components, to preclude the possibility of trace elements from entering the solution and causing contamination.

An advantage of thin film cathodes (coating thicknesses varied in the range of 500–3000 Å) is that high deuterium or hydrogen loadings could be obtained in time durations as short as an hour or two. Also the nuclear products would constitute a larger fraction of the metallic mass, minimizing doubts that the new elements found could be due to impurities deposited from the electrolyte. Miley and his colleagues carried out more than a dozen electrolytic runs with various types of coatings. Following several weeks of electrolysis, beads from the upper layers of the packed bed cathode were retrieved for analysis.

A variety of measurement techniques such as Secondary Ion Mass Spectrometry (SIMS), Energy Dispersive X-ray (EDX) analysis, Auger Electron Spectroscopy (AES), and Neutron Activation Analysis (NAA) were employed. While EDX gave confirmatory data for the higher concentration elements, AES was used for depth profiling of these elements. SIMS was used to obtain an overall picture of the various nuclides present and their relative isotopic ratios while NAA gave a quantitative measure of eight key elements, namely Al, Ag, Cr, Fe, Cu, V, Co, and Zn, present in a gross sample

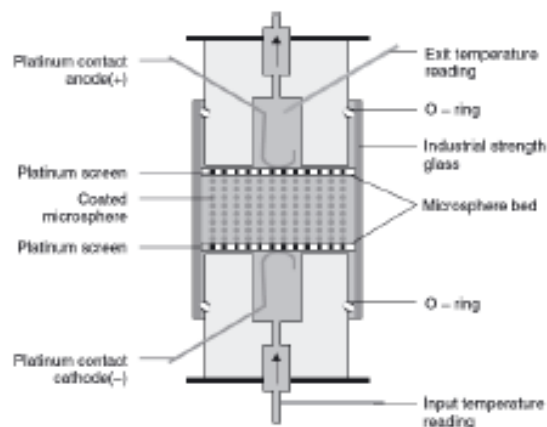


Figure 2. Schematic of Patterson power cell.

containing 10 microspheres. In the case of Cu and Ag, NAA helped establish deviations of isotopic composition from their natural abundance values. NAA has the advantage that it circumvents the molecular ion interference problem. Since NAA typically gives an average value integrated over 10 beads, it averages out the significant bead-to-bead variations in the reaction product yields, which are known to be sensitive to the location of the microspheres in the packed bed.

The results confirmed the presence of a wide range of new elements in the post-run thin films. The reaction products had mass numbers ranging both below and above the atomic mass number of the host metal, spanning across the entire periodic table. Figure 3 is a smoothened out plot of the reaction product yields plotted against the atomic number (Z value) of the product elements. A characteristic four-humped yield spectrum is evident with humps occurring at $Z = 6-18$ (peak at Mg–Si), $Z = 22-30$ (peak at Fe–Zn), $Z = 44-50$ (peak at Ag–Cd), and $Z = 75-85$ (peak at Au). In some of the runs, as much as 40% of the initial metal atoms of the thin film coating was transmuted. Miley speculates that each of these groups of elements is derived from one of the main elemental components used in the construction of the cell such as sulphur, nickel, palladium, and platinum (which was the anode material).

SIMS results indicated that the isotopic composition of most of the elements showed substantial deviation from natural abundance, whereas data of the control beads corresponded to natural isotopic ratios only. NAA data for Ag and Cu also confirmed significant deviations from natural abundance. It was however not possible to discern any systematic in the isotopic shift results, since there was considerable scatter in the cathode bed.

Miley's papers have also discussed the differences in yield spectrum between different base metal coatings, differences in product yield between plastic beads and glass microspheres and differences between H_2O runs and D_2O runs. The similarity of this four humped yield curve with the well-known double-humped yield curve observed in neutron induced fission has led to speculation that there could be an analogous proton or deuteron induced fission of the compound nucleus formed between a host metal nucleus and one or more protons or deuterons in LENR configurations.

Inspired by Miley's findings reported at the First International Conference on Low Energy Nuclear Reactions held at College Station, Texas, in June 1995, Mizuno of Hokkaido University, carried out a systematic analysis of his post-run Pd cathodes that had earlier been electrolyzed in heavy water solutions and to his pleasant surprise also found a four humped yield spectrum similar to that of Miley (see Fig. 4). Mizuno has elaborated on the details of his transmutation quest both in his book [10] as well as a recent review paper [11].

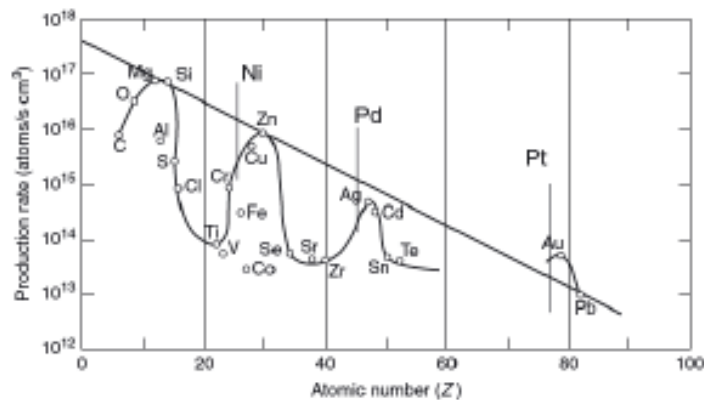


Figure 3. Reaction product yield vs. atomic number (Miley).

5. Deuterium Gas Permeation (Iwamura)

Possibly the most spectacular of transmutation findings in the CF/LENR field are those of Yasuhiro Iwamura and his colleagues at the MHI Laboratories in Japan who have been systematically studying the nuclear products formed during the loading and diffusion of deuterium in single and multilayer nano-structured Pd foil complexes, for close to two decades. Suspecting that impurities could play an important role in the nuclear processes, Iwamura incorporated CaO in the form of alternate layers of CaO and Pd in a multilayer foil complex. CaO was selected because of its low work function [12]. In an early experiment they mounted such a multilayer foil complex at the bottom of an electrolytic cell and evacuated the chamber underneath the cell to promote diffusion of deuterons towards the outer evacuated face. Subsequent post run examination of the inner (electrolyzed) face showed the presence of large amounts of Ti

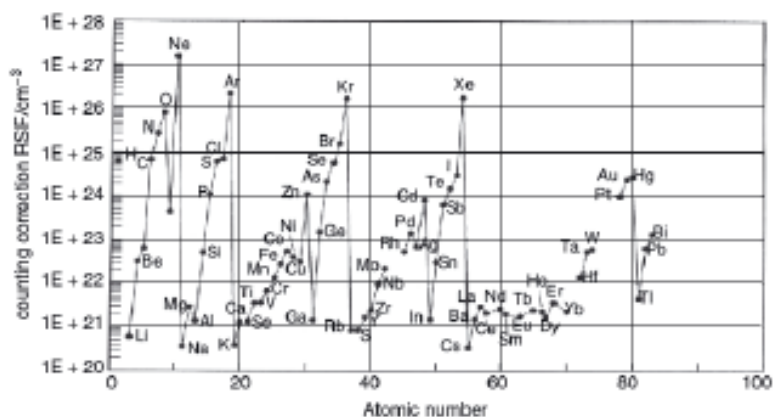


Figure 4. Yield of elements formed on Pd surface (Mizuno).

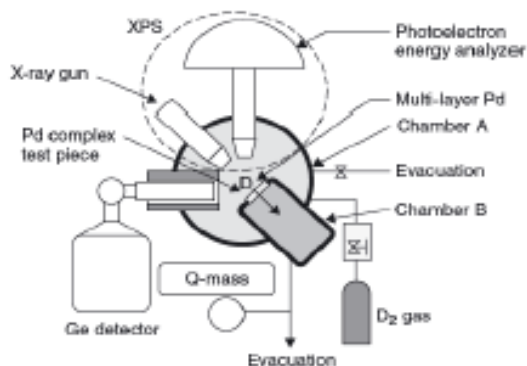
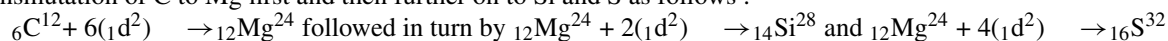


Figure 5. Iwamura's gas diffusion apparatus.

and ($\text{Fe}^{57}/\text{Fe}^{56}$) ratios as high as 1.8 in selected spots, compared to the ratio's natural abundance value of 0.023. This surprising finding set the stage for Iwamura's long "Transmutation journey".

Having experienced the advantage of vacuum assisted permeation, they reverted back to pure gas loading, incorporating instrumentation which enabled *in situ* elemental analysis (using XPS) and measurement of isotopic ratios (using SIMS) without having to take the sample out for analysis, thereby eliminating the possibility of contamination.

Figure 5 is a schematic diagram of the apparatus used by them in most of their subsequent investigations. In one of their first experiments with this set up they observed carbon as an initial impurity on the surface prior to filling D_2 gas in the chamber, a phenomenon well known to those handling vacuum systems. But it was what they observed after D_2 gas permeation over a period of a few days that surprised them. They had obtained evidence [13] for the sequential transmutation of C to Mg first and then further on to Si and S as follows :



In these experiments some nuclides present on the surface appear to be absorbing deuterons in pairs of 2 or multiples thereof such as 4 or 6. Such multiheavy ion nuclear reactions have never been observed even in the most advanced

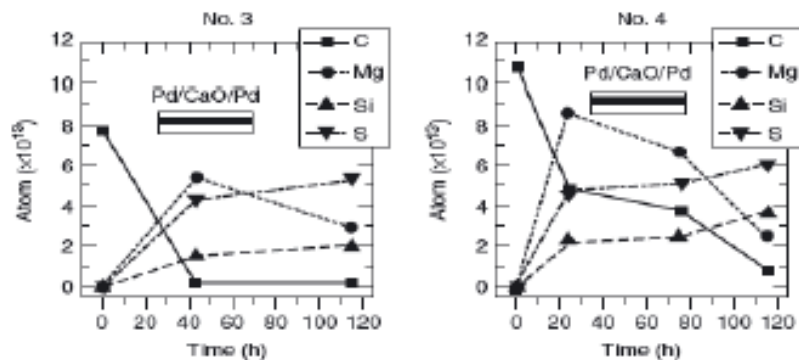


Figure 6. XPS measurement of time dependence of C, Mg, Si, and S on surface of multilayer Pd samples.

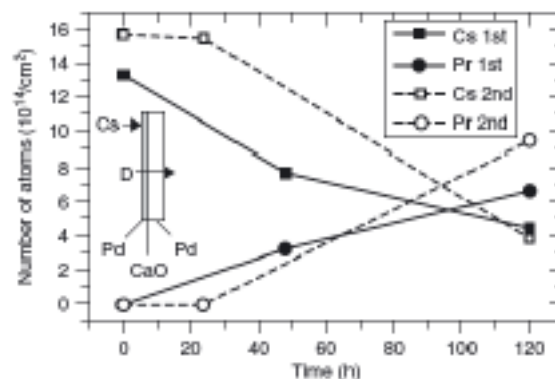


Figure 7. Variation of Cs and Pr concentration.

nuclear physics laboratories elsewhere, let alone the fact that this unbelievable reaction seems to be taking place during the simple act of deuterons diffusing through a foil complex, that too at room temperature (actually they found keeping the foil complex at a slightly higher temperature helped deuteron diffusion rate).

With a view to further confirm occurrence of such multi deuteron capture transmutations, in the next step they deposited a thin layer of a test element on top of the multilayer complex and followed the progressive formation of new elements and isotope species during the D_2 permeation, over a period of 1 or 2 weeks, through periodic *in situ* measurements, using XPS and SIMS.

In the first of such “designed transmutation” studies they coated ${}^3\text{Li}^7$ as a dopant on the surface and observed the production of ${}^9\text{F}^{19}$ following capture of six deuterons which then went on to become ${}^{13}\text{Al}^{27}$ following a further capture of four more deuterons. In a subsequent series of experiments [13] they studied the conversion of ${}^{55}\text{Cs}^{133}$ to ${}^{59}\text{Pr}^{141}$ following four deuteron captures. This is brought out in Fig. 7.

In a recent overview [14] of their two decade long pursuit of LENR transmutations, Iwamura has placed his findings in perspective. He confesses that he still does not understand why exactly addition of CaO (or Y_2O_3) works but not MgO and why such multideuteron captures work mostly only with intermediate layer coatings of alkali and alkaline earth elements and not others.

6. Biological Transmutations

In the 1960s a book was published [15] by a French medical doctor titled “Biological Transmutations” which summarized the results of a number of prior experiments conducted over the previous couple of centuries that seemed to suggest that elemental (nuclear) transmutations do occur in plants and animals and even human beings. Of course the techniques for analysis of elemental composition of substances in those days were rather crude and as such the scientific community did not take the claims of Biological Transmutation seriously. With availability of improved analytic methods, evidence for this Biological phenomenon has continued to be reported. Since the cold fusion era began many such papers have been presented at various ICCF series conferences, especially on the topic of Microbial Transmutation. In recent years with mass spectroscopic instrumentation becoming more commonly available, isotopic anomalies in Biological Transmutation experiments have also been published. During the last decade Vladimir Vysotskii of Keiv, Ukraine, has conducted a series of systematic measurements carrying forward the field from where Kervran left it. The most impressive of Vysotskii’s recent work reports on the transmutation of radioactive Cs^{137} to stable Ba^{138} using microbial colonies in light water based cultures. Due to space restriction we are however unable to discuss more about Vysotskii’s

work here and refer interested readers to his review paper published in the ACS LENR Source book Vol. 1 [16] and his book published in 2009 [17].

Biberian has recently published a review article [18] and a book in French [19] on the historical evolution of “Biological Transmutations”.

7. Conclusions

In this brief overview we could discuss the work of only about half a dozen researchers, but there are many more. We selected examples each from glow discharge, electrolysis, gas loading and biological transmutation. Almost all the results reveal a pattern of essentially similar behavior :

In all the experiments the newly found elements or isotopes appear to be explainable through occurrence of multiple deuteron captures in one or more of the isotopes of the high-Z elements in/on the cathode, followed by fission of some of the complex intermediate compound nuclei.

In Iwamura’s D₂ permeation runs, 2, 4 or 6 deuterons are absorbed by certain test elements deposited on the surface, during the simple act of diffusion. (However Iwamura has not reported observing any evidence for occurrence of fission following multiple deuteron captures.)

All the results, clearly point to the phenomenon occurring mostly in highly localized spots. Russian investigators have suggested that these spots appear to be associated with grain boundaries, in the case of bulk metal electrodes. Several researchers have observed microcraters on the surface and along whose rims transmutation products are found.

Although the best results are obtained with Pd and D, glow discharge experiments show that other combinations of cathode material and fill gas environments also seem to support such transmutation reactions.

The question arises as to whether these transmutations are merely an “academically interesting side show” in the overall field of CF/LENR or do they play a central role in macroscopic (industrial) scale energy production? While in PdD systems Helium appears to be the main nuclear product, in the case of Ni–H systems the question is still open. Miley had earlier suggested that transmutation products are most likely the source of excess heat in their thin film cathode light water runs. Similarly Karabut and Savvatimova started looking for transmutation products primarily because neutrons, tritium and helium could not be detected in quantities commensurate with the observed excess heat in their glow discharge runs. Andrea Rossi has recently gone on record to state that transmutation of Ni to Cu is the source of nuclear heat in their Ni–H devices. Reliable experimental data from analysis of spent Ni fuel powders is keenly awaited to settle this question.

Vysotskii’s microbial transmutation experiments are the only reliable measurements to date wherein radioactive nuclei have been transmuted to stable nuclei, to the best of this authors knowledge, although there were many experimental attempts and claims of electrolytic remediation of Thorium radioactivity in the mid-1990s.

The occurrence of transmutation reactions in simple LENR configurations has however a more profound implication, namely it questions a 300 year old “dogmatic belief” of Science, prevalent from the days of Lavoisier, that one cannot transmute one element into another in any simple laboratory experiment, no matter what you do, such as heating, cooling, applying pressure, passing a current, etc., other than by bombarding the target nuclei with nuclear particles such as neutrons or high energy alpha particles or using particle accelerators.

These results are clearly suggesting that the age old claims of Alchemy may perhaps be true after all, however unpalatable it may be to the Scientific community [20]. In this context it may be worth mentioning that at least two groups [21,22] of LENR researchers have during the last one year come up with exploratory proposals to manufacture rare and valuable stable elements including gold, deploying LENR based processes.

References

- [1] M. Srinivasan, G.H. Miley and E. Storms, *Low Energy Nuclear Reactions: Transmutations*, Chapter 43 in *Nuclear Energy Encyclopedia*, Wiley, New York, 2011
- [2] M. Srinivasan, G.H. Miley and E. Storms, *Low Energy Nuclear Reactions: Transmutations*, <http://lenr-canr.org/acrobat/Srinivasanlowenergyn.pdf>, 2011.
- [3] G.H. Miley and P.J. Shrestha, Overview of light water/hydrogen-base low energy nuclear reactions, *Proc. 12th Int. Conf. on Cold Fusion*, A. Takahashi, K. Ota and Y. Evamura (Eds.), Yokohama, Japan, November 27– December 2, 2005, World Scientific, Singapore, 2006, pp. 34–43.
- [4] G.H. Miley and P.J. Shrestha, Transmutation reactions and associated LENR effects in solids, in *Low Energy Nuclear Reactions Sourcebook*, J. Marwan and S. B. Krivit (Eds.), American Chemical Society, Washington, DC, Oxford University Press, Oxford, 2008.
- [5] E. Storms, *The Science of Low Energy Nuclear Reaction*, World Scientific, Singapore, 2007.
- [6] A.B. Karabut, Analysis of experimental results on with high current glow discharge, *Proc. 8th International Conference on Cold Fusion*, F. Scaramuzzi (Ed.), May 21– 26, 2000, Lerici (La Spezia), Italy, Italian Physical Society, Bologna, Italy, 2000, pp. 329–334.
- [7] A.B. Karabut, Excess heat power, nuclear products and X-ray emission in relation to the high current glow discharge experimental parameters, *Proc. 9th Int. Conf. on Cold Fusion*, X. Z. Li (Ed.), May 19–24, 2002, Beijing, China, Tsinghua University Press, Beijing, China, 2002, pp. 151–154.
- [8] I.B. Savvatimova, and D.V. Gavritenkov, Influence of the parameters of the glow discharge on change of structure and the isotope composition of the cathode materials, *Proc. 12th Int. Conf. on Condensed Matter Nuclear Science*, Nov. 27 to Dec. 2, 2005, Yokohama, Japan, World Scientific, Singapore, 2006, p. 231.
- [9] G.H. Miley et al., Quantitative observations of transmutation products occurring in thin film coated microspheres during electrolysis, *Proc. 6th Int. Conf. on Cold Fusion*, Hokkaido, Japan, Oct. 13–18, 1996, M. Okamoto (Ed.), *New Energy and Industrial Technology Development Organization*, Tokyo, 1996, pp. 629–644.
- [10] T. Mizuno, *Nuclear Transmutation : The Reality of Cold Fusion*, Infinite Energy Press, NH, USA, 1998.
- [11] T. Mizuno, *Transmutation Reactions in Condensed Matter*, *Low Energy Nuclear Reactions Sourcebook*, Vol. 1, Marwan, J. and Krivit, S. B., (Eds.), American Chemical Society, Washington D.C, Oxford University Press, Oxford, 2008.
- [12] Y. Iwamura, T. Itoh and M. Sakano, Nuclear products and their time dependence induced by continuous diffusion of deuterium through multi-layer palladium containing low work function, *Proc. 8th Int. Conf. on Cold Fusion*, May 21–26, 2000, Lerici, Italy, *SIF Conf. Proc.*, 2000, Vol. 70, pp. 141–146.
- [13] Y. Iwamura, et al., Observation of low energy nuclear reactions induced by D₂ gas permeation through Pd complexes, *Proc. 9th Int. Conf. on Cold Fusion*, Beijing, 2002, pp 141–146.
- [14] Y. Iwamura et al., Observation of low energy nuclear transmutation reactions induced by deuterium permeation through multilayer Pd and CaO thin film, *Electronic J. Condensed Matter Nucl. Sci.* **4** (2011) 132–144.
- [15] L.C. Kervran, *Biological Transmutations*, Swan House Publishing Co., New York, 1972.
- [16] V.I. Vysotskii, A.B. Tashyrev and A.A. Kornilova, Experimental observation and modeling of Cs 137 isotope deactivation and stable isotopes, *Proc. ICCF 9, Beijing*, transmutation in biological cells, in *American Chemical Society Sourcebook*, Vol. 1, Oxford University Press, Oxford, 2008, pp. 295–303.
- [17] V.I. Vysotskii and A.A. Kornilova, *Nuclear Transmutation of Stable and Radioactive Isotopes in Biological Systems*, Pentagon Press, New Delhi, India, 2009.
- [18] J. P. Biberian, Biological Transmutations : Historical Perspective, *J. Condensed Matter Nucl. Sci.* **7** (2011) 11–25.
- [19] J.P. Biberian, La fusion dans tous ses états: *Fusion Froide, ITER, Alchimie, Transmutations Biologiques*, Guy Trédaniel, 2012.
- [20] R. A. Monti, Low energy nuclear reactions: the revival of Alchemy . *Proc. Int. Conf. Space and Time*, St. Petersburg, Russia, 2001, p. 178.
- [21] Lattice Energy LLC, Commercializing a next Generation Source of Valuable Stable Elements, Unpublished Report, May 19, 2012.
- [22] E. Esko and Alex Jack, *Cool Fusion, A Quantum Approach to Peak Minerals and Nuclear Waste*, Amber Waves, Becket, MA, USA, Second Edition, June 2012.



Research Article

Sonofusion's Transient Condensate Clusters

Roger S. Stringham*

4124 Kapuna Rd. Kilauea, HI 96754, USA

Abstract

D₂O cavitation produces Z-pinch jets implanting a target lattice. Measurements, data interpretations, and FE SEM photos explain products heat and ⁴He produced in target foils. The picosecond dynamics of a deuteron electron plasma charge separation and pressure pulse produce alpha particles and heat.

© 2014 ISCMNS. All rights reserved. ISSN 2227-3123

Keywords: Cavitation, Condensate, Deuteron, Image

1. Introduction

Over twenty years of work including thousands of experiments have contributed to the explanation of the puzzling and disjointed aspects of sonofusion technology. Using new analytical techniques and data interpretations gives a fresh look at sonofusion processes at a megahertz frequency. Among the resolved problems was the target foil destruction associated with kilohertz low frequency problems. As time passed it appeared that BECs in the form of nuclear condensates would lead to paths that resolved some major problems [1–3]. The excess heat (Q_x) was not accompanied by any long-range radiation products. The high densities required to produce the products of alpha particles and heat in sonofusion are similar to the densities of muon fusion. Conditions found in astrophysical steady state systems can be drawn from to help explain what is a very transient terrestrial environment. It might be expected to exist in a picosecond timeframe culminating in a single alpha particle event per implanted cluster. During some sonoluminescence (SL) measurements a new technique was developed for counting photons in the MPPC energy range by the manipulation of the device's saturation mode.

2. Review

Sonofusion in the megahertz range uses a 20 mm disk piezo driving the D₂O cavitation bubble process. The red acoustic wave amplitude, Q_a , P^+ to P^- , finds a resonant bubble, blue R_i bubble, Fig. 1. Within this μs cycle, the bubble grows to R_o , then violently collapses to R_f , dark blue. The emitted photon pulse, SL, shown in green, originates from many R_f

*E-mail: firstgate@earthlink.net

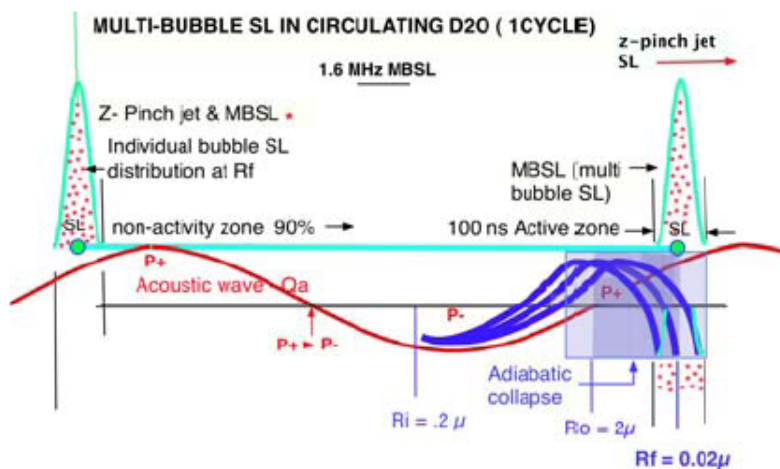


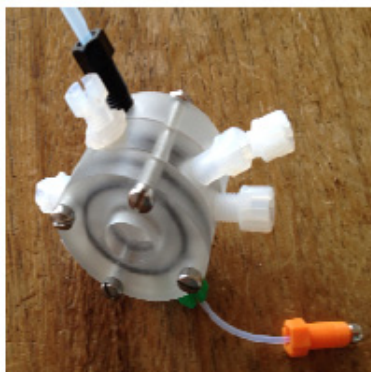
Figure 1. The megahertz D₂O cavitation bubble cycle and violent adiabatic collapse, blue, noted by a 100-fold change in radius, produces Z-pinch jets with SL plasma, green. Z-pinch jets implant the target foil producing DD fusion.

bubbles (10^3 – 10^5), red stars [4–9]. To maximize the SL's photon count and the high-density Z-pinch D⁺ jet intensity, one adjusts the acoustic power input, Q_a . During a 1.6 MHz cycle in the 100 ns active zone, the SL emission pulse and the Z-pinch implantation jets are distributed into a target foil. Over 90% of the cycle is without of any activity. The SL emission shows a 100 ns time period of implant activity when transient charge separated deuteron clusters are produced. An expanded view using the larger knowledge base of low frequency resonant bubbles, 20–46 kHz, in H₂O and D₂O studies is extended to the higher megahertz frequency of the D₂O bubble systems [4,5].

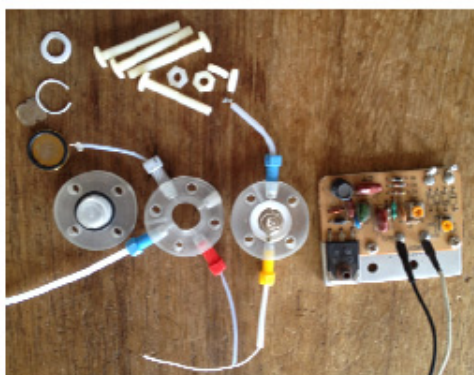
These systems require control over the parameters of temperatures, pressure, and acoustic input. The general piezo bubble mechanics holds for all frequencies studied. The same bubble mechanics should hold for frequencies up to 20 MHz. These higher frequencies systems have the following advantages: they are easier to study; more economical; they produce less damage to target foils; and they produce the same energy density in smaller and more numerous bubbles. Coincidental to the SL emission is the Rf bubble formation of a Z-pinch jet that is located close to the surface of the target foil lattice. The jet is a partial plasma that is squeezed by sheath electrons accelerating and squeezing the jet's contents to higher densities before implanting into the lattice. The jet formation from bubbles is well known, and damage to water handling mechanical devices like pumps and propellers is common.

3. Experimental

The megahertz cavitation experiments were carried out in a black felt lined light-proof box 0.4 m on a side, with a fan circulating air through the totally dark experimental system so that the SL could be monitored. SL was a tool, a method of photon monitoring of the plasma character of the collapsed cavitation bubble's target implanting Z-pinch jet. The three parameters controlling SL and cavitation were; the temperature of the D₂O in the reactor, the argon pressure over the circulating D₂O, and the acoustic power, Q_a . It was important to keep the acoustic megahertz piezo polycarbonate reactor cool at its resonance. This is accomplished with the circulation of D₂O. Small changes in the temperature were accommodated using a feedback type acoustic oscillator that sensed and adjusted to changes in the natural resonating frequency of the reactor. Input power (Q_i) was measured by a 0–100 W wattmeter from Ohio Semiconductor, where $Q_a = 0.3 Q_i$. The 20 cm³ of circulating D₂O via a 6 mm FMI displacement pump operated at a flow rate of 1.02 g D₂O/s.



2(a)



2(b)

Figure 2. (a) The 1.6 MHz reactor. (b) The disassembled reactor and Q_a oscillator, Pd target foil is third object from bottom, left corner. It was clamped together with Nylon or stainless steel bolts.

The tubing was 1.5 mm stainless steel and fluorinated ethylene polymer. They were used as reactor connections for D_2O , argon gas, electrical acoustic ports, and 0.07 mm diameter K-type thermocouples (TCs). These connections were completed at the polycarbonate reactor, with 6 mm tapped Omnifit fittings, Fig. 2(a). Temperature data was collected every second. In the pump's D_2O circulation path was a 1.5 m \times 1.5 mm stainless steel coil tube heat exchanger in 2 L of water and a sintered stainless steel 10 μ m filter that removed particulates. Next in the flow path was the TC used to measure D_2O_{in} at the reactor inlet. The cavitation residence time of D_2O in the reactor was about 1 s. The TC measurement at the reactor outlet monitored D_2O_{out} . The other TC was located at the bottom as the D_2O_{in} flow entered, completing the ΔT measurement. As the flow continued it passed through a visual flow meter, from K/E, with a 100 cm³/min maximum. From there the D_2O passed to a 50 cm³ stainless steel and Pyrex bubbler that was connected to a vacuum line that managed the fluids and gases. In the bubbler was 20 cm³ of argon saturated D_2O that circulated to the pump, completing the D_2O cycle. Figure 2(a) shows the disassembled 1.6 MHz reactor and the acoustic oscillator.

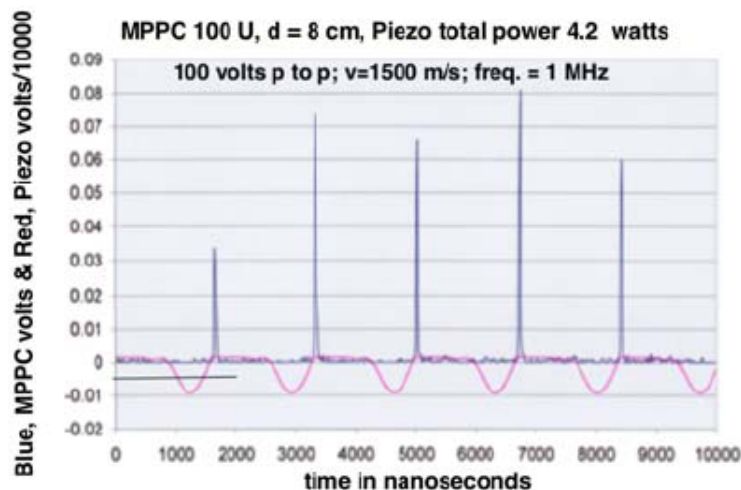


Figure 3. Measurements of SL MPPC differences between blocked and unblocked photons were made, blue trace. The MPPC was located 8 cm from the megahertz reactor. The red trace is a 100 V MHz acoustic wave the Q_a input, note the coupling of SL to Q_a . The SL trace in Fig. 1 green trace of 100 ns SL photons. Only in 100 ns was there any activity.

3.1. SL and photon counting

The acoustic input (Q_a) of 1–16 W powered the piezo at a megahertz frequency and was monitored by channel 1 of the oscilloscope. The photon counter, Multi Pixel Photon Counter, MPPC S510362-11 series from Hamamatsu, with a millivolt output was monitored by channel 2. The DC volt input to the MPPC was from a HP 6634A power supply. The MPPC device had a photon counting area of 1 mm² that was placed 8 or 16 cm from the reactor window. The MPPC outputs were frequency and pressure coupled shown in Fig. 3 in blue and red. It took many runs to establish the separation of MPPC dark current from the SL photon emission.

There was no radio frequency (RF) interference in the difference measurements (MPPC open-beam SL minus blocked-beam SL) of the SL photon count. The D₂O photon intensity was 10⁹ per cycle and more diffuse than single bubble SL. It has an order lower intensity than H₂O, and was not visible to the naked eye [9].

3.2. Piezos, Z-pinch jets

The favored 1.6 MHz piezos, run at 50 W from the wall, Q_i , rather than the 20 kHz at 600 W Q_i , and they produce in 10⁴ smaller volume 100 times more bubbles, which have the same energy density of the low frequency systems. The bubbles collapse adiabatically producing the dissociated plasma of D₂O. At the collapse at Rf, SL and a Z-pinch jet are produced, Fig. 1. The velocity of the Z-pinch jet's sheath electrons generates a magnetic compression, a Z-pinch. The magnetically compressed Z-pinch jet transmits the dense plasma, implanting deuterons and free electrons into the target lattice forming the concentric condensates that will be shown later. Coincident with the Z-pinch jets is the SL monitored with a MPPC and suggests the condition of the plasma via SL photon intensity.

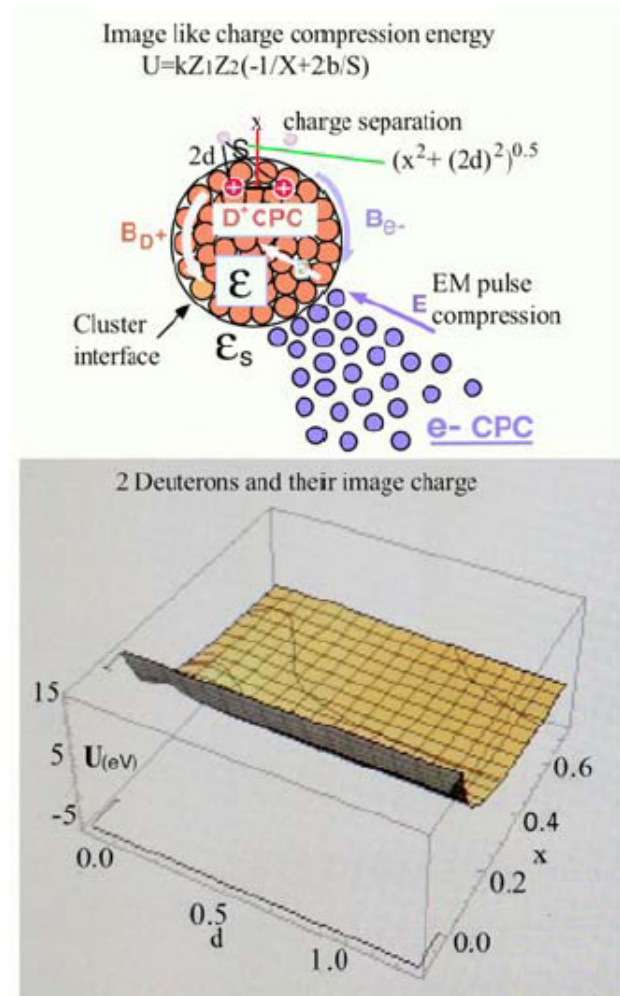


Figure 4. Top is the cluster implosion image and EM pulse energy of the 2 concentric charged particle condensates that form the 2 concentric condensates of D+ and $2e^-$. Blue balls represent Cooper Pairs and orange balls, deuterons. The cluster's unit image is formed of the 2 D+ red balls, and across the interface are the 2 D+ violet image balls of the electron condensate. The d, in Å, is the interface distance to the D+ image charge, pink ball, and to the D+, red ball. The image-charge particle separation x, in Å, between 2 deuterons, red balls, is squeezed during the concentric condensate implosion [1]. Altogether they form the geometry of the image charge attractive energy of deuteron separation. Bottom shows the beginning implosion of particle closing separation energy $U_{(eV)}$. The fusion squeeze is a picosecond event. Apply the image units to $n = 10^2$ pairs that make up the total spherical interface system. Blue and white arrows show the EM E field compression. The EM B fields, white and blue arrows, tend to cancel.

3.3. Cluster EM compression pulse

The EM driven implosion of the sub-nanometer deuteron cluster is represented as a spherical cluster of high density orange balls, Fig. 4, with a surface interface area of $4\pi r^2$ squeezed by an equally high density of free electrons. The

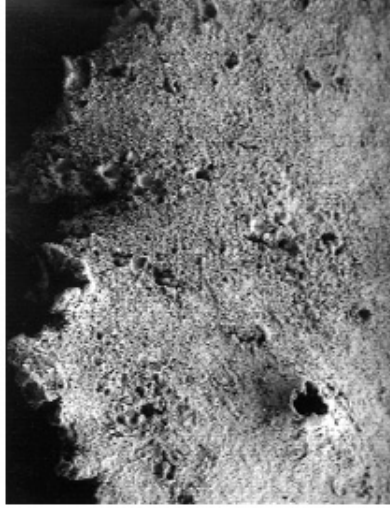


Fig. 5(a)

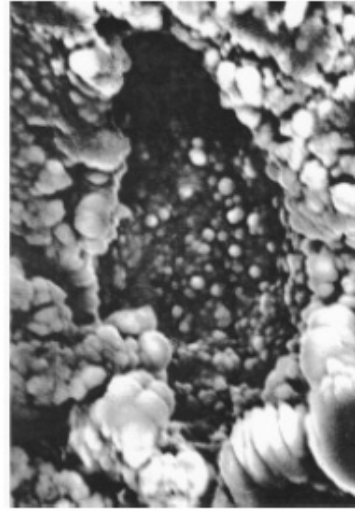


Fig. 5(b)

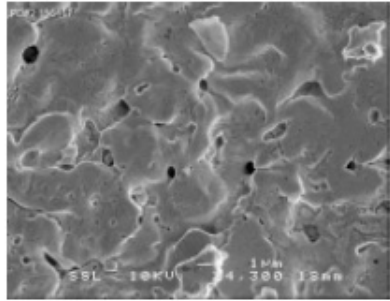


Fig. 5(c)

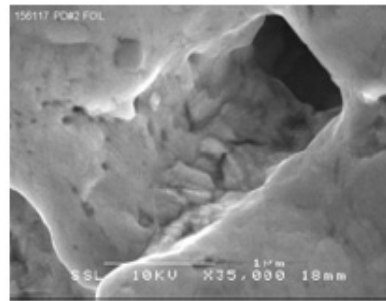


Fig. 5(d)

electrons, violet balls, spherically surround the deuteron cluster, and at these extreme densities will likely be coupled as Cooper Pairs, bosons [2]. These densities will form a free electron condensate phase that squeezes the interface surface with coulombic plasma pressure power. For a time period of less than a picosecond these particles move towards their common center. The EM pressure power pulse increases to values in spherical symmetry equivalent to those spatial separations in the muon molecular ion. The density is high enough to allow for one destructive fusion event, and this is what is measured in ejecta sites. See FE SEM photos of Fig. 5(e). The high density picosecond electron electromagnetic pressure power pulse, EM, at the cluster interface $k\Sigma q_1 Q_2 / r^4 \text{sec}_1$ is the squeezing pressure power, where q_1 is 1 electron, Q_2 is D+ cluster, r is the interface radius, and k the constant for SI units. Opposing this squeezing pressure power is the Coloumb repulsion pressure power at the interface $k\Sigma q_3 (Q_2 - q_3) / r^4 \text{sec}_2$, where q_3 is a D+. The ratio is $\text{sec}_2 / \text{sec}_1$ equals 10^{12} more pressure power at the interface during the interface compression.

There is no chemical activity at the interface as it is too hot and fast for the deuterium atom formation. The deuterons and free electrons have the same compressing acceleration at the interface. The magnetic fields and forces are tangent to the interface and surround the cluster's compression space. These magnetic fields cancel at the interface, with equal

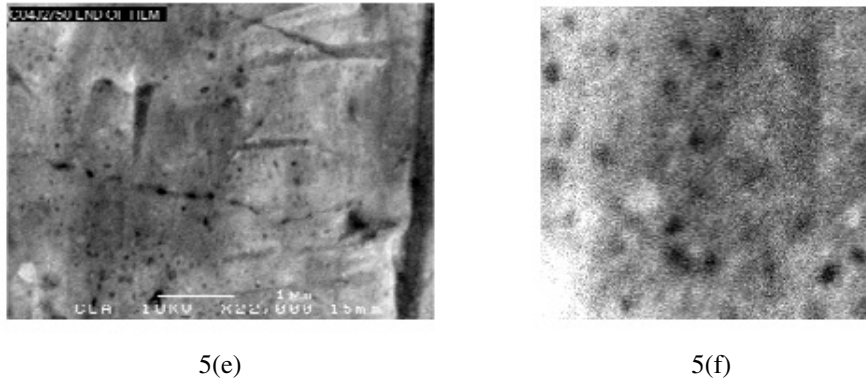


Figure 5. (a) SEM photo of a Pd target foil with multi-size ejecta sites; frequency of 20 kHz; scale 0.5 mm = 10 μ . (b) SEM photo of an ejecta site detail of 5a; scale 1 mm = 1 μ . Photos by John Dash. SEM photo of a Pd target foil with multi-size ejecta sites; frequency of 46 kHz; scale 1 mm = 1 μ . (c) SEM photo of a Pd target foil with multi-size ejecta sites; frequency of 46 kHz; scale 1 mm = 1 μ . Detail from 5c SEM photo; scale 1 cm = 1 μ . Photos by Jane Wheeler. (d) Detail from 5c SEM photo; scale 1 cm = 1 μ . Photos by Jane Wheeler. (e) SEM photo of a Pd target foil with a single size ejection site; 1600 kHz sites; scale 0.5cm = 1 μ . (f) A 1 square μ m detail from 5e SEM photo showing ejecta sites of single DD fusion events ◇ about 20 MeV; scale, one ejecta site = about 50 nm in diameter. Jane Wheeler.

compression collapse velocities. The E fields, green and blue, from the imploding deuterons and electrons are additive. The picosecond EM pulse at the interface is compressed by an increasing like-charge cluster compressing pressure at the interface, but is eventually overcome by the increasing repulsive pressure. The EM pulse reaches the critical fusion density before the pressure pulse collapse. The adiabatic compression heating of the cluster is reduced by the loss of surface deuterons, evaporative cooling. This adds to the momentum of the cluster's implosion. This cooling gives the deuteron condensate more stability during compression. As the pulse compresses the cluster, a fusion environment is reached; fusion occurs and the cluster's particles revert back to D₂O. The ejecta carry the Q_x and ${}^4\text{He}$ into the D₂O circulation. For a cluster originating from $n_{\text{D}_2\text{O}}$ equaling 10,000 D+ the recombination energy is 0.007 that of a single 24 MeV fusion event. Note this when looking at ejecta sites (Fig. 5(f)).

3.4. Image charge of two deuterons and CP

At the accelerating interface both D⁺ and e⁻ accelerate together to the center of the cluster. Residual concentric spherical magnetic fields with the same center are sandwiched at the interface between two condensates in compression [1,2], with a large difference in their respective permittivity, ϵ . The image-charge system provides an alternate mechanism to the EM pressure power pulse for reducing deuteron separations. Under the conditions of high density, charged particles across an interface of a large ϵ g differences, these like-charge particles become attractive. The implanted imploding clusters consist of two concentric BECs Cooper Pairs (CP) and deuterons. These two particle groups have relative permittivities proportional to their mobility across their mutual surface interface, Fig. 4. top. The electron cluster has a relative permittivity of ϵ_s . The imploding accelerating interface of the deuteron BEC has a permittivity ϵ . At the interface, between the two condensates, the ϵ_s/ϵ ratio of the relative permittivities is 10³ based on their relative mobilities. The image charge system's permittivity factor $b = (\epsilon - \epsilon_s)/(\epsilon + \epsilon_s) = -1$ (see Lawandy's description [1]). The effective squeeze range for b is from -0.5 to -1.0, with -1 giving the maximum effect. This sonofusion system's b is close to -1.0, and provides an excellent environment for the deuteron's attractive image charge energies to reduce deuteron separation x as d diminishes below Å levels. The cluster's particles are arranged as onion-skin d layers, from the interface to the center (five layers of deuterons, $n = 10^2$). A collective application of $n = 10^2$ of paired

like-charges produces $U(x)$ in eV. When $b = -1$, it shows the mechanics of reduced separation x of like-charge image energies in the deuteron cluster in the sub-picosecond range. $U(x)$ is 15 eV and increasing. A picosecond duration at these densities is a satisfactory period for DD fusion to occur. The number of fusion events is measured by the survey count of ejecta sites shown in SEM photos in Fig. 5(f).

3.5. The nuclear and electron condensate environment

These condensates in this case are different, and not like the more often discussed condensate of cold Boson atoms. The cluster is a self-focusing layered spherical collection of Bosons, deuterons and CP, Fig. 4. For a picosecond there are no associated electrons inside the interface of the cluster during the EM pressure power pulse. The cluster is expected to have the properties of a deuteron nuclear Boson condensate cluster. The cluster is squeezed by the exterior CP condensate, as the separation between fm sized charged deuteron particles is decreasing. The two concentric condensates have very high critical temperatures, T_c , across their interface [3].

The uniqueness of the D+ condensate character is outlined here. The deuterium atom, after removal of its one e^- , is a single charged boson nucleus and is unique in the family of particles at 2.14 fm. Its nucleus is the most easily dissociated. The deuteron has only one measured energy level, its ground state, E_0 . The deuteron has a large $E_1 - E_0$ energy level separation greater than its dissociation of 2.23 MeV and supports a high T_c of millions of degrees. A picosecond environment of compressing condensates produces DD fusion events with no measurable radiation products. The energy levels are nuclear, not chemical. Experiments show that sonofusion's Q_x cluster dynamics is the sum of the DD fusion events at a rate of 10^{13} per second that is also the sum of the frozen target cluster ejecta site count, Fig. 5(e). The two deuterons and CP, are separated and compressed at the cluster's spherical interface. The residual of opposite and tangent magnetic fields generated by the separated charge movement to their common center, Fig. 4, are excluded from the condensates. The canceling magnetic fields at the interface are compatible with the condensate's Meissner exclusion. The BEC compression heating from within the deuteron cluster looks for relief through a cooling mechanism presented as the evaporation of deuterons from the cluster interface [9]. This flow of mass also provides momentum compression, and may progress to the point of less than 100 remaining deuterons in the deuteron cluster for the single DD fusion event per cluster at a megahertz frequency.

3.6. The DD fusion in the cluster

The deuteron cluster's compression movement during a picosecond approaches 10^{-12} m or closer, a separation that is similar to that of muon fusion [1,2]. The DD fusion has the time and the density (separation) for a product path to ^4He and Q_x . The immediate rate-energy transfer in the deuteron CP condensate as the Q_x , the heat of fusion in a disrupted cluster, quenches the potential for a 24 MeV gamma. The mechanism is too slow (in the range of one gamma photon oscillation, 10^{-22} s). The target foil's SEM photos show, at these megahertz frequencies, that the DD fusions are single events and leave ejecta sites as their footprint [4,8]. The measurement of target foil severity of damage is related to the piezo acoustic driven frequency. The information gathered from SEM photos of target foil damage at the low frequency of 20 and 46 kHz shows extensive foil damage from multiple fusion events. Some larger $10\ \mu\text{m}$ ejecta sites from the low frequency piezos show many sub-micron spheres of recondensed vaporous target foil in the ejecta cavity, and few single fusion events. The megahertz exposed foils in Fig. 5 show a trend to much less target foil damage and many more eject sites, all of the same energy. The energy on the megahertz exposed foils showed these sites, Fig. 5(f), are 20 ± 10 MeV ejecta sites, with a single event of one alpha particle per cluster [9].

3.7. Acoustic frequency effect

The measurement of target foil damage severity is related to the piezo acoustic driven frequency. The lower the frequency the more severe the target foil damage. The information gathered from SEM photos of target foil

3.8. Cluster's ejecta site at low frequency

The cluster's single DD fusion event is generated during the picosecond after the Z-pinch plasma implantation of deuterons and electrons. Fusion products and debris are ejected into circulating D₂O. The ejecta site size and depth are shown in the SEM photos, Fig. 5 [4]. A survey of the size distribution of ejecta sites in the Pd target foil exposed to 46 kHz of cavitating D₂O are shown in Fig. 6. The single events are few, and quite different than the megahertz system, and are surveyed in the 1 μ m square at three times the resolution, lower left in Fig. 6. The larger SEM field of ejecta site damage represents thousands of DD fusion events.

3.9. Data, heat (calorimetry) and ⁴He

The 1.6 MHz reactor flow-through calorimetry using K-type thermocouples measured $T_{\text{out}} - T_{\text{in}}$, ΔT , of the circulating D₂O. And an in-line flow-meter measured the D₂O mass-flow/second. The low mass of the reactor at half the mass of the D₂O flow per minute is an advantage. The ΔT_x (D₂O flow in g/s) \times 4.184 = watts out (Q_o). Q_a is the measured acoustic power input. $Q_o - Q_a = Q_x$ and is the heat of fusion for the reaction $2D^+ = \alpha + 23.8$ MeV and equals mc^2 (the mass deficit as heat not a gamma ray). The graph Q_a versus Q_x indicates close to a linear relationship shown in Fig. 4. DOE mass spectral analyses of sampled gases circulating with the D₂O from a 20 kHz reactor after a 19 h run established the presence of ⁴He in an amount of 552 ± 2 ppm in their report [4,6].

4. Discussion

It is remarkable that sub-nanometer transient clusters will fuse when compressed as in Inertial Confined Fusion to produce fusion heat, Q_x , and ⁴He with no measureable neutrons or gammas. Sonofusion does that, and depends on

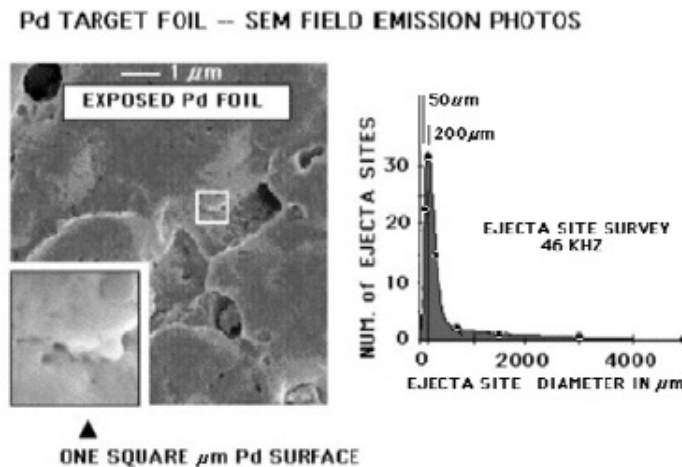


Figure 6. SEM survey of an exposed 46 MHz Pd target foil and the distribution of ejecta sites produced by DD fusion in cluster ejecta sites.

a picosecond spherical subatomic size cluster, 10^{-11} m, in a deuteron condensate cluster implosion where densities equivalent to those of muon fusion produce Q_x and ${}^4\text{He}$. Sonofusion energy production is focused just below the target foil lattice surface in clusters that produce ejecta sites. Experimental results can be expanded to explain other low temperature fusion technologies. The megahertz cavitation of argon gas saturated D_2O produces transient spherical condensate deuteron clusters that drive the cluster's interface like a spherical piston into the DD fusion mode. Condensates of deuterons and CP and their subtractive tangent magnetic fields, and their respective perpendicular additive electric fields form a spherically centered dipole pulse, Fig. 4. Both CP and deuterons, on either side of their common interface, accelerate to the cluster's center during the picosecond compression pulse. In these extreme high-density cluster compression environments of CP, two electrons will be favored over one. Some deuterons will ultimately fuse, destroying the cluster, and are identified by their FE SEM ejecta site photos and calculated energies, Fig. 5(e). The rest of the clusters will revert back to D_2O , a path thousands of times less energetic than the Q_x of a single fusion event. The cluster survey count extrapolates to $10^{13}/\text{s}$ of the 50 nm diameter ejecta sites per second (a survey estimate and also the calorimetry heat measurements) in a 1.6 MHz exposed target foil. The exposure indicates that less than 10% of a 1 cm^2 Pd-target foil is used and less than 10% of the time is actively involved. Each acoustic megahertz cycle destroys old sites as new sites are produced in the next cycle. Each ejecta site originates from a single 23.8 MeV fusion event, see Fig. 5(f). The number of ejecta sites is equivalent to the number of fusion events per second. The ejecta site count calculation is 38 W of Q_x , The measured calorimetric calculation is $57\text{ W} \pm 10\%$ for a $15.2\text{ W } Q_a$ input, shown in Fig. 7. The deuteron cluster's evaporative cooling, where interface surface deuterons are ejected through a mass of free electrons that are too hot to recombine until cool-off that is well beyond the interface. D_2O is the choice of cavitating liquids because of its recombination characteristics after the heat pulse. The deuteron spherical size is 2^+ fm and expands at recombination to an atom size of 2^+ \AA . Adding an electron to D^+ effectively removes heat from the cluster and adds compression and momentum from the surrounding exterior of the Pd lattice [9].

Nabil Lawandy [1] explains into cluster squeezing pressures via the accelerating CP– D^+ interface. The image-charge separation reduction of like-charge particles is the mechanism that produces fusion events. Compressive pressures result from large permittivity differences between free e^- as CP and D^+ cluster condensates across the interface depend on their relative mobility. Image-charge energies reduce deuteron separations that parallel other transient EM pressure pulses that coulombically squeeze the cluster's DD fusion probability into reality. The cluster's transient lifetime of a picosecond, with its small squeezed deuteron clusters, have densities close to $10^{36}\text{ D}^+/\text{m}^3$. The squeeze produces one

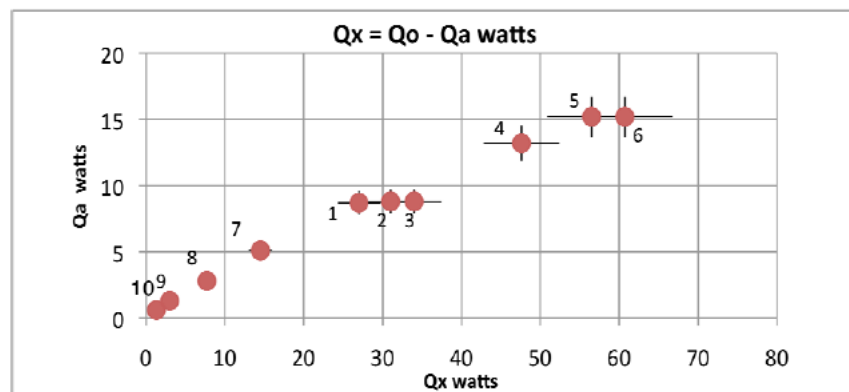


Figure 7. The megahertz Q_x flow-through calorimetry is shown in the time sequence of the acquired 10 data points [7].

fusion event per cluster in megahertz driven D₂O cavitation. The deficit energy, Q_x , will be dispersed from a nuclear D⁺ condensate as heat. A superconducting environment rejects any radiation mechanism.

The T_c measurements were made at intervals at the beginning of the off mode as the reactor piezo drive was programmed with a duty cycle of 120 s on and 120 s off. T_c measurements were made every second and were back calculated to the time of the start of the off mode to determine the ΔT and Q_o . This eliminated any possible radio frequency interference from the megahertz piezo during T_c measurements. The low mass reactor was close to steady state temperature after one minute of piezo running time. The total power in, Q_i was measured by 0–100 W power meter from an Ohio Semiconductor, $Q_a = 0.3 Q_i$, where Q_i was the measured total input power. The data was taken at different Q_a measuring the SL intensity and the watts out, Q_o , where $Q_x = Q_o - Q_a$ (see Fig. 7). The length of each series of runs was about 20 min at a measured acoustic power input, Q_a .

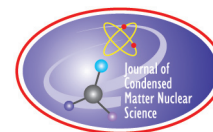
These small 20–50 g single unit megahertz sonofusion reactors, with a 2×20 mm piezo disk, can be ganged together to make any sized device. ⁴He in target foils will be stable for years, and can be analyzed for ⁴He content and stable isotope changes at any time. Sonofusion's energy future can be viewed as a high impact energy technology that may eventually replace the need for hydrocarbon based energy providers. D converts to non-polluting ⁴He and radiation free heat, Q_x . No long-range radiation products have been measured during experiments on a variety of target foils. The total calculated sonofusion energy, excluding Q_x , should not exceed the Q_a input. At 100 deuterons the value is 0.2 W, when Q_a is 15 W producing 10^{13} fusion events per second. Smaller clusters and higher megahertz frequencies show a promising future for sonofusion. This is a changing model for sonofusion.

Acknowledgements

Support of this work is in the form of moral support from my family and friends.

References

- [1] N.M. Lawandy, Interaction of charged particles on surfaces, *Appl. Phys. Lett.* **95** (2009) 234101-1-3.
- [2] H Abuki, T. Hatsuda and K. Itakura, Color superconductivity in dense QCD and structure of Cooper Pairs, NSF-ITP-02-45 hep-ph/0206043, 4 June 2002.
- [3] Masahito Ueda, *Fundamentals and New Frontiers of BEC* (World Scientific, Singapore, 2010). ISBN-10 981-283-959-3.
- [4] R. Stringham, Sonofusion, deuterons to He experiments, *ACS source book #2*, 2009, pp. 160–167.
- [5] R. Stringham, When bubble fusion becomes sonofusion, *J. Cond. Nucl. Sci.* **8** (2012) 1–12.
- [6] R.S. Stringham, Ti produces tritium that decays to helium 3, *CMNS, Proceedings 15*, Rome Italy, V. Violante and F. Sarto (Eds.), 5–9 Oct. 2009.
- [7] R.S. Stringham, Low Mass 1.6 MHz sonofusion reactor, *Proc. ICCF-9*, Marseille, France, J.P. Biberian (Ed.), 31 Oct.–5 Nov. 2004.
- [8] R.S. Stringham, Cavitation and fusion, *Proc. ICCF 10*, Boston, USA, P.L. Hagelstein and S.R. Chubb (Eds.), 24–29 Aug. 2003.
- [9] R.S. Stringham, Model for electromagnetic pulsed BEC experiments, *JCMNS, Proceedings ICCF 16*, Chennai, India, M. Srinivasan and J.P. Biberian (Eds.), p.257, 6 Feb.–11, 2011.



Research Article

Demonstration of Energy Gain from a Preloaded ZrO_2 –PdD Nanostructured CF/LANR Quantum Electronic Device at MIT

Mitchell R. Swartz*

JET Energy Inc., Wellesley Hills, MA 02481-0001, USA

Peter L. Hagelstein†

Research Laboratory of Electronics, Massachusetts Institute of Technology, Cambridge, MA 02139, USA

Abstract

A self-contained, preloaded CF/LANR quantum electronic component, a NANOR[®]-type LANR device containing active ZrO_2 –PdD nanostructured material at its core, showed energy gain during, and after, the January, 2012 IAP MIT Course on CF/LANR. The Series VI two terminal device featured new composition, structure, and superior handling properties. Most importantly it was preloaded so that LANR activation is separated from loading. The calorimeter had parallel diagnostics, including heat flow measurement, and calibrations included an ohmic (thermal) control located next to the NANOR[®]-type device. The preloaded LANR device demonstrated energy gain which ranged generally from 5 to 16. It was 14.1 energy gain while the MIT IAP course was ongoing. During February and March, through a range of experiments, the NANOR[®] continued to produce excess energy, confirmed by daily calibrations. This open demonstration has confirmed the existence, reproducibility, and improved control of CF/LANR reactions, and as importantly, has shown a possibly superior preloaded nanostructured LANR material and driving device.

© 2014 ISCMNS. All rights reserved. ISSN 2227-3123

Keywords: Dry, NANOR, Preloading, Reproducibility

1. Introduction

Clean, high efficiency energy production is very important today, and in the foreseeable future, from whatever source. Lattice assisted nuclear reactions (LANR, also known as cold fusion and LENR) use hydrogen-loaded alloys to create heat and other products [1]. The “excess heat” is energy derived from what is believed to be deuteron fusion in aqueous, non-preloaded, earlier systems, and so the deuterons are the fuel and are extremely slowly consumed. LANR will

*E-mail: mica@theworld.com

†Email: plh@mit.edu

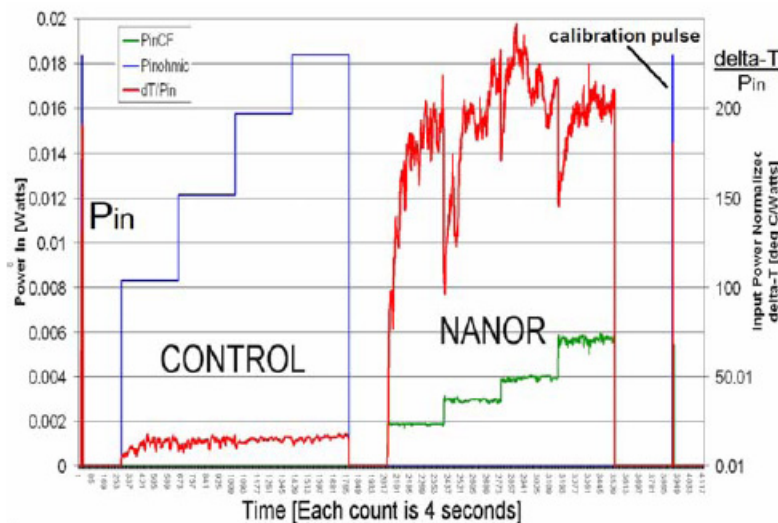


Figure 1. Input power and resulting output temperature rise (normalized to input electrical power) of a self-contained CF/LANR quantum electronic component Series 6–33; run EJan30B, a two terminal NANOR[®]-type device containing active preloaded ZrO₂–Pd nanostructured material at its core.

be an important source of energy for this planet, for artificial internal organs, for interstellar probes, and robotics, transportation, and electricity production. With LANR we also get to transfer the use of petrochemicals and gasoline into making useful pharmaceuticals and plastics and perhaps even nanomaterials. In the case of LANR, there can rarely occur, in a lattice under special conditions, the fusion of two heavy hydrogen nuclei to form a helium nucleus at near room temperature. The product helium-4, or simply helium, is *de novo* meaning that this helium-4 is created new and fresh, generated directly from two, driven by more, deuterons physically located within the loaded palladium, nickel or one of their nanostructured materials. These reactions were first reported as CMNS, LANR, LENR or cold fusion, and it involves a palladium-alloyed lattice where the process occurred irregularly at low efficiency. Most importantly, the product with LANR, helium, is environmentally safe and does not produce global contamination or warming. One such cold fusion device (PHUSOR[®]) was openly shown at MIT during August 2003 [2]. This paper reports a second open demonstration; confer Figs 1,3–5; and, therefore, it is important to compare this to the previous LANR demonstration and technology. For example, we previously demonstrated success in LANR aqueous systems, linked to high solution resistance (impedance) and shaped-metamaterial LANR devices, with power gains more than 200–500%; and short term power gains using codepositional high impedance devices DAP (Dual anode Phusor[®]-Type LANR device; Pd/D₂O, Pd(OD)₂/Pt–Au have reached energy outputs of up to ~8000% compared to input energy, where ohmic controls are defined as 100% [3–5].

The results of the previous open demonstrations of the PHUSOR[®]-type LANR devices including BOTH at MIT and later developed integrated larger systems involving paired Stirling engines driven by LANR to beyond 19 W of excess power [2]. These devices (cathode volume ~0.47 cm³, area ~6.4 cm²) yield significant excess heat after full loading, with a peak excess power production circa 1.5 W, and a peak power gain of ~2.4 or higher. Their output depends upon loading rate, loading achieved, and confinement time. The palladium Pd/D₂O/Pt devices demonstrate a critical threshold input electrical current density circa 1.5 ± 0.3 mA/cm², and a possible activation energy of ~60.7 kJ/mol. Open circuit voltage (V_{oc}) greater than 1.8–2.70 V is useful and heralds excess heat. The mean excess power gain (compared

to an ohmic joule control) during the week was 2.30 ± 0.84 for electrical input powers of 120–750 mW. The system developed 338 ± 67 mW of excess power compared to a joule (thermal) control which is defined as 100%.

However, successful LANR requires engineering of multiple factors including loading, adequate confinement time (sometimes weeks within the component container because the materials can be potential toxic if inhaled), loading rate, and prehistory (with careful avoidance of contamination and materials and operational protocols which quench performance). Specifically, nanostructured materials [6], metamaterials [7], and their controlled operation [8,9] improve success. At LANR's nanostructured material “core” is an isotope of hydrogen, usually deuterons, which are tightly packed (“highly loaded”) into binary metals, alloys, or nanostructured compounds, containing palladium or nickel, loaded by an applied electric field or elevated gas pressure which supply deuterons from heavy water or gaseous deuterium.

ZrO₂–(PdNi)–D LANR/CF nanostructured materials generate excess heat [10], including with acoustic and electric fields [11–13], with additional effects from orthogonal applied DC magnetic field intensities [12]. They have been made into LANR/CF transistors [3] which exhibit energy gain and simultaneous non-thermal near infrared emission. There are complicated polarization/transconduction phenomena including an “avalanche (transconduction electrical breakdown) effect” which has a critical role in excess heat. Nanostructured materials are important in LANR produced in codeposition structures [14], observed in non-thermal near infrared emissions [15,16], and exhibiting LANR excess heat correlated with the size of the Pd–D nanostructures [12,13]. Relevant to LANR and the future of LANR devices, nanostructured materials offer great opportunity. These nanostructured LANR materials include nanoparticles, nanocrystals, quantum dots, nanocatalysts, nanowires, nanocrystals, nanoclusters, nanodendrimers and higher polymer aggregates, and metallic-organic hybrids. They are made from metals, semiconductors, oxides, ceramics, polymers, composite materials, glasses, alloys and combinations of the above. As a result of the small size, nanotechnology built using these new nanostructured materials have two amazing properties. First, nanostructured materials have incredibly large surface area to volume ratios. Second, many also have new unexpected quantum mechanical properties. Nanostructured materials enable quantum confinements, surface plasmon resonances, and superparamagnetism. Examples of material properties which unexpectedly change by nanostructured utilization include significantly decreased melting temperatures (gold), significantly increased electrical conductivity (silicon), increased flammability (aluminum), improved catalytic properties (platinum), and unexpected transparency of metals (copper). Solvated gold nanoparticles have colors which range from red to black. Palladium nanoparticles often have a vacancy in their center. Similarly, LANR nanostructures include vacancies within them. In the alloys, they must drift into the bulk from the surface. This diffusion is slightly facilitated by the loading itself. *de novo* Pd–D vacancies have been made in loaded Pd (and Ni) with electron beam irradiation [17]. Codeposition has been used to make palladium, nickel and alloyed loaded materials on top of electrodes, and used dual anode LANR systems to produce very high levels of such LANR nanostructured materials locally [13,14]. In addition, nanostructured materials have been used in LANR using palladium black [10] in a double structure (DS)-cathode. They reported more than 200 MJ of excess energy was continuously produced for over 3000 h at an average rate of 50–100 kJ/h. The DS-cathode is a Pd cathode with “an internal vacuum zone filled with a deuterium storage type powder” and an outer cylindrical vessel of Pd metal (wall thickness of 3 mm). Such bulk cathodes rely on diffusion, making it difficult to reach 100 at% concentration solid solution of D in Pd or the other nanostructured material. The D ions are postulated to move over the surfaces of the Pd black by the “spillover-effect”, without the need to becoming D₂ molecules. We have reported successful production of excess heat using nanomaterial palladium, nickel, and newer alloyed compounds, such as ZrO₂PdNi, and in a LANR transistor configuration, driven by two applied electric field intensities, which demonstrate LANR heat associated with low level near-infrared emission, controlled by two optimal operating point manifolds.

2. Experimental

We report a new generation of LANR (CF) preloaded nanocomposite $\text{ZrO}_2\text{--PdNiD}$ CF/LANR quantum electronic devices which are active, and capable of energy gain. These feature two terminals and self-contained superior handling properties enabling portability and transportability. NANOR-type lattice assisted nuclear reaction (LANR) devices use hydrogen alloys to create heat and other reactions. Most importantly, the activation of the desired cold fusion reactions is, for the first time, separated from the loading. These proprietary prepared preloaded $\text{ZrO}_2\text{--(PdNi)}$ LANR/CF nanostructured materials are dry, and glued into electrically conductive, sealed configurations. The core is $\text{ZrO}_2\text{--(PdNiD)}$ [Zr ($\sim 66\%$), Ni (0–30%), and Pd (5–25%) by weight before additional D_2 and H_2 are added to achieve more than 130% D/Pd. These are potentially very useful. Their complex development has required control of their breakdown states and quenching tendencies. Series VI NANORs feature new composition, structure, and superior handling properties. Again, most importantly, they are preloaded so that LANR activation is separated from loading. The current driver system incorporates our proprietary third generation LANR (CF) Integrated Circuit which is microprocessor controlled and coupled to a Series V or VI preloaded CF/LANR nanocomposite $\text{ZrO}_2\text{--PdD}$ and $\text{ZrO}_2\text{--PdNiD}$ electronic devices to activate them. It is combined with a new type calorimeter and data processing which is used to evaluate and verify activity of the NANOR[®], controls, and others materials. This system has already been demonstrated using the more reproducible nanostructured CF/LANR quantum electronic devices at MIT in 2012.

The LANR preloaded, stabilized NANOR[®]s were driven by a high voltage circuit up to 3000 V rail voltage. The duty cycle was split with half going to a control portion consisting of a carefully controlled electrical DC pulse into an ohmic resistor which was used to thermally calibrate the calorimeter. We also employed a new series of LANR-directed light indicator outputs to define states which has been a matter of incredible utility and assistance almost every time the system and device has been used. The new controlled driving system uses pulse wave modulated microcomputer control of specialized very high voltage semiconductors linked to a current source driving system driving system coupled to the NANOR[®]-type LANR system. It provides an improved method of current control, enabling new activation, a new method of driving, an improved and better paradigm system and the ability to evolve paradigms. Furthermore, the system is excellent for preliminary tests for usefulness to detect LANR activity, and by serially examining multiple samples of the same CF/LANR material to look for changes from doping, contaminants, and quenching materials. The new controlled driving system can be used for open demonstrations as discussed above, and to more closely examine LANR and other systems for their activity, linearity, time-invariance, and even the impact of additives. For example, a very successful investigation of silver doping was made. This system can easily detect the impact of impurities, dopants, contaminants, quenching agents, accelerants, and other factors. Basically, there are two levels of operation for NANOR[®] LANR systems, low and high power. High power is useful for applications requiring larger amounts of power such as transportation, heating, and artificial organs. In this case, however, low power is used for several reasons including to facilitate the rapid time constant, and because this is for demonstration and teaching purposes.

Data is taken from voltage, current, temperatures at multiple sites, and even as a 4-terminal measurement of the NANOR's internal electrical conductivity. Data acquisition has all temperature and electric measurements sampled at data rates of 0.20–1 Hz, with 24+ bit resolution (e.g. Measurement Computing (MA) USB-2416, or a Omega OMB-DaqTemp or equivalent; voltage accuracy 0.015 ± 0.005 V, temperature accuracy $< 0.6^\circ\text{C}$). All connections are isolated when possible, including where possible with Keithley electrometers, or their equivalent, for computer isolation. All leads are covered with dry, electrically insulating tubes, such as medical grade silicone, Teflon, and similar materials, used to electrically isolate wires. To minimize quantization noise, if necessary, 1 minute moving averages may be used for some signals. The noise power of the calorimeter is in the range of $\sim 1\text{--}30$ mW. The noise power of the Keithley current sources is generally ~ 10 nW. Input power is defined as $V * I$. There is no thermo-neutral correction in denominator. Therefore, the observed power is a lower limit. The instantaneous power gain (power amplification factor (non-dimensional)) is defined as $P_{\text{out}}/P_{\text{in}}$. The energy is calibrated by at least one electrical joule control (ohmic

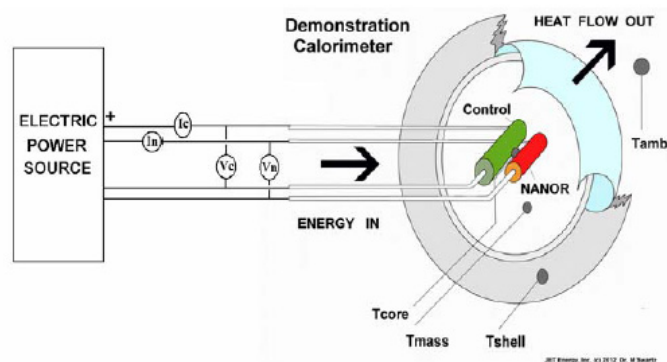


Figure 2. Electric driver and calorimeter showing parallel diagnostics consisting of heat flow measurement and temperature, and the ohmic (thermal) control. The electric power supply provided a high voltage DC rail voltage with the electronics controlling the applied voltage across the component.

resistor) used frequently, and with time integration for additional validation. The excess energy, when present, is defined as $(P_{\text{out}} - P_{\text{in}}) \times \text{time}$. The amount of output energy is determined from the heat released producing a temperature rise, which is then compared to the input energy.

3. Experimental – Methods

Figure 2 is a three-dimensional (3D) schematic perspective view of the NANOR[®] and control and sensors located inside, and monitored by, several systems and a calorimeter. The distances shown, and relative sizes of objects, in the figure are not actual, simply schematic to help demonstrate what is occurring. At the center are the NANOR[®] and the ohmic thermal control. Additional temperature measurements are used for further accuracy and verification. Physically located between them, is one of the Calorimeter's three central core temperature probes. To ensure thermal contact, a thermally conductive, electrically resistive material can be used. Thermal compounds can include Wakefield Thermal compound (Pelham, NH). Some of the heat flow was measured by an Omega HFS Thin Film Heat flux sensor. In all cases, a thin layer of electrically insulating, but thermally conductive material is placed above and below these three elements of the system. Very thin insulating ceramics can be used, such as Wesgo AL-500 and Molecular Dielectrics, Inc (Clifton, NJ) MYKROY J11. There are also specialized additional thermal masses which are for the most part completely and adiabatically isolated from the ambient environment by a series of five insulating barriers. One of these barriers enable the leads from the NANOR[®], ohmic control, and temperature sensors (and other diagnostics such as heat flow sensors) to leave the calorimeter through specially modified firebricks.

Using a low power type system for open demonstrations, the output of this system was presented at MIT from January 30, 2012 through mid May 2012. The input powers were below 100 mW [19], because the set-up was designed to run at low power input levels to increase the safety at the educational institution for its multi month-long stay at MIT. A range of experiments were conducted examining the impact of various driving sequences, and the NANOR[®] continued to produce excess energy. There were daily calibrations using input current and voltage standards.

The 2012 Open LANR/CF Demonstration at MIT had parallel diagnostics including calorimetry, input-power-normalized delta- T , and focused heat flow measurement, and several calibrations. One of the calibrations included an ohmic (thermal) control located next to the NANOR, used to ascertain activity. To enable demonstrations at MIT for the NANOR[®]-type LANR system, including in the MIT IAP class where multiple experiments had to be shown to classes, or otherwise run over times of 2 h, a specialized heat flow semiquantitative analyzer was specially developed. The heat which this preloaded NANOR[®]-type LANR device demonstrated was monitored three ways by three (3) independent systems for semiquantitative measurement of the energy produced. Furthermore, the output of the NANOR is compared to an ohmic control. First, the energy produced is instantaneously and kinematically determined by the ratio of the input power normalized temperature increase, called by the symbol ' $\Delta T/P_{in}$ ' referring to the increase of temperature (ΔT), divided by the input electrical power (P_{in}). Second, it is also instantaneously and kinematically evaluated over a wide area by the ratio of the input power normalized heat flow leaving it, called by the symbol ' HF/P_{in} ' referring to the heat flow (HF) divided by the input electrical power (P_{in}). Third, it is examined by calorimetry, calibrated by the thermal ohmic control, and confirmed by long-term time integration. These three methods of verification are pooled to derive very useful information, semiquantitatively ascertain energy produced, and infer activity.

4. Results

The self-contained CF/LANR quantum electronic component and a two-terminal NANOR[®], containing active ZrO₂–PdD nanostructured material at its core, showed energy gain during, and after, the January, 2012 IAP MIT Course on CF/LANR. The results are shown in Figs. 1, 3–5. In this case, the mini-sized NANOR is a sixth generation CF/LANR device, and it is smaller than 2 cm, with less than 1 g of active material. However, this is actually a matter which is not *de minimus* because the LANR excess power density was more than 19,500 W/kg of nanostructured material. The preloaded NANOR-type LANR device demonstrated an average energy gain (COP) of $\sim 14 \times$ ($\sim 1412\%$) the input for a duration of several hours that it was observed during the MIT IAP course on the first day, and levels of that order continued. Over several weeks, CF/LANR quantum device demonstrated more reproducible, controllable, energy gain which ranged generally from 5 to 16 (14.1 while the course was ongoing).

In the case of this NANOR (the sixth generation of these microminiaturized CF/LANR devices), the activation of this cold fusion reaction is, for the first time, separated from its loading. In every other system known, Fleischmann and Pons, Arata, Miles, and the others, the loading was tied to activation. By contrast, in the case of the sixth generation NANOR[®]s, unlike the others, the preloaded devices can be simply electrically driven.

This is a high efficiency heat producing system, and within it, a unique calorimeter and a unique driving system whose design, driving configuration and implementations, in conjunction with the NANOR have made portability of LANR to MIT, and elsewhere, possible. Furthermore, the proprietary microprocessor controlled system has also led to an evolving series of improved driving paradigms to qualitatively explore and then exploit loaded nanostructured, nanocomposite, and other materials including semiquantitatively examining them for usefulness, heat-production activity, linearity, time-invariance, and even the impact of additives and contaminants.

The NANOR[®]-type LANR device was able to generate large amounts of heat ($> 100\%$ compared to the expected dissipation by $V * I * \text{time}$). This excess energy clearly heralds a high efficiency of driving energy use. The entire system was put onto three electronic boards enable an entire new generation of activated CF/LANR nanocomposite ZrO₂–PdNiD electronic devices. This second Open Demonstration of LANR devices featuring the preloaded NANOR turns out to have been more important than initially realized. First, this demonstration confirmed the existence, reproducibility, and now improved control, of CF/LANR reactions. For the entire months of February through April 2012, the NANOR[®] continued to produce excess energy, with daily calibrations against an ohmic thermal control; thus, it also confirmed the existence of CF/LANR daily during that time. By comparison, and also worth noting, the historic 2003 open demonstration of CF/LANR at MIT needed two full tables for the setup, whereas the 2012 NANOR

demonstration at MIT needed only a single standard sized desk top. And most of that space was taken up by the computer and confirming meters (five of them), rather the device itself. In addition, the new calorimeter was cyclable in hours rather than requiring an entire day, making it applicable to the MIT course. In addition, compared to the 2003 LANR Open Demonstration at MIT, this second open demonstration featured a more sophisticated calorimeter shown at the MIT RLE laboratory. It had additional monitoring diagnostics for improved verification, such as the measurement of heat flow, to thereby provide for three independent ways of monitoring excess heat semiquantitatively compared to a thermal ohmic control.

Second, it has shown a possibly superior nanostructured material and configuration. The NANOR[®]-type preloaded LANR device openly demonstrated features include its convenient size (much smaller) and its superior handling properties which enable unique portability, and transportability. Like its 2003 (ICCF-10) predecessor demonstration, this preloaded NANOR-type LANR device also showed excess energy and also obvious improvements of size, response time, diagnostics, and total output energy.

Third, it had a much higher energy gain compared to the 2003 demonstration unit (Energy gain 14.1 in 2012 vs an energy gain ~ 2.7 in 2003). In fact, the current NANOR Series VI NANORs have had even higher gains (to beyond 30).

Fourth, another unique quality is the graphs were generated by an open demonstration proving also precise, safer containment.

Fifth, the Internet blogs and visitors to the open demonstration have indicated that the public wants cold fusion by whatever name, and therefore, these activated preloaded CF/LANR nanocomposite materials and LANR electronic devices do have usefulness and importance.

These preloaded NANOR[®]-type LANR devices have shown significant improvement over their predecessors, including the highly successful metamaterial PHUSOR[®]-type of LANR device. At their core is the proprietary preloaded nanostructure material specially prepared by several new processing steps. Could these dry, preloaded, ready-to-be-activated, NANOR[®]-type LANR devices/systems/materials, including in preassembled IC devices and systems, be the future of clean efficient energy production [20]?

Figures 1 and 3–5 show this entirely new, more reproducible, much more powerful configuration of clean, efficient energy production from several points of view. The figures include raw data and derived information from the runs which show conclusively LANR excess energy heralded by calorimetry and by input power normalized incremental temperature (ΔT) changes. These graphs show a small portion of the collected data and derived information which was actually collected and analyzed by the class, and later in a four-month interval. Confirmatory measurement of the operability and utility of the system include the first day of the 3 months open demonstration of the NANOR[®]-type LANR device at MIT during the 2012 IAP course on CF/LANR in the Department of Electrical Engineering.

Figure 3 is a set of curves which plot the differential incremental increase in temperature ($^{\circ}\text{C}$) for case with no input (“Background”), and for the case of an ohmic thermal control at the same location, and for the NANOR[®]-type LANR device. The graph presents several curves which plot the temperature rise in response to four different levels of electrical input power, and the response of an ohmic control to same electrical input power. The x -axis represents time, and each count represents 4 s. The y -axis on the left-hand side represents electrical input power in watts. The y -axis on the right-hand side represents the amount of temperature rise (differential temperature increase) in response to the electrical input power ($^{\circ}\text{C}$). The input to the thermal ohmic control is shown, followed by the preloaded NANOR[®]-type device, as are the thermal output (heat output generated) for both the ohmic control and the preloaded NANOR[®]-type device. The graph shows first the response of the ohmic control, and then the response of the NANOR, then a second ohmic control. Each of the outputs are read off of the right-hand side. Calibration pulses, used for accuracy and precision checks of voltages and currents, are also shown.

Compare the output for NANOR[®]-type LANR device to the thermal (ohmic) control. Figure 3 clearly demonstrates the larger differential incremental increase in temperature ($^{\circ}\text{C}$) for the NANOR[®] compared to the ohmic. Attention

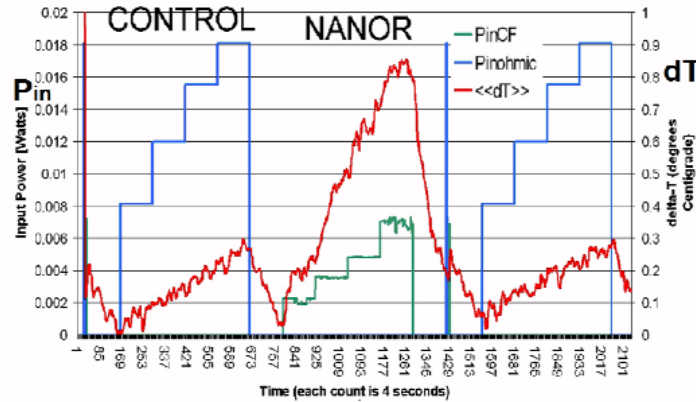


Figure 3. Input power and incremental output temperature rise of a self-contained CF/LANR quantum electronic Series VI NANOR[®] device. These curves plot the raw data as incremental temperature rise and the applied input electrical power.

is directed to the fact that the active preloaded LANR quantum electronic device clearly shows a larger, significant improvement in differential thermal output compared to a standard ohmic control (a carbon composition resistor). That amount of differential temperature increase for the preloaded NANOR[®]-type device heralds great utility for the energy output as a heat source.

Figure 1 is set of curves which plot the temperature rise (ΔT (in $^{\circ}\text{C}$)) of the preloaded NANOR[®]-type LANR device and the ohmic control normalized to four levels of input electrical power. Each is shown with as a thermal output response to its electrical input. The several regions present the differential temperature rise normalized to input electrical power for the preloaded NANOR, for the case with no input power (“Background”), and for the case of input to the ohmic thermal control, located at the core. The x -axis represents time, and each count represents 4 s. The y -axis on the left-hand side represents electrical input power in watts. Each of the outputs are read off of the right-hand side. The y -axis on the right-side represents the amount of temperature rise (differential temperature increase) normalized (that is, divided by) to the electrical input power. The units of this axis are in $^{\circ}\text{C}/\text{W}$. Calibration pulses, used for accuracy and precisions checks of voltages and currents, are also shown.

Figure 1 heralds the excess energy achieved by the NANOR type of LANR device. Compare the ΔT output normalized to input power for preloaded NANOR[®]-type LANR device to the thermal (ohmic) control. It can be seen that the input power normalized delta measurements suggest strongly the presence of excess heat. Observe that despite lower input electrical power to the NANOR, the temperature rise normalized to input electrical power observed in the core was higher than expected, as compared to the ohmic control. Attention is directed to the fact that the active preloaded LANR quantum electronic device again clearly shows significant improvement in thermal output, here input-power-normalized compared to a standard ohmic control (a carbon composition resistor).

Figure 4 is set of curves which plot the heat flow, normalized to input electrical power, leaving the system while driving the preloaded NANOR[®]-type LANR device and the ohmic control at four different electrical input powers. The heat flow is in response to the electrical input. The figure presents the output heat flow for the preloaded NANOR, for the case with no input, and for the ohmic thermal control, located at the calorimeter’s core. The x -axis represents time, and each count represents 4 s. The y -axis on the left-hand side represents the electrical input power in watts. The y -axis on the right-hand side represents the Heat Flow output normalized (that is, divided by) to the electrical input power. Calibration pulses, used for accuracy and precisions checks of voltages and currents, are also shown.

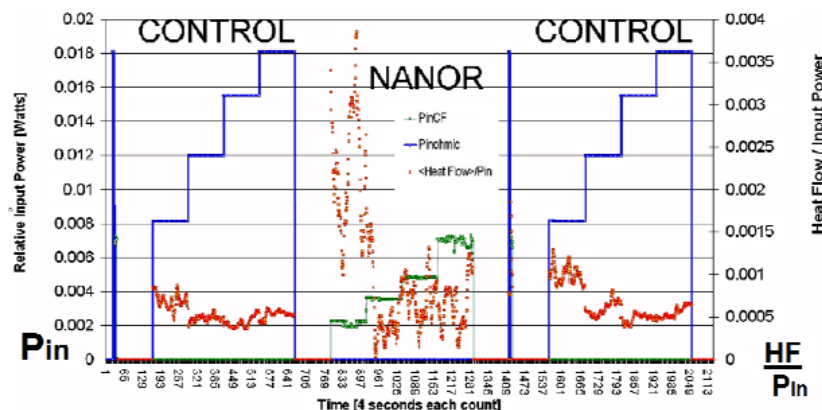


Figure 4. Input power and output heat flow normalized to input electrical power of a self-contained CF/LANR quantum electronic component NANOR 6-33.

In Fig. 4, compare the output heat flow normalized to input power for NANOR[®]-type LANR device to that for the thermal (ohmic) control. The long term heat flow measurements (using calibrated devices) confirm the presence of excess energy, and validate the other measurements. It can be seen that despite lower input electrical power to the NANOR, the heat flow out in response, normalized to input electrical power observed in the core, was higher than expected, as compared to the ohmic control – especially at lower input power levels. The response of the NANOR[®]-type LANR device is consistent with very efficient energy gain, with the energy output as heat. The changes of the output with input power is consistent with the optimal operating point manifold of the LANR material. Therefore, the figure heralds the great efficiency of, and the excess energy coming from, the preloaded NANOR[®]-type of LANR device. Attention is directed to the fact that the active preloaded LANR quantum electronic device clearly again shows significant improvement in energy generated compared to a standard ohmic control (a carbon composition resistor) by this method, too, using heat flow. This information corroborates the marked and substantive incremental increase in energy output as heat for the preloaded NANOR[®]-type of LANR device.

Figure 5 shows curves which plot the electrical input power, at several input power levels, and the calorimetric responses of both the preloaded NANOR[®]-type device and the ohmic control. The x -axis represents time, and each count represents 4 s. The y -axis on the left-hand side represents electrical input power in watts. The y -axis on the right-hand side represents the amount of energy released. The units of this axis are in joules. The figure shows the input, and the calorimetry, of preloaded NANOR along with that for the ohmic thermal control used to calibrate the system. Those calibration pulses, used for accuracy and precisions checks of voltages and currents and time, are also shown. The inputs to the thermal ohmic control, followed by the preloaded NANOR[®]-type device, are shown, as are the calibrated calorimetric outputs for both.

Each of the outputs are read off of the right-hand side. The latter curves represent time integration to determine total energy. They thus rule out energy storage, chemical sources of the induced heat, and other sources of possible false positives. Compare the output for NANOR[®]-type LANR device to the thermal (ohmic) control. As can be seen, this semiquantitative calorimetry, itself calibrated by thermal waveform reconstruction, was consistent with excess heat being produced only during energy transfer to the NANOR[®]-type LANR device.

Notice that the active preloaded LANR quantum electronic device clearly shows significant improvement in thermal output compared to a standard ohmic control (a carbon composition resistor). The graph, taken from the MIT IAP January

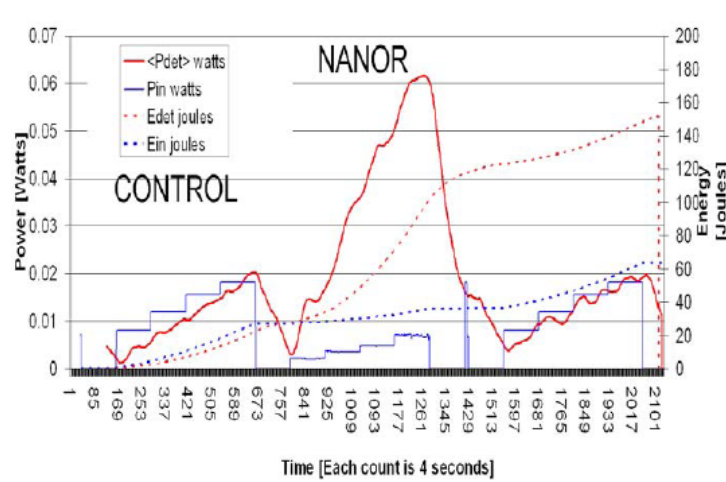


Figure 5. Input and Heat Output of a two terminal NANOR[®]-type device Series 6-33 device, showing the calorimetric response at several input powers, for the device and the ohmic control.

2012 class, is representative of the NANOR-type of CF/LANR technology, and it shows quite clearly demonstrated over unity thermal output power from the NANOR, at a level close to 78 mW.

5. Conclusion

In summary, the uniqueness of the preloaded LANR nanostructured material-device includes its high activity, its preloaded nature, its dryness, its precise containment, and its easy portability. It begins a new generation of CF/LANR nanostructured materials and devices. In the case of this NANOR (the sixth generation of these CF/LANR devices), the activation of this cold fusion reaction is, for the first time, separated from its loading. In every other system known, Fleischmann and Pons, Arata, Miles, and the others, the loading was tied to activation. As importantly, the semiquantitatively measured output energy IS a significant energy gain. This has always been a ‘goal post’ for cold fusion, one which so far remains beyond the realm for hot fusion on Earth. The present device and driving technology have provided high-efficiency pre-loaded energy-, heat-, and product-producing devices which can be electrically driven and has provided a method of improved activation and reproducibility for controlling lattice assisted reactions and their generated products using nanostructured, nanocomposite, and other materials.

Preloaded CF/LANR nanocomposite materials in CF/LANR Electronic Devices do have usefulness today and tomorrow. Today, they can be clearly examined with this system for demonstrations of their CF/LANR activity, linearity, time-invariance, and the impact of additives. For example, the present device, and controlling/driving system provided a reliable low power, high-efficiency, energy production device for demonstration and teaching purposes of size smaller than a centimeter, with an active site weight of less than 100 mg. The preloaded nanostructured LANR material and accompanying controller and driver have shown at MIT a successful (second) open demonstration of CF/LANR heat production and energy conversion device. This confirms LANR/CF. Also, compared to the first LANR/CF open demonstration at MIT, the new device and accompanying driver and other technologies have shown obvious improvements of size, response time, diagnostics, and even total output energy.

This open demonstration over months has demonstrated that microprocessor controlled integrated circuits using LANR quantum optical devices containing preloaded nanostructured LANR material can be used as an effective very

clean, energy production system, apparatus, and process. We have run the component over a year with evanescent loss which is attributed to fuel loss, or redistribution, or inactivation (perhaps by reaction with another material). Whether they can be refueled or simply replaced, is under investigation. In addition, elsewhere, this driving and monitoring system was useful to easily convert conventional monitoring and conventional thermometry into fine calorimetry. Calorimetry and input-power-normalized delta T were used to ascertain activity. For example, this system has been used to show the calorimetry of a nanostructured composite CF/LANR Device using twenty different levels of input. This method is similar to, but beyond, that suggested by Dr. Robert W. Bass [18]. After testing it, we have determined that it was highly useful, and now use it routinely, wherever possible.

Tomorrow, preloaded LANR nanostructured materials and devices will also be useful for integrated circuits and other applications using a pre-activated nanostructured and other materials. These include high power, effectively ‘over-unity’, self-contained, microprocessor-controlled, preloaded, energy production devices and systems enabling their remote activation for electronic, bioelectronics, space and avionic circuits, IC devices, and AI systems.

Acknowledgements

The authors gratefully thank Gayle Verner and Jeffrey Tolleson for meticulous help in the manuscript, and Jeffrey Tolleson for help with the computer programming; also Jeffrey Shapiro, Alex Frank, Allen Swartz, Charles Entenmann, Alan Weinberg, Dennis Cravens, Dennis Letts, Brian Ahern, Jeff Driscoll, Larry Forsley, Pamela Mosier-Boss, Robert Smith, Robert Bass, Robert Godes and the late Talbot Chubb; and JET Energy and New Energy Foundation for support. NANOR[®]-type and PHUSOR[®]-type technologies, and other discussed IP herein, is protected by USA Patents D596724, D413659 and other Patents pending.

References

- [1] M. Swartz, Survey of the observed excess energy and emissions in lattice assisted nuclear reactions, *J. Sci. Exploration* **23**(4) (2009) 419–436.
- [2] M. Swartz, Can a Pd/D₂O/Pt device be made portable to demonstrate the optimal operating point? Condensed Matter Nuclear Science, *Proc. of ICCF-10*, Peter L. Hagelstein, Scott, R. Chubb (Eds.), World Scientific, NJ, ISBN 981-256-564-6, (2006), pp. 29–54.
- [3] M. Swartz, Excess power gain using high impedance and codepositional LANR devices monitored by calorimetry, heat flow, and paired stirling engines, *Proc. ICCF-14*, 10–15 August 2008, Washington, D.C., David J. Nagel and Michael E. Melich (Eds.), ISBN: 978-0-578-06694-3, 2010, p. 123.
- [4] M. Swartz and G. Verner, Excess heat from low electrical conductivity heavy water spiral-wound Pd/D₂O/Pt and Pd/D₂O–PdCl₂/Pt devices, Condensed Matter Nuclear Science, *Proc. ICCF-10*, P. Hagelstein (Ed.), Chubb, World Scientific, NJ., ISBN 981-256-564-6, 2006, pp. 29–54.
- [5] M. Swartz, The impact of heavy water (D₂O) on nickel-light water cold fusion systems, *Proc. of the 9th Int. Conf. on Cold Fusion (Condensed Matter Nuclear Science)*, Beijing, China, 2002, pp. 335–342.
- [6] M. Swartz, Optimal operating point manifolds in active, loaded palladium linked to three distinct physical regions, *Proc. of the 14th Int. Conf. on Condensed Matter Nuclear Science and the 14th Int. Conf. on Cold Fusion (ICCF-14)*, 10–15 August 2008, Washington, D.C., ISBN: 978-0-578-06694-3, 2010, p. 639.
- [7] M. Swartz and G. Verner, The Phusor[®]-type LANR cathode is a metamaterial creating deuteron flux for excess power gain, *Proc. of the 14th Int. Conf. on Condensed Matter Nuclear Science and the 14th Int. Conf. on Cold Fusion (ICCF-14)*, 10–15 August 2008, Washington, D.C., ISBN: 978-0-578-06694-3, 2010, p. 458.
- [8] M. Swartz, Quasi-one-dimensional model of electrochemical loading of isotopic fuel into a metal, *Fusion Technol.* **22** (2) (1992) 296–300.
- [9] M. Swartz, Consistency of the biphasic nature of excess enthalpy in solid state anomalous phenomena with the quasi-1-dimensional model of isotope loading into a material, *Fusion Technol.* **31** (1997) 63–74.

- [10] Y. Arata and Y.C. Zhang, Observation of anomalous heat release and He4 production from highly deuterated palladium particles, *Jpn. J. Appl. Phys.* **38** (Part 2, No. 7A) (1999) L774–L776.
- [11] M. Swartz, G Verner and J. Tolleson, Energy gain from preloaded ZrO₂-(PdNi)-D nanostructured CF/LANR quantum electronic components, *Proc. ICCF17*, 2012.
- [12] M. Swartz, Impact of an applied magnetic field on the electrical impedance of a LANR device, Volume 4, *JCMNS, Proc. 239th Am. Chemical Soc.*, 2011.
- [13] M. Swartz, LANR nanostructures and metamaterials driven at their optimal operating point, 3rd Vol *LANR/LNR Sourcebook*, October 21, 2011.
- [14] M. Swartz, Codeposition of palladium and deuterium, *Fusion Technol.* **32** (1997) 126–130.
- [15] M. Swartz, G.Verner and A.Weinberg, Non-thermal near-IR emission from high impedance and codeposition LANR devices, *Proc. of the 14th Int. Conf. on Condensed Matter Nuclear Science and the 14th Int. Conf. on Cold Fusion (ICCF-14)*, 10–15 August 2008, Washington, D.C., ISBN: 978-0-578-06694-3, 2010, p. 343.
- [16] M. Swartz and G. Verner, Bremsstrahlung in hot and cold fusion, *J. New Energy* **3** (4) (1999) 90–101.
- [17] M. Swartz, P.L. Hagelstein, G. Verner and K. Wright, Vacancy-phase nickel cathodes, Abstracts ICCF7, 1997, p.137.
- [18] R.W. Bass, Five frozen needles CF protocol, *J. New Energy* **6**(2) (2002) 30.
- [19] These low power NANOR[®] -type components have been driven up to the two watt level.
- [20] Similar aqueous systems of Pd D indicate the fuel, D, is used to make ⁴He (Miles), and there are no biologically significant neutron, or ionizing radiation, output hazards known.



Research Article

Energy Gain From Preloaded $\text{ZrO}_2\text{--PdNi--D}$ Nanostructured CF/LANR Quantum Electronic Components

Mitchell R. Swartz*, Gayle Verner and Jeffrey Tolleson

JET Energy Inc., Wellesley Hills, MA 02481-0001, USA

Abstract

Previously, we reported that such nanocomposite $\text{ZrO}_2\text{--PdNiD}$ LANR materials have been made into LANR/CF transistors which exhibit energy gain and simultaneous non-thermal near infrared emission. This is accompanied by complicated polarization/transconduction phenomena including an avalanche transconduction electrical breakdown, which has a critical role in excess heat generation. This paper presents a new generation of preloaded LANR (CF) activated nanocomposite $\text{ZrO}_2\text{--PdNiD}$ CF/LANR quantum electronic devices capable of energy gain. These devices dry, glued into electrically conductive, sealed, configurations. The core is $\text{ZrO}_2\text{--(PdNiD)}$ with additional D_2 and H_2 . They are self-contained CF/LANR quantum electronic components containing $\text{ZrO}_2\text{--PdNi--D}$ LANR/CF nanostructured materials which generate significant excess heat from applied electric fields. They also feature two terminals and self-contained superior handling properties enabling portability and transportability. Most importantly, the activation of the desired LANR reactions is, for the first time, separated from the loading of the substrate. Although their development has required control of their breakdown states and the quenching tendencies of nanostructured materials, these $\text{ZrO}_2\text{--PdNiD}$ CF/LANR quantum electronic devices are potentially very useful because they are reproducible active nanostructured CF/LANR quantum electronic devices.

© 2014 ISCMNS. All rights reserved. ISSN 2227-3123

Keywords: Dry cold fusion, NANOR[®], Preloading, ZrO_2PdNiD , ZrO_2PdD

1. Introduction

We report a new generation of LANR (CF) activated nanocomposite $\text{ZrO}_2\text{--PdNiD}$ CF/LANR quantum electronic devices capable of significant energy gain [1]. Lattice assisted nuclear reactions (LANR) are also known as CF, CMNS, and LENR. These self-contained, two-terminal, CF/LANR quantum electronic components (NANOR[®]-type LANR devices) feature new composition, structure, and superior handling properties enabling portability and transportability. Most importantly, they are preloaded so that LANR activation is separated from loading. These devices contain active ZrO_2PdD nanostructured material at their core. The preloaded nanocomposite LANR/CF materials are made into dry electronic circuit devices, which required surmounting their extremely high electrical resistances. They are then,

*E-mail: mica@theworld.com

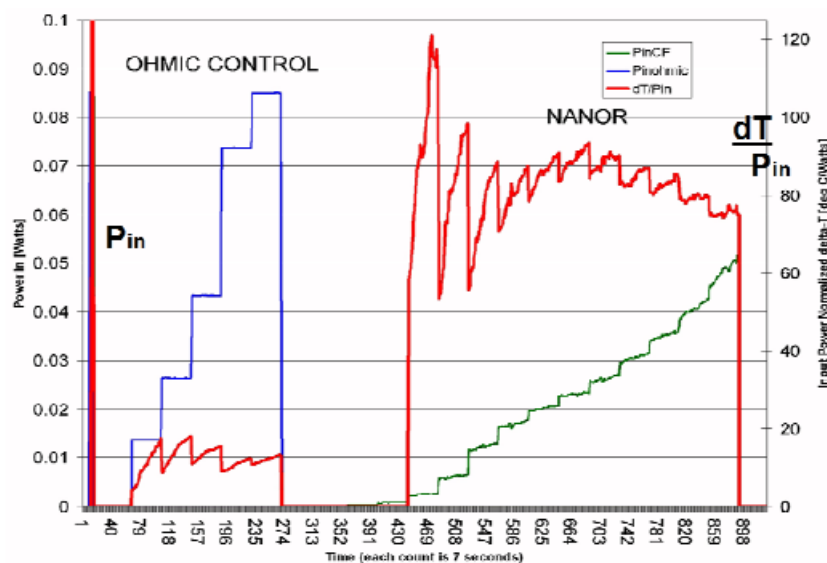


Figure 1. Input Power and Resulting Output Temperature rise (normalized to input electrical power) of a self-contained CF/LANR quantum electronic component, a Series V two terminal NANOR[®]-type device containing active preloaded ZrO₂/PdNiD nanostructured material at its core. These curves plot the temperature rise normalized to input electrical power as a function of time.

remotely, easily activated, driven by an electrical circuit and controlled by an electrical driver (cf. Figs. 1,3–5). They have been carefully evaluated for energy gain, including during, and after, the January, 2012 IAP MIT Course on CF/LANR (Figs. 3,4; [1]). That calorimeter had parallel diagnostics, such as heat flow measurement, and calibration including an ohmic (thermal) control located next to the NANOR[®].

This demonstrates that these NANORs can be fashioned into completely preloaded easily activated LANR (CF) Integrated Circuits which enable an entire new generation of ZrO₂-PdNiD preassembled IC electronic devices. The importance is they enable LANR devices and their integrated systems to now be fabricated, transported, and then activated. They *are* the future of clean, efficient energy production.

2. Background

Clean energy production is critically important today, and in the foreseeable future, from whatever source. LANR use hydrogen-loaded alloys to create heat and other reactions. They are an energy multiplier because the energy density of LANR reactions is ten million times that of gasoline. LANR will play a critical role in all future technologies with potential revolutionary applications to all energy issues – robotics, transportation, electricity production, artificial internal organs, and space travel [2]. In the case of LANR, there can rarely occur, in a lattice under special conditions, the fusion of two heavy hydrogen nuclei to form a helium nucleus at near room temperature. The product helium-4, or simply helium, is *de novo* meaning that this helium is created new and fresh, generated directly from two, driven by more, deuterons physically located within the loaded palladium, nickel or one of their nanostructured materials. These reactions were first reported in aqueous. Today, they involve a palladium-alloyed lattice or nanomaterials where the process occurred irregularly at low efficiency. Most importantly, the product with LANR, helium, is environmentally safe and does not produce global contamination or warming. We previously demonstrated success in LANR aqueous

systems, linked to high solution resistance (impedance) and shaped-metamaterial PHUSOR[®]-type LANR devices, with power gains more than 200–500%; and short term power gains using codepositional high impedance devices DAP (Dual anode Phusor[®]-Type LANR device; Pd/D₂O, Pd(OD)₂/Pt–Au have reached ~8000% compared to input energy and to input energy transferred to control dissipative devices (100%) [3–8]. However, successful LANR requires engineering of multiple factors including loading, adequate confinement time (sometimes weeks to generate vacancies in non-nanomaterial systems), loading rate, and prehistory (with careful avoidance of contamination and materials and operational protocols which quench performance). Specifically, nanostructured materials, metamaterials, and their controlled operation improve success [9–11].

Nanostructured materials are important in LANR, and are also produced in codeposition structures [12], observed producing non-thermal near infrared emissions when active [13,14], and exhibiting LANR excess heat correlated with the size of the Pd–D nanostructures [6,7]. Relevant to LANR and the future of LANR devices, nanostructured materials offer great opportunity. As a result of the small size, nanotechnology built using these new nanostructured materials have two amazing properties. First, nanostructured materials have incredibly large surface area to volume ratios. Second, many also have new unexpected quantum mechanical properties. Nanostructured materials enable quantum confinements, surface plasmon resonances, and superparamagnetism. Examples of material properties which unexpectedly change by nanostructured utilization include significantly decreased melting temperatures (gold), significantly increased electrical conductivity (silicon), increased flammability (aluminum), improved catalytic properties (platinum), and unexpected transparency of metals (copper). Solvated gold nanoparticles have colors which range from red to black.

These nanostructured LANR materials include nanoparticles, nanocrystals, quantum dots, nanocatalysts, nanowires, nanocrystals, nanoclusters, nanodendrimers and higher polymer aggregates, and metallic-organic hybrids. They are made from metals, semiconductors, oxides, ceramics, polymers, composite materials, glasses, alloys and combinations of the above.

LANR devices use hydrogen-loaded alloys of nanostructured materials to create heat and other reactions. At LANR's nanostructured material "core" is an isotope of hydrogen, usually deuterons, which are tightly packed ("highly loaded") into the binary metals, alloys, or in this case, nanostructured compounds, containing palladium or nickel, loaded by an applied electric field or elevated gas pressure which supply deuterons from heavy water or gaseous deuterium. Loaded are isotopes of hydrogen -protons, protium, deuterons, deuterium, and hydrogenated organic compounds, deuterated organic compounds, D₂, H₂, deuterides and hydrides. Precisely for these NANOR[®]-type LANR devices, the fuel for the nanostructured material in the core, is deuterium.

Palladium nanoparticles often have a vacancy in their center. Similarly, LANR nanostructures include vacancies within them. In the alloys, they must drift into the bulk from the surface. This diffusion is slightly facilitated by the loading itself. *de novo* Pd–D vacancies have been made in loaded Pd (and Ni) with electron beam irradiation [15]. Codeposition has been used to make palladium, nickel and alloyed loaded materials on top of electrodes, and used dual anode LANR systems to produce very high levels of such LANR nanostructured materials locally. In addition, nanostructured materials have been used in LANR using palladium black [16] in a double structure (DS)-cathode. They reported more than 200 MJ of excess energy was continuously produced for over 3000 h at an average rate of 50–100 kJ/h. The DS-cathode is a Pd cathode with an internal vacuum zone filled with a deuterium storage type powder and an outer cylindrical vessel of Pd metal (wall thickness of 3 mm). Such bulk cathodes rely on diffusion, making it difficult to reach 100 at% concentration solid solution of D in Pd or the other nanostructured material. The D ions are postulated to move over the surfaces of the Pd black by the "spillover-effect", without the need to becoming D₂ molecules. Previously, we reported production of excess heat using nanomaterial palladium, nickel, and newer alloyed compounds, such as ZrO₂PdNi, and in a LANR transistor configuration, driven by two applied electric field intensities, which demonstrate LANR heat associated with low level near-infrared emission, controlled by two optimal operating point manifolds.

ZrO₂–(PdNi)–D LANR/CF nanostructured materials generate excess heat [3], including with acoustic and electric fields, and with additional significant effects from orthogonal applied DC magnetic field intensities [6]. There are complicated polarization/transconduction phenomena including an “avalanche (transconduction electrical breakdown) effect” which has a critical role in excess heat. The LANR nanostructured materials have been made into LANR/CF transistors [7] which exhibit energy gain and simultaneous non-thermal near infrared emission.

LANR materials and nanostructured materials, when active at their OOP, generate non-thermal near infrared (NT–NIR) emission. Dr. Stan Szpak (SPAWAR) et alia reported the emission of infra-red from LANR codeposition devices. However, they did not use a control or calibration. In 2008, Swartz demonstrated that two controls are needed, including normalization of NIR emission intensities to both non-energized background and to ohmic control areas; in experiments involving a variety of LANR metamaterial spiral-wound and other Phusor®-type lattice assisted nuclear reaction (LANR) systems, including high impedance palladium (Pd/D₂O/Pt, Pd/D₂O/Au), codepositional (Pd/Pd(OD)₂/Pt) heavy water, and nickel (Ni/H₂O_xD₂O_{1–x}/Pt, Ni/H₂O_xD₂O_{1–x}/Au) light water Phusor-type LANR devices. Swartz demonstrated that the emission of near-IR from the electrodes coupled with LANR operation is only observed when active electrodes operated at their optimal operating point, and that there was a linkage of excess power gain and heat flow with simultaneous NT–NIR emission [13]. Most importantly, NT–NIR is coupled and specific to the LANR devices’ excess heat production and not its physical temperature.

3. Experimental – Materials

We designed and prepared several generations of active LANR (CF) preloaded nanocomposite ZrO₂–PdNiD CF/LANR quantum electronic devices capable of significant, reproducible energy gain (Fig. 2). The preactivated LANR nanostructured material is incorporated into a proprietary self-contained CF/LANR quantum electronic component, called a two terminal NANOR®-type of LANR device. These feature two terminals and self-contained superior handling properties enabling portability and transportability. The Series V NANOR®-type LANR devices feature new structure and superior handling properties. Series VI NANOR®-type LANR devices augment that with new composition, and, most importantly, are preloaded so that LANR activation is separated from loading. The symbol N in a solid circle is used here to denote the active preloaded NANOR-type LANR device.

These are potentially very useful and more reproducible nanostructured CF/LANR quantum electronic devices, whose development has required control of their breakdown states and quenching tendencies. Most importantly, the activation of this cold fusion reaction is, for the first time, separated from its loading at room temperature [17,18]. As a result, these are called preloaded NANOR®-type nanocomposite LANR materials and devices. Generally speaking, nanostructure preparation, assembly, and driving are very complicated and there are several methods of each which will be briefly reviewed.

The NANOR®-type of LANR devices contain active nanostructured material in the core, which is ZrO₂–PdNiD, ZrO₂–Pd, ZrO₂–NiD, ZrO₂–NiH, ZrO₂–PdNiDAg, and the like, with the atomic ratios being usually in the range of Zr (~60–70%), Ni (0–30%), and Pd (0–30%) by weight, with the weights being before the oxidation step, and several later additional preparation steps. The additional D₂ and H₂ yield loadings (ratio to Pd) of up to more than 130% D/Pd. For simplicity, all of these nanostructured materials in the core, in their range of deuterations, will henceforth simply be referred to as ZrO₂–PdD, ZrO₂–NiHD, and ZrO₂–PdNiD.

For the NANOR-type LANR devices reported in this paper, although the nanostructured LANR material might be loaded with either hydride, at this time we have focused solely on D, and used experimental structures, paradigms, materials for that.

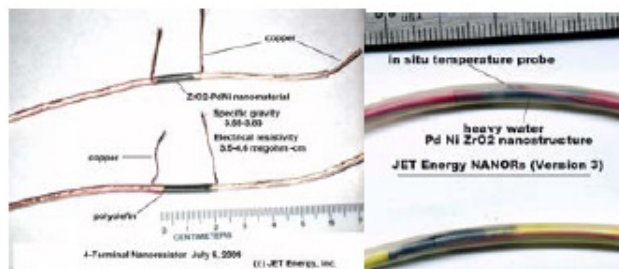


Figure 2. Series II and III two terminal NANOR[®]-type devices containing active ZrO₂–PdNiD nanostructured material at their core.

There are issues of particle size, electrical conductivity, potential contamination, and potential toxicity, that each must be discussed first. The size of nanostructured materials is key. The desired nanostructure islands of NiPd have characteristic widths of 2–20 nm size. This nanostructure size is selected because it can react cooperatively, generating large amplitude, low frequency oscillations. The characteristic width is between 7 and 14 nm. These size structures tend to be Raman active, with the islands having anharmonic terahertz vibrations. Furthermore, the storage capacity decreases rapidly when the nanostructure size is greater 30 nm. It is not unreasonable to see rapid drop off in LANR success if sizes are larger than 20–30 nm. The vibrations of nanostructured materials are very important for activity. The nanostructured vibrational modes are maximized with softening of the material in which they are contained. It is reported that some of the modes are so large that they can cause a sudden structural phase change to a lower free energy state.

Preparation of active nanostructured materials, able to undergo preloading, requires very pure materials. Contamination remains a major problem, with excess heat potentially devastatingly quenched. Contaminants can appear from both electrode and container degradation and leeching, from atmospheric contamination, especially after temperature cycling. Furthermore, the heavy water and D₂ are hygroscopic, therefore must be kept physically isolated from the air by seals.

Potential toxicity must be considered. Nanostructured and nanocomposite materials have potential human and environmental health hazards. The large number of particles, and greater specific surface area, yield increased absorptive risk through the skin, lungs, and digestive tract. In 2008, the Karolinska Institute (Sweden) examined the impact of metallic nanoparticles on human lung epithelial cells. Ferric oxide nanoparticles produced the smallest amount of DNA damage and were relatively non-toxic. Titanium and zinc oxide nanoparticles were more toxic, and carbon nanotubes also produced DNA damage. Cupric oxide nanoparticles were the most toxic, and are avoided here.

The preloaded NANORs involve palladium as one of the elements within the zirconia nanostructured material. Palladium powder can be obtained (Goodfellow, Alpha Aesar) which usually present sizes from 60 to 200 nm. Most relevant is deuterided palladium-black, palladium black dual cathode, glass ZrO palladium-black systems, and a wide variety of other nanostructures.

Pd and Ni nanoparticles can be made by chemical solution deposition, also known as the solution–gelation (sol–gel) process, used in ceramic engineering for making metal oxides. The precursor substrates are metallic alkoxides and chlorides which polymerize by hydrolysis forming a colloidal suspension. Solvent removal controls hydration, shrinkage and porosity. The deposition method controls whether films (dip- or spin-coating), ceramics, glasses, fibers, membranes, aerogels, or powders result. The technologies began in 1880 when it was noted that tetraethyl orthosilicate in acid forms SiO₂ monolithic fibers.

Nanocrystalline palladium has been made by inert gas condensation and compaction with grain, crystallite, sizes ranging from 5 to 50 nm. Palladium nanodendrimers of ~ 300 Pd atoms in a metallic core of 2.0 nm diameter are also fabricated with nearly 90% of the metal nanoparticle surface is unpassivated and available for catalysis. The dendrons inhibit metal agglomeration without adversely affecting chemical reactivity. Palladium nanoparticles and nanowires are also created by electrochemical deposition, usually on a carbon surface. Pd nanoparticles made on a gold surface show proton reduction catalytic activity enhanced by more than two orders of magnitude, as the diameter of the palladium particles decreases from 200 to 6 nm. As an alternative, there are the zirconium oxide binary and ternary Group VIII LANR materials. $\text{ZrO}_2\text{--PdNiD}$ and $\text{ZrO}_2\text{--PdH}$ are made by the initially by the Yamaura protocol and are used to store hydrogen gas for fuel cells. Arata used this powder for his LANR work. Today, second and third generation nanostructured powders, such as Zr 67% Ni 29% Pd 4% (by weight before the oxidation step), absorb a very large number of deuterons for each and every nickel and palladium nuclei. There are reports of numbers in the order of 3.5. Close up, in $\text{ZrO}_2\text{--PdNi--D}$ LANR/CF nanostructured materials, the lattice of Pd is expanded by Zr. There are then also wrought other major changes by the oxidation of the Zr. The nanostructured material, $\text{ZrO}_2\text{--(Pd}_x\text{Ni}_{1-x})$, is a composite distribution of nanostructured ferromagnetic “islands” separated among a vast dielectric zirconia “ocean”. The dielectric zirconia embeds uncountable numbers of nanostructured metal ternary alloy islands of the material containing now NiPdD. The appearance is like a chocolate chip cookie on the nanoscale. The “chips” are hydrided palladium nickel metallic alloy embedded in a zirconium oxide dielectric matrix (“cookie”).

The $\text{ZrO}_2\text{--(Pd Ni)D}$ is prepared in a complicated process that begins by oxidizing a mixture of zirconium oxide surrounding metallic palladium, nickel, or Pd–Ni islands. This raw materials, PdZr oxide and ZrPdNi oxide, are available from Santoku Corporation (Japan) and Ames National Laboratory (Iowa). These are made as follows. First, there is made a co-melt (e.g. Zr (65%), Ni (30%), Pd (5%)) in a silica ampoule by the arc technique. The molten alloy is then dripped, and rapidly cooled, into a glassy form. This is done by taking the co-melt, adding the additives at this point, and the dropping the glassy material slowly between two water-cooled copper wheels, each with an angular velocity of ~ 25 m/s. The sudden glassy freezing of the molten alloy produces an amorphous, metallic tinsel ribbon of size ~ 0.5 mm \times 2 to 20 mm \times ca 0.1 mm thick. Thus, the majority of the Pd and Ni alloys appear as a foil; silvery-colored, shiny bright, and smooth. The next step is to bake the prenanostructure material in the air for 25–75 h at temperatures in the range of 270–390°C. Upon heating in air, the zirconium metal oxidizes into the oxidized ZrO_2 (zirconia) matrix which surrounds, encapsulates, and separates the NiPd alloy into 7–10 nm sized ferromagnetic nanostructured islands located and dispersed within the electrically insulating zirconia dielectric. The metallic ribbons are not magnetic prior to the air bake oxidation. However, they become magnetic, and semiconducting after the bake. We use several additional steps. For example, the size must be decreased further. This can be achieved by a rotary polishing drum (Thumler’s Tumbler, Mod B). The rotary drum may take in the range of one to several days to achieve the size decrease, which must be carefully monitored. Flammability increases markedly as the size is decreased and finely powdered form appears; and therefore caution must be taken. Another series of steps are the backings of the prenanostructure material. On of these occurs over several days, at temperatures in the range of 270–390°C. Upon heating in air the zirconium metal oxidizes into the oxidized ZrO_2 (zirconia) matrix which surrounds, encapsulates, and separates the NiPd alloy into 10 nm sized ferromagnetic nanostructured islands in the insulating zirconia dielectric. The metallic ribbons are not magnetic prior to the air bake oxidation. They become magnetic, and semiconducting after the bake. If possible, the humidity should be removed because it can contribute to heterogeneity and inactive materials. Excessive temperatures should be avoided, because oxidation at 420°C for 24 h in air eliminates the smooth surface and makes the material inactive, as judged by in part to poor hydridation. The second baking is the vacuum bake at 200°C for 12–24 h. This is done to drive off any and all residual water vapor. Finally, the material can be very carefully ground in a mortar and pestle. The air bake temperature and time, and final proprietary dopants and processing appear to have critical importance.

The LANR nanostructured material is contained in the core volume (or chamber). The preloaded nanostructured material is placed into the hermetically sealed enclosure which is specially designed to withstand pressure, minimize

contamination, enable lock on of wires connecting to it. The enclosure is tightly fit because contamination is a potential problem, and because of the potential toxicity from the nanomaterial.

4. Experimental – Methods

The NANOR and the thermal control are at the center of much larger thermal mass in the calorimeter which is discussed in more detail in Ref. [1] (Fig. 2). The heat loss is the same for both the control and the component. One portion of the heat flow was measured by an Omega HFS Thin Film Heat flux sensor, with effort made to have significant heat flow go in one direction through the sensor.

The LANR preloaded, stabilized NANORs were driven by a high voltage circuit up to 3000 V rail voltage. The duty cycle was split with half going to a control portion consisting of a carefully controlled electrical DC pulse into an ohmic resistor which was used to thermally calibrate the calorimeter. These low power NANOR[®]-type components have been driven up to the two watt level.

The new controlled driving system uses pulse wave modulated microcomputer control of specialized very high voltage semiconductors linked to a current source driving system driving system coupled to the NANOR[®]-type LANR system. It provides an improved method of current control, enabling new activation, a new method of driving, an improved and better paradigm system and the ability to evolve paradigms. Furthermore, the system is excellent for preliminary tests to detect LANR activity, including for monitoring and/or examining changes in doping, and to examine different CF/LANR regions. We also employed a new series of LANR-directed light indicator outputs to define states which has been a matter of incredible utility and assistance almost every time the system and device has been used.

Basically, there are two levels of operation for NANOR LANR systems, low and high power. High power is useful for applications requiring larger amounts of power such as transportation, heating, and artificial organs. In this case, however, low power is used for several reasons including to facilitate the rapid time constant, and because this is for demonstration and teaching purposes. The new controlled driving system at low power was also very useful to more closely examine LANR and other systems for their activity, linearity, time-invariance, and even the impact of additives.

The instantaneous power gain (power amplification factor (non-dimensional)) is defined as $P_{\text{out}}/P_{\text{in}}$. The energy is calibrated by at least one electrical joule control (ohmic resistor) used frequently, and with time integration for additional validation. The excess energy, when present, is defined as $(P_{\text{output}} - P_{\text{input}}) * \text{time}$. The amount of output energy is determined from the heat released producing a temperature rise, which is then compared to the input energy. Data is taken from voltage, current, temperatures at multiple sites of the solution, and outside of the cell, and even as a 4-terminal measurement of the NANOR's internal electrical conductivity. Data acquisition has all temperature and electric measurements sampled at data rates of 0.20–1 Hz, with 24⁺ bit resolution (e.g. Measurement Computing (MA) USB-2416, or a Omega OMB-DaqTemp or equivalent; voltage accuracy 0.015 ± 0.005 V, temperature accuracy $< 0.6^\circ\text{C}$). All connections are isolated when possible, including where possible with Keithley electrometers, or their equivalent, for computer isolation. All leads are covered with dry, electrically insulating tubes, such as medical grade silicone, Teflon, and similar materials, used to electrically isolate wires. To minimize quantization noise, if necessary, 1 min moving averages may be used for some signals. The noise power of the calorimeter is in the range of ~ 1 –30 mW. The noise power of the Keithley current sources is generally ~ 10 nW. Input power is defined as $V * I$. There is no thermoneutral correction in denominator. Therefore, the observed power is a lower limit.

It is a long, expensive, arduous, effort to prepare these devices. The preloading of the nanostructured material is begun after preparation to the extent previously reported. This preloading system has achieved calculated loadings of 90 to $> 130\%$, with impressive results of excess heat over months at modest input power levels. The production of the preloaded core material involves preparation, production, proprietary pretreatment, loading, postloading treatment, activation, and then adding the final structural elements, including holder and electrodes. These are assembled to create the complete preloaded LANR nanomaterial package.

5. Results

It is clear that these preloaded nanostructured CF/LANR quantum electronic devices are very useful. The development of a more reproducible nanostructured CF/LANR quantum electronic device has not been easy, and has directly been linked to improved material, and avoidance of low-threshold breakdown states and quenching tendencies. Electrically, the response is complex. There are complicated polarization/transconduction phenomena including an “avalanche (transconduction electrical breakdown) effect” which has a critical role in excess heat generation [4]. The zirconia dielectric matrix is insulating at low voltage and keeps the nanoscale metal islands electrically separated. It also prevents the aggregation of the islands. Each nanostructured island acts as a short circuit elements during electrical discharge. These allow deuterons to form a hyperdense state in each island, where the deuterons are able to be sufficiently close together. In addition, the nanomaterial lattice of Pd is expanded by Zr, and also, but less so, by the H and D. In the former, there are then also wrought other major changes by the oxidation of the Zr. We previously reported sudden changes of, and generally large, electrical impedances of such NANOR[®]-type devices containing nanostructured materials. Several were ~ 3 m Ω when lower voltages were applied, but then as the voltage was increased to ~ 24 V, the impedance suddenly decreased to very low values. It was shown theoretically that this sudden reduction can be attributed to an “avalanche effect” that is typical of the current–voltage behavior that occurs in Zener diodes, and noted that this NANOR device, in principle, could be used in similar applications where Zener diodes have been used (e.g., for stabilizing circuits against potential surges in applied power). Control of the breakdown states and quenching tendencies has been critical. The newer materials have had transsample impedances of ~ 300 g Ω , creating several serious problems. Surmounted them has been difficult but of value.

First, these preloaded NANOR[®]-type LANR devices have significant high efficiency heat production, with significant improvement over all of their predecessors in sustained activity, including the highly successful metamaterial PHUSOR[®]-type of LANR device. At their core is the proprietary preloaded nanostructure material specially prepared by several new processing steps. As a result, they had a much higher energy gain, even compared to the 2003 demonstration unit (Energy gain 14.1 in 2012 vs an energy gain ~ 2.7 in 2003). In fact, the current Series VI NANORs have had even higher gains (to beyond 30).

Second, these JET Energy Inc. devices are conveniently preloaded, mountable as easily activated LANR (CF) components into Integrated Circuits. They are a new generation of activated CF/LANR nanocomposite ZrO₂–PdNiD electronic devices.

In the case of the Series V and VI NANOR[®]s ((miniature preloaded CF/LANR devices), the activation the activation of this cold fusion reaction is, for the first time, separated from its loading at room temperature. In every other system known, Fleischmann and Pons, Arata, Miles, and the others, the loading has been tied to activation.

By contrast, in the case of the sixth generation NANOR[®]s, unlike the others, the preloaded devices can be simply electrically driven.

Third, combined with a surrounding calorimeter and a unique driving system whose design, driving configuration and implementations, in conjunction with the NANOR[®] have made portability of LANR to MIT, and elsewhere, possible. This has created two spin-offs. The first is that the proprietary microprocessor controlled system has also led to an evolving series of improved driving paradigms to qualitatively explore and then exploit loaded nanostructured, nanocomposite, and other materials including semiquantitatively examining them for usefulness, heat-production activity, linearity, time-invariance, and even the impact of additives and contaminants. The other has been the demonstrated superior operation through preloaded nanostructured LANR material and requisite driving configuration over months. This has been shown by low power open demonstration, including the 2012 Open Demonstration at MIT which ran from January 30, 2012 through mid May 2012 (Figs. 1, 3, 4).

The self-contained CF/LANR quantum electronic component, a two terminal NANOR[®] containing active ZrO₂–PdNiD nanostructured material at its core, showed energy gain during, and after, the January, 2012 IAP MIT Course on

CF/LANR. In this case, the mini-sized NANOR is a 6th generation CF/LANR device, and it is smaller than 2 cm, with less than 1 g of active material. However, this is actually a matter which is not *de minimus* because the LANR excess power density was more than 19,500 W/kg of nanostructured material. The preloaded NANOR[®]-type LANR device demonstrated an average energy gain (COP) of $\sim 14\times$ ($\sim 1412\%$) the input for a duration of several hours that it was observed during the MIT IAP course on the first day, and levels of that order continued.

Over several weeks, the CF/LANR quantum device demonstrated more reproducible, controllable, energy gain which ranged generally from 5 to 16 (14.1 while the course was ongoing). The NANOR[®]-type preloaded LANR device openly demonstrated features include its convenient size (much smaller) and its superior handling properties which enable unique portability, and transportability. Like its 2003 (ICCF-10) predecessor demonstration, this preloaded NANOR[®]-type LANR device also showed excess energy and also further improvements of decreased size, decreased response time, improved and dual diagnostics, and increased total output energy density. The set-up was designed to run at low power input levels to increase the safety at the educational institution for its multi month-long stay at MIT. A range of experiments were conducted examining the impact of various driving sequences, and the NANOR[®] continued to produce excess energy, confirmed by daily calibrations. That system had parallel diagnostics including calorimetry, input-power-normalized ΔT , and focused heat flow measurement, and several calibrations. One of the calibrations included an ohmic (thermal) control located next to the NANOR, used to ascertain activity. To enable demonstrations at MIT for the NANOR system, including in the MIT IAP class where multiple experiments had to be shown to classes extending over times of 2 h, a specialized heat flow semiquantitative analyzer was specially developed. The heat which this preloaded NANOR[®]-type LANR device demonstrated was monitored three ways by three independent systems for semiquantitative measurement of the energy produced. Furthermore, the output of the NANOR[®] is compared to an ohmic control. First, the energy produced is instantaneously and kinematically determined by the ratio of the input power normalized temperature increase, called by the symbol ' $\Delta T/P_{in}$ ' referring to the increase of temperature (ΔT), divided by the input electrical power (P_{in}). Second, it is also instantaneously and kinematically evaluated over a wide area by the ratio of the input power normalized heat flow leaving it, called by the symbol ' HF/P_{in} ' referring to the heat flow (HF) divided by the input electrical power (P_{in}). Third, it is examined by calorimetry, calibrated by the thermal ohmic control, and confirmed by long-term time integration. These three methods of verification are pooled to derive very useful information, semiquantitatively ascertain energy produced, and infer activity.

Figures 1,3,4 show this entirely new, more reproducible, much more powerful configuration of clean, efficient energy production from several points of view. The figures include raw data and derived information from the runs which show conclusively LANR excess energy heralded by calorimetry and by input power normalized incremental temperature (ΔT) changes. These graphs shows a small portion of the collected data and derived information which was actually collected and analyzed by the class, and later in a four month interval.

Figure 1 is set of curves which plot the temperature rise (ΔT in $^{\circ}\text{C}$) of the preloaded NANOR[®]-type LANR device and the ohmic control normalized to input electrical power. The NANOR[®] device received more than 10, and the ohmic control received five, levels of input electrical power. Each is shown with its thermal output response to its electrical input. Figure 1 presents the differential temperature rise normalized to input electrical power for the preloaded NANOR[®], for the case with no input power ("Background"), and for the case of input to the ohmic thermal control, located at the core. The x -axis represents time, and each count represents 7 s. The y -axis on the left-hand side represents electrical input power in watts. Each of the outputs is read off of the right-hand side. The y -axis on the right-hand side represents the amount of temperature rise (differential temperature increase) normalized (that is, divided by) to the electrical input power. The units of this axis are in $^{\circ}\text{C}/\text{W}$. Calibration pulses, used for accuracy and precisions checks of voltages and currents, are also shown. Compare the ΔT output normalized to input power for preloaded NANOR[®]-type LANR device to the thermal (ohmic) control. Observe that despite lower input electrical

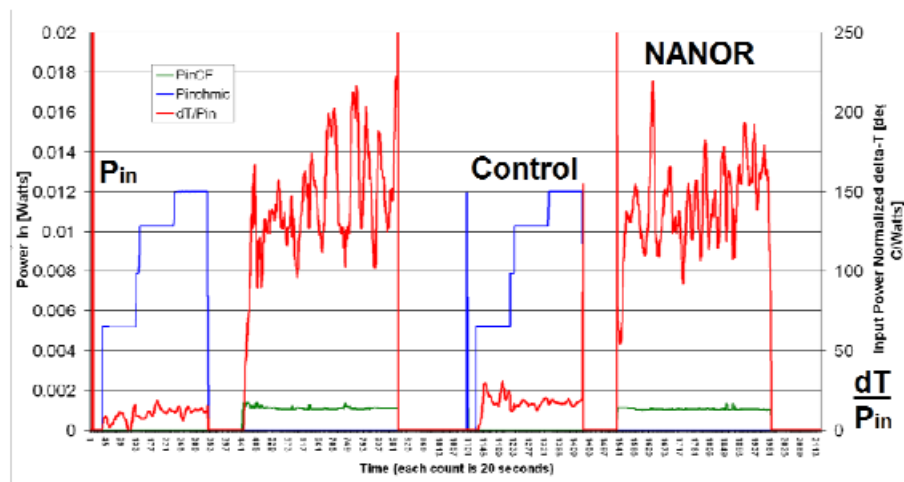


Figure 3. Input Power and Resulting Output Temperature rise (normalized to input electrical power) of a self-contained CF/LANR quantum electronic component, a Series VI two terminal NANOR[®]-type device containing active preloaded ZrO₂/PdD nanostructured material at its core. These curves plot the temperature rise normalized to input electrical power.

power to the NANOR[®], the temperature rise normalized to input electrical power observed in the core was higher than expected, as compared to the ohmic control. Note the active preloaded LANR quantum electronic device again clearly shows significant improvement in thermal output, here input-power-normalized compared to a standard ohmic control (a carbon composition resistor). Figure 1 heralds the excess energy achieved by the Series V NANOR[®] type of LANR device. It can be seen that the input power normalized delta-measurements suggests strongly the presence of excess heat.

Figure 3 shows the excess energy achieved by a slightly different type of self-contained CF/LANR quantum electronic component. This Series VI, preloaded, two terminal NANOR[®]-type device contained active preloaded ZrO₂/PdD nanostructured material at its core. These curves plot the temperature rise normalized to input electrical power. It can be seen that the input power normalized delta-measurements suggests strongly the presence of excess heat.

Figure 3 is set of curves which plot the temperature rise (ΔT in °C) of the preloaded NANOR[®]-type LANR device and the ohmic control normalized to input electrical power. The NANOR[®] device received a single level of electrical input power and the ohmic control received three levels of input electrical power. Each is shown with its thermal output response to its electrical input. Figure 3 presents the differential temperature rise normalized to input electrical power for the preloaded NANOR[®], for the case with no input power ("Background"), and for the case of input to the ohmic thermal control, located at the core. The x -axis represents time, and each count represents 20 s. The y -axis on the left-hand side represents electrical input power in watts. Each of the outputs is read off of the right-hand side. The y -axis on the right-hand side represents the amount of temperature rise (differential temperature increase) normalized (that is, divided by) to the electrical input power. The units of this axis are in °/W. Calibration pulses, used for accuracy and precisions checks of voltages and currents, are also shown.

Compare the ΔT output normalized to input power for preloaded NANOR[®]-type LANR device to the thermal (ohmic) control. Observe that despite lower input electrical power to the NANOR[®], the temperature rise normalized to input electrical power observed in the core was higher than expected, as compared to the ohmic control. Attention is

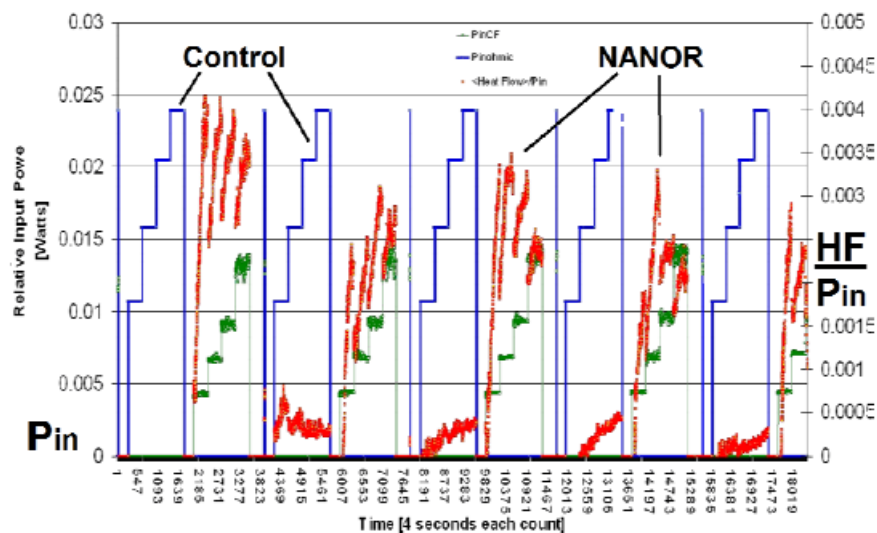


Figure 4. Input Power and Output Heat Flow normalized to input electrical power of a self-contained CF/LANR quantum electronic component 6-33.

directed to the fact that the active preloaded LANR quantum electronic device again clearly shows significant improvement in thermal output, here input-power-normalized compared to a standard ohmic control (a carbon composition resistor).

Figure 3 heralds the excess energy achieved by the Series V NANOR[®] type of LANR device. It can be seen that the input power normalized delta-measurements suggests strongly the presence of excess heat.

Figure 4 is set of curves which plot the heat flow, normalized to input electrical power, leaving the system while driving the preloaded NANOR[®]-type LANR device and the ohmic control at four different electrical input powers. The heat flow is in response to the electrical input. The figure presents the output heat flow for the preloaded NANOR[®], for the case with no input, and for the ohmic thermal control, located at the calorimeter's core. In Fig. 4, the x-axis represents time, and each count represents 4 s. The y-axis on the left-hand side represents the electrical input power in watts. The y-axis on the right-hand side represents the Heat Flow output normalized (that is, divided by) to the electrical input power. Calibration pulses, used for accuracy and precisions checks of voltages and currents, are also shown. In Fig. 4, compare the output heat flow normalized to input power for NANOR[®]-type LANR device to that for the thermal (ohmic) control. The long term heat flow measurements (using calibrated devices) confirm the presence of excess energy, and validate the other measurements.

It can be seen that despite lower input electrical power to the NANOR[®], the heat flow out in response, normalized to input electrical power observed in the core, was higher than expected, as compared to the ohmic control – especially at lower input power levels. The response of the NANOR[®]-type LANR device is consistent with very efficient energy production, with the energy output as heat. The changes of the output with input power is consistent with the optimal operating point manifold of the LANR material. Therefore, the figure heralds the significant excess energy coming from, the preloaded NANOR[®]-type of LANR device.

Attention is directed to the fact that the active preloaded LANR quantum electronic device clearly again shows significant improvement in energy generated compared to a standard ohmic control (a carbon composition resistor) by

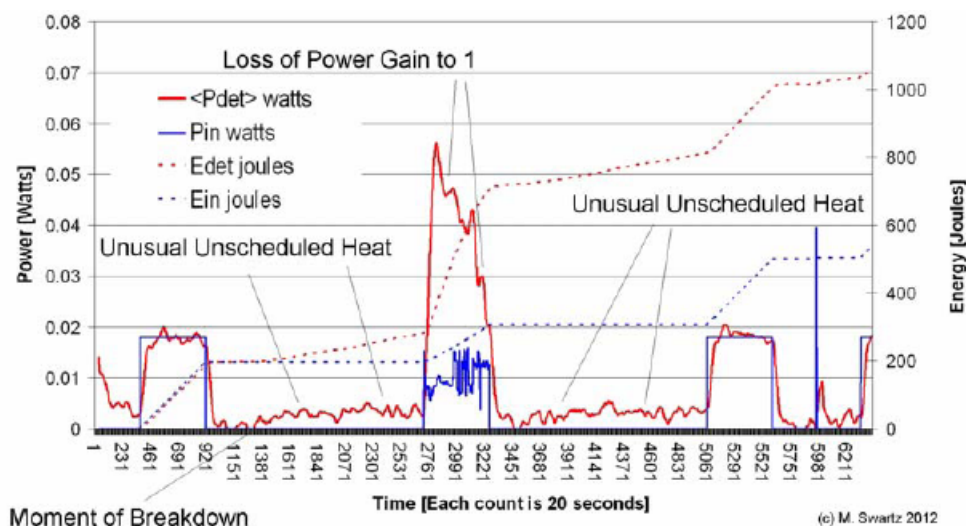


Figure 5. Electrical Input Power and Output Calorimetric response of a se NANOR[®]-type of CF/LANR quantum electronic component and the Catastrophic loss resulting in loss of excess energy.

this method, too, using heat flow. This information corroborates the marked and substantive incremental increase in energy output as heat for the preloaded Series VI NANOR[®]-type of LANR device.

Figure 5 is set of curves showing that under some conditions the NANOR[®] can actually catastrophically lose its excess energy producing properties becoming the exact equivalent of the ohmic control, and under some conditions creating distinguishing features in the calorimetry. Figure 5 shows curves which plot the electrical input power, at one input power level each to the preloaded NANOR[®]-type LANR device and the ohmic control, and the calorimetric responses of both.

The x -axis represents time, and each count represents 20 s. The y -axis on the left-hand side represents electrical input power in watts. The y -axis on the right-hand side represents the amount of energy released. The units of this axis are in joules. The figure shows the input, and the calorimetry, of preloaded NANOR[®] along with that for the ohmic thermal control used to calibrate the system. Those calibration pulses, used for accuracy and precisions checks of voltages and currents and time, are also shown. The inputs to the thermal ohmic control, followed by the preloaded NANOR[®]-type device, are shown, as are the calibrated calorimetric outputs for both.

Each of the outputs is read off on the right-hand side. The latter curves represent time integration to determine total energy. They thus rule out energy storage, chemical sources of the induced heat, and other sources of possible false positives. Compare the output for NANOR[®]-type LANR device to the thermal (ohmic) control. As can be seen, this semiquantitative calorimetry, itself calibrated by thermal waveform reconstruction, was consistent with excess heat being produced only during energy transfer to the NANOR[®]-type LANR device.

Notice that the active preloaded LANR quantum electronic device clearly shows significant improvement in thermal output compared to a standard ohmic control (a carbon composition resistor), however, in this case, there is instability in electrical input, at which time the excess energy produced by the device falls precipitously until the efficiency falls toward the equal to that of an ohmic thermal resistor (i.e. 100%). Note also that there was a sudden leakage of D from preloaded NANOR[®]-type LANR device with the “candle meltdown”-signature and the appearance of excess energy

from the exogenous nanostructure material. This refers only to the “melted candle”-shape of the temperature curve. This breakdown is the reason for the importance of the hermetic shields and the careful control via the sketch-driver system. It is also consistent with the catastrophic active media (CAM) theory of LANR/CF [19,20]. The graph is representative of the NANOR[®]-type of CF/LANR technology, and it shows quite clearly demonstrated over unity thermal output power from the NANOR[®] until the catastrophic event.

6. Conclusion

In summary, most importantly, for these NANOR[®]-type CF/LANR devices, the semiquantitatively measured output energy *is* a significant energy gain. This has always been a goal post for cold fusion, and one which so far remains beyond the realm for hot fusion on Earth by engineering means. As importantly, for these NANOR[®]-type CF/LANR devices, the activation of this cold fusion reaction is, for the first time, separated from its loading, at room temperature. Furthermore, the uniqueness of the preloaded LANR nanostructured material-device includes, beyond its high LANR activity, and its preloaded convenient nature, includes its dryness, its precise containment, and its easy portability. It begins a new generation of CF/LANR nanostructured materials and devices.

The present device and driving technology have provided high-efficiency preloaded energy-, heat-, and product-producing devices which can be electrically driven and has provided a method of improved activation and reproducibility for controlling lattice assisted reactions and their generated products using nanostructured, nanocomposite, and other materials.

Preloaded CF/LANR nanocomposite materials in CF/LANR Electronic Devices do have usefulness today and tomorrow. Today, they can be clearly examined with this system for demonstrations of their CF/LANR activity, linearity, time-invariance, and the impact of additives. For example, the present device, and controlling/driving system provided a reliable low power, high-efficiency (compared to an ohmic control; i.e. 100%) energy production device for demonstration and teaching purposes of size smaller than a centimeter, with an active site weight of less than 100 milligram.

The preloaded nanostructured LANR material and accompanying controller and driver shown at MIT was a successful (second) open demonstration of CF/LANR heat production and energy conversion device. This again confirms LANR/CF.

This open demonstration over months has demonstrated that microprocessor controlled integrated circuits using LANR quantum optical devices containing preloaded nanostructured LANR material can be used as an effective very clean, highly efficient, energy production system, apparatus, and process. In addition, elsewhere, this driving and monitoring system was useful to easily convert conventional monitoring and conventional thermometry into fine calorimetry. Calorimetry and input-power-normalized ΔT were used to ascertain activity. For example, this system has been used to show the calorimetry of a nanostructured composite CF/LANR Device using twenty different levels of input. This method is similar to, but beyond, that suggested by Dr. Robert W. Bass [21]. After testing it, we have determined that it was highly useful, and now use it routinely, wherever possible.

We have run the component over a year with evanescent loss which is attributed to fuel loss, or redistribution, or inactivation (perhaps by reaction with another material). Whether they can be refueled or simply replaced, is under investigation. Going forward, preloaded LANR nanostructured materials and devices will also be useful for integrated circuits and other applications using a pre-activated nanostructured and other materials. These include high power, self-contained, microprocessor controlled, preloaded, energy production devices and systems enabling their activation for electronic, medical, space and avionic circuits, integrated circuit devices, and artificial intelligence systems.

Acknowledgements

The authors gratefully thank Peter Hagelstein, Alex Frank, Alan Weinberg, Allen Swartz, Charles Entenmann, Dennis Cravens, Dennis Letts, Brian Ahern, Jeff Driscoll, Larry Forsley, Pamela Mosier-Boss, Robert Smith, Robert Bass, and the late Talbot Chubb; and JET Energy and New Energy Foundation for support. PHUSOR[®] and NANOR[®] are registered trademarks. NANOR[®]-type and PHUSOR[®]-type technologies, and other discussed IP herein, is protected by U.S. Patents D596724, D413659 and other patents pending.

References

- [1] M. Swartz and P.L. Hagelstein, Demonstration of energy gain from a preloaded ZrO₂–Pd nanostructured CF/LANR quantum electronic device at MIT, *ICCF17*, 2012.
- [2] M. Swartz, Survey of the observed excess energy and emissions in lattice assisted nuclear reactions, *J. Sci. Exploration* **23** (4) (2009) 419–436.
- [3] M. Swartz, Excess power gain using high impedance and codepositional LANR devices monitored by calorimetry, heat flow, and paired stirling engines, *Proc. 14th Int. Conf. on Cold Fusion (ICCF-14)*, 10–15 August 2008, Washington, D.C., D.J. Nagel and M. Melich (Eds.), ISBN: 978–0–578-06694-3, 2010, p. 123.
- [4] M. Swartz and G. Verner, Excess heat from low electrical conductivity heavy water spiral-wound Pd/D₂O/Pt and Pd/D₂O–PdCl₂/Pt devices, *Condensed Matter Nuclear Science, Proc. ICCF-10*, P. Hagelstein and S Chubb (Eds.), World Scientific, NJ, ISBN 981–256–564-6, 2006, pp. 29–44, 45–54.
- [5] M. Swartz, The impact of heavy water (D₂O) on nickel-light water cold fusion systems, *Proc. the 9th Int. Conf. on Cold Fusion (Condensed Matter Nuclear Science)*, Beijing, China, Xing Z. Li (Ed.), May 2002, pp. 335–342.
- [6] M. Swartz, Impact of an applied magnetic field on the electrical impedance of a LANR device, Volume 4 JCMNS, Proc. of the March 2010, New Energy Technology Symposium held at the 239th American Chemical Society National Meeting and Exposition in San Francisco (2011).
- [7] M. Swartz, LANR Nanostructures and Metamaterials Driven at their Optimal Operating Point, 3rd Volume of the LANR/LENR Sourcebook, October 21, 2011
- [8] M. Swartz and G. Verner, The Phusor[®]-type LANR cathode is a metamaterial creating deuteron flux for excess power gain, *Proc. the 14th Int. Conf. on Condensed Matter Nuclear Science and the 14th Int. Conf. on Cold Fusion (ICCF-14)*, 10–15 August 2008, Washington, D.C., ISBN: 978–0–578-06694-3, 2010, p. 458.
- [9] M. Swartz, Optimal operating point manifolds in active, loaded palladium linked to three distinct physical regions, *Proc. of the 14th Int. Conf. on Condensed Matter Nuclear Science and the 14th Int. Conf. on Cold Fusion (ICCF-14)*, 10–15 August 2008, Washington, D.C., David J. Nagel and Michael E. Melich (Eds.), ISBN: 978–0–578-06694-3, 2010, p. 639.
- [10] M. Swartz, Quasi-one-dimensional model of electrochemical loading of isotopic fuel into a metal, *Fusion Technol.* **22**(2) (1992) 296–300.
- [11] M. Swartz, Consistency of the biphasic nature of excess enthalpy in solid state anomalous phenomena with the quasi-1-dimensional model of isotope loading into a material, *Fusion Technol.* **31** (1997) 63–74.
- [12] M. Swartz, Codeposition of palladium and deuterium, *Fusion Technol.* **32** (1997) 126–130.
- [13] M. Swartz, G. Verner and A. Weinberg, Non-thermal near-ir emission from high impedance and codeposition LANR devices, *Proc. the 14th Int. Conf. on Condensed Matter Nuclear Science and the 14th Int. Conf. on Cold Fusion (ICCF-14)*, 10–15 August 2008, Washington, D.C., ISBN: 978–0–578-06694-3, 2010, p. 343.
- [14] M. Swartz and G. Verner, Bremsstrahlung in hot and cold fusion, *J New Energy* **3**(4) (1999) 90–101.
- [15] M. Swartz, P.L. Hagelstein, G. Verner and K. Wright, Vacancy-phase nickel cathodes, Abstracts, ICCF7, 1997, p. 137.
- [16] Y. Arata and Y.C. Zhang, Observation of anomalous heat release and helium-4 production from highly deuterated palladium fine particles, *Jpn. J. Appl. Phys.* **38** (Part 2, No. 7A) (1999) L774–L776.
- [17] F.L. Tanzella and M.C.H. McKubre, Calorimetry of pulse electro-melting of PdD_x wires, *Proc ICCF15*, 2009, pp. 42–46
- [18] F. Tanzella, J. Bao, M. McKubre and P.L. Hagelstein, Stimulation of metal deuteride wires at cryogenic temperatures, *J. Cond. Matter Nucl. Sci.* **8** (2012) 176–186.

- [19] M. Swartz, Catastrophic active medium hypothesis of cold fusion, Vol. 4. *Proc. Fourth Int. Conf. on Cold Fusion* sponsored by EPRI and the Office of Naval Research (1994).
- [20] M. Swartz, Hydrogen redistribution by catastrophic desorption in select transition metals, *J. New Energy* **1**(4) (1997) 26–33.
- [21] R.W. Bass, Five frozen needles CF protocol, *J. New Energy* **6**(2) (2002) 30.



Research Article

Forcing the Pd/¹H–¹H₂O System into a Nuclear Active State

Stanislaw Szpak and Frank Gordon*

SPAWAR Systems Center (Retired), San Diego, CA USA

Abstract

In cells employing cathodes prepared by the co-deposition process, the polarized Pd/D–D₂O system becomes nuclear active when the concentration of deuterium, expressed as D/Pd atomic ratio, is equal to or greater than one. In contrast, to activate the polarized Pd/H–H₂O system, action of an external magnetic field and modulation of cell current or both are required. Evidence for the nuclear active state in the Pd/H–H₂O system, namely deuterium production, particle emission and catastrophic thermal event, is presented. Extension of nuclear active state to the Pd¹H/¹H₂O system under the application of an external magnetic field and modulated cell current profile is discussed.

© 2013 ISCMNS. All rights reserved. ISSN 2227-3123

Keywords: Nuclear Active State, Electron capture

1. Introduction

The emission of soft X-rays [1] and production of tritium [2] led us to the conclusion that an electron capture by a deuteron might be one of the nuclear reactions generating the F–P effect in the polarized Pd/D–D₂O system. We reviewed the available empirical evidence and concluded that the proper course of action is to examine in detail the content and meaning of the electron capture reaction. While the essential goal of nuclear physics is to interpret the nature of nuclear forces, that of nuclear chemistry is to cast transmutation in terms used in chemical reactions [3]. It does not matter which methodology is employed, because the governing laws are the same. In what follows, the discussion is limited to chemical reasoning and terminology. The transition from chemical to physical terminology is by substituting negative binding energy, $-\epsilon$, for chemical potential, μ , i.e. $\mu(p) = -\epsilon(p)$.

1.1. The content and meaning of the electron capture reaction

In the Landau and Lifshitz Treatise [4] we find a nuclear reaction, which may be symbolically written as $A_Z + e^- \rightarrow A_{Z-1} + \nu$, where A_Z denotes a nucleus of atomic weight A and charge Z , e^- an electron and ν a neutrino. The neutrinos are not retained by matter and leave the body. Nuclear reaction of this type may be represented by equations

*E-mail: dr.frank.gordon@gmail.com

which correspond exactly to those employed in chemical reactions. Consequently, it is not difficult to write down the thermodynamic conditions for the reaction



to proceed, namely that the inequality $\mu(e^-) > \mu(n) - \mu(p^+)$ is positive.

Equation (1) as written is the usual representation of a chemical reaction. It provides only limited information, namely it is the statement of conservation of mass, energy and charge. Since the initial and final states are not specified, it simply means that the system consists of unbounded particles in the sense that there is a continuous range of possible energies. Since there are two partners, electrons and lattice interacting protons, energies of both must be considered, a conclusion neglected in the Widom–Larsen theory.

1.2. Protons in lattice

All protons located in the reaction volume interact with the Pd lattice to a various degree. The chemical potential of interacting protons, p_l^+ , is of the form $\mu(p_l^+) = \mu(p^+) + u(r)$ where $u(r)$ denotes the energy of interaction. To evaluate the $u(r)$ function, we consider the relation $\mu(p) = -\epsilon(p)$, i.e. the chemical potential of a particle p is its negative binding energy. In this representation, the $u(r)$ term indicates that a part of the interacting site is incorporated into the proton itself, i.e. it represents the degree of an overlap which, in turn, determines whether or not the electron capture by proton can occur. For an electron capture by a proton to occur, the quantity $\mu(n) - \mu(p_l^+)$ must be positive. Since light water electrolysis alone does not produce a nuclear active state, it follows that $\mu(p_l^+)$, is greater than that of the neutron, $\mu(n)$, i.e. irrespective of its energy, the electron capture by proton cannot occur.

1.3. Sequence of events

The sequence of events leading to the initiation of the nuclear active state is shown in a diagram, Fig. 1.

Here, the events within the metal side of the interphase are: an exchange between the adsorbed and absorbed hydrogen, H_{ad}, H_{ab} , the transition from atomic to nuclear state that occurs when the hydrogen atom gives up an electron and becomes a proton, denoted $H_{ab} \rightarrow p^+$, followed by $p^+ \rightarrow p_l^+$, the latter identifies a proton interacting strongly with the Pd lattice with the formation of a metallic bond. When an external magnetic field, ψ , is applied, a new set of processes can be identified, viz weakening of the interaction, $p_l^+ \rightarrow p_*^+$, electron capture by proton, $e^- + p_*^+ \rightarrow n$, with

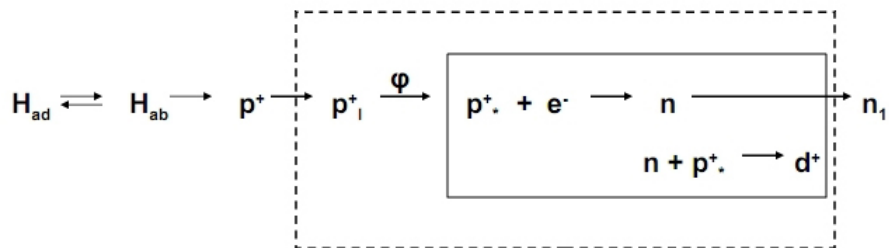


Figure 1. Schematic diagram showing events within the interphase. Enclosed by broken lines are processes affected by an external field; by solid line – coupled nuclear reactions.

neutrons either escaping, n_1 , or reacting with proton to yield deuteron, $n + p_*^+ \rightarrow d^+$. At the beginning, the simplest, and the only reaction that yields neutrons in this system is the electron capture by proton.

2. Coupled Reaction

Under the action of an external magnetic field, the transition $p_1^* \rightarrow p_*^+$ takes place and, as indicated, reaction $e^- + p_*^+ \rightarrow n$ occurs. With the passage of time, the second, highly energetic reaction $n + p_*^+ \rightarrow d^+$, takes place to become the primary energy supplier for the first reaction. The reaction product, the deuteron, reacts with an electron, $e^- + d^+ \rightarrow 2n$. Here, we have a situation in which the first reaction is accelerated by its product via the energy supplied by the chemical change in the substance (here neutrons) which induces the first reaction. Restating: the first reaction is induced by the second and third reaction via the energy transfer. Such kinetics is referred to as induction kinetics [6].

3. Forcing into Nuclear Active State – Effect of Magnetic Field

The interaction of a magnetic field with electrochemical systems can be divided into three main areas: (i) magneto-hydrodynamic effects, i.e. those affecting mass transport via the reduction of the diffusion layer thickness, (ii) magneto-mechanical effects, i.e. those that involve the shape change of micro-globules as well as complex macro-molecules, Fig. 2, and (iii) non-specific interactions of electronic nature, i.e. those affecting dynamics of the highly concentrated hydrogen in the Pd lattice. These effects are attributed to forces generated by the gradients of magnetic energy density, i.e. by forces that arise from non-homogeneity of the paramagnetic entity and those associated with non-uniformity of the magnetic field.

The data presented in Fig. 3 show typical potential/time curve for the desorption of hydrogen from the electrode having structure shown in Fig. 2b, in absence and presence of an external magnetic field, curves a and b, respectively. Here, the electrode potential/time relation, $\Phi(t)$, shows, Fig. 3, that the time for the transition from transport to surface controlled desorption of hydrogen, segments AB and BC, is substantially shorter when an external magnetic field was applied. Such behavior indicates that magnetic field weakens the proton/Pd defect interaction, i.e. $\mu(p_1^+) > \mu(p_*^+)$.

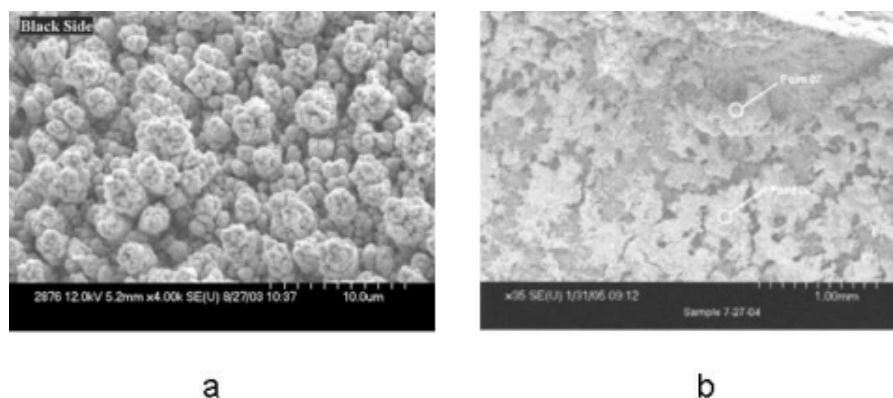


Figure 2. (a) SEM photograph of the electrode surface with no magnetic field applied. (b) Applied magnetic field.

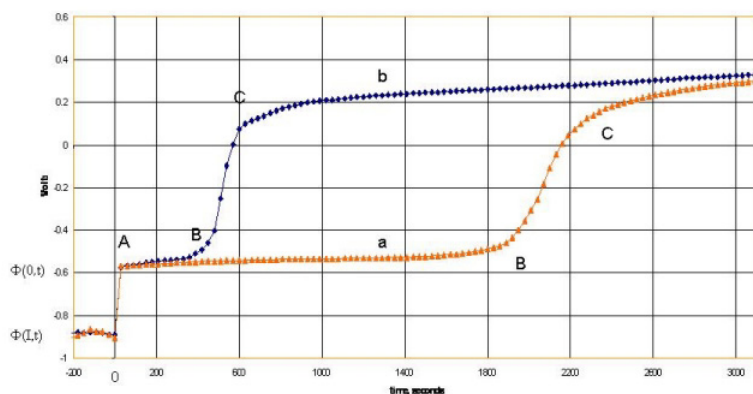


Figure 3. Hydrogen desorption rates. Curve a in the absence of magnetic field. Curve b in the presence of external magnetic field.

4. Experimental

4.1. Cell construction and operation

A rectangular cell, made of clear plastic, with affixed neutron detectors (CR-39 chips) and electrodes connected to a galvanostat (Princeton Applied Research, model 363) was placed in an external magnetostatic field. Upon placing an operating cell (with $i = -30 \text{ mA cm}^{-2}$) in the magnetic field, Fig. 4, electrochemical compression of absorbed hydrogen was put under computer controlled regime (LabView program) with $i = -400 \text{ mA}$ for 90 s and $i = 5.0 \text{ mA}$ for 5 s. The fabrication of cathodes involves (a) co-deposition from a solution of 0.03 M PdCl_2 and 0.3 M LiCl dissolved in H_2O at $i = -1.0 \text{ mA/cm}^2$ for the first 24 h followed by $i = -3.0 \text{ mA/cm}^2$ for the time required to reduce all the Pd^{2+} ions; (b) a 3–4 h stabilization period at $i = -30 \text{ mA/cm}^2$, i.e. the time needed to assure uniform distribution of absorbed hydrogen throughout the electrode volume. Additional detail is provided by Szpak et al. [6].

4.2. The art of Pd + H co-deposition

The Pd + H co-deposition may be viewed as a special case of production of alloys by electrochemical processing. It involves simultaneous deposition of more than one component. This is done by the reduction of ions present in the electrolyte. Briefly, for the production of Pd/H alloy, the relevant reactions are: $\text{Pd}^{2+} + 2\text{e}^- \rightarrow \text{Pd}$ and $\text{H}_2\text{O} + \text{e}^- \rightarrow \text{H} + \text{OH}^-$. In practice, however, these reactions depend on the electrolyte composition. For the co-deposition from a solution containing PdCl_4^{2-} complexes, Naohara [7] found that the reduction of Pd^{2+} proceeds via the reduction of an adsorbed PdCl_4^{2-} complex resulting in a layer-by-layer growth of the Pd film. However, the orderly growth of deposited palladium is disturbed by the adsorbed hydrogen generated by the reduction of water. Ohmori et al. [8] using a scanning tunneling microscope, proposed a model where the H^+ ions are adsorbed and reduced at the surface. A part of the adsorbed hydrogen enters the Pd lattice and accumulates around lattice defects. Through this process, the surface is transformed into a modular-like structure. Figure 5 showing mechanism of growth and SEM of actual deposit.

Figure 6 illustrates the procedure when (i) reduction of PdCl_4^{2-} and H_2O are independent of each other, (ii) electrolyte

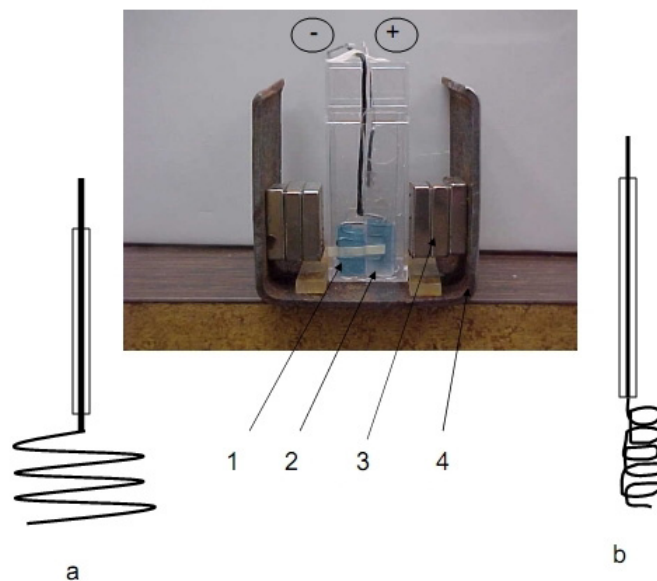


Figure 4. Electrochemical cell. 1–outside CR–39 detector, 2 – double CR–39 stock located inside the cell, 3 – neodymium magnets, 4 – magnet holder. Cathode and anode identified by Fig. 1a. Cathode assembly designed for neutron detection, 1 – CR–39 chips inside the cell, 2 – CR–29 outside the cell; Fig. 1b – for determination of deuterium content.

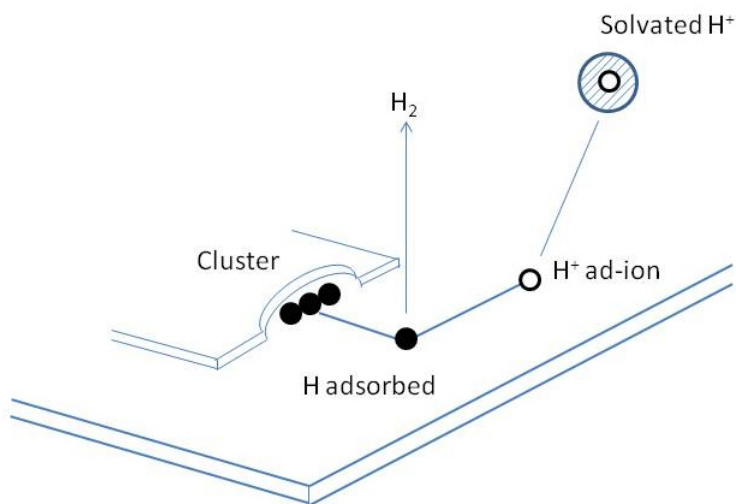


Figure 5. Representation of the development of micro-globules during co-deposition.

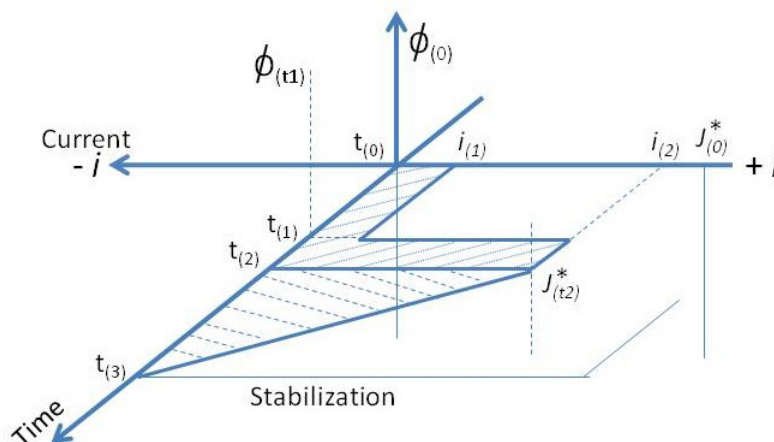


Figure 6. Cell current profile during the co-deposition process.

volume and electrode surface remain constant, (iii) reduction of Pd ions is diffusion controlled^a and (iv) no other charge transfer reactions occur. Under these conditions the electrode rest potential, $\Phi(0)$, is determined by solution composition. At $t = 0$, a constant cell current, I_1 , is applied. In practice it is much smaller than the limiting current, $I_1 \ll j_{1,\text{lim}}$. Note that in Fig. 6, j^* denotes the limiting current. This is done to assure an adherent Pd deposit. With the passage of time, the Pd^{2+} ions are depleted, the electrode potential, driven by the cell current, becomes more negative. At $t = t_1$ the cell current is increased to I_2 , i.e. to a value very close to the limiting current. This is done to assure a long co-deposition period. When the applied current density, I_2 , by reducing the concentration of Pd^{2+} ions, becomes the limiting current (for that concentration), the electrode potential is driven into the region of heavy water instability and at $t = t_2$, the reduction of D^+ ions commences

5. Evidence

5.1. Detection of neutrons

Figure 7 shows typical images of tracks recorded on CR-39 chips. The examination of the CR-39 chips, located inside and outside, indicates no difference in the type of tracks but in their number, the latter being highest on the CR-39 detector facing the cathode and the lowest on the chip located outside the cell. In particular, Fig. 7(a) shows a typical distribution of images of circular and elliptical tracks, Fig. 7(b) and (c) illustrate the case of ionizing particle entering either perpendicular to the detector's surface or at an oblique angle, and Fig. 7(d) a double track. The physical meaning of the images recorded by CR-39 detectors is discussed in detail by Mosier-Boss et al. [9].

5.2. Deuterium detection

The mass spectrograph was used to analyze for deuterium. The Pd/H film co-deposited onto a thin coiled palladium wire was employed to assure retention of the electrochemically compressed hydrogen isotopes, Fig. 4(b). This electrode

^aThe diffusion limited current density is estimated by substituting $\delta = 0.05$ cm which yields $j^* = j_{\text{lim}} = 0.025zc \text{ Acm}^{-2}$, where z is the number of positive charges and c in g-ion/l.

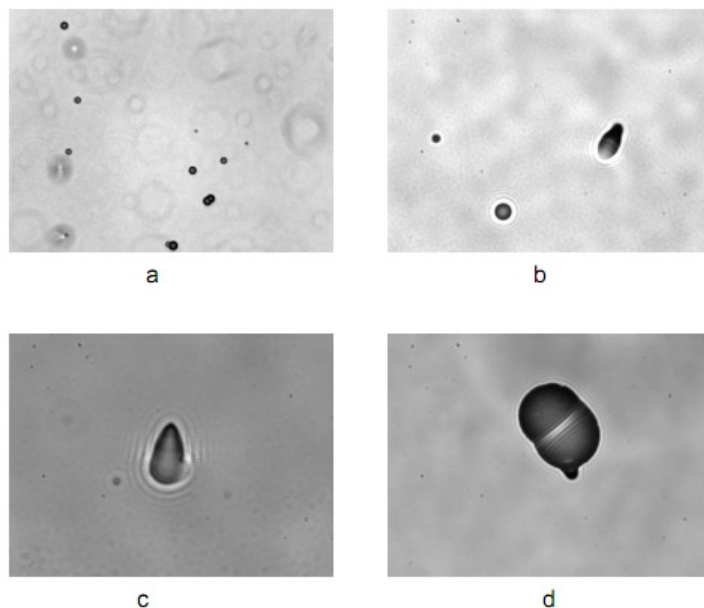


Figure 7. Images of tracks in CR-39 detectors created in the course of an experiment; a – distribution of tracks at 40 \times , b – illustrates the angle of impingement at 500 \times , c – shows a single track at 1000 \times , d – image of a double track at 500 \times .

design was selected to meet the requirements imposed by mass spectrograph. To minimize the desorption of hydrogen isotopes the following procedure was adapted (a) remove the cell from magnetostatic field, (b) stop the cell current flow, (c) take out the cathode, (d) cut-off the coiled part of the cathode and (e) analyze as soon as possible (e.g. within 15 min), utilizing the high vacuum of the mass spectrometer to greatly reduce the possibility that the hydrogen isotopes will form molecules as they diffuse out of the lattice.

The mass spectroscopic analysis, performed upon completion of a run, showed the presence of all hydrogen isotopes. Qualitatively, deuterium was the dominant isotope with negligible amounts of tritium. Typically, the D/H atomic ratio greater than one, with a value as high as 5:1, was recorded. Needless to say, that the presence of deuterium in the cathode is of utmost importance because it might provide decisive insight into the mechanism of nuclear reactions in condensed matter.

As a rule, mass spectroscopic analysis yields results that are unambiguous. However, if additional identification is required, then this can be done by (i) changing the method of analysis while retaining the sampling procedure or (ii) employing the original procedure (e.g. mass spectroscopy) and analyze after electrolysis of water with known D/H atomic ratios. Here, the latter was employed in which the desired D/H atomic ratios were obtained by electrolysis of a mixture of H_2O and D_2O in corresponding proportions using thin palladium wires as cathodes.

5.3. Catastrophic thermal events

Several catastrophic thermal events were observed (three out of ten). In one case, after three days of electrolysis with cell current varying between -300 mA cm^{-2} and 5 mA cm^{-2} , a catastrophic thermal event occurred that resulted in cell deformation, loss of electrolyte due to evaporation and leaking through a punctured cell bottom, Fig. 8.

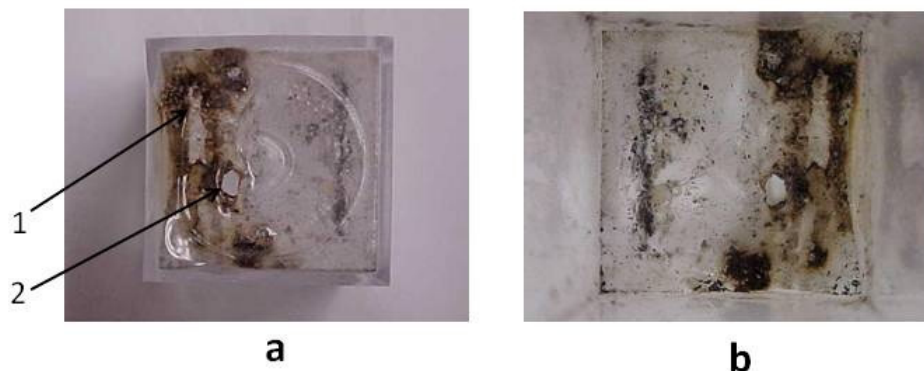


Figure 8. Damaged cell bottom: a – outside view, b – inside view. Arrows indicate the well defined damage areas (1 – thinning, 2 – hole, 3 – embedded particles).

The damage, about 1/3 of total area, viewed from the outside, Fig. 8(a), and inside the cell, Fig. 8(b), is consistent with placing a very hot object in contact with plastic material. Examination of Fig. 8(a) of the cell damage, suggests that an explosive fragmentation of the Pd/H deposit occurred and a large segment hit the surface. The wall deformation implies that sufficiently high temperature softened the acrylic plastic. The intensity of the heat source can be estimated from the temperature raise of the electrolyte during the last 170 min of cell operation, Fig. 9.

Here, a cell, charged with 3.0 ml of 0.03 M PdCl_2 and maintained at a constant volume of 5.0 ml, was operated for two days before recording the solution temperature, with the thermocouple located below the cathode. Within the last 160 min the electrolyte temperature remained constant (at 50 C) followed by, at first, a slow raise for the next 4 min, section ABC, followed by a rapid increase, at 2.6 C/s, section DE. During the next 3–4 min, the electrolyte evaporated and the temperature returned to ambient. For this run, the intensity of the heat source, based on the heat generated by the minute amount of the PD/H film and transferred to the electrolyte, can be estimated to be more than 10 eV/Pd atom, i.e. outside the limits of chemical reaction. Moreover, the temperature raise of the source of ca 250 C/s means that substantial amount of the electrolyte was lost by “film boiling”.

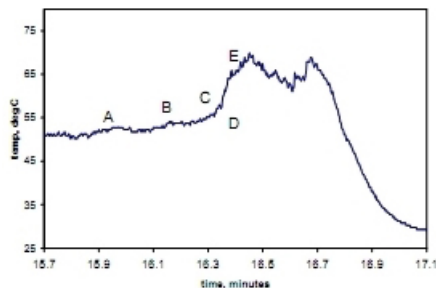


Figure 9. Temperature profile during thermal run-a-way.

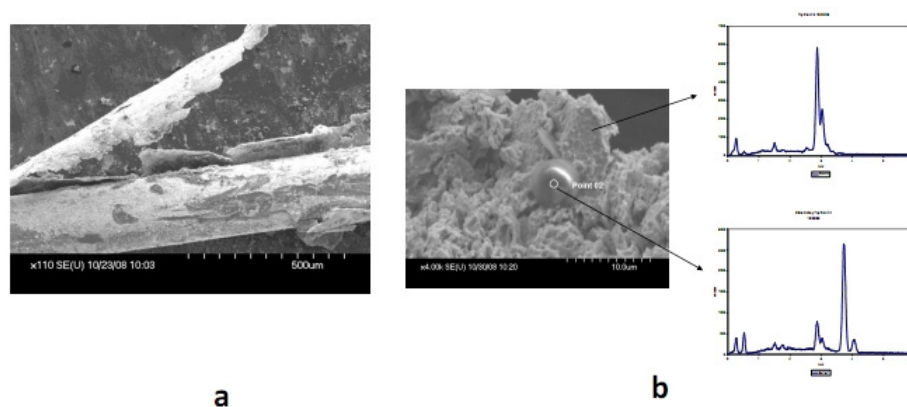


Figure 10. SEM/EDX SEM photograph illustrating separation of a Pd/H film during a mild run-a-way run. (a) – SEM photograph showing single reaction site; (c) – EDX of single reaction site (b) showing localized transmutation.

5.4. Mechanism of the Pd/H film separation

A probable, but speculative, mechanism of Pd/H film separation from the Pt substrate can be deduced using photograph, Fig. 10. The separation shown in Fig. 10 illustrates the separation of a Pd/D deposit in another set of experiments.

In particular, examination of Fig. 10(a) suggests the following: (i) a number of localized reactions at the Pt/Pd/D interface, indicated by an arrow, forced the separation of the Pd/D deposit from the Pt substrate, (ii) the SEM/EDX analysis of reaction sites contains participation of a nuclear event (transmutation) is involved in forcing film separation. The Pd/H film separation, shown in Fig. 8, occurred during a mild thermal run-a-way during electrolysis of light water is almost identical to that heavy water, thus suggesting the same mode of separation.

The film separation may be explosive. The damage, shown in Figs. 8a and (b), indicates that a Pd/H sleeve, after separation, was propelled away from the cathode and came in contact with the cell bottom. The high temperature and the amount of thermal energy necessary to generate the observed damage implies that thermal activity did not terminate upon separation from the cathode but persist during flight as well as after landing at the cell bottom.

6. Relevance

We have shown that chemical methodology is useful in studying conditions that initiate and maintain processes involving hydrogen and occurring within the confines of the palladium lattice. Here, we consider three cases: (i) the Widom–Larsen theory and experiment, (ii) reaction products and their usefulness and (iii) conceptual design of a power source.

6.1. The Widom–Larsen theory and experiment

Three facts that question the applicability of the Widom–Larsen theory to real systems, as applied to the polarized Pd/¹H–H₂O system, are considered. Those are: (i) the minimum value of heavy electrons, (ii) the ultra-low momentum neutrons and (iii) the location of the nuclear reactions.

6.1.1. Heavy electrons

Through the interpretation of the meaning of the reaction $e^- + p_1^+ \rightarrow n$ one can specify the necessary conditions for it to proceed, namely $\mu(n) - \mu(p_1^+) > 0$. Clearly, energies of both electron and proton must be considered. The energy

(heaviness) of the captured electron depends on the strength of p_1^+ /Pd lattice defect interaction.

6.1.2. Ultra-low momentum neutrons

Qualitatively, viewing the electron capture as a chemical step, an addition of an electron (mass 0.91×10^{-27} g) to a proton (mass 1.66×10^{-24} g) does not substantially change the displacement velocity of the generated neutrons, i.e. neutron kinetic energy is that of the producing proton.

6.1.3. Location of nuclear event

Experimental evidence (specifically the emission of α^{2+} particles) shows that the nuclear event occurs within the interphase region. The exact location cannot be determined because it depends on the dynamics of the interphase region. Certainly, they do not occur at the contact surface which is occupied by hydrogen ad-ions subject to reduction to hydrogen atoms via the orbital capture of electrons. Incidentally, there is no known experimental method that would provide definite answer.

6.2. Reaction products and their usefulness

The sequence of events illustrated in Fig. 1 suggests some practical applications, arising from the kinetics of coupled reactions, e.g. (i) extraction of deuterium to increase D_2O/H_2O concentration in water, or as a neutron source and (ii) excess enthalpy production.

6.2.1. Deuterium, and neutron extraction

Both, deuterium and neutrons are the reaction products and both can be extracted. The specification of the correct procedure for maximum efficiency is dictated by the kinetics of coupled reactions (work currently in progress).

6.3. Excess enthalpy

Another, more interesting observation is that of excess enthalpy production. Returning to the temperature/time of Fig. 9, section BCD, the excess enthalpy is generated safely at high rates, i.e. just before the onset of the catastrophic event. Whether or not the high rate of excess enthalpy can be controlled cannot be determined before the reaction kinetics is known.

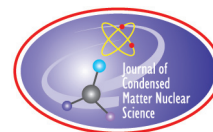
6.4. Conceptual design of power source

In principle, it is possible to design an electrochemical cell that utilizes the concept of power production. The set of reactions $e^- + p_1^+ \rightarrow n$, $e^- + d_1^+ \rightarrow 2n$ and $n + p_1^+ \rightarrow D^+$ forms the basis for a conceptual design of a power source. The co-deposited Pd/H film is the location of electrons and protons. If, within the film there is an added component, a substance, X, and if the $n + X \rightarrow X^* + Q$ reaction occurs, then it is possible to build a functioning device.

References

- [1] S. Szpak, P.A. Mosier-Boss and J.J. Smith, *Phys. Let.* **A221** (1996) 141.
- [2] S. Szpak, *J. Electroanal. Chem.* **373** (1994) 1.

- [3] H. Remy, *Treatise on Inorganic Chemistry*, Vol. II, Elsevier, Amsterdam, 1956, p.563.
- [4] L.D. Landau and E.M. Lifshitz, *Statistical Physics*, Vol. 5, part 1, Pergamon, Oxford, 1957, pp.318–319.
- [5] R. Haase, *Thermodynamics of Irreversible Processes*, Adison-Wiley, London, 1969.
- [6] S. Szpak, *J. Dea, J. Condensed Matter Nucl. Sci.* **9** (2012) 21.
- [7] H. Naohara, S. Ye and K. Uosaki, *J. Phys. Chem B* **102** (1998) 4366.
- [8] T. Ohmori, K. Sohamaki, K. Hashimoto and A. Fujishima, *Chemistry Letters*, The Chemical Society of Japan, 1991, p. 93.
- [9] P.A. Moser-Boss, S. Szpak, F. Gordon and L.P.G. Forsley, *Naturwissenschaften* **96** (2005) 135.



Research Article

Nickel Transmutation and Excess Heat Model using Reversible Thermodynamics

Daniel S Szumski*

Independent Scholar, 513F Street, Davis, CA 95616, USA

Abstract

This research develops the Least Action Nuclear Process (LANP) model of cold fusion, by assuming that the process is thermodynamically reversible. This requires: (1) one element of new physical theory, a far-from-equilibrium black body equation having a second temperature scale and (2) a nuclear reaction selection method based on the Principle of Least Action. The model appears to predict nuclear transmutations observed in Miley's nickel microspheres, without false positives, and provides a plausible explanation of loading and ignition processes, excess heat, no excess heat, and the absence of gamma radiation. The model shows how solar core temperatures can exist in a laboratory temperature device. This presentation is abstracted from a larger technical paper.

© 2014 ISCMNS. All rights reserved. ISSN 2227-3123

Keywords: LANP model, Least action, Reversible process, Theory

1. Introduction

During the last two decades it has become evident that low energy nuclear reactions are occurring in Fleischmann–Pons (F–P) electrolytic cells [1]. These reactions are unprecedented in nuclear physics, and are at least for now, hidden from understanding because a suitable theoretical framework has not been forthcoming [2]. The degree to which new physics underlies these experimental observations is not known. But, among theoreticians it is considered more likely that the present conundrum will be resolved by extensions of known physical principles.

This research endeavors to provide insight into three theoretical issues. First, it explores a mechanism for accumulating the ignition energy. Second, it explores how this energy might be stored until the moment of ignition. And third, it proposes how the accumulated energy partitions to specific nuclear transformations, and not others. The goal here is to show how a different view of heat processes, one that includes both irreversible and reversible thermodynamics, might inspire a comprehensive cold fusion theory.

*E-mail: Danszumski@sbcglobal.net

2. Theory of Heat

Heat exists in two domains that continually exchange energy as any arbitrary thermal system tends toward new quasi-equilibrium states. These are the domain of molecular motion, and the domain of heat radiation. The first might be referred to as the *mass domain*. It was Helmholtz who first showed that molecular motion is equivalent to heat; an observation that is central to what follows.

Heat energy also exists in the *radiation domain*. The theoretical framework describing equilibrium conditions there bears the revered names of Rayleigh, Wien, and Planck. Planck's equation [3] describes the equilibrium temperature dependence of black body spectral emittance.

Reversible thermodynamic processes are believed to be rare in nature. These are processes that produce a net zero free energy change, and are described by the thermodynamic treatment of Helmholtz, but not that of Gibbs. In all cases, reversible processes can be completely described by the Principle of Least Action [4].

I have proposed [5] a mathematical form for the black body spectral distribution that permits a glimpse into its non-equilibrium, and far-from-equilibrium characteristics.

$$K(\nu_1) = \frac{\varepsilon_\nu}{a_\nu} = k_b T_m \frac{\nu_1^2}{c^2} \frac{1}{e^{f_3(\nu_1/\nu_m)}}, \quad (1)$$

Black body spectra = Emittance (Rayleigh Law)/Absorptance (Ref. [5]),

where

$$f_3(\nu_1/\nu_m) = \left(\frac{\nu_1}{\nu_m}\right)^2 \left[\frac{1}{2} \left(\ln \left(\frac{\nu_1}{\nu_m} \right) \right)^2 - \frac{3}{2} \ln \left(\frac{\nu_1}{\nu_m} \right) + \frac{7}{4} \right] \quad (2)$$

and

$$\nu_m = 5.89 \times 10^{10} T_R \text{ (K)} \quad \text{(Wein frequency)}, \quad (3)$$

where T_m is the thermodynamic temperature, T_R is a new quantity called the radiation temperature, and $K(\nu_1)$ exists where the number of quanta is equal to or greater than 1.

Planck's equilibrium equation is given by:

$$K(\nu_1) = h \nu_1 \frac{1}{c^2} \frac{1}{e^{h\nu/k_b T - 1}}. \quad (4)$$

The non-equilibrium form in Eq. (1) is close to, but not exactly, Planck's at equilibrium.

This theory suggests that independent temperature scales might represent the mass and radiation domains. Figure 1 illustrates characteristics of the far-from-equilibrium, black body radiation spectra.

Curve A, refers to the transient initial condition where heating is initiated by increasing molecular motion, for example, by frictional input of heat.

If an identical amount of heat is initially added to the radiation domain alone (i.e. higher energy radiation), T_m , is initially constant, and the Wein frequency increase shifts the emittance spectra to higher frequencies (curve B). Both of these cases decay to equilibrium spectra similar to, but with higher total energy than the initial equilibrium case. At the new equilibrium condition, the mass and radiation temperatures become identical, and it is not possible to determine from which of the two domains the original heating took place. However, as will be shown in what follows, there are circumstances under which the second of these spectra might be held in a far-from-equilibrium state, and in this way store vast amounts of energy in a nickel or palladium cathode that is apparently at about 60°C.

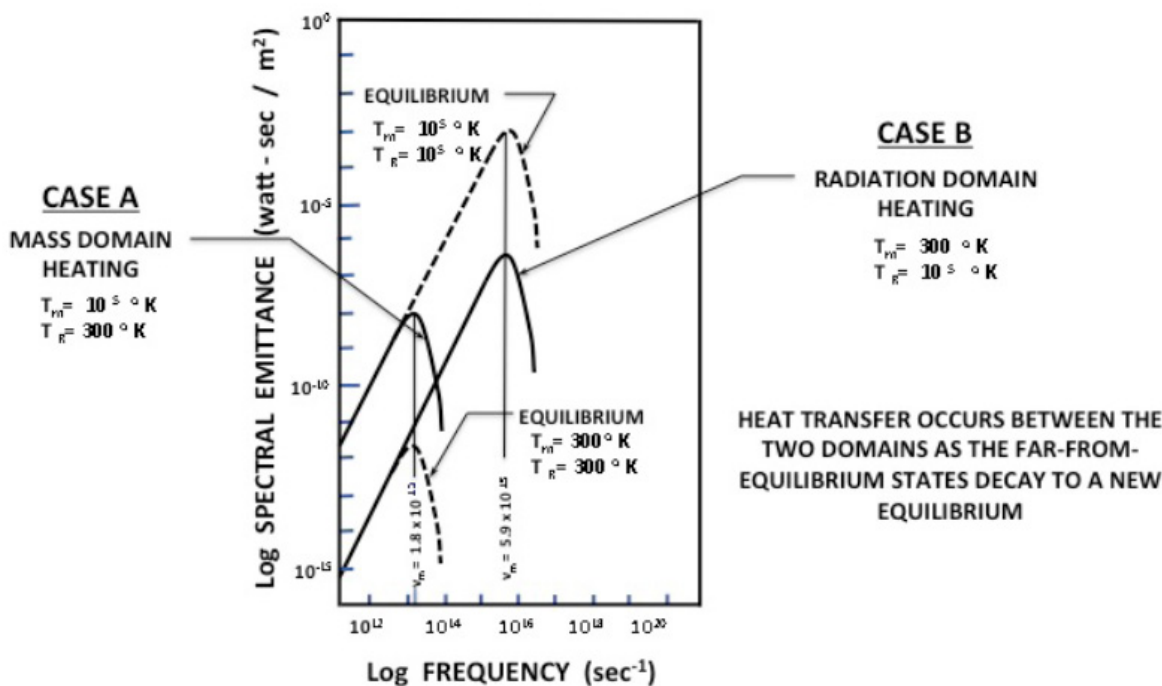


Figure 1. Illustration of non-equilibrium changes in the heat radiation spectra (Eq. (1)). Case A represents instantaneous mass domain heating (i.e. friction) at constant radiation temperature. Case B represents adiabatic heat accumulation at a constant thermodynamic temperature.

3. Consider a Thermodynamically Reversible Process

In thermodynamically reversible processes, be they chemical or nuclear, all of the process energy must be in a usable form. Thermal motion is specifically excluded, or it must be quieted; i.e. converted to radiation domain energy, as it enters the reaction space. In our case, a deuteron's kinetic energy is captured ('quieted') as it is absorbed from the heavy water into the metal lattice, adding to the internal lattice energy, and more specifically storing that captured kinetic energy in excited electron and excited nuclear states.

To place an order of magnitude estimate on this energy storage, we will use the 0.2 cm diameter \times 10 cm Pd electrode from Fleischmann and Pons 1989 experiments [1]. The surface area of the cathode is $6.28 \times 10^{-4} \text{ m}^2$. Assuming α -phase absorption approximating β -Pd D_{0.85}, and having a lattice parameter of 0.405 nm, the number of filled sites at the surface of the cathode, is approximated as 3.26×10^{15} sites in a single atomic layer at the cathode surface. If we assume that the average deuteron velocity is 0.2 m/s, the average kinetic energy of the deuterons in the cell can be calculated as $6.68 \times 10^{-22} \text{ erg}$, or a total of $2.2 \times 10^{-6} \text{ erg} = 1.35 \text{ MeV}$ in a single surface atomic layer. Thus, deuterium's 'quieted' thermal motion is more than sufficient for ignition. Where the electrode is being loaded in a deuterium gas environment the average molecular energy is $\frac{3}{2} k_b T$ at, or $6.89 \times 10^{-14} \text{ erg}$.

The loading energetics for metal hydrides are well understood [6–8] and the research reported here takes no issue with the known thermodynamics. Nevertheless, this theory is alone in associating the cold fusion ignition and process

Table 1. Selected nuclear reactions in Miley's nickel coated microspheres

Nuclear reaction	Initial isotope	Stable isotope	Energy change (amu)
$^{58}_{28}\text{Ni} + (6) \text{}^2_1\text{H} \xrightarrow{\text{fusion}}$	$^{70}_{34}\text{Se}$	$^{70}_{32}\text{Ge}$ absent	-0.095706
$^{70}_{32}\text{Ge} \xrightarrow{\text{fission}}$		$(2) \text{}^{35}_{16}\text{S} \xrightarrow{\beta^-} (2) \text{}^{35}_{17}\text{Cl} \uparrow$	-0.082248
$^{62}_{28}\text{Ni} + (1) \text{}^2_1\text{H} \xrightarrow{\text{fusion}}$	$^{64}_{29}\text{Cu}$	$^{64}_{28}\text{Ni}$	-0.014480
		$^{64}_{30}\text{Zn}$ absent (note 1)	-0.013304
$^{64}_{30}\text{Zn} \xrightarrow{\beta^+ \beta^+}$		$^{64}_{28}\text{Ni}$	-0.014480
$^{64}_{30}\text{Zn} \xrightarrow{\text{fission}}$	$(2) \text{}^{32}_{15}\text{P}$		+0.005368
$(2) \text{}^{32}_{15}\text{P} \xrightarrow{\beta^-}$		$(2) \text{}^{32}_{16}\text{S}$	+0.001696
$(2) \text{}^{32}_{16}\text{S} \xrightarrow{\text{fission}}$		$(4) \text{}^{16}_8\text{O}$ Example	+0.037212
$^{58}_{28}\text{Ni} - (2) \text{}^4_2\text{He} \xrightarrow{\alpha}$	$^{50}_{24}\text{Cr} \xrightarrow{\beta^+ \beta^+}$ (Note 2)	$^{50}_{22}\text{Ti}$	+0.014654
$^{58}_{28}\text{Ni} \xrightarrow{\text{fission}}$	$(2) \text{}^{29}_{14}\text{Si}$		+0.0176465
$(2) \text{}^{58}_{28}\text{Ni} \xrightarrow{\text{fusion}}$	$^{116}_{56}\text{Ba}$	$^{111}_{48}\text{Cd}, ^{112}_{50}\text{Sn}, ^{114}_{50}\text{Sn},$ $^{115}_{50}\text{Sn}, [^{116}_{50}\text{Sn}]$ abs	-0.0310552
$^{116}_{50}\text{Sn} \xrightarrow{\text{fission}}$		$(2) \text{}^{58}_{26}\text{Fe}$	-0.0020673
$(2) \text{}^{60}_{28}\text{Ni} \xrightarrow{\text{fusion}}$	$^{120}_{56}\text{Ba}$	$^{116}_{50}\text{Sn}, ^{118}_{50}\text{Sn}, [^{120}_{51}\text{Te}]$ absent	+0.0424482
$^{120}_{51}\text{Te} \xrightarrow{\text{fission}}$		$(2) \text{}^{60}_{28}\text{Ni}$	0.0000000
$(2) \text{}^{58}_{28}\text{Ni} + \text{}^2_1\text{H}^+ \xrightarrow{\text{fusion}}$	$^{118}_{57}\text{La}$	$^{114}_{50}\text{Sn}, ^{116}_{50}\text{Sn}, ^{117}_{50}\text{Sn}, [^{118}_{50}\text{Sn}]$	+0.016815
$(2) \text{}^{60}_{28}\text{Ni} + \text{}^2_1\text{H}^+ \xrightarrow{\text{fusion}}$	$^{122}_{57}\text{La}$	$^{118}_{50}\text{Sn}, ^{121}_{51}\text{Sb}, [^{122}_{52}\text{Te}]$ absent (note 3)	+0.027369
$^{122}_{52}\text{Te} \xrightarrow{\text{fission}}$		$(2) \text{}^{61}_{28}\text{Ni}$	+0.013562
$(2) \text{}^{58}_{28}\text{Ni} + (3) \text{}^2_1\text{H}^+ \xrightarrow{\text{fusion}}$	$^{122}_{59}\text{Pr}$	$^{118}_{50}\text{Sn}, ^{120}_{52}\text{Te}, ^{121}_{51}\text{Sb}, [^{122}_{52}\text{Te}]$ absent	-0.0099461

$^{122}_{52}\text{Te} \xrightarrow{\text{fission}}$		$(2) \text{ }^{61}_{28}\text{Ni}$	-0.050878
$^{122}_{52}\text{Te} \xrightarrow{\alpha} {}^4_2\text{He}$		$^{118}_{50}\text{Sn}$	+0.001162
$(2) \text{ }^{60}_{28}\text{Ni} + (3) \text{ }^2_1\text{H}^+ \xrightarrow{\text{fusion}}$	$^{126}_{59}\text{Pr}$	$^{125}_{52}\text{Te}, [^{126}_{54}\text{Xe} \uparrow]$	0.0003958
$^{60}_{28}\text{Ni} + {}^{61}_{28}\text{Ni} - {}^4_2\text{He} \xrightarrow{\text{fusion}}$	$^{117}_{54}\text{Xe}$	$^{116}_{50}\text{Sn}, [^{117}_{50}\text{Sn}]$	+0.015139
$^{58}_{28}\text{Ni} + {}^{60}_{28}\text{Ni} - (2) \text{ }^4_2\text{He} \xrightarrow{\text{fusion}}$	$^{110}_{52}\text{Te}$	$^{109}_{47}\text{Ag}, [^{110}_{48}\text{Cd}]$ absent	+0.042079
$^{110}_{48}\text{Cd} \xrightarrow{\text{fission}}$		$[(2) \text{ }^{55}_{24}\text{Mn}]$	+0.015167
$^{58}_{28}\text{Ni} + {}^{61}_{28}\text{Ni} - (2) \text{ }^4_2\text{He} \xrightarrow{\text{fusion}}$	$^{111}_{52}\text{Te}$	$^{110}_{48}\text{Cd}, [^{111}_{48}\text{Cd}]$	+0.042985
$^{58}_{28}\text{Ni} + {}^{62}_{28}\text{Ni} - (2) \text{ }^4_2\text{He} \xrightarrow{\text{fusion}}$	$^{112}_{52}\text{Te}$	$[^{112}_{50}\text{Sn}]$	+0.046336
$^{112}_{50}\text{Sn} \xrightarrow{\text{fission}}$		$[(2) \text{ }^{56}_{26}\text{Fe}]$ (note 4)	+0.019328
$^{58}_{28}\text{Ni} + {}^{64}_{28}\text{Ni} - (2) \text{ }^4_2\text{He} \xrightarrow{\text{fusion}}$	$^{114}_{52}\text{Te}$	$[^{114}_{50}\text{Sn}]$	+0.044676
$^{114}_{50}\text{Sn} \xrightarrow{\text{fission}}$		$[(2) \text{ }^{57}_{26}\text{Fe}]$	+0.012685
$(3) \text{ }^{64}_{28}\text{Ni} \xrightarrow{\text{fusion}}$	$^{192}_{84}\text{Po}$	$^{176}_{72}\text{Hf}, ^{184}_{76}\text{Os}, ^{188}_{76}\text{Os}, [^{192}_{78}\text{Pt}]$	+0.207437
$^{192}_{84}\text{Po} \xrightarrow{\text{fission}}$	$(2) \text{ }^{96}_{39}\text{Y}$	$(2) [^{96}_{40}\text{Zr}]$	+0.032648
$^{58}_{28}\text{Ni} + ^{107}_{47}\text{Ag} + {}^2_1\text{H}^+ \xrightarrow{\text{fusion}}$	$^{167}_{76}\text{Os}$	$^{143}_{60}\text{Nd}, ^{147}_{62}\text{Sm}, [^{155}_{64}\text{Gd}],$ $^{159}_{65}\text{Tb}, ^{163}_{66}\text{Dy}, [^{167}_{68}\text{Er}]$	+0.0775065
$^{167}_{68}\text{Er} \xrightarrow{\alpha}$		$^{163}_{66}\text{Dy}$	+0.0767937

${}^{61}_{28}\text{Ni} + {}^{107}_{47}\text{Ag} + (2) {}^2_1\text{H}^+ \xrightarrow{\text{fusion}}$	${}^{172}_{77}\text{Ir}$	${}^{164}_{68}\text{Er}, {}^{168}_{70}\text{Yb}, [{}^{172}_{70}\text{Yb}]$	+0.0720249
${}^{61}_{28}\text{Ni} + {}^{107}_{47}\text{Ag} + (2) {}^2_1\text{H}^+ \xrightarrow{\text{fusion}}$	${}^{114}_{55}\text{Cs}$	${}^{106}_{48}\text{Cd}, {}^{107}_{47}\text{Ag}, {}^{108}_{48}\text{Cd}, {}^{109}_{47}\text{Ag}, {}^{110}_{48}\text{Cd},$ ${}^{111}_{48}\text{Cd}, {}^{112}_{50}\text{Sn}, {}^{113}_{49}\text{In}, {}^{114}_{50}\text{Sn}$	
${}^{114}_{50}\text{Sn} - {}^4_2\text{He} \xrightarrow{\alpha}$		${}^{110}_{48}\text{Cd}$	-3.95358
${}^{112}_{50}\text{Sn} \xrightarrow{\beta^+\beta^+}$		${}^{112}_{48}\text{Cd}$	-1.951766
${}^{113}_{49}\text{In} - {}^4_2\text{He} \xrightarrow{\alpha}$		${}^{109}_{47}\text{Ag}$	-4.951832
${}^{114}_{50}\text{Sn} \xrightarrow{\text{fission}}$ (Note 3)		$[(2) {}^{57}_{26}\text{Fe}]$	-0.014203

Note 1: Believed to undergo $\beta^+\beta^+$ decay to ${}^{64}_{24}\text{Ni}$ with half-life of over 2.3×10^{18} years.

Note 2: Suspected of $\beta^+\beta^+$ decay to ${}^{50}_{22}\text{Ti}$ with half-life of not less than 1.3×10^{18} years.

Note 3: Theoretically capable of spontaneous fission.

Note 4: Lowest mass/nucleon of all nucleides. End product of Stellar nucleosynthesis.

Table notes were taken from “Isotopes of Elements”, Wikipedia, http://en.Wikipedia.org/wiki:Main_page,4/13/12

energy with the loading process. All other theoretical constructs take the matrix loading as a given, and then look for the ignition energy within the metal hydride matrix.

Hydrogen storage within the lattice structure is known to occur in distinct thermodynamic phases: α , $\alpha + \beta$, β . These are known to be thermodynamically reversible [6]. Let us now look at that next step.

How is this energy stored during the loading phase of the experiment? We will begin by assuming that deuterium loading is a singular, multi-site, reversible process. During loading, no energy is lost to thermal motion. Thus, the stored energy is either entirely in the radiation domain, or it moves to another energy type where it can be held in a completely reversible state. We will partition this energy storage into two components. The first is the mechanical work involved in expanding the metal lattice by up to 15% to accommodate high deuterium loadings. This is an adiabatic volume expansion, and thus, a reversible process. The second is the adiabatic storage of radiation domain energy to achieve ignition energies.

It appears to me that the best explanation for the lower bound for energy storage is within discrete covalent bonds; each covalent electron pair alternately absorbing and emitting electro-magnetic energy that remains in a wholly reversible state. As the total energy storage increases further, excited nuclear states become active bringing the reversibly stored cathode energy to gamma levels, where Mössbauer resonance, a reversible process, prevails, and energy storage occurs as resonant gamma exchange. This energy is stored entirely within the atomic structure of the lattice, and without any external manifestation. It is masked from observation.

In order to inquire about temperatures achieved in this reversible energy storage, we note that temperature is a derivative [4, p. 105], dQ/dt , measuring the emittance from any closed volume contained completely within the nickel electrode's interior, and where the Joules/s crossing the surface area of that volume completely describes its temperature. If our free body volume is around one of the electrons participating in covalent bond resonant energy

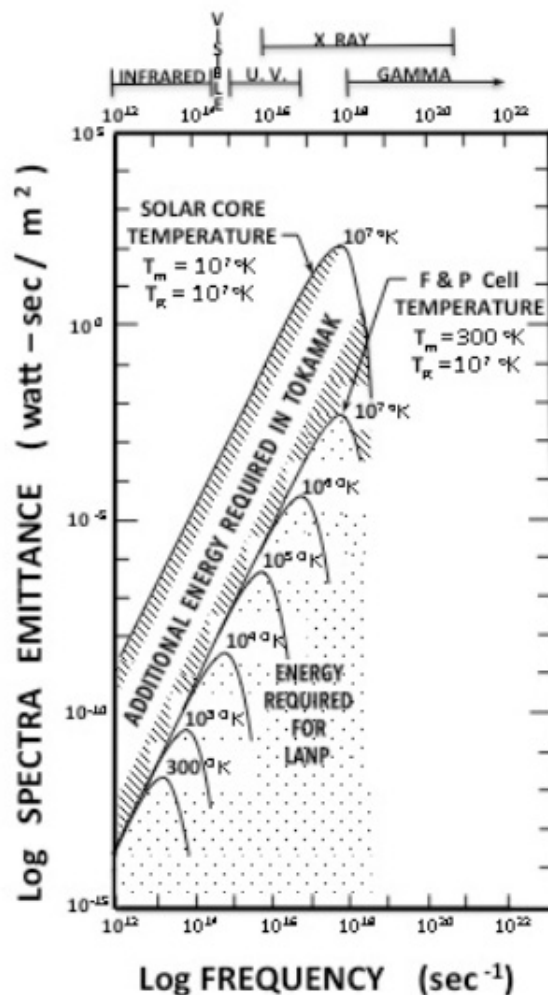


Figure 2. Comparison of theoretical radiation temperature structure in the F&P electrode with the solar core temperature. Both exhibit 10^7 K radiation temperature, but very different thermodynamic temperatures.

storage, the temperature is above the ambient thermodynamic temperature, T_m , but relatively small. However, as the frequency of the shared photon approaches gamma energies, the exchange takes place between nuclei, and the heat derivative, and thus the temperature within the volume containing one of these nuclei can become enormous, approaching and exceeding solar core temperatures.

The spectra labeled B in Fig. 1 represents the distribution of energy levels corresponding to this storage of heat energy. Eventually, the Wein frequency reaches gamma intensities, and the radiation temperature approximates that in the solar core, about 10^7 K as illustrated in Fig. 2. The figure contrasts the temperature regime (T_m and T_R) that this theory postulates to that in the solar core. It suggests that the energy spectra required for ignition in the Tokamak is about four orders of magnitude higher than that operative in the F&P cell, and much larger on a total energy basis. In essence,

the cold fusion process takes an energy shortcut around the enormous kinetic energy required for thermonuclear fusion. In this way, we see that the LANP is actually quite hot.

But, where are the Gamma emissions? We need to recall that we are dealing here with an extension of black body theory wherein electromagnetic energy of all wavelengths is emitted and absorbed within the lattice. The mass quantities involved in this absorption and emission are presumed to be electrons at the low energy end of the spectrum, and atomic nuclei as the energies increase through gamma intensities. Mass changes from any overall reaction occur as gamma emissions into the black body spectral distribution. Gamma emission and absorption are intrinsic to this system, internal to it, and in effect masked by it.

4. Experimental

Let us return to the mechanism of thermo-nuclear fusion/fission under these conditions. Miley's data from electrolysis of nickel coated microspheres [9] provides a suitable data set for analysis. I have inventoried what I believed are the most likely nuclear reactions occurring in the nickel coated microspheres. A small sampling of the 210 reactions (column 1) analyzed during this research is presented in Table 1. Isotope data are extracted from Wikipedia [10]. The second and third columns are the initial isotope formed, and the final stable product(s) of its decay. The last column is the total mass change in the nuclear reaction sequence that ends with the isotope in column 3.

Overall the data analysis shows that the reactions producing the lower atomic weight portion of the final electrode composition are: (1) fusion reactions of initial electrode isotopes (including impurities) with one or more deuterons, (2) fission reactions of initial electrode isotopes or isotopes that were *absent* from Miley's table, or (3) alpha decay. Some of the higher atomic weight isotopes result from fusion reactions involving nickel–nickel and nickel–impurities with deuterium nuclei. Because the initial electrode is severely neutron deficient relative to the final electrode, many of the high nuclear weight products probably have their origin in more complex stellar nucleosynthesis reactions. One thing that is clear is that neutron production is fundamental to the underlying nuclear process.

Many of these nuclear reactions have multiple isotope end points, and many of those are not in Miley's Table 3 [9]. I have identified one rule that determine which of these multiple isotope products will occur.

Rule 1: All fusion and fission reactions that can occur, are candidates. The one that actually produces a product along any reaction pathway is the reaction sequence that satisfies the Principle of Least Action (smallest overall mass change).

For each reaction shown, the isotope product that satisfies this condition is in **bold** type. Consider the nuclear reaction involving Miley's nickel electrode and one of its impurities: $^{58}_{28}\text{Ni} + ^{107}_{47}\text{Ag} + ^2_1\text{H}^+ \xrightarrow{\text{fusion}}$. It normally produces 38 intermediate radioactive isotopes and seven stable isotope products, three of which are in Miley's Table 3: $^{151}_{63}\text{Eu}$, $^{155}_{64}\text{Gd}$ and $^{163}_{66}\text{Dy}$. The results obtained from this reaction sequence are shown in Table 1 where the Principle of Least Action correctly selects for $^{163}_{66}\text{Dy}$, but not along the normal decay pathway. Instead the Principle of Least Action selects for $^{167}_{69}\text{Er}$ with a mass change of +0.0775065 amu. This is followed by alpha decay to $^{163}_{66}\text{Dy}$, still within the domain of reversible thermodynamics. The energy change drops accordingly to +0.0767937 amu. The overall mass change which normally manifests as gamma absorption, occurs instead as Mössbauer resonance; part of the far-from-equilibrium black body spectra..

I have chosen to call this mode of nuclear decay, where no intermediate radioactive products occur, and where half-life time delays are nonexistent, sigma-decay.

We are finally ready to look at the issue of excess heat generated in Miley's experiment. The LANP reversibility constraint requires that the core process be adiabatic. Therefore, we need to explore the limits of that process to identify the step at which it crosses over the line into the domain of irreversibility.

Because there are both exothermal (– mass change) and endothermal (+ mass change) reactions occurring, the excess heat is probably a net heat measure, and most probably has its origin in the circumstance where the far-from-equilibrium

spectrum is already filled at the gamma emission's frequency, and the energy must instead flow into the spectra's mass domain. There it enters the domain of irreversible processes, and results in an increase in T_m . The transfer function that re-distributes the gamma energy is theorized to be Eq. (2). Furthermore, experiments where no excess heat is observed could be either: (1) dominated by endothermal reactions, or (2) have a net zero heat production. The electrodes from these 'failed' experiments need to be checked for transmutation products. It is entirely possible that these experiments were successful in some way other than excess heat production.

5. Discussion

The LANP theory is unique in its ability to describe many of the unexplained phenomena occurring in a F&P electrolytic cell including:

- (1) A mechanism for loading energy into the metal hydride lattice,
- (2) A mechanism for storing that energy until ignition,
- (3) A theoretical basis for the fusion temperature requirement and how it is masked,
- (4) A mechanism for selecting products that do and do not occur,
- (5) An explanation for the absence of radioactivity.

The theory also has appeal in that it is not nickel specific, or even metal lattice specific, and it provides a plausible mechanism for the solar temperatures that thermonuclear fusion is known to require. LANP is a very hot process.

The mechanism that causes excess heat may require more detailed work, particularly with the nuclear event sequence that fills the far-from equilibrium spectra, and the meaning of equation [2], including its more rigorous derivation. Nevertheless, the model demands additional study and experimental work. It answers too many questions to be dismissed.

On the other hand, theoreticians and experimentalists in the field should contain their exuberance for this, or any other promising model. This field is simply too controversial to allow missteps, or premature dialog with the non-scientific community.

Places where LANP departs from current theory, and more importantly, from common sense, need immediate study. For example, is it even plausible that all of the intermediate radioactive decay steps, and half-life constraints of σ -decay can be bypassed by LANP. The absence of any radiation signature in F&P cells, and the observed transmutation products make that conclusion tantalizing. And yet, it is contrary to everything that we currently know about nuclear processes. The same is true of more fundamental aspects of the theory such as its claim of reversibility. This one feature of the theory is without precedent in modern science, and will be attacked vigorously in peer review. Perpetual motion machines, quite simply, are not supposed to exist. Even more implausible is the claim that stellar and supernova processes might occur within a laboratory device.

These claims are almost untenable, and yet they seem to constitute a cohesive theoretical framework that is consistent with the data. We should be very careful not to give LANP too much credibility at this point in its short life, and instead design a scientific plan to achieve rigorous experimental proof one way or the other.

Appendix A - The Tunneling Issue

The fundamental problem in cold fusion theory is overcoming the coulomb barrier between reacting nuclei. The barrier can be represented by the electro-static potential energy:

$$U_{\text{Coulomb}} = 2kZ_1Z_2e^2/l,$$

($Z_1 = 1$, $Z_2 = 28$)

where k is the Coulomb's constant, e the elementary charge, l the charge separation, and Z_1, Z_2 are the atomic numbers of the interacting nuclei. Overcoming this potential barrier for deuterium–deuterium fusion requires kinetic energies in the MeV range, essentially solar surface temperatures.

Parmenter and Lamb [11] showed how dual deuterons in a single potential well might achieve the required resonant energies in the presence of large numbers of conduction electrons which effectively masked the coulomb barrier. Subsequent investigators have proposed refinements to this resonant tunneling model, incorporating enhanced electron mass [12], resonant nuclear states [13], and calculated tunneling enhancements [14]. None of the tunneling theories put forward to date has proven sufficient to explain cold fusion experiments.

This issue is magnified in the current research because fusion reactions beyond the elementary four nucleon model are not only proposed, but presented without reference to the enormous coulomb barriers that they imply. For example, the $H + Ni$ and $Ni + Ni$ ($Z_1 = 1, Z_2 = 28$) Coulomb barriers are approximately 25 and 750 times greater, staggering energy barriers relative to the simple four nucleon problem. And yet, if the experimental results of Miley [15] and Mizuno [16] are to be believed, nature overcomes these incredible coulomb barriers in room temperature experiments every day.

The one remarkable characteristic of the reversible thermodynamic, framework employed by the LANP model, is the way that the time differentials, regardless of their mechanism, become identically zero. This occurs regardless of the order of the derivative (second order in the case of coulomb barrier repulsive force). Therefore, it is entirely possible that when we treat the cold fusion *process* as a reversible thermodynamic system, all of the repulsive coulomb barrier acceleration terms disappear from our model, and reactions that are possible at the operative radiation temperature, all become candidates for the reactor's next step. Possible reactions do not cascade randomly, but proceed stepwise in a systemized manner described entirely by the Principle of Least Action. One occurs. Then the next step occurs, and the next, and so on. This is the Least Action Nuclear Process. I discuss some of the fundamentals involved in [17], where I have included a calibration of my Theory of Heat; the larger research project that this paper is derived from. The LANP theory does not require tunneling. The coulomb repulsion terms \mathbf{a} in $f_{\text{Coulomb}} = m\mathbf{a}$ have all gone to zero.

Appendix B. The Gamma Conundrum

The LANP model differs from all other nuclear models in two important ways. First, it produces only stable nucleotides, and in fact, expected unstable isotopes and excited nuclear states *never* occur within the process. These are entropic quantities that are foreign to the reversible thermodynamic state, and cannot be produced within it. The only relevant quantities are the initial and final (Least Action) states.

Gamma energies are produced. For example, in Section 4, I refer to a fusion reaction: ${}^{58}_{28}\text{Ni} + {}^{107}_{47}\text{Ag} + {}^2_1\text{H}^+ \xrightarrow{\text{fusion}} {}^{162}_{66}\text{Dy}$ which normally results from six discrete beta decays and an alpha decay. Yet, no beta decay products are measured, nor are any of the intermediate unstable isotopes detected. The reversible thermodynamic process began with the three reactants, and produced one stable isotope and consumed a gamma photon ($0.07607937 \text{ amu} = 70.86489 \text{ MeV}$).

Secondly, although the LANP model produces these gamma energies, it liberates no gamma photons. Instead gamma quanta are theorized to be absorbed and emitted within the far-from-equilibrium blackbody spectra where these quanta are Mössbauer resonant between identical nuclei, and thus masked from observation beyond the limits of that absorption/emission process. In the circumstance where the far-from-equilibrium blackbody spectra has no vacancies to accommodate the gamma photon, its energy dissipates into the low energy spectra where it deteriorates to heat of motion, i.e. 'excess heat'.

Section 3 describes how Mössbauer resonant gamma energy alone defines the effective temperature within the LANP's metal lattice. For this model to evolve, it is a sufficient condition, that the lattice's *radiation temperature*, T_R , described by the Mössbauer resonant gamma field, achieve solar core temperatures.

We might ask the question: Is this temperature real? I am not questioning the heat content of the system. The gamma energies place the intra-nuclear temperature at solar core conditions. But at the boundary of this nuclei pair there exists no heat flux, a zero derivative, and all appearances of room temperature conditions. In other words, the gamma energy exists, but not in a form that can be observed. It seems only accessible through theory.

This is a radically different view than is found in the high-energy physics literature. There, the fusion temperature condition is the sum of enormous kinetic energy, and the same high, gamma dominated, radiation conditions employed here. The difference is in the way that this theory finds *radiation temperatures* in the solar core range entirely sufficient to carry forward nuclear transmutations in the absence of the equilibrium blackbody's kinetic energy pool.

Finally, I note the extraordinary amount of misinformation regarding reversible thermodynamic processes in the literature and in physics textbooks. If we are going to have this discussion, we need to go back to the one reliable source, Planck's 1909 Lectures at Columbia University (4 above). I believe that this paper's interpretation is entirely consistent with Planck's presentation in Lectures 1 and 7. The only place where we differ is on pages 19 and 20, where he makes this often quoted statement regarding reversible processes:

"Reversible processes have, however, the disadvantage that singly and collectively they are only ideal: in actual nature there is no such thing as a reversible process. ..."

Nevertheless, Planck cites several reversible processes elsewhere in the Lectures, and speaks of the ultimate division of all physical processes into two categories: reversible and irreversible.

It is my carefully considered opinion that the common belief, quoted above, is at the very heart of our inability to understand the cold fusion process, and possibly, the process that gives rise to matter's living state.

References

- [1] M. Fleischmann, S. Pons and M. Hawkins, Electrochemically induced nuclear fusion of deuterium, *J. Electroanal. Chem.* **261** (1989) 301 and errata in **263** (1989).
- [2] P. Hagelstein et al., Input to theory from experiment in the Fleischmann–Pons effect, *ICCF-14 Int. Conf. on Condensed Matter Nuclear Science*, Washington, DC., 2008.
- [3] M. Planck, *Verhandlungen der Deutschen Physikalischen Gesellschaft* **2** (1900) 237 or in English translation: *Planck's Original Papers in Quantum Physics*, Vol. 1 of *Classic Papers in Physics*, H. Kangro (Ed.), Wiley, New York, 1972.
- [4] M. Planck, *Eight Lectures in Theoretical Physics*, 1909, translated by A.P. Wills, Columbia University Press, NY, 1915.
- [5] D.S. Szumski, Consequences of partitioning the photon into its electrical and magnetic vectors upon absorption by an electron, *Proc. SPIE* **8832** (2013).
- [6] T.R. Gibb, *Primary Solid Hydrides*, in *Progress in Organic Chemistry*, F.A. Cotton (Ed.), Wiley, NY, 1962.
- [7] G.G. Libowitz, *The Solid State Chemistry of Binary Metal Hydrides*, W.A. Benjamin, NY, 1965.
- [8] E. Storms, *The Science of Low Energy Nuclear Reaction*, World Scientific, Singapore, 2007 [6].
- [9] G. Miley and J. Patterson, Nuclear transmutations in thin-film nickel coatings undergoing electrolysis, *J. New Energy* **1**(3) (1996) 5–38.
- [10] Isotopes of *element* in Wikipedia, Retrieved 1/04-07/12 from <http://en.wikipedia.org>
- [11] R.H. Parmenter and W.E. Lamb, *Proc. Natl. Acad. Sci USA*, 86,8614,1989, 87,3177, 8652, 1990.
- [12] A. Widom and L. Larsen, Ultra low momentum neutron catalyzed nuclear reactions on metallic hydride surfaces, *Euro. Phys. J.* **46** (1) (2006) 107.
- [13] P.L. Hagelstein, Resonant tunneling and resonant excitation transfer, *Proc. 10th Intl Conf Cold Fusion*, Cambridge, MA, 2003.
- [14] Y. Kim et al., Reaction barrier transparency for cold fusion with deuterium and hydrogen, *Fourth Intl Conf Cold Fusion*, Lahaina, Maui, USA, 1994.
- [15] G. Miley and J. Patterson, Nuclear transmutations in thin-film nickel coatings undergoing electrolysis, *J. New Energy* **1**(3) (1996) 5–38.
- [16] T. Mizuno et al., *Nuclear Transmutation: The Reality of Cold Fusion*, Infinite Energy Press, Concord, NH, 1998.
- [17] D.S. Szumski, *Introduction to Theoretical Biology- A Theory of Heat*, Amazon.com, 2013.



Research Article

Physics of Cold Fusion by TSC Theory

Akito Takahashi^{*,†}*Technova Inc., 1-1 Uchisaiwaicho 1-chome, Chiyoda-ku, Tokyo 100-0011, Japan*

Abstract

This paper explains the basic physics of cold fusion by the tetrahedral symmetric condensate (TSC) theory. Models of TSC formation conditions in condensed matter are first proposed. Secondly formulas for cold fusion rates per D(H)-cluster are explained with typical quantitative results. The 4D/TSC fusion and the 4H/TSC WS fusion describe the D (deuterium)-system and the H (protium)-system, respectively.

© 2014 ISCMNS. All rights reserved. ISSN 2227-3123

Keywords: D(H)-cluster, 4D fusion, 4H WS fusion, TSC theory

1. Introduction

The tetrahedral symmetric condensate (TSC) theory has been elaborated for 23 years beginning in April 1989 [1]. The basic concept (by intuition) is that the ordering/constraint conditions of particles (namely deuterons, protons and electrons) in condensed matter containing deuterium (D) and/or protium (H) should make unique heretofore unknown D(H)-cluster fusion reactions measurable, while the known fusion reactions in high temperature plasma are two-body reactions such as p–d, d–d, d–t, d–³He and so on, which take place in random free particle motions. Here, D(H)-cluster includes two deuterons (or protons) systems as d–e–d (p–e–p) and d–e–e–d (p–e–e–p), as well as 3D(H), 4D(H), 6D(H) and so forth. Here e denotes electron. D denotes deuteron (d) + electron (e), and H denotes p + e.

The study of D(H)-cluster dynamics using the quantum mechanical (QM) Langevin equation [2] shows that any transient entity (condensate state) as small as a few tens of femtometers will not be possible for the d–e–d and d–e–e–d systems or a 3D-cluster. On the other hand, a 4D/TSC- or a 6D/OSC-neutral-clusters may ultimately condense to a very small charge-neutral entity, as small as a few tens of femtometer or less. In this state, it will induce significant reaction rates of nuclear strong interaction between deuterons. The condensation time for 4D/TSC is as short as 1.4 fs and the yield of 4D/TSC fusion per TSC is 1.0 (100%) [3].

The macroscopic fusion rate by the TSC theory is given by the product of two rates as,

$$\langle \text{Macroscopic fusion rate} \rangle = \langle \text{D(H) – Cluster formation rate} \rangle \times \langle \text{Microscopic fusion yield per TSC} \rangle. \quad (1)$$

^{*}E-mail: akito@sutv.zaq.ne.jp

[†]Also at: Osaka University, 1-1 Yamadaoka, Suita, Osaka 565-0871, Japan.

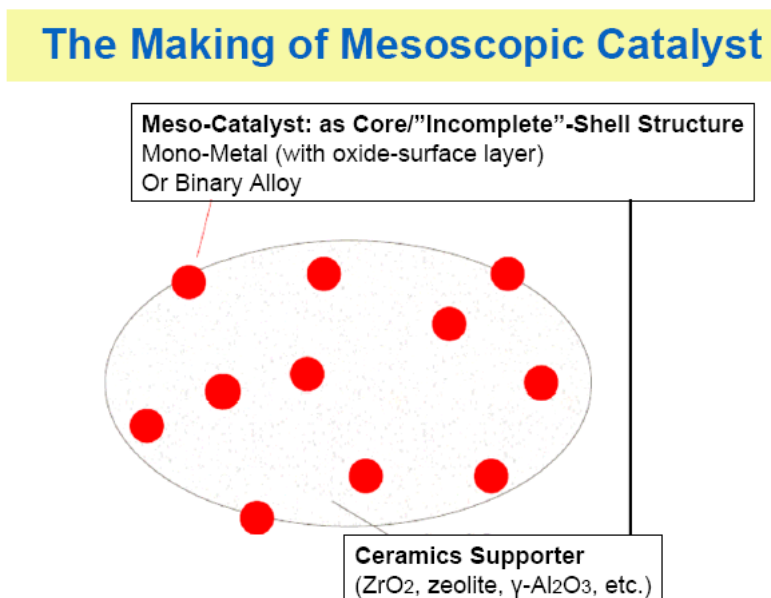


Figure 1. Design of nano-composite sample for D(H)-gas loading.

The microscopic fusion rate is defined by the time-dependent cluster condensation motion (inter-nuclear d–d distance R_{dd} and relative d–d kinetic energy) and the rate of strong interaction, using Fermi's first golden rule [4]. The D(H)-cluster formation rate should be defined to reflect, in dynamic conditions of near-surface-physics/chemistry and finite lattice of solid state physics/chemistry of condensed matter as D(H)-loaded metal electrodes, D(H)-loaded nano-metal-powder composites or some other materials used for cold fusion studies. No formulas of D(H)-cluster formation rate have been given until now, and only speculative models have been given [5,6], since the relevant dynamic conditions in condensed matter are so complex with many-particle systems. Our progress in experiments will provide hints to develop the formulas.

2. Model of TSC Formation States

We employ the idea of 'mesoscopic catalyst' [5,6] for the near-surface condition of condensed matter to provide states of dynamic TSC formation. A typical design of nano-composite metal powder in current D(H)-gas loading experiments is shown in Fig. 1. An isolated nano-binary-metal particle (1–10 nm diameter) is thought to be optimum [5,6]. It has a 'fractal' surface with many sub-nano-holes (SNH) and an inner finite lattice (Bloch) structure. The D(H)-adsorption/absorption process is illustrated in Fig. 2. An image of a TSC formation state of SNH is shown in Fig. 3. First a D₂ molecule is adsorbed at a SNH and before its dissociation the second D₂ molecule is 'orthogonally' adsorbed onto it to form a TSC ($t = 0$) state.

A diagram of absorbed D(H)s in a finite lattice of nano-particle is shown in Fig. 4 conceiving the case of Ni-core binary nano-particle at lower and higher ambient temperature.

The D₂ molecule is adsorbed and dissociated at deep trapping potential, due to many dangling chemical electron bonds there at SNH on surface. The deuterons then diffuse into inner finite lattice sites by the quantum-mechanical

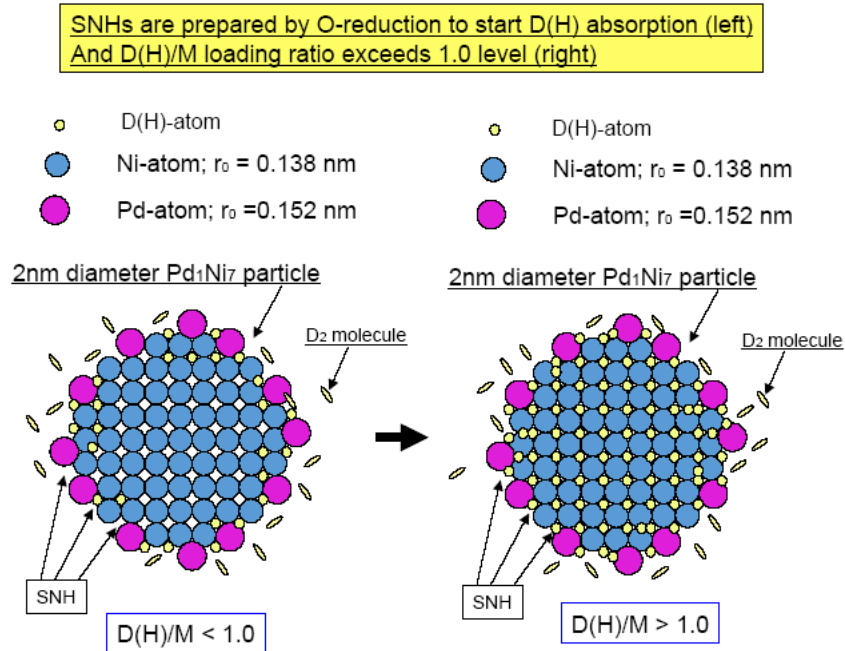


Figure 2. D(H)-adsorption/absorption image via SNHs of nano-particle.

(QM) tunneling effect, which is enhanced at elevated temperature. From the point of view of thermodynamics, system energy is transferred via phonon energy exchange between trapped D(H)s in QM oscillation and outside phonons of the substrate (a ceramic supporter) as shown in Fig. 5. The temperature dependence of phonon-frequency distribution of trapped D(H)s in GMPW (global mesoscopic potential well) should be studied.

At elevated temperature conditions, the probability of TSC ($t = 0$) formation at inner finite lattice sites may be significantly enhanced [1] as illustrated in Fig. 6. Quantitative QM calculations for these TSC formation process are very complex due to so many-body time-dependent problems under the ordering/constraint conditions of condensed matter. They will require further study.

3. Cluster Fusion Rates

Once a TSC ($t = 0$) state forms, the time-dependent TSC condensation motion is so fast, it finishes 4D/TSC condensation in 1.4 fs [2,3]. During the continuous condensation motion, we can employ an ‘adiabatic’ state (for digitizing very small time-steps) of ‘quasi-molecule’ confining potential and 4D (or d-d pair) wave function, as illustrated in Fig. 7. In the QM-Langevin calculation, Gaussian-type wave functions were employed [2,3] to implement the ‘quasi-eigen-values’ search for the adiabatic state, by using the variational method [3]. The detail of QM-Langevin equation and TSC-trapping potential is fully given in [2,3].

The cluster fusion rate for an adiabatic quasi-molecule state is given by Fermi’s golden rule under the Born–Oppenheimer approximation.

Image on Formation of TSC($t=0$) at Sub-Nano-Hole (SNH) Of Nano (Mesoscopic) Catalyst

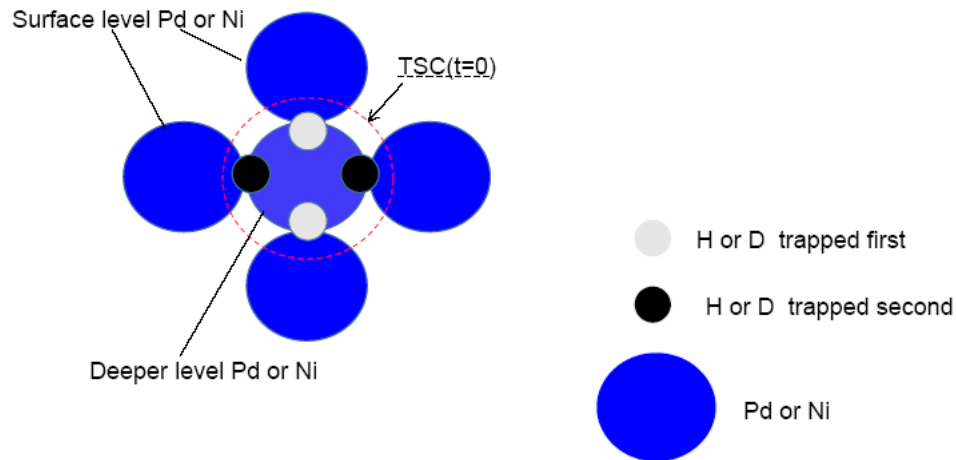


Figure 3. Image of TSC ($t = 0$) formation at a SNH state.

$$\langle \text{FusionRate} \rangle = \frac{2}{\hbar} \langle \Psi_{\text{nf}} | W(r) | \Psi_{\text{ni}} \rangle_{V_n} \cdot \langle \Psi_{\text{cf}} | \Psi_{\text{ci}} \rangle_{V_n} . \quad (2)$$

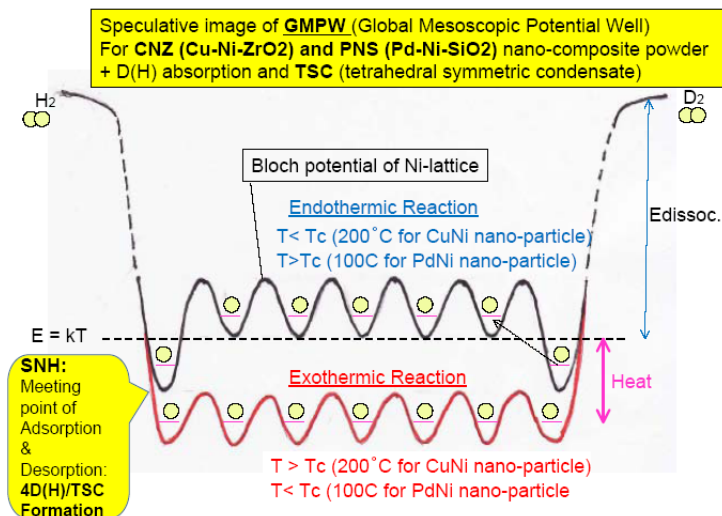


Figure 4. Diagram of absorbed D(H)s in a global mesoscopic potential well (GMPW) of binary nano-particles.

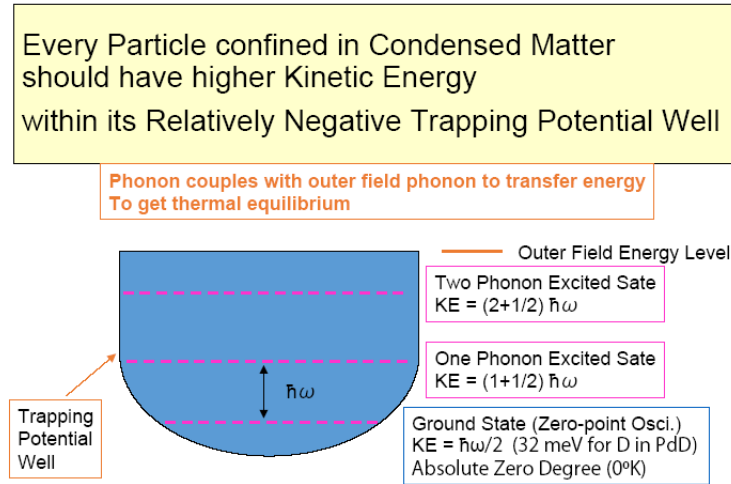


Figure 5. Phonon-energy exchange of trapped D(H)s and outer phonons in the substrate (a ceramic supporter).

Here, Ψ_{ni} and Ψ_{nf} are inter-nuclear wave functions, respectively for the initial state and the final state. Ψ_{ci} and Ψ_{cf} are outer-nuclear wave functions in the electro-magnetic field, respectively for the initial and the final state of interaction. V_n is the effective volumetric domain of nuclear interaction by strong (or weak) force to be given approximately as,

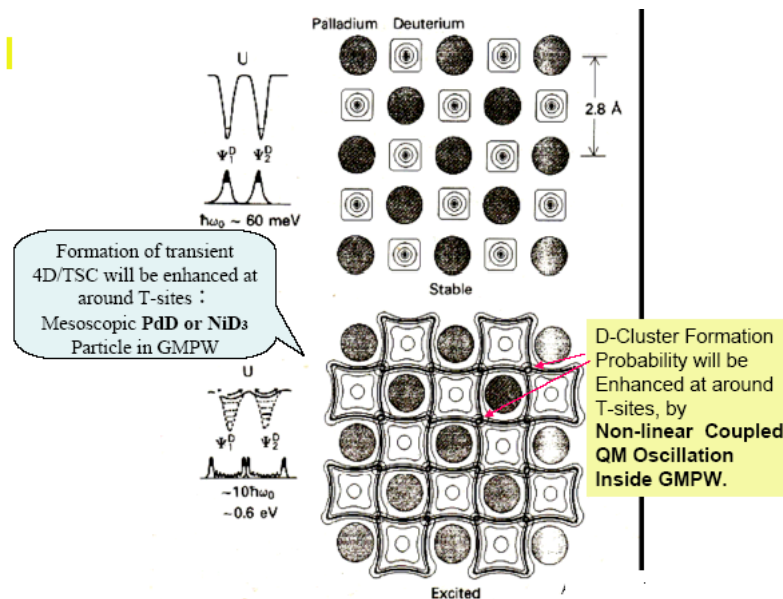


Figure 6. Possibility of enhanced TSC formation at inner lattice sites of nano-particle as mesoscopic catalyst, at elevated ambient temperature (lower figure).

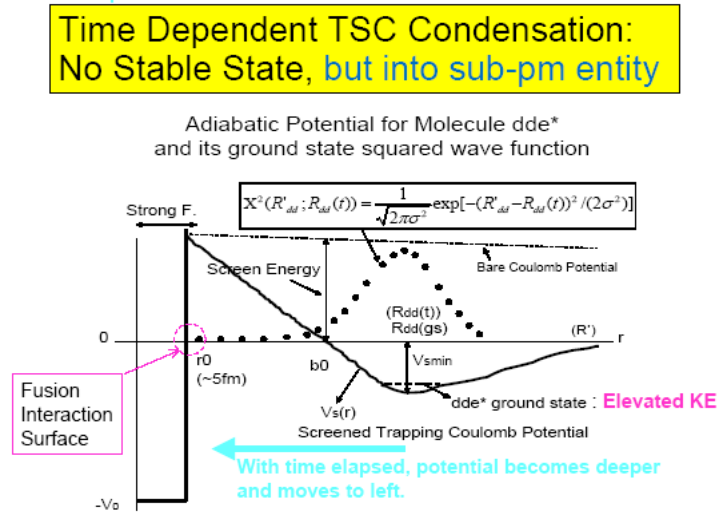


Figure 7. Illustration of ‘adiabatic state’ under continuous condensation motion of 4D(H)/TSC.

$$V_n \approx 4\pi R_n^2 \lambda_\pi. \quad (3)$$

Here R_n is the radius of nuclear-interaction surface as shown in Fig. 7, and λ_π is the Compton wavelength (1.4 fm) of pion as virtual force-exchange boson for strong interaction. (In the case of weak interaction, we replace it with the

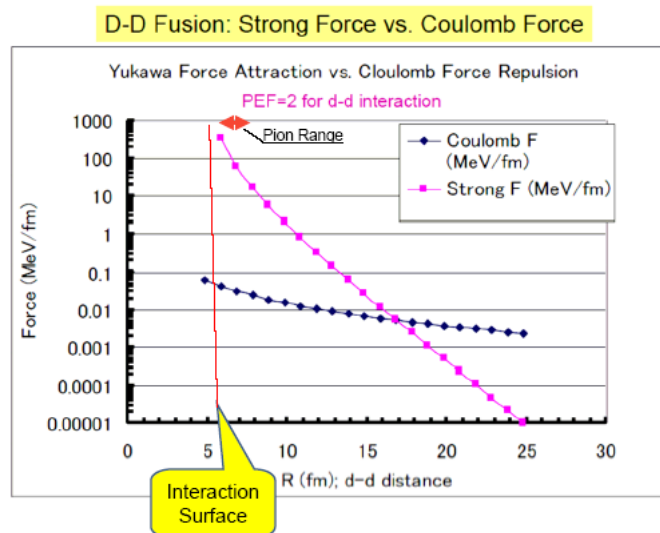


Figure 8. Strong force (attractive) is compared with Coulombic force (repulsive) for the d–d interaction.

Optical Potential for Strong Interaction

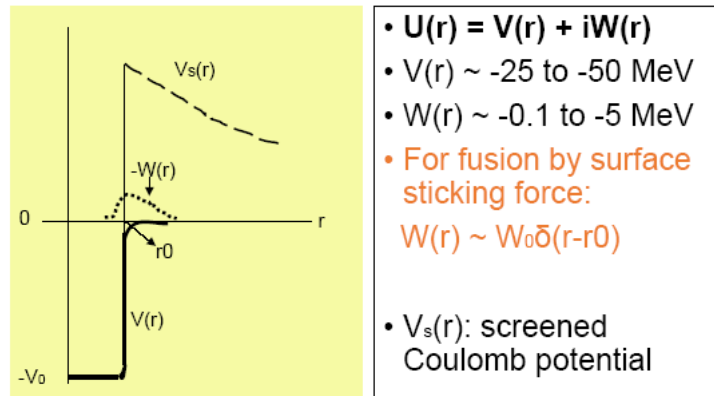


Figure 9. General features of nuclear optical potential.

Compton wavelength of weak boson 2.5 am.)

$W(r)$ is the imaginary part of the nuclear optical potential, which is the main factor of strong (or weak) interaction near around the interaction surface $r = R_n$. To estimate the fusion rate by Eq. (2), we need to calculate two adiabatic terms: the first is the inter-nuclear fusion rate, and the second is the effective QM wave-function-weight for that inter-

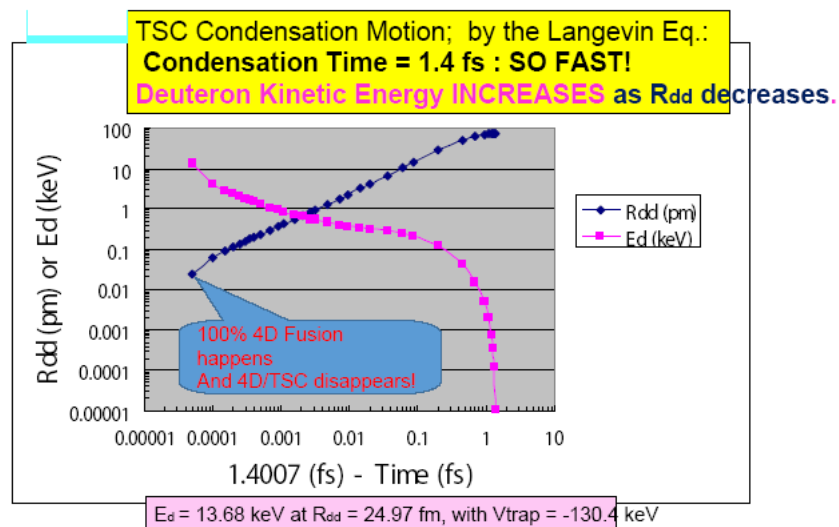


Figure 10. Time variation of R_{dd} and relative d–d kinetic energy under the 4D/TSC condensation.

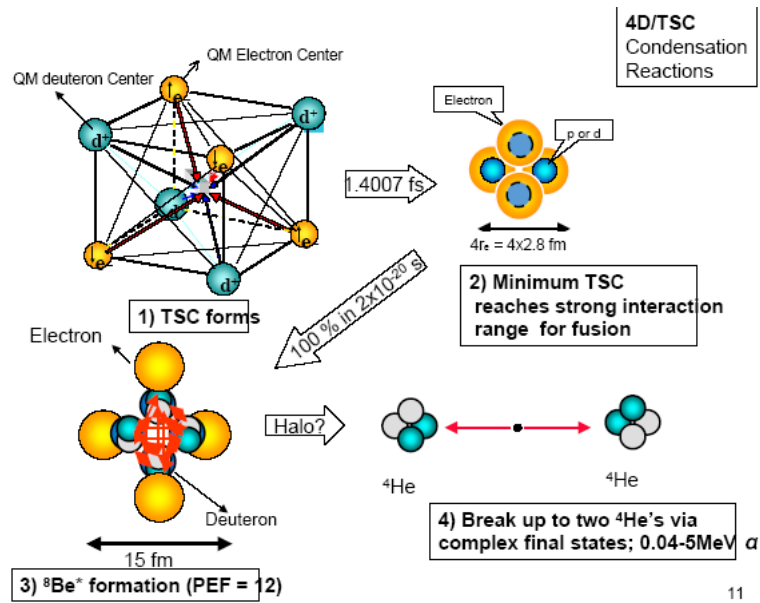
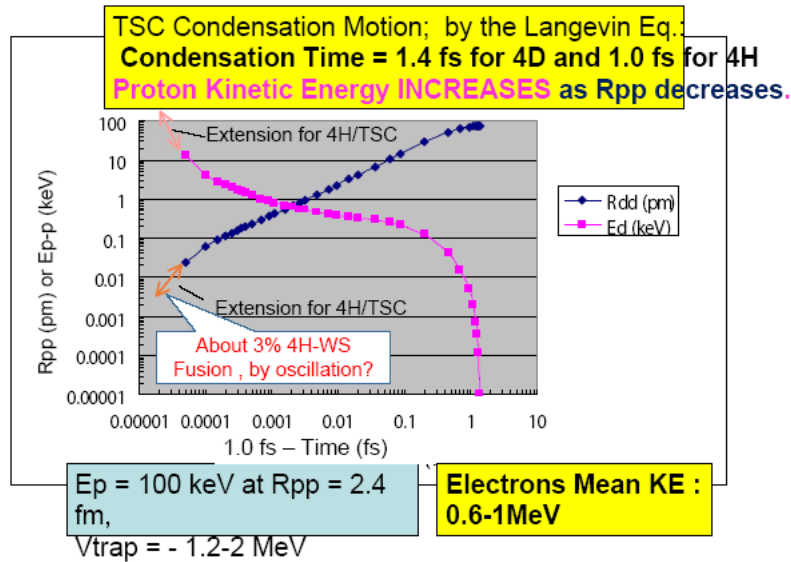


Figure 11. Brief view of 4D/TSC condensation and 4D fusion.

Figure 12. Time variation of R_{pp} and relative p-p kinetic energy under the 4H/TSC condensation.

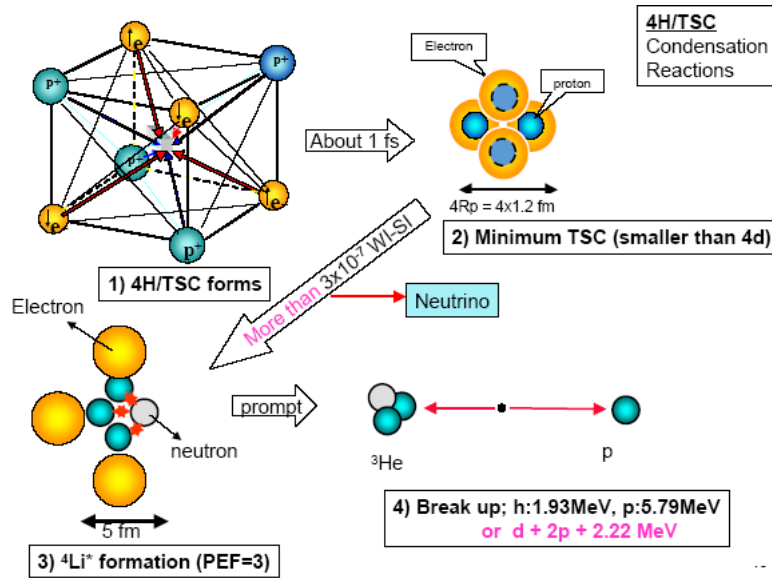


Figure 13. Brief view of 4H/TSC condensation and 4H weak-strong fusion interaction.

nuclear fusion rate [4]. In an approximate treatment, the second term is calculated by using the WKB approximation with Gamow integral, which is called the ‘barrier penetration probability.’ The approximation of the first term (W), an

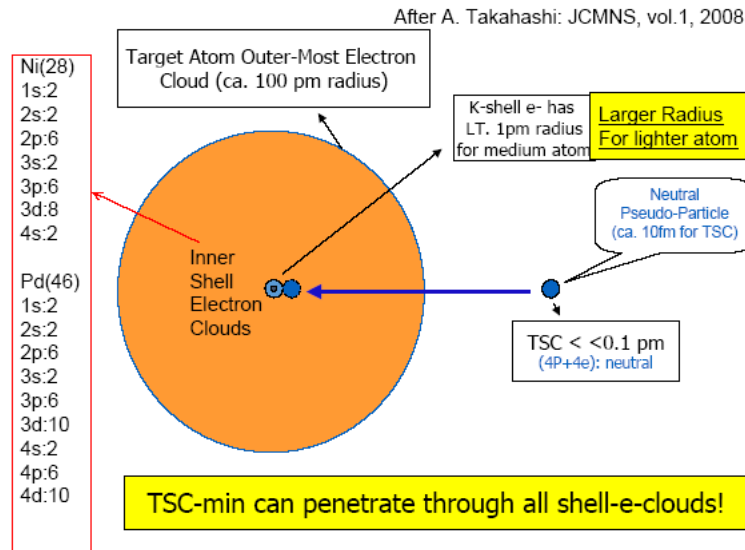
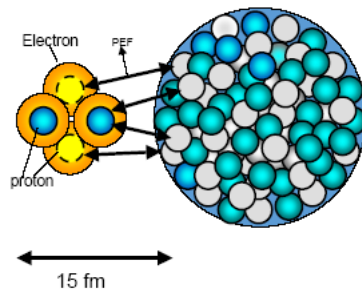


Figure 14. 4H/TSC-minimum may approach Ni-nucleus to make strong interaction (4p capture and fission).

After A. Takahashi: JCMNS, vol.1, 2008

M + 4p/TSC Nuclear Interaction Mechanism



- Topological condition for Pion-Exchange (PEF): 4p's are within pion ranges.
- Selection of simultaneous pick-up of 4p looks dominant.
- M + 4p capture reaction.

Figure 15. 4H/TSC-minimum can make 4p capture into Ni nucleus.

empirical approach with pion exchange force-values (PEF-values), was used [3,4].

A graph of PEF as a measure of strong interaction is drawn in Fig. 8 for the case of PEF =2 (d-d fusion), using

Major Fission Channels from Ni + 4p (2)	
<ul style="list-style-type: none"> • $^{62}\text{Ni}(3.6\%) + 4p \rightarrow ^{66}\text{Ge}(\text{Ex}=24.0\text{MeV})$ $[^{60}\text{Ni} + 4d \rightarrow ^{64}\text{Ge}(\text{Ex}=53.937\text{MeV})]$ <ul style="list-style-type: none"> → 11.0MeV + n + $^{65}\text{Ge}(\text{EC})^{65}\text{Ga}(\text{EC})^{65}\text{Zn}$ → 21.4MeV + ^4He + $^{62}\text{Zn}(\text{EC})^{62}\text{Cu}(\text{EC})^{62}\text{Ni}$ → 11.5MeV + ^8Be + ^{56}Ni → 18.9MeV + ^{12}C + ^{54}Fe → 10.5MeV + ^{14}N + $^{52}\text{Mn}(\text{EC})^{52}\text{Cr}$ → 8.2MeV + ^{16}O + ^{50}Cr → 13.9MeV + ^{20}Ne + ^{46}Ti → 15.2MeV + ^{24}Mg + ^{42}Ca → 13.7MeV + ^{27}Al + ^{39}K → 18.9MeV + ^{28}Si + ^{36}Ar → 18.6MeV + ^{32}S + ^{34}S • Neutron emission channel may open! • S-values for higher mass Ni may be larger than Ni-58 and Ni-60, due to more p-n PEF interaction. 	<ul style="list-style-type: none"> • $^{64}\text{Ni}(0.93\%) + 4p \rightarrow ^{68}\text{Ge}(\text{Ex}=29\text{MeV})$ $[^{60}\text{Ni} + 4d \rightarrow ^{64}\text{Ge}(\text{Ex}=55.048\text{MeV})]$ <ul style="list-style-type: none"> → 16.7MeV + n + $^{67}\text{Ge}(\text{EC})^{67}\text{Ga}(\text{EC})^{67}\text{Zn}$ → 25.6MeV + ^4He + ^{64}Zn → 10.0MeV + ^6Li + $^{61}\text{Cu}(\text{EC})^{61}\text{Ni}$ → 13.2MeV + ^8Be + $^{57}\text{Ni}(\text{EC})^{57}\text{Co}(\text{EC})^{57}\text{Fe}$ → 10.9MeV + ^{10}B + $^{58}\text{Ni}(\text{EC})^{58}\text{Co}$ → 9.9MeV + ^{10}B + $^{58}\text{Co}(\text{EC})^{58}\text{Fe}$ → 22.7MeV + ^{12}C + ^{56}Fe → 14.8MeV + ^{14}N + $^{54}\text{Mn}(\text{EC})^{54}\text{Cr}$ → 12.7MeV + ^{16}O + ^{52}Cr → 17.6MeV + ^{20}Ne + ^{47}Ti → 12.7MeV + ^{23}Na + ^{45}Sc → 17.5MeV + ^{24}Mg + ^{44}Ca → 14.8MeV + ^{27}Al + ^{41}K → 18.7MeV + ^{28}Si + ^{40}Ar → 18.7MeV + ^{32}S + ^{36}S

56

Figure 16. Expected major fission products by Ni + 4p process.

the simplified one-pion exchange potential of Hamada–Johnston [7] the main part of which is the Yukawa potential of meson exchange. $\langle W \rangle$ values for multi-body fusion as 3D, 4D and 6D were roughly estimated by using the scaling law with (PEF)⁵ and cross sections of p–d, d–d and d–t reactions and were given in [3]. The general features of the nuclear optical potential is illustrated in Fig. 9.

4. D-Cluster Fusion

As soon as a 4D/TSC ($t = 0$) state with a D₂ molecule of size ($R_{dd} = 74$ pm) is formed, our code calculation by the QM-Langevin equation gives a numerical solution for time-dependent R_{dd} and mean relative kinetic energy of d–d pair of a face of six TSC (d–e–d-type) faces, as copied from Refs. [2,3] and shown in Fig. 10. The adiabatic size of 4D/TSC reaches few tens of femtometers in 1.4 fs, which is fast. With adiabatic 4D/TSC size around 20 fm, 4D-fusion takes place by 100% yield [2,3] in 2×10^{20} s, namely,



The break up channels of ${}^8\text{Be}^*$ are very complex, because break-up occurs with a very deformed nucleon (n or p) halo admixture, which may have a very small level-gap (possibly 1–10 keV) vibration/rotation band structure with relatively long life time, from where complex EM transitions to emit low energy (1–10 keV, possibly) gamma-rays and excitation-damping to the ${}^8\text{Be}$ ground state (two alphas decay) may occur [8]. 4D/TSC disappears after 1.4 fs.

The fusion yield per 4D/TSC generation is calculated by integrating the time-dependent fusion rate by Fermi's first golden rule as precisely explained in reference [3], that was very close to 1.0, namely 100%, during the very small time interval of ca. 2×10^{-20} s in the final stage of condensation. The mean relative kinetic energy of neighboring d–d pairs of 4D/TSC-minimum is ca. 14 keV, which by coincidence resembles the value of DT plasma fusion experimental devices such as ITER. A discussion of the mean kinetic energies of d–d pairs was given in [7] for the D₂ molecule (2.7 eV) and muonic d–d molecule (180 eV). These are not 'cold' values as 0.025 eV of room-temperature matter. The reason is that the confined d–d pair in a 'deep' electromagnetic (or Coulombic) trapping potential should decrease its de Broglie wave length to be constrained by the Heisenberg Uncertainty Principle (HUP).

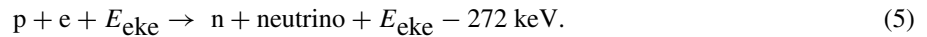
A simplified image of 4D/TSC condensation and fusion reaction is copied [1–3] as shown in Fig. 11.

5. 4H/TSC WS Fusion

According to the formula of the QM-Langevin equation, the velocity of condensation (time dependent) is inversely proportional to the square root of the mass of the confined particle. Therefore, 4H/TSC will condense in 1.0 fs to the small size region of a few tens of femtometers. However, there is no strong-fusion interaction (PEF = 0) between 4 protons of TSC to finally destroy the TSC state. We believe that 4H/TSC can condense further to be ultimately as small as the 4H/TSC-minimum state, a few femtometers in size (where 2.4 fm p–p distance is the limit, due to the hard core of the proton with 1.2 fm radius). The problem there is how long the 4H/TSC-minimum state can survive.

As a future task, we need a study of this extremely condensed state using a relativistic QM equation (the Dirac equation or some equivalent one). The TSC trapping potential can be modified with an additional term of spin-tensor force of electrons and protons in combination of ordered directions [8]. The converted figure of condensation motion for 4H/TSC is shown in Fig. 12.

The depth of adiabatic p–p trapping potential on a face of TSC is as deep as –1.2 to –2.0 MeV in the 4H/TSC-minimum state. There the mean relative kinetic energy of electron E_{eke} in a p–e–e–p system on one face of TSC would be 0.6–1.0 MeV. Therefore, we may expect the electron capture process to occur with one proton of 4H/TSC-minimum, by the weak interaction [9].



Once a proton-to-neutron transition is generated by the electron capture, we expect instantaneous strong interaction between the newly born neutron and closely available three protons within the Compton wave length of charged pions 1.4 fm (PEF = 3) as illustrated in step (3) of Fig. 13. As the pion range 1.4 fm is the Heisenberg uncertainty in distance, the $n + 3p$ reaction takes place by 100% with $\langle W \rangle$ value of PEF = 3 (comparable to d-t fusion) [9].



The intermediate compound ${}^4\text{Li}^*$ has two break-up channels.



The branch (7) is thought to be a major out-going channel and we expect ${}^3\text{He}$ to be the main nuclear product.

Also 5.79 MeV proton will produce secondary neutron by $\text{Ni}(n,p)$ reactions with higher mass nickel isotopes, on the order of 10^{-13} of ${}^3\text{He}$ production rate and $\text{Ni}(p,\gamma)$ secondary gamma-rays on the order of 10^{-11} per 5.79 MeV proton. Characteristic X-rays from nickel ionization by the proton are also expected.

However, we do not know the branching ratio to the branch (8), which will not produce secondary neutrons and gamma-rays at all.

So the key problem is how probable is it that a weak interaction rate will suffice to generate neutron–nucleon (not a free neutron) during the duration of the 4H/TSC-minimum state. The weak interaction rate is given by

$$\langle W \text{rate} \rangle = (4\pi/h) \langle W \rangle_w \langle \Psi_e(r_w) \rangle^2. \quad (9)$$

The details of the weak interaction rate calculation are given in [9]. As the Compton wave length of weak bosons (W^+, W^-) is extremely short, at 2.5×10^{-18} m (2.5 am), the second term of Eq. (9), namely, the weight of electron wave function from outer EM field, is as small as 5.9×10^{-5} , and the $\langle W \rangle$ value is also small, 78 eV [9].

If we assume the lifetime of 4H/TSC minimum is the same as the 4D/TSC-minimum, namely ca. 2×10^{-20} s, the weak interaction yield is very small, 3×10^{-7} fusion/TSC.

However, if the lifetime of 4H/TSC-minimum would be elongated to ca. 1 fs, which is comparable to the condensation time, the weak interaction yield can become as large as 3×10^{-2} (3%)/TSC, which is a reasonably large enough level to explain 100 W/mol-Ni-H level excess heat evolution in the Ni-based gas-loading experiments [10,11].

The other weak interaction channel is the $p + p \rightarrow d + \beta^+ + Q$ reaction. The p–p fusion rate at the 4H/TSC-minimum state is estimated to be 10^{-38} f/s, by using the S value 3.4×10^{-22} keV and the relative p–p kinetic energy 100 keV for the two-body reaction rate formula (Fermi's second golden rule [4]). Assuming that the lifetime is 1 fs of 4H/TSC-minimum, the p–p weak-fusion yield is 10^{-53} f/TSC, which is negligibly small.

6. Possibility of 4H/TSC + Ni Fission

As the inner-most (K) electron shell of the nickel atom has ca. 1 pm radius of 1s orbit and additional shell electrons 'protect' the nickel nucleus from an in-coming proton to make Ni + p nuclear reaction. This makes a two-body strong interaction between metal nucleus and proton (or deuteron) impossibly difficult. However, as the 4H/TSC-minimum state may have a very small size (as small as a few femtometers) and charge-neutrality, it would easily penetrate through the multi-shell barrier of electrons of metal nucleus. As nickel has a much larger 1s orbit than that of palladium, the 4H/TSC-minimum may more easily approach to the Ni-nucleus than palladium. Because the 4D/TSC disappears at sizes of a few tens of femtometers, only 4H/TSC has a good probability of approaching the nickel nucleus. This feature is illustrated in Fig. 14.

We have reported that fission products from Ni + 4p fission are predicted to be mainly clean stable isotopes, according to the selected channel scission theory [12]. As discussed in the previous section, the lifetime of the 4H/TSC-minimum state may be much longer than we conceived previously, and the size of its neutral entity is much smaller than previously thought. The strong interaction with nickel nucleus would be selective to the Ni + 4p capture and 1p to 3p capture processes will be neglected as shown in Fig. 15.

Fission products are considered to be mostly from the near symmetric fragmentations of Ge* intermediate compound state as shown in Fig. 16. In the past, there were reports on production of foreign elements, which were thought to be transmutation by several authors, such as Miley and Patterson [13].

Their data were analyzed by TSC-induced fission in reference [12]. Mass spectral analysis for samples before and after use is recommended for Ni–H system experiments as being done by the Piantelli-group, Kobe-Technova-group (Sakoh et al.) and Celani-group (INFN).

7. Conclusions

A systematic theoretical study on the possible physics mechanisms of cold fusion in D(H)-contained condensed matter is briefly explained.

As the nature of condensed matter is the ordering/constraint dynamic conditions on confining particles of deuterons, protons and electrons in electro-magnetically induced trapping potentials, D(H)-cluster formation and its transient motion is considered a clue to solve the puzzle of cold fusion.

The TSC theory has been proposed and elaborated since April 1989 by the author in three main steps [1]. The most realistic solution with quantitative results of microscopic D(H)-cluster fusion rates has been obtained recently (step 3) by using the QM-Langevin equation for studying their dynamic condensation processes and relevant strong and/or weak nuclear interactions as a many-body system. The conventional two-body system has not been able to provide meaningfully observable nuclear reaction rates, in contrast to the hot fusion process.

The 4D simultaneous fusion (^4He : ash) and the 4H simultaneous weak-strong fusion (^3He , d: ash) are the consequence of the TSC theory that the author has developed until now.

The quantitative formulation of microscopic fusion rates for D(H)-cluster fusion has been made by one-through work. However, the remaining work, namely the quantitative study on the TSC formation probability in D(H)-loaded metal systems is yet to be done. It might be accomplished by solving many-body time-dependent problems under organization of the field of condensed matter. This will be challenging.

Acknowledgment

The author is grateful to Technova colleagues (A. Kitamura, R. Seto and Y. Fujita) for their support.

References

- [1] A. Takahashi, Progress in condensed cluster fusion theory, *J. Cond. Mat. Nucl. Sci.* **4** (2011) 269–281.
- [2] A. Takahashi, *The Basics of Deuteron Cluster Dynamics as Shown by Langevin Equation*, American Chemical Society, Oxford Univ. Press, Oxford, LENR-NET Sourcebook, Vol.2, 2009, pp. 193–217.
- [3] A. Takahashi, N. Yabuuchi, Study on 4D/TSC condensation motion by non-linear Langevin equation, American Chemical Society, Oxford Univ. Press, LENR-NET Sourcebook Vol.1, pp.57–83 (2008)
- [4] A. Takahashi and N. Yabuuchi, Fusion rates of bosonized condensates, *J. Cond. Mat. Nucl. Sci.* **1** (2007) 106–128.
- [5] A. Takahashi et al., Role of PdO surface coating in CMNE D(H)-gas loading experiments, *J. Cond. Mat. Nucl. Sci.* **5** (2011) 17–33.
- [6] A. Takahashi et al., Mesoscopic catalyst and D-cluster fusion, *Proc. JCF11*, pp. 47–52, JCFRS web-site, (2011).

- [7] A. Takahashi, Kinetic reaction energy of cold fusion, *Proc. JCF12*, Dec. 2011, Kobe, pp. 67–76 (2012).
- [8] D. Rocha, Private communication with A. Takahashi, 2012.
- [9] A. Takahashi, 4HTSC fusion by simultaneous weak/ and strong interactions, *Proc. JCF12*, Dec. 2011, Kobe, pp.115–122 (2012).
- [10] F. Piantelli et al., Some results from the Nichenergy laboratory, presentation at the 10th Int. Workshop, Siena, April 2012 (see ISCMNS web site).
- [11] H. Sakoh et al., Hydrogen isotope absorption and heat release characteristics of a Ni-based sample, *Proc. ICCF17*, Daejeon Korea, August 2012,, to be published.
- [12] A. Takahashi, TSC-induced nuclear reactions and cold transmutations, *J. Cond. Mat. Nucl. Sci.* **1** (2007) 86–96.
- [13] G. Miley and J. Patterson, *J. New Energy* **1** (1996) 5.



Research Article

Detection of Pr in Cs Ion-implanted Pd/CaO Multilayer Complexes with and without D₂ Gas Permeation

Naoko Takahashi*, Satoru Kosaka, Tatsumi Hioki and Tomoyoshi Motohiro

Toyota Central R&D Labs. Inc., Japan

Abstract

Iwamura-type nuclear transmutation, $^{133}\text{Cs} \rightarrow ^{141}\text{Pr}$, with D₂ permeation through Pd/CaO multilayer complexes, was examined. Using ICP-MS, the amounts of Pr were measured in the range 10^{10} atoms/cm². The amounts of Pr measured in D₂ permeated samples were larger than samples that were not permeated.

© 2014 ISCMNS. All rights reserved. ISSN 2227-3123

Keywords: CaO/Pd multilayer complex, Cs→Pr, Deuterium permeation, Nuclear transmutation

1. Introduction

Iwamura et al. have published several reports claiming that nuclear transmutation occurs with D₂ gas permeation through Pd substrates covered with a Pd/CaO multilayer film (multilayer complexes) [1]. The elements to be transformed are deposited on to the surface of the multilayer complex by the electrochemical method or by ion implantation, and the complex is subjected to D₂ permeation at 343 K for a week or so. The selected nuclear transmutations reported so far are ^{88}Sr to ^{96}Mo , ^{133}Cs to ^{141}Pr and ^{138}Ba to ^{150}Sm [1,2].

Few replication attempts at other laboratories have succeeded. One of the difficulties in reproducing the results of the Iwamura group may be that the amounts of the transformed element are too small to be detected by surface elemental analysis such as XPS, which has often been used in Iwamura-type nuclear transmutation replication experiments [3,4].

In this study, we focused on the Cs to Pr transmutations. We investigated the performance of trace Pr detection by several analysis methods. We compared the detection sensitivity among Glow Discharge Mass Spectrometry (GD-MS), Laser Ablation Inductively Coupled Plasma Mass Spectrometry (LA-ICP-MS) and Inductively Coupled Plasma Mass Spectrometry (ICP-MS), using reference samples that were doped with different concentrations of Pr. We concluded that ICP-MS is the best technique for detecting small amounts of Pr. Using ICP-MS, we measured the amounts of Pr in samples with and without D₂ permeation treatment, and in some reference samples. Our goal was to discover whether the observed Pr is generated as a result of a nuclear reaction during the D₂ permeation process, or whether it is simply

*E-mail: nao-t@mosk.tytlabs.co.jp

chemical contamination. In this study, efforts were made to examine chemical contamination in the materials used and in the process of sample preparation, e.g., surface concentration of impurities in Pd during the D₂ permeation process.

2. Experimental

2.1. Materials

Substrates of Pd (purity: 99.95%) 100 μm thick were obtained from Tanaka Kikinzoku Kogyo. The as-purchased substrates were heat-treated in vacuum (5×10^{-5} Pa) at 1173 K for 15 h and subsequently in the air at 873 K for 10 min to remove impurity atoms. With this pre-treatment, S impurities in the Pd substrates were greatly reduced [5]. The D₂ gas for permeation treatments with purity of more than 99.995% was obtained from Takachiho Chemical Industrial Co. Ltd. The impurity concentrations listed by the supplier were less than 5 ppm for oxygen, nitrogen and water, and less than 1 ppm for carbon monoxide, carbon dioxide and total hydrocarbons.

2.2. Sample preparation

A multilayer film of Pd/CaO was formed on the Pd substrates by pulsed laser deposition (PLD). The multilayer complex was similar to the ones used by Iwamura et al., i.e., Pd (40 nm), CaO (2 nm), Pd (18 nm), CaO (2 nm), Pd (18 nm), CaO (2 nm), Pd (18 nm), CaO (2 nm), Pd (18 nm), CaO (2 nm), and Pd substrate (100 μm).

Cs atoms were implanted in the multilayer complex at 65 keV to a dose of 1.5×10^{15} atoms/cm². The range of the implanted Cs was estimated to be 11.8 nm. The Pd substrates were then heat-treated in air at 573 K for 10 min to remove carbonaceous materials deposited during the ion implantation.

The deposition of Cs on the top of the multilayer film was also carried out with the electrochemical method in the same manner as reported in the original paper by Iwamura et al. [1].

The samples were then subjected to D₂ gas permeation treatments at 343 K or 423 K for a period of 150–250 h. The deuterium gas was supplied to the up-stream side (the multilayer film side) of the sample via a reservoir tank of about 1 L, which was connected with a 6 MPa cylinder (D₂: 200 L) through a pressure regulator. Table 1 shows a list of the samples prepared in this study.

2.3. ICP-MS

The ICP-MS instrument used was an Agilent 7700X. The samples were dissolved partially or totally by nitric acid or aqua regia. Most samples were partially dissolved. The depth of dissolution was about 100 nm.

In order to evaluate the detection limit of the ICP-MS analysis, we prepared reference samples, i.e., Si wafers and Pd substrates with the CaO/Pd multilayer complexes, which were implanted with Pr ions at doses of 10^{12} , 10^{13} , and 10^{14} atoms/cm².

3. Results and Discussion

3.1. Structure of multilayer complex

An X-ray diffraction pattern using Cu ($K\alpha$) radiation was made to confirm the structure of the multilayer complex of the samples. Figure 1 shows the pattern for a Si wafer on which the multilayer structure was formed with the PLD technique.

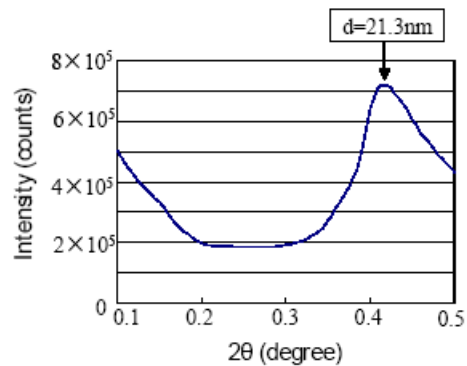
A peak is seen at very low angles indicating a super lattice structure with a spacing of 21.3 nm, which is close to the planned spacing of 20 nm. The PLD conditions, under which the multilayer film on the Si wafer was formed, were also used to form multilayer film on Pd substrates.

Table 1. Samples prepared for ICP-MS analysis (–: no data)

Sample No.	Multilayer	Cs deposition	D ₂ permeation	Max. upstream D ₂ pressure (atm)	Premeation Temp. (°C)	Average D ₂ flux (sccm)	Total permeated D ₂ (L)
1	Yes	Electro-chemical	Yes	5	70	0.77	18.7
2	Yes	Electro-chemical	Yes	9	70	1.6	45.4
3	Yes	Electro-chemical	Yes	5	150	1.6	34
4	Yes	Electro-chemical	Yes	2	70	0.71	14.3
5	Yes	Electro-chemical	Yes	9	150	3.6	111
6	Yes	Ion implantation	Yes	9	150	5.3	43
7	Yes	Ion implantation	Yes	9	150	2.6	74
8	Yes	Ion implantation	Yes	9	150	–	–
9	Yes	No	Yes	9	150	2	27
10	No	No	Yes	9	150	–	–
11	No	No	Yes	9	150	–	–
12	Yes	Ion implantation	No				
13	Yes	Ion implantation	No				
14	No	No	Yes				
15	No	No	Yes				
16	No	No	No				

3.2. Deuterium permeation

According to Iwamura et al. [6], the conversion rate of Cs to Pr increases with increasing D₂ gas permeation flux. The D₂ flux is sensitive to the surface conditions of the sample. Furthermore, it is generally observed that the permeation

**Figure 1.** Low angle X-ray diffraction pattern for the multilayer structure prepared on a Si wafer by PLD.

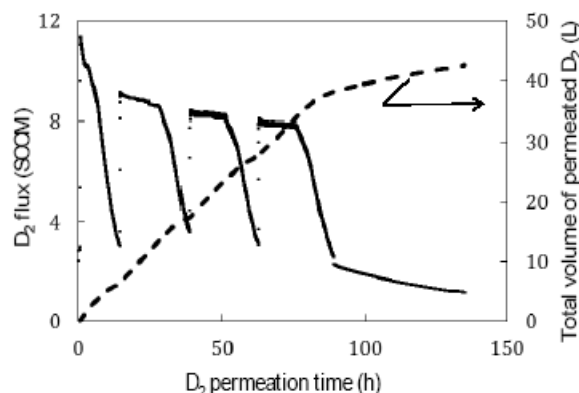


Figure 2. Permeation flux and total permeated D_2 volume vs. time for sample #6.

flux is relatively higher at the beginning of permeation but it decreases as permeation continues [7]. Therefore, it is not easy to keep a high D_2 flux during the whole duration of a D_2 permeation test.

Figure 2 shows an example of D_2 flux as a function of permeation time. As seen in Fig. 2, when the reservoir tank and the upstream side was filled up to about 900 kPa and kept at that pressure, the permeation flux was very high; about 8 sccm or more. The abrupt decreases of the flux sometimes seen in Fig. 2 were caused when the supply of D_2 to the tank was stopped. Under such condition, the D_2 pressure in the upstream side decreases with time and so does the permeation flux.

In Table 1, the average permeation flux and total permeated D_2 volume are shown for each sample.

3.3. Calibration of ICP-MS to detect Pr

In Fig. 3, the amounts of Pr measured by ICP-MS analysis were plotted as a function of the given doses of Pr ion implantation for the two series of samples. The amounts of Pr measured by ICP-MS is in close agreement with the ion implantation doses for both the Si wafer samples and CaO/Pd multilayer samples. It is seen that ICP-MS is capable of accurately detecting amounts of Pr as small as 1×10^{11} atoms/cm² in the samples of CaO/Pd multilayer complex as well as in high purity Si wafers. Figure 3 also indicates that contamination is low; nearly all of the Pr atoms in the multilayer complexes were implanted. The contamination level is estimated to be at most 10^{11} atoms/cm².

3.4. Amount of Pr in deuterium permeated samples

Figure 4 compares the amount of Pr measured by the ICP-MS technique for samples #1–#11. The results for the amount of Cs are also shown.

In Fig. 4, all the samples were treated with deuterium permeation. The samples #1–#8 are deposited with Cs either by electrochemical method or by ion implantation, while #9, #10, and #11 are samples without Cs deposition. Samples #10 and #11 are Pd substrates treated only with D_2 permeation.

It is seen in Fig. 4 that significant amounts of Pr are detected in the three samples #6, #7, and #8. In samples #2 and #4, amounts of Pr far exceeding 1×10^{11} atoms/cm² are also detected. From this figure, it is suggested that Pr is not detected in the samples which are not deposited with Cs before D_2 permeation treatment (#9, #10, and #11). This seems to be consistent with the idea that Pr emerges as a result of nuclear transmutation from Cs.

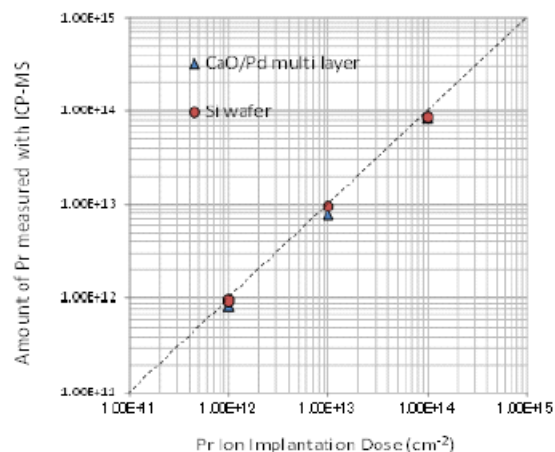


Figure 3. The amount of Pr measured by ICP-MS vs. ion implantation dose.

The samples #1–#5 are deposited with Cs by the electrochemical method. In these samples, however, as seen in Fig. 4, the amounts of Cs detected after D₂ permeation treatments are much smaller compared to the samples deposited with Cs by ion implantation. The detected amounts of Cs in samples #6–#8 are comparable with the ion implantation dose of 1.5×10^{15} atoms/cm². The electrochemical method seems to be unable to control the amount of Cs to be deposited.

If we assume that the Pr atoms detected in samples #6–#8 are converted from Cs atoms, the conversion rates, Pr/Cs, are in the order of 0.1% as shown in Table 2. The conversion rates are 1 to 2 orders of magnitude smaller than those reported by Iwamura et al.

Table 2 suggests that the conversion efficiency is more correlated with the total volume of permeated D₂, rather than the average D₂ flux.

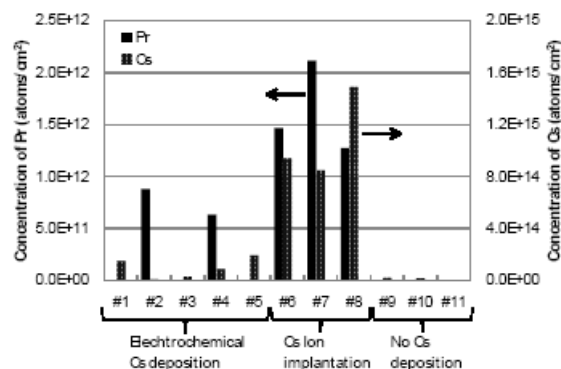


Figure 4. The detected amounts of Pr and Cs in the samples with D₂ permeation treatments.

Table 2. Conversion rate and permeation conditions

Sample No.	Pr/Cs (%)	Average D ₂ flux (sccm)	Total permeated D ₂ (L)
6	0.16	5.3	43
7	0.25	2.6	74
8	0.086	–	–

3.5. Amount of Pr in samples that were not permeated

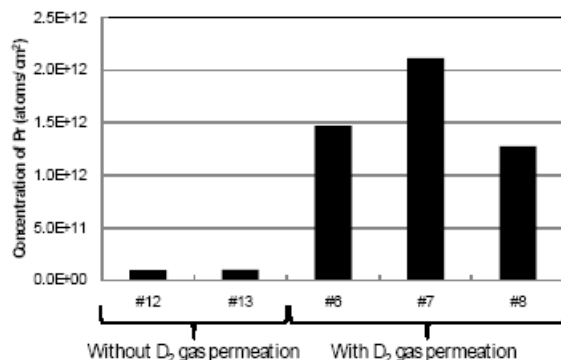
To confirm the effect of deuterium permeation on the emergence of Pr, the ICP-MS analyses were performed on control samples #12 and #13. These multilayer samples are deposited with Cs by ion implantation but not subjected to D₂ permeation treatment. The results are shown in Fig. 5. For comparison, the data for samples #6, #7, and #8 is shown. These were deposited with Cs by ion implantation and subjected to D₂ permeation.

As seen in Fig. 5, small amounts of Pr are detected in the control samples: 0.98×10^{11} atoms/cm² and 1.0×10^{11} atoms/cm² in #12 and #13, respectively. Such small amounts of Pr can be expected in the impurities in an ordinary environment. The amounts of Pr detected in the D₂ permeated samples are more than one order of magnitude larger than those detected in the control samples.

3.6. Amount of Pr in Pd substrates

In order to determine the amount of Pr contained in the Pd substrates, 3 Pd samples (#14 and #15) in the as-purchased state were analyzed with ICP-MS. These samples are totally dissolved. The results are shown in Fig. 6. For comparison, the result of #6–#8 is also shown.

As shown in the figure, Pd substrates contained small amount of Pr: 2.3×10^{10} atoms/cm², 9.0×10^{10} atoms/cm² and 7.9×10^{10} atoms/cm² for #14, #15, and #16, respectively. Therefore, the contamination of Pr in Pd substrates is at most 1.0×10^{11} atoms/cm². We conclude that the amounts of Pr detected in the samples #6–#8 are more than one order of magnitude larger than the total amount of Pr impurities in the Pd substrates used in the present study.

**Figure 5.** Comparison of the amounts of Pr in samples with and without D₂ permeation.

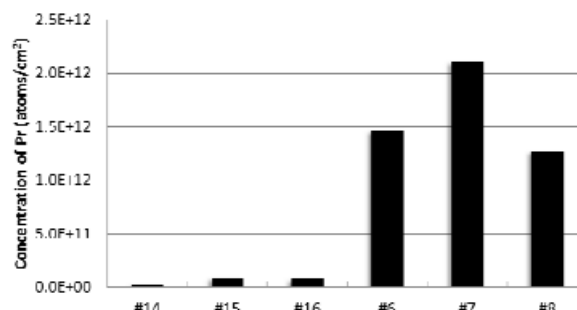


Figure 6. The amount of Pr in Pd substrates #14–#16. The result of #6–#8 is included for comparison.

4. Conclusions

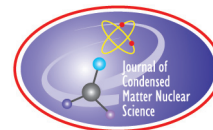
Using ICP-MS, we measured the concentration of Pr in the range of 1.0×10^{10} atoms/cm². The amounts of Pr in the D₂ permeated samples were one order of magnitude larger than those in the control samples not permeated with D₂. We detected approximately 1.0×10^{12} atoms/cm² of Pr in the D₂ permeated Pd/CaO multilayer samples with ion-implanted Cs atoms. On the other hand, in the control samples, the amount of Pr was at most 1.0×10^{11} atoms/cm². If we assume that the Pr atoms detected were converted from Cs atoms, the conversion rates, Pr/Cs, were in the order of 0.1%. This value is much smaller than those reported by the Iwamura group.

Acknowledgment

We would like to thank T. Nishi, H. Azuma, S. Hibi for their discussions and support in the experiments. We are also grateful to N. Nakamura of Toyota Motor Corporation for discussions and encouragement.

References

- [1] Y. Iwamura, M. Sakano and T. Itoh, Elemental analysis of Pd complexes: effects of D₂ gas permeation, *Jpn. J. Appl. Phys.* **41** (2002) 4642–4648.
- [2] Y. Iwamura, T. Itoh, M. Sakano, N. Yamazaki and S. Kuribayashi, Observation of nuclear transmutation reactions induced by D₂ gas permeation through Pd complexes, *Proc. ICCF-11*, Marseilles, France, October 2004, pp. 339–350.
- [3] A. Kitamura, R. Nishio, H. Iwai, R. Satoh, A. Taniike and Y. Furuyama, In situ accelerator analyses of palladium complex under deuterium permeation, *Proc. ICCF-12*, Yokohama, Japan, October 2004, pp. 339–350.
- [4] T. Hioki, N. Takahashi and T. Motohiro, XPS study on surface layer elements of Pd/CaO multilayer complex with and without deuterium permeation, *Proc. ICCF-13*, Sochi, Russia, June 2007, pp. 518–528.
- [5] T. Hioki, J. Gao, N. Takahashi, S. Hibi, A. Murase, T. Motohiro and J. Kasagi, Influence of deuterium gas permeation on surface elemental change of ⁸⁸Sr ion-implanted Pd and Pd/CaO multi-layer system, *Proc. ICCF-14*, Washington DC, USA, August 2008, pp. 203–211.
- [6] Y. Iwamura, T. Itoh, M. Sakano, N. Yamazaki and S. Kuribayashi, Low energy nuclear transmutation in condensed matter induced by D₂ gas permeation through Pd complexes: correlation between deuterium flux and nuclear products, *Proc. ICCF-10*, Cambridge, Massachusetts, USA, August 2003, pp. 435–446.
- [7] T. Hioki, N. Takahashi, J. Gao, A. Murase, S. Hibi and T. Motohiro, Effects of self-poisoning of Pd on the deuterium permeation rate and surface elemental analysis for nuclear transmutation, *J. Cond. Mat. Nucl. Sci.* **6** (2012) 64–76.



Research Article

Excess Heat Triggered by Different Current in a D/Pd Gas-loading System

Jian Tian*, Bingjun Shen, Lihong Jin, Xinle Zhao and Hongyu Wang

Clean Energy Technology Lab, Changchun University of Science and Technology, Changchun 130022, People's Republic of China

Xin Lu

School of Science, Changchun University, Changchun 130022, People's Republic of China

Abstract

In order to study the relationship between the triggering current, deuterium pressure and the excess heat, a series of experiments were made in a D/Pd gas-loading system. By comparing the system constants ($k = \Delta T / \Delta P$) in both nitrogen and deuterium atmosphere we found an optimum current (8 A) and a deuterium pressure (9×10^4 Pa) in which the system could release a maximum excess power (more than 80 W). The reproducibility was 16/16 and the excess energy released in the longest experiment was about 300 MJ within 40 days, which was corresponding to 10^4 eV for each palladium atom. Analysis of the palladium surface with a scanning electron microscopy (SEM) and an energy dispersive spectrometer (EDS) revealed that some new surface topographical feature with concentrations of unexpected elements (such as Ag, Sn, Pb and Ca) appeared after the current triggering. The results implied that the excess heat might come from a nuclear transmutation.

© 2014 ISCMNS. All rights reserved. ISSN 2227-3123

Keywords: Current triggering, Deuterium pressure, D/Pd gas-loading system, Excess heat

1. Introduction

Focardi et al. [1] reported on the existence of a large excess heat production observed in a H/Ni gas-loading system. Rossi [2] developed the method and enlarged the phenomenon into 1 MW power generation device afterwards. In recent days some reported their new achievements in this field and many had skeptics on the demonstration reactor [3–8]. With a curiosity to that event a D/Pd gas-loading system was chosen and a series of similar experiments were made in order to prove if the evidence could be true and if the excess heat could be also occurred in other different system.

*E-mail: tian2281@126.com; tianjian@cust.edu.cn

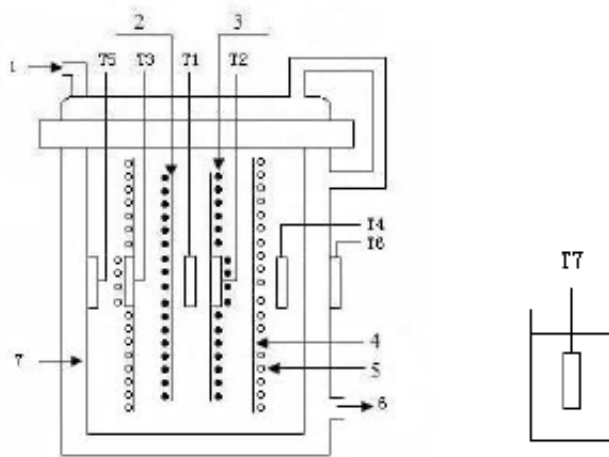


Figure 1. The chamber structure. Here 1 is the inlet of circulating water, 2,4 the ceramic tubes, 3 the Pd wire for triggering, 5 the Pd wire for being triggered, 6 the outlet of circulating water, 7 the double-jacket, the $T_1 - T_7$ Pt100 resistor thermometers were used for taking the temperatures in different positions, T_1 the center of the chamber inside the ceramic tube, T_2 wound on triggering Pd wire, T_3 wound on being triggered Pd wire, T_4 inside the chamber between inner wall and outer wall of the ceramic tube, T_5 inner wall of the chamber, T_6 outside wall of the chamber and T_7 ambient temperature.

2. Experimental

2.1. Materials and apparatus

Figures 1 and 2 show the schematic of the experimental system. Figure 1 is a reaction chamber that made up of stainless steel with a double-jacket structure, where the circulating water could flow through. It has internal dimension of diameter = 100 mm and height = 240 mm with a useful capacity of about 1.9 L. Two Pd wires were 99.98% in purity (made by General Research Institute of Nonferrous Metals, Beijing), one of them was for being triggered with the dimension of 0.5 mm in diameter and 210 cm in length ($V = 4.1 \times 10^{-1} \text{ cm}^3$). And the other was for triggering with the same size in diameter and 400 cm in length ($V = 7.854 \times 10^{-1} \text{ cm}^3$). In order to monitor the temperature at different positions continuously, Seven Pt100 resistor thermometers were placed inside and outside the reaction chamber. The chamber structure as shown in Fig. 1,

The apparatus connected to the reaction chamber is shown as in Fig. 2,

2.2. Calibration

Two palladium wires for triggering and being triggered were placed, respectively, in the reaction chamber. At the beginning some natural nitrogen gas was introduced into the chamber by four steps of $P_{N_2} = 20, 1 \times 10^4, 5 \times 10^4$ and 9×10^4 Pa. In each step, an initial current of 1 A and at a regular increase ($\Delta I = 1 \text{ A}$) were passed through the triggering Pd wire. The maximum current was 8 A. Then the relation between the temperature increases and different input power was obtained. The same process was done exactly when the nitrogen was replaced by deuterium. The promising result was occurred in $P_{N_2/D_2} = 9 \times 10^4$ Pa and calibration were shown in Figs. 3 and 4.

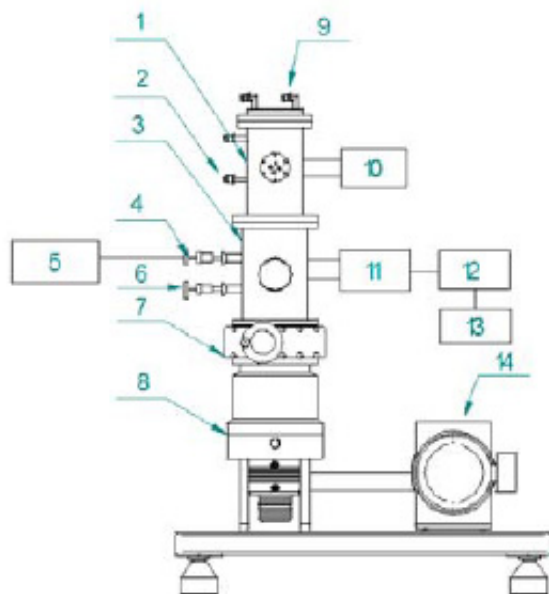


Figure 2. The apparatus connected to the reaction chamber. Here 1 is the chamber, 2 the inlet and outlet for circulation water around the chamber, 3 the transition chamber, 4 the D_2 needle valve, 5 the D_2 generator, 6 the air-released valve, 7 the gate valve, 8 the turbo-molecular pump, 9 the inlet and outlet mouth for water circulation on the top, 10 the DC power supply, 11 the vacuum gauge, 12 the Keithley 2700 multifunction data-inquisition meter, 13 a computer for data recording and controlling, 14 the mechanical pump.

2.3. Current triggering

From the data, the correlation between input power and $k = \Delta T / \Delta P$ [3] on being triggered Pd wire in N_2 and D_2 were fitted. The fitting curves were as shown as in Fig. 4. From this we can see that the value of k in N_2 atmosphere was

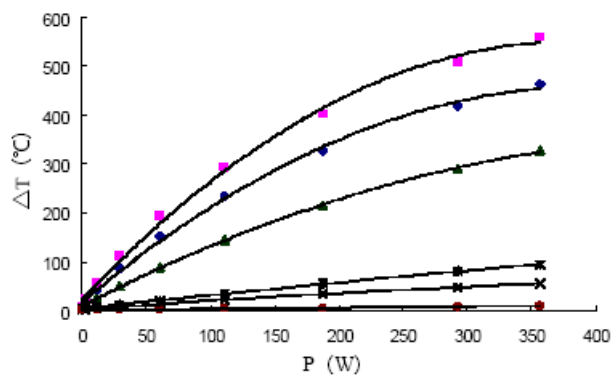


Figure 3. Calibration curves: temperature (relative to the T_7) vs. power under N_2 environment at 9×10^4 Pa. (T_1 (), T_2 (), T_3 (Δ), T_4 (\times), T_5 () and T_6 (\bullet)).

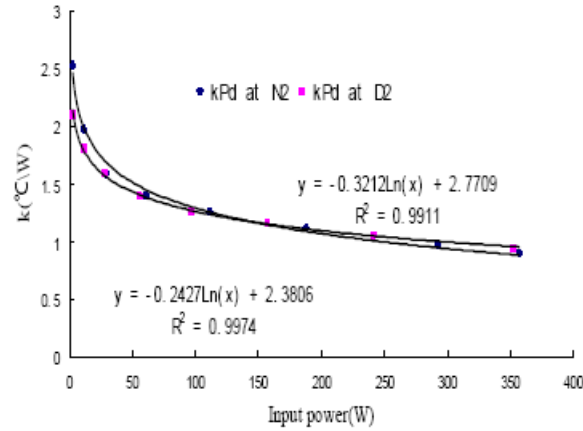


Figure 4. The fitting curve of input power and k under N_2 (), D_2 () environment at 9×10^4 Pa.

higher than that in the D_2 when input power was less than 150 W. But when the input power was more than 150 W, the value of k in D_2 was higher than that in the N_2 at high temperature. And with the input power is increasing, the difference between k in D_2 and k in N_2 became larger. However, taking into account the specific circumstances of laboratory equipment and the palladium wire, the triggering current of 8.0 A and $P_{D_2} = 9 \times 10^4$ Pa were chosen in the whole experiment. The triggering result is shown in Fig. 5.

The drawing in Fig. 5 is only the first four times' triggering in our experiment. The total was as many as 16 times.

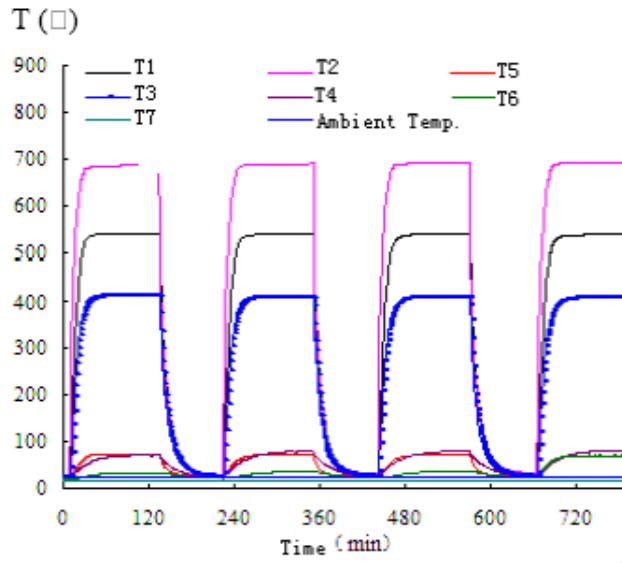


Figure 5. Current triggering results at 8 A in $P_{D_2} = 9 \times 10^4$ Pa.

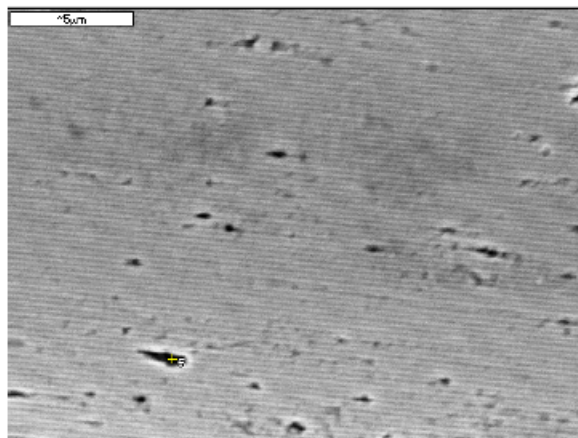


Figure 6. SEM of palladium wire before triggering (400 \times).

There were 80–90 W excess power in these experiments. The longest one was lasted for 40 days. It looked like the experiment could keep going on as long as possible.

3. Results and Discussion

3.1. Calculation for excess heat

The main purpose of this experiment was to investigate whether the excess heat could also appear in D/Pd gas-loading system by current triggering as in Focardi's H/Ni system. The next was whether the excess energy obtained in the system could be higher than chemical heat triggered by different electric current when deuterium atoms were charged into metal

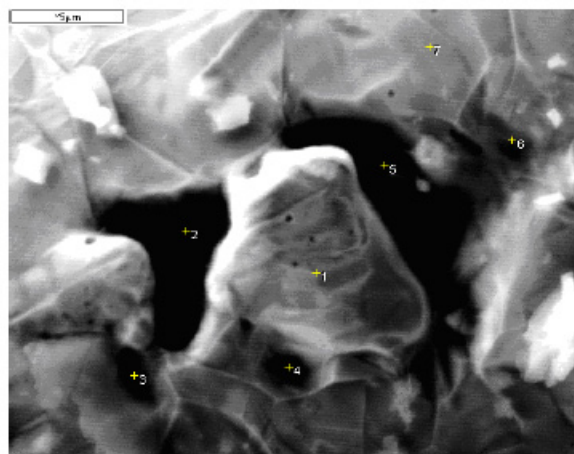


Figure 7. SEM of palladium wire after triggering (400 \times).

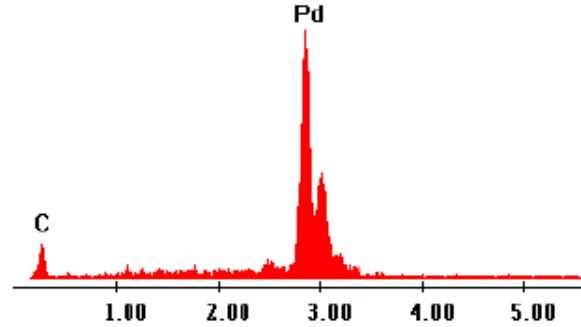


Figure 8. EDS of Pd origin sample before triggering.

palladium lattice. Let P_i be the electrical power supplied into the reaction chamber. At the thermal equilibrium the difference between the T_6 and T_7 could be measured. If k is the system heat equilibrium constant, which was determined by the rise of temperature with a unit power input into the system, the following relation must be verified:

$$P_i = k(T_6 - T_7). \quad (1)$$

If some kind of physical–chemical process occur into the system and palladium wire is the related enthalpy variation, the following relation holds:

$$P_i + \sum_{i=1}^n \frac{dH_i}{dt} = C \frac{dT_5}{dt} + k(T_6 - T_7), \quad (2)$$

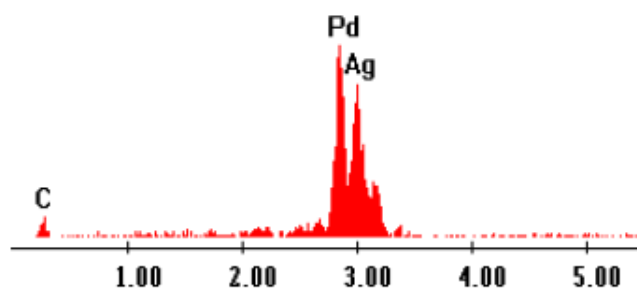
where C is the heat capacity. Equation (2) is valid if the characteristic times of the heat exchanges inside the reaction chamber are shorter than $\tau_c = C/k$ (chamber time constant). If all the physical–chemical processes last for a limited period before stopping, Eq. (2) reduces to Eq. (1). In the case for which one process excess heat power (P_o) does not stop and $P_o = dH_i/dt \rightarrow \text{constant}$, on assuming quasi-stationary conditions, that is, the temperatures of the chamber remain practically constant during a few chamber time constants. The excess heat power can be calculated by using Eq. (3).

$$P_o = P_i - \frac{T_6 - T_7}{k}. \quad (3)$$

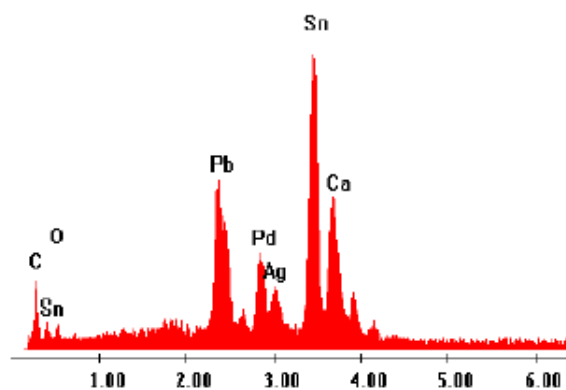
According to Eq. (3), the excess heat power could be calculated as in Table 1.

Table 1. 8 A Current triggering results in $P_{D_2} = 9 \times 10^4 \text{ Pa}$

Triggering	P_{input} (W)	Loading ratio	Equilibrium temperature ($^{\circ}\text{C}$)	Excess heat power (W)
0	–	0.094	23.959 ± 0.003	–
1	416.875 ± 0.011	0.018	409.138 ± 0.022	90.629 ± 0.002
2	416.689 ± 0.015	0.029	407.166 ± 0.037	88.380 ± 0.015
3	416.778 ± 0.019	0.092	406.408 ± 0.156	87.399 ± 0.019
4	416.71 ± 0.004	0.032	405.532 ± 0.022	88.217 ± 0.004



(a) Element Ag was found (point 2)



(b) Element Pb, Sn, Ca were found (point 5)

Figure 9. EDS of Pd sample after triggering.

The longest triggering experiment lasted for 40 days. The average excess heat power was more than 87 W, the total excess heat energy was about 300 MJ, which was corresponding to 1.8×10^4 eV/atom Pd. Apparently it was more than the energy for each Pd atom released in a chemical process.

3.2. SEM and EDS analysis

The SEM image of original Pd wire before triggering was shown in Fig. 6. From this many scratches on Pd wire surface could be seen due to its industrial production. The SEM of Pd wire charged by deuterium for 5 times was given in Fig. 7. Where many small cavities on Pd wire surface occurred. Comparison to Figs. 6 and 7, Pd wire had an apparently morphological difference in the surface before and after deuterium loading and current triggering. Because a certain number of deuterium atoms went into the Pd lattice, many cavities formed on the surface. These cavities or channels, made it easy that deuterium atoms charged into the Pd lattice. This is the reason why deuterium charging repeatedly into Pd became more easily afterwards.

The original Pd wire was analyzed with an EDS (Fig. 8). The result indicated that the purity of sample was of nearly 100%. The EDS analysis of palladium wire after being triggered was shown in Fig. 9. It is very clear that new

elements of Ag, Pb, Sn and Ca were appeared after the triggering process. Also it is necessary to investigate how they did form on the palladium surface or inside the body. These elements might be produced during some transmutation process.

4. Conclusions

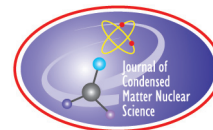
Being triggered by current large amount of excess heat could be produced in D/Pd gas-loading system as same as in H/Ni system. Under the condition of bellowing an atmosphere, the higher of deuterium pressure, the larger of triggering current, the better the triggering effect. By this way even larger excess heat could be obtained under some other conditions (such as 2 atm, 500°C). The reproducibility of our experiments was good as 16/16 in the conditions of 8 A triggering current and 9×10^4 Pa deuterium pressure. 300 MJ excess energy was obtained within 40 days, which was corresponding to the energy of 1.8×10^4 eV for each Pd atom. This is clear that gratitude was much higher than the energy for each Pd atom released in a chemical process. And on the surface of Pd after being triggered some new elements were found by SEM and EDS analysis. This phenomenon needs further studies and its origin might come from a nuclear transmutation process.

Acknowledgement

This work was financially supported by the Projects from Science and Technology Bureau of Changchun City (2009099), Jilin Provincial Science and Technology Department (20090541) and National Natural Science Foundation of China (21153003).

References

- [1] S. Focardi, V. Gabbani and V. Montalbano, Large excess heat production in Ni–H systems, *J. IL Nuovo Cimento* **A111** (1998) 1233–1242.
- [2] L. Mortensen, Rossi ECat To Breed Across USA, available online at: <http://ecatnews.com/?p=1160> /2011/10/30.
- [3] J. Tian et al., “Excess Heat” and “Heat after Death” in a gas-loading hydrogen/palladium system, *The 9th Int. Conf. On Cold Fusion, Condensed Matter Nuclear Science*, ICCF-9, 2002, Beijing, China, May 2002.
- [4] M. Macy, Defkalion Press Conference in Athens Introduces Rossi Energy Catalyzer, *Infinite Energy* **97** (2011) 3–5.
- [5] G. Levi and D. Bianchini, Report on heat production during preliminary tests on the Rossi “Ni–H” reactor, Bologna University, 2011.
- [6] D.J. Nagel, Potential advantages and impacts of LENR generators of thermal and electrical power and energy, *Infinite Energy* **103** (2012) 11–16.
- [7] L. Popa-Simil, Roadmap to fusion battery a novel type of nuclear battery and potential outcomes and applications, in *International Low Energy Nuclear Reactions Symposium*, ILENRS-12, 2012. The College of William and Mary, Williamsburg, VA 23185, USA.
- [8] J. Tian, X. Lu, L.H. Jin, B.J. Shen, L.Z. Zhu, X.L. Zhao, H.Y. Wang, X.H. Zheng and H.Y. Zhang, An excess heat phenomenon triggered by pressure in a H/Pd gas-loading system, *Adv. Materials Res.* **399–401** (2012) 1433–1438



Research Article

A Self-Consistent Iterative Calculation for the Two Species of Charged Bosons Related to the Nuclear Reactions in Solids

Ken-ichi Tsuchiya *

*Department of Chemical Science and Engineering, Tokyo National College of Technology (TNCT),
1220-2 Kunugida, Hachioji, Tokyo 193-0997, Japan*

Abstract

Many theoretical studies on cold fusion have been done by many workers using Bose–Einstein condensation (BEC) in order to find a possible mechanism of this phenomenon. In our previous work on BEC approach to the theoretical interpretation of cold fusion, we estimated the transition temperature of BEC in palladium deuteride [1]. It was based on the Y.E.Kim’s work by using equivalent linear two-body (ELTB) method to the many-body problems of charged bosons trapped in an ion trap [2]. Recently, Kim et al. tried to explain the results of Rossi’s experiment [3] by using the ELTB method for a mixture of different two species of positive charged bosons trapped to the harmonic potential [4]. In this study, we verified Kim’s theory and considered how to perform the numerical calculation. A self-consistent iterative calculation was introduced and the coupled two equations corresponding to the two species of positive charged bosons were solved.

© 2014 ISCMNS. All rights reserved. ISSN 2227-3123

Keywords: Bose–Einstein condensation, Cold fusion, Rossi’s experiment, Self-consistent method

1. Introduction

Here, we briefly introduce the theory of Kim et al [4]. In their theory, the Schrödinger equation for the mixture of two different species of positive charged bosons are written as

$$\left\{ -\frac{\hbar^2}{2m_i} \nabla^2 + V_i(\mathbf{r}) + W_i(\mathbf{r}) \right\} \psi_i(\mathbf{r}) = \mu_i \psi_i(\mathbf{r}), \quad (1)$$

where the two species are labeled by $i = 1, 2$. The first term on the left-hand side means the kinetic energy of the boson i and the second and third terms mean the following. The potential V_i means the harmonic potential induced by the electromagnetic ion trap. In the real lattice, it corresponds to the interaction between a boson and host metal ions. The potential W_i corresponds to the electro-static potential, which means the interaction between bosons. Therefore, W_i depends on the states ψ_i and ψ_j . The energy eigenvalue μ_i means chemical potential of the system.

*E-mail: tsuchiya@tokyo-ct.ac.jp

The solutions of Eq. (??) give the number densities of each boson, which means the probability density of the particle. They are written as

$$n_i(\mathbf{r}) = |\psi_i(\mathbf{r})|^2. \quad (2)$$

The normalized states should satisfy the volume integration of the number densities over the all space, which is written as

$$\int d\mathbf{r} n_i(\mathbf{r}) = N_i. \quad (3)$$

This means that the total number of the boson i is always N_i . We can normalize ψ_i by using Eq. (??).

On the other hand, it is well-known that the charge distributions in the system and the electro-static potentials should satisfy the Poisson's equation which is written as

$$\nabla^2 W_i(\mathbf{r}) = -\frac{e^2}{\varepsilon_0} Z_i \{Z_i n_i(\mathbf{r}) + Z_j n_j(\mathbf{r})\}, \quad (4)$$

where eZ_i is the charge of an ionized boson i and ε_0 means the dielectric constant of the vacuum.

Kim et al. have proposed the method in order to describe the states of the Bose–Einstein condensation (BEC) for the mixture of two different species of positive charged bosons by using Eqs. (1) and (4). They also emphasized the nuclear reactions in solids can be explained by using BEC, which can achieve the large overlap of the wave functions of charged bosons.

2. Self-consistent Solution

We can easily understand that Eqs. (1) and (4) for each boson are linked each other. For example, the states ψ_i and ψ_j are linked each other. The state ψ_i and the potential W_i are also linked each other. Therefore, we cannot obtain the solutions by simple method. In this study, we have tried to obtain the self-consistent solution of them by iterative substitutions.

Firstly, we introduce the Green's function for the well-known Helmholtz equation [5] ARFKEN which is written as

$$G_k(\mathbf{r}) = \frac{e^{-k|\mathbf{r}|}}{4\pi|\mathbf{r}|}, \quad (5)$$

where k is a positive real constant. This function satisfies the differential equation of

$$(\nabla^2 - k^2) G_k(\mathbf{r}) = -\delta(\mathbf{r}), \quad (6)$$

where $\delta(\mathbf{r})$ is the 3-dimensional Dirac's delta function. By using this Green's function, Eq. (??) is translated from the differential equation into the integral equation. As a result, it is rewritten in the form of the density functional formalism as

$$W_i(\mathbf{r}) = \int d\mathbf{r}' G_k(\mathbf{r} - \mathbf{r}') \times \left[\frac{e^2}{\varepsilon_0} Z_i \{Z_i n_i(\mathbf{r}') + Z_j n_j(\mathbf{r}')\} + k^2 W_i(\mathbf{r}') \right]. \quad (7)$$

This is a typical formula for the iterative substitutions. If we regard $W_i(\mathbf{r}')$, $n_i(\mathbf{r}')$ and $n_j(\mathbf{r}')$ on the right-hand side of Eq. (??) as old quantities, they will make new $W_i(\mathbf{r})$ on the left-hand side through the volume integration over the

all space. Fundamentally, the constants k in Eqs. (5)–(7) are arbitrary when they are positive and real, because the subtraction of $k^2 W_i(\mathbf{r})$ from both side of Eq. (??) leads to Eq. (??). When we solve Eq. (??) numerically, Runge–Kutta–Gill method is used for the calculation. Usually, we start the calculation from $r = 0$ and proceed it to large r . At the final region of these calculations, the errors are accumulated larger and larger. However, these errors included in the number density n_i and n_j are eliminated by the damping factor of the Green's function in Eq. (??).

If we consider the ground state of the system, n_i and W_i should have spherical symmetries. Then, we can easily calculate the angular components of the volume integration in Eq. (??) and it becomes the function of $r = |\mathbf{r}|$ as

$$W_i(r) = \frac{e^{-kr}}{kr} \int_0^r dr' r' \sinh(kr') F_i(r') + \frac{\sinh(kr)}{kr} \int_r^\infty dr' r' e^{-kr'} F_i(r'), \quad (8)$$

where the function F_i is defined as

$$F_i(r) = \frac{e^2}{\varepsilon_0} Z_i \{Z_i n_i(r) + Z_j n_j(r)\} + k^2 W_i(r). \quad (9)$$

The electro-static potential written in this formula has no divergence difficulties in the numerical calculations at the origin. The harmonic potential is also defined as

$$V_i(r) = \frac{1}{2} m_i \omega_i^2 r^2. \quad (10)$$

Using these potentials, the radial Schrödinger equation for s-like ground state is written as

$$\left\{ -\frac{\hbar^2}{2m_i} \frac{1}{r^2} \frac{d}{dr} \left(r^2 \frac{d}{dr} \right) + V_i(r) + W_i(r) \right\} \psi_i(r) = \mu_i \psi_i(r), \quad (11)$$

where the angular momentum term $l(l+1)\hbar^2/2m_i r^2$ is omitted because $l = 0$ for the ground state.

In order to begin the iterative calculations, we assumed the initial functions for the quantities on the right-hand side of Eq. (??) as

$$W_i(r') = 0 \quad (12)$$

and

$$n_i(r') = n_{0i} \theta(R_i - r'), \quad (13)$$

where the step function θ is defined as $\theta(x) = 1$ for $x > 0$ and $\theta(x) = 0$ for $x < 0$. The parameters n_{0i} and R_i in Eq. (??) should satisfy

$$\frac{4}{3} \pi R_i^3 n_{0i} = N_i. \quad (14)$$

This means that the initial boson distributions are uniform in the sphere of radius R_i neglecting the interaction between charged bosons. Starting from these assumptions, we can solve Eq. (??) numerically, and the first solutions give the normalized new densities by using Eqs. (2) and (3). These densities are used for obtaining the new W_i by solving Eq. (??). After that, new W_i is substituted into Eq. (??) again and the second wave functions are obtained. These procedures will be continued until the enough self-consistency is obtained. It is checked by seeing the stability of the energy eigenvalue. The flow chart for the self-consistent calculation is shown in Fig. 1.

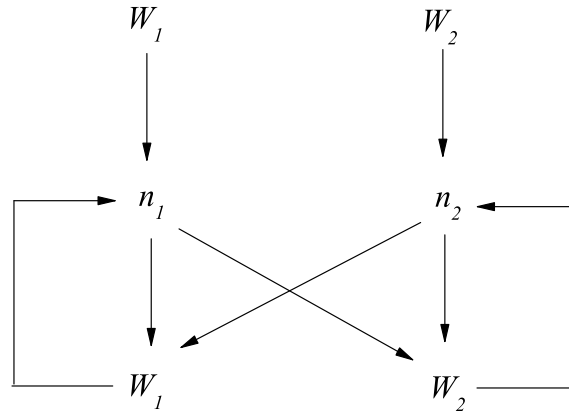


Figure 1. The flow chart for the self-consistent calculation. Using Eqs. (12)–(14), the initial function of W_i can be given by Eq. (7). The densities n_i and the electro-static potentials W_i are obtained alternatively by using Eqs. (1) and (7). The self-consistencies should be checked on the two loops in this diagram connected in parallel.

3. Units of the Calculations

We used the same unit with the pure harmonic problem. Here, they are explained briefly. It is well-known that the position r of a particle is translated into the non-dimensional quantity ξ_i by using

$$\xi_i = \alpha_i r, \quad (15)$$

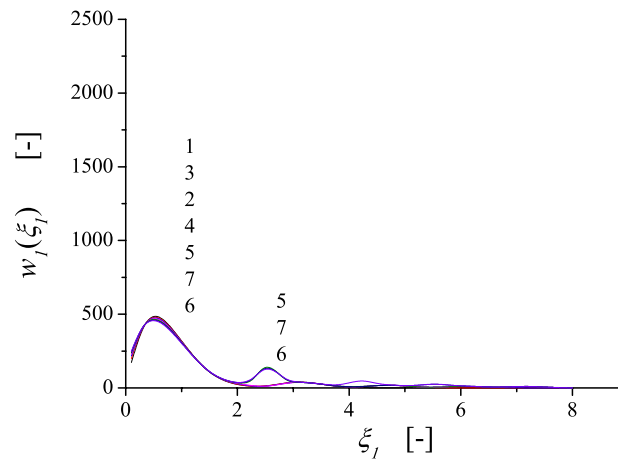


Figure 2. Change of the electro-static potential for D^+ along the iteration. The iteration numbers are also shown at the right sides of the first and second peaks. The array of them corresponds to the heights of the peaks.

where parameter α_i is given by

$$\alpha_i = \sqrt{\frac{m_i \omega_i}{\hbar}}. \quad (16)$$

In Eq. (??), the inverse of α_i corresponds to the classical turning point of a particle with energy $\hbar\omega_i/2$, which means the ground state energy of the quantum mechanical harmonic oscillator. Therefore, Eq. (??) means that ξ_i is the normalized position of the particle by the classical turning point. In Eq. (??), ω_i and m_i mean a frequency of the harmonic ion trap and mass of the particle, respectively. The chemical potential μ_i is also normalized by the ground state energy as

$$\varepsilon_i = \frac{2\mu_i}{\hbar\omega_i}. \quad (17)$$

By using these transformations, the radial Schrödinger equation is rewritten as

$$\left\{ -\frac{d^2}{d\xi_i^2} - \frac{2}{\xi_i} \frac{d}{d\xi_i} + \xi_i^2 + w_i(\xi_i) \right\} \psi_i(\xi_i) = \varepsilon_i \psi_i(\xi_i), \quad (18)$$

where w_i means the normalized electro-static potential. It is written as

$$w_i(\xi_i) = \frac{e^{-k_i \xi_i}}{k_i \xi_i} \int_0^{\xi_i} d\xi'_i \xi'_i \sinh(k_i \xi'_i) f_i(\xi'_i) + \frac{\sinh(k_i \xi_i)}{k_i \xi_i} \int_{\xi_i}^{\infty} d\xi'_i \xi'_i e^{-k_i \xi'_i} f_i(\xi'_i), \quad (19)$$

where function f_i is defined as

$$f_i(\xi_i) = C_i Z_i \left\{ Z_i n_i(\xi_i) + Z_j n_j \left(\frac{\alpha_j}{\alpha_i} \xi_i \right) \right\} + k_i^2 w_i(\xi_i). \quad (20)$$

In these equations, constants k_i and C_i are defined as

$$k_i = \frac{k}{\alpha_i} \quad (21)$$

and

$$C_i = \frac{2e^2}{\hbar\omega_i \alpha_i^2 \varepsilon_0}. \quad (22)$$

In Eq. (??), it should be noticed that ξ_i and $\xi_j = \frac{\alpha_j}{\alpha_i} \xi_i$ indicate a same point $r = \frac{\xi_i}{\alpha_i} = \frac{\xi_j}{\alpha_j}$ in the original coordinate. Therefore, the argument of n_j in Eq. (??) is not ξ_i but $\frac{\alpha_j}{\alpha_i} \xi_i$. This means that the function f_i is not identical with f_j for the case of $\alpha_j \neq \alpha_i$.

Furthermore, we can obtain simpler expression by using a new function $u_i(\xi_i)$, which is defined as

$$\xi_i \psi_i(\xi_i) = u_i(\xi_i). \quad (23)$$

The new expression is written as

$$\left\{ -\frac{d^2}{d\xi_i^2} + \xi_i^2 + w_i(\xi_i) \right\} u_i(\xi_i) = \varepsilon_i u_i(\xi_i). \quad (24)$$

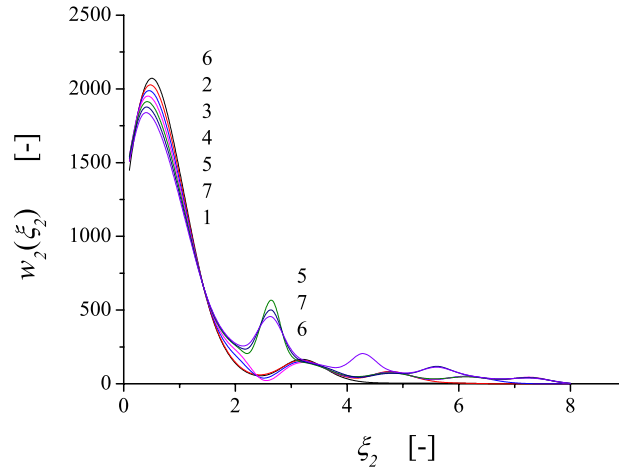


Figure 3. Change of the electro-static potential for ${}^6\text{Li}^+$ along the iteration. The iteration numbers are also shown at the right sides of the first and second peaks. The array of them corresponds to the heights of the peaks.

The relation between the solution of Eq. (??) and the number density is written as

$$n_i(\xi_i) = \left\{ \frac{u_i(\xi_i)}{\xi_i} \right\}^2. \quad (25)$$

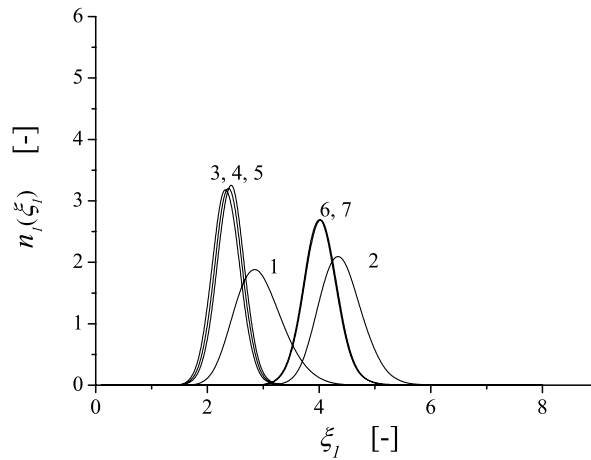


Figure 4. Change of the density for D^+ along the iteration. The iteration numbers are also shown in the figure.

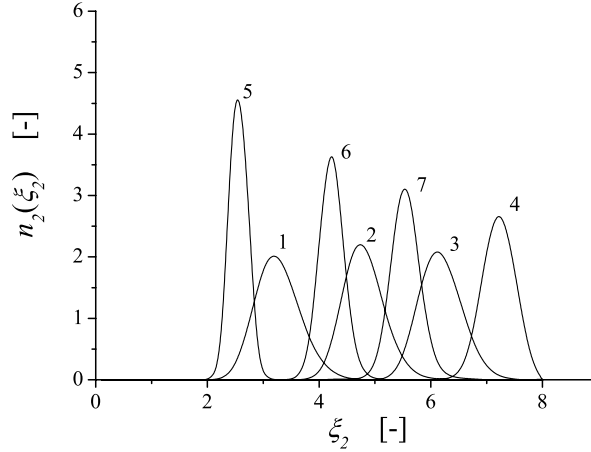


Figure 5. Change of the density for ${}^6\text{Li}^+$ along the iteration. The iteration numbers are also shown in the figure.

Therefore, the normalized solution of the new equation should satisfy

$$4\pi \int_0^\infty d\xi_i \{u_i(\xi_i)\}^2 = N_i. \quad (26)$$

In Eq. (??), the number density $n_i(\xi_i)$ for boson i is a non-dimensional function, because ξ_i is a dimensionless variable. If we need to know the number density in the original coordinate system, $\alpha_i^3 n_i(\alpha_i r)$ with a dimension of the reciprocal volume should be used.

The unperturbed eigenvalue of the ground state is $\varepsilon_i = 3$, because it is a radial component of a 3-dimensional problem. The unperturbed solution corresponding to $\varepsilon_i = 3$ is written as

$$u_i(\xi_i) = \xi_i H_0(\xi_i) e^{-\xi_i^2/2}, \quad (27)$$

where the function $H_0(x) = 1$ is the well-known Hermite polynomials in the 0th order [6]. At first, the eigenvalues for the perturbed system are unknown. However, we can find them by using the fact that Eq. (??) can be regarded as an asymptotic solution of the perturbed system for large ξ_i .

4. Results and Discussions

We have tried the calculations for $3\text{D}^+ + 3{}^6\text{Li}^+$ in an ion trap. In this case, D^+ and ${}^6\text{Li}^+$ are bosons, because they are composite particles with even number of fermions. For example, D^+ consists of a proton and a neutron, and ${}^6\text{Li}^+$ consists of three protons and three neutrons. The combinations of the positively charged two bosons and their numbers are arbitrary. However, we have chosen $3\text{D}^+ + 3{}^6\text{Li}^+$ case as a first step trial. The labels for D^+ and ${}^6\text{Li}^+$ are $i = 1$ and 2, respectively. In this study, $\omega_i = 4.79 \times 10^{14} \text{s}^{-1}$ is assumed for both particles. Using this frequency, the parameters α_i 's for $i = 1$ and 2 are 1.23×10^{11} and $2.14 \times 10^{11} \text{m}^{-1}$, respectively. And the parameters k_i 's for $i = 1$ and 2 are 29.1 and 16.8, respectively. For the initial density, we assume that $\alpha_i R_i$'s for $i = 1$ and 2 are 3.23 and 5.60, respectively.

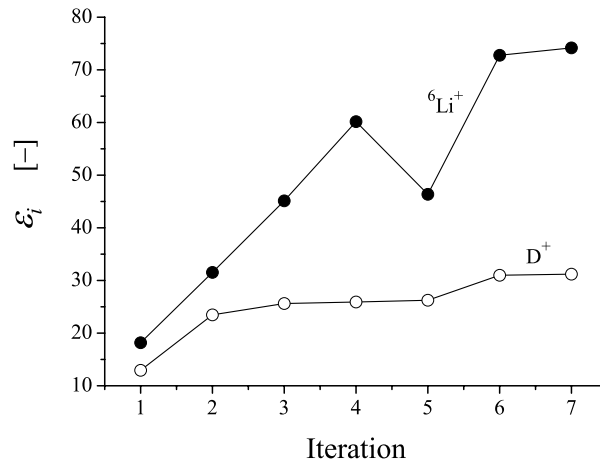


Figure 6. Energy eigenvalues for D^+ and ${}^6\text{Li}^+$ as a function of iterations.

Results for the electro-static potentials are plotted in Figs. 2 and 3. And results for the densities are plotted in Figs. 4 and 5. The check of self-consistency is done in Fig. 6. Seeing Figs. 2 and 3, the electro-static potentials are well converged. In both figures, changes of the first peaks are very small. And we can find the almost convergent second peak when the iteration is larger than 4.

On the other hand, seeing Figs. 4 and 5, the convergences are incomplete. In both figures, we can see the inversions of the gaussian-like peak positions. For example, the peak of n_2 suddenly shifts to the left after the 4th iteration in Fig. 5. The energy eigenvalue depression for ${}^6\text{Li}^+$ at the 5th iteration in Fig. 6 may cause the inversion in Fig. 5. However, the entire aspects of energy eigenvalue changes in Fig. 5 show the good convergences. If we continue the iteration, the inversion of the densities will appear again and again but gradually be smaller.

5. Conclusions

In this study, we have done the self-consistent iterative calculations for the two species of charged bosons. We have adopted $3\text{D}^+ + 3{}^6\text{Li}^+$ case for the mixtures of charged bosons and obtained the self-consistent densities. As a result, we have confirmed that 3D^+ and $3{}^6\text{Li}^+$ coexist at a time in an ion trap with $\omega_i = 4.79 \times 10^{14} \text{s}^{-1}$ for both particles.

In the next step, we will calculate the fusion rate by using Kim's theory [4]. The overlaps of the wave functions will make the finite value of fusion rates. In the near future, we will do it and report the results to some CF societies.

Acknowledgements

The author would like to thank Professor Y.E. Kim of Purdue University and Professor H. Yamada of Iwate University for helpful discussions and encouragements. The author also would like to thank students of TNCT for their fruitful collaborations. They are Mr. S. Asami, Mr. S. Kikuchi and Mr. O. Tamagawa.

References

- [1] K.Tsuchiya, Quantum states of deuterons in Pd, *Int. J. Hydrogen Energy* **29** (2004) 1513–1519.
- [2] Y.E. Kim and A.L. Zubarev, Nuclear fusion for bose nuclei confined in ion trap, *Fusion Technol.* **37** (2000) 151–156.
- [3] S. Focardi and A. Rossi, *A New Energy Source from Nuclear Fusion*, March 22, 2010, Ny Teknik.
- [4] Y.E. Kim and A.L. Zubarev, Mixtures of charged bosons confined in harmonic traps and Bose–Einstein condensation mechanism for low energy nuclear reactions and transmutation process in condensed matter, *Condensed Matter Nuclear Science, Proc. of ICCF11*, France, pp.711–717.
- [5] G. Arfken, *Mathematical Methods for Physicists*, the 3rd Edition, Section 16.6, Academic Press, New York.
- [6] L.I. Schiff, *Quantum Mechanics*, 3rd Edition, Section 4.13, McGraw-Hill, New York.



Research Article

Features and Giant Acceleration of “Warm” Nuclear Fusion at Interaction of Moving Molecular Ions (D-...-D)⁺ with the Surface of a Target

Vladimir I. Vysotskii*

Kiev National Shevchenko University, 64/13, Volodymyrska Street, City of Kyiv, Kiev 01601, Ukraine

Alla A. Kornilova and Vladimir S. Chernysh

Lomonosov Moscow State University, GSP-1, Leninskie Gory, Moscow 119991, Russian Federation

Abstract

The nuclear interaction mechanism and optimization methods of (dd) synthesis under bombardment of solid targets by linear oriented molecular ions consisting of a few deuterium atoms (nano-clusters) are discussed. Preliminary results on observation of optimized $d + d = \text{He}^3 + n$ reaction during collective interaction are presented.

© 2014 ISCMNS. All rights reserved. ISSN 2227-3123

Keywords: Moving nano-clusters, Correlated states, Neutron generation, Warm nuclear fusion

1. Introduction

The search for optimal systems to produce nuclear fusion effectively is one of most important problem in science today. About two decades ago the abnormally high yield of synthesis products (p, t and He^3) was observed experimentally under collisions of single charged cluster ions of heavy water $(\text{D}_2\text{O})_N$ with energy 0.12–6 keV/nucleus with TiD target. Every cluster consisted of a big group of identical molecules (e.g. D_2O) connected by hydrogen bonds.

It was found that the synthesis efficiency depended on the number of nuclei N in the clusters: $25 < N < 1300$ [1].

In the absence of D in cluster ions (i.e. at light water use $(\text{D}_2\text{O})_N \rightarrow (\text{H}_2\text{O})_N$) or when using targets formed on the basis of hydrogen ($\text{D} \rightarrow \text{H}$), the reaction products were not observed.

A mechanism leading to the enhanced yield was not revealed in [1]. However, it has been suggested in [2] that the anomalies can arise due to collisions between cluster components. Moreover, the environment surrounding moving cluster ions in a solid influences these collisions.

*E-mail: vivysotskii@gmail.com

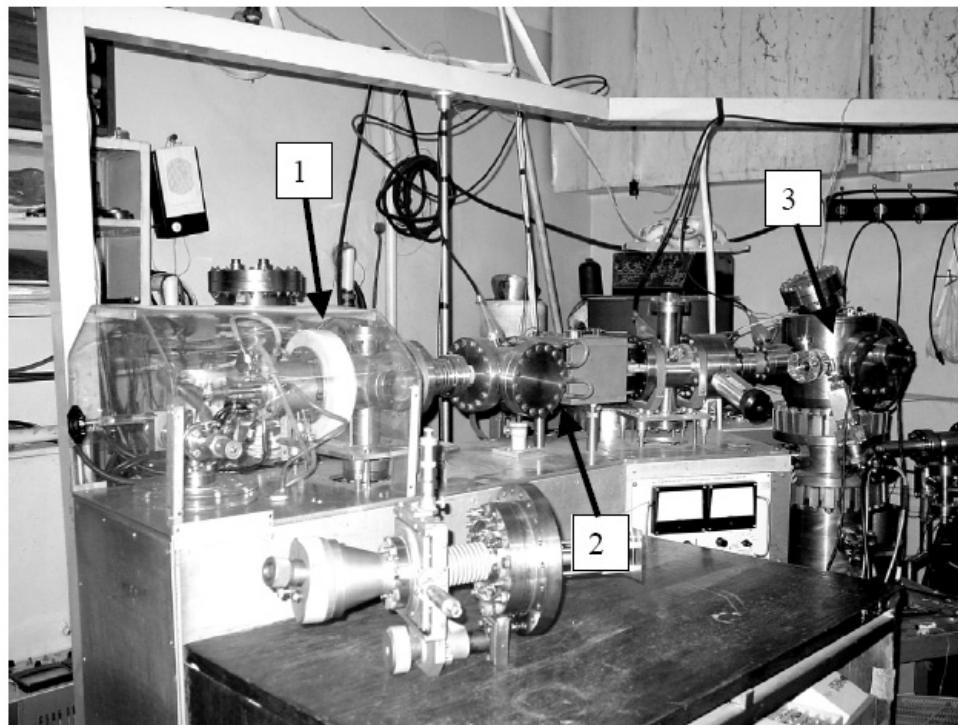


Figure 1. A general view of experimental installation.

Since a detailed dynamic calculation for a system with $N \gg 1$ is impossible, the main objective of the present work is to study mechanisms of this phenomenon for nano-clusters with $N = 2$ and 3.

In this report new experiments and theoretical models are discussed.

2. Experiments on Controlled Warm dd-fusion

Experiments were done with beams of accelerated molecular ions (D_2^+ and D_3^+ with energy 3.3 keV/nucleon) bombarding a stainless steel target. The analysis and calculation of processes in this system were carried out. The current of the ion beam was $J_D \leq 5 \mu A$, and the diameter of beam was about 2.5 mm.

These ions were formed at single ionization of gas molecules D_2 and D_3 in duoplasmatron (see Fig. 1).

A duoplasmatron ion source (Fig.1, item 1) of different atomic and molecular ions ($D^+ \equiv d$, D_2^+ and D_3^+) with the system of magnetic separation (Fig. 1, and item 2) was used.

A Duoplasmatron is a gas-fed source of light ions capable of producing positive or negative ion beams. The working principle is based on a two-stage discharge.

The target made of stainless steel and mounted in UHV chamber (Fig.1, item 3) and bombarded with the mass separated ion beam along the surface normal.

A background pressure in the target chamber was 2×10^{-6} Pa, while the density of the ion beam current was 0.2–0.3 mA/cm². The monochromaticity of a beam was about $\Delta E/E \approx 10^{-4}$.

A large aperture neutron detector was placed behind glass window of the vacuum chamber (Fig. 1, item 3).

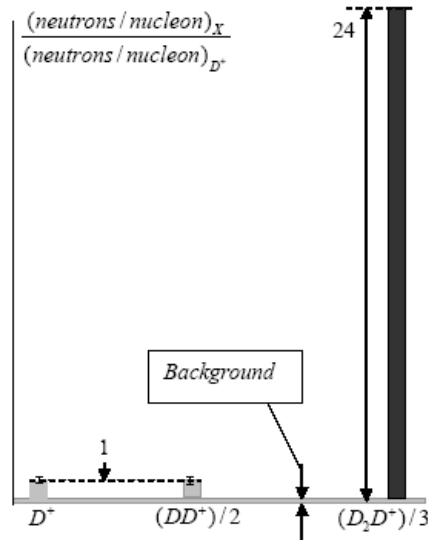


Figure 2. Effectiveness of dd-fusion with neutron generation for different accelerated nano-clusters $D^+ \equiv d, D_2^+ \text{ or } D_3^+$ with the same specific energy 3.3 keV/nucleon.

In preliminary experiments to investigate the reaction

$$d + d \rightarrow \text{He}^3 + n + \Delta E_{d+d},$$

$$\sigma_{d+d} \approx 0.09 \text{ bn} \approx 10^{-25} \text{ cm}^2 \quad \text{at } E \approx 100 \text{ keV}, \quad \Delta E_{d+d} \approx 4 \text{ MeV},$$

it was found that the neutron yield (neutron/nucleon) increased more than an order (typically by 20–25 times) under transition from bombardment by D_2^+ (and $D_1^+ \equiv d$) ions to D_3^+ ions (see Fig.2). All these additional fast neutrons were connected with dd-reaction. and are essentially the result of an increase the fusion efficiency.

It was shown during preliminary analysis that the yield increase of nano-cluster dd-fusion can be connected with:

- (1) cumulative effects at cluster component collisions in a target;
- (2) satisfaction of the conditions of coherent correlated states formation [3–9] in nano-cluster volume (in potential well formed for atom 2 by atoms 1 and 3 (see Fig. 3).

Our analysis shows that the formation of coherent correlated particle states is a very efficient method of significantly suppressing the action of the Coulomb potential barrier during pair interactions of charged particles (including the nuclear dd-fusion problem and other nuclear reactions). This method provides a great increase of sub-barrier transparency (by $10^{40} - 10^{100}$ and more times). The formation of coherent correlated states in charged moving oriented $(D-D-D)^+$ clusters may be connected with periodical or monotonous modulation of interatomic distance during acceleration in duoplasmatron or deceleration on the target surface. The detailed description of such processes at different types of modulation of potential wells is presented in [3–9].

On the other hand in the $(D-D)^+$ molecular ion this effect is absent.

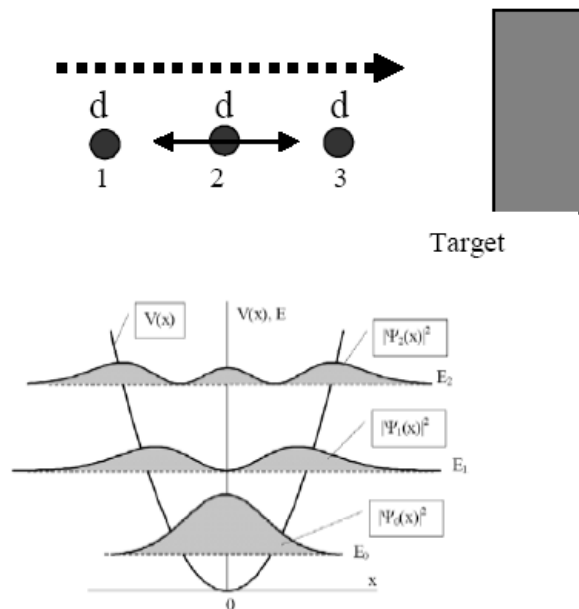


Figure 3. Principle of formation of correlated states of interacting deuterons in moving D3+ nano-cluster.

3. Summary

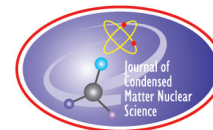
Our method of optimization of medium-scale energy (“warm” energy) accelerating synthesis at rather small nano-cluster energy can be used to optimize neutron generators to increase the neutron release from dd-reactions. The typical efficiency of a neutron source on the basis of dd-reaction with a fixed target (e.g. LiD crystal) and accelerated nucleus does not exceed $\eta \approx 10^{-7} - 10^{-10}$ (created neutrons/one accelerated nucleus) for fast and medium energy particles. The increase in this efficiency leads to an increase in the neutron flux.

References

- [1] R.J.Beuler, G. Fridlander and L. Friedman, *Phys. Rev. Lett.* **63** (1989) 1289.
- [2] V.B. Leonas, The new approach to realization of d–d-fusion reactions, *Soviet Phys.-Uspekhi* **160**(11) (1990) 135–141.
- [3] V.I. Vysotskii and S.V.Adamenko, Correlated states of interacting particles and problems of the coulomb barrier transparency at low energies in nonstationary systems, *Technical Phys.* **55**(5) (2010) 613–621.
- [4] V.I. Vysotskii and S.V.Adamenko, Low energy subbarrier correlated nuclear fusion in dynamical systems, *J. Cond. Mat. Nucl. Sci.* **8** (2012) 91–104.
- [5] V.I. Vysotskii, M.V. Vysotskyy and S.V. Adamenko, Formation and application of correlated states in nonstationary systems at low energies of interacting particles, *J. Exp. Theoret. Phys.* **114**(2) (2012) 243–252.
- [6] V.I. Vysotskii, M.V. Vysotskyy and S.V. Adamenko, The formation of correlated states and the increase in barrier transparency at a low particle energy in nonstationary systems with damping and fluctuations, *J. Exp. Theoret. Phys.* **115**(4) (2012) 551–566.
- [7] V.I. Vysotskii and M.V.Vysotskyy, Coherent correlated states and low-energy nuclear reactions in non stationary systems, *Euro. Phy. J. A* **49**(8) (2013): 99 DOI 10.1140/epja/i2013-13099-2.
- [8] V.I.Vysotskii, S.V.Adamenko and M.V.Vysotskyy, Acceleration of low energy nuclear reactions by formation of correlated states

of interacting particles in dynamical systems, *Ann. Nucl. Energy* **62** (2013) 618–625.

- [9] V.I.Vysotskii and M.V.Vysotsky, Application of coherent correlated states of interacting particles in non-stationary controlled LENR, *Infinite Energy* **112** (2013) 71–76.



Research Article

Stimulated ($B^{11}p$) LENR and Emission of Nuclear Particles in Hydroborates in the Region of Phase Transfer Point

Vladimir I. Vysotskii*

Kiev National Shevchenko University, 64/13, Volodymyrska Street, City of Kyiv, Kiev 01601, Ukraine

Alla A. Kornilova, Vladimir S. Chernysh,
Nadezhda D. Gavrilova and Alexander M. Lotonov

Lomonosov Moscow State University, GSP-1, Leninskie Gory, Moscow 119991, Russian Federation

Abstract

In this work, we consider the characteristics of proton (hydrogen) processes that take place in a special class of crystals (hydroborates), linked to the task of isolating and separating hydrogen and nuclear fusion with the participation of hydrogen. Preliminary results on observation of stimulated $B^{11} + p = He^4 + \Delta E$ reaction in hydroborates are presented.

© 2014 ISCMNS. All rights reserved. ISSN 2227-3123

Keywords: LENR, Hydroborates, Nuclear fusion

1. Introduction

The search of optimal systems for effective implementation of low energy nuclear fusion (LENR) is one of most important problems in this field. One of the most interesting systems for this is hydroborates. Interest in hydroborates is connected to the large quantity of hydrogen bonds and water molecules in these structures. In the process of heating crystals, the hydrogen bonds break and it is possible to release molecular water and also a large number of protons in the process of decomposition. Such processes have been observed in natural borates, from room temperature up to the temperature of full break-down of the crystal.

Practically, hydroborates can be donors of free hydrogen just as metal are donors of free electrons. The typical concentration of protons in hydroborates is about $n_p \approx 10^{22} \text{ cm}^{-3}$. One more reason for the big interest in hydroborates is connected to how their composition ideally corresponds to the precondition for producing the synthesis reaction with the formation of helium nuclei. One more doubtless advantage of hydroborates is the following – they are stable natural

*E-mail: vivysotskii@gmail.com

materials and contained in a giant quantity in earth's crust. These crystals may play an essential role in natural power of the Earth and may be one of the essential sources of natural thermal energy!

2. Physical and Electrodynamical Properties of Reality of Hydroborates

The general scheme of the behavior of hydroborate gratings during phase transfer come down to the following stages:

- The loss of absorbed water and water, filling the pores in the crystal (this process is observed during the heating of crystals up to 100°C – 120°C).
- Transformation of part of the OH[−] of the group in H₂O.
- Decay of H₂O and its connection to borate anions and then “exiting” the framework of all the water.

As a result of a process of dehydration, a change takes place in the structure: a less hydrated structure forms as a result of the loss of crystallized water. In these processes, a large quantity forms of quasi-free hydrogen in the grating (strong proton conductivity appears).

In the course of doing this work the following research was conducted.

- **Differential scanning calometry (DSC)** is a method used for registering heat flow, which characterizes the changes taking place in a substance as a result of heating or cooling. The sample and the standard are both heated or cooled at identical speeds, and their temperatures are kept the same. Experimental curves show the dependence of heat flow on temperature.
- **Thermo-gravimetric analysis (TGA)** is a method of thermal analysis which registers the change of sample mass depending on temperature.
- Gaseous products are analyzed with **Fourier infrared spectroscopy (FIRS)**.
- Researching the **dielectric and conducting properties** of hydroborates.

The results of conducted investigation of physical properties of different hydroborates are presented in Figs. 1–4.

For single crystals of colemanite a temperature–frequency dependence was obtained for dielectric permittivity. The analysis of this dependence leads to the following conclusions.

Practically all types of natural hydroborates show phase transfer and sporadic changes of conductivity, which is connected with the remolding of the structure of the crystals. The temperature of these phase transfer lies at a very low interval. For example, in *colemanite* the phase transfer corresponds to the temperature of 0°C; or in *interboride*, at 40°C and 100°C; and in *Ulexite*, at 40°C and 80°C. These anomalies are observed only at very low frequencies (indicating proton conductivity!).

3. Preliminary Research into Processes of Stimulated Nuclear Fusion in Hydroborates in the Neighborhood of Phase Transfer Point

The dependencies, obtained above, which determine the properties of hydroborates all over the interval of temperatures and frequencies under study, enable us to pose a question about the possibility of producing nuclear fusion in such crystals. We base this statement about the experiment on the following. It is well known that one of the most attractive nuclear reactions



is characterized by a large release of energy $\Delta E = 8.7 \text{ MeV}$ and by the nearly complete absence of induced radioactivity. In ordinary conditions of a paired collision of free nuclei, this reaction has a maximal cross-section under relative energy

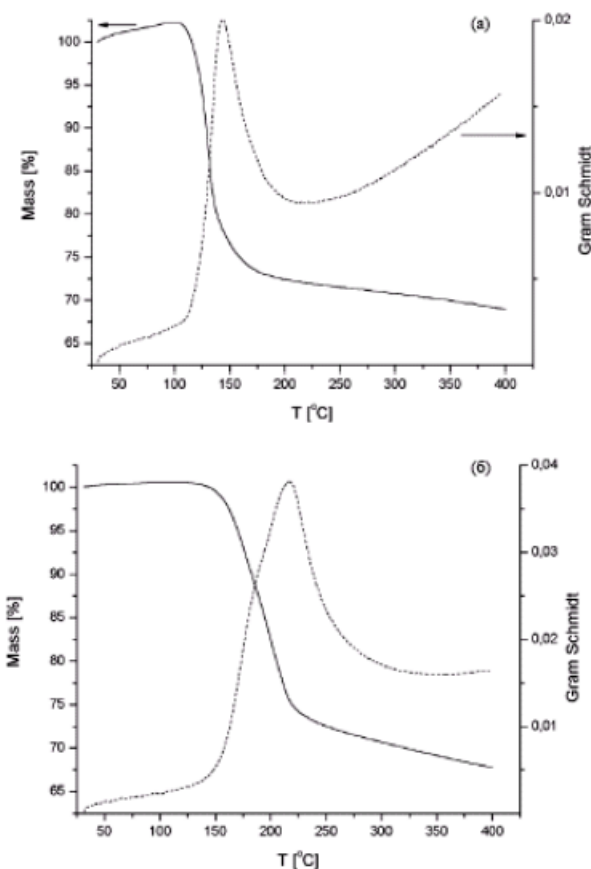


Figure 1. TGA (Thermo-gravimetric analysis) analysis for *interboride* (top) and *ulexite* (bottom).

of colliding particles $T_{pB^{11}} = 675$ keV. This is large energy and usually, to obtain it, highly precise ionic accelerators are needed.

However, in cases when the interacting particles are located in non-stationary microcavities and in the volume of non-standard crystals (crystals which are in the stage of transition processes like phase transfer) the fusion process may occur even at low energy of relative motion. Such processes were observed in, for example, deuterated crystals like *KDP* crystal during phase transfer, when the local deformation of crystalline grating led to a stable and recurrent generation of a small number of neutrons by the formula



In the hydroborate crystals under consideration there are all the prerequisites for realizing the reaction for the synthesis of $He^4(1)$ (quasi-free hydrogen in a state with large mobility; the boron ions, representing local targets and variable local conditions (the presence of phase transfers and local high pressure)).

The presence of phase transfers at different temperatures is very important and may be used for safe auto-control of LENR with negative temperature feedback. Practically all types of natural hydroborates show phase transfer and

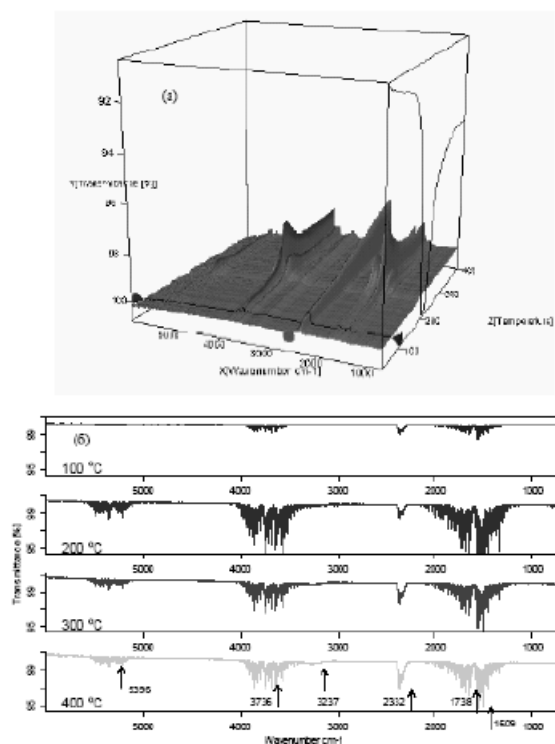


Figure 2. IR absorption for *interboride*.

spasmodic change of conductivity, which is connected with the re-moulding of the structure of crystals.

The mechanism of suppression of the Coulomb barrier to nuclear reactions in such crystals is, most probably, connected with the process of formation of correlated states in continuously changing potentials holes during phase transfer [1–3].

The temperature of these phase transfers occurs at very low temperature change. For example, in *colemanite* the phase transfer corresponds to the temperature of 0°C; in *interboride* at 40°C and 100°C; in *ulexite* at 40°C and 80°C. These anomalies are observed only at very low frequencies. This is the result of proton conductivity in hydroborate crystals! For convenience, the research conducted is adduced below with the use of more “burning” phase transfer for which it is necessary to heat the sample of hydroborate to temperatures exceeding 100°C. At the beginning of this cycle of measurements a calibration of the measuring device was done. In Fig. 5 the calibration spectrum is presented for an alpha-particle source of the isotope Pu^{239} with maximal energy of about 5.2 MeV.

The unit of scale division was calculated by formula $5.2 \text{ MeV}/N_{\text{max}}$. The initial experiments on controlled (B^{11}p)LENR were conducted in the following way. A fresh single crystal of hydroborate was placed directly on an alpha-particle sensor. To heat the local temperature to the point of phase transfer, the sample was touched by the tip of a soldering iron. To eliminate interference, the soldering iron was first heated, and then unplugged from the electric power mains. On heating the samples, a light crackling noise was heard. The samples at the point of contact with the heater became opaque and turned a milky white color. These phenomena are explained by how in the process of gradient heating used in our experiments, internal tensions arise in the crystal followed by cracking of the samples. For

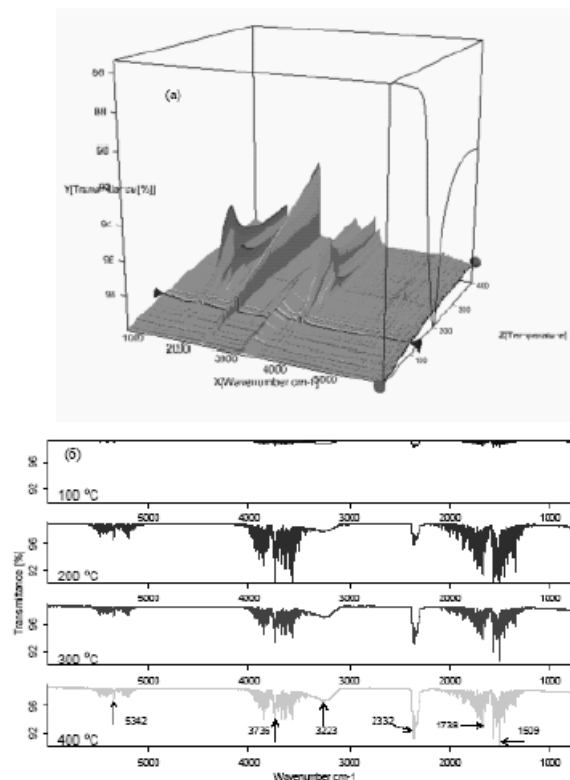


Figure 3. IR absorption for *ulexite*.

each sample, several trials were conducted. For each separate measurement a fresh crystal was used.

In Fig. 6, the data from measurements of alpha-particles emission from different crystals of hydroborates are presented.

For the *ulexite* crystal (Fig. 6, top) in the course of 10 s a signal was observed in the region of 200–210 channels on the lower scale. The signals in the neighborhood of the 60th channel are a hindrance which can be eliminated by weakening the sensitivity of the amplifier. The calculation by the above formula gives, for channels 200–210, a value of energy particles of about 60.6 keV. That emission of particles, which was observed in the course of the initial phase of heating, testifies to how nuclear transformation occurs during phase transfer caused by heating.

In Fig. 6 (bottom), experimental results are given for *inderborite* crystal. Together with the parasitic noise signal lower than the 50th channel, there are also individual pulses in the region of channels 100–130. These signals were detected in the first ten seconds after the start of heating. The calculated value of energy turns out to be 29.5 keV in the neighborhood of the 125th channel.

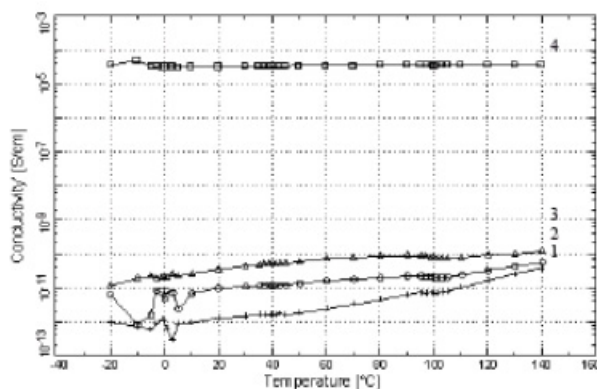


Figure 4. Temperature dependence of conductivity of *colemanite* at frequencies of 1-0,1; 2-1;3-10;4-10-7 Hz .

4. Summary

The adduced data indicate how in the crystal of hydroborates, nuclear reactions of synthesis can take place. Of course, the preliminary results do not enable one to conclude that these reactions are effective. Also unknown is the spatial location deep within the crystal, where the fusion conditions are fulfilled. Obviously, these reactions occurred at a relatively great depth, which led to the low energy of the emitted alpha-particles.

We plan to conduct these investigations with controlled contactless heating of the sample with step-by step research throughout the whole temperature range. In the course of carrying out this work, we also considered methods and perspectives on fusion in synthetic borates.

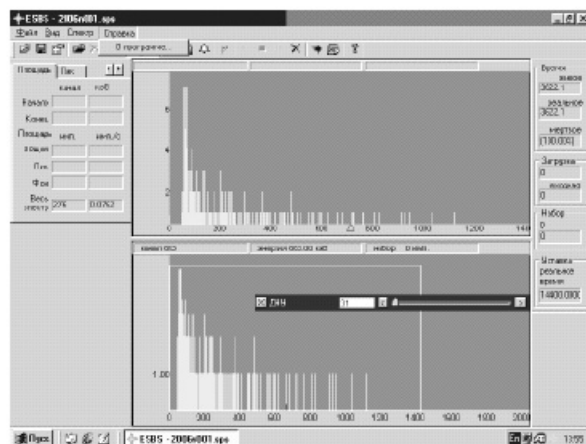


Figure 5. Calibration spectrum of alpha-particles source with the use of isotope Pu^{239} .



Figure 6. Registration of alpha-particles, flying out in the course of a local heating from crystals of *ulexite* (top) and *inderborate* (bottom).

References

- [1] V.I. Vysotskii, M.V. Vysotskyy and S.V. Adamenko, Formation and application of correlated states in nonstationary systems at low energies of interacting particles, *J. Exp. Theoret. Phys.* **114**(2) (2012) 243–252.
- [2] V.I. Vysotskii and S.V. Adamenko, Correlated states of interacting particles and problems of the coulomb barrier transparency at low energies in nonstationary systems, *Technical Phys.* **55**(5) (2010) 613–621.
- [3] V.I. Vysotskii and S.V. Adamenko, Low energy subbarrier correlated nuclear fusion in dynamical systems, *J. Cond. Matter Nucl. Sci.* **8** (2012) 91–104.



Research Article

On Problems of Widom–Larsen Theory Applicability to Analysis and Explanation of Rossi Experiments

Vladimir Vysotskii *

Kiev National Shevchenko University, Kiev, Ukraine

Abstract

The effectiveness and possibility of application of Widom–Larsen (W–L) theory for explanation of Rossi experiments on stimulation of (p, Ni^A) low-energy nuclear reactions (LENR) is analyzed. The carried out analysis has shown that W–L theory, which is connected with the inverse reaction of beta-decay in variable electric field of surface plasmon in metal hydride, is unsuitable for the description and explanation of Rossi experiments in metal hydrides.

© 2014 ISCMNS. All rights reserved. ISSN 2227-3123

Keywords: Inverse beta-decay, LENR, Ponderomotive force, Rossi experiments, Widom–Larsen theory

1. Introduction

Theoretical explanation of important Rossi–Focardi (R–F) experiments (e.g. [1,2]) is usually associated with Widom–Larsen (W–L) theory (see [3–8]).

The general scenario of such theory includes three consecutive steps.

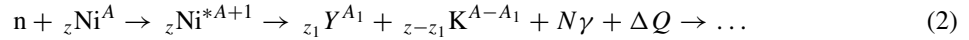
- Process of increase of electron mass with $\Delta m_e > 0$ by “dressed up” effect and formation of slow heavy electrons by ponderomotive nonlinear action of variable electric field of surface plasmon;
- Transformations of protons, which are situated in the form of monoatomic hydrogen layer on Ni surface, into slow neutrons in inverse reaction of beta-decay

$$\begin{aligned} \tilde{e}^- + p &\rightarrow n + \nu, & \tilde{m}_e &\equiv m_e + \Delta E/c^2, \\ \Delta E &= \Delta m_e c^2 > |Q_{e-p}|, & Q_{e-p} &\approx -0.78 \text{ MeV} \end{aligned} \quad (1)$$

with the help of “dressed up” heavy electrons. For realization of such reaction the variable electric field $|E(\vec{r}, t)|_{\max} \geq |E(\vec{r}, t)|_{\text{thresh}} \approx 3 \times 10^{10} \text{ V/cm}$ is needed [1,2].

*E-mail: vivysotskii@gmail.com

- Immediate absorption of these slow neutrons in a matrix and stimulations of nonbarrier nuclear reactions



The main questions are the following: are the process of stimulated inverse beta-decay reaction in metal hydrides like Ni + H possible (a) and efficient enough (b)?

The general idea of such method is very attractive. Its ideological part is close to well-known process of inverse beta-decay reaction



which takes place during the neutronization process that is stimulated by gravitational collapse of stars with masses $M > 1.45M_\odot$ and leads to the formation of neutron stars (M_\odot is the mass of the Sun). This process is connected with the increase of Fermi energy

$$W_F \equiv (3\pi^2)^{1/3} \hbar c n_e^{1/3} \geq (M_{(A,Z-1)} - M_{(A,Z)} - m_e)c^2 \quad (4)$$

of relativistic degenerate electron gas with electron number density

$$n_e \geq m_e^3 c^3 / 3\pi^2 \hbar^3 \approx 10^{30} \text{ cm}^{-3}$$

during gravitational collapse.

Both processes (W–L process and process of astrophysical neutronization (AN)) are connected with the increase of electron energy but in different ways:

- AN process is connected with the formation of relativistic electrons with great momentum

$$p_e = \sqrt{\gamma^2 - 1} m_e c \geq m_e c$$

and great relativistic energy

$$W_e = \gamma m_e c^2 \quad (5a)$$

- predicted W–L process is connected with the formation of fixed or slow “dressed up” heavy electrons with low momentum $p_e \ll m_e c$, great renormalized mass and great energy

$$W_e = \tilde{m}_e c^2. \quad (5b)$$

AN process is real and plays very important role in the evolution of the Universe. Reality of W–L process in R–F experiments will be discussed below.

2. Reality of W–L Process in Rossi Experiments

2.1. Influence of electron motion on electric field of surface plasmon of metal hydride

In works [3,4] it was supposed that surface electrons of metal hydride are under the influence of strong variable electric field

$$\vec{E}(\vec{r}, t) = \vec{E}_0(\vec{r}) \cos \Omega t \quad (6)$$

with intensity

$$\left\langle \left| \vec{E}_0^{(\max)} \right| \right\rangle \approx en_p^{2/3} \approx 10^{10} \text{ V/cm}$$

and frequency $\Omega = \omega_p \approx 10^{13} \text{ s}^{-1}$, generated by plasma fluctuations of ions with concentration n_p .

From the other hand it is implicitly supposed that these electrons do not react the field $\vec{E}(\vec{r}, t)$, do not change own (electron) state of motion under the influence of the field $\vec{E}(\vec{r}, t)$ and do not influence this field. It means that authors of [3,4] have used the assumption of a invariance of electron state at periodical oscillations of surface nuclei (protons) near the equilibrium position.

According to the general concepts of quantum mechanics and quantum statistics such assumption corresponds to the condition of ideality of degenerated electron gas, when average kinetic electron energy \bar{T}_e exceeds greatly the average potential energy $|\bar{V}_e|$.

On the other hand in the same work [4] (see Eq. (24)) the following expression for electron density was used:

$$n_e = 1/\pi a^3 \approx 3 \times 10^{23} \text{ cm}^{-3},$$

which corresponds to the opposite condition $\bar{T}_e < |\bar{V}_e|$. More exact analysis based on *Virial theorem* shows that in atom of hydrogen the similar opposite condition $\bar{T}_e = 0.5|\bar{V}_e|$ takes place.

At the breaking of the condition of electron gas ideality the situation cardinally changes in comparison with assumptions used in [3,4]. In this case electrons (as easier particles) move much faster then protons and immediately react to the breaking of both local charge equilibrium and formation of additional local electric field $\vec{E}(\vec{r}, t)$ during plasma oscillation. Motion of electrons leads to the adiabatic compensation of electric field $\vec{E}(\vec{r}, t)$ connected with the motion of protons. From the plasma theory follows that any local nonequilibrium in plasma exists for no more than the period $T_e = 2\pi/\omega_e$ of electron plasma frequency

$$\omega_e = \sqrt{4\pi n_e e^2 / m_e}. \quad (7a)$$

In metals $T_e \approx (1-3) \times 10^{-16} \text{ s}$ that is by 100–1000 times less then the period of heavy ion (proton) plasma frequency

$$\omega_p = \sqrt{4\pi n_p e^2 / M_p}. \quad (7b)$$

The same effect takes place for surface plasmon oscillations. At such relation of T_e and T_p all electrons in plasma and in metals always follow protons and movement of protons is be close to adiabatic.

Hence, actual electric field in the volume of ionic surface plasmon is by many orders (in $\omega_e/\omega_p \gg 1$ times) less then the value $\left\langle \left| \vec{E}_0^{(\max)} \right| \right\rangle \approx en_p^{2/3} \approx 10^{10} \text{ V/cm}$ predicted in [3,4].

Another approach also shows that this electric field is much lower then the predicted value $\langle |\vec{E}_0^{(\max)}| \rangle \approx 10^{10} \text{ V/cm}$, which is based on the analysis of the method of $E_0^{(\max)}$ calculation used in [4].

In this work the main model was connected with proton embedded in a sphere with a mean electronic charge density $\rho_e = -en$. It is standard Wigner–Zetitz cell. If the proton suffers a small displacement u then an electric field $\vec{E}(\vec{r})$ will appear (see [4], Eq. (22))

$$\text{div } \vec{E}(\vec{r}) = 4\pi\rho_e, \quad E(r) = -\frac{4\pi}{3}enr, \quad \vec{r} \equiv \vec{u}. \quad (8)$$

The strength of the mean electric field in [4]

$$|E(u)| = \frac{4e}{3a^3}u = E_{\text{atom}}(a) \left(\frac{4}{3} \right) \frac{u}{a}, \quad E_{\text{atom}}(a) = e/a^2 \approx 5.1 \times 10^9 \text{ V/cm} \quad (9)$$

was estimated by taking the mean electron number density at the position of the proton (see [4], Eqs. (24) and (26))

$$n(r=0) = |\Psi_{1s}(0)|^2 = 1/\pi a^3,$$

$$a \equiv r_B = \frac{\hbar^2}{m_e e^2} = 5.3 \times 10^{-9} \text{ cm.} \quad (10)$$

The next calculation of electric field was conducted in [4] basing on these formulas. From neutrons scattering experiments on palladium hydride follows that the amplitude of collective proton oscillations on palladium surface equals $\bar{u}_p \approx 2.2 \text{ \AA}$ [4]. At such value \bar{u}_p the mean electric field was estimated through Eq. (??) (see [4], Eq. (26)) and equals (see also [4], Eq. (27))

$$|E(r = \bar{u}_p)| = E_{\text{atomic}}(a) \left(\frac{4}{3}\right) \frac{\bar{u}_p}{a} \approx 2.9 \times 10^{10} \text{ V/cm.} \quad (11)$$

It is incorrect estimation! The expression (??) is correct only for very small displacements $u \ll a$ and at $\bar{u}_p \ll a$ (see expression for $n(r=0)$ in (??))! If $\bar{u}_p > a$, we need to use the correct (screened) expression for mean electron number density at the position of the proton

$$|E(r \approx \bar{u}_p)| = -\frac{4\pi}{3} e r |\Psi_{1s}(r)|^2 \Big|_{\bar{u}_p} = -\frac{4e}{3a^3} \bar{u}_p e^{-2\bar{u}_p/\Lambda} = -E_{\text{atomic}}(a) \left(\frac{4}{3}\right) \frac{\bar{u}_p}{a} e^{-2\bar{u}_p/\Lambda}. \quad (12)$$

Here Λ is a radius of electron screening:

$$\Lambda_B = \hbar^2/m_e e^2 = 0.53 \text{ \AA} \quad (\text{for atom}),$$

$$\Lambda_D = \sqrt{kT/4\pi\bar{n}e^2} \quad (\text{for classical electron gas}), \quad (13)$$

$$\Lambda_{\text{TF}} = \sqrt{\varepsilon_F/3\pi\bar{n}e^2} \quad (\text{for degenerate electron gas}).$$

In all metals (including Ni) $kT > \varepsilon_F$ and $\Lambda = \Lambda_{\text{TF}} \approx 0.6 \text{ \AA}$. At such parameters we have $|E(r \approx \bar{u}_p)| \approx 2 \times 10^7 \text{ V/cm}$ that is too low for the formation of heavy “dressed” electrons needed for inverse reaction of beta-decay (1).

2.2. Analysis of the action of variable nonuniform electric field of surface plasmon on electrons

According to the date of [3,4] the energy of ponderomotive interaction of electric field

$$\vec{E}(\vec{r}, t) = \frac{1}{c} \frac{\partial \vec{A}(\vec{r}, t)}{\partial t} = (\Omega/c) \vec{A}_0(\vec{r}) \cos \Omega t \equiv \vec{E}_0(\vec{r}) \cos \Omega t \quad (14)$$

(generated by plasma oscillation of protons situated on metal surface) with electron

$$W_{\text{pond}}(\vec{r}, t) = \sqrt{m_e^2 c^4 + e^2 c^2 |\vec{E}(\vec{r}, t)|^2 / \Omega^2} - m_e c^2 \quad (15)$$

is much greater then the binding energy

$$W_{\text{coulomb}} = -Ze^2 e^{-r/a} / r \quad (16)$$

of electron with nucleus and equals

$$W_{\text{pond}}^{(\text{max})} \approx 1 \text{ MeV.}$$

Action of spatially nonuniform periodic ponderomotive force on electrons

$$\vec{F}_{\text{pond}}(\vec{r}, t) = -\nabla W_{\text{pond}}(\vec{r}, t) = -\frac{(ec/\Omega)^2 \nabla |\vec{E}(\vec{r}, t)|^2}{2\sqrt{m_e^2 c^4 + e^2 c^2 |\vec{E}(\vec{r}, t)|^2 / \Omega^2}}, \quad (17)$$

which is synchronised with variable electric field $\vec{E}(\vec{r}, t)$, leads to their acceleration and expulsion from the area of increasing field. Such effect is used at the formation of a bunch of relativistic electrons with energy $T_e \geq 100 \text{ MeV}$ at the action of femtosecond laser pulse on a solid-state matrix. In this case the increase of electron energy $W_e = \gamma m_e c^2$ is connected with the increase of relativistic momentum

$$p_e = \sqrt{\gamma^2 - 1} m_e c$$

instead of formation of “dressed up” electron with $W_e = \tilde{m}_e c^2$ and low momentum $p_e \ll m_e c$.

The alternative effect of increase of effective mass of this electron $m_e \rightarrow \tilde{m}_e$ without acceleration (without increase of electron momentum) at ponderomotive nonlinear interaction with electric field (effect of “dressed up” electron) is possible only in the case of completely spatial-homogeneous variable field $\vec{E}(\vec{r}, t) \equiv \vec{E}(t)$, when there is no pushing out force and

$$\vec{F}_{\text{pond}} \sim \nabla |\vec{E}(\vec{r}, t)|^2 \equiv 0. \quad (18)$$

However in considered model of surface plasmon the field

$$\vec{E}(\vec{r}, t) \approx \vec{e}_x E_0 e^{-x/l} \cos \Omega t, \quad l \approx n_p^{1/3} \quad (19)$$

is extremely nonuniform and localized in very thin surface layer (see Fig. 1).

Hence, the main result of ponderomotive action of strong nonuniform variable electric field $\vec{E}(\vec{r}, t)$ of surface plasmon is the acceleration of both free conduction electrons and coupled atom electrons.

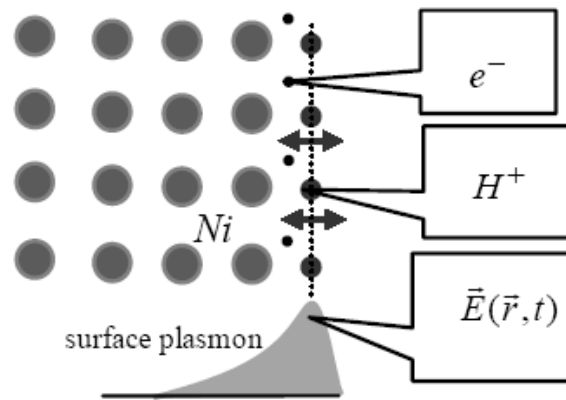


Figure 1. The model and space structure of surface plasmon.

2.3. Analysis of effectiveness of neutron production by inverse reaction of beta-decay at ponderomotive action of variable electric field of surface plasmon.

Let us consider the efficiency of inverse reaction of beta-decay $\tilde{e}^- p \rightarrow n\nu$ taking into account the formation of such accelerated relativistic electrons.

Mean free path of these fast electrons in relation to the process of inverse reaction of beta-decay $\tilde{e}^- p \rightarrow n\nu$ is

$$\langle l_{\tilde{e}^- p \rightarrow n\nu} \rangle \approx \langle v \rangle \tau_{\tilde{e}^- p \rightarrow n\nu}. \quad (20)$$

Here

$$\tau_{\tilde{e}^- p \rightarrow n\nu} = 1/\Gamma_{\tilde{e}^- p \rightarrow n\nu}$$

is the duration of return beta-decay reaction (see [3], Eqs. (29) and (30)),

$$\Gamma(\tilde{e}^- p \rightarrow n\nu) \approx (G_F m_e^2 c / \hbar^3)^2 (m_e c^2 / \hbar) \left(\frac{\tilde{m}_e - \Delta}{\Delta} \right)^2 \approx 1.2 \times 10^{-3} (\beta - \beta_0)^2 \text{ s}^{-1},$$

$$\beta = \tilde{m}_e / m_e, \quad \Delta = M_n - M_p \approx 1.3 \text{ MeV}/c^2 \quad (21)$$

is the probability of return beta-decay reaction.

From the other hand the same mean free path may be written

$$\langle l_{\tilde{e}^- p \rightarrow n\nu} \rangle \approx 1/\sigma_{\tilde{e}^- p \rightarrow n\nu} n_t \quad (22)$$

using the cross-section $\sigma_{\tilde{e}^- p \rightarrow n\nu}$ of $\tilde{e}^- p \rightarrow n\nu$ reaction and total concentration n_t of atoms (nuclei) in a target.

From the last equations follows the following expression for cross-section $\sigma_{\tilde{e}^- p \rightarrow n\nu}$ of return beta-decay reaction with the participation of fast electron with averaged velocity $\langle v \rangle$

$$\sigma_{\tilde{e}^- p \rightarrow n\nu} \approx \Gamma_{\tilde{e}^- p \rightarrow n\nu} / n \langle v \rangle \approx \left\{ 1.2 \times 10^{-3} (\beta - \beta_0)^2 / n \langle v \rangle \right\} \text{ cm}^2. \quad (23)$$

For typical parameters $n_t \approx 3 \times 10^{22} \text{ cm}^{-3}$, $\langle v \rangle \approx c/3 = 10^{10} \text{ cm/s}$, $\beta - \beta_0 \approx 0.5$ we have the final values for cross-section

$$\sigma_{\tilde{e}^- p \rightarrow n\nu} \approx \Gamma_{\tilde{e}^- p \rightarrow n\nu} / n \langle v \rangle \approx 10^{-36} \text{ cm}^2 = 10^{-12} \text{ bn} \quad (24)$$

and mean free path of these fast electrons

$$\langle l_{\tilde{e}^- p \rightarrow n\nu} \rangle \approx 3 \times 10^{13} \text{ cm} \quad (25)$$

in relation to the process of inverse reaction of beta-decay.

This cross-section of neutronization is by $10^{14} - 10^{15}$ times less then the cross-section

$$\sigma_{\text{ion.rad.loss}} = 1/n_t \langle l_{\text{ion.rad.loss}} \rangle \quad (26)$$

of ionization and radiative loss (including ionization and excitation of atoms of target and X-ray bremsstrahlung).

In particular for electron with the energy about 0.8 MeV the mean free path and cross-section of ionization and radiative loss in Ni or Pd matrix are equal

$$\langle l_{\text{ion.rad.loss}} \rangle \approx 1 - 2 \text{ mm}, \quad (27)$$

$$\sigma_{\text{ion.rad.loss}} \approx (3 - 1.5) \times 10^{-22} \text{ cm}^{-2} = 300 - 150 \text{ bn.} \quad (28)$$

In the result at surface density of heavy electron–proton pairs $N/S = 10^{16} \text{ cm}^{-2}$ the maximal possible rate of neutron production on a metal hydride surface is much lower then it was presented in [4] (see Eq. (31) where $\tilde{w}(\tilde{e}^- p \rightarrow n\nu) \approx 10^{13} \text{ cm}^{-2} \text{ s}^{-1}$ at $\beta - \beta_0 \approx 0.5$) and equals to very low value

$$\tilde{w}(\tilde{e}^- p \rightarrow n\nu) \approx 10^{13} (\beta - \beta_0)^2 \frac{\langle l_{\tilde{e}^- p \rightarrow n\nu} \rangle}{\langle l_{\text{ion.loss}} \rangle} \text{ cm}^{-2} \text{ s}^{-1} \leq 0.03 \text{ cm}^{-2} \text{ s}^{-1}. \quad (29)$$

2.4. The problem of additional localized energy for the generation of heavy electrons

According to Fermi theory of weak interaction the rate of $\tilde{e}^- p \rightarrow n\nu$ reaction is the following (see [3], Eqs. (29) and (30))

$$\Gamma(\tilde{e}^- p \rightarrow n\nu) \approx \left(\frac{G_F m_e^2 c}{\hbar^3} \right)^2 (m_e c^2 / \hbar) \left(\frac{\tilde{m}_e - \Delta}{\Delta} \right)^2 \approx 7 \times 10^{-3} \left(\frac{\tilde{m}_e - \Delta}{\Delta} \right)^2 \text{ s}^{-1} \approx 1.2 \times 10^{-3} (\beta - \beta_0)^2 \text{ s}^{-1}. \quad (30)$$

At surface density of heavy electron–proton pairs $N/S = 10^{16} \text{ cm}^{-2}$ [4] the rate of weak neutron production on a metal hydride surface is (see [4], Eq.(31))

$$\tilde{w}(\tilde{e}^- p \rightarrow n\nu) \approx 1.2 \times 10^{13} (\beta - \beta_0)^2 \text{ cm}^{-2} \text{ s}^{-1}. \quad (31)$$

For formation of such surface density of heavy (“dressed up”) electrons we need additional density of:

localized specific surface energy

$$W/S \geq (\tilde{m}_e - m_e) c^2 (N/S) \geq 10^{16} \text{ MeV/cm}^2 \approx 2 \times 10^3 \text{ J/cm}^2, \quad (32)$$

localized specific volume energy

$$(W/S) n_p^{1/3} \geq 10^{24} \text{ MeV/cm}^3 \approx 10^{11} \text{ J/cm}^3, \quad (33)$$

localized specific surface power

$$P/S \approx \tilde{w}(\tilde{e}^- p \rightarrow n\nu) (\tilde{m}_e - m_e) c^2 \approx 2 \times 10^{13} \text{ MeV/cm}^2 \approx 3 \text{ W/cm}^2 \quad (34)$$

and localized specific volume power

$$(P/S) n_p^{1/3} \approx 10^{21} \text{ MeV/cm}^3 \approx 3 \times 10^8 \text{ W/cm}^3. \quad (35)$$

There are no sources of such concentrated energy and power on the surface of metal hydride!

Decrease of total proton mass (including the mass of proton electrostatic field) cannot be the source of this energy because in such case the conditions of inverse reaction of beta-decay (1) cannot be satisfied.

At the same time the thermal energy of these N/S surface hydrogen atoms is only

$$(3kT/2)N/S \leq 4 \times 10^{-5} \text{ J/cm}^{-2}. \quad (36)$$

The real maximally possible total number of heavy electron–proton pairs with additional energy

$$E \geq (\tilde{m} - m) c^2 \geq 0.8 \text{ MeV}$$

at averaged (thermal) energy

$$kT \approx 0.025 - 0.075 \text{ eV} \quad (T = 300 - 900 \text{ K})$$

of each proton in considered system is very small and equals

$$N^*/N = \int_{(\tilde{m}-m)c^2}^{\infty} \frac{1}{kT} e^{-E/kT} dE = e^{-(\tilde{m}-m)c^2/kT} \approx (10^{-14000000} - 10^{-4500000}) \rightarrow 0, \quad N^*/S \rightarrow 0. \quad (37)$$

Such negligible quantity of surface concentration of heavy electron–proton pairs N^*/S does not allow to explain observable effects.

3. Summary

The carried out analysis has shown that Widom–Larsen theory, which is connected with the inverse reaction of beta-decay in variable electric field of surface plasmon in metal hydride, is unsuitable for the description and explanation of Rossi experiments in metal hydrides.

Authors of works [3–7] have not considered very essential features of interaction of electrons with a strong nonuniform field of surface high-frequency plasmon in condensed matters. Result of such interaction is acceleration of electrons due to action of ponderomotive force and formation of “fast heavy electrons”, instead of formation of “slow heavy electrons”, that is possible only in uniform high-frequency field.

Such accelerated (relativistic) electrons spend the own energy not for initiation of inverse reaction of beta-decay in target but to electromagnetic radiating processes and generation of bremsstrahlung. Such result directly follows from comparison of cross-sections of bremsstrahlung

$$\sigma_{\text{ion.rad.loss}} \approx 300 - 150 \text{ bn}$$

and inverse reaction of beta-decay

$$\sigma_{\tilde{e}^- p \rightarrow n \nu} \approx 10^{-12} \text{ bn}$$

for these “fast heavy electrons”

Such method of realization of inverse reaction of beta-decay may be effective in the area of action of uniform plane electromagnetic waves [9] of very high intensity

$$J \geq c |E_0^{(\text{max})}|^2 / 4\pi \approx 10^{20} \text{ W/cm}^2 \quad (38)$$

in uniform substance. Such intensities are reached in experiments with femtosecond laser pulses. Unfortunately, electromagnetic fields of such squeezed optical laser pulses are very nonuniform. In this case at interaction of these pulses with any substance appearing of pushing out ponderomotive force and formation of relativistic electrons take place (e.g. [10]).

The same effect of electrons acceleration takes place at interaction of external soft electromagnetic waves (e.g. action of IR laser) with metal surface. In this case the surface electromagnetic field will be nonuniform because of total reflection. From the other hand, in the case of action of stationary radiation of hypothetical X-ray and gamma-ray lasers [11] on thin layer, process of surface reflection is absent, electromagnetic field would be close to uniform and it would be no effect of acceleration.

In our opinion the most optimal method of optimization of LENR is connected with the formation of correlated states of interacting particles in nonstationary potential wells without the increase of total energy of these particles. This mechanism provides the great increase of very small subbarrier transparency (by $10^{40} - 10^{100}$ and more times [12–15]) and can be efficiently applied to different nonstationary experiments (e.g. [16–20] and Rossi–Focardi experiments [1,2]).

Additional analysis of application of Widom–Larsen theory to LENR phenomena is presented in [21].

References

- [1] John Michell. Rossi's eCat. Free Energy, Free Money, Free People. Xecnet, 2011.
- [2] Andrea Rossi, Method and apparatus for carrying out nickel and hydrogen exothermal reaction, United States Patent Application Publication (Pub. No.: US 2011/0005506 A1, Pub. Date: Jan. 13, 2011).
- [3] A. Widom and L. Larsen, Ultra low momentum neutron catalyzed nuclear reactions on metallic hydride surfaces, *European Phys. J. C* **46** (2006) 107–112.
- [4] Y.N. Srivastava, A. Widom and L. Larsen, A primer for electroweak induced low-energy nuclear reactions, *Pramana J. Phys.* **75**(4) (2010) 617–637.
- [5] A. Widom and L. Larsen, Theoretical Standard Model Rates of Proton to Neutron Conversions Near Metallic Hydride Surfaces (arXiv:nucl-th/0608059v2 25 Sep 2007).
- [6] A. Widom and L. Larsen, Nuclear Abundances in Metallic Hydride Electrodes of Electrolytic Chemical Cells (arXiv:cond-mat/0602472 v1 20 Feb 2006).
- [7] A. Widom and L. Larsen, Absorption of Nuclear Gamma Radiation by Heavy Electrons on Metallic Hydride Surfaces (arXiv:cond-mat/0509269 v1 10 Sep 2005).
- [8] A. Widom, Y.N. Srivastava and L. Larsen, Energetic Electrons and Nuclear Transmutations in Exploding Wires (arXiv: nucl-th/0709.1222v1 8 Sep 2007).
- [9] L.D. Landau and E.M. Lifshitz, *The Classical Theory of Fields*, Sections.17 and 47, Prob.2 (Pergamon Press, Oxford, 1975).
- [10] V.I. Vysotskii, S.V. Adamenko, V.A. Stratienco, N.G. Tolmachev, Creating and using of superdense micro-beams of relativistic electrons. *Nucl. Instr. Methods Phys. Res.* **455A**(1) (2000) 123–127.
- [11] V.I. Vysotskii and R.N. Kuzmin. *Gamma-Ray Lasers* (Moscow State Univ. Publ. House, Moscow, 1989).
- [12] V.I. Vysotskii and S.V. Adamenko, Correlated states of interacting particles and problems of the Coulomb barrier transparency at low energies in nonstationary systems, *Technical Phys.* **55**(5) (2010) 613–621.
- [13] V.I. Vysotskii and S.V. Adamenko, Low energy subbarrier correlated nuclear fusion in dynamical systems, *J. Cond. Mat. Nucl. Sci.* **8** (2012) 91–104.
- [14] V.I. Vysotskii, M.V. Vysotskyy and S.V. Adamenko, Formation and application of correlated states in nonstationary systems at low energies of interacting particles, *J. Experimental and Theoret. Phys.* **114**(2) (2012) 243–252.
- [15] V.I. Vysotskii, M.V. Vysotskyy and S.V. Adamenko, The formation of correlated states and the increase in barrier transparency at a low particle energy in nonstationary systems with damping and fluctuations, *J. Experimental Theoret. Phys.* **115**(4) (2012) 551–566.
- [16] S.V. Adamenko and F. Selleri (Eds.), *Controlled Nucleosynthesis. Breakthroughs in Experiment and Theory* (A. van der Merwe, Springer, 2007).
- [17] V.I. Vysotskii and A.A. Kornilova, Nuclear fusion and transmutation of isotopes in biological systems (MIR, Publ. House, Moscow, 2003).
- [18] V.I. Vysotskii and A.A. Kornilova, *Nuclear Transmutation of Stable and Radioactive Isotopes in Biological Systems* (Pentagon Press, India, 2010).
- [19] D. Letts, D. Cravens and P.L. Hagelstein, Dual laser stimulation and optical phonons in palladium deuteride, in low-energy nuclear reactions and new energy technologies, *Low-Energy Nuclear Reactions Sourcebook*, Vol. 2 (American Chemical Society, Washington DC, 2009). pp. 81–93.
- [20] P.L. Hagelstein, D.G. Letts and D. Cravens, Terahertz difference frequency response of PdD in two-laser experiments, *J. Cond. Mat. Nucl. Sci.* **3** (2010) 59–76.
- [21] V.I. Vysotskii, Critique of the Widom–Larsen theory, *Infinite Energy* **105** (2012) 37–41.



Research Article

Application of Correlated States of Interacting Particles in Nonstationary and Periodical Modulated LENR Systems

Vladimir I. Vysotskii*[†] and Mykhaylo V. Vysotskyy

Kiev National Shevchenko University, Kiev, Ukraine

Stanislav V. Adamenko

Electrodynamics Laboratory, “Proton-21”, Kiev, Ukraine

Abstract

In the report the universal mechanism of optimization of low energy nuclear reactions (LENR) on the basis of coherent correlated states of interacting particles at different kinds of nonstationary periodical action to the system is considered. We have considered the peculiarities and investigated the efficiency of the creation of a correlated state under a periodic action on a harmonic oscillator. This method is shown to lead to rapid formation of a strongly correlated particle state that provides an almost complete clearing of the potential barrier even for a narrow range of oscillator frequency variations. Several successful low-energy fusion experiments based on usage of correlated states of interacting particles are discussed.

© 2014 ISCMNS. All rights reserved. ISSN 2227-3123

Keywords: Coherent correlated states, LENR, Transparency of Coulomb potential barrier

1. Introduction

The problem of overcoming the Coulomb potential barrier during the interaction of charged particles is the key one in modern atomic and nuclear physics. This problem is of particular importance in controlled nuclear fusion, for which the action of the Coulomb barrier leads to a very low tunneling probability for low energy particles.

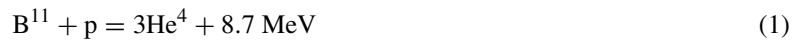
This fundamental constraint leads to extremely big problems related to the necessity of very rapid heating of a target composed of hydrogen isotopes (deuterium, D and tritium, T) to a state of thermonuclear plasma with a temperature of about 10 keV and its additional compression by a factor of $k \geq 10^3$ (in the case of “inertial” nuclear fusion with a confinement time of 10^{-9} s based on an initial target with an atomic concentration of 10^{23} cm^{-3}) as well as similar heating of a low density target to the same temperature with its subsequent confinement for a long time (for TOKAMAK or STELLARATOR systems).

*E-mail: vivysotskii@gmail.com

[†]Also at: Electrodynamics Laboratory, “Proton-21”, Kiev, Ukraine

Extremely big obstacles that should be overcome for a successful solution of such global problems in future are well known. In addition, the studies of controlled $d + d$ and $d + t$ fusion carried out for 60 years have shown that using the “thermonuclear” way of overcoming the Coulomb barrier makes any attempt to use the controlled thermonuclear fusion reactions based on isotopes heavier than deuterium or tritium under terrestrial conditions virtually unrealistic [1,2].

It is well known that the $d + d$ and $d + t$ fusion reactions are not optimal due to an intense flux of fast neutrons accompanying these reactions. This leads to induced radioactivity and critical radiation damage of the reactor vessel (the first wall problem). In this respect, for example, fusion based on the ecologically pure reaction



involving B^{11} and p nuclei is more optimal: it does not produce neutrons and does not induce activity.

In these circumstances, the topicality of new approaches that can provide an increase in the transparency of potential barriers through the application of quantum processes determining the interaction of low energy particles with these barriers without any compulsory use of a high temperature plasma under conditions of either long confinement or super-strong compression is obvious. In [1–3], we have shown that the use of coherent correlated states can lead to such effect.

A specific quantitative analysis of the condition for the formation of a strongly correlated state has been performed in [1–4] basing on one particular and specially chosen deformation regime of an oscillator with a particle located in its parabolic field irrespective of the possibility of its practical realization. Below, we consider in detail the possible methods of the formation of such states, determine the conditions of their realization, and show that there exist many different and simple (compared to [3]) realization scenarios close to the conditions of a real experiment.

2. The General Foundations of Formation of Coherent Correlated States of Particles

The Heisenberg uncertainty relation for the coordinate and momentum,

$$\sigma_q \sigma_p \geq \hbar^2/4 \quad (2a)$$

and its generalization

$$\sigma_A \sigma_B \geq |\langle [\widehat{A}\widehat{B}] \rangle|^2/4, \quad \sigma_C = \langle (\Delta\widehat{C})^2 \rangle \equiv (\delta C)^2, \quad \Delta\widehat{C} = \widehat{C} - \langle C \rangle \quad (2b)$$

made in 1929 by Robertson for arbitrary dynamical variables A and B are base relations of quantum mechanics. In modern interpretation these relations correspond to uncorrelated states.

In 1930, Schrodinger [5] and Robertson [6] generalized relation (2b) and derived a more universal inequality called the Schrodinger–Robertson uncertainty relation

$$\sigma_A \sigma_B \geq |\langle [\widehat{A}\widehat{B}] \rangle|^2/4(1 - r^2), \quad (3a)$$

$$r = \sigma_{AB}/\sqrt{\sigma_A \sigma_B},$$

$$\begin{aligned}
\sigma_{AB} &= \langle \{\Delta \hat{A}, \Delta \hat{B}\} \rangle / 2 \\
&\equiv \langle ((\hat{A} - \langle A \rangle) (\hat{B} - \langle B \rangle) + (\hat{B} - \langle B \rangle) (\hat{A} - \langle A \rangle)) \rangle / 2 \\
&= (\langle \hat{A} \hat{B} + \hat{B} \hat{A} \rangle) / 2 - \langle A \rangle \langle B \rangle,
\end{aligned}$$

where r is the correlation coefficient between quantities A and B with $|r| \leq 1$, σ_{AB} is the mutual variance of A and B corresponding to the mean value of the anticommutator of the error operators $\Delta \hat{K} = \hat{K} - \langle K \rangle$.

The Schrodinger–Robertson uncertainty relation (3a) is an obvious generalization of the Heisenberg–Robertson uncertainty relation (2b) for correlated states and is reduced to it at $r = 0$.

In [1–4,7,8] it was shown that for a model system including a particle with coordinate $q(t)$ and momentum $p(t)$ in the field of a nonstationary harmonic oscillator

$$V(q, t) = \frac{mq(t)^2 \omega^2(t)}{2}, \quad (3b)$$

a decrease in the particle oscillation frequency $\omega(t)$, leads to an increase in the correlation coefficient $|r(t)|$, and a change of the uncertainty relation,

$$r(t) = \langle q \hat{p}_q + \hat{p}_q q \rangle / 2 \delta q \delta p_q,$$

$$\delta q \equiv \sqrt{\langle q^2 \rangle}, \quad \delta p_q \equiv \sqrt{\langle p_q^2 \rangle},$$

$$\delta q \delta p_q \geq \hbar / 2 \sqrt{1 - r^2}. \quad (3c)$$

Formally, the change in the correlation coefficient in the uncertainty relation can be taken into account by the formal substitution

$$\hbar \rightarrow \hbar^* \equiv \hbar / \sqrt{1 - r^2}. \quad (4)$$

In the absence of a correlation the uncertainty relation takes the form of the “standard” Heisenberg relation (2a).

When a strongly correlated particle state with $|r| \rightarrow 1$ is formed, the product of the variances of the coordinate $\langle q^2 \rangle$ and momentum $\langle p_q^2 \rangle$ increase indefinitely. This leads to the possibility of a much more efficient particle penetration into the sub-barrier region $V(q)$ than that for the same particle in an uncorrelated state.

It was shown in [1–4] that the very low barrier transparency (tunneling probability) for the initial uncorrelated state,

$$D_0 \equiv D_{r=0} = \exp\{-W(E)\} \ll 1, \quad (5)$$

$$W(E) = \frac{2}{\hbar} \int_R^{R+L(E)} |p(q)| \, dq \equiv \frac{2}{\hbar} \langle |p(q)| \rangle L(E),$$

$$|p(q)| = \sqrt{2M} \left\langle \sqrt{V(q) - E} \right\rangle$$

that corresponds to the conditions $E \ll V_{\max}$, $W(E) \gg 1$ for the formation of a strongly correlated superposition particle state can increase to a very large value, $D_{|r| \rightarrow 1} \rightarrow 1$ at the same low energy $E \ll V_{\max}$.

In (5) R is the nuclear radius, L is the “barrier width” and M is the reduced particle mass.

In a very simplified form, this effect can be taken into account by the formal (not quite correct) substitutions

$$W_{r=0}(E) \rightarrow W_{r \neq 0}(E, \hbar) \equiv W_{r=0}(E, \hbar^*) = W_{r=0}(E, \hbar) \sqrt{1 - r^2} \quad (6)$$

in (5) and

$$D_{r \neq 0} \approx \exp \left\{ -\frac{2\sqrt{1 - r^2}}{\hbar} \int_R^{R+L(E)} |p(q)| \, dq \right\}, \quad (7)$$

from which it follows that

$$D_{|r| \rightarrow 1} \rightarrow 1 \text{ even if } E \ll V_{\max} \text{ and } W_{r=0}(E) \gg 1. \quad (8)$$

In this case, the potential barrier transparency increases by a factor of

$$D_0^{\sqrt{1-r^2}} / D_0 = 1 / D_0^{1-\sqrt{1-r^2}} \gg 1, \quad (9)$$

which is close in order of magnitude to the result of exact barrier clearing calculations using rigorous quantum-mechanical methods [1,3,4]. Although these estimates with the substitution $\hbar \rightarrow \hbar^*$ are not quite correct (they are made just for illustration of order of the effect) and must be justified every time, they clearly demonstrate a high efficiency of the use of coherent correlated states in solving of applied tunneling related problems in the case of a high potential barrier and a low particle energy.

The physical causes of the huge increase in barrier transparency for a particle in coherent correlated superposition state were discussed in our works [1,3,4]. The physical reason for the increase of the probability of tunneling effect is related to the fact that the formation of a coherent correlated state leads to the cophasing and coherent summation of all fluctuations of the momentum for various eigenstates forming the superpositional correlated states. This leads to great dispersion of the momentum correlated state, very great fluctuations of kinetic energy of the particle in the potential well and increasing of potential barrier penetrability.

A coherent correlated state can be formed in various quantum systems. The most easy way to form such state is when the particle is in a nonstationary parabolic potential well (3b).

The formation mechanism in such system was considered in [1–4,7,8].

There are two different methods for analyzing and optimizing the process of formation of a correlated state.

The first method [1] is that a prespecified form of the specific dependence $r(t)$ that must simultaneously satisfy condition of adiabaticity

$$\left| \frac{dr(t)}{dt} \right| \leq \omega_0 \sqrt{1 - r(t)^2} / \left| \frac{r(t)}{|r(t)|} + 2\omega_0 \int_0^t \frac{r(t') \, dt'}{\sqrt{1 - (r(t'))^2}} \right| \quad (10)$$

and the optimal condition $|r| \rightarrow 1$ should be used to find the optimal condition for the change in

$$\omega(t) = A \sqrt{\frac{1}{(g(t))^2(1-r^2)}} \left\{ 1 - \frac{g(t)}{\omega_0 \sqrt{1-r^2}} \frac{dr}{dt} \right\}. \quad (11)$$

Although this method seems to be logically correct, it is not optimal. In most cases the prespecified “convenient” form of the dependence $r(t)$ is inconsistent with the adiabaticity condition (10) or leads to an expression for $\omega(t)$ that is very difficult to realize in an experiment.

The second more optimal method [2–4] consists in solving the inverse problem-finding $r(t)$ for a specified law of change in the oscillator frequency $\omega(t)$ that is consistent with the possibilities of a real experiment.

In this case, the problem of ensuring the adiabaticity condition is solved automatically by using the real dependence $\omega(t)$. A parametric form of the solution $r(\omega(t))$ inverse to (11) and equivalent to it that is more convenient for calculations can be used to find such solutions.

This solution can be obtained by analyzing the complex equation of motion for a classical oscillator with a variable frequency that in dimensionless form is

$$\frac{d^2\varepsilon}{dt^2} + \omega^2(t)\varepsilon = 0, \quad \varepsilon(0) = 1, \quad \left. \frac{d\varepsilon}{dt} \right|_0 = i, \quad \omega(0) = \omega_0, \quad (12)$$

where ε is the complex amplitude of the harmonic operator normalized to $x_0 = \sqrt{\hbar/M\omega_0}$.

The correlation coefficient is defined by the expression [1–3,6,7]

$$r = \operatorname{Re} \left\{ \varepsilon^* \frac{d\varepsilon}{dt} \right\} / \left| \varepsilon^* \frac{d\varepsilon}{dt} \right|, \quad r^2 = 1 - \omega_0^2 / \left| \varepsilon^* \frac{d\varepsilon}{dt} \right|^2. \quad (13)$$

The general solution of (12) is

$$\varepsilon(t) = e^{\varphi(t)}, \quad \varphi(t) = \alpha(t) + i\beta(t). \quad (14)$$

Substituting (14) into (12) and (13), using the initial conditions

$$\varphi(0) = \alpha(0) = \beta(0) = 0,$$

$$\left. \frac{d\varphi}{dt} \right|_0 = i, \quad \left. \frac{d\alpha}{dt} \right|_0 = 0, \quad \left. \frac{d\beta}{dt} \right|_0 = 1 \quad (15)$$

that follow from (12), and separating the real and imaginary parts of the derived equation, we find

$$\frac{d^2\alpha}{dt^2} + \left(\frac{d\alpha}{dt} \right)^2 - \exp(-4\alpha) = -\omega^2(t), \quad (16a)$$

$$\beta(t) = \int_0^t \exp\{-2\alpha(t')\} dt', \quad (16b)$$

$$|r| = \sqrt{\frac{\left(\frac{d\alpha}{dt}\right)^2 \exp(4\alpha)}{\left\{1 + \left(\frac{d\alpha}{dt}\right)^2 \exp(4\alpha)\right\}}}. \quad (16c)$$

The system of Eqs. (16a)–(16c) is equivalent to Eq. (11), but it is more convenient to analyze and allows one initially to find the exponent of the oscillation amplitude for the oscillator $\alpha(t)$ from Eq. (16a) based on a specified law of change in frequency $\omega(t)$ and subsequently to find $r(t)$ from Eq. (16c) based on $\alpha(t)$.

Note that our analysis disregards the influence of the damping of the oscillations of a nonstationary harmonic oscillator on the formation of a correlated state of the quantum system. This damping can be taken into account by analyzing a more general equation of oscillator motion

$$\frac{d^2\varepsilon}{dt^2} + 2\gamma \frac{d\varepsilon}{dt} + \omega^2(t)\varepsilon = 0, \quad \varepsilon(0) = 1, \quad \left.\frac{d\varepsilon}{dt}\right|_0 = i, \quad \omega(0) = \omega_0 \quad (17a)$$

and the equations following from it,

$$\frac{d^2\alpha}{dt^2} + \left(\frac{d\alpha}{dt}\right)^2 + 2\gamma \frac{d\alpha}{dt} - \exp(-4\alpha - 4\gamma t) = -\omega^2(t), \quad (17b)$$

$$\beta(t) = \int_0^t \exp\{-2\alpha(t') - 2\gamma t'\} dt'. \quad (17c)$$

The problem of influence of both damping and presence of additional fluctuation force was solved also [4] and will be discussed later.

3. Formation of Correlated States of Interacting Particles under Nonstationary Periodical Action

Using solutions (16a)–(16c), we will determine the formation dynamics of correlated states for different regimes of change in frequency $\omega(t)$.

In our works [1,3] the method of formation of coherent correlated states of particle at monotonic decrease in the frequency $\omega(t)$ of a nonstationary harmonic oscillator (e.g. $\omega(t) = \omega_0 \exp(-t/T)$) was discussed.

A more interesting and realizable situation takes place for a harmonic law of change in $\omega(t)$ in the case of a full-scale (maximally possible) change of the oscillator frequency,

$$\omega(t) = \omega_0 |\cos \Omega t| \quad (18)$$

or a change of this frequency in a limited range,

$$\omega(t) = \omega_0 (1 + g_\Omega \cos \Omega t), \quad (19)$$

where $|g_\Omega| < 1$ is the modulation depth.

This regime can be provided, for example, at a constant depth of the potential well V_{\max} in which the particle is located and for a periodic change in its width in the interval

$$L_0/(1 + |g_\Omega|) \leq L \leq L_0/(1 - |g_\Omega|), \quad L_0 = \sqrt{8V_{\max}/M\omega_0^2}. \quad (20)$$

The efficiency of excitation of the correlated states greatly depends on a ratio of frequencies ω_0 and Ω .

Figure 1 presents the time dependences of the correlation coefficient $r(t)$ for a periodic and limited change in the oscillator frequency (19) at $\Omega = \omega_0, 2\omega_0$ and at various frequency modulation depths g_Ω .

It follows from these results that a completely correlated state is formed not only for a monotonic–asymptotic [1,3] or periodic full-scale (in the range $0 \leq \omega(t) \leq \omega_0$) change in the oscillator frequency, but also for its change in the limited range

$$\omega_0(1 - g_\Omega) \leq \omega(t) \leq \omega_0(1 + g_\Omega) \quad (21)$$

and even for $|g_\Omega| \ll 1$ [3,4].

The duration of formation of correlated state decreases with the increase of frequency modulation depth and reaches its minimum for $|g_\Omega| \rightarrow 1$. For example, for the case, presented on Fig. 1(d) ($g_\Omega = 0.1$, $\Omega = 2\omega_0$), we have $|r|_{\max} = 0.999998$ at $\omega_0 t = 500$. For such value of $|r|_{\max}$ the probability of tunneling effect for two possible reactions

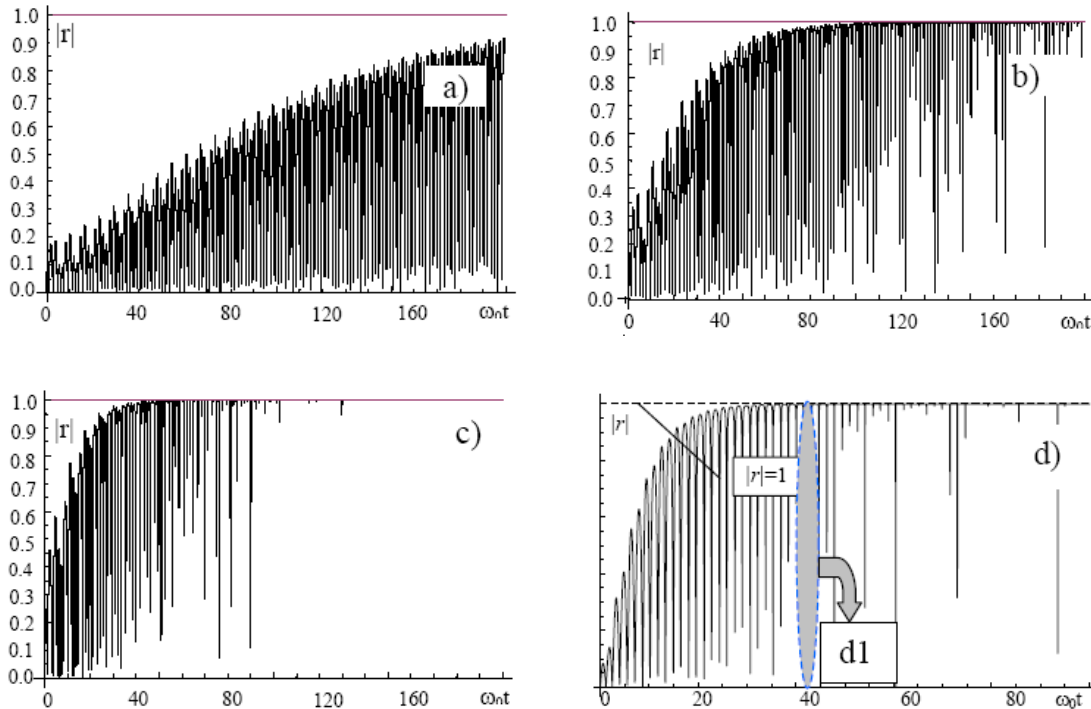


Figure 1(a–d)

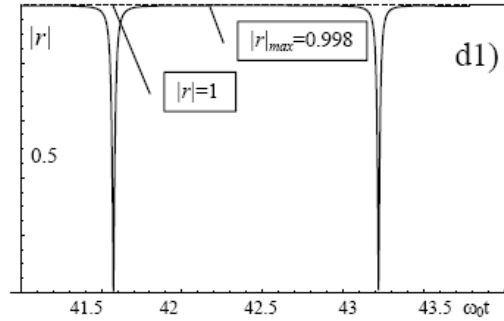


Figure 1. Time dependences of the correlation coefficient r for a limited change in the oscillator frequency $\omega(t) = \omega_0 (1 + g_\Omega \cos \Omega t)$ for various frequency modulation depths g_Ω and various frequency modulation: (a) $g_\Omega = 0.1$, $\Omega = \omega_0$; (b) $g_\Omega = 0.2$, $\Omega = \omega_0$; (c) $g_\Omega = 0.3$, $\Omega = \omega_0$; (d) $g_\Omega = 0.1$, $\Omega = 2\omega_0$, (d1) increased fragment of (1d).



at room temperature increases from $D_{r=0} \approx 10^{-100}$ (for non-correlated state of interacting deuterons in reaction (22)) to $D_{r=0.999998} \approx 0.8$ (for correlated state of d) and from $D_{r=0} \approx 10^{-4600}$ (for non-correlated state of interacting particles d and Pd^A in reaction (23)) to $D_{r=0.999998} \approx 10^{-8}$ in potential well made of nearest Pd^{A+} ions!

From the detailed analysis follows that the process of correlated states formation at the action of limited periodic modulation $\omega(t) = \omega_0 (1 + g_\Omega \cos \Omega t)$ is possible only at any of two conditions:

$$\Omega = \omega_0 \quad (24a)$$

or Ω is close to $2\omega_0$ and lies inside the interval P

$$(2 - g_\Omega)\omega_0 \leq \Omega \leq (2 + g_\Omega)\omega_0. \quad (24b)$$

The results of calculation of averaged correlation coefficient

$$\langle |r(t)| \rangle_t \equiv \frac{1}{\Delta t} \int_{t_0 - \Delta t/2}^{t_0 + \Delta t/2} |r(t)| dt \quad (25)$$

are presented on Fig.2a,b for $\Delta t = 10^3/\omega_0$ and different values of modulation depths $g_\Omega = 0.1$ ($t_0 = 1500/\omega_0$), and $g_\Omega = 0.01$ ($t_0 = 10^4/\omega_0$).

In Fig. 2(b), the results of calculation the averaged coefficient of barrier transparency

$$\langle \langle D(t, \Omega) \rangle_t \rangle = \frac{1}{\sqrt{\pi \delta \Omega}} \int \left\{ \frac{1}{\Delta t} \int_{t_0 - \Delta t/2}^{t_0 + \Delta t/2} D(t, \Omega') dt \right\} e^{-\frac{(\Omega - \Omega')^2}{(\delta \Omega)^2}} d\Omega' \quad (26)$$

at non-monochromatic periodic modulation with $\Omega/\delta \Omega = 10$ are presented also

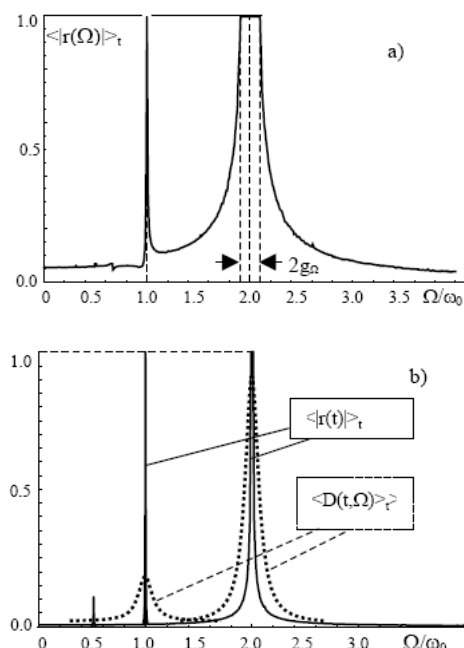


Figure 2. Dependences of averaged correlation coefficient $\langle |r(t, \Omega)| \rangle_t$ and normalized averaged coefficient of barrier transparency on frequency of modulation Ω at $|g_\Omega| = 0.1$ (a) and $|g_\Omega| = 0.01$ (b).

So the essential suppression of action of potential barrier on the effectiveness of nuclear reaction with the participation of charged particles at limited periodic modulation of the oscillator frequency (19) is possible only for two frequencies (24a) and (24b).

From this result very important statement follows: in any experiments with the use of external periodic modulation with limited frequency interval, two resonances of energy release on frequencies $\Omega = \omega_0$ or $|\Omega - 2\omega_0| \leq g_\Omega \omega_0$ should be observed!

This statement are in good correlation with “Terahertz” laser experiments of Letts, Hagelstein and Cravens [9,10] on the stimulation of nuclear reaction at joint action of two laser beams with variable beat frequency $\Omega = 3 - 24$ THz on the cathode surface during the electrolysis in PdD system with the presence of heavy water D_2O .

Figure 3 shows the experimental frequency dependencies of thermal energy release [10] in these experiments.

Formation of correlated states in this system is connected with the direct or indirect (by plasmon excitation or phonon mode modulation) action of electromagnetic radiation with frequencies Ω on optical phonon modes $\omega_0^{(k)}$ of deuterons in PdD compound.

Four main resonances of energy release $\Omega_1 \approx 7.8 - 8.2$ THz, $\Omega_2 \approx 10.2 - 10.8$ THz, $\Omega_3 \approx 15.2 - 15.6$ THz and $\Omega_4 \approx 20.2 - 20.8$ THz in Fig. 3 are the result of averaging of about 30 experiments and subsequent statistical processing of experimental data. In work [9] the second resonance with frequency $\Omega_2 \approx 10.2 - 10.8$ THz was not separated.

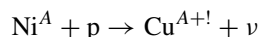
Comparison of frequencies of all four resonances shows that the ratios between these frequencies are $\Omega_3 \approx 2\Omega_1$ and $\Omega_4 \approx 2\Omega_2$ with good accuracy. By the way, from the given experiments follows that the amplitude of high-frequency maxima in each of these pairs (accordingly Ω_3 and Ω_4) greatly exceeded the amplitudes of the maxima corresponding

to the “basic” frequencies Ω_1 and Ω_2 . Such relation directly follows from comparison of Figs. 2(b) and 3. These experimental results completely correspond to theoretical model of the coherent correlated states that was discussed above.

This model also allows to explain the presence of a resonance of nuclear reactions (??) and (23) on frequency $\Omega_4 \approx 20.2 - 20.8$ THz (at action of beat frequency Ω_4). It is known that in the region $\omega_0^{(k)} > 16$ THz there is no optical phonon modes for PdD compound (see analysis in [9]). So, the resonance of nuclear reactions (??) and (23) at action of beat frequency Ω_4 is connected (by parametric interaction at formation of coherent correlated state) with the optical phonon mode in PdD with the frequency $\omega_0^{(2)} = \Omega_4/2 = \Omega_2$!

The different situation takes place if there is a full-scale (maximally possible) change of the oscillator frequency $\omega_0(t)$ (18). In this case the process of formation of totally correlated state is possible at various actions on the system (including the use of low frequency $\Omega \ll \omega_0$). Figure 4 presents the time dependencies of the correlation coefficient $r(t)$ for full-scale (18) change in the oscillator frequency $\omega(t)$ at $\Omega = \omega_0/100\pi \approx 0.03\omega_0$.

Obtained results can explain Rossi–Focardi experiments at action of radio-frequency irradiation to hot NiH nano-powder situated in closed chamber with the presence of compressed H_2 gas [11,12]. In this case the action of RF-irradiation on surface of nano-particles leads to modulation of acoustic phonon and plasmon modes of these nano-particles. At such modulation the processes of formation of correlated states and stimulation of nuclear reactions



are possible. Barrier transparency for these reactions at temperature $T \approx 400 - 600^\circ\text{C}$ increases from $D_{r=0} \approx 10^{-1000}$ (for non-correlated states of interacting p and Ni^A nuclei) to $D_{r=0.999993} \approx 10^{-6} - 10^{-4}$ (for correlated state of p)!

The similar effect of formation of coherent correlated states of D^+ ions and stimulation of effective nuclear dd-fusion

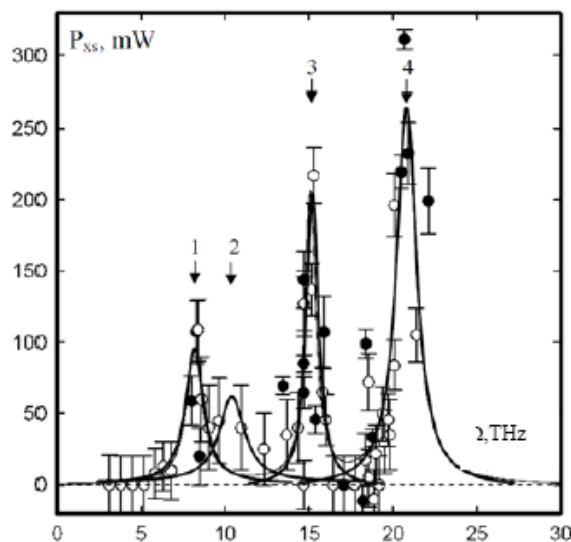


Figure 3. Frequency dependencies of energy release at combined action of beat frequency of two different lasers on surface of cathode during the electrolysis [9].

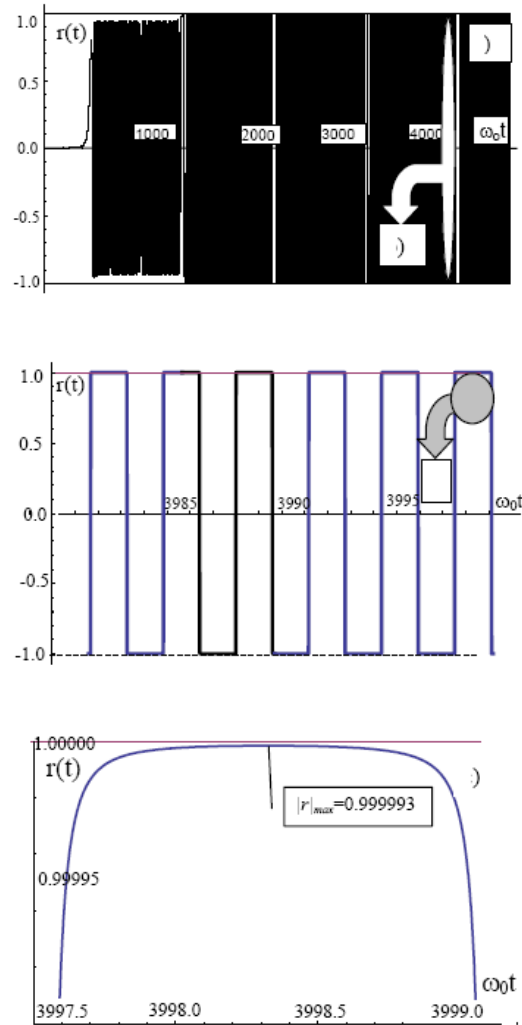


Figure 4. Dynamics of change of correlation coefficient during the action of parametrical perturbation with the frequency $\Omega = \omega_0/100\pi$ at full modulation $\omega(t) = \omega_0 \cos \Omega t$ of oscillator. Figure 4(b) corresponds to the increased fragment of Fig 4(a) and Fig. 4(c) corresponds to the increased fragment of the Fig. 4(b).

(including generation of neutron bursts) takes place in cooled D_2 gas at changing of strong external magnetic field in interval 8–10 Oe [16].

4. Summary

In conclusion, note that a coherent correlated state whose influence on the penetration probability into the region under the potential barrier is associated with the synchronization of the momentum fluctuations at different levels of the

superposition state and the particle kinetic energy fluctuation caused by this synchronization can be realized not only in a parabolic field [2]. Such state can be formed, at least in principle, within any system of levels of quantized motion that is not subjected to an external intense dephasing action, provided that a certain coherent action is superimposed on it.

These effects may play the important role in processes of controlled nucleosynthesis in different potential wells and systems with nonstationary action on active systems (e.g. in experiments with high-current electron driver in Kiev Laboratory “Proton-21” [13] and in experiments on nuclear transmutation of stable and radioactive isotopes in growing biological systems [14,15]).

Another method of nuclear reaction optimization is connected with the process of creation of the spatially-compressed states of particle beam under action of crystal fields.

In ordered crystal lattice there is very strong influence of crystal axes and planes electrical field on motion and interaction of fast charged particles with crystal atoms and nuclei. It was shown in our old articles [17,18] that in monocrystal targets like LiD the rate of fusion process with the participation of both target nuclei (e.g. D) and beam of fast nuclei (e.g. T), directed at *Lindhard* angle, may be increased by 10–100 times compared to the alternative process of deceleration on atomic electrons. Such changes are based on the use of specific channeling physics regime of motion – “overbarrier motion” At such regime the processes of spatial redistribution and dechanneling of accelerated ions take place.

References

- [1] V.I. Vysotskii, M.V. Vysotskyy and S.V. Adamenko, Formation and application of correlated states in nonstationary systems at low energies of interacting particles. *J. Experimental Theoret. Phys.* **114**(2) (2012) 243–252.
- [2] V.I. Vysotskii and S.V. Adamenko, Correlated states of interacting particles and problems of the Coulomb barrier transparency at low energies in nonstationary systems, *Technical Phys.* **55**(5) (2010) 613–621.
- [3] V.I. Vysotskii and S.V. Adamenko, Low energy subbarrier correlated nuclear fusion in dynamical systems, *J. Cond. Mat. Nucl. Sci.* **8** (2012) 91–104.
- [4] V.I. Vysotskii, M.V. Vysotskyy and S.V. Adamenko, The formation of correlated states and the increase in barrier transparency at a low particle energy in nonstationary systems with damping and fluctuations, *J. Experimental Theoret. Phys.* **115**(4) (2012) 551–566.
- [5] E. Schrodinger, *Ber. Kgl. Akad. Wiss.*, Berlin, S.296 (1930).
- [6] H.P. Robertson, A general formulation of the uncertainty principle and its classical interpretation. *Phys. Rev. A* **35** (1930) 667.
- [7] V.V. Dodonov and V.I. Man'ko, *Tr. Fiz. Inst. im. P. N. Lebedeva, Akad. Nauk SSSR* **183** (1987) 71.
- [8] V.V. Dodonov, A.V. Klimov and V.I. Man'ko, *Tr. Fiz. Inst. im. P. N. Lebedeva, Akad. Nauk SSSR* **200** (1991) 56.
- [9] D. Letts, D. Cravens and P.L. Hagelstein, Dual laser stimulation and optical phonons in palladium deuteride, in low-energy nuclear reactions and new energy technologies, *Low-Energy Nuclear Reactions Sourcebook*, Vol. 2 (American Chemical Society, Washington DC, 2009) pp. 81–93.
- [10] P.L. Hagelstein, D.G. Letts and D. Cravens, Terahertz difference frequency response of PdD in two-laser experiments, *J. Cond. Mat. Nucl. Sci.* **3** (2010) 59–76.
- [11] John Michell, Rossi's eCat. Free Energy, Free Money, Free People. Xecnet, 2011.
- [12] Andrea Rossi, Method and apparatus for carrying out nickel and hydrogen exothermal reaction, United States Patent Application Publication (Pub. No.: US 2011/0005506 A1, Pub. Date: Jan. 13, 2011).
- [13] S.V. Adamenko, F. Selleri and A. van der Merwe (Eds.), *Controlled Nucleosynthesis. Breakthroughs in Experiment and Theory* (Springer, Berlin, 2007).
- [14] V.I. Vysotskii and A.A. Kornilova, *Nuclear Fusion and Transmutation of Isotopes in Biological Systems* (MIR Publ. House, Moscow, 2003).
- [15] V.I. Vysotskii and A.A. Kornilova, *Nuclear Transmutation of Stable and Radioactive Isotopes in Biological Systems* (Pentagon Press, India, 2010).

- [16] T. Mizuno, T. Akimoto, A. Takahashi and F. Celani, *Proc. ICCF-11 Conf.*, France, 31 Oct.–5 Nov. 2004, World Scientific, Singapore, 2006, pp. 312–323.
- [17] V.I. Vysotskii and R.N. Kuzmin, Reactions of controlled fusion in crystal targets, *Soviet. Tech. Phys. Lett.* **7** (1981) 422–424.
- [18] V.I. Vysotskii and R. N.Kuzmin, Optimization of controlled fusion in crystals, *Soviet Phys. Tech. Phys.* **28**(9) (1983) 1144–1146.